ISTITUTO NAZIONALE DI FISICA NUCLEARE

Laboratori Nazionali di Frascati

INFN – 2026-01-LNF
Feb 5 th, 2026

EuPRAXIA@SPARC_LAB

Technical Design Report

Istituto Nazionale di Fisica Nucleare

INFN 2026 - 1 - LNF
Feb 5th, 2026

EuPRAXIA@SPARC_LAB

Technical Design Report

Authors

D. Alesini[1], M. P. Anania[1], F. Anelli[1], P. Angeletti[1], M. Angelucci[1], G. Armenti[1], M. Arpaia[1], R. Assmann[2], L. Avaldi[3], A. Bacci[4], C. Badiali[5], A. Balerna[1], I. Balossino[1], M. Bellaveglia[1], A. Biagioni[1], D. Bleiner[6], P. Bolognesi[3], C. Bortolin[1], F. Bossi[1], B. Buonomo[1], L. Cacciotti[1], P. Campana[1], M. Campolucci[1], G. Campri[7,8], S. Cantarella[1], L. B. D. Capuano[1], F. Cardelli[1], M. Carillo[1], L. Carlini[3], A. Casamatta[1], G. Catuscelli[1], M. Ceccarelli[1], R. Ceccarelli[1], V. Ceccarelli[1], A. Cecchinelli[1], E. Chiadroni[1,7], F. Chiarelli[1], J. Chiarinelli[3], P. Chimenti[1], D. Chiti[1], A. Cianchi[9,10], M. Cianfrini[1], R. Cimino[1], F. Cioeta[1], G. A. P. Cirrone[11], R. Clementi[1], L. Crincoli[1], M. Coreno[1,12], G. Costa[1], F. Curciarello[13], A. Curcio[7,14], G. D'Auria[8], G. De Bernardis[1], A. Del Dotto[1], M. Del Franco[1], M. Del Giorno[1], M. Dell'Angela[15], G. Delzeri[1], R. Demitra[1], F. Demurtas[1,7], T. De Nardis[1], E. De Santis[9,10], M. De Simone[15], C. Di Giulio[1], S. Di Mitri[8], M. Diomede[16], E. Di Pasquale[1], G. Di Pirro[1], G. Di Raddo[1], R. Di Raddo[1], V. Dompè[1], R. Donghia [1], Z. Ebrahimpour[1,8], A. Esposito[1], L. Faillace[1], A. Falone[1], X. Fang[1,7], M. Ferrario[1], G. Franzini[1], F. Frisinelli[13], F. Galdenzi[9,10], F. Galletti[1], M. Galletti[1], A. Gallo[1], M. Gaobardi[9,10], A. Ghigo[1], L. Giannessi[1,8], P. Gianotti[1], A. Giribono[1], L. Giuliano[7,14], L. Gizzi[17], G. Grilli[1], M. Ianni[1], S. Incremona[1], L. Ioannucci[1], A. Iungo[1], F. Iungo[1], L. Labate[17], G. Latini[1], S. Lauciani[1], A. Liedl[1], M. Loffreda[1], V. Lollo[1], G. Lombardo[1], G. Luminati[1], S. Lupi[7,14], R. Magnanimi[1], A. Marcelli[12,18], M. Marchetti[1], S. Martelli[1], M. Martini[1], R. Mascio[1], A. Mascioli[1], F. Mazzoni[1], C. Mencarelli[1], A. Michelotti[1], M. Migliorati[7,14], A. Mostacci[7,14], T. Napolitano[8], B. Nese[1], F. Nguyen[1,19], M. Opromolla[1], G. Parise[1], L. Palumbo[7,14], M. Pedio[20], D. Pellegrini[1], L. Pellegrino[1], A. Pesce[21], A. Petralia[19], M. Petrarca[7,14], V. Petrillo[4], L. Petrucciani[1], G. Piermarini[1], L. Piersanti[1], S. Pioli[1], R. Pompili[1], E. Principi[8], S. Quaglia[1], R. Quaranta[1], D. Quartullo[1], R. Ricci[1], E. Romano[1], S. Romeo[1], M. Rossetti Conti[4], A. R. Rossi[4], L. A. Rossi[1], J. B. Rosenzweig[22], U. Rotundo[1], L. Sabbatini[1], M. F. Sardone[1], M. Scampati[1], G. Scarselletta[1], L. Serafini[4], B. Serenellini[1], G. J. Silvi[1], L. Spallino[1], B. Spataro[1], A. Stella[1], F. Stellato[9,10], A. Stecchi[1], F. Stocchi[1,9], S. Strabioli[1], S. Tocci[1], P. Tomassini[23], A. Trigilio[1], P. Tuscano[1], C. Vaccarezza[1], A. Vannozzi[1], L. Verra[1], S. Vescovi[1], F. Villa[1], C. Zannini[1], M. Zarlenga[1], A. Zigler[24], M. Zottola[1]

[1] *INFN - Laboratori Nazionali di Frascati, via E. Fermi 54, 00044 Frascati (Rome), Italy*

[2] *GSI Helmholtzzentrum für Schwerionenforschung GmbH Planckstraße 1, 64291 Darmstadt, Germany*

[3] *CNR - Istituto di Struttura della Materia (CNR-ISM), Sede Secondaria di Montelibretti, Area della Ricerca di Roma 1, Via Salaria km 29.300, 00015 Monterotondo Stazione (Rome), Italy*

[4] *Universitá degli Studi di Milano and INFN sez. Milano, Via Celoria 16, 20133 Milan, Italy*

[5] *GoLP/Instituto de Plasmas e Fusão Nuclear, Instituto Superior Técnico, Universidade de Lisboa, 1049-001 Lisbon, Portugal*

[6] *OST Eastern Switzerland University of Applied Sciences, Werdenbergstrasse 4, 9471 Buchs SG, Switzerland*

[7] *Sapienza University of Roma, P.le Aldo Moro 2, 00185 Rome, Italy*

[8] *Elettra-Sincrotrone Trieste S.C.p.A., Area Science Park Strada Statale 14 km 163.5, 34149 Basovizza - Trieste, Italy*

[9] *Universitá degli Studi di Roma Tor Vergata, Via della Ricerca Scientifica 1, 00133 Rome, Italy*

[10] *INFN sez. Roma Tor Vergata, Via della Ricerca Scientifica 1, 00133 Rome, Italy*
[11] *INFN - Laboratori Nazionali del Sud, Via S. Sofia 62, 95125 Catania, Italy*,
Centro Siciliano di Fisica Nucleare e Struttura della Materia, Via S. Sofia 64, 95125 Catania, Italy
[12] *CNR - Istituto di Struttura della Materia (CNR-ISM), Area Science Park Strada Statale 14 km 163.5, 34149 Basovizza - Trieste, Italy*
[13] *ENEA - Centro Ricerche Casaccia, Via Anguillarese 301, 00123 S. Maria di Galeria - Rome, Italy*
[14] *INFN sez. Roma, P.le Aldo Moro 2, 00185 Rome, Italy*
[15] *CNR - Istituto Officina dei Materiali (CNR-IOM), Area Science Park Strada Statale 14 km 163.5, 34149 Basovizza - Trieste, Italy*
[16] *Deutsches Elektronen-Synchrotron (DESY), Notkestr. 85, 22607 Hamburg, Germany*
[17] *CNR - Istituto Nazionale di Ottica (CNR-INO), Intense Laser Irradiation Laboratory, via G. Moruzzi 1, 56124 Pisa, Italy*
[18] *Università di Camerino, Physics Division, School of Science and Technology, Via Madonna delle Carceri 9, 62032 Camerino (Macerata), Italy*,
INFN sez. Torino, Via Giuria 1, 10125 Turin, Italy,
RICMASS, Rome International Center for Materials Science Superstripes, Via dei Sabelli 119A, 00185 Rome, Italy
[19] *ENEA - Centro Ricerche Frascati, Via E. Fermi 45, 00044 Frascati (Rome), Italy*
[20] *CNR - Istituto Officina dei Materiali (CNR-IOM), Università degli Studi di Perugia, Via A. Pascoli, 06123 Perugia, Italy*
[21] *INFN - Amministrazione Centrale, via E. Fermi 54, 00044 Frascati (Rome), Italy*
[22] *University of California Los Angeles, Department of Physics and Astronomy, 90095 Los Angeles, California, USA*
[23] *Extreme Light Infrastructure - Nuclear Physics (ELI-NP), IFIN-HH, 30 Reactorului Street, 077125 Magurele, Romania*
[24] *The Hebrew University of Jerusalem, Racah Institute of Physics, 91904 Jerusalem, Israel*

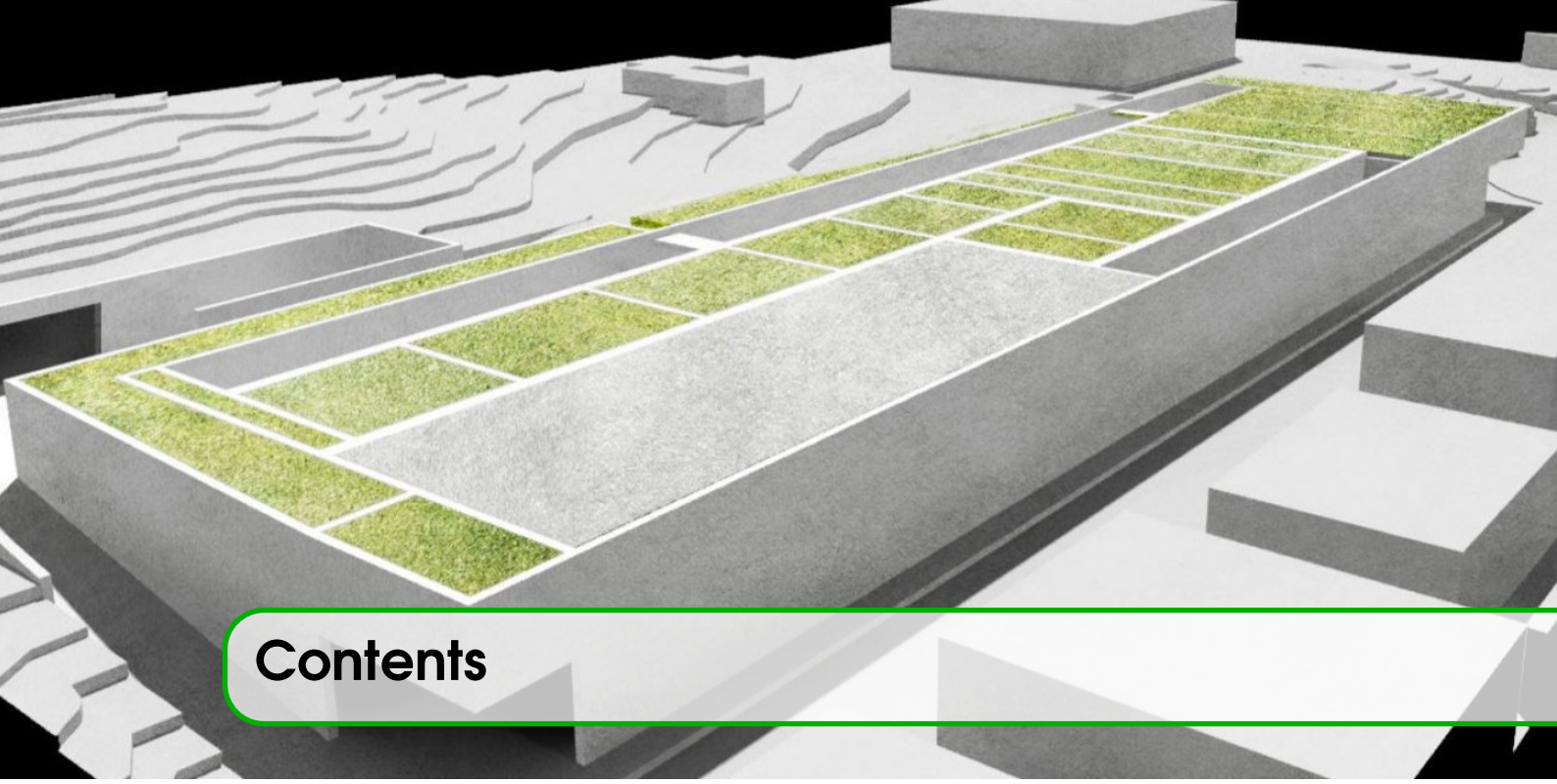

Contents

1 Executive Summary 33
1.1 Introduction 33
1.2 The EuPRAXIA Concept 34
1.2.1 Plasma Acceleration 34
1.2.2 The pan-European EuPRAXIA Project 35
1.3 The EuPRAXIA@SPARC_LAB User Facility 38
1.4 The AQUA FEL in the International context 39
1.5 FEL Scientific Case and Applications 39
1.6 Machine Expected Performances 42
1.6.1 FEL Radiation Stability 44
1.7 Machine Layout 46
1.7.1 Technology Readiness Levels 49
1.7.2 Contribution of SPARC_LAB to EuPRAXIA 49
1.8 Electron and Photon Beam Diagnostics 50
1.9 Other Technical Sub-Systems Supporting Operational Reliability 52
1.10 Civil Infrastructure 54
1.11 Integrated Safety 57
1.12 Implementation Methodology 58
1.13 Consideration about Sustainability 59
1.14 Project Cost, Timeline, and Management 60
1.14.1 Implementation Timeline 61
1.14.2 Management Structure and Project Governance 62
1.15 Risk Mitigation and Project Robustness 62
1.16 Conclusions and Future Outlook 63

1.17 Acknowledgments 65

2 FEL Scientific Case . . . 73

2.1 Introduction 73

2.2 Science @ FELs in the soft X-ray region 74

2.2.1 Photon Science Applications at AQUA . . . 75

2.3 Experimental techniques @ AQUA 76

2.3.1 Coherent imaging . . . 78
2.3.2 X-ray spectroscopies . . . 80
2.3.3 Ion and Electron Spectroscopies . . . 82
2.3.4 Conclusions . . . 84

3 Beam Physics . . . 91

3.1 Overview of the start to end simulations 91

3.2 Start to end simulation for the plasma acceleration case 93

3.2.1 Photoinjector . . . 94
3.2.2 Linac . . . 97
3.2.3 Plasma acceleration stage . . . 99
3.2.4 Driver separator . . . 103
3.2.5 FEL performances . . . 106
3.2.6 Jitters and tolerance studies results . . . 109
3.2.6.1 Active elements jitter . . . 110
3.2.6.2 Misalignments and trajectory corrections . . . 111
3.2.6.3 FEL performance with statistical approach . . . 113
3.2.6.4 Optical transport simulations . . . 118

3.3 Start to end simulation for the X-band RF acceleration case 119

3.3.1 Photoinjector and linac . . . 119
3.3.2 TransferLine and Undulator Matching . . . 123
3.3.3 FEL performance . . . 123
3.3.4 Jitter and misalignment analysis . . . 125

3.4 Microbunching instability 127

3.4.1 Full RF configuration . . . 128
3.4.2 Laser heater . . . 129
3.4.2.1 Effects on the electron beam . . . 130
3.4.3 Comments on the results with the MBI semi analytical model . . . 131

3.5 Conclusions 132

4 Facility layout . . . 137

4.1 Introduction 137

4.2 EuPRAXIA@SPARC_LAB Building Layout 137

4.2.1 General description . . . 137
4.2.2 The accelerator and undulator tunnel . . . 139
4.2.3 Modulator & Klystron gallery and power supplies area . . . 139
4.2.4 Laser Rooms . . . 140
4.2.5 Beamlines and Users area . . . 141

4.3 The facility layout 141
4.3.1 Introduction . . . 141
4.3.2 S-band photo-injector . . . 142
4.3.3 X-band linac . . . 143
4.3.4 Plasma accelerating section . . . 144
4.4 Free Electron Laser radiation 145
4.4.1 The FEL undulators . . . 145
4.4.2 FEL radiation beam transport lines . . . 146
4.4.3 End station and users area . . . 147
4.5 Conclusions 148

5 RF Photo-Injector . . . 149
5.1 Introduction 149
5.1.1 Injector requirements . . . 151
5.2 Electron source and injection system 151
5.2.1 Electron source and RF gun . . . 152
5.2.1.1 Compensation solenoid . . . 154
5.2.2 X-band linearising cavity . . . 155
5.2.3 Gun-to-first boosting section . . . 157
5.2.4 Booster accelerating modules . . . 159
5.3 Laser heater section 161
5.4 Diagnostics beamline design and performances 163
5.4.1 Low energy diagnostic beamline . . . 164
5.4.2 High energy diagnostic beamline . . . 165
5.5 Injector performance studies 165
5.6 Final considerations 167

6 RF X-band Linac . . . 171
6.1 Introduction 171
6.2 X-band RF module 171
6.3 X-band TW structures 172
6.3.1 Electromagnetic design . . . 173
6.3.2 Thermo-mechanical design . . . 175
6.3.3 Vacuum . . . 176
6.3.4 Prototyping activity . . . 176
6.4 X-band waveguide components 177
6.5 BOC pulse compressor 178
6.6 RF power source 179
6.7 Quadrupole and diagnostics inter-modules 180
6.8 Supports 180
6.9 Magnetic chicane 181
6.10 Conclusions and Technical Readiness Level 182

7 Plasma Accelerating Module 187
7.1 Introduction 187
7.2 Plasma module design 188
7.2.1 Plasma sources 190
7.2.2 High repetition rate operation 195
7.2.3 High-Voltage discharge pulser 198
7.2.4 Plasma discharge stabilization 199
7.3 Plasma chamber integration in the accelerator layout 200
7.3.1 Beam transport upstream and downstream of the vacuum chamber 200
7.3.2 Focusing and extraction quadrupoles 200
7.4 Vacuum pumping system 201
7.5 Diagnostics 204
7.5.1 Plasma source diagnostics 204
7.5.2 Electron beam diagnostics 206
7.6 Plasma module safety system 206
7.7 Conclusions 209

8 FEL and Undulators 211
8.1 Introduction 211
8.2 AQUA FEL 211
8.2.1 Introduction to the Undulator Design for the AQUA Beamline 211
8.2.2 Undulator Technology 212
8.2.3 Undulator parameters 215
8.2.4 FEL operation tuning range and performance 216
8.2.5 Magnetic lattice and beam transport 221
8.3 AQUA undulator 223
8.3.1 Magnetic Modeling 223
8.3.1.1 Undulator K parameter and tuning range 225
8.3.1.2 Field Profile 225
8.3.1.3 End magnets design 226
8.3.1.4 Field integrals 228
8.3.1.5 Trajectory 229
8.3.1.6 Correction coils system 229
8.3.2 Mechanical design 231
8.3.2.1 Magnetic Forces 231
8.3.2.2 Experience from the SABINA APPLE-X Undulator 233
8.3.2.3 Undulator Mechanical considerations 235
8.3.2.4 Undulator positioning system 237
8.3.2.5 Temperature stability 237
8.3.3 Phase shifter for the AQUA undulator 238
8.3.3.1 Phase Shifter requirements 238
8.3.3.2 Phase Shifter modeling 240
8.3.3.3 Phase Shifter properties 241
8.3.3.4 Phase Shifter positioning 244
8.4 Analysis of tolerances 244
8.4.1 Trajectory Injection jitters 245
8.4.2 Sensitivity to magnetic errors 247
8.4.3 Sensitivity to quadrupole misalignment 249

8.5 Vacuum chamber 249
8.5.1 Analysis of wakefields . . . 250
8.5.1.1 Longitudinal . . . 250
8.5.1.2 Transverse . . . 252
8.5.2 Vacuum properties . . . 255
8.5.3 Vacuuum chamber mechanical design and supports . . . 256
8.5.4 Conclusion . . . 259
8.6 Intra-undulator sections 259
8.7 Conclusion 262

9 Photon Beamline . . . 267
9.1 Introduction 267
9.2 AQUA beamline 267
9.2.1 Layout . . . 269
9.2.2 Overview of the beam parameters along the beamline . . . 271
9.2.3 Technology Readiness Level of the beamline elements . . . 273
9.3 Photon beam transport and optics for AQUA beamline 275
9.3.1 Defining apertures . . . 275
9.3.2 Gas Attenuators and Solid Filters . . . 275
9.3.2.1 Solid filters . . . 276
9.3.2.2 Gas attenuator . . . 276
9.3.3 Mirrors . . . 277
9.3.3.1 General Description . . . 278
9.3.3.2 Mirror Specification . . . 278
9.3.3.3 Mirror position specification . . . 279
9.3.3.4 Mirror support and UHV chamber description . . . 279
9.3.3.5 Mirror Coating . . . 280
9.3.4 Focusing system . . . 281
9.3.4.1 System Description . . . 281
9.3.4.2 Optical Performance . . . 282
9.3.5 Monochromator . . . 283
9.3.6 Split and Delay line . . . 283
9.4 Photon Diagnostics 284
9.4.1 Gas Monitor Detectors . . . 284
9.4.1.1 Beam Intensity Monitoring . . . 285
9.4.1.2 Beam Position Monitoring . . . 286
9.4.2 Viewing screens . . . 286
9.4.3 Plate Beam Position Monitors . . . 286
9.4.4 Grating spectrometer . . . 288
9.4.5 Temporal and polarization characterization . . . 289
9.4.6 Wavefront Sensor . . . 290
9.4.7 Coherence . . . 291
9.4.7.1 Temporal Coherence Characterization . . . 291
9.4.7.2 Spatial Coherence Characterization . . . 292
9.5 Operation 292
9.5.1 Alignment Protocols . . . 292
9.5.2 User Operation Workflows . . . 293
9.5.3 Safety . . . 294
9.6 Conclusions 295

10 Experimental End-stations 299
10.1 The AQUA endstation 299
10.2 Instrumentation 300
10.2.1 Experimental chambers 300
10.2.1.1 Vacuum requirements 302
10.2.1.2 Short focal length optics 303
10.2.1.3 External lasers 303
10.2.2 Sample delivery systems 303
10.2.2.1 Fixed targets 304
10.2.2.2 Gas-phase molecular injectors 304
10.2.2.3 Liquid jet injectors 305
10.2.2.4 Aerosol injectors 306
10.2.3 Detectors 307
10.2.3.1 Photon detectors 308
10.2.3.2 Ions and electron detectors 308
10.3 Data Acquisition and Management 310
10.4 Sample preparation and characterization laboratories 311
10.4.1 Technology Readiness Level of the endstation components 312

11 Electron Diagnostics 317
11.1 Introduction 317
11.2 Electron beam diagnostics 318
11.2.1 Integrated current transformer 318
11.2.2 Faraday cup 319
11.2.3 Strip-line Beam Position Monitors 320
11.2.4 Cavity Beam Position Monitors 321
11.2.5 View Screens 325
11.2.6 Emittance Measurements 327
11.2.7 Magnetic spectrometers 329
11.2.8 Transverse deflecting structure 332
11.2.9 Electro Optical Sampling 335
11.2.10 Coherent radiation monitor 338
11.2.11 Plasma entrance diagnostics 340
11.2.11.1 OTR screen 342
11.2.11.2 Microwire scanner 342
11.2.12 Beam Loss Monitors 343
11.3 Layout integration 347
11.4 Technology Readiness Level and List of Elements 351
11.5 Artificial Intelligence 352
11.6 Conclusions 352

12 Laser System 357
12.1 Introduction 357
12.2 The Photocathode Laser 357
12.2.1 Location and Infrastructure 357
12.2.2 Laser Requirements 359
12.2.3 Photocathode Laser Subsystems 359
12.2.4 Example of a Commercial IR Laser System 359

12.2.5 Laser Layout after Pulse Compression . . . 360
12.2.6 Transverse Beam Profile on the Cathode . . . 361
12.2.6.1 Peak-to-peak uniformity . . . 361
12.2.6.2 Energy Stability . . . 362
12.2.7 Estimation of Energy Losses . . . 362
12.2.8 Final Scheme of the Laser Systems . . . 363
12.2.9 Laser Diagnostics . . . 364
12.2.10 Summary of the Laser Parameters . . . 366
12.3 The Probe Beamlines 366
12.3.1 Laser Beams for Diagnostics . . . 366
12.3.2 Laser System for the Laser Heater . . . 367
12.4 Laser System for FEL Users 367
12.5 Laser Safety System 368
12.6 Conclusions 368

13 RF systems . . . 371
13.1 Introduction and general description 371
13.2 The S-band injector RF systems 371
13.2.1 The RF Gun . . . 372
13.2.2 The Travelling Wave S-band accelerating sections . . . 372
13.2.2.1 Brazing-free design and realization of sections . . . 375
13.2.3 RF Power distribution network . . . 376
13.3 The S-band and X-band RF power sources 377
13.3.1 RF source safety . . . 381
13.4 Low Level RF systems 383
13.4.1 LLRF System Architecture and Challenges . . . 383
13.4.2 R&D Efforts for X-Band and S-Band LLRF Systems . . . 383
13.4.3 Key Features of the LLRF System . . . 384
13.5 Technology readiness level 385
13.6 Conclusions 385

14 Timing and Synchronisation . . . 389
14.1 Introduction 389
14.2 System overview and specifications 389
14.2.1 Timing . . . 389
14.2.2 Synchronization . . . 390
14.3 System implementation 390
14.3.1 Timing system . . . 391
14.3.2 Synchronization system . . . 392
14.3.2.1 Reference generation . . . 392
14.3.2.2 Reference distribution . . . 392
14.3.2.3 Client locking systems . . . 394
14.3.2.4 Residual drift compensation . . . 395
14.3.2.5 RF plant stability enhancement . . . 395
14.4 Conclusions 396

15 Control System ... 399
15.1 Introduction 399
15.2 Overview 399
15.2.1 Architecture ... 401
15.2.2 Hardware and Software Integration Schemes ... 401
15.2.2.1 Hardware ... 402
15.2.2.2 Software ... 403
15.2.3 Control Equipment Catalogue ... 403
15.3 Services 405
15.3.1 Design and Architecture ... 405
15.3.2 Functionality ... 405
15.3.3 High Level Applications ... 406
15.4 Graphic and Not-Graphic Interfaces 406
15.5 AI for EuPRAXIA@SPARC_LAB control system 407
15.6 E-infrastructure 409
15.6.1 Data Management & Access Policy ... 409
15.6.2 Network ... 410
15.7 Conclusions 411

16 Vacuum System ... 415
16.1 Introduction 415
16.2 Vacuum System: Requirements and General Evaluations 415
16.3 Vacuum Layout 416
16.3.1 RF-Gun Section ... 417
16.3.2 S-Band Linac Injector ... 418
16.3.3 Laser Heater ... 420
16.3.4 X-Band Linac ... 421
16.3.5 Plasma Interaction Area ... 422
16.3.6 Undulator Section ... 424
16.3.7 Photon beamline ... 425
16.3.8 Waveguide Systems ... 426
16.4 Manufacturing and Cleaning Procedures 426
16.5 Conclusions 427

17 Magnets and Power Converters ... 429
17.1 Introduction 429
17.2 Magnets for the injector 431
17.2.1 Gun solenoid ... 431
17.2.2 Gun quadrupole ... 432
17.2.3 Gun steerers ... 433
17.2.4 Focusing solenoids for accelerating sections ... 434
17.2.5 Steerers between accelerating sections ... 437
17.2.6 Quadrupoles before laser heater chicane ... 437
17.2.7 Laser heater chicane dipoles ... 438
17.2.8 Laser heater chicane sextupole ... 438

17.3 Magnets for the linac **441**
17.3.1 Steerers between X band accelerating sections . . . 441
17.3.2 Quadrupoles between X band accelerating sections . . . 441
17.4 Bunch compressor magnets **443**
17.4.1 Bunch compressor chicane dipoles . . . 443
17.4.2 Bunch compressor section quadrupoles . . . 444
17.4.3 Bunch compressor chicane sextupole . . . 444
17.5 Magnets for the plasma section **445**
17.5.1 Beam focusing requirements . . . 445
17.5.2 Tunable permanent magnet preliminary design . . . 446
17.5.3 Current status and next steps . . . 448
17.6 Driver-witness separator **448**
17.7 Spectrometer Dipoles **452**
17.8 Magnets for the undulator line **453**
17.8.1 Intra-undulators quadrupoles . . . 453
17.8.2 Intra-undulators steerers . . . 453
17.9 Dump dipole **455**
17.10 Power Converter Sizing and Specifications **456**
17.11 Safety for magnets and power supplies **456**
17.11.1 Magnets . . . 456
17.11.2 Cables . . . 458
17.11.3 Power converters . . . 459
17.12 Conclusions **459**

18 Civil Infrastructures . . . 463
18.1 Civil engineering **463**
18.1.1 Geology and environment . . . 463
18.1.2 Buildings . . . 464
18.1.2.1 Main Buildings . . . 466
18.2 Electrical installations **474**
18.2.1 LNF Power supply . . . 474
18.2.2 EuPRAXIA@SPARC_LAB Load estimation . . . 474
18.2.3 Electrical network and Redundancy criteria . . . 475
18.2.4 Critical issues and proposed solutions . . . 476
18.2.5 Electrical installation in the accelerator tunnel . . . 476
18.2.6 Grounding, bonding and low voltage distribution system . . . 477
18.2.7 Electromagnetic compliance . . . 477
18.2.8 Technological plants automation and control . . . 477
18.3 Fluid plants **478**
18.3.1 Process Cooling System . . . 478
18.3.1.1 Primary Water Cooling System . . . 479
18.3.1.2 Secondary Water Cooling System . . . 479
18.3.1.3 Demineralized Water Production System . . . 480
18.3.1.4 Leak Control and Water Collection System . . . 483
18.3.2 Ventilation and HVAC Systems . . . 483
18.3.3 Compressed Air System . . . 491
18.4 Conclusions **491**

19 Integrated safety 493
19.1 Introduction 493
19.2 Reference Regulations 495
19.2.1 Building Works and structures 495
19.2.2 Occupational Health & Safety 495
19.2.3 Radiation Protection 496
19.2.4 Installations 496
19.2.5 Fire Prevention 496
19.3 Conventional safety 498
19.3.1 Fire safety 498
19.3.1.1 Reaction to fire 499
19.3.1.2 Fire resistance 499
19.3.1.3 Compartmentation and evacuation 499
19.3.1.4 Fire safety management 501
19.3.1.5 Fire control 502
19.3.1.6 Fire detection and alarm 503
19.3.1.7 Smoke and heat control 504
19.3.1.8 Firefighting operations 505
19.3.1.9 Safety of technological systems 506
19.3.2 Safety of equipment and accident prevention 506
19.3.2.1 Requirements for the safe operation of equipment 506
19.3.2.2 Occupational Health & Safety requirements for the construction phase 507
19.3.3 Emergency preparedness and response 507
19.3.3.1 Staff Training 507
19.3.3.2 Specialized Training for the Emergency Response Teams 508
19.3.3.3 General Training for All Personnel 508
19.3.3.4 General Emergency Drills 508
19.3.3.5 Radiological Emergency Drills 509
19.4 Radiation Safety and protection 510
19.4.1 Preliminary Radiation Safety Program 510
19.4.1.1 Radiation monitoring System 510
19.4.1.2 Data acquisition and management 515
19.4.1.3 Personnel Dosimetry Systems 515
19.4.1.4 Access control system requirements 516
19.4.1.5 Interlock requirements 516
19.4.1.6 Area classification 517
19.4.2 Radiation protection evaluations 517
19.4.2.1 Operating parameter 518
19.4.2.2 Shielding Approach and Design Criteria 519
19.4.2.3 Radiation Source Terms 519
19.4.3 Lateral shielding and beam dumps design 521
19.4.3.1 Lateral shielding design 521
19.4.3.2 Electron Beam Dump design 523
19.4.3.3 Diagnostic Beam Dumps 523
19.4.3.4 Diagnostic Beam Dump FLUKA simulation 524
19.4.3.5 Fixed Beam Dump 530
19.4.3.6 FEL Beam Dump (AQUA beamline) 530
19.4.3.7 Driver Beam Dump 533
19.4.4 Other Radiation Sources 537

19.5 Functional Safety 538
19.5.1 Compliance and Risk Assessment Procedure . . . 538
19.5.2 Machine Protection System . . . 539
19.5.2.1 MPS Requirements and Specifications . . . 539
19.5.2.2 MPS Architecture and device support . . . 540
19.5.2.3 MPS Risk Assessment . . . 541
19.5.2.4 MPS Software and Hardware Design . . . 543
19.5.2.5 Validation and Verification . . . 543
19.5.3 Personnel Safety System . . . 543
19.5.3.1 PSS Requirements and Specifications . . . 544
19.5.3.2 PSS Architecture and device support . . . 547
19.5.3.3 PSS Risk Assessment . . . 548
19.5.3.4 PSS Software and Hardware Design . . . 548
19.6 Conclusions 549

20 Implementation Methodology . . . 553
20.1 Introduction 553
20.2 Integration of the Accelerator Machine with Civil Infrastructure 553
20.2.1 Building Acceptance Test . . . 554
20.2.1.1 Geometric and Dimensional Characteristics of the Building . . . 555
20.2.1.2 Short- and Long-Term Building Settlements . . . 555
20.2.2 Key Integration Areas Between Machine and Civil Infrastructure . . . 556
20.2.3 Design and Implementation Strategy . . . 558
20.2.4 Designing for Mechanical and Thermal Stability . . . 558
20.2.5 Spatial Planning and Functional Layout . . . 559
20.2.6 Utilities and Infrastructure Services . . . 559
20.2.7 Radiation Safety and Shielding . . . 560
20.2.8 From Design to Commissioning . . . 560
20.3 Naming Convention 560
20.4 Schematic Layout 563
20.5 Asset Management 568
20.5.1 The PBS and Utility Matrix in the Context of EuPRAXIA@SPARC_LAB . . . 569
20.6 Conclusions 574

21 Sustainability . . . 577
21.1 Introduction 577
21.2 LNF campus greening strategies 577
21.3 Sustainability Regulation and duties in Italy 578
21.4 EuPRAXIA@SPARC_LAB Building 579
21.4.1 Integration of the new building into the naturalistic and landscape context . 579
21.4.2 Design techniques to ensure good energy performance . . . 580
21.4.3 Choice of building products and materials . . . 580
21.4.4 Specific design choices for the construction phase . . . 580
21.5 Sustainability Aspects of RF systems 580
21.6 HVAC 582
21.7 Process cooling 586
21.8 Greenhouse gas 587

21.9 Energetic mix and CO2 587
21.10 Sustainability Benefits of Plasma-Based Acceleration 588
21.11 Conclusions 589

22 Project Cost, Timeline and Management Structure 591
22.1 Introduction 591
22.2 Project Management Methodology 591
22.3 Cost Baseline and cost assessment methodology 592
22.3.1 Time Line 597
22.3.2 Work Breakdown Structure resource associated and correlation with Lab . . 598
22.3.3 Correlation with the European context 599
22.4 Conclusions 600

A Appendix: TRL reference table 601

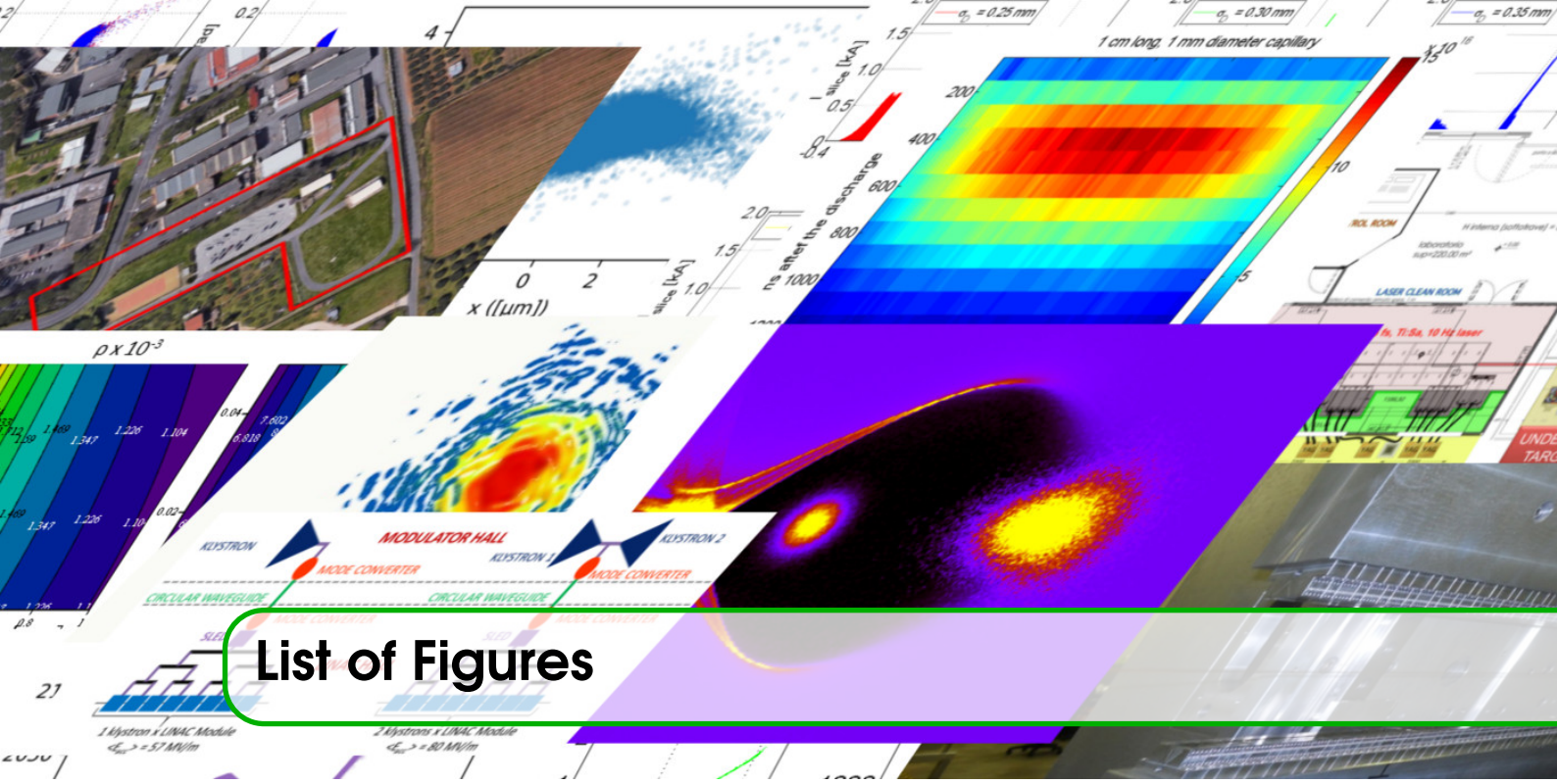

List of Figures

1.1 Wakefield acceleration scheme. 35
1.2 Geographical distribution of EuPRAXIA Research Infrastructure 36
1.3 Architectural rendering of EuPRAXIA@SPARC_LAB 38
1.4 Genesis simulation results for PWFA 45
1.5 Genesis simulation results for Full RF 45
1.6 Photon number versus wavelength for 100 random events 47
1.7 Layout of the accelerator and beamlines 48
1.8 Facility top view and internal ground level layout 55
1.9 EuPRAXIA@SPARC_LAB schedule 61

2.1 Images of relevant scientific targets 77
2.2 Schematics of some complementary X-ray–based techniques 78
2.3 Simulated CDI pattern of a poliovirus in AQUA beamline 79
2.4 Simulated CEI footprints in AQUA beamline 83

3.1 FEL saturation length and number of photons 92
3.2 The layout of the EuPRAXIA@SPARC_LAB accelerator 93
3.3 Electron Beam transverse phase space (PWFA case) 98
3.4 Electron beam longitudinal profile (PWFA case) 98
3.5 X-band wakefields 99
3.6 Longitudinal and transverse phase space at the plasma injection . . . 100
3.7 Normalized optimal β-function at the entrance of a plasma ramp . . . 101
3.8 Energy spread of the electron bunch vs the plasma density 102
3.9 Slice analysis of the witness bunch in the accelerator 103
3.10 Longitudinal phase space of the driver and witness bunches 104
3.11 Energy distribution of the comb beam at the plasma exit 105
3.12 Witness beam Twiss parameters between plasma and undulators . . 105
3.13 Slice analysis of the witness beam in the undulator 107
3.14 FEL simulation results for PWFA nominal working point 109
3.15 Evaluation of plasma vs linac contribution to energy gain jitter 110

3.16 Witness-driver relative offset and divergence 113
3.17 Photon number versus wavelength for 100 random events 116
3.18 Time duration histogram of the radiation pulse over 100 events 117
3.19 Photon number vs λ in the extended electron energy range 117
3.20 e^- beam transverse phase space emittance and envelope (Full RF) 120
3.21 e^- beam longitudinal phase space through the linac (Full RF) 122
3.22 Electron beam slice analysis (Full RF) 123
3.23 Electron beam parameters in the undulator (full RF case) 124
3.24 FEL simulation results (Full RF case) 126
3.25 Electron beam phase space for MBI study (Full RF case) 129
3.26 MBI spectral gain 130
3.27 Slice energy spread induced by the LH 130

4.1 Top view of the building with accelerator and FEL beam lines 138
4.2 Functional areas of EuPRAXIA@SPARC_LAB ground floor 138
4.3 Accelerator and undulators tunnel and Modulator & klystron gallery . 139
4.4 Laser clean rooms 140
4.5 Layout of the accelerator and beamlines 141
4.6 Layout of the S-band photo-injector 142
4.7 Layout of the X-band accelerator 143
4.8 Layout of the area dedicated to plasma acceleration 144
4.9 Layout of the Free Electron Laser undulators area 146
4.10 Schematic layout of the FEL beamlines and experimental stations . . 147

5.1 Injector layout. 150
5.2 Prospective view of the laser injection scheme. 153
5.3 Electromagnetic model of the RF gun. 154
5.4 2D geometry of the gun with electric field modes 154
5.5 S-band RF gun installed at SPARC_LAB 155
5.6 RF rendering of the optimized SW RF cavity 156
5.7 Reflection coefficient at the port of the input waveguide. 157
5.8 RF power splitter. 157
5.9 RF power splitter reflection and transmission coefficients. 158
5.10 Linearizer full structure 158
5.11 On-axis electric field profile. 158
5.12 Gun to first boosting section layout. 159
5.13 S-band boosting section layout. 160
5.14 CAD view of the long solenoid 160
5.15 Layout for the S-band power distribution 161
5.16 Layout for the X-band power distribution 161
5.17 Layout of the Laser Heater section. 162
5.18 Layout of the high energy injector diagnostic. 165

6.1 X-band linac layout. 172
6.2 X-band RF module mechanical layout. 172
6.3 X-band RF module schematic layout. 173
6.4 Schematic layout of two consecutive modules. 173
6.5 HFSS model of the X-band accelerating structure 174
6.6 Amplitude and phase of the accelerating field along the structure . . 175
6.7 Peak accelerating field in each cell 175
6.8 Mechanical drawing of the X-band structure. 176
6.9 Results of the thermo-mechanical analysis performed by ANSYS 176
6.10 Simulated pressure along the X-band structure 177
6.11 X-band accelerating structure prototypes 177

6.12 X-band components under test at the LNF TEX test facility. 178
6.13 Rectangular X-band flange for waveguide connections 179
6.14 Rectangular to circular mode converter 179
6.15 Mechanical design of waveguide distribution components 180
6.16 Cooling system of the waveguides 180
6.17 Picture and e.m. configuration of BOC 181
6.18 Girder of the X-band module 182
6.19 Support of the X-band structure. 183
6.20 Detail of the granite support of the X-band structure. 183
6.21 Schematic layout of the magnetic chicane. 184
6.22 Layout of the magnetic chicane. 184

7.1 Plasma module placed within the layout of the accelerator 187
7.2 Plasma module layout 188
7.3 Plasma source housing chamber 189
7.4 Gas-filled discharge capillary design with CFD simulations 191
7.5 Plasma module designed for EuPRAXIA@SPARC_LAB 192
7.6 60 cm-long capillary discharge 192
7.7 60 cm-long capillary discharge characterization 193
7.8 Final construction of the Shapal capillary 193
7.9 Plasma module designed for EuPRAXIA@SPARC_LAB 194
7.10 Test sample of the gas-filled discharge capillary 195
7.11 Deterioration assessment of gas-filled discharge capillary 196
7.12 Evolution of the laser spot deformation with plasma shots 197
7.13 Longitudinal profile and electrodes after millions shots 197
7.14 High-voltage source design 198
7.15 High-voltage source characterization 199
7.16 Current discharge waveforms 200
7.17 Layout of the chicane line 201
7.18 Plasma chamber and vacuum pumping system 202
7.19 Sizing of the vacuum pumping system near the X-band 203
7.20 Setup in *Plasma_lab* for the Stark broadening technique 204
7.21 Characterization of the gas-filled discharge capillaries 205
7.22 Layout of the beam diagnostics 207

8.1 Dependence of the period length vs. the beam energy 212
8.2 Undulator on axis field as a function of the aperture/period ratio 214
8.3 FEL saturation length vs. period length and resonant wavelength. . . . 215
8.4 Photon count per pulse vs. resonant wavelength and beam energy . 216
8.5 FEL parameters vs. norm. emittance and relative energy spread, CP 217
8.6 FEL parameters vs. norm. emittance and relative energy spread, LP . 218
8.7 FEL parameters vs. normalized emittance and the average β_T, CP . . 218
8.8 FEL parameters vs. normalized emittance and the average β_T, LP . . . 219
8.9 FEL parameters vs. relative energy spread and peak current, CP 220
8.10 FEL parameters vs. relative energy spread and peak current, LP 220
8.11 AQUA FODO cell schematic layout. 221
8.12 Twiss β values vs. integral quadrupole strength 221
8.13 Electron beam transverse rms size subject to undulator plus FODO . . 222
8.14 Quadrupole Integrated gradient vs. beam energy (Twiss $\beta = 8\,m$) . . . 222
8.15 Quadrupole Integrated gradient vs. beam energy (Twiss $\beta = 5\,m$) . . . 223
8.16 Structure of the AQUA APPLE-X undulator 224
8.17 Undulator K parameter variation 225
8.18 K_{rms} and wavelength tuning range for different gaps 225
8.19 Longitudinal field profile of the AQUA undulator 226

8.20 Transverse field profile of the AQUA undulator 226
8.21 End magnets design scheme after optimization. 227
8.22 Undulator field integrals 228
8.23 Electron trajectory in the undulator 229
8.24 Correction coils scheme and its displacement 230
8.25 Correction coils system 230
8.26 Corrected trajectory by means of the Correction Coils system 231
8.27 Integrated magnetic forces acting on the four undulator girders . . . 232
8.28 Compensating magnets scheme of the undulator array. 233
8.29 Integrated magnetic forces acting on the girders with comp. mag. 233
8.30 Mechanical structure under investigation. 234
8.31 Rendering of one of the AQUA undulator modules. Front view. 236
8.32 Rendering of one of the AQUA undulator modules. Side view. 236
8.33 Undulator lower frame 237
8.34 FEL radiation energy vs. the intraundulator phase advance 239
8.35 Intraundulator phase delay and corrections vs. wavelength 239
8.36 Scheme of the phase shifter for the AQUA undulator 241
8.37 Vertical component of the field B_y 242
8.38 Peak B field and of second integral vs. phase shifter gap 242
8.39 Trajectory and kick angle of a electron in the phase shifter 243
8.40 Phase Integral in the phase shifter vs. gap 243
8.41 Phase shifter correction vs. gap and wavelength 243
8.42 Electron trajectory in the undulator, coupled with the phase shifter . 244
8.43 Electron RMS matched transverse size along AQUA undulator, CP . . 245
8.44 FEL emission from the nominal electron bunch, CP 246
8.45 FEL emission from the nominal electron bunch, LP 247
8.46 Average energy loss and output power vs. undulator propagation . 251
8.47 Energy loss at undulator exit and power output with RW wakefields . 251
8.48 Kick angle/m for different vacuum chamber inner radii, short 253
8.49 Kick parameter/m^2 and uncertainty vs. VC inner radius, short 253
8.50 Kick angle/m for different vacuum chamber inner radii, long 254
8.51 Kick parameter/m^2 and uncertainty vs. VC inner radius, long 254
8.52 Front view of the undulator vacuum chamber 257
8.53 Side view of the undulator vacuum chamber 258
8.54 Undulator frame with vacuum chamber holders 258
8.55 Undulator frame with the vacuum chamber, side 259
8.56 Intra-undulator section elements 260

9.1 Layout of the AQUA and ARIA beamlines 269
9.2 Layout detail of AQUA beamline inside undulator area 270
9.3 Layout detail of AQUA beamline inside shielded area 270
9.4 Layout of the AQUA beamlines inside the user area 271
9.5 BDA layout 275
9.6 Transmission for different filter materials 276
9.7 Layout of the gas absorber 277
9.8 Gas absorber attenuation 277
9.9 Mirror layout 278
9.10 Mirror reflectivity 280
9.11 K-B system 281
9.12 3D schematic view of K–B mirrors configurations 282
9.13 Draft of the GMD 284
9.14 Expected current from GMD 285
9.15 Layout of the plate BPM 287

9.16 Schematic of the HWFS 291
9.17 Schematic of the coherence measurement setups 292

10.1 Schematic of the experimental AQUA chamber 301
10.2 Sample injection systems that will be installed at AQUA. 306
10.3 Schematic of the electrospray-based aerosol injector system 307

11.1 Faraday Cup 319
11.2 Technical design of the strip-line BPM pickup 320
11.3 Design of cavity BPM 322
11.4 Cavity BPM PSI model "BPM8". 322
11.5 LIBERA Cavity BPM Electronics 323
11.6 Mechanical drawing of the compact view screen 325
11.7 Screen holder in the view screen 326
11.8 Particle beam image with COTR 326
11.9 COTR filtering with spatial mask 327
11.10 View screens RF Shield 327
11.11 Magnetic spectrometers lattice schemes 330
11.12 Spectrometer simulation results for driver and witness at 120 MeV . . 330
11.13 Working principle of the PolariX TDS 332
11.14 2D layout of the beamlines hosting the PolariX TDS 333
11.15 Longitudinal resolution for the electron bunches 334
11.16 Measured EOS signal of the driver and witness bunches 335
11.17 EOS spatial decoding configuration 336
11.18 Experimental setup of the EOS system 337
11.19 CDR target 338
11.20 CDR monitor as a function of compression at TTF VUV-FEL. 339
11.21 Axonometric projection of the plasma entrance device 340
11.22 Design of the plasma entrance device 341
11.23 GEANT4 simulations of the wire scanner 343
11.24 Lost electron Cherenkov coupled by optical fiber 344
11.25 Cherenkov UV BLM Scheme 344
11.26 Setting for time-of-flight beam loss measurement 345
11.27 Internal structure of high-OH silica core fiber. 345
11.28 Hamamatsu MPPC sensor structure. 346
11.29 WaveCatcher 8-channels. 346
11.30 Description of the detection flow of Cherenkov BLM. 347
11.31 Diagnostics positions between gun and first accelerating module . 348
11.32 Diagnostics positions in the injector area INJ-LA-002-003 348
11.33 Diagnostics positions in the injector area section INJ-LA-004-005. . . 348
11.34 Positions of screens and BPM between dipole and compressor 349
11.35 Diagnostics positions in bunch compressor 349
11.36 Diagnostics positions in the high energy linac 349
11.37 Diagnostics position in the plasma module. 350
11.38 Diagnostics positions in the undulator. 350

12.1 Layout of the EuSPARC laser rooms 358
12.2 Transport beamline from cleanroom to cathode. 358
12.3 Commercial IR laser system suitable for photocathode applications. 360
12.4 Schematic of the laser chain after compression. 360
12.5 Transverse uniformity requirement of the laser beam. 361
12.6 Measured transverse profile of the laser beam 362
12.7 Estimated energy losses throughout the laser system. 363
12.8 Simplified schematic of the complete laser systems. 363

12.9 Side view of the gun with the optical table for laser diagnostics. 364
12.10 Laser diagnostics installed near the cathode 364
12.11 Top view of the gun and associated diagnostics. 365
12.12 Schematic of the Laser Heater (LH) beamline. 367

13.1 Picture of the S-band RF Gun realized for the CLEAR injector 373
13.2 Computed RF pulses at the SLED for the 3 m S-band structures 374
13.3 Quasi-constant accelerating gradient across the 3 m structure 375
13.4 Computed RF pulses at the SLED for the 1.5 m S-band structures 375
13.5 Quasi-constant accelerating gradient across the 1.5 m structure . . . 375
13.6 Mechanical design and realization of the variable RF power divider 377
13.7 Picture of the Canon E37119 klystron 378
13.8 Picture of the solid-state RF sources at the TEX facility 379
13.9 Measured klystron anode voltage and beam current waveforms . . . 381

14.1 Timing and synchronization hardware map 391
14.2 Layout of the synchronization system. 392
14.3 Phase noise of the reference generator 393
14.4 Special cable duct design 394
14.5 Insulated duct network layout 395

15.1 Three tier architecture scheme. 401
15.2 Hardware and software vertical columns. 402
15.3 Control System Services architecture scheme. 405
15.4 AI functionality for control system 407
15.5 Q-learning system adjusting beam energy with RF power and phase 409
15.6 Communication between AI framework and control system 409
15.7 EuPRAXIA network design scheme. 411

16.1 Vacuum Schematic Layout Legend 416
16.2 Vacuum Schematic Layout Legend 417
16.3 RF-gun Vacuum System: Schematic Layout 418
16.4 RF-gun Vacuum System: CAD Layout 418
16.5 RF-gun Vacuum System: Pressure Simulation 418
16.6 S-Band Linac: Schematic Vacuum Layout 419
16.7 S-Band Linac: Pressure Simulations 419
16.8 S-Band Linac: Pressure Distribution 419
16.9 Laser Heater Chamber: Pressure Simulations 420
16.10 Laser Heater Chamber: Pressure Distribution 420
16.11 X-Band Linac Module: Vacuum Schematic Layout 421
16.12 X-Band Accelerating Structure: Pressure Simulations 421
16.13 X-Band Accelerating Structure: Pressure Distribution 422
16.14 X-Band Linac: Simulation of Pressure Distribution 422
16.15 Plasma Area: Vacuum Schematic Layout 423
16.16 Plasma Area: CAD representation for simulation 423
16.17 Undulators: Vacuum Schematic Layout 424
16.18 Undulators: Pressure Simulations 425
16.19 Undulators: Pressure Distribution 425

17.1 Gun solenoid 431
17.2 Gun solenoid during measurements 431
17.3 Gun quadrupole design 432
17.4 Gun quadrupole 433
17.5 Gun steerer 433

17.6 Measurements of solenoid 436
17.7 Installation of solenoid 436
17.8 Alignment of solenoid 436
17.9 Steerer between accelerating sections 437
17.10 Laser heater chicane 440
17.11 Laser heater chicane dipole 440
17.12 Laser heater chicane sextupole 440
17.13 Steerer between X band accelerating sections 442
17.14 Bunch compressor chicane dipole 443
17.15 Bunch compressor chicane sextupole 444
17.16 3D model of TPMQ 446
17.17 3D model of compact TPMQ 448
17.18 Separator chicane dipole 449
17.19 Separator chicane 450
17.20 Septum dipole 450
17.21 Septum dipole face 451
17.22 Septum dipole details 451
17.23 3D model of intra-undulators quadrupoles 453
17.24 3D model of intra-undulators steerers 454

18.1 INFN-LNF and EuPRAXIA@SPARC_LAB area. 464
18.2 Excerpt from the geological report 465
18.3 EuPRAXIA@SPARC_LAB facilities top view. 465
18.4 3D view of the EuPRAXIA@SPARC_LAB facilities 466
18.5 EuPRAXIA@SPARC_LAB building functional layout - Level 0. 467
18.6 EuPRAXIA@SPARC_LAB building Level 0 - Entrances. 468
18.7 Removable blocks dividing walls between Undulators and Exp. halls 468
18.8 EuPRAXIA@SPARC_LAB building functional layout - Level 1. 469
18.9 Views of the Exp. halls with systems ducts and penetrations 470
18.10 Structural joint of the EuPRAXIA@SPARC_LAB building. 470
18.11 EuPRAXIA@SPARC_LAB Building cross section. 471
18.12 Views for equipment accessibility during maintenance stops 471
18.13 Current Waveform for 100 Hz operated Modulator. 476
18.14 Current Waveform FFT. 477
18.15 Cooling System Schematic. 478
18.16 Monthly operating hours and consumptions - dry/adiab. mode . . . 481
18.17 Monthly operating hours and consumptions - chillers 482
18.18 HVAC ducts and distribution. 483
18.19 LINAC ventilation system. 485
18.20 Undulators Hall ventilation system. 486
18.21 Experimental Hall ventilation system. 486
18.22 CleanRoom HVAC schematic. 487
18.23 CleanRoom ventilation system. 488
18.24 Technical balconies for AHUs. 489
18.25 LINAC room Temperature simulation map. 490
18.26 LINAC room Velocity vectors simulation map. 490
18.27 Undulators enclosure ventilation system. 491

19.1 Conventional, Radiation, and Functional Safety Interconnections . . 494
19.2 Example of emergency exit signs 500
19.3 Example of emergency signage UNI EN ISO 7010 compliant 500
19.4 Example of automatic extinguishing system 503
19.5 Section of a SHEVS exhaust opening 505
19.6 Access routes for firefighting vehicles 506

19.7 Planned detector position on the first (b) and ground (a) floor. 512
19.8 Irradiation geometry considered for the lateral shielding evaluation. 521
19.9 Ambient dose equivalent rate (4 m - 90°). 522
19.10 Ambient dose equivalent rate (20 m - 90°). 522
19.11 Diagnostic beam dump layout in 2D (a) and 3D (b). 523
19.12 Technical and simulated layout in 2D (a-b) and 3D (c-d). 524
19.13 Measurement points - diagnostic beam dump simulations. 525
19.14 H*(10) - 300 MeV diagnostic beam dump - xz plane. 527
19.15 H*(10) - 300 MeV diagnostic beam dump - xy plane. 527
19.16 H*(10) - 800 MeV diagnostic beam dump - xz plane. 528
19.17 H*(10) - 800 MeV diagnostic beam dump - xy plane. 528
19.18 H*(10) - 1.2 GeV diagnostic beam dump - xz plane. 529
19.19 H*(10) - 1.2 GeV diagnostic beam dump - xy plane. 529
19.20 FEL Beam Dump (AQUA beamline) layout on yz plane. 531
19.21 FEL Beam Dump Simulation area 531
19.22 H*(10) - FEL beam dump - without plasma acceleration - xz plane. 532
19.23 H*(10) - FEL beam dump - without plasma acceleration - yz plane. 533
19.24 Driver beam dump layout 2D (a) and 3D (b). 534
19.25 Driver Beam Dump Simulation area 534
19.26 H*(10) - driver beam dump - xz plane. 536
19.27 H*(10) - driver beam dump - xy plane 536
19.28 Risk assessment procedure to evaluate risk reduction measures. . . . 538
19.29 Overview of the devices and subsystems connected to the MPS . . 539
19.30 MPS Architecture 541
19.31 FPGA state machine implementing read–search–set cycle in MPS . 543
19.32 Diagram of the Personnel Safety System 544
19.33 PSS Architecture 547

20.1 EuPRAXIA 3D View Project 554
20.2 Alignment apertures 556
20.3 Labyrinths in Experimental Area 557
20.4 Door closure near plasma area 557
20.5 Matching between Machine with Civil Infrastructure 559
20.6 Sample identification code 561
20.7 PBS layout - RF Gun 563
20.8 PBS layout - Accelerator 564
20.9 PBS layout - Undulator 565
20.10 PBS layout - Beamline 566
20.11 PBS layout - Klystron gallery 567
20.12 Sample list of machine components in Hexagon database 568
20.13 Scale of Maturity Levels in Project Configuration Management. . . . 569
20.14 Sample detail of PBS schematic layout 571
20.15 Example of Machine Component Classification. 573

21.1 Annual electrical power demand 578
21.2 Trend of Natural gas annual demand 578
21.3 EER depending on outdoor air temperature without free cooling . . . 583
21.4 Cooling capacity without free cooling 583
21.5 EER depending on outdoor air temperature with free cooling 584
21.6 Cooling capacity with free cooling 584
21.7 Interpolating surface for partial load operation 585
21.8 COP depending on outdoor air temperature 585
21.9 Italian energy mix 588

22.1 Cost and schedule baseline methodology 592
22.2 Cost distribution per functional area. 594
22.3 Cost distribution per subsystem. 595
22.4 Cost distribution 596
22.5 Cumulative Distribution Function of the project cost. 596
22.6 High Level time line - Machine & Building 597
22.7 RI Lifecycle approach in the ESFRI Context 600

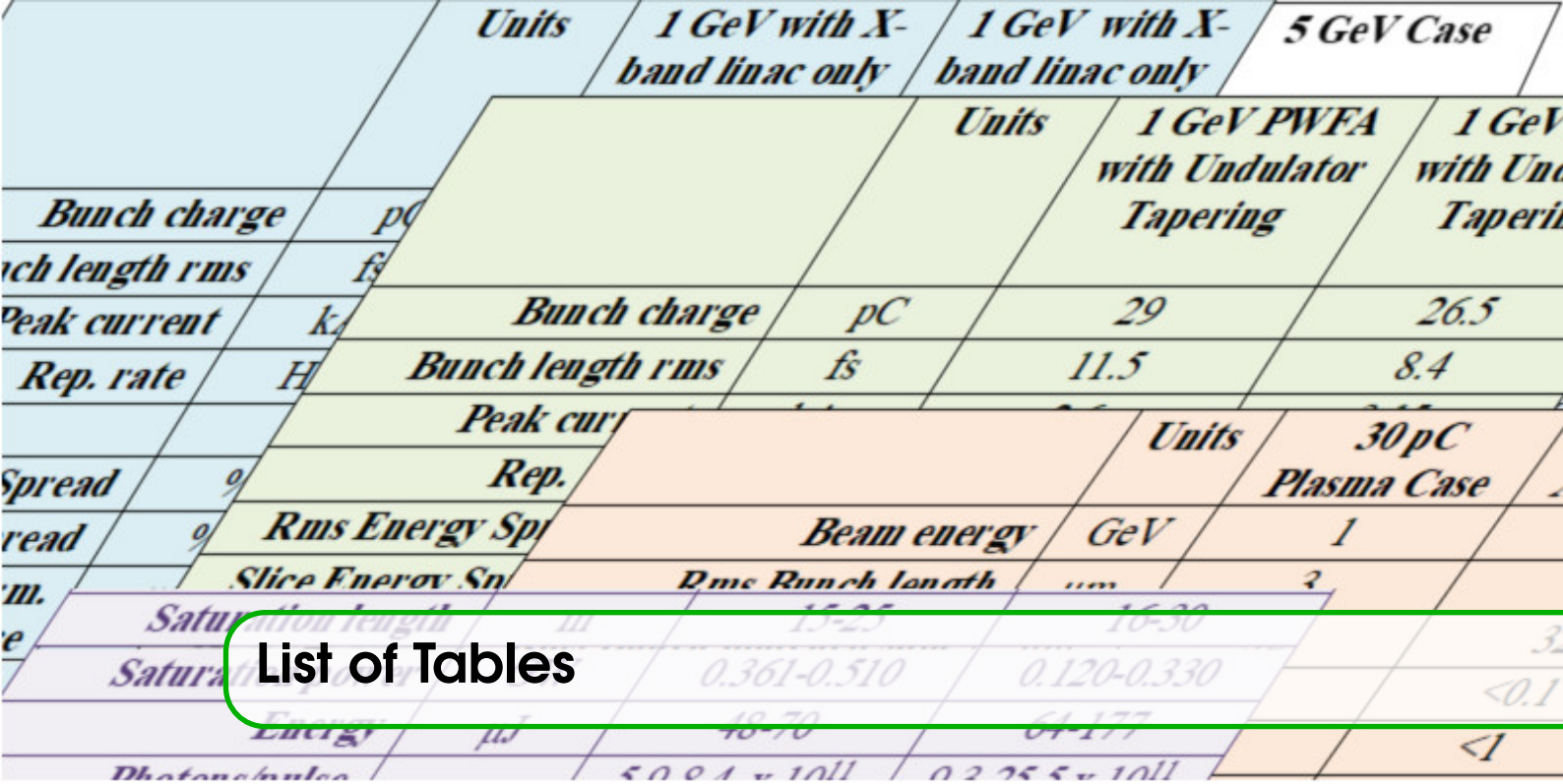

List of Tables

1.1 Major Short-Wavelength FEL User Facilities 40
1.2 AQUA Scientific case and applications 41
1.3 Electron beam and FEL radiation main parameters 43
1.4 TRL level of the main components 50
1.5 Electron Beam Diagnostics 51
1.6 Photon Pulse Diagnostics 51
1.7 Expected power consumption 56
1.8 Aggregated cost per functional area (values in k€) 60

3.1 Electron beam and FEL radiation main parameters 94
3.2 e^- beam parameters at plasma entrance for the ref. working point . . 95
3.3 Reference input parameters at injector for comb beam production . . 97
3.4 Witness parameters at the injection and extraction of plasma channel 102
3.5 Layout parameters of the separator chicane 105
3.6 Electron beam parameters at the undulator entrance (PWFA case) . 106
3.7 Reference beam main radiation parameters (PWFA case) 108
3.8 Undulator tapering values 108
3.9 Summary of jitter values used in the sensitivity analysis 111
3.10 Statistical values of the witness bunch at undulator entrance 111
3.11 Undulator parameters for $\lambda_r = 4$ nm at 1 GeV 114
3.12 Theoretical 3-D radiation parameters results (PWFA case) 114
3.13 Statistical values of FEL radiation parameters (PWFA case) 115
3.14 Undulator parameters and wavelength tuning 116
3.15 Transport efficiency as a function of the surface rms roughness. 119
3.16 Photoinjector main parameters for the Full RF case 120
3.17 Photoinjector output beam parameters for the Full RF case 120
3.18 Linac setup for the Full RF case 121
3.19 Layout parameters of the BC chicane 122
3.20 e^- beam parameters at the undulator entrance (Full RF) 124
3.21 FEL radiation parameters for the Full RF case 125

3.22 CompactLight-XLS: Main electron beam and FEL parameters. 125
3.23 CompactLight Linac performance Analysis, static imperfections . . . 126
3.24 RMS dynamic imperfections of CompactLight subsystems 127
3.25 CompactLight Linac performance Analysis, dynamic jitters 127
3.26 Main parameters related to the use of the laser heater 131
3.27 Technology Readiness Level of the Start-to-End Simulations. 132

4.1 Lengths of the EuPRAXIA@SPARC_LAB parts 142

5.1 Injector requirements 151
5.2 Summary of the required photocathode laser parameters. 153
5.3 Main parameters of the new SPARC_LAB RF gun 155
5.4 Main parameters of the X-band linearising cavity. 156
5.5 Main specifications of the LH system. 163
5.6 e^- beam parameters in the low energy beamline 163
5.7 e^- beam parameters in the high energy beamline. 164
5.8 Jitter values used in the simulations 166
5.9 S-band injector jitters without the HHC 166
5.10 Summary of jitter sources affecting the witness bunch 166
5.11 TRL level of the photoinjector and its sub-systems. 168

6.1 Parameters of the EuPRAXIA@SPARC_LAB accelerating structures . . . 174
6.2 Parameters of the BOC-type pulse compressor. 178
6.3 Parameters of the X-band Canon klystron E37119. 181
6.4 Parameters of the Solid state pulsed Modulator. 182
6.5 Parameters of the magnetic chicane. 184
6.6 TRL of the X band linac. 185

7.1 Plasma source key parameters 190
7.2 Vacuum pumping system design 203
7.3 Vacuum pumping system sizing 204
7.4 Plasma module safety system 208
7.5 TRL of the plasma module sub-systems. 209

8.1 Reference set of target beam parameters 212
8.2 Undulator basic parameters 224
8.3 Undulator transverse field homogeneity 227
8.4 Undulator field integrals at minimum gap 228
8.5 Correction coils modeling parameters as defined in Fig. 8.25. 230
8.6 Undulator field integrals at minimum gap with corr. coils 231
8.7 SABINA undulator parameters. 234
8.8 Phase shifter main parameters. 241
8.9 AQUA undulator tolerance to electron beam transverse misalignment 247
8.10 AQUA undulator tolerance to magnetic errors 249
8.11 RMS kick, divergence angles and emittance growth due to wakefields 255
8.12 Intra-undulator elements 261
8.13 AQUA undulator physical specifications summary 262
8.14 TRL level of the FEL system 263

9.1 FEL radiation parameters from S2E simulations. 268
9.2 Relevant photon pulse parameters for diagnostics 268
9.3 Beamline subsystem list 269
9.4 AQUA beam parameters along the beamline 272
9.5 AQUA beam parameters scan 273

9.6 TRL of photon beamline optics. 274
9.7 TRL of photon beamline diagnostics. 274
9.8 Mirror dimensions in the AQUA beamline 279
9.9 Parameters for the spectrometer gratings 289

10.1 TRL level of the endstation equipment. 313

11.1 Relevant electron beam parameters and measurements 318
11.2 Strip-line BPM parameters 321
11.3 Main parameters of PSI cavity BPM 323
11.4 Main parameters of the "LIBERA Cavity BPM". 324
11.5 Nominal beam parameters at the emittance diagnostics 328
11.6 Emittance diagnostic resolutions 328
11.7 Magnetic spectrometer parameters 331
11.8 Parameters of TDS Measurements 334
11.9 EOS parameter employed at the SPARC_LAB 337
11.10 Parameters of optical fiber. 345
11.11 Digitizer specifications. 347
11.12 TRL level of the electron beam diagnostics 351
11.13 List of electron beam diagnostics with section reference. 351

12.1 Infrared laser parameters. 366
12.2 Ultraviolet laser parameters. 366
12.3 Laser Heater parameters. 367
12.4 Technological Readiness Level (TRL) of the laser subsystems. 369

13.1 Parameters of the S-band sections 374
13.2 RF sources parameters 380
13.3 Klystrons nominal parameters 381
13.4 RF solid state driver amplifier parameters 382
13.5 LLRF main specifications 384
13.6 TRL of RF subsystems 385
13.7 Radiofrequency subsystem list 386

14.1 Timing jitter specifications 390
14.2 Synchronization expected performance for the RF and laser clients . 397
14.3 TRL level of the timing and synchronization systems 397

15.1 Requirements for control systems 400
15.2 Technology Readiness Level of Control System sub-components. . . . 412

16.1 Vacuum System Main Elements 417
16.2 Plasma Chamber: Calculated and Simulated Pressure Distribution . . 424
16.3 TRL level of the Vacuum 427

17.1 Magnets list 430
17.2 Gun Solenoid Parameters. 432
17.3 Gun steerers Parameters. 434
17.4 Injector accelerating-structure solenoid parameters. 435
17.5 Steerer between sections parameters. 437
17.6 Quadrupole triplet before LH chicane. 438
17.7 Laser heater chicane dipoles parameters 439
17.8 Laser heater chicane sextupole parameters 441
17.9 Steerers between X band sections parameters. 442
17.10 Quadrupole between X band accelerating sections. 443

17.11 Bunch compressor chicane dipoles parameters. 444
17.12 Bunch compressor chicane sextupole parameters 445
17.13 TPMQ requirements upstream and downstream plasma capillary . 445
17.14 Parameters of upstream TPMQ 446
17.15 Parameters of downstream TPMQ 447
17.16 Downstream short TPMQ: compact and normal parameters 447
17.17 Separator chicane dipoles parameters. 449
17.18 Separator chicane parameters. 450
17.19 Septum dipole parameters. 452
17.20 Spectrometer dipoles main parameters. 452
17.21 Intra-undulators quadrupoles parameters 454
17.22 Intra-undulators steerers parameters 455
17.23 Dump dipole parameters 456
17.24 Power converter sizing 457
17.25 Power converter technical specifications 457
17.26 TRL level of the magnets 460

18.1 Soleil Synchrotron long time settlement 470
18.2 EuPRAXIA@SPARC_LAB Building Level 0 main halls dimensions 472
18.3 EuPRAXIA@SPARC_LAB Building Level 1 main halls dimensions 472
18.4 EuPRAXIA@SPARC_LAB Building Level 0 main halls interior finishes . . . 473
18.5 EuPRAXIA@SPARC_LAB Building Level 1 main halls interior finishes . . . 473
18.6 Legend of Tables 18.4 and 18.5 473
18.7 EuPRAXIA@SPARC_LAB Main loads estimation 475
18.8 Expected power consumption for the AQUA beamline 475
18.9 Power demand for the primary cooling circuits. 479
18.10 Secondary Cooling System Users 479
18.11 Primary and secondary circuits pumps design data 480
18.12 Total Electrical Power demand. 480
18.13 Total Electrical Power demand, Water @28 °C 481
18.14 Total Electrical Power demand, Water @20 °C 482
18.15 Design values for the ventilation system 484
18.16 AHUs main values 489

19.1 Detector location. 513
19.2 Area classification planned for the EuPRAXIA@SPARC_LAB facility . . 517
19.3 Operational parameter considered for radiation safety 518
19.4 Diagnostic Beam Dump Measurement point 526
19.5 H*(10) values for diagnostic scenarios. 530
19.6 FEL Beam Dump Simulation point 532
19.7 H*(10) - FEL beam dump - only RF scenario 533
19.8 Driver Beam Dump Simulation point 535
19.9 H*(10) values - Driver Beam Dump 536
19.10 MPS System Requirements 539
19.11 MPS Technical Specifications 540
19.12 Traceability Matrix: Requirements vs Specifications 540
19.13 Overview of the quantity of devices connected to the MPS 542
19.14 MTBF values hardware devices 542
19.15 SIF versus PFH according to mode of operation. 542
19.16 PSS Requirements for EuPRAXIA@SPARC_LAB 545
19.17 PSS System Specifications for EuPRAXIA@SPARC_LAB 546
19.18 Matrix relationship between SR and SS for the PSS 547
19.19 Quantity of devices monitored and controlled by the PSS 548
19.20 TRL of the Conventional Safety. 550

19.21 TRL level of the radiation protection system. 550
19.22 TRL of the functional safety subsystems. 551

20.1 System Descriptions. 562
20.2 Technical specifications for component LEL-A-ACC-XBD-005. 572
20.3 Summary of Main Machine Elements by System. 574

21.1 Main specification of the VKX83113 CPI klystron prototype 581

22.1 Methodology for cost accuracy assessment 593
22.2 Aggregated cost per functional area (values in k€) 593
22.3 Estimated costs by system 595
22.4 Main structure of the Work Breakdown Structure 598

A.1 Reference TRL description 601

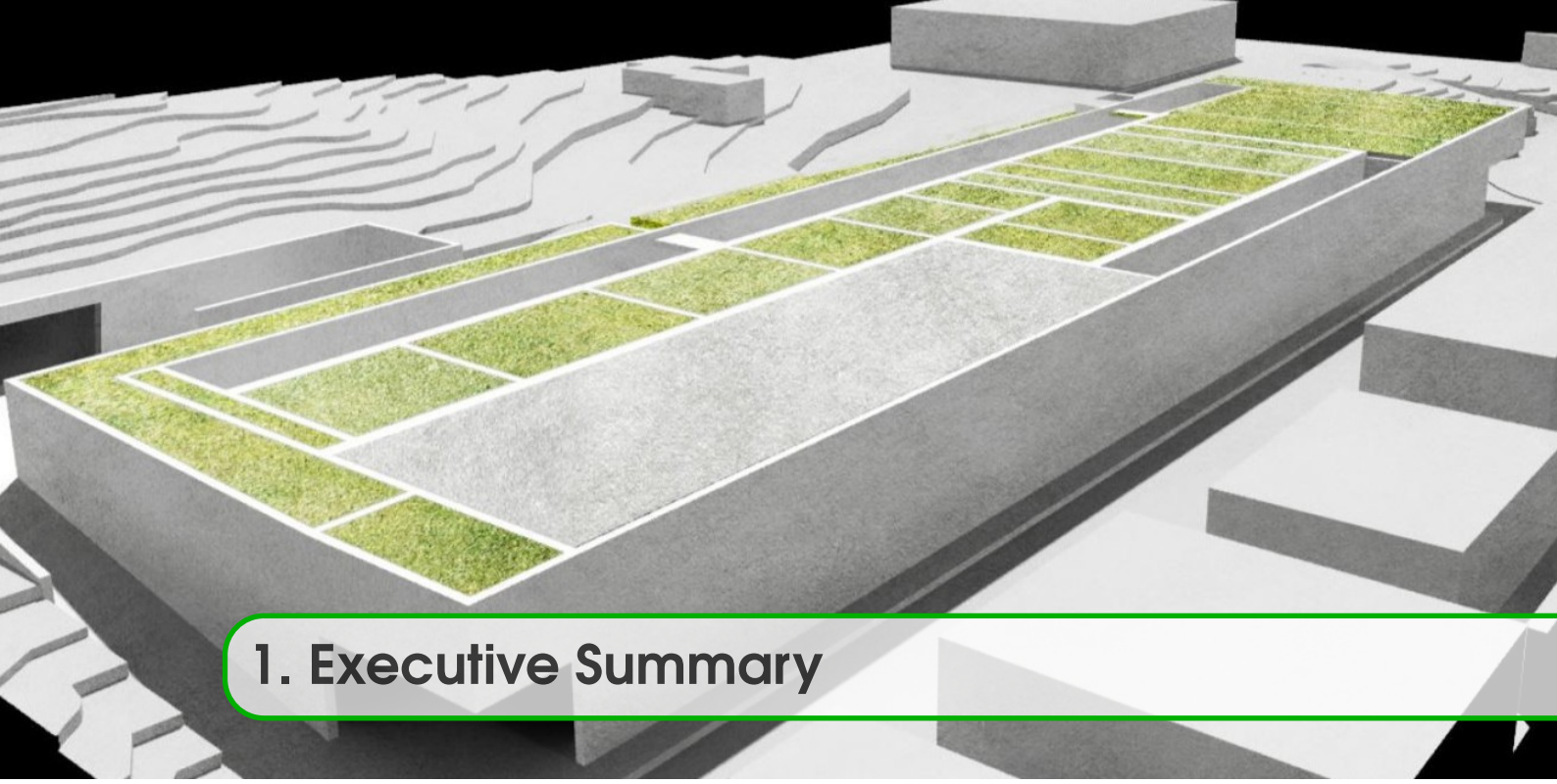

1. Executive Summary

1.1 Introduction

The purpose of the EuPRAXIA@SPARC_LAB User Facility is to **establish a research infrastructure that pioneers the use of Plasma Wake-Field Acceleration (PWFA) for driving a high-brightness Free-Electron Laser (FEL) user facility** in the soft X-ray regime.

As one of the two core pillars of the pan-European Plasma Research Accelerator with eXcellence In Applications (EuPRAXIA) Research Infrastructure [1, 2], EuPRAXIA@SPARC_LAB will be hosted at the INFN Frascati National Laboratory (LNF) serving both as a cutting-edge scientific facility for users and as a technological demonstrator [3]. It will validate the integration of high-gradient plasma acceleration and X-band RF technology within a compact FEL light source, laying the groundwork for future compact user facilities. This will improve their **sustainability** by significantly reducing the size, energy consumption, and operational costs typically associated with conventional accelerator-based FEL light sources, making advanced photon science more accessible and environmentally responsible in the long term (see Chapter 21).

The user facility is expected to begin operations in 2031. Its first user beamline, AQUA, will deliver ultrashort femtosecond soft X-ray pulses within the biologically relevant "water window" spectrum, enabling real-time imaging, advanced materials development, and investigation of chemical processes with unprecedented spatial and temporal resolution.

By transitioning plasma-based accelerators from proof-of-concept to operational systems and validating them under real user facility conditions, EuPRAXIA@SPARC_LAB closes a critical gap in the Technology Readiness Level (TRL) chain (from the current TRL ≈ 5 to the final TRL > 7). This will position Europe at the forefront of global innovation in compact accelerators and strengthen its capacity to lead future high-energy physics, photon science, and interdisciplinary research programs. **The inclusion in the European Strategy Forum on Research Infrastructures (ESFRI) roadmap since 2021** [4] marks the strategic importance of the project at the European level.

The realization of the facility entails the construction of new buildings to host the accelerator systems, experimental halls, and support laboratories. This new infrastructure, to be built within the INFN LNF site, represents the project's first significant step and challenge. From the outset, the

design and construction will prioritize incorporating energy-efficient solutions, environmentally responsible materials, and infrastructure choices aligned with long-term ecological and operational resilience.

The **Technical Design Report** (TDR) for the EuPRAXIA@SPARC_LAB facility presents a comprehensive technical reference for the construction and scientific exploitation of the user facility. The TDR is structured to:

- Define the scientific and technological objectives of the facility (this Executive Summary);
- Outline the scientific cases and user applications (Chapter 2);
- Demonstrate feasibility through simulations and design studies (Chapter 3);
- Deliver a technical description of the facility and its components including technical readiness and potential risks evaluation (Chapters 4-21);
- Support funding efforts and stakeholder engagement (Chapter 22).

This **Executive Summary** aims to define the scientific and technological objectives of the facility and to provide a concise overview of the full TDR, tailored for funding agencies, institutional stakeholders, and expert reviewers. It distills the key content into an accessible format that emphasizes the facility's maturity, technical feasibility, and scientific relevance. The summary is also intended to support informed decision-making and alignment with European research priorities and funding instruments, particularly those related to ESFRI and Horizon Europe.

1.2 The EuPRAXIA Concept

Modern science and technology rely heavily on particle beams from fundamental physics [5], photon science [6], and a wide range of industrial and medical applications [7]. However, traditional RF-based accelerators face practical limitations in cost and size as high beam energies are needed. This has prompted a global effort to develop more compact and cost-effective alternatives [8]. Plasma acceleration, proposed in 1979 [9], has demonstrated potential energy gradients up to 100 GV/m [10], orders of magnitude higher than conventional RF systems [11], limited by metallic surface breakdown. Using lasers [9] or particle beams [12] to drive plasma waves, this technology replaces metal cavities with plasma structures, allowing for ultra-high acceleration fields. Despite challenges in stability, recent advancements have shown that plasma-based systems can meet the quality required for VUV FELs [13, 14], with international efforts making significant progress [15–23].

1.2.1 Plasma Acceleration

Plasma accelerators exploit charge density oscillations in an ionized gas (plasma) to generate ultra-high accelerating gradients [24]. These oscillations, plasma waves, are driven by the passage of a high-energy beam through a dense plasma. The plasma wave **driver** can be either an **ultra-relativistic electron bunch** (as it is in our case) [12, 25] or an intense laser pulse [9]. As the driver propagates through the plasma, it displaces plasma electrons outward via its space-charge field (in the case of an electron beam) or the ponderomotive force (for a laser pulse), leaving behind a positively charged ion cavity, illustrated in Figure 1.1. The resulting electric fields in the ion-filled cavity can reach several GV/m, far exceeding the breakdown limits of conventional RF accelerating structures, which are currently limited to $\sim$ 100 MV/m. These extreme fields depend not only on the plasma density but also on the driver's current, bunch length, and transverse size, and are maximized when the bunch length is shorter than half the plasma wavelength [25, 26].

To exploit this accelerating field, a second trailing electron bunch, called the **witness**, is injected into the appropriate phase of the wake. For efficient energy gain with minimal energy spread and beam divergence, the witness must be precisely placed within the region of the wake where the electric field is simultaneously accelerating longitudinally and focusing transversely. In the highly

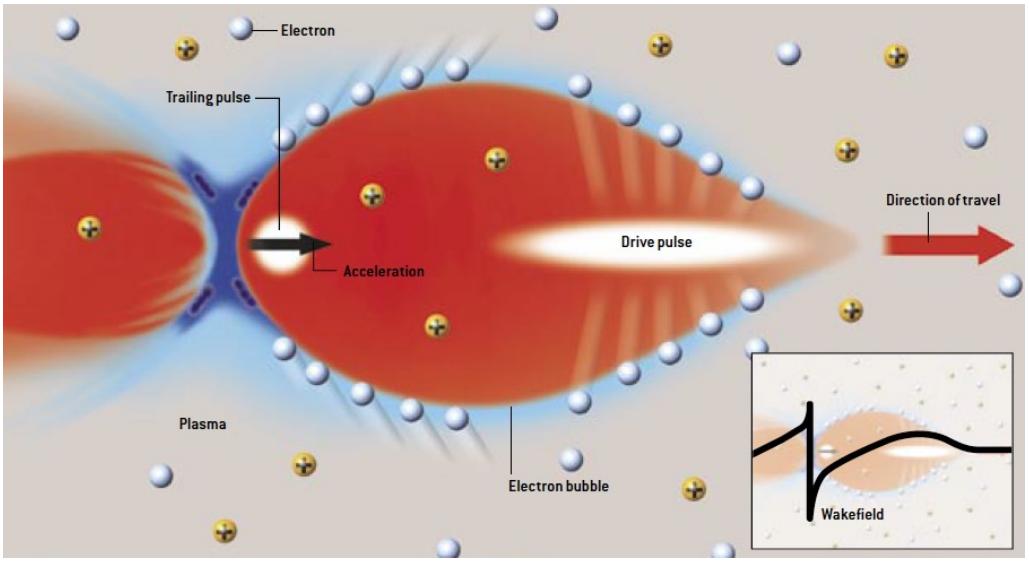

Figure 1.1: Plasma wakefield accelerators rely on charge separation in the plasma sustaining fields known as a wakefield. The drive bunch blows the electrons (blue) away from axis , leaving behind a region of positive charge (red). Along the axis where the bunches propagate, the electric field (plotted in the little box) causes the drive bunch to lose energy, and a trailing pulse of electrons injected near the rear of the bubble to experience strong acceleration [24].

nonlinear "blowout" regime [26, 27] (as in our case), this optimal region lies behind the center of the ion cavity. When correctly phased, the **witness beam** can experience a nearly uniform accelerating gradient and a constant focusing field, allowing it to reach GeV-scale energies over distances of just a few tens of centimeters.

To match the dimensions of the plasma bubble—typically 100-300 µm in length and 10-30 µm in width—both the driver and witness beams must be significantly shorter and narrower than the plasma wavelength, while maintaining high charge densities. In particular for FEL applications this demands beams of exceptional quality: ultrashort duration, low emittance, narrow energy spread, and high peak current. **Achieving and maintaining these beam parameters represents one of the key challenges of the EuPRAXIA project.**

Before the formal launch of EuPRAXIA, plasma-based accelerator research had been advancing rapidly through both theoretical studies and experimental breakthroughs. Significant progress in Laser Wakefield Acceleration (LWFA) [28] and Particle Wakefield Acceleration (PWFA) [25] demonstrated the potential of these novel technologies. EuPRAXIA represents the coordinate European effort to drive the transition from proof of principle experiments to industrial and user machine applications.

1.2.2 The pan-European EuPRAXIA Project

The idea of EuPRAXIA emerged in 2012 within the framework of the European Network for Novel Accelerators (EuroNNAc) [29], under the umbrella of the EU-funded EuCARD project. The concept was further refined during the first European Advanced Accelerator Concepts Workshop in September 2013 [30], ultimately leading to the preparation of a proposal for a Design Study, submitted in 2014 to the Horizon 2020 programme.

The EuPRAXIA Design Study [31] officially began in November 2015, supported by 3 M€ EU funding over four years. Coordinated by DESY (Germany), the project brought together 16 core partners and 25 associated institutions across nine countries. Its main objective was to develop a Conceptual Design Report (CDR) for a European plasma accelerator facility capable of delivering

high-quality electron beams up to 5 GeV for scientific and technological applications.

Delivered in October 2019, the CDR presented multiple technical configurations and proposed four candidate sites. These configurations combined advanced laser and conventional accelerator technologies to drive the plasma accelerating module and to produce electron beams powering advanced radiation sources (FEL, betatron, Compton) and secondary sources of particles including positrons. EuPRAXIA's envisioned applications span a wide range of fields, including structural biology, medicine, archaeology, and industry.

The CDR underwent international peer review and was published in 2020 [1]. With government endorsements from Italy, Portugal, the Czech Republic, Hungary, and the UK, the EuPRAXIA consortium applied for inclusion in the ESFRI roadmap. In 2021, EuPRAXIA was officially included [4], becoming the first plasma-based accelerator project on the ESFRI roadmap and the first accelerator infrastructure to be added since the High-Luminosity LHC in 2016.

The EuPRAXIA Research Infrastructure is conceived as a distributed research facility [32] (see Fig. 1.2), leveraging the combined expertise and resources of numerous institutions across Europe and beyond. It will be structured around two major construction and user sites, supported by a network of specialized national nodes. The first EuPRAXIA User Site is under development at INFN-LNF in Italy [33]. This site will host EuPRAXIA@SPARC_LAB, a plasma–beam-driven FEL user facility. The Italian Ministry of University and Research, through INFN, is investing over 108 M€ to establish this EuPRAXIA site in Frascati. The effort, coordinated by INFN, involves also Elettra, ENEA, CNR, and the Universities of Rome ("La Sapienza" and "Tor Vergata") and Milan.

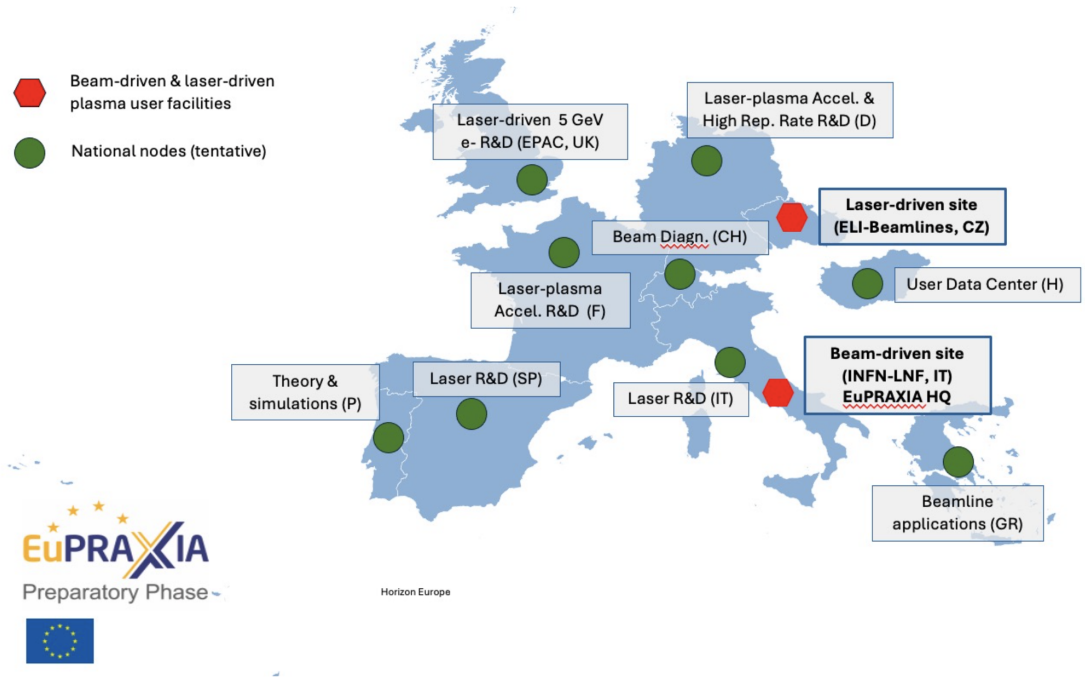

Figure 1.2: Geographical distribution of the EuPRAXIA Research Infrastructure, showing the two User Sites (Italy and Czech Republic) and the network of contributing Nodes.

The second User Site has recently been awarded to the ELI-ERIC Beamlines facility in Dolní Břežany, Czech Republic, which will focus on the laser-driven branch of the project [34].

Additional Nodes distributed across Europe will contribute to the two User Sites through R&D, component prototyping, training, and technical support. This distributed model is intended to foster international collaboration, optimizing the use of existing infrastructure while actively enhancing

funding acquisition strategies, thus reinforcing Europe's leadership in accelerator science.

In the EuPRAXIA project, the user facility is conceived as a cutting-edge, distributed European research infrastructure that provides open access to advanced plasma-based accelerator technologies and associated beamlines. Users will access beamlines including plasma-driven FELs, betatron and Inverse Compton Scattering (ICS) X-ray sources, and ultrashort electron and positron beams. It is designed not only to serve the needs of the scientific community but also to act as a platform for innovation, integrating academia, industry, and technology developers, including users working on the development and consolidation of plasma acceleration science and technology. A distinctive element of the EuPRAXIA user facility is actually its commitment to open innovation, where collaboration between research institutions, industrial partners, and technology providers is central to the development and application of new accelerator concepts [1].

In 2023, the project entered its preparatory phase (EuPRAXIA_PP) [35], funded with over 2.7 M€. This phase aims to develop the legal, financial, organizational, and technical foundations of the EuPRAXIA infrastructure, in line with ESFRI's recommendations. It also includes the formal selection of the second EuPRAXIA Pillar, mentioned above. The preparatory phase, coordinated by INFN (Italy), involves 38 participating institutes and 8 associated partners across Europe and will culminate in a proposal for a legal governance structure recognized under EU law. Following the conclusion of the Preparatory Phase in 2026, EuPRAXIA is expected to move into construction, aiming for initial operation in the early 2030s.

In parallel, a 2.53 M€ doctoral network (EuPRAXIA_DN) [36] is training 12 young fellows in advanced accelerator technologies, with a strong focus on innovation and collaboration with industry.

A further 22 M€, awarded under the Next Generation EU recovery plan, is funding the EuPRAXIA Advanced Photon Sources (EuAPS) project [37]. This initiative will develop an X-ray betatron radiation source at INFN-LNF, along with high-power, high-repetition-rate laser facilities at INFN-LNS (Catania) and CNR-INO (Pisa). These facilities, expected to become operational for users from 2026, will form the first building block of EuPRAXIA as a distributed user facility.

Most recently, in March 2025, the EU approved the Plasma Accelerator systems for Compact Research Infrastructures (PACRI) project [38], coordinated by Elettra (Trieste), under the Horizon Europe programme. It is a collaborative effort involving 19 universities and international research laboratories, supported by seven industrial partners. With 10 M€ in funding, PACRI aims to develop high-repetition-rate plasma accelerator components to support next-generation infrastructures such as EuPRAXIA and ELI Beamlines.

The Lazio Region has supported the EuPRAXIA@SPARC_LAB project since 2018 through the grants LATINO (Laboratory in Advanced Technologies for INnOvation) [39] and SABINA (Source of Advanced Beam Imaging for Novel Applications) [40], which have strengthened some of the strategic infrastructures at LNF. These projects supported the realisation of a regional technology hub in the field of advanced accelerators using technologies critical for EuPRAXIA. More recently (2025), INFN and the Lazio Region have signed an agreement to further support EuPRAXIA, whereby 10 M€ from European Regional Development Funds are made available for the implementation at EuPRAXIA@SPARC_LAB of an additional VUV FEL beamline named ARIA [41], dedicated to academic and industrial users. The design of the ARIA beamline is still at an early stage; therefore, detailed specifications are not included in this TDR, except for the essential provisions required to ensure its seamless integration within the infrastructure.

The present Technical Design Report refers to the EuPRAXIA@SPARC_LAB facility and constitutes also a major deliverable (D15.2) of the EuPRAXIA_PP project, scheduled for submission in April 2026.

1.3 The EuPRAXIA@SPARC_LAB User Facility

As described in the CDR in 2018 [33], EuPRAXIA@SPARC_LAB aims to be a research infrastructure that pioneers the use of PWFA for driving a high-brightness FEL in the soft X-ray regime. It will be located at the LNF, see Figure 1.3.

Figure 1.3: Architectural rendering of the EuPRAXIA@SPARC_LAB building at the INFN - LNF campus, which will host the 1 GeV accelerator and the AQUA FEL beamline.

The choice of using a plasma-driven FEL is very attractive for a broad scientific user base, facilitating the transition from accelerator R&D to industrial and scientific application and justifying further investment. In other words, the FEL serves as a strategic and technically demanding application that not only showcases the potential of plasma accelerators but also accelerates their integration into user-oriented scientific infrastructure.

The design of EuPRAXIA@SPARC_LAB is driven by a set of physical and technical principles aimed at achieving high-brightness FEL operation while demonstrating the maturity of PWFA high-gradient acceleration preserving high beam quality. At the beam-physics level, the facility relies on ultra-low-emittance photo-injector capabilities [42–44] to generate **both the driver and witness beams directly in the RF gun** [45]. Velocity bunching in the S-band [46, 47], combined with harmonic linearisation in the X-band [48], allows reaching the expected bunch peak current and driver/witness separation, suppresses the RF curvature and limits the onset of Coherent Synchrotron Radiation (CSR) related degradation at the earliest stages of acceleration [49]. Subsequent compression and matching strategies are defined through full start-to-end simulations, reported in Chapter 3, ensuring that beam transport preserves electron beam brightness, controls wakefield effects in the X-band linac, CSR in the bending magnets, and provides optimal matching of the driver and witness beams into the plasma wave [50]. The PWFA stage is operated in the nonlinear blowout regime, maximizing transverse focusing, energy uniformity, and robustness to timing jitter [51]. In addition, a carefully designed driver–witness separation scheme ensures clean driver extraction and transport of the witness bunch to the FEL undulator chain (see Chapter 3). FEL operation in the Self Amplified Spontaneous Emission regime (SASE) [52] with undulator tapering [53] has been chosen because it provides the most robust and efficient pathway to high photon flux and high pulse energy [54] within the compact footprint of the EuPRAXIA@SPARC_-LAB facility. At the system-engineering level, the architecture prioritizes modularity, enabling smooth switching between pure RF operation and the combination of RF with plasma acceleration

and supporting upgrades such as higher-energy plasma stages or seeded FEL configurations [55].

These design principles form the foundation for meeting the stability, reproducibility, and performance requirements expected of the EuPRAXIA@SPARC_LAB user facility.

EuPRAXIA@SPARC_LAB, in its first phase, will deliver a 1 GeV electron beam to generate, within the **AQUA beamline**, ultrashort ($<$ 10 fs), high-brightness X-ray pulses in the water-window spectral range (3–5 nm) via the SASE FEL mechanism. **The facility is expected to begin operations in 2031**.

1.4 The AQUA FEL in the International context

A comparative snapshot of leading short-wavelength FELs user facilities worldwide is shown in Table 1.1, profiling them by location, operational wavelength range, accelerator length, electron beam energy, RF band and key capabilities, including the proposed EuPRAXIA@SPARC_LAB FEL beamline named AQUA.

While major facilities like LCLS, European XFEL, and PAL-XFEL require linac drivers that approach kilometer length and operate at multi-GeV energies to access the hard X-ray regime, EuPRAXIA@SPARC_LAB takes a different approach:

- **Moderate Energy with High Impact**: Operating at 1 GeV, will deliver soft X-rays radiation in the "water window". This range is crucial for imaging biological specimens in aqueous environments, allowing measurements in almost native conditions, positioning AQUA as a valuable tool for structural biology, chemistry, and material science.
- **Compact Design**: With an accelerating length shorter than 50 meters, it is the most compact facility in the soft X-rays list, at least by a factor 3. This reflects its use of the combination of high-gradient X-band linac technology and plasma acceleration. Compact accelerator footprint reduces the need for large-scale infrastructure and land use.
- **Technology Demonstrator and R&D bench for plasma acceleration**: it will be also a strategic testbed for integrating advanced acceleration schemes and short period undulators into user-oriented FELs marking a paradigm shift toward compact and cost-effective light sources.

Aligned with the EuPRAXIA mission, EuPRAXIA@SPARC_LAB aims to broaden access to ultrafast X-ray science while enhancing sustainability by significantly reducing facility size, energy consumption, and operational costs.

1.5 FEL Scientific Case and Applications

The AQUA beamline of EuPRAXIA@SPARC_LAB will open a scientific window onto the ultrafast world of atoms, molecules, and soft condensed matter. Able to operate in the **3.2–10 nm** spectral region with the current foreseen hardware, with **nominal performance in the 3.2–5.2 nm water-window range** as supported by start to end simulations, AQUA will deliver intense, femtosecond soft X-ray pulses ideally suited to probe matter on its natural spatial and temporal scales. With pulse durations **shorter than 10 fs** and more than $\mathbf{10^{11}}$ **photons per shot**, the beamline will provide the essential conditions to explore electronic and structural dynamics with high temporal resolution, complementing existing soft X-ray FELs and enabling studies not feasible at synchrotron sources.

Consistent with the implementation strategy outlined in Chapter 22, AQUA will adopt a **phased approach** that supports both the scientific program and the accelerator development goals:

- **Phase 0**: commissioning on fixed, calibration samples, to allow beam and detectors characterization and alignment.
- **Phase 1**: first user experiments in the gas phase, focused on Atomic, Molecular, and Optical (AMO) physics and simple model systems.

Table 1.1: Major Short-Wavelength FEL User Facilities

Facility	Location	Wavelength [nm]	Linac [km]	Energy [GeV]	RF (MV/m)	Key Features
Soft X-rays radiation						
AQUA	Frascati, Italy	3.2 – 10	<0.05	1.0	X/Plasma (60/1000)	Compact facility; targets the water window.
FLASH [56, 57]	Hamburg, Germany	4.1 – 45	0.2	1.25	L (30)	Pioneering SASE FEL; testbed for SC RF and FEL technologies.
FERMI [58]	Trieste, Italy	10 – 100	0.15	1.67	S (28)	Seeded FEL; very high spectral purity in VUV – soft X-ray region.
SXFEL [59]	Shanghai, China	1.2 – 24	0.3	1.5	S / C (27/38)	First Chinese soft X-ray FEL; seeded + SASE operation.
Hard X-ray radiation						
LCLS 1 [60]	SLAC, United States	0.13 – 6.2	1.0	14	S (25)	First hard X-ray FEL; ultrafast imaging capabilities.
European XFEL [61]	Hamburg, Germany	0.05 – 4.7	2.1	17.5	L (24)	High rep-rate; multi-beamline architecture.
SACLA [62]	Harima, Japan	0.06 – 0.2	0.4	8.5	C (38)	Compact design; hard X-ray operation.
SwissFEL [63]	Villigen, Switzerland	0.1 – 5.0	0.5	5.8	C (28)	Two beamlines covering soft + hard X-ray.
PAL-XFEL [64]	Pohang, South Korea	0.06 – 4.5	0.78	10	S (27)	Covers both soft and hard X-ray.
SHINE/ HXFEL [65]	Shanghai, China	0.06 – 0.3	1.2 – 1.5	8 – 12	S (27)	High-repetition-rate hard X-ray FEL; multibeamline; under commissioning.

- **Phase 2**: expansion to condensed-phase samples, including liquid jets and aerosol injectors, enabling Warm Dense Matter (WDM) studies and imaging of hydrated biological specimens.

This roadmap ensures that the scientific program evolves coherently with the technological readiness of the facility while maintaining a clear focus on experiments that are tightly linked to the accelerator's performance evolution.

AQUA's scientific reach is enabled by an extensive set of experimental techniques, presented in detail in Scientific Case Chapter 2. Among these are:

- **Coherent Diffraction Imaging** (CDI) for lensless, native conditions reconstructions of biological and soft-matter samples.
- **Ion and electron spectroscopies**, such as velocity-map imaging and momentum-resolved detection, to study fundamental processes in isolated molecules and clusters.
- **X-ray Absorption and Emission Spectroscopies** (XAS/XES) for element-specific probing of ultrafast electronic and structural dynamics (on a longer time scale in phase 2).

This combination of approaches enables researchers to investigate systems ranging from isolated atoms to complex biological assemblies, all within a unified, flexible beamline architecture. The following Tab. 1.2 outlines the main application areas, along with their corresponding scientific focus, the experimental techniques employed, the anticipated key impact and the planned Phase (1 or 2) as extensively discussed in Scientific Case Chapter 2 and Experimental End-Station Chapter 10.

Table 1.2: Main application areas, associated scientific focus, experimental techniques, expected impact, and planned implementation phase.

Application Area	Scientific Focus	Techniques	Phase	Key Impact
Atomic, Molecular, and Optical Physics	Ultrafast electron dynamics, core-level excitation, fragmentation pathways	Time-resolved photoabsorption, photoemission, ion/electron spectroscopy (time-of-flight (TOF), velocity map imaging (VMI)), Coulomb explosion imaging	**P1**	Fundamental insights into charge migration, excited-state dynamics, and molecular structure
Ion & Electron Spectroscopy (Gas Phase)	Ionization and fragmentation of molecules, clusters, aerosols; selected environmental and astrochemical model systems	Photo-ionization mass spectroscopy (PI-MS), TOF detectors, momentum imaging	**P1**	Proof-of-principle user experiments; benchmarking FEL performance and machine stability
Warm Dense Matter	Non-equilibrium states, ultrafast structural transitions, electron–ion equilibration	Time-resolved XAS/XES	**P2**	Advances in planetary science, dense plasmas, and fusion-relevant materials
Biology & Soft-Matter Imaging	CDI of hydrated biological specimens (viruses, macromolecular assemblies)	CDI, and single-pulse "diffraction-before-destruction"	**P2**	High-resolution reconstructions in the water window; foundations for future bio-imaging program

The main foreseen application areas are:

- **Atomic and Molecular Physics and Gas-phase Systems**: In its first phase of operation,

AQUA will primarily support experiments in **AMO physics** with a particular focus on **gas-phase systems**, an area in which soft X-rays and ultrafast temporal resolution provide powerful and versatile tools. Using techniques such as time-resolved soft X-rays absorption, photoemission, ion and electron momentum spectroscopy, and Coulomb explosion imaging, it will be possible to track the evolution of excited molecular states, map ultrafast charge migration, and resolve fragmentation pathways with elemental and site specificity. These studies take full advantage of the coherence and peak brilliance of the AQUA FEL, allowing researchers to observe the evolution of electronic wavepackets or transient molecular structures with femtosecond precision. As described in Chapter 2, this class of experiments forms the natural starting point of the scientific program, requiring limited infrastructure while offering high scientific impact.

- **Warm Dense Matter**: As the facility matures, AQUA will extend its reach to the study of **WDM**, a regime of extreme temperature and density relevant to planetary interiors, inertial confinement fusion, and ultrafast solid–plasma transitions. In this domain, soft X-ray absorption and emission spectroscopies, performed with femtosecond pump–probe sequences (using a dedicated **Ti:sapphire femtosecond laser system** (30 fs, $\sim$10 mJ), with an OPA tunable from 200 nm to 20 μm), offer a uniquely sensitive probe of the transient structural and electronic changes that occur as materials pass through non-equilibrium states. The brightness of AQUA and its tunability within the water-window make it possible to study electron-ion equilibration, short-range order, and the evolution of local atomic environments on sub-picosecond timescales. These experiments, identified as Phase-2 activities in Chapter 2, will contribute to bridging the gap between theoretical models and experimental measurements in this challenging and technologically relevant regime.
- **Biology and Soft Matter**: Within the water window, carbon-rich biological samples exhibit strong natural contrast against their aqueous environment, making coherent diffraction imaging (CDI) an exceptionally powerful technique. Using the "diffraction-before-destruction" principle demonstrated at several FELs worldwide, AQUA will enable high-resolution imaging of biological specimens such as viruses, macromolecular assemblies, and hydrated cellular structures. Chapter 2 presents simulations performed using AQUA's expected photon parameters, showing that single-particle imaging of objects in the sub-micrometer range is feasible at design performance. In later phases, the facility may also support time-resolved imaging of radiation damage, membrane dynamics, or conformational changes, although these more advanced biological studies will be developed progressively as beam stability and diagnostic capabilities are refined.

1.6 Machine Expected Performances

Based on extensive start to end beam dynamics studies (Chapter 3), the nominal electron beam and FEL parameters are reported in Tab. 1.3. The facility is designed to operate in two fully complementary modes:

- **PWFA Mode**: The X-band linac generates the 550 MeV driver-witness bunches to be injected into the plasma-wakefield acceleration stage, whose goal is to boost the witness bunch energy up to 1 GeV. This configuration represents the core technological demonstrator for plasma-based FEL user operation and fulfills the ESFRI requirement that EuPRAXIA be implemented as a plasma-accelerator–driven research infrastructure.
- **Full RF Mode**: The X-band linac accelerates the beam to 1 GeV, as required for FEL operation, using a single-bunch configuration that bypasses the plasma module. This provides a mature and reliable acceleration pathway for initial commissioning, early user operation, subsystem benchmarking, and performance validation. Notably, it will also be the first 1 GeV X-band–based user facility.

While the **PWFA mode defines the ESFRI-compliant baseline**, the facility is conceived with broad versatility. Applications and experiments that do not rely on plasma acceleration will also be supported, thereby broadening the scientific reach of EuPRAXIA@SPARC_LAB and reinforcing its role as a flexible, high-performance user facility. In its initial phase, the facility will operate at a **repetition rate of 100 Hz**, with a planned upgrade to 400 Hz in a future phase.

Table 1.3: Electron beam and FEL radiation main parameters at the undulator entrance for the two considered machine configurations: plasma acceleration (PWFA) and conventional (Full RF) one. For both the two configurations we reach saturation inside the undulator length at $\lambda_r = 4$ nm with the expected number of photons per second.

	Units	**PWFA** Velocity bunching	**Full RF** Velocity Bunching + Magnetic Compression
Electron Energy	GeV	1	1
Repetition Rate	Hz	100	100
Bunch charge	pC	30	200
Peak current	kA	3.3	3.4
RMS bunch length	μm	1.4	16.9
RMS normalized emittance (x,y)	mm mrad	0.7, 0.7	2.1, 1.0
RMS energy spread	%	0.5	0.2
Slice length	μm	0.5	0.5
Slice normalized emittance (x,y)	mm mrad	0.7, 0.7	0.3, 0.3
Slice energy spread	%	0.04*	0.02
ρ 3D	$\times 10^{-3}$	0.77	1.49
Radiation wavelength	nm	4.06	4.06
Saturation length	m	20.5	20.0
Photon Pulse Energy	μJ	16	150
Photon per pulse	$\times 10^{11}$	3.2	31.3
Photon pulse length (FWHM)	fs	2.33	33.0
Photon bandwidth	%	0.4	0.5
Average photon brilliance	$\#\times 10^{30}$	0.12	2.1

#= N_{phot}/s/m^2/rad^2/0.1%bw.
* Calculated with the 5 % cut of off-energy charge, not lasing, see details in FEL performances Section 3.2.5.

Some key features that emerge from the table are the following:

- The **parameters represent the fully consistent working point** obtained by start-to-end simulations from the photocathode to the end of the AQUA undulator, including RF jitters, transport optics, plasma acceleration and collective effects. These values therefore correspond to an experimentally achievable configuration rather than ideal design numbers.
- The **beam quality** at the undulator entrance **satisfies** all requirements for **SASE lasing**, with slice emittance < 1 mm mrad, slice energy spread $\approx 0.04\%$, and peak current ≥ 3 kA. These values place the EuPRAXIA@SPARC_LAB working point well within the region of acceptable FEL gain length, as shown in the FEL performance maps of Chapter 3 and

Chapter 8.

- The **PWFA** and the **Full RF** configurations provide **complementary FEL operating regimes**. The PWFA option delivers electron beam and FEL parameters that are fully adequate for a significant class of scientific applications, while prioritizing compactness and cost effectiveness, and it therefore constitutes the baseline solution for future energy upgrades. The Full RF configuration, instead, ensures robust Day-1 operability up to 1 GeV and offers enhanced photon pulse energy through its capability to accelerate higher-charge electron bunches, thereby extending operational flexibility.
- The nominal beam energy of 1 GeV and undulator K parameter **allow tuning over the 3.2 - 5.2 nm range**. This range partially covers the water window, including the carbon K-edge at ≈ 4.35 nm and other biologically relevant wavelengths. Energy variations from 720 MeV to 1.25 GeV further extend in principle the accessible range to 10–2 nm, as shown in Fig. 3.19.
- The repetition-rate upgrade **from 100 to 400 Hz** is already anticipated in the RF, Plasma and infrastructure design (Chapter 18). This upgrade will increase average brightness by almost one order of magnitude and is compatible with the thermal load and refresh time of the plasma capillary [66].
- The listed photon-beam parameters (pulse energy, brilliance, bandwidth) refer to the **tapered undulator configuration**, which is the reference working point for AQUA (see Chapter 3 and Chapter 8). Tapering is adopted to enhance output power within the same undulator length.
- All parameters reported in the table represent the reference working points around which a **statistical analysis** has been performed, including the effects of expected jitters in RF phases, laser arrival times, and synchronization(Chapter 14).

These values therefore reflect realistic user-facility operation. These parameters demonstrate that the EuPRAXIA@SPARC_LAB facility satisfies all beam-quality requirements for SASE operation at 4 nm.

Figures 1.4 and 1.5 provides a comparative overview of the FEL simulation results for the two reference working points described in Table 1.3 — PWFA (Figure 1.4) and Full RF (Figure 1.5) — both optimized with undulator tapering. The figure illustrates how the two acceleration configurations perform in terms of FEL gain, pulse structure, and spectral properties.

1.6.1 FEL Radiation Stability

EuPRAXIA@SPARC_LAB is designed around a target shot to shot **electron beam energy stability requirement of $\approx$ 0.1–0.2% rms** at the undulator entrance for the Full RF mode and **<1% rms** for the PWFA mode.

The stability of the FEL wavelength is directly linked to the stability of the accelerator parameters that determine the resonance condition inside the undulator. The resonant wavelength [52]: $\lambda_r = \lambda_u/(2\gamma^2)(1+K/2)$ which relates the emitted radiation wavelength λ_r to the undulator period λ_u, the undulator parameter K and the electron beam energy γ, is particularly sensitive to variations of γ, with a quadratic dependence such that a relative energy jitter $\Delta\gamma/\gamma$ produces approximately twice as much wavelength jitter ($\Delta\lambda/\lambda \approx 2\Delta\gamma/\gamma$). This makes **electron beam energy stability** the dominant requirement for reliable FEL operation. In EuPRAXIA@SPARC_LAB, start-to-end simulations (Sections 3.2.6 and 3.3) show that the expected energy jitter from the RF linac and from the plasma acceleration stage leads to a wavelength fluctuation of the order of 0.2–2%, depending on the operating mode (Full RF vs PWFA). In the PWFA configuration, the larger shot-to-shot energy jitter is addressed through **systematic single-shot photon diagnostics and energy tagging** [67], enabling post-acquisition sorting and correlation-based data analysis. This operational approach, already adopted at SASE FEL facilities [68], ensures that the PWFA mode delivers scientifically robust and exploitable photon beams despite intrinsically larger fluctuations and is fully aligned

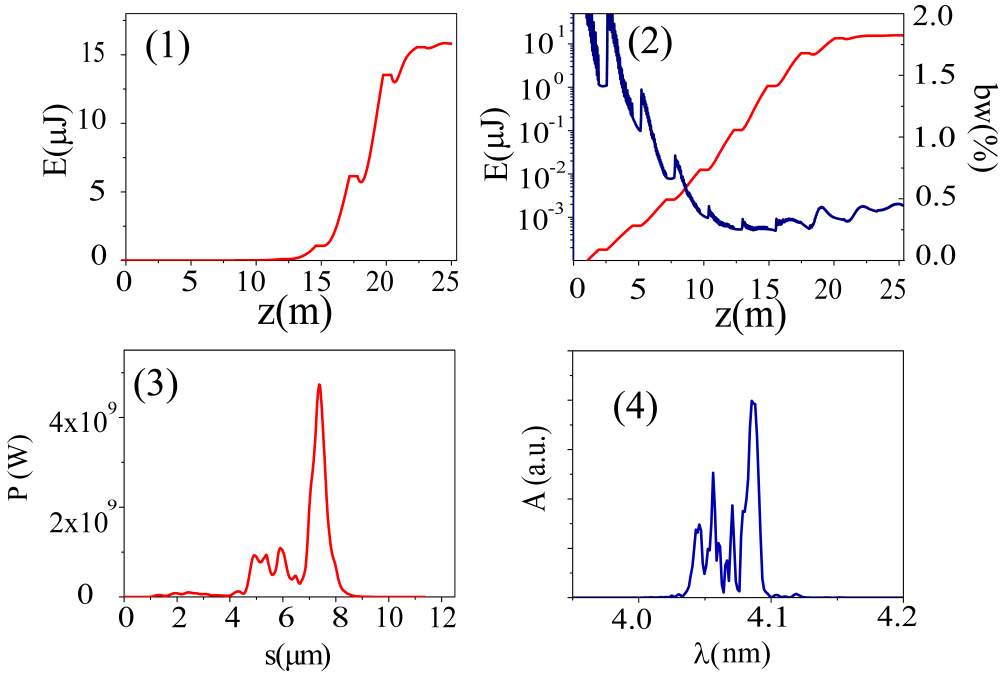

Figure 1.4: Genesis simulation results for PWFA working points with Undulator Tapering, Plot (1): energy growth in linear scale. Plot (2): energy growth in logarithmic scale and bandwidth in %. Plot (3): power distribution. Plot (4): amplitude of spectral distribution.

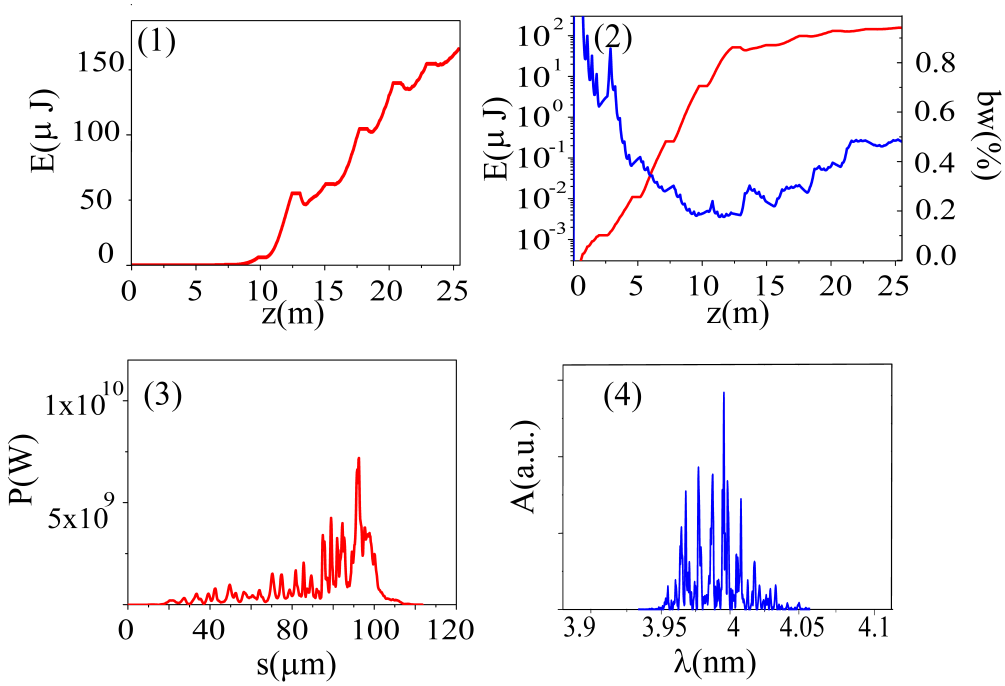

Figure 1.5: Genesis simulation results for Full RF working points with Undulator Tapering, Plot (1): energy growth in linear scale. Plot (2): energy growth in logarithmic scale and bandwidth in %. Plot (3): power distribution. Plot (4): a smplitude of spectral distribution.

with the operational model as elaborated in the EuPRAXIA Preparatory Phase user studies and access policy reports [69, 70].

A specific consideration applies to the PWFA configuration, where **plasma density fluctuations** directly affect the accelerating gradient and thus the final beam energy. Because the witness energy gain scales with the plasma frequency, a relative density variation $\Delta n/n$ translates into a comparable relative variation in energy ($\Delta\gamma/\gamma \approx \frac{1}{2}\Delta n/n$ for the operating regime considered), making shot to shot plasma density stability the key contributor to the FEL wavelength jitter. Driver–witness **delay jitter** introduces a similar sensitivity, as timing errors modify the phase at which the witness samples the wakefield. The design, characterization, and stabilization strategies for the 60 cm plasma module — including discharge control, gas-feed uniformity, and shot-to-shot reproducibility — are described in detail in Section 7.2 and their effect on FEL wavelength stability is quantified in the jitter analysis of Section 3.2.6. The expected plasma density stability is: $\Delta n/n \leq$ **1% rms**, and the driver–witness delay jitter: $\leq$ **10 fs rms**. Further improvements in shot-to-shot plasma stability are identified as an important objective for reliable long-term operation and user exploitation. In this context, the ongoing experimental and R&D activities at the SPARC_LAB facility provide a controlled environment for systematic validation, optimization, and risk mitigation of plasma-source stability, constituting a key contribution to the maturation of PWFA technology for of EuPRAXIA. The new facility EuPRAXIA@SPARC_LAB will allow investigating and reducing the energy/wavelength jitters.

Other accelerator parameters play a secondary but important role in preserving the spectral purity and shot-to-shot reproducibility of the FEL. Variations in the undulator parameter K, driven by mechanical vibrations of the gap, introduce direct shifts of the resonant wavelength at the 10^{-3} level, and are controlled through the high-precision magnetic and mechanical systems described in Section 8.3. Beam emittance, beta-function matching, and trajectory jitter do not significantly shift the central wavelength, but they strongly influence the gain process and thus the effective spectral width. Their impact on FEL performance is documented through tolerance studies in Section 3.2.6 and detailed undulator-lattice analyses in Section 8.4. Fluctuations in peak current, slice energy spread, and longitudinal chirp, produced respectively by shot to shot fluctuations of the electron beam parameters translating in bunch compression and plasma energy gain fluctuation, also affect the FEL bandwidth, with mitigation strategies described in Section 5.2, Section 3.4, and Section 3.2.5. The complete set of jitter analyses, tolerance budgets, and mitigation strategies supporting FEL wavelength stability are presented in Beam Physics Chapters 3 and FEL and Undulators Chapter 8, with complementary information for the injector (Chapter 5), RF linac (Chapter 6), and Plasma Stage (Chapter 7).

The statistical analysis described in Section 3.2.6 has been performed considering an ensemble of 100 electron beams accelerated in the PWFA mode each affected by jitter and alignment errors. The results reported in Figure 1.6 shows the photon number versus wavelength for each event, with and without tapering. The rms wavelength jitter results to be about 2% as expected ($\Delta\lambda/\lambda \approx 2\Delta\gamma/\gamma$).

More than 85% of the events exceed 10^{11} photons without tapering, while this fraction increases to 95% when tapering is applied. These findings highlight the robustness of the design and identify the most critical tolerances, particularly timing and energy jitter, that require careful stabilization and monitoring.

1.7 Machine Layout

The machine architecture integrates high-gradient accelerator modules, precision magnetic optics, state-of-the-art diagnostics, and photon transport systems into a coherent infrastructure optimized for both performance and flexibility. Each segment of the machine has been designed to preserve

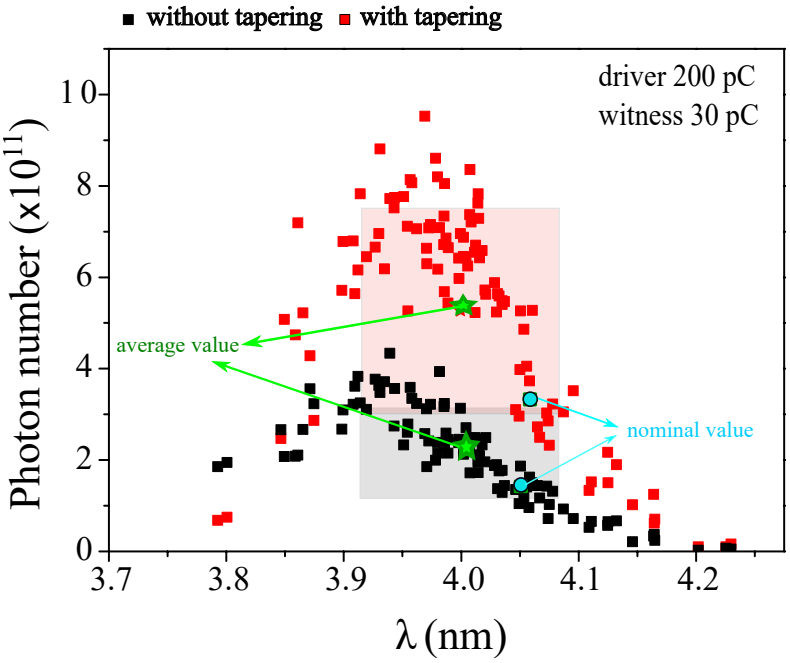

Figure 1.6: Photon number versus wavelength for 100 random events of the reference case at 1 GeV. Black squares: without tapering. Red squares: with a tapering with the K_{rms} values of Table 3.8. Green stars represent the average values. Cyan circles represent the values obtained with the reference beams. The shaded areas (light gray for the case without tapering and light pink for the case with tapering) around the average values have the half hight equal to the rms deviation of the photon number (1 and 2.33×10^{11}) and the half bases equal to the rms deviation of the peak wavelength (85 pm).

emittance, minimize energy spread, and support high-repetition-rate (100 Hz) FEL operation in both Full RF and PWFA modes. See Chapter 4 for more details.

This machine layout implements the baseline design validated in beam dynamics, plasma physics and FEL performance simulations (Chapters 3 - 8), and supports PWFA operation to demonstrate the first plasma-accelerated soft X-ray FEL under user-facility conditions.

The layout of the EuPRAXIA@SPARC_LAB machine is schematically illustrated in Fig. 1.7.

The main sections and components of the facility are briefly outlined below and with more details in Chapters 5 to 10.1:

- **RF Photo-Injector** (Chapter 5): The injector comprises a 1.6-cell S-band (2.99855 GHz) RF gun equipped with a copper photocathode and a solenoid, capable of producing low-emittance electron bunches with initial energies of 5.5 MeV. Both the driver and witness bunches are generated within the same RF bucket and accelerated by four S-band accelerating structures up to the injection in the X-band Linac. By operating the first two structures off-crest, the bunches can be velocity-compressed reaching energies of approximately 120 MeV that is actually the current operating mode of the SPARC_LAB photo-injector. If all four structures are run on-crest, as possibly required in the case of using magnetic compressions only, the beams can be accelerated up to a maximum energy of about 250 MeV.
- **X-band Linac** (Chapter 6): The linac comprises 16 high-gradient 90 cm long accelerating

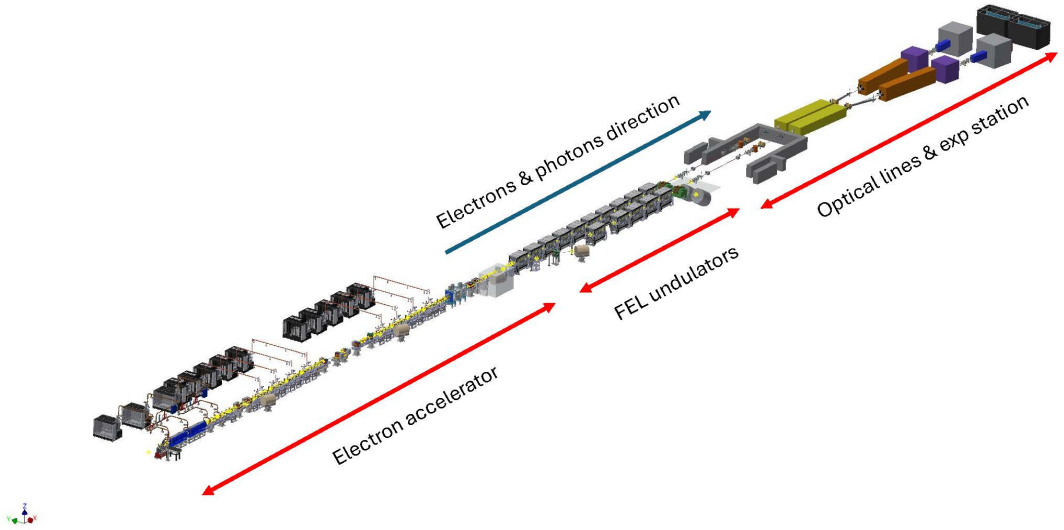

Figure 1.7: Layout of the accelerator and beamlines

structures operating at X-band (11.9942 GHz). At their maximum power, these structures operate at an accelerating field of 60 MV/m, enabling acceleration of the beam up to 1 GeV, sufficient to directly drive the FEL without the use of the plasma stage. When the plasma module is employed, the linac can be operated at a reduced gradient of 30 MV/m, delivering a total beam energy of ∼550 MeV, including ∼120 MeV from the injector, which is subsequently boosted by the plasma stage to meet the nominal 1 GeV FEL energy requirement. The beamline is equipped with essential components including quadrupoles, beam diagnostics, trajectory correctors and a magnetic bunch compressor.

- **Plasma Module** (Chapter 7): Positioned downstream of the X-band linac, the plasma stage consists of a 60 cm long plasma channel, including 10 + 10 cm of in/out density ramp, generated within a gas filled (Nitrogen) discharge capillary (operating at 10-50 mbar gas pressure and a voltage of 5-25 kV). In this section, the plasma wakefield boosts the witness bunch from ∼550 MeV to energies reaching the nominal 1 GeV with an accelerating field of ∼1 GV/m (and possibly beyond) in the 40 cm active length. Critical components includes a dedicated vacuum chamber, plasma diagnostics, electron spectrometers, and appropriate radiation shielding. Driver and witness are separated in a dispersive section of a dedicated magnetic chicane with a septum magnet at the exit of the plasma vacuum chamber.
- **Transport and Matching Sections** (Chapter 3): Upstream and downstream the Plasma Module beam matching is achieved using Permanent Magnet Quadrupoles, providing focusing gradients up to 510 T/m. Downstream Transport section ensures proper beta function and phase-space matching into the undulator while maintaining beam trajectory within tight tolerances ($\leq$10 μm).
- **Undulator Line** (Chapter 8): The design foresees 10 planar undulator modules on the APPLE X permanent magnet configuration, each module is 2 m long interleaved with a 60 cm long sections hosting diagnostics and quadrupoles. The baseline undulator has an 18 mm period, 1.5 mm minimum gap, and consists of Neodymium-Iron-Boron magnets arranged to allow both linear and circular polarization with tunable wavelengths.
- **Photon Beamlines** and **End-Stations** (Chapters 9 and 10): The radiation emitted in the

SASE process is extracted and directed via grazing-incidence optics to the experimental stations. Beamlines include focusing mirrors, attenuators, shutters, and diagnostics for intensity, spectrum, and profile measurements. Experimental end-stations are equipped for coherent imaging, time-resolved spectroscopy, and sample manipulation with sub-micron precision.

This modular beamline layout allows for staged commissioning, ease of maintenance, and future upgrades such as seeding schemes, higher energy plasma stages, or additional user beamlines.

1.7.1 Technology Readiness Levels

The Technology Readiness Levels (TRL) of the main components are summarized in Table 1.4, based on the detailed assessments provided in the corresponding reference chapters. Each subsystem chapter contains a dedicated section where the technological maturity of its components is assessed according to the TRL definitions [71] adopted by the European Commission for research infrastructures (see Appendix A). The TRL values were aggregated into a single table, providing a coherent snapshot of the technological maturity of all major components of EuPRAXIA@SPARC_LAB.

Table 1.4 highlights the need for continued R&D efforts focused on both plasma and X-band technologies, which are currently underway at LNF. Two dedicated test facilities, **SPARC_-LAB** [72] and **PLASMA_LAB** [66], are actively supporting the development and validation of plasma acceleration concepts , while the **TEX** [73] facility is dedicated to high power testing of X-band performance. Achieving an overall TRL above 7 for these subsystems will only be possible following the successful construction and operation of the EuPRAXIA@SPARC_LAB facility which is one of the scientific goals of the project.

1.7.2 Contribution of SPARC_LAB to EuPRAXIA

A substantial part of the credibility and technical maturity of the EuPRAXIA research infrastructure is rooted in the long-standing experience of **SPARC_LAB at INFN–LNF**, which for more than two decades has operated as a leading European test facility for high-brightness electron beams, advanced beam physics, and novel radiation sources [74]. SPARC_LAB has demonstrated Free-Electron Laser operation from the visible to the extreme-ultraviolet, culminating in the first FEL lasing driven by a plasma-accelerated electron beam [16, 17], a landmark result that directly underpins the EuPRAXIA concept and provides a key element of technical risk mitigation [75]. SPARC_LAB combines a mature S-band photo-injector [76] with extensive expertise in C-band and high-gradient accelerating structures, state-of-the-art beam diagnostics [77], and the FLAME high-intensity laser [78], enabling comprehensive investigations of both beam- and laser-driven plasma acceleration schemes. Within this framework, SPARC_LAB operates as a dedicated test bench for innovative plasma concepts [79–81], including high-stability discharge capillaries [82], controlled density ramps, tailored plasma profiles, beam-loading optimization, and advanced injection schemes [83], providing critical experimental input for the realization of reproducible plasma accelerator stages. In addition, SPARC_LAB will hosts by the end of 2026 the EuPRAXIA Advanced Photon Source, a laser–plasma betatron radiation beamline fully integrated into the EuPRAXIA roadmap and identified as one of its flagship early user facilities [84]. **EuAPS** will deliver ultrashort, broadband soft X-ray pulses and will represent the **first operational implementation of EuPRAXIA** as a distributed research infrastructure [1], providing early user access while validating plasma-based photon sources in a user-oriented framework. In addition, EuAPS will be spectrally complementary to EuPRAXIA, extending the accessible photon energy range towards hard X-rays, while EuPRAXIA will mainly address the water-window region. The laboratory has also developed the **SABINA THz FEL** beamline [85], currently in the installation and commissioning phase, employing **APPLE-X undulators** of the same type foreseen for EuPRAXIA@SPARC_LAB. This ensures direct technological validation and continuity of the undulator solution adopted for the

Table 1.4: TRL level of the main components

Sub - systems	TRL	Comments
Injector	9	S-Band injectors are widely used in many facilities including SPARC_LAB. S-Band technology is fully available in the market.
X-Band Linac	6	X-Band Linacs are relatively new. Impressive progress has been made. The final testing of the accelerating section prototype will upscale the corresponding TRL level in the upcoming months.
Plasma Module	5	Extensive R&D has been made to validate the plasma capillary technology and solid results have proved the validity of the technical choice. A full system proven in a real environment is expected to be done in the next year.
AQUA Undulators	7	Technology demonstrated in other facilities (FERMI, SwissFEL, etc.).
FEL Beamline	8	Most of the components of the photon beamline are implemented at other facilities and are commercially available. Few systems (needed only for a subset of possible experiments) are still in development.
RF power system	8	X-Band RF power system has been already tested and operated in normal condition in the test-stand. The final operational test will prove the validity and reproducibility of the technical choices in the real setting, including control of amplitude and phase jitters.
Timing and Synchronization systems	7	A similar system has been in operation at SPARC_LAB since 2006 on S-band RF power stations and has been tested on the C-band station using solid state modulator. Tests are planned at TEX to confirm the compliance on the X-band RF stations using the same architecture of EuPRAXIA@SPARC_LAB.
Laser system	9	Photocathode laser is now a proven technology tested in real facilities (including SPARC_LAB). The systems are fully available on the market almost as off-the-shelf products.
General elements	9	Other elements (Control, mechanics etc.) are based on standardized components daily used in other facilities and in other contexts (e.g. industrial).

EuPRAXIA user facility [86].

1.8 Electron and Photon Beam Diagnostics

EuPRAXIA@SPARC_LAB relies on an integrated suite of electron- and photon-beam diagnostics to monitor the beam quality and stability required for reliable FEL operation.

As summarized in Table 1.5, the electron-beam diagnostics distributed along the injector, linac, plasma module, and undulator provide shot-to-shot measurements of the electron beam parameters governing FEL performance—charge, energy, energy spread, emittance, peak current, bunch length and spot size, and arrival time. These instruments enable continuous verification of the electron beam parameters defined in Chapter 3 and support machine protection, feedback, and automated optimization.

Complementing this, the AQUA beamline incorporates a complete photon-diagnostic chain (see

Table 1.5: Electron Beam Diagnostics

Function	Diagnostic Tools	Main Measured Quantities	Typical Resolution / Performance	TDR Reference
Charge Measurement	ICTs, Faraday Cup	Bunch charge, dark current discrimination	pC-level accuracy	Sec. 11.2.1, 11.2.2
Beam Position & Trajectory	Stripline BPMs, Cavity BPMs	Beam orbit, shot-to-shot jitter	tens of µm → sub-µm	Sec. 11.2.3, 11.2.4
Transverse Beam Profile & Emittance	View screens (OTR / YAG), Emittance stations, Wire scanner	Beam size, Twiss parameters, emittance	few µm; ~ 0.3 mm mrad	Sec. 11.2.5, 11.2.6, 11.2.11
Energy & Energy Spread	Magnetic spectrometers	Beam energy, ΔE/E before & after plasma	O(10 keV), $\Delta E/E \sim 10^{-4}$	Sec. 11.2.7
Longitudinal Phase Space & Timing	TDS (PolariX), EOS, CDR monitor	Bunch length, chirp, driver–witness delay	fs-class	Sec. 11.2.8, 11.2.9, 11.2.10
Plasma-Related Diagnostics	Plasma entrance OTR, wire scanner, Balmer-line spectroscopy*, fast optics*	Witness/driver transverse size, plasma density, discharge uniformity	few µm (beam); sub-% plasma density*	Sec. 11.2.11; *plasma tools in Ch. 7
Machine Protection	Cherenkov Beam Loss Monitors	Localized beam losses, halo, mis-steering	cm localization	Sec. 11.2.12
Digital Acquisition & AI Tools	Digitizers, AI-based virtual diagnostics	Real-time data capture, virtualized beam parameters	3.2 GS/s, 12-bit; ML resolution varies	Sec. 11.5

Table 1.6) that measures pulse energy, spectrum, arrival time, spatial profile, wavefront, coherence, and polarization with high accuracy. These observables provide direct, physics-relevant feedback on FEL performance, allowing rapid identification of drifts and enabling fine tuning of accelerator and undulator settings.

Table 1.6: Photon Pulse Diagnostics

Function Group	Diagnostic Tools	Measured Photon Quantities	Typical Resolution / Performance	TDR Reference
Pulse Energy & Intensity Monitoring	Gas Intensity Monitors, Photodiodes, View Screens	Pulse energy, shot-to-shot intensity	Sensitivity: 10^9 photons; sub µJ-level pulse energy	Sec. 9.4.1, 9.4.2, 9.4.5
Spectral & Temporal Diagnostics, Wavefront & Polarization Measure	Spectrometer, Transient Reflectivity ToA, Wavefront Sensor, Linear Polarimeter, Radial ion. ToF, THz Streaking	Spectrum, arrival time, pulse duration, wavefront errors, polarization	$\Delta\lambda/\lambda \approx 3 \cdot 10^{-5}$; timing ~ 10 fs, $\lambda/10$ wavefront; 1° polarization	Sec. 9.4.4, 9.4.5, 9.4.6,
Spatial Profile & Pulse positioning Diagnostics	View Screens, Bladed BPMs, Gas Intensity Monitors	Transverse profile, divergence, position, direction	µm size & position, µrad direction & divergence	Sec. 9.4.1, 9.4.2, 9.4.3
Coherence Diagnostics	Double-Slit and Michelson Interferometer, Spectrometer	Transverse coherence, longitudinal coherence, FEL mode properties	10% coherence resolution	Sec. 9.4.4, 9.4.7

Together, the diagnostics listed in Tables 1.5 and 1.6 form a unified, shot-to-shot monitoring system that stabilizes both the electron beam and the FEL output, ensuring the reproducibility and spectral purity required for demanding soft-X-ray user experiments.

1.9 Other Technical Sub-Systems Supporting Operational Reliability

Beam dynamics investigation also set the requirements for other important technical sub-systems whose contributions have been investigated to ensure operational stability and, ultimately, FEL wavelength reproducibility. These systems act by reducing jitter sources, improving environmental and mechanical stability, and ensuring reliable and repeatable beam quality transport from the photocathode to the undulator. Key features are described hereafter, for a more detailed description refers to the dedicated Chapters indicated in the brackets. Overall, **the proposed Sub-Systems meet beam dynamics specifications**, with most subsystems at high TRLs.

- **Laser Systems (Chapter 12):** Three laser subsystems contribute to machine performance and user capabilities: the **photocathode laser**, the **laser heater**, and the **pump laser for user science** at the AQUA endstation. The **photocathode laser** defines the initial beam phase space and must ensure sub-percent energy stability, few-µrad pointing stability, and timing jitter below ∼10–20 fs with respect to the RF. Operating at 266 nm and 100 Hz, it provides up to ∼2 mJ on the cathode and supports multi-pulse configurations required for PWFA external injection. Its Chirped Pulse Amplification architecture allows precise control of pulse duration (down to 35 fs), transverse homogeneity (<10% p-p), and multi-pulse timing (few-fs relative jitter), enabling stable high-brightness beam generation. Enclosed beam-transport lines with active diagnostics maintain long-term position stability (<5 µm). The laser pulse for the **laser heater** is extracted from the first amplifier of the photocathode laser and transported to the chicane where it is required. It uses a dedicated optical transport system to impose a controlled electron beam energy modulation (∼20–40 keV) in a dedicated magnetic chicane. For **Pump and Probe experiments** in the user area, the AQUA endstation includes a dedicated **Ti:sapphire femtosecond laser system** (30 fs, ∼10 mJ), with an OPA tunable from 200 nm to 20 µm. All user lasers are synchronized to the facility's optical master oscillator, ensuring pump–probe timing jitter within a few tens of femtoseconds, with active feedback for fs-level drift correction [87]. Transport optics are enclosed, thermally stabilized, and continuously monitored to guarantee reproducible experimental conditions. The laser pulse arrival time, and in the future also the FEL pulse arrival time, will be monitored on a single-shot basis for post-processing and data sorting.
- **RF Systems (Chapter 13):** Together with the photo-cathode laser the RF is the main source of jitter for the electron beam energy, peak current, and arrival time. RF power delivery is based on **solid-state modulators** for their superior pulse-to-pulse stability, modularity, compactness, and safety. **The Low-Level RF** (LLRF) system provides precise phase and amplitude control for all 13 RF stations (3 S-band, 10 X-band). Plasma external-injection imposes extremely strict jitter tolerances; consequently, the LLRF must limit added phase jitter to $\leq$**0.005° rms** in S-band and $\leq$**0.015° rms** in X-band. Meeting these requirements necessitates custom X-band LLRF development, including high-bandwidth ADCs, temperature-stabilized analog front-ends, and intra-pulse feedback systems capable of fs-level phase correction within a single RF pulse. Table 13.5 presents the full performance specifications.
- **Timing and Synchronization (Chapter 14):** The **timing system** uses an event-based architecture to distribute triggers synchronized with the Reference Master Oscillator through a tree topology network. This approach ensures flexibility, scalability, and low jitter (<35 ps), supporting over 100 trigger points. It employs EVG/EVR modules connected via fiber optics and integrates White Rabbit technology for sub-nanosecond absolute time synchronization. The **synchronization system** ensures the femtosecond-level timing stability that is crucial for controlling the injection phase in the RF structures, the laser-to-RF synchronization at the gun and at the laser heater, and the driver–witness delay in PWFA operation. This also limits the beam arrival-time jitter and it prevents induced energy chirp or peak-current fluctuations directly supporting the stability of beam parameters feeding the undulator. The

synchronization system generates and distributes a high-frequency reference signal (2998.55 MHz) and its 42nd sub-harmonic (71.39 MHz) for laser locking. Reference distribution relies on the leading-edge RF-over-Fiber technology that exploit stabilized optical fiber links with active compensation for environmental changes and guarantees an added jitter below 8 fs RMS. Coaxial cables are used for less critical signals. Both the fibers and the coaxial cables are placed inside thermally and vibration insulated ducts to minimize added drifts and jitters. Optical clients (lasers) require dedicated locking electronics based on Balanced Optical-Microwave Phase Detector, achieving residual jitter below 15 fs RMS. RF systems are stabilized using intra-pulse feedback on klystrons, reducing jitter to less than 10–15 fs. Performance requirements are extremely tight: maximum jitter of 20 fs RMS for lasers and 18–23 fs RMS for RF stations. Critical components such as fiber-stabilized ducts and optical locking systems are under validation.

- **Control System and AI-based Optimization (Chapter 15):** The control architecture provides interlocks, active feedback loops, and machine-learning tools for slow and fast correction of trajectory, energy, phase, and charge fluctuations. The system is designed to meet the demanding requirements of a next-generation plasma-based User Facility: scalability, high performance, maintainability, reliability, and usability throughout decades of operation. All major accelerator components — motors, cameras, vacuum pumps, magnet power converters, RF modulators and LLRF, timing and synchronisation systems, and diagnostic devices — are integrated through standardized EPICS modules. Approximately $\mathbf{10^3}$ hardware devices and $\mathbf{10^5}$ – $\mathbf{10^6}$ Process Variables will be incorporated. The **Services Tier** implements essential functionalities: the **EPICS Archiver Appliance** for massive real-time and historical data handling; the **Alarm Handling** with hierarchical propagation across subsystems; the **Logging** for operational traceability through iocLogServer and CaPutLog; and the integration with the **Machine Protection System**. A major innovation is the integration of **Artificial Intelligence**, used for system-wide anomaly detection, predictive maintenance of RF/magnet/vacuum systems, and reinforcement-learning-based optimization of beam tuning and stability. Examples include time-series forecasting via recurrence plots and Q-learning regulation of beam energy.
- **Vacuum System (Chapter 16):** Stable vacuum conditions reduce outgassing and improve long-term reliability of RF structures. Pressure stability in the plasma area and the undulator vacuum chamber is essential for consistent beam transport. The machine operates in a **fully non-cryogenic ultra-high-vacuum** environment, with pressures across most sections kept between $\mathbf{5 \cdot 10^{-8}}$ **and** $\mathbf{5 \cdot 10^{-9}}$ **mbar**, dominated by hydrogen. The vacuum regime is **conductance-limited**, due to beam pipes apertures as small as 8 – 15 mm in the injector and linac, and down to 5.5 mm inside the undulators. The system is divided into independently pumped regions separated by **all-metal gate valves**, with a vacuum architecture built around **lumped pumping** using NEG pumps, ion pumps, turbomolecular pumps, and manual isolation valves. A dedicated Section (Sec. 16.3.5) is devoted to the **plasma interaction region**, the only part of the accelerator where gas loads are intentionally introduced. Gas injection in the capillary produces pressures of $\sim \mathbf{5 \cdot 10^{-3}}$ **mbar** in the plasma vacuum chamber, with rapid staged reduction to $\mathbf{10^{-9} - 10^{-11}}$ **mbar** using large turbomolecular pumps and intermediate pumping chambers. The **Undulator Section** represents a challenge for the vacuum. With ultra-narrow 5.5 mm diameter and 2 m long chamber, Monte Carlo simulations predict pressures up to $\mathbf{6.5 \cdot 10^{-7}}$ **mbar** for standard copper outgassing. Meeting EuPRAXIA requirements ($\leq 3 \cdot 10^{-6}$ mbar) demands outgassing rate levels $\leq \mathbf{5 \cdot 10^{-10}}$ **mbar L/s cm^2**, making chamber material selection and prototype testing essential.
- **Magnets and Power Converters (Chapter 17):** Quadrupole and steering magnets, powered by stabilized and low-ripple converters, determine the reproducibility of the beta functions and

beam trajectory. Power converters must deliver highly stable, low-ripple currents—typically at the 10^{-4} to 10^{-5} level—to ensure trajectory, optics, and energy stability across the injector, linac, and undulator. High mechanical precision and thermal stability in the magnet supports (Sections 17.2 - 17.8) ensure nm–μm level reproducibility in the beam orbit, limiting trajectory-induced FEL performance degradation (Section 8.4). All magnet families were modeled using **Opera 3D**, with attention to field quality, thermal stability, alignment constraints, and integration within extremely limited longitudinal spaces. Many components draw from established LNF experience (SPARC, SABINA, ELI, BTF), while others — such as the permanent magnet quadrupoles and septum dipole — required new, space-optimized designs. In the **injector**, key elements include the high-stability **gun solenoid**, skew/normal **gun quadrupole**, trajectory-correction steerers, and the long water-cooled solenoids surrounding the S-band accelerating structures for velocity bunching. Quadrupoles and integrated steerers upstream of the laser-heater section provide flexible matching into the chicane. The **Laser Heater** section features four high-field dipoles (up to 1.54 T) enabling both chicane and spectrometer modes, along with a compact sextupole for second-order correction. The **X-band linac** uses standardized steerers and compact water-cooled quadrupoles (100–150 mm length; 30 T/m gradient) placed between structures together with cavity BPMs. The **bunch compressor** incorporates four identical C-shaped dipoles, two quadrupole triplets, one doublet, and a sextupole optimized for chromatic compensation. The **plasma-interaction region** requires a dedicated set of **Tunable Permanent Magnet Quadrupoles** with gradients of **300–510 T/m**, 7 mm apertures, and very short lengths (17–100 mm). These Halbach-array-based magnets provide strong focusing with minimal power consumption and high mechanical compactness. Simulations validate field quality and tunability, and prototyping is underway. Downstream, the **driver–witness separator** employs a four-dipole chicane followed by a high-performance **septum dipole**, enabling clean spatial separation between the GeV-class witness and the lower-energy driver beam. The **undulator line** includes compact air-cooled quadrupoles (40.7 T/m) and lightweight air-core steerers, minimizing magnetic cross-talk with undulator modules and ensuring fast actuation.

1.10 Civil Infrastructure

EuPRAXIA@SPARC_LAB will be constructed within the INFN LNF site, on the southern slope of a small hill as described in **Chapter 18**. Geotechnical surveys confirm the ground is stable and well-suited for precision infrastructure, being composed of layered volcanic soils typical of the Colli Albani region. The site is free from environmental or archaeological constraints, with full planning and construction approvals secured by mid-2023.

The main infrastructure includes a new building of approximately 5,600 m^2, purpose-built to house the accelerator, the FEL, various experimental areas, and supporting technical rooms. It consists of two floors above ground with main vehicular and pedestrian accesses (north-west facade), while, in the upstream part (south-east facade) only one floor above ground provides secondary accesses reserved purely for maintenance. At its maximum extension above ground, the building is approximately 140 m long and 45 m wide, with a narrowing to 36 m towards the north-west; it ends on the ground floor with a rectangular appendix measuring 21 m by 13 m completely underground. This structure has been carefully engineered to accommodate complex equipment with stringent requirements on radiation shielding and vibration suppression. Reinforced concrete walls and roofs, up to 2 meters thick, ensure radioprotection and operational integrity, while structural joints isolate sensitive experimental spaces from mechanical vibrations. Building construction is expected to start by the end of 2026 and to be completed in 3 years.

The **architectural layout** of the main building has been carefully designed to meet the specific requirements of the experimental equipment and associated systems.

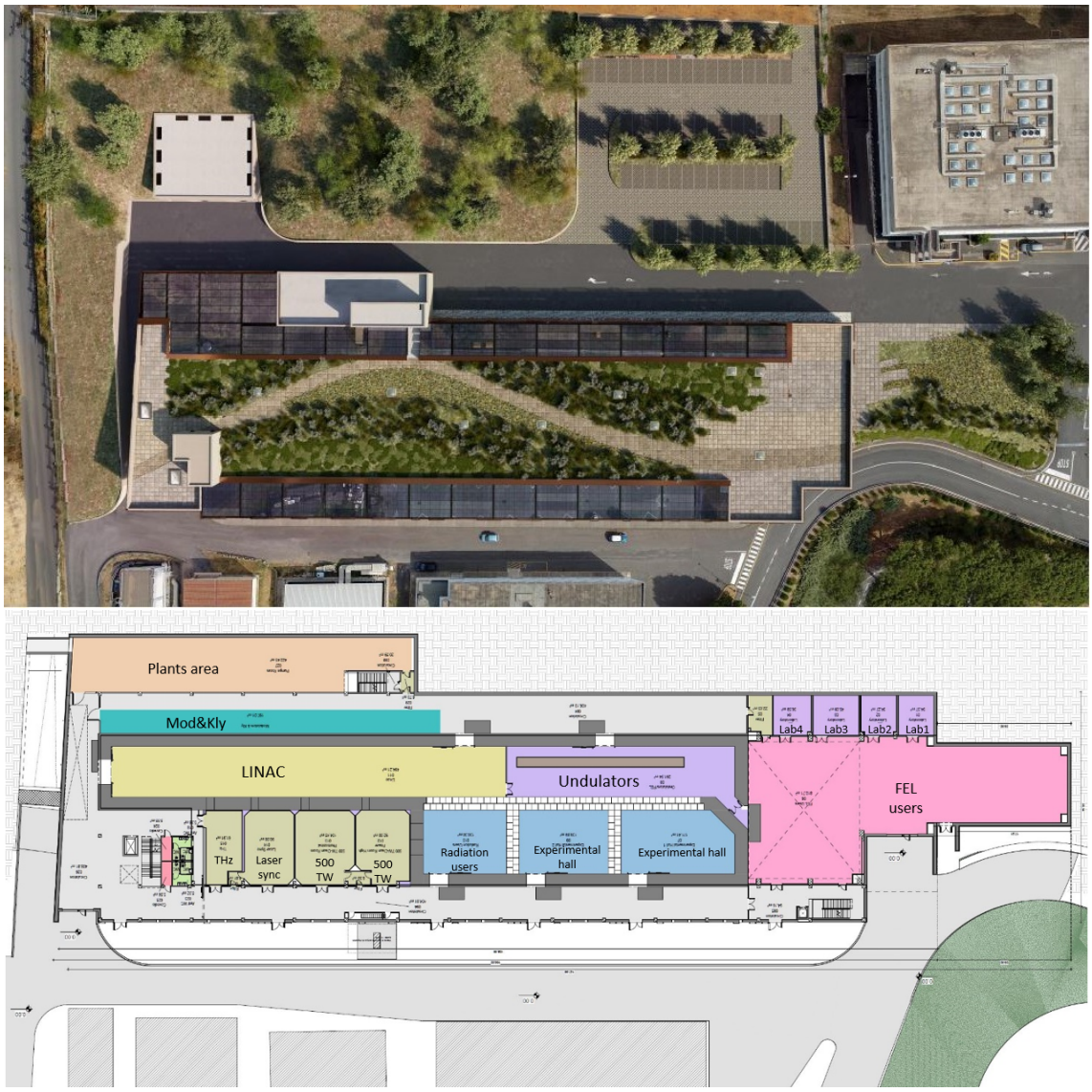

Figure 1.8: Facilities top view (upper picture) and corresponding ground floor building functional layout (lower scheme).

At the **ground floor** (Figure 1.8 from left to right), the following functional areas are foreseen:

- **A LINAC tunnel**, approximately 62 meters long, 8 meters wide, and 6 meters high.
- **Four clean rooms** dedicated to laser and synchronization systems, varying in size and distributed along the LINAC tunnel, accessible via a wide service corridor.
- **A radiation user room**, located adjacent to the LINAC tunnel and near the last clean room.
- **An Undulator/FEL hall**, positioned downstream of the LINAC, measuring approximately 36 meters by 8 meters, with a height of 6 meters.
- **Two experimental halls**, situated adjacent to the undulator hall and separated by a 2-meter-thick radiation shielding wall.
- **A Modulators and Klystrons gallery**, running parallel and adjacent to the LINAC tunnel, 6 meters wide and 6 meters high, designed to host RF systems and to allow waveguide access to the LINAC sections through dedicated penetrations.
- **The FEL Users Hall**, a large open space of approximately 50 meters by 23 meters.
- **Four user laboratories**, located near the FEL Users Hall, intended for sample preparation and ancillary activities.
- **An auxiliary technical area** designated for infrastructure systems (e.g., pumps room), positioned near the Modulators and Klystrons gallery.

On the first floor there are a Control Room, the Racks Room, a meeting room, offices and services.

To support the operation of the infrastructure, the building has been specifically designed to accommodate the following critical utility systems:

Electrical Systems: The facility will be supplied by the 150/20 kV LNF substation and with a total installed power capacity of 10 MW that ensure an high availability of the power. The maximum expected power demand of the facility, used for the electrical installation design, is about 2.8 MVA for all the site. A dedicated MV substation is equipped with 3 transformer each 1.6 MVA. Space has been also reserved for future facility expansion. The expected power consumption for the AQUA operation at 100 Hz repetition rate, delivering up to 1.2 GeV electron beams is 1.1 MW, as detailed in Tab. 1.7.

Table 1.7: Expected power consumption for the AQUA beamline operation at 100 Hz, 1 GeV

Electrical loads	**kW**
RF Modulators	575
Magnet PSU	300
Laser	15
Experimental users	10
Vacuum, electronics and controls	30
Cooling magnet + RF	45
HVAC	120
Total Expected power consumption	**1095**

Reliability and resilience are ensured through redundant feeders and transformers. Supercapacitor-based Uninterruptible Power Supplies will be used to mitigate harmonic distortion, unbalance and voltage dips, especially important for the RF modulators. The design also incorporates Electromagnetic Compatibility standards and a Common Bonding Network to reduce electrical noise.

Cooling and Fluid Systems: To support the stable operation of accelerator components, a sophisticated cooling infrastructure is in place, see Section 18.3.1. The primary water cooling system is divided into two distinct circuits in order to optimize different operational temperatures

requested by the secondary circuits. The maximum total thermal power to be dissipated for the baseline accelerator configuration is 700 kW. Users requiring a temperature set above 28 °C are served by adiabatic dry coolers, while loads requiring lower temperature set, for example the RF accelerating structures, which require thermal stability at 25 °C, are served by an adiabatic free cooling chiller that can operate in free cooling mode as long as the outdoor temperature allows it, and the compressor is optimized for water production at temperatures above 20 °C. The secondary cooling system will manage the different cooling lines dedicated to specific subsystems like Magnets, RF Modulators, RF Systems and Vacuum Pumps. The Heating, Ventilation, and Air Conditioning (HVAC) systems are designed to maintain tight environmental control in sensitive areas. Dedicated Air Handling Units serve each major room—including ISO7 cleanrooms for laser and THz systems—with temperature stability within ± 0.5 °C and relative humidity control between 40–60%. CFD simulations have confirmed the design's ability to keep airflow and temperature within strict tolerances required by the LINAC and undulator systems. A centralized compressed air network delivers stable pressure for actuating valves and pneumatic devices across the entire facility. The system is fully monitored to ensure efficient and reliable performance in all operating conditions.

1.11 Integrated Safety

The facility safety framework is structured into three main areas: Functional Safety and Machine Protection Systems, Conventional Safety, and Radiation Safety and Beam Dumps (Chapter 19). Together, these elements form a coherent and integrated safety strategy ensuring the protection of personnel, infrastructure, and equipment throughout all operational phases of the facility.

- **Functional Safety and Machine Protection Systems**
  Operational functional safety is implemented through two dedicated and clearly separated subsystems the **Machine Protection System (MPS)** and the **Personnel Safety System (PSS)** . Both systems are classified as **Safety Instrumented Systems** and are designed in compliance with the **IEC 61508** standard, following a structured lifecycle approach that includes risk assessment, requirements definition, verification, and validation.
  The **MPS** is responsible for protecting accelerator components by continuously monitoring critical machine parameters such as RF and LLRF status, vacuum conditions, temperature, timing signals, and interlock states, and by promptly inhibiting operation in the presence of abnormal or hazardous conditions.
  The **PSS** is dedicated to personnel protection and prevents access to radiation areas during accelerator operation by supervising access points, shielding doors, emergency stop systems, and safety-related devices, while enforcing controlled-access procedures.
  The combined action of MPS and PSS ensures safe and reproducible accelerator operation in compliance with applicable functional and radiation safety requirements.
- **Conventional Safety**
  The conventional safety strategy is based on national legislation and European standards and encompasses fire protection, emergency preparedness and response, safe operation of equipment, and occupational health and safety measures. The entire design has been validated and authorized by the competent Italian authorities as part of the approved executive project. Fire safety is ensured through structural compartmentation, the use of non-combustible materials, and fire resistance ratings of at least **120 minutes** across the accelerator complex. Evacuation routes are protected and redundant, with maximum path lengths limited to **60 m**, and are equipped with certified signage and emergency lighting. Fire detection is provided by a fully addressable system with optical and thermal sensors, manual call points, and EN 54–certified control units.
  Fire suppression systems include hydrants, portable extinguishers, and gas-based extinguish-

ing systems (Inergen and CO_2) for technical areas, complemented by certified smoke and heat extraction systems. Personnel protection is further reinforced by a redundant personnel interlock system employing fail-safe logic, emergency stops, door interlocks, and controlled-access procedures, all supervised from the control room. These measures, together with periodic testing and dedicated safety coordination during construction and operation, ensure a robust and regulation-compliant safety environment.

- **Radiation Safety and Beam Dumps**
  Radiation safety is addressed through a comprehensive analysis of radiation source terms, including bremsstrahlung photons, photoneutrons, muons, gas bremsstrahlung, and induced activation, evaluated for electron energies up to 1–1.2 GeV under conservative operating assumptions. To ensure compliance with regulatory limits, accessible areas are maintained below **1 µSv/h** for controlled zones and **0.25 µSv/h** for free-access or supervised areas.
  The shielding strategy includes typically **2 m of concrete** for walls and roof, with additional localized shielding at beam dumps and other critical components. A preliminary radiation protection program has been defined, including area classification, interlocked access control, radiation monitoring systems, personnel dosimetry, and centralized data acquisition and supervision.
  The facility includes three **diagnostic beam dumps** designed for 300, 800, and 1200 MeV operation, as well as two **fixed beam dumps** for the FEL beamline and the PWFA driver beam. All beam dump designs have been optimized and validated through detailed FLUKA simulations, demonstrating compliance with dose constraints. Predicted dose rates at the boundaries of free-access or supervised areas remain below **0.15 µSv/h** for all considered configurations. Additional radiation sources, including RF stations, cooling systems, and ventilation components, have also been assessed for induced activity and are addressed within the overall radiation safety framework.

1.12 Implementation Methodology

The successful realization of EuPRAXIA@SPARC_LAB relies on the close integration of accelerator design, civil infrastructure, and a structured system-engineering methodology, as discussed in Chapter 20.

The **integrated implementation strategy** guides the transition from conceptual design to construction and, ultimately, to beam operation. This strategy ensures that all accelerator subsystems are embedded within a building designed to meet stringent requirements in terms of mechanical stability, controlled thermal environments, low vibration levels, and safe installation logistics. It further defines how spatial planning, utilities routing, electrical distribution, HVAC control, shielding provisions, and radiation-protection requirements are coordinated to support the precision, alignment, and overall stability requirements of the facility. The chapter also outlines a staged approach to installation and technical system commissioning, ensuring that each subsystem is validated, aligned, and progressively brought into operation in an efficient and coherent manner.

The **system-engineering** framework complements this perspective by ensuring consistency, traceability, and long-term reliability across the entire project. It introduces standardized practices for configuration and interface management, unified schematic layouts for all major systems, and asset-tracking and lifecycle-management tools that support operation and the future evolution of the facility well beyond first light. In this context, the application of the Verification & Validation (V&V) model proves particularly valuable as a method for assessing the project's progress, from the implementation phase through to operational deployment. Together, these methodologies provide the organizational and technical backbone needed to deploy, commission, operate, and upgrade EuPRAXIA@SPARC_LAB with the rigor expected of a modern European research infrastructure.

1.13 Consideration about Sustainability

The civil infrastructure of EuPRAXIA@SPARC_LAB has been conceived not only to meet the demanding mechanical, thermal, and radiological requirements of a next-generation accelerator facility, but also to comply with the energy-efficiency and environmental-sustainability principles outlined in **Chapter 21**.

The building layout, utility systems, and supporting infrastructure incorporate multiple design measures aimed at minimizing the facility's energy footprint while ensuring stable operating conditions for the LINAC, undulator, lasers, RF systems, and experimental halls. In line with the **DNSH** (Do No Significant Harm [88]) framework and regional **CAM** (Criteri Ambientali Minimi [89]) requirements, the architectural design — together with the building's mechanical and electrical systems — adopts high-efficiency insulation, low-thermal-transmittance structures, and optimized solar-exposure geometries to reduce HVAC loads. The electrical system is dimensioned for high availability while allowing the integration of renewable energy sources including the integrated photovoltaic field. As described in Chapter 21, the choice of **adiabatic dry coolers** for all medium-temperature accelerator loads (30–40 °C) represents a key sustainability action, reducing electricity consumption by more than 40% compared to conventional chiller-based cooling. Where chilled water is required (e.g., for precision thermal control of the X-band structures), the design prioritizes chillers with a high Coefficient of Performance, and therefore improving energy efficiency and incorporates heat-recovery loops to reuse waste heat from RF stations and technical rooms cooling system. HVAC systems rely on **dedicated Air Handling Units**, ensuring ± 0.5 °C temperature stability in laser and synchronization clean rooms. CFD simulations confirm that thermal stratification and turbulent airflow are kept within strict tolerances to protect beam stability in the LINAC and undulator halls. The water-cooling system implements variable-flow pumps, high-efficiency motors, and optimized ΔT design, as recommended in Chapter 21 to reduce ancillary power consumption. A centralized monitoring and control layer integrates energy-metering, HVAC performance, and cooling-loop efficiency, enabling the real-time optimization strategies described in the chapter.

In addition, the facility is being evaluated through a **Life-Cycle Assessment** approach, to confirm that the chosen construction materials, reinforcement methods, and civil-work practices minimize embodied carbon relative to baseline solutions. The design also incorporates measures to reduce operational environmental impact, such as the use of low-Global Warming Potential refrigerants and limited town water usage. Together, these elements ensure that the EuPRAXIA@SPARC_LAB civil infrastructure supports the stringent technical requirements of the accelerator while contributing to a measurable reduction of environmental impact, energy demand, and CO_2 emissions throughout the facility's lifetime.

Although the current RF linac layout has been intentionally designed to be longer than strictly necessary for risk mitigation, **an optimized EuPRAXIA@SPARC_LAB configuration** would accelerate the beam to approximately 550 MeV using only the S-band injector (about 120 MeV in velocity-bunching configuration) and four X-band modules operating at 60 MV/m (providing an additional $\sim$ 480 MeV), with the remaining energy supplied by the plasma booster. Operating in this minimized-RF mode would reduce the RF power demand from 575 kW to 400 kW, corresponding to a **reduction greater than** 30% with respect to the Full RF configuration. The plasma booster also **replaces a significant fraction of conventional RF infrastructure**: a plasma module approximately 6 m long (including matching sections, vacuum chamber (3.7 m) and the driver–witness separator (2.3 m)) substitutes for about 10 m of X-band linac, **reducing the associated capital investment from roughly** 9.8 M€ **to about** 2.2 M€**.**

Plasma acceleration therefore enables GeV-scale beam energies with a substantially smaller RF footprint, reduced capital costs, and significantly lower electrical power consumption, cooling requirements, and associated CO_2 emissions over the facility lifetime.

1.14 Project Cost, Timeline, and Management

The TDR provides the consolidated assessment of the Project Cost, Implementation Timeline, and Management Structure of the EuPRAXIA@SPARC_LAB facility, as discussed in **Chapter 22**. The **Budget at Completion** for the full baseline configuration is estimated at 115.7 M€, depending on the final procurement strategy and market conditions, see Tab. 1.8. This figure results from the **Project Breakdown Structure**, which aggregates costs by functional areas and system families, including civil engineering, accelerator systems, photon beamlines, RF power sources, diagnostics, and integration activities.

Concerning personnel, at this stage around **70 - 80** Full Time Equivalent **(FTE)** are expected to be needed for the implementation of the project and to comply with the aggressive and successfull-oriented project plan. This figure will be assessed during the course of the implementation phase.

Table 1.8: Aggregated cost per functional area (values in k€)

Functional Area	Estimated Cost (k€)
Injector	11,000
Low Energy Line	9,600
Bunch Compressor	1,200
High Energy Line	9,800
Plasma Module	2,300
AQUA FEL	12,000
AQUA Beamlines	7,100
General Elements	4,000
Building Construction	47,935
Building Ancillary costs	4,765
Hi-Tech Utilities	6,000
TOTAL	**115,700**

The cost coming from the PBS are then aggregated in two different way:

- Aggregation per functional area.
- Aggregation per work package (System).

The current budget allocation is of 108 M€ which part of them has been already used in the R&D phase (9 M€). A budget gap of about 17 M€ must be addressed. The following strategy will be adopted:

- Priority to the more mature items;
- Priority to the minimum configuration scenario needed;
- Make or buy scenario;
- Additional funding line to support the activities;
- Phasing approach.

The first (and largest) procurement will be the building construction for which the full budget will be allocated. The final offer will be expected to be lower, the difference will be used as additional resources for the machine implementation. Additional funding lines might be in synergy with the machine implementation providing a more structured and elaborated financial framework. The above mentioned initiative will be fully analyzed and structured in the project management

plan.

A key finding of the cost analysis is the markedly different cost profile of plasma-based acceleration compared with conventional RF technology. The Plasma Accelerating Module, despite providing an energy gain comparable to the High Energy X-band Linac, accounts for roughly one quarter of the corresponding linac cost, illustrating the economic advantage of compact plasma-based stages. This considerable advantage becomes even more compelling when accounting for operational expenditures, as the running costs associated with a plasma accelerator module are substantially lower than those of conventional RF-based technologies.

This cost asymmetry reinforces the long-term rationale of EuPRAXIA, where plasma technology is expected to significantly reduce footprint and capital investment for future facilities.

1.14.1 Implementation Timeline

The EuPRAXIA@SPARC_LAB **schedule**, shown in Fig. 1.9, is structured around three main project phases and highlights the coordinated progression from civil construction to first FEL operation. The figure illustrates the **critical sequencing** between building completion, accelerator installation, and beam commissioning, while also displaying the **interface dependencies** that drive the overall timeline. The overall schedule is aligned with the **ESFRI Landmark** [90] preparation horizon and ensures that the facility reaches its first operational capability in 2031.

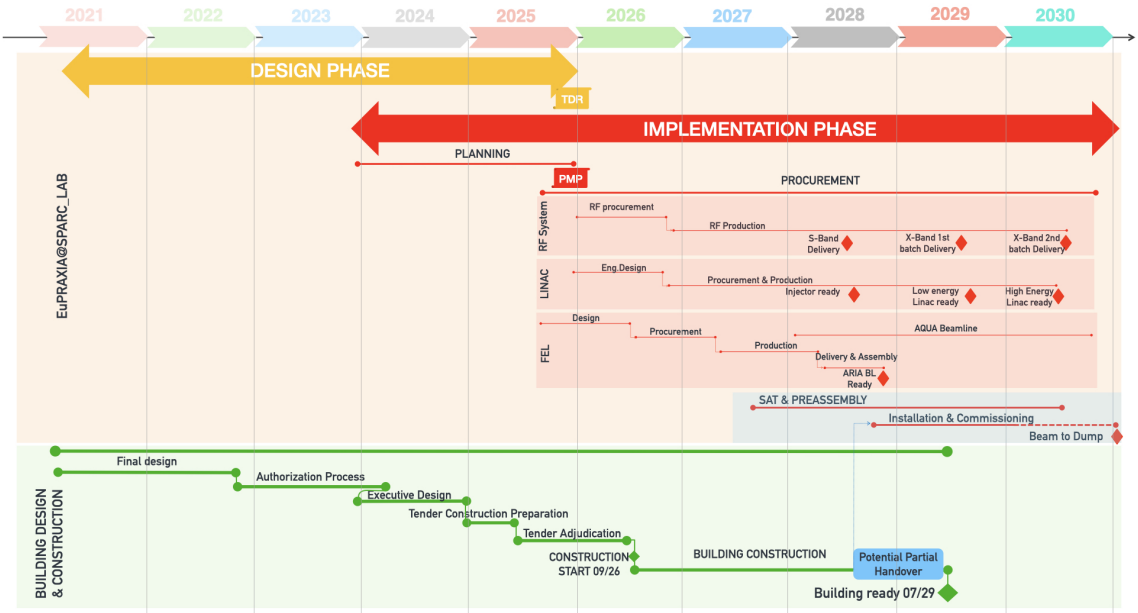

Figure 1.9: EuPRAXIA@SPARC_LAB schedule

Construction and Infrastructure Completion (2026–2029): Civil engineering, building services, and technical utilities will be completed by mid-2029, providing the environmental and mechanical stability required for accelerator installation. The timeline includes the commissioning of HVAC, cooling systems, radiation shielding, power distribution, and laboratory spaces, and is fully consistent with the ESFRI preparation roadmap. The RF modules will be pre-assembled and tested in a dedicated storage and preparation hall prior to completion of the main building. This approach allows mechanical integration and cabling to be carried out in parallel with civil construction activities, ensuring that the modules are ready for installation as soon as the accelerator tunnel becomes available.

Installation, Integration, and Commissioning (2029–2031): Accelerator subsystems, photon

beamlines, undulators, plasma module, RF systems, and diagnostics will be installed between 2029 and 2031, followed by an integrated commissioning phase. This period includes:

- subsystem acceptance tests;
- alignment and metrology;
- staged beam commissioning (photoinjector →linac →plasma →undulator →FEL);
- V&V according to the project's system-engineering model.

Early Operation and Pilot User Facility (2031 and beyond): The facility is planned to reach minimum operational capability by 2031, corresponding to the delivery of qualified electron beams and first photon production from the undulator line, rather than immediate full-scale user operation. By this milestone, EuPRAXIA@SPARC_LAB will have all the subsystems fully commissioned and demonstrate stable beam delivery together with first SASE FEL radiation thus enabling repeatable and reproducible beam and photon parameters. This phase fulfills the ESFRI "early operation" requirement, ensuring that the infrastructure is technically operational and scientifically exploitable while allowing for a controlled ramp-up of complexity. Early scientific activities (Phase 1) will focus on a limited and well-defined set of experiments, initially centered on beam characterization and gas-phase photon science, fully compatible with the expected Day-1 beam parameters. More complex experimental programs will be progressively enabled in subsequent years as operational maturity, reliability, and availability are consolidated. As shown in Fig. 1.9, this milestone anchors EuPRAXIA@SPARC_LAB within the ESFRI timeline for the first operational nodes of the distributed research infrastructure, while explicitly balancing technology validation of plasma-driven acceleration in a user environment with the initial delivery of beams and photons by 2031.

1.14.2 Management Structure and Project Governance

The management framework described in Chapter 22 adopts a structured project-management approach ensuring coordinated control of scope, schedule, and cost baselines. This framework includes:

- a **Project Steering Committee** overseeing strategic decisions;
- a **Technical Coordination Board** responsible for system integration across Work Packages;
- a **Configuration and Change Control process**, ensuring consistency with requirements;
- periodic **milestones** and **Key Performance Indicators** for risk tracking, subsystem maturity, and schedule adherence.

A detailed description of the project management methodologies will be examined in the Project Management Plan that will follow the approval of the Technical Design Report.

The project also follows a **System Engineering V-model** (see Sec. 20.5), linking design, procurement, installation, and verification/validation activities to formal deliverables. This approach ensures traceability and compliance with technical requirements, especially at subsystem interfaces.

1.15 Risk Mitigation and Project Robustness

The EuPRAXIA@SPARC_LAB design incorporates a comprehensive risk-mitigation strategy aimed at ensuring reliable delivery of FEL performance under varying operational conditions. Key technological risks — such as PWFA plasma-density fluctuations and X-band RF breakdown probability — are mitigated through **redundancy**, pre-series component testing, and extensive use of feedback and diagnostic systems. The facility retains a fully independent Full RF operational mode as a fallback solution, guaranteeing Day-1 user capability even in the event of plasma-module unavailability or in the worst-case scenario, if the required plasma operating conditions cannot be achieved. Parallel development lines at SPARC_LAB, PLASMA_LAB, and the TeX test stand for X-band systems, ensure that all critical technologies reach TRL ≥ 6 before integration. The

modular building layout further enables staged installation, early subsystem commissioning, and progressive risk retirement, consistent with INFN system-engineering standards.

1.16 Conclusions and Future Outlook

The scientific and technological ecosystem developed for EuPRAXIA@SPARC_LAB is designed not only to meet the immediate performance objectives of a compact soft X-ray FEL but also to establish the foundations for the next generation of high-brightness, plasma-enabled accelerators. Several enabling technologies are central to this long-term vision, with significant implications for both fundamental research and applied innovation.

Among the key innovations, the integration of high-gradient **X-band** accelerating structures, delivering fields of $\sim$60 MV/m, allows for a dramatic reduction in the RF linac footprint while preserving beam brightness and stability. The use of **plasma channels** for wakefield acceleration represents a transformative step toward ultra-compact energy boosting, offering gradients in excess of 1 GV/m and paving the way for reproducible, beam-quality-preserving plasma stages. Advances in **ultrafast synchronization**, with sub-10 fs rms timing jitter between lasers and electron bunches, are essential enablers for pump–probe experiments and for precise control of beam–plasma interactions. The undulator system introduces additional flexibility through the adoption of **APPLE-X** variable-polarization undulators, enabling on-axis generation of tunable linear, circular, and elliptical polarization states with high stability, an essential capability for a broad class of soft-X-ray spectroscopy and imaging experiments. In **diagnostics and control**, the facility introduces real-time, non-invasive beam monitoring, machine learning assisted predictive tuning, and scalable, modular data acquisition systems, tools that support high repetition rate user operation and that are readily transferable to other infrastructures such as FELs, Linear Colliders, Compton sources, or medical accelerators.

Looking ahead, EuPRAXIA@SPARC_LAB has been conceived with clear upgrade and diversification pathways. These include the addition of new beamlines such as **ARIA** for VUV radiation, implementation of seeded FEL schemes for improved spectral purity, and expansion of the plasma module to higher energies or multi-stage acceleration. R&D toward operating at **400 Hz** repetition rate - enabled by the forthcoming **C-band photo-injector** - is already underway [91], in particular in the framework of the PACRI project. The facility also allows accommodating in the future frontier concepts such as dielectric acceleration, THz-driven structures, and plasma photocathode injection, ensuring long-term technological relevance.

The modular architecture of the PWFA section naturally supports future **energy-upgrade** paths. Operating the X-band linac at its full installed RF power and coupling it to a **high-transformer-ratio** PWFA stage [92], optimized through tailored driver shaping, would allow the facility to reach **multi-GeV** electron energies (up to $\approx$5 GeV).

Reaching this energy range, combined with a dedicated R&D program on **short period undulators**, including plasma-based undulators, would dramatically extend the reachable photon energies and spectral flexibility of the FEL. In particular, plasma undulators [93–98], with their millimeter-scale periods and high effective field amplitudes, could push the emission wavelength below 1 nm in an ultra-compact footprint, far beyond the limits of conventional magnetic undulators. At shorter wavelengths, the requirements on electron beam quality become significantly more stringent, with tighter tolerances on transverse emittance, relative energy spread, and shot-to-shot stability. In parallel, the photon transport system and optics would need to be adapted to operate efficiently at higher photon energies and higher peak power densities. These aspects are therefore an integral part of the long-term upgrade perspective and will require targeted R&D on beam generation, plasma acceleration stability, advanced electron beam and **X-ray** photon diagnostics.

Beyond the FEL science mission, EuPRAXIA@SPARC_LAB offers unique opportunities for broader scientific domains.

On the photon side, the availability of high-brightness, tunable electron beams provides the basis for developing a **gamma-ray Compton source** [99], enabling precision studies in **nuclear physics**, including photonuclear reactions, photofission, nuclear structure, astrophysical processes, isotope production, and non-destructive analysis for cultural heritage and security applications.

On the accelerator side, the PWFA module, positions EuPRAXIA@SPARC_LAB as a testbed for **multi-stage** beam-driven plasma acceleration [100–102], directly contributing to the road-map for a future plasma-based Linear Collider. In a dedicated R&D future program, staging can be explored by installing a second plasma module downstream and off-line with respect to the first module, complemented by a compact inter-stage extraction and matching section for both the second driver and the witness beams. In addition, the flexibility of the injector and timing systems allows the generation and synchronization of two high-charge drive bunches together with a low-emittance witness bunch, with independently adjustable relative delays. This configuration enables controlled experimental studies of stage-to-stage coupling, cumulative energy gain, beam-loading efficiency, and emittance preservation at the GeV scale, providing critical input for next-generation high-energy physics facilities, including plasma-based Higgs factories such as **HALHF** [103] and future textbfmulti-TeV collider concepts, as recommended by the **European Strategy for Particle Physics** [104].

The facility layout has been designed to accommodate also secondary particle production, including **positron** [105] generation via high-Z targets driven by the high-brightness electron beam or high power PW-class laser systems, with the possibility of subsequent capture, pre-acceleration, and injection into dedicated beamlines.

The high-gradient capabilities of plasma accelerators have direct relevance also for the short-lived particles like **muons**: these particles must be rapidly collected, cooled, and accelerated before decaying [106]. Plasma-based acceleration present a promising approach to minimizing particle losses for the acceleration of both muons and pions.

EuPRAXIA@SPARC_LAB will also generate substantial **industrial impact**, strengthening high-tech sectors in RF technologies, ultrafast lasers, photon instrumentation, advanced diagnostics, and plasma-source engineering at the **European and Regional (Lazio) levels**. The procurement and co-development of components - including X-band structures, undulator magnets and AI-driven control electronics - will foster new collaborations with industry and stimulate technology transfer to markets such as medical accelerators, semiconductor lithography, security scanners, cultural-heritage imaging, and compact radiation sources.

Equally important is the facility's role in **training** the next generation of accelerator and photon-science researchers. EuPRAXIA@SPARC_LAB and in particular its test facility SPARC_LAB will serve as a hands-on training ground for students and young scientists through the EuPRAXIA Doctoral Network, national PhD programs, and dedicated fellowship programs. The installation, commissioning, and operation of cutting-edge technologies will provide unique educational opportunities. This will help build a highly skilled workforce capable of driving future innovation in high-energy physics, materials science, and accelerator-based technologies across Europe.

In conclusion this Technical Design Report demonstrates the feasibility of realizing a plasma-based user facility capable of reliable delivery of high-brightness soft X-ray FEL radiation. The EuPRAXIA@SPARC_LAB baseline integrates validated accelerator concepts, coherent performance assumptions, and a realistic combination of RF and plasma technologies into a mature facility design. The project incorporates also a clear technical risk-mitigation strategy ensuring early user capability and scientific productivity. With construction completion targeted around 2031, we are confident that the facility will play a leading role in advancing accelerator and photon science research in Europe.

1.17 Acknowledgments

The preparation of this Technical Design Report and the EuPRAXIA@SPARC_LAB project development have been made possible through the support of several European and national funding agencies and research institutions, which we wish gratefully to acknowledge here.

EuPRAXIA is included in the ESFRI Roadmap and has received funding from the European Union within the framework of Horizon 2020 and Horizon Europe, in particular through the EuPRAXIA Design Study, the EuPRAXIA Preparatory Phase, and the EuPRAXIA Doctoral Network. The inclusion of EuPRAXIA in the 2021 ESFRI Roadmap represents a key milestone for the project, providing strategic recognition at the European level and enabling its further development toward implementation. We gratefully acknowledge the ESFRI Executive Board for its essential role in this process, and in particular Prof. Gelsomina Pappalardo, Italian representative on the ESFRI Board, for her continuous encouragement and support during the preparation of the ESFRI application.

The Italian Pillar, EuPRAXIA@SPARC_LAB, is supported by the Italian Ministry of University and Research through INFN, which is providing the main financial contribution for the realization of the user facility at the INFN Frascati National Laboratories. Additional support has been provided by the Lazio Region through regional and European structural funds, including the LATINO, SABINA, and ARIA related initiatives. We wish to acknowledge the strong and continuous support of the INFN President Prof. Antonio Zoccoli and former INFN President Prof. Fernando Ferroni.

The project further benefits from strong synergies with complementary European initiatives, including EuPRAXIA Advanced Photon Sources, funded under the Next Generation EU framework, and the PACRI project, supported by the European Union to advance high-repetition-rate plasma accelerator technologies and I.FAST project for the essential networking opportunities.

Last but not least the authors gratefully acknowledge the continuous guidance and constructive feedback provided by the Project Advisory Committee (Patric Muggli, Chair; Deepa Angal-Kalinin; Martin Beye; Majed Chergui, Marco Pedrozzi; Luigi Scibile and Sigfried Schreiber who sadly passed away during the course of the project), whose continuous commitment and expertise have been invaluable in strengthening the project.

We also acknowledge the in-kind contributions of all EuPRAXIA@SPARC_LAB partner institutions (CNR, Elettra, ENEA, Sapienza University of Rome, and the University of Rome 'Tor Vergata'), whose staff effort and institutional resources have supported the work of their personnel involved in the project.

We further recognize the commitment of the LNF Accelerator and Technical Divisions and the support of the Administration Service, as well as the contributions of all students participating in the EuPRAXIA programme, in particular those from the PhD programme in Accelerator Physics and Technology at Sapienza University of Rome.

Together, these contributions have been essential in advancing the project from conceptual design toward a user oriented European research infrastructure. Last but not least, we deeply acknowledge the support of all our international and associated partners within the EuPRAXIA consortium. Their contributions have been, and will remain, an essential pillar in the realization of a European research facility strongly integrated at the international level.

Bibliography

[1] R. W. Assmann et al. "EuPRAXIA conceptual design report". In: *The European Physical Journal Special Topics* 229.24 (2020), pp. 3675–4284.

[2] *EuPRAXIA Web Site*. URL: https://www.eupraxia-facility.org/.

[3] M. Ferrario et al. "EuPRAXIA@ SPARC_LAB Design study towards a compact FEL facility at LNF". In: *Nuclear Instruments and Methods in Physics Research Section A: Accelerators, Spectrometers, Detectors and Associated Equipment* 909 (2018), pp. 134–138.

[4] *ESFRI Roadmap 2021 Announcement*. URL: https://www.esfri.eu/latest-esfri-news/new-ris-roadmap-2021.

[5] J. de Blas et al. *Physics Briefing Book: Input for the 2026 update of the European Strategy for Particle Physics*. 2025. DOI: 10.17181/CERN.35CH.2O2P. URL: http://cds.cern.ch/record/2944678.

[6] T. Ishikawa. "Synchrotron radiation, X-ray free-electron lasers and beyond". In: *Philosophical Transactions of the Royal Society A* 377.2145 (2019), p. 20180023. DOI: 10.1098/rsta.2018.0231.

[7] S. Sheehy. "Applications of Particle Accelerators". In: (2024). arXiv: 2407.10216 [physics.acc-ph]. URL: https://arxiv.org/abs/2407.10216.

[8] M. Ferrario and R. W. Assmann. "From dreams to reality: prospects for applying advanced accelerator technology to next generation scientific user facilities". In: *Proc. 10th Int. Particle Accelerator Conf.(IPAC'19)(Melbourne, Australia, 19–24 May 2019)(Int. Particle Accelerator Conf. vol 10)*. 2019, pp. 1–5.

[9] T. Tajima and J. M. Dawson. "Laser electron accelerator". In: *Physical Review Letters* 43.4 (1979), p. 267.

[10] D. Gordon et al. "Observation of electron energies beyond the linear dephasing limit from a laser-excited relativistic plasma wave". In: *Physical review letters* 80.10 (1998), p. 2133.

[11] T. Argyropoulos et al. "Design, fabrication, and high-gradient testing of an X-band, traveling-wave accelerating structure milled from copper halves". In: *Physical Review Accelerators and Beams* 21.6 (2018), p. 061001.

[12] P. Chen et al. "Acceleration of electrons by the interaction of a bunched electron beam with a plasma". In: *Physical review letters* 54.7 (1985), p. 693.

[13] C. Pellegrini, A. Marinelli, and S. Reiche. "The physics of x-ray free-electron lasers". In: *Reviews of Modern Physics* 88.1 (2016), p. 015006.

[14] M. Galletti et al. "Prospects for free-electron lasers powered by plasma-wakefield-accelerated beams". In: *Nature Photonics* 18.8 (2024), pp. 780–791.

[15] W. Wang et al. "Free-electron lasing at 27 nanometres based on a laser wakefield accelerator". In: *Nature* 595 (2021), pp. 516–520. DOI: 10.1038/s41586-021-03678-x.

[16] R. Pompili, D. Alesini, M. P. Anania, et al. "Free-electron lasing with compact beam-driven plasma wakefield accelerator". In: *Nature* 605 (2022), pp. 659–662. DOI: 10.1038/s41586-022-04589-1.

[17] M. Galletti et al. "Stable operation of a free-electron laser driven by a plasma accelerator". In: *Physical review letters* 129.23 (2022), p. 234801.

[18] M. Labat, J. C. Couperus Cabadağ, A. Ghaith, et al. “Seeded free-electron laser driven by a compact laser plasma accelerator”. In: *Nature Photonics* 17 (2023), pp. 150–156. DOI: 10.1038/s41566-022-01104-w.

[19] S. K. Barber, J. van Tilborg, C. Schroeder, et al. “Greater than 1000-fold gain in a free-electron laser driven by a laser-plasma accelerator with high reliability”. In: *Physical Review Letters* 135.5 (2025), p. 055001. DOI: 10.1103/vh62-gz1p.

[20] C. Joshi et al. “Plasma wakefield acceleration experiments at FACET II”. In: *Plasma Physics and Controlled Fusion* 60.3 (2018), p. 034001.

[21] Collaboration AWAKE. *AWAKE Status Report 2025*. Tech. rep. 2025.

[22] B. Hidding et al. *Directions in plasma wakefield acceleration*. 2019.

[23] C. Zhang et al. “Plasma-wakefield accelerator simultaneously boosts electron beam energy and brightness”. In: *Nature Communications* 16.1 (2025), p. 10719.

[24] C. Joshi. “Plasma accelerators”. In: *Scientific American* 294.2 (2006), pp. 40–47.

[25] C. A. Lindstrøm et al. “Beam-driven plasma-wakefield acceleration”. In: *arXiv preprint arXiv:2504.05558* (2025).

[26] W. Lu et al. “Nonlinear Theory for Relativistic Plasma Wakefields in the Blowout Regime”. In: *Physical Review Letters* 96 (2006), p. 165002. DOI: 10.1103/PhysRevLett.96.165002.

[27] J. B. Rosenzweig. “Nonlinear plasma dynamics in the plasma wake-field accelerator”. In: *Phys. Rev. Lett.* 58 (6 1987), pp. 555–558. DOI: 10.1103/PhysRevLett.58.555.

[28] V. Malka. “Plasma wake accelerators: introduction and historical overview”. In: *arXiv preprint arXiv:1705.09584* (2017).

[29] *EuroNNAc 2012 Meeting*. URL: https://indico.cern.ch/event/187383/.

[30] *First EAAC Workshop 2013*. URL: https://agenda.infn.it/event/5564/.

[31] *EuPRAXIA Design Study (2015-2021)*. URL: https://www.eupraxia-project.eu/ (visited on 11/24/2025).

[32] *EuPRAXIA web site*. URL: https://www.eupraxia-facility.org/ (visited on 11/24/2025).

[33] *EuPRAXIA@SPARC_LAB CDR 2018*. URL: https://sparclab.lnf.infn.it/wp-content/uploads/sites/30/2023/03/Eupraxia@sparc_lab_CDR.pdf.

[34] *ELI-ERIC facility*. URL: https://www.eli-beams.eu/.

[35] *EuPRAXIA Preparatory Phase*. URL: https://www.eupraxia-pp.org/about.

[36] *EuPRAXIA Doctoral Network*. URL: https://www.eupraxia-dn.org/about.

[37] *EuPRAXIA Advanced Photon Sources*. URL: https://euaps.infn.it/.

[38] *PACRI - Plasma Accelerator systems for Compact Research Infrastructures*. URL: https://www.pacri.eu/.

[39] *LATINO web site*. URL: https://latino.lnf.infn.it/?lang=en (visited on 11/24/2025).

[40] *SABINA web site*. URL: https://sabina.lnf.infn.it/?lang=en (visited on 11/24/2025).

[41] F. Villa et al. “ARIA—a VUV beamline for EuPRAXIA@SPARC_LAB”. In: *Condensed Matter* 7.1 (2022), p. 11.

[42] B. E. Carlsten. "Space charge induced emittance compensation in high brightness photoinjectors". In: *Part. Accel.* 49 (1995), pp. 27–65.

[43] L. Serafini and J. B. Rosenzweig. "Envelope analysis of intense relativistic quasilaminar beams in rf photoinjectors: mA theory of emittance compensation". In: *Physical Review E* 55.6 (1997), p. 7565.

[44] M. Ferrario et al. "Direct Measurement of the Double Emittance Minimum in the Beam Dynamics of the Sparc High-Brightness Photoinjector". In: *Physical review letters* 99.23 (2007), p. 234801.

[45] M. Ferrario et al. "Laser comb with velocity bunching: Preliminary results at SPARC". In: *Nuclear Instruments and Methods in Physics Research Section A: Accelerators, Spectrometers, Detectors and Associated Equipment* 637.1 (2011), S43–S46.

[46] L. Serafini and M. Ferrario. "Velocity bunching in photo-injectors". In: *AIP conference proceedings*. Vol. 581. 1. American Institute of Physics. 2001, pp. 87–106.

[47] M. Ferrario et al. "Experimental demonstration of emittance compensation with velocity bunching". In: *Physical review letters* 104.5 (2010), p. 054801.

[48] P. Emma et al. "X-band RF harmonic compensation for linear bunch compression in the LCLS". In: *SLAC, Stanford, CA, USA, Rep. ILCLS-TN-01-1* (2001).

[49] Z. Huang and K. J. Kim. "Formulas for coherent synchrotron radiation microbunching in a bunch compressor chicane". In: *Physical Review Special Topics-Accelerators and Beams* 5.7 (2002), p. 074401.

[50] S. Romeo, M. Ferrario, and A. R. Rossi. "Beam loading assisted matching scheme for high quality plasma acceleration in linear regime". In: *Physical Review Accelerators and Beams* 23.7 (2020), p. 071301.

[51] James B. Rosenzweig et al. "Acceleration and focusing of electrons in two-dimensional nonlinear plasma wake fields". In: *Physical Review A* 44.10 (1991), R6189.

[52] R. Bonifacio, C. Pellegrini, and L. M. Narducci. "Collective instabilities and high-gain regime in a free electron laser". In: *Opt. Commun.* 50 (1984), p. 373.

[53] N. Kroll, P. Morton, and M. Rosenbluth. "Free-electron lasers with variable parameter wigglers". In: *IEEE Journal of Quantum Electronics* 17.8 (2003), pp. 1436–1468.

[54] R. Bonifacio et al. "Hamiltonian model and scaling laws for free-electron-laser amplifiers with tapered wiggler". In: *Optics communications* 66.2-3 (1988), pp. 133–139.

[55] L. Giannessi et al. "High-order-harmonic generation and superradiance in a seeded free-electron laser". In: *Physical review letters* 108.16 (2012), p. 164801.

[56] J. Andruszkow et al. "First Observation of Self-Amplified Spontaneous Emission in a Free-Electron Laser at 109 nm Wavelength". In: *Phys. Rev. Lett.* 85 (18 2000), pp. 3825–3829. DOI: 10.1103/PhysRevLett.85.3825.

[57] M. Beye et al. "FLASH and the FLASH2020+ project—current status and upgrades for the free-electron laser in Hamburg at DESY". In: *The European Physical Journal Plus* 138.3 (2023), p. 193.

[58] E. Allaria et al. "Highly coherent and stable pulses from the FERMI seeded free-electron laser in the extreme ultraviolet". In: *Nature Photonics* 6.10 (2012), pp. 699–704.

[59] Z. Zhentang et al. "Shanghai soft X-ray free-electron laser facility". In: *Chinese Journal of Lasers* 46.1 (2019), p. 0100004.

[60] P. Emma et al. “First lasing and operation of an ångstrom-wavelength free-electron laser”. In: *nature photonics* 4.9 (2010), pp. 641–647.

[61] T. Tschentscher et al. “Photon beam transport and scientific instruments at the European XFEL”. In: *Applied Sciences* 7.6 (2017), p. 592.

[62] T. Ishikawa et al. “A compact X-ray free-electron laser emitting in the sub-ångström region”. In: *nature photonics* 6.8 (2012), pp. 540–544.

[63] C. J. Milne et al. “SwissFEL: the Swiss X-ray free electron laser”. In: *Applied Sciences* 7.7 (2017), p. 720.

[64] I. S. Ko et al. “Construction and commissioning of PAL-XFEL facility”. In: *Applied Sciences* 7.5 (2017), p. 479.

[65] Z. Zhao, H. Ding, and B. Liu. “Shanghai hard X-ray FEL facility progress status”. In: *15th International Particle Accelerator Conference, Nashville, TN, USA*. 2024, p967–972.

[66] L. Crincoli et al. “Meter Scale Discharge Capillaries for Plasma Based Accelerators”. In: *Applied Sciences* (2025). submitted.

[67] G. Brenner et al. “First results from the online variable line spacing grating spectrometer at FLASH”. In: *Nuclear Instruments and Methods in Physics Research Section A: Accelerators, Spectrometers, Detectors and Associated Equipment* 635.1 (2011), S99–S103.

[68] M. Braune et al. “A non-invasive online photoionization spectrometer for FLASH2”. In: *Synchrotron Radiation* 23.1 (2016), pp. 10–20.

[69] E. Principi and F. Stellato. *User and Market Study Including Research Infrastructure Potential User Base and Needs*. Tech. rep. WP5 Milestone MLS5.1. Horizon Europe Grant Agreement No. 101079773. EuPRAXIA Preparatory Phase (EuPRAXIA-PP), Oct. 2023.

[70] E. De Santis et al. *EuPRAXIA Report on Access Policy*. Tech. rep. WP5 Milestone MLS5.2. Horizon Europe Grant Agreement No. 101079773. EuPRAXIA Preparatory Phase (EuPRAXIA-PP), Apr. 2025.

[71] M. Héder. “From NASA to EU: the evolution of the TRL scale in Public Sector Innovation”. In: *The Innovation Journal* 22.2 (2017), pp. 1–23.

[72] *SPARC_LAB website*. URL: `https://sparclab.lnf.infn.it/`.

[73] *TEX website*. URL: `https://tex.lnf.infn.it/`.

[74] M. Ferrario et al. “SPARC_LAB present and future”. In: *Nuclear Instruments and Methods in Physics Research Section B: Beam Interactions with Materials and Atoms* 309 (2013), pp. 183–188.

[75] R. Pompili et al. “The SPARC_LAB Facility for Advanced Acceleration and Radiation Experiments”. In: *Physical Review Accelerator and Beams* (2026). submitted.

[76] A. Cianchi et al. “High brightness electron beam emittance evolution measurements in an rf photoinjector”. In: *Physical Review Special Topics-Accelerators and Beams* 11.3 (2008), p. 032801.

[77] R. Pompili et al. “Femtosecond timing-jitter between photo-cathode laser and ultra-short electron bunches by means of hybrid compression”. In: *New Journal of Physics* 18.8 (2016), p. 083033.

[78] M. Galletti et al. “Overview and Recent Developments of the Frascati Laser for Acceleration and Multidisciplinary Experiments Laser Facility at SPARC_LAB”. In: *Applied Sciences* 14.19 (2024), p. 8619.

[79] R. Pompili et al. “Experimental characterization of active plasma lensing for electron beams”. In: *Applied Physics Letters* 110.10 (2017), p. 104101.

[80] V. Shpakov and et al. In: *Phys. Rev. Lett.* 122 (2019), p. 114801.

[81] R. Pompili et al. “Guiding of charged particle beams in curved plasma-discharge capillaries”. In: *Physical Review Letters* 132.21 (2024), p. 215001.

[82] F. Filippi et al. “Spectroscopic measurements of plasma emission light for plasma-based acceleration experiments”. In: *Journal of Instrumentation* 11.09 (2016), p. C09015.

[83] L. Verra et al. “Resonant excitation of plasma wakefields with a train of relativistic particle bunches”. In: *Phys. Rev. E* 112 (4 Oct. 2025), p. 045205. DOI: 10.1103/x4xl-4fnp. URL: https://link.aps.org/doi/10.1103/x4xl-4fnp.

[84] F. Galdenzi et al. “The EuAPS Betatron Radiation Source: Status Update and Photon Science Perspectives”. In: *Condensed Matter* 9.3 (2024), p. 30.

[85] *Source of Advanced Beam Imaging for Novel Applications*. URL: https://sabina.lnf.infn.it/.

[86] I. Balossino et al. “Mechanical strength investigations of the APPLE-X undulator using Fiber Bragg Grating strain measurements”. In: *arXiv preprint arXiv:2501.11531* (2025).

[87] S. Schulz and H. Schlarb. “Latest achievements in femtosecond synchronization of large-scale facilities”. In: *13th International Beam Instrumentation Conference No. 13 (IBIC2024)*. 2024, pp. 457–464.

[88] The European Parliament and the Council of the European Union. “Regulation (EU) 2020/852 of the European Parliament and of the Council of 18 June 2020 on the establishment of a framework to facilitate sustainable investment, and amending Regulation (EU) 2019/2088”. In: *Official Journal of the European Union* L 198.63 (2020), p. 13. URL: https://eur-lex.europa.eu/legal-content/EN/TXT/PDF/?uri=CELEX:32020R0852.

[89] Il Ministro della transizione ecologica. “Criteri ambientali minimi per l’affidamento del servizio di progettazione di interventi edilizi, per l’affidamento dei lavori per interventi edilizi e per l’affidamento congiunto di progettazione e lavori per interventi edilizi”. In: *Gazzetta Ufficiale della Repubblica Italiana* 183 (2022). URL: https://www.gazzettaufficiale.it/eli/id/2022/08/06/22A04307/sg.

[90] *details on Landmark requirements can be found in:* URL: https://www.esfri.eu/sites/default/files/ESFRI_Roadmap2026_Public%20Guide_approved_FINAL.pdf.

[91] D. Alesini et al. “Design, realization, and testing of a brazing-free C-band radio frequency photogun”. In: *Phys. Rev. Accel. Beams* 29 (1 Jan. 2026), p. 012001. DOI: 10.1103/jrth-j9sf. URL: https://link.aps.org/doi/10.1103/jrth-j9sf.

[92] G. Loisch et al. “Observation of High Transformer Ratio Plasma Wakefield Acceleration”. In: *Phys. Rev. Lett.* 121 (6 Aug. 2018), p. 064801. DOI: 10.1103/PhysRevLett.121.064801. URL: https://link.aps.org/doi/10.1103/PhysRevLett.121.064801.

[93] C. Joshi et al. “Plasma wave wigglers for free-electron lasers”. In: *IEEE journal of quantum electronics* 23.9 (1987), pp. 1571–1577.

[94] D. H. Whittum, A. M. Sessler, and J. M. Dawson. “Ion-channel laser”. In: *Physical review letters* 64.21 (1990), p. 2511.

[95] I. A. Andriyash et al. “An ultracompact X-ray source based on a laser-plasma undulator”. In: *Nature communications* 5.1 (2014), p. 4736.

[96] S. G. Rykovanov et al. “Plasma undulator based on laser excitation of wakefields in a plasma channel”. In: *Physical Review Letters* 114.14 (2015), p. 145003.

[97] A. Frazzitta et al. “Extreme radiation emission regime for electron beams in strong focusing ion channels and undulators”. In: *Physical Review Accelerators and Beams* 28.4 (2025), p. 040703.

[98] A. Frazzitta. “Plasma Discharge Undulator: a novel concept for plasma-based radiation sources”. In: *arXiv preprint arXiv:2601.06717* (2026).

[99] L. Serafini et al. “Considerations for a Gamma Source at EuPRAXIA”. In: *arXiv preprint arXiv:2601.07897* (2026).

[100] J. B. Rosenzweig et al. “Towards a plasma wake-field acceleration-based linear collider”. In: *Nuclear Instruments and Methods in Physics Research Section A: Accelerators, Spectrometers, Detectors and Associated Equipment* 410.3 (1998), pp. 532–543.

[101] S. Gessner et al. *arXiv: Design Initiative for a 10 TeV pCM Wakefield Collider*. Tech. rep. 2025.

[102] C. A. Lindstrøm. “Staging of plasma-wakefield accelerators”. In: *Physical Review Accelerators and Beams* 24.1 (2021), p. 014801.

[103] B. Foster et al. “Proceedings of the Erice workshop: A new baseline for the hybrid, asymmetric, linear Higgs factory HALHF”. In: *Physics Open* 23 (2025), p. 100261.

[104] J. F. Kamenik et al. *Physics Briefing Book: Input for the 2026 update of the European Strategy for Particle Physics*. Tech. rep. CERN, 2025.

[105] G. Sarri, L. Calvin, and M. Streeter. “Plasma-based positron sources at EuPRAXIA”. In: *Plasma Physics and Controlled Fusion* 64.4 (2022), p. 044001.

[106] C. Badiali et al. “Plasma Accelerator For Decaying Particle”. In: *arXiv preprint arXiv:2506.23668* (2025).

2. FEL Scientific Case

2.1 Introduction

The purpose of this chapter is to present the scientific motivation for the EuPRAXIA@SPARC_-LAB facility, focusing on the opportunities enabled by a plasma-driven Free Electron Laser (FEL) operating in the soft X-ray water window. The goals of this chapter are threefold:

1. General Motivation – to outline the broader vision of plasma-driven FELs as compact, cost-effective light sources, highlighting their potential to democratize access to ultrafast, high-brilliance X-ray science in the medium to long term.
2. Specific Science Case for AQUA – to define the photon science program realistically achievable with the AQUA beamline, based on the electron beam and FEL parameters derived in Beam Physics Chapter 3 and Undulator Chapter 8. The expected FEL performance—sub-percent bandwidth, more than 10^{11} photons per pulse, and few-femtosecond pulse duration—defines the operational envelope for the photon science program. This includes experiments that can be performed with the initial operating range of 3.2–5.2 nm, partially covering the water window, and extending to the range 3.2-10 nm that will be achievable with modest energy variations of the accelerator. Regarding the fluence and wavelength jitter across different pulses, shot-to-shot diagnostics, as described in Sec. 9.4, will be implemented to monitor the spectral properties of the incident beam and to enable appropriate correction procedures. Post-acquisition energy sorting and energy tagging will be employed to properly take into account shot-to-shot variations.
3. Staged Approach and Integration with Machine Development – to describe a phased strategy in which early experiments (gas-phase spectroscopy, ion spectroscopy, proof-of-principle bio-imaging) provide essential feedback for accelerator optimization, while subsequent phases progressively expand into more complex regimes (warm dense matter, aerosol studies, hydrated biological systems).

The chapter emphasizes the dual role of EuPRAXIA@SPARC_LAB as both a user facility and a development platform for advanced accelerator technology.

2.2 Science @ FELs in the soft X-ray region

FELs operating in the soft X-ray region are powerful tools for studying the structure and dynamics of matter at atomic and molecular scales [1]. Indeed, thanks to the high intensity and short duration of their pulses, FELs enable the exploration of fundamental processes such as electronic dynamics, chemical reactions, and phase transitions with unprecedented temporal and spatial resolution. Crucially, FELs allow experiments that are not feasible even at the brightest synchrotron sources, owing to their orders of magnitude higher peak brilliance and ultrashort pulses. This unique capability allows to obtain images of an object before the object itself is disintegrated by the FEL pulse [2–5]. The ultra-short FEL pulses also support time-resolved measurements—such as attosecond streaking of photoelectrons and investigations of saturable absorption in core-electron transitions—that reveal the intricate dynamics of electronic processes, chemical reactions, and phase transitions in extreme conditions [6–9].

At present, there are a few FEL facilities operational in the soft X-ray region, including FLASH [10], the EuropeanXFEL [11, 12], FERMI [13], SwissFEL [14], SACLA [15, 16], PAL [17] and LCLS [18]. The wide range of scientific opportunities offered by FELs is reflected in the distribution of allocated proposals, which, at operational soft X-rays FEL user facilities, spans condensed matter, low-density matter, magnetism, atoms, molecules, plasmas, polymers, and soft matter research employing techniques such as diffraction imaging, time-resolved photoemission and elastic and inelastic scattering. A survey conducted within the EuPRAXIA Preparatory Phase project (EuPRAXIA-PP [19]) among prospective international users confirms strong interest in these same scientific areas, indicating that the topics of highest relevance for AQUA closely mirror those already prominent at existing soft X-ray FEL facilities. EuPRAXIA@SPARC_LAB will extend the list of FEL sources by hosting a soft X-ray SASE FEL beamline, delivering, according to start-to-end simulations, more than 10^{11} photons/pulse with a pulse duration of about 10 femtoseconds and a wavelength of around 4 nm within the AQUA operational range of 3.2–5.2 nm, with possible extension toward longer wavelengths up to 10 nm in a later stage (see Chapter 3). This energy range partially falls within the so-called water window, i.e. the wavelength range between carbon (4.40 nm) and oxygen (2.33 nm) K-edges. For this reason, the beamline exploiting the FEL beam to perform photon science experiments has been termed AQUA, which stands for "water" in Latin. Moreover, the possibility of exploiting higher harmonics for shorter wavelength experiments, thus going to and beyond the oxygen K-edge, will be explored. However, these possible future developments are not discussed in the present document.

Notably, EuPRAXIA@SPARC_LAB represents more than just another FEL facility at the disposal of the scientific community. Its innovative character lies in the use of plasma-based acceleration, with the ultimate goal of developing a technology that will enable the construction of compact and therefore cost-effective FEL sources. As highlighted in the Executive Summary, the adoption of plasma acceleration is expected to reduce the overall facility length by a factor of three compared to conventional machines operating at the same wavelength, and to lower the cost of accelerating modules by a factor of four while delivering the same energy gain. In the medium to long term, these advances will enable the emergence of smaller-scale FEL facilities, promoting wider access to ultrafast X-ray science and accelerating progress across multiple disciplines.

The scientific program will be aligned with this challenging objective. To achieve this, it is structured to evolve through successive phases, each designed to exploit the machine technological developments in support of increasingly advanced photon-beam experiments. This phased strategy will support the integration of emerging innovations, systematically address and provide feedback on technical challenges, and progressively optimize system performance. The subsequent phases of the program are described in more detail in Section 2.2.1.

It is worth pointing out that obtaining beamtime at a FEL source is still a major bottleneck to perform experiments requiring high-brilliance, ultra-short pulses. Unlike synchrotrons, which can

support simultaneous experiments across multiple beamlines, FELs operate as inherently "serial" sources — accommodating only one (or in some cases, two) experiments at a time. Consequently, there is a significant fraction (depending on the facility specifications, on its photon wavelength and on the specific beamline features) of the submitted proposals not receiving beamtime at currently operational facilities. Looking ahead, the applicant pool is likely to grow as synchrotron users port time-resolved and element-specific studies to FEL platforms, further increasing demand for limited beamtime. The AQUA beamline will therefore contribute to increase the availability of beamtime and to enlarge the community of active FEL users. Given the nature of the EuPRAXIA@SPARC_-LAB plasma-based source, photon science users will work in close collaboration with accelerator physics scientists. This interaction will give the possibility to tailor the beam properties to adapt to niche applications which might be difficult to perform at larger scale FEL facilities. In the end, the facility will contribute to the development of new FEL methodologies and diagnostics schemes. Although not present in the baseline of the project and therefore falling outside the scope of the present document, it is worth mentioning here that a second accelerator branch line called ARIA (which stands for "air" in Italian), producing seeded FEL radiation in the VUV (50 nm - 180 nm) range, is being evaluated and will likely be present on the side of the AQUA beamline [20]. The ARIA beamline would constitute a unique opportunity to achieve innovation in XUV optics and detector developments for an optimal exploitation of FEL radiation for investigating the physics of matter and materials.

2.2.1 Photon Science Applications at AQUA

Thanks to its bright, ultra-short, coherent photon pulses, AQUA will in principle be able to support a photon science program spanning diverse fields such as atomic and molecular physics, chemistry, including photochemistry, atmospheric and astrochemistry, and life science. As detailed in the next section, experimental techniques, including coherent imaging, X-ray absorption and ion and electron spectroscopies will be implemented to pursue the photon science program. However, given the novel, plasma-based electron acceleration method, the photon experiments will grow in complexity as the performance and stability of the beam improves. Therefore, in this section, we showcase a few examples of the scientific challenges that EuPRAXIA@SPARC_LAB will be able to address, while the description of the experimental techniques is given in Section 2.3.

Atomic, Molecular and Optical physics

The availability of ultrashort, coherent soft X-ray pulses enables Atomic, Molecular and Optical (AMO) experiments with a particular focus on gas-phase systems. Gas-phase targets provide isolated, solvent-free environments where electronic and nuclear dynamics can be tracked on their natural femtosecond timescales, yielding molecule-specific fingerprints that are difficult to extract in condensed phases. Soft-X-ray excitation at AQUA gives access to site-specific processes—including core-hole decay, charge migration and dissociation—as well as nonlinear X-ray interactions at high peak brightness. These molecular-frame measurements permit quantitative determination of cross sections, fragmentation pathways and ultrafast dynamics in isolated molecules, clusters and aerosol proxies.

AQUA will further enable the combination of X-ray absorption, imaging of injected nanoparticles or model aerosols, and photo-ionization mass spectrometry (PI-MS), which provides selective detection of molecular species based on their ionization and fragmentation signatures. This capability is particularly relevant for fundamental atmospheric chemistry: PI-MS can probe the ultrafast photophysics of volatile organic compounds (VOCs) and nitrogen oxides (NOx) under controlled gas-phase conditions. By resolving prompt ionization and fragmentation on the femtosecond scale, these experiments deliver benchmark data on elementary photochemical steps that complement measurements performed under realistic atmospheric conditions. With time-resolved ion detection,

AQUA can finally follow the evolution of these species on ultrafast timescales, revealing the primary pathways that initiate atmospheric reactions.

Warm Dense Matter

The AQUA instrument is ideal both to generate and to investigate the behavior of materials under extreme conditions resulting from the interaction with the FEL beam [21]. At intensities of 10^{11} photons/pulse a soft X-ray FEL can bring a sample to a regime known as Warm Dense Matter (WDM) in a few tens of femtoseconds. WDM is a state of matter at the boundary between condensed matter and plasma. It typically occurs at temperatures ranging from thousands to millions of degrees and at high densities where electrons and ions are strongly coupled exhibiting kinetic energies comparable to the Coulomb potential energy. Under these conditions both condensed matter and plasma theoretical frameworks fail to describe the properties of matter, thus demanding deeper experimental insight. Warm Dense Matter is of great interest in several fields. In astrophysical and planetary sciences, WDM is found in the interiors of stars, giant planets, and white dwarfs. Understanding the properties of WDM helps to model the behavior of matter in systems, such as the core of gas giants, where the pressure and temperature are incredibly high. In the field of fusion research, studying WDM can help improve the efficiency and achieving the technological feasibility of inertial confinement fusion and magnetic confinement fusion reactors. In general, studying WDM provides insights into the behavior of materials under extreme stresses and temperatures, as those encountered during high-energy events, such as explosions or rapid compressions, which is essential for material science applications.

Biology and Health

For what concerns biological samples, EuPRAXIA@SPARC_LAB will allow studying cells and bacteria in their native conditions. The ultrashort pulse durations and high brilliance of the FEL allow to capture time-resolved images and spectra of living cells (as in Figure 2.1) and microbial communities. It is worth pointing out that, given the accessible wavelength range, the expected resolution is of tens of nanometers, thus not going down to atomic resolution. However, imaging in native conditions will still enable the investigation of dynamic cellular processes—such as stress responses, membrane dynamics, and intracellular signaling. By directly probing these processes in situ, experiments at EuPRAXIA@SPARC_LAB offer unique insights into the structure–function relationships that govern microbial adaptation and pathogenesis, ultimately paving the way for innovative therapeutic strategies. In addition, FEL-based photoinduced fragmentation studies will help unravel fundamental DNA damage mechanisms, providing insights that may lead to improved cancer therapies and radioprotection strategies. Finally, AQUA will allow performing photochemistry and astrochemistry relevant experiments. As an example, it will be possible to study how short wavelength radiation exposure can influence the chemical composition and abundance of molecules in space, unraveling the process leading to the formation of molecules, including organic ones, in the interstellar space.

2.3 Experimental techniques @ AQUA

This section presents the main experimental techniques planned for the AQUA beamline. As previously noted, the scientific program will follow a phased approach: it will begin with experiments that are less demanding in terms of photon beam parameters, characterization, and setup requirements, and then progress toward more complex investigations. The technical requirements for the various phases detailed here below are described in the endstation Chapter 10.1. The FEL will first be commissioned by characterizing the spectral features and by performing Coherent Diffraction Imaging (CDI) measurements on fixed, calibration samples, to allow beam and detectors

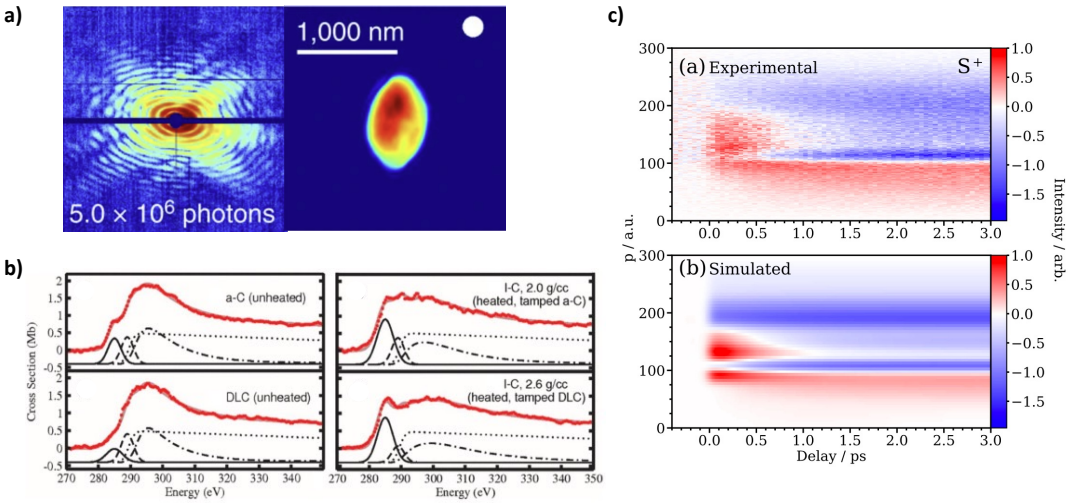

Figure 2.1: Literature examples corresponding to the scientific areas described above. a) Diffraction pattern and reconstructed electron density of an aerosolised living cyanobacterium. Image adapted from [22] b) TR-XAS measurements on liquid carbon reveal changes in bonding structure and bond length under varying densities, providing insights into its behavior as warm dense matter. Image adapted from [23]. c) Time-resolved Coulomb explosion imaging of photoexcited CS_2 using soft X-ray pulses. Image adapted from [24].

characterization and alignment (Endstation Phase 0 (*P0*)). CDI provides an excellent benchmark for coherence, photon energy, spectral bandwidth, and spatial stability, and serves as a testbed for assessing instrument resolution. Starting in Phase *P1*, we will prioritize ion and electron spectroscopy on fixed and gas-phase targets, complemented by CDI and X-ray absorption spectroscopy (XAS). The initial Endstation Phase 1 experiments will focus on static measurements, serving as a baseline for system characterization and optimization. Still within Endstation Phase 1 (*P1*), the program will advance to time-resolved studies, employing an external laser to optically excite (pump) the sample, followed by probing with the FEL pulses. This pump–probe configuration will allow the investigation of ultrafast dynamics in excited states, providing insights into transient phenomena at femtosecond timescales. In Endstation Phase 2 (*P2*), the experimental scope will expand to include samples in aerosols and liquid environments. As detailed in the experimental endstation Chapter 10.1 this development introduces technical challenges, particularly related to maintaining vacuum conditions and ensuring operational cleanliness. However, it also unlocks the possibility of studying samples under close-to-native, fully hydrated conditions, which is critical for probing biological systems and chemical processes in realistic environments. Moreover, in the later stage of *P2* the possibility of using the FEL both as a pump and as a probe with a the split-and-delay scheme will be explored.

The phased experimental approach at EuPRAXIA@SPARC_LAB is designed to ensure a smooth transition from initial beam characterization and system calibration to advanced, time-resolved scientific investigations. This strategy not only maximizes the scientific output from the FEL source but also provides a flexible and robust platform capable of addressing a wide range of research challenges. By integrating techniques such as CDI, XAS, emission, and scattering spectroscopies, along with ion and electron analyses, the facility is well-positioned to make significant contributions across multiple disciplines.

This diverse palette of experimental techniques will enable the investigation of a wide range of phenomena spanning multiple scientific fields. In materials science, they allow detailed characterization of quantum materials, nanostructures, and magnetic systems. In chemistry and catalysis,

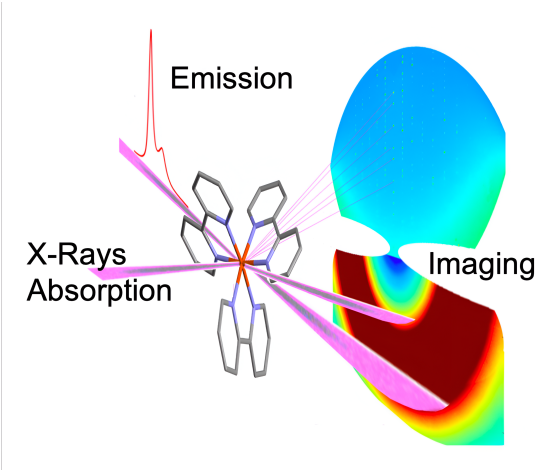

Figure 2.2: Schematics of some complementary X-ray–based techniques, such as spectroscopy and imaging, that could be employed at the new EuPRAXIA@SPARC_LAB. By probing in the ultrafast time domain, these methods enable us to capture the evolving electronic and structural dynamics of molecular systems, solutions, solids, and biosystems, thus providing deeper insights into the nature of dynamical matter. Image adapted from [25].

they provide real-time access to chemical reactions and catalytic processes, yielding insight into reaction intermediates and transition states. In biological and biomedical research, imaging and spectroscopic approaches enable the study of biological molecules and entire cells, deepening our understanding of biomolecular dynamics. In environmental science, in situ studies of chemical processes in environmental samples support the analysis of pollutants and atmospheric reactions.

2.3.1 Coherent imaging

CDI has emerged as a powerful technique in the field of X-ray science, enabling the study of non-crystalline and weakly scattering specimens at nanometer-scale resolution [26–28]. In particular, thanks to the high spatial coherence and extreme brightness of FELs, CDI measurements performed at FELs allow to record diffraction patterns of complex objects and subsequently reconstruct the sample's electron density in real space without relying on crystallinity [3, 29]. Unlike conventional microscopy methods that suffer from depth-of-focus or lens limitations, CDI utilizes the intrinsic coherence of synchrotrons or FEL beams to illuminate samples in a lensless geometry [4]. Through iterative phase retrieval algorithms [30–32], the complex scattering amplitudes can be recovered, thereby reconstructing high-resolution images of targets. One of the key challenges in FEL CDI is sample damage induced by the intense FEL pulses. However, the "diffraction-before-destruction" concept—initially predicted by theory [33–35] and later confirmed by experiments [2] — circumvents this issue. By using a single femtosecond FEL pulse to capture a diffraction snapshot before significant radiation damage occurs, sensitive targets such as nanostructured particles or biological molecules can be imaged in their native state, which would otherwise be irreversibly altered during prolonged exposure. CDI has been successfully applied at FELs to diverse samples [36], including single bio-molecules [37], viruses [38], organelles, and entire cells [39, 40]. Besides biological systems, single shot diffractive imaging has been used to study the morphology of nanoparticles [41], aerosols [42] and combustion products [43], power density dependent damage processes in atomic clusters [44], and superfluid quantum systems [45]. In addition to conventional CDI, advanced holographic approaches, most notably X-ray Fourier-transform holography, have expanded the lensless imaging capabilities at FEL sources [46]. By introducing a well-defined reference object in the beam path, the phase information is directly

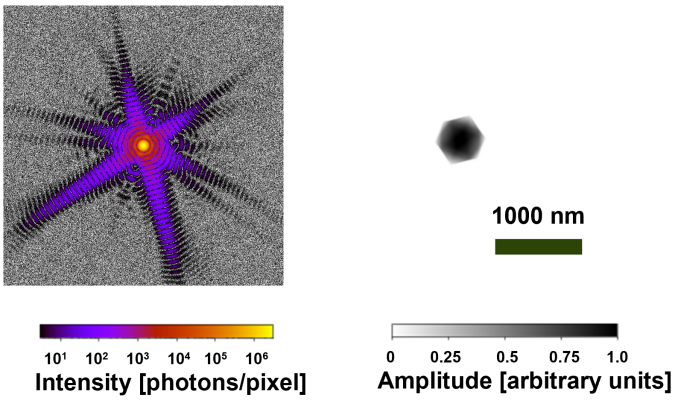

Figure 2.3: Simulated, ideal CDI diffraction pattern of a poliovirus. The simulation was performed using the Condor software [49], assuming the FEL beam parameters expected at AQUA, namely 10^{11} photons per pulse at a wavelength of 4.3 nm, focused onto a 5 μm spot size. Gaussian (detector readout) and Poisson (FEL shot) noise were added to emulate experimental conditions.

encoded in the resulting interference pattern, removing the need for fully iterative reconstruction. Such an approach has already enabled single-shot or time-resolved imaging of rapidly evolving structures—from magnetic domain rearrangements [22] to conformational transitions [47] — while also benefiting from more flexible reference designs and potentially higher signal-to-noise ratios [48]. For these reasons, these advanced CDI techniques will be particularly suitable for experiments at AQUA.

As mentioned previously, the AQUA beamline will supply photons in the so-called water window, in which biological materials, mainly constituted by carbon atoms, exhibit strong natural contrast against water. The water window energy range is particularly advantageous for CDI, as carbon containing structures absorb X-rays more strongly than the surrounding water, thereby enabling high-resolution imaging of biological samples in their native, hydrated state. Thanks to this, at AQUA it will be possible to acquire diffraction patterns from living cells and to reconstruct their electron density at a resolution of few tens of nanometers. Just for the sake of visualization, an idealized pattern of a large virus simulated under the AQUA experimental conditions is given in Figure 2.3.

Since, although it has not yet been investigated in detail, the EuPRAXIA@SPARC_LAB photon range could extend beyond the water window towards longer wavelengths (up to about 10 nm), the AQUA beamline will be able to accommodate CDI experiments over this extended range. Energy and wavelength jitter effects will be considered by incorporating shot-to-shot spectral diagnostics (as detailed in 9.4) into the reconstruction pipeline, enabling wavelength-dependent phase retrieval corrections and, when necessary, sorting or rebinning of diffraction patterns according to their measured incident photon energy. Depending on the wavelength and the focusing options, the AQUA endstation will deliver approximately about 10^{10} - 10^{11} photons per pulse in ultra-short pulses — on the order of ten femtoseconds. These short pulses are essential for freeze-frame imaging capturing transient states or rapid dynamics, enabling experiments in which a pump laser triggers a reaction and the FEL probe pulse records the ensuing structural changes.

With a 100 Hz repetition rate, thousands of diffraction patterns can be collected in just a few minutes, ensuring robust data statistics. For samples that, at the achievable resolution, can be considered identical - as viruses observed at tens of nanometers resolution - it will be also possible to acquire multiple diffraction patterns from different, random orientations and obtain a

3D tomographic reconstruction [50].

The EuPRAXIA@SPARC_LAB FEL beam stands as highly suitable for a broad range of CDI investigations when coupled with efficient detectors and optimized sample delivery methods. High-throughput sample injection schemes—ranging from solid supports (e.g., thin membranes, meshes, and conveyor belts) to liquid jets and aerodynamic lens stacks (see details in Sections 10.2.2.3 and 10.2.2.4 of Chapter 10) — will facilitate the delivery of fresh samples at each pulse. These methods minimize sample consumption while increasing the probability of intercepting a target with each shot. Furthermore, improved detector technologies, featuring a higher dynamic range and lower noise levels, are expected to enhance the signal-to-noise ratio under low-photon conditions. Recent advances in data processing and phase retrieval algorithms [31, 32, 51] have demonstrated that successful reconstructions are achievable from diffraction patterns with fewer photons, underscoring the adaptability of CDI techniques even with lower brilliance sources.

Time-resolved CDI experiments can be conducted by pairing the FEL pulses with an ultrafast pump source, such as an optical laser or terahertz pulse. When the sample is excited, driven, or perturbed by the pump, the FEL probe arrives at a precisely controlled delay, capturing the evolution of the sample's structure in "snapshot" increments down to femtosecond timescales. By systematically scanning the delay, time series of diffraction patterns that map out reaction pathways or transient phases can be obtained, reconstructing a movie of structural changes at the atomic or nanometer scale. This approach is invaluable for elucidating ultrafast processes in protein folding and functioning, chemical reactions, or phase transitions in correlated electron materials.

In summary, AQUA's intense, femtosecond pulses in the XUV wavelength range will significantly broaden access to lensless imaging, enabling studies in structural biology, nanoscience, and materials research. In particular, the photon wavelength falling between the C and O K-edge will allow collecting high-contrast images of biological samples under hydrated conditions. Moreover, the femtosecond pulse length allows collecting diffraction patterns before significant damage of the samples. Enhanced detection schemes, exploiting small-pixel, low-intrinsic noise detectors and state-of-the-art computational algorithms will ensure that experiments continue to achieve tens of nanometers-resolution reconstructions, even under modest photon flux conditions.

2.3.2 X-ray spectroscopies

X-ray Absorption Spectroscopy (XAS) is an invaluable technique for elucidating the local structural and electronic properties of samples due to their inherent element- and site-specific sensitivity. These techniques enable detailed investigation of local structural configurations, electronic states, and even nonlinear optical phenomena across broad spectrum of targets — including organic molecules, biomolecules, polymers, nanostructured compounds, and solids. XAS will benefit from the tuneable, intense and short FEL pulses, facilitating the exploration of time-resolved processes, ultrafast chemical reactions (including photochemical ones) in both liquid and gas phases, and the probing of the electronic structure of transition-metal complexes in solution or under operando conditions [52]. Applications extend to research on solar energy conversion systems, small molecules, organic frameworks, and surface chemical reactions.
At the AQUA beamline, the target energy range is particularly suited for investigating the K-edge of carbon. At a later stage, when also longer wavelength pulses will be produced, the L-edges of elements such as phosphor, sulfur and chlorine, and the M-edges of higher-Z elements, will become accessible. This versatility opens up applications in catalysis, solar energy conversion, small organic molecules, polarization-dependent phenomena, non-adiabatic dynamics of photoexcited molecular systems, and surface reactions [53]. XAS pump-probe experiments will allow the study of ultra-fast processes, such as charge transfer, bond-breaking, structural isomerization, electronic relaxation, and vibrational dynamics.

A significant challenge when performing XAS at a SASE FEL is the inherent spectral jitter,

which results in a variable spectral structure from shot to shot (see Chapter 3 for details). One common approach to manage this variability is the use of a monochromator to exploit the natural jitter of the radiation and scan the photon energy across the desired spectral range [54]. However, this method reduces the photon flux at the sample due to the limited transmission of optical elements and the intrinsic spectral jitter. Consequently, during the initial operation phase of AQUA, no monochromator will be installed. Instead, alternative schemes for XAS measurements that are compatible with variable SASE sources will be implemented. These schemes are referred to as "correlation spectroscopies", since they perform correlations either between spectra upstream and downstream of the sample [55–57], or between the upstream FEL beam spectrum with the beam intensity downstream of the sample [58]. This latter scheme is referred to as "ghost spectroscopy". The former approach requires the simultaneous use of two spectrometers, one upstream and one downstream from the sample interaction region, to monitor the incident and transmitted spectra on a shot-to-shot basis in a dispersive geometry, thereby allowing for proper normalization [59–61]. In "ghost spectroscopy" [58, 62, 63], the sample's absorption spectrum is reconstructed by correlating the measured input spectral profile of each pulse with the integrated detector signal—typically from a photodiode — after the sample. The detector's response effectively maps the overlap between the variable pulse spectrum and the sample's transmission function, enabling a reconstruction of the absorption features over multiple pulses with varying spectra. Assembling diverse spectral regions obtained by tuning the FEL central photon energy, one can obtain high energy resolution XAS, extending over tens of eV. The correlation spectroscopy requires a spiky broadband spectrum, and is therefore in line with the AQUA SASE FEL spectrum. Moreover, correlation spectroscopy has to be operated below the sample damage threshold. Finally, the correlation spectroscopy scheme is based on the shot-to-shot measurements of each FEL pulse, thus naturally correcting for energy and wavelength jitter. Therefore, the technique is ideal for the AQUA FEL pulse intensity, does not require a tight focus, thus facilitating the transverse superposition with the laser pump beam and drastically limiting the issues related to FEL beam pointing instability.

The soft-X rays XAS measurements performed at AQUA will be a framework for investigating a wide range of atomic and molecular structures. In order to perform time-domain spectroscopy, the FEL pulses will be combined with synchronized optical lasers in the pump-probe configuration. To ensure precise temporal overlap between the FEL pulses and the optical or other external laser pulses on the femtosecond timescale, timing jitter correction systems will be used. Ultrafast processes, such as charge transfer, electronic relaxation, and vibrational dynamics will be studied in this scheme. As pointed out above, the AQUA accessible energy range spans K, L and M edges, allowing XAS measurements on different elements. Considering the K-edge, it will be possible to perform experiments on carbon. Carbon is particularly interesting, since C is the basic constituent of all organic and biological molecules, and therefore spectroscopy at its K edge allows the study of a very broad range of systems [64]. When longer wavelengths will become accessible, L-edge measurements on P, S and Cl will be possible. Although L-edge spectroscopy poses experimental challenges, its cross section can be even two orders of magnitude higher than that at the K-edge, thus enabling the acquisition of higher signal to noise ratio from low concentrated samples. As a side effect, this implies that severe radiation damage can cause problems in experiments performed on sensitive samples. Since the damage is mainly caused by radical diffusion, which takes place in the picosecond time regime, the femtosecond-pulses FEL sources are an ideal tool to overcome/minimize this problem [65]. Potential applications of L-edge (mass) spectroscopy at the sulfur L-edge have demonstrated its capability to probe the inner shells of sulfur atoms using synchrotron sources [66]. Moreover, lanthanides N-edges are accessible, thus allowing oxidation state and ligand field effect studies for characterizing magnetic, luminescent, and redox-active lanthanide systems with element-specific sensitivity. When coupled to an ultrafast laser as a pump, the intrinsic time-resolution capabilities of AQUA will also enable the exploration

of the complex photophysics of transition metal complexes [67].

In the end, the SASE nature of the FEL radiation will allow performing correlation XAS measurements, thus not requiring the installation of a monochromator. The details of the spectrometers required to perform this kind of measurements are provided in the chapter dedicated to the experimental endstation 10. On the photon wavelength side, it will allow studying the K-edge of C, thus accessing a wealth of organic and biological systems. The extension towards longer wavelengths could then broaden the accessible elements. Finally, thanks to the ten(s) fs pulse-length, AQUA will allow performing ultrafast experiments.

2.3.3 Ion and Electron Spectroscopies

X-ray ion and electron spectroscopies are analytical techniques used to study how X-ray photons interact with matter by inducing ionization. Electron spectroscopies (e.g. Photoemission Spectroscopy, PES) detect the emitted electrons and provide direct access to binding energies and electronic structure, whereas ion spectroscopies analyze the resulting charged fragments. In this section we focus primarily on ion spectroscopy, with PES discussed as a potential future capability in Endstation Phase 2. When a sample is exposed to an intense X-ray pulse, the high-energy photons can eject inner-shell electrons from the atoms or molecules. This primary ionization event often triggers secondary processes—such as Auger decay or fluorescence—resulting in the formation of various charged species. By measuring the mass-to-charge ratios, kinetic energies, and abundances of these ions using instruments like time-of-flight mass spectrometers, information about the electronic structure, chemical composition, and dynamic behavior of the sample can be obtained. Rather than only revealing *what* absorbs, ion spectroscopy reports *what changes, how far, and how fast*—capturing bond breaking, charge migration, and Coulomb explosion in real time. Ion spectroscopy is particularly powerful when combined with ultrafast X-ray sources such as FELs, capturing rapid ionization dynamics on femtosecond timescales and allowing the study of transient states and reaction pathways that are crucial in fields ranging from materials science and chemistry to biology and plasma physics. Thanks to the peak brightness and femtosecond AQUA pulse duration, techniques such as time-of-flight mass spectrometry and ion coincidence measurements enable the precise determination of ion yields, kinetic energies, and charge states following intense light–matter interactions. These measurements provide critical insights into the mechanisms of multiphoton ionization and Coulomb explosion, which are essential for understanding transient molecular and plasma states.
In the context of the EuPRAXIA@SPARC_LAB facility, the incorporation of advanced ion spectroscopy capabilities is expected to play a pivotal role in characterizing the interplay between photon-induced ionization processes and subsequent fragmentation, ensuring a comprehensive understanding of both fundamental and application-oriented phenomena. In the AQUA energy range, ion spectroscopy can access critical absorption edges such as the carbon K-edge, other light-element L-edges and lanthanides N-edges.

One particularly interesting application of ion spectroscopy at AQUA is Coulomb Explosion Imaging (CEI) [24, 72]. By analyzing the trajectories of ions produced by intense FEL-induced multi-ionization, CEI can enable the reconstruction of three-dimensional molecular geometries. The planned experiments will exploit this technique to capture transient structural changes in molecules undergoing chemical reactions, including isomerization, bond breaking, and complex formation. These studies will provide real-time insight into how molecular structures evolve, shedding light on reaction mechanisms and molecular dynamics. Moreover, theoretical works suggest that coupling CEI data with CDI can reveal the orientation of individual molecules at the moment of X-ray irradiation, which is critical for improving single-particle CDI reconstructions [73–76]. The dual CDI/CEI approach promises a powerful strategy for capturing atomic-resolution structures of biomolecules in their native state, offering deeper insights into both their shape and function.

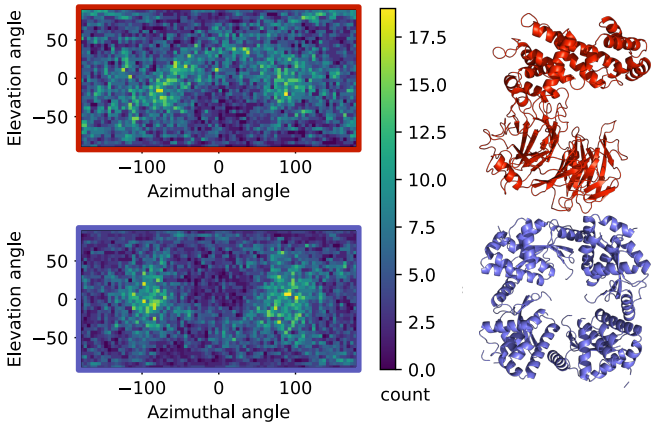

Figure 2.4: Simulated CEI footprints under AQUA beamline experimental conditions. Simulations were performed using the MOLDSTRUCT software [68] for two proteins of similar mass: one originating from the cell nucleus (Nucleoporin, PDB ID: 4mhc [69], shown in red) and one derived from a virus (avian influenza virus PA_N Apo, PDB ID: 4e5e [70], shown in blue). Differences between the footprints enable clear differentiation of the two proteins upon explosion. Image adapted from [71].

Fragmentation studies will also profit substantially from the AQUA's capabilities [77, 78]. Ion spectroscopy allows for the identification of dissociation channels and bond strengths in diverse systems, from small organic molecules to large biomolecules. By probing charge redistribution and fragmentation pathways, these investigations aim to reveal the fundamental principles governing molecular stability and decay processes. This knowledge will enrich our understanding of gas-phase molecular dynamics and inform related fields such as mass spectrometry, where fragmentation data is essential for molecular identification. Moreover, elucidating the fragmentation pathways of DNA and its constituent molecules—such as nucleobases, deoxyribose sugars, and phosphate groups—under intense radiation is critical for enhancing our understanding of radiation-induced damage, thereby opening avenues for more targeted cancer therapies [79, 80].

Another central focus is the study of cluster and nanoparticle dynamics. Nanoscale systems exhibit unique electronic and structural properties that are highly sensitive to ionization and fragmentation processes. Through ion spectroscopy, the effect of electronic excitations on the ionization behavior and on the fragmentation patterns in clusters and nanoparticles can be studied. These efforts will involve exploring size-dependent effects, charge delocalization, and energy dissipation mechanisms, ultimately influencing the development of advanced nanostructured materials and devices. Finally, the FEL's ultrafast pulse structure will enable time-resolved ion spectroscopy, capturing ionization and fragmentation processes as they unfold. By synchronizing FEL pulses with external laser systems in a pump-probe configuration, ultrafast phenomena such as charge migration, electron correlation effects, and nuclear rearrangements can be tracked. These studies will contribute to the understanding of the intricate interplay between electronic and nuclear motion in complex systems, providing a comprehensive view of molecular and nanoscale dynamics.
On a more applicative track, coupling tunable soft X-ray excitation with photoionization mass spectrometry (PI-MS) is under consideration as a complementary diagnostic. If implemented, this approach may enable time-resolved detection of selected gas-phase and aerosol species and the characterization of their fragmentation patterns. The achievable selectivity and sensitivity will depend on source parameters, ion-optics, and calibration, and will be established in proof-of-principle tests (e.g., [81–83]). Relevant application areas include hydrogen-related chemistry [84], pollutant identification [85], and energy-storage materials [86, 87].

In Endstation Phase 2 (P2), PES may be implemented to probe core and valence electronic states, offering direct insight into the electronic structure and local chemical environment [88]. Key applications include revealing intermediates and adsorbates on catalytic surfaces, studying redox processes in energy materials, and probing functional groups in biological macromolecules, thereby providing essential information on their electronic structure and properties [89–92]. A fundamental prerequisite for PES is the use of monochromatic radiation. Thus, it will be introduced only in a later phase of AQUA operation, when a monochromator will be added to the beamline, and it can be coupled with higher harmonics of the FEL beam.

The main requirements to perform the experiments described above include high photon flux, ultrashort pulses, tunability around relevant absorption edges, and a suitable repetition rate (with monochromatic bandwidth for future PES), which are in line with the AQUA performances.

2.3.4 Conclusions

In conclusion, the AQUA scientific program has been defined within a realistic and staged framework that reflects the expected performance of the EuPRAXIA@SPARC_LAB FEL. Initial experiments will concentrate on gas-phase AMO physics, ion and electron spectroscopy, and fundamental photochemical studies, which represent robust, high-impact use cases compatible with early beam parameters and essential for providing immediate feedback to accelerator optimization. As the facility matures, this program will progressively extend toward more demanding measurements, including warm dense matter studies, liquid-phase spectroscopy, and coherent imaging of hydrated biological systems within the water window range.

This staged evolution mirrors the broader mission of EuPRAXIA@SPARC_LAB: to deliver competitive soft X-ray FEL capabilities while acting as the first plasma-wakefield-driven FEL demonstrator operated under user-facility conditions. The scientific activities described in this chapter are therefore tightly coupled to machine development, ensuring that user experiments and accelerator innovation advance in synergy. Through this dual role, EuPRAXIA@SPARC_LAB will not only open new opportunities in ultrafast X-ray science but will also contribute to establishing the foundations of future compact, high-brightness FEL sources.

Bibliography

[1] N. Huang et al. “Features and futures of X-ray free-electron lasers”. In: *The Innovation* 2.2 (2021).

[2] H. N. Chapman et al. “Femtosecond diffractive imaging with a soft-X-ray free-electron laser”. In: *Nature Physics* 2.12 (2006), pp. 839–843.

[3] A. P. Mancuso et al. “Coherent imaging of biological samples with femtosecond pulses at the free-electron laser FLASH”. In: *New Journal of Physics* 12.3 (2010), p. 035003.

[4] H. N. Chapman and K. A. Nugent. “Coherent lensless X-ray imaging”. In: *Nature photonics* 4.12 (2010), pp. 833–839.

[5] A. V. Martin et al. “Single particle imaging with soft X-rays at the Linac Coherent Light Source”. In: *Advances in X-ray free-electron lasers: radiation schemes, X-ray optics, and instrumentation*. Vol. 8078. SPIE. 2011, pp. 39–47.

[6] B. Nagler et al. “Turning solid aluminium transparent by intense soft X-ray photoionization”. In: *Nature Physics* 5.9 (2009), pp. 693–696.

[7] I. Grguraš et al. “Ultrafast X-ray pulse characterization at free-electron lasers”. In: *Nature Photonics* 6.12 (2012), pp. 852–857.

[8] N. Hartmann et al. “Attosecond time–energy structure of X-ray free-electron laser pulses”. In: *Nature Photonics* 12.4 (2018), pp. 215–220.

[9] S. Schulz et al. “Femtosecond all-optical synchronization of an X-ray free-electron laser”. In: *Nature communications* 6.1 (2015), p. 5938.

[10] M. Beye et al. “FLASH and the FLASH2020+ project-current status and upgrades for the free-electron laser in Hamburg at DESY”. In: *The European Physical Journal Plus* 138.3 (2023), p. 193.

[11] M. Altarelli. “The European X-ray free-electron laser facility in Hamburg”. In: *Nuclear Instruments and Methods in Physics Research Section B: Beam Interactions with Materials and Atoms* 269.24 (2011), pp. 2845–2849.

[12] T. Tschentscher et al. “Photon beam transport and scientific instruments at the European XFEL”. In: *Applied Sciences* 7.6 (2017), p. 592.

[13] E. Allaria et al. “The FERMI free-electron lasers”. In: *Journal of synchrotron radiation* 22.3 (2015), pp. 485–491.

[14] C. J. Milne et al. “SwissFEL: the Swiss X-ray free electron laser”. In: *Applied Sciences* 7.7 (2017), p. 720.

[15] Z. Huang and I. Lindau. “Free-electron lasers: SACLA hard-X-ray compact FEL”. In: *Nature Photonics* 6.8 (2012), p. 505.

[16] S. Owada et al. “A soft X-ray free-electron laser beamline at SACLA: the light source, photon beamline and experimental station”. In: *Journal of Synchrotron Radiation* 25.1 (2018), pp. 282–288.

[17] S. H. Park et al. “PAL-XFEL soft X-ray scientific instruments and X-ray optics: First commissioning results”. In: *Review of Scientific Instruments* 89.5 (2018).

[18] W. F. Schlotter et al. “The soft x-ray instrument for materials studies at the linac coherent light source x-ray free-electron laser”. In: *Review of Scientific Instruments* 83.4 (2012).

[19] EuPRAXIA Preparatory Phase. *EuPRAXIA-PP — Towards revolutionary applications and benefits for society*. `https://www.eupraxia-pp.org/`. Accessed: 2025-11-28. 2025.

[20] F. Villa et al. “Aria-a vuv beamline for eupraxia@ sparc_lab”. In: *Condensed Matter* 7.1 (2022), p. 11.

[21] R. W. Lee et al. “Finite temperature dense matter studies on next-generation light sources”. In: *Journal of the Optical Society of America B* 20.4 (2003), pp. 770–778.

[22] C. von Korff Schmising et al. “Imaging ultrafast demagnetization dynamics after a spatially localized optical excitation”. In: *Physical review letters* 112.21 (2014), p. 217203.

[23] G. Kang and B. I. Cho. “Investigation of warm dense matter using time-resolved X-ray absorption spectroscopy with third-and fourth-generation light sources”. In: *Current Applied Physics* 30 (2021), pp. 58–68.

[24] J. Unwin et al. “X-ray induced Coulomb explosion imaging of transient excited-state structural rearrangements in CS2”. In: *Communications Physics* 6.1 (2023), p. 309.

[25] M. Chergui and E. Collet. “Photoinduced structural dynamics of molecular systems mapped by time-resolved X-ray methods”. In: *Chemical reviews* 117.16 (2017), pp. 11025–11065.

[26] J. Miao, R. L. Sandberg, and C. Song. “Coherent x-ray diffraction imaging”. In: *IEEE Journal of selected topics in quantum electronics* 18.1 (2011), pp. 399–410.

[27] J. Miao et al. “Beyond crystallography: Diffractive imaging using coherent x-ray light sources”. In: *Science* 348.6234 (2015), pp. 530–535.

[28] P. A. Prosekov, V. L. Nosik, and A. E. Blagov. “Methods of coherent X-ray diffraction imaging”. In: *Crystallography reports* 66 (2021), pp. 867–882.

[29] I. A. Vartanyants et al. “Coherence measurements and coherent diffractive imaging at FLASH”. In: *Journal of Physics B: Atomic, Molecular and Optical Physics* 43.19 (2010), p. 194016.

[30] V. Elser. “Phase retrieval by iterated projections”. In: *JOSA A* 20.1 (2003), pp. 40–55.

[31] S. Marchesini. “Phase retrieval and saddle-point optimization”. In: *JOSA A* 24.10 (2007), pp. 3289–3296.

[32] D. Russell Luke. “Relaxed averaged alternating reflections for diffraction imaging”. In: *Inverse problems* 21.1 (2004), p. 37.

[33] R. Neutze et al. “Potential for biomolecular imaging with femtosecond X-ray pulses”. In: *Nature* 406.6797 (2000), pp. 752–757.

[34] M. Bergh, N. Tîmneanu, and D. van der Spoel. “Model for the dynamics of a water cluster in an x-ray free electron laser beam”. In: *Physical Review E-Statistical, Nonlinear, and Soft Matter Physics* 70.5 (2004), p. 051904.

[35] S. Marchesini et al. “Coherent X-ray diffractive imaging: applications and limitations”. In: *Optics Express* 11.19 (2003), pp. 2344–2353.

[36] A. Aquila et al. “The linac coherent light source single particle imaging road map”. In: *Structural Dynamics* 2.4 (2015).

[37] T. Ekeberg et al. “Observation of a single protein by ultrafast X-ray diffraction”. In: *Light: Science & Applications* 13.1 (2024), p. 15.

[38] M. M. Seibert et al. “Single mimivirus particles intercepted and imaged with an X-ray laser”. In: *Nature* 470.7332 (2011), pp. 78–81.

[39] G. Van Der Schot et al. “Imaging single cells in a beam of live cyanobacteria with an X-ray laser”. In: *Nature communications* 6.1 (2015), p. 5704.

[40] M. F. Hantke et al. “High-throughput imaging of heterogeneous cell organelles with an X-ray laser”. In: *Nature Photonics* 8.12 (2014), pp. 943–949.

[41] D. Starodub et al. “Single-particle structure determination by correlations of snapshot X-ray diffraction patterns”. In: *Nature communications* 3.1 (2012), p. 1276.

[42] M. J. Bogan et al. “Aerosol imaging with a soft x-ray free electron laser”. In: *Aerosol Science and Technology* 44.3 (2010), pp. i–vi.

[43] M. J. Bogan et al. “Single-particle coherent diffractive imaging with a soft x-ray free electron laser: towards soot aerosol morphology”. In: *Journal of Physics B: Atomic, Molecular and Optical Physics* 43.19 (2010), p. 194013.

[44] T. Gorkhover et al. “Nanoplasma dynamics of single large xenon clusters irradiated with superintense x-ray pulses from the linac coherent light source free-electron laser”. In: *Physical review letters* 108.24 (2012), p. 245005.

[45] L. F. Gomez et al. “Shapes and vorticities of superfluid helium nanodroplets”. In: *Science* 345.6199 (2014), pp. 906–909.

[46] S. Eisebitt et al. “Lensless imaging of magnetic nanostructures by X-ray spectro-holography”. In: *Nature* 432.7019 (2004), pp. 885–888.

[47] C. H. Yoon et al. “Conformation sequence recovery of a non-periodic object from a diffraction-before-destruction experiment”. In: *Optics express* 22.7 (2014), pp. 8085–8093.

[48] A. V. Martin et al. “X-ray holography with a customizable reference”. In: *Nature communications* 5.1 (2014), p. 4661.

[49] M. F. Hantke, T. Ekeberg, and F. R. N. C. Maia. “Condor: a simulation tool for flash X-ray imaging”. In: *Applied Crystallography* 49.4 (2016), pp. 1356–1362.

[50] T. Ekeberg et al. “Three-dimensional reconstruction of the giant mimivirus particle with an x-ray free-electron laser”. In: *Physical review letters* 114.9 (2015), p. 098102.

[51] A. Colombo et al. “SPRING, an effective and reliable framework for image reconstruction in single-particle Coherent Diffraction Imaging”. In: *npj Computational Materials* 11.1 (2025), p. 265.

[52] P. Wernet. “Chemical interactions and dynamics with femtosecond X-ray spectroscopy and the role of X-ray free-electron lasers”. In: *Philosophical Transactions of the Royal Society A* 377.2145 (2019), p. 20170464.

[53] U. Bergmann et al. “Using X-ray free-electron lasers for spectroscopy of molecular catalysts and metalloenzymes”. In: *Nature Reviews Physics* 3.4 (2021), pp. 264–282.

[54] R. Y. Engel et al. “Shot noise limited soft x-ray absorption spectroscopy in solution at a SASE-FEL using a transmission grating beam splitter”. In: *Structural Dynamics* 8.1 (2021).

[55] Y. Kayser et al. “Core-level nonlinear spectroscopy triggered by stochastic X-ray pulses”. In: *Nature communications* 10.1 (2019), p. 4761.

[56] W. Błachucki et al. “Resonant X-ray Emission Spectroscopy with a SASE Beam”. In: *Applied Sciences* 11.18 (2021), p. 8775.

[57] D. De Angelis et al. “Free electron laser stochastic spectroscopy revealing silicon bond softening dynamics”. In: *Physical Review B* 107.21 (2023), p. 214305.

[58] Y. Klein et al. “High-spectral-resolution absorption measurements with free-electron lasers using ghost spectroscopy”. In: *Physical Review A* 107.5 (2023), p. 053503.

[59] M. Harmand et al. “Single-shot X-ray absorption spectroscopy at X-ray free electron lasers”. In: *Scientific Reports* 13.1 (2023), p. 18203.

[60] C. Svetina et al. “PRESTO, the on-line photon energy spectrometer at FERMI: design, features and commissioning results”. In: *Journal of Synchrotron Radiation* 23.1 (2016), pp. 35–42. DOI: 10.1107/S1600577515021116. URL: https://doi.org/10.1107/S1600577515021116.

[61] E. Principi et al. “A versatile wide energy range spectrometer for soft X-ray FELs”. In: *Nuclear Instruments and Methods in Physics Research Section A: Accelerators, Spectrometers, Detectors and Associated Equipment* 1058 (2024), p. 168856. ISSN: 0168-9002. DOI: https://doi.org/10.1016/j.nima.2023.168856. URL: https://www.sciencedirect.com/science/article/pii/S0168900223008471.

[62] T. Driver et al. “Attosecond transient absorption spooktroscopy: a ghost imaging approach to ultrafast absorption spectroscopy”. In: *Physical Chemistry Chemical Physics* 22.5 (2020), pp. 2704–2712.

[63] S. Li et al. “Time-resolved pump–probe spectroscopy with spectral domain ghost imaging”. In: *Faraday Discussions* 228 (2021), pp. 488–501.

[64] Z. Ebrahimpour et al. “Progress and Perspectives of Spectroscopic Studies on Carbon K-Edge Using Novel Soft X-ray Pulsed Sources”. In: *Condensed Matter* 7.4 (2022). ISSN: 2410-3896. DOI: 10.3390/condmat7040072. URL: https://www.mdpi.com/2410-3896/7/4/72.

[65] R. Mitzner et al. “L-edge x-ray absorption spectroscopy of dilute systems relevant to metalloproteins using an x-ray free-electron laser”. In: *The journal of physical chemistry letters* 4.21 (2013), pp. 3641–3647.

[66] L. Schwob et al. “Site-selective dissociation upon sulfur L-edge X-ray absorption in a gas-phase protonated peptide”. In: *The journal of physical chemistry letters* 11.4 (2020), pp. 1215–1221.

[67] K. Zhang et al. “Tracking the metal-centered triplet in photoinduced spin crossover of Fe (phen) 32+ with tabletop femtosecond M-edge X-ray absorption near-edge structure spectroscopy”. In: *Journal of the American Chemical Society* 141.43 (2019), pp. 17180–17188.

[68] I. Dawod et al. “MolDStruct: Modeling the dynamics and structure of matter exposed to ultrafast x-ray lasers with hybrid collisional-radiative/molecular dynamics”. In: *The Journal of Chemical Physics* 160.18 (May 2024), p. 184112. ISSN: 0021-9606.

[69] H. S. Seo et al. “Structure and nucleic acid binding activity of the nucleoporin Nup157”. In: *Proceedings of the National Academy of Sciences* 110.41 (2013), pp. 16450–16455.

[70] R. M. DuBois et al. “Structural and biochemical basis for development of influenza virus inhibitors targeting the PA endonuclease”. In: *PLoS pathogens* 8.8 (2012), e1002830.

[71] E. De Santis et al. “Biological applications at the AQUA beamline of the EuPRAXIA@ SPARC_LAB free electron laser”. In: *European Biophysics Journal* (2025), pp. 1–9.

[72] R. Boll et al. “X-ray multiphoton-induced Coulomb explosion images complex single molecules”. In: *Nature Physics* 18.4 (2022), pp. 423–428.

[73] C. Östlin et al. “Reproducibility of single protein explosions induced by X-ray lasers”. In: *Physical Chemistry Chemical Physics* 20.18 (2018), pp. 12381–12389.

[74] E. De Santis et al. “Ultrafast X-ray laser-induced explosion: How the depth influences the direction of the ion trajectory”. In: *Europhysics Letters* 148.1 (2024), p. 17001.

[75] T. André et al. “Protein structure classification based on X-ray laser induced Coulomb explosion”. In: *Physical Review Letters* (2025).

[76] T. André et al. “Partial orientation retrieval of proteins from X-ray free-electron-laser induced explosions for single particle imaging”. In: *Scientific Reports* 15.1 (2025), p. 37160.

[77] B. Iwan et al. “Explosion, ion acceleration, and molecular fragmentation of methane clusters in the pulsed beam of a free-electron laser”. In: *Physical Review A-Atomic, Molecular, and Optical Physics* 86.3 (2012), p. 033201.

[78] J. Ullrich, A. Rudenko, and R. Moshammer. “Free-electron lasers: New avenues in molecular physics and photochemistry”. In: *Annual review of physical chemistry* 63.1 (2012), pp. 635–660.

[79] L. Pihlava et al. “Shell-dependent photofragmentation dynamics of a heavy-atom-containing bifunctional nitroimidazole radiosensitizer”. In: *Physical Chemistry Chemical Physics* 26.11 (2024), pp. 8879–8890.

[80] E. Kukk et al. “Molecular dynamics of XFEL-induced photo-dissociation, revealed by ion-ion coincidence measurements”. In: *Applied Sciences* 7.5 (2017), p. 531.

[81] D. Bleiner. “Tabletop beams for short wavelength spectrochemistry”. In: *Spectrochimica Acta Part B: Atomic Spectroscopy* 181 (2021), p. 105978.

[82] T. J. Kauppila, J. A. Syage, and T. Benter. “Recent developments in atmospheric pressure photoionization-mass spectrometry”. In: *Mass spectrometry reviews* 36.3 (2017), pp. 423–449.

[83] Y. Arbelo and D. Bleiner. “Tabletop extreme ultraviolet time-of-flight spectrometry for trace analysis of high ionization energy samples”. In: *Rapid Communications in Mass Spectrometry* 33.14 (2019), pp. 1196–1206.

[84] A. Borgschulte and D. Bleiner. “Laser-Stimulated Desorption of Hydrogen in Palladium for Dynamic Hydrogen Sorption Microanalysis”. In: *Analytical Chemistry* 96.50 (2024), pp. 19889–19897.

[85] J. V. Goodwin et al. “Initial demonstration of microplasma ionization/Orbitrap mass spectrometry for molecular screening of perfluorinated compounds”. In: *Journal of Analytical Atomic Spectrometry* 39.10 (2024), pp. 2353–2362.

[86] D. Larcher and J. M. Tarascon. “Towards greener and more sustainable batteries for electrical energy storage”. In: *Nature chemistry* 7.1 (2015), pp. 19–29.

[87] A. Borgschulte et al. “Imaging the Chemistry of Materials Kinetics”. In: *Chimia* 76.3 (2022), pp. 192–202.

[88] F. Reinert and S. Hüfner. “Photoemission spectroscopy-from early days to recent applications”. In: *New Journal of Physics* 7.1 (2005), p. 97.

[89] L. Nguyen et al. “Understanding catalyst surfaces during catalysis through near ambient pressure X-ray photoelectron spectroscopy”. In: *Chemical reviews* 119.12 (2019), pp. 6822–6905.

[90] B. Philippe et al. “Photoelectron spectroscopy for lithium battery interface studies”. In: *Journal of The Electrochemical Society* 163.2 (2015), A178.

[91] H. Nakajima. “Photoemission Spectroscopy for Energy Storage Materials”. In: *Energy Storage Materials Characterization: Determining Properties and Performance* 1 (2025), pp. 67–97.

[92] O. Plekan et al. “Investigation of the amino acids glycine, proline, and methionine by photoemission spectroscopy”. In: *The journal of physical chemistry A* 111.43 (2007), pp. 10998–11005.

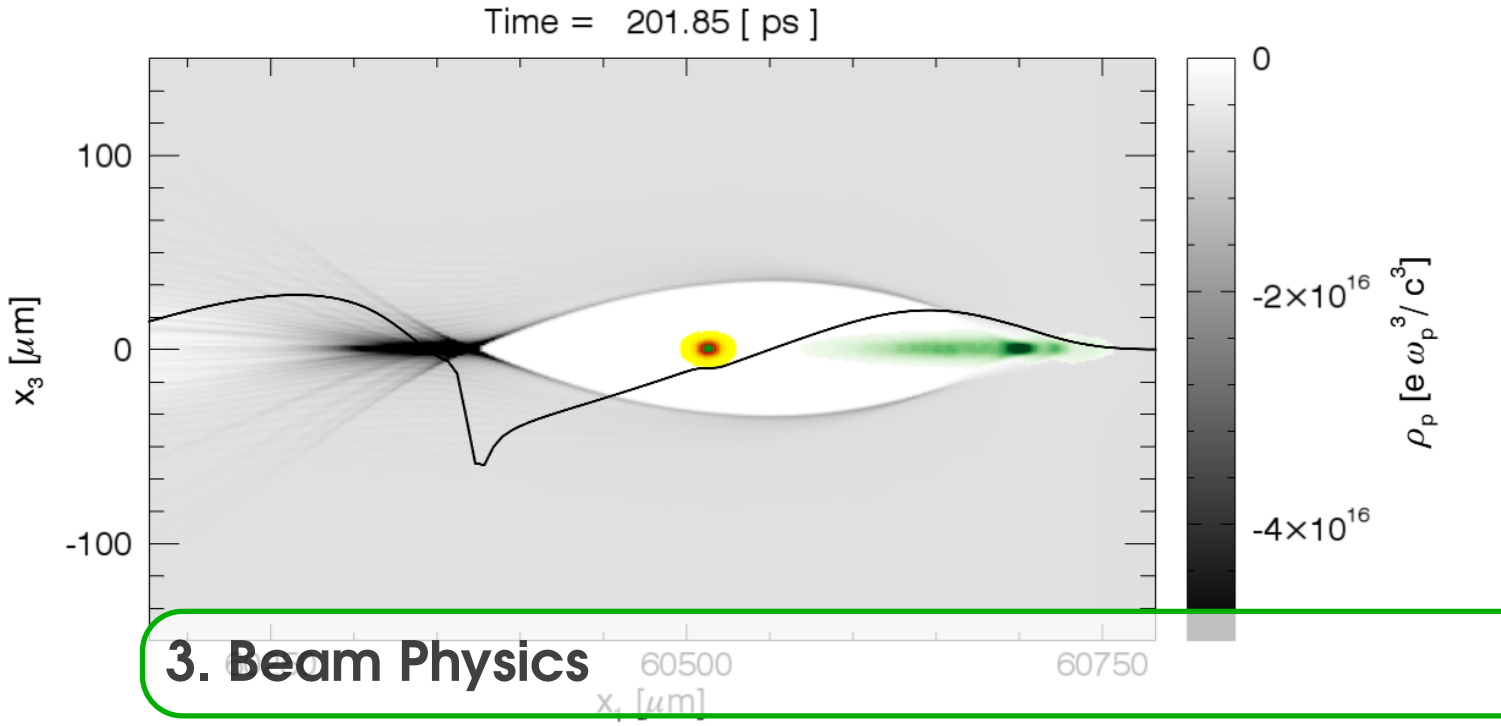

3. Beam Physics

3.1 Overview of the start to end simulations

This chapter presents the results of the start-to-end simulations performed for EuPRAXIA@SPARC_-LAB facility, with the purpose of validating the accelerator design and confirming its capability to drive the FEL beamline AQUA. The simulations follow the beam through the entire accelerator chain — from the photo-injector, through the X-band linac and plasma acceleration stage, up to the undulator exit — using the well established codes TStep [1], Elegant [2], Architect [3], and GENESIS [4]. In particular, they demonstrate the feasibility of delivering an electron beam with an energy of 1 GeV, a normalized emittance below 1 mm mrad, a relative slice energy spread below 0.1%, and peak currents in the 2-3 kiloampere range, enabling FEL lasing in the water window ($\lambda_r \approx 4$ nm) with a photon output exceeding 10^{11} photons per pulse.

FEL radiation at $\lambda_r = 4$ nm is generated by injecting a 1 GeV electron beam into a 25 m long undulator (see Fig. 3.2), with period $\lambda_w = 1.8$ cm, an rms undulator parameter K in the range 0.6–1.1, and variable polarization, as described in Chapter 8.

According to Ref. [5], we can analytically evaluate the FEL saturation length (left figure of Fig. 3.1) and the number of photons (right figure) as functions of the current I(A) and of the energy spread ΔE/E while keeping fixed the value of the normalized emittance. To determine the suitable electron-beam parameters for the plasma-acceleration case, we consider a beam energy of 1 GeV and two values of the transverse normalized rms emittance, $\varepsilon_{n,x,y} = 0.7$ or 1.2 mm mrad, which represent the typical performance range of a plasma-accelerated beam. The undulator parameter is set to $K_{\rm rms} = 0.84$ (corresponding to a radiation wavelength of $\lambda = 4$ nm), with a transverse beam size of 50 μm at the undulator entrance and a total charge of 30 pC, assuming a Gaussian current profile.

The results are presented in Fig. 3.1, showing the saturation length (left figures), and the number of photons (right figures), mapped in the plane (I(A), Δ E/E), for the two emittance values. The saturation length is assumed to be 20 times the three-dimensional gain length L_{g3D} [5]. It must remain <20 m to let the radiation saturate within the design magnetic length of the undulator. The graphs show that more than 10^{11} photons/shot can be generated in less than 20 m of magnetic undulator length with an energy spread lower than 10^{-3} and current $I \geq 2.5$ kA, when the normalized emittance is $\varepsilon_{nx,y} = 0.7$ mm mrad (Fig. 3.1). If the normalized emittance is larger, such limits

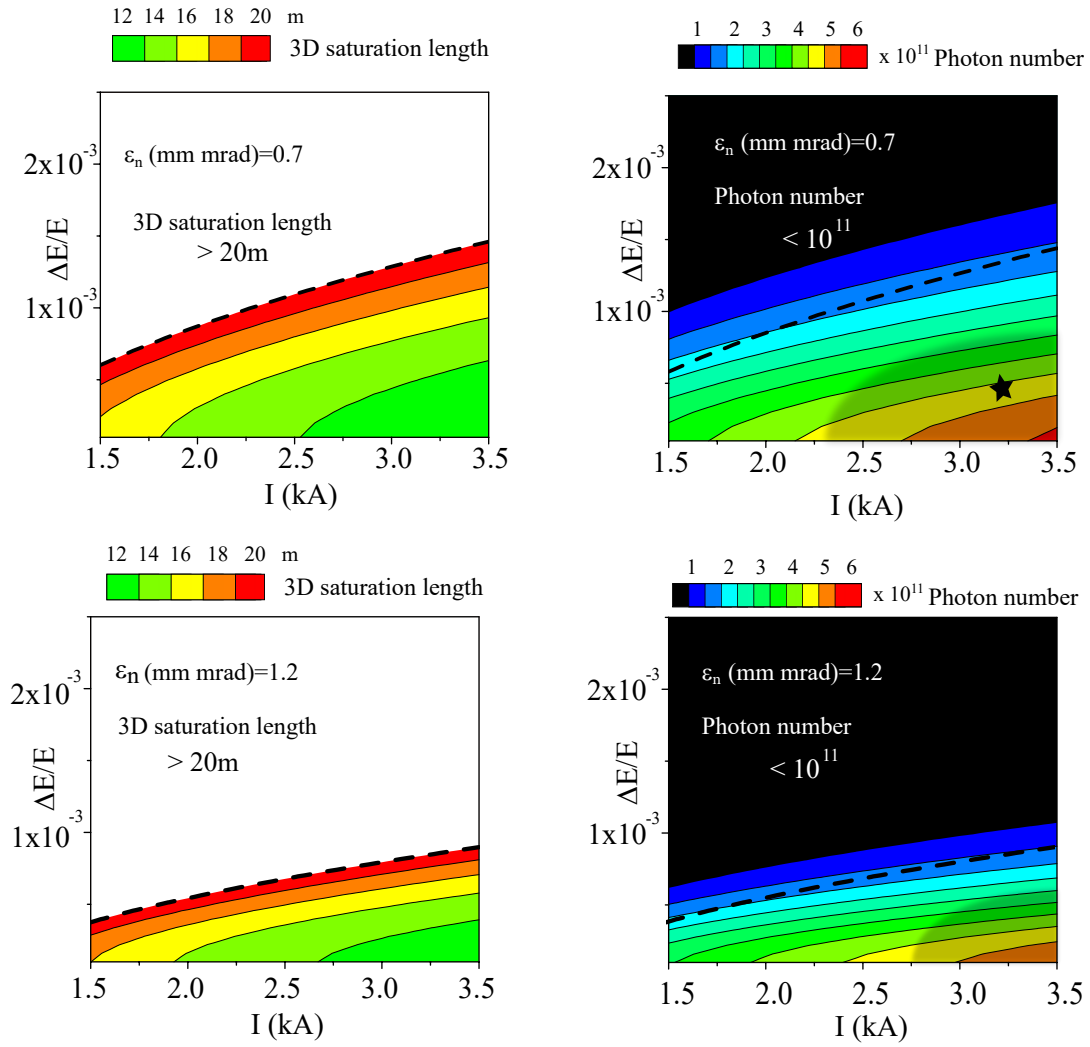

Figure 3.1: FEL saturation length and number of photons: Q= 30 pC, E=1 GeV, K_{rms} = 0.84, $\lambda = 4$ nm for normalized emittance ε_n = 0.7 mm mrad (top figures), ε_n = 1.2 mm mrad (bottom figures). Left figures: saturation length (evaluated as 20 times the three-dimensional gain length) mapped in the plane I(A) vs. ΔE/E. In the white region, the saturation length is larger than 20 m. The dotted black line indicates the edge of the 20 m. Right figures: photon number per shot. In the black region the number of photons is less than 10^{11}. The black dotted line is the limit of saturation length equal to 20 m. The star in the top-right window is the start to end simulated working point for the plasma acceleration configuration, referring as well to Fig. 8.10.

become more demanding. The star in the top-right window is the working point obtained by the start to end simulation in the plasma acceleration configuration that will be discussed in Section 3.2.

Figure 3.2 shows the facility layout (see as well Chapter 4 for details).

The high-brightness 1 GeV accelerator complex is 55 meters in length. This comprises an S-band RF photo-injector, two X-band RF Linacs interleaved with a magnetic chicane, and a plasma accelerator section at the end. The diagnostic and matching sections are located towards the undulator entrance. The 25-meter-long undulator section is located in the downstream area, followed by a 50-meter-long photon diagnostic and transport section that delivers radiation to the user end-station.

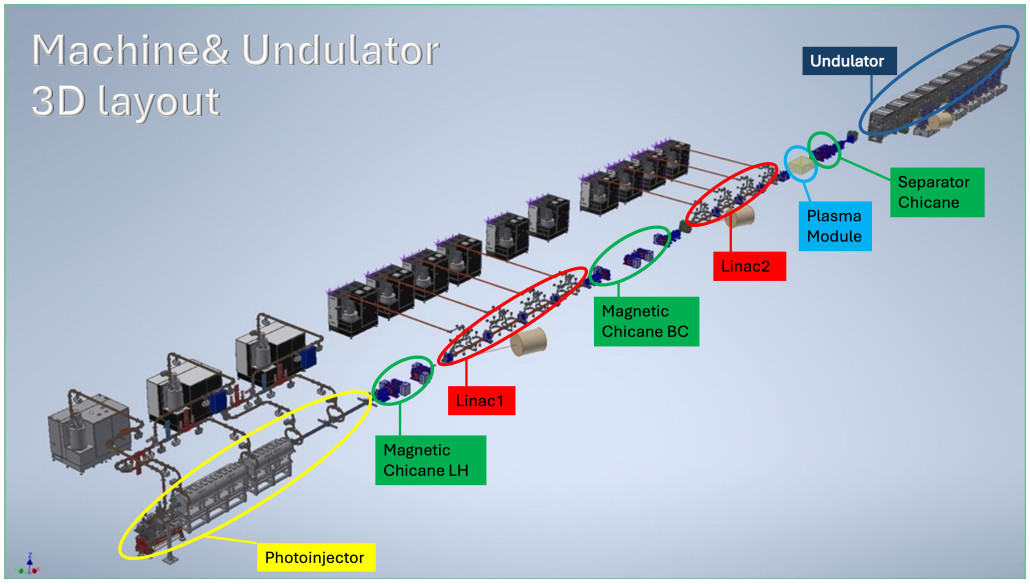

Figure 3.2: The layout of the EuPRAXIA@SPARC_LAB accelerator

The linac is capable of being operated in two different configurations providing both 1 GeV beams:

- **Plasma acceleration case**: the comb scheme (driver plus witness), provides a 30 pC charge beam (witness), with an energy doubling in the plasma module, where accelerating fields, on the order of $E_{acc} \approx 1$ GV/m, can be excited by the driver bunch traveling ahead in a plasma filled capillary. In this case the RF linac provides ≈ 500 MeV, operating the X-band sections at $E_{acc} \approx 0.03$ GV/m, (see Section 3.2).

- **X-band RF acceleration case:** using RF acceleration only, a single bunch with a charge of approximately 200 pC can reach a kinetic energy of $E_{\text{kin}} \approx 1$ GeV while preserving the required beam quality. This is achieved with the X-band accelerating sections operating at full power, i.e. at an accelerating gradient of $E_{\text{acc}} \approx 0.06$ GV/m, thus providing a high-charge operating point for the X-ray source (see Section 3.3).

To check the feasibility and the robustness of the accelerator design, a computational-theoretical work has been performed following the electron beam properties evolution from its generation up to the radiation emission, so called start to end simulations, aiming and reaching final compliance with the 4 nm FEL source requirements outlined above for the two possible configurations, i.e the plasma acceleration and the conventional all RF one. Table 3.1 lists the electron-beam parameters at the undulator entrance (i.e., after the separator chicane), as obtained from the start-to-end simulations described in this chapter, for both configurations, together with the resulting FEL radiation parameters. Also reported are the electron-beam slice emittance and slice energy spread, calculated for an average slice length of 0.5 μm, on the order of the average cooperation length L_c [6]. For the two configurations we reach saturation inside the undulator length at $\lambda_r = 4$ nm with the expected number of photons per pulse.

3.2 Start to end simulation for the plasma acceleration case

This section presents the start-to-end simulation results for the plasma acceleration case. The configuration consists of a driver with 200 pC charge and a witness with 30 pC charge. The target is

Table 3.1: Electron beam and FEL radiation main parameters at the undulator entrance, as obtained from the start-to-end simulations described in this chapter, for the two considered machine configurations: plasma acceleration (PWFA) and conventional (Full) RF one. For the two configurations we reach saturation inside the 25 m floor length of the undulator at $\lambda_r = 4$ nm with the expected number of photons per pulse.

	Units	PWFA Velocity bunching	Full RF Velocity Bunching + Magnetic Compression
Electron Energy	GeV	1	1
Repetition Rate	Hz	100	100
Bunch charge	pC	30	200
Peak current	kA	3.3	3.4
RMS bunch length	μm	1.4	16.9
RMS normalized emittance (x,y)	mm mrad	0.7, 0.7	2.1, 1.0
RMS energy spread	%	0.5	0.2
Slice length	μm	0.5	0.5
Slice normalized emittance (x,y)	mm mrad	0.7, 0.7	0.3, 0.3
Slice energy spread	%	0.04*	0.02
ρ_{3D}	$\times 10^{-3}$	0.77	1.49
Radiation wavelength	nm	4.0	4.0
Saturation length	m	20.5	20.0
Photon Pulse Energy	μJ	16	150
Photon per pulse	$\times 10^{11}$	3.2	31.3
Photon bandwidth	%	0.4	0.5
Photon brilliance per pulse	# $\times 10^{30}$	0.12	2.1

* Calculated with the 5 % cut of off-energy charge, not lasing, see details in FEL performances section.
# = N_{phot}/s/m^2/rad^2/0.1%bw.

to reach 1 GeV energy for the witness while preserving beam quality for FEL operation within an accelerating distance shorter than one meter. This corresponds to an average accelerating gradient on the order of one GeV/m in the plasma section, while maintaining beam quality compatible with the FEL operation.

Establishing the working point parameters required a systematic optimization to control emittance growth and energy spread of the witness bunch throughout the acceleration process. In addition, the optimization must incorporate the effects of expected jitters originating from the RF acceleration stage, the beam transport line, and the plasma module [7].

3.2.1 Photoinjector

High brightness electron beams can be generated in high-brightness RF photo-injectors coupled with a high gradient booster linac, in our case operating at higher harmonic frequency. Typical electron beams, useful for EuPRAXIA@SPARC_LAB project applications and able to couple with the wavelength of the plasma accelerating wakefield, are tens of femtoseconds long with transverse projected emittance lower than 1 mm mrad at up to 1 GeV energy. This is accomplished using an

RF gun, equipped with a laser-driven photo-cathode S-band RF gun, followed by followed by a S-band linac boosting the energy up to 120 MeV, interleaved with beam phase space manipulation sections, see Chapter 5 for details.

The transverse beam quality is reached at the source adopting the well-known emittance compensation scheme proposed in [8], based on a focusing channel at very low energy to control emittance growth due to space charge effects, together with the matching conditions based on the invariant envelope theory proposed in [9]. This scheme helps in limiting the transverse beam projected emittance down to the intrinsic value, i.e. the lowest achievable in the photoemission process at the cathode, and that scales as $\varepsilon_n \approx \sigma_{cath} \approx \sqrt{Q}$, where σ_{cath} is the laser spot size on the photocathode, and Q the extracted electron charge. The longitudinal beam phase space optimization takes also place at low energy, through RF compression in the photoinjector with the velocity bunching technique [10].

The RF compression integrated with the emittance compensation process [10, 11] can provide up to kA bunch peak current with low transverse emittance, with the advantage of machine compactness and absence of Coherent Synchrotron Radiation (CSR) effects, that may occur in magnetic compression chicanes. Additional magnetic compression can be applied at high energy (higher than 300 MeV), if needed, as described in details below.

A reference working point has been studied for the plasma wakefield based operation optimizing beam charge and distance separations between the driver and the witness; in Table 3.2 the obtained electron beam parameters at the plasma entrance are reported. It should be noted that the witness peak current reported in Table 3.1 differs from that in Table 3.2, as the electron beam undergoes additional compression after the plasma acceleration stage within the separator device, as described in Sec. 3.2.4.

Table 3.2: Electron beam parameters at plasma entrance for the reference working point.

Parameter	**Symbol**	**Unit**	**Witness**	**Driver**
Charge	Q	pC	30	200
Energy at plasma module entrance	E	MeV	562.5	563.8
RMS energy spread	$\Delta\gamma/\gamma$	(%)	0.06	0.13
RMS normalized emittance	ε_n	mm mrad	0.7	1.6
RMS bunch length	σ_z	µm	5.4	46
Slice length	$\sigma_{z-slice}$	µm	0.50	0.50
Slice peak current	$I_{peak-slice}$	kA	2.1	0.5
Witness-Driver separation	Δl	µm	162	-

Since the beams experience different dynamic regimes, to properly account for the different physical forces acting along the accelerator, the simulations are divided into multiple stages, each one addressed with the proper code: TStep [1], used for the photoinjector, from the cathode to the entrance of the X-band linac, where the beam is in the space charge regime; Elegant [2], from the entrance of the X-band linac to the plasma stage, and from the exit of the plasma to the injection into the FEL, to take into account wakefields and CSR; Architect [3], hybrid fluid code, for the plasma acceleration stage; and Genesis, 3D time-dependent code [4], for the radiation generation and electron tracking.

The S-band photoinjector is based on the experience at the SPARC_LAB test facility in operation at INFN-LNF since 2006, and currently devoted to plasma-based experiments both to accelerate and focus electron beams, and to the advanced radiation generation concepts. The layout is described in details in Chapter 5 and it consists of a 1.6 cell RF gun [12] including a copper

photocathode with an emittance compensating solenoid followed by four S-band traveling wave sections operating at 2.998 GHz. The first two acceleration sections are 3 m long, each incorporated into a solenoid channel to control the emittance compensation process while compressing longitudinally the beam via velocity bunching. Each solenoid is composed of twelve coils in groups of three independently powered. The third and fourth S-band accelerating structures are 1.5 m long and their phase and voltage are set to let the electron bunch gain energy while freezing the phase space good quality and consequently reducing the space charge effects.

As mentioned above, the simulations have been performed with the multi-particles code TStep [1] which takes into account space charge effects, relevant at low energies, and the intrinsic thermal emittance at the cathode, considered to be $\varepsilon_t \simeq 0.6 \pm 0.01[\text{mm mrad}/\text{mm}] \cdot \sigma_{\text{r}}[\text{mm rms}]$ [13] with the gun operating at 120 MV/m peak field at the cathode. The code calculates the self-fields by solving Poisson equation for the electrostatic field in the reference frame where the beam may be considered at rest and then transforming the fields back into the laboratory frame where kicks to the particles are applied. In our calculations the cylindrical symmetry of the beam has been assumed, in order to allow the adoption of a 2D model which requires a reasonable number of particles and mesh points, and so computational time, with respect to a 3D model.

The driver and trailing beams are generated within the same RF bucket in the photo-injector by means of the combination of the so called laser-comb technique [14], consisting of a train of laser pulses (in this case two pulses) spaced in time that illuminates the photocathode, and of RF compression. The laser pulse extracting the witness arrives on the photocathode about 5.0 ps earlier than the one for the driver and then they are reversed in time at the end of the velocity bunching process, during which the longitudinal phase space is rotated. Experimental results have been obtained at SPARC_LAB where the laser-comb technique is routinely used in order to produce trains of multiple electron bunches [15]. The comb-like configuration for the electron beam consists of a 200 pC driver followed by a 30 pC witness bunch, as already mentioned, it has been widely explored to optimize the witness bunch parameters and to set the longitudinal distance between the two bunches at a desired value. The witness bunch is represented in simulations by 30k macroparticles, while the 200 pC driver is represented by 200k macroparticles.

Computational studies have been devoted to provide, at the plasma entrance, driver and witness bunches separated by $\lambda_p/2$, with the plasma wavelength inversely proportional to the plasma background density n_p on the order of (10^{16} cm^{-3}). Both driver and witness bunches must be compressed down to $\simeq$ 45.4 and 5.4 μm (154 and 18 fs) rms, respectively. Since the accelerating gradient inside the plasma wave grows linearly in the longitudinal direction, the witness bunch length must be kept as short as possible respect to the plasma wavelength in order to minimize the energy spread growth. An rms length equal to 1-2% of the plasma wavelength guarantees the conditions for an acceptable energy spread growth and the correct current in order to allow beam loading compensation of the residual energy spread of the core as discussed in a dedicated section. Additionally, the transverse normalized emittance of the witness, defined as the RMS projected value, must be below 1 mm mrad.

The photoinjector is set to perform adiabatic RF bunch compression within. the two accelerating structures immediately after the gun, ensuring good flexibility and precise parameter definition in terms of beam temporal separation (less than 1 ps), witness peak current up to 2 kA, and emittance below 1 mm mrad. The RF compression is applied to the first two S-band cavities to shorten the bunch length from tens of microns to $\simeq$ 6 μm rms, both cavities working close to the zero crossing of the field. A slightly off-crest operation of the third and fourth S-band cavities further reduces the energy spread at the injector exit. The longitudinal profile of the bunch exiting the photoinjector is typical of the velocity bunching process, showing a spike of current in the head of the bunch, and a long tail. In this configuration, the longitudinal crossing of the driver and witness bunches takes place within the second S-band TW accelerating section. Consequently, at the photoinjector exit

the longitudinal ordering of the two beams is reversed, with the witness beam trailing the driver beam. The emittance minimization is obtained by setting the gun solenoid to $\simeq 3$ kG and those surrounding the first and second S-band cavities to 0.32 kG and 0.50 kG, respectively. To further minimize the growth of witness emittance, that occurs due to the overlap of the bunches in time at the crossing point, the laser spot size on the cathode relative to the driver bunch, is chosen based on the desired witness quality, longitudinal profile and transverse normalized emittance, ensuring the latter remains below 1 mm mrad [16].

Best compromise in terms of final spacing, witness normalized emittance and current profile has been obtained with the photocathode laser pulse parameters at the cathode and the machine parameters shown in Table 3.3.

Table 3.3: Reference input parameters at the injector for comb beam production.

Parameter	**Symbol**	**Unit**	**Value**
Number of bunches			2
Witness Charge	Q_W	pC	30
Driver Charge	Q_D	pC	200
RMS Laser pulse length (W/D)	σ_t	fs	350/550
RMS Laser pulse spot size (W/D)	σ_r	μm	175/285
Laser pulses separation at the cathode	Δt	ps	4.8
Peak electric field on the cathode	E_{acc}	MV/m	120
Solenoid center longitudinal position (with respect to cathode)		m	0.204
Solenoid peak field	B_{max}	T	0.38
S1-S2 average accelerating field	E_{acc}	MV/m	21
S3-S4 average accelerating field	E_{acc}	MV/m	35

The simulation results are shown in Fig. 3.3 for the optimized comb-like beam for the reference working point: the left and right plots show the evolution of the transverse normalized emittance (red line), spot size (blue line) and bunch length (green line) of the witness and driver, respectively, from the cathode to the photoinjector exit, as obtained with the TStep code. The obtained results are in agreement with the requirements for the normalized emittance, driver and witness bunch length and proper distance between the two bunch distribution centroids (see Table 3.3), apart from the energy spread which required value is obtained at the end of the X-band linac.

In Fig. 3.4 the beam longitudinal profiles in terms of slice current are shown as obtained with TStep for the 200+30 pC beams.

3.2.2 Linac

The X-band RF linac, operating at 11.994 GHz, consists of two sections Linac1 and Linac2, equipped each with eight, 90 cm long, X-band accelerating sections. According to the RF power system design (see RF X-band linac Chapter 6) the maximum accelerating field applied is $E_{acc} = 60$ MV/m through both Linac1 and Linac2. Before and after the Linac1 there are two magnetic chicanes named Laser Heater (LH) and Bunch Compressor (BC), respectively 2.4 and 10 m long. The shorter LH is meant to also host a 50 cm long wiggler insertion where the electron beam can interact with a laser pulse to increase the uncorrelated energy spread of the bunch in such a way to mitigate detrimental effects of the eventual microbunching instability. At the same time, when the two chicane dipoles are switched off, the straight beamline can accommodate the low and middle energy diagnostic station for 6D beam parameters measurement. The matching sections at the

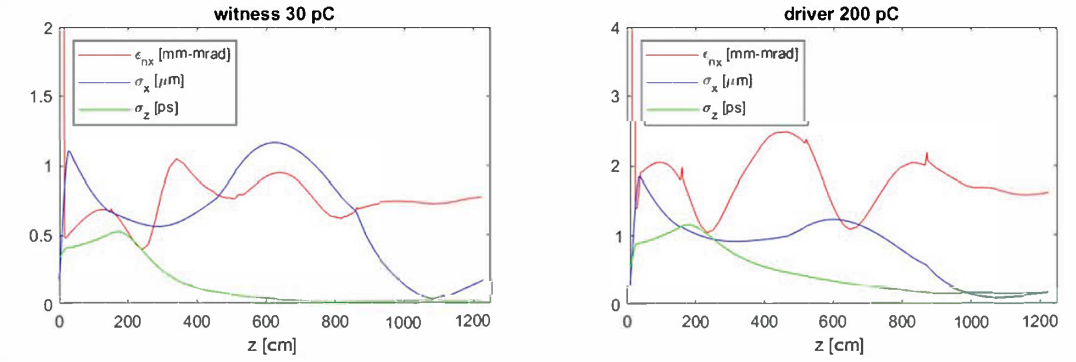

Figure 3.3: Evolution of the electron beam transverse normalized emittance (red line), spot size (blue line) and bunch length (green line) of the witness and driver, respectively, from the cathode to the photoinjector exit as obtained with the TStep code for the PWFA case. The picture shows the control on the transverse emittance value through all the RF compression process in the photoinjector that leads to the desired bunch length, at the same time optimizing the beam transverse envelope.

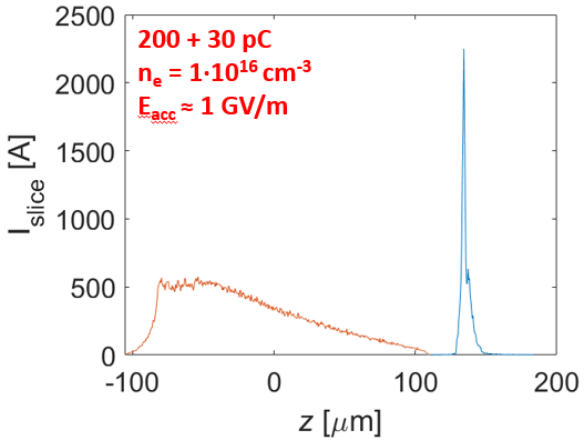

Figure 3.4: Electron beam longitudinal profile (PWFA case) in terms of slice current as obtained with TStep for the 200+30 pC comb beam.

entrance of Linac1 and Linac2 have been optimized to provide the required beam acceptance, from the photo-injector and after the magnetic chicane, for the working points described in this chapter: the best focusing strength for the lattice has been found with a betatron phase advance per cell of about 20° and 30° for Linac1 and Linac2, respectively.

Electron beam dynamics simulations have been performed with the Elegant code [2] that includes longitudinal space charge effects and both coherent and incoherent synchrotron radiation effects in the bending magnets, and the wakefield effects generated by the electron beam inside the accelerating structures. To simulate the electron beam dynamics, the 230k macroparticles, (200k for the driver and 30k for the witness), generated and tracked in the photoinjector with the TSTEP code [1], are tracked trough the linac using the Elegant code, where we use asymptotic values of the longitudinal and transverse wake functions calculated according to [17] and reported in Fig. 3.5.

The Twiss parameters in the X-band linac evolve on a FODO-like lattice structure with a maximum beta function value below 30 m in both planes, that helps in controlling transverse

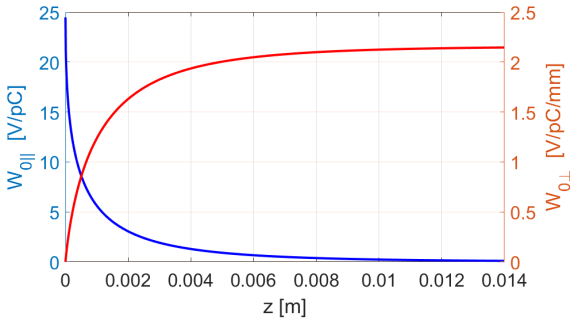

Figure 3.5: X-band longitudinal and transverse wakefield calculated for an average iris radius of 3.5 mm and a cell length of 8.332 mm.

wakefield drawbacks in case of misalignment (see Section 3.2.6.2 for the evaluation of off-axis beam dynamics for the comb beam along the linac). The beam is then transversely matched to the plasma by means of a focusing system comprising an electromagnetic quadrupole triplet followed by a permanent-magnet triplet. This configuration allows the injection of electron beams with a minimum achievable beta function at the waist of approximately 1 mm. However, the optimization study presented here instead considers the inclusion of 10 cm long plasma density ramps inside the capillary (see Section 3.2.3), which enable a gradual transition of the beam into the plasma. This smooth entrance, occurring over the first and last 10 cm of the 60 cm capillary, relaxes the required beta function at the capillary entrance to approximately 1 cm. In contrast, in the presence of a sharp plasma density transition—i.e., in the absence of density ramps—the required beta function is reduced to 1 mm, as it is shown in Fig. 3.7. These density ramps facilitate a controlled adjustment of the beam phase space and help minimize emittance growth throughout its interaction with the plasma, as detailed in Section 3.2 and in [18]. The beam dynamics in this part of the machine has also been evaluated with TStep in case of absence of plasma density ramps, i.e. with the strongest focusing applied, to take into account the space charge contribution to the transverse emittance, that came out to be negligible.

Figure 3.6 shows the longitudinal and transverse phase space of witness and driver bunches at the plasma entrance, as obtained with TStep and Elegant codes. In particular the witness twiss parameters are reported that fulfill the matching conditions in presence of a 10 cm ramp with one order of magnitude excursion in the plasma density (from plateau to capillary end), i.e. $\alpha_{x,y} \approx 1$ and $\beta_{x,y} \approx 2.5$ cm.

3.2.3 Plasma acceleration stage

The plasma wakefield section operates in a nonlinear regime, with a peak plasma density of approximately $10^{16}\,\mathrm{cm}^{-3}$. This ensures a competitive accelerating gradient together with optimal focusing conditions and a stable wakefield response. To realize this configuration, the driver density must exceed the background plasma density while maintaining a relatively low charge with respect to the effective interaction region. This requirement is fulfilled when the normalized driver density $\alpha = n_b/n_p \gg 1$ and the normalized charge $\tilde{Q} = N_b k_p^3/n_p < 1$.

Since both the driver and the witness must remain fully contained within the plasma bubble, the machine will operate with short, narrow bunches satisfying $k_p\sigma_r < 1$ and $k_p\sigma_z < 1$.

Taking into account the overall dimensional constraints of the RF linac, a conservative choice has been made: 200 pC for the driver and 30 pC for the witness. These values lie within our estimated maximum transportable charge of 400 pC, ensuring preservation of the beam quality.

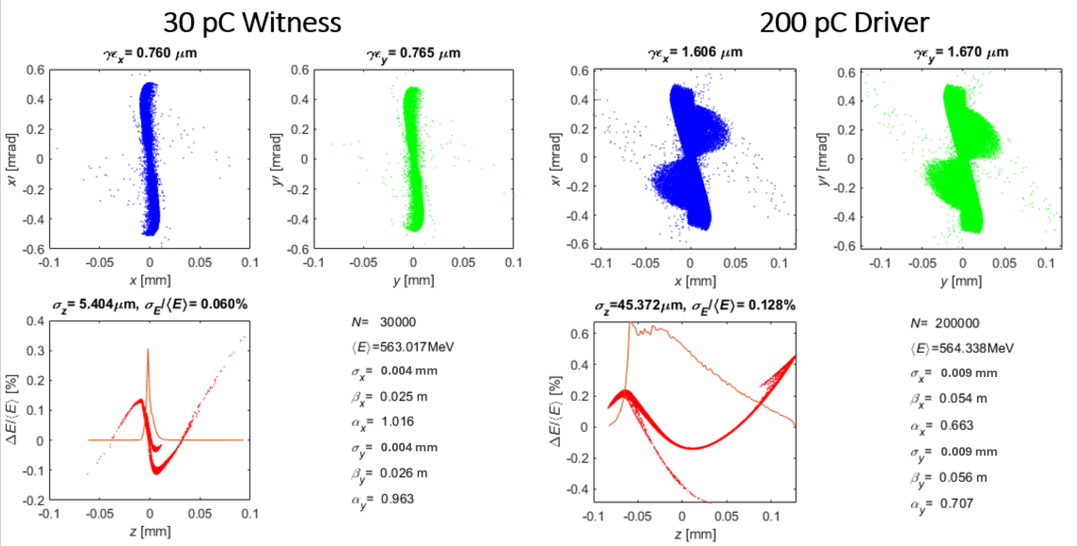

Figure 3.6: Longitudinal and transverse phase space of the electron beam at the plasma injection for the reference working point as obtained with TStep and Elegant codes.

With this configuration, the normalized charge of the driver is $\tilde{Q} \approx 1$, while the normalized density, which also depends on the transverse spot size—and is therefore linked to the transport of the driver inside the plasma channel—is estimated to reach $\alpha \approx 5-10$ at the peak plasma density.

Beam Quality Preservation

The preservation of the energy spread can be achieved by tuning the witness injection phase so that the accelerating field E_z is flat only in the proximity of the current peak, as will be shown below.

The emittance growth inside plasma channels in the quasi non linear regime is mostly due to betatron de-phasing. This can be avoided by matching the bunch(es) transverse size to the plasma focusing force. If the transition between the empty space and the plateau of the plasma channel is sharp enough, the ion column model foretells the matching conditions for the Twiss functions [19], β_0 and α_0, at the plasma entrance:

$$\beta_0 = \frac{\sqrt{2\gamma}}{k_p} \qquad \text{and} \qquad \alpha_0 = 0\,. \tag{3.1}$$

However, the presence of a smooth transition region inside the plasma channel (i.e., a plasma ramp) significantly alters the matching conditions at the entrance of the plasma. To evaluate these conditions analytically, the density profile has been approximated by an injection and extraction ramp with a $\cos^2$ shape and total length $L = 10$ cm [18, 20], connected to a 40 cm long plateau, as also shown in Fig. 7.5.

Under this approximation, the injection Twiss parameters at the plasma entrance, β_{inj} and α_{inj}, relax to:

$$\beta_{\text{inj}} = 3\sqrt{\frac{L\beta_0}{\pi}}, \qquad \alpha_{\text{inj}} = 1, \tag{3.2}$$

thereby simplifying the transport upstream of the RF injector as pointed out in Fig. 3.7.

Simulation setup

As already mentioned the considered configuration consists of a 200 pC driver and a 30 pC witness, and we the hybrid kinetic-fluid code Architect [3], that models the beam particles using a Particle-

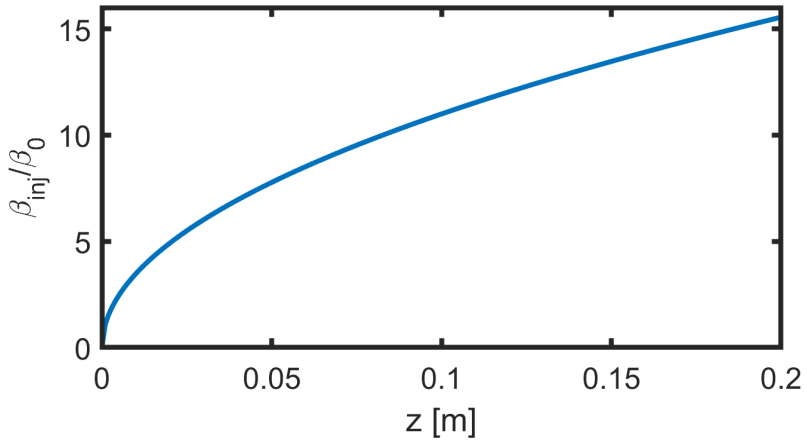

Figure 3.7: Normalized optimal β-function at the entrance of a plasma ramp, expressed as a function of the ramp length. The β-function is normalized to the matched value at the peak plasma density, β_0. In this evaluation, the bunch has a Lorentz factor of $\gamma = 1000$ and is assumed to be injected into a plasma channel with a peak density of $n_p = 10^{16}$ cm^{-3}.

In-Cell (PIC) scheme, while the background plasma is described as a fluid. In this hybrid approach, the driver beam is treated kinetically through the PIC method, whereas the background plasma is approximated as a cold fluid.

To accelerate the simulations without loss of generality, the fluid and Maxwell equations are solved under the assumption of cylindrical azimuthal symmetry. The bunch particles, however, are tracked in the full six-dimensional phase space. This simplification allows to perform meter scale simulations avoiding high levels of numerical noise and keeping a reasonable computational time in a single core for numerical scans. The 3D kinetic evaluation of the particles trajectory allows at the same time to assess realistically the evolution of the beam distributions in 6D phase space. The simulations are performed within a computation box of dimensions 2048×512 µm^2, where the first value corresponds to the longitudinal extent and the second to the radial extent. The spatial resolution is set by defining a single grid cell with a size of 3×3 µm^2, ensuring a sufficient level of detail for accurately resolving the plasma dynamics while maintaining computational efficiency. The convergence of the numerical results has been checked with respect to the number macro-particles and 230k macro-electrons (200k for the driver and 30k for the witness with a macro charge of 1 fC per macro particle) and gave us a satisfactory result for the chosen configuration.

As a result of the optimization study of the transverse and longitudinal phase space of the electron beam after acceleration in the capillary, the most effective plasma profile—providing the best compromise between energy gain and beam quality preservation—consists of a central plateau of approximately 40 cm, preceded and followed by two symmetric 10 cm ramps. In these ramp regions, the optimized plasma density follows a squared-cosine longitudinal distribution, as illustrated by the blue curve in Fig. 7.9.

The optimized working point consists of a driver with an RMS length of $\sigma_{z,D} \approx 50$ µm, followed by a witness with an RMS length of $\sigma_{z,W} \approx 5$ µm, and a bunch separation of $\Delta z \approx 160$ µm.

The length of the driver has been determined by balancing the expected performance of the RF photo-injector with the requirement of operating at a plasma density on the order of 10^{16} cm^{-3}. The witness length has been selected to yield a peak current of $I \approx 2$ kA, which was identified as the optimal choice for maximizing the beam-loading effect and minimizing the energy spread within the plasma. This configuration is particularly advantageous in view of the additional longitudinal compression introduced by the driver–separator chicane located upstream of the undulator entrance. Several simulation scans, simultaneously varying the driver–witness separation and the plasma

density around the nominal value, have been performed [7]. The results show that, in the proposed configuration, the energy spread growth remains below 1% and is only weakly sensitive to variations in bunch separation and plasma density on the order of 10%. The transverse distribution of both bunches has been designed in order to be consistent with the matching conditions Eq. 3.2, which are $\alpha_{inj} = 1$ and $\beta_{inj} \approx 25$ mm.

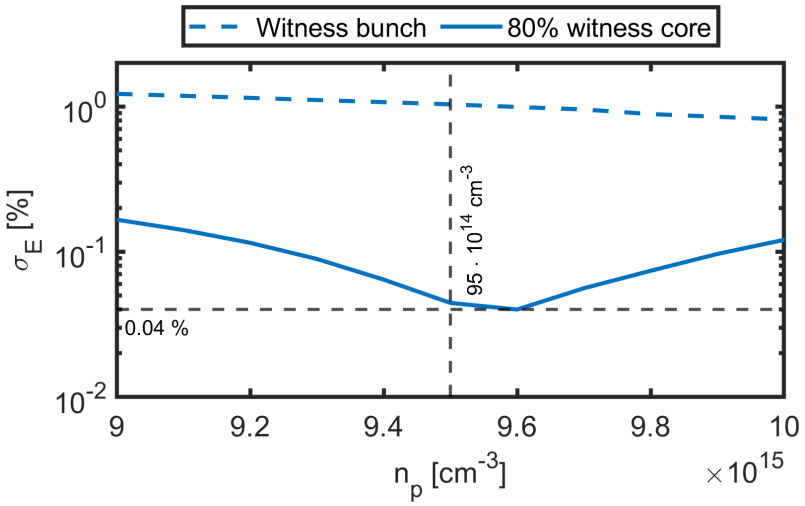

Figure 3.8: Energy spread of the bunch σ_E as a function of the input plateau density for the reference charge configuration 30 pC (dashed line) and for the 80% core of the distribution (continuous line).

Table 3.4: Witness parameters at the injection and extraction of plasma channel for the 30 pC charge reference configuration (projected values).

Beam Parameter	**Unit**	**Injection**	**Extraction**	**80% Core**
Energy	GeV	0.56	1.01	1.01
Energy Spread	%	0.06	1.03	0.04
Charge	pC	30	30	24
$\varepsilon_{n,x}$	mm mrad	0.7	0.7	0.7
$\varepsilon_{n,y}$	mm mrad	0.7	0.7	0.7
σ_x	µm	4.1	3.2	3.2
σ_y	µm	4.2	3.0	3.1
σ_z	µm	5	5	2

Numerical scans have been performed in order to retrieve the optimal density of the plateau that gives the minimum energy spread growth for the reference configuration. The optimal density was retrieved by optimizing the energy spread of the witness beam core, estimated containing 80% of the charge. The minimum energy spread growth is obtained as shown in Fig. 3.8 with a plasma density $\approx 9.5 \cdot 10^{15}$ cm^{-3}, that represents our final choice for the working point (nominal case). The beam parameters at injection, at extraction and for the core are shown in Table 3.4, where it can be noticed that there is a significant reduction of emittance and bunch length. Slice analysis of the bunches, pictured in Fig. 3.9, shows that the current profile is preserved throughout acceleration, while a slight emittance dilution is located, as expected, in the head and the tail of the bunch. Figure 3.10 shows the phase space of the bunch at the extraction (a) and focuses on the witness

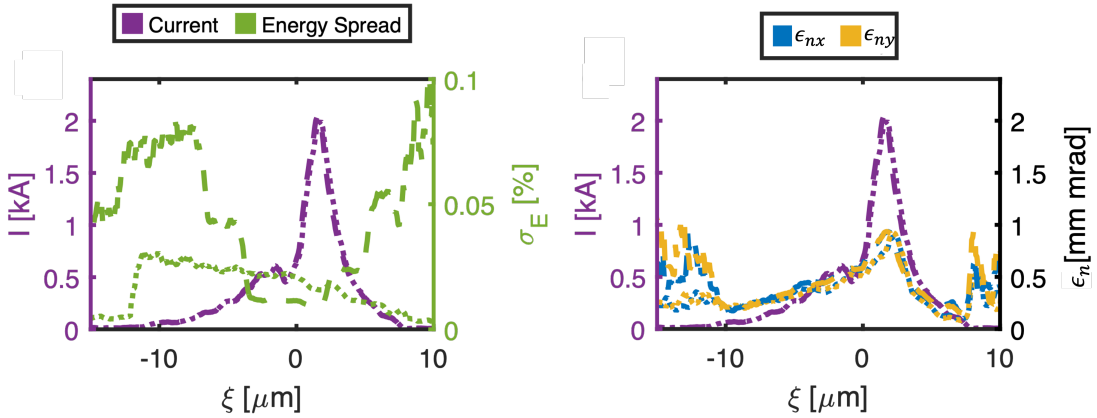

Figure 3.9: Slice analysis of the witness bunch at the injection (dots) and the extraction (dashed lines) of the plasma for the 30 pC charge reference working point: current and energy spread profile (left), transverse normalized emittance for both x,y planes (right). The coordinate ξ denotes the separation of the single slice centroid respect to the position of the longitudinal centroid of the witness charge distribution.

phase space only in (b). The average obtained accelerating field is of the order of $\approx$ 800 MV/m, $\approx$ 1 GV/m in the plateau region (c), for a final energy of 1.1 GeV (c). The overall energy spread (d) is kept at a reasonable level ($\approx$ 1%), while the normalized energy spread of the core (80 % of the total charge), that is substantially uncorrelated, is reduced. Finally the transverse matching (e) is well performed.

3.2.4 Driver separator

The transfer line from the plasma to the FEL consists of three main sections: a capture channel for the highly divergent electron beam emerging from the plasma, a magnetic chicane (Driver separator) to separate the driver from the witness, and a beamline equipped with electromagnetic quadrupoles to match the Twiss parameters of the witness to the FEL requirements. In more details, the capture section is composed of a 1-meter-long FODO structure based on permanent magnets and it is optimized for large energy acceptance (see Chapter 7 for details). This enables simultaneous transport of both the accelerated witness and the decelerated driver without significant charge loss along the capture FODO, thanks to its optimized acceptance energy of about 50% and proper iris width of the permanent quadrupoles, that counteract the $\approx$ 80% energy spread of the accelerated comb beam. Thanks to this significant energy difference between the witness and the driver after the acceleration in plasma, see Fig. 3.11, the magnetic chicane, two meters long and with an R_{56} typically around 0.8 mm, directs the witness towards the FEL while deflecting the driver towards the beam dump (see Sec. 19.4.3.7 in Chapter 19), by means of a three-ways vacuum chamber and a C-shape bending dipole equipped with a septum, see details in Chapter 17. A set of scrapers/collimators is also foreseen to clean the witness distribution from the residual off-energy driver particles.
A final longitudinal compression of the witness takes place in the driver-separator chicane, taking advantage of the strong energy–time correlation (chirp) naturally produced during plasma acceleration, and the non-zero momentum compaction R_{56} of the chicane. The witness current then rises from $I_{peak} \approx 2$ kA at the plasma exit to $I_{peak} \geq 3$ kA at the undulator entrance, as reported in Table 3.1.
The transfer line is also equipped with a Polarix RF deflector followed by a bending dipole that

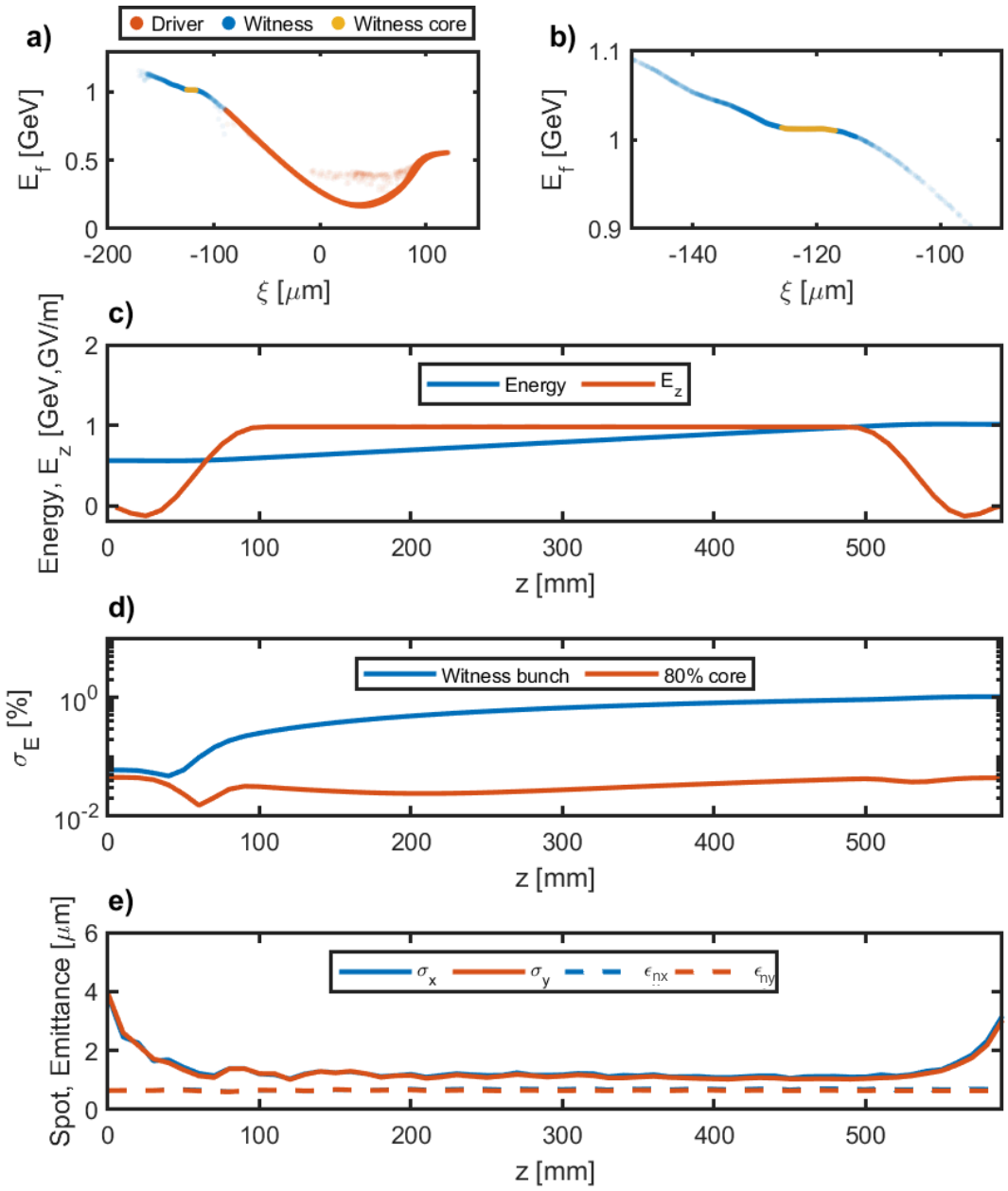

Figure 3.10: Longitudinal phase space of the driver and witness bunches (a) and of the witness only (b) at the end of the capillary. The coordinate ξ denotes the separation of the single particles respect to the position of the longitudinal centroid of the driver z. The witness energy evolution and its experienced accelerating gradient inside the plasma module are shown in (c), where a decelerating zone close to the capillary ends can be noticed, due to the fact that for low densities the witness is in the decelerating phase of the accelerating field. Energy spread evolution of the entire bunch and the witness core (d). Transverse size inside the capillary and normalized emittance evolution (e).

provide the diagnostic system for the 6D analysis of the beam prior the injection in the undulator.

Figure 3.12 shows the evolution of the Twiss parameters along the transfer line, from the plasma exit to the FEL entrance for the comb beam working point. In Table 3.5 the layout parameters of the separator (S) chicane are given. As far as the drawbacks due to the Micro Bunching Instability (MBI) effect are concerned (see Sec. 3.4), the estimate given by the semi-analytical model shows

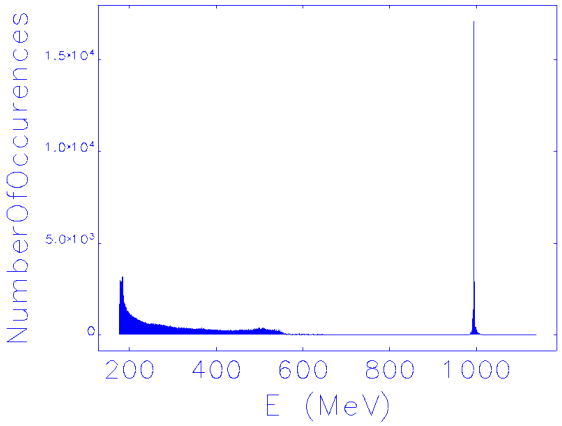

Figure 3.11: Energy distribution of the comb beam at the plasma exit: the witness bunch is located around the 1 GeV peak, while most of the driver particles are distributed between 200 and 500 MeV

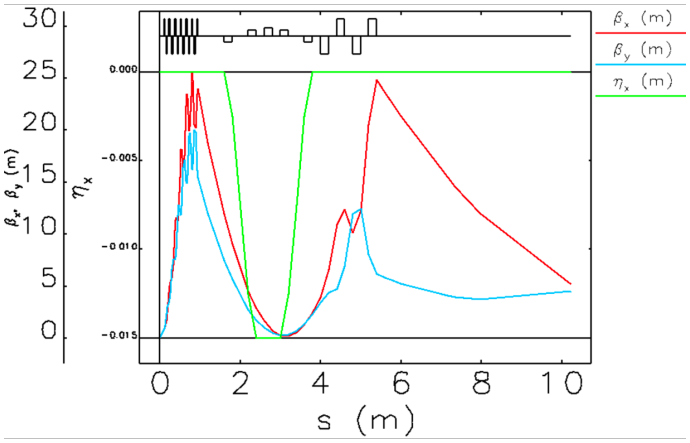

Figure 3.12: Twiss parameters of the witness along the capture/separation transfer line between the plasma capillary exit and the undulator entrance.

Separator chicane parameter	**Symbol**	**Units**	**S**
Total chicane length (1^{st} bend to last)	L_{total}	m	2.40
Floor length of each dipole	L_b	m	0.25
Floor length of drift between first two and last two dipoles	ΔL	m	0.40
Floor length of drift between center two dipoles	ΔL_c	m	0.60

Table 3.5: Layout parameters of the separator chicane

that at the undulator entrance the relative energy spread given by collective effects (MBI and Intra Beam Scattering) is $\approx 0.01\%$, for both witness and driver. The spectral gain of the witness, generated in the separation chicane after the plasma, shows the presence of moderate current modulations, as depicted in Fig. 3.22. The contribution of the MBI to the rms energy spread is limited to $\approx 0.01\%$, that does note compromise the SASE FEL performance.

3.2.5 FEL performances

The properties of the simulated 30 pC witness beam at the entrance of the undulator are reported in Table 3.6. The second column lists the parameters of the full beam, while the slice emittance and slice energy spread are evaluated for the slice yielding the highest expected brilliance, both for the complete beam and for the beam after a 5% removal of the outer 6D halo (third column).

Table 3.6: Reference witness main parameters at the beginning of the undulator. 200 pC of charge in the driver and 30 pC in the witness. Whole beam (second column) and beam with a cut of 5%, located mainly in the bunch distribution tails. (third column). The slice values of emittance and energy spread are evaluated for the best slice, in terms of radiation brilliance, of the whole beam (second column) and for the beam with a 5% cut (third column). The slightly higher value of the slice emittance vs the projected one for best slice of the whole beam are discussed at the beginning of this section.

Parameter	Units	No charge cut	95% of charge
Charge	pC	29.5	28.
Electron energy	GeV	0.995	0.994
Lorentz factor	γ	1946.0	1945.
Peak current	kA	3.3	3.2
(x,y) proj. normalized emittance	mm mrad	0.7, 0.7	0.6, 0.6
(x,y) slice emittance	mm mrad	0.7, 0.7	0.6, 0.6
Proj. energy spread	%	0.48	0.24
Slice energy spread	%	0.25	0.04
x,y rms dimension	µm	36.3, 37.2	34., 37.

The slightly larger slice emittance observed for the full beam is due to the fact that the slice providing the maximum brilliance is primarily determined by the minimum slice energy spread, which is only weakly correlated with the emittance. In addition, the presence of small secondary clusters of particles with large phase-space excursions artificially inflates the projected rms values, although these particles do not contribute to FEL emission.

For this reason, we also report the beam parameters after a 5% charge cut, which effectively removes these satellites and isolates the true beam core. Without the cut, the full-beam energy spread ($\simeq 0.24\%$) would correspond to a low-performance region in Fig. 3.1, with saturation lengths exceeding 20 m. After the cut, the reduced slice energy spread ($\sigma_\delta \simeq 0.04\%$) places the beam in a region of Fig. 3.1 where more than 10^{11} photons are expected within less than 20 m of undulator length, better reflecting the effective beam conditions.

In the FEL simulations, however, the GENESIS code takes into account all the particles and the selection occurs intrinsically by the FEL emission mechanism. Figure 3.13 shows current (red curve), (a) Lorentz factor γ, (b) x and y rms dimensions σ_x and σ_y, (c) x and y normalized emittance ε_{nx} and ε_{ny} and (d) the relative energy spread $\Delta\gamma/\gamma$ along the beam. The profiles are calculated with the rolling window procedure, assuming a slice width of 0.5 µm.

As can be seen in Fig. 3.13, the current is not Gaussian, but presents two peaks. The best slice (indicated by red columns) has a peak current of about 3.2 kA, contains 5.4 pC of charge with normalized emittance that is below 0.7 mm mrad in both planes and relative energy spread (without cut) below $3 \cdot 10^{-3}$. The energy of the best slice is about 0.991 GeV ($\gamma = 1940$). In the best slice, a residual energy chirp of about 1.4 MeV/µm has been evaluated. With these values, however, Fig. 3.1 shows that emission of radiation with more than 10^{11} is not guaranteed. A more reliable estimate is given by considering the case of the beam with the cut of 5% in charge, where the projected energy

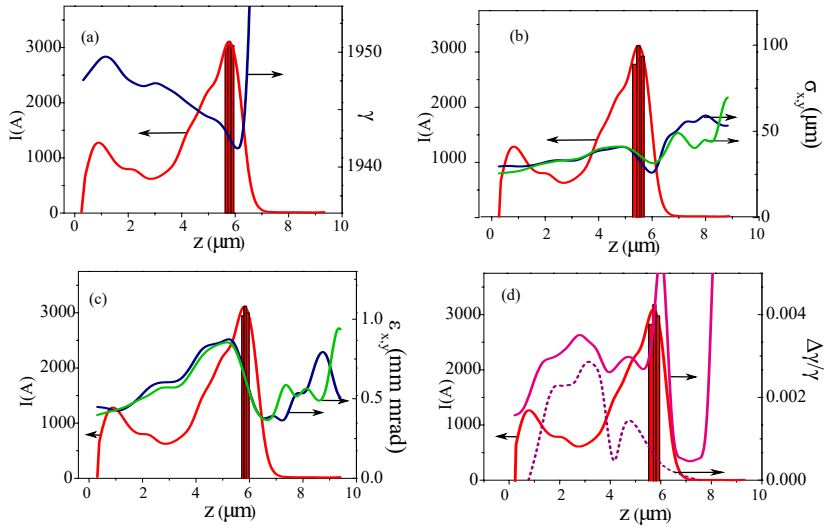

Figure 3.13: Slice analysis of the electron beam in the undulator: Beam current in red on the left axis in all the figures as function of the beam coordinate z(μm). The red columns indicate the best slices in terms of radiation brilliance. On the right axes, (a) Lorentz factor γ (blue curve), (b) x and y rms dimensions σ_x and σ_y (green and blue curve respectively), (c) x and y normalized emittance ε_{nx} and ε_{ny} (green and blue curve respectively), and (d) the relative energy spread $\Delta\gamma/\gamma$ for the whole beam (magenta solid line) and with a cut of 5% of charge (magenta dotted line).

spread is halved and the slice energy spread goes down to $4 \cdot 10^{-4}$ on the best slice. We can see that, in this way, more than 10^{11} photons are foreseen.

The undulator layout of AQUA, used in all FEL simulations of this chapter, is the one widely described in Chapter 8, and we refer to it for all the technical details regarding the undulator line. The transverse sizes σ_x and σ_y, at the beginning of the undulator, after the process of matching the beam to the undulator, are about 36.3 μm and 37.2 μm, respectively. With the undulator period λ_w = 1.8 cm and the undulator parameter K_{rms} = 0.84, the radiation wavelength is about λ_r = 4.05 nm, in agreement with the nominal wavelength value discussed in the Executive Summary Chapter 1 and in Scientific Case Chapter 2. The 1D FEL parameter ρ_{1D} of the best slice is about $2.5 \cdot 10^{-3}$, while 3D effects decrease it to $7.7 \cdot 10^{-4}$ for a gain length $L_{g3D} \simeq 1$ m considering the whole beam, a value corresponding to a saturation at the end of the undulator. For the beam cut at 5% of charge, a condition that gives more reliable estimates, the 3-D ρ_{3D} is $1.7 \cdot 10^{-3}$ for a gain length of about 0.48 m.

The FEL performances of the electron beam, obtained with GENESIS 1.3 [4] start-to-end simulations, are presented in Table 3.7. The 3-D, time-dependent simulations have been done with the maximum precision allowed by the code and by uploading in GENESIS 1.3 the file with the whole phase space of the electron beam. The emission follows the typical behavior of the short growth regime [6], with a first saturation at 15 m at 1.3 μJ, marking the end of the exponential phase. A further linear growth phase then follows, leading the energy to about 6.5 μJ at 25 m. In this last phase, however, a deterioration of the temporal and spectral properties of the pulse takes place, with the formation of secondary peaks, corresponding to the features of the FEL superradiance [6]. Without tapering, (second column of Table 3.7) the number of photons produced per shot is about $2.35 \cdot 10^{10}$ at saturation and $1.31 \cdot 10^{11}$ at the end of the undulator. The expected number of spikes [6] is about one at saturation at 15 m. In the superradiant phase, however,

Table 3.7: Main radiation parameters for the reference beam (PWFA case). Case with 200 pC of charge in the driver and 30 pC in the witness. Without tapering (column 3) and with the tapering of Table 3.8 (column 4). In bold, the nominal working point with plasma acceleration.

Parameter	(Unit)	Without tapering	**With tapering**
Radiation wavelength	nm	4.05	**4.06**
3-D ρ	$\times 10^{-3}$	0.77	**0.77**
3-D gain length	m	1	**1**
3-D cooperation length	μm	0.26	**0.26**
Pulse energy	μJ	6.5	**15.8**
Photon number	$\times 10^{11}$	1.31	**3.22**
Saturation length	m	22	**20.5**
Bandwidth	%	0.48	**0.44**
Transverse size	μm	220	**230**
Divergence	μrad	34	**34**
FWHM length	μm	4.8	**0.7**
FWHM time duration	fs	16	**2.33**
Average brilliance	$\# \times 10^{30}$	0.048	**0.12**
x,y displacements	μm	-12.1, 7	**4.58, 6.7**
x,y angular deviation	μrad	0.93, 1.15	**0.07, 8.6**

#= N_{phot}/s/m^2/rad^2/0.1%bw.

secondary maxima develop. Moreover, since the beam current distribution is not gaussian-like, but double-peaked, the other parts of the beam arrive sequentially at saturation, deteriorating further the structure of the pulse. Considering a 100 Hz repetition rate, the average brilliance of the pulse is $4.8 \cdot 10^{28}$ photons/s/m^2/rad^2/0.1%bw.

Table 3.8: Undulator parameter values of the various sections in the case of step-tapering.

Undulator	1	2	3	4	5	6	7	8	9	10
K_{rms}	0.84	0.84	0.84	0.84	0.8392	0.8384	0.8376	0.8368	0.836	0.8352

Thanks to the short bunch length, the application of a tapering to the magnetic field of the undulator favors a stronger emission and a shortening of the radiation pulse. The tapering has been applied to the undulator by tuning the K_{rms} values of each single section of the undulator to different values ("step-tapering" [21]), according to Table 3.8. The step-tapering procedure is described in detail in Chapter 8. Such sequence of values of K_{rms} have been chosen as the result of an a optimization with respect to the emitted power, with a procedure simulating the operations that can be performed experimentally. The variation of the values of K_{rms} of the tapering sequence are well within in the tunability range of the undulator, as described in Chapter 8 devoted to the technology of the undulators. The results of the GENESIS 1.3 simulation are reported in column 4 of Table 3.7 and in Fig. 3.14. The case with tapering has been considered as our reference working point. It widely satisfies all the requirements of the scientific case described in Chapter 2 in wavelength, photon number, bandwidth and pulse duration. The acceptability of the average position and angle displacements of the radiation pulse at the end of the undulator will be discussed in Section 3.2.6.4,

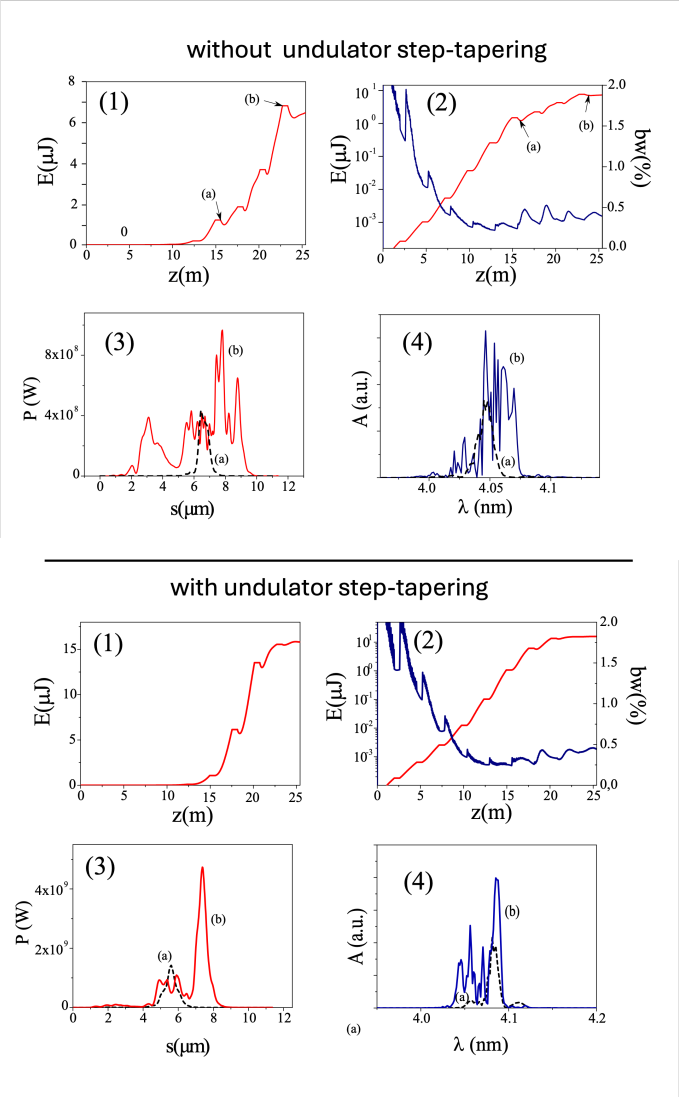

Figure 3.14: FEL simulation results for PWFA nominal working point. Top: case without tapering. Bottom: case with tapering, the corresponding values of the undulator parameters along the line are given in Table 3.8. Picture (1): energy growth in linear scale. Picture (2): energy growth in logarithmic scale and bandwidth in %. Picture (3): power distribution at (a) 17 m and (b) 25 m along the undulator ($s = z - 17$ m and $s = z - 25$ m respectively) Picture (4): spectral distribution at (a) 17 m and (b) 25 m along the undulator.

dedicated to the transport of the radiation along the beamlines.

3.2.6 Jitters and tolerance studies results

Tolerance studies are a key component of the TDR workflow, aimed at verifying the robustness and reliability of the chosen working point. These studies focus in particular on the temporal stability of the RF and photocathode laser systems, as well as the alignment of both active and passive components. While jitter in the RF and laser systems significantly affect the shot-to-shot performance of the plasma accelerator, misalignment can lead to off-axis beam trajectories in the X-band linac. This, in turn, degrades beam quality and reduces acceleration effectiveness due to misalignment between the witness and driver at the plasma entrance.

3.2.6.1 Active elements jitter

The sensitivity analysis to temporal jitters has been carried out by evaluating beam quality and stability at the FEL entrance. The corresponding FEL performance metrics are shown in Section 3.2.6.3. The dominant source of FEL performance variation is the energy deviation at the plasma exit that primarily originates from shot-to-shot jitter in the relative timing between the witness and driver at the plasma entrance, as well as from fluctuations in plasma density. To keep the energy jitter of the witness beam below 1%, according to the analytical estimation shown in the Figure 3.15 [7], the timing jitter between the witness and driver must be below 5 fs, assuming a jitter of the plasma density of the order of 1%.

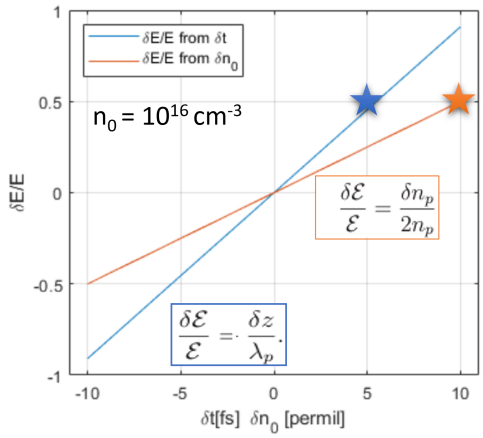

Figure 3.15: Analytical evaluation of the plasma vs the linac contribution to energy gain jitter at the plasma exit [7]. The stars represent the contribution to the energy spread due to the 5 fs jitter of the witness and driver temporal separation (blue) and the contribution due to the 1% plasma density variation (orange)

Jitter sources have been introduced throughout the machine — including both the RF and plasma acceleration — as summarized in Table 3.9 (for the Time of Arrival value reported in this table see details in Chapter 14). These values have been defined on the base of the state-of-the-art technological capabilities of the machine elements, and are consistent with what will be achieved, as shown in the respective chapters.

Machine sensitivity studies were conducted using samples comprising 100 machine runs, a limit imposed by computational constraints. These samples were generated by executing 50 machine runs for two randomly selected plasma-density values, chosen within the specified 1% stability range of the plasma source. Each run incorporates the accelerator jitter and misalignment described later in this paragraph, thereby ensuring that the plasma contribution to the overall machine jitter is appropriately accounted for. For each machine we have generated a tracking input code whose element errors are provided by means of the Matlab Latin Hypercube function [22], that returns an n-by-p matrix containing a sample of n machine run identifier on each of the p element errors. The n values are randomly distributed with one from each interval (0,1/n), (1/n,2/n), ..., (1-1/n,1), and they are randomly permuted. Furthermore a normal random distribution of minus and plus signs is also applied. In this way, for each parameter, the error matrix randomly factorizes from -100% to +100% the error values listed in Table 3.9.

The data analysis shows that RF jitter in the photoinjector — that primarily affects the witness bunch length and the witness-driver timing — together with plasma density fluctuations, results in energy variations of the same order of magnitude as those predicted by analytical estimates. On the other hand the X-band longitudinal wakefields in the linac help in stabilizing the witness

Table 3.9: Summary of jitter values used in the sensitivity analysis. The quantities are intended as RMS values, except for charge and spot size of the cathode laser system, which are instead drawn from uniform distributions and oscillate within the indicated range.

Subsystem	Parameter	Symbol	Jitter
S-band Gun and Accelerating Sections	RF Voltage	ΔV	0.02 %
	RF Phase	$\Delta\phi$	0.02°
X-band Accelerating Sections	RF Voltage	ΔV	0.02 %
	RF Phase	$\Delta\phi$	0.10°
Plasma Accelerator	Density	n_0	1%
Cathode Laser System	Time of arrival	Δt	20 fs
	Charge	ΔQ	±1 %
	Spot size	$\Delta\sigma$	±1 %

peak current to fluctuations on the order of 10 %. A detailed study of individual RF errors shows that the laser pulse arrival time and the RF voltage and phase of the first accelerating section are the primary sources of jitter; the witness–driver delay scales linearly with the magnitude of each error. The linear trend allows for evaluating the jitter of the witness-driver delay on the basis of analytical calculation, as described in [23], so to not rely on hundreds of simulations. Analytical and numerical studies, that are in good agreement, indicate a time delay jitter between the beams on the order of 5 fs rms in case of same power source for the first two accelerating sections (the ones involved in the compression).

The 100 sample beams exiting from the plasma module are then tracked through the transfer line up to the FEL entrance (see Section 3.2.6.3). Table 3.10 shows the results obtained for the witness at the FEL entrance, it can be seen that in the worst case scenario, a degradation occurs of about the 30% for the slice transverse emittance, while for the peak current the variation is on the order of 20%. However, all the values still remain within specifications.

Table 3.10: Statistical values of the whole witness bunch main parameters at the beginning of the undulator. All quantities are averaged over 100 events.

Parameter	Units	Value	Absolute error	Relative % error
Charge	pC	29.51	0.06	0.2
Electron energy	GeV	1.001	0.011	1.1
γ		1959.5	22	1.1
Peak current	kA	3.075	0.6	19
(x,y) proj. norm. emittance	mm mrad	0.68, 0.67	0.023, 0.021	3.4, 3.1
(x,y) slice emittance	mm mrad	0.73, 0.69	0.22, 0.2	30, 29
Proj. energy spread	%	0.44	0.02	4.5
Slice energy spread	%	0.26	0.05	19
x,y rms dimension	µm	43.4, 43.4	10.4, 16.2	24, 37

3.2.6.2 Misalignments and trajectory corrections

To assess the robustness of the accelerator design and the steerer-magnet configurations, a random misalignment kick was applied to the transverse centroid of the comb beam distribution. This

accounts for trajectory deviations at the S-band photoinjector exit, before the injection in the X-band linac, where off-axis wakefield effects become particularly significant. Additionally, static alignment errors in both the accelerating structures and magnetic elements across the entire linac sections (Linac1 and Linac2) were incorporated following alignment specifications of static and electromagnetic elements as described Chapter 5 and Chapter 17.

The analysis has been carried out using the ELEGANT code, focusing on the performance of the Comb working point at the plasma entrance. Particular attention has been given to beam quality and the transverse alignment between the witness and driver, as these factors critically influence the injection efficiency and the subsequent acceleration in the plasma stage.

The study has been conducted in two steps, reflecting the progressive refinement of beamline alignment. In the first step, static errors representative of the mechanical alignment process have been introduced, based on the specifications mentioned above. The second step has involved the application of residual misalignment resulting from a Beam-Based Alignment (BBA) procedure, which has improved component positioning through beam trajectory measurements, thereby simulating more realistic operational conditions after alignment corrections.

In summary we assume that after the mechanical alignment we can have a maximum 70 μm offset in the x,y plane for the X-band sections, similarly for the quadrupole magnets, together with a maximum 70 μrad angle of rotation around the longitudinal axis. For the electron beam trajectory coming from the photoinjector we assume a maximum residual error value of 50 μm for the offset and 50 μrad for the angle of the beam centroid in the x,y plane. All these values are considered as root mean square (RMS) quantities, assuming a Gaussian distribution with a 2σ cutoff to exclude extreme deviations. After a BBA all the previous values should reasonably decrease to 25 μm x,y and 25 μrad.

In this way to simulate upstream imperfections, an initial transverse offset has been applied at the Linac1 entrance, modeling a possible off-axis injection from the photoinjector. Furthermore, the X-band accelerating structures have been modeled in pairs, consistent with their actual layout in the machine, to provide a more realistic representation of alignment tolerances. Beam Position Monitors (BPMs) and steerers have been placed at critical locations along the linac, where active trajectory correction has been essential to preserve beam quality and minimize emittance growth. Their distribution has been extensively discussed in Chapters 5 and 17.

Beam dynamics simulations have been carried out over a sample of 50 machine runs, incorporating trajectory correction procedures. In the X-band linac, cavity BPMs with a resolution of 1 μm were employed to monitor and adjust beam trajectories. Both global and one-to-one correction approaches have been successfully implemented. The one-to-one method applies local corrections using the nearest steerer-BPM pair, offering a fast but less optimized solution. In contrast, the global method uses all BPMs and steerers to compute a more precise, system-wide correction via response matrix inversion.

Figure 3.16 presents the witness-driver relative offset (top row), relative angle (middle row), and witness beam emittance (bottom row) at the plasma entrance, comparing conditions before and after the application of the BBA procedure. The left column shows the beam properties prior to alignment, while the right column illustrates the improvements achieved through BBA. The transverse centroid offset between witness and driver is presented as normalized to the driver spot size (W-D δ centroid / σ_D). This normalization allows for a more meaningful comparison across different configurations, accounting for the varying beam and plasma conditions. The results indicate that the plasma module can successfully operate with the reference comb beam even in the absence of BBA, since the distribution of witness-driver offset falls almost in the 20% of the driver rms spot size, while the relative angle distribution falls in the range of $\pm$ 0.2 mrad, as can be seen in the left column pictures of Fig. 3.16. Under these conditions, the system's performance remains

robust, functioning effectively despite lacking the advanced alignment corrections provided by BBA. The results demonstrate a reduction of a factor 4 of the relative offset and angle distribution limits, see right column pictures of Fig. 3.16, while the relative emittance degradation value decreases from the 0.4% (left column) to the 0.1% (right column).

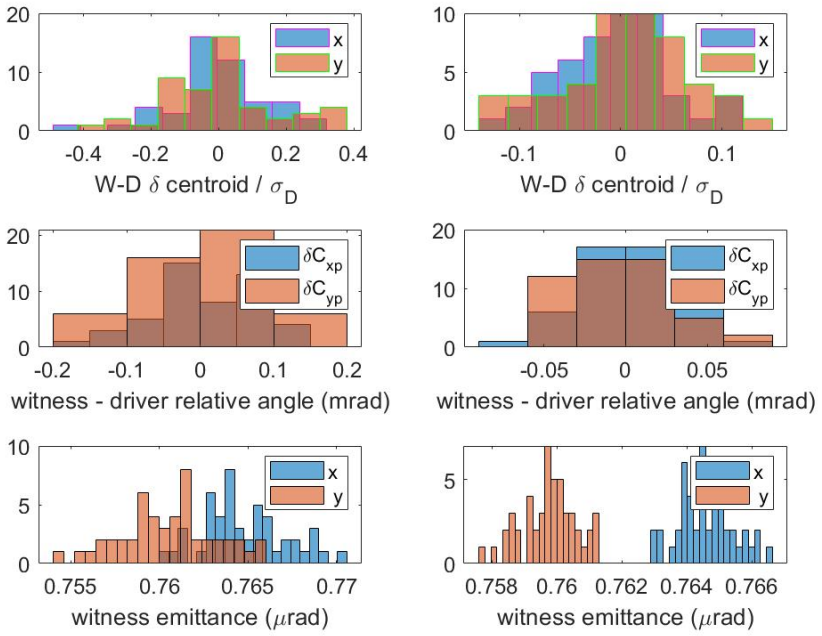

Figure 3.16: Witness-driver relative offset (top row), relative angle (middle row), and witness beam emittance (bottom row) at the plasma entrance, before (left) and after (right) the Beam-Based Alignment procedure.

3.2.6.3 FEL performance with statistical approach

Following the statistical analysis described above, the ensemble of 100 electron beams/events coming from the accelerator, has been tracked in the undulator for an in-depth study of the statistical efficiency of the radiation source. Each comb beam had an energy of approximately 1 GeV and a total charge of 200+30 pC. Table 3.10 summarizes the average beam parameters at the undulator entrance, including charge, energy, Lorentz factor γ, peak current, projected and slice normalized emittance, as well as projected and slice relative energy spread. For each quantity, averages over the 100 shots are reported together with the corresponding absolute errors.

The beams were transported through the separator, removing the driver component, and matched to the undulator, tuned to emit radiation at $\lambda_r = 4$ nm. The parameters of the separation chicane and transfer line were optimized to match the transport of all 100 separated witness bunches, rather than a single one, in line with operating procedures of a real experiment. The undulator lattice was then configured to maximize the FEL output at the reference wavelength, for an average electron energy close to 1 GeV.

Table 3.11 summarizes the parameters of the undulator in these conditions.

FEL simulations were performed with GENESIS with maximum temporal and spatial resolution. Each one of the 100 beams was propagated independently through the separator–transfer–undulator line, with fixed optics for all runs. Due to differences in beam energy, emittance, energy spread,

Table 3.11: Undulator parameters for $\lambda_r = 4$ nm at 1 GeV

Parameter	Value
λ_w	1.8 cm
K_{rms}	0.84
Electron energy	1 GeV
λ_r	4 nm
Quadrupole gradient	8 T/m
tapering	step-like, see Table 3.8
polarization	circular

and current, the FEL radiation fluctuates in both intensity and wavelength. Table 3.12 reports the average FEL performance parameters for the nominal on axis case, including the resulting radiation offset and angle, without and with step tapering of the undulator (K_{rms} values from Table 3.8). The quantities in the table were evaluated at 25 m from the undulator entrance (corresponding to 19.8 m of magnetic length), averaged over the 100 events, with absolute variations also indicated.

Table 3.12: 3-D Theoretical radiation parameters (Pierce parameter ρ, gain and cooperation length) as given by the Ming Xie analytical analysis [5]) and averaged radiation simulation results (PWFA case) for $\lambda_r = 4$ nm at 1 GeV.

Parameter	Unit	No tapering	RMS Error	With tapering	RMS Error
3-D ρ	$\times 10^{-3}$	0.66	0.46	0.66	0.46
3-D gain length	m	1.98	1.72	1.98	1.72
3-D cooperation length	μm	0.3	0.06	0.3	0.06
Pulse energy	μJ	10.54	5.2	25.54	11.6
Photon number	$\times 10^{11}$	2.1	1	5.26	2.33
Saturation length	m	20.5	2	20.16	1.3
Peak wavelength	nm	4.003	0.085	4.003	0.085
Bandwidth	%	0.37	0.09	0.27	0.06
Transverse size	μm	150	41	160	43.4
Divergence	μrad	28.5	4.2	30.31	4.3
FWHM length	μm	3.55	2.2	1.7	0.8
FWHM time duration	fs	11.7	7.3	5.6	2.6
Average brilliance	$\#\times 10^{30}$	0.77	0.92	1.66	1.39
x,y displacements	μm	-11.1, 2.5	10, 9	-11.9, 6.2	4.2, 6.2
x,y angular deviation	μrad	2.7, 10.6	5, 4.6	6, 8.6	4, 2.9

#= N_{phot}/s/m^2/rad^2/0.1%bw.

Figure 3.17 shows the photon number versus wavelength for each event, with and without tapering. When adopting the photon number per event as the figure of merit for the radiation source, it is observed that over 85% of the events surpass $1 \cdot 10^{11}$ photons in the absence of tapering, whereas this proportion increases to 95% when tapering is implemented. The overall photon yield spans the interval from $1 \cdot 10^8$ to $1 \cdot 10^{12}$, corresponding to variations of a few tenths of a percent in the parameters listed in the Table 3.12.

Figure 3.18 shows the distribution of pulse durations: without tapering, values extend up to 20 fs, whereas with tapering, 98% of the cases exhibit pulse durations shorter than 10 fs.

Table 3.13: 3-D Theoretical radiation parameters (Pierce parameter ρ, gain and cooperation length) as given by the Ming Xie analytical analysis [5]) and statistical values of FEL radiation parameters (PWFA case): average values over the 100 events. Random displacements in x and y (Gaussian distribution with rms width equal to 50 μm) and angular deviations in x and y (Gaussian distribution of θ_x and θ_y with rms width of 25 μrad) have been superimposed to the 100 shots of the electron beam ensemble, leading to an increase in the deviations of the displacement and exit angle of the radiation.

Parameter	**Unit**	**No tapering**	**RMS Error**	**With tapering**	**RMS Error**
3-D ρ	$\times 10^{-3}$	0.66	0.46	0.66	0.46
3-D gain length	m	1.98	1.72	1.98	1.72
3-D cooperation length	μm	0.3	0.06	0.3	0.06
Pulse energy	μJ	5.81	3.8	10.2	6.9
Photon number	$\times 10^{11}$	1.16	0.76	2.04	1.37
Saturation length	m	22.9	1.6	23.4	1.2
Bandwidth	%	0.59	0.18	0.48	0.16
Transverse size	μm	175	52.5	178	45
Divergence	μrad	33.5	5.8	36	5.2
FWHM length	μm	2.1	1.5	1.3	0.44
FWHM time duration	fs	7	5	4.2	1.5
Average brilliance	$\# \times 10^{30}$	0.22	0.36	0.17	0.2
x,y displacements	μm	0.14, 15.5	127, 66	9, 15	132, 50
x,y angular deviation	μrad	0.7, 1.1	20, 14	3, 2	23, 9.6

#= N_{phot}/s/m^2/rad^2/0.1%bw.

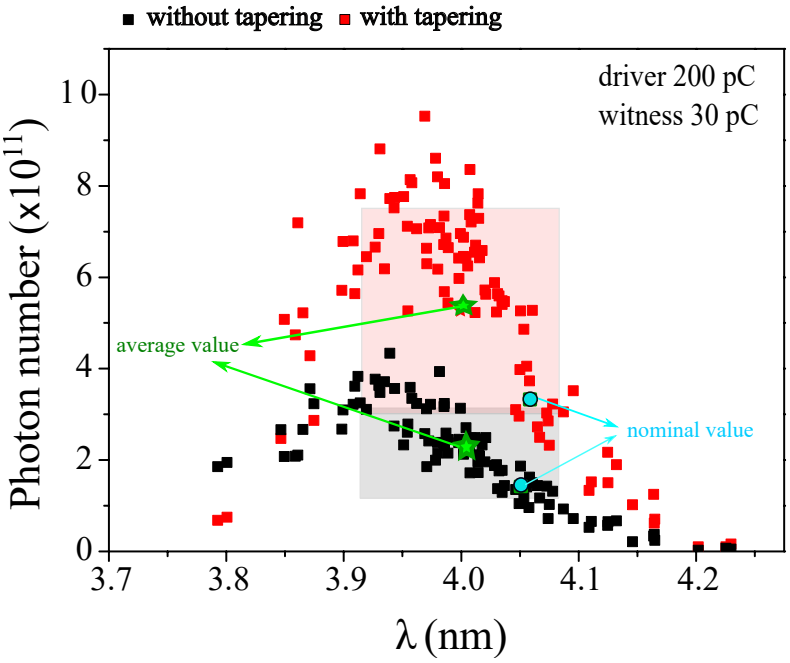

Figure 3.17: Photon number versus wavelength for 100 random events of the reference case at 1 GeV. Black squares: without tapering. Red squares: with a tapering with the K_{rms} values of Table 3.8. Green stars represent the average values. Cyan circles represent the values obtained with the nominal beams. The shaded areas (light gray for the case without tapering and light pink for the case with tapering) around the average values have the half hight equal to the rms deviation of the photon number (1 and $2.33 \cdot 10^{11}$) and the half bases equal to the rms deviation of the peak wavelength (85 pm).

Using the same 100 event ensemble, only changing the K_{rms} of the undulator it is possible to explore a wider wavelength range. Table 3.19 illustrates the achievable wavelength tuning by varying only the undulator parameter within its allowed range ($K_{rms} = 0.6 \div 1.11$, see Chapter 8).

Table 3.14: Undulator parameters and wavelength tuning

K_{rms}	0.6	0.84	1.11
Wavelength	3.2 nm	4 nm	5.2 nm

This corresponds to a tuning range between 3.2 and 5.2 nm for the 1 GeV beams, although here a detailed tolerance study has been performed only in the nominal operational range from 3.6 to 5.2 nm. This range partially covers the water window, including the carbon K-edge at ≈ 4.35 nm and other biologically relevant wavelengths. Energy variations from 720 MeV to 1.25 GeV further extend in principle the accessible range to 2–10 nm, as shown in Fig. 3.19 but a more detailed analysis of this range is out of the scope of this TDR. In all cases with $\lambda_r > 3.6$ nm, the FEL consistently delivers photon numbers above 10^{11}, both with and without tapering, thus meeting the requirements of the scientific case, see introduction of Chapter 2.
Operation at shorter wavelengths is also possible in principle, though not yet optimized. Finally,

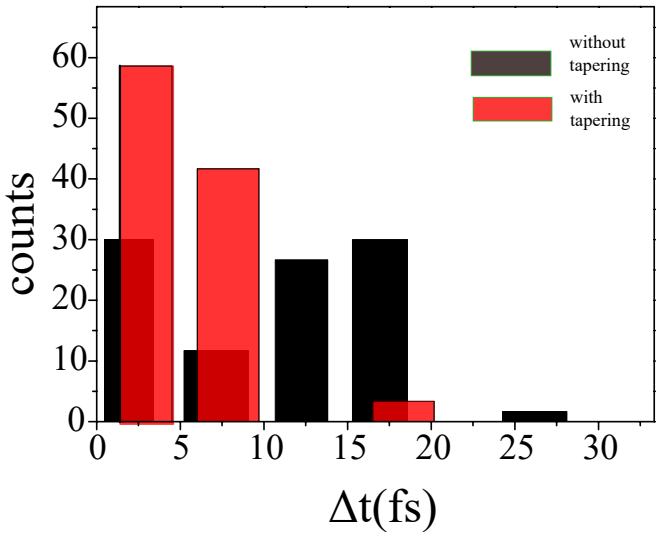

Figure 3.18: Histogram of the number of event as function of the FEL photon pulse length Δt in fs. Black columns: without tapering, red columns: with tapering

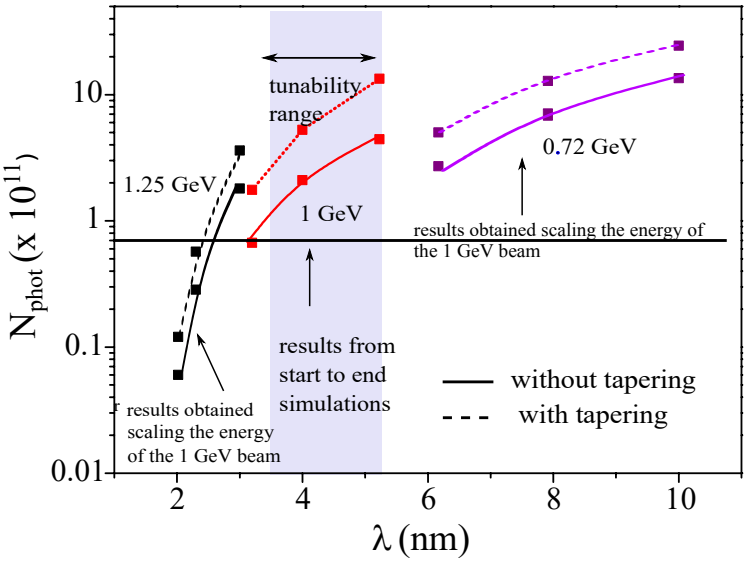

Figure 3.19: Number of photons vs wavelength in the extended electron energy range for $K_{rms} = 0.6, 0.84, 1.11$. Solid lines: without tapering. Dashed lines: with the tapering of Table 3.8.

Table 3.13 presents the impact of transverse displacement and angular deviation at the undulator entrance, again the he quantities in the table were evaluated at 25 m from the undulator entrance (corresponding to 19.8 m of magnetic length). Random Gaussian offsets ($\sigma_{x,y} = 50$ μm, $\sigma_{\theta_{x,y}} = 25$ μrad), representing a pessimistic scenario for the alignment between the accelerator and the

undulator, were applied to the 100 beams. Even under these conditions, the FEL output remains above 10^{11} photons per pulse, with pulse properties compliant with the requirements of the scientific program. This statistical approach demonstrates that, while the spread in output energy is non-negligible, the FEL remains capable of reaching saturation at 4 nm with photon numbers exceeding 10^{11} per pulse in more than 90% of the simulated cases. These findings highlight the robustness of the design and identify the most critical tolerances—particularly timing and energy jitter—that require careful stabilization and monitoring.

3.2.6.4 Optical transport simulations

Ray tracing simulations with OASYS SHADOW4 code [24] have been performed to validate the photon transport line. The analysis focuses on tolerance studies at $\lambda = 4$ nm, using input source parameters obtained from the start-to-end simulations (Tab. 3.12) and the optical layout described in Chapter 9. The steering mirror and the grating are modeled as plane mirrors, while the K–B mirrors are represented as ideal elliptical mirrors with different focal lengths to achieve a coincident focus 1.5 m downstream of the last mirror.

For the baseline case, the source parameters of 160 µm (rms spot size) and 30.3 µrad (rms divergence) were varied by $\pm 1\sigma$. The resulting focal spot at the sample plane is 0.5×0.4 µm (rms), with an increase of about 1×0.7 µm for $\pm 1\sigma$ variation of the source spot dimension using the same K–B mirror curvatures. The focal size is dominated by the source spot size, while the divergence contributes only marginally (0.4×0.3 µm at 1σ). The focal spot position is largely unaffected: position fluctuations remain below the $\sim$0.1 µm numerical accuracy of the simulation, while angular variations at 1σ lead to a ± 0.5 µm displacement. All 2×10^5 rays are transmitted to the focus without geometrical losses for parameter variations up to $\pm 2\sigma$, without considering the effects of plate BPM apertures (described in Sec. 9.4.3). The variations scale linearly when the simulation is extended to 2σ source fluctuations, obtaining double the stated values. Simulations including wavefront propagation, using OASYS SRW code, give a small increase in the focal spot, due to diffraction, to a value of 2.2×1.6 µm.

Tolerance studies on source pointing and position errors confirm robustness against realistic shot-to-shot fluctuations. For angular deviations of 8 µrad (2σ from Tab. 3.12), the focal spot remains unchanged within 0.1 µm compared to the unperturbed case, with a slight loss on the Plate BPM apertures (0.3% total additional losses, going to 1.6% for double the fluctuation due to the gaussian shape of the pulse). A 50 µrad angular mismatch induces a ± 5 µm shift and a 2 µm increase in the rms size, while a 100 µrad mismatch produces a 19 µm displacement, a doubling of the spot dimensions, and $\sim$ 1.5% losses on the grating interface. Plate BPM apertures should be adjusted for strong pointing fluctuation, as 50 µrad source deflection will increase the losses by $\sim$15% from the aperture calculated for a stable pulse. No losses occur at the K–B mirrors; however, future wave-optics simulations are expected to reveal additional diffraction losses due to the mirror edges. For position mismatches of ± 12 µm (2σ from Tab. 3.12), the spot position shifts only ± 0.4 µm. Even for ± 100 µm offsets, the full transmission is preserved, with spot displacements below 3.5 µm and no significant enlargement or losses (0.1% on the plate BPM apertures).

Tolerance studies have also been extended to other wavelengths (Tab. 3.14). At 3.2 nm, the focal spot is 1.3×0.9 µm rms, with similar sensitivity to source misalignment, wavefront propagation has rms values of 1.2×1.2 µm with significant deformation from the gaussian shape. For ± 50 µrad angular mismatch, the spot enlarges by ~ 2 µm and shifts by 3.5 µm, while ± 100 µrad produces a doubling of the spot dimensions, an 18 µm shift, and $\sim$ 1% ray losses. At 5.2 nm, the focus is 1.2×0.9 µm rms (2.2×1.2 µm with wavefront propagation), with ± 50 µrad causing a ~ 2 µm enlargement, a 3.5 µm displacement, and 0.1% losses, while ± 100 µrad results in doubling of the size, $\sim$ 18 µm displacement, and $\sim$ 5% losses (again only at the grating).

The reflectivity of the optical surfaces used in the transmission calculations has also been

simulated with the internal OASYS library, assuming Ni coatings with rms roughness values between 0 and 5 nm. The resulting transmission values are reported in Tab. 3.15. The simulations show that maintaining surface roughness below 1 nm rms ensures transmission above 50%, while values below 0.5 nm rms, if achievable in a cost-effective manner, provide a modest additional increase in efficiency.

Table 3.15: Transport efficiency as a function of the surface rms roughness.

Roughness (rms nm)	**Transmission at 3.2 nm** (%)	**Transmission at 4 nm** (%)	**Transmission at 5.2 nm (%)**
0	56.0	56.9	57.8
0.5	55.0	56.2	57.4
1	52.0	54.2	56.3
2	41.5	46.9	51.8
5	8.6	17.1	29.3

In conclusion, the simulation campaign demonstrates that the proposed optical transport line provides stable focusing performance at the design wavelength and across the target photon energy range. For baseline parameters, the system achieves micrometer-scale focal spots with minimal sensitivity to source fluctuations, that are not affecting the transmission efficiency. Realistic shot-to-shot variations, as predicted by start-to-end simulations, remain well within acceptable limits. Only large angular deviations (≥ 50 µrad) or position offsets beyond ± 100 µm induce significant shifts or transmission losses, mainly at the grating. These values also provide a clear indication for the optics stability required in the transport line. Simulations also confirm that Ni-coated mirrors with rms roughness below 1 nm ensure transmission above 50%, defining a realistic specification for optical surface quality.

3.3 Start to end simulation for the X-band RF acceleration case

With the full RF acceleration in the X-band linac a hybrid compression scheme can be adopted to meet the FEL requirements for the $\lambda_r = 4$ nm radiation production, with a first stage of RF compression in the photoinjector applying the velocity bunching technique and final magnetic compression in the BC chicane. A 200 pC charge has been chosen for this case, and to simulate the electron beam dynamics, around 400k macroparticles are generated and tracked in the photoinjector with the Tstep code and then tracked trough the linac using the Elegant code, where the CSR (Coherent Synchrotron Radiation) effects are taken into account.

3.3.1 Photoinjector and linac

The beam dynamics of the velocity bunching for the hybrid compression scheme mentioned before, has been investigated with numerical simulations to demonstrate the generation in the photoinjector of high-brightness beams with projected emittance values lower than 1 mm mrad and bunch length shorter than 450 µm, as described in the following section.

3.3.1.0.1 Velocity bunching mode

An extensive simulation campaign led to the selection of an 200 pC electron beam with a photocathode laser pulse with a gaussian longitudinal profile and an RMS duration of 0.9 ps, combined with a truncated gaussian transverse distribution with standard deviation $\sigma_r = 170$ µm and cutoff at two sigma.

The main operating parameters of the photoinjector are summarized in Table 3.16.

Table 3.16: Photo-injector main parameters for the full RF case - hybrid compression mode: velocity bunching plus magnetic compression.

Parameter	**Unit**	**Value**
Gun electric field amplitude	MV/m	120
Gun electric field operation phase	deg.	30
Output beam energy	MeV	5.6
Amplitude of electric field in TW sections	MV/m	22.0 / 22.5 / 35.0 / 35.0
Magnetic field in the emittance compensating solenoid	kG	3
Magnetic field in the TW section solenoids	kG	0.3 0

The velocity bunching scheme in the first S-band cavity is adopted to achieve a longitudinal compression of the beam by a factor of 4.3, reducing the bunch length to 120 µm by operating the cavity at a phase slightly off the zero-crossing. Emittance minimization is achieved by setting the gun solenoid to 3 kG and the solenoid surrounding the first accelerating section to 0.30 kG. A slight off-crest operation of the following S-band accelerating cavities allows for additional compensation of the energy spread at the entrance of the X-band booster. In this configuration, the main parameters of the electron beam at the photo-injector exit are given in Table 3.17.

Table 3.17: Photoinjector output beam parameters for the Full RF case - velocity bunching mode.

Beam Parameter	**Unit**	**Value**
Charge	pC	200
Energy	MeV	185
Energy spread (RMS)	%	0.66
RMS bunch length	µm	120
RMS normalized emittance	mm mrad	0.40
RMS transverse size	µm	430

The simulation results are illustrated in Fig. 3.20. The left plot shows the evolution of the transverse normalized emittance (red), transverse spot size (blue), and bunch length (green), while the right plot displays the energy (blue) and energy spread (red) along the beamline, from the cathode to the photo-injector exit, as obtained with the TStep code.

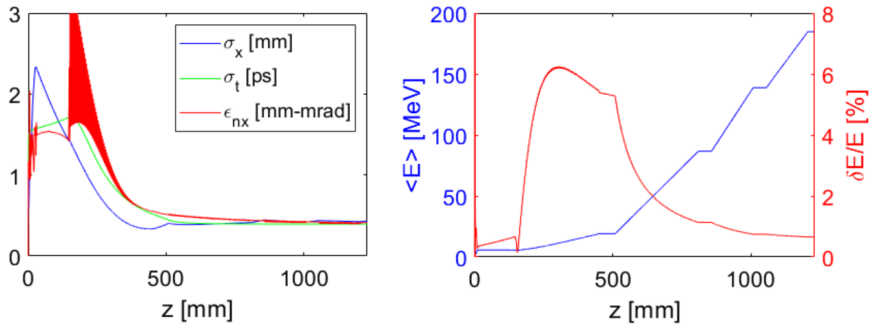

Figure 3.20: Electron Beam transverse phase space emittance and envelope (Full RF case). Left: evolution of transverse normalized emittance, spot size, and bunch length. Right: energy and energy spread along the beamline.

The full X-band linac configuration is designed to provide a single bunch electron beam able to drive SASE-FEL radiation in the AQUA undulator. The 200 pC charge electron beam coming from the photo-injector is accelerated with the RF linac only, and a second stage longitudinal compression needed for the SASE-FEL operation is provided in the BC magnetic chicane in between Linac1 and Linac2 sections. The main setup of the X-band traveling wave (TW) sections, for the full RF acceleration case, is reported in Table 3.18, in terms of average gradients and phases, along with the expected beam parameters at the entrance and exit of each linac section.

Table 3.18: Main setup of the X-band TW sections for the RF acceleration case: average gradients and phases, along with expected beam parameters at the entrance and exit of sections Linac1 and Linac2.

Main setup parameters of the X-band TW sections for the hybrid compression scheme			
	Unit	Linac1	Linac2
Active linac length	m	7.2	7.2
Accelerating gradient	MV/m	54.0	54.0
RF phase (0 = crest)	deg.	-10.7	0.0
Expected beam parameters at the entrance and exit of Linac1 and Linac2			
Initial energy	GeV	0.17	0.60
Final energy	GeV	0.60	1.02
Initial energy spread	%	0.70	0.44
Final energy spread	%	0.44	0.19
Final bunch length	mm	0.120	0.015

The Bunch Compressor chicane (BC), 6.3 m long, can provide a maximum momentum compaction factor $R_{56} = 30$ mm. Between the second and third dipole a quadrupole doublet is foreseen for helping the comb beam transport when the chicane dipoles are switched off for the plasma acceleration configuration. In Table 3.19 the main parameters of the BC magnetic chicane are given, while in Figure 3.21 the evolution of the longitudinal phase space is shown as obtained from Elegant simulations. In Fig. 3.22, the slice analysis of the beam transverse emittances (x and y, top left and right), the slice energy spread (bottom left), and the current distribution (bottom right) at the entrance of the undulator is shown, obtained by selecting different fractions of the beam core according to the core-emittance criterion [25], being the core emittance the emittance of the lowest-amplitude (core) particles, excluding the halo.

Table 3.19: Layout parameters of the BC chicane

BC chicane parameter	Symbol	Units	BC
Total chicane length (1^{st} bend to last)	L_{total}	m	6.3
Floor length of each dipole	L_b	m	0.35
Floor length of drift between first two and last two dipoles	ΔL	m	2.35
Floor length of drift between center two dipoles	ΔL_c	m	0.90
Beam Energy	E	GeV	0.67
Beam Charge	Q	pC	200
Initial rms bunch length	σ_{z_i}	µm	120.0
Final rms bunch length	σ_{z_f}	µm	15.0
Rms total incoming relative energy spread	σ_δ	%	0.44
Momentum Compaction	R_{56}	mm	23.2
Second order momentum compaction	T_{566}	mm	16.6
Dipole bend angle	$\lvert\theta_B\rvert$	deg	4.1
Maximum dispersion at chicane center	η_{max}	m	0.17

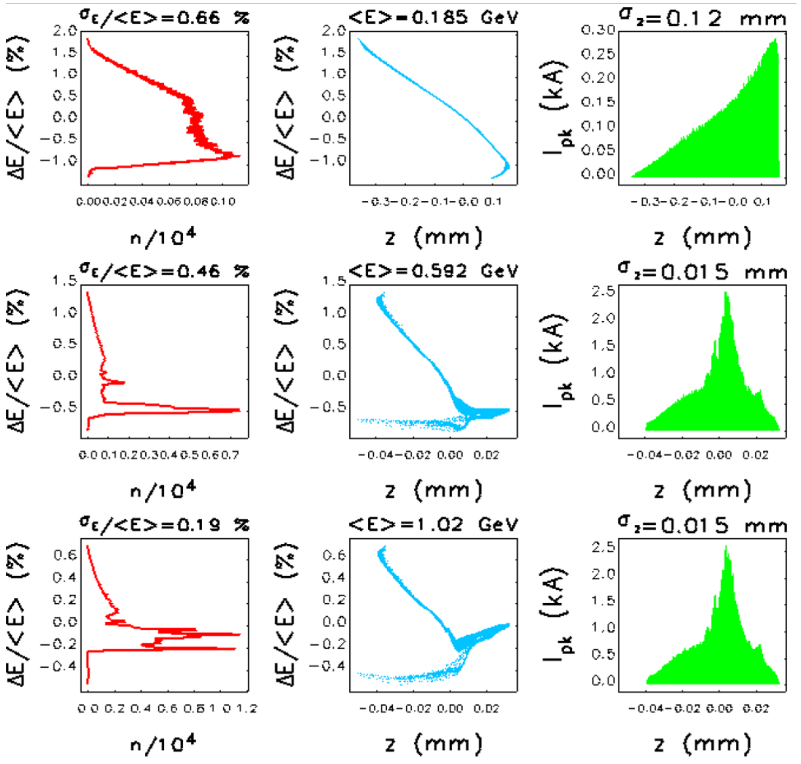

Figure 3.21: Electron beam longitudinal phase space evolution through the linac (Full RF case): Energy (left), longitudinal phase space (center) and axial (right) e-beam distributions after Photoinjector (top), after BC chicane (center row) and at undulator entrance (bottom), as obtained with Tstep-Elegant simulation of 400k macroparticles.

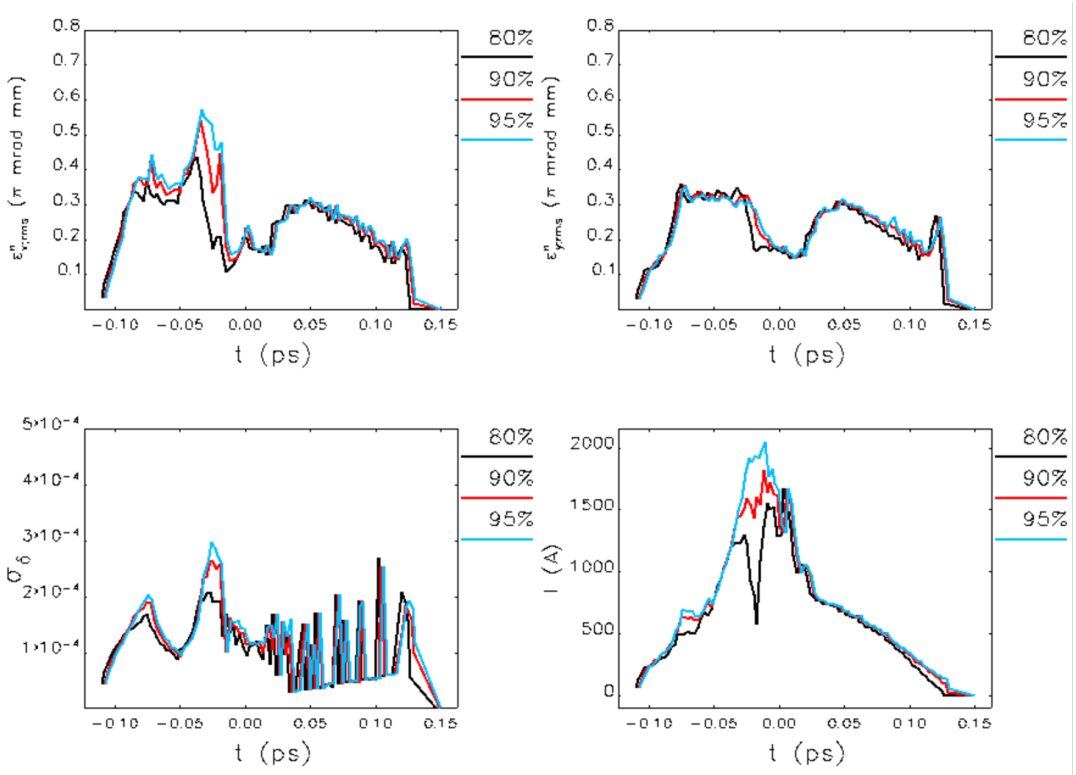

Figure 3.22: Electron beam slice analysis at the entrance of the undulator (Full RF case): x-y transverse emittance (top) and energy spread (bottom left), together with the current profile (bottom right), obtained by selecting different fractions of the beam core according to the core-emittance criterion [25].

3.3.2 TransferLine and Undulator Matching

When the plasma capillary and the in-out permanent quadrupole arrangement are not inserted, a 14 m transfer line is available, downstream the linac exit, to match the electron beam transverse phase space dimensions with the undulator lattice requirements; the e.m. quadrupole arrangement can flexibly provide the required spot size and divergence for the electron beam at the undulator entrance.

3.3.3 FEL performance

Table 3.20 and Fig. 3.23 summarize the parameters of the electron beam obtained for the full RF case.

Table 3.20: Electron beam parameters at the undulator entrance for the Full RF case

Parameter	Unit	Value
Charge	pC	200
Electron energy	GeV	1.02
γ		1999.85
Peak current	kA	3.4
(x,y) projected emittance	mm mrad	2.14, 0.95
(x,y) slice emittance	mm mrad	0.26, 0.25
Energy spread	%	0.19
Slice energy spread	%	0.021
x,y rms dimension	μm	77, 69

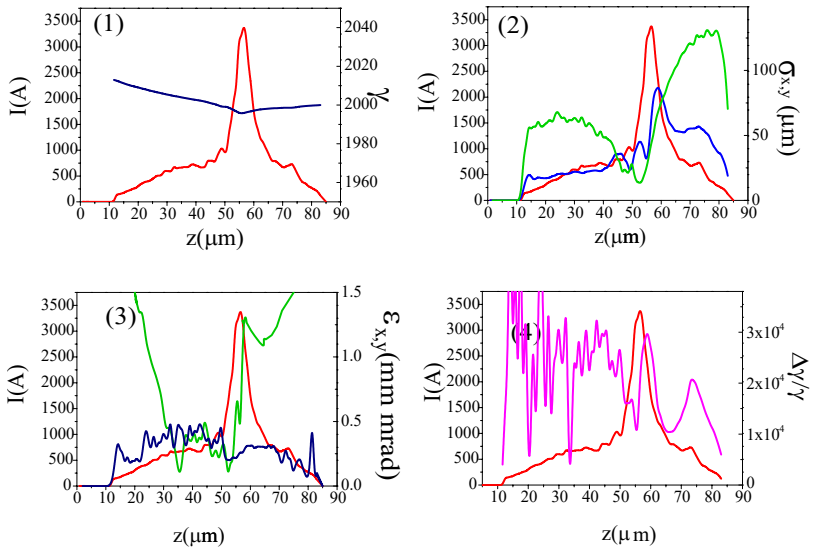

Figure 3.23: Electron beam parameters in the undulator (Full RF case): Beam current (red curve) on the left axis in all the figures as function of z(μm) and, on the right vertical axes, (1) Lorentz factor (blue curve), (2) x and y rms dimension (green and light blue, respectively), (3) x and y normalized emittance (green and light blue, respectively), and (4) relative energy spread (magenta).

The results of the radiation obtained with this beam with three values of the undulator parameter, i.e., $K_{rms} = 1.1$, corresponding to a resonant wavelength equal to $\lambda_r = 4.99$ nm , $K_{rms} = 0.878$ for $\lambda_r = 4.0$ nm and $K_{rms} = 0.7$ for $\lambda_r = 3.37$ nm, are presented in Table 3.21 and Fig. 3.24.

The results of the FEL simulations show that, with this configuration, it is possible to generate a pulse with tunable wavelength in the range of about 3.4-5 nm, with more than 10^{12} photons and duration between 20 and 30 fs. This is considered as the nominal working point, with high-charge, large flux and long pulse.

Table 3.21: Full Rf case: theoretical FEL parameters and radiation simulation results for (a) 4.95 nm (b) 4.0 nm and (c) 3.37 nm at 1.02 GeV.

Parameter	(Unit)	case (a)	case(b)	case(c)
K_{rms}		1.1	**0.878**	0.7
λ_r	nm	4.95	**4.00**	3.37
3-D ρ	$\times 10^{-3}$	1.7	**1.49**	1.25
3-D gain length	m	0.48	**0.55**	0.65
3-D cooperation length	μm	0.42	**0.4**	0.39
Pulse energy	μJ	255	**156**	89
Photon number	10^{12}	6.4	**3.13**	1.47
Saturation length	m	20	**20**	23
Bandwidth	%	0.6	**0.48**	0.45
Transverse size	μm	200	**160**	140
Divergence	μrad	37	**34.5**	31
FWHM length	μm	7	**10**	8
FWHM time duration	fs	23	**33**	27
Average brilliance	# $\times 10^{30}$	1.9	**2.14**	1.74

#= N_{phot}/s/m^2/rad^2/0.1%bw.

3.3.4 Jitter and misalignment analysis

For the full RF case we refer to the study results reported in the Conceptual Design Report of the CompactLight X-ray FEL-XLS [26], to which many among the authors of this document participated in work packages such as RF systems and beam dynamics. In paragraph 5.3.2 of CompactLight CDR the performance of the Linac is discussed taking into account static and dynamics machine imperfections, i.e. misalignments and active element jitters. The 190 m long CompactLight linac [27] employs C-, X-, and K_a-band RF systems. It consists of a 300 MeV injector equipped with a high-brightness electron source and a laser heater, followed by a first magnetic bunch compressor. Downstream of the injector, two X-band linacs—comprising a total of 104 accelerating structures and separated by a second bunch compressor operating at 1–2 GeV—accelerate the beam to a final energy of 5.5 GeV, see Table 3.22. As in our case static

Table 3.22: CompactLight-XLS: Main electron beam and FEL parameters.

Parameter	Value
Max energy	5.5 GeV @ 100 Hz
Peak current	5 kA
Normalised emittance	0.2 mm mrad
Bunch charge	$<$ 100 pC
RMS slice energy spread	10^{-4}
Max photon energy	16 keV

imperfections include quadrupole and accelerating-structure misalignment and BPM errors, while dynamic errors originate from injector-laser timing/charge jitter, RF phase and amplitude jitter, and transverse beam jitter amplified by long-range wakefields. In Table 3.23 the considered static

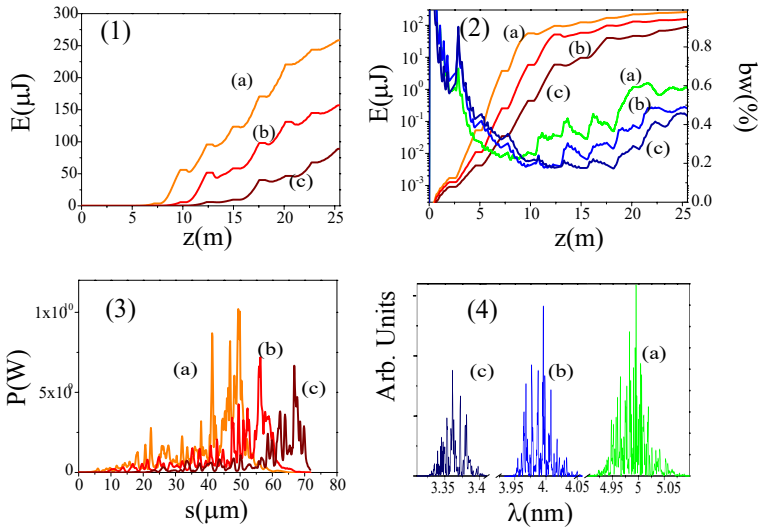

Figure 3.24: FEL simulation results (Full RF case). Case (a) K_{rms} =1.1, corresponding to λ_r = 4.95 nm, (b) K_{rms} = 0.878, corresponding to $\lambda_r = 4.0$ nm and (c) K_{rms} =0.7, corresponding to $\lambda_r = 3.37$ nm . Figure (1): pulse energy growth in linear scale. Figure (2): pulse energy growth in logarithmic scale and bandwidth in %. Figure (3): power distributions at 25 m, ($s = z - 25$m). Figure (4): spectral distributions at 25 m.

imperfections for the CompactLight Linac performance study are reported, while in Table 3.24 the expected jitter levels of the RF and laser systems are listed. It can be noticed that the static error

Table 3.23: CompactLight Linac performance Analysis [26]: RMS static imperfections considered in the simulations.

Element	**Pos. offset** [μm]	**Angle error** [μrad]	**Roll** [μrad]
Quadrupoles	100	100	200
C-band structures	100	100	–
Ka-band structure	100	100	–
X-band structures	100	100	–
BPMs	100	100	200
BPM resolution	5	–	–
Correctors	–	100	200

values for CompactLight are slightly higher than those we considered for EuPRAXIA, (70 μm offset in the x,y plane and 70 μrad angle of rotation around the longitudinal axis). For CompactLight an ensemble of 100 randomly misaligned machines has been tracked and after the simulated dispersion-free beam based alignment, aiming also to minimize the short range wakefield effect, the required transverse emittance average value of 0.2 mm mrad has been obtained at the linac exit. For the CompactLight dynamic errors, the considered values are with some small differences comparable with the ones we adopted for our machine (see Table 3.9). About 500 simulations

Table 3.24: RMS dynamic imperfections of CompactLight subsystems considered in the simulations [26].

Parameter	Unit	Value
Incoming bunch energy jitter	%	0.01
Incoming bunch charge jitter	%	1
Incoming bunch timing jitter	fs	25
C-band phase stability	deg	0.04
C-band voltage stability	%	0.02
X-band phase stability	deg	0.08
X-band voltage stability	%	0.02
Ka-band phase stability	deg	0.16
Ka-band voltage stability	%	0.02

have been performed for the shortest and most demanding wavelength case of CompacLight and the results are reported in Table 3.25. The CompactLight stability goals were determined from the SASE dynamics by analyzing the fluctuations of the FEL process assuming a beam arrival time jitter on the order of the photon pulse-length ($\approx$ 10 fs) and a mean energy jitter of 0.035% that would keep the resonant condition within the FEL bandwidth, while the horizontal emittance of 0.029 mm mrad still allows the saturation within their 36 m undulator length. The conclusion of this study was that the inclusion of dynamic errors in the bunch distributions causes a small decrease in averaged peak brightness and pulse energy, and does increase the fluctuations in the FEL output, but however, the user requirements that RMS fluctuations in pulse energy should be less than 10% and that the peak brightness should exceed 10^{33} ph/s/mm^2/mrad^2/0.1 %bw are both satisfied. We refer to this conclusion for our full RF case presented here.

Table 3.25: CompactLight Linac performance Analysis [26]: Summary of dynamic jitters of electron beam parameters.

Parameter	Units	Value
RMS mean energy error	%	0.016
RMS arrival time error	fs	8.52
RMS energy spread	keV	165
RMS bunch length error	mm	0.28
RMS horizontal emittance	mm mrad	0.029
RMS peak current error	kA	1.05

3.4 Microbunching instability

Microbunching instability (MBI) is a highly relevant phenomenon for linac-driven FELs [28–31]. Such an instability is a collective effect arising from small inhomogeneities in the beam longitudinal charge distribution that gives rise to energy modulation in the longitudinal phase space. These are then transformed into current modulation through non-isochronous dispersive sections ($R_{56} \neq 0$), and the phenomenon iterates itself in a positive feedback loop enhancing the effect. If not properly treated, MBI can be disruptive for FEL performance, in particular in terms of spectral purity (for externally-seeded FEL) and intensity (for SASE). Hence, a laser heater (LH) can be used to increase

the uncorrelated energy spread of the electron beam before the instability builds up, providing an effective longitudinal Landau damping of the MBI [32, 33].

To study the growth and magnitude of MBI for the various machine configurations, we made use of a semi-analytical model, namely the Huang-Kim model [34, 35], that describes the stepwise formation of microbunching along the different sections of the machine, driven by both longitudinal space-charge (LSC) and coherent synchrotron radiation (CSR) impedance. It also incorporates the physics of intrabeam scattering (IBS) and Landau damping, including a possible arbitrary transverse mismatch of laser and electron beam in the laser heater (LH) undulator. The model is valid in the ultra-relativistic regime and averages over betatron oscillations making use of 1D approximations in the Coulomb interaction calculations. The formalism summarizes the phenomenon of MBI formation along a machine section (composed of a straight section followed by a 4-dipole chicane) as an integral equation whose kernel contains the physics of collective effects:

$$b(\lambda(s);s) = b_0(\lambda(s);s) + \int_0^s K(s;s')b(\lambda(s');s')ds', \tag{3.3}$$

where $\lambda(s)$ is the modulation wavelength, b is the bunching factor, i.e. the Fourier transform of the current modulation relative to the local peak current. Here we use the relative energy spread and the spectral gain as main figures of merit to quantify the presence of MBI. The former is defined as:

$$\sigma_\delta = \frac{1}{E}\sqrt{\sigma_{int}^2 + \sigma_{IBS}^2 + \sigma_{MBI}^2 + \sigma_{LH}^2}, \tag{3.4}$$

where the σ_{int} is the intrinsic uncorrelated energy spread, i.e. the initial one (here assumed ~ 2 keV [36, 37], to consider a beam prone to instability) multiplied by the compression factor (considering an approximate preservation of the longitudinal emittance), σ_{IBS} is the one given by IBS, σ_{MBI} is the energy spread given by the energy modulations cumulated through LSC, σ_{LH} is the energy spread induced by the LH and E is the beam energy. The spectral gain can give a clear indication of the more critical bandwidth for the MBI growth, and is defined as:

$$G(\lambda) = \left|\frac{b_f(\lambda)}{b_0(\lambda)}\right|, \tag{3.5}$$

where b_f is the final bunching factor and b_0 is the initial one. It is important to mention that, while the spectral gain is normalized to the initial bunching factor, thus independent of its value, σ_{MBI} scales linearly with b_0 [35], here assumed to have a shot noise distribution with values in the range $10^{-4} - 10^{-3}$, in the bandwidth of interest (condition of ideal uniformity of the photocathode laser pulse). Hence the estimate of the energy spread given here has to be considered as a reference, as photocathode laser irregularities larger than b_0, at critical wavelengths, may cause larger beam energy spread.

The case discussed here is the full RF scheme. Unless specified, all the results presented here are obtained with the LH switched off.

3.4.1 Full RF configuration

For the microbunching effect analysis in the full RF configuration a more critical scenario has been considered than the one previously presented as our reference case, namely featuring two-stage magnetic compression and a slightly higher charge, in order to evaluate a worse-case condition from the perspective of MBI. In this case, the first longitudinal compression takes place not in the photoinjector but in the LH chicane positioned downstream, while the second occurs in the BC. A longitudinal phase space linearization is also needed and can be provided by a 30 cm long X-band section that can take place upstream the LH, to remove the non linear contribution to the

longitudinal phase space distribution of the electron beam coming from the S-band photo-injector. The LH can provide a momentum compaction $R_{56} = 60$ mm with an off axis deviation of about 14 cm, it can also host an up to 60 cm wiggler where the uncorrelated energy spread of the beam can be adjusted by means of the interaction with a laser pulse. Sextupole magnets are also needed in this case in both LH and BC chicanes for tuning the second order momentum compaction T_{566} contribution.

In Figure 3.25 the longitudinal phase space distribution of the electron beam is shown as obtained at the photoinjector exit and at the undulator entrance; in the bottom left picture a modulation can be seen of the longitudinal profile of the peak current I_{pk} as evidence of a microbunching effect, in this case originated by numerical, noise and still present even tracking a 3.2 M macroparticles ensemble.

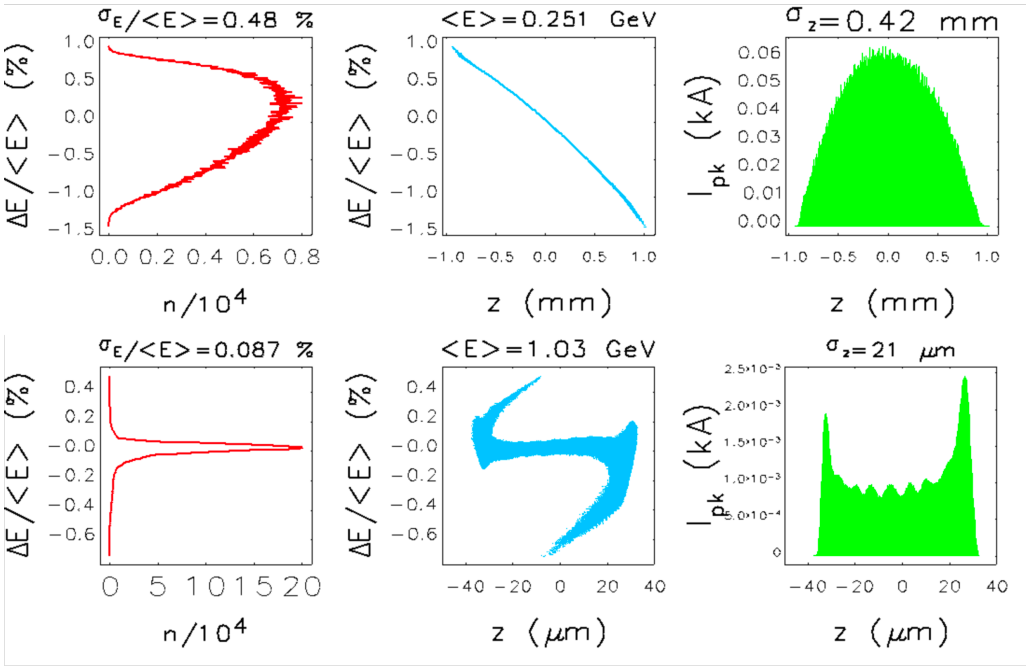

Figure 3.25: Full Rf case with purely magnetic compression: Energy (left column), longitudinal phase space (center column), and axial e-beam distributions (right column) at the photoinjector exit (above), and at undulator entrance (below), obtained with Tstep-Elegant simulation of 3.2 M macroparticles.

No plasma acceleration is involved and no beam separation mechanism is needed, hence, the separation chicane is disabled. For this configuration we consider a bunch charge of 250 pC, a compression factor of ~ 3.9 for the LH chicane and ~ 6.5 for the BC chicane. As shown in Fig. 3.26 (left), we expect a spectral gain peaking in the λ_0 range of 20–30 μm, translating into a compressed wavelength $\lambda \sim 1$ μm, and a final energy spread $\sigma_\delta < 0.01\,\%$. In this specific case the energy spread is dominated by σ_{int} and σ_{IBS}, and introducing any LH contribution would only increase the final energy spread, as shown in Fig. 3.26 (right). However, it may be required to make use of the LH to suppress the spectral gain and energy spread if larger laser pulse irregularities are present. Nevertheless for the tested configurations with 250 pC we obtained at the undulator $\sigma_\delta < 0.01\%$.

3.4.2 Laser heater

The LH concept was first introduced by Saldin et al. [38] and its usefulness first proven at the LCLS hard-X-ray FEL, where the use of the LH shortened the FEL gain length and boosted

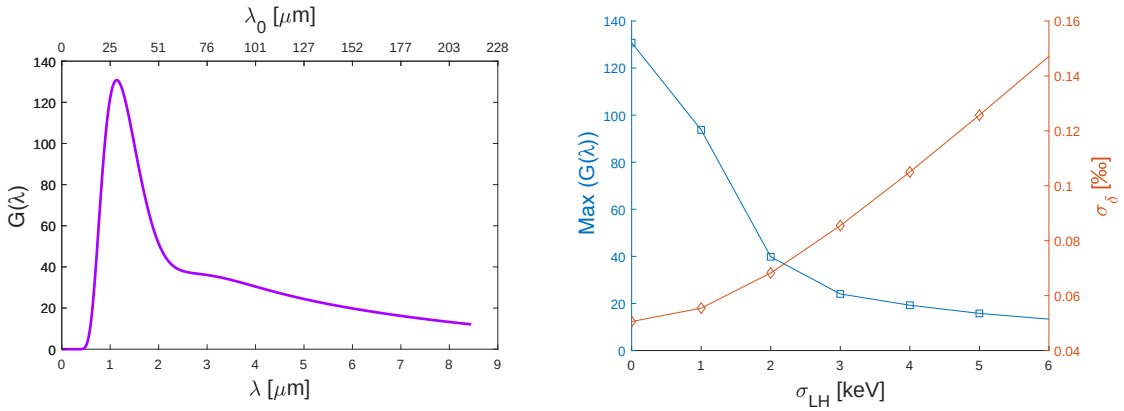

Figure 3.26: MBI spectral gain $G = \left|\frac{b_f}{b_0}\right|$. Left: spectral gain for the full RF -only magnetic- (250 pC). λ_0 and λ are the initial and compressed wavelength, respectively (two-stage magnetic compression). Right: peak spectral gain and respective σ_δ as a function of the energy spread induced by the LH.

the photon flux [32]. It has to operate within the beam energy range of 100–250 MeV, i.e. the maximum operation range set for the full RF working point, and with adjustable bending angles of the chicane between 4–14.5°. Such flexibility is provided by the possibility to use both the fundamental ($\lambda_l \sim 800$ nm) and second harmonic ($\lambda_l \sim 400$ nm) of the Ti:Sapphire laser. This, combined with the remotely controllable undulator gap (15–35 mm), can resonantly match the full electron-energy working range. For an electron beam duration FWHM < 5 ps, a ~ 10 ps FWHM of laser pulse duration favors the temporal alignment while keeping the required energy per pulse below 50 μJ. Figure 3.27 shows the expected sensitivity of the resonance condition to small variations of the undulator gap. The values shown here are analytically computed from well-known, already benchmarked formulas [32, 39].

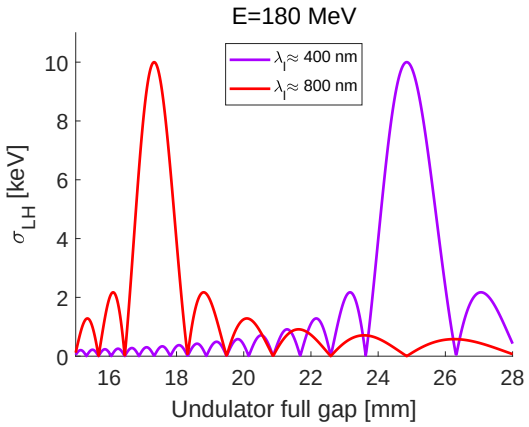

Figure 3.27: Slice energy spread induced by the LH vs undulator full gap (target $\sigma_{LH} = 10$ keV), for the two possible laser wavelengths, in the case of an electron beam energy of 180 MeV.

3.4.2.1 Effects on the electron beam

These LH parameters are specified to ensure an increase of the slice energy spread of the electron bunch by up to $\sigma_{LH_{max}} = 30$ keV, with a full coverage of both electrons energy and bending angle ranges, although, by choosing small values for the latter, for example $|\theta_B| = 4°$, one can reach up

to $\sigma_{LH_{max}} \sim 50$ keV. This upper limit for the energy spread ensures a generous tuning margin for a proper Landau damping of the MBI. The horizontal emittance growth caused by the particles energy change in the undulator dispersive region, induced by the interaction with the laser beam, can be estimated, assuming the pessimistic case of a full chromatic filamentation of the transverse phase space, as:

$$\frac{\Delta\varepsilon_x}{\varepsilon_x} = \sqrt{1 + \frac{\gamma_x \eta_x^2 \sigma_{LH}^2}{\varepsilon_x E^2}} - 1\,, \tag{3.6}$$

where $\gamma_x = (1+\alpha_x^2)/\beta_x$ is the Twiss parameter defined at the undulator location and E is the electron beam energy. For the foreseen configurations, the expected emittance growth induced by the LH remains below 15 %. The main parameters related to the LH are collected in Table 3.26.

Table 3.26: Main parameters related to the use of the laser heater

Parameter	Unit	Value
Laser wavelength, λ_l	nm	400, 800
Laser pulse duration, FWHM	ps	≤ 10
Laser peak power	MW	≤ 5
e-beam energy, E	MeV	100–290
LH-induced maximum slice energy spread, $\sigma_{LH_{max}}$	keV	30–50
LH-induced horizontal emittance growth, $\Delta\varepsilon_x/\varepsilon_x$	%	< 15
LH Chicane bending angle, $\lvert\theta_B\rvert$	°	4–14.5
Horizontal offset in the chicane	mm	39–139
RMS Horizontal e-beam spot size in the undulator	mm	0.2–0.8
RMS Vertical e-beam spot size in the undulator	mm	< 0.1
Electron beam duration, FWHM	ps	< 5

3.4.3 Comments on the results with the MBI semi analytical model

To evaluate the accelerator sensitivity to the detrimental effects of MBI, in addition to the reference scenarios described earlier, we examined the worst-case case for the full RF acceleration configuration, i.e. using magnetic longitudinal compression only and with slightly higher charge. Unfortunately the results cannot be considered conclusive mostly looking at the Fig. 3.25 where the current profile at the undulator entrance (bottom right) shows an evident modulated profile even simulating 3.2 M macroparticles. A more in-depth numerical study is needed to reach a conclusive insight getting rid of the numerical noise contribution. The major effort made so far has been devoted to allocate space and magnetic components for an eventual LH setup that could also permit the first evaluations, but that is not foreseen in the first phases. The LH chicane can be hosted in the diagnostic section needed at the photoinjector exit with no extra length requirements, the dipole magnets have been studied and fit within the machine design. Two additional sextupole magnets can also be inserted in the LH and BC chicanes to properly tune the second order momentum compaction if needed, they also have been studied and fitted in the CAD drawing of the machine, for the sake of brevity, the relative beam dynamics studies are not reported here. For the longitudinal phase space linearization, only needed with the full magnetic compression, an additional 30 cm long X-band section can find a location prior the LH chicane entrance, fitting also with the RF distribution system. The laser pulse needed for the interaction can be obtained from the photocathode laser of the photoinjector. After a more dedicated numerical study, a final decision will be taken also looking at the realization phases and priorities of the machine.

3.5 Conclusions

The beam dynamics studies and start-to-end simulations presented in this chapter confirm that the EuPRAXIA@SPARC_LAB accelerator can deliver electron beams that meet the stringent requirements for Day-One operation of the AQUA FEL beamline. Both the plasma-accelerated and the RF-only configurations have been benchmarked, demonstrating the capability to reach 1 GeV beam energy, normalized emittance below 1 mm mrad, energy spread below 0.1%, and peak currents in the 2-3 kA range. Statistical analyses including jitter and alignment errors show that FEL saturation at 4 nm can be robustly achieved with more than 10^{11} photons per pulse in the majority of cases. Critical aspects such as energy jitter, timing stability between driver and witness, and microbunching instability have been identified as key challenges, with mitigation strategies discussed in connection to Chapters 4, 6, 7, 10, and 14. Future beam tests at SPARC_LAB will be essential to validate these results experimentally and to provide feedback for further optimization. Overall, the simulations results demonstrate that the accelerator design provides a solid foundation for reliable day-one FEL operation and a flexible platform for future upgrades. Based on what stated above the Technology Readiness Level of the start-to-end simulations tools is shown in Tab. 3.27.

Table 3.27: Technology Readiness Level of the Start-to-End Simulations.

Sub - systems	TRL	Comments
Electron beam tracking codes (2D - 3D)	9	Several codes are immediately available, most of them are open source or commercial, optimized for multi-core and cluster operation (Tstep (Parmela commercial), Astra, Elegant, Genesis, CST, HFSS).
Cluster Technology	9	High level computational systems able to perform state of the art level simulations of plasma acceleration, are available and commercialized.
Fast 2D tracking plasma codes	8	Several codes are available which can perform meter scale plasma acceleration simulations with a hybrid fluid-PIC framework (Architect) and quasi-static framework (HiPACE). Another 3D fluid code is currently under development within an INFN-Tor Vergata collaboration.
Plasma PIC 3D Simulation Codes	7	Full PIC 3D code Osiris is open source and available for the EuPRAXIA project, currently in use to cross check the start to end nominal working points of the TDR. Its use to perform simulation scans for stability analysis with reasonable computational resources is still not possible.
Plasma Discharge Simulation Codes	4	Despite several codes are currently being developed for simulating a plasma capillary discharge, there are several doubts over the applicability of underlying models, due to the difficulty in correctly modeling the electron-wall interaction which is of primary importance in our density range.

Bibliography

[1] L. Young and J. Billen. "The particle tracking code PARMELA". In: *Proceedings of the Particle Accelerator Conference*. Vol. 5. 2003, pp. 3521–3523.

[2] M. Borland. *Elegant: A flexible SDDS-compliant code for accelerator simulation*. Tech. rep. Argonne National Lab., IL (US), 2000.

[3] A. Marocchino et al. "Efficient modeling of plasma wakefield acceleration in quasi-non-linear-regimes with the hybrid code Architect". In: *Nuclear Instruments and Methods in Physics Research Section A: Accelerators, Spectrometers, Detectors and Associated Equipment* 829 (2016), pp. 386–391.

[4] S. Reiche. "GENESIS 1.3: a fully 3D time-dependent FEL simulation code". In: *Nuclear instruments and methods in physics research section a: accelerators, spectrometers, detectors and associated equipment* 429 (1999), pp. 243–248.

[5] M. Xie. "Design optimization for an X-ray free electron laser driven by SLAC linac". In: *Proceedings Particle Accelerator Conference. IEEE* 1 (1995).

[6] R. Bonifacio, B. W. J. McNeil, and P. Pierini. "Superradiance in the high-gain free-electron laser". In: *Physical Review A* 40.8 (1989), p. 4467.

[7] S. Romeo et al. "Numerical studies for EuPRAXIA@ SPARC_LAB plasma beam driven working point". In: *Journal of Physics: Conference Series*. Vol. 2687. 4. IOP Publishing. 2024, p. 042008.

[8] B. E. Carlsten. "New photoelectric injector design for the Los Alamos National Laboratory XUV FEL accelerator". In: *Nuclear Instruments and Methods in Physics Research Section A: Accelerators, Spectrometers, Detectors and Associated Equipment* 285.1-2 (1989), pp. 313–319.

[9] L. Serafini and J. B. Rosenzweig. "Envelope analysis of intense relativistic quasilaminar beams in rf photoinjectors: mA theory of emittance compensation". In: *Physical Review E* 55.6 (1997), p. 7565.

[10] L. Serafini and M. Ferrario. "Velocity bunching in photo-injectors". In: *AIP conference proceedings*. Vol. 581. 1. American Institute of Physics. 2001, pp. 87–106.

[11] M. Ferrario et al. "Experimental demonstration of emittance compensation with velocity bunching". In: *Physical review letters* 104.5 (2010), p. 054801.

[12] V. Shpakov et al. "Design, optimization and experimental characterization of RF injectors for high brightness electron beams and plasma acceleration". In: *Journal of Instrumentation* 17.12 (2022), P12022.

[13] W. Graves et al. "Measurement of thermal emittance for a copper photocathode". English (US). In: *Proceedings of the IEEE Particle Accelerator Conference*. Ed. by P Lucas and S Webber. Vol. 3. 2001 Particle Accelerator Conference ; Conference date: 18-06-2001 Through 22-06-2001. 2001, pp. 2227–2229.

[14] M. Ferrario et al. "Laser comb with velocity bunching: Preliminary results at SPARC". In: *Nuclear Instruments and Methods in Physics Research Section A: Accelerators, Spectrometers, Detectors and Associated Equipment* 637.1 (2011), S43–S46.

[15] E. Chiadroni et al. "Beam manipulation for resonant plasma wakefield acceleration". In: *Nuclear instruments and methods in physics research section a: accelerators, spectrometers, detectors and associated equipment* 865 (2017), pp. 139–143.

[16] A. Giribono et al. "EuPRAXIA@ SPARC_LAB: The high-brightness RF photo-injector layout proposal". In: *Nuclear Instruments and Methods in Physics Research Section A: Accelerators, Spectrometers, Detectors and Associated Equipment* 909 (2018), pp. 282–285.

[17] K. L. F. Bane. *Short-range dipole wakefields in accelerating structures for the NLC*. Tech. rep. SLAC National Accelerator Lab., Menlo Park, CA (United States), 2003.

[18] S. Romeo et al. "Evaluation of the transfer matrix of a plasma ramp with squared cosine shape via an approximate solution of Mathieu differential equation". In: *Plasma Physics and Controlled Fusion* 65.11 (2023), p. 115005.

[19] M. Reiser. *Theory and design of charged particle beams*. John Wiley & Sons, 2008.

[20] S. Koscielniak and C. Johnstone. "Analytic model for quadrupole fringe-field effects". In: July 2007, pp. 1386–1388. DOI: 10.1109/PAC.2007.4440764.

[21] L. Giannessi et al. "Self-Amplified Spontaneous Emission Free-Electron Laser with an Energy-Chirped Electron Beam and Undulator Tapering". In: *Phys. Rev. Lett.* 106 (14 2011), p. 144801. DOI: 10.1103/PhysRevLett.106.144801.

[22] M. D. McKay, R. J. Beckman, and W. J. Conover. "A Comparison of Three Methods for Selecting Values of Input Variables in the Analysis of Output from a Computer Code". In: *Technometrics* 21.2 (1979), pp. 239–245. ISSN: 00401706. DOI: 10.2307/1268522.

[23] R. Pompili et al. "Femtosecond timing-jitter between photo-cathode laser and ultra-short electron bunches by means of hybrid compression". In: *New Journal of Physics* 18.8 (2016), p. 083033.

[24] M. S. del Rio and L. Rebuffi. "OASYS: A software for beamline simulations and synchrotron virtual experiments". In: *AIP Conference Proceedings*. Vol. 2054. 1. AIP Publishing LLC. 2019, p. 060081.

[25] C. Davut et al. "Balance of bunch compression and emittance preservation for high-brightness x-ray free electron laser injectors". In: *Phys. Rev. Accel. Beams* 28 (9 Sept. 2025), p. 091602. DOI: 10.1103/rjns-vqzt.

[26] G. D'Auria et al. *XLS - D2.3: Conceptual Design Report*. Version v1. 2021. DOI: 10.5281/zenodo.6375645. URL: https://doi.org/10.5281/zenodo.6375645.

[27] G. D'Auria et al. "CompactLight design study". In: *10th International Particle Accelerator Conference*. 2019, TUPRB032. DOI: 10.18429/JACoW-IPAC2019-TUPRB032.

[28] Z. Huang et al. "Suppression of microbunching instability in the linac coherent light source". In: *Physical Review Special Topics—Accelerators and Beams* 7.7 (2004).

[29] Z. Huang and G. Stupakov. "Control and application of beam microbunching in high brightness linac-driven free electron lasers". In: *Nuclear Instruments and Methods in Physics Research Section A: Accelerators, Spectrometers, Detectors and Associated Equipment* 907 (2018). Advances in Instrumentation and Experimental Methods (Special Issue in Honour of Kai Siegbahn), pp. 182–187. ISSN: 0168-9002. DOI: https://doi.org/10.1016/j.nima.2018.02.030.

[30] S. Di Mitri. "Coherent Synchrotron Radiation and Microbunching Instability". In: *CERN Yellow Rep. School Proc.* 1 (2018). Ed. by R. Bayley, p. 381. DOI: 10.23730/CYRSP-2018-001.381.

[31] A. Brynes. "Characterisation of microbunching instability at the FERMI Free Electron Laser". In: *JACoW* IPAC2023 (2023). DOI: 10.18429/JACoW-IPAC2023-MOOG2.

[32] Z. Huang et al. “Measurements of the linac coherent light source laser heater and its impact on the x-ray free-electron laser performance”. In: *Physical Review Special Topics—Accelerators and Beams* 13.2 (2010), p. 020703.

[33] S. Di Mitri and S. Spampinati. “Microbunching instability suppression via electron-magnetic-phase mixing”. In: *Physical Review Letters* 112.13 (2014), p. 134802.

[34] Z. Huang and K. J. Kim. “Formulas for coherent synchrotron radiation microbunching in a bunch compressor chicane”. In: *Physical Review Special Topics-Accelerators and Beams* 5.7 (2002), p. 074401.

[35] S. Di Mitri et al. “Systematic and comprehensive comparison of two semianalytical models of microbunching instability”. In: *Physical Review Accelerators and Beams* 28.4 (2025), p. 044401.

[36] Z. Huang et al. “Uncorrelated energy spread and longitudinal emittance of a photoinjector beam”. In: *Proceedings of the 2005 Particle Accelerator Conference*. IEEE. 2005, pp. 3570–3572.

[37] S. Tomin et al. “Accurate measurement of uncorrelated energy spread in electron beam”. In: *Physical Review Accelerators and Beams* 24.6 (2021), p. 064201.

[38] E. L. Saldin, E. A. Schneidmiller, and M. V. Yurkov. “Longitudinal space charge-driven microbunching instability in the TESLA Test Facility linac”. In: *Nuclear Instruments and Methods in Physics Research Section A: Accelerators, Spectrometers, Detectors and Associated Equipment* 528.1 (2004). Proceedings of the 25th International Free Electron Laser Conference, and the 10th FEL Users Workshop, pp. 355–359. ISSN: 0168-9002. DOI: https://doi.org/10.1016/j.nima.2004.04.067.

[39] S. Spampinati et al. “Laser heater commissioning at an externally seeded free-electron laser”. In: *Physical Review Special Topics-Accelerators and Beams* 17.12 (2014), p. 120705.

4. Facility layout

4.1 Introduction

This chapter provides an overview of the activities underway at the INFN Frascati National Laboratories (LNF), which will contribute to the European distributed research infrastructure *EuPRAXIA*. The building currently under construction, its functional areas, the electron accelerator, the undulator responsible for producing FEL radiation, and the optical beamlines delivering X-rays to the users' experimental stations are briefly described. References to the chapters containing detailed discussions of these systems are also provided.

The *EuPRAXIA@SPARC_LAB* research infrastructure has been designed to meet the required functionalities while accommodating the limited space available on the INFN-LNF site. Particular attention has been given to the needs of future users conducting experiments across different scientific disciplines with EuPRAXIA. Furthermore, the design considers possible future expansions and developments of the facility by including a very large machine tunnel and provisions for additional shielded experimental areas and laboratory spaces.

4.2 EuPRAXIA@SPARC_LAB Building Layout

4.2.1 General description

The EuPRAXIA@SPARC_LAB building extends over an area approximately 150 m long and 35 m wide. Figure 4.1 shows the top view of the building, including the accelerator and the FEL beam line. The detailed design of the new building and its technical systems is presented in Chapter 18.

The functional areas of the ground floor of the EuPRAXIA@SPARC_LAB building are shown in Figure 4.2.

As illustrated in Figure 4.2, the internal tunnel—approximately 100 m long and 8 m wide and shielded by 2 m-thick concrete walls—hosts the electron accelerator in its first section and the magnetic undulator in the second section.

Adjacent to the shielded tunnel lies another service tunnel, known as the Modulator & klystron gallery, which houses the radio-frequency (RF) power systems. This is followed by an area dedicated to the magnet power supplies and the racks for instrumentation and diagnostic electronics.

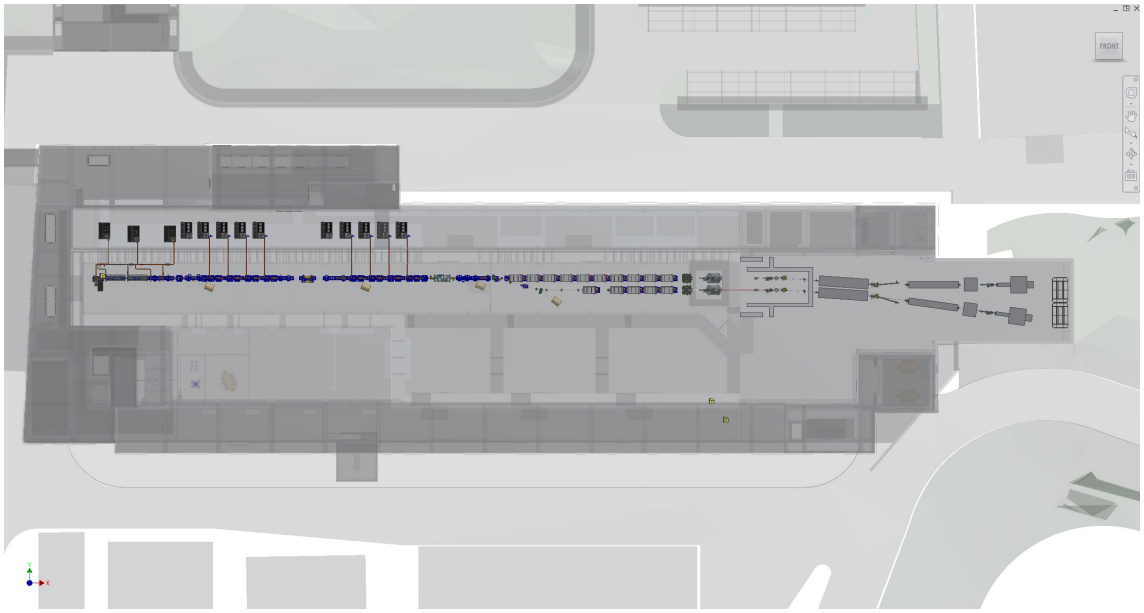

Figure 4.1: Top view of the building with accelerator and FEL beam lines

On the right side of the main tunnel, in the direction of the electron beam, are the laser clean rooms, followed by three shielded experimental areas designed to host experiments that directly use either the accelerated electron beam or the high-power laser located in the adjacent clean room.

A large area, approximately 50 m long and located downstream of the shielded tunnel, accommodates the optical beamlines and the experimental apparatus that utilize the produced radiation, along with laboratories available to users for experiment preparation.

The ground floor also includes the area hosting the cooling and electrical power systems. The first floor, starting from the east side, contains the control room, rack room, meeting rooms, and common areas for operators and users, together with the required service facilities.

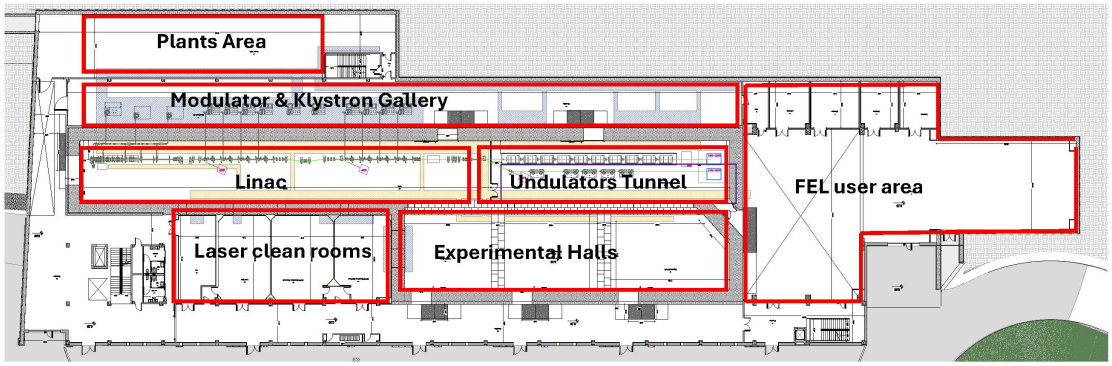

Figure 4.2: Functional areas of EuPRAXIA@SPARC_LAB ground floor

4.2.2 The accelerator and undulator tunnel

The core of the facility is the tunnel that houses the linear electron accelerator and the undulators responsible for generating the FEL radiation.

The tunnel is enclosed by two-meter-thick concrete walls to shield against radiation generated during operation. The roof is covered with an additional two meters of soil to further enhance radiation protection and to allow the area above to be used as a garden. To satisfy the strict temperature stability requirements (see Chapter 8), a partition wall has been designed to thermally isolate the accelerator section from the undulator section.

Two overhead cranes in the two parts of the tunnel are installed to move the accelerator and undulators components.

A longitudinal service shaft located beneath the walking surface, wider in the accelerator area and narrower in the undulator area, accommodates the cooling system pipes and magnet power cables. Two additional trenches are provided for the laser optical lines: one directed toward the photocathode and the other toward the undulator hall, extending up to the users' area.

The accelerator and undulators tunnel together with the klystron gallery are shown in Figure 4.3

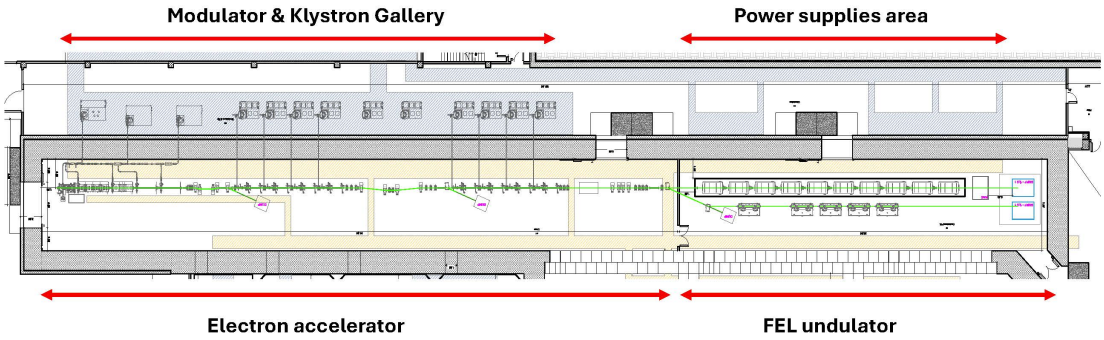

Figure 4.3: Accelerator and undulators tunnel and Modulator & klystron gallery

Within the tunnel, several cable trays will carry the diagnostic signal cables, optical fibers, and control system wiring. The final layout and routing of the cables will be defined during the detailed engineering design phase.

4.2.3 Modulator & Klystron gallery and power supplies area

The RF power, generated by modulators and klystron installed in the gallery, is transmitted through waveguides that connect the klystron RF output windows to the accelerating sections via openings in the 2-meter-thick shielded wall. These penetrations are distributed evenly along the entire length of the accelerator tunnel to provide maximum flexibility for the linac installation as well as for possible future modifications or upgrades.

The modulators are installed above a trench where the cooling pipes, the magnet power cables and the modulator cables pass from the modulator room to the accelerator tunnel through another series of penetrations. This trench is located below the level of the klystron gallery and linac floors

for radiation protection reasons. The area is equipped with a bridge crane both to install and replace the klystrons and other components; an electrical busway running along the entire room distributes the electrical power to the utilities. The whole klystron gallery is protected by two interlocked gates to prevent unauthorized access to the area. The second section of this long corridor, adjacent to the undulator shielded tunnel, houses the power supplies that deliver DC current to the magnets responsible for bending and focusing the electron beam. In the same area, racks are installed for the electronics associated with diagnostics and control systems. This section is also equipped with a bridge crane, a busbar, and dedicated cable ducts to facilitate maintenance and future expansion.

4.2.4 Laser Rooms

On the right side of the building's ground floor, immediately after the main entrance, are four clean rooms (Fig. 4.4) that house the lasers and optical equipment. These systems require exceptionally stable environmental conditions — including precise control of temperature and humidity — and an extremely clean atmosphere to ensure optimal performance and prevent damage. In addition to these requirements, air turbulence must be minimized; therefore, quasi-laminar flow systems have been designed and installed above the areas where the optical tables are located. The clean-room specifications are described in Chapter 18, while the laser systems themselves are discussed in detail in Chapter 12.

The first room is dedicated to instrumentation for measuring terahertz radiation produced by the electron beam, used for both diagnostic and experimental purposes.

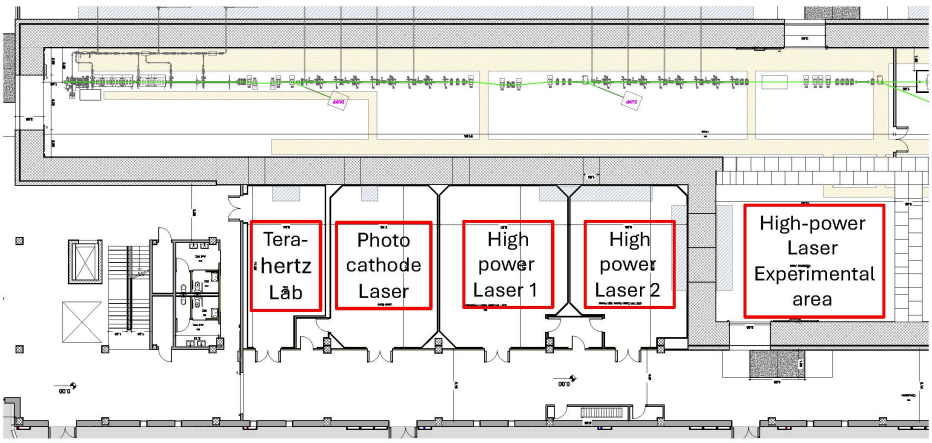

Figure 4.4: Laser clean rooms

In the second clean room the laser that produce the optical pulses that extract the electrons from the injector photocathode is installed. The clean rooms are connected to the previously described trenches in the tunnel through passages below floor level for radiation protection reasons.

The second clean room houses the laser system that generates the optical pulses used to extract electrons from the injector photocathode. For radiation protection reasons, the clean rooms are connected to the trenches described previously via underground passages.

The other two large clean rooms are designed to accommodate high-power, petawatt-class lasers. These systems can be used for particle generation and plasma acceleration experiments

conducted in the adjacent shielded area. The high-power laser beam can be transported into the experimental area through the radiation-protected penetrations provided for this purpose. This portion of the infrastructure has been configured to support potential future upgrades, which are not included in the short-term scope of the present TDR.

4.2.5 Beamlines and Users area

The optical beamlines that transport the FEL-generated X-ray radiation, together with the users' experimental instrumentation, are located in a large area situated immediately downstream of the shielding wall of the undulator tunnel.

Right after the wall separating the tunnel from this room, a shielded chamber is installed at the beginning of the optical transfer lines. This chamber is designed to absorb the unwanted gamma-photon beam produced by the interaction of the electrons with the residual gas along the linac and in the subsequent vacuum chambers.

Four laboratories, located on the right side of the users' hall and in line with the area dedicated to modulators and power supplies, are available for users to install their instruments and prepare or characterize samples prior to FEL irradiation.

4.3 The facility layout

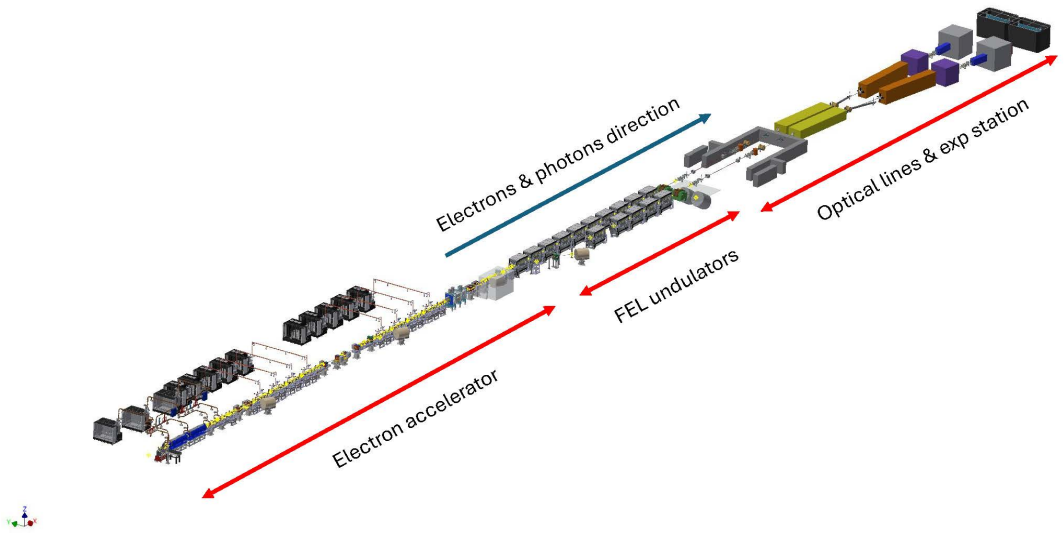

Figure 4.5: Layout of the accelerator and beamlines

4.3.1 Introduction

The EuPRAXIA@SPARC_LAB electron accelerator is a linear accelerator composed of several sections that incorporate innovative technologies. For descriptive purposes, it is divided into three functional areas, each of which is characterized in separate chapters of this TDR.

This subdivision is functional both for the machine description and for the nomenclature that will be used to identify its various components. An overview of the accelerator, the undulators, and the FEL optical beamline components is shown in Figure 4.5. Table 4.1 shows the lengths of the various parts that make up the facility.

Table 4.1: Lengths of the EuPRAXIA@SPARC_LAB parts

Part	Length (m)	Note
Photoinjector	14.219	
Laser heater	3.319	
Linac 1	10.604	
Bunch compressor	10.989	overall dimensions
Bunch compressor	6.264	only chicane
Linac 2	10.719	
Plasma	5.532	
Matching (with AQUA line)	5.616	
AQUA line	29.536	
Photon beam transport line	52.602	

In the following sections, the components located within the tunnel are described in sequence, starting from the electron source and following the acceleration path up to the undulators entrance.

4.3.2 S-band photo-injector

The first section of the accelerator is the injector, described in detail in Chapter 5. In this subsystem, electron bunches are generated, manipulated, and transported to energies of approximately 100–200 MeV before being injected into the X-band linac for further acceleration (Fig. 4.6).

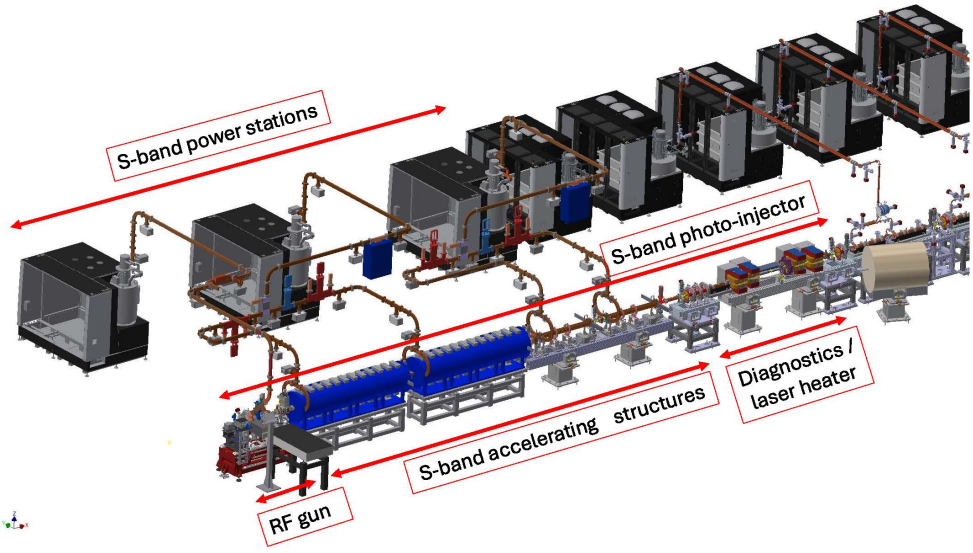

Figure 4.6: Layout of the S-band photo-injector

The first element of the injector is the electron source, a normal-conducting RF gun in which electrons are extracted from a copper photocathode by means of the photoelectric effect. The photocathode is located inside a 1.6-cell S-band RF structure operating at 3 GHz.

The longitudinal electric field of the RF gun accelerates the electrons to an energy of up to 6 MeV, while a solenoid surrounding the cavity exit ensures proper transverse focusing. A complete set of diagnostics is installed between the RF gun and the first long accelerating section to measure the characteristics of the emitted electron bunches. All diagnostic systems installed in the

accelerator are described in detail in Chapter 11. A short X-band cavity is also included to linearize the longitudinal phase space.

Downstream of the RF gun, the injector comprises four S-band accelerating sections. The first two, each 3 m long, are used to compress the electron bunch in time using the velocity bunching technique, while the remaining two, each 1.5 m long, provide the final energy gain. The four accelerating sections are powered by two high-power RF stations, each consisting of a modulator and klystron assembly, whereas the RF gun is driven by a dedicated lower-power klystron. RF pulse-compression cavities, located between the klystrons and the accelerating structures, are used to increase the peak RF power delivered to the sections. All RF power stations are installed in the klystron gallery, which runs parallel to the accelerator tunnel (Fig. 4.6).

Following the injector, a complete set of diagnostic tools is installed to further characterize the electron beam, together with a chicane that serves a dual purpose: acting either as a bunch compressor or as a laser heater. The laser-heater configuration is used to suppress micro-bunching instabilities that can develop when operating at high bunch charges (see Beam Physics, Chapter 3).

4.3.3 X-band linac

Chapter 6 discusses all aspects of the X-band linac, including the magnetic bunch-compression chicane. The electron bunches generated and transported through the S-band injector are subsequently accelerated in a linac consisting of 8 + 8 X-band accelerating structures. The choice of the higher 12 GHz RF frequency allows the achievement of significantly higher accelerating gradients compared to lower-frequency technologies (Fig. 4.7).

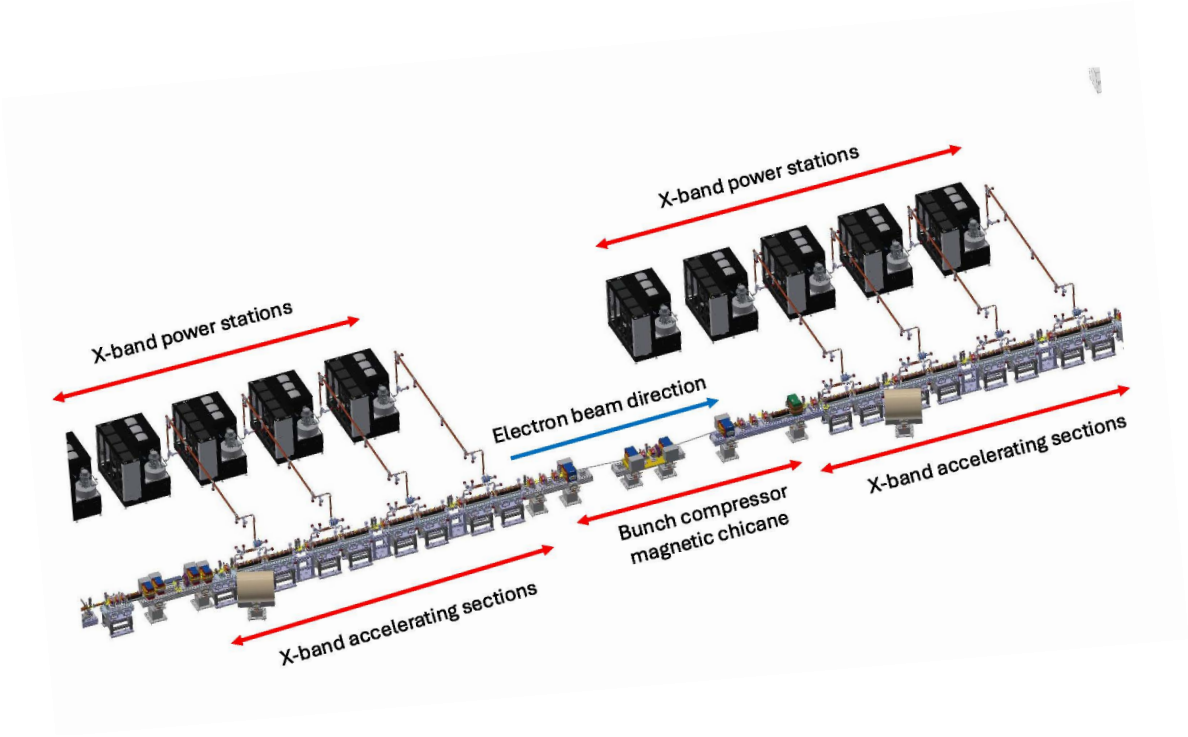

Figure 4.7: Layout of the X-band accelerator

The high-power RF pulse generated in the X-band power station is sent to an RF compression system to increase its peak power. The compressed RF pulse is then split and delivered to two X-band accelerating sections, each 1 m long. The complete assembly, consisting of the power source, compression system, and two accelerating structures, is referred to as an X-band RF module.

A nominal accelerating gradient of 60 MeV/m is routinely achieved with this configuration. This design choice results from an optimization process balancing the total length of the 1 GeV linac with considerations of energy consumption, performance, and both construction and operating costs.

A full set of diagnostic devices is installed at each X-band RF module. These include an intercepting YAG screen for measuring the transverse beam profile and a non-intercepting RF cavity beam position monitor. Between the two accelerating sections of each module, an X–Y corrector is placed to compensate for trajectory deviations and mitigate possible transverse wakefield effects.

Between the first part of the linac — consisting of eight accelerating sections (four modules) — and the second part, which includes another eight sections, a magnetic chicane is installed to further compress the electron bunches.

When operating in the comb-beam configuration produced by velocity bunching, the electron beam must propagate along a straight path through the chicane region. When the chicane is used for bunch compression, it is desirable to vary the compression factor continuously. Achieving this flexibility with a fixed magnetic geometry would require an impractically large vacuum chamber and magnets with wide gaps. To overcome this limitation, a system already adopted in other accelerators was chosen: the central section of the chicane is mounted on a linear translation stage. This allows for smooth transverse movement, while the ends of the vacuum chamber are connected by flexible bellows that compensate for the angular displacement of the adjoining sections.

4.3.4 Plasma accelerating section

For a complete description of the plasma acceleration section, including the beam-focusing systems and the magnetic separator between the driver and witness beams, please refer to Chapter 7.

At the exit of the X-band linac begins the area dedicated to plasma acceleration. A triplet of quadrupole electromagnets is first used to focus the electron beam at the entrance of the chamber that houses the plasma acceleration section (Fig. 4.8).

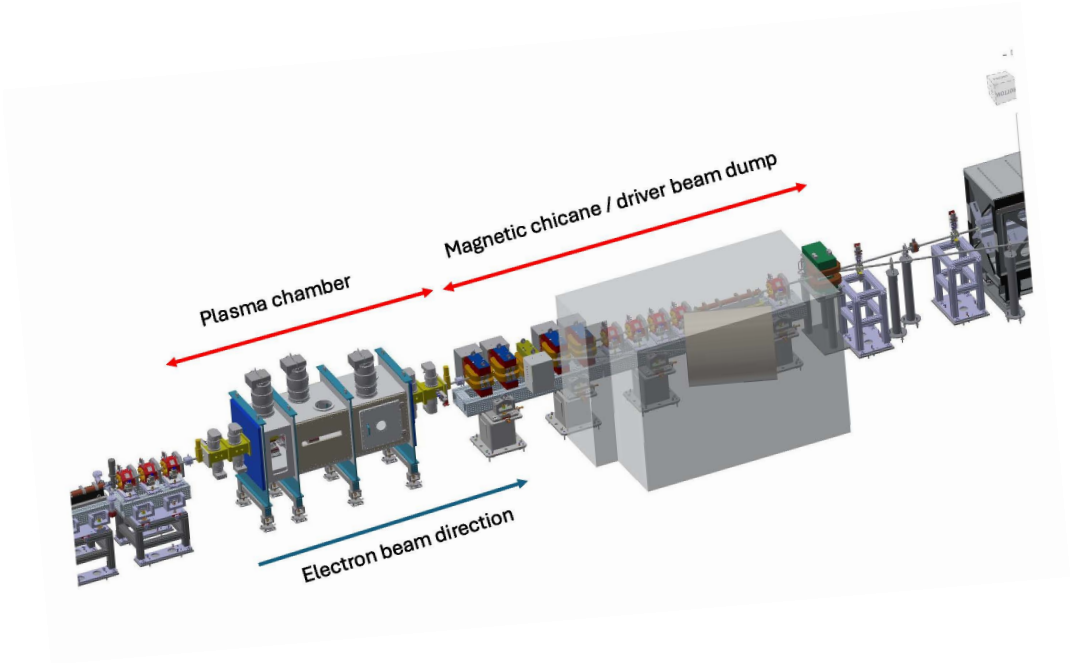

Figure 4.8: Layout of the area dedicated to plasma acceleration

The plasma vacuum chamber consists of three interconnected sections. The two lateral chambers are dedicated to high-capacity vacuum pumping in order to prevent gas backflow toward the linac.

These side chambers are separated from the central chamber by narrow tubes with a small internal diameter, which increase the vacuum impedance and thus limit gas propagation. The central chamber, which has a larger volume, houses the permanent magnet quadrupoles that focus the electron beam at the entrance of the capillary, where the gas is pre-ionized.

In the comb-beam scheme, the first bunch—called the driver—propagates through the plasma and excites a plasma wave, within which the second bunch, the witness, is subsequently accelerated. The acceleration gradient achieved in this configuration is extremely high: within just 60 cm, the energy of the witness bunch, initially around 500 MeV, is doubled, reaching the nominal beam energy of 1 GeV.

A series of permanent magnet quadrupoles, positioned within the same vacuum chamber downstream of the capillary, transport the beam toward another magnetic chicane located outside the plasma chamber. This chicane separates the driver particles—having transferred most of their energy to the plasma—from the witness particles, which have been accelerated to nearly twice the driver energy. Due to their different momenta, the two beams follow distinct trajectories through the first dipole magnet: they diverge in the drift section and, after the second dipole, are separated by more than 15 mm. A septum magnet, positioned between the second and third dipoles, diverts the driver beam toward a dedicated beam dump through a separate vacuum line, without perturbing the trajectory of the witness bunch.

A set of quadrupole magnets ensures proper beam matching for injection into the undulators. Before entering the undulator section, the beam phase space is carefully characterized using a complete suite of diagnostics, including transverse RF deflectors in both X and Y planes, Polarix, a spectrometer, view screens, and beam position monitors.

4.4 Free Electron Laser radiation

4.4.1 The FEL undulators

The undulator magnets responsible for generating the FEL radiation are installed just beyond the wall separating them from the linac tunnel (Fig. 4.9). A detailed discussion of the undulator region, where the FEL radiation is produced, is provided in Chapter 8.

The undulator line, named AQUA, delivers FEL radiation in the XUV–soft X-ray range, using an electron beam energy of 1 GeV. To reach saturation—corresponding to the maximum photon yield achievable with the beam parameters provided by plasma acceleration—a total undulator magnetic length of 20 m is required.

The system consists of ten undulator modules, each 2 m long, separated by 60 cm sections housing the diagnostics, as well as the electron beam focusing and trajectory correction systems. The undulators are of the APPLE-X type, enabling variable polarization of the emitted radiation.

Each undulator module consists of a series of permanent magnets arranged to produce an alternating magnetic field with a period of 18 mm. The magnet arrays are mounted on supports capable of transverse motion relative to the electron beam direction, following an X-shaped trajectory. Additional longitudinal motion is implemented to allow control over the polarization state of the emitted radiation.

Precise temperature stabilization around the undulator is essential to prevent variations in the magnetic field strength and, consequently, in the emitted wavelength. To avoid conditioning the entire tunnel volume, each undulator is enclosed within a compact structure of minimal necessary volume, where the air temperature is controlled with a stability of 0.1 °C.

At the exit of the undulator line, a magnetic element is installed to separate the trajectories of the electrons and the X-ray photons. The photons continue in a straight path toward the experimental hall, while the electrons are deflected toward the beam dump. The beam dump is located in a dedicated pit below the floor, designed to ensure that no radiation—whether photons, electrons, or

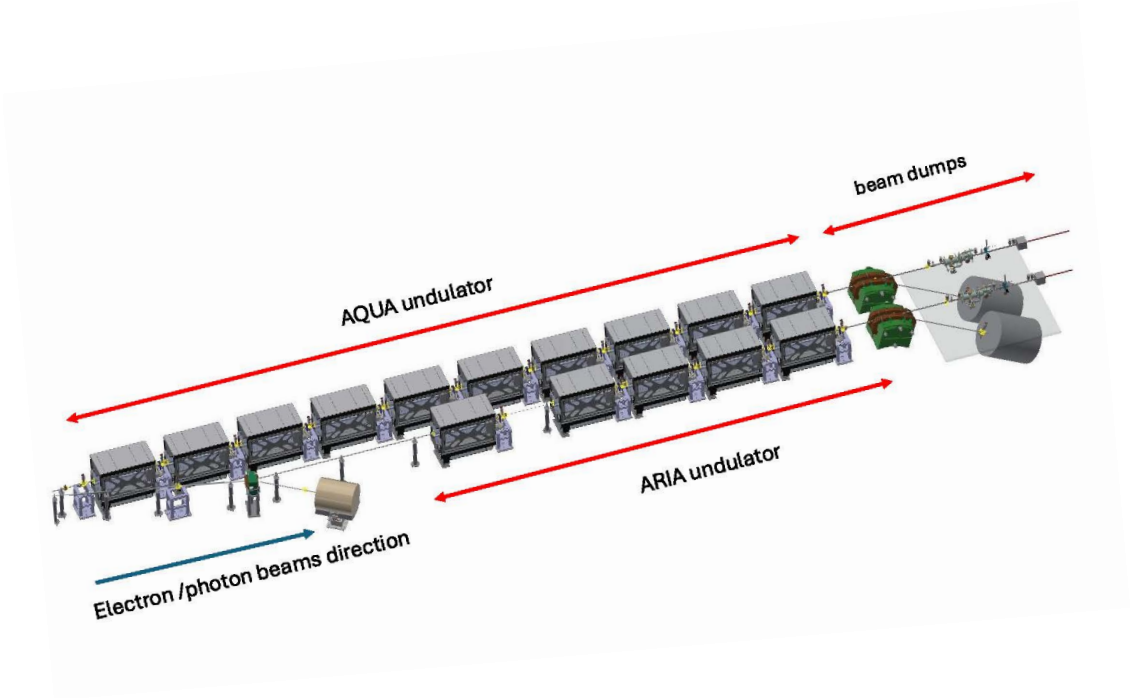

Figure 4.9: Layout of the Free Electron Laser undulators area

neutrons—can reach the experimental area.

4.4.2 FEL radiation beam transport lines

The photon beamlines are installed downstream of the FEL undulator line (Fig. 4.10).

Some components of the photon transport line are located upstream of the shielding wall, within the undulator tunnel. Following the photon propagation direction, the various elements are arranged as described below. A detailed description can be found in the photon beamlines chapter of this TDR (Chapter 9).

The first element encountered is a beam stopper, which allows the photon transport toward the experimental hall to be safely interrupted. Downstream of the beam stopper, and after the vacuum valve that isolates the photon line—with pumping sections on both sides—a Gas Monitor Detector is installed. This device, equipped with a split electrode, performs non-destructive measurements of the photon beam intensity and position on both the horizontal and vertical planes. The transverse beam profile is then measured using a YAG scintillating screen that intercepts the beam.

A gas absorber, consisting of a long tube with a gas injection station and differential pumping system, is embedded within the shielding structure. This configuration takes advantage of the concrete wall thickness, optimizing space usage in the experimental area.

A second Gas Monitor Detector is positioned downstream of the absorber to measure the photon beam intensity after attenuation and to verify beam alignment before the beam-defining aperture. This aperture acts as a collimator for the spontaneous undulator emission, which exhibits a larger divergence compared to the coherent FEL radiation.

Following the second YAG screen, a small-angle reflecting mirror deflects the X-ray beam into its transport line. Unwanted high-energy gamma photons—possibly generated by interactions between the electron beam and residual gas in the linac and undulator vacuum chambers—pass through the mirror and are absorbed by a dedicated dump located in a lead-shielded area.

A solid attenuator equipped with filter wheels is installed at the entrance of the monochromator area. Downstream of this section, a plate beam position monitor based on the interception of the

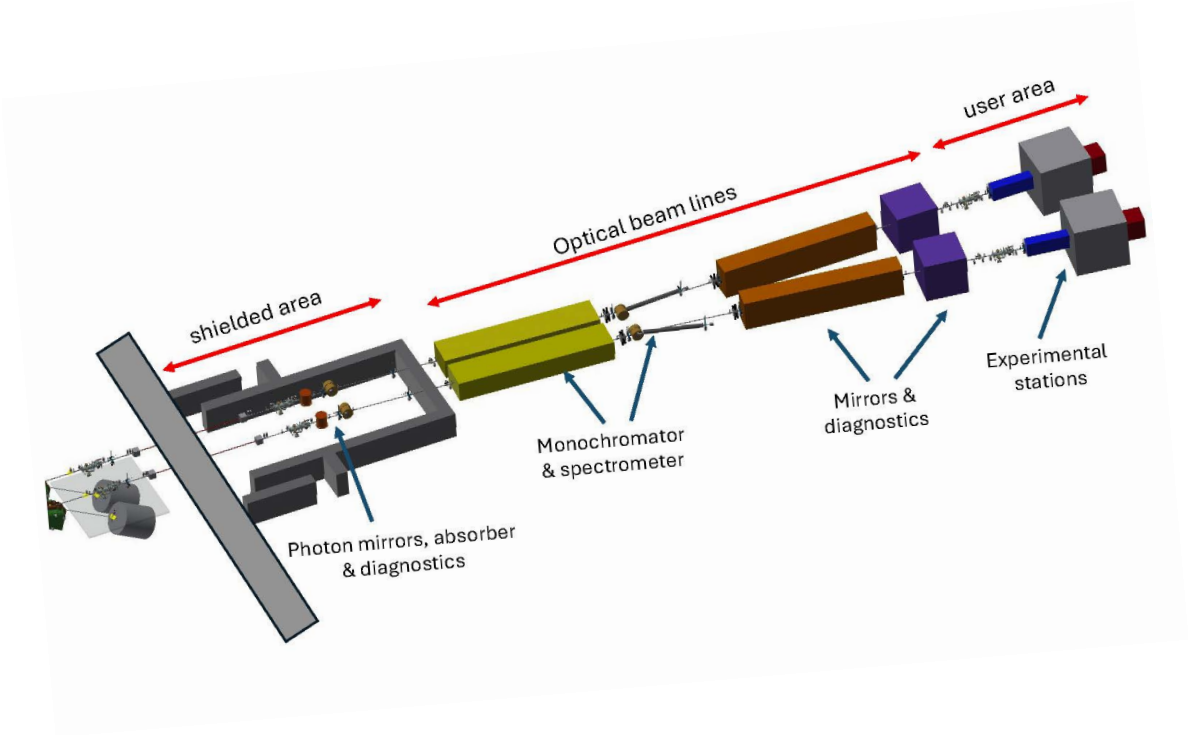

Figure 4.10: Schematic layout of the FEL beamlines and experimental stations

photon beam tails by four metallic blades—collecting a drain current—is positioned to measure the beam position from the transverse intensity distribution.

To characterize the radiation spectrum, a high-resolution grating spectrometer is installed downstream of a YAG scintillating screen. The spectrometer consists of a variable line-spacing grating surface with high reflectivity in the zero-order reflection, while the higher diffraction orders are focused onto a scintillating target to record the spectral distribution.

A second pair of YAG screen and beam position monitors is located upstream of the optional Split-and-Delay Line system, which enables division of the photon beam into two parts and introduces a controllable delay between them, allowing refined pump–probe experiments.

For pulse length characterization, a gas ionization chamber with radial time-of-flight measurements will be installed, operated in conjunction with a THz streaking pulse to determine the temporal duration and arrival time of the FEL pulses at the end station.

Another gas monitor detector and YAG screen station are positioned before the pair of focusing mirrors in Kirkpatrick–Baez configuration. These mirrors are essential for reducing the final photon spot size to the micrometer range (a few μm rms) at the experimental station. Multi-channel plates are employed for coherent X-ray imaging applications.

The transverse coherence of the FEL beam is evaluated through the visibility of the interference fringes produced by a double-slit setup. The wavefront is characterized using a Hartmann sensor, while the longitudinal coherence length is measured with an interferometer operating in either Michelson or Fizeau configuration and via the spectral statistical information in the spectrometer measure.

4.4.3 End station and users area

The User Experimental Station is located at the end of the photon beamlines and is equipped with instrumentation capable of supporting a wide range of experimental configurations. Chapter 10 provides a detailed discussion of the experimental stations and their capabilities.

The experimental vacuum chamber is designed to accommodate solid samples mounted on motorized stages and can be connected to a sample delivery system capable of handling liquid and gaseous targets as well. Several detectors are integrated into the chamber; among them, a time-of-flight spectrometer is connected directly to the chamber to analyze the molecular fragments and ions generated by the sample–beam interaction.

On the left side of the FEL User Area, a set of laboratories is available for experimental setup, last-minute sample preparation, and characterization activities. A high-power, synchronized optical laser system is provided to enable laser-pump/FEL-probe experiments. Dedicated servers and control computers are also available for beamline operation, data acquisition, storage, and real-time processing.

4.5 Conclusions

This chapter describes the entire research infrastructure being developed within the INFN Frascati Laboratories, including the new building that is being constructed to host it. The electron accelerator, the undulators that generate the radiation, the optical beamlines and the experimental stations—together with the spaces that house them—are briefly outlined here, with references to the chapters of this TDR where they are discussed in detail. The preparation of the layout for the scientific equipment and their auxiliary systems has enabled a space design optimized for the available areas, resulting in a functional and harmonious project. Particular attention has been paid to ensuring comfort for the personnel operating and using the infrastructure, as well as to potential future developments and upgrades.

5. RF Photo-Injector

This chapter outlines the layout and overall design of the RF injector system (see Fig. 5.1) that will achieve the performance and parameters listed in the Beam Physics chapter (Ch. 3). Ancillary components, such as laser, magnets, RF structures and diagnostics, are also introduced, while a more detailed description is done in the corresponding chapters.

5.1 Introduction

The S-band injection complex generates high brightness electron beams that determine the performances of both plasma and full RF acceleration, setting the quality of the GeV witness beam to drive FEL radiation for user applications.

The injector is optimized for providing a two-bunches beam, i.e. witness (W) and driver (D), generated in the same RF bucket. Therefore the overall sub-systems layout and parameters are chosen to provide the best performances under the injector operation in the laser comb technique [1] to generate directly at the cathode two bunches separated at the picosecond scale [2]. For its successful implementation, we rely on the long standing experience matured at SPARC_LAB on the generation, manipulation and characterization of such high brightness electron beams [3].

For this reason, based on the past experimental and operational experience, from the beam dynamics point of view, the injector follows in its design the SPARC_LAB photo-injector [4], except for

- a recent update of the RF gun [5];
- the length and number of the S-band accelerating structures;
- the choice of the S-band European frequency;
- the renovation of the power and water plants;
- the insertion of an X-band linearizing cavity.

The injector layout is shown in Fig. 5.1.

The electron bunch is emitted by a Cu cathode illuminated by a UV laser pulse in a high accelerating field (120 MV/m peak gradient on the cathode) and accelerated up to 5.6 MeV in the standing wave (SW) normal conducting RF gun cavity, operating at the European S-band (2.998 GHz). The gun cavity [5] is composed of 1.6 cells requiring 15 MW from a dedicated klystron to

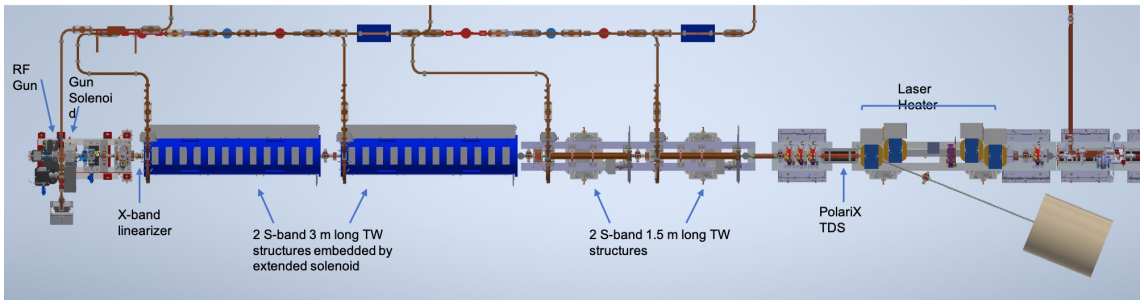

(a) Top view.

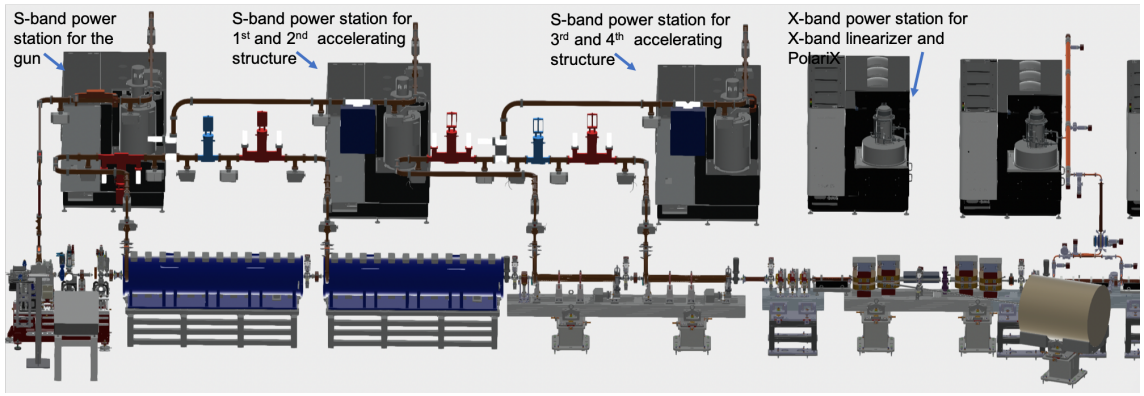

(b) Side view.

Figure 5.1: Injector layout.

achieve the nominal gradient. A solenoid, centered at 0.204 m downstream of the cathode, focuses the beam into the first accelerating module, which is located at 1.534 m from the cathode to satisfy the nominal working point for high brightness photo-injectors [6]. The solenoid for emittance compensation is composed by two coils fed by two power supplies. It implements a remote control of the transverse position (by means of step motor) with a resolution <10 µm. A corrector composed by a variable quadrupole and skew quadrupole is mounted on the vacuum chamber at the center of the solenoid. It is used to compensate the residual quadrupole component induced by the input coupler and non idealities of the solenoid and of the laser pulse shape. It is based on the design made at PSI [7]. No bucking coil is foreseen due to the fact that the estimated solenoid field on the cathode is negligible.

A complete diagnostic section for the very low energy beam (i.e. 5.6 MeV kinetic energy) consists of a Faraday cup, a scintillator screen and a toroid. Steering magnets for trajectory optimization and gun energy measurement, together with beam position monitors, are also foreseen. An X-band linearizing cavity is installed before the first accelerating structure to enhance the stability of the temporal separation between driver and witness bunches for the two-bunch workng point needed for PWFA mode. Jitter studies conducted on the 200 pC driver and 30 pC witness beams, with and without the X-band cavity, demonstrate that the cavity significantly improves the temporal separation between the two bunches at the injector exit. Specifically, activating the X-band linearizer increases the bunch separation in accordance with plasma acceleration requirements. Even in the worst-case scenario, the resulting temporal jitter is reduced to 3.9 fs—lower than in the case without the linearizer. Detailed results are presented in Section 5.5.

The following S-band traveling wave (TW) accelerating modules increase the energy to 80 MeV and up to 250 MeV, depending on the settings of the first two accelerating structures, which can operate in the velocity bunching regime [8] to properly manipulate the driver-witness

beam longitudinal phase space accordingly to the PWFA transverse and longitudinal matching conditions [9, 10]. The S-band section is then composed of two, 3 m long TW structures, both powered by a 45 MW klystron, followed by two 1.5 m long TW structures, powered by a second 45 MW klystron. The S-band accelerating section is followed by the laser heater section, the magnetic lattice for transport and normalized transverse emittance measurement by means of the quadrupole scan, a Polarizable X-band Transverse Deflection Structure (PolariX TDS [11]) for slice emittance and bunch length measurement and, when operated together with a magnetic spectrometer, for longitudinal phase space characterization. More details of the injector components can be found in the corresponding chapters, i.e. RF (Ch. 13), Magnets (Ch. 17) and Diagnostics (Ch. 11).

The main parameters of the injector for the two bunches, driver and witness, working point, as required for the PWFA configuration, are summarized in Tables 3.2 and 3.3 of the beam physics chapter.

A second working point is foreseen to operate with a single 200 pC electron bunch in the all X-band case. The main parameters of the injector are listed in the beam physics chapter, Tables 3.16 and 3.17.

5.1.1 Injector requirements

To inject the driver and witness bunches, with proper temporal separation and current distribution into the plasma module, both transverse and longitudinal phase spaces must be manipulated at the photo-injector. In this regard, the requirements on beam parameters for PWFA must be satisfied at the exit of the photo-injector area and then preserved, during acceleration up to 500 MeV, in the linac. Table 5.1 shows the beam parameters as required for stable and efficient injection in the linac of the driver and witness bunches. In the beam physics chapter, detailed sensitivity studies are presented and results summarized in Tables 3.9 and 3.10.

Table 5.1: Electron beam requirements at exit of the injector for the two bunches, driver and witness, baseline working point.

Parameter	Symbol	Unit	Value
# of bunches			2
Driver Charge	Q_D	pC	200
Witness Charge	Q_W	pC	30
Beam energy	$E_{D/W}$	MeV	119/118
Driver normalized emittance	ε_{n_D}	mm mrad	1.5
Witness normalized emittance	ε_{n_W}	mm mrad	0.7
Driver energy spread	σ_{E_D}	%	0.7
Witness energy spread	σ_{E_W}	%	0.1
Driver bunch duration	σ_{t_D}	fs	193
Witness bunch duration	σ_{t_W}	fs	17

5.2 Electron source and injection system

The electron source is a metallic photocathode (polycrystalline copper) illuminated by an intense, $\sim$266 nm wavelength UV laser, whose longitudinal shape is chosen to set the proper working point, either in the multi-bunch operation, namely laser comb technique [1], or in the single high charge mode, and transverse pulse shape to fulfill the required beam quality. The maximum charge

foreseen in operation is 450 pC (400 pC driver and 50 pC witness bunches); therefore, given the best measured values of the quantum efficiency of copper, in the range 10^{-5}-10^{-4} at 266 nm, the laser must deliver on the cathode at least 200 μJ energy. The photocathode also serves as the conducting back plane of the 1.6 cell RF gun. The gun and the ancillary components are designed for a pulse repetition rate of 100 Hz. An eventual upgraded version, reaching up to 400 Hz repetition rate, is under study.

5.2.1 Electron source and RF gun

The photocathode laser is a fundamental element in all user-oriented photo-injector driven FEL facilities. The pulse and beam quality of this system is crucial to the overall FEL performance, as it is directly imprinted on the emittance of the generated electron bunch. Indeed both temporal and spatial shaping of the drive laser radiation will strongly influence the achievable beam brightness, finally the transversal homogeneity of the electron beam which depends on the convolution of cathode quantum efficiency and laser flatness. In this regard, the metal cathode surface roughness must be much better than $\lambda/10$ (with λ = 266 nm, the UV wavelength), requiring nm scale copper machining. For RF guns based on metal (e.g. copper) photocathode, the required laser pulse energy in the UV is on the order of hundreds of μJ to generate several hundreds of pC, thus implying at least one multipass amplifier, followed by two harmonic generation stages.

The photocathode laser system is a SPARC-like one, updated with respect to the present state-of-the-art to account for a better transverse uniformity and a more demanding energy stability as required for stable and efficient operation of a plasma-based accelerator. The photocathode laser is based on the laser developed for the SPARC_LAB test facility [3] and its upgrade in the framework of the SABINA project [12]. In the present configuration, the laser is based on the Ti:Sa technology, which is mature and commercially available, delivering pulses of high energy and down to 35 fs range duration, as required by the relatively large bandwidth needed for pulse shaping. The 1 ns long infrared (IR) beam from the amplifiers is compressed and converted in UV beam. It is then split in n lines, as required for the laser comb technique. The manipulation of the laser pulses, in terms of length, intensity and separation, is described in the laser system chapter (Chapter 12).

The laser is injected into the accelerator vacuum chamber through one window, which allows for a normal incidence on the cathode. A second window allows for the observation of the reflection from the cathode surface for diagnostic purposes. The second viewport also serves for cathode inspection. Figure 5.2 shows the laser injection area. The chosen architecture of the photo-cathode laser system is all set already for a future upgrade to 400 Hz repetition rate.

Beam dynamics simulations have set the final requirements on the laser pulse parameters and their stability, in particular in terms of the minimum pulse length, transverse uniformity and energy stability. Table 5.2 shows the main laser parameters, details on how they can be achieved and verified can be found in Chapter 12, together with a detailed description of the photo-cathode laser system and ancillary components.

The gun design is based on a 1.6 cell European (EU) S-band RF gun fabricated with the new brazing-free technology, developed at the INFN-LNF [13]. This approach has been proven to substantially simplify the manufacturing procedure, preserving the hard-copper characteristics that are instead compromised by the material softening at the brazing temperatures. The LNF team has fabricated, tested and put in operation 5 of such devices of various frequencies in last few years, including the one with EU S-Band frequency in operation at the CLEAR facility [14] (CERN). The EuPRAXIA@SPARC_LAB RF gun will be a copy of this already realized device.

The e.m. design has been accomplished using ANSYS-HFSS [15] and the e.m. model is given in Fig. 5.3. The overall design follows the same criteria already implemented in the gun fabricated at INFN for SPARC_LAB [16, 17]. Three additional holes have been made in the coupling cell to have a full compensation of both, the dipole and quadrupole field components, introduced by

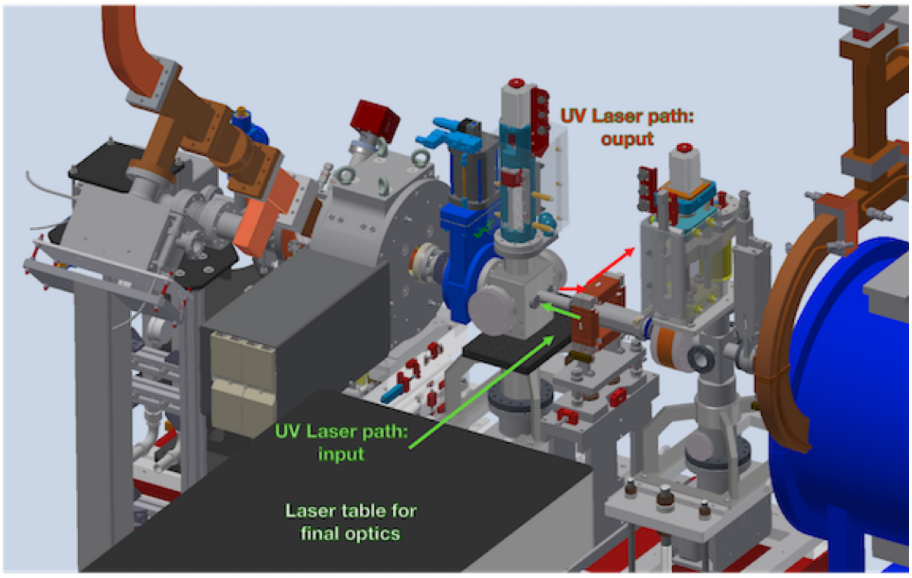

Figure 5.2: Prospective view of the laser injection scheme.

Table 5.2: Summary of the required photocathode laser parameters.

Parameter	Symbol	Unit	Value
Rep. Rate	f_{rep}	Hz	100
Min pulse duration (IR FWHM)		fs	35
Pulse shape			Flat top
Spatial profile			Flat top
IR central wavelength	λ	nm	780 ± 20
UV wavelength (3rd harm.)	λ_{UV}	nm	263 ± 3
Max UV pulse energy (on the cath.)		mJ	1.75
Timing stability (wrt RF)		fs rms	20
Energy stability in UV		%	<1

the coupling hole itself. These holes can be connected to vacuum pumps allowing for a vacuum pressure that, in operation, is of few 10^{-10} mbar. The gun has been designed with a coupling coefficient equal to 2 to allow for short RF filling time (<1μs), thus reducing the breakdown rate probability [18] and the power dissipation. An elliptical profile of the iris with large aperture (ϕ = 36 mm) has been also implemented to reduce the peak electric field, to increase the 0–π mode frequency separation (thus avoiding excitation of the 0 mode with short RF pulses) and to obtain a better pumping speed on the cathode cell. Figure 5.4 shows the 2D geometry of the gun with the electric field of the working mode (π-mode) and of the 0-mode. A picture of the RF gun in operation at SPARC_LAB is shown in Fig. 5.5. The final RF gun parameters are listed in Table 5.3. Realization details, low power RF tests, conditioning procedure and characterization results are shown in [5].

The cathode system is based on the present SPARC_LAB RF gun, composed by a custom flange connected to the gun body and a CF100 flange for vacuum pumping.

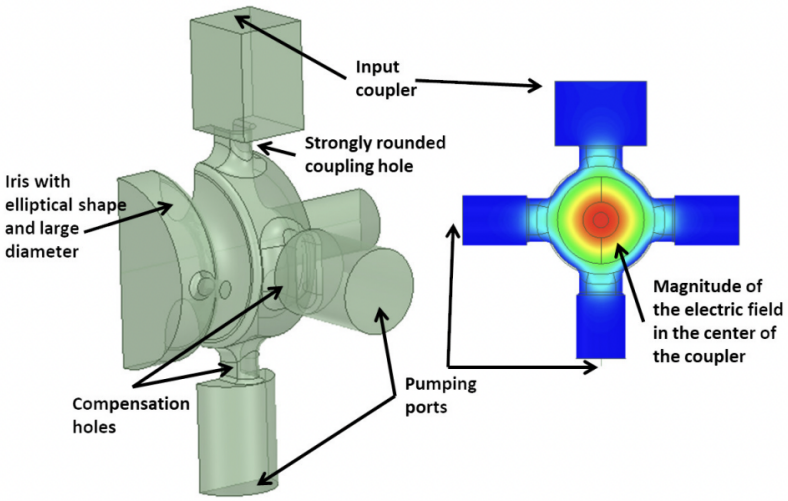

Figure 5.3: Electromagnetic model of the RF gun.

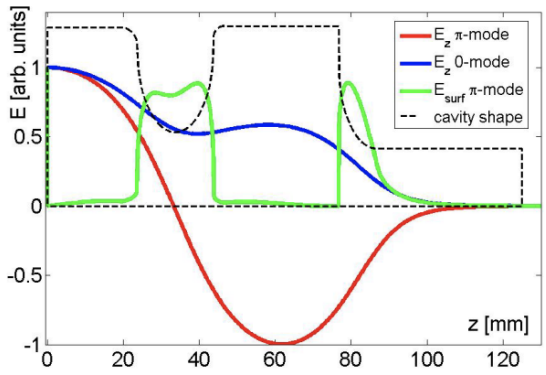

Figure 5.4: 2D geometry of the gun with an electric field of the working mode (π-mode) and of the 0-mode.

5.2.1.1 Compensation solenoid

The solenoid, placed right after the RF gun, at 0.2 m from the cathode, is composed of two coils fed by two power supplies [20]. It implements a remote control of the transverse position (by means of step motor) with a resolution < 10 µm, with a residual misalignment less than 150 µm which, according to our simulations, is proved to be enough for a well aligned downstream trajectory. The solenoid magnet is water cooled with a maximum magnetic field of 0.38 T, and a residual field on the cathode surface, less than 6 10^{-4} T. Aside from the motorized solenoid, the RF gun solenoid design includes an additional quadrupole, which is intended for emittance compensation and manipulation in case of asymmetry of the emittance source. Indeed, a steering magnet composed of a skew quadrupole is mounted on the vacuum chamber at the center of the solenoid. It is used to compensate for the residual quadrupole component induced by the input coupler and for asymmetries in the laser spot size. The skew quadrupole, air cooled, is based on the design made at PSI [7], with a maximum field of 2 mT/m and a magnetic length of 10 cm.

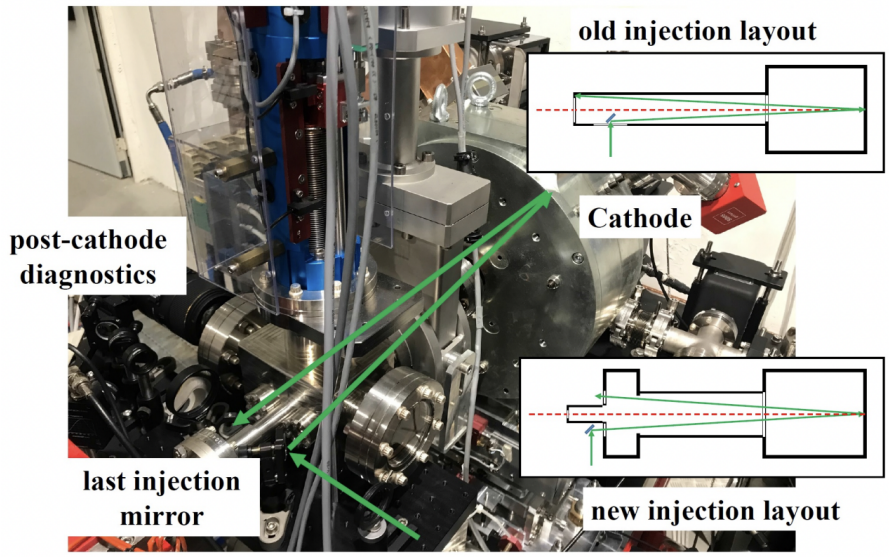

Figure 5.5: S-band RF gun installed at SPARC_LAB with highlighted the new laser injection system. On the insets are the layouts of the new and old systems [19].

Table 5.3: Nominal parameters for the RF gun.

Parameter	Symbol	Unit	Value
Resonant frequency	f_{RF}	GHz	2.99855
$E_{cath}/\sqrt{P_{diss}}$	...	$\mathrm{MV}/(\mathrm{m}\cdot\mathrm{MW}^{0.5})$	37.5
RF input power	P_{input}	MW	15
Cathode peak field	E_{cath}	MV/m	120
Repetition rate	f_{rep}	Hz	100
Quality factor	Q		14300
Filling time	τ_F	ns	515
Coupling coefficient	β		2
RF pulse length		µs	1
E field ratio	E_{surf}/E_{cath}		0.88
Pulsed heating		°C	<30
Working temperature		°C	25
$0-\pi$ mode frequency separation		MHz	44

5.2.2 X-band linearising cavity

An X-band SW RF cavity is foreseen in the gun area between the RF gun and the first S-band TW accelerating structure to manipulate the longitudinal phase space and increase the control on witness-driver peak current and bunch separation when operating in the two-bunches mode. Table 5.4 shows the main parameters of the X-band linearising cavity, located 1.40 m from the cathode surface. The RF rendering of the optimized SW RF cavity is shown in Fig. 5.6. The use of elliptical irises and rounded cell fillets allow for lower surface electric fields and higher quality factor, respectively. The envelope of the on-axis electric field profile is shown in the bottom figure. The accelerating field is 20 MV/m and the electric peak value is 38 MV/m, as required. The

Table 5.4: Main parameters of the X-band linearising cavity.

Parameter	Symbol	Unit	Value
Resonant frequency	f_{RF}	GHz	11.9942
Quality factor	Q		9900
Accel. field	E_{acc}	MV/m	20
Peak field	E_{peak}	MV/m	38
Number of cells			7
Cavity cell radius	r	mm	4
Cavity length		cm	10
Filling time	τ_F	ns	117
Coupling coefficient	β		1.23
Input RF power	P_{in}	kW	400

required input RF power is 400 kW. The coupler design features dual-feed and racetrack geometry

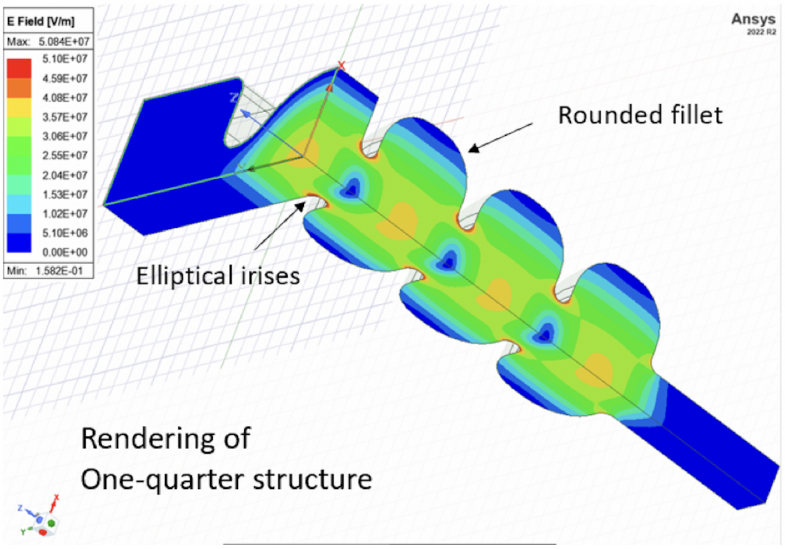

Figure 5.6: Rendering of one quarter structure of the RF cavity from Ansys.

in order to cancel the dipole and quadrupole field components. Moreover, the coupler hole has a fat-lip geometry to minimize the surface magnetic field, thus mitigating the RF pulsed heating effect. The reflection coefficient at the port of the input waveguide is given in Fig. 5.7. The minimum is equal to -20 dB at the operation frequency. The mode separation is 62 MHz. A custom designed power splitter (Fig. 5.8) was integrated to couple the RF power into the X-band cavity from the distribution system. Figure 5.9 shows the reflection and transmission coefficients of the optimized RF power splitter. Figure 5.10 shows the full structure after optimization, i.e. RF power splitter and X-band cavity. The reflection coefficient at the port of the input waveguide of the full structure is less than -20 dB at the operation frequency. In Fig. 5.11, the on-axis electric field profile is plotted with a peak value of 38 MV/m for an input RF power of 400 kW.

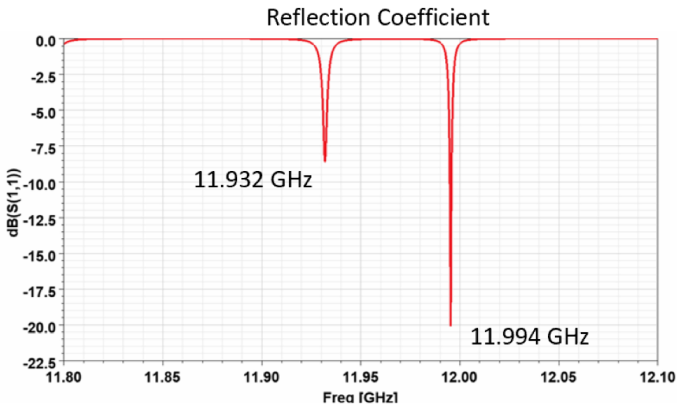

Figure 5.7: Reflection coefficient at the port of the input waveguide. The minimum is equal to -20 dB at the operation frequency. The mode separation is 62 MHz.

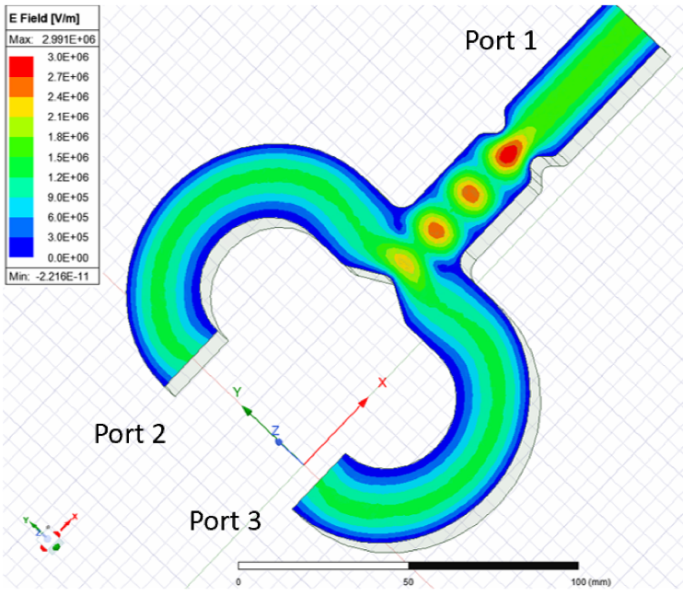

Figure 5.8: RF power splitter.

5.2.3 Gun-to-first boosting section

The gun-to-first boosting section covers the beamline from the gun exit to the entrance of the first booster accelerator. A zoomed view of the layout is shown in Fig. 5.12.

The beamline contains the instrumentation for the low energy beam diagnostics and trajectory correction, and the vacuum instrumentation.

A couple of dipole magnets (HOR/VER) allow correcting beam offset and angle for injection into the X-band linearizing cavity. A stripline beam position monitor (BPM) is placed in the first HOR/VER steering magnet to evaluate the offset from the main trajectory. Two vacuum crosses support movable actuators for beam profile image screens and a charge-measuring Faraday cup. The first vacuum cross foresees also two CF16 windows for on-axis injection and extraction of the photocathode drive laser pulse, the extraction line being used also as photocathode and laser diagnostic. The vacuum pumping system is also located under vacuum crosses. Two valves, a fast a one before the X-band linearizer, and a conventional one right after the gun solenoid, allows for vacuum protection. An Integrating Current Transformer (ICT) is placed at 1.3 m from the cathode

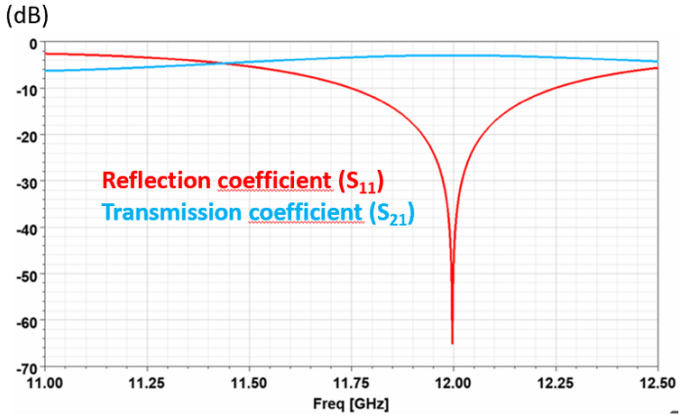

Figure 5.9: Reflection coefficient (in red) and transmission coefficient (in blue) of the RF power splitter.

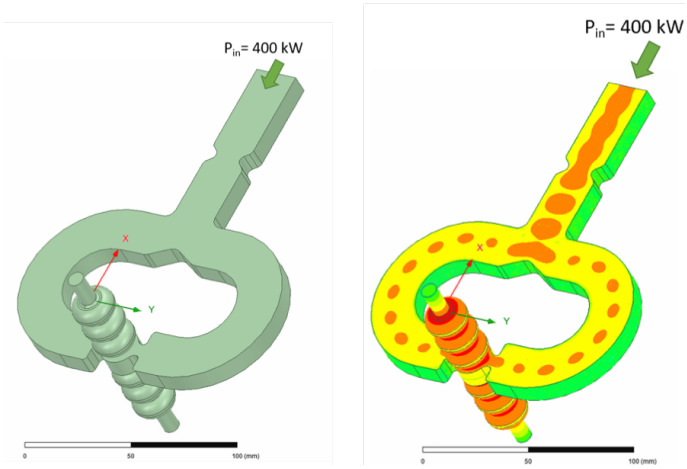

Figure 5.10: Full structure: RF power splitter and X-band cavity. Rendering, left; surface electric field distribution, right.

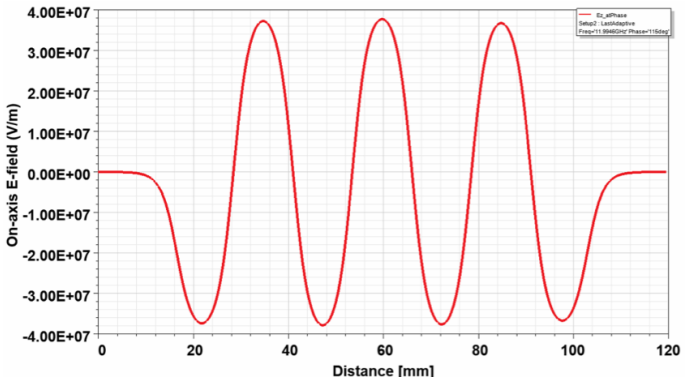

Figure 5.11: On-axis electric field profile.

for non-destructive bunch charge measurements. Details on the devices can be found in the specific chapters.

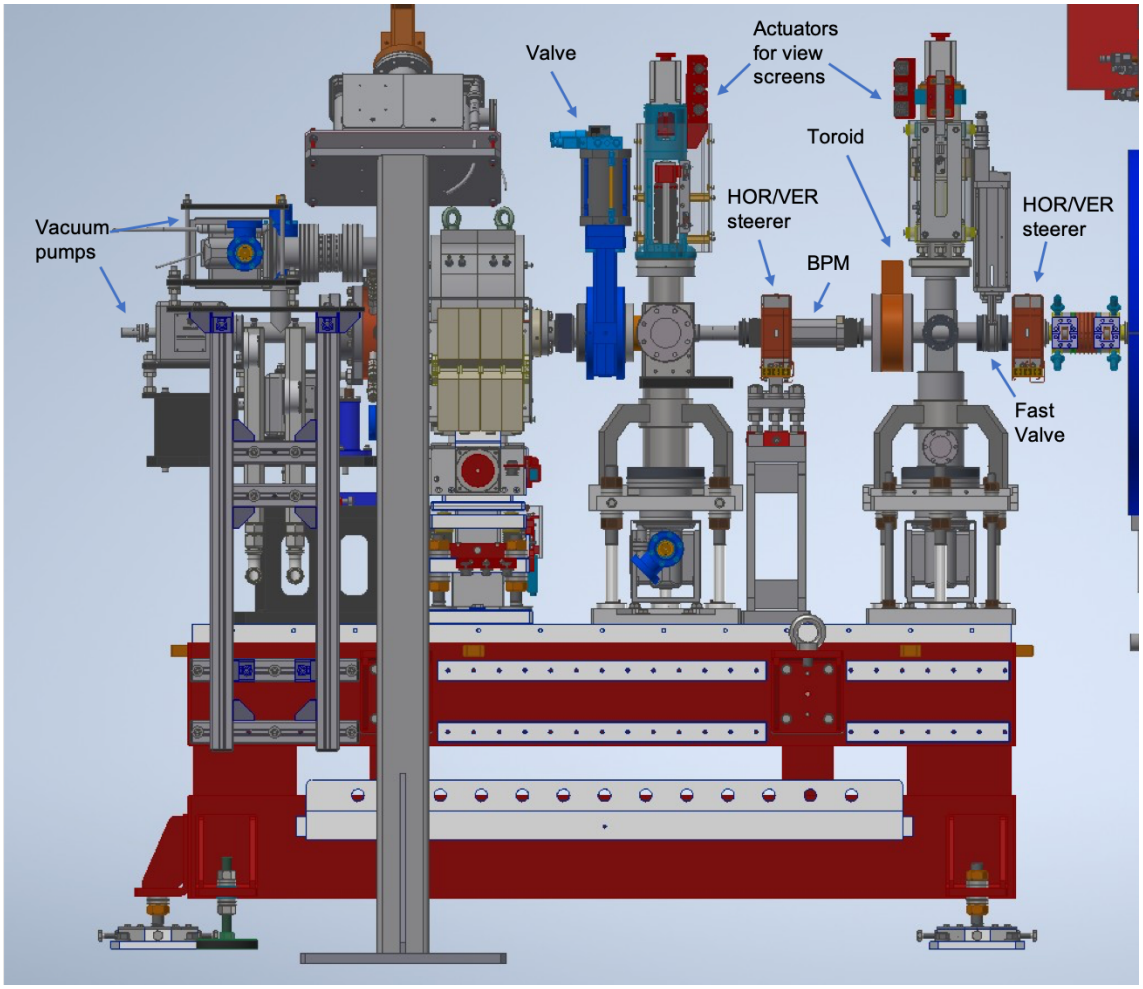

Figure 5.12: Gun to first boosting section layout.

5.2.4 Booster accelerating modules

Two 3-meter-long booster TW accelerating structures are followed by two additional TW structures, each 1.5 meters long, as shown in Fig. 5.13. Each 3-meter section consists of 88 identical on-axis, iris-coupled cells resonating at 2.998 GHz, while the 1.5-meter sections comprise 44 cells each. The end cells in each structure serve to couple the RF power in and out of the system. Each 3-meter structure requires 3.3 meters of beamline, which also accommodates an in-vacuum image profile diagnostic, a stripline BPM, and horizontal and vertical steering magnets. The 36 cm gap between the two 1.5-meter TW structures includes a vacuum cross equipped for beam imaging and vacuum pumping, followed by another BPM and steerers.

All TW structures operate in the $2\pi/3$ mode. The maximum peak accelerating fields are 25 MV/m for the 3-meter sections and 35 MV/m for the 1.5-meter ones. The longer booster sections are equipped with solenoids to provide transverse focusing and support emittance compensation during velocity bunching. These solenoids also assist in matching the optical lattice functions to subsequent linac sections (see Fig. 5.14 for a detailed view). The injector RF system includes three RF power stations operating at the European S-band frequency of 2.998 GHz: one station delivers up to 16 MW to the RF gun, while the other two supply 45 MW to the four TW structures, powered in pairs via a pulse compressor (as shown in Fig. 5.13). Each RF station comprises a klystron, high-voltage (HV) modulator, pulse transformer, HV cables, a waveguide distribution network, and a Low-Level RF system that controls the RF pulse shape, amplitude, and phase. These parameters

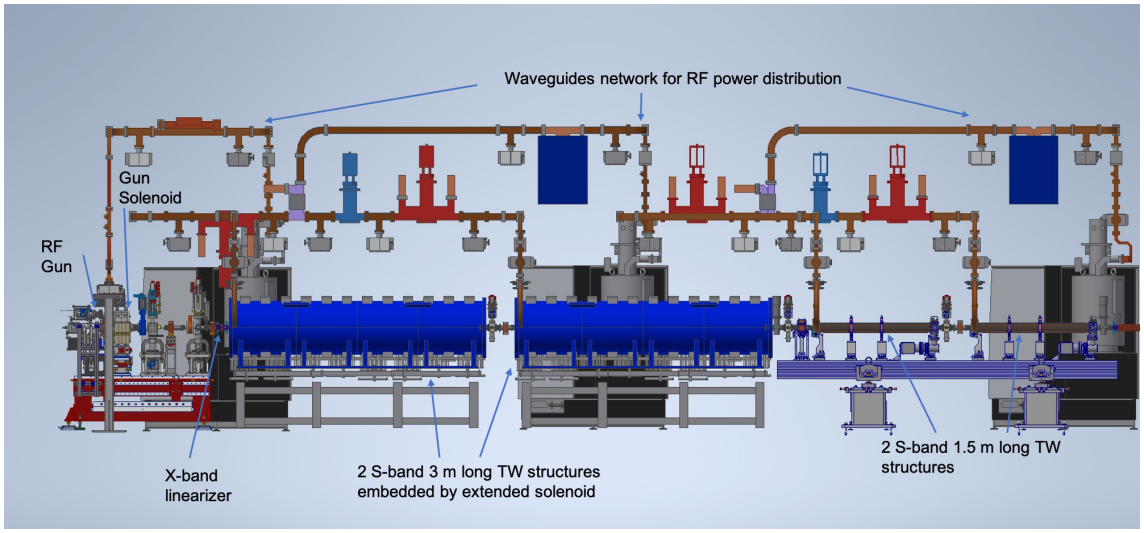

Figure 5.13: S-band boosting section layout.

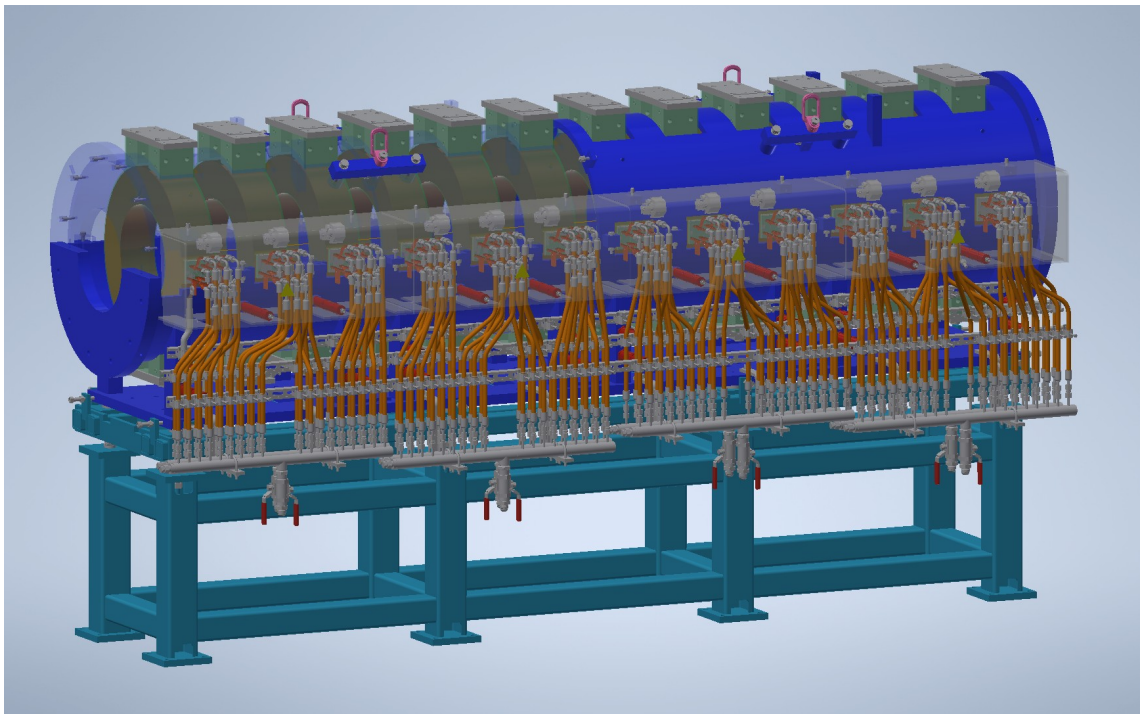

Figure 5.14: CAD view of the long solenoid foreseen to surround the first two S-band accelerating structures: coils and the iron yoke (blue shielding) are highlighted. The exploded layout highlights the arrangement of the coils.

are tightly regulated to meet the stability requirements outlined in the jitter studies (Section 5.5).

Further information about the high-power RF system and technical requirements is detailed in the RF Chapter 13.

The layout of the S-band RF power distribution is shown in Fig. 5.15, while Fig. 5.16 illustrates the X-band configuration. The latter includes a SW X-band linearizing cavity located at the entrance of the first S-band TW structure, and the PolariX transverse deflecting structure. Additional details are provided in the chapter dedicated to the RF system.

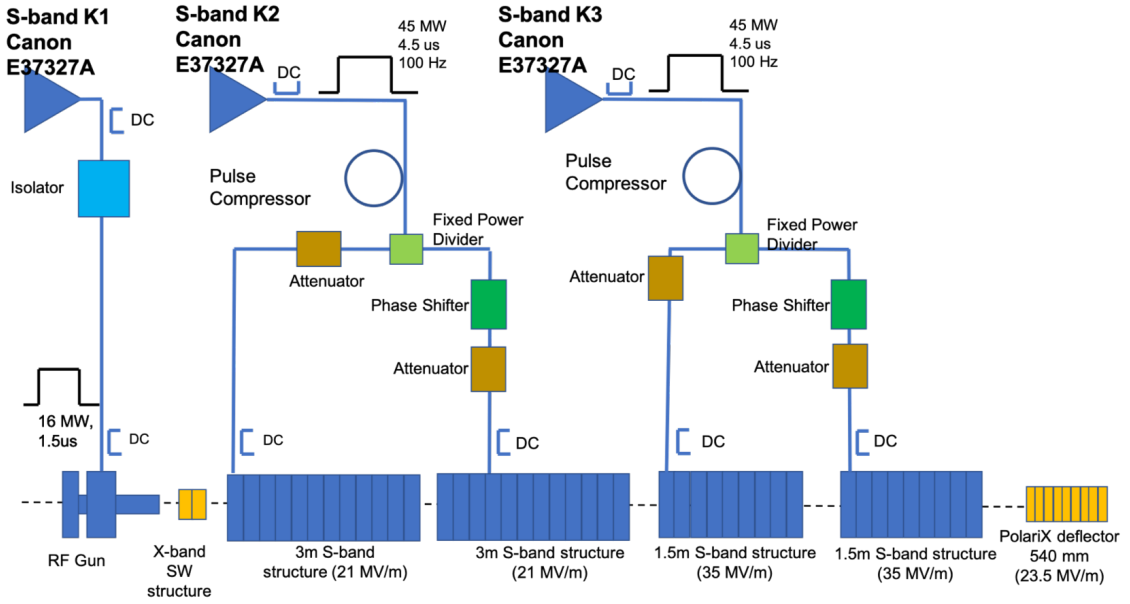

Figure 5.15: Layout for the S-band power distribution system taking into account the four S-band accelerating structures.

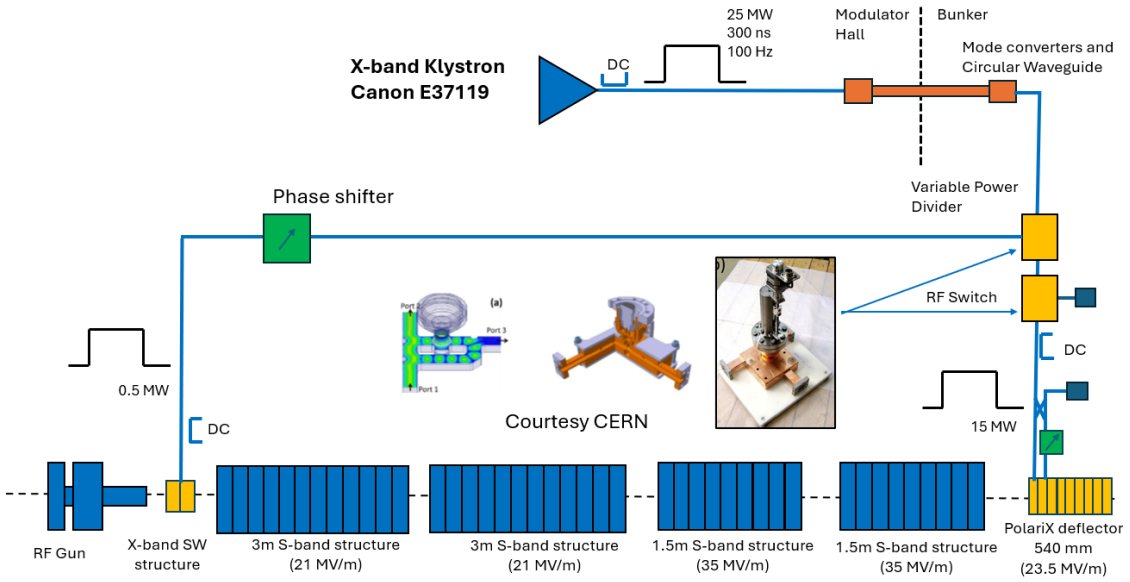

Figure 5.16: Layout for the X-band power distribution taking into account the X-band linearizer and the PolariX Transverse Deflecting Structure [11].

5.3 Laser heater section

The laser heater (LH) consists of an undulator, placed in the magnetic chicane at the exit of the S-band booster linac. A laser pulse, interacting with the electron beam in the undulator, causes an energy modulation within the bunch on the scale of the optical wavelength. The corresponding density modulation is negligible and the coherent energy–position correlation is smeared by the chicane.

The LH section described below is based on a semi-analytical model. However, since the

two-bunch operation mode for PWFA does not require its use, a more detailed numerical study will be carried out at a later stage to provide the executive design of the main components. However, the LH chicane has been embedded in the high-energy diagnostics section at the photoinjector exit, with space and magnetic devices allocated, ensuring that the overall layout remains unaffected.

The LH layout is shown in Fig. 5.17.

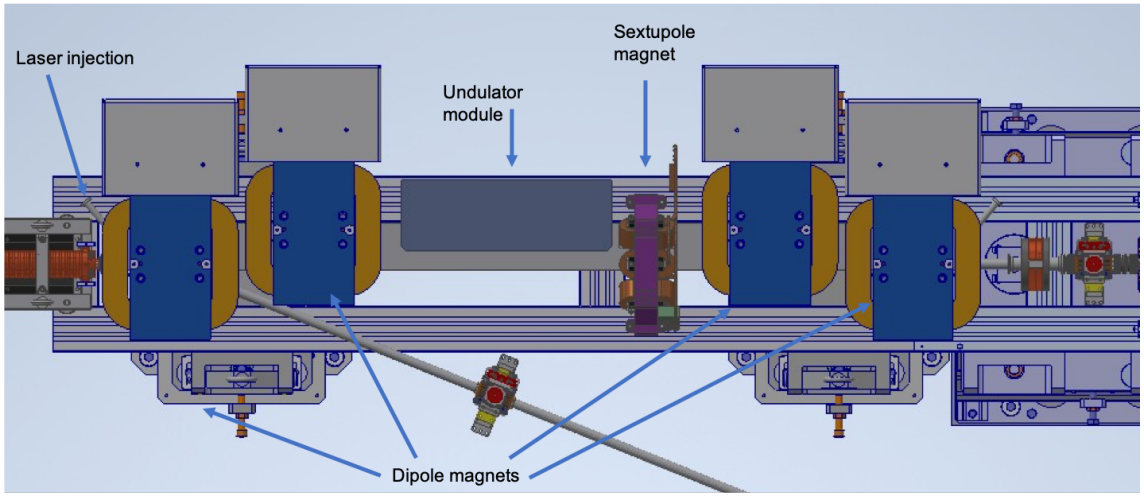

Figure 5.17: Layout of the Laser Heater section.

The laser pulse is split from the photocathode laser pulse, extracted upstream of third-harmonic generation. Making both the fundamental ($\lambda_l \sim 800$ nm) and its second harmonic ($\lambda_l \sim 400$ nm) available guarantees the spectral flexibility required to accommodate an electron-beam energy range of $\sim$ 100–290 MeV.

The ability to freely adjust the dispersive section requires an independent laser beam focusing system for the vertical and horizontal planes to minimize the laser pulse power required, as the horizontal electron beam spot size in the undulator approaches the value of ~ 1 mm (rms), for the larger chicane bending angles, while the vertical size should remain < 0.1 mm. A pair of orthogonally mounted cylindrical lenses (or, at high fluence, cylindrical mirrors) provides independent control of the horizontal and vertical waists without adding appreciable aberrations. Each LH pulse is specified to deliver up to 50 μJ in 10 ps FWHM, providing a maximum laser pulse peak power of 5 MW. A polarimeter offers continuous attenuation, while a fast shutter can extinguish the beam completely for alignment or diagnostics. The LH section has to include two screen stations for spatial alignment of the laser and electron beam and two BPMs for on-line control of the electron beam trajectory (position and angle).

The modulator undulator consists of 10 periods of 45 mm, with remanent field permanent magnets of $B_r = 1.2$ T, for a total length of 0.45 m. Its full gap can be remotely controlled within a range of 15–35 mm and, combined with the choice of the fundamental or second harmonic of the laser pulse, can resonantly match the full electron-energy working range.

The LH magnetic chicane is designed to operate with adjustable deflection angles between 4 and 14.5°. The vacuum chamber must provide at most 13 mm of external vertical width at the undulator location to accommodate the minimum undulator full gap of 15 mm. Since the electron trajectory shifts with the dipoles varying bending angle, the vacuum pipe, the undulator and laser optics and diagnostic have to be mounted on a common transverse translation stage, that can move in a range of about 110 mm.

The main LH specification are collected in Tab. 5.5.

These integrated specifications ensure that the LH can supply the required Landau damping

Table 5.5: Main specifications of the LH system.

Laser	**Value**
Wavelength, λ_l [nm]	400, 800
Pulse duration, FWHM [ps]	≤ 10
Pulse energy [μJ]	≤ 50
Peak power [MW]	≤ 5
Undulator	
Permanent magnets remanent field, B_r [T]	1.2
Period length [mm]	45
Number of periods	10
Undulator parameter, K	0.8–3.0
Undulator full gap [mm]	15–35
Electron beam	
e-beam energy, E [MeV]	100–290
LH-induced maximum slice energy spread, $\sigma_{LH_{max}}$ [keV]	30–50
LH-induced horizontal emittance growth, $\Delta\varepsilon_x/\varepsilon_x$ [%]	< 15
LH chicane	
LH chicane bending angle, $\lvert\theta_B\rvert$ $[deg]$	4–14.5
Vacuum chamber external vert. width [mm]	≤ 13

across all planned operating modes of EuPRAXIA@SPARC_LAB while preserving overall beam brightness as shown by studies discussed in Chapter 3.

5.4 Diagnostics beamline design and performances

In this section both techniques and instrumentation needed to set up and measure beam parameters as generated along the injector area are introduced. A more detailed description of each specific diagnostic is shown in the diagnostics chapter (Ch. 11).

Two main beamlines can be identified in the injector area: the low energy beamline consists in the region from the cathode up to the first TW accelerating section, and the high energy beamline from the first TW section up to the end of the injector area, where the full 6D electron beam characterization can be performed. The expected electron beam parameters are listed in Table 5.6 for the low energy beam and in Table 5.7 for the high energy beam.

Table 5.6: Electron beam parameters for the driver and witness bunches in the low energy beamline. The beam energy refers to the energy of the beam out of the RF gun.

Parameter	Symbol	Unit	Value
RF injection phase	$\phi_{RF_{inj}}$	deg	35
Beam energy	E	MeV	5.6
Number of bunches			2
Driver charge	Q_D	pC	200
Witness charge	Q_W	pC	30

Table 5.7: Electron beam parameters for the driver and witness bunches in the high energy beamline.

Parameter	Symbol	Unit	Value
Beam energy	E	MeV	120
Number of bunches			2
Driver charge	Q_D	pC	200
Witness charge	Q_W	pC	30
Driver beam normalized emittance	ε_{nD}	mm mrad	1.60
Witness beam normalized emittance	ε_{nW}	mm mrad	0.70
Driver energy spread	σ_E	%	0.65
Witness energy spread	σ_E	%	0.13
Driver beam duration	σ_{tD}	fs	154.00
Witness beam duration	σ_{tW}	fs	18.00
Driver-witness beam separation	T_{DW}	ps	0.54

5.4.1 Low energy diagnostic beamline

The low energy diagnostic (LED) refers to the electron beam characterization at 5-6 MeV, being the energy gained by the electron beam by the gun exit. The gun area is particularly critical because the ultimate quality of the electron beam is the one of the electron source. Several checks are required and, in particular, the proper alignment of the laser beam at the cathode, the proper set of the RF gun injection phase, the measurement of the operational charge. The LED beamline requires diagnostics to accurately and adequately measure the electron beam and optimize the RF gun and photo-injector laser parameters. Measurements of the electron beam include:

- bunch charge and photocathode quantum efficiency;
- transverse beam position;
- beam energy;
- transverse beam profile;
- intrinsic emittance.

Only bunch charge and transverse beam position measurements can be performed with non-interceptive diagnostics. All other measurements require beam interception and/or deflection. In this regard, to perform all the above measurements, the following instrumentation is placed in the RF gun area (see Fig. 5.12):

- Faraday cup for charge measurement
- YAG:Ce screen for checking laser alignment on the cathode, transverse beam size measurement, RF injection phase scan, low energy measurement, emittance measurement through solenoid scan, and for imaging the cathode
- Horizontal and vertical steering magnets for beam trajectory correction and as low energy spectrometer
- Integrated Current Transformer for non-invasive charge measurements
- Beam Position Monitors for measuring beam offset from the reference trajectory.

Additional measurements need to be performed on the photoinjector laser beam: laser beam spot size, energy distribution and total energy deposited at the photocathode, for instance. They are provided by optical diagnostics (virtual cathode and camera, laser pulse joule-meter, etc.) located close to the RF gun. Information on the longitudinal laser pulse distribution will be obtained from the optical spectrum, and/or by indirect measurement with a cross-correlator (details in the laser chapter, Sec. 12.2.9). Figure 5.12 shows the layout of diagnostic components in the gun-to-boost

area. More details are shown in the diagnostics chapter.

5.4.2 High energy diagnostic beamline

The high energy diagnostics has to provide 6D phase space characterization of both driver and witness bunches. Normalized emittance measurements are foreseen at the end of the injector by means of the conventional quadrupole scan technique. In this regard, a quadrupole triplet is placed downstream from the fourth accelerating structure, with the first quadrupole centered at 12.506 m from the cathode. Downstream from the quadrupole triplet, a PolariX transverse deflecting structure is foreseen. Both bunch length and normalized slice emittance are retrieved by measuring the transverse beam size on the screen placed at 2.87 m from the PolariX exit. When operating together with the first laser heater dipole, the PolariX allows for the longitudinal phase space measurement in the dogleg. A schematic layout is shown in Fig. 5.18. Further details on the instrumentation here shown can be found in Chapter 11. Along the injector line, viewscreens are placed at 1.109 m, 4.567 m, 8.047 m, 9.910 m and 12.346 m to measure the transverse beam envelope, needed for validating the model and the working point. Each screen station is preceded by a BPM surrounded by a HOR/VER steerer to ensure and measure the alignment.

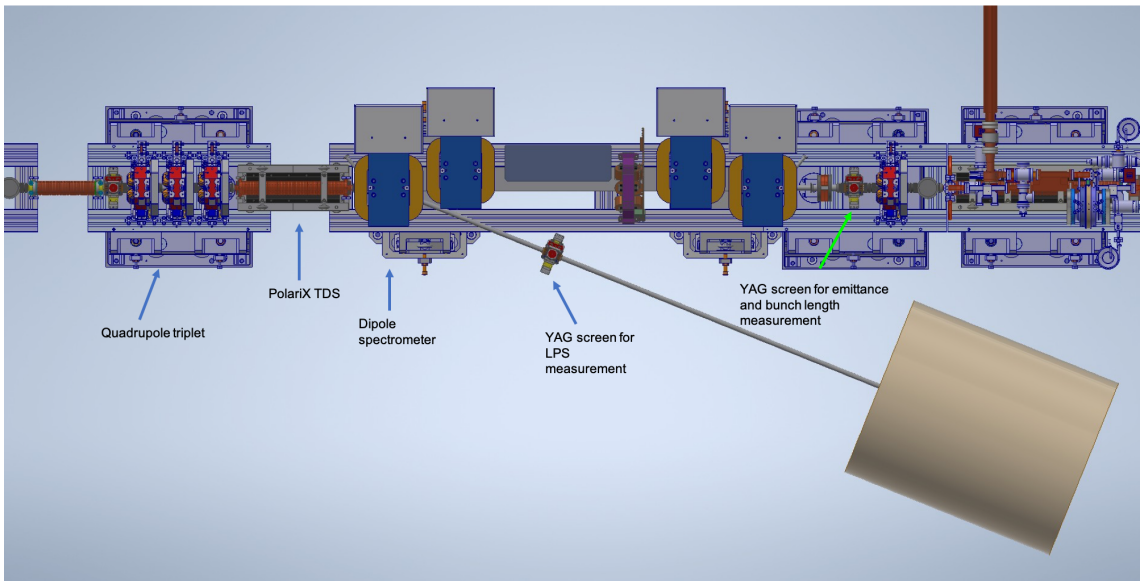

Figure 5.18: Layout of the high energy injector diagnostic.

5.5 Injector performance studies

The SPARC_LAB test facility has been used as a reference and a testing ground for the optimizations implemented in the photoinjector of EuPRAXIA@SPARC_LAB. To complement the study on the generation and optimization of a high-brightness two-bunches beam for the injector, a systematic study on machine jitters on how the high-brightness parameters of interest are affected has been performed. The study also revealed which jitters most affect the stability of the PWFA working point. This study focuses on a comprehensive analysis of injector jitter, a key factor that influences machine stability, particularly in relation to RF and laser jitters. The stability and reproducibility of the electron beam are primarily governed by both, the RF generation system, which drives the accelerating structures, and the laser timing with respect to the RF, determining the timing and energy of the beam. The sensitivity of the entire RF injector chain to jitters is shown in this section, together with studies to mitigate it. In this regard, the X-band linearising cavity

described in Section 5.2.2 is employed to counteract these potential instabilities [21–23]. The X-band cavity is designed to pre-correct the longitudinal phase space of the electron bunch before it undergoes further acceleration. Its implementation allows for fine-tuning of both the longitudinal and transverse beam parameters at the photoinjector exit. The X-band (11.99424 GHz) SW RF structure, placed between the RF gun and the first accelerating structure, is used as an intermediary to manipulate the LPS. Downstream from the drift, the bunch enters the 10 cm long linearizer that decelerates it by 1.27 MeV. Taking into account the main sources of jitters in RF photoinjectors (see Table 5.8), a comprehensive sensitivity jitter study has been conducted for all RF injector components, comparing the resulting beam stability both with and without the implementation of the X-band cavity. Jitter values without and with X-band cavity are listed in Table 5.9 and in Table 5.10, respectively.

Table 5.8: Jitter values used in the simulations based on SPARC_LAB experience and state-of-the-art (see Table 5.1).

Parameter	Symbol	Unit	Value
Charge	ΔQ (max)	%	$\pm$ 1
Laser arrival time	Δt (rms)	fs	$\pm$ 20
Laser spot size	$\Delta\sigma$	%	$\pm$ 1
RF Voltage	ΔV	%	$\pm$ 0.02
RF Phase	$\Delta\phi$	%	$\pm$ 0.02

Table 5.9: S-band injector jitters without the Higher Harmonic Cavity (HHC).

injector	witness emittance	bunch separation	witness bunch length
S-band no HHC	0.573 ± 0.003 (mm-mrad)	0.460 ± 0.005 (ps)	0.0185 ± 3.0e-4 (ps)

Table 5.10: Summary of jitter sources affecting the witness bunch. A check mark (X) indicates the parameter is jittering, otherwise it is fixed. The worst-case scenario results in a 4 fs bunch separation jitter ($\sigma_t(DW)$).

Jitter							**Witness bunch**		
Phase HHC	**Grad. HHC**	**Phase S**	**Grad. S**	**Charge**	**Spot**	**ToA**	ε (mm-mrad)	$\sigma_t(DW)$ (ps)	Length (ps)
X	X	X	X	X	X	X	0.66 ± 0.02	0.547 ± 0.004	$0.0132 \pm 4\times10^{-4}$
X	X	X	X	X	X		0.67 ± 0.02	0.546 ± 0.004	$0.0138 \pm 4\times10^{-4}$
X	X		X	X	X		0.67 ± 0.02	0.546 ± 0.003	$0.0138 \pm 4\times10^{-4}$
		X	X	X	X		0.66 ± 0.02	0.546 ± 0.003	$0.0136 \pm 4\times10^{-4}$
X	X		X	X			0.66 ± 0.02	0.547 ± 0.002	$0.0136 \pm 1\times10^{-4}$
X	X		X				0.66 ± 0.01	0.546 ± 0.002	$0.0136 \pm 1\times10^{-4}$
X	X	X	X				0.67 ± 0.02	0.545 ± 0.003	$0.0137 \pm 1\times10^{-4}$
X	X						0.658 ± 0.004	0.546 ± 0.001	$0.0136 \pm 2\times10^{-5}$

5.6 Final considerations

The studies carried out on the RF photo-injector confirm its central role in enabling beam-driven plasma-based acceleration. Indeed, the analysis highlights the critical interplay between injector parameters and the downstream plasma stage. The optimization of the two-bunches working point is carried out by applying the laser-comb technique within the solenoid-based emittance compensation scheme. This approach is further complemented by the inclusion of the X-band linearizing cavity, which plays a key role in mitigating the temporal jitter between driver and witness at the entrance of the linac, thus ensuring more stable and reproducible operating conditions, as also shown in detail in the Beam Physics chapter.

The results show that the state-of-the-art photo-injectors provide a solid basis for the delivery of electron beams with the quality needed to sustain efficient plasma wakefield excitation and subsequent acceleration of witness bunches. The EuPRAXIA@SPARC_LAB RF photoinjector presented here provide the two bunches with parameters required as determined from S2E simulation results.

In conclusion, RF photo-injector specifications align with the required two-bunches beam configuration for the PWFA, i.e., the requirements on stability and reproducibility, the versatility needed for exploring different working points.

The injector layout is consistent with the requirements from beam dynamic studies, virtual diagnostics and multi-working point operation.

Based on what stated above, the Technological Readiness Level (TRL) of the photoinjector and its sub-components is shown in Table 5.11. At TRL 9, the RF photoinjector demonstrates reliable, stable, and reproducible operation in real-world conditions. It is expected to provide a high percentage of up-time (i.e., larger than 95%) with consistent beam quality and minimal downtime for routine maintenance. The system can be fully integrated into control and safety procedures, ensuring robustness and user-readyness.

Table 5.11: TRL level of the photoinjector and its sub-systems.

Sub - systems	TRL	Comments
RF gun	9	S-Band RF guns are widely used in many facilities including SPARC_LAB. S-Band technology is fully available in the market.
Solenoids	9	Technology demonstrated in other facilities (FERMI, SwissFEL, etc.)
X-band linearizer	7	Higher harmonic cavities are used already in several facilities for manipulating the LPS; X-band linearizer is still relatively new in daily user operation.
S-band linac	9	S-Band linac structures are widely used in many facilities including SPARC_LAB. S-Band technology is fully available in the market.
Laser heater	8	Laser heater systems are routinely in operation in several facilities (FERMI, SwissFEL, etc.), a design more suitable for our layout is needed.
Diagnostics	8	Diagnostics instrumentation is based on standardized components daily used in other facilities; only very few devices cannot be considered plug-and-play.
Photo-cathode laser	9	Photocathode laser is now a proven technology tested in real facilities (including SPARC_LAB). The systems are fully available in the market almost as off-the shelf products.

Bibliography

[1] M. Boscolo et al. “A Train of Micro-bunches for PWFA Experiments produced by RF Photoinjectors”. In: *International Journal of Modern Physics B* 21.03n04 (2007), pp. 415–421.

[2] F. Villa et al. “Laser pulse shaping for high gradient accelerators”. In: *Nuclear Instruments and Methods in Physics Research Section A: Accelerators, Spectrometers, Detectors and Associated Equipment* 829 (2016), pp. 446–451.

[3] R. Pompili et al. “Beam manipulation with velocity bunching for PWFA applications”. In: *Nuclear Instruments and Methods in Physics Research Section A: Accelerators, Spectrometers, Detectors and Associated Equipment* 829 (2016), pp. 17–23.

[4] D. Alesini et al. “The SPARC project: a high-brightness electron beam source at LNF to drive a SASE-FEL experiment”. In: *Nuclear Instruments and Methods in Physics Research Section A: Accelerators, Spectrometers, Detectors and Associated Equipment* 507.1 (2003). Proceedings of the 24th International Free Electron Laser Conference and the 9th Users Workshop., pp. 345–349. ISSN: 0168-9002. DOI: https://doi.org/10.1016/S0168-9002(03)00943-4.

[5] D. Alesini et al. “The New SPARC_LAB RF Gun Photoinjector”. In: *13th Int. Particle Acc. Conf.* MOPOMS019 (2022).

[6] M. Ferrario et al. “Direct Measurement of double emittance minimum in the SPARC high brightness photo-injector”. In: *Phys. Rev. Lett.* 99.234801 (2007).

[7] T. Schietinger et al. “Commissioning experience and beam physics measurements at the SwissFEL Injector Test Facility”. In: *Phys. Rev. Accel. Beams* 19 (10 2016), p. 100702. DOI: 10.1103/PhysRevAccelBeams.19.100702.

[8] L. Serafini and M. Ferrario. “Velocity bunching in photoinjectors”. In: *AIP Conf. Proc.* 581.1 (2001), pp. 87–106.

[9] E. Esarey, C. Schroeder, and W. Leemans. “Physics of laser-driven plasma-based electron accelerators”. In: *Reviews of Modern Physics* 81 (2009), p. 1229.

[10] A. R. Rossi et al. “Stability study for matching in laser driven plasma acceleration”. In: *Nuclear Instruments and Methods in Physics Research Section A: Accelerators, Spectrometers, Detectors and Associated Equipment* 829 (2016). 2nd European Advanced Accelerator Concepts Workshop - EAAC 2015, pp. 67–72. ISSN: 0168-9002. DOI: https://doi.org/10.1016/j.nima.2016.02.015.

[11] P. Craievich et al. “Novel X-band transverse deflection structure with variable polarization”. In: *Phys. Rev. Accel. and Beams* 23.112001 (2020).

[12] L. Sabbatini et al. “SABINA: A Research Infrastructure at LNF”. In: *Proc. IPAC’21* (Campinas, Brazil, May 2021). JACoW Publishing, Geneva, Switzerland, 2021, pp. 4505–4507. DOI: 10.18429/JACoW-IPAC2021-THPAB372.

[13] D. Alesini et al. *International Patent Publication No. WO 2016/147118 A1, assigned to INFN*.

[14] R. Corsini et al. “The Future of the CLEAR Facility: Consolidation, Ongoing Upgrades and its Evolution Towards Future Electron Facilities at CERN”. In: *Proc. IPAC’25* (Taipei, Taiwan, June 2025). JACoW Publishing, Geneva, Switzerland, 2025, pp. 1220–1223. DOI: 10.18429/JACoW-IPAC2025-TUPM027. URL: https://proceedings.jacow.org/ipac2025/pdf/TUPM027.pdf.

[15] ANSYS Electronics Desktop website.

[16] D. Alesini et al. “New technology based on clamping for high gradient radio frequency photogun”. In: *Phys. Rev. Spec. Top. Accel. Beams* 18.092001 (2015).

[17] D. Alesini et al. “Design, realization, and high power test of high gradient, high repetition rate brazing-free S-band photogun”. In: *Phys. Rev. Accel. Beams* 21.112001 (2018), P12022.

[18] A. Grudiev et al. “New local field quantity describing the high gradient limit of accelerating structures”. In: *Phys. Rev. Spec. Top. Accel. Beams* 12.102001 (2009).

[19] V. Shpakov et al. “Design, optimization and experimental characterization of RF injectors for high brightness electron beams and plasma acceleration”. In: *Journal of Instrumentation* 17.12 (2022).

[20] A. Vannozzi et al. “Design and Realization of New Solenoids for High Brightness Electron Beam Injectors”. In: *12th Int. Particle Acc. Conf.* TUPAB366 (2021), p. 2377.

[21] A. Bacci, L. Faillace, and M. Rossetti Conti. “Extreme High Brightness Electron Beam Generation in a Space Charge Regime”. In: *Proc. 29th Linear Accelerator Conference (LINAC’18), Beijing, China, 16-21 September 2018*. 2018, pp. 314–319. DOI: doi:10.18429/JACoW-LINAC2018-TU1P01.

[22] A. Gallo et al. “Study of a C-band Harmonic RF System to Optimize the RF Bunch Compression Process of the SPARC Beam”. In: *Proc. 6th International Particle Accelerator Conference (IPAC’15), Richmond, VA, USA, May 3-8, 2015*. 2015, pp. 1552–1555. DOI: https://doi.org/10.18429/JACoW-IPAC2015-TUPWA058.

[23] P. Emma. *X-Band RF harmonic compensation for linear bunch compression in the LCLS*. SLAC Nation Accelerator Laboratory Technical Note SLAC-TN-05-004, LCLS-TN-01-1. Nov. 2001.

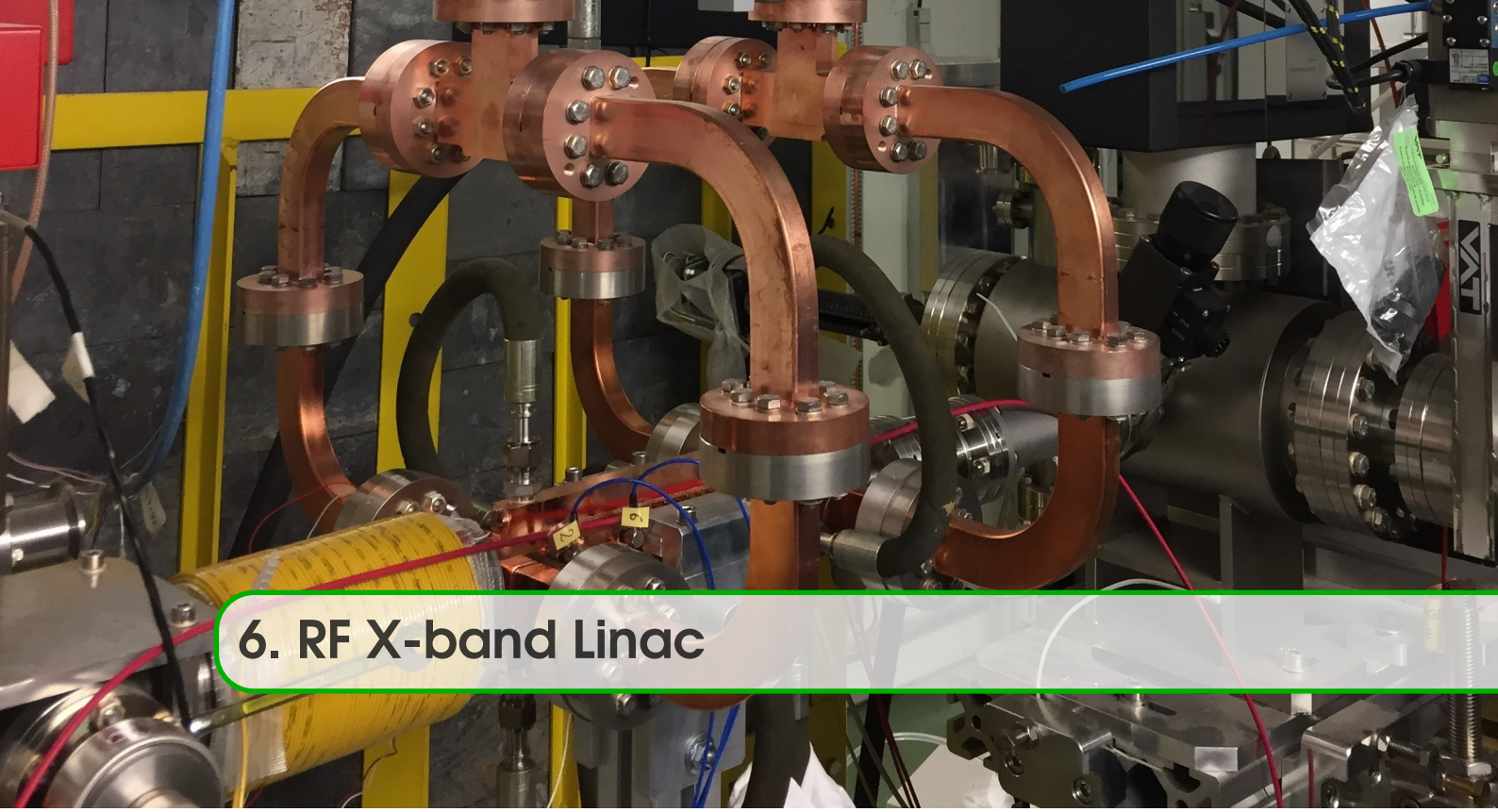

6. RF X-band Linac

6.1 Introduction

The EuPRAXIA@SPARC_LAB X-band linac is designed to accept the beam coming from the photo-injector and to accelerate it to the final energy with the proper characteristics to match the requirements of the various specific applications as given in Chapter 3. The overall linac layout is given in Fig. 6.1. After the S-band (2.99855 GHz) photo-injector the beam is accelerated through an X-band (11.9942 GHz) linac consisting of 16, 0.9 m-long traveling wave (TW) accelerating sections operating up to a maximum accelerating field of 60 MV/m and 100 Hz repetition rate. The goal of this chapter is to describe the X-band linac in term of layout, components and main parameters. The X-band linac is divided into two parts: low energy and high energy, separated by a magnetic chicane used for bunch compression for the full RF acceleration case. The linac consists of eight accelerating modules, in which two pairs of TW structures are fed in parallel by a single power source, as described in detail in Sec. 6.2. The linac RF design has been driven by the need for a high accelerating gradient, i.e., well above the operational values of existing FEL sources. This has been required by the limited space available in the new building and, more generally, to achieve facility compactness, which is one of the main goals of the EuPRAXIA project. The final choice of the X-band frequency has been guided by various reasons: it is more efficient, it has been operated in prototypes, at high accelerating field (>100 MV/m), its development is supported by a strong international effort, and experimental data are abundant. Moreover, the possibility to establish a partnership with CERN (CLIC project) represents an added value to the project itself.

6.2 X-band RF module

The mechanical layout of the RF module is shown in Fig. 6.2 while its schematic layout is given in Fig. 6.3. It includes a 25 MW RF power source (implemented as a solid state pulsed modulator combined with a Canon klystron E37119, as described in Sec. 6.6), that is connected to an RF pulse compressor of the Barrel Open Cavity (BOC) type through a low loss, $\approx$ 6 m-long, transport line. The transport line consists of two vertical straight double-height WR90 (DHWR90) waveguides and a 6-meter-long WC50 overmoded circular waveguide. The 25 MW, 1.5 µs rectangular pulse

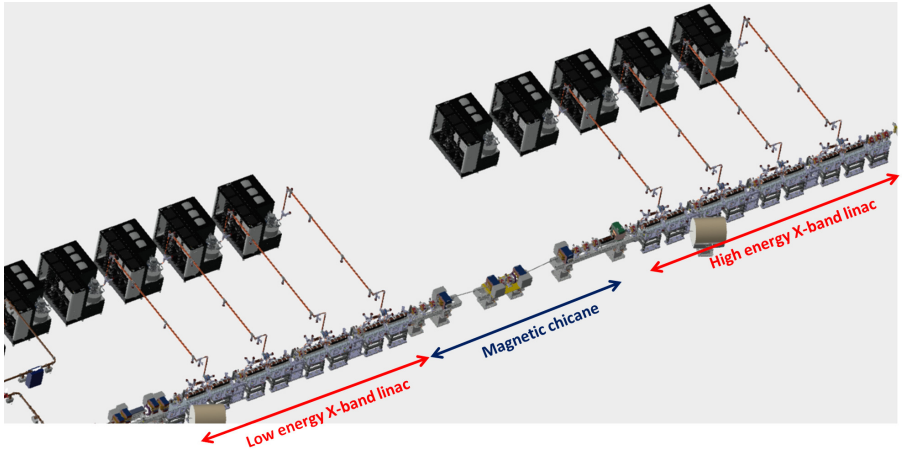

Figure 6.1: X-band linac layout.

produced by the power source is compressed, through the BOC, into a 130 ns typical trapezoidal-shaped compressed pulse [1] of 140-70 MW. After compression the power is split in two branches with a 3dB hybrid, and feeds the two TW X-band accelerating structures in parallel. The module integrates several waveguide components, such as pumping units, directional couplers to measure the forward and reflected powers, splitters for a symmetric feeding of the structures, and spiral RF loads at the end of the structures to dissipate the residual power out from the TW sections. Between the two accelerating structures of each module a horizontal-vertical corrector magnet is inserted. The schematic layout of two consecutive modules is shown in Fig. 6.4. Between the modules we have a sector vacuum valve, a screen chamber, a cavity BPM and a quadrupole. These elements are described in Sections 16, 11.2.5,11.2.4, 17.3.2.

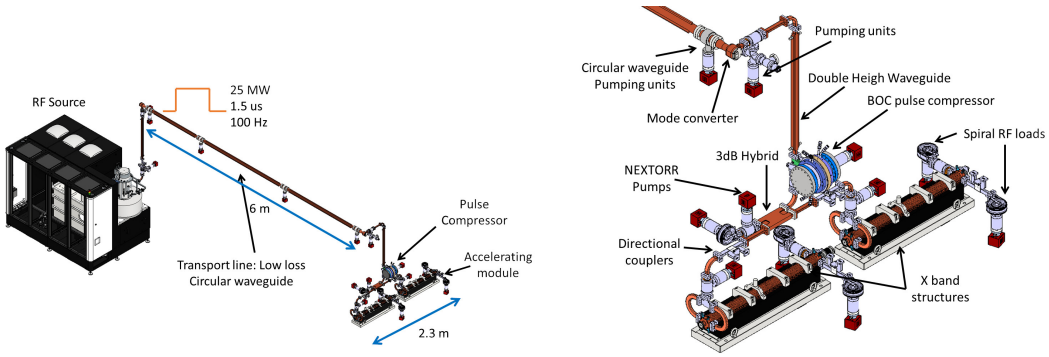

Figure 6.2: X-band RF module mechanical layout.

6.3 X-band TW structures

The accelerating structures are disc-loaded quasi-constant gradient TW sections powered by an RF compressed pulse. To maximize their efficiency, the radii of the irises have a linear tapering along the structure itself that has been optimized following the criteria illustrated in [2, 3]. The average dimensions of the irises have been chosen as a compromise between efficiency and beam dynamics requirements (Chapter 3) [4]. The input and output couplers have been designed to minimize reflections and multipolar field components. The final TW structure parameters are given in Table 6.1

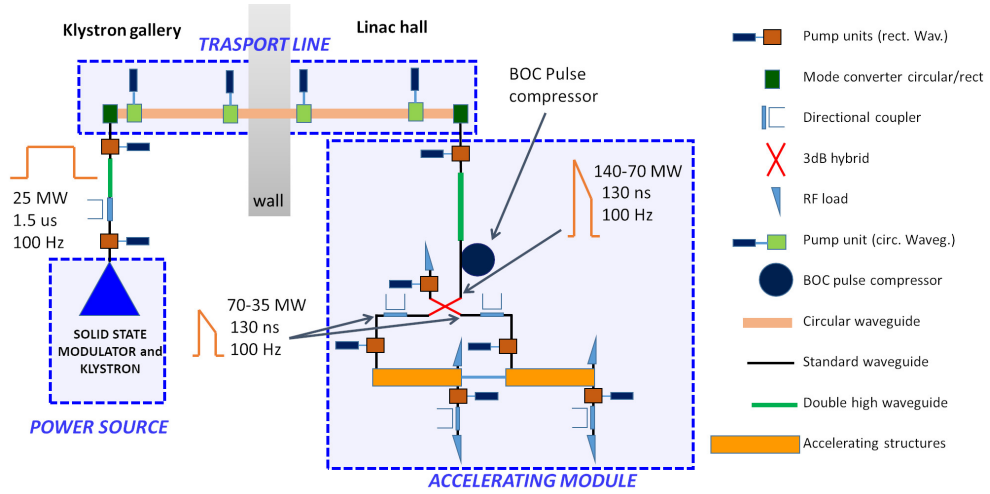

Figure 6.3: X-band RF module schematic layout.

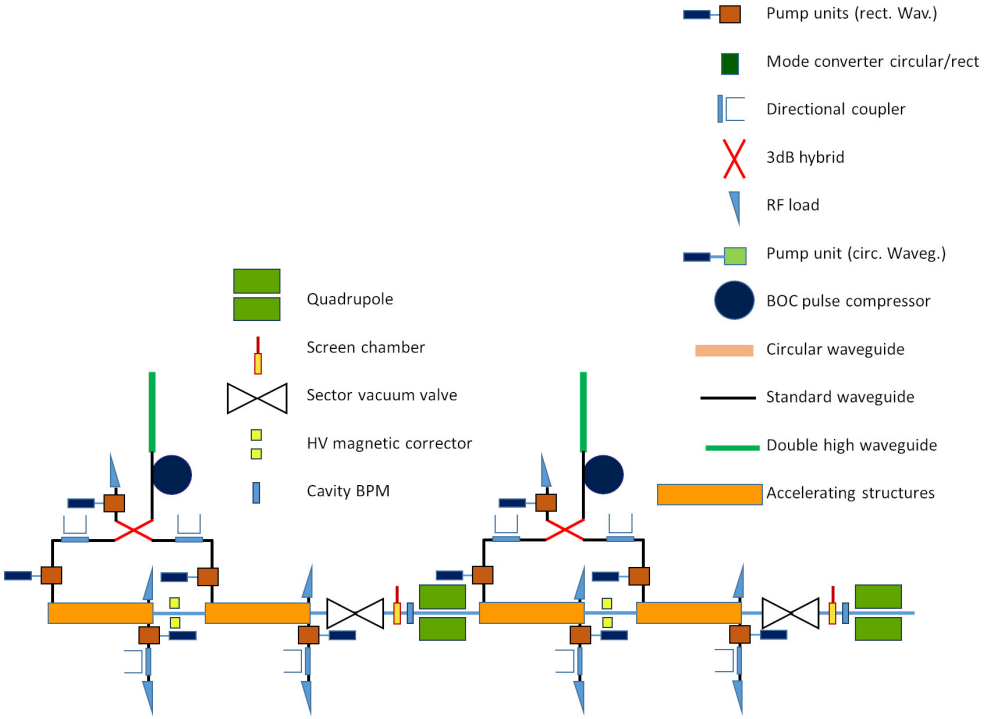

Figure 6.4: Schematic layout of two consecutive modules.

6.3.1 Electromagnetic design

The electromagnetic (e.m.) design of the cells and couplers has been performed using the 3D e.m. code ANSYS Electronics Desktop [5], and the final simulated model is given in Fig. 6.5. An elliptical shape of the irises has been considered in the single-cell profile to minimize the modified Poynting vector and the peak surface electric field. The average radius of the cells has been fixed, according to beam dynamics simulations and beam break-up limits, to a value of 3.5 mm, while the overall iris radii have a linear tapering along the structure that has been chosen to maximize the effective shunt impedance [2]. The input and output couplers have a symmetric dual feed, and a racetrack geometry, in order to simultaneously cancel the dipole and quadrupole

Table 6.1: Parameters of the EuPRAXIA@SPARC_LAB accelerating structures (in parenthesis the values in the case of a constant impedance structure, if different from the quasi-constant gradient case). * This corresponds to the maximum achievable accelerating field assuming klystrons operating at full power (25 MW) and 10% waveguides power attenuation.

Accelerating structures parameter	Symbol	Unit	Value
Frequency	f_{RF}	GHz	11.9942
Iris radius (linear tapered)	a	mm	3.85-3.15 (3.5)
Structure active length	L_s	m	0.94
Number of cells	N_{cell}		113
Shunt impedance per unit length	R	MΩ/m	93-107 (100)
Effective shunt impedance per unit length	R_s	MΩ/m	350 (347)
Average accelerating field*	E_{acc}	MV/m	60
Peak input power per structure	P_{peak}	MW	70
Input power per structure averaged over the pulse	P_{in}	MW	51
P_{out}/P_{in}		%	25
Filling time	τ_F	ns	130
Peak mod. Poynting Vector	S_c	W/μm^2	3.6 (4.3)
Peak Surf. E field	E_P	MV/m	160 (190)
Quality factor	Q		6400
Phase advance per cell	ϕ		$2\pi/3$
Repetition rate	f_{rep}	Hz	100

field components introduced by the coupling holes. The e.m. design has also been optimized to keep pulsed heating [6] below 30K and the modified Poynting vector below 5 W/μm^2. The final reflection coefficient is well below -30 dB. Figure 6.6 shows, as an example, the electric field profiles, in magnitude and phase, of a structure with a reduced number of cells, while Fig. 6.7 shows the accelerating field sampled by a particle accelerated on crest. In the figure we show the constant impedance case and the case with a linear tapering of the irises.

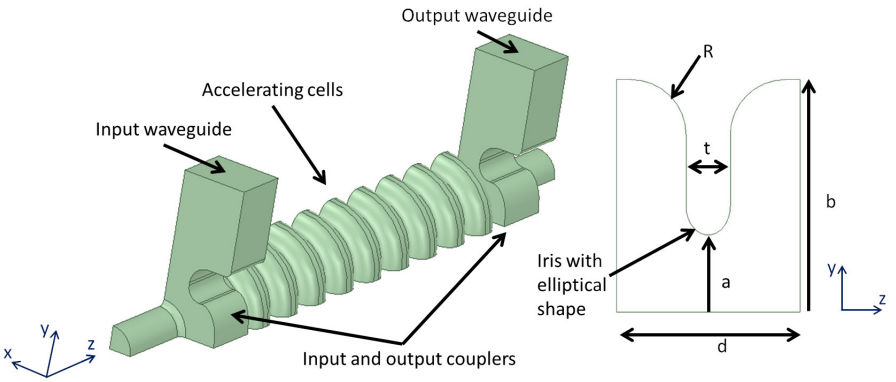

Figure 6.5: HFSS model of the X-band accelerating structure (reduced number of cells).

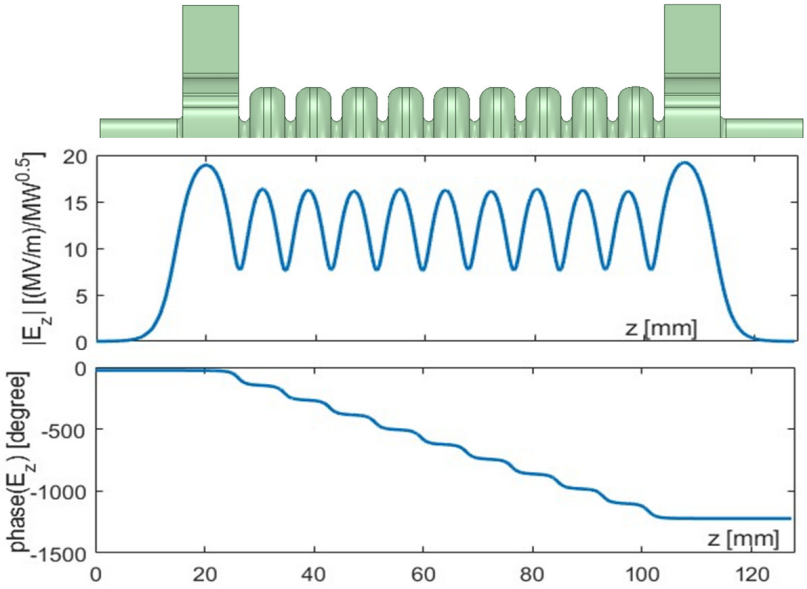

Figure 6.6: Amplitude and phase of the accelerating field along the structure (ANSYS-HFSS simulation result with a reduced number of cells, 9 instead of 113).

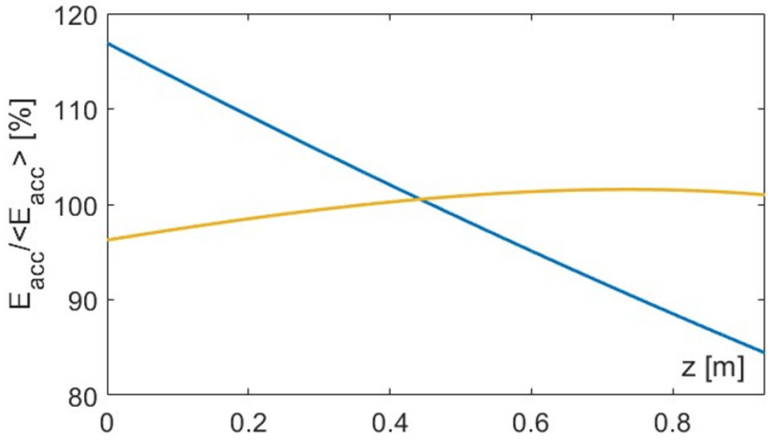

Figure 6.7: Peak accelerating field in each cell in case of constant impedance (blue curve) and tapered irises (yellow curve) structures (in the two cases the energy gain per structure is the same).

6.3.2 Thermo-mechanical design

The mechanical drawing of the accelerating structures is given in Fig. 6.8. Each structure incorporates four cooling channels that have been designed using a combined electromagnetic and thermo-mechanical analysis in ANSYS workbench [5]. Each structure requires a total flow rate of 16 l/min while the working temperature of each structure has been fixed to 25°C. The calculated equilibrium temperature at full power is shown in Fig. 6.9. In the same figure, we also show the radial mechanical deformations. The increase in temperature under powering, detunes the structure and we have calculated that, to compensate this temperature increase the input water temperature has to be reduced by 2°C. The temperature stability required for the water is ± 0.1°C (Sec. 18.3.1.2). The structure cell-to-cell alignment required by the beam dynamics has been fixed to ± 30 µm. The realization process we have developed for the structures allows these specifications to be met, and these requirements have already been achieved in prototypes [7].

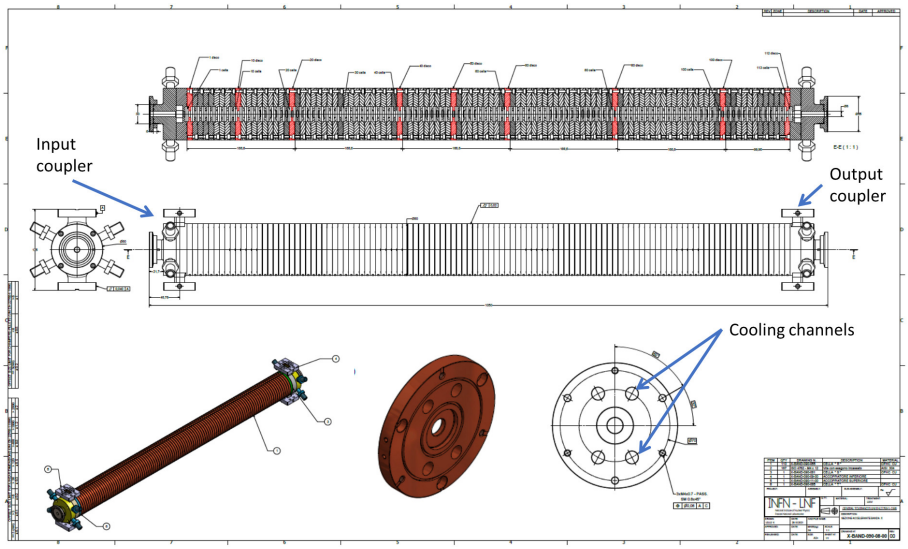

Figure 6.8: Mechanical drawing of the X-band structure.

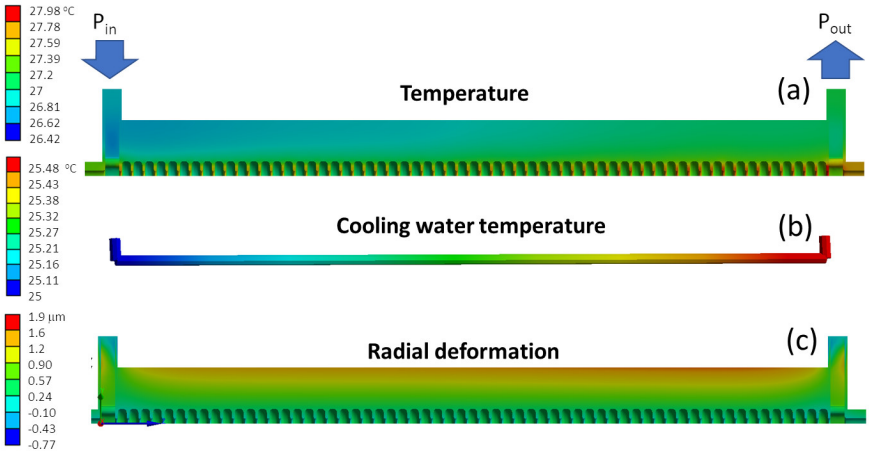

Figure 6.9: Results of the thermo-mechanical analysis performed by ANSYS (model with a reduced number of cells).

6.3.3 Vacuum

According to the module layout, each structure is vacuum pumped through the waveguides connected to the input and output couplers. The type of pumps that will be used are neg-type pumps combined with ion pumps (NEXTorr Z100 [8]). The vacuum pressure along the structure has been calculated assuming an effective pumping speed of 10 l/s at the waveguide apertures. The results are shown in Fig. 6.10 for different values of the specific outgassing rate. According to our experience this value, for pure brazed copper is, after several hour of pumping well below 10^{-12} mbar/l/sec/cm^2 that give a pressure in the center of the structure below 10^{-8} mbar.

6.3.4 Prototyping activity

Several prototypes of the X-band accelerating structure have been fabricated. The performed activities are illustrated in [7] and have been focused on demonstrating the feasibility of the proposed scheme. All these components have been tested at the Frascati TEX Facility, which is exclusively dedicated to testing the feasibility of the X-band linac. All the waveguide components

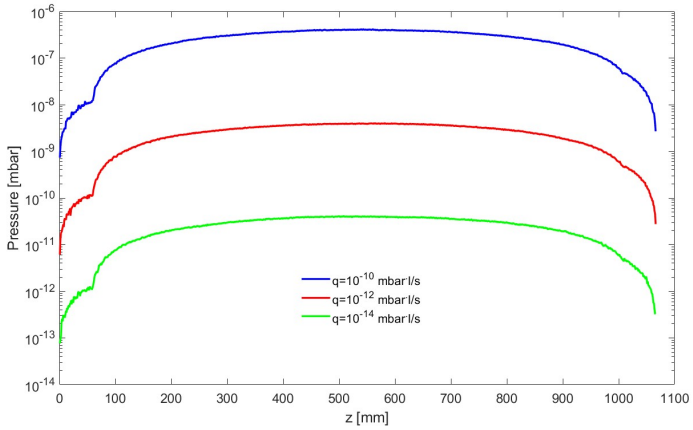

Figure 6.10: Simulated pressure along the X-band structure assuming different specific outgassing rates for copper (in $mbar/l/sec/cm^2$).

have been successfully tested almost at the nominal parameters (see TRL Table 6.6 for details). A 20-cell X-band short RF prototype (shown in Figure 6.11) has been tested, successfully reaching the nominal parameters. The pulse compressor system (BOC), along with the full-scale RF prototype (shown in Figure 6.11), will be tested in the coming months.

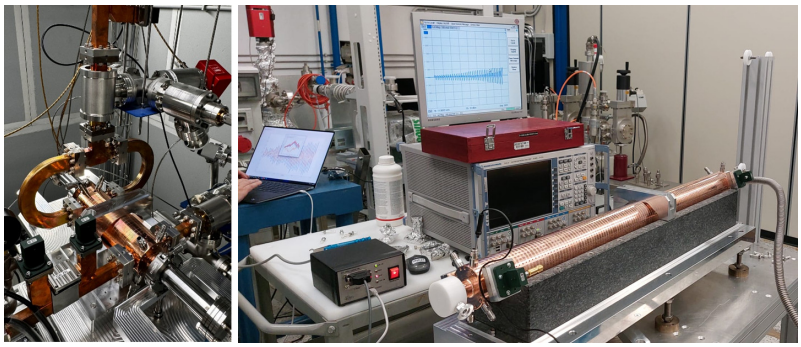

Figure 6.11: X-band accelerating structure prototypes: 20 cell structure under high power testing at the LNF TEX test facility (left); full scale rf structure under low power rf characterization (right).

6.4 X-band waveguide components

The waveguide standard we adopted is WR90 and the RF module integrate several different waveguide components. Many of them are based on design developed at CERN [9] while, for the others, we have not found an already developed or available commercial solution, and they have been designed by INFN [10]. All the waveguide components have been (or will be) tested at their nominal power in the INFN-LNF TEX Facility [11, 12]. Figure 6.12 shows some of them under test. For all the waveguide components we have adopted the International Vacuum Flange given in Fig. 6.13. Below we give the complete list of these components[1]:

- circular-to-rectangular waveguide mode converter (INFN design based on [13], shown in Fig. 6.14);
- circular waveguide pumping unit (INFN design, shown in Fig. 6.14);

[1] For some of these components (directional coupler, pumping port, 3dB power splitter, RF water load), a PSI design also exists and will be considered as a possible alternative solution.

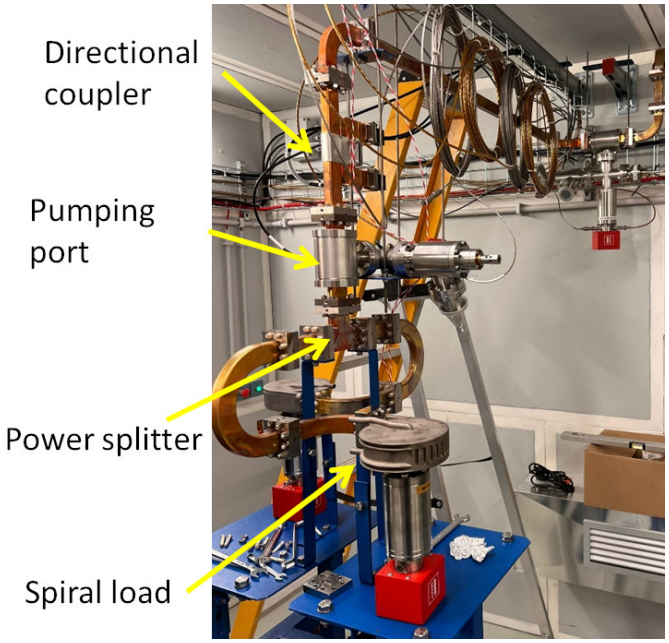

Figure 6.12: X-band components under test at the LNF TEX test facility.

- 3 dB hybrid (CERN design, shown in Fig. 6.15);
- 60 dB directional couplers (CERN design, shown in Fig. 6.15);
- pumping units (CERN design, shown in Fig. 6.15);
- power divider (CERN design, shown in Fig. 6.15);
- spiral loads (CERN design);

The total attenuation of the different components has been calculated, and we expect a power attenuation from the klystron output flange to the accelerating structures of about 10%. This inevitable attenuation has been considered in all calculations related to the effective accelerating field and power.

The waveguide straight sections and the circular waveguide will be cooled with brased copper rectangular pipes (internal dimensions 20mm x 12mm, wall thickness 2mm) as given in Fig. 6.16. For the cooling of the other components we will adopt, if necessary, a clamping system that will be tested at TEX.

Table 6.2: Parameters of the BOC-type pulse compressor.

Parameter	Value
Type	Barrel Open Cavity
Frequency	11.9942 GHz
Resonant Mode	$TM_{18,1,1}$
Q_0	150000
Coupling factor β	7.1

6.5 BOC pulse compressor

Pulse compressors are widely used devices in the RF systems of room temperature linacs. By constructively interfering reflected power pulses of very high-Q cavities with properly phase

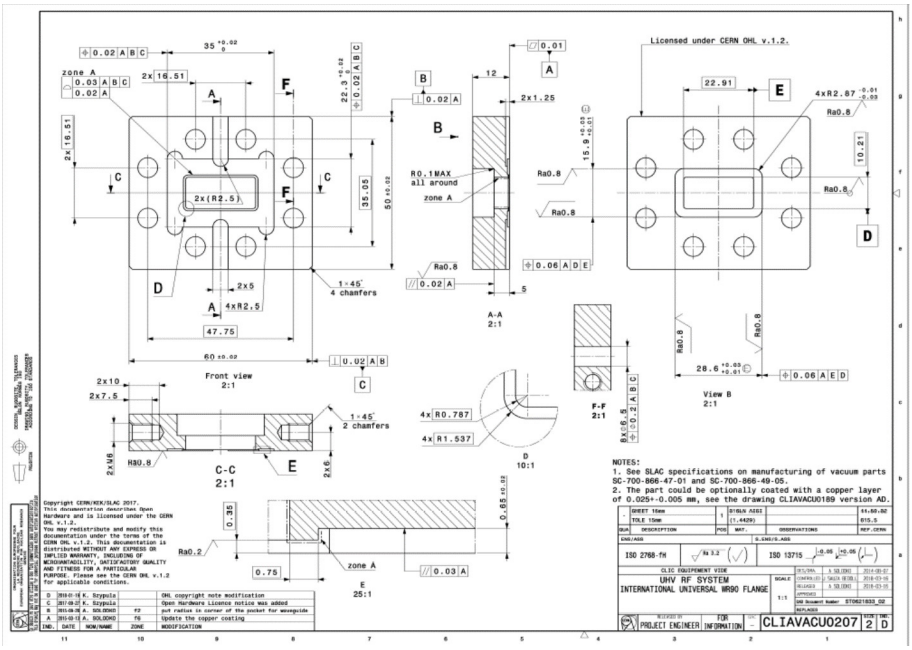

Figure 6.13: Rectangular X-band flange (International flange) adopted for waveguide connections CERN drawing (CERN design and open source repository).

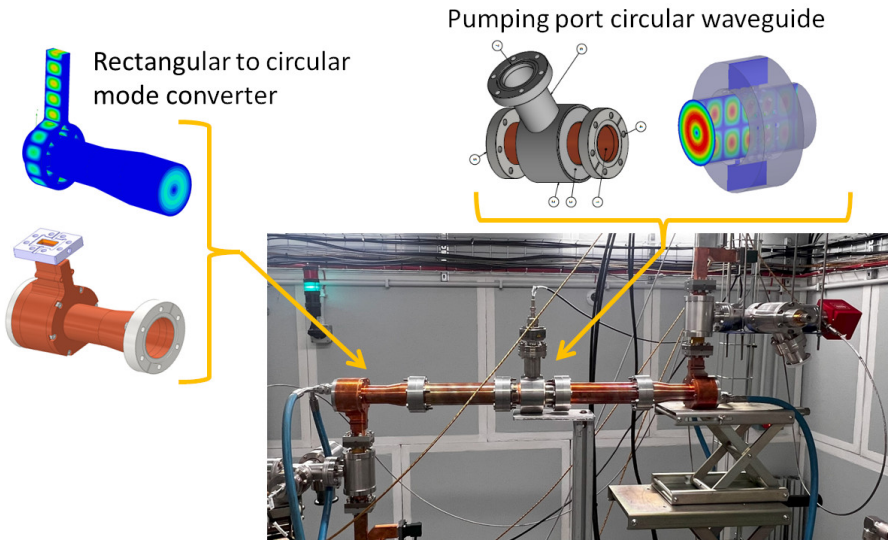

Figure 6.14: Rectangular to circular mode converter, pumping units and circular waveguide installed in the TEX facility.

modulated forward pulses, it is possible to concentrate a large portion of a klystron RF pulse energy into a small fraction of the original pulse duration [1]. The rf pulse compression in the X-band linac is performed through a BOC-type cavity [14] shown in Fig. 6.17. The design adopted for the linac baseline is that of PSI with the parameters given in Table 6.2.

6.6 RF power source

The X-band power source is based on klystron Canon E37119 driven by a commercial solid state pulsed modulator, capable of generating 1.5 µs RF pulses of 25 MW with a repetition rate up

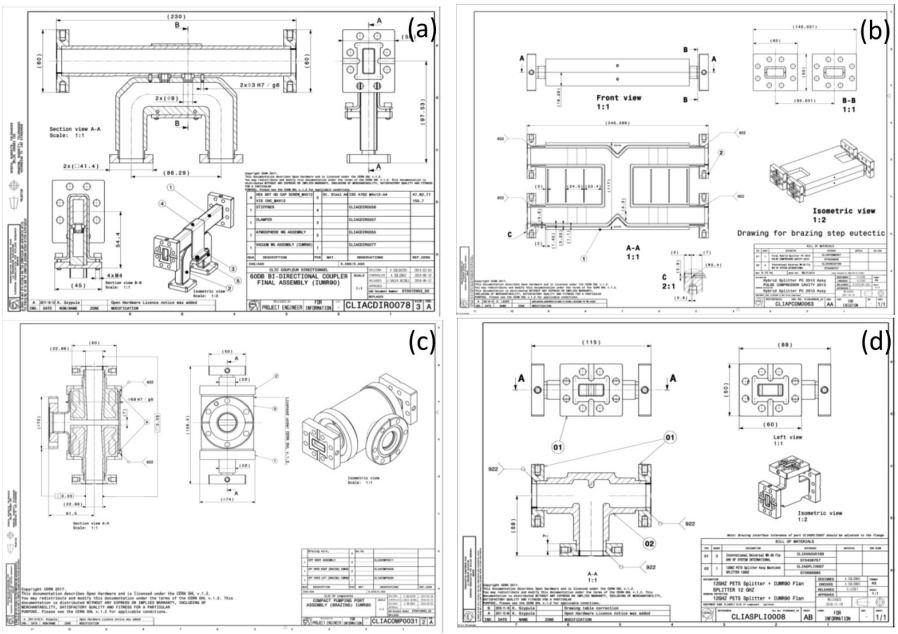

Figure 6.15: Mechanical design of the X-band components adopted in the waveguide distribution of the X-band linac (CERN design and open source repository).

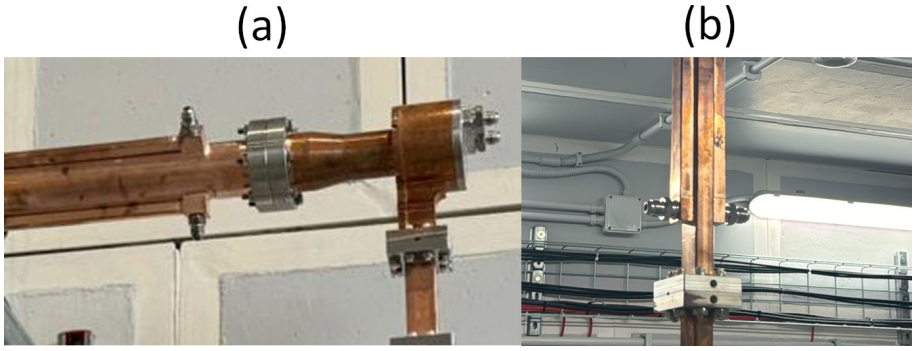

Figure 6.16: Detail of the cooling system of the circular (a) and rectangular (b) waveguides.

to 400 Hz (the baseline for the X-band linac is 100 Hz). The linac needs eight power sources each feeding a pairs of structures as illustrated in Fig. 6.2. The picture of the power station with Scandinova Solid state modulator, installed in the TEX facility is given in Section 13.3. The main klystron and modulator parameters are given in Tables 6.3 and 6.4.

6.7 Quadrupole and diagnostics inter-modules

As already illustrated in Fig. 6.2, between the modules we have a screen chamber, a cavity BPM and a quadrupole. The characteristics of these devices are given in Sections 11.2.5, 11.2.4, 17.3.2.

6.8 Supports

All the components of X-band modules will be supported by girders, as shown in Fig. 6.18. The girder is made of iron and equipped with precise rectified rails to host the X-band structures. The four pedestals allow for a precise regulation of the height and tilt of the overall module with a

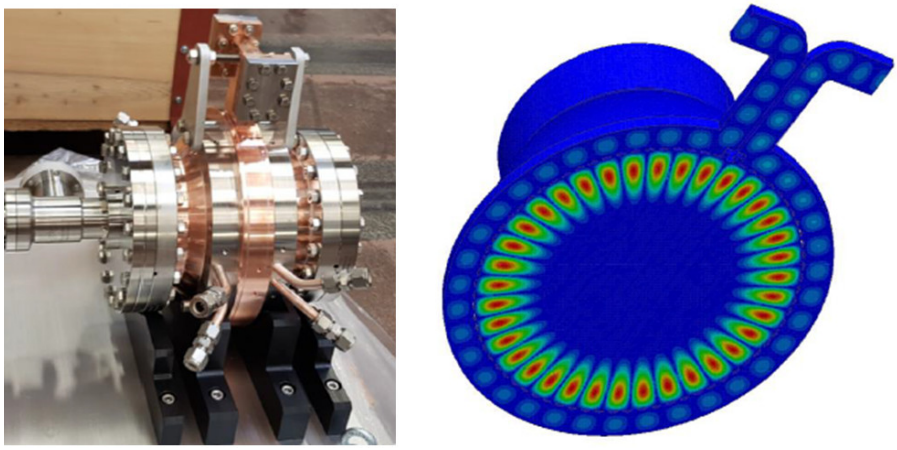

Figure 6.17: Picture of the X-band BOC (left); electromagnetic field configuration of the BOC operating mode $TM_{18,1,1}$ [14].

Table 6.3: Parameters of the X-band Canon klystron E37119.

Parameter	Unit	Value
Frequency	GHz	11.9942
Beam Voltage (V_k)	kV	320
Cathode current (I_k)	A	200
Peak RF output Power	MW	25
Average RF output power	kW	15
RF pulse length	µs	1.5
Repetition rate	Hz	0-400
Gain	dB	49
Efficiency	%	40
Preveance	µP	1.16

precision of better than 0.05 mm in all directions, according to the beam dynamics requirements (Chapter 3). The details of the support of the X-band structure are given in Fig. 6.19. This support is made of a rectified "V"-shaped granite support detailed in Fig. 6.20 that allows to maintain the straightness of the accelerating structure at the level of ±30 µm. This granite support is fixed to an aluminum plate that allows a regulation with a precision better than 0.05 mm in all directions.

6.9 Magnetic chicane

The schematic layout of the magnetic chicane between the low and high X-band energy linacs is given in Fig. 6.21. As illustrated in Section 3.3, the magnetic compression is used in the X-band full RF accelerator case. A C-shape chicane with rectangular dipoles has ben considered, and the parameters have been chosen in order to minimize the emittance dilution due to the Coherent Synchrotron Radiation in the bends. At the same time the chicane length has been kept as short as possible. To allow for different compressions factors for the different working points the central magnets of the chicane and the vacuum chambers are mounted on a movable support that allows to change the bending angle from 0 to 4°. The 3D CAD details is given in Fig. 6.22. A diagnostic screen chamber (Sec. 11.2.5) is foreseen at the center of the chicane, and five stripline BPMs

Table 6.4: Parameters of the Solid state pulsed Modulator.

Parameter	Unit	Value
Peak power	MW	78.2
Average Power	kW	94.4
Voltage range	kV	0-340
Current range	A	0-230
Repetition rate	Hz	0-400
Top Flatness	$\pm$% s	1.0
Pulse to pulse stability rms (max)	ppm	20
Rate of rise	kV/µs	<306
Rate of fall	kV/µs	<303
Trig delay	µs	≈ 1.2
Pulse to pulse time jitter	ns	$< \pm 4$
Pulse width time jitter	ns	$< \pm 8$

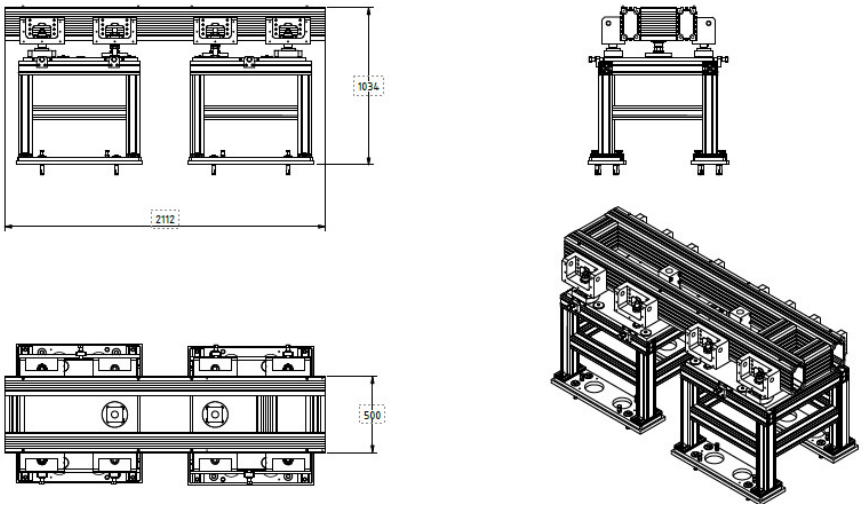

Figure 6.18: Girder of the X-band module supporting the two X-band structures and components.

(Sec. 11.2.3) are planned to be integrated into the quadrupoles. The main parameters of the magnetic chicane are given in Table 6.5.

6.10 Conclusions and Technical Readiness Level

The goal of this chapter has been to describe the X-band linac in terms of its layout, components, and main parameters. All components of the linac have been clearly defined and fabricated. They are currently undergoing high-power RF testing at the Frascati X-band Test Facility (TEX) [11]. Table 6.6 finally summarize the Technical Readiness Level (TRL) of the X band linac components.

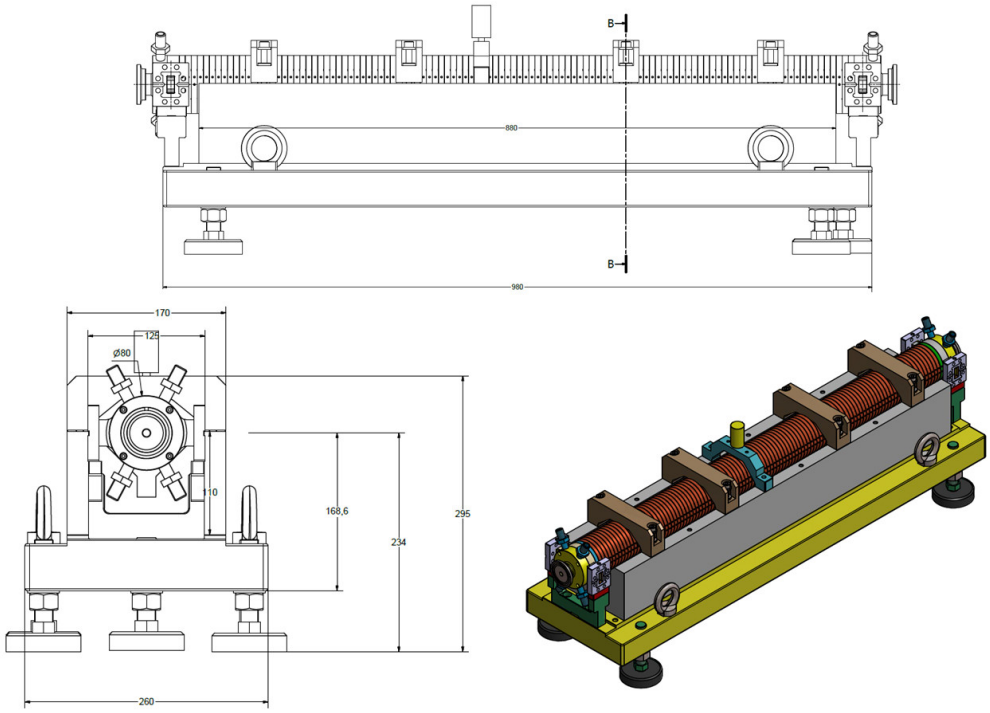

Figure 6.19: Support of the X-band structure.

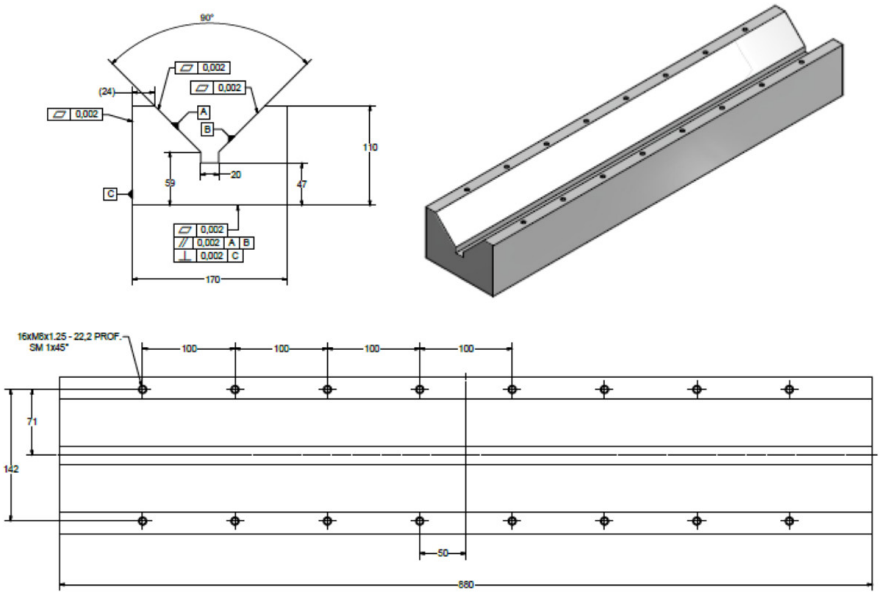

Figure 6.20: Detail of the granite support of the X-band structure.

Table 6.5: Parameters of the magnetic chicane.

Parameter	Unit	Value
Beam Energy at chicane entrance (Echic)	GeV	0.67
Total chicane length (LC1)	m	6.3
Internal magnetic chicane length (LC2)	m	0.9
Dipole magnetic length (LM)	m	0.35
Chicane variable angle (θ)	deg	0-4
First order momentum compaction (R56)	mm	30
Second order momentum compaction (T566)	mm	25
Maximum dispersion at chicane center (η MAX)	m	0.18

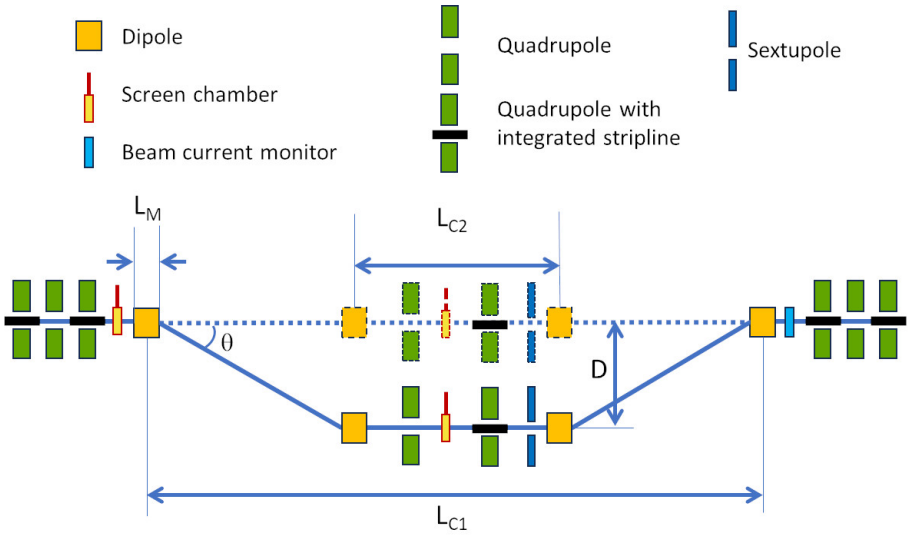

Figure 6.21: Schematic layout of the magnetic chicane.

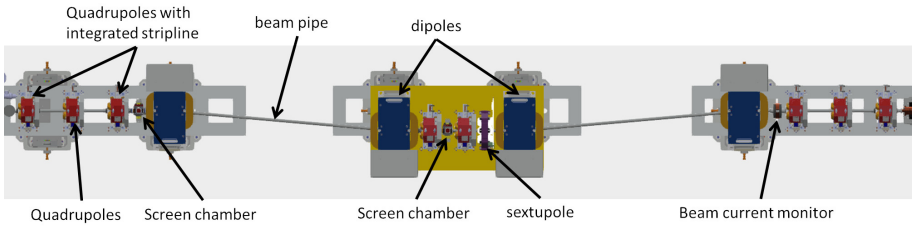

Figure 6.22: Layout of the magnetic chicane.

Table 6.6: TRL of the X band linac.

Sub - systems	TRL	Comments
X band Power Source	6	Commercially available (Scandinova Modulator and Canon klystron) ready to be tested at TEX to reach the nominal parameters
X band structure	6	In-house design. Final full-scale prototype ready to be tested. 20-cell prototype successfully tested with uncompressed pulse at 50 Hz, tuning free technology to be finalized
Mode converter rectangular-circular waveguide	8	In-house design. Prototype fabricated and tested at 21 MW, 50 Hz, 1 µs(nominal 25 MW, 100 Hz, 1.5µs)
Pumping unit circular waveguide	8	In-house design. Prototype fabricated and tested at 21 MW, 50 Hz, 1 µs(nominal 25 MW, 100 Hz, 1.5 µs)
Pumping unit rectangular waveguide	7	CERN Design. Prototype tested at 45 MW, 1 µs, uncompressed pulse, 50 Hz. Needs to be tested at 100 Hz with compressed pulse 70-35 MW, 0.13 µs
Directional coupler	7	CERN Design. Prototype tested at 45 MW, 1 µs, uncompressed pulse, 50 Hz. Needs to be tested at 100 Hz with compressed pulse 70-35 MW, 0.13 µs.
BOC pulse compressor	6	PSI design. Device ready to be tested with the nominal power source at TEX. Device already tested in other laboratories, but at reduced repetition rate and peak power.
3dB splitter	6	CERN Design. Fabricated, to be tested at TEX at nominal full power. Already tested in other lab but at a reduced power.
RFf load	8	Fabricated and tested at nominal peak and average power (50 Hz, 0.6 µs)

Bibliography

[1] Z. D. Farkas et al. “SLED: A method of doubling SLAC’s energy”. In: *Proc. Of 9th Int. Conf. On High Energy Accelerators, SLAC*. 1974, p. 576.

[2] M. Diomede et al. “Preliminary RF design of an X-band linac for the EuPRAXIA@ SPARC_LAB project”. In: *Nuclear Instruments and Methods in Physics Research Section A: Accelerators, Spectrometers, Detectors and Associated Equipment* 909 (2018), pp. 243–246.

[3] M. Diomede. “High-gradient structures and rf systems for high brightness-electron linacs, PhD Thesis”. In: https://iris.uniroma1.it/handle/11573/1357033 (2020).

[4] C. Vaccarezza et al. “EUPRAXIA@ SPARC_LAB: Beam dynamics studies for the X-band Linac”. In: *Nuclear Instruments and Methods in Physics Research Section A: Accelerators, Spectrometers, Detectors and Associated Equipment* 909 (2018), pp. 314–317.

[5] URL: https://www.ansys.com/it-it/products/electronics/ansys-hfss.

[6] V. A. Dolgashev. “High magnetic fields in couplers of X-band accelerating structures”. In: *Proceedings of the 2003 Particle Accelerator Conference*. Vol. 2. IEEE. 2003, pp. 1267–1269.

[7] F. Cardelli et al. “Preliminary results on X-Band structures for the Eupraxia@SPARC_LAB project”. In: *14th International Particle Accelerator Conference*.

[8] URL: https://www.saesgetters.com/highvacuum/solution/nextorr-hv/.

[9] N. Catalan-Lasheras et al. “High Power Conditioning of X-Band RF Components”. In: *Proc. 9th Int. Particle Accelerator Conf.(IPAC’18)*. 2018, pp. 2545–2548.

[10] F. Cardelli et al. “Preliminary R&D on X-band components for the X-band based user facility EuPRAXIA@SPARC_LAB”. In: *The European Physical Journal Special Topics* (2025). DOI: 10.1140/epjs/s11734-025-01828-0. URL: https://doi.org/10.1140/epjs/s11734-025-01828-0.

[11] S. Pioli et al. “TEX-an X-Band Test Facility at INFN-LNF”. In: *12th Int. Particle Accelerator Conf.(IPAC’21), Campinas, Brazil*. 2021.

[12] C. Di Giulio et al. “TEX (TEst stand for X-band) at LNF”. In: *arXiv preprint arXiv:2308.03053* (2023).

[13] S. G. Tantawi et al. “Evaluation of the TE 12 mode in circular waveguide for low-loss, high-power rf transmission”. In: *Physical review special topics-accelerators and beams* 3.8 (2000), p. 082001.

[14] P. Craievich et al. “Novel X-band transverse deflection structure with variable polarization”. In: *Phys. Rev. Accel. Beams* 23 (11 2020), p. 112001. DOI: 10.1103/PhysRevAccelBeams.23.112001. URL: https://link.aps.org/doi/10.1103/PhysRevAccelBeams.23.112001.

7. Plasma Accelerating Module

7.1 Introduction

This chapter provides a detailed description of the design of the plasma module that will be implemented at EuPRAXIA@SPARC_LAB. Figure 7.1 shows an overview of the plasma vacuum chamber and the magnetic optics, starting from the end of the X-band linac and up to the driver-witness separation chicane. While the electromagnetic quadrupoles are located upstream and downstream of the vacuum chamber, the permanent magnet quadrupoles (PMQ) are hosted directly into it. The overall performances of the plasma module have been validated with the start-to-end simulations reported in Chapter 3, especially in terms of the longitudinal plasma density distribution and related stability.

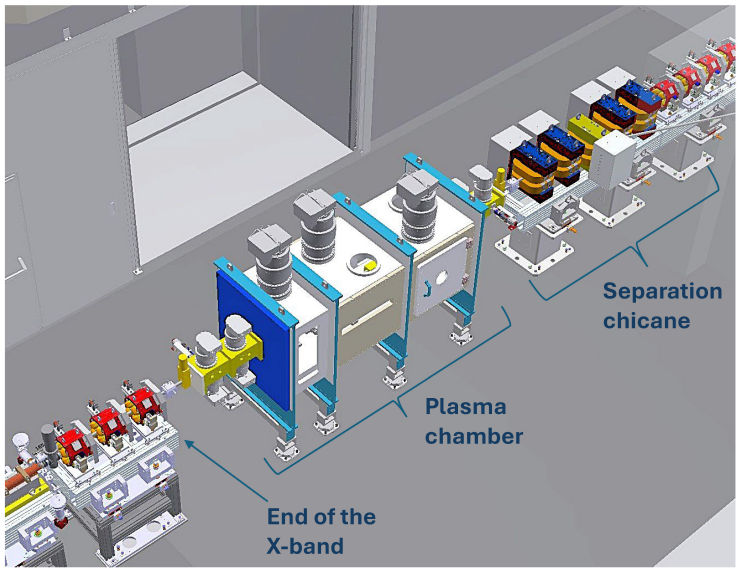

Figure 7.1: Plasma module zoomed view in the accelerator layout.

7.2 Plasma module design

Figure 7.2 shows the entire apparatus used for the plasma formation, control and characterization. The plasma is confined in a cylindrical capillary with 60 cm length and 2 mm diameter and is generating by ionizing Nitrogen gas. The ionization is achieved by using high-voltage discharge pulses applied to two tungsten electrodes, located at the capillary ends. The plasma generation process and its evolution are controlled by tuning the discharge current and the nitrogen gas pressure, by means of a fast electro-mechanical valve, in order to adapt longitudinal and transverse plasma density profiles as required by the electron beam matching. High-voltage pulses for the ionization of the neutral gas column are produced by a RLC pulser circuit, in turn fed by a high-voltage generator. The plasma module includes a diagnostics system for the plasma characterization, which is based on a spectroscopic technique, relying on the Stark effect, for the measurement of the electron plasma density distribution within the plasma channel (see Section 7.5). Shot-to-shot stability is strictly required in a FEL radiation user facility. In order to improve it, the high-voltage plasma discharge is stabilized by triggering the ignition with an external laser pulse (see Section 7.2.4). In such a way the resulting discharge-current timing and plasma density jitters are reduced below 1%.

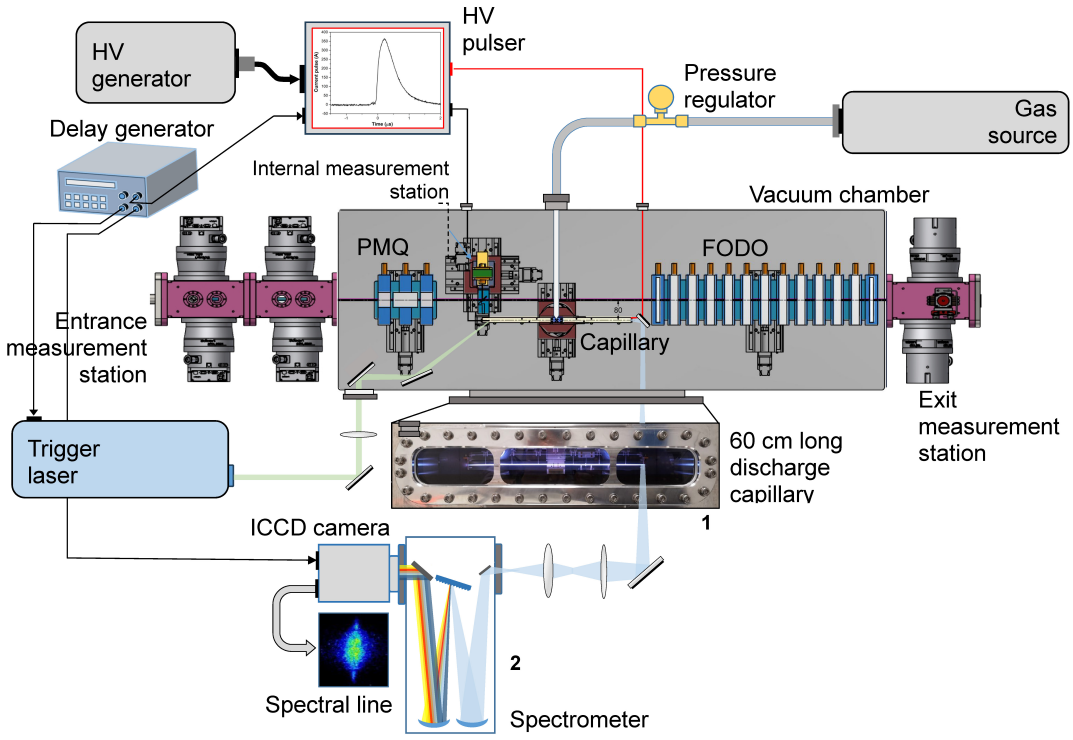

Figure 7.2: Schematic representation of the plasma module. A picture of a 60 cm long gas-filled discharge capillary (1) is shown in this scheme. The plasma diagnostics is based on the Stark broadening technique, for which the emitted plasma light is collected into an imaging spectrometer allowing to measure the spectral wavelengths of the hydrogen Balmer series (2).

Considering that a nominal repetition frequency of 100 Hz is foreseen for EuPRAXIA@SPARC_-LAB, with the possibility of reaching 400 Hz in the future, an appropriate design of all the components (vacuum chamber, capillary and high-voltage discharge pulser) has been carried out. Such working conditions, indeed, require the injection of considerable amounts of gas in the capillary, which must be removed by the vacuum pumping system, carefully designed to meet the vacuum requirements in the experimental chambers. The technical configuration of the plasma chamber pumping system is presented in Section 7.4. Beam matching and extraction systems are discussed

in Section 7.3. Figure 7.3 provides a detailed representation of the layout of the chamber, housing the plasma source.

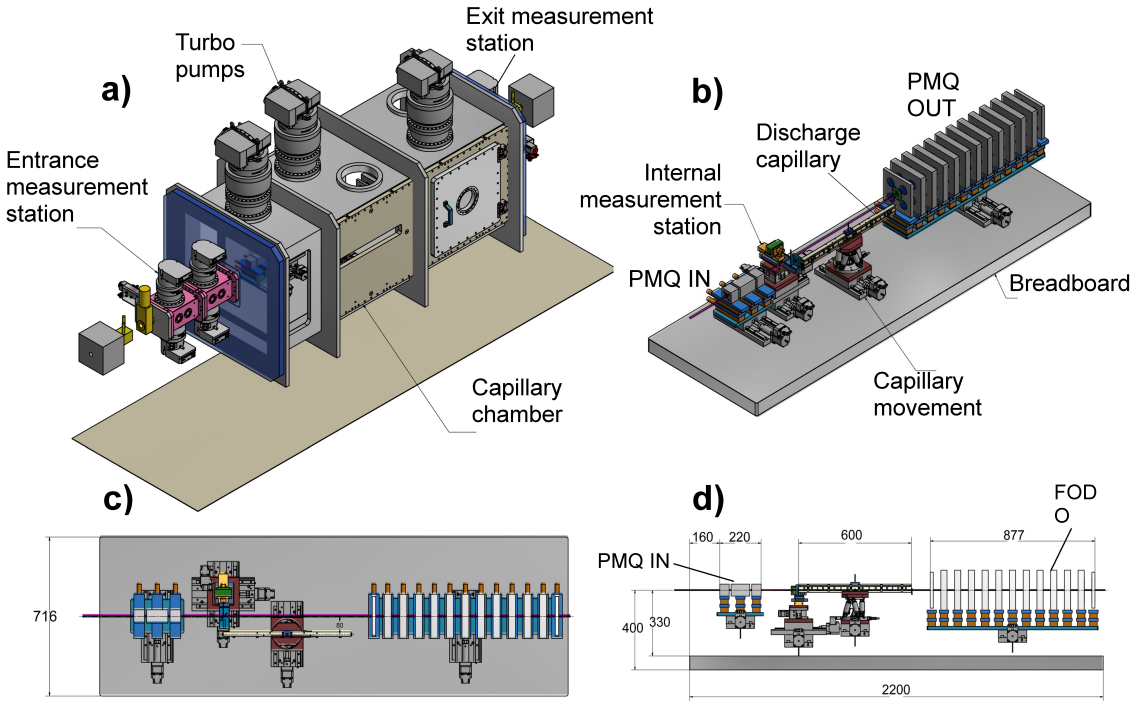

Figure 7.3: Plasma source housing chamber. a) Chamber external view. All turbo pumps are mounted on the top of the chamber. Two small auxiliary chambers are positioned upstream and downstream to accommodate the entrance and exit beam diagnostics. b) Chamber inside view: a PMQ triplet is positioned at the entrance and a FODO cell at the exit. c) Top view and d) side view of the internal elements of the plasma chamber.

The main chamber (see Figure 7.2 and 7.3) is designed to house the three main components of the plasma module: the gas-filled discharge capillary, a PMQ triplet at the entrance and a FODO cell at the exit, which are respectively used to match the beam at the capillary entrance and capture it after plasma acceleration. The plasma source is 60 cm long with a single gas feed connected to a horizontal service injection pipe, which in turn supplies the vertical injectors (see Section 7.2.1). These injectors, ranging between 8 and 15, depending on the desired plasma profile, are used to feed the channel for the plasma formation, with the possibility of shaping them according to the requirements of uniformity of the neutral gas (and plasma) distribution. In addition, two small side chambers housing the beam diagnostics (described in Section 7.5) are located upstream and downstream of the plasma-accelerating stage. Six additional turbo pumps are installed in these chambers, four in the entrance chamber and two in the exit chamber, to maintain the nominal pressure level in the X-band linac sections and in the undulator vacuum chambers.

The discharge capillary is equipped with a fine alignment system consisting of a hexapod and a horizontal translation, while all the PMQs and the FODO cell have dedicated positioning systems. Moreover, an internal diagnostics station for the characterization of the incoming beam is placed between the PMQs and the capillary entrance, as described in detail in Chapter 11.

7.2.1 Plasma sources

The main component of the plasma accelerating module is the 60 cm long discharge capillary with 2 mm diameter cylindrical cross section, whose key design parameters are discussed in this section and summarized in Table 7.1.

Key design parameters for the plasma discharge capillary source	
Source type	Gas-filled discharge capillary
Geometry	60 cm in length 2 mm in diameter
Gas (continuous flow)	Nitrogen
Gas pressure	10-20 mbar
Discharge repetition rate	100 Hz
Discharge circuit parameters	15 kV, 500 A
Materials	Channel: Sapphire, Shapal Holder: Macor Electrodes: Tungsten
Plasma density	$10^{15} \div 10^{17}$ cm^{-3}
Lifetime	$> 1 \times 10^8$ shots
Shot-to-shot stability	$< 1\%$ rms plasma density jitter with laser stabilization

Table 7.1: Plasma source key parameters

The plasma source has been designed relying on Computational Fluid Dynamics (CFD) simulations of the neutral N_2 gas distribution, performed with the open source code OpenFOAM [1]. The use of nitrogen gas represents a compromise between the ease of extraction by the pumping system and the low ionization energy required to ionize it. Figure 7.4 shows two different geometric configurations, designed to test the modularity of the longitudinal gas (and plasma) density profile, and simulated with the injection of 100 mbar of pure N_2 in continuous flow regime. The first configuration is shown in Figure 7.4a. The capillary design involves the use of 10 gas injectors with the same diameter of 1 mm, with closer spacing towards the extremities of the capillary in order to counteract the rapid loss of gas at the ends. The simulation of the corresponding longitudinal gas density profile is shown in Figure 7.4c (green curve), characterized by a central "flat-top", with a 10% density variation over 25 cm from the center towards the outer region of the capillary, and an overall 80% density decrease from the central peak to the capillary extremities. The second configuration, shown in the Figure 7.4b, is characterized by the same number of gas injectors in the same positions as the previous case, but with increasing diameter towards the extremities. In this second case, the longitudinal gas density profile, reported in Figure 7.4c (blue curve), shows a higher uniformity in the central region, with less than 10% density variation over 45 cm, and an overall center-to-exit density decrease of 60%. Both solutions include a 2 mm diameter plasma channel and an upper service tube parallel to the plasma channel, connecting all injectors. As described above, both the position and size of the injectors are key elements to control the longitudinal gas distribution, on which the plasma electron distribution depends.

Such simulations show that the capillary geometry, in particular the neutral gas injection system, allows to control the longitudinal profile of the plasma density, which is a crucial factor for

achieving the accelerating gradients of around 1 GeV/m described in Section 3.2.

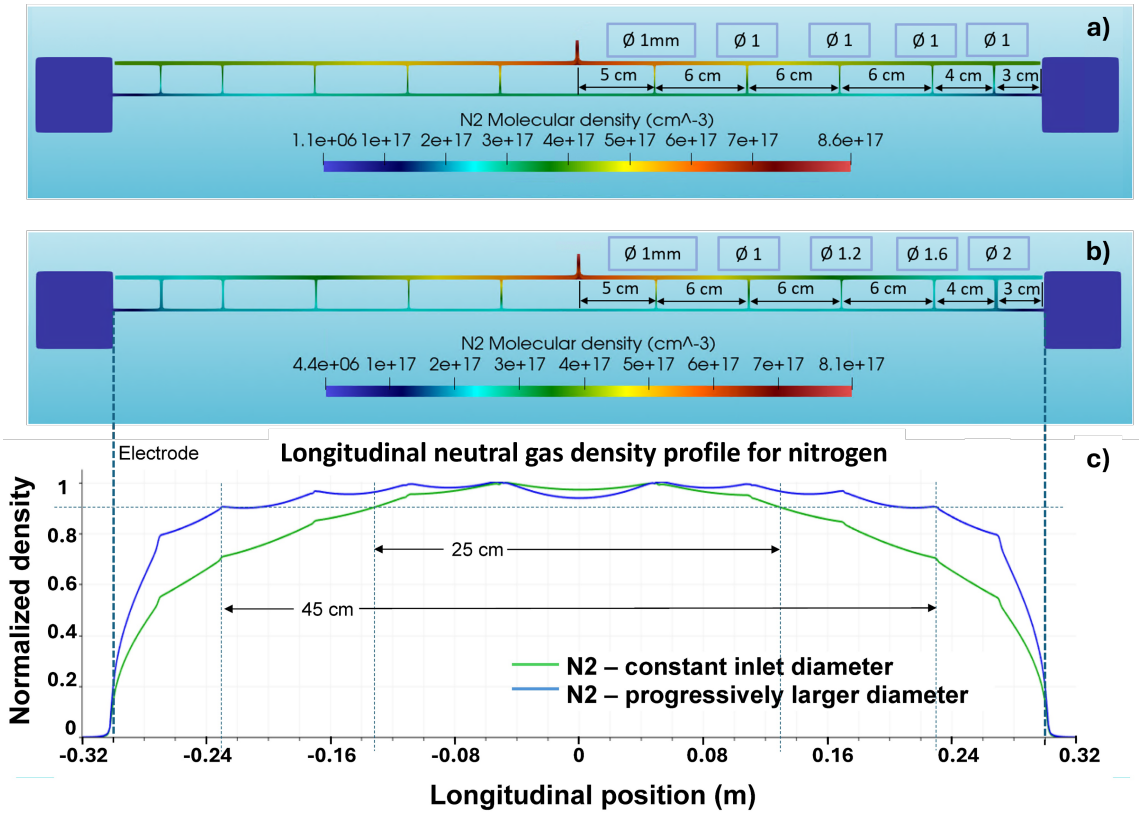

Figure 7.4: Numerical design of 60 cm long discharge capillaries performed with CFD simulations. a) Capillary design composed of ten gas injectors with the same diameter of 1 mm, b) Capillary design composed of ten gas injectors with increasing diameter towards the extremities, c) Longitudinal nitrogen density profiles for both solutions.

The design of the 60 cm-long discharge capillary is depicted in Figure 7.5, based on previous studies concerning the distribution of neutral gas within the capillary channels. The adopted technical solution relies on simulation results, concerning the tunability of the longitudinal profiles, and other aspects related to the operating conditions, such as the capability of reaching high repetition rates above 100 Hz, as well as reliability and cost-effectiveness.

The device is composed of two different sections, as shown in the figure: a holder onto which the gas feeding tube and electrodes are attached, and an inner supporting structure composed of two horizontal and ten vertical blocks, hosting the channels for the gas injection and the plasma formation. The two components of the capillary are made of different materials. The holder is made of *Macor*®, a ceramic material which remains stable at 800 °C, with a maximum operating temperature of 1000 °C, and unlike ductile materials, it does not creep or deform. *Macor* is easy to machine and offers tight tolerances capabilities, allowing complex shape design (tolerances up to ±0.013 mm). Its coefficient of thermal expansion is 1.46 W/m·K. This insulating material is chosen because it can be easily machined and at the same time it can withstand the heat flux produced by the plasma. The inner supporting structure for gas injection and plasma channel confinement, on the other hand, is made of *Shapal*, a ceramic material that is more resistant to thermal stress, although it is less easy to machine than *Macor*. *Shapal* is a hybrid type of Aluminum Nitride (AlN) ceramic that offers high mechanical strength and high thermal conductivity (92 W/m·K at 25 °C). Its properties result particularly useful for the dissipation of the thermal energy deposited by the plasma discharge onto the confinement structure, thus avoiding severe damage of the device.

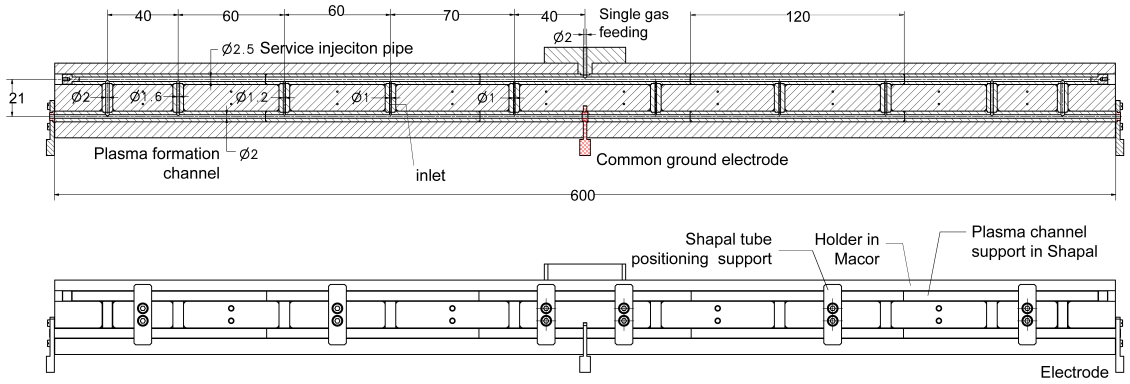

Figure 7.5: Design of the 60 cm long discharge capillary, composed of an external holder, connected to the gas injection pipe and the electrodes, and an internal support structure, into which the gas injectors and the plasma confinement channel are created.

The suitability of such ceramic materials for long-term high repetition rate operation is discussed in more detail in the Section 7.2.2. As shown in the Figure 7.5, the 60 cm-long support structure is sectioned into five parts, each with a length of 12 cm (Figure 7.6a), in order to fabricate the device by machining both the inlets and the plasma formation channel. Figure 7.6a shows a plastic implementation of the 60-cm-long capillary, in which the two structures that compose it, i.e. holder and internal support structure, are highlighted. *Macor* and *Shapal* materials will be used for the final version of the plasma source (Figure 7.8). Figure 7.6b represents a picture of the gas-filled discharge capillary during the plasma formation process to test basic parameters, such as pressure, voltage, gas injection system and synchronization.

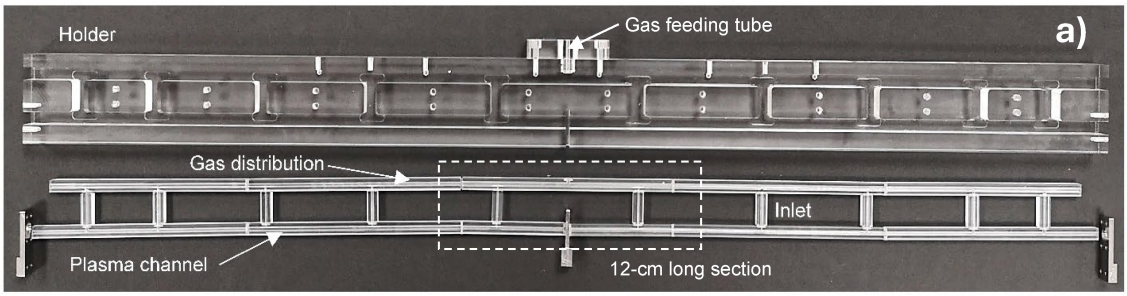

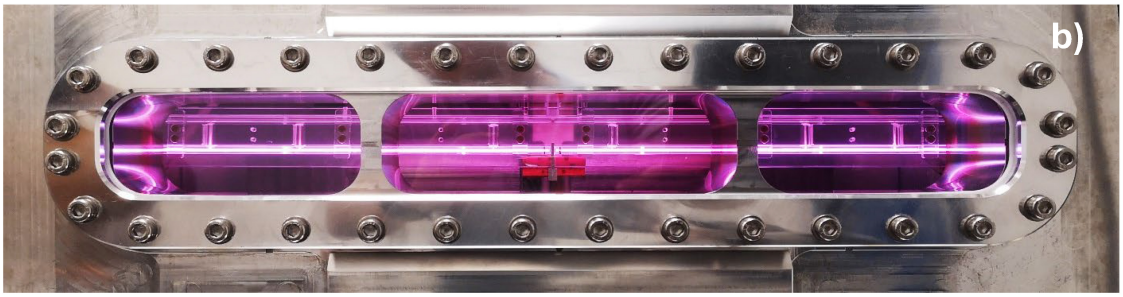

Figure 7.6: 60 cm-long gas-filled discharge capillary. a) Single components before the capillary assembly. b) Plasma discharge generated after the assembly.

Figure 7.7a presents the experimental characterization of the discharge capillary. The figure reports the comparison between the measurements of the longitudinal plasma density, taken over

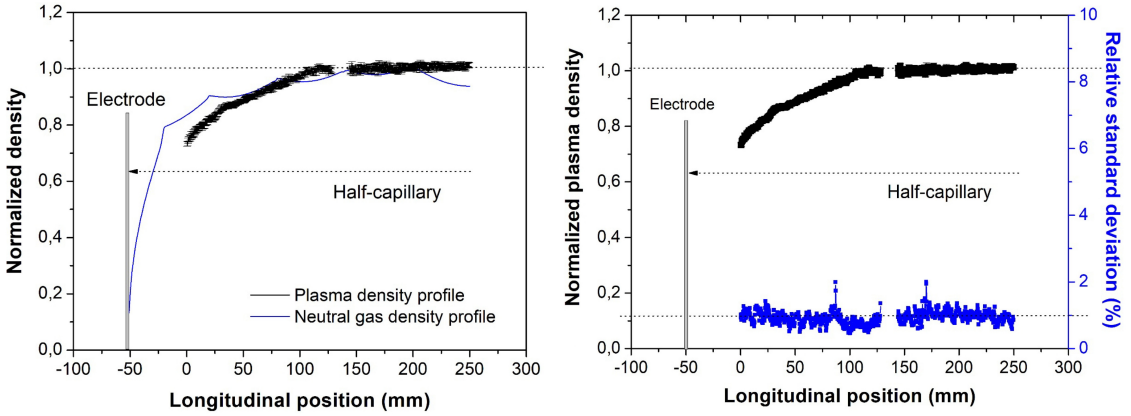

Figure 7.7: Characterization of a 60 cm-long capillary equipped with inlets having an increasing diameter toward the ends. a) Comparison of the longitudinal plasma profile measured using the Stark broadening technique with simulations of the N_2 gas distribution (blue curve in Figure 7.4). b) Longitudinal plasma density and relative standard deviation.

half of the capillary length, and the neutral gas simulations used in the capillary design (described in Figure 7.4c), corresponding to the configuration with injectors having progressively increasing diameters. Given the symmetry of the device, the longitudinal profiles were acquired over only half of the capillary. However, since the total length of the capillary exceeds the observation window of the experimental test chamber, the measurements of the longitudinal plasma profiles do not include the outermost 50 mm, which are instead visible in the simulated neutral gas curves. From the comparison, it emerges that the neutral gas profiles provide a good approximation of the longitudinal plasma distribution, successfully predicting both the uniform central region and the decreasing ramps. Figure 7.7b shows the longitudinal plasma density profile along with the standard deviation calculated with respect to the measured average density. This parameter, obtained by performing a statistical analysis over 2000 acquired images of the Balmer H_β spectral line, describes the shot-to-shot stability of the plasma formation process, which remains confined within approximately 1%, as required by beam physics simulations.

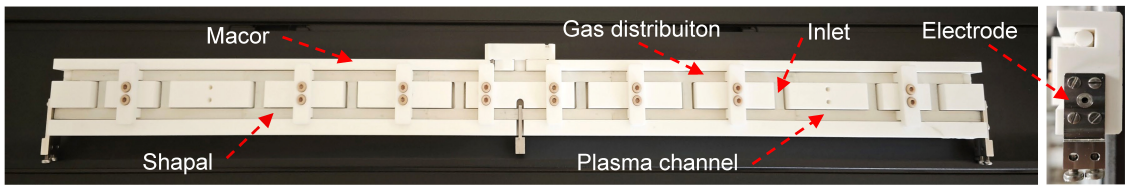

Figure 7.8: Final construction of the gas-filled discharge capillary in Shapal/Macor. The project is a copy of the prototype built in plastic, on which operational tests and characterization of the plasma properties were carried out.

Figure 7.8 illustrates the 60-cm-long gas discharge capillary, fully fabricated from ceramic materials, specifically *Shapal* for the plasma and auxiliary channels, and *Macor* for the supporting structure. In order to reproduce the ideal plasma density profile described in Section 3.2, characterized by 10 cm-long squared cosine density ramps at the entrance and exit of the plasma channel and a 40 cm-long central plateau, an optimized capillary geometry has been designed, as shown in Figure 7.9a. The optimized device includes 8 gas injectors with increasing diameter towards the exit (from 1 mm to 2 mm) and a channel shaping to create the squared cosine ramps, with a widening from 2 mm to 3 mm in the outer 5 cm of the channel at both sides. In addition, Figure 7.9b reports

a direct comparison between the ideal plasma density profile and the molecular nitrogen density profile simulated with such capillary geometry.

The neutral nitrogen gas has been simulated with an injection pressure of 100 mbar, resulting into a molecular density profile in the range of $1 \div 3 \times 10^{17}$ cm^{-3}, which matches the operating conditions foreseen for the discharge capillary, with plasma density peaks of around 1×10^{17} cm^{-3}. On the other hand, the working point for electron beams acceleration foresees a plasma density of around 9.5×10^{15} cm^{-3} (central plateau), as discussed in Section 3.2, which is reached during the plasma recombination into neutral nitrogen. Such operating conditions allow to precisely tune the plasma density, characterized by a slow time variation in the recombination phase, by means of a proper temporal synchronization with the arrival time of electron beams. For this reason, the comparison between simulated nitrogen gas and ideal plasma density is obtained by normalizing both longitudinal profiles to the respective density peaks. As shown in the figure, the optimized geometry, with 8 gas injectors and channel widening at the capillary ends, provides a neutral gas distribution that suitably fits the plasma profile required for electron beams acceleration. Hence, such geometric configuration will be adopted for the final capillary device, realized in *Macor* and *Shapal*.

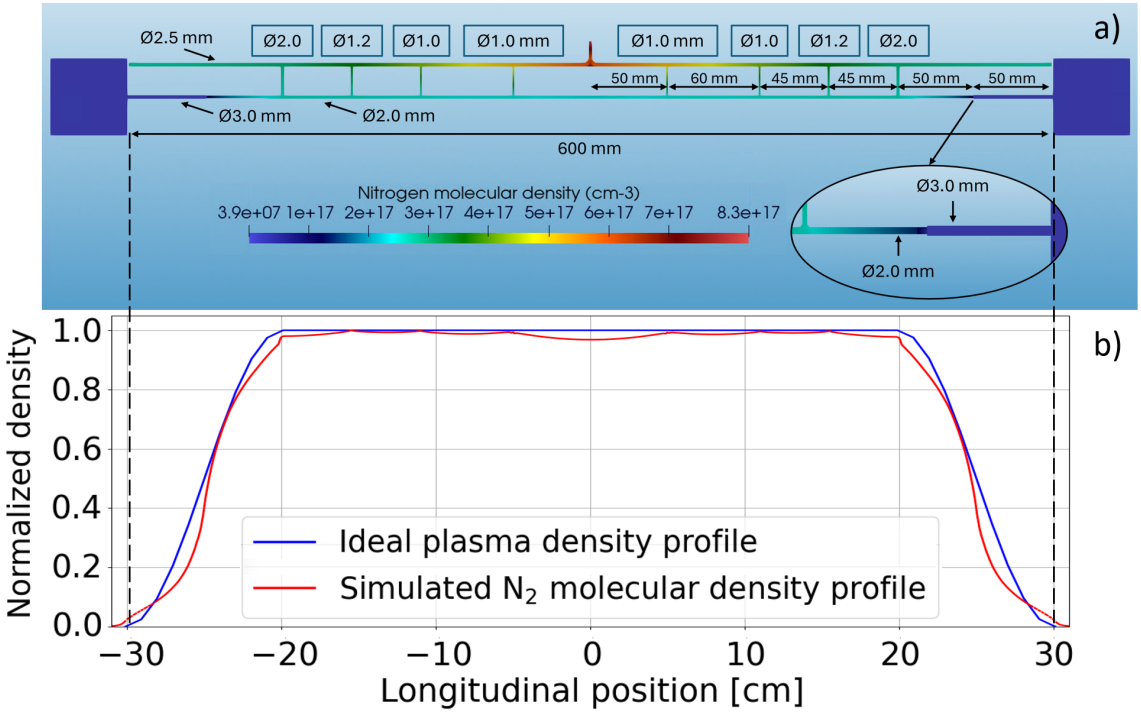

Figure 7.9: Numerical design of the 60 cm long gas-filled discharge capillary to reach the final energy of 1 GeV. a) 2D nitrogen density distribution showing the geometrical design of the capillary, constituted by 8 inlets, whose diameter ranges from 1 to 2 mm, and a widening of the horizontal channel diameter from 2 mm to 3 mm in the outer 5 cm of the channel at both sides. b) Comparison between the ideal plasma density profile described in Sec. ??, with squared cosine ramps and a 40 cm long density plateau, and the simulated nitrogen density profile.

In conclusion, we showed how to control the longitudinal density profile of the plasma by adjusting (i) the geometry of the capillary, in particular the neutral gas injection system, (ii) the high-voltage pulse used to ionize the neutral gas and (iii) the neutral gas pressure. The latter one, in particular, is set by means of the pressure regulator shown in the Figure 7.2, which directly connects the gas source with the discharge capillary.

7.2.2 High repetition rate operation

The standard working conditions include the operation at a repetition rate of 100 Hz, with the possibility to reach 400 Hz. The main potential limitation to the operativity of the discharge capillaries is represented by the erosion of the walls material, exposed to the heat power deposited by the plasma discharge. The erosion of the capillary walls results in a change of the shape of the plasma formation channel and consequently a variation in the electron distribution of both longitudinal and transverse plasma density profiles. As a result, this effect alters the matching conditions between the particle beams and the plasma channel. The erosion of the capillary walls depends on several design factors of the plasma source, including the diameter of the channel and the current used for plasma formation, which affects the plasma temperature and the heat flux to the capillary walls. Indeed, Equation 7.1 of the quasi-static model of the plasma discharge, developed by Bobrova [2], describes the temperature reached on the capillary axis as a function of the current density flowing through the plasma channel during the arc discharge, i.e. as a function of the peak current and the channel radius:

$$T_p[eV] = 5.27 \times \left(\frac{Ipeak[kA]}{r[mm]} \right)^{2/5}, \tag{7.1}$$

with typical values of 1-10 eV (tens of thousands of Celsius degrees) resulting from peak currents of hundreds Amps in capillaries with 1-2 mm diameter. Therefore, the use of materials capable of dissipating high amounts of thermal energy, that is, with high thermal conductivity k (defining the heat flux as $\mathbf{q} = -k(T)\nabla T$), plays a crucial role for operating at high repetition rate. Materials such as sapphire or diamond show high values of this parameter (about 40 W/m·K for sapphire and up to about 2400 W/m·K for diamond at 25 °C), but they are unsuitable for the fabrication of thin channels where gas can be injected and plasma created, because of their poor machinability and high costs.

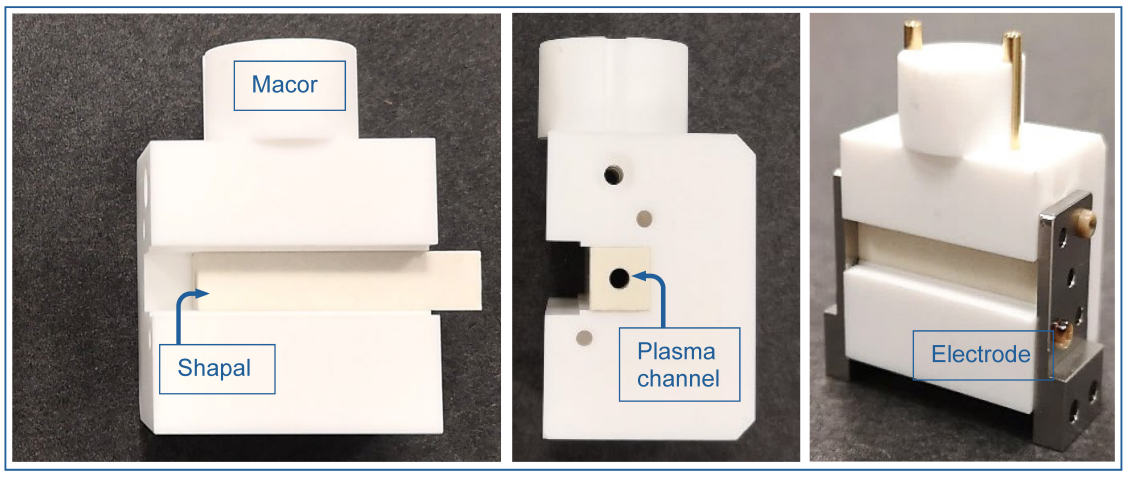

Figure 7.10: Image of basic elements that make up the test sample of the gas-filled discharge capillary for high repetition rate operation. The holder is composed of *Macor* ceramic and the support for the plasma formation channel is made of *Shapal* ceramic. The plasma formation channel is 30 mm in length and 2 mm in diameter.

For these reasons, as described in the previous section, the choice of materials for the realization of the discharge capillaries lead to *Macor* and *Shapal*. Both materials exhibit excellent machinability, low cost, and high melting temperatures. In addition, *Shapal* shows twice the thermal conductivity of sapphire, specifically 92 W/(m·K) at 25 °C.

Testing of a gas-filled discharge capillary composed of *Macor-Shapal* ceramics has been performed by producing plasma discharges for up to 20 millions of shots at repetition rates from 30 Hz to 150 Hz, corresponding to around 55 hours of operation, with the aim of assessing the capability of the ceramic capillary to sustain the heat flux produced by the plasma in long-term high repetition rate operation, and hence its lifetime [3]. Figure 7.10 shows a 3 cm-long 2 mm-diameter gas-filled discharge capillary made of *Macor-Shapal* ceramic, used for high repetition rate tests. Since the plasma channel is opaque, the presence of possible deformations in its structure is investigated both through microscopic analysis and by observing the alterations of a laser beam propagating longitudinally through the channel. A Compact Laser Module (Thorlabs) is employed to observe any geometrical variation in the capillary channel cross section, eventually caused by erosion of Shapal. The laser beam enters the capillary with a spot size larger than the channel diameter and is guided through the beam transport line to an intensified CCD camera, positioned on the imaging spectrometer of the diagnostic line.

A mirror implemented inside the spectrometer guides the laser beam into the ICCD camera. In this way, the shape of the laser spot image, acquired by the camera, is directly related to the capillary wall profile and any variation represents a deformation of the capillary. Figure 7.11 shows the comparison between the laser spots acquired after traversing the capillary channel without plasma, for both the newly installed capillary (zero discharges produced) and after performing 2×10^7 discharges, working at a repetition frequency varied from 30 to 150 Hz. Using this technique, laser spots were acquired at different stages of capillary aging, as shown in Figure 7.12, where the vertical and horizontal profiles of the laser spots are compared. This comparison shows that there are no changes for the transverse dimension of the laser spots, demonstrating that after such a number of discharges no alteration is observed in the geometrical profile of the capillary channel.

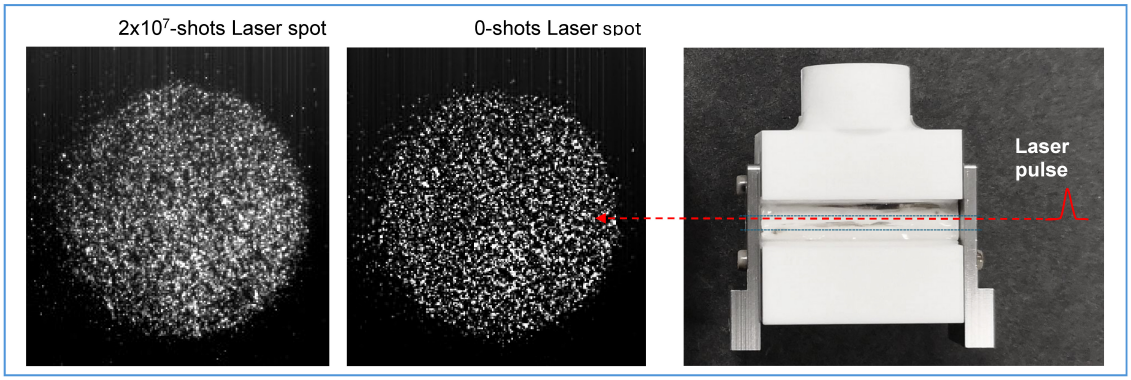

Figure 7.11: Comparison of laser spots to assess the deterioration of gas-filled discharge capillary made in *Macor-Shapal* ceramics before and after performing 2×10^7 shots at up to 150 Hz.

A second diagnostic tool, used to evaluate the deterioration of the Shapal, is based on acquiring microscope images at various positions along the plasma channel, again before and after producing 2×10^7 discharges. This microscopic analysis is performed by means of an optical stereomicroscope (Euromex) to characterize the entire channel profile with high precision, scanning the transverse cross section along the capillary channel to assess if any deformation is present due to *Shapal* erosion. Figure 7.13 reports the capillary channel profile measured by the optical microscope before and after the experimental testing at high repetition rate. For each longitudinal position, the reported diameter is obtained by measuring the cross section diameter both in the horizontal and vertical planes and computing the average, in order to take into account possible deformations that would determine a transverse elliptical shape. Measured error bars result from 200 acquired images. As shown in Figure 7.13a, the normalized channel diameter is close to unity along the entire longitudinal profile, proving that the capillary channel is well preserved after 20 million

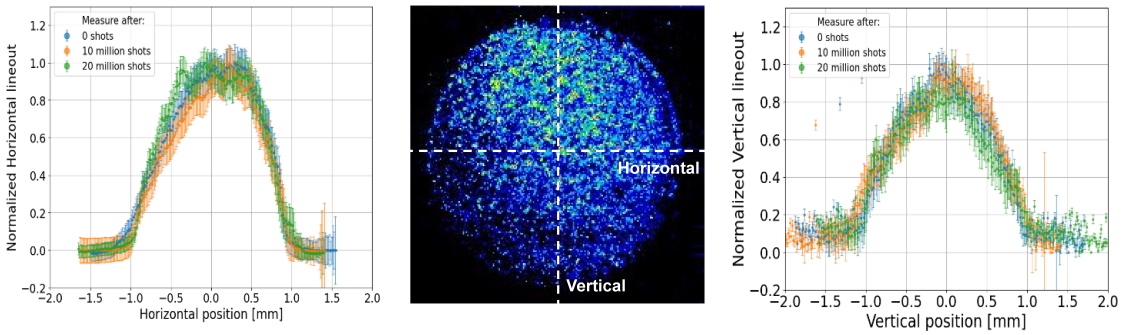

Figure 7.12: Measurement of the laser spot deformation as a function of the number of plasma discharges, up to 2×10^7 shots, produced inside the gas-filled Shapal capillary to assess its degradation.

plasma discharges at up to 150 Hz.

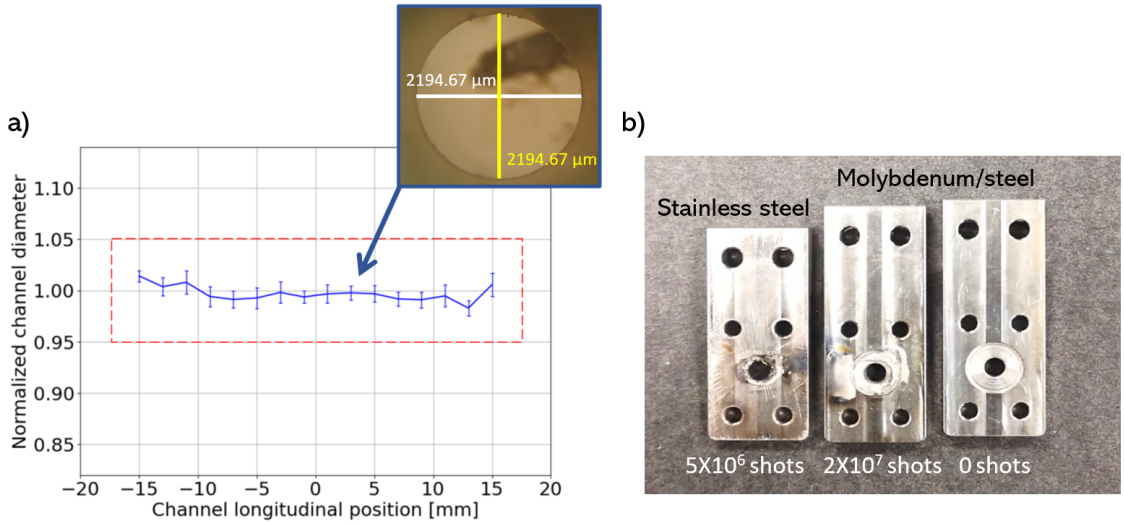

Figure 7.13: a) Longitudinal profile of the capillary channel cross section, measured after 20 million shots at 30-150 Hz and normalized to the channel profile measured at 0 shots. The insert shows a microscopic image acquired from the capillary center, in which the cross section diameter is computed by the average of the horizontal and vertical measurements, that in this case are coincident. b) Comparison between different electrode configurations, tested at high repetition rate with the ceramic capillary. The use of an inner disk made of molybdenum allows to better preserve the integrity of the electrodes after 20 million shots.

In addition, Figure 7.13b shows a comparison between different electrodes tested together with the Shapal capillary at up to 150 Hz. Stainless steel electrodes are strongly damaged by exposure to the plasma after only 5×10^6 shots. On the other hand, the use of an inner molybdenum disk, inserted into a stainless steel plate and directly exposed to the plasma, allows to better preserve the integrity of the whole electrode after 2×10^7 discharges, thanks to the high melting temperature of molybdenum (2623 °C). Based on such experimental results, the final design of the 60 cm long plasma source will involve, together with ceramic materials, also electrodes entirely made of high melting temperature metals, such as molybdenum or tungsten.

7.2.3 High-Voltage discharge pulser

The high-voltage source, providing the energy to ionize the neutral gas and generate the plasma, consists of a high-voltage generator and a pulser circuit, composed essentially of a resistor-capacitor circuit, as depicted in Figure 7.14. In the pulser circuit, in addition, a high-voltage solid state switch (SCR, semiconductor controlled rectifier) is inserted to regulate the voltage pulse formation. To reach the required plasma density, 10÷15 kV voltage pulses are required, with plasma currents on the order of 400÷500 A. The high-voltage generator must be chosen to be capable of charging the capacitor C to the voltage required for ionization of the 60-cm-long gas column at repetition rates in the range of 100÷400 Hz. For the latter purpose, it is important to consider the use of high-voltage generators capable of providing average output currents I larger than 200 mA, working at the nominal ionization voltages of up to 15 kV. Indeed, such current affects the capacitor charging time required for each shot, given by $t_C = Q/I$, where Q is the amount of charge required to reach the ionization voltage V, with $Q = CV$. Therefore, the maximum theoretical repetition rate is proportional to $f = 1/t_C = I/Q$. The circuit design involves the use of a capacitance of 40 nF, by which the maximum current value achievable is about 2.5 kA using 20 kV voltage from the high-voltage generator. Such values represent the measured characteristics of the real current pulse produced; the inductive components are not taken into account in the circuit diagram. These parameters ensure a minimum repetition rate larger than 100 Hz, which represents the starting operating frequency foreseen for the FEL source. In any case, the value of the current pulse achievable during the plasma ionization process depends essentially on the pressure and length of the gas column in the source.

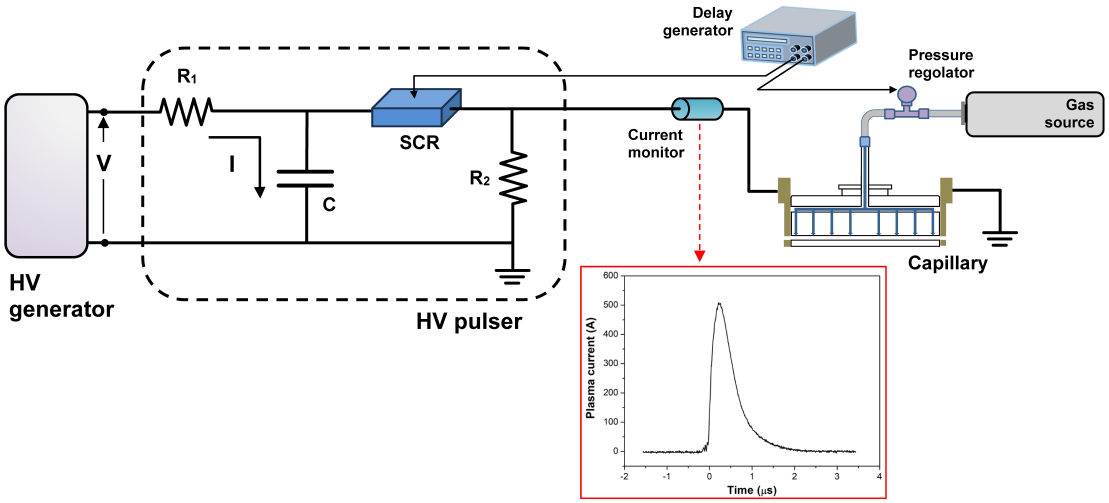

Figure 7.14: High-voltage source designed for plasma creation inside gas-discharge-filled capillaries. There are three different parts: the high-voltage generator that supplies power to a pulser consisting of an RC circuit that, in turn, is capable of producing high-repetition frequency current pulses (100-400 Hz) and a load represented by the plasma source.

The characterization of the high-voltage source is shown in Figure 7.15. Figure 7.15a shows the current-voltage characteristics measured in short-circuit configuration and with a 40 cm-long capillary connected to the pulser circuit. In the voltage range 5-25 kV, the peak current spans from a few hundred amperes up to 1.5 kA with the discharge capillary, and up to 2.5 kA in short-circuit. The reduced current observed with the capillary is attributed to the electrical resistance of the plasma channel, which increases with capillary length. Figure 7.15b shows a typical current waveform acquired with an oscilloscope for 11 kV pulses applied to the 40 cm-long, 2 mm-diameter capillary,

filled with 20 mbar of N_2 gas. The pulser circuit itself has no intrinsic electronic limitations for operation at the required repetition frequencies, since the high-voltage source generates pulses with a duration of about 1 µs, as shown in Figure 7.15b. The only constraint on high-repetition-rate operation is the thermal load on the SCR switch. Adequate air cooling is sufficient up to ∼100 Hz, whereas oil cooling is required to reach 400 Hz.

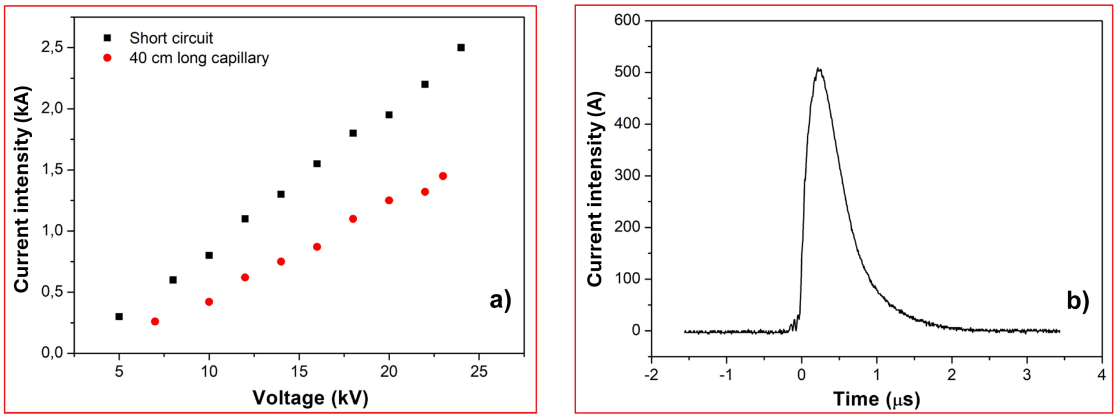

Figure 7.15: High-voltage source characterization: a) Current pulse peak, measured at the output of the pulser circuit as a function of the generator voltage, under short-circuit conditions (black squares) and closed circuit conditions on a 40-cm-long gas-filled discharge capillary (red circles); b) Single current profile measured at the output of the pulser circuit with 11 kV generator voltage, when the circuit is closed on a 40-cm-long capillary.

7.2.4 Plasma discharge stabilization

Due to the stochastic behavior of electrical discharges, the instant of the voltage breakdown is affected by an intrinsic time jittering, which results in a shot-to-shot variation of the plasma density at the arrival time of the electron beams. In order to stabilize the plasma formation and thus produce high quality accelerated beams, the plasma module includes a laser system for triggering the electrical discharge, as shown in Figure 7.2. Indeed, a laser pulse, impinging onto the negative capillary electrode few tens-hundreds of ns before the high-voltage discharge, allows to control the production of the first free electrons that onset the electrical breakdown, thus resulting in a remarkable reduction of the time jitter and an enhancement of the shot-to-shot stability [4].

For the purpose of showing the usefulness of the laser discharge ignition technique, measurements of current pulses with and without the use of the stabilizing laser pulse are reported in Figure 7.16. A 3 cm-long hydrogen-filled capillary has been employed, using a laser energy of 80 mJ and approximately 200 µm spot sizes at the capillary entrance. The corresponding laser intensity is on the order of 10^{10} W/cm^2. The laser beam, used to pre-ionize the gas [5, 6], is focused into the gas near the negative electrode by means of an optical system. It should be noted that such laser pulses are not able to ionize the entire hydrogen gas column, but they only create first free electrons to ignite the high voltage discharge along the capillary, according to the laser collisional absorption model [7]. Figure 7.16(a) shows 50 consecutive current discharge waveforms acquired by means of a digital scope at 1 Hz repetition rate. A large shot-to-shot variation of the plasma current shape is observed when the laser is switched off, while keeping the voltage stable at 5 kV. In this case, the current amplitude changes from 70 to 110 A, with RMS amplitude jitter of 10.7 A, and also its starting time jitters by tens of nanoseconds, with RMS time jitter of 32 ns. On the contrary, by turning on the laser (with 80 mJ energy), the discharge waveform becomes very reproducible, as shown in Figure 7.16(b), while maintaining the same value of the discharge voltage at 5 kV. The

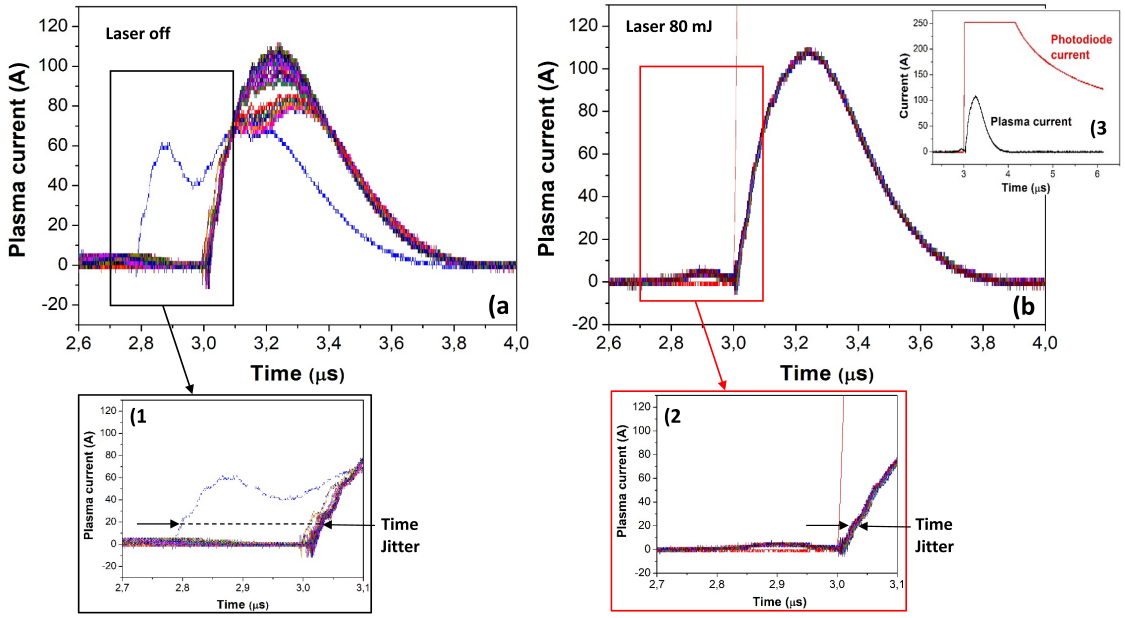

Figure 7.16: Current discharge waveforms obtained with laser turned off (a) and on with 80 mJ pulse energy (b). Each plot shows a set of 50 measurements obtained by applying 5 kV between the capillary electrodes. Insets 1) and 2) show the time jitter without and with the use of the stabilizing laser, respectively. The inset 3) shows the laser pulse signal measured with a photo-diode.

RMS amplitude oscillation is now 1 A and the RMS rising edge time-jittering is around 1.7 ns.

7.3 Plasma chamber integration in the accelerator layout

In this section a brief overview of the magnetic optics upstream and downstream of the capillary is provided. More details can be found in the dedicated chapters of the TDR (Chapter 17.6).

7.3.1 Beam transport upstream and downstream of the vacuum chamber

The operation of a plasma-based accelerator requires the beams to be transversely handled both upstream and downstream of it. Indeed, the accelerated witness bunch usually emerges from the plasma with a rather large divergence that may cause an increase of its emittance [8]. Moreover, in the case of a beam-driven plasma-wakefield accelerator, the witness bunch must be focused at the plasma entrance to transversely match the plasma [9]. These tasks are performed with a triplet of permanent-magnet quadrupoles (PMQ), that allow to reach very large magnetic gradients (order of hundreds of T/m) and, in turn, very short focal lengths [10]. In our case, numerical simulations indicate that a witness spot size of ≈ 1.5 μm with a Twiss-β function $\beta_{eq} \approx 2.4$ mm satisfies the matching condition. This can be accomplished using PMQs with 7 mm diameter aperture, 300 T/m average gradient and 5-10-5 cm magnetic lengths (see Table 17.13).

7.3.2 Focusing and extraction quadrupoles

The reduction of the bunch transverse dimensions is accomplished by means of a triplet consisting of three small-bore PMQs, each one made of several magnetized segments combined in circular arrays. They currently represent the state-of-the-art since it has been demonstrated that PMQ-based focusing systems are able to provide field gradients as strong as 560 T/m when employing neodymium-iron-boride (NdFeB) materials [11]. Similarly, to catch the plasma accelerated witness and the energy-depleted driver bunches, an array of thirteen consecutive PMQs is foreseen. In this

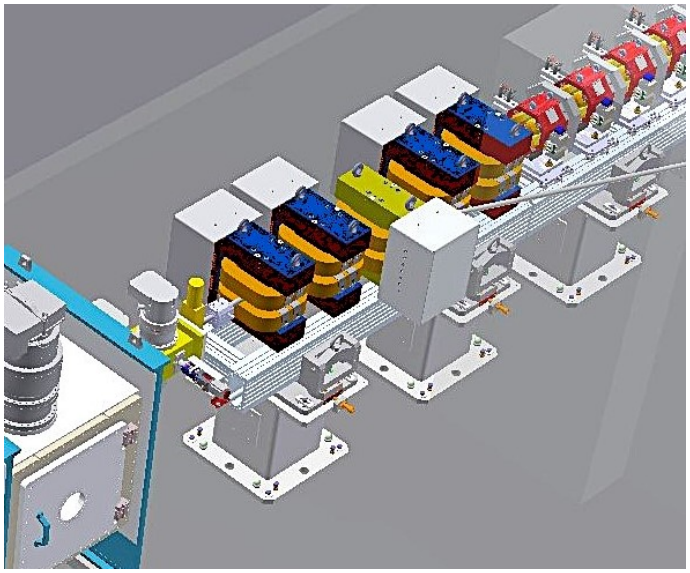

Figure 7.17: Layout of the chicane line where the energy-depleted driver is spatially separated from the witness beam. The driver is then transported up to the beam dump.

case the primary goal is to remove the large divergence of the witness bunch while, at the same time, keeping a large enough acceptance for the energy-depleted driver bunch, ensuring its transport out of the plasma vacuum chamber. This layout is shown in Figure 7.3(b). Figure 7.17 shows the layout of the magnetic chicane located downstream of the plasma chamber, whose purpose is to separate the energy-depleted driver from the plasma-accelerated witness bunch. The chicane consists of four bending magnets and it is able to spatially separate the driver bunch by several millimeters from the witness beam trajectory. The driver bunch is then transported to the beam dump while the witness bunch is guided to the downstream undulators.

7.4 Vacuum pumping system

Plasma wakefield acceleration involves injecting a certain amount of gas into specifically designed chambers, that are typically located near radio frequency accelerating sections. Given the high repetition frequencies expected for such plasma-based accelerator (100-400 Hz), gas injection into the plasma source needs to be performed in continuous flow regime, since commercial electro-mechanical valves are not able to support such high frequencies, due to their ms-scale activation times. This results in a large amount of injected gas that needs to be removed from the plasma source chamber by means of a proper vacuum pumping system, whose ability to maintain acceptable vacuum levels in the chamber plays a crucial role. Indeed, while the gas quantities are on the order of 10-12 mbar·l/s in continuous flow injection, a minimum vacuum level of $5-8\times10^{-9}$ mbar is required in the X-band accelerating sections, located approximately 2-meters away from the plasma source chamber. Less stringent conditions are required on the side facing the FEL, around 10^{-8} mbar. Such a request strongly affects the entire plasma module design, both chamber geometry and vacuum pumping system, since during the plasma formation at densities useful for the acceleration (between 10^{16} and 10^{17} cm^{-3}) we need to reach pressures up to 50 mbar inside the plasma sources.

The gas injection inside the discharge capillary (2 mm in diameter and 60 cm in length) is controlled by means of a pressure regulator placed between the N_2 gas tank and the plasma source itself (as shown in Figure 7.2). Figure 7.18 shows in a simplified way the vacuum pumping system needed to meet the requirements given above. For this purpose, a differential pumping technique has been adopted, separating the plasma module chamber into three pumping sections.

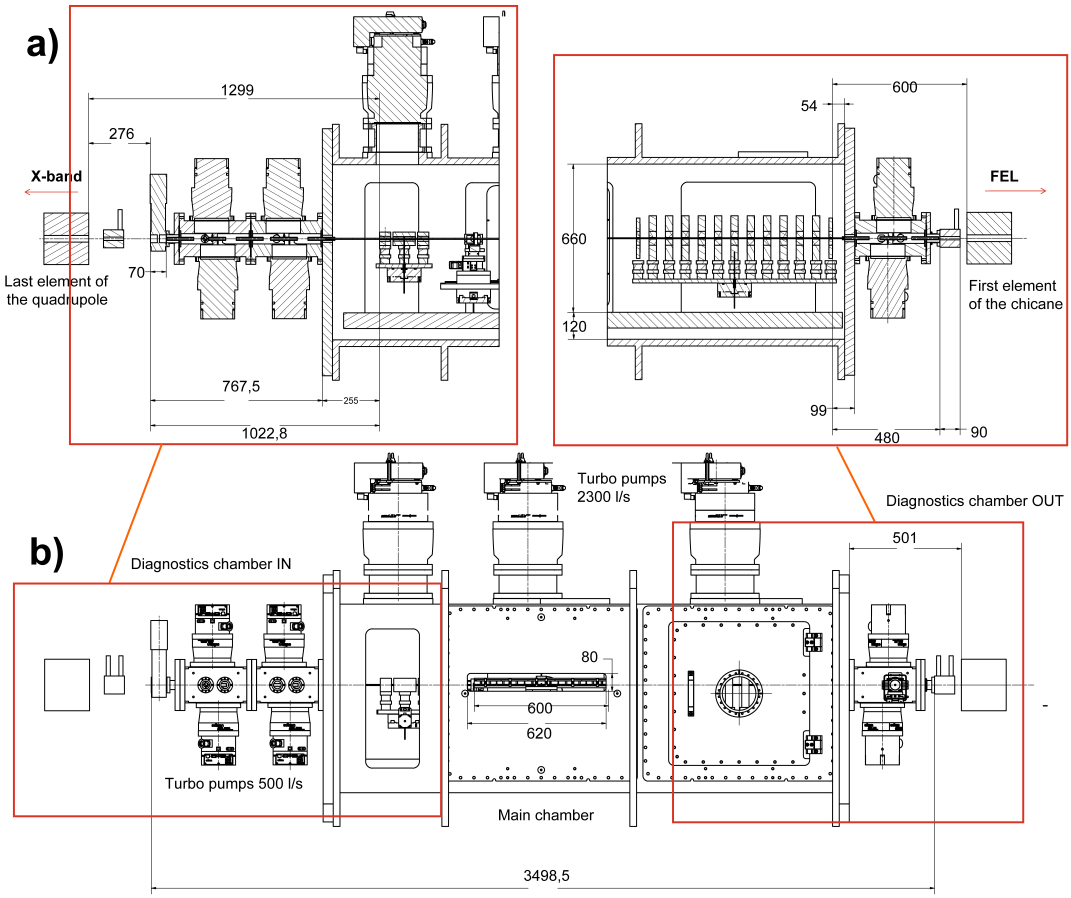

Figure 7.18: Plasma chamber and vacuum pumping system. a) Detailed view of the side chambers containing beam diagnostics and mounting part of the vacuum pumping system. b) Overview of the plasma chamber.

There is a main chamber, i.e. the capillary chamber, where the gas-filled discharge capillary, diagnostics and magnets for focusing and beam extraction are mounted, as well as two side buffer chambers, referred to as diagnostics chambers IN and OUT, in which additional turbo pumps are installed to further cut the gas flow to the outer sections, such as the X-band sections on one side and the undulators on the other. These two side chambers are also used to house beam diagnostic instruments (see Section 7.5.2). In addition, given the role of user facility, the workload for the vacuum pumping system is very high and, as a result, each pump installed in the chamber needs to be equipped with an auxiliary water cooling system.

The following is a brief description of how the pumping system, consisting of elements reported in the Table 7.2, is able to maintain the required vacuum values in the most sensitive work zone, i.e. that of the X-band accelerating sections. On the FEL side, where reduced pumping is used compared to the X-band side, the vacuum levels can still be extrapolated from the presented analysis.

A schematic representation of the sizing of the vacuum pumping system towards the X-band structures is shown in Figure 7.19. The flow entering the capillary chamber for plasma production is about Q_0 = 10-12 mbar·l/s. Considering the use of two turbo pumps (T_{R1} and T_{R2}), with nominal suction speed S = 2100 l/s (the actual speed is about S_e = 1200 l/s, as it depends on the working pressure P_0), it is possible to maintain the pressure in the capillary chamber at the value $P_0 = Q_0/(2 \cdot S_e) = 5 \times 10^{-3}$ mbar. Starting from these values in the capillary chamber, a second

Vacuum pumping system design	
Gas	Nitrogen
Turbo pumps	$3-5\times 2300$ l/s
Turbo pumps	$6-8\times 500$ l/s
Primary pumps	$2-5\times 480$ m^3/h multi-stage roots pumps
Water cooling system	3-5 chillers Nominal flow rate 20-30 l/min and cooling capacity 4500 W

Table 7.2: Vacuum pumping system design

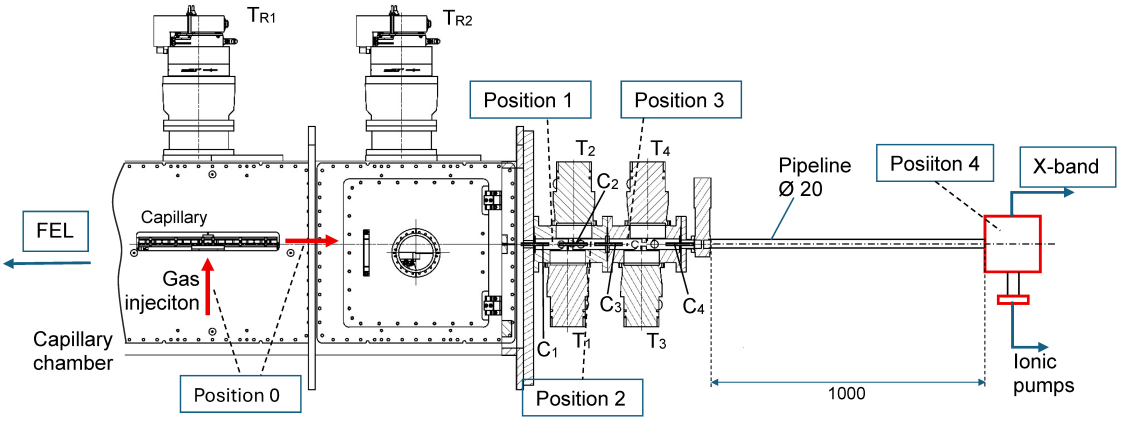

Figure 7.19: Sizing of the vacuum pumping system under the most stringent conditions near the X-band, based on continuous nitrogen gas injection for plasma production in a 60-cm long capillary.

pumping station with the possibility of mounting up to four turbo pumps (T_1 - T_4) with nominal (actual) suction speed S = 350 l/s (S_e = 280 l/s), is used to reach the vacuum level reduction till the requested values in the X-band structures. Indeed, the joint work of turbo pumps together with four vacuum impedances (C_1 - C_4), with a diameter of 12 mm and a length of 120 mm, allows a cascade reduction of the flow rate and pressure according to the relationships $Q_1 = P_0 \cdot C_1 = 3\times 10^{-2}$ mbar·l/s and $P_1 = Q_1/S_1 = 1\times 10^{-5}$ mbar, and so on until the vacuum value required by the specifications is reached (Q_4, P_4). The vacuum impedance can be expressed as $C = 12.1\cdot(d^3/L)\cdot\alpha$, where d is the diameter of the hole, L the length and α an empirical coefficient. Table 7.3 shows a simulation of the behavior of the vacuum system when subjected to the required gas injection. Regarding the FEL side, considering a pumping system up to the third station, together with the vacuum system designed downstream of the plasma chamber, it is plausible to consider achieving a vacuum level on the order of $7-9\times 10^{-9}$ mbar.

The vacuum chambers and pumping system are designed to make the plasma module flexible in anticipation of future applications requiring larger gas flow conditions, as well as the use of lighter gases such as hydrogen and helium. Indeed, more turbo pumps and additional impedance can be installed (T_4 and C_4 were not used to obtain the data in the Table 7.3) in order to handle larger gas flows than those just considered. As a final consideration, it should be noted that the primary pumps that collect the gas expelled from the turbo pumps, directly connected to the vacuum chamber, have to be at least two and provide a nominal suction speed of 480 m^3/h each, in order to avoid gas accumulation between the turbo pumps and the primary pumps.

7.5 Diagnostics

This section describes the diagnostics foreseen for the plasma interaction area. The diagnostics can be separated in two main categories: (i) the diagnostics of the plasma source and (ii) the diagnostics of the electron beams. Details are provided in the following.

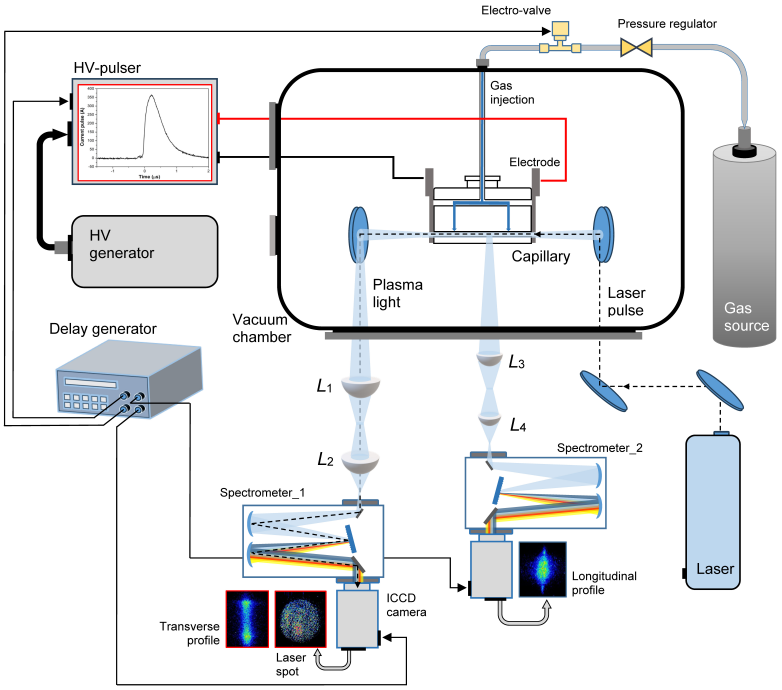

Figure 7.20: Experimental setup installed in the *Plasma_lab* of the INFN-LNF, used to implement the Stark broadening technique to characterize the gas-filled discharge capillaries.

7.5.1 Plasma source diagnostics

This section describes the experimental setup currently used for the characterization of the plasma sources, as shown in Figure 7.20. Through this setup, it is possible to measure the plasma properties required for discharge capillaries, such as stability, density, and temporal evolution. Longitudinal and transverse plasma density profiles presented in this section, used to describe the Stark broadening method, refer to a plasma source composed of 3D-printed capillaries with lengths of 3 cm and 60 cm, each featuring a 1–2 mm diameter channel. The capillaries are filled with

Vacuum pumping system sizing		
Position	**Pressure (mbar)**	**Gas flow (mbar·l/s)**
0	5×10^{-3}	12
1	1×10^{-5}	3×10^{-2}
2	4×10^{-8}	1×10^{-5}
3	3×10^{-10}	8×10^{-8}
4	1×10^{-11}	2×10^{-10}

Table 7.3: Vacuum pumping system sizing for Nitrogen gas injected in continuous flow. Reported positions refer to those indicated in Figure 7.19.

hydrogen gas, supplied through two symmetric inlets in the shorter capillary and through a more complex injector system in the 60 cm-long one.

The gas is produced by an electrolytic generator and injected through a pressure regulator and an electro-mechanical valve with 3-5 ms aperture time. The pressure inside the capillary is on the order of 10-50 mbar. The capillary is installed inside the vacuum chamber, operating at 10^{-5} mbar when the repetition rate is 1 Hz and at around 10^{-3} mbar in continuous flow injection, which is performed to operate with high repetition rate discharges in the range 100-150 Hz. Two electrodes are attached to the capillary ends and connected with a high-voltage discharge pulser, providing up to a maximum current value around 2 kA with 20 kV voltage [12]. The emitted light is then collected both from the front and the side of the capillary into two different imaging spectrometers, equipped with an intensified camera, allowing to retrieve the longitudinal and the transverse density profiles of the plasma channel (as shown in Figure 7.21). For opaque materials, such as *Shapal* and *Macor*, the light is collected only from the side, so the transverse density distribution is directly measured, while longitudinal density profiles are determined with transparent capillaries having identical geometric configurations.

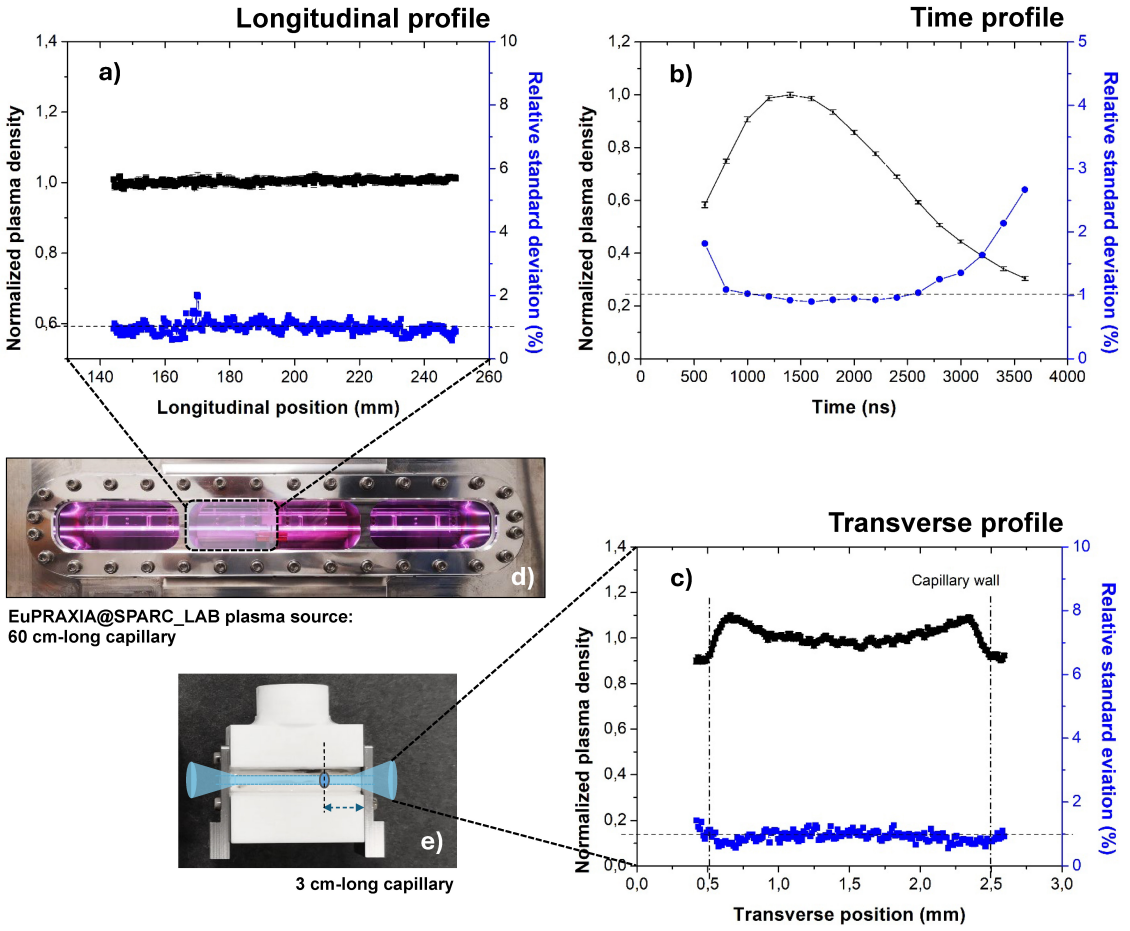

Figure 7.21: Characterization of gas-filled discharge capillaries: a) Longitudinal plasma profile obtained for 60 cm long capillary by using the optical line 2; b) Longitudinal plasma profile measured as a function of the plasma recombination time for 60 cm long capillary; c) Transverse plasma profile obtained for 3 cm long capillary by using the optical line 1; d) Measurement area for 60 cm-long capillary: e) Measurement area for 3 cm-long capillary.

The measurement of the plasma density profiles is performed by employing a spectroscopic

technique based on the Stark-broadening effect [13]. In the visible range, the emission spectrum of the ionized hydrogen plasma is characterized by a series of spectral lines at different wavelengths (the Balmer series). In the presented characterization, we select one specific wavelength of the Balmer series, centered at 486.1 nm (H_β), and, by measuring its spectral line width, the plasma electron density n_e is retrieved as [14, 15]:

$$n_e[cm^{-3}] = 8.02 \times 10^{12} \left(\frac{\Delta\lambda_{1/2}}{\alpha_{1/2}} \right)^{3/2}, \tag{7.2}$$

where $\Delta\lambda_{1/2}$ is the full width at half maximum (FWHM) of the spectral line in Angstroms and $\alpha_{1/2}$ is a parameter, related to H_β line, whose values are tabulated for different ranges of plasma densities and temperatures [16]. According to Equation 7.2, a wider (thinner) spectral line corresponds to a larger (smaller) plasma density. The emitted light is thus imaged onto the camera so that the x-axis represents the spectral wavelength and the y-axis the longitudinal or transverse coordinate of the capillary. The imaging system allows to perform single-shot measurements of the entire capillary over a spatial extension of about 5 cm, thus also the density of the plasma plumes outside the capillary can be measured. Finally, by delaying the camera trigger with respect to the discharge one, snapshots at different times can be acquired, allowing to measure the temporal evolution of the plasma density during the plasma formation and recombination in neutral gas.

The transparent implementation of the 60 cm-long capillary was tested using the optical Line 2 to investigate the plasma's longitudinal behavior, while the transverse diagnostics, crucial for characterizing opaque materials, is illustrated through results obtained on 3 cm-long capillaries. Both profiles exhibit shot-to-shot stability better than 1%, measured by acquiring 1000 images for each time delay.

7.5.2 Electron beam diagnostics

This section gives a brief description of the beam diagnostics installed in the area of the plasma source chamber, shown in Figure 7.22. A more detailed description of their operation is provided in the Chapter 11.

Three distinct measuring stations are used to characterize the particle beams: one inside the chamber at the entrance of the plasma capillary (Figure 7.22c), and two just outside the chamber, at the entrance and exit, shown in Figures 7.22b) and 7.22d), respectively. The beam diagnostics at the entrance of the discharge capillary include a wire scanner system, which allows to measure very small spot sizes, on the order of few microns. In this position, there is a longitudinal movement capable of covering up to approximately 10 cm, which is used for the focal point assessment, and two transverse movements, the first for positioning the wire scanner reticle in front of the beam and the second for its fine movement. In the entrance measurement station, the one located before the electron beams enter the plasma acceleration section, a measurement system based on the electro-optical sampling (EOS) technique is installed, which is used to analyze the longitudinal charge density of the ultrashort electron beams, required for the plasma acceleration experiments. Finally, in the exit measurement station, which is smaller than the first one, a series of scintillating targets are mounted for characterizing the electron beams with and without plasma.

7.6 Plasma module safety system

Operation of the beamline follows a strict protocol to protect personnel, equipment and the facility. Safety measures are integrated into all stages of the beamline operations, including experimental and maintenance activities. Below are some more detailed directions regarding safety regulations for some components of the plasma accelerator module, such as the high-voltage section for plasma production, the gas generation and distribution system within the plasma source, and the use of

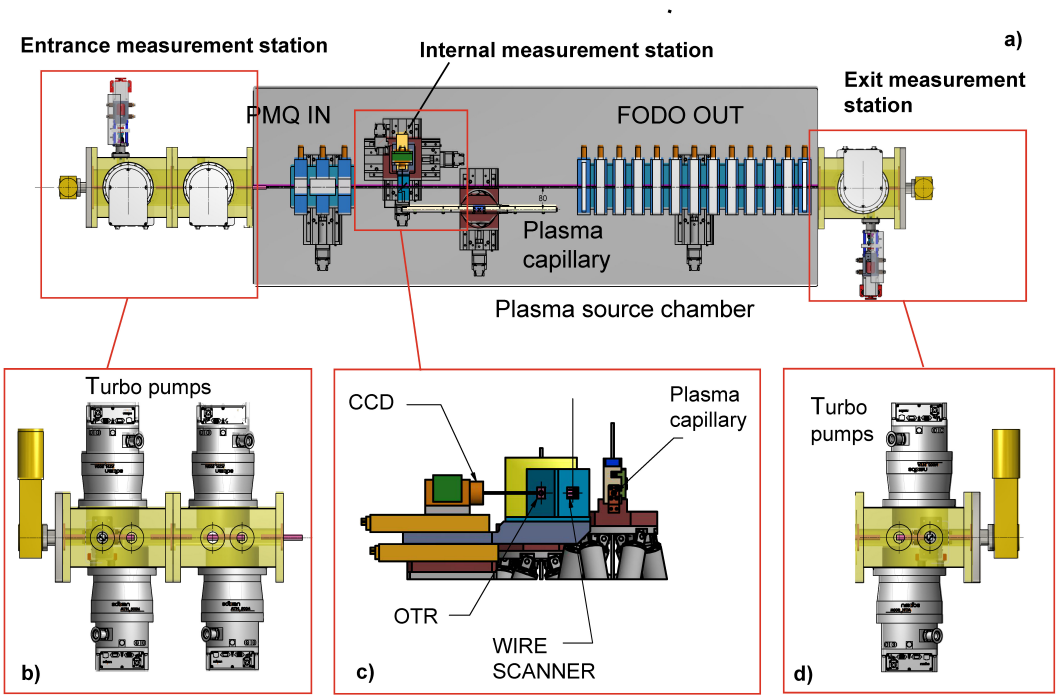

Figure 7.22: a) Top view of the layout of the beam diagnostics provided in the plasma source housing chamber area. b) Side view of the chamber housing the incoming beam diagnostics. c) Side view of the diagnostics of the beam entering the capillary. d) Side view of the chamber housing the outgoing beam diagnostics.

the laser systems. Table 7.4 summarizes the safety systems implemented and the elements of the plasma module to which these are addressed.

Regarding the high-voltage source, produced voltage pulses are in the range of 5-20 kV, with currents on the order of 100 to 1000 A, with repetition rates up to 100 Hz. As shown in the Figure 7.2, the high-voltage production system consists of two separate components, a commercial-grade HV generator capable of producing constant voltages up to 50 kV and output currents up to 200 mA, and a home-made HV pulser circuit. Active safety for both of these components involves connection to the common ground wires installed in the machine installation area. In addition, the power supply from the mains is provided by means of a dedicated electrical panel, on which an interlock system is mounted to allow immediate disconnection in the event of improper use by personnel, such as disconnection of electrical cables for maintenance operations or accidental causes. Both components, in addition to a dual key and switch on/off system, are also equipped with visual signaling systems during operations, indicating voltage and current values reached. Regarding the safety rules for the use of the HV generator, reference should be made to the manuals provided by the manufacturer, while for the HV pulser circuit, a special document is prepared in agreement with the LNF safety manager, in which the operations that must be followed for the safe switching on, switching off and controlling of the device are described.

Regarding the gas production system, Nitrogen gases will be used for plasma formation, which are found to be non-toxic and pose no flammability hazards. However, the danger of using the aforementioned gases is related to the possibility of saturation of the environment at the expense of oxygen. For this reason, the safety protocol requires the presence of a ventilation system capable of ensuring three complete air changes per hour of the entire operation volume. Gas storage is arranged in special tanks system capable of providing a gas flow of about 6 m^3/day, assuming a 24-hour load per day. The gas storage system must ensure a continuity of operation of at least

Plasma module safety system	
Element	**Safety rules**
HV source	• Manual manufacturer for both HV generator and HV pulser • All electrical components connection to the common ground wires • Interlock system with dedicated panel
Gas production system	• Safety protocol provided by the manufacturer • Interlock system with dedicated panel • Ventilation system able to ensure three complete air changes per hour of the entire operation volume
Laser system	• Shielding structure arranged around the laser area affected by the propagation of the laser beam until it reaches the plasma source • Interlocking system to visually warn laser operations • Personal Protective Equipment

Table 7.4: Safety system design for the plasma accelerating module.

fifteen days. The gas distribution system from the tanks to the vacuum chamber containing the plasma source is calibrated and certified to withstand pressures up to 70 bar. In addition, this system is equipped with pressure reduction systems down to about 1 bar at the inlet of the plasma chamber. Safety protocols for the use of pressurized gases are drawn up by the company implementing the gas distribution system.

Regarding the use of the laser system used for stability control in plasma formation, safety protocols involve several solutions. A shielding structure is arranged around the area exposed to the propagation of the laser beam until it reaches the plasma source, to prevent accidental reflections of the laser beam. In addition, an interlocking system is provided to visually warn of the start of laser operations as soon as the laser is turned on. This warning will be mounted at the entrance to the accelerator area. Finally, the laser operation area will be equipped with personal protective equipment for laser system operators.

7.7 Conclusions

The EuPRAXIA@SPARC_LAB plasma accelerating module has been designed and validated to meet the requirements for operation in a plasma-driven FEL facility. The main target parameters of the plasma source have been demonstrated and are consistent with the facility goals: (i) A 60 cm-long gas-filled discharge capillary has been characterized both experimentally and theoretically, the latter using fluid-dynamics codes to study the neutral gas distribution. (ii) Plasma density in the range $\approx 10^{15-17}$ cm^{-3}, with flat-top regions and controlled density ramps, has been achieved and reproduced. (iii) Shot-to-shot stability has been improved by laser-triggered discharge, reducing the current jitter from ≈ 10 A to ≈ 1 A and the temporal jitter from 32 ns to 1.7 ns. (iv) Capillary lifetime has been experimentally verified up to 2×10^7 shots at 30–150 Hz without measurable degradation. Extrapolation to the 60 cm device supports long-term operation at 100 Hz, with prospects for scaling to 400 Hz, pending further dedicated tests. (v) Laser triggering system parameters (80 mJ, $\approx 10^{10}$ W/cm^2) have been defined and successfully applied, ensuring reproducibility of plasma discharges under the EuPRAXIA operating conditions.

Integration with the machine has been addressed: (i) Beam transport and matching are ensured by high-gradient PMQs upstream and downstream of the capillary, together with a dedicated magnetic chicane for driver-witness separation. (ii) Vacuum system design allows continuous gas injection at $\approx$ 10-12 mbar·l/s while maintaining UHV conditions (10^{-9} mbar) in adjacent RF structures (iii) Plasma diagnostics based on Stark broadening provide single-shot longitudinal and transverse density measurements, enabling direct monitoring of the accelerating medium. In conclusion, within the present experimental limitations, the plasma accelerating module fulfills the baseline requirements for EuPRAXIA@SPARC_LAB. At this regard, Tab. 7.5 describes the technology readiness level of each sub-system of the plasma module.

Technology readiness level of the Plasma module sub-systems		
Sub-system	**TRL**	**Description**
Plasma chamber	8	Plasma chamber designed for differential pumping are widely used in many facilities, including SPARC_LAB. Actual system proven in operational environment.
Vacuum pumping system	8	Pumping system appropriate to the gas quantities required for plasma formation in acceleration experiments have already been tested at the SPARC_LAB and other facilities.
HV source	8	The high-voltage system to produce ionization of 60 cm long gas columns in thin capillaries has been fully designed and tested in the laboratory at the operating repetition rates.
Gas-filled discharge capillary	5	Extensive R&D has been made to validate the plasma capillary technology and solid results have proved the validity of the technical choice. A full system proven in a real environment is expected to be done in the next year.
Magnetic separator	5	The separation chicane between the driver and the witness in plasma accelerators has never been experimentally tested and, although it exists at the design level, it has not yet been technically implemented.

Table 7.5: TRL of the plasma module sub-systems.

Bibliography

[1] H. G. Weller et al. “A tensorial approach to computational continuum mechanics using object-oriented techniques”. In: *Computer in Physics* 12.6 (Nov. 1998), pp. 620–631. ISSN: 0894-1866. DOI: 10.1063/1.168744.

[2] N. A. Bobrova et al. “Simulations of a hydrogen-filled capillary discharge waveguide”. In: *Physical Review E* 65.1 (2001), p. 016407.

[3] L. Crincoli et al. “Advanced ceramic plasma discharge capillaries for high repetition rate operation”. In: *Scientific Reports* 15.12456 (2025).

[4] A. Biagioni et al. “Gas-filled capillary-discharge stabilization for plasma-based accelerators by means of a laser pulse”. In: *Plasma Physics and Controlled Fusion* 63.11 (2021), p. 115013.

[5] N. J. Bednar, J. W. Walewski, and S. T. Sanders. “Assessment of multiphoton absorption in inert gases for the measurement of gas temperatures”. In: *Applied spectroscopy* 60.3 (2006), pp. 246–253.

[6] N. A. Bobrova et al. “Laser-heater assisted plasma channel formation in capillary discharge waveguides”. In: *Physics of Plasmas* 20.2 (2013).

[7] A. Poyé et al. “Dynamic model of target charging by short laser pulse interactions”. In: *Physical Review E* 92.4 (2015), p. 043107.

[8] M. Migliorati et al. “Intrinsic normalized emittance growth in laser-driven electron accelerators”. In: *Physical Review Special Topics-Accelerators and Beams* 16.1 (2013), p. 011302.

[9] N. Barov and J. B. Rosenzweig. “Propagation of short electron pulses in underdense plasmas”. In: *Physical Review E* 49.5 (1994), p. 4407.

[10] S. Becker et al. “Characterization and tuning of ultrahigh gradient permanent magnet quadrupoles”. In: *Physical Review Special Topics-Accelerators and Beams* 12.10 (2009), p. 102801.

[11] J. K. Lim et al. “Adjustable, short focal length permanent-magnet quadrupole based electron beam final focus system”. In: *Physical Review Special Topics-Accelerators and Beams* 8.7 (2005), p. 072401.

[12] M. P. Anania et al. “Plasma production for electron acceleration by resonant plasma wave”. In: *Nuclear Instruments and Methods in Physics Research Section A: Accelerators, Spectrometers, Detectors and Associated Equipment* 829 (2016), pp. 254–259.

[13] H. R. Griem, A. C. Kolb, and K. Y. Shen. “Stark broadening of hydrogen lines in a plasma”. In: *Physical Review* 116.1 (1959), p. 4.

[14] D. G. Jang et al. “Density evolution measurement of hydrogen plasma in capillary discharge by spectroscopy and interferometry methods”. In: *Applied physics letters* 99.14 (2011).

[15] H. Griem. *Spectral line broadening by plasmas*. Elsevier, 2012.

[16] C. R. Vidal, J. Cooper, and E. W. Smith. “Hydrogen Stark-broadening tables”. In: *Astrophysical Journal Supplement, vol. 25, p. 37 (1973)* 25 (1973), p. 37.

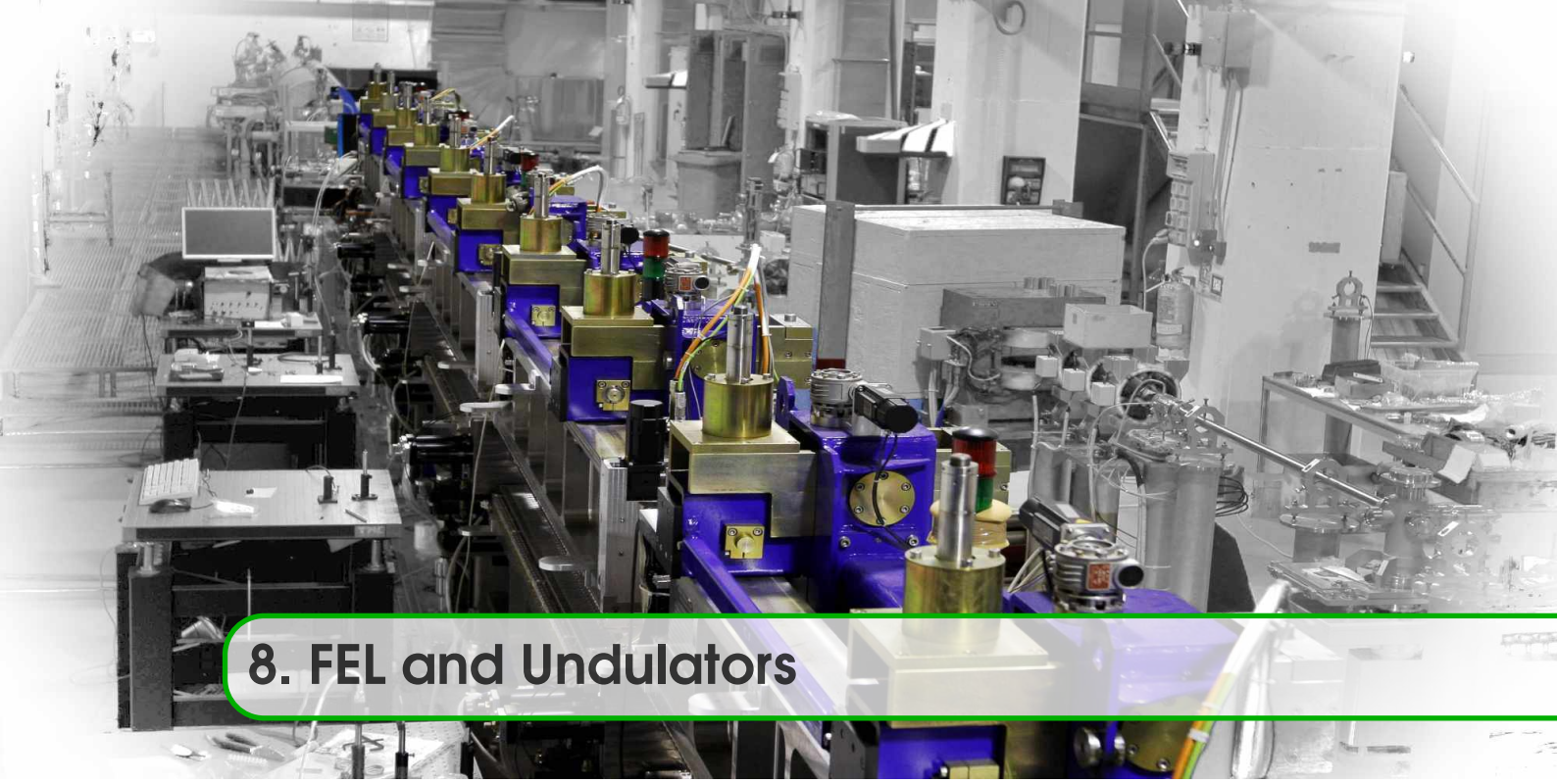

8. FEL and Undulators

8.1 Introduction

The facility relies on a first Free Electron Laser (FEL) line, named AQUA, with the target of reaching the carbon K-edge of the water window at the minimum beam energy of 1 GeV, which could be extended to the nitrogen K-edge with a boosted energy of 1.2 GeV. This is a self amplified spontaneous emission (SASE) FEL, where the main features are the control of the polarization, the high field intensity of the undulator combined to a short period, in order to minimize the undulator length and maximize the FEL amplification gain. The Plasma Wakefield Accelerator (PWFA) operation gives the best performances with low charge (few pC), short duration beams (few fs). This FEL will therefore provide the best performance in the generation of ultrashort radiation pulses.

The ensuing sections of this technical design report will delve into the requirements of the AQUA FEL. The subsequent analyses and discussions aim at providing a comprehensive understanding of the design considerations and requirements of the facility. This chapter aims to analyze the key parameters of the FEL design, including the magnetic length, undulator period and specifications, focusing optics, and vacuum chamber layout. It also provides a preliminary assessment of the expected FEL performance, along with tolerance studies concerning component alignment, temporal and spatial jitters, and sensitivity to magnetic imperfections that can lead to residual field integrals. Building on the undulator parameters and specifications outlined in this chapter, a detailed analysis of FEL performance is presented in Chapter 3. This chapter includes start-to-end simulations, providing an in-depth examination of the beam dynamics from the gun through to the FEL.

8.2 AQUA FEL

8.2.1 Introduction to the Undulator Design for the AQUA Beamline

The AQUA FEL line is designed as a Soft-X-ray SASE FEL optimized for operation in the 4 nm range, with a focus on achieving lasing within the "water window". The ability to control the polarization of the emitted light is considered a valuable advantage, and the associated technology

should be considered in the undulator design. The facility aims to be a benchmark in advancing FEL technology through the integration of beam-driven Plasma Wakefield Accelerator systems with both advanced undulator designs and x-band accelerator technology. The undulator design is based on a reference set of target beam parameters as outlined in Table 8.1. These parameters were derived from [1]. Based on the findings presented in Chapter 3, it is reasonable to expect that a beam with parameters that are either close to or better than those listed in Table 8.1 can be achieved.

Table 8.1: Reference set of target beam parameters

Beam Energy E_{beam}	0.7-1.0 GeV
Peak Current I_{peak}	1.5 kA
Slice norm. emittances ε_n	0.7 mm-mrad
Slice energy spread σ_γ	0.03%

The AQUA FEL undulator, with the target of including the carbon K-edge and of reaching the water window at such a relatively low electron beam energy, presents unique challenges. The resonant wavelength λ_0 and the undulator period λ_u are linked by the relation

$$\lambda_0 = \frac{\lambda_u}{2\gamma^2}\left(1 + K_{rms}^2\right) \tag{8.1}$$

where γ is the ratio between the electron beam energy E and the electron rest energy m_0c^2 and where $K_{rms} = \frac{e_0 B_{RMS} \lambda_u}{4\pi m_0 c}$ is the (RMS) undulator strength.

In Fig. 8.1 we show the dependence of the period length vs. the beam energy, which is required to set the resonance condition at the carbon K-edge ($\approx$ 300 eV). The plot shows three curves calculated at different undulator deflection parameters or strengths. A higher K_{rms} at fixed undulator period provides a higher FEL gain. At the same time low K_{rms} values cause a reduction of gain and an increase of the undulator magnetic length required for saturation. This operational domain requires therefore the exploration of advanced undulator technologies, to achieve both a short undulator period, in the range $\lambda_u \sim 15 - 20\,\text{mm}$, and a strong magnetic strength $K_{rms} \sim 1$.

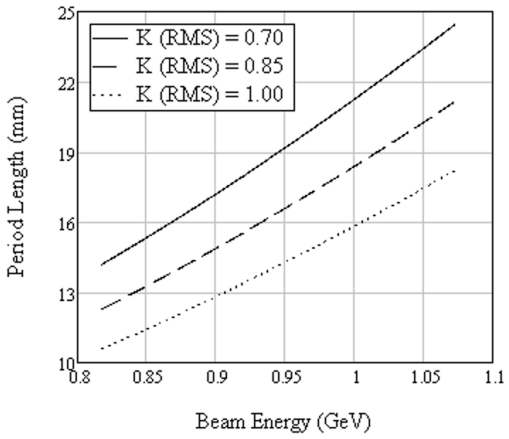

Figure 8.1: Relation between the beam energy and the undulator period ensuring the undulator resonance at the carbon K-edge (300 eV).

8.2.2 Undulator Technology

In pursuit of these requirements, the forefront technologies which were considered are:

- **Cryogenic/in vacuum undulators (IVU):** these undulators are placed within a vacuum chamber and are capable of achieving shorter periods (down to the sub-centimeter range) due to their closer magnetic poles. This reduces the gap between the magnets, allowing for stronger magnetic fields and shorter wavelengths. Cooling the undulator magnets to cryogenic temperatures enhances their performance by increasing the magnetic field strength. In-vacuum undulators with variable polarization have been designed and built [2–4] but their main drawbacks are related to increased complexity and higher costs. IVUs are more challenging to design and manufacture compared to traditional undulators. In permanent magnets (PM) in-vacuum undulators, the maximum gap aperture is constrained by the outer vacuum chamber. As a result, it is generally not possible to open the undulator gap wide enough to limit the radiation dose delivered to the magnets under imperfect conditions. In the context of a PWFA-based facility, this limitation could lead to early degradation of the field properties due to radiation damage.
- **Superconducting Undulators (SCU)** are probably the best choice in terms of high field combined to a shorter period. Superconducting materials allow SCUs to generate much higher magnetic fields compared to traditional permanent magnet or electromagnet undulators. Superconducting undulators are also generally considered to be quite robust in terms of radiation hardness. We explored this solution and an undulator prototype was designed in collaboration with FERMILAB [5]. The associated costs for SCU-based FEL lines are substantially higher than those of a permanent magnet undulator. The main drawback is indeed again related to the complexity and associated costs. In this case also the operational costs have to be considered for the cryogenic system operation: assuming the SCU option, we estimated more than 300 kW (cw) power to keep the AQUA undulator modules in operation. Even though this undulator technology was proposed in several cases, there are nowadays no FEL facilities using a FEL line entirely based on SCUs. Polarization switching would require specific and additional development studies.
- **Open Permanent Magnets undulators (PMU):** the use of high-strength rare-earth magnets, such as Neodymium-Iron-Boron (NdFeB), allows PMUs to achieve strong magnetic fields. The mechanical design of PMUs is simpler compared to SCUs or to IVUs. The use of permanent magnets simplifies the undulator's infrastructure, leading to reduced complexity and maintenance compared to technologies that require cryogenic cooling systems. PMUs do not require an external power source to generate the magnetic field, this results in lower operational costs, as there is no need for cryogenic cooling or RF power to maintain the magnetic field, unlike SCUs. PMU APPLE-X/APPLE-II configurations [6, 7] ensure the possiblity to tune the light polarization properties. Open undulator structures (i.e., not in-vacuum) allow the gap to be adjusted such that the magnets can be fully retracted from the beam path, minimizing radiation damage associated with beam loss. This is particularly beneficial during beam size/shape measurements using an intercepting screen at one of the undulator intersections.

Naturally, each technology presents its own set of benefits and challenges. Based on the previous discussion, it is desirable to have an undulator with a high K_{rms} and a short period. While the undulator strength is influenced by the undulator technology, as discussed earlier, even when limiting the options to PMU solutions, it also depends on the configuration, including factors such as geometry and magnetic material. As a reference, in Fig. 8.2 we show the undulator strength as a function of the ratio between the undulator gap and the undulator period for four different types of PMUs:

1. **The SPARC Undulator** (Planar PM 28 mm period, vert. field NdFeB ($B_r = 1.31$T). Measured data.
2. **The FERMI FEL-1 radiators** (APPLE-II PM, 55.2 mm period, NdFeB ($B_r = 1.25$T) linear

and circular polarizations. Measured data.

3. **The FERMI FEL-2 radiators** (APPLE-II PM, 34.8 mm period, NdFeB ($B_r = 1.25$T) linear and circular polarizations. Measured data.
4. **APPLE-X PM Field** (18, 28, 38, 48 mm period, NdFeB $B_r = 1.35$T). RMS peak field independent from the polarisation (linear or circular). The design assumes a minimum separation between the magnets (effective gap) of 1.5 mm. The field is calculated in RADIA [8].

The field is plotted vs the "aperture", where we define an aperture d as the maximum diameter of a cylindrical pipe which can be inserted in the undulator set at the minimum gap. This quantity coincides with the minimum gap separating the arrays of magnets in a planar or in a APPLE-II undulator. Due to its different geometry, there is an offset between the minimum gap and the aperture in the case of the APPLE-X undulator. In the APPLE-X case, the plots in Fig. 8.2 were obtained assuming a minimum gap of 1.5 mm, but with the same minimum aperture of the SPARC PMU (6 mm).

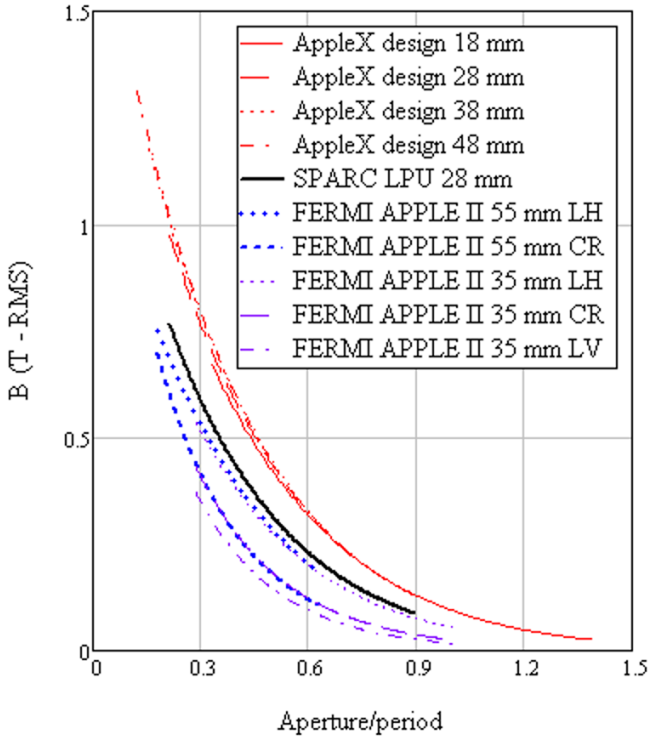

Figure 8.2: Undulator on axis field (RMS) as a function of the aperture/period ratio for different undulator types and polarizations. Data for SPARC and FERMI undulators correspond to measurements on real devices. The APPLE X undulator is designed and simulated in RADIA [8]. The RMS field in APPLE-X type undulator devices is independent from the polarisation.

While the APPLE-X undulator geometry allows for polarization control as the APPLE-II undulator, it also offers a distinct advantage in terms of on-axis field strength vs. the ratio aperture/period compared to all other geometries. **For this reason, the proposed undulator baseline is an APPLE-X Permanent Magnet Undulator (PMU), ensuring switchable polarization, high peak field and K_{rms} parameter in combination with a short period length.** The primary disadvantage of open PMUs is the necessity of a vacuum chamber to separate the undulator from the beam transport system, which reduces the maximum achievable on-axis field. To minimize this limitation, we propose an innovative design strategy for the vacuum chamber, as outlined in a

further dedicated paragraph. This design evolution is supported by collaborations with ENEA and through side initiatives such as the SABINA project [9]. In the following we discuss the choice of the undulator parameters.

8.2.3 Undulator parameters

In Fig. 8.3, we present the FEL saturation length as a function of both the resonant wavelength and the undulator period. The saturation length is calculated using a modified version of the Xie FEL scaling relations [10], with the primary adjustment being the inclusion of beam shot noise power for determining the initial conditions of amplification (see e.g. [11]). The blue shaded area indicates the region where the saturation condition is not achieved. The operational range is constrained at short wavelengths by the available undulator length, which is assumed to be 20 m. This is close to the maximum undulator magnetic length that can fit within the ~ 25 m allocated in the undulator section of the building. At longer wavelengths, the operational range is limited by the maximum strength of the undulator. We have assumed an APPLE-X undulator with a minimum magnetic aperture of 6 mm.

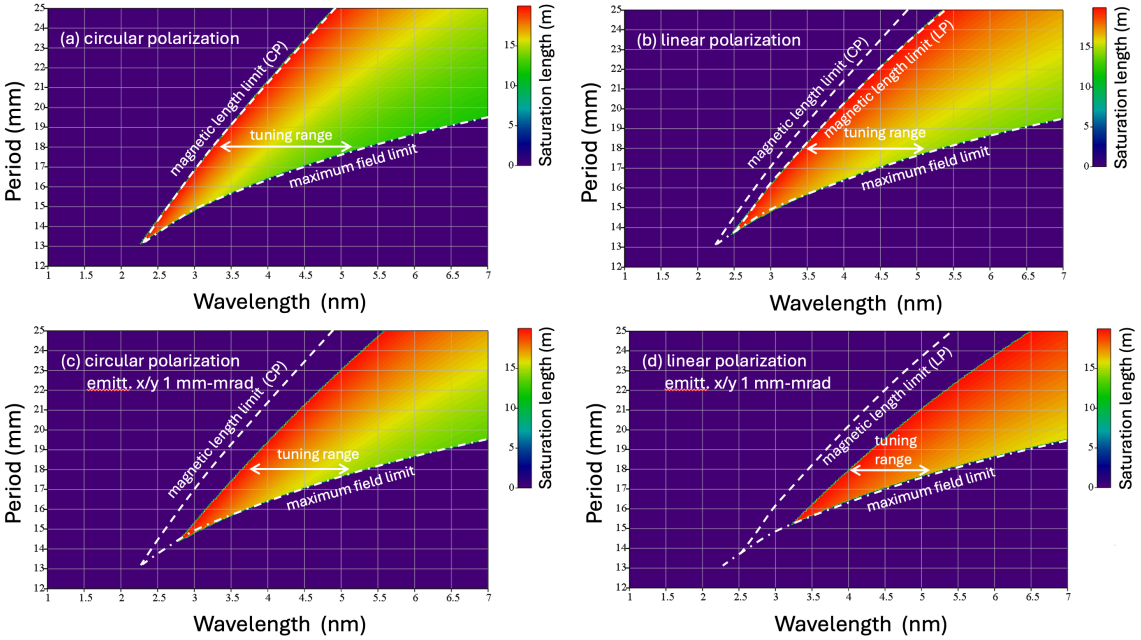

Figure 8.3: FEL saturation length vs. period length and undulator resonant wavelength. The parameters of an APPLE-X undulator with minimum magnetic aperture of 6 mm ($B_r = 1.35T$) have been assumed. In (a) and (c) the polarization is circular; in (b) and (d) the polarization is linear. In (a) and (b) the beam parameters are those in Table 8.1. In (c) and (d) the slice x/y emittances are increased to 1.0 mm-mrad.

The plot in Fig. 8.3 (a) illustrates the condition for the undulator operating in circular polarization, assuming the beam parameters in Table 8.1, and an average Twiss $\beta_{x,y} = 10$ m. The shortest wavelength which could theoretically be reached, is ~ 2.4 nm with an undulator period of 13.5 mm. In this case, the tuning range at a fixed beam energy $E = 1$ GeV would be extremely limited. This condition is also critical in terms of the system parameters. In the case of linear polarization (Fig. 8.3 (b)), the saturation condition would not be achievable, primarily due to the small gain reduction associated with the longitudinal dephasing characteristic of electron motion in a linear undulator. The situation becomes even more critical in Fig. 8.3 (c) and (d), where the emittances in both the x/y planes are increased to 1.0 mm mrad. A longer undulator period prevents

from achieving the shortest wavelength, but allows a larger tuning range and greater tolerance with respect to beam quality and beam current. In circular polarization (Fig. 8.3 (a)), the target wavelength of 4 nm lies in the middle of the tuning range for an undulator period $\lambda_u = 18$ mm. **Thus, we adopt $\lambda_u = 18$ mm undulator period as the reference.**

8.2.4 FEL operation tuning range and FEL performance dependence on the beam parameters

The tuning range of the AQUA undulator is shown in Fig. 8.4 (a) for circular polarization and (b) for linear polarization. The model allows to calculate the pulse peak power, which is then converted to a number of photons per pulse by assuming a pulse duration of ~ 15 fs (FWHM). The white dashed line represents the nominal maximum beam energy.

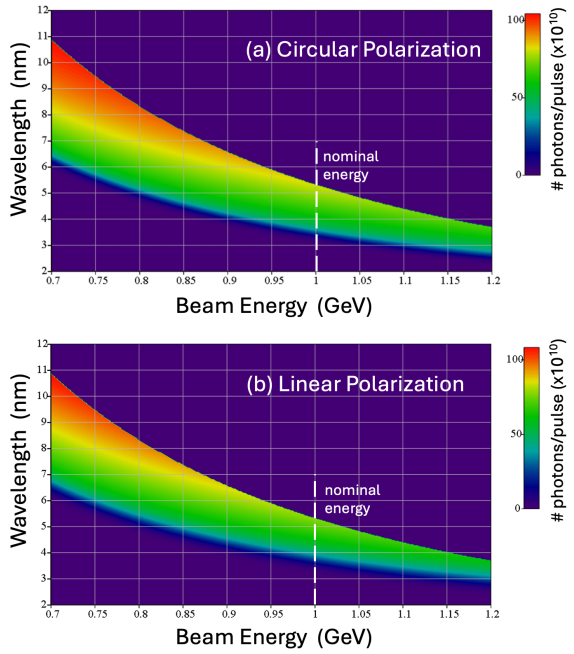

Figure 8.4: Photon count per pulse as a function of both resonant wavelength and beam energy, assuming an APPLE-X type undulator with a minimum magnetic aperture of 6 mm, a minimum gap of 1.5 mm, and $B_r = 1.35$ T. Panel (a) shows results for circular polarization, while panel (b) shows results for linear polarization. The conservative beam parameters of Table 8.1 and a pulse duration of ~ 15 fs (FWHM) have been assumed.

The plot range has been extended up to 1.2 GeV to illustrate that, if a higher beam energy with suitable quality becomes available, the device's operational range could potentially extend below 3 nm, including the nitrogen K-edge.

By varying the beam energy in the range shown in Table 8.1 the spectral range extends from 10.7 nm down to include 4 nm for both the circular and the linear polarizations. A broader spectral range, extending towards longer wavelengths to include, for example, the Si_{23} threshold, can be achieved by further reducing the beam energy. The tuning range at fixed beam energy (1 GeV) is upper limited by the maximum undulator strength to $\lambda_0 \sim 5.3$ nm, regardless of the polarization mode. The low wavelength limit depends on the FEL gain, therefore on the effective beam parameters and on the polarization mode. Considering the parameters in Table 8.1, the model predicts more than 10^{10} photons/pulse for $\lambda_0 \gtrsim 3.1$ nm in circular polarization and $\lambda_0 \gtrsim 3.3$ nm in linear polarization. This result is strongly affected by the beam quality.

We show in Figs. 8.5 and 8.6 the dependence of the peak power (a), the pulse energy (b),

the number of photons per pulse (c) and the saturation length (d) as functions of both the beam emittances and the energy spread.

The plots illustrate the beam parameter space required for achieving saturation and efficient beam energy conversion into light in a magnetic length of 20 m. The calculations assume an average β_T function of 10 m in both planes and a peak current of 1.5 kA. The effect of larger beam transverse emittances or of a larger energy spread can be partially compensated by a reduction of the β_T function or by an increase of the peak current.

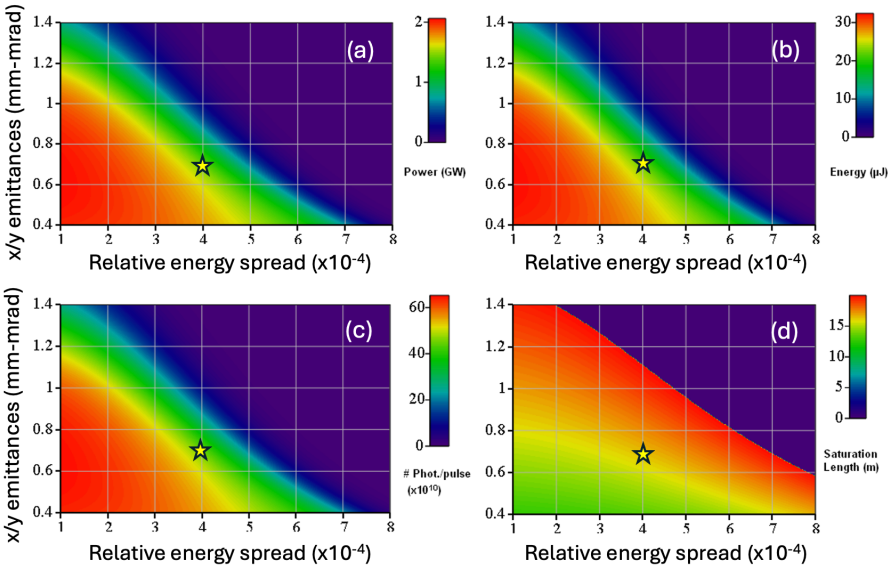

Figure 8.5: The four panels represent the dependence of the peak power (a), the pulse energy (b), the number of photons per pulse (c) and the saturation length (d) as functions of both the slice normalised beam emittances and the energy spread. The undulator is in circular polarisation. The yellow star symbol indicate energy spread and emittances of the working point simulated in the beam physics, Tab. 3.1. Note that the simulated working point presents a substantially higher peak current with respect to the conservative value used in this example (3.3-3.4 kA vs 1.5 kA).

The behavior of the system vs. the β_T function is illustrated in Figs. 8.7 and 8.8 in circular and linear polarizations respectively.

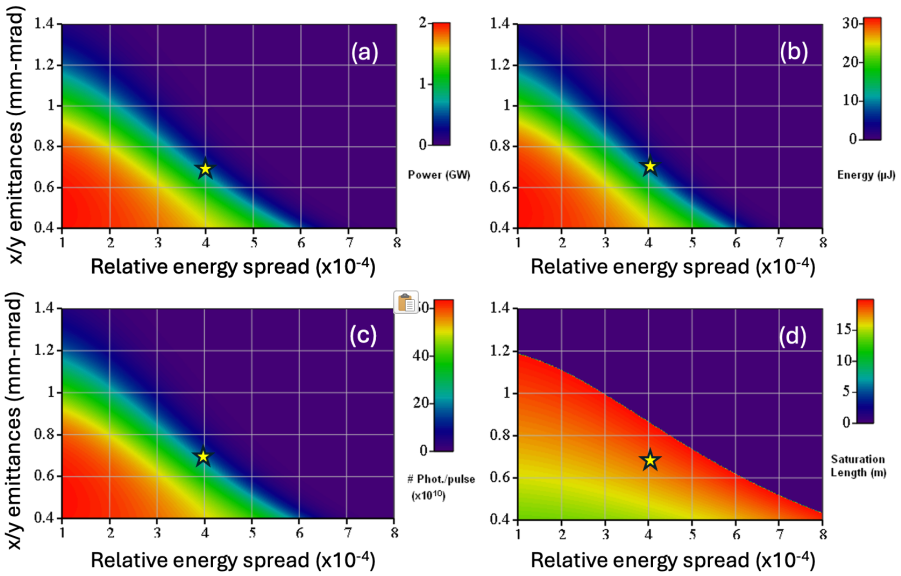

Figure 8.6: As in Fig. 8.5, the four panels represent the dependence of the peak power (a), the pulse energy (b), the number of photons per pulse (c) and the saturation length (d) as functions of both the beam emittances and the energy spread, but with the undulator in linear polarization mode. The yellow star symbol indicate the working point simulated in the beam physics chapter, Tab. 3.1. Note that the simulated working point presents a substantially higher peak current with respect to the conservative value used in this example (3.3-3.4 kA vs 1.5 kA).

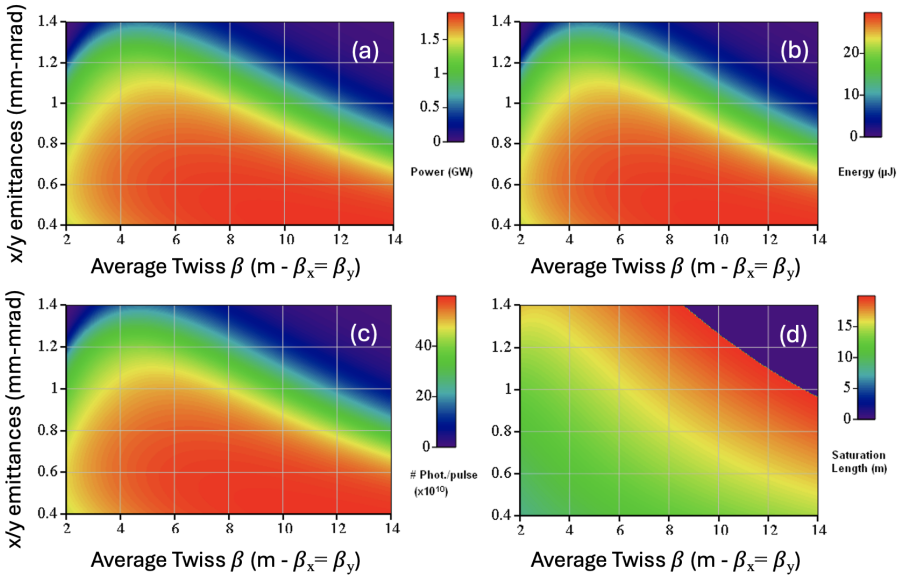

Figure 8.7: The four panels represent the dependence of the peak power (a), the pulse energy (b), the number of photons per pulse (c) and the saturation length (d) as functions of the transverse normalised emittances and the average β_T. The undulator is in circular polarisation, the energy spread and peak current are the one of Table 8.1.

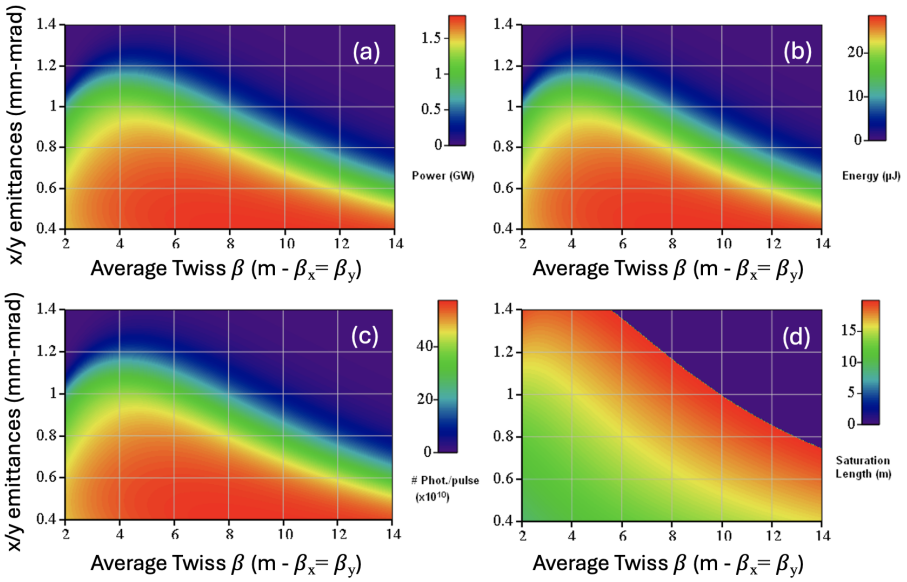

Figure 8.8: As in Fig. 8.7, the four panels represent the dependence of the peak power (a), the pulse energy (b), the number of photons per pulse (c) and the saturation length (d) as functions of the transverse normalised emittances and the average β_T, but with the undulator in linear polarisation.

The plots indicate that, regardless of the polarisation, the optimum average β_T is of the order of 5 m. However, transporting a tightly focused beam could amplify trajectory jitters, increasing the beam pointing instability. While these effects will be analysed later, we have assumed a conservative reference value $\beta_T = 10$ m. The effective β_T will be determined through an optimisation process.

The effect of an increase of the peak current and of the relative slice energy spread is illustrated in Figs. 8.9 and 8.10 in circular and linear polarisations respectively.

Peak current values below 1 kA hinder efficient FEL operation, particularly in linear polarization. On the other hand, current values exceeding 2 kA allow for a larger acceptable slice energy spread, which could increase to as much as $4 - 5 \cdot 10^{-4}$.

We have illustrated the expected FEL performance by exploring the system's parameter space, assuming a magnetic length of 20 m. Such a magnetic length is achieved through stacking a sequence of independent undulator sections. A low number of long sections results in fewer segments between the undulators, where diagnostics, correctors, and quadrupoles for beam transport are placed. This is advantageous for minimizing the overall device length. Achieving saturation within 20 m also requires the FEL gain length to be shorter than 1 m, which has to be significantly shorter than the length of a single undulator section to reduce losses due to the lack of gain guiding along the intersections.

On the other side the length of each section has to be sufficiently small to ensure the possibility to modulate the beam Twiss average beta functions in the undulator, in the range shown in Figs. 8.7 and 8.10. Given the extremely short period (18 mm), the small gap (1.5 mm), the associated high on-axis field, and the need to tune the transverse beta parameter down to 5 m, each undulator section should not exceed 2 m in length. The undulator chain would be composed by ten undulator sections separated by a intra-undulator.

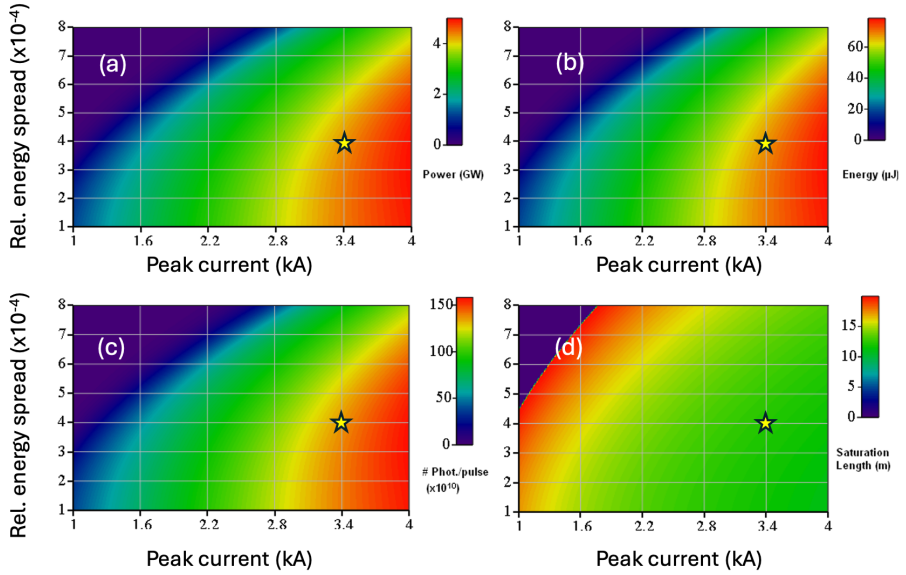

Figure 8.9: The four panels represent the dependence of the peak power (a), the pulse energy (b), the number of photons per pulse (c) and the saturation length (d) as functions of both the slice beam relative energy spread and the peak current. The undulator is in circular polarisation. The yellow star symbol indicate the working point simulated in the beam physics chapter, Tab. 3.1.

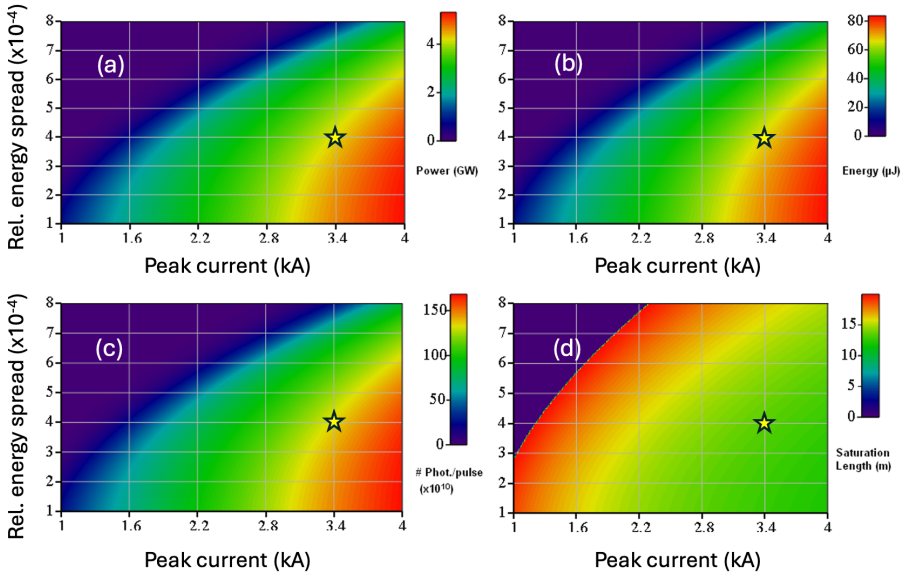

Figure 8.10: As in Fig. 8.9, the four panels represent the dependence of the peak power (a), the pulse energy (b), the number of photons per pulse (c) and the saturation length (d) as functions of both the slice beam relative energy spread and the peak current, but with the undulator in linear polarisation. The yellow star symbol indicate the working point simulated in the beam physics chapter, Tab. 3.1.

In the following section, we will analyze the focusing properties of the beam transport through the AQUA undulator.

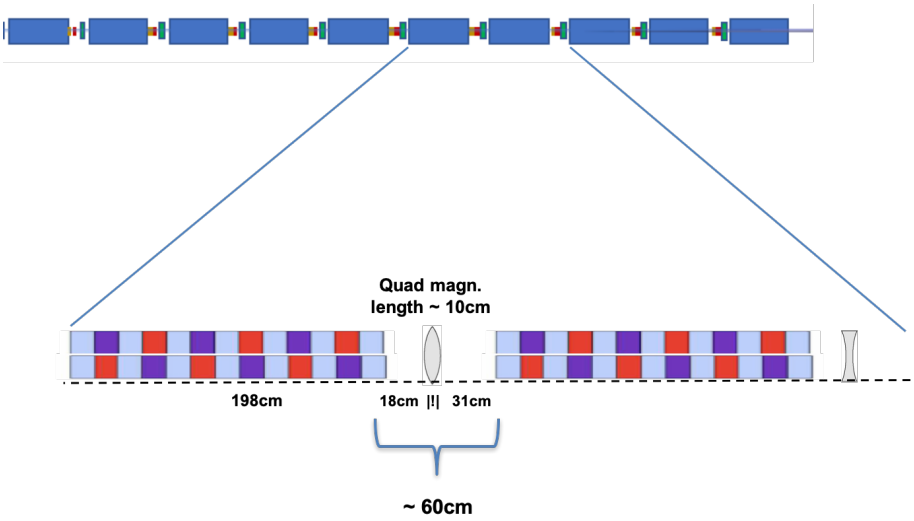

Figure 8.11: AQUA FODO cell schematic layout.

8.2.5 Magnetic lattice and beam transport

The design under consideration [12] envisages a 2 m long module, namely about 110 periods, with variable polarization and deflection strength parameter K that can be accordingly tuned to a maximum value: $K_{max} = 1.1$ ($K_{max} = 1.5$) in case of circular (linear) polarization.

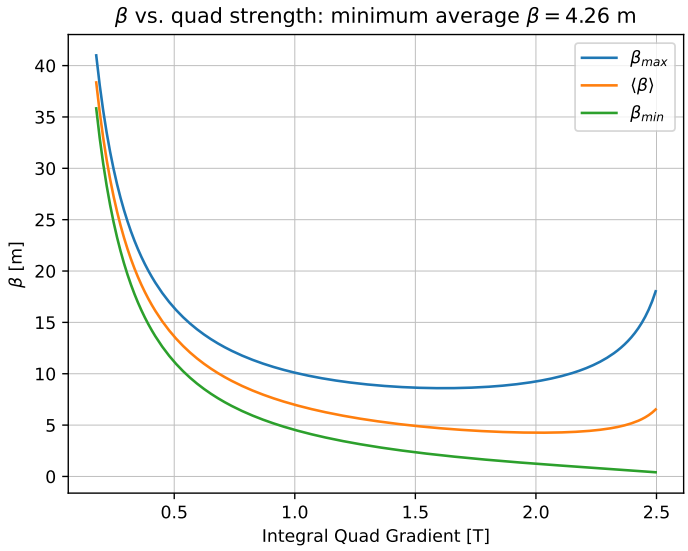

Figure 8.12: Maximum, average and minimum Twiss β values as a function of the integral quadrupole strength (@ 1 GeV).

Figure 8.11 shows the scheme of the undulator section, featuring the inset zoom of the magnetic unit cell made of the undulator and FODO sections (for more details on the components of the intra-undulator section refer to Sec. 8.6).

This beamline layout drives the choice of the betatron Twiss parameter as a function of the quadrupole strength, within the FODO cell between two undulator modules. Figure 8.12 shows the β Twiss parameter values, at increasing integrated quadrupole gradient. The minimum value for the average β function is $\langle\beta\rangle_{min} = 4.26$ m.

For a 1 GeV electron beam energy, the choice to have the intra-undulator distance of about 60 cm, together with Twiss average β parameter and K values constrain the quadrupole integrated gradient requested to operate the APPLE-X modules at 4 nm wavelength, in either linear or circular polarization.

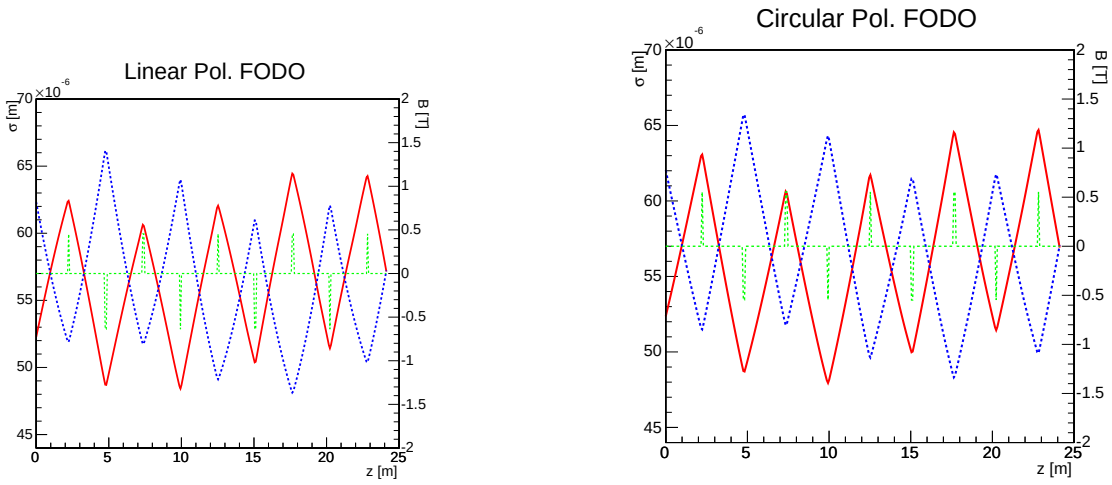

Figure 8.13: Transverse rms size of the electron beam subject to the undulator plus FODO sections in Linear (left) and Circular (right) polarization operations.

Figure 8.13 shows the transverse profile of the electron beam subject to the undulator plus FODO sections in linear (left) and circular (right) polarization operations with $\langle\beta_{x,y}\rangle = 8$ m, and integrated gradient values on the second y-axis. These results are obtained with the Genesis1.3 simulation code for evaluating the transverse size of the nominal electron beam subject to the undulator plus FODO line sketched in Figure 8.11. The behavior of the integrated gradient is investigated with increasing the electron beam energy, while keeping constant all other parameters. In order to accommodate the same focusing factors, the integrated gradient have to be increased, as shown in Figure 8.14.

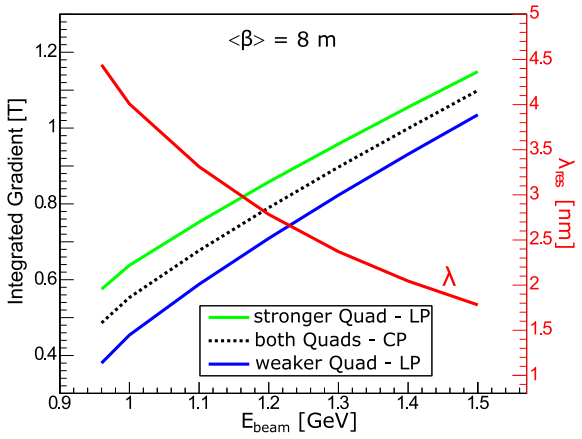

Figure 8.14: Quadrupole Integrated gradient as a function of beam energy with a Twiss $\beta = 8$ m, for both LP and CP configurations, superimposed to the achievable wavelength λ as a function of the electron beam energy. Calculated for $\lambda_u = 18$ mm, $K_{rms} = 0.84$.

The field values stay on the order of about 1 Tesla or even smaller. These estimates imply that the same structure under design (see Sec. 17.8.1) can operate at higher energies, in such a way to

cover shorter resonant FEL wavelengths in a more efficient way.

Figure 8.14 shows these values for both LP and CP configurations, superimposed to the achievable wavelength as a function of the electron beam energy.

If the beamline is operated at $\langle\beta_{x,y}\rangle = 5\,\mathrm{m}$, the quadrupole strengths have to be increased accordingly. Within this latter configuration, Figure 8.15 shows these values for both LP and CP

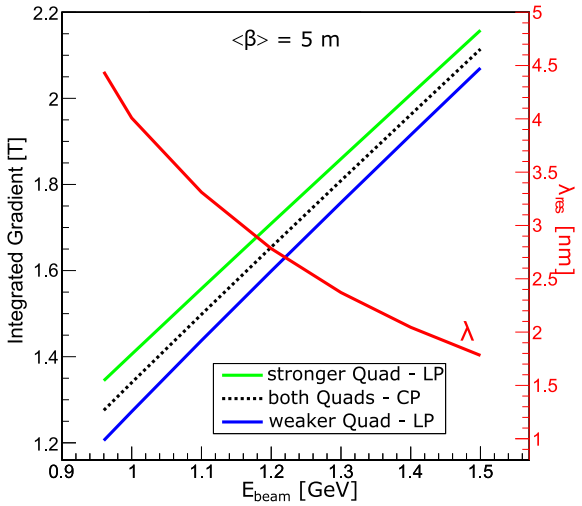

Figure 8.15: Quadrupole Integrated gradient as a function of beam energy with a Twiss $\beta = 5\,m$, for both LP and CP configurations, superimposed to the achievable wavelength λ as a function of the electron beam energy. Calculated for $\lambda_u = 18\,mm$, $K_{rms} = 0.84$.

configurations, superimposed to the achievable wavelength as a function of the electron beam energy. In this case, the field values are required to be around 2 Tesla, only if the beamline has to be operated at electron beam energies larger than 1.4 GeV.

8.3 AQUA undulator

8.3.1 Magnetic Modeling

The AQUA undulator is a variable polarization device with APPLE-X type configuration [6]. As explained in the previous section, given the beam energy ($E = 1$ GeV) and the desired resonance, the undulator must have a short period ($\lambda_u = 18$ mm) and a peak magnetic peak B that results in a deflection parameter $K_{\mathrm{rms}}\,(= a_w) \approx 1$, in accordance with the FEL resonant condition Eq. (8.1).

The APPLE-X undulator, due to its geometry, is well-suited to meet the required parameters for the FEL operation. Additionally, the characteristics of this undulator ensure that the resonance wavelength and tuning range remain consistent across all polarization settings.

Given the period length $\lambda_u = 18$ mm, the required deflection parameter $K_{\mathrm{rms}} = 0.8$ is hence required for the operation at 4 nm, according with Eq. (8.1).

The undulator structure is made of four Neodymium-Iron-Boron (NdFeB) permanent magnet blocks with octagonal shape with a magnetization at 45° and a remanent field $B_r = 1.35$ T, with a locking tooth to fix the block magnets to the holder. The magnets are disposed radially at equal distance around the electron beam axis. The resultant square hole in the centre of the structure, with a diameter $\phi = 6$ mm (namely the aperture), allows the installation of a 5.5 mm external diameter vacuum pipe for the propagation of the electrons. Longitudinally we have four blocks per period arranged according to the Halbach [13] configuration. The block size in the x, y, z dimensions are $18x18x4.4$ mm, the z size is less than $\lambda_u/4$ (= 4.5 mm) since a distance of 0.1 mm between magnets has been assumed as typical to take into account the mounting issues. The minimum achievable

gap is settled as 1.5 mm, being this a good compromise between the maximum wanted magnetic field value (and hence the maximum K), and some constructive constraints due to the mounting tolerances of the magnets, the movement of the girders and the holders for the vacuum chamber (see Fig. 8.16). We remind here that the gap is defined as the distance between magnets on the sides of the undulator.

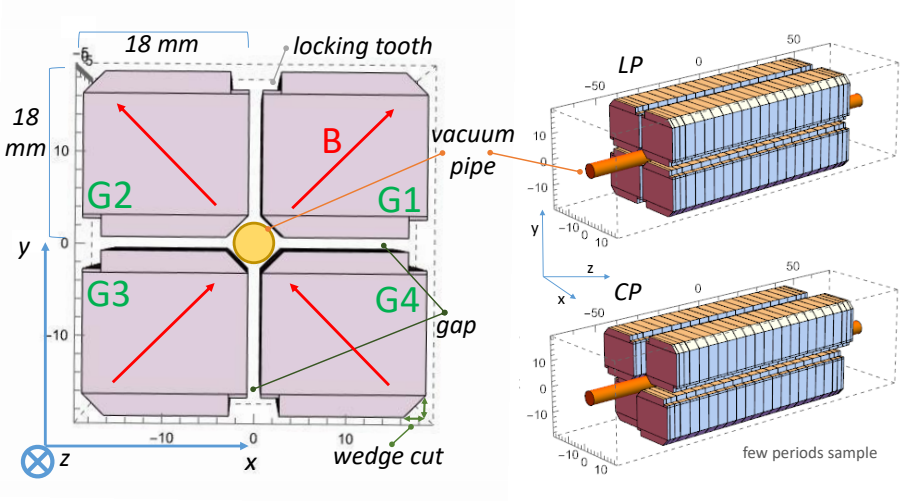

Figure 8.16: Structure of the AQUA APPLE-X undulator, transverse (left) and longitudinal (right) view. The positioning for the two linear (LP) and circular (CP) polarization modes are also plotted for a sample of few periods.

The magnetic modeling of the undulator has been performed by means of the RADIA code [8]. The main considered parameters and the resulting capabilities are summarized in Table 8.2.

Table 8.2: Undulator basic parameters

Parameter	**Value**
Material	NdFeB
Remanent field B_r	1.35
Period λ_u	18 mm
Blocks per period	4
Block magnet x,y,z size	18 mm x 18 mm x 4.4 mm
Aperture diameter ϕ	6 mm
Minimum gap	1.5 mm
B_{max} (in LP)	0.93 T
K_{max} (in LP)	1.57
K_{rms} range	1.11 - 0.6
Resonance tuning range (1 GeV)	3.5 - 5.24 nm
N periods	110
Module length	2 m

8.3.1.1 Undulator *K* parameter and tuning range

The wavelength tuning is obtained by moving the four magnets arrays radially in order to adjust the magnetic gap, while the polarization control is realized by shifting longitudinally (namely a "phase" shift) two diagonally opposite girders with the magnets arrays respect to the other two. The general expression for the undulator parameter K_{rms} in a variable polarization undulator is:

$$K_{\mathrm{rms}} = \sqrt{\frac{K_x^2}{2} + \frac{K_y^2}{2}} \tag{8.2}$$

where K_x and K_y are the undulator deflection parameters associated to the peak magnetic field for respectively the horizontal and the vertical components B_x and B_y. The symmetrical geometry of the APPLE-X gives the same K_{rms}, and hence the same tuning range, for all polarization modes (Fig. 8.17). The maximum achievable K is limited by the longitudinal dimension of the blocks magnet (one quarter of the undulator period), for this reason we do not have a large tuning range but the parameters have been optimized to increase it as much as possible. Of course, as explained in the previous section, the resonance capability of the undulator can be eventually extended by varying the electron beam energy (Fig. 8.18).

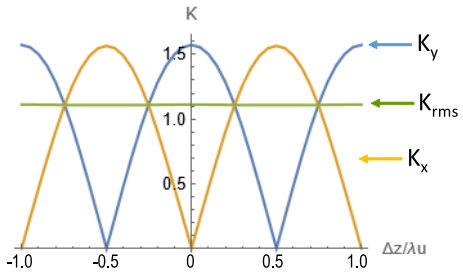

Figure 8.17: Undulator K parameter variation with different polarization setting given by a phase shift Δz in unit of λ_u, at the minimum gap 1.5 mm.

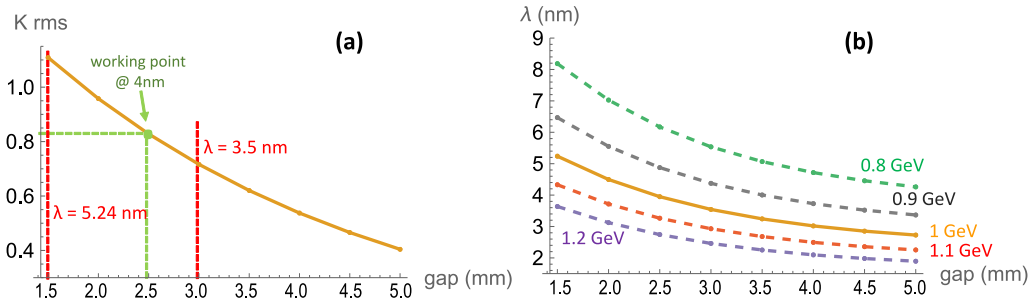

Figure 8.18: (a) K_{rms} variation vs gap and tuning range. Tuning range is the same for all operation modes of polarization. (b) Wavelength tuning range for different values of the e-beam energy; the continuous line stands for the reference case at 1 GeV.

8.3.1.2 Field Profile

The field profile estimation, for the so designed undulator, reveals perfect symmetry between the horizontal (x) and vertical (y) directions when the device operates in circular polarization mode. This symmetry is reflected in both the field gradients and the undulator's focusing properties. The transverse field gradients exhibit a parabolic profile, but with significant variation, particularly for

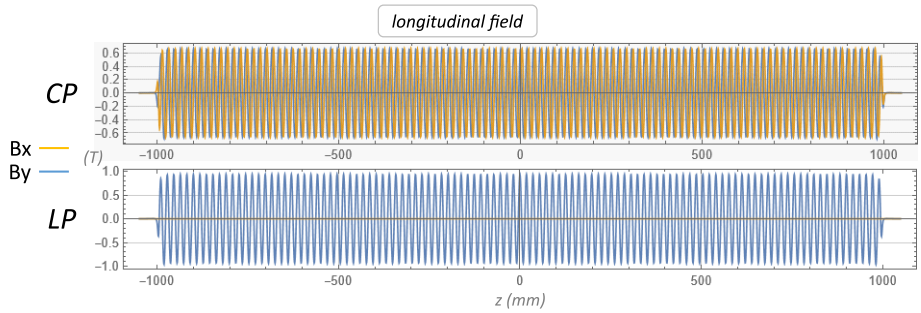

Figure 8.19: Longitudinal field profile of the AQUA undulator in Linear (LP) and Circular (CP) polarization.

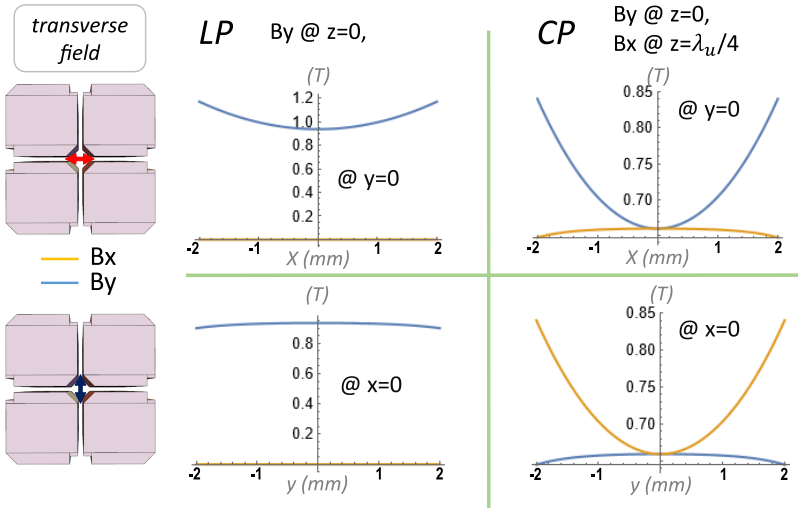

Figure 8.20: Transverse field profile of the AQUA undulator in Linear (LP) and Circular (CP) polarization.

the cross components $\Delta B_y/\Delta x$ and $\Delta B_x/\Delta y$, due to the small gap and the aperture of the central hole, which leads to a loss of homogeneity (see Figs. 8.19 and 8.20).

The homogeneity map illustrates the good field region for undulator operation. The variation in the transverse field (and thus in K) affects the radiation bandwidth as off axis injected electrons experience a different K and therefore have a different average longitudinal velocity. The effect can be normally neglected if the K variation is of the order of few per mill. For the undulator under study this happens if $x, y < 200$ µm from axis, where the maximum B field variation is $< 0.3\%$. Considering a distance of $x, y = 200$ µm, the field variation goes down to less than 0.3%. The transverse field variations within 400 µm from axis in both x and y are listed in Table 8.3 for linear and circular mode. This fixes the homogeneity region of the AQUA APPLE-X undulator. According to the electron beam parameters (see Tab. 3.1 and Sec. 8.2.5), the transverse rms size of the electron beam is of the order of 100 µm which is four times less than the field homogeneity range. Anyway this gives constraints on the precision of the beam alignment tool and trajectory jitters.

8.3.1.3 End magnets design

The design of the end magnets configuration is a crucial item which determines the quality of the field integrals and then the effect on the beam trajectory of the electrons passing trough the undulator. To find the best option for the end magnets design of the AQUA undulator, some

Table 8.3: Undulator transverse field homogeneity at a distance x, y of 100 µm, 200 µm and 400 µm from axis, for Linear (LP) and Circular (CP) polarization mode.

	@ 100 µm		@ 200 µm		@ 400 µm	
	LP	**CP**	**LP**	**CP**	**LP**	**CP**
$\Delta B_y/\Delta y$	0.005%	0.002%	0.002%	0.009%	0.08%	0.04%
$\Delta B_y/\Delta x$	0.06%	0.07%	0.25%	0.27%	1%	1.07%
$\Delta B_x/\Delta x$	—	0.02%	—	0.007%	—	0.03%
$\Delta B_x/\Delta y$	—	0.07%	—	0.27%	—	1.06%

different schemes have been considered. The aim is to minimize the effect of the non-zero magnetic susceptibility of NdFeB since this affects the values of the field integrals, this giving non zero offset and angle at the exit of the module for a on-axis injected electron even for an ideal undulator. This compensation can be obtained by choosing the end magnets scheme but in practice a further optimization is required with varying the block size and position of the end magnets respect to the more standard cases [14, 15]. We started from a conventional configuration where the end part is made by three magnets at each side of the undulator girders with a longitudinal width of respectively $1/4$, $1/2$ and $3/4$ of the full block size. In this scheme the external magnet has a field orthogonally oriented respect to the propagation axis z. However with this scheme it turns not to be possible to minimize the field integrals for both Circular and Linear setting of the undulators. The solve as much as possible this inconvenient a fourth magnets is added at the begin (and at the end) of the girder with a field orientation parallel to the z-axis. This scheme is borrowed from the SABINA APPLE-X undulator [16], which has been already realized for a THz FEL operation [9]. The chosen end magnets design is finally given by four magnets at both end and begin of the girders with dimensions different from the full block size. Block size's and positions have been optimized to match the requirements on field integrals. The variation step of the size and positioning of the magnets has been assumed as 0.1 µm which is consistent with real mechanical capabilities for the precision on the block size and mounting. The conceptual scheme of the optimized ends design is described in Fig. 8.21.

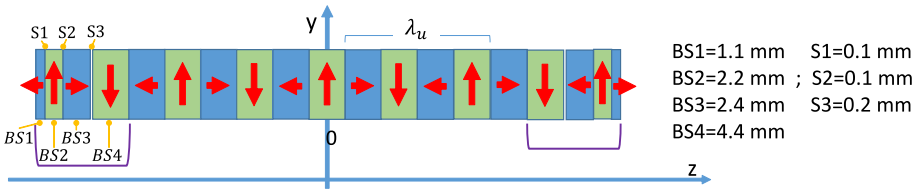

Figure 8.21: End magnets design scheme after optimization.

By including the effects of the NdFeB susceptibility, this configuration ensures values of the first and second field integrals close to zero and hence it minimize the exit angle and offset of an on-axis propagating electron (for the ideal undulator). Here we are not considering the effects of the tolerances on block sizes, field and positioning which are crucial for a real device. This last effect will be treated in the following paragraphs. The ending magnets are additional to the ones which define the undulator number of periods. This means that effective number of periods of the full array is larger than the one assumed as reference for the FEL process. The reference number of period is $N = 110$ for the single undulator module while the effective, in term of module length, is close to $N_{end} = 111.5$.

8.3.1.4 Field integrals

The field integrals obtained as a result of the end magnets optimization are described in Tab. 8.4 for the radial (x) and vertical (y) field components. The outgoing values are given in linear Horizontal, Circular and linear Vertical polarization mode, for the ideal model of the undulator. Fig. 8.22 shows the dependence of field integrals values on the undulator phase and gap. The values of the field integrals decrease with opening the gap, as expected.

Table 8.4: Undulator first (I) and second (II) field integrals at minimum gap, for the radial (x) and vertical (y) field components, in linear horizontal (HP), Circular (CP) and linear vertical (VP) polarization mode.

	HP	**CP**	**VP**	units
I_x	0	0	0.06	$10^{-4}\ T \cdot m$
I_y	0.022	-0.005	0.378	$10^{-4}\ T \cdot m$
II_x	0	-0.019	-0.121	$10^{-4}\ T \cdot m^2$
II_y	0	0	0	$10^{-4}\ T \cdot m^2$

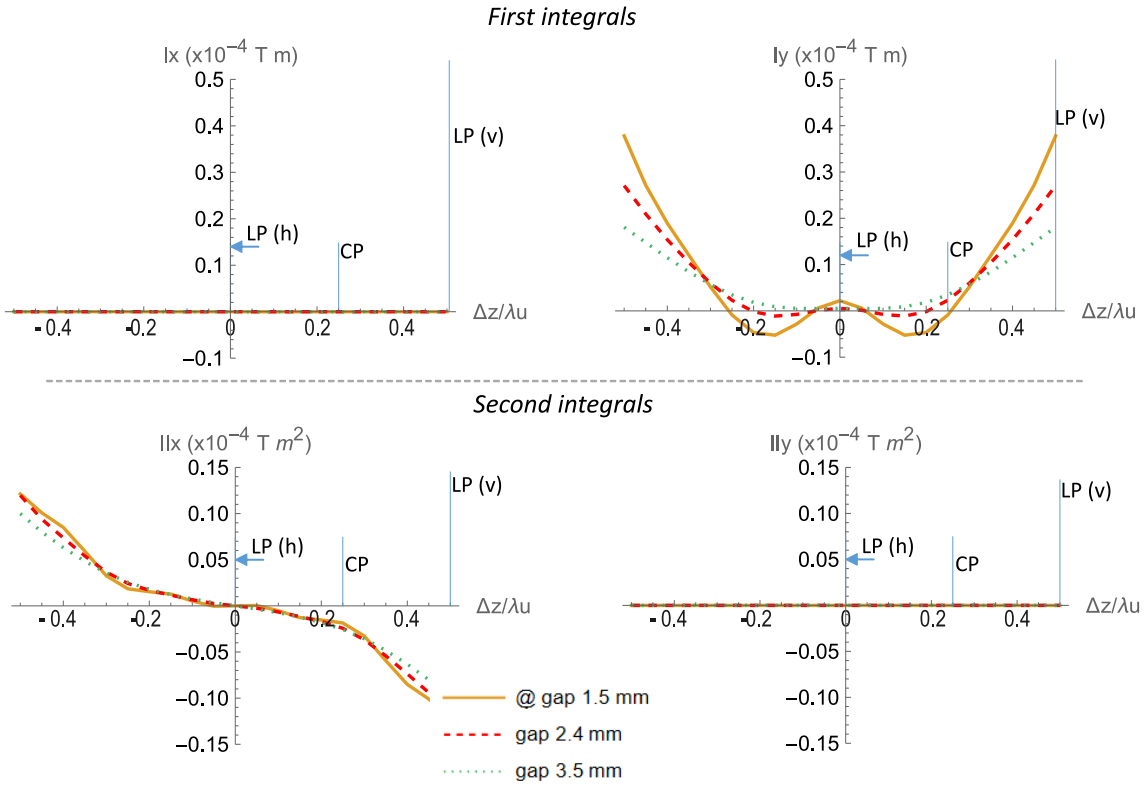

Figure 8.22: Undulator field integrals. The first $I_{x,y}$ and the second $II_{x,y}$ integrals are plotted for the for the radial (x) and vertical (y) components depending on the phase value ($\Delta z/\lambda_u$) which determines the polarization mode. Different lines refer to different gap values, 1.5 mm (minimum gap), 2.4 mm (resonance 4 nm) and 3.5 mm ($K_{rms} \approx 0.6$).

The largest values arise in the vertical mode. All values are however small enough for the purpose of the basic modeling. We remark that the present analysis holds for an ideal undulator. The values of the field integrals in a real device are mainly determined by uncertainty in the size and mounting of the magnets. The actual field integrals values will be measured and minimized with

the effective construction of the device. The previous experiences for APPLE-X undulators suggest that correction coils are required to manage the proper values of the integrals in a real device. The procedure to define the maximum acceptable values of the first and second field integrals for the FEL operation will be treated in the following sections.

8.3.1.5 Trajectory

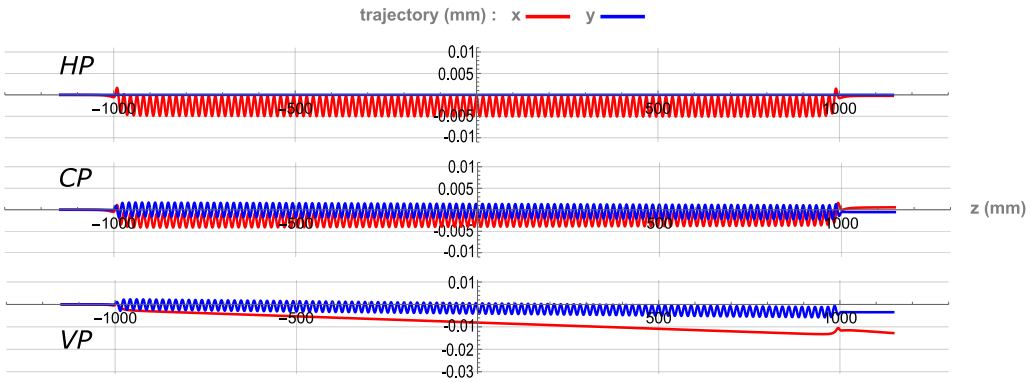

Figure 8.23: Trajectory in the undulator for an electron with initial null offset and angle at the entrance in the undulator. The linear Horizontal (HP), Circular (CP) and linear Vertical (VP) polarization cases are plotted.

The resulting field integrals are strictly related to the electron beam trajectory trough the undulator. The best would be to have a zero-displacement oscillation and to have a null offset and angle at the exit of the undulator, in both x and y direction, for an electron entering in the undulator with null offset and angle respect to the longitudinal axis. However, because of the non-zero susceptibility of the NdFeB magnets and of the complex geometry of the APPLE-X, a small deviation from the desired condition arises even for an "ideal" undulator, where the errors due to precision on blocks properties and mounting are not considered. As described in the previous paragraph, the effect has been minimized by playing with the end magnets to find the best configuration to operate at any phase with different polarization mode. The resulting trajectory is plotted in Fig. 8.23 for linear horizontal, circular and linear vertical polarization cases.

Indeed, the resulting trajectory does not exhibit zero displacement due to the specific arrangement of the end magnets. As shown in Fig. 8.23, the electrons oscillate around a point a few microns off-axis in the radial direction. However, this does not pose any issues, as this displacement remains well within the homogeneity region of the radial field. The exit angle α and offset Δ values for both the radial (x) and vertical (y) coordinates are anyway within $|\alpha_{x,y}| < 1$ µrad and $|\Delta_{x,y}| < 1.5$ µm.

8.3.1.6 Correction coils system

The resulting field integrals give the worst effect in the linear vertical polarization mode but all resulting values can be considered still acceptable according to the tolerance study (see next sections). However this result is given by an "ideal" undulator where neither the precision on magnets block sizes and fields nor the mounting accuracy effects are considered. To further minimize the residual field integrals a correction coils system can be foreseen to be installed on the undulator. The conceptual scheme of the coils system is given by two blocks (C1 and C2), made of four coils each, one at the begin of the undulator and another one at the end. The correction coils scheme is described in Figs. 8.24 and 8.25, the modeling parameters of each coil are detailed in Tab. 8.5.

The coils are coupled in such a way that the two coils of the first and third quadrants and the

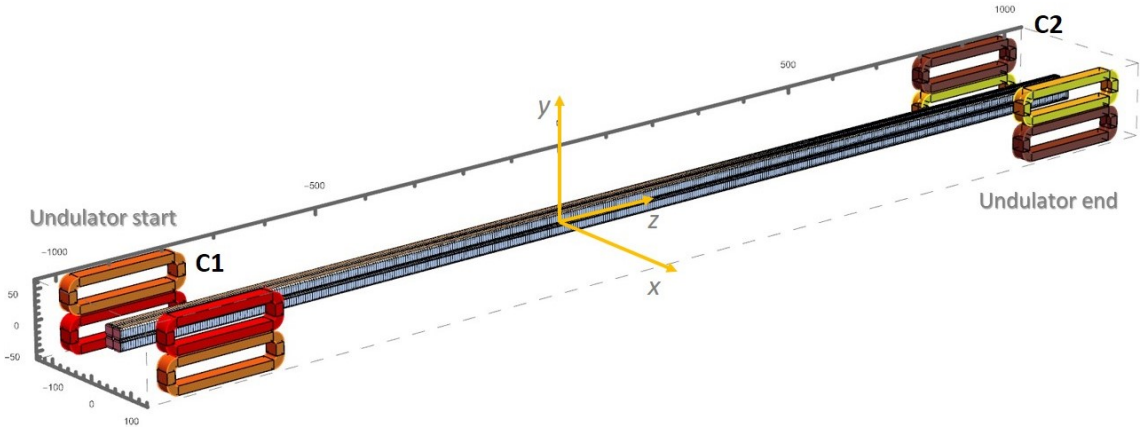

Figure 8.24: Correction coils scheme and its displacement at the begin (C1) and at the end (C2) of the undulator magnets array. Coils with the same color are electrically coupled in series.

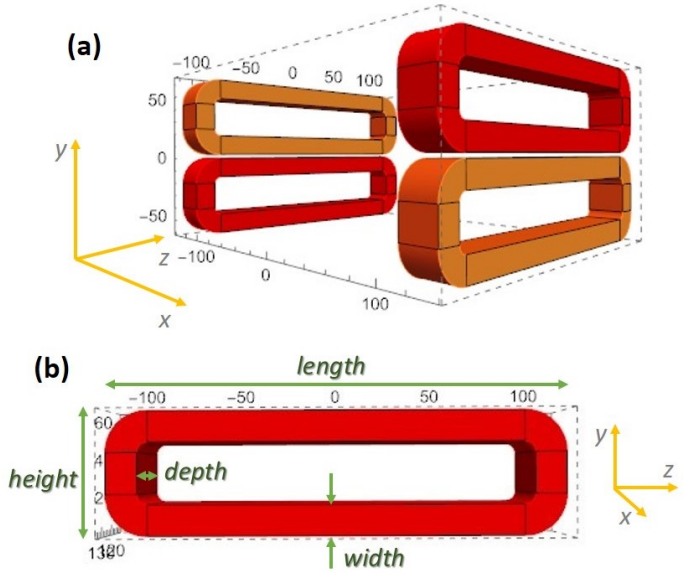

Figure 8.25: (a) Single block of the correction coils system. The horizontal distance form the undulator axis (x = 0) takes reasonably into account the size of the magnets' holders. (b) Scheme and dimensions of the single coil.

Table 8.5: Correction coils modeling parameters as defined in Fig. 8.25.

Parameter	**Value**
Length	220 mm
Height	60 mm
Width	15 mm
Depth	25 mm
# wire turns	10
Wire sizes	2 mm x 1 mm
Max. current density	1-2 A/mm^2

two of the second and fourth quadrants are electrically connected in series with each other (and therefore powered by the same current). Each coil is assumed to be made by 10 turns of a wire with a 2 mm $\times$ 1 mm rectangular section, where a maximum current of few amps flows This is typically sufficient to correct the residual field integrals. Once optimized the coils, by varying the current, the field integrals are further decreased respect to the ones of Tab. 8.4, these values are compared in Tab. 8.6. The resulting correction effect on the trajectory is evident in Fig. 8.26.

Table 8.6: Undulator first (I) and second (II) horizontal (x) and vertical (y) field integrals at minimum gap. Comparison between with and without using the correction coils for the Horizontal (HP), Circular (CP) and Vertical (VP) polarization mode.

	corr. coils off			***corr. coils on***			
	HP	**CP**	**VP**	**HP**	**CP**	**VP**	units
I_x	0	0	0.6	0	0	0.54	$10^{-5}\ T \cdot m$
I_y	0.22	-0.05	3.78	0.22	0.08	-0.32	$10^{-5}\ T \cdot m$
II_x	0	-0.19	-1.21	0	-0.09	-0.67	$10^{-5}\ T \cdot m^2$
II_y	0	0	0	0	0	0.42	$10^{-5}\ T \cdot m^2$

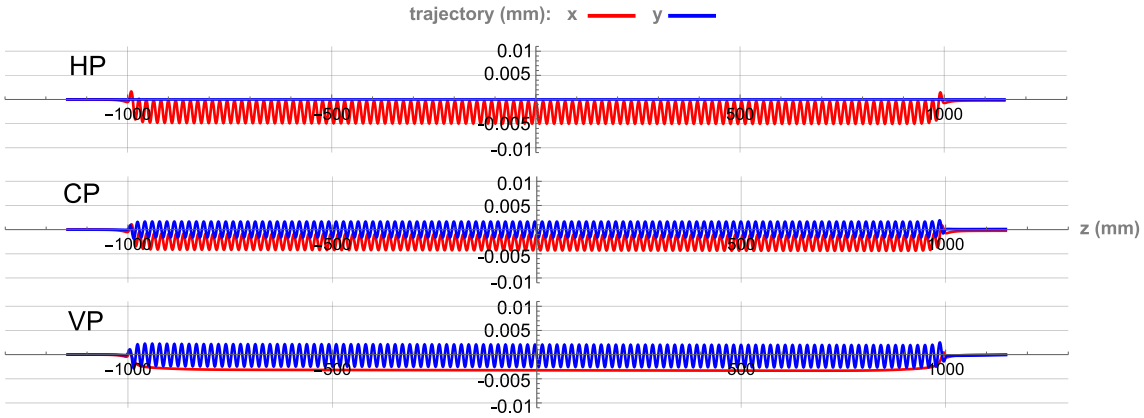

Figure 8.26: Corrected trajectory by means of the Correction Coils system. The three cases of linear Horizontal (HP), Circular (CP) and linear Vertical (VP) polarization mode are plotted.

8.3.2 Mechanical design

In this section we analyse the mechanical stress induced by the intense magnetic fields at minimum gap (Sec. 8.3.2.1) and we present a summary of the measurements of mechanical deformation of the SABINA undulator, which were investigated on the real device, and compared to the finite element analysis provided by the producer prior to the realisation. In Sec. 8.3.2.3 we report on the results of a prototypical study of the AQUA undulator, conducted using the SABINA undulator (realised by KYMA [17]) as the baseline design.

8.3.2.1 Magnetic Forces

The magnetic field generated by the magnetic elements of the undulator, and its superposition in each point, determines some attractive or repulsive force which in particular acts on the girders. This point is crucial to define the the mechanical structure of the undulator and to estimate the stress at which the motors, which move the undulator axis, have to work. In principle the lower the

forces the best is the work condition. Anyway also the capability of the commercial motors have to be considered as a reference. In addition, since the undulator is both gap and phase variable, the forces change with changing gap and phase. The highest value, then the worst case, holds for the smallest gap. In that condition, the variation of the girders shift leads to different values and shape of the variation for the three horizontal, vertical and longitudinal forces acting on the four girders. The longitudinal forces are however systematically weaker than the transverse ones.

The basic structure of the AQUA APPLE-X undulator is made of the four magnets arrays which have to generate the field useful for the FEL process. The forces acting on the four girder, due to the effect of the other three, can be estimated numerically from the undulator magnetic model by means of the code RADIA. The results are plotted in in Fig. 8.27. The maximum intensity is for the radial and vertical forces where the absolute value reaches respectively 1000 Kg and 1200 Kg.

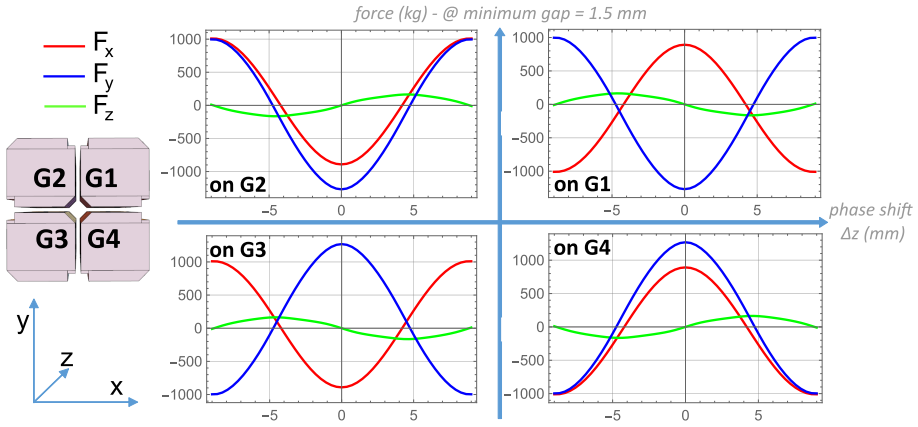

Figure 8.27: Integrated magnetic forces acting on the four undulator girders supporting the magnet arrays ($G1, G2, G3, G4$). Forces are of the order of 1 ton.

The evaluated forces can be actually manageable by commercial motors. However the magnetic forces can have some effects on the deformation of the undulator girders supporting the magnet arrays and then on the magnetic uniformity which the electrons feel. This effect can be neglected if the planarity of the girders while subjected to the magnetic forces remains within few microns.

The magnetic forces distribution can be compared with the case of the SABINA undulator [16, 18] where the forces variation with phase shift show a similar shape with an absolute maximum value of 1020 Kg. Also in this case the intensity of the longitudinal force is much lower than in the other coordinates. The effects of the forces on the stability of the structure have been experimentally tested as discussed in the following section, giving anyway negligible effects on the uniformity of the surface flatness of the girders.

The present analysis, together with the experimental results on the SABINA undulator, suggests that no further precaution would be necessary to manage the magnetic forces.

Anyway, if during the mechanical design phase of the structure it turns out that the required flatness is not obtainable by assuming a mechanical structure similar to that of the SABINA undulator, a possible solution to reduce the intensity of the magnetic forces could be taken into account. In this case a force compensation scheme can be considered by adding supplementary arrays of magnets with the same Halbach scheme of the undulator and choosing in an opportune way the transverse orientation of the field in the magnets as in [19]. The considered scheme is better detailed in Fig. 8.28. In this configuration the magnetic force can be significantly reduced up to a factor 5 as well evident in Fig. 8.29. To be noticed that the presence of the additional magnets does not affect the field and the field integrals in the undulator aperture. Also the requirements on remanent field intensity and block to block magnetic and mounting precision can be relaxed respect to the main arrays. For the considered case the remanent field for the compensating magnets have

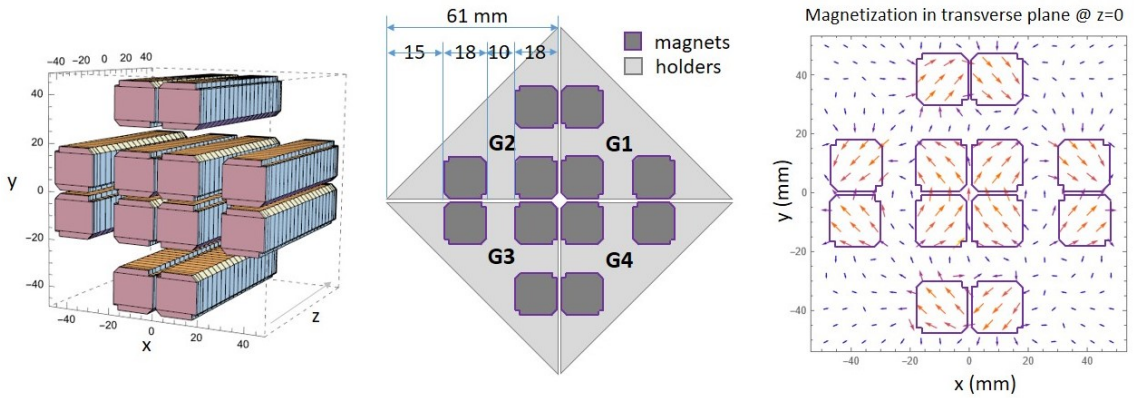

Figure 8.28: Compensating magnets scheme of the undulator array.

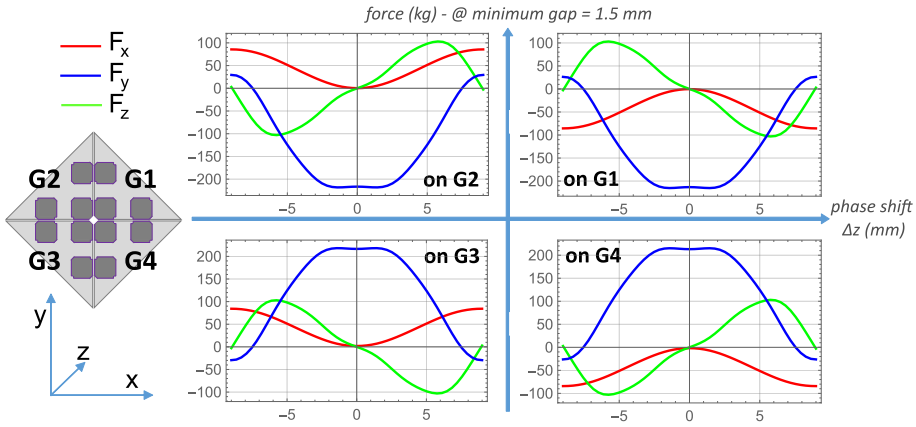

Figure 8.29: Integrated magnetic forces acting on the four undulator girders ($G1, G2, G3, G4$) in presence of the compensating magnets array.

been fixes as B_{rC} = 1.26 T (B_r = 1.35 T for the undulator main blocks).

The compensating magnets scheme would be useful to strongly reduce the magnetic forces and then the mechanical stress on the undulator structure. This anyway would increase the complexity of the magnetic structure and than the costs of realization.

8.3.2.2 Experience from the SABINA APPLE-X Undulator

SABINA is a THz FEL facility in commissioning at INFN-LNF. The undulators of the SABINA FEL line are APPLE-X undulators with some characteristics in common with the future AQUA undulator. An analysis of the SABINA undulator mechanical structure was performed in the undulator design phase (undulator realized by KYMA S.p.a). This analysis predicted the level of expected deformations when varying the undulator operating conditions (gap/phase). In order to measure directly the magnitude of the deformations and to verify the reliability of the mechanical design, a set of tests has been performed with FBG acting as strain sensors, after the undulator delivery in Frascati, with the support of the ENEA Fiber Optic Sensors Laboratory [20]. An FBG [21] is a phase grating inscribed in the core of a single-mode fiber, whose Bragg-diffracted light propagates back along the fiber. Any deformation of the grating affects its pitch, which changes the diffracted Bragg wavelength thus giving information about the occurred deformation. Application of the technique at the state-of-the-art level allows performing strain measurements with 1 µm strain resolution. The undulator parameters are listed in Tab. 8.7.

With respect to the AQUA undulator module, the two undulators have several characteristics in

Table 8.7: SABINA undulator parameters.

Parameter	Value
Material	NdFeB
Remanent field B_r	1.28-1.31
Period λ_u	55 mm
Blocks per period	4
Block magnet x,y,z size	28 mm × 28 mm × 13.65 mm
Aperture diameter ϕ	14.84 mm
Minimum gap	5 mm
B_{max} (in LP)	0.97 T
K_{max} (in LP)	4.9
K_{rms} max	3.5
N periods	22 (23.5)
Module length	1.35 m
Max Magnetic force at min. gap	750 kg/m

common: they are both APPLE-X devices with a similar mechanical layout. In the case of SABINA the undulator is shorter, and the minimum gap is 5 mm instead of 1.5 mm, but with the longer period (3 times longer in the case of SABINA) the specific magnetic forces are comparable.

The undulator [16] consists of four magnetic arrays mounted on identical magnetic girders, which are fixed to the guide rail carriages of the gap drive mechanism (see Fig. 8.30). The gap between the arrays can be varied by simultaneous movements of the girders hosting the magnets. Two of the four arrays, positioned diagonally, can also be moved longitudinally to induce a field phase displacement between the arrays of half period. Each magnet block is precisely positioned on a magnet holder. Along the length of the array, the magnet holders are screwed on top of three aluminum plates. The latter are then sustained by one interface plate towards the girder. The three holder plates and the interface plate are shown in Fig. 8.30 and are the structures under investigation.

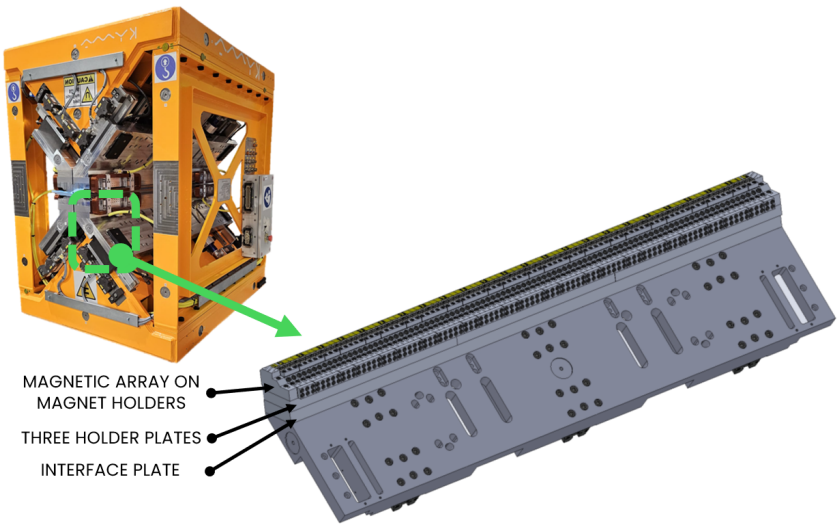

Figure 8.30: Mechanical structure under investigation.

The Fiber Bragg Grating [22] selected sensors were 1 cm long (Broptics OS 1500 optical sensors) and were used with Micron Optics FBG interrogation instruments [23]. The sensors were bonded to the surfaces facing the inside part of the undulator using Araldite epoxy adhesives.

The wavelength shift induced by the deformation of the fiber $\Delta\lambda$ can be converted into a strain parameter considering that 1 strain ($=1$ μm/m) of deformation corresponds to $\Delta\lambda = 1.2$ pm. These sensors were used in two different ways: as *strain measurements*, by gluing the fiber fully adhered to the surface of the magnet holder-plates; as *gap measurement* devices, by placing the sensors between adjacent plates. In both cases the measurement is local, but in the first case, the reference length is the length of the sensor. In the second case, the reference length is the separation between the adjacent plates.

We address to [24] for a detailed description of the setup and of the carried out measurements. The extremely high sensitivity of the measurement method allowed to measure a variation of the order of $\approx 150-200$ nm in the connections between the elements composing each girder, and local deformations of the order of ≈ 300 nm/cm of the structure where the senors were installed. These deformations are considered compatible or lower than those calculated by finite elements methods [17] and confirm the reliability of the undulator mechanical structure and design. These measurements validate the technical solutions adopted for the APPLE-X device, providing confidence in their effectiveness. Consequently, it is reasonable to extend this design to meet AQUA's requirements, while assessing deformations associated with the longer structure. Compensation methods, such as the one described in the previous Magnetic Forces section, should be considered only if finite element analysis of the AQUA undulator suggests their necessity.

8.3.2.3 Undulator Mechanical considerations

A prototypical study of the AQUA undulator was developed for the FEL line as a mechanical evolution of the previously realised SABINA undulator. While retaining the core architecture of SABINA, the AQUA design incorporates several structural modifications to meet the requirements for greater length, precision, and load capacity. Mechanically, the AQUA undulator can be seen as a longer version of the SABINA design, with key enhancements including a longer structure and the capability to reduce the gap to as small as 1.5 mm. Other variations are aimed at reinforcing the frame to withstand higher stresses and achieve tighter mechanical tolerances. However when the study will enter the finite-element analysis, the use of compensation magnets as described in Sec. 8.3.2.1 could be envisaged to mitigate the mechanical stresses.

A CAD representation of the undulator is shown in Figs. 8.31 and 8.32.

The entire frame should adopt motors to ensure positioning of the undulator in the transverse x-y plane (beam propagating along z). According to the analysis developed in Sec. 8.4 a movement range of 1 mm with a step of 5 μm should be sufficient for enabling remote beam based alignment.

The frame (see Fig. 8.33) has been strengthened by integrating internal bulkheads with a smaller pitch, thus increasing the number of reinforcements to sustain the higher loads. For longitudinal displacement, the system has moved from using one motor (as in SABINA) to two motors. These two motors act on two separate points, pushing the single girder forward or backward along the line, parallel to the beamline, to enable phase shifting. As seen in the design images, the radial movement system has also evolved, moving from two to three motors, thus providing a redundant driving force relative to the expected proportional load increase.

Compared to SABINA's 1.35-meter length, the AQUA undulator reaches approximately 2 meters. By doubling the motors for longitudinal phase shifting, the system is intentionally over-engineered, as with two motors it would theoretically be possible to move girders along a 3-meter length, making the setup more robust than strictly necessary. For radial movement, the system has also moved from two to three motors, again providing an overcapacity relative to the estimated mechanical demands.

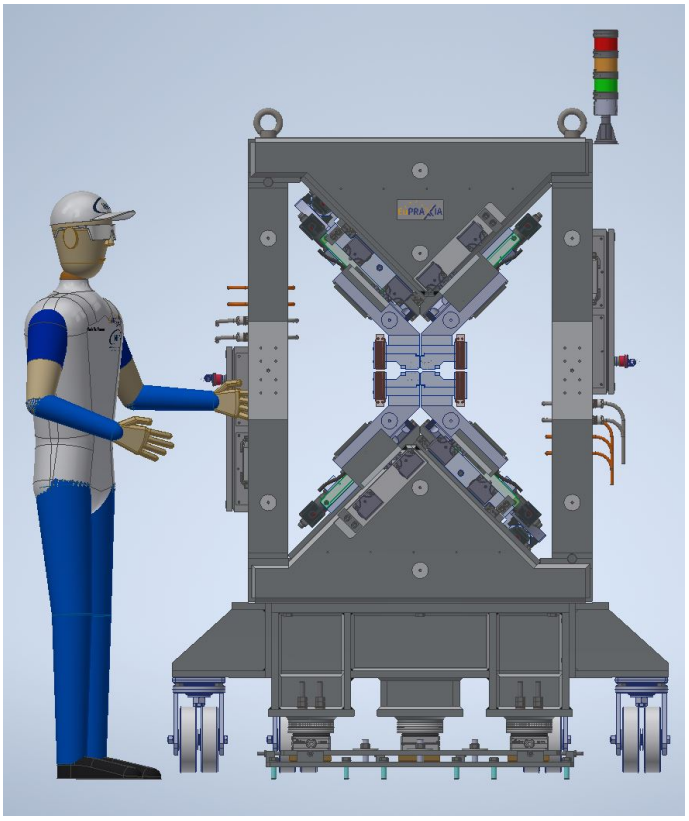

Figure 8.31: Rendering of one of the AQUA undulator modules. Front view.

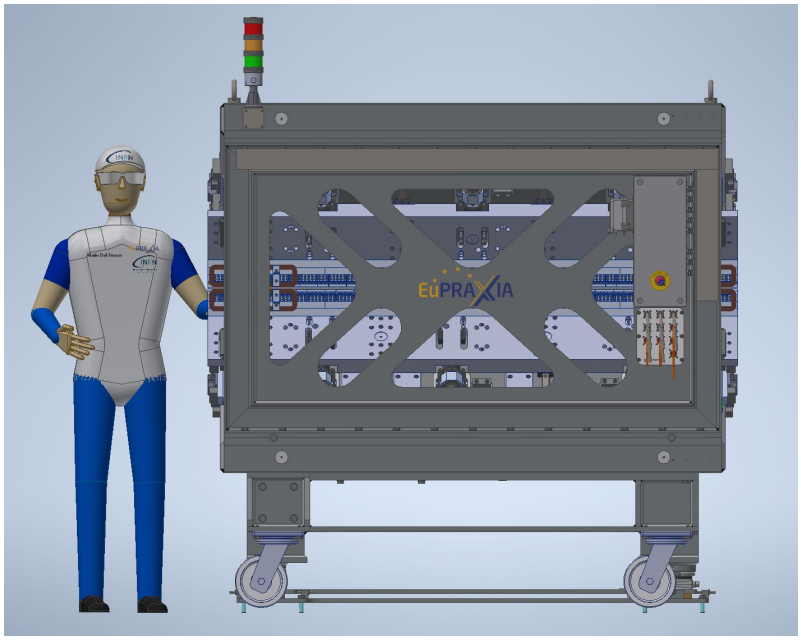

Figure 8.32: Rendering of one of the AQUA undulator modules. Side view.

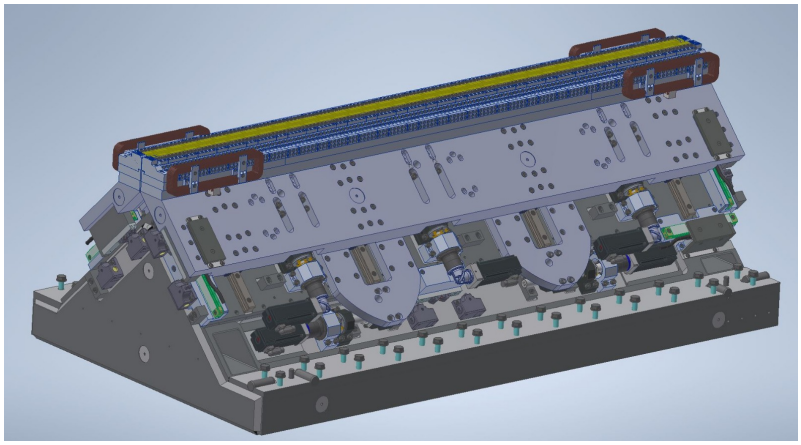

Figure 8.33: Undulator lower frame

The motion control system relies on the use of optical encoders, which monitor the undulator's position. While continuous feedback on left-right positioning and potential tapering effects is not implemented, the optical encoders provide sufficient control to ensure that the undulator's motion remains within the required tolerances.

8.3.2.4 Undulator positioning system

To successfully implement beam-based alignment (BBA) procedures, the undulator must be mounted on an active, motorized positioning system capable of precise and repeatable transverse motion. This system should allow the undulator to be shifted horizontally and vertically over a range of at least ± 1 mm, with step sizes on the order of 5 µm or finer. Such fine control is essential to align the undulator axis with the electron beam trajectory, compensate for installation tolerances, and correct for slow drifts over time. The motorized stages (not implemented in the CAD model of Fig. 8.31) must provide not only high resolution but also excellent mechanical stability, ensuring that movements are smooth and free of backlash or vibrations that could compromise beam quality. Integration with the accelerator control system is also critical, as it enables automated scans, automated step-tapering of the undulator chain and closed-loop BBA routines that use beam position monitors and other diagnostics to iteratively optimize the undulator positions and resonances. By equipping the undulator with this level of active control, the facility ensures that optimal overlap between the electron beam and the magnetic axis can be maintained, maximizing FEL gain and efficiency, reducing beam losses, and preserving the quality of the emitted radiation across varying operating conditions.

8.3.2.5 Temperature stability

The temperature stability plays a critical role in ensuring both magnetic field uniformity and precise beam alignment, both of which are essential for achieving optimal FEL performance. In undulators based on NdFeB permanent magnets, the magnetic field exhibits a negative temperature coefficient of approximately -0.1% per degree Celsius. This means that even small temperature fluctuations can induce measurable variations in the undulator field, which directly affect the photon wavelength, gain length, and saturation behavior of the FEL. For example, to maintain a relative field stability below 5×10^{-3} (0.5%), the temperature of the magnets should be controlled within a tight band of about ± 2.5°C; a stricter control of ± 1°C or better is desirable to account for other sources of variation and to maintain performance margins. Beyond the magnetic effects, the mechanical stability of the undulator axis with respect to the electron beam trajectory is another critical aspect influenced by temperature. The undulator frame, mostly made by structural steel or iron, is subject

to thermal expansion governed by the linear coefficient of thermal expansion $\alpha \approx 12 \times 10^{-6}/°\text{C}$. For a frame height of ≈ 120 cm, a temperature change of just 1°C produces a vertical displacement of about 14.4 µm. To meet stringent beam alignment tolerances—typically on the order of 10 µm or less in the vertical direction—the temperature of the support structure must therefore be controlled within about ± 0.7°C. This alignment sensitivity becomes particularly relevant when operating at short wavelengths.

The combined influence of thermal effects on both the magnetic field and mechanical stability means that the undulator system requires an integrated approach to thermal management. Passive approaches, such as thermal insulation and the use of low-expansion materials (e.g., Invar or granite), can help mitigate the effects of ambient temperature variations. Active measures, including temperature-controlled enclosures, water-cooled thermal jackets, may be necessary for achieving the required stability. Moreover, when thermal gradients exist along the length of the undulator, they can induce not only vertical displacement but also bending or torsional deformations, leading to misalignments between segments and to phase errors that degrade FEL gain.

An option to ensure thermal stability is that of implementing active temperature stabilization of the undulator cage. To achieve precise thermal stabilization of the undulator, a highly effective approach is to thermalize the supporting cage or frame, rather than attempting to control the temperature of the entire undulator environment. The cage is the structural backbone that determines the position and alignment of the undulator relative to the electron beam. By equipping the cage with an active thermalization system — such as circulating thermostabilized fluid, embedded heating elements, or temperature-controlled insulation panels — the temperature of the frame can be maintained within a narrow band, typically within ± 0.5°C or better. This ensures that thermal expansion effects on the frame are minimized, maintaining the undulator axis stability within micrometer tolerances, even if the surrounding tunnel or hall environment fluctuates by few degrees. Because the magnetic and vacuum components are rigidly mounted to the cage, stabilizing the frame effectively stabilizes their position without requiring complex or costly full-environment climate control. This strategy allows for a highly efficient and targeted solution: the thermal mass of the frame is relatively modest, making it feasible to apply active control, while the undulator magnets and vacuum chamber can remain passively shielded with minimal additional thermal management.

8.3.3 Phase shifter for the AQUA undulator

In a single-pass FEL designed with a segmented undulator, the breaks between each undulator segment introduce a phase shift between the electron density modulation and the phase of the electromagnetic field. Such a phase mismatch causes the electrons to momentarily recover energy at the expense of the radiation field amplification.

The ≈ 25-m long undulator of the AQUA line [25] is divided into ten segments each separated by a $L_d = 600$ mm long break section. The effect of a phase mismatch at the nine breaks between the undulators is shown in Fig. 8.34 where time dependent simulation has been obtained with the GENESIS1.3 (version 4) code [26] with the electron beam parameters of the AQUA FEL case [25].

8.3.3.1 Phase Shifter requirements

The phase shift ϕ_d induced by a drift L_d between two segments is given by:

$$\frac{\phi_d}{2\pi} = \frac{L_d}{2\gamma^2\lambda_0} = \frac{L_d}{\lambda_u(1+K_{rms}^2)} \tag{8.3}$$

The K value changes with varying the undulator gap and so the phase advance in the break section for different tuning of the operational resonance wavelength. A Phase Shifter (PS) can introduce a supplementary phase delay so that the total phase advance (break section + phase

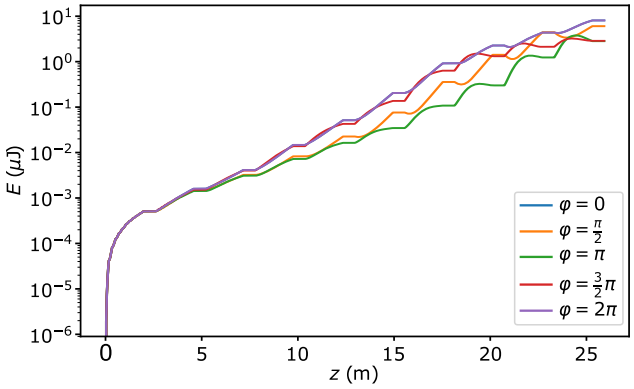

Figure 8.34: Intensity growth of the FEL radiation as a function of the phase advance in the separations between the modules of the AQUA undulator line. Cases for $\phi = 0$ and $\phi = 2\pi$ are equivalent and then overplotted.

shifter) is an integer multiple of 2π. The effective phase advance to be compensated by the phase shifter is better defined as:

$$\frac{\phi_d}{2\pi} = \frac{L_d - L_p}{2\gamma^2\lambda_0} \tag{8.4}$$

where L_d is the break section length from the cell boundary of the previous undulator to the cell boundary of the next undulator. The phase shifter magnetic length L_p is subtracted from L_d since the drift phase advance in L_p is part of the phase shifter correction. When the phase shifter is off ($L_p = 0$) the previous formula takes again the form of Eq. (8.3).

For the present case, with a 600 mm long break section and a 1 GeV energy of the electron beam ($\gamma = \frac{E}{m_o c^2} = 1957$), the phase advance introduced in the break section is plotted in Fig. 8.35 with dependence on the wavelength, together with the correspondent required phase correction of the phase shifter. Here we assume a constant magnetic length of $L_p = 90$ mm for the phase shifter.

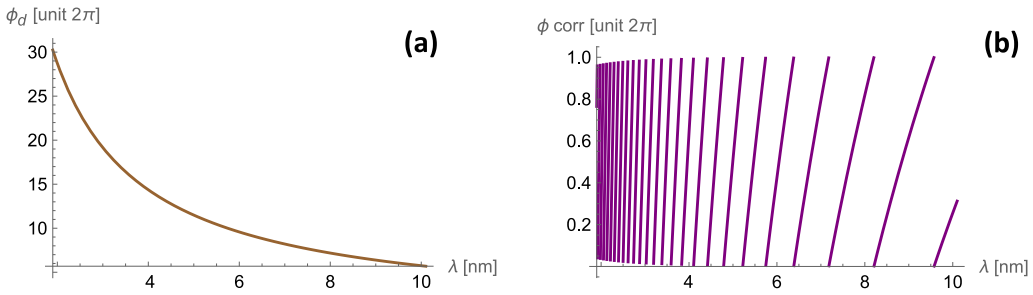

Figure 8.35: (a) Phase delay introduced by the break section with variation of the resonant wavelength of operation. (b) Required phase correction from the phase shifter in the operational wavelength range. The phase values are given in units of 2π.

If no correction occurs, the electrons would enter the next undulator with the wrong phase with a consequent degradation of the FEL amplification as described before. The phase shifter compensates for this changing phase advance. The phase change in the phase shifter can be calculated as [27]:

$$\frac{\phi_p}{2\pi} = \frac{L_p + (\frac{e_0}{m_0 c})^2 PI}{\lambda_u(1 + K_{rms}^2)} \tag{8.5}$$

here L_p is the magnetic length of the phase shifter. *PI* is the so called "phase integral" which, if we consider only a planar phase shifter with one (vertical) field components B_y, is defined as:

$$PI = \int_{-L_p/2}^{L_p/2} \left(\int_{-L_p/2}^{z} B_y(z')\, dz' \right)^2 dz \tag{8.6}$$

Then the phase change depends only on the phase shifter's and undulator's mechanical and magnetic properties. Since all the parameters of the two devices are specified, the phase integral is the key parameter which describes the phase shifter action. To be noticed that the phase advance to be corrected variates with the different undulator tuning. For this reason also the phase shifter must have variable gap independently from that of the undulator, varying then the peak magnetic field and slightly the magnetic length. If L_b is the break section between two undulators, the effective free space length L_0 changes with the phase shifter tuning as $L_0 = L_b - L_p$. However we assume a constant magnetic length for the phase shifter, being this is good approximation for the purpose of the present case.

As described in Fig. 8.35, in order to compensate all possible phase advances from the break section, the phase change of the phase shifter should be well over 2π when it works at its minimum gap, at the longest foreseen value of FEL radiation wavelength (largest K value) at operation. A permanent magnet phase shifter has been then designed to achieve the required electron beam delay in a compact structure that could be installed in close proximity to the undulators. The phase shift is obtained by a magnetic chicane that delays the beam due to a longer path, which in principle may be realized as in the main undulator, with the same kind of permanent magnets, in a similar arrangement. However in our case, because of the more complex geometry of the APPLE-X undulator and since a delay in only one coordinate is enough for the purpose, we prefer not to reply the APPLE-X scheme also for the phase shifter, opting rather for the more simply planar configuration. In addition to the requirements on the phase correction value, another constraint for such a phase corrector is that the field integrals must vanish at any gap.

8.3.3.2 Phase Shifter modeling

The magnetic scheme of the Phase Shifter is a classic 1 period planar Halbach displacement [13] with 4 block per period with a fifth block at the end to ensure the symmetry in the field. The chosen geometry is borrowed and rescaled from the SPARC phase shifter [28]. The choice of the constructive parameters is related to the desired performances. An optimization of the parameters have been done according to the following considerations:

- the longitudinal width of the PS cell must be compatible with the installation of the other elements foreseen in the break section (quadrupole, bpm, correctors, diagnostics, vacuum pumping stage); this fix the dimension of the PS as of few centimeters;
- the block longitudinal width has not necessary to be so small as in the undulator since the geometry itself is not the same. In addition also the remanent field B_r can be decreased to the more manageable value 1.26 T.
- the magnetic gap, namely the vertical distance between the planar faces of the magnets, should be as small as possible to maximize the peak magnetic field but at the same time it must allow the installation of the 5.5 mm (external diameter) vacuum pipe for the electrons. We choose a gap g = 7 mm to consider some tolerance in mounting and alignment of the pipe;
- the AQUA line is optimized to operate at 1 GeV with a resonant wavelength of 4 nm. The range allowed by the tuning of the undulator is 3-5 nm. However the resonance can be extended up to 10 nm with decreasing the electron beam energy down to 0.7 GeV. The PS have then to be designed to consider also this eventuality;

- the end magnets dimension and the positioning of the block have to be optimized to minimize the field integrals and hence the effect of the PS on the trajectory and kick angle of the electron passing inside the device.

The magnetic design of the phase shifter has been performed by means of the RADIA code [8]. The final scheme is then a planar geometry as described in Fig. 8.36, with the parameters in Tab. 8.8.

This geometry are suitable to fulfill the requirement on field integrals (which must be equal to zero at the nominal gap), phase integral and the desired phase correction for the whole range of operational wavelength.

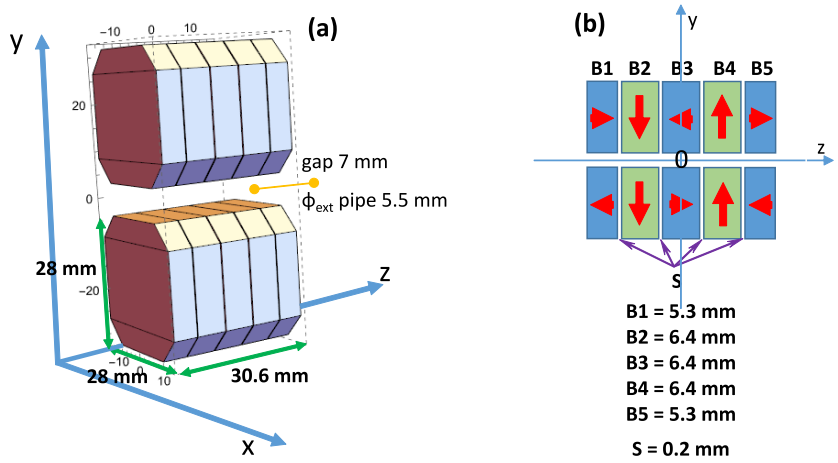

Figure 8.36: (a) Structure of the phase shifter for the AQUA undulator. (b) Longitudinal scheme showing the orientation of the magnetic field in the blocks and the end magnets design.

Table 8.8: Phase shifter main parameters.

Parameter	Value
Geometry	Planar
Material	NdFeB
Remanent field B_r	1.26 T
Total # blocks	5
Block magnets x,y size	28 mm × 28 mm
B2, B3, B4 block z width	6.4 mm
B1, B5 end blocks z width	5.3 mm
Space between blocks	0.2 mm
Mechanical length	30.6 mm
Effective cell length	90 mm
Minimum gap	7 mm
B_{max}	0.94 T
Operational wavelength range	3 - 10 nm

8.3.3.3 Phase Shifter properties

According to the chosen geometry, the central magnets of the top and bottom phase shifter array have the field oriented parallel to the longitudinal z axis (see Fig. 8.36), this giving a null field at

its center. This geometry causes a full one period oscillation of the field along the longitudinal coordinate. The planar geometry causes the presence of the vertical component B_y only of the field.

The vertical component of the magnetic field at the nominal gap, as well as the consequent first and second field integrals, are shown in Fig. 8.37. The scheme is such that the field integrals are equal to zero at the minimum gap (g = 7 mm). However we have a slight dependence of the second field integral with the gap, but it remains within the tolerances (Fig. 8.38).

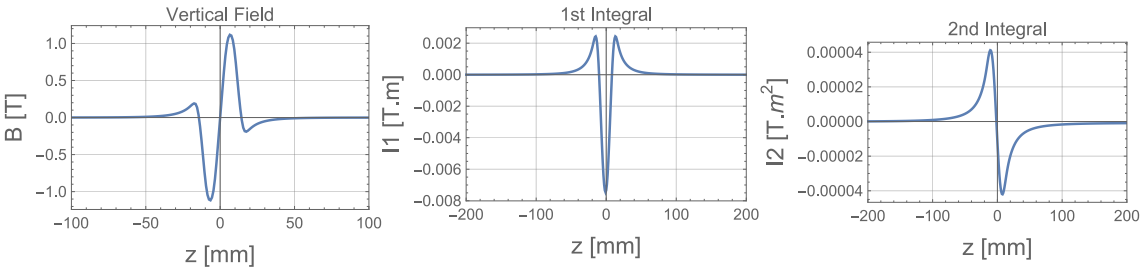

Figure 8.37: Vertical component of the field B_y, first and second field integrals for the AQUA phase shifter.

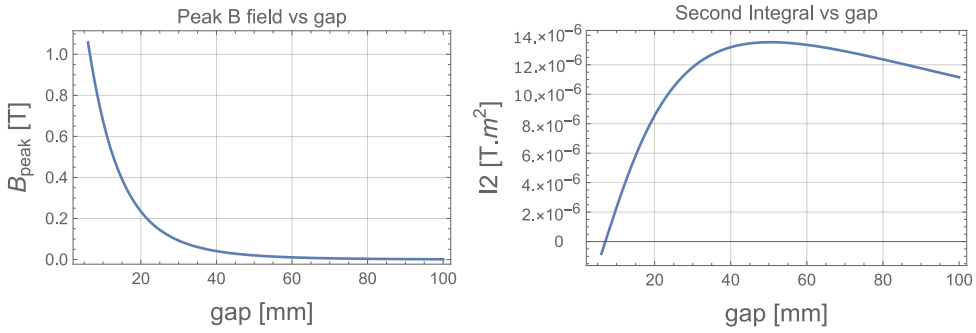

Figure 8.38: Variation of the peak B field and of the second integral with changing phase shifter gap. We do not report the variation of the first integral since it is negligible. Variation of the second integral is anyway within tolerances.

The transverse field profile ensure a variation of the field no more than 0.1% for $y < 200$ µm from axis in the vertical direction. This is to be considered as the homogeneity region which is anyway comparable with that of the undulator which still drives the constraints on beam alignment precision. A much large value (some millimeters) stands for the horizontal homogeneity region of the field, this because of the planar geometry of the phase shifter.

In Fig. 8.39 we can also see the trajectory and kick angle of a electron entering in the phase shifter with null offset and angle at minimum gap.

Following the procedure in [27], the required maximum value of the phase integral is $PI_{max} = 3.2 \cdot 10^{-7}$ T^2 m^3. The geometry of the phase shifter has then been optimized to have more than this value when the devices works at minimum gap and for the maximum FEL resonance wavelength of operation (λ = 10 nm in this case). This ensure the phase shifter can operate in all the foreseen configuration of the undulator. The resulting phase integral inside the phase shifter is plotted in Fig. 8.40 for different values of the gap. The phase correction can then be evaluated from Eq. (8.5) for different wavelength in the undulator tuning range: the shorter the wavelength the larger is the maximum achievable correction. Such a large range of values depends on the range of wavelength in which the phase shifter is foreseen to operate. The variation of the phase advance in the PS with varying the gap is also plotted in Fig. 8.41.

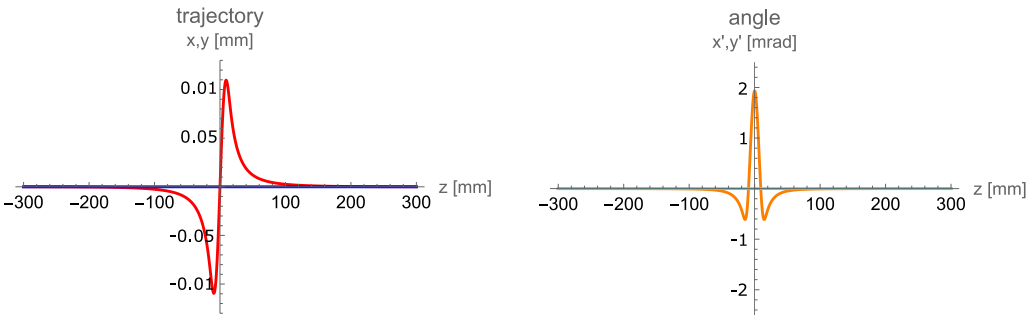

Figure 8.39: Trajectory and kick angle of a electron entering in the phase shifter with null offset and angle at minimum gap. Since the planar geometry, one electron oscillates, and its angle varies, only in the horizontal plane.

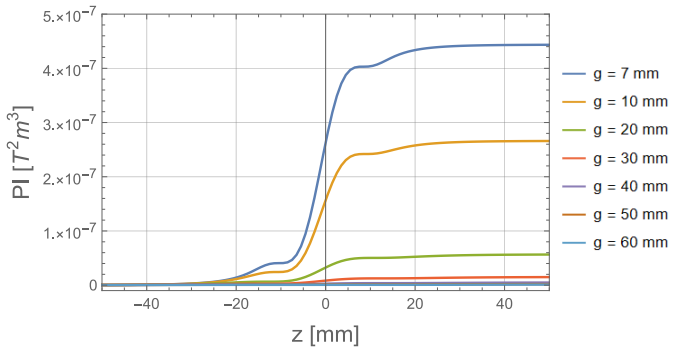

Figure 8.40: Phase Integral (PI) in the phase shifter for different values of the operational phase shifter gap.

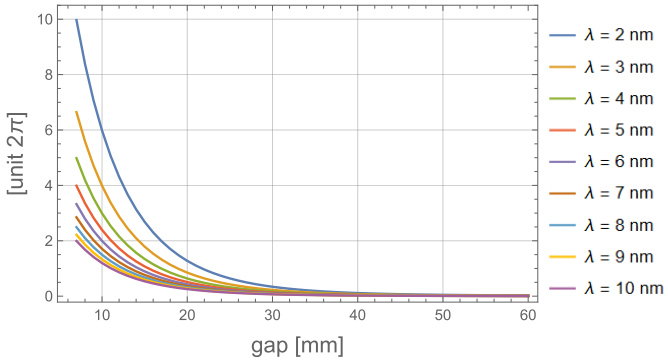

Figure 8.41: Phase correction as a function of the phase shifter gap, for different values of operational wavelength.

The minimum correction arises for the longest wavelength but the maximum value is still enough to compensate any phase delay up to 4π. The maximum phase advance occurs at the minimum wavelength and we have a value of 5 times 2π for the working point at 4 nm. In that case, increasing the gap from 7 to 8.3 mm allows to shift the phase by a whole period and switching the phase shifter off at gap > 60 mm for all values of operational wavelength.

Finally by evaluating the phase advance for all gaps and wavelength in the range of operation we can estimate the effective length in which the PS works by finding the distance from the PS centre at which the phase advance varies no more than 0.1%. This can be considered the PS cell length $L_p = 90$ mm.

8.3.3.4 Phase Shifter positioning

The phase shifter should be placed soon at the exit of the undulator. Anyway a certain distance from the undulator magnets array has to be considered in order to avoid a superposition of the fringe fields of the two devices which may affect the electron beam trajectory. This because the undulator has some residual field within few millimeters beyond the physical end of the magnets array. The estimated best position is at a distance of 34.5 mm from the edge of the last undulator magnet when the undulator is settled in horizontal polarization mode (no shift of the movable girders).

The effect of the coupling of PS with undulator is better evident in Fig. 8.42 on the trajectory of an electron moving across undulator and phase shifter, entering with null offset and angle (no correction coils are used). The trajectory is plotted for the cases of horizontal, circular and linear vertical polarization mode of the undulator. In all three cases the residual offset and angle at the end of the line is due to the residual field integrals of the undulator itself (see Fig. 8.23). The PS has no effect on the trajectory when placed at no less than 34.5 mm from the undulator magnets edge (in HP mode). The effective open distance becomes less, with varying the polarization mode of the undulator (shifting the movable girders), down to 30 mm for the linear vertical polarization. This value is consistent with the estimated effective cell length of the phase shifter (see previous paragraph).

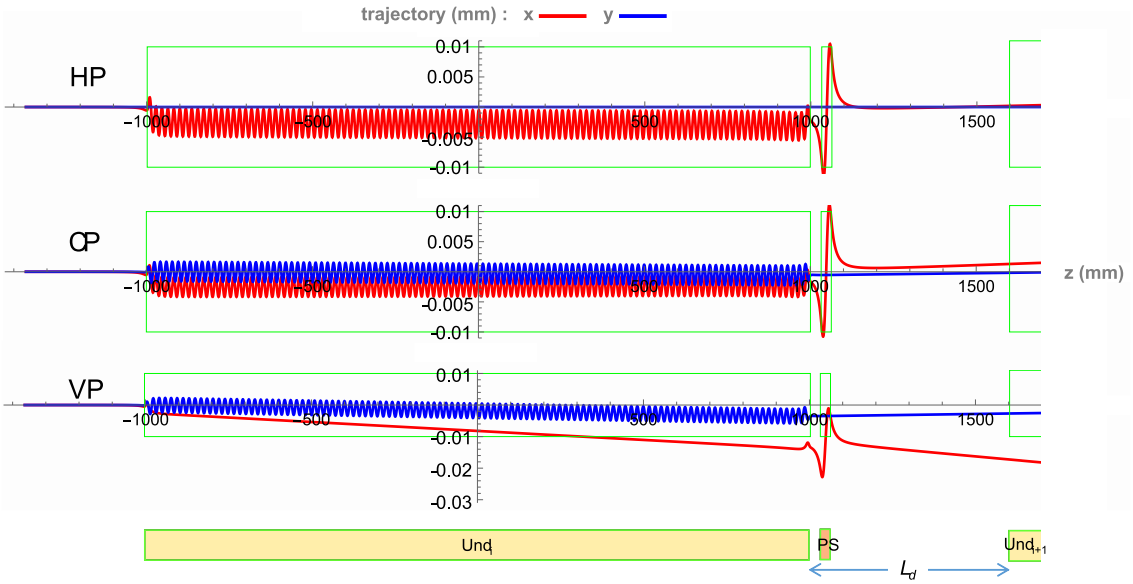

Figure 8.42: Trajectory (vertical blue, horizontal red) of an electron moving in the undulator coupled with the phase shifter. The electron is entering with null offset and angle in the undulator (with no contribution from correction coils). The cases of Horizontal (LP), Circular (CP) and Vertical (VP) polarization mode are considered with the phase shifter placed soon after at a distance of 34.5 mm from the undulator edge (in HP mode). The rectangular boxes correspond to the devices on the line, one undulator (U_i) and the following (U_{i+1}), the phase shifter (PS).

8.4 Analysis of tolerances

We have employed both analytical models and numerical simulations to study the impact of parameter fluctuations and beam degradation, and to assess their tolerances. In the introduction, and in Section 8.2.4, we discussed the effects of variations in electron beam energy spread, current, emittance, and beta functions. We now turn our attention to other critical aspects, such as tolerances related to beam injection into the undulator line. These can also be interpreted as alignment

tolerances for individual undulator sections, quadrupole positioning, and undulator magnetic field errors, and their combined impact on the FEL amplification process.

When driven by the short electron bunch delivered by the plasma stage, the FEL operates in a regime close to the single-spike limit, where fluctuations are strongly influenced by shot noise in the electron beam. This regime is not ideal for defining tolerances related to trajectory alignment or injection jitters at the entrance of the undulator line, as the inherent statistical fluctuations obscure the effects of systematic variations. To disentangle the effects of macroscopic jitters and errors in the undulator line parameters from the microscopic statistical fluctuations of the electron beam—and to reduce computational time, we consider steady-state single-mode simulations with the beam specified in Tab. 8.1 or a longer, 200 pC-200 fs electron bunch, corresponding to a peak current of 1.3 kA.

8.4.1 Trajectory Injection jitters

Transverse misalignment of the electron beam in the undulator FODO line induces oscillations in the beam trajectory, which can degrade the FEL performance. We can distinguish between two types of effects: (1) static offsets of magnetic elements—such as an individual undulator module, the entire undulator line, a quadrupole, or localized magnetic field errors—which can be partially compensated using corrector magnets to restore the average trajectory; and (2) shot-to-shot trajectory jitters, which cannot be corrected in advance due to their unpredictability before the beam passes through. Although these effects differ in origin, they produce similar consequences. Therefore, analyzing a single instance provides insights into both the alignment tolerances of beamline components and the sensitivity to trajectory jitters arising during acceleration and transport.

Transverse position jitters can include beam trajectory offsets and tilts with respect to the conventional on-axis electron beam propagation. FEL emission is evaluated for both positive and negative electron beam trajectory offsets and tilts at injection, considering off-axis injection in one transverse plane (horizontal and vertical).

The impact of the beam matching conditions on FEL performance is investigated using the reference electron bunch parameters for the undulator design (see Table 8.1) with a transverse Twiss beta function of $\beta_T = 8$ m, as well as a smaller beta function of $\beta_T = 5$ m, corresponding to a smaller average transverse beam size. The FODO matching of these two working conditions used in the simulations is shown in Fig. 8.43.

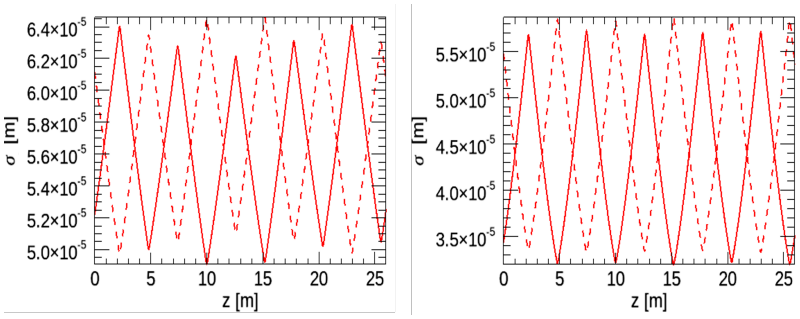

Figure 8.43: Electron beam RMS matched transverse size $\sigma_{x,y}$ (m) along the AQUA undulator coordinate z (m) in circular polarization. Nominal case with β_T= 8 m (left) for quadrupole field gradients 5.6/-5.5 T/m, and case with β_T= 5 m (right) for quadrupole field gradients 12.5/-12 T/m. Solid lines σ_x, dashed lines σ_y.

When the initial transverse tilt θ_0 of the electron beam at injection increases, the FEL saturation length also increases. This degradation in performance is accompanied by a small redshift of the resonant wavelength.

FEL emission from electron bunches injected off-axis into the ideal AQUA undulator line is simulated using GENESIS 1.3: a sequence of steady-state runs for different values of initial trajectory offset and tilt is performed, resulting in a 25×40 matrix recording the achieved FEL power along the undulator line versus the initial tilt angle and offset in the range [-40, +40] μrad and [-120, +120] μm respectively.

In circular polarization, the results of the analysis are summarized in the plots of Fig. 8.44, where the maximum achieved radiation power level P_0 along the undulator for a given transverse misalignment, normalized to the maximum FEL power $P_{0,max}$ achieved in the whole range of offsets and tilts investigated, is mapped as function of the trajectory offset and tilt values at the entrance of the undulator.

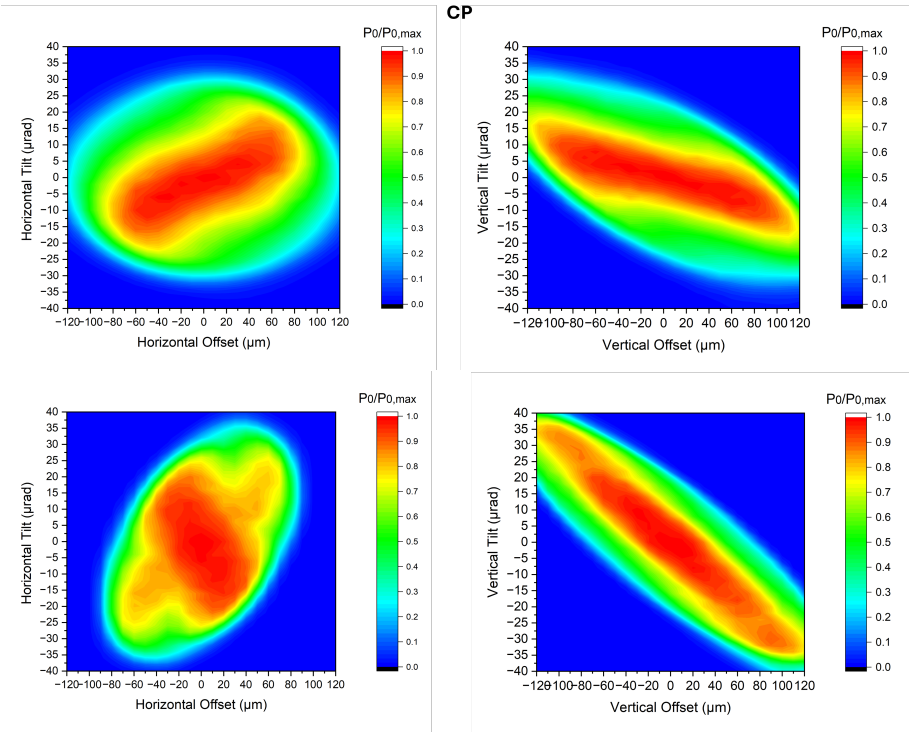

Figure 8.44: FEL emission from the nominal electron bunch with $\beta_T = 8$ m (top line) and $\beta_T = 5$ m (bottom line). Maximum achievable radiation power level P_0 for a given transverse misalignment, normalized to the maximum FEL power $P_{0,max}$ achieved along the undulator line in the whole range of explored misalignments in circular polarization (CP) as a function of the initial horizontal (left) and vertical (right) tilt angles (μrad) and offsets (μm).

The acceptable electron beam transverse misalignments, that cause a FEL power reduction of less than 30%, are the ones corresponding to the red and yellow areas of the plots in Figs. 8.44 and 8.45. The emission areas located on the diagonal of the plots, separated from the central part, are an effect of the matching optics. If operating in circular polarization, the tolerance of electron beam misalignments in one single plane is slightly more stringent for the lower β_T electron beam.

The tolerances in linear polarization are similar to the ones in circular polarization and are shown in Fig. 8.45.

The supported electron beam position jitters at injection in the AQUA FEL undulator are summarized in Table 8.9. Such values provide a degradation of the emission of the order of 10-15% of FEL peak power), still allowing to achieve FEL saturation within the 10 undulator modules foreseen for AQUA.

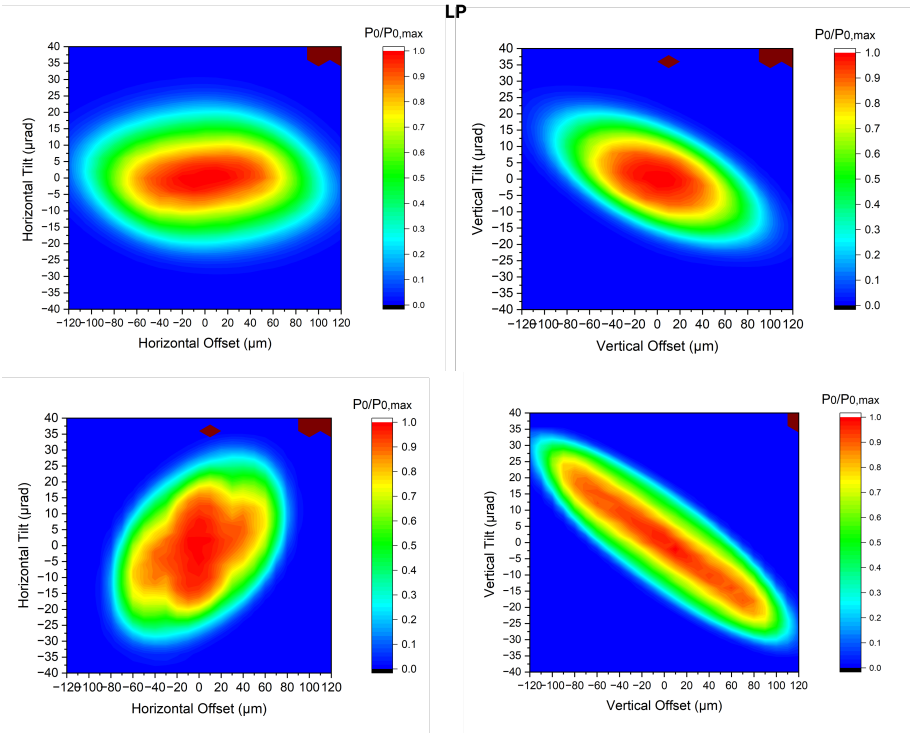

Figure 8.45: FEL emission from the nominal electron bunch with $\beta_T = 8$ m (top line) and $\beta_T = 5$ m (bottom line). Maximum achievable radiation power level P_0 for a given transverse misalignment, normalized to the maximum FEL power $P_{0,max}$ achieved along the undulator line in the whole range of explored misalignments in linear polarization (LP) as a function of the initial horizontal (left) and vertical (right) tilt angles (μrad) and offsets (μm).

Table 8.9: AQUA undulator tolerance to electron beam misalignments in one transverse plane or symmetrically in both transverse planes (horizontal = vertical) at injection and in circular polarization, for nominal electron bunches (properties in Table 8.1) with $\beta_T = 8$ m and $\beta_T = 5$ m.

	Tilt	**Offset**
β_T**= 8 m**	$\pm$ 8 μrad	$\pm$ 40 μm
β_T**= 5 m**	$\pm$ 8 μrad	$\pm$ 20 μm

8.4.2 Sensitivity to magnetic errors

The FEL process can be affected by two types of errors within the undulator beamline:

- non-steering errors, depending on the peak field variations and causing broadening of the bandwidth and shift of the resonance independently on the beam energy
- steering errors, comprehending various effects able to cause beam wander and leading to mismatch in the transverse overlap between the gain-guided optical mode of the radiation field and the beam itself.

In order to investigate how the FEL amplification process responds to magnetization errors in individual poles, we analyzed the sensitivity of FEL radiation growth to magnetic imperfections using a procedure that simplifies and mimics the protocols typically employed by undulator manufacturers.

We extracted random independent values ($\delta B_{x,+}$,$\delta B_{x,-}$,$\delta B_{y,+}$,$\delta B_{y,-}$) from four Gaussian distributions $\{\Theta_{x,+,n}\}$ and $\{\Theta_{x,-,n}\}$ $\{\Theta_{y,+,n}\}$ $\{\Theta_{y,-,n}\}$ representing magnets with different + or - polarity

and errors along the two coordinates x and y. The index n ranges between 1 and 70. For both components and both polarities. Randomly distributing these errors along the undulator imposes stringent constraints on the allowable spread of the distributions. A realistic model must consider the optimization procedures that can be applied—such as discarding a subset of magnets to eliminate distribution tails, and pairing magnets to minimize off-axis trajectory deviations. A first selection is done by removing the worst 10 magnets from each ensemble. We extracted then a set of 55 errors for each polarity corresponding to the minimum average of the whole sequence, taking into account that the magnets are aligned alternating the polarity. The first integral at the end of each undulator (110 errors, corresponding to the number of the periods, L_u is the module length):

$$I_{1,x} = \int_0^{L_u} dz' \delta B_x(z') \; = \sum \delta B_x \lambda_w \tag{8.7}$$

(and similarly for y) is therefore minimized. A third round consists in sorting the 110 items, always with alternating polarity, by minimizing step by step the second integral of the x-component:

$$I_{2,x} = \int_0^{L_u} dz \int_0^z (\delta B_x(z'))\, dz' \tag{8.8}$$

(and similarly for y). Such a protocol permits to reach a very high level of optimization of the magnetic error sequence for a given error rms value. We incorporated into the procedure the potential degradation from optimal error selection and alignment by introducing two additional features. First, we allowed for arbitrary changes to the final value of the first field integral—this reflects, in practice, the use of correctors at the ends of the undulator module or the application of shimming and pole-height adjustment techniques. Second, we modified the sorting by randomly inserting magnets from the distribution at a few locations with variable probability, without enforcing the constraint of minimizing the second field integral. As a result, the second integral is generally larger than in the fully optimized configuration. This protocol is similar to those used by the manufacturers, although the actual procedures are much more complex, could rely on groups of 3 and 5 magnets and take into account the natural link between the x and y components. Table 8.10 summarizes the required specifications of precision and stability of the magnetic field of the undulator modules and of the beam orbit correctors in order to guarantee the full FEL emission with the nominal electron beam parameters, i.e. more than 95% of the saturation power value obtained in the absence of magnetic errors. In Table 8.10, we have adopted the following denominations:
we introduce:

$$\delta B_r(z') = \sqrt{\delta B_x(z')^2 + \delta B_y(z')^2}, \tag{8.9}$$

and:

$$I_{1,rms} =< \int_0^z dz' \delta B_r(z') > \tag{8.10}$$

$$I_{2,rms} =< \int_0^z dz'' \int_0^{z''} dz' \delta B_r(z') > \tag{8.11}$$

the rms values along the undulator of the first and second integral, respectively. The functions $I_{1,max}$ and $I_{2,max}$ are the maximum value along the line of such integrals and correspond to the maximum angle and position offset of the average trajectory along the undulator. The parameters and $I_{1,res}$ and $I_{2,res}$ represent the average of their residual values at the end of the undulator modules.

Rms error values lower than 9×10^{-3} T do not prevent the full radiation growth (>95%) in the nominal electron beam condition, provided that the conditions in Table 8.10 are fulfilled. Even if the electron beam arrives straight on axis at the entrance of the undulator first module, its propagation in the following segments, cumulating offsets and tilts, can strongly diverge from the axis. It is necessary therefore to operate on the beam with orbit magnetic correctors to bring back the

Table 8.10: AQUA undulator tolerance to magnetic errors: specifications of phase error and field integrals as a function of the local magnetic error $\delta B_{x/y,rms}$

Quantity	**Unit**			
$\delta B_{x/y,rms}$	T	3×10^{-3}	6×10^{-3}	9×10^{-3}
σ_ϕ	deg	0.82	1.65	2.4
$I_{1,rms}$	$T\cdot m$	$<7\times10^{-5}$	$<6\times10^{-5}$	$<5\times10^{-5}$
$I_{2,rms}$	$T\cdot m^2$	$<5\times10^{-6}$	$<4\times10^{-6}$	$<3.1\times10^{-6}$
$I_{1,max}$	$T\cdot m$	$<4.5\times10^{-5}$	$<4\times10^{-5}$	$<3.6\times10^{-5}$
$I_{2,max}$	$T\cdot m^2$	$<3\times10^{-5}$	$<2.7\times10^{-5}$	$<2.5\times10^{-5}$
$I_{1,res}$	$T\cdot m$	$<2.1\times10^{-5}$	$<1.6\times10^{-5}$	$<1.1\times10^{-5}$
$I_{2,res}$	$T\cdot m^2$	$<2.5\times10^{-6}$	$<2.5\times10^{-6}$	$<2.5\times10^{-6}$

trajectories on axis. We chose to pre-compensate the offset at the entrance of each undulator module by inserting a magnetic corrector before the previous one.

It is reasonable to require local magnetic errors $\delta B_{x/y,\mathrm{rms}}$ to remain below approximately $5\text{–}6\times10^{-3}$. From Table 8.10, we can estimate the corresponding maximum acceptable trajectory offset. For the values in the middle column—corresponding to $\delta B_{x/y,\mathrm{rms}} = 6\times10^{-3}$ at 1 GeV—we obtain a maximum deflection angle of 12 µrad and a resulting trajectory offset of about 8 µm. From the same column we estimate that the maximum phase error should not exceed 5° (3 standard deviation σ_ϕ).

8.4.3 Sensitivity to quadrupole misalignment

A quadrupole offset is equivalent to introducing a first field integral at the quadrupole position within the undulator intersection. The maximum acceptable field integral at the undulator exit is listed in Tab. 8.10, namely $I_{1,\mathrm{res}} < 1.6\times10^{-5}$. Such a residual field integral is expected to be detrimental to the FEL amplification, whether it originates from imperfections in the undulator field or from a quadrupole offset. To quantify the maximum acceptable quadrupole offset that does not degrade FEL performance, we compare this allowable field integral to the contribution from a displaced quadrupole. We assume the worst-case scenario, corresponding to a quadrupole operating at its maximum integrated gradient of 1.7 T. Under these conditions, a quadrupole offset of approximately 15 µm would induce a field integral comparable to the threshold of $I_{1,\mathrm{res}}$.

A quadrupole offset can be corrected by repositioning the quadrupole using a system of transverse movers, which are rigidly coupled to a corresponding beam position monitor operating in closed loop with the trajectory feedback system. Any residual kick that remains after this correction can be further compensated by beam steerers distributed along the beamline.

8.5 Vacuum chamber

A key innovation in the AQUA FEL undulator line lies in the design of its vacuum chamber. The AQUA vacuum chamber represents a substantial leap forward in terms of mechanical and electromagnetic integration. The chamber is designed as a circular titanium pipe with a thin wall, internally coated with gold to reduce wakefield impedances.

The move toward a thinner vacuum chamber wall in the AQUA design is motivated by several intertwined technical goals. One of the most important is the increase of the effective magnetic field on axis. The peak magnetic field that can be achieved for a given undulator period is strongly dependent on the minimum achievable magnetic gap. The presence of a vacuum chamber inside

the undulator introduces a physical constraint: its external diameter subtracts directly from the mechanical gap that can be closed between the magnetic poles. Traditionally, this has been one of the main limitations of so-called "out-of-vacuum" undulators, where the vacuum chamber physically separates the magnets from the electron beam. In contrast, "in-vacuum" undulators eliminate the chamber wall entirely by operating the magnets directly in the vacuum, thus maximizing the on-axis field and minimizing the magnetic gap. However, in-vacuum undulators come with a host of challenges, including the need for radiation-resistant materials, bake-out procedures, complex assembly processes, and often more demanding magnetic correction schemes. The AQUA vacuum chamber is envisioned to close this performance gap.

The geometry and dimensions of the pipe are set to take into account the effects associated to longitudinal and transverse wake-fields, to maximize the useful aperture for electron propagation (also considering the dimensions of the undulator aperture equal to 6 mm) and to take into account the mechanical positioning tolerances of the pipe itself. A second critical aspect for a small diameter cylindrical pipe is associated to the vacuum impedance, which may limit the quality of vacuum in the middle of the 2 m long pipe. We analyse these two aspects in Sec. 8.5.1 and in Sec. 8.5.2. The mechanical design is then discussed in Sec. 8.5.3.

8.5.1 Analysis of wakefields

Wakefields critically affect the beam quality and overall performance of the FELs. They arise from the interaction between the charged particle beam and the structures of the accelerator: as the electron beam moves through the metallic vacuum chamber within the undulator and break sections, it excites longitudinal and transverse wakefields due to the resistance and the discontinuities in the beam tube wall.

Assuming cylindrical symmetry for the wall geometry, the longitudinal (monopole) wakefield generates an energy loss and an increase in energy spread independent of the beam orbit, while the transverse (dipole) wakefield generates an emittance growth that actually depends on the orbit.

8.5.1.1 Longitudinal

When propagating inside a vacuum chamber (VC) with finite conductivity, electrons experience self-induced fields, described by the resistive wall (RW) impedance model.

The resulting longitudinal RW wakefield introduces a significant energy spread, affecting the FEL gain length and overall performance. Energy loss and FEL power are evaluated with the RW wakefield model presented in [29], assuming a copper VC with different inner radii.

Figure 8.46 shows the average energy loss (left panel) and the average FEL power (right panel) as a function of the coordinate along the undulators beamline, for the electron bunch with 30 pC charge and 2 µm RMS length moving inside an ideal copper vacuum chamber with inner radius of 2 mm and 3 mm, compared with the case of neglecting RW wakefields. Although the average energy loss is significant, especially in the case of 2 mm VC inner radius, no detrimental loss of FEL average power as well as no relevant increase in the saturation length is found.

The electron bunch with 300 pC and 20 µm RMS length is also analyzed. Figure 8.47 shows the energy loss at the exit of the undulators beamline superimposed to the current profile as a function of the bunch coordinate (left panel) and the average FEL power as a function of the propagation coordinate (right panel), for a copper vacuum chamber with inner radius of 2 mm and 3 mm, compared with the case of neglecting RW wakefields. The energy loss – and so the average FEL power – for both inner radii is comparable to the case of no wakefields at all.

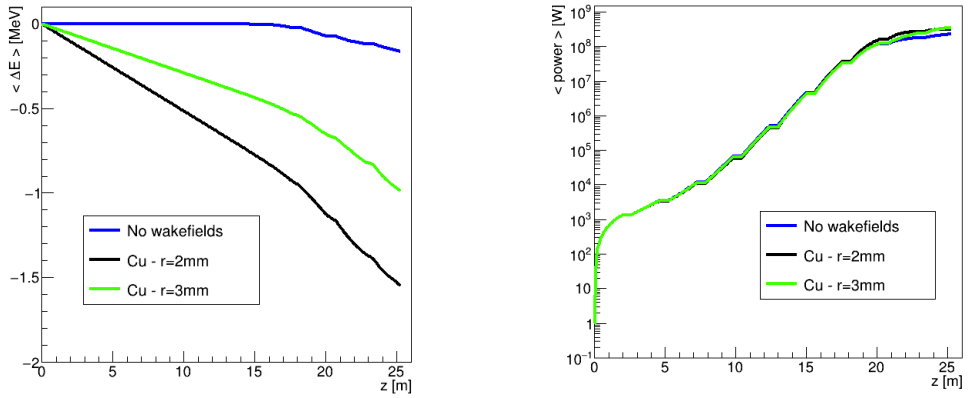

Figure 8.46: Electron bunch with 30 pC charge and 2 µm RMS length. Average energy loss (left) and average FEL output power (right) as a function of the propagation coordinate for VC inner radius of 2 mm (black) and 3 mm (green), compared with the no wakefield effects case (blue).

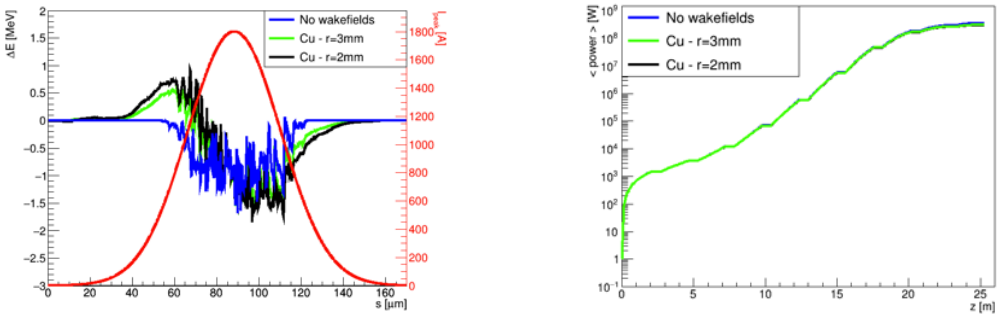

Figure 8.47: Electron bunch with 300 pC charge and 20 µm RMS length. Energy loss at undulator exit superimposed to the current profile (left frame) and average FEL output power along the propagation coordinate (right frame) for VC inner radius of 2 mm (black) and 3 mm (green), compared with the no wakefield effects case (blue).

8.5.1.2 Transverse

The transverse wakefields affect the electrons trajectory along the undulator line. The scope of this section is to assess the trajectory uncertainty induced by the RW wakefields, as a result of transverse offsets of any source: for instance misalignment between adjacent undulator modules or between vacuum chamber and undulator within the same module.

Analytical formulae are obtained by exploiting the special relationship between the RW longitudinal $Z_{\parallel}$ and transverse $Z_{\perp}$ impedances (and so the related $W_{\parallel}, W_{\perp}$ wakefields) within a vacuum pipe of radius r:

$$Z_{\perp}(k) = \frac{2}{r^2}\frac{Z_{\parallel}(k)}{k}, \quad W_{\perp}(s) = \frac{2}{r^2}\int W_{\parallel}(s)ds \tag{8.12}$$

where k, s indicate wavevector and intra-bunch coordinate, respectively.

After checking that the RW longitudinal wakefield effects on the FEL performance show consistent results either with the model in [29] or with the analytical short-range approximation [30], Eq. 8.12 is used to evaluate the transverse wakefields and express their impact by means of the kick angle per unit length per transverse offset:

$$\varkappa(r) = \frac{eQ}{E_{beam}}\int W_{\perp}(s-s',r)\lambda(s')ds', \quad [\varkappa] = \frac{rad}{m^2} \tag{8.13}$$

where $\lambda(s)$ is the line charge density and the dependence on the vacuum chamber inner radius r is included in the wakefield function, once the surface wall material is fixed.

The following results are recast in terms of the transverse kick angle per unit length κ_T[rad/m], calculated for several transverse offset values, describing different possible misalignment extents in both horizontal and vertical planes:

$$\begin{aligned} \kappa_{Tx} &= \varkappa(r)\cdot x_{\text{off}}, \quad \sigma_{\kappa_{Tx}} = \varkappa(r)\cdot\sigma_{x_{\text{off}}} \\ \kappa_{Ty} &= \varkappa(r)\cdot y_{\text{off}}, \quad \sigma_{\kappa_{Ty}} = \varkappa(r)\cdot\sigma_{y_{\text{off}}} \end{aligned} \tag{8.14}$$

where the kick angle error σ_{κ_T} scales linearly with any transverse offset jitter $\sigma_{x(y)_{\text{off}}}$.

Short bunch

The electron beam with parameters specified on Table 8.1 is analyzed. In particular, a Gaussian current profile with σ_z = 2 μm and charge $Q = 30$ pC is assumed. Figure 8.48 shows the kick angle per unit length as a function of the bunch time, for different vacuum chamber inner radii, and for a generic transverse offset of 50 μm, superimposed to the current profile. For the short bunch case, the kick angle increase happens well outside the current peak area.

For each different inner radius, values for $\varkappa$ and σ_{κ_T} are evaluated at a distance of about $2\sigma_z$ from the current peak position. The exact coordinate is shown on Figure 8.48 with a vertical dot-dashed line.

Left panel of Figure 8.49 shows the kick $\varkappa$ parameter per unit length per transverse offset as a function of the vacuum chamber inner radius. Right panel of Figure 8.49 shows uncertainty in the kick angle per unit length as a function of the misalignment jitter σ_{off} value, for different vacuum chamber inner radii.

For a vacuum chamber inner radius of 2.3 mm, only 3% of the bunch is affected by a 60×10^{-9} rad/m kick angle per unit length jitter, assuming 300 μm of misalignment error.

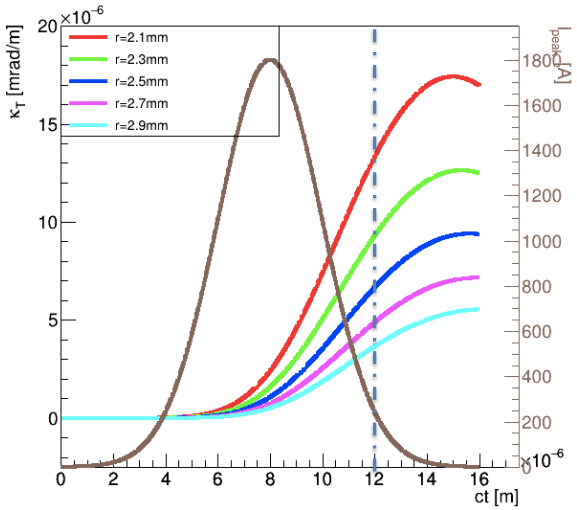

Figure 8.48: Kick angle per unit length for different vacuum chamber inner radii, and for a transverse offset of 50 µm, superimposed to the short bunch current profile (brown curve).

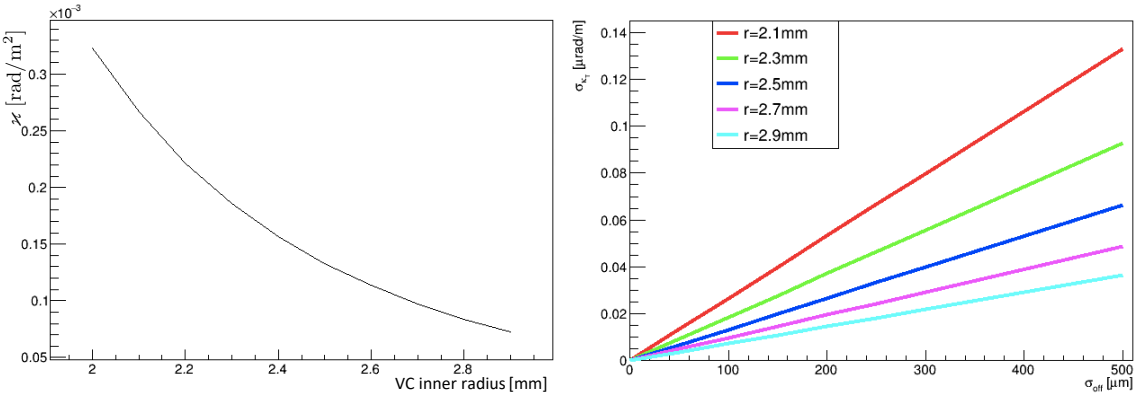

Figure 8.49: Left: kick parameter per unit length per transverse offset as a function of the vacuum chamber inner radius. Right: uncertainty in the kick angle per unit length as a function of the misalignment jitter value, for different vacuum chamber inner radii.

Long bunch

An electron beam with a higher charge of 300 pC and a Gaussian current profile, is analyzed: in fact σ_z = 20 µm and charge Q = 300 pC, for a broader wakefield assessment of the higher charge values was considered as a reference for a high charge pure RF acceleration case (see Section 3.3).

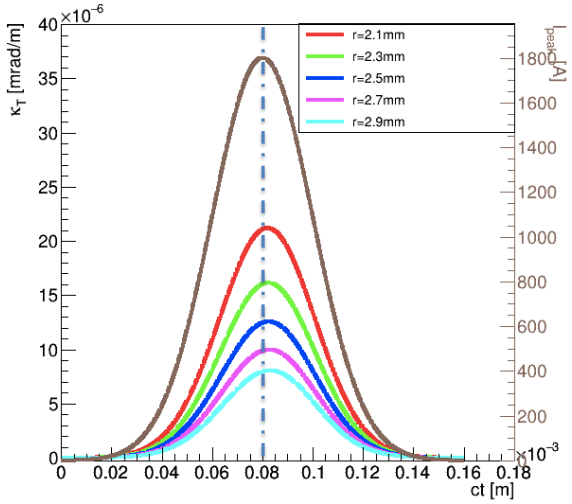

Figure 8.50: Kick angle per unit length for different vacuum chamber inner radii, and for a transverse offset of 50 µm, superimposed to the long bunch current profile (brown curve).

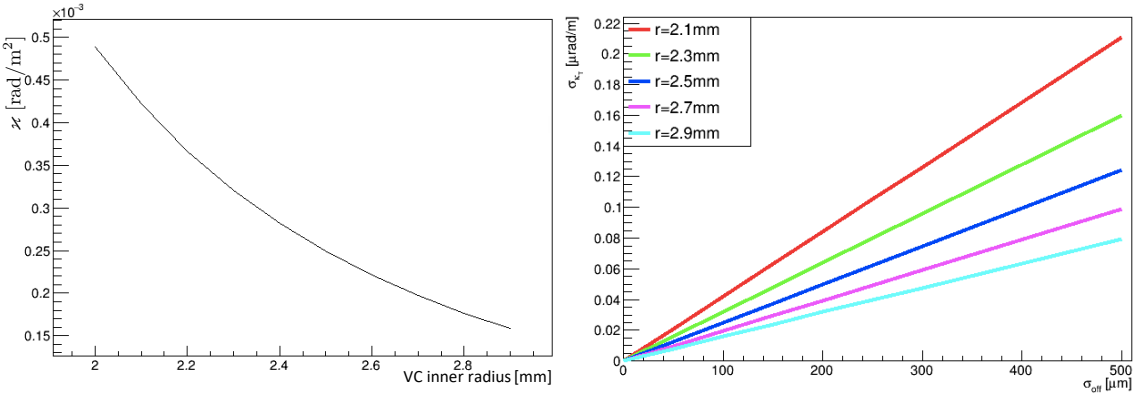

Figure 8.51: Left: kick parameter per unit length per transverse offset as a function of the vacuum chamber inner radius. Right: uncertainty in the kick angle per unit length as a function of the misalignment jitter value, for different vacuum chamber inner radii.

Figure 8.50 shows the kick angle per unit length as a function of the bunch time, for different vacuum chamber inner radii, and for a generic transverse offset of 50 µm, superimposed to the current profile.

For the long bunch case, the kick angle distribution nearly reflects that of the current profile: the maximum κ_T position almost coincides with that of the current peak.

For each different inner radius, values for $\varkappa$ and σ_{κ_T} are precisely evaluated at the current peak position. The exact coordinate is shown on Figure 8.50 with a vertical dot-dashed line.

Left panel of Figure 8.51 shows the kick $\varkappa$ parameter per unit length per transverse offset as a function of the vacuum chamber inner radius. Right panel of Figure 8.51 shows uncertainty in the kick angle per unit length as a function of the misalignment jitter σ_{off} value, for different vacuum

chamber inner radii.

For a vacuum chamber inner radius of 2.5 mm, the peak current region of the bunch is affected by a potential kick angle per unit length of $0.12\,\mu\text{rad}/\text{m}$, assuming 500 µm of misalignment error.

Transverse emittance increase

The transverse wakefields cause the beam centroid oscillation which may be corrected by orbit feedback and an emittance growth due to the fact that the kicks vary along the bunch or from bunch to bunch.

In a FODO lattice, the focusing optics devices transform these kicks into oscillations that increase the transverse emittance. The initial unpertubed geometric emittance ε gets added in quadrature by a contribution [31, 32], described by the mean square angular divergence $\langle\theta^2\rangle$, resulting in an effective geometric emittance ε_{eff}. Assuming that the electron beam transverse distribution at the undulator is matched to the design Twiss parameters, the effective projected emittance is modified as follows:

$$\varepsilon_{eff} \simeq \varepsilon\sqrt{1+\frac{\bar{\beta}}{\varepsilon}\langle\theta^2\rangle}, \quad \bar{\beta} = \frac{1}{L_{cell}}\int_0^{L_{cell}} \beta(z)\,dz \tag{8.15}$$

where the angular divergence is averaged over the bunch current density, and the Twiss β function is averaged over the length of the FODO cell period L_{cell}.

Transverse wakefields generate a kick angle $\varkappa$ per unit propagation length per transverse offset given in Eq. 8.13. The angular divergence contributing to the emittance growth over the entire undulator beamline, due to the transverse wakefields, is estimated through the following formula:

$$\sqrt{\langle\theta^2\rangle} \approx L_{AQUA}\,\ell_{off}\sqrt{\langle\varkappa^2\rangle} \tag{8.16}$$

where $\langle\varkappa^2\rangle$ is the mean square kick angle averaged over the bunch current density, ℓ_{off} is the generic transverse offset and L_{AQUA} is the AQUA undulator beamline length. Table 8.11 shows

Table 8.11: Root mean square kick and divergence angles, evaluated for both short and long bunches, considering a 2.5 mm inner radius vacuum chamber, and associated emittance fractional increase, assuming $\bar{\beta} = 8\,\text{m}$, $L_{AQUA} = 26\,\text{m}$, and $\ell_{off} = 500\,\mu\text{m}$.

	Unit	Short bunch	Long bunch
$\sqrt{\langle\varkappa^2\rangle}$	$[\text{rad}/\text{m}^2]$	0.49×10^{-4}	1.75×10^{-4}
$\sqrt{\langle\theta^2\rangle}$	[µrad]	0.637	2.275
$\Delta\varepsilon_n/\varepsilon_n$		4 ‰	5 %

the root mean square kick and divergence angles, evaluated for both short and long bunches, for the case of a vacuum chamber with inner radius of 2.5 mm. Moreover, the fractional normalised emittance growth over the undulator beamline length of 26 m, corresponding to about four FODO cells and one betatron period with an average $\bar{\beta} = 8\,\text{m}$, is considered for the worst case (see right panel of Figures 8.49 and 8.51) scenario of a 1 GeV beam transverse offset with respect to the vacuum chamber axis of 500 µm.

Under the discussed operation conditions, the normalised emittance increase due to the transverse wakefields is acceptable, in both bunch configurations.

8.5.2 Vacuum properties

The acceptable vacuum level in an electron beam single-pass transport line, such as the FODO lattice traversing the undulator is crucial for minimizing beam loss, emittance growth, and preserving beam quality.

At ≈ 1 GeV, the dominant concern in a relatively short (26 m), single-pass line is small-angle Coulomb scattering (Molière scattering [33]) from residual gas atoms. Since the average beam current is extremely low, beam-induced ion instabilities, and beam-induced gas desorption are negligible.

The rms scattering angle over distance L due to residual gas is approximately [34]:

$$\theta_{\mathrm{rms}} \approx \frac{13.6\,\mathrm{MeV}}{\beta pc}\sqrt{\frac{L}{X_0}},$$

where X_0 is the radiation length of the gas, which scales inversely with pressure.

At $P = 10^{-6}$ mbar, the scattering angle is roughly:

$$\theta_{\mathrm{rms}} \sim 100\,\mathrm{nrad},$$

over 20–30 m of beamline, which is smaller than the angular divergence of a high-quality 1 GeV beam with the parameters of Table 8.1. Therefore, the induced emittance growth is negligible.

The beam-gas interaction loss probability is [35]:

$$\frac{\Delta N}{N} \sim \sigma n_{\mathrm{gas}} L.$$

At $P = 3 \times 10^{-6}$ mbar, the beam loss per meter is on the order of 10^{-9}, and over 26 m, the total loss remains $\ll 10^{-7}$, which is negligible.

In summary, a vacuum at the level of few 10^{-6} should be acceptable in terms of beam loss, emittance growth and ionization instabilities. The Bremsstrahlung background should also be negligible at this charge level, but the possibility of forward scattered high energy radiation to reach the user operation area should be considered and minimised by proper shielding and FEL beam transport.

Given the geometrical constraints of the vacuum chamber placed in the small aperture of the undulator, vacuum pumps can operate only at the two boundaries of the vacuum chamber. The vacuum can be much lower at the pumping stations, but the vacuum impedance along the pipe causes a degradation of the vacuum in the centers of the undulator module.

In Fig. 16.19 we show the trend of the pressure along the undulator pipe. The vacuum level in this case reaches the level $\approx 3 \times 10^{-6}$ mbar in the middle of the chamber.

To determine the actual vacuum performance and pumping efficiency, a test bed incorporating the elements of the intrasection will be constructed.

8.5.3 Vacuuum chamber mechanical design and supports

The chamber is a circular titanium pipe with a thin wall thickness of just 300 µm, internally coated with gold to reduce wakefield impedances. It has an internal diameter of 5 mm and an external diameter of 5.6 mm, fitting into the 6 mm physical aperture of the undulator gap. The dimensional tolerance for rectilinearity is tight, with a target allowed deviation of less than 500 µm from the undulator axis over the entire length of the chamber.

The choice of titanium as the base material was driven by its favorable combination of mechanical strength, low density, and compatibility with UHV conditions. Titanium offers excellent resistance to deformation even at minimal wall thicknesses, while its low atomic number minimizes absorption and scattering effects that could degrade beam quality. The internal gold coating improves surface conductivity, thereby reducing wakefields and enhancing the long-term vacuum stability by providing a chemically inert surface. The circular cross-section, with its small internal diameter of 5 mm, is particularly advantageous compared to elliptical or rectangular designs, as it offers symmetric impedance characteristics and simplifies the modeling of beam–vacuum

interaction. This configuration also facilitates manufacturing and quality control during the coating process, ensuring uniform surface properties throughout the length of the chamber. In Figs. 8.52 and 8.53 the vacuum chamber in shown in front and side views respectively.

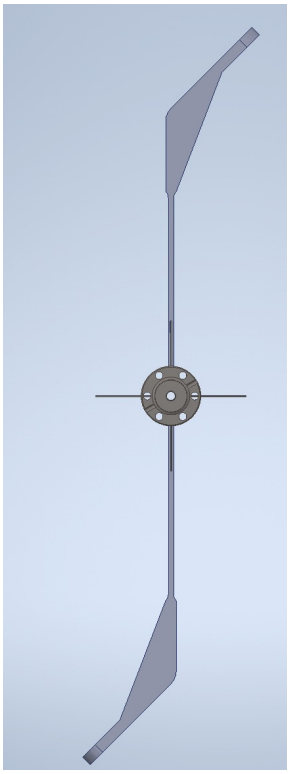

Figure 8.52: Front view of the undulator vacuum chamber. The holders to be fixed to the undulator frame are visible in the upper and lower side of the chamber axis.

Achieving the targeted rectilinearity of 500 µm over the length of the chamber represents a mechanical challenge. To maintain the required stiffness and rectilinearity over the entire length of the chamber, the mechanical design includes four thin laminations, or stiffeners, welded along the pipe—two in the vertical plane and two in the horizontal plane—arranged at 90 degrees relative to each other. These stiffeners act as structural ribs, increasing the flexural rigidity of the thin-walled pipe without significantly increasing its outer dimensions. The stiffeners are critical not only for maintaining the straightness of the chamber during installation and operation but also for ensuring that the mechanical load is uniformly distributed along the support points.

To meet the requirements, the support system—although inspired by SABINA's design—has to be fundamentally re-engineered to provide fine vertical and horizontal adjustments. For example, the mechanical support points are spaced more densely than in SABINA, and the adjustment mechanisms are designed to allow micrometer-level corrections. Maintaining an ultra-high vacuum inside such a thin-walled chamber introduces additional complexities. The thin walls, while beneficial for magnetic field performance, are inherently more sensitive to mechanical stress, thermal cycling, and vibration.

In Figs. 8.54 and 8.55 we provide a view of the integration of the vacuum chamber in the undulator frame. The lower and upper undulator frames are prepared with dedicated areas to retain the vacuum chamber blade holders.

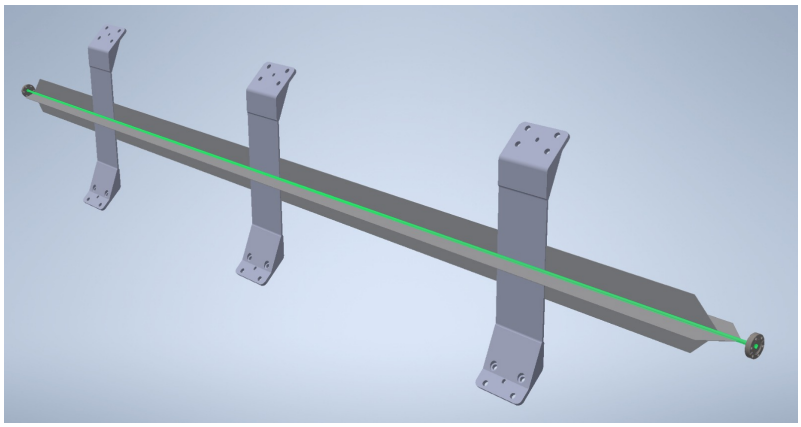

Figure 8.53: Side view of the undulator vacuum chamber. The three sets of holders are meant to sustain the chamber in place from the lower and upper gilders of the undulator

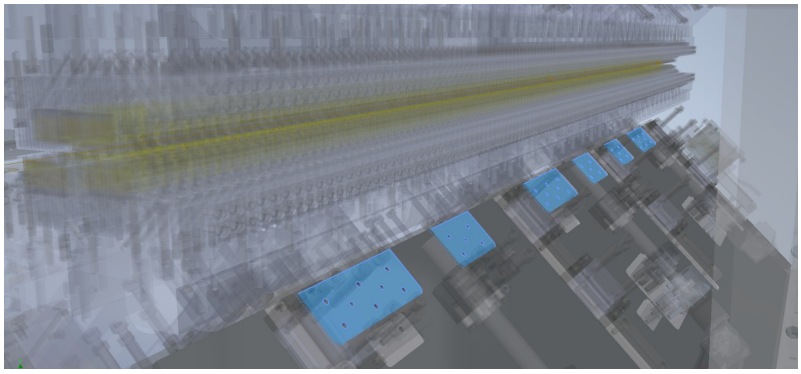

Figure 8.54: Representation of the undulator frame where the areas holding the vacuum chamber are highlighted in blue.

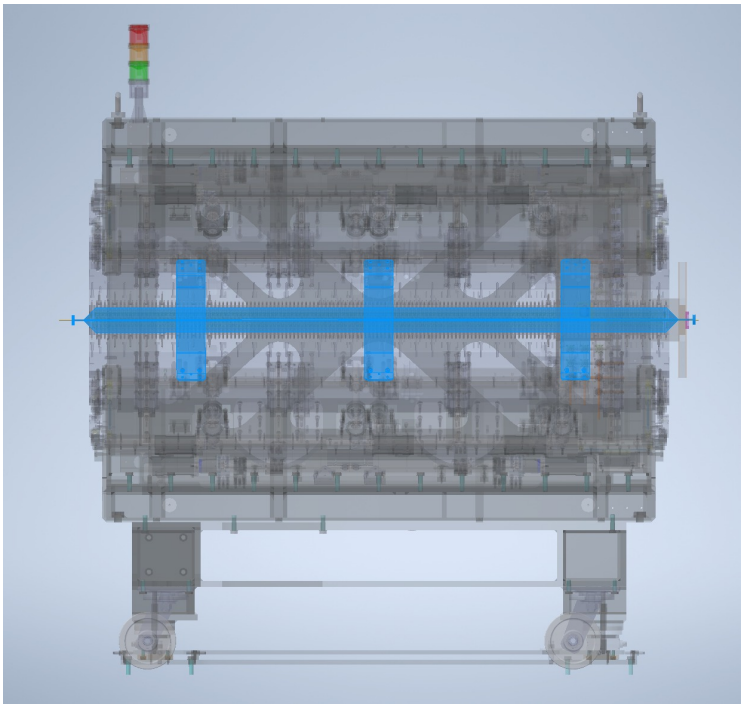

Figure 8.55: Undulator frame with the vacuum chamber in place. On the right side it is visible the vacuum chamber extension required to host the phase shifter (see Sec. 8.6)

8.5.4 Conclusion

In summary, the vacuum chamber of the AQUA undulator is a 300-µm thin titanium cylindrical pipe, with an internal diameter of 5 mm (radius 2.5 mm) and an external diameter 5.6 mm and 2 m length. It is internally gold-coated, with stiffening laminations; it is held in place by a system of fingers which ensure positioning in the undulator gap with a precision (distance from an ideal axis) of ≈ 500 µm.

The design addresses the simultaneous challenges of structural integrity, ultra-high vacuum performance, and magnetic optimization. By reducing the effective magnetic gap, the AQUA vacuum chamber allows the undulator to deliver on-axis magnetic fields that approach those of in-vacuum undulators, without the associated operational complexity.

8.6 Intra-undulator sections

The intra-undulator section consists of a 60 cm-long, free-space segment between two undulator modules, taking into account the mechanical shifts associated with undulator phase movements. This section hosts several essential components required for beam tuning and control along the undulator line, including supports for the vacuum chamber and elements of the vacuum system. Figure 8.56 shows a schematic of this region. The same configuration is identically repeated after each of the ten undulator modules.

In sequence from left to right, the elements are:

- **The phase shifter.** The phase shifter is the first element following the undulator. It is mounted on the external frame of the undulator and shares the same vacuum chamber segment that passes through the undulator. The magnetic length of the phase shifter is 10 cm, so no magnetic element should be placed 3.5 cm before and after it. A detailed description is provided in Sec. 8.3.3.

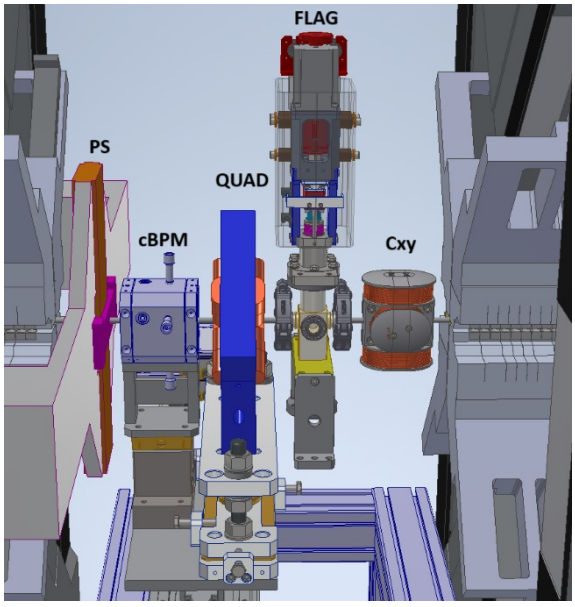

Figure 8.56: Intra-undulator section elements. From left to right: phase shifter (PS), cavity BPM (cBPM), quadrupole (QUAD), photons diagnostic chamber (FLAG) and steerers (Cxy).

- **The Cavity Beam Position Monitor.** The cavity Beam Position Monitor (BPM) is the main beam diagnostic tool within the intra-undulator section. It will positioned upstream the quadrupole, on the same motorized stage. The BPM will be manufactured by PSI and features a 5 mm diameter aperture with a longitudinal length of 80 mm. For further details see Section 11.2.4.
- **The Quadrupole.** As discussed in Sec. 8.2.5, focusing quadrupoles are necessary along the undulator line to ensure the correct periodic beam focusing. The required quadrupole strength is defined in Figs. 8.14 and 8.15. The highest field gradient corresponds to the condition β = 5 m at E = 1.2 GeV, where an integrated gradient 1.7 T is required. The quadrupole design is described in Section 17.8.1. The cavity BPM and the quadrupole will be mounted together on the same motorized stage, which is preceded and followed by bellows to allow precise alignment with respect to the beam.
- **The Photons Diagnostic Chamber.** The primary photons diagnostic system will consist of a view screen made of scintillator crystals (see Sec. 11.2.5), housed in a 80 mm-long chamber. A vacuum pump will be connected to the chamber. For more details, see Section 11.2.5 and Fig. 11.6 for the mechanical drawing of the device.
- **The Steerers.** The magnetic steerers for the intra-undulator section should provide angular correction of at least 0.3 mrad for 1.5 GeV in both transverse axis (x and y), and must support a high rate feedback system (at least 100 Hz). This can potentially be achieved using in-air steerers (without iron yoke) which are capable of sustaining high rate. Various configurations are currently under study to optimize angular correction capability, field quality and longitudinal space usage. For technical details, see Sec. 17.8.2.

In conclusion, we summarize the physical requirements of the elements along the intra-undulator sections in Tab. 8.12.

Table 8.12: Intra-undulator elements

Item	Quantity	Units
Phase shifter	see Sec. 8.3.3	
Geometry	Planar	
Magnetic mat.	NdFeB	
Phase shift (@10 nm)	2π	
Length	30.6	mm
Magnetic length	100	mm
Min gap	7	mm
Supported by UM frame		
Decoupling Bellow	25	mm
Quadrupole	see Secs. 17.8.1 and 8.2.5	
Length	70	mm
Max. Int. Gradient	1.7	T
Alignment	15	μm
on motorised board with BPM		
Beam Pos. Monitor	see Sec. 11.2.4	
Accuracy	< 1	μm
Range of operation	1	mm
Length	80	mm
Inner aperture	5	mm
on motorised board with Quad.		
Decoupling Bellow	25	mm
Flag/Pump Chamber	see Sec. 11.2.5	
Length	80	mm
3 flag positions:		
Flag with reference		
Flag no reference		
Metal plate with hole	1	mm
Steerers	see Sec. 17.8.2	
Angle @1.5 GeV	300	μm
In air		
Decoupling Bellow	25	mm
Next Undulator		

8.7 Conclusion

This chapter presented a detailed analysis of the AQUA undulator system, highlighting its design, optimization, and performance under realistic operating conditions. We summarise in Tab. 8.13 the main constraints for the undulator specifications resulting from the analysis of the AQUA FEL line.

Table 8.13: AQUA undulator physical specifications summary

Parameter	Quantity	Units
Number	10	Undulators
Period length	18	mm
Number of periods	110	
Minimum gap	1.5	mm
Aperture at min. gap	6	mm
K_{RMS} at min. gap	1.11	
Peak Field error	0.5	%
Max. phase error	5	deg
1^{st} Field Integral (res LH,CR)	$2 \cdot 10^{-6}$	$\mathrm{T \cdot m}$
1^{st} Field Integral (res LV)	10^{-5}	$\mathrm{T \cdot m}$
2^{nd} Field Integral (res LH,CR)	10^{-6}	$\mathrm{T \cdot m^2}$
2^{nd} Field Integral (res LV)	10^{-5}	$\mathrm{T \cdot m^2}$
Max. Trajectory offset (@1GeV)	8	µm
Max. Trajectory angle (@1GeV)	15	µrad
Quadrupole (x,y)	$5 \cdot 10^{-2}$	T
Sextupole (x,y)	1	T/m
Transverse positioning system range (x/y)	1	mm
Transverse positioning system accuracy (x/y)	5	µm
Temperature stability	± 0.5	°C

Beginning with the fundamental undulator parameters and their resonance conditions across a broad photon energy range, the chapter explores the relationships between undulator period, beam energy, and polarization modes. It provides in-depth characterization of field profiles, field integrals, and K-parameter variations, supported by extensive simulation and experimental data. The interplay between beam dynamics and undulator performance is carefully examined, including FEL saturation length, peak power, photon output, and sensitivity to beam emittance and energy spread under both circular and linear polarization. These calculations are based on the conservative beam parameters listed in Tab. 8.1. A more comprehensive analysis of the expected FEL performance is provided in Chapter 3, where start-to-end simulations demonstrate that these parameters can be achieved and even exceeded at the undulator. In Chapter 3, FEL performance is extensively simulated using GENESIS 1.3, taking into account the potential for step-tapering the undulator. Given that the 10 modules are independent, step-tapering can be easily implemented by tuning individual undulator modules to different resonances.

Particular attention is also given to mechanical and magnetic aspects, such as the design and optimization of end magnets, correction coils, and compensating magnets, as well as their role in improving beam trajectory and magnetic force balance. The chapter addresses the impact of vacuum chamber geometry and wakefield effects on beam stability, providing quantitative

assessments of kick angles, energy loss, and FEL power degradation for both short and long bunch configurations. Phase shifter integration and intra-undulator components are also discussed, underscoring their importance for phase control and diagnostics. Overall, the chapter delivers a comprehensive framework for achieving the demanding requirements of the facility, balancing magnetic precision, mechanical stability, beam alignment tolerances, and wakefield mitigation. The combination of simulation results, analytical modeling, and physical specifications establishes a robust foundation for the realization of high-performance, tunable FEL operation across a wide range of user applications. We summarise in Tab. 8.14 the technological readiness level of the FEL system and it's sub-components.

Table 8.14: TRL level of the FEL system

Sub - systems	TRL	Comments
FEL	9	FEL design based on reliable simulations (Genesis 1.3) and calculations which were benchmarked with real devices.
Undulators	7	Short period undulators were realised at many facilities. Apple X - Type undulators Technology demonstrated in other facilities (SwissFEL, EuXFEL, etc.)
Phase Shifters	9	Phase shifters are operational at most multi-undulator FEL beamlines
Vacuum chamber	4	Vacuum chamber with 300 μm walls, tolerance on alignment 500 μm. Vacuum levels simulated in comparable operational environment.
Quadrupoles	9	Quadrupoles are within standard parameters
Steerers	9	In-air steerers with the required specifications are standard at many facilities
C-BPM	9	Cavity BPM with the required specifications are available at many facilities (e.g. PSI))
YAG – CCD-Diagnostics	9	Standard hardware

Based on this approach, we anticipate that the undulator system should be fully capable of achieving FEL lasing within the 4-5.2 nm range, while adhering to the constraints imposed by the facility.

Acknowledgments

Firstly, we acknowledge the special support of M. Caponero[b] and A. Polimadei[b] from the ENEA Holographic Interferometry & Fibre Optic Sensors (HIFOS) Laboratory for their significant contribution to the structural tests of the SABINA undulator.

We also wish to recognize the work of F. Bosco[e] and M. Migliorati[e] for their efforts in implementing the MILES code, which was instrumental in the study of the wakefield impedance of the AQUA FEL vacuum pipe.

Our thanks also go to C. Boffo[f] for his insightful discussions on superconducting undulator technology, as well as his thorough research on the realization of a complete superconducting undulator prototype for AQUA, a design that, although excluded from the AQUA undulator baseline, provided invaluable technical insights.

We are grateful to N. Mirian[g] for her stimulating discussions on FEL simulations for the AQUA

beamline, which have significantly advanced our understanding of the beam dynamics.

[f] University of Rome "La Sapienza", Rome, Italy
[e] Fermilab National Laboratory, Kirk Road and Pine Street, Batavia IL 60510-5011, USA
[g] Helmholtz-Zentrum Dresden - Rossendorf (HZDR) Bautzner Landstr. 400, 01328 Dresden, Germany

Bibliography

[1] M. Ferrario et al. *EuPRAXIA Conceptual Design Report*. URL: https://www.eupraxia-project.eu/eupraxia-conceptual-design-report.html.

[2] R. Kinjo and T. Tanaka. "Undulator configuration for helicity switching in in-vacuum undulators". In: *Physical Review Accelerators and Beams* 23.2 (2020), p. 020705.

[3] J. Bahrdt et al. "In-vacuum APPLE II undulator". In: *Proc. 9th International Particle Accelerator Conference (IPAC '18), Vancouver, BC, Canada, April 29-May 4, 2018*. 2018, pp. 4114–4116.

[4] T. Tanaka et al. "In-vacuum figure-8 undulator for hard X-rays with both horizontal and vertical polarization". In: *Synchrotron Radiation* 5.3 (1998), pp. 412–413.

[5] C. Boffo et al. "Design of the Superconducting Undulator for EuPRAXIA@SPARC_LAB". In: *40th International Free Electron Laser Conference (FEL'22), Trieste, Italy*. 2022.

[6] T. Schmidt and M. Calvi. "APPLE X undulator for the SwissFEL soft X-ray beamline Athos". In: *Synchrotron Radiation News* 31.3 (2018), pp. 35–40.

[7] S. Sasaki et al. "Performance of APPLE-II type quasi periodic undulator at Hisor". In: *proceedings of Int. Particle Accelerator Conf.(IPAC'12), New Orleans, USA*. 2012.

[8] URL: https://www.esrf.fr/Accelerators/Groups/InsertionDevices/Software/Radia.

[9] L. Sabbatini et al. "SABINA: A RESEARCH INFRASTRUCTURE AT LNF". In: *proceedings of 12th Int. Particle Accelerator Conf.(IPAC'21), Campinas, Brazil*. 2021.

[10] M. Xie. "Design optimization for an X-ray free electron laser driven by SLAC linac". In: *Proceedings Particle Accelerator Conference*. Vol. 1. IEEE. 1995, pp. 183–185.

[11] L. Giannessi. "Seeding and Harmonic Generation in Free-Electron Lasers". In: *Synchrotron Light Sources and Free-Electron Lasers: Accelerator Physics, Instrumentation and Science Applications*. Ed. by E. Jaeschke et al. Cham: Springer International Publishing, 2014, pp. 1–27. ISBN: 978-3-319-04507-8. DOI: 10.1007/978-3-319-04507-8_3-2. URL: https://doi.org/10.1007/978-3-319-04507-8_3-2.

[12] A. Petralia et al. "Short Period Apple-X Undulator Modeling for the AQUA Line of the Future EuPRAXIA@SPARC_LAB Facility". In: *Proc. 40th International Free Electron Laser Conference*. 2022, pp. 454–457.

[13] K. Halbach. "Physical and optical properties of rare earth cobalt magnets". In: *Nuclear Instruments and Methods in Physics Research* 187.1 (1981), pp. 109–117.

[14] J. A. Clarke. *The science and technology of undulators and wigglers*. Vol. 4. OUP Oxford, 2004.

[15] B. Diviacco and R. P. Walker. *Pure permanent magnet end-configurations*. Tech. rep. Sincrotrone Trieste Internal Report, ST/M-TN-92/5. 1992.

[16] J. Počkar et al. "Design of the innovative APPLE-X AX-55 for SABINA project, INFN Laboratori Nazionali di Frascati". In: *Proc. FEL2022* (2022), pp. 475–478.

[17] KYMA SpA. *Final Mechanical Design, 3 module APPLE-X undulator for SABINA project at INFN Frascati*. Tech. rep. 2022.

[18] KYMA SpA. *Final Magnetic Design, APPLE-X typ undulator for SABINA beamline at INFN Frascati*. Tech. rep. 2022.

[19] M. Tischer et al. "Development of an APPLE-III undulator for FLASH-2". In: *Journal of Physics: Conference Series*. Vol. 2380. 1. IOP Publishing. 2022, p. 012017.

[20] M. A. Caponero. “Use of FBG sensors in advanced civil engineering applications”. In: *Journal of Instrumentation* 18.07 (2023), p. C07020.

[21] K. T. V. Grattan and T. Sun. “Fiber optic sensor technology: an overview”. In: *Sensors and Actuators A: Physical* 82.1-3 (2000), pp. 40–61.

[22] URL: https://www.broptics.com/products_sensors.htm/%20..

[23] URL: http://micronoptics.ru/sensing_tech.html%20..

[24] I. Balossino et al. “Strain measurements of the Apple-X SABINA undulator with fiber Bragg grating”. In: *Proc. IPAC’24* (2024), pp. 3777–3780.

[25] M. Ferrario et al. “EuPRAXIA@ SPARC_LAB Design study towards a compact FEL facility at LNF”. In: *Nuclear Instruments and Methods in Physics Research Section A: Accelerators, Spectrometers, Detectors and Associated Equipment* 909 (2018), pp. 134–138.

[26] S. Reiche and C. Lechner. “Status of the time-dependent FEL code Genesis 1.3”. In: *Proc. IPAC’24* (Nashville, TN). JACoW Publishing, Geneva, Switzerland, May 2024, pp. 2631–2634. ISBN: 978-3-95450-247-9. DOI: 10.18429/JACoW-IPAC2024-WEPR58. URL: https://indico.jacow.org/event/63/contributions/4480.

[27] Z. Wolf. “A PPM phase shifter design”. In: *Technical Note, LCLS-TN-11-2* (2011).

[28] G. Parisi et al. “Phase shifters for the SPARC Undulator System”. In: *Proceedings of the 27th International Free Electron Laser Conference* (2005), p. 188.

[29] F. Bosco et al. “Advanced Studies for the Dynamics of High Brightness Electron Beams with the Code MILES”. In: *Journal of Physics: Conference Series* 2687.6 (2024), p. 062018. DOI: 10.1088/1742-6596/2687/6/062018. URL: https://dx.doi.org/10.1088/1742-6596/2687/6/062018.

[30] K. L. F. Bane and G. Stupakov. *Resistive wall wakefield in the LCLS undulator beam pipe*. Tech. rep. SLAC-PUB-10707, LCLS-TN-04-11. Sept. 2004.

[31] S. Di Mitri and S. Spampinati. “Estimate of free electron laser gain length in the presence of electron beam collective effects”. In: *Phys. Rev. ST Accel. Beams* 17 (11 2014), p. 110702. DOI: 10.1103/PhysRevSTAB.17.110702. URL: https://link.aps.org/doi/10.1103/PhysRevSTAB.17.110702.

[32] G. Dattoli et al. “Slice collective dynamics, projected emittance deterioration and free electron laser performances detrimental effects”. In: *Journal of Plasma Physics* 86.6 (2020), p. 845860601. DOI: 10.1017/S0022377820001324.

[33] H. A. Bethe. “Molière’s theory of multiple scattering”. In: *Physical Review* 89 (1953), pp. 1256–1266. DOI: 10.1103/PhysRev.89.1256.

[34] G. R. Lynch and O. I. Dahl. “Approximations to multiple Coulomb scattering”. In: *Nuclear Instruments and Methods in Physics Research Section B* 58 (1991), pp. 6–10. DOI: 10.1016/0168-583X(91)95671-Y.

[35] H. Wiedemann. *Particle Accelerator Physics*. 4th ed. Springer, 2015. DOI: 10.1007/978-3-319-18317-6.

9. Photon Beamline

9.1 Introduction

This chapter presents the design and technical specifications of the FEL beamline, called AQUA, dedicated to photon pulses in and near the water window spectral range.

The scientific motivations driving the beamline specifications, including target applications in life sciences, ultrafast dynamics, and nanoscale imaging, were presented in a previous section of this document (Chapter 2). Initially, the beamline will serve a single experimental end-station, designed to support a broad range of photon-science applications within the water window as described in Chapter 10. The layout and infrastructure allow for future expansion to additional beamlines, as the facility evolves through subsequent phases of construction and commissioning.

Following a brief overview of the beamline layout, key parameters, and technological readiness in Sec. 9.2, the optics are presented in Sec. 9.3, and the diagnostics in Sec. 9.4.

Starting downstream of the undulator, the design includes a series of grazing-incidence mirrors, focusing optics, and filtering elements that preserve the coherence, brightness, and ultrashort duration of the FEL pulses while minimizing losses and wavefront distortion. Pulse diagnostics also play a central role in ensuring stable and reproducible beam delivery, covering aspects such as intensity, spectrum, position and transverse dimensions, wavefront, and arrival time. This chapter illustrates the choices and specifications of the instruments needed to fully characterize the pulses.

At the end of the chapter (Sec. 9.5), the main procedures for alignment, operation, and safety to be implemented are briefly outlined.

9.2 AQUA beamline

The first foreseen FEL operational mode is based on the Self-Amplified Spontaneous Emission (SASE) mechanism [1] in the AQUA beamline. Other schemes, like seeded and higher harmonic generation configurations, will be also investigated and implemented in a second beamline, called ARIA, but they are not reported in this document. A detailed discussion of beam physics is provided in Chapter 3; here, the reference photon parameters used for designing the beamline capabilities are summarized in Tab. 9.1, considering, for the PFWA case, the slightly intense case from Tab. 3.12 to

have additional margins on equipment safety.

Table 9.1: FEL radiation parameters from start-to-end simulation (Tab. 3.12, 3.21).

	Units	**PWFA**	**Full RF**
Radiation Wavelength	nm	4.0	4.0
Pulse Energy	μJ	25.5	156
Photons/pulse	$\times 10^{11}$	5.3	31.3
Pulse Bandwidth	%	0.27	0.48
Pulse FWHM duration	fs	5.6	33
Pulse RMS trans. size	μm	160	160
Pulse waist divergence	μrad	30.3	34.5

Once the photon pulse is produced in the undulators via the FEL process, it is fully characterized and delivered to users. The main parameters to be diagnosed are listed in Tab. 9.2, together with the required sensitivity and precision, as well as the corresponding diagnostic instruments foreseen for their measurement.

Table 9.2: Relevant photon pulse parameters, required range of measurement and resolution, and corresponding envisioned diagnostic tool.

Parameter	**Range**	**Resolution**	**Tool**
Photon number	10^9-10^{13}	$\mathcal{O}(10^9)$	Gas Monitor Detectors, Photodiodes
Spectrum	2-15 nm	$\mathcal{O}(1/30000\ \Delta\lambda/\lambda)$	Grating spectrometer
Arrival time (rms)	± 20 ps	$\mathcal{O}$(10 fs)	Transient reflectivity, Indirect from electron arrival time
Time length (FWHM)	1 fs - 1 ps	$\mathcal{O}$(10 %)	Indirect from electron time length, Ionization Streaking
Transverse position	± 10 mm	$\mathcal{O}$(10 μm)	Gas Monitor Detectors, Plate Beam Position Monitors, View screens
Transverse dimensions (rms)	2 μm - 4 mm	$\mathcal{O}$(μm)	View screens, Wire scanner on Plate BPM, Hartmann sensor
Polarization	linear - circular	$\mathcal{O}(1°)$	Polarizing Polarimeter, Ionization Polarimeter
Wavefront	$\pm\lambda$	$\mathcal{O}(\lambda/10)$	Hartmann sensor
Transverse Coherence	200-1000 μm	$\mathcal{O}$(10 %)	Double slit interferometry
Longitudinal Coherence	0.5-5 fs	$\mathcal{O}$(10 %)	Michelson interferometer, spectrometer

9.2.1 Layout

Fig. 9.1 shows the general layout of the two beamlines inside the building, with a total available space of approximately 60 m between the end of the undulator lines and the external wall of the building.

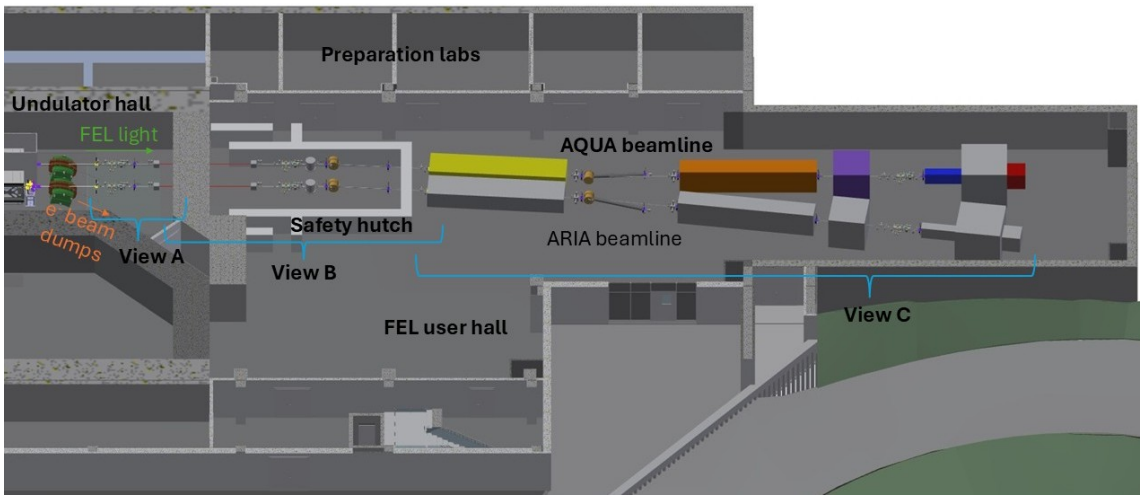

Figure 9.1: Layout of the AQUA (upper) and ARIA (lower) beamlines in the FEL user hall

Table 9.3: Beamline subsystems list with section reference and typical transmission per element at 4 nm. "0 or 1" is listed for intercepting diagnostics that are removed after the measurements. The two values for the monochromator correspond to the double- or single-grating configurations.

Subsystems	**Number**	**Description**	**Typ. Trans. (per element) @4 nm**
Beam defining aperture	1	Sec. 9.3.1	1
Filter wheels	2	Sec. 9.3.2.1	from $\sim 10^{-6}$ to 1
Gas absorber	1	Sec. 9.3.2.2	from ~ 0.01 to 1
Steering mirror	1	Sec. 9.3.3	0.84
Focusing system	1	Sec. 9.3.4	0.84
Monochromator	0 (1)	Sec. 9.3.5	0.02 or 0.08
Split&delay line	0 (1)	Sec. 9.3.6	0.5
Gas Monitor Detectors	3	Sec. 9.4.1	~ 0.99
Screen stations	7	Sec. 9.4.2	0 or 1
PlateBPMs	2	Sec. 9.4.3	~ 0.97
Spectrometer	1	Sec. 9.4.4	0.74
Polarization and time diagnostics	1	Sec. 9.4.5	0 or ~ 0.99
Wavefront measurement	1	Sec. 9.4.6	0
Shutters	1+1	Sec. 9.5.3	0
Experimental chamber (with diagnostics)	1	Chapter 10	–

The second beamline is presented here only for spatial reference, assuming similar occupancy

to the AQUA beamline. This allows proper evaluation of the space required within the user hall and dimensioning of the gas bremsstrahlung safety hutch, avoiding extended shutdowns during future upgrades. The actual distance from the source to the target is slightly longer than 52 m. There are approximately 5.5 m of free space between the user end-station and the wall, available for future upgrades or for installing larger experimental instruments (e.g., for spectroscopy). Tab. 9.3 lists the planned beamline subsystems, with references to their description sections and expected transmission values at the reference wavelength of 4 nm.

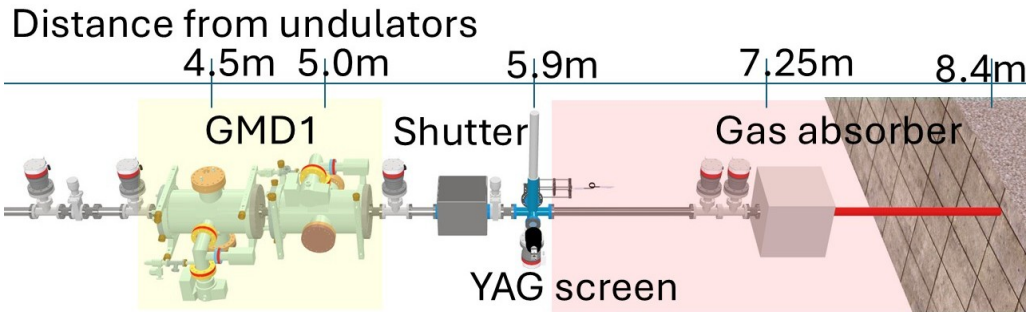

Figure 9.2: Details of the layout of the AQUA beamlines inside the undulator hall (Fig. 9.1, view A). GMD: Gas Monitor Detectors, Shutter: bremsstrahlung radiation stopper (for maintenance), YAG screen: transverse diagnostic chamber with scintillating screen and alignment laser, Gas absorber: gas attenuation module with gas insertion station and differential pumping

Before the main 2 m concrete shielding (Fig. 9.2), only a few diagnostics are foreseen to characterize the FEL pulses directly after the undulators: a scintillating screen (Sec. 9.4.2) and a Gas Monitor Detector (Sec. 9.4.1) to measure the pulse size, position, and intensity at the beamline entrance. A beam stopper can be inserted when the FEL radiation is suppressed - e.g., when the undulator gaps are open and the electron beam is properly dumped - to allow maintenance within the safety hutch while maintaining feedback from the accelerator (see Sec. 9.5.3 for further details). Within the shielding, a gas absorber (Sec. 9.3.2.2) will provide controlled attenuation. Its operation at relatively high pressure requires sufficient space for differential pumping.

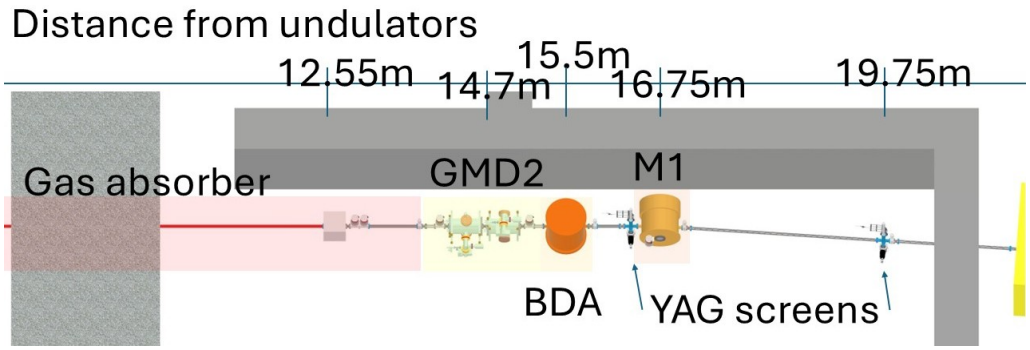

Figure 9.3: Layout of the AQUA beamline inside the bremsstrahlung shielding area (Fig. 9.1, view B). BDA: beam defining aperture; M1: mirror chamber.

Beyond the main shielding, a smaller radiation-shielded area (Fig. 9.3) is dedicated to suppressing copropagating bremsstrahlung radiation. This section also contains the downstream end of the gas absorber and its differential pumping stages. A second GMD will be placed after the differential pumping section to provide feedback on gas absorber pressure required to achieve the desired photon energy per pulse. It will also monitor the beam position along a straight reference axis, enabling precise steering of the FEL pulse. A beam-defining aperture (Sec. 9.3.1) safeguards

the downstream optics from missteered pulses and suppresses the broad spectral halo surrounding the XUV beam. Finally, a mirror (Sec. 9.3.3) redirects the FEL pulse away from the high-energy radiation.

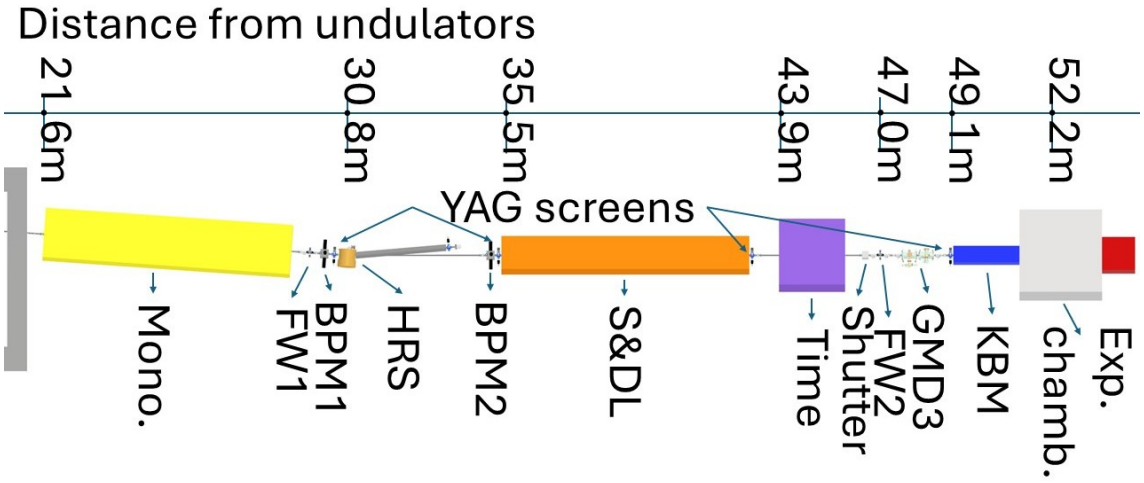

Figure 9.4: Details of the layout of the AQUA beamlines inside the user area (Fig. 9.1 view C). Mono.: monochromator area, FW: filter wheels, BPM: bladed beam position monitors, HRS: high resolution spectrometer, S&DL: split and delay line area, Time: time and polarization measurement area, Shutter: FEL photon shutter, KBM: K-B mirror chamber, Exp. chamb.: experimental chamber area.

Most of the space between the shielding wall and the spectrometer grating, shown in Fig. 9.4, is reserved for a monochromator (Sec. 9.3.5), to be designed and implemented in a second phase. Immediately after this area, a first filter wheel (Sec. 9.3.2.1) will be installed for spectral calibration and characterization of filters used in the second filter wheel, located farther downstream where the radiation intensity is lower. Because the intensity incident on the filters in the first position is close to the damage threshold, this filter wheel will operate only during single-shot calibration procedures or under low-intensity FEL configurations.

A plate Beam Position Monitor (Sec. 9.4.3), together with a pair of scintillating screens, will monitor the pulse position after the steering mirror inside the radiation shielding area. The high resolution grating spectrometer (Sec. 9.4.4) will provide shot-to-shot measurements on the pulse spectrum.

Downstream of the spectrometer, a second BPM will verify the pulse alignment. Two additional reserved areas are foreseen for second-phase instrumentation: the first (highlighted in orange) is dimensioned to host a split-and-delay line system (Sec. 9.3.6) with picosecond delay capability, while the second (in violet) will accommodate diagnostic instruments for pulse duration, polarization, and arrival time characterization (Sec. 9.4.5).

Following the timing diagnostics section, the beamline will include the main filter wheels (Sec. 9.3.2.1) and a final GMD to measure the pulse energy after all beamline attenuators and most optical elements. The focusing system, based on Kirkpatrick–Baez mirror pair (Sec. 9.3.4), will be installed just upstream of the user experimental chamber (Chapter 10) at the end of the beamline.

9.2.2 Overview of the beam parameters along the beamline

Tab. 9.1 summarizes the FEL pulse parameters at the end of the undulator. After the undulator, the beam propagates in vacuum, undergoing only planar reflections and filter absorptions, up to the focusing mirrors.

Tab. 9.4 reports the evolution of the pulse size and fluence on the optic surfaces along the beamline, considering the highest values obtained for the PWFA and Full RF configurations presented earlier. Wavefront propagation simulations, performed using the OASYS code [2], were used to estimate the pulse size evolution up to the focal spot inside the experimental chamber. The focal spot RMS is affected by fine adjustments of the mirror figure, and the intensity distribution is often non-Gaussian, exhibiting broader tails. Consequently, the reported fluence values for the focal spot — calculated assuming the RMS of an ideal Gaussian beam — are likely slightly underestimated (the FWHM of the focal spot is typically comparable to, or smaller than, the RMS value).

Table 9.4: AQUA beam parameters along the beamline for the reference 4 nm case. Fluence is calculated including losses and the inclination of the optic surfaces.

element	**distance (m) from the undulators**	**dimension (σ, mm) PWFA**	**dimension (σ, mm) Full RF**	**fluence (μJ/mm^2) PWFA**	**fluence (μJ/mm^2) Full RF**
1st YAG screen	5.9	0.34	0.36	70.8	375
BDA	15.5	0.63	0.70	3.56	17.8
1st mirror	16.8	0.67	0.74	0.63	3.16
1st filter wheel	29.8	1.00	1.13	6.82	34.5
1st blade BPM	30.1	1.01	1.14	6.43	31.3
spectrometer	30.8	1.04	1.16	0.16	0.78
2nd blade BPM	35.5	1.12	1.27	3.75	18.2
2nd filter wheel	47.0	1.44	1.63	2.28	11.0
last YAG screen	49.1	1.50	1.70	2.11	10.1
KB first mirror	50.6	1.53	1.73	0.06	0.29
KB last mirror	51.2	1.09×1.55	1.24×1.75	0.07	0.33
on the sample	52.7	2.2×1.6 (μm)	2.3×1.4 (μm)	0.90 10^6	6.28 10^6

All calculated fluences on optical surfaces remain below the single-shot damage threshold, which represents the most critical limit for ultrafast operation. Only the first scintillating Ce:YAG screen and some filters in the first filter wheel may occasionally experience damage from strong FEL intensity fluctuations. Mitigation strategies include operation at reduced repetition rates or in single-shot mode, the use of larger components to allow translation to undamaged regions, and the selection of more robust materials.

Considering the tuning range simulated in the Beam Physics Chapter (Tab. 3.14), the expected boundary parameters for the beamline at 3.2 and 5.2 nm are reported in Table 9.5. Looking toward future perspectives, shorter wavelengths can be effectively transported down to approximately 2 nm (near the Ni *k*-edge), although mirror reflectivity at these wavelengths requires smaller grazing angles to remain efficient (see Section 9.3.3). Conversely, longer wavelengths are well reflected by the system, but the intrinsic divergence of the beam can lead to significant geometrical losses due to the finite size of the optical elements. For example, a 10 nm wavelength pulse with a 0.68 mm dimension and 90 μrad divergence at undulator exit would experience about 13% geometrical losses, with approximately 90% of these occurring at the spectrometer grating. The lost photons will impinge on the optical mounts inside the vacuum chambers or on uncoated or differently coated regions of the combined mirror (grating) assembly (none of which exhibit absorption edges in the

Table 9.5: AQUA beam parameters along the beamline for the extreme edges simulated in Tab. 3.14.

element	distance (m) from the undulators	dimension (σ, mm) 3.2 nm case	dimension (σ, mm) 5.2 nm case	fluence (µJ/mm^2) 3.2 nm case	fluence (µJ/mm^2) 5.2 nm case
1st YAG screen	5.9	0.35	0.41	28.1	94.1
BDA	15.5	0.63	0.80	1.52	4.36
1st mirror	16.8	0.67	0.85	0.23	0.66
1st filter wheel	29.8	0.99	1.29	4.44	12.5
1st blade BPM	30.1	1.00	1.31	2.81	7.65
spectrometer	30.8	1.02	1.33	0.07	0.19
2nd blade BPM	35.5	1.10	1.45	1.63	4.47
2nd filter wheel	47.0	1.40	1.87	1.00	2.69
last YAG screen	49.1	1.46	1.95	0.93	2.48
KB first mirror	50.1	1.49	1.99	0.03	0.07
KB last mirror	50.7	1.06×1.50	1.42×2.01	0.03	0.08
on the sample	52.2	1.2×1.2 (µm)	2.2×1.2 (µm)	$0.95\ 10^6$	$2.56\ 10^6$

longer-wavelength range; see Fig. 9.10).

To estimate the overall beamline transmission, Table 9.3 lists the number of components and their associated transmission values for the reference case at 4 nm. The total transmission of the AQUA beamline, excluding the monochromator and the split & delay line, is 41% for the reference wavelength. A modest degradation of the mirror reflectivity (10% less transmission per surface, i.e., down to 0.74) would reduce the total transmission to 24%. Including the optional vertical steering mirror in the focusing system would lower the transmission to 35% (18% in the degraded-reflectivity case).

9.2.3 Technology Readiness Level of the beamline elements

Tab. 9.6 summarizes the Technology Readiness Level (TRL) of the main photon beamline optics subsystems. Most components are already mature and commercially available (TRL 8–9). A few systems, such as the split-and-delay line and the monochromator, are still under active R&D and standardization (TRL 6). For this reason, these instruments will not be installed during the first project phase; however, sufficient space has been reserved in the beamline layout for their future integration.

Table 9.7 presents the TRL of the photon diagnostics subsystems. Most monitoring devices are fully mature and commercially available (TRL 8–9). More advanced diagnostic techniques, such as transient reflectivity time-of-arrival (ToA) and THz streaking, are currently at lower readiness levels (TRL 4–5) and remain under active development. As for the optical systems, these diagnostics will be introduced in a later phase; in this TDR, they are described only at a conceptual level, with indicative positioning and space allocation along the beamline.

Table 9.6: TRL of photon beamline optics.

Subsystem	TRL	Comments
Defining apertures	9	Commercially available; standard design and implementation.
Solid filters	9	Fully commercial components; standard design.
Mirrors	9	Coatings and substrates meet specifications; commercial motors and vessels; standard design. Ongoing R&D focuses on improved surface quality and contamination control.
Focusing system	9	Commercially available systems (e.g. Elettra ILO).
Gas attenuator	8	Based on established designs; differential pumping and gas systems are custom-integrated, using commercial components.
Split & delay line	6	Prototype systems exist at several FEL facilities; ongoing R&D on automated alignment and reproducibility of delay scans.
Monochromator	6	Standard single-grating designs are well established; dispersion-compensating versions (with bypass option) are implemented only in a few facilities (e.g. DESY).
Other elements	9	Vacuum and mechanical components are fully commercial.

Table 9.7: TRL of photon beamline diagnostics.

Subsystem	TRL	Comments
Gas intensity monitor	9	Fully commercial system.
Wavefront sensor	9	Fully commercial system.
Photodiode	9	Commercially available device.
Linear polarimeter	9	Commercially available device.
Plate BPM	9	Commercial components; standard and reliable design.
Transverse coherence diagnostics	9	Standard technique using commercial components.
Longitudinal coherence diagnostics	8	Based on commercial components; requires custom configuration.
Grating spectrometer	8	Uses commercial elements; facility-specific customization.
Viewing screen	8	Commercial components with custom mechanical design.
Radial TOF chamber	6	Custom-built system; successfully used in a few facilities (e.g. PETRA@DESY).
Transient reflectivity ToA	5	Demonstrated at other FELs; optimization and standardization still ongoing.
Radial TOF chamber with THz streaking	4	Proof of concept and beamline tests completed (e.g. FLASH); R&D ongoing for routine operation.

9.3 Photon beam transport and optics for AQUA beamline

This section describes the optical components and beam manipulation systems implemented in the photon beamlines.

9.3.1 Defining apertures

Apertures are implemented to ensure high-contrast spectral purity at the experimental chamber and to protect the machine from accidental misalignments or failures.

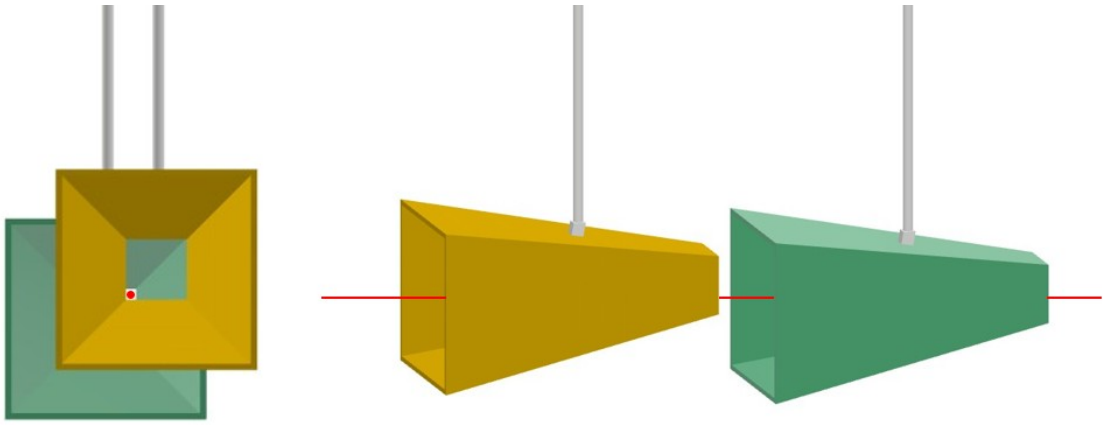

Figure 9.5: Schematic layout of the two consecutive truncated pyramids forming the BDA. Left: frontal view; right: side view. The red line represents the photon beam.

Mechanically, the Beam Defining Aperture (BDA) is similar to other FEL BDAs (i.e. [3]). It consists of two consecutive aluminum truncated pyramids, each with a central aperture of 20×20 mm^2 (see Fig. 9.5). Each pyramid trunk can be independently moved vertically and horizontally by ± 12.5 mm from the nominal reference axis, allowing the effective aperture to be adjusted up to complete closure using UHV-compatible stages.

The aperture is typically closed such that its edges intercept the far tails of the photon beam. This ensures minimal perturbation of the main beam while protecting downstream optics and components from large beam fluctuations or accidental misalignment.

The BDA side walls are tilted at a grazing angle of 10°, which spreads the incident flux over a larger area (factor ≈ 6) to reduce ablation. The expected energy deposition on the aluminum walls is ~ 0.05 eV/atom in the highest intensity scenarios reported in Tab. 9.4 and 9.5, well below typical single-shot damage thresholds [3]. Each pyramid trunk is approximately 120 mm in length.

Since the FEL radiation emitted from the undulators contains an intense coherent core with an angular divergence of a few tens of μrad, surrounded by a broader spontaneous emission with larger divergence, this aperture also functions as a collimator. Further downstream, plate BPMs (Sec. 9.4.3) will also act as collimating apertures.

9.3.2 Gas Attenuators and Solid Filters

In the AQUA beamline, an attenuator is an optical component designed to control and regulate the intensity of the XUV beam. For effective experiments and measurements, it is crucial to control the FEL pulse intensity. Users can reduce the pulse intensity across several orders of magnitude using solid filters, while fine-tuning of the average intensity can be performed with a gas attenuator.

9.3.2.1 Solid filters

A solid filter device is a mechanical assembly containing a set of interchangeable filters made from solid materials. Each filter has specific optical properties, allowing it to attenuate selected wavelengths while blocking others. Materials are chosen for their absorption characteristics in the XUV range, and filter selection depends on the experimental attenuation requirements of the AQUA beamline.

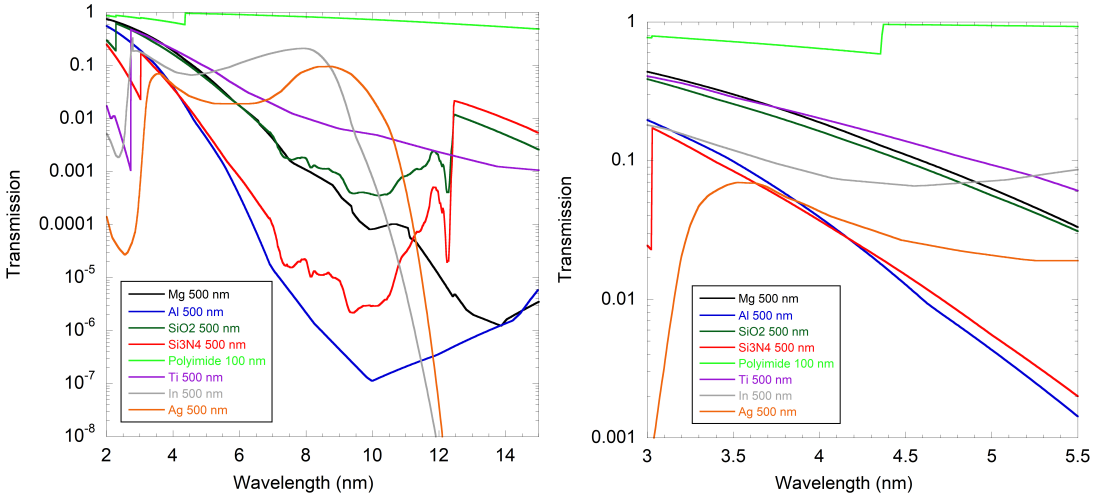

Figure 9.6: Transmission of 500 nm filter made from various materials. Some materials require a polyimide substrate (plotted separately). The right plot zooms in around the carbon K-edge.

Common XUV filter materials include silica, aluminum, magnesium, and sapphire. Fig. 9.6 shows the predicted transmission for 500 nm filters. Typical filter thickness ranges from 100 nm to a few µm. Filters may also include a thin polyimide substrate to improve mechanical stability. The exact composition and thickness will be determined based on operational wavelength and experimental requirements.

Filters are mounted on a wheel, with each angular position corresponding to a specific filter. Multiple wheels can be combined to achieve different filter compositions. Each filter wheel assembly includes two wheels, each capable of holding 12 filters (one slot empty to allow unperturbed propagation). Each slot matches the beam pipe diameter (40 mm), and filters are mounted in frames to maintain mechanical stability with a minimum clear width of ∼10 mm to avoid clipping the beam.

A filter wheel assembly is planned before the final intensity monitor, where the beam has near-maximum diameter and lower intensity (energy deposition ∼0.1–0.2 eV/atom for the considered materials under the highest XUV flux). A second filter wheel assembly is planned before the spectrometer to enable characterization of the filter spectral properties. Since the fluence is roughly three times higher at this location (similar to the 1st blade BPM line in Tabs. 9.4 and 9.5), operation of this assembly is only permitted in single-shot mode or with low-energy FEL configurations.

9.3.2.2 Gas attenuator

A gas attenuator consists of a chamber filled with a specific gas (typically N_2 or noble gases such as Ar, Xe or Kr) through which the XUV beam passes. The degree of attenuation can be controlled by changing the gas pressure within the cell. By adjusting the gas pressure, users can precisely control the average amount of light that reaches the experimental sample. This precise control is critical when working with sensitive samples, for example during measurements of nonlinear properties.

Gas attenuators are widely used in FEL beamlines [4–6] as they provide dynamic and continuous beam attenuation for a variety of experiments. Careful evaluations of the vacuum system for the differential pumping are ongoing and in the beamline it is reserved adequate space and budget, based on other facilities experience.

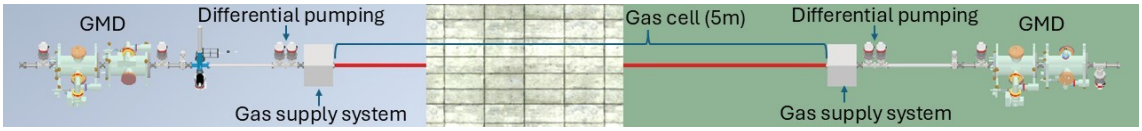

Figure 9.7: Schematic layout of the gas absorber: 5 m gas cell (within the shielding wall), Gas supply system and differential pumping at the edges of the gas cell, GMDs before and after the gas absorber

The gas attenuator layout (Fig. 9.7) includes:

- **Gas cell:** The primary component; a ∼5 m long chamber provides 1–5 orders of magnitude of attenuation.
- **Gas supply system:** Provides a controlled flow of N_2, Kr, or Xe depending on operation wavelength (Fig. 9.8).
- **XUV beam inlet/outlet:** Windowless entry and exit ports minimize disturbance to the beam, with differential pumping and conductance-limited vacuum sections.
- **Diagnostics:** Photodiodes and GMDs before and after the gas cell monitor the beam and provide feedback for gas pressure control.

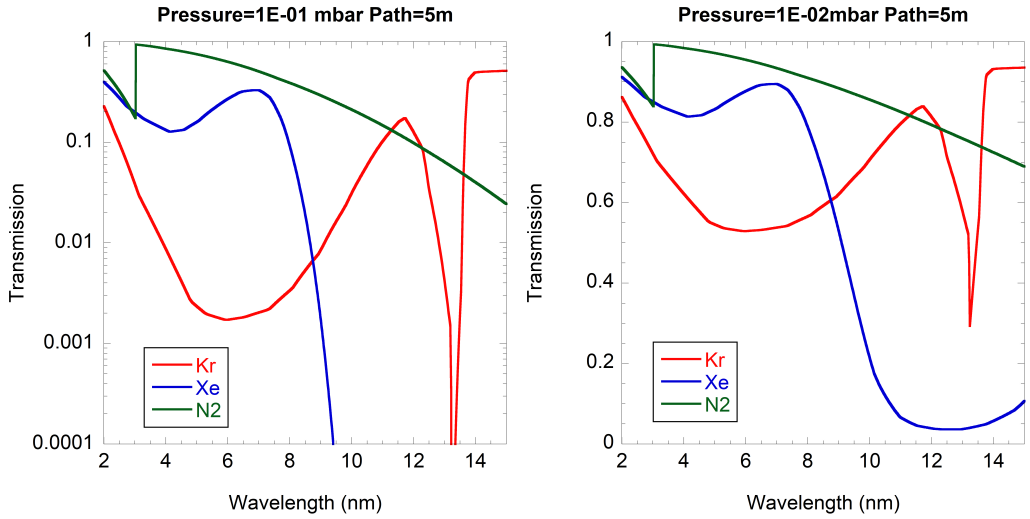

Figure 9.8: Transmission for 0.1 mbar (left) and 0.01 mbar gas pressure in a 5 m gas cell for N_2 (green line), Kr (red), Xe (blue)

The choice of attenuation method (gas attenuator or solid filter) depends on experimental needs. Both options will be available to beamline users.

9.3.3 Mirrors

The beamlines will require a few plane mirrors for steering the beam away from the undulator line, for the split-and-delay system, for the monochromator, and for the optional vertical steering before the final beam focusing. The mirrors operate at a grazing incidence angle of 2°, ensuring high reflectivity and a large illuminated area, which helps keep the surface intensity well below the damage threshold of the mirror coatings (on the order of several hundred μJ/cm^2). Considering

the conservative damage threshold for Ni reported in [7], corresponding to an energy deposition of 0.57 eV/atom for ultrafast pulses (< 100 fs), the fluence values from Tab. 9.4 for the first mirror, subject to the highest fluence, yield deposited energies of 4×10^{-5} eV/atom (PWFA case) and 2×10^{-4} eV/atom (Full RF case), calculated following the method of [8].

9.3.3.1 General Description

The mirrors are mounted inside ultra-high-vacuum (UHV) chambers on adjustable support structures capable of fine control in pitch, yaw, and both vertical and lateral translations. The support structures can be secured to the chamber and allow manual adjustment in all six degrees of freedom for initial alignment.

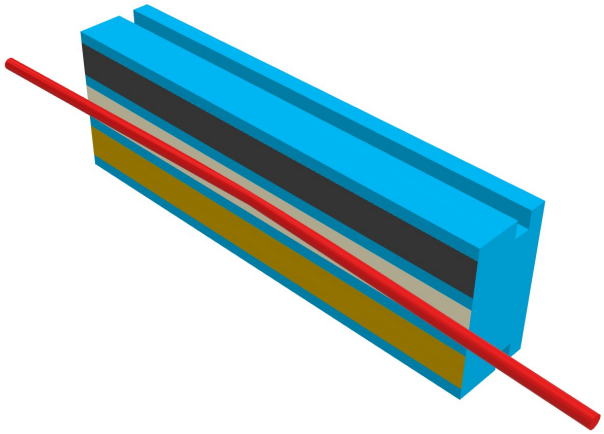

Figure 9.9: Mirror layout

9.3.3.2 Mirror Specification

The mirror shape and mounting design ensure optimal stability and positioning within the UHV chamber. Two longitudinal slots along the sides of the mirror serve primarily for mounting (see Fig. 9.9).

In the following table (Tab. 9.8) the different specifications for each mirror are listed.

The longitudinal length (X) of each mirror is approximately twice the 6σ dimension of the FEL pulse at 4 nm, accounting for the projected footprint at grazing incidence, and is sufficient to enclose the 4σ extent of the largest simulated beam. The vertical width (Y) allows three separate coatings for different spectral regions, each significantly larger than the pulse footprint to provide clean, undamaged region access during operation. A 3 mm separation margin is maintained between coatings.

Using SHADOW simulations, maintaining a focal variation below 10% requires mirror flatness exceeding $\sim$3 km radius in the sagittal and $\sim$30 km in the tangential direction. Commercial high-quality mirrors (e.g., Zeiss [9]) routinely achieve flatness of $\sim$100 km.

A small conductive contact plate is installed to measure current drawn by the metallic coating. This plate will touch the mirror surface over an area of less than a few mm^2 and connect via a screened cable to a BNC feedthrough outside the UHV chamber.

Additional mirrors for the monochromator and split-and-delay systems will be specified later in the project when those components are implemented.

Table 9.8: Mirror dimensions in the AQUA beamline

Mirror	**Shape**	**Size (mm)** Length (X) Width (Z) Thickness (Y)	**Incident Angle**	**Fixing**	**Cooling**
Steering mirror	Flat	250 ±1 40 ±0.1 30 ±0.1	2	Lateral Slot	No
Optional steering mirror before the K-B system	Flat	500 ±1 55 ±0.1 20 ±0.1	2	Lateral Slot	No
K-B mirror vertical	Bendable	500 ±1 55 ±0.1 20 ±0.1	2	Lateral Slot	No
K-B mirror horizontal	Bendable	500 ±1 55 ±0.1 20 ±0.1	2	Lateral Slot	No

9.3.3.3 Mirror position specification

The mirror system will be mounted along the beamline and fixed to the floor. Its position will be surveyed and manually adjusted to meet nominal alignment and altitude specifications. Mounting feet will be bolted to the floor for stability.

Manual adjustment must compensate for variations in floor height and allow fine tuning of roll, pitch, yaw, lateral, and longitudinal positioning. The altitude and nominal center position of each mirror will be referenced to external fiducial monuments with an accuracy of ± 0.1 mm.

9.3.3.4 Mirror support and UHV chamber description

Each mirror will have two angular degrees of freedom, plus insertion and vertical alignment controls — all remotely actuated. Angular adjustment will allow beamline alignment corrections with a resolution better than 10 µrad. Vertical motion will enable selection of the appropriate coating for the experimental wavelength and repositioning of the beam within the coated area to avoid damaged regions. The expected vertical resolution is about 10 µm. Insertion control will allow fine longitudinal tuning with $\sim$10 µm resolution and reproducibility better than 100 µm.

After alignment, each mirror will be able to move reproducibly between two positions:

1. Mirror fully intercepting the beam at 2° incidence;
2. Mirror fully retracted from the beam path.

The final supplier may implement these long-travel and fine-adjustment motions using any suitable, cost-effective solution meeting specifications — such choices will be considered valuable design contributions.

Auxiliary flanges for visual inspection and vacuum pumping will be included, with final positioning proposed by the supplier and subject to approval.

Mirrors and mechanisms shall be supported by a rigid platform secured to the UHV chamber floor. Mirror positioning must be unaffected by vacuum pressure or moderate thermal variations. The chamber support frame shall allow full six-degree-of-freedom adjustment. The final supplier

may choose between adjustable feet, kinematic mounts, or equivalent solutions (e.g., Bosch-type supports or sand-filled structures), which will be evaluated for suitability. Each chamber will provide mounting for UHV components such as ion gauges and pumps, with provisions for supporting heavy equipment where necessary.

9.3.3.5 Mirror Coating

Mirrors will have coatings optimized for high reflectivity in the target spectral range. Different coating materials have been analyzed (see Fig. 9.10).

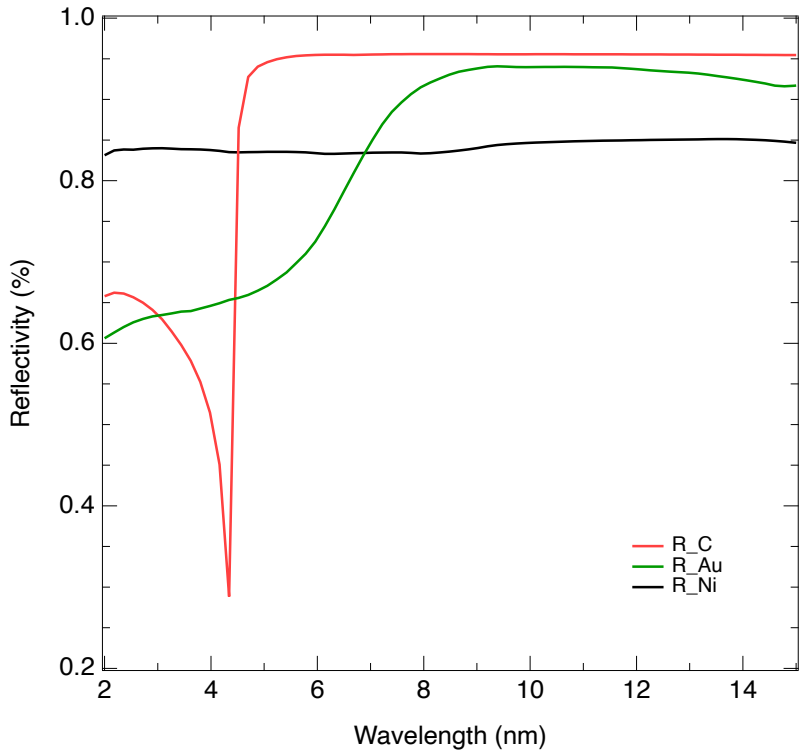

Figure 9.10: Mirror reflectivity as function of the wavelength at 88° angle of incidence under ideal conditions (no roughness, no contamination).

Carbon (graphite) coatings offer the highest reflectivity—up to 95%—up to their K-edge and will be the default choice for wavelengths from the longest usable values down to about 4.5 nm.

Nickel provides nearly flat reflectivity (∼84%) across the AQUA beamline range and will be used for shorter wavelengths (< 4.5 nm). Nickel is known to be reactive, so the reflectivity is expected to degrade in time due to exposure to contaminants. While oxidation is not affecting the reflectivity too much outside the oxygen K-edge at 2.34 nm, carbon contamination from hydrocarbons or from spattered sample can severely affect the reflectivity. Standard plasma-based cleaning techniques (e.g., inductively coupled plasma [10]) may not be suitable for in-situ cleaning due to limited selectivity between carbon contamination and the mirror coating [11]; however, mirrors can be cleaned offline with care to preserve the carbon coating.

Gold will serve as a backup coating option due to its chemical stability and ease of cleaning, despite its lower reflectivity in the relevant spectral range.

Polarization-dependent reflectivity differences are below 1% across the considered wavelengths. Surface roughness must be below 1 nm rms to limit scattering losses, as reported in Sec. 3.2.6.4.

9.3.4 Focusing system

To achieve the desired beam spot size on the target inside the experimental chamber, a focusing system is required that can vary the spot size from the millimeter scale — corresponding to the natural propagation from the undulators — to a tightly focused spot for high-intensity experiments.

State-of-the-art focusing systems for XUV and soft X-ray FELs employ two mirrors in a Kirkpatrick–Baez (K–B) configuration [12], where each concave elliptical mirror focuses the beam in one transverse direction. Many facilities include bendable mirrors that allow dynamic adjustment of the curvature during operation, enabling control of the longitudinal focal position and, consequently, the beam size at the target.

Because each K–B mirror introduces an angular deflection of 4° (twice the grazing angle), a removable plane mirror is included upstream of the K–B system to compensate for vertical deviation, ensuring a horizontally aligned beam when required by specific experiments. This additional reflection introduces an estimated transmission loss of about 20%.

Commercial K–B systems, such as the KAOS system developed at Elettra — one of the first laboratories to implement this approach [13] — illustrate the compactness and precision achievable with such designs (see Fig. 9.11).

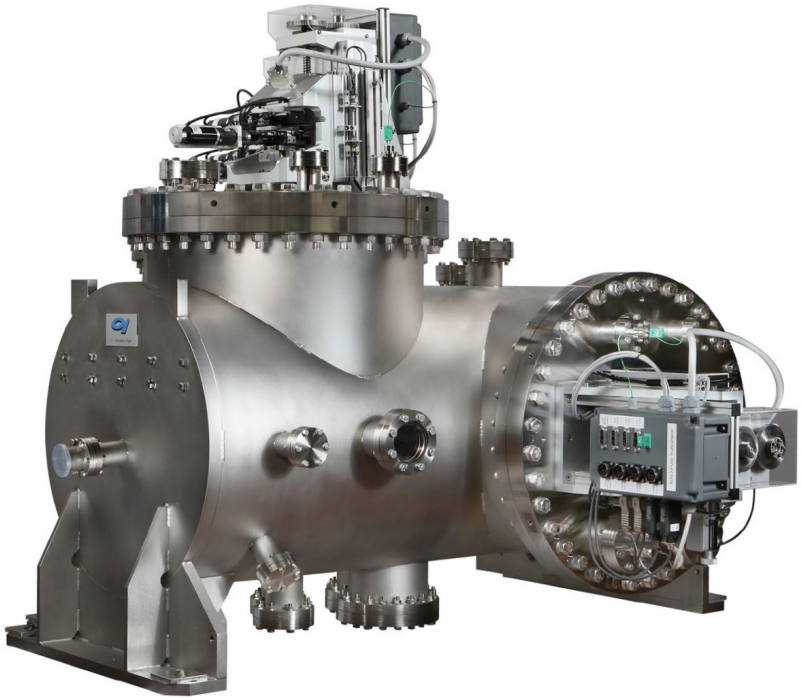

Figure 9.11: An example of commercial K-B system: the KAOS system developed at Elettra (from [14]).

9.3.4.1 System Description

The final focusing system will consist of:

- a first vertical deflecting mirror that can be inserted or removed from the beamline,
- two mechanically bendable mirrors arranged in a K–B configuration,
- the corresponding vacuum vessels and support frames, with two exit ports to accommodate configurations with and without the vertical deflecting mirror,
- all mechanical and vacuum-pumping components required for UHV operation.

The total system length will be approximately 2 m, with the last element being the horizontally

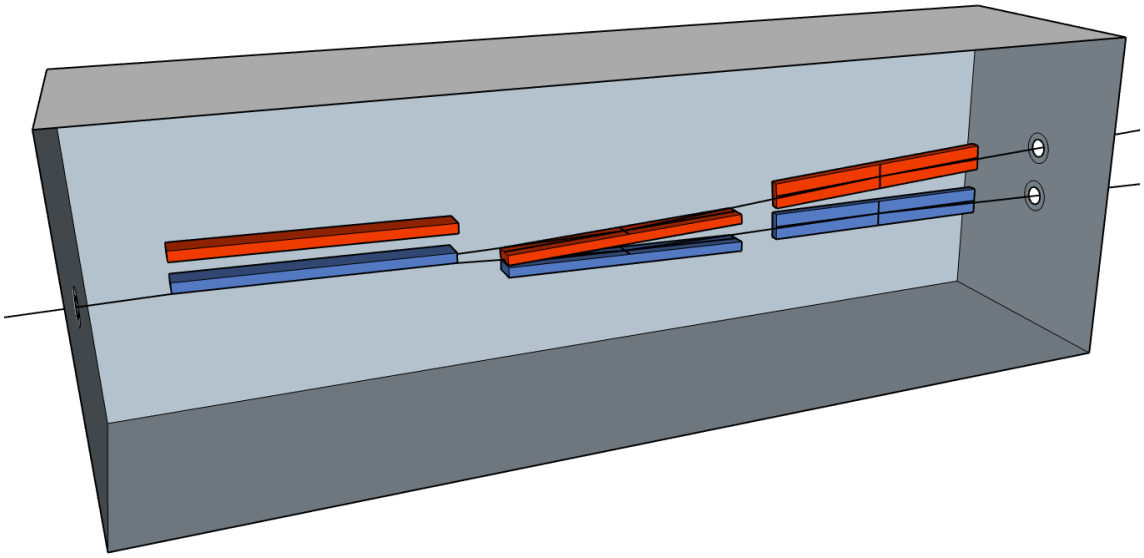

Figure 9.12: 3D schematic view of mirror configurations with (blue) and without (red) the vertical steering mirror.

deflecting K–B mirror. Each mirror inside the vacuum vessel will be 500 mm long, with a center-to-center separation of 600 mm.

All mirrors will be motorized for two rotational degrees of freedom (pitch and yaw), with an additional degree for the final mirror to match the propagation direction in both configurations. Typical angular adjustment ranges are $\pm 2°$ for the vertical deflecting mirror and $\pm 4°$ for the K–B mirrors. Two translational degrees of freedom will be available to insert or retract each mirror and to select the appropriate coating or configuration.

In particular, the K–B mirrors will have two reference positions corresponding to configurations with and without the vertical steering mirror. These positions will be separated by approximately 4 cm (vertical mirror) and 8 cm (horizontal mirror), resulting in a total exit shift of about 11 cm (see Fig. 9.12). The separation is sufficient to accommodate independent CF40 flange connections toward the experimental chamber.

All mechanical alignment, motorization, and performance tests will be carried out by the suppliers before installation at the AQUA beamline. Upon installation, the suppliers will also provide on-site training and final configuration verification.

9.3.4.2 Optical Performance

The expected focal range of the K–B system extends from a nearly plane-mirror configuration — yielding a beam size of approximately 1 mm rms (slightly larger at longer wavelengths) — to a tight focus at about 2.1 m (vertical) and 1.5 m (horizontal) focal lengths. At these conditions, the beam focus is expected to have a RMS spot size smaller than 4×3 µm for the reference 4 nm FEL pulse, consistent with the simulations presented in Tab. 9.4 and accounting for potential aberrations in the beam profile or mirror surfaces not included in the simulations. This range of tunable focusing will allow experiments spanning from low-intensity, wide-field illumination to tightly focused, high-intensity regimes — providing versatility for both linear and nonlinear XUV interaction studies.

9.3.5 Monochromator

SASE FELs produce a noisy, broadband spectrum. Some experiments, such as absorption spectroscopy, require a narrow spectral bandwidth. A monochromator can select a small portion of the spectrum, significantly improving spectral purity, and also removing higher harmonics and unwanted background photons coming from the FEL or upstream sources, that can also interfere with measurements.

While a monochromator enhances energy resolution and spectral selectivity, it introduces some important drawbacks, such as the reduction of the total photon throughput due to diffraction efficiency and path length dispersion, stretching femtosecond pulses to longer durations and potentially affecting ultrafast time-resolved studies. More complex configurations using two gratings for dispersion compensation may be envisaged [15], but at the cost of larger losses on the photons per pulse. In addition, at least at the beginning of the facility operation, the pulse will have energy jitters larger than the FEL spectral width (see for example Fig. 3.17).

For those reasons, the AQUA beamline will not have a monochromator at the beginning of its life, but it may be implemented in a later phase. Consequently, a space of approximately 7.5 m between the safety hutch and the spectrometer (indicated as the yellow area in Fig. 9.1) is foreseen, with the option to extend it by an additional 2.5 m within the safety hutch.

9.3.6 Split and Delay line

A split-and-delay line (SDL) system is an optical apparatus in a FEL beamline to generate two temporally separated copies of a single X-ray pulse with low relative timing jitters.

Many SDL systems operate by spatially splitting the incoming FEL wavefront into two parts using the edge of a mirror, directing each part along a separate optical path, and then recombining them with a controlled time delay. Stability is critical: to ensure the coherence and wavefront integrity of the FEL pulses, the SDL system must maintain angular deviations below a few μrads and positional repeatability within tens of nm. As the pulse is geometrically cut by a hard edge, the expected focal spot on the sample will also have different dimensions from unperturbed configuration and possible diffraction fringes may occur. Other possible schemes involve spectral splitting (in particular for two color FEL configurations).

The SDL system will be implemented in the beamline at a later phase, beyond the scope of this TDR, as it is critical only for a specific class of experiments requiring high temporal resolution in UV pump–UV probe measurements. Accordingly, space is reserved in the beamline for future implementation, while this document provides only design considerations of the potential systems for footprint evaluation.

In case of multi ps delay, a long delay line is required due to the small incidence angles on the mirrors. As a first evaluation, using 2° grazing incidence for the fixed line and 3° for the movable one, and considering to recombine the beam on a mirror before the experimental target, about 7.5 m are required and a similar area is reserved after the spectrometer (the orange area in Fig. 9.4). The expected transmission for the SDL system alone will be about 35% for the fixed delay line and 18% for the movable line, and the total delay range will be from -1 to +26.7 ps. Examples of similar systems are present at FERMI facility [16] or LCLS [17].

In case of sub-ps delay, a more compact configuration can be installed directly inside the experimental chamber, having the two beams going back together on the sample. In this configuration, less mirrors are required for the SDL, but the total delay is reduced in the 100s fs and the angle of the delayed pulse is slightly larger (thus with larger reflection losses, having in the end a similar transmission with respect to the other longer configuration). Example of similar systems are present at FERMI TIMER beamline [18] or at FLASH [19].

9.4 Photon Diagnostics

This section presents the diagnostics systems implemented in the FEL photon beamlines.

9.4.1 Gas Monitor Detectors

Properties such as beam position and intensity of the FEL radiation will be measured and monitored on a shot-by-shot basis in a non-invasive manner by means of three Gas Monitor Detectors (GMD) installed along the beamline. GMDs represent the state-of-the-art diagnostic technology for characterizing and monitoring FEL radiation across a wide wavelength range, from the XUV range [20] to the X-ray regime [21, 22]. Their operation relies on the photoionization of a rare gas, followed by the analysis of the emitted electrons and ions generated in the process.

Originally developed at DESY (Hamburg) for the FLASH SASE FEL [23], the GMD design has since been optimized and is now commercially available (e.g. from DESY) with customizable specifications. An overall view of the vacuum chamber housing the GMD is shown in Figure 9.13.

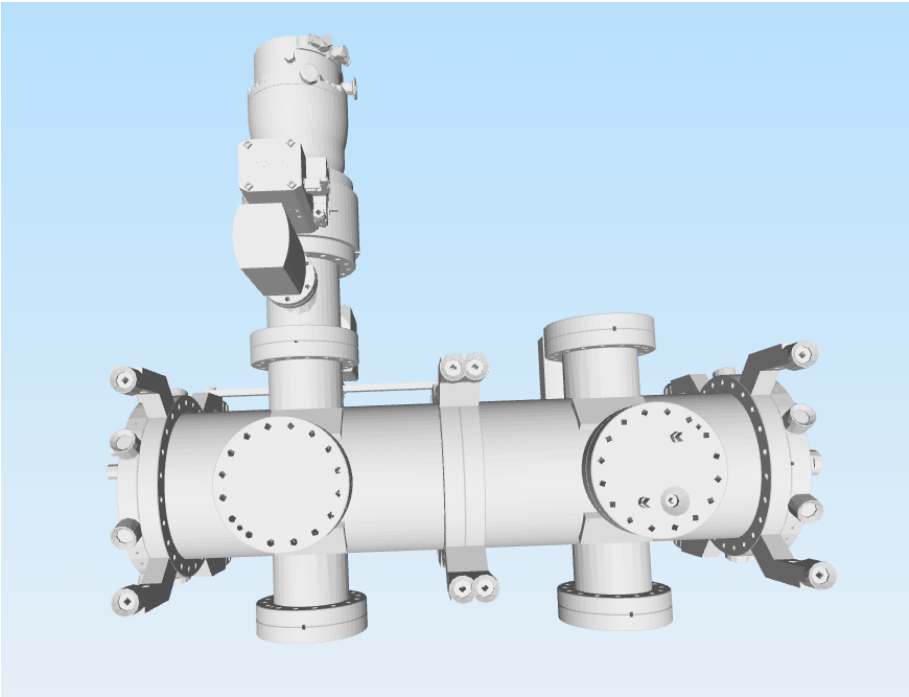

Figure 9.13: Draft of the GMD, Courtesy of Dr. K. Tiedke, Photon Diagnostic Team DESY, Hamburg.

The vacuum chamber, approximately 1 m in length, functions as a gas cell filled with a target rare gas, typically neon, argon, or krypton, at a pressure of about 10^{-5} mbar. As the FEL pulse traverses the GMD, it ionizes the gas atoms while undergoing negligible absorption due to the low gas density. The resulting ions and electrons are extracted from the interaction volume, accelerated by an electric field, and collected by electrodes functioning as Faraday cups. The measured ion current is directly proportional to the pulse's total intensity, enabling an accurate determination of the photon flux.

To allow beam position monitoring, the electrodes are arranged in a split geometry. Additionally, a time-of-flight (TOF) mass spectrometer can also be positioned behind the ion electrodes, providing additional diagnostic capabilities.

GMDs are typically calibrated by manufacturers at national metrology institutes, such as the Physikalisch-Technische Bundesanstalt (PTB, Germany) in Germany, using dispersed synchrotron

radiation in the microwatt range and a calibrated photodiode as reference detector.

Two GMD units — each equipped with horizontal and vertical split electrodes — will be installed downstream of the undulator sections, with the gas attenuator (Sec. 9.3.2.2) positioned in between. This setup enables machine commissioning, beam tuning, and continuous monitoring of the absolute FEL intensity and photon beam pointing. A third GMD will be located just upstream of the focusing mirrors, allowing full characterization of the FEL radiation at the experimental stations.

9.4.1.1 Beam Intensity Monitoring

The expected beam intensity at a fixed photon energy can be determined using Eq. 9.1 from Sorokin et al. [22]:

$$N_{photon} = \frac{0.862\, I_{ion}[A]\ (273\ +\ t[^{\circ}C])}{\sigma_{ph}[cm^2]\ z_{eff}[cm]\ p[mbar]\ \gamma\ \nu} \tag{9.1}$$

where I_{ion} is the total ion current, ν the repetition rate, σ_{ph} the total photoionization cross section [24], z_{eff} the effective interaction length (typically ~ 22 cm, [22]), p the gas pressure, t the temperature and γ the mean charge of the photoions [23].

GMDs have been successfully used to measure individual femtosecond pulses containing 10^7 - 10^{15} photons at photon energies ≥ 14 eV with an absolute measurement accuracy of 7–10 % [22]. Under AQUA beamline conditions, assuming 10^{10} photons/shot, 100 Hz repetition rate, 10^{-5} mbar of gas pressure, and literature values for σ_{ph} and γ [23], ion currents on the order of tens of pA are expected. The most suitable rare gas will be selected based on its ionization cross section at the relevant photon energy. A simulation of the expected current is shown in Fig. 9.14.

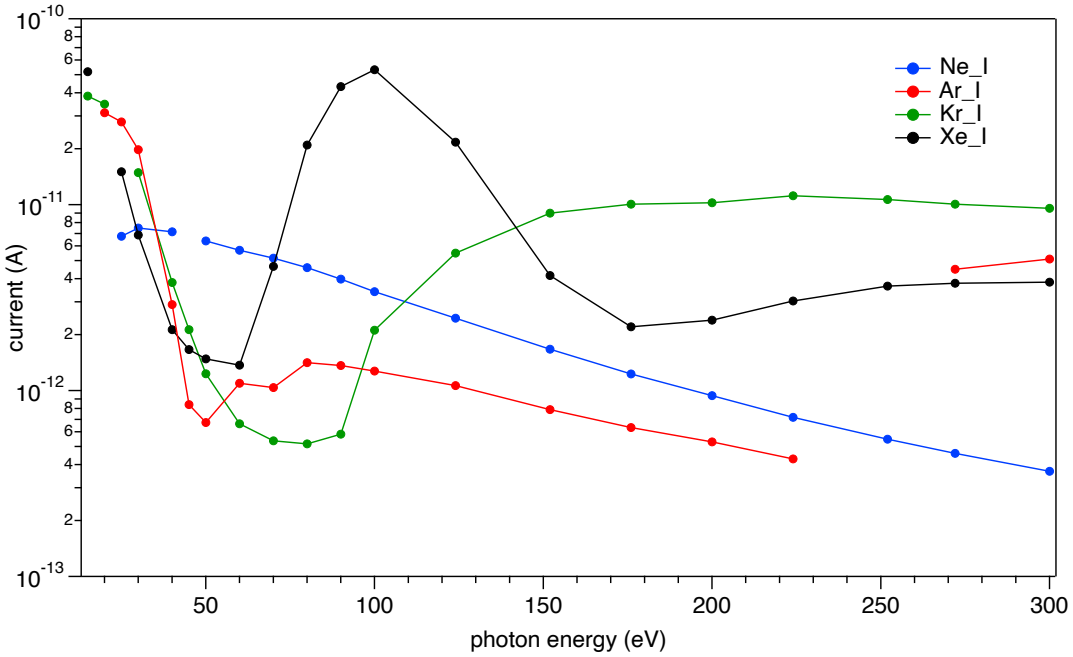

Figure 9.14: Estimate of the expected current from a GMD according to Eq. (9.1), using $z_{eff} =$ 22 cm, $p = 10^{-5}$ mbar, 10^{10} photons/pulse, and 100 Hz repetition rate at room temperature. Four different rare gases are considered. Breaks in the curves correspond to resonance regions. Cross section and mean charge data from [23].

9.4.1.2 Beam Position Monitoring

The GMD will also serve as a non-invasive monitor of the beam position, achieved through the split geometry of the ion electrodes. Due to the homogeneous extraction field, the charged particles generated by a single photon pulse represent, on the plane of the split electrode, a projection of the photon beam. The lengths z_1 and z_2 of this projection on each electrode half define the ratio of the corresponding ion current I_1 and I_2 as:

$$\frac{I_1}{I_2} = \frac{z_1}{z_2} = \frac{b-2\Delta x}{b+2\Delta x} \tag{9.2}$$

where Δx is the beam displacement from the center, and b is the width of the split electrode. With a typical effective total length of 22 cm, an accuracy of 20 µm can be achieved [23]. Comparison of the signals from the first two GMDs, located approximately 10 m apart, will provide information on the beam direction with an accuracy of about 10 µrad.

A rectangular aperture in the ion extraction electrode, covered with a high-transparency Au mesh, can also serve as the extractor electrode for the drift tube of a TOF spectrometer. This instrument enables mass-over-charge analysis of the produced ions and can be used for additional photon diagnostics, including the detection of higher FEL harmonics - leading to more highly charged ions - and direct determination of the mean charge state of the photoions.

9.4.2 Viewing screens

Similar to the approach used for the electron beam diagnostics (Sec. 11.2.5), several viewing screen stations will be installed along the beamline to monitor the transverse profile of the FEL photon beam.

Each station consists of a scintillator mounted perpendicular to the beam path, coupled with a 45° mirror that redirects the emitted light through a vacuum viewport towards a CCD camera equipped with imaging optics for image acquisition. The scintillator screen can be precisely inserted and retracted from the beam path by means of a stepper motor driving a double ball screw mechanism, ensuring high accuracy and repeatability. A bellows integrated within the vertical support column maintains vacuum integrity during motion.

The selected scintillator material is Ce:YAG, widely used in FEL beamline diagnostics [25–27] due to its high light yield per incident photon (typically ∼30 photons/keV, depending on the cerium concentration). The single-shot damage threshold fluence for Ce:YAG under ultrafast irradiation is approximately 2.5 mJ/mm^2 [28], which exceeds the expected fluence on the AQUA beamline screens, ranging from about 0.375 mJ/mm^2 at the station closest to the undulators down to 0.01 mJ/mm^2 before the K-B mirrors in the highest flux scenario (Full RF case, longer and more charged pulses). Response linearity is maintained up to roughly one-third of the damage threshold [28].

Should FEL performance increase substantially or if crystal damage becomes frequent, more robust scintillating materials such as CVD diamond can be considered [29].

Below the screen holder, an auxiliary mirror is installed at a -45° angle, orthogonal to the one used for the Ce:YAG screen, to facilitate laser alignment of the beamline toward the user end-station, via the viewport opposite to that used by the CCD camera assembly.

Finally, a second, empty slot located beneath each mounting is foreseen to accommodate alternative diagnostic devices, such as photodiodes or double slits for coherence measurements (Sec. 9.4.7).

9.4.3 Plate Beam Position Monitors

Plate Beam Position Monitors [3, 26] are planned along the photon beamline to complement the information on the pulse trajectory collected by GMD and screens (when inserted) and to act as

collimators for the peripheral radiation surrounding the FEL pulse. Each BPM consists of four metallic blades that intercept the outer edges of the beam to collect a drain current (Fig. 9.15).

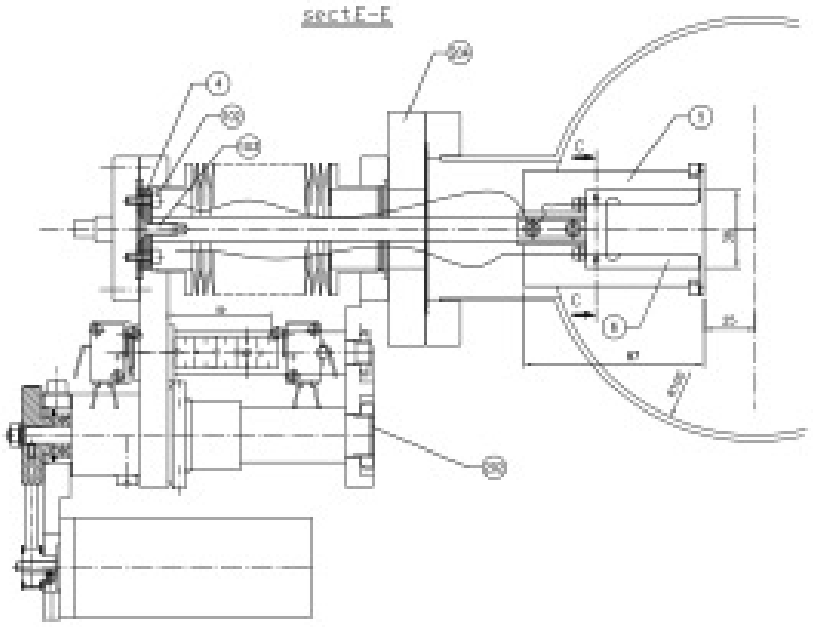

Figure 9.15: Layout of the plate BPM

The expected spatial resolution of this system is approximately 2 µm displacement from the reference position, while minimally perturbing the beam's shape and energy. The slit assembly is designed to intercept the beam at the center of the chamber, allowing controlled profiling. Each slit is larger than the full transverse size of the beam, and the total motion range ensures complete coverage.

The BPM consists of four independently movable blades—two vertical and two horizontal—each translating perpendicular to the beam axis. The blades are electrically isolated and connected to external feedthroughs for current readout.

The slits are fully retractable and can be positioned with a precision of 2 µm using linear translators actuated by remotely controlled motors. Copper is chosen for the blade material due to its high thermal conductivity and mechanical stability, ensuring reproducible beam interception. Assuming a photon flux of 10^{10} photons per pulse, a beam interception fraction of 3%, and a total electron yield of 0.05 for copper, the expected current per pulse on a single plate is $\sim 4 \cdot 10^6$ electrons ($\sim$60 pA at 100 Hz repetition rate).

For accurate current readout, a high-resolution picoammeter, such as the CAENels 4-Channel Charge-Integration Picoammeter AD401D [30], will be employed to monitor the signal from the four plates. Comparison of the signals from each blade allows real-time reconstruction of the beam position.

In addition to slit-based position monitoring, the system includes a wire scanner for transverse beam profile measurements. The scanner uses a 1 µm metallic wire mounted on a spring-loaded support to maintain constant tension and minimize thermal elongation effects. The wire is electrically isolated and connected to a picoammeter via feedthroughs to measure the current generated by intercepted photons.

The BPMs are positioned at 30.1 m and 35.5 m from the effective photon source. The expected transverse RMS beam dimensions at these locations are 1.0 mm and 1.1 mm for PWFA cases, and 1.1 mm and 1.3 mm for Full RF cases. Accordingly, the BPM apertures will have an operation

aperture of about 5–6 mm. The estimated beam fluences at full interception are 6 and 4 μJ/mm^2 for PWFA, and 31 and 18 μJ/mm^2 for Full RF cases, all below levels that could induce surface ablation.

9.4.4 Grating spectrometer

High spectral resolution is a fundamental requirement for the spectrometer, but equally important is the preservation of the photon beam properties. Furthermore, due to the stochastic nature of the FEL emission, the spectral diagnostics must operate in a shot-to-shot mode. Several approaches have been developed over the years to achieve high-resolution spectral measurements while minimizing perturbation to the transmitted beam across various photon energy ranges [31].

The adopted solution employs a diffraction grating with Variable Line Spacing (VLS), designed to ensure high reflectivity in the zero-order direction. This configuration allows most of the incoming beam to propagate toward the experimental stations with minimal disruption, requiring a reflectivity exceeding 70% to ensure adequate pulse delivery. Higher diffraction orders are spatially separated and focused onto the detection system by the action of the VLS grating.

The optical path of a beam diffracted by a VLS grating can be described by a power series expansion, where the dominant terms are [31, 32]: the grating equation F_{100}, the sagittal focus F_{200}, the tangential focus F_{020}, and the primary coma F_{300}:

$$
\begin{aligned}
F_{100} &= mD_0\lambda - (sin(\alpha) - sin(\beta)) \\
F_{200} &= \frac{1}{2}\left[-mD_1\lambda + \left(\frac{cos^2\alpha}{r} + \frac{cos^2\beta}{r'}\right)\right] \\
F_{020} &= \frac{1}{r'} + \frac{1}{r} \\
F_{300} &= -\frac{1}{3}mD_2\lambda + \frac{1}{2}\left(\frac{cos^2\alpha sin\alpha}{r^2} + \frac{cos^2\beta sin\beta}{r'^2}\right)
\end{aligned}
\tag{9.3}
$$

where α and β are the incidence and diffraction angles, respectively; m is the diffraction order; r and r' denote the distances from the source and to the detector; and the groove density is expressed as a power series in the tangential coordinate x: $N(x) = D_0 + D_1x + D_2x^2 + O(x^3)$.

A fixed incidence angle α = 88° relative to the grating normal has been selected to ensure high reflectivity. As the distances between the preceding mirror and the spectrometer, and between the spectrometer and the detector, are defined, the diffraction angle β becomes a function of the photon wavelength λ, enabling full spectral reconstruction on a shot-by-shot basis.

The detector system, comprising a scintillator and a camera assembly, will be positioned approximately 3 m downstream of the grating (r') in a dedicated vacuum chamber oriented at an angle with respect to the main photon beam path. The diffraction grating will be installed along the beamline in a separate vacuum chamber, located 30.8 m (r) downstream of the undulators.

Simulations based on the beamline parameters yield optimal diffraction angles β between -75° and -79° relative to the grating normal, covering the photon energy range from 15 nm (∼85 eV) to 3 nm (∼420 eV). Each grating will be fabricated on a 250 mm-long, 40 mm-thick silica substrate, with three different line distributions and coating materials. Each grating has a clear height of 10 mm.

The detection system consists of a Ce:YAG scintillator housed in a dedicated vacuum chamber, coupled to a CCD camera mounted on a viewport flange. The camera must operate in the visible range with a quantum efficiency (QE) above 60%, compensating for the relatively low diffracted intensity (the Ce:YAG QE ranges between 35% and 80%, depending on wavelength). For low photon flux operation, the chamber will also accommodate an in-vacuum XUV-sensitive camera mounted on the opposite flange.

To achieve the required spectral resolution, CCD sensors with at least 1000 $\times$ 1000 pixels are foreseen. The overall power density on the YAG screen is expected to remain low, avoiding any risk of damage. For precise alignment and focusing, the grating and detection assemblies will be mounted on remotely controlled micrometric actuators to ensure accurate and repeatable positioning.

All the relevant parameters are summarized in Table 9.9.

Table 9.9: Baseline parameters of the gratings foreseen for the beamline, derived from the system implemented at FERMI and adapted to the AQUA beamline using Ray-UI [33] simulations.

Parameter	**First Grating**	**Second grating**	**Third Grating**
Wavelength (nm / eV)	3.1 / 400	4.4 / 282	12.5 / 99
Resolution (meV)	$\approx$ 11.1	$\approx$ 1.6	$\approx$ 0.5
Groove Height (nm)	$\approx$ 7	$\approx$ 4	$\approx$ 12
Material	Nickel(50 nm)	Nickel(50 nm)	Amorph. Carbon (50 nm)
D_0 (l/mm)	3500	1700	600
D_1 (l/mm^2)	2.68	1.36	0.35
D_2 (l/mm^3)	8.3 x10^{-3}	1.4 x10^{-3}	1.7 x10^{-4}

9.4.5 Temporal and polarization characterization

Direct temporal and polarization measurements in the XUV range remain highly challenging due to the lack of phase-matched nonlinear media, commonly used in ultrafast laser diagnostics, and the absence of dedicated ultrafast detectors with adequate reliability and temporal resolution.

To address these limitations, a phased strategy has been adopted, implementing diagnostic techniques with progressively increasing precision and complexity. The initial stage employs simpler, well-established devices with limited temporal resolution or intercepting operation, followed by the integration of advanced, non-intercepting, single-shot techniques that are currently under development or require careful customization for the specific pulse parameters.

The first diagnostic tool to be implemented is a fast silicon photodiode, providing temporal resolution in the tens-of-picoseconds range. Although interceptive, the photodiode is mounted beneath the mirror/YAG support within the diagnostic flags and can be inserted into the beam path only when required. Its main functions include pulse energy calibration and coarse timing measurements, such as pre-alignment of external devices (e.g., laser delay lines) and verification of trigger synchronization with slower instrumentation. Additional information on pulse duration and arrival time can be indirectly derived from electron beam diagnostics. In particular, data obtained from transverse deflecting cavities (Sec. 11.2.8) and electro-optic sampling (Sec. 11.2.9) systems, providing the longitudinal profile of the lasing electron bunch, can be combined with beam dynamics models to estimate the corresponding FEL photon pulse characteristics.

Polarization measurements of linearly polarized FEL pulses at arbitrary angles can be performed using single-shot, intercepting polarimeters based on Brewster-angle reflections. Such systems, developed and commercialized at FERMI@ELETTRA [34, 35], provide reliable, real-time characterization of polarization. The polarimeter requires a minimum of 10^7 photons per shot and achieves a polarization sensitivity of approximately 1°. It will be installed inside the experimental chamber for offline characterization of the FEL pulse prior to user experiments and subsequently removed during data acquisition.

In a later development phase, not covered by this TDR, a more accurate, single-shot measurement of both the temporal and polarization properties of the FEL pulse will be implemented. To

properly allocate the necessary space and infrastructure, two complementary approaches are being considered for successive installation.

The first approach relies on the transient reflectivity of a thin film to provide shot-to-shot timing information [36]. Although this method offers excellent temporal resolution, it requires a significant fraction of the available photon flux. The diagnostic will be installed downstream of the user target, behind the experimental chamber (Sec. 10.2, red box in Fig. 10.1), exploiting the non-diffracted portion of the beam, which remains too intense for diffraction-based user detectors.

In parallel, a second strategy will be implemented based on radial TOF measurements of gas ionization products, enabling the determination of pulse polarization. By analyzing the asymmetry and yield of ion signals detected along different axes of a TOF spectrometer, it is possible to accurately infer the degree and orientation of linear or circular polarization. Differential pumping stages are included before and after the apparatus to preserve ultra-high vacuum conditions along the beamline. Adequate space has been reserved for this system (purple box in Fig. 9.4), consistent with similar setups at other FEL facilities.

For time-resolved characterization, THz streaking techniques offer a direct and absolute measurement of FEL pulse temporal profiles by monitoring photoelectron emission dynamics in the presence of a synchronized THz electric field [37, 38]. The resulting momentum modulation encodes the temporal envelope of the XUV pulse and allows sub-femtosecond, single-shot determination of both its temporal shape and arrival time relative to the THz field phase. To further enhance analysis speed and robustness, artificial intelligence methods, particularly convolutional neural networks, have been successfully applied to process and reconstruct streaking data [39].

9.4.6 Wavefront Sensor

The Hartmann Wavefront Sensor (HWFS) is an optical diagnostic tool used to measure wavefront distortions in light beams. Originally developed for adaptive optics in astronomy, it has since found widespread application in high-precision laser diagnostics, FEL, and synchrotron radiation facilities.

In the XUV range, the HWFS setup consists of an array of pinholes positioned in front of a CCD or CMOS detector [40]. Each pinhole samples a small portion of the incoming wavefront, projecting a spot onto the detector. The resulting grid of spots (Fig. 9.16) encodes the local slopes of the wavefront: deviations of the measured spot positions from those of an ideal planar wavefront indicate wavefront distortions. Assuming the wavefront is locally flat over each pinhole aperture, the full wavefront can be reconstructed from these local gradient measurements.

Compared to the Shack–Hartmann approach, which employs a microlens array (in the XUV range typically realized using Bragg–Fresnel zone plates), the Hartmann sensor offers a key advantage: achromatic response. This makes it particularly suitable for FEL beamlines, where the photon energy can be tuned over a wide range.

The reference centroids are obtained from a well-characterized beam at a wavelength selected within the calibration range. For a perfect wavefront (WF), the distance between adjacent spots is directly related to the local curvature of the WF. However, producing an ideal planar wavefront in the XUV and X-ray domains is extremely challenging. Therefore, during calibration, a spherical wavefront is preferred. A common approach to generate a well-defined spherical WF is to place a small circular aperture in the beam path, which diffracts a known spherical wave [41].

Calibration of the Hartmann WF sensor at a specific wavelength ensures accurate measurements across a broad wavelength range, and the sensor can maintain its calibration stability for many years [40].

When applied to photon beams in synchrotron radiation facilities or high-intensity laser setups, the HWFS delivers essential real-time information about the beam's phase distortions, intensity distribution, and optical aberrations. By analyzing deviations in the measured WF, the system can

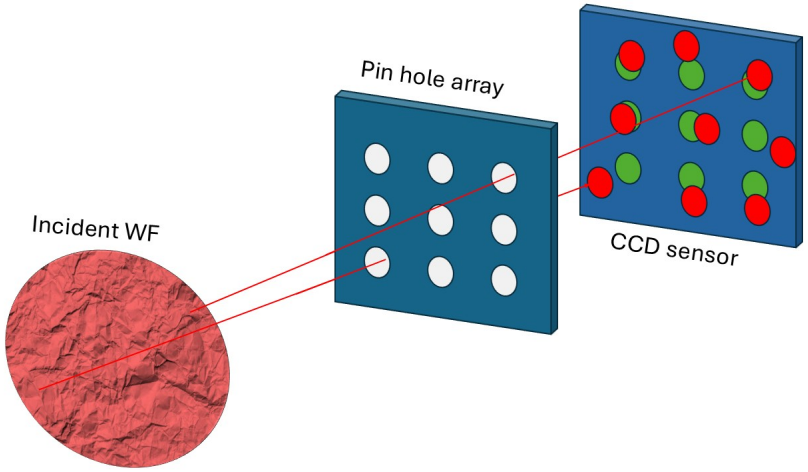

Figure 9.16: Schematic of the HWFS. Green dots on the detector plane correspond to the reference spot positions for a planar wavefront, while red dots indicate the displaced positions for an aberrated wavefront.

evaluate beam quality and identify optical imperfections caused by beamline components, thermal effects, or misalignments. Additionally, the HWFS enables non-destructive reconstruction of the FEL pulse focal spot parameters [42].

A major advantage of the HWFS is its compatibility with active feedback systems for real-time beam correction [43]. Wavefront data from the sensor is fed into a control loop that adjusts deformable mirrors at the final focus, optimizing transverse beam quality and focus. Commercial HWFS units—such as those from Imagine Optics—are available with wavefront resolution better than $\lambda/10$ rms [40]. The HWFS is planned for installation downstream of the experimental chamber (cylindrical yellow area in Fig. 10.1).

9.4.7 Coherence

A SASE FEL can amplify multiple transverse modes simultaneously. The same electron-bunch instabilities that limit spatial coherence also lead to partial temporal coherence, since the FEL photon pulse is not composed of a single longitudinal mode but of multiple temporal spikes, each with a duration on the order of the coherence time. These longitudinal modes can exhibit mutual correlations and interference, thereby influencing the overall temporal coherence of the pulse. Characterization of both the longitudinal and transverse coherence of the FEL radiation is therefore very useful [44], particularly for experiments sensitive to coherence effects, such as coherent diffraction imaging.

9.4.7.1 Temporal Coherence Characterization

To characterize the longitudinal coherence, a split-and-delay interferometer based on grazing-incidence optics will be employed (see Fig. 9.17, left) [45], in conjunction with mode retrieval from the grating spectrometer. From the cooperation lengths (L_c) reported in Table 3.12 and 3.21, we expect to have a coherence length of $\approx$1 fs in both PWFA and Full RF cases.

The FEL pulse is split using a Ni-coated beamsplitter system, spatially aligned with sub-micron accuracy, and temporally recombined with variable delay up to 200 fs. Interferograms are recorded on an XUV CCD detector installed in the user experimental chamber, allowing for the retrieval of the autocorrelation function. The analysis enables the evaluation of the number of longitudinal modes M via fringe contrast detection.

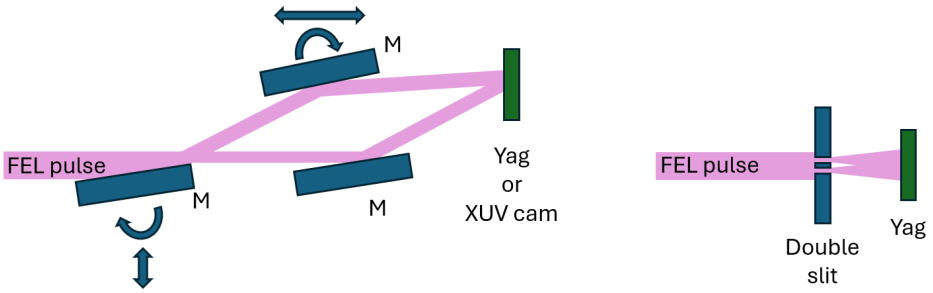

Figure 9.17: Schematic of the two different coherence measurement setups. The FEL pulse is split using a Ni-coated mirror pair for temporal coherence measurement (left), and directed through a variable double-slit apparatus for spatial coherence assessment (right). The recombined or diffracted beams are recorded on XUV-sensitive detectors downstream.

The diagnostic setup will consist of motorized optics with steps shorter than the coherence length, i.e. sub-micrometric step resolution. This diagnostic setup will be implemented for the preliminary phase related to the pulse spectro-temporal characterization, and it will be removed before the installation of the user equipment.

In a later development, beyond the scope of this TDR, the setup will be upgraded to a full TG-FROG, similar to [46], with the addition of a external laser pump and a nonlinear target such as Si_3N_4. This configuration will allow the measurement of both phase and intensity of the FEL electric field, and thus the reconstruction of the spectral phase via FFT.

In parallel, the temporal coherence of the FEL pulse will also be inferred from the spectral intensity measured by the grating spectrometer (Sec. 9.4.4). From a statistical analysis of the spectral intensity, the pulse coherence length can be estimated, as each spike in the SASE spectrum corresponds to a temporal duration of about $2\pi L_c$ [47]. For short pulses, such as those obtained in the PWFA case, the method provides limited resolution because the bunch length approaches the duration of a single spike, resulting in a quasi-single-spike spectral profile.

9.4.7.2 Spatial Coherence Characterization

Spatial coherence is assessed using Young's double-slit interferometry (see Fig. 9.17, right) [48, 49]. Slits with separations of 0.03–1 mm are patterned via electron beam lithography on 50 nm Si_3N_4 membranes coated with 20 nm of Au, and mounted on nanopositioning stages in the YAG station after the Split and Delay Line system area (in orange in Fig. 9.4).

Measurements are taken $\sim$ 5.5 m downstream of the slits on the next Ce:YAG station (before the K-B mirrors). Fringe contrast as a function of slit separation yields the transverse coherence length.

9.5 Operation

This section outlines the standard procedures and configurations for operating the beamline. It includes details on alignment protocols, typical user operation workflows and safety recommendations. Emphasis is placed on reproducibility, uptime optimization, and the integration of control systems to ensure consistent performance throughout experimental runs.

9.5.1 Alignment Protocols

Beamline alignment is a multi-stage process designed to ensure precise beam transport from the source to the experimental end-stations. The procedure includes both coarse and fine alignment

steps and is typically performed after major maintenance, energy changes, or significant shifts in experimental configuration.

Coarse alignment is performed using a continuous-wave alignment laser that is co-aligned with the FEL source via a retractable alignment assembly integrated with the vacuum vessels for the scintillating screens. The alignment laser propagates through the beamline under atmospheric pressure or vacuum, providing a visible reference for the positioning of optical components. Motorized actuators bring mirrors, slits, gratings, and apertures to nominal positions based on previously recorded fiducials or optical encoders.

Fine alignment begins once the beamline is under operational vacuum and low-energy FEL pulses are available. Scintillators or retractable targets located at key positions (e.g., after major mirrors or focusing optics) are used to observe beam position and size. Alignment is refined iteratively by adjusting mirror pitch, yaw, and translation stages to center the beam and maintain consistent beam quality throughout transport.

For focusing optics (e.g., the K-B mirrors), the focal position is optimized using in-situ targets and diagnostic tools located at the sample plane (cameras and wavefront detectors). Beam pointing is monitored continuously during the alignment process and recorded to ensure reproducibility in future sessions.

Active feedback systems may be employed during alignment to maintain beam stability in the presence of thermal drift or mechanical vibration. Alignment routines can be partially automated via predefined scripts integrated into the beamline control system, reducing setup time between experiments.

9.5.2 User Operation Workflows

User operation is structured to balance experimental flexibility with operational stability. Standard workflows are designed to support both short-term access and extended experimental campaigns, with dedicated support from beamline scientists throughout.

In preparation for user access, beamline parameters such as photon energy, polarization (if applicable), focal spot size, and pulse duration will be configured according to the experimental plan submitted during proposal review. In order to maximize the efficiency of beamtime, experiments requiring similar parameters and setups will be scheduled in the same block. Sample environments - such as vacuum chambers, sample holders, manipulators, and environmental controls - are installed and tested in coordination with the user team.

Users interact with the beamline through a dedicated control interface, based on EPICS, allowing intuitive access to beamline functions. The interface provides control of motorized stages, sample positioning systems, beamline shutters, and alignment optics, along with real-time visualization of beam parameters and sample interaction. More details on the control system are described in its dedicated Chapter 15.

Experiments are conducted in scheduled shifts, with users collecting data according to predefined acquisition protocols. Beamline staff will be working together with the users during shifts to assist with troubleshooting, parameter adjustments, or realignment as needed.

Data acquired during operation are automatically archived in a centralized storage system, with metadata tags for experimental parameters and timestamps. Users have remote or on-site access to data processing pipelines for preliminary analysis. More details on data acquisition and management are described in the end-station Chapter 10.

Each shift concludes with logging of system status, any changes to beamline configuration, and experimental progress. Deviations from nominal performance, unexpected interruptions, or user feedback are documented to facilitate continuous improvement.

After the experiment, the beamline is returned to a baseline state, and alignment is verified. A debrief with users may be conducted to review data quality, provide support for further analysis,

and gather feedback for future beamtime optimization.

9.5.3 Safety

The operation of the beamline adheres to strict safety protocols to protect personnel, equipment, and the facility. Safety measures are integrated into all phases of beamline use, including alignment, experimental operation, and maintenance.

A safety beam stopper will be installed in the undulator hall, upstream of the gas absorber. This shutter can block gas bremsstrahlung radiation during maintenance operations in the subsequent safety hutch, allowing the accelerator to remain operational and reducing downtime associated with warming-up procedures. Its main component is a tungsten rod; FLUKA [50–52] simulations confirm that a total length of 10 cm and a diameter of 5 cm provide sufficient attenuation to ensure safe access to the hutch. This shutter is intended exclusively for blocking bremsstrahlung radiation. Accelerated electrons are always directed to the dedicated dump, or, in the event of faults, a machine shutdown is triggered and managed by the personnel safety systems. Furthermore, the FEL radiation is still too intense at this location, and ablation of the tungsten surface is expected if directly intercepted. For this reason, the undulator gaps will be opened before shutter insertion, thereby suppressing FEL emission. In the event of a malfunction in the undulators' control, the vacuum system will generate an interlock signal due to pressure variations caused by material ablation, shutting down the electron beam.

A fast photon beam shutter will be installed upstream of the last GMD, where the FEL intensity is lower, allowing machine feedback to operate while blocking radiation from reaching the user experimental chamber. The shutter is composed of a 10-mm-thick aluminum plate, 150 mm by 60 mm, set at a grazing angle of 20° to reduce the surface intensity to approximately 3.9 $\mu J/mm^2$ (corresponding to an energy deposition of 0.01 eV/atom) in the most intense case considered, while covering the entire beam pipe diameter. The plate is equipped with a motorized side-rotation mechanism that enables fast motion between a fully open configuration, parallel to the beam propagation, and the grazing-incidence position used to stop the FEL pulse.

Access to the beamline is controlled via an interlock system that enforces safe conditions before FEL radiation can be generated or transmitted. This includes verification of vacuum integrity, correct positioning of shutters and beam stop, and the absence of personnel in restricted areas. Beamline doors and experimental hutch enclosures are fitted with fail-safe sensors that immediately disable beam delivery if a breach is detected. Radiation shielding is designed according to regulatory standards and facility-specific hazard assessments, accounting for both prompt electron bunches (electron, FEL or otherwise) and secondary emissions other elements (i.e. gas bremsstrahlung, diffused radiation from electron beam dump, induced activity from materials). The FEL user hall, excluding the safety hutch, is designed, as radioprotection classification, to be "supervised" during electron acceleration, and of "free access" otherwise.

Class 3 or 4 lasers (e.g. for pump-probe experiments or for diagnostics) will propagate in the hall in a enclosed beam distribution, with interlocked apertures for installation and maintenance and clear, visible signs of the status in the hall and before the hall accesses.

All users and staff are required to complete mandatory safety training, which includes instruction on laser safety, vacuum and pressure systems, electrical hazards, and radiation protection. Operational procedures and emergency protocols are documented and available on-site, and safety drills are conducted regularly in collaboration with facility safety officers.

During beamline operation, status indicators, warning lights, and audible alerts provide continuous feedback on the machine and beamline states. Any deviation from nominal operating conditions automatically triggers a controlled shutdown, with logs recorded for subsequent analysis.

Personal protective equipment, such as laser safety eyewear or grounding devices, must be used in designated areas and situations as specified in the beamline's safety documentation. Visitors are

only permitted in operational areas under direct supervision and after completing the appropriate orientation.

Ongoing risk assessments and safety reviews are conducted to adapt procedures to evolving experimental requirements and to incorporate lessons learned from operational experience.

More details on the safety systems are described in the Safety Chapter 19.

9.6 Conclusions

The AQUA photon beamline has been designed, validated, and finalized to meet the operational requirements of both PWFA and Full RF configurations. The layout ensures reliable FEL pulse transport and conditioning from the undulator to the experimental end-station, while reserving space for future installations, such as monochromator and advanced temporal and polarization diagnostics. The overall design is fully compatible with integration and operation, with no critical technical blockers. A few subsystems, such as specific vacuum management, are still under development; in these cases, references to analogous components successfully operating in other facilities have been adopted, and similar solutions are implemented.

The beamline delivers well-characterized photon pulses to users, with parameters precisely monitored and reproducible along the line. Key photon characteristics at the experimental station include pulse energies on the order of 10^{10} photons per shot (accounting for the overall transmission of $\lesssim 40\%$, with attenuation up to 10^6 available if needed), transverse RMS beam sizes ranging from $\sim$1 µm to 1.3 mm depending on the operating regime, spectral coverage from 2 nm to 15 nm (designed for transporting the 3.2 - 5.2 nm range detailed in this TDR and ready for future upgrades) with shot-to-shot spectral resolution of 11 - 0.5 meV, and pointing reproducibility at the $\sim$10 µrad level. Grazing-incidence mirrors, reflective coatings, and diagnostic insertion points are optimized to preserve these parameters with minimal losses and wavefront distortion.

User-accessible diagnostics provide comprehensive, single-shot-resolved information. Key detectors include gas monitor detectors, which deliver absolute pulse energy and beam position; grating spectrometers, which retrieve spectral profiles; and scintillating screens and Hartmann wavefront sensors, which map transverse intensity and aberrations. The layered instrumentation described in this chapter enables full characterization of energy, spectrum, spatial mode, wavefront quality, coherence and pointing stability, supporting both routine operation and advanced physics experiments from the outset, while leaving space for future upgrades in temporal, polarization, and coherence diagnostics.

Bibliography

[1] R. Bonifacio, C. Pellegrini, and L. M. Narducci. "Collective instabilities and high-gain regime in a free electron laser". In: *Opt. Commun.* 50 (1984), p. 373.

[2] M. S. del Rio and L. Rebuffi. "OASYS: A software for beamline simulations and synchrotron virtual experiments". In: *AIP Conference Proceedings*. Vol. 2054. 1. AIP Publishing LLC. 2019, p. 060081.

[3] M. Zangrando et al. "The photon analysis, delivery, and reduction system at the FERMI@ Elettra free electron laser user facility". In: *Review of Scientific Instruments* 80.11 (2009), p. 113110.

[4] U. Hahn and K. Tiedtke. "The gas attenuator of FLASH at DESY". In: *AIP Conference Proceedings*. Vol. 879. 1. American Institute of Physics. 2007, pp. 276–282.

[5] L. Rumiz et al. "The gas attenuator vacuum system of FERMI@ Elettra". In: *2nd International Particle Accelerator Conference (IPAC)*. JACoW. 2011, p. 1530.

[6] C. Pradervand et al. "A compact gas attenuator for the SwissFEL ATHOS beamline realized using additive manufacturing". In: *Synchrotron Radiation* 30.4 (2023), pp. 717–722.

[7] K. J. Kapcia et al. "Ultrafast demagnetization in bulk nickel induced by X-ray photons tuned to Ni M 3 and L 3 absorption edges". In: *Scientific reports* 14.1 (2024), p. 473.

[8] M. Tavakkoly et al. "Simulations about stability, damage, and heating impacts for an x-ray optical delay line at sase3". In: *Journal of Physics: Conference Series*. Vol. 2380. 1. IOP Publishing. 2022, p. 012066.

[9] ZEISS SMT. *Zeiss specification for high quality mirror, with realization examples*. URL: https://www.zeiss.com/semiconductor-manufacturing-technology/products/semiconductor-manufacturing-optics/synchrotron-optics.html (visited on 10/21/2025).

[10] H. Moreno Fernández et al. "Towards chemically neutral carbon cleaning processes: plasma cleaning of Ni, Rh and Al reflective optical coatings and thin Al filters for free-electron lasers and synchrotron beamline applications". In: *Synchrotron Radiation* 25.6 (2018), pp. 1642–1649.

[11] H. Moreno Fernández et al. "Characterization of carbon-contaminated B4C-coated optics after chemically selective cleaning with low-pressure RF plasma". In: *Scientific reports* 8.1 (2018), p. 1293.

[12] P. Kirkpatrick and A. V. Baez. "Formation of optical images by X-rays". In: *Journal of the optical society of America* 38.9 (1948), pp. 766–774.

[13] L. Raimondi et al. "Microfocusing of the FERMI@ Elettra FEL beam with a K–B active optics system: Spot size predictions by application of the WISE code". In: *Nuclear Instruments and Methods in Physics Research Section A: Accelerators, Spectrometers, Detectors and Associated Equipment* 710 (2013), pp. 131–138.

[14] ELETTRA. *KAOS K-B focusing system*. URL: https://www.elettra.eu/images/Documents/ILO/Componenti%20di%20Acceleratori/03_Elettra_KAOS%20Refocusing%20Mirror%20System.pdf (visited on 05/09/2025).

[15] F. Frassetto et al. "Double-grating monochromator for ultrafast Free-Electron-Laser beamlines". In: *FEL conference, Basilea (CH)*. 2014.

[16] A. Simoncig et al. "AC/DC: The FERMI FEL Split and Delay Optical Device for Ultrafast X-ray Science". In: *Photonics*. Vol. 9. 5. MDPI. 2022, p. 314.

[17] W. K. Peters et al. “Hard x-ray–optical four-wave mixing using a split-and-delay line”. In: *Optics Express* 31.19 (2023), pp. 31410–31418.

[18] F. Bencivenga et al. “Short-wavelength four wave mixing experiments using single and two-color schemes at FERMI”. In: *Journal of Electron Spectroscopy and Related Phenomena* 257 (2022), p. 146901.

[19] S. Usenko et al. “Split-And-Delay Unit for FEL Interferometry in the XUV Spectral Range”. In: *Applied Sciences* 7.6 (2017). ISSN: 2076-3417.

[20] M. Richter et al. “Measurement of gigawatt radiation pulses from a vacuum and extreme ultraviolet free-electron laser”. In: *Applied physics letters* 83.14 (2003), pp. 2970–2972.

[21] J. Grünert et al. “X-ray photon diagnostics at the European XFEL”. In: *Journal of Synchrotron Radiation* 26.5 (2019), pp. 1422–1431.

[22] A. A. Sorokin et al. “An X-ray gas monitor for free-electron lasers”. In: *Journal of synchrotron radiation* 26.4 (2019), pp. 1092–1100.

[23] K. Tiedtke et al. “Gas detectors for x-ray lasers”. In: *Journal of Applied Physics* 103.9 (2008).

[24] J. A. R. Samson and W. C. Stolte. “Precision measurements of the total photoionization cross-sections of He, Ne, Ar, Kr, and Xe”. In: *Journal of electron spectroscopy and related phenomena* 123.2-3 (2002), pp. 265–276.

[25] K. Tiedtke et al. “The soft x-ray free-electron laser FLASH at DESY: beamlines, diagnostics and end-stations”. In: *New journal of physics* 11.2 (2009), p. 023029.

[26] M. Zangrando et al. “Recent results of PADReS, the Photon Analysis Delivery and REduction System, from the FERMI FEL commissioning and user operations”. In: *Synchrotron Radiation* 22.3 (2015), pp. 565–570.

[27] C. J. Milne et al. “SwissFEL: the Swiss X-ray free electron laser”. In: *Applied Sciences* 7.7 (2017), p. 720.

[28] T. Burian et al. “Soft x-ray free-electron laser induced damage to inorganic scintillators”. In: *Opt. Mater. Express* 5.2 (2015), pp. 254–264.

[29] A. Koch and J. Grünert. “Radiation hardness of luminescent screens under FEL radiation”. In: *Optics Damage and Materials Processing by EUV/X-ray Radiation (XDam8)*. Vol. 12578. SPIE. 2023, p. 1257803.

[30] CAEN ELS s.r.l. *AH401D 4-channel Charge Integration Picoammeter*. URL: `https://www.caenels.com/product/ah401d/` (visited on 11/24/2025).

[31] C. Svetina et al. “PRESTO, the on-line photon energy spectrometer at FERMI: design, features and commissioning results”. In: *Journal of Synchrotron Radiation* 23.1 (2016), pp. 35–42.

[32] W. B. Peatman. *Gratings, mirrors and slits: beamline design for soft X-ray synchrotron radiation sources*. Routledge, 2018.

[33] P. Baumgärtel et al. “RAY-UI: new features and extensions”. In: *AIP Conference Proceedings*. Vol. 2054. 1. AIP Publishing. 2019.

[34] ELETTRA. *Tonix polarimetry systems*. URL: `https://www.elettra.eu/images/Documents/ILO/Strumenti%20Scientifici/21_Elettra_Tonix.pdf` (visited on 04/30/2025).

[35] A. Caretta et al. “A novel free-electron laser single-pulse Wollaston polarimeter for magneto-dynamical studies”. In: *Structural Dynamics* 8.3 (2021).

[36] M. B. Danailov et al. “Towards jitter-free pump-probe measurements at seeded free electron laser facilities”. In: *Optics express* 22.11 (2014), pp. 12869–12879.

[37] I. Grguraš et al. “Ultrafast X-ray pulse characterization at free-electron lasers”. In: *Nature Photonics* 6.12 (2012), p. 852.

[38] N. Hartmann et al. “Attosecond time–energy structure of X-ray free-electron laser pulses”. In: *Nature Photonics* 12.4 (2018), pp. 215–220.

[39] K. Dingel et al. “Artificial intelligence for online characterization of ultrashort x-ray free-electron laser pulses”. In: *Scientific reports* 12.1 (2022), p. 17809.

[40] O. de La Rochefoucauld et al. “EUV and Hard X-ray Hartmann Wavefront Sensing for Optical Metrology, Alignment and Phase Imaging”. In: *Sensors* 21.3 (2021). ISSN: 1424-8220.

[41] K. A. Goldberg. *Extreme ultraviolet interferometry*. University of California, Berkeley, 1997.

[42] C. Svetina et al. “The Low Density Matter (LDM) beamline at FERMI: optical layout and first commissioning”. In: *Journal of synchrotron radiation* 22.3 (2015), pp. 538–543.

[43] P. Mercère et al. “Automatic alignment of a Kirkpatrick-Baez active optic by use of a soft-x-ray Hartmann wavefront sensor”. In: *Optics letters* 31.2 (2006), pp. 199–201.

[44] A. Singer et al. “Spatial and temporal coherence properties of single free-electron laser pulses”. In: *Opt. Express* 20.16 (2012), pp. 17480–17495.

[45] V. Hilbert et al. “Spatio-temporal coherence of free-electron laser radiation in the extreme ultraviolet determined by a Michelson interferometer”. In: *Applied physics letters* 105.10 (2014), p. 101102.

[46] F. Elverson et al. “Single-shot measurements of shaped XUV FEL pulses with frequency-resolved optical gating”. In: *Opt. Express* 33.9 (2025), pp. 19936–19950. DOI: 10.1364/OE.549398.

[47] R. Bonifacio et al. “Spectrum, temporal structure, and fluctuations in a high-gain free-electron laser starting from noise”. In: *Phys. Rev. Lett.* 73 (1 1994), pp. 70–73. DOI: 10.1103/PhysRevLett.73.70.

[48] R. Ischebeck et al. “Study of the transverse coherence at the TTF free electron laser”. In: *Nuclear Instruments and Methods in Physics Research Section A: Accelerators, Spectrometers, Detectors and Associated Equipment* 507.1-2 (2003), pp. 175–180.

[49] A. Singer et al. “Transverse-coherence properties of the free-electron-laser FLASH at DESY”. In: *Physical Review Letters* 101.25 (2008), p. 254801.

[50] A. Ferrari et al. *FLUKA: A Multi-particle Transport Code (Program Version 2005)*. Tech. rep. CERN-2005-10. CERN, 2005.

[51] T. T. Böhlen et al. “The FLUKA code: Developments and challenges for high energy and medical applications”. In: *Nuclear Data Sheets* 120 (2014), pp. 211–214.

[52] F. Ballarini et al. “The FLUKA code: Overview and new developments”. In: *EPJ Nuclear Sci. Technol.* 10 (2024), p. 16.

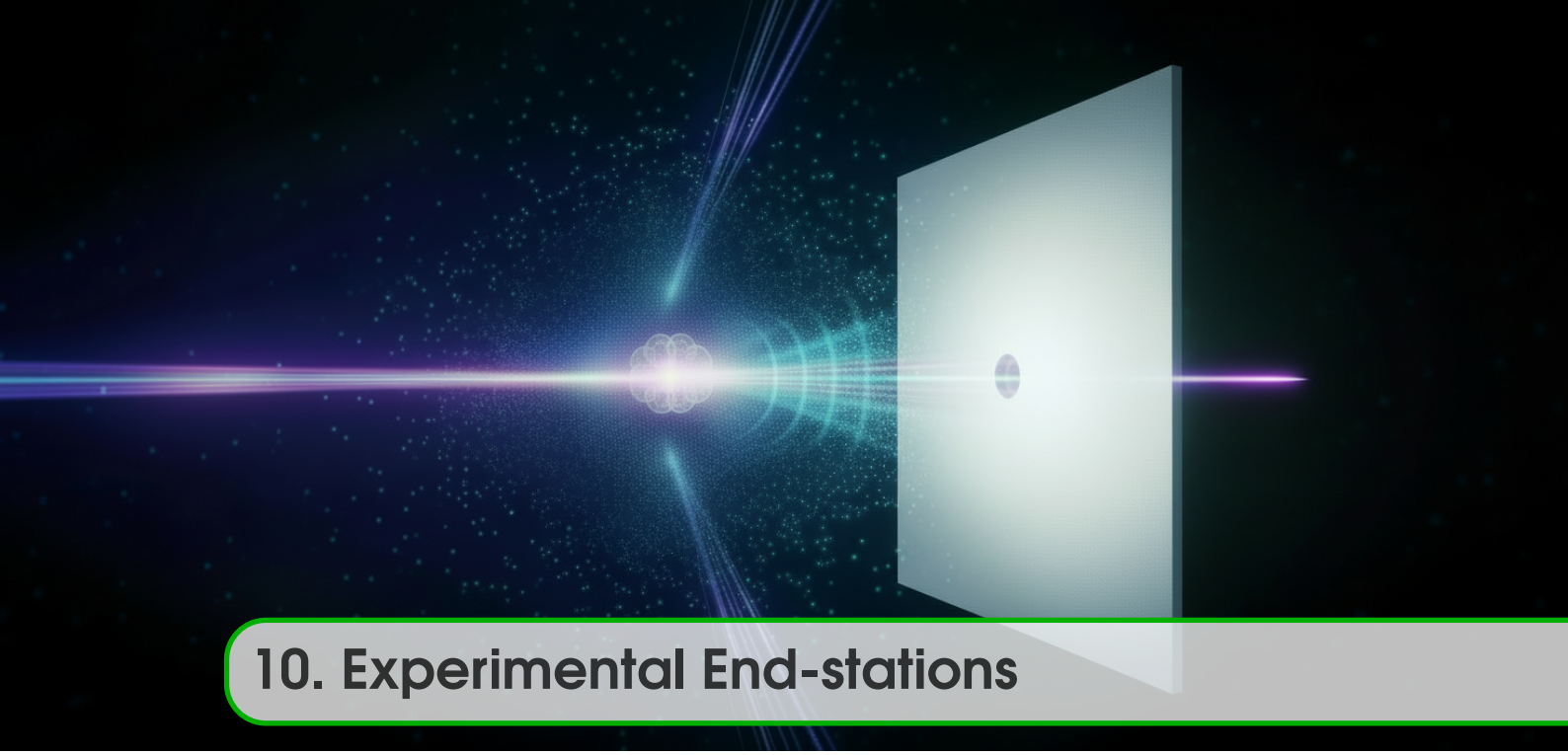

10. Experimental End-stations

10.1 The AQUA endstation

This chapter describes the experimental endstation to be installed to perform experiments at the EuPRAXIA XUV SASE FEL, which supplies the AQUA beamline. Named after the Latin word for “water”, AQUA operates in the XUV region (Fig. 8.4), with the design wavelength around 4 nm, further extending in the range 3.2–10 nm (although a detailed analysis of the FEL performance in this extended range is out of the scope of this TDR).

A beamline with the AQUA photon beam features can support a wide range of techniques, including imaging, X-ray absorption and scattering, and ion and electron spectroscopy. However, given the peculiar feature of the EuPRAXIA@SPARC_LAB infrastructure, which is focused on the development of novel, plasma-based acceleration schemes, it is important to define an implementation roadmap that foresees a phased implementation. The facility photon science program will indeed start with the less demanding experimental techniques, and then progressively expand into more complex regimes as the accelerator performance is consolidated. This staged evolution ensures that early scientific results will directly feed back into accelerator development while progressively enabling a broader range of photon-science applications.

- **Endstation Phase 0 (*P0*):** Initial Commissioning. Fixed-target experiments dedicated to photon beam characterization, calibration of diagnostics, and detector alignment, providing the baseline for subsequent user operation.
- **Endstation Phase 1 (*P1*):** First user-oriented experiments in the gas-phase, employing injectors to study atomic and molecular dynamics under ultrafast X-ray excitation.
- **Endstation Phase 2 (*P2*):** Expansion to condensed-phase systems, with liquid-jets and aerosol injectors integrated in a second version of the experimental chamber, enabling studies of complex soft- and bio-matter under realistic conditions.

As the facility evolves, user-driven contributions will enable more advanced and focused applications.

10.2 Instrumentation

The schematic layout of the chamber represented in Fig. 10.1 shows the setups in the different phases of operation. Panel a illustrates the *P0* setup for CDI experiments, where a fixed sample—mounted on a motorized stage for precise positioning —is illuminated by the FEL beam. Scattered photons are collected by a pixel array detector. Panels b and c represent possible configurations of the experimental chamber for *P1* and *P2*. In panel b, the pixel array detector is replaced by a photodiode used for correlation X-ray spectroscopy measurements. Panel c shows a configuration allowing ion and electron spectroscopy. The chamber hosts a magnetic bottle electron spectrometer (in blue) and a velocity map imaging (VMI) spectrometer (in orange). Beam diagnostic tools, shown in red, are used to monitor the beam position and intensity. Starting from *P1*, a pump–probe configuration is enabled by coupling an optical laser from the side of the chamber. Using a system of mirrors, the laser can be aligned to propagate parallel to the X-ray beam, allowing precise temporal and spatial overlap at the sample interaction point. From this phase onward, a second vacuum chamber, hosting gas and liquid sample injection systems—such as aerosol or liquid-jet nozzles (depicted in the figure as a white cone)— will be made available, thus broadening the range of sample delivery modes without contaminating the first chamber. It is worth noting that these configurations represent only a subset of the possible experimental setups. The chamber has been designed with modularity and flexibility in mind, allowing for customized layouts within defined spatial and mechanical constraints. Components not foreseen within the present TDR phases (such as the optional monochromator) are planned as future upgrades, with dedicated space and flanges already reserved for their integration.

10.2.1 Experimental chambers

The AQUA experimental chambers are designed to support a broad range of experiments, including imaging as well as photon, electron, and—at a later stage—ion spectroscopy. To accommodate these diverse applications, the chamber will adopt a highly flexible and modular design, following the approach of multi-purpose instruments developed at several FEL facilities, such as CAMP at FLASH [1], DiProI [2] and LDM [3] at FERMI, among others. Two versions of the chamber will be built, one dedicated to solid targets and gas-phase experiments, the other to liquid samples.
Both will consist of a stainless steel box with approximate dimensions of $100 \times 60 \times 60$ cm^3. It will be possible to replace the rear panel of each chamber with an expansion module to allow positioning further downstream the X-ray detectors, if required by a particular experiment. One of the side panels will have a large aluminum flange to allow an easy access to the sample region. The chamber will feature a dozen of viewports and will include flanges for beam apertures, a flange for an aerosol particle delivery system and a flange to host devices such as evaporators, mass spectrometers, or a soft X-ray spectrometer to allow X-ray spectroscopy measurements. Where possible, the distances from the flanges to the interaction point and the flange sizes will be homogenized with those of established endstations such as LDM at FERMI or CAMP at FLASH, facilitating the re-use and interchangeability of detectors and sample delivery systems across facilities.
The sample will be mounted on a high-precision, motorized multi-axis manipulation stage (XYZ plus rotation), allowing micrometer-level positioning and angular alignment of fixed-targets, injectors, and diagnostic tools with respect to the FEL focus. The manipulator will support remote operation and integration with the beamline control system to ensure reproducible positioning during alignment and data collection. On one viewport, a high-magnification telemicroscope for monitoring the sample surface in a region of a few hundreds μm, will be installed. Illumination of the sample will be provided by vacuum compatible LED lights.
The chamber will be mounted on a rigid mechanical support frame equipped with vibration-damping elements, following the layout adopted at similar endstations such as CAMP at FLASH and LDM at FERMI, to ensure mechanical stability and precise alignment with the beamline optics. The

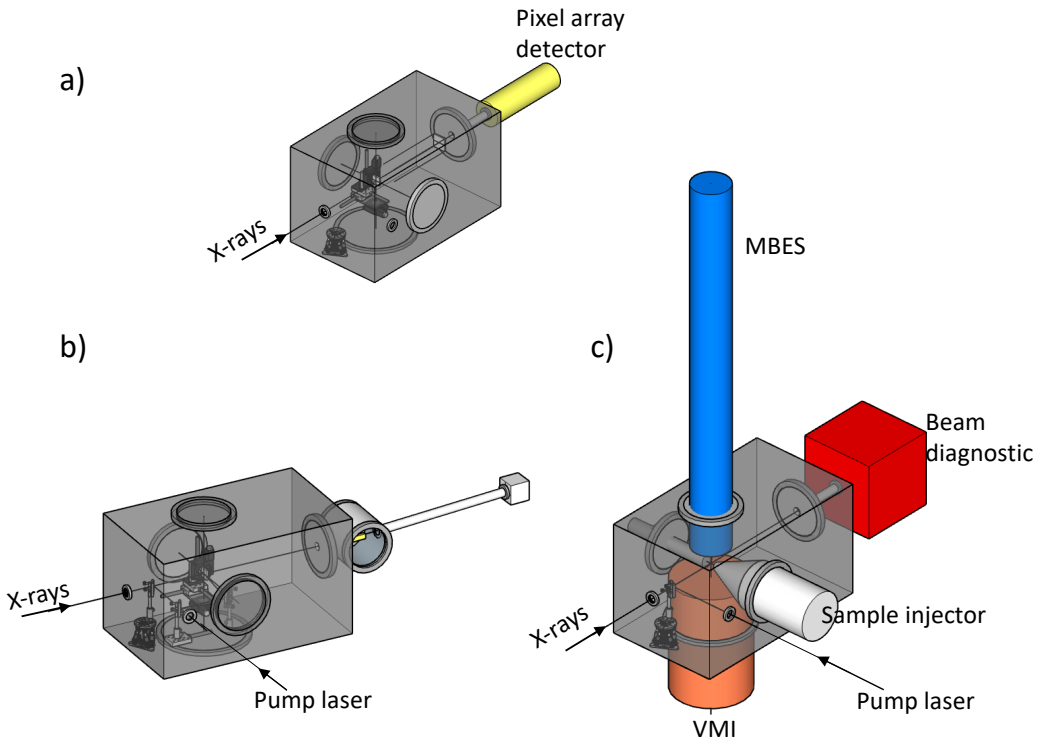

Figure 10.1: Schematic representation of planned configurations for the experimental chambers during *P0–2*. Panel (a) illustrates the *P0* setup for CDI experiments, featuring the pixel-array detector positioned downstream of the sample. Panels (b) and (c) depict possible configurations for *P1* and *P2*, corresponding to XAS and ion/electron spectroscopy, respectively. In panel (b), soft X-ray absorption signals are measured with a photodiode placed downstream of the sample, used together with an upstream spectral measurement for correlation spectroscopy. Panel (c) shows an arrangement combining a sample injector, velocity-map imaging (VMI) spectrometer, and beam-diagnostic module (i.e. Hartmann sensor).

support frame will include survey fiducials and adjustable mounts to align the chamber with the beamline reference within sub-millimeter tolerances.
Since the AQUA photon wavelength falls into the soft X-ray region, where the air absorption is significant, the experimental chamber will be maintained under HV conditions (down to 10^{-8} mbar). The vacuum system will have two independent pumping systems, each with a turbo-molecular pump backed by a scroll roughing pump. Venting will be performed via a nitrogen line and a manual valve, while setup changes in the sample region will be made possible by a fast-locking flange.
Since the experiments involve a variety of samples, each class being delivered by means of different kinds of injectors, the vacuum systems will have to take into account the specific features and gas loads associated with the different sample delivery methods.
Two versions of the experimental chamber will be made available to users: the first, available from *P0*, is dedicated to solid and gas-phase samples; the second, introduced in *P2*, is designed for volatile targets such as liquid-jets and aerosol injectors.

10.2.1.1 Vacuum requirements

The vacuum requirements for the solid samples are such that the chamber has to be kept as clean as possible, with particular attention to nitrogen and carbon pollution. On the other hand, experiments on volatile samples introduce further challenges, especially for the vacuum system. These samples will increase the pressure in the chamber, so the installation of extra turbo pumps, capable of handling a higher workload for extended periods without overheating, is foreseen. Specific differential pumping setups are required to guarantee an acceptable vacuum level in the chamber and not to contaminate the beamline when injecting liquids and aerosols in the chamber. To prevent contamination of the beamline and protect upstream optical elements, specific differential pumping setups will be implemented at the interface between the chamber and the beamline. This approach is inspired by advanced schemes such as those adopted at the SPB/SFX instrument at the European XFEL, where multi-stage differential pumping with narrow apertures and high-throughput turbo pumps maintains a large pressure gradient between the sample interaction region and the ultra-high vacuum required for sensitive X-ray optics [4]. Similar strategies have been successfully implemented at other FEL instruments, including the CAMP endstation at FLASH BL1 and the PRESTO system at FERMI, demonstrating effective isolation of high-pressure sample regions from clean beamline environments. In the AQUA endstation, at least three differential pumping stages will be integrated to separate the high-pressure sample interaction region from the ultra-high vacuum of the beamline. The first stage will be mounted directly on the chamber extension surrounding the sample, featuring sub-millimeter apertures and a dedicated turbomolecular pump capable of thousands of liters per second. The second stage will be located in the interface section between the chamber and the beamline, also equipped with narrow apertures and a high-speed turbo pump, forming an additional vacuum barrier. The third stage will be positioned along the upstream beamline just before sensitive optical elements, providing final isolation and maintaining clean vacuum conditions. The differential pumping stages are designed to cumulatively reduce the pressure from the 10^{-2}–10^{-1} mbar in the sample region to the 10^{-8}–10^{-9} mbar range required upstream, with each stage contributing a pressure drop of approximately 1–2 orders of magnitude. Dedicated vacuum lines and pumps for volatile (“dirty”) samples will be kept separated from those serving the optics (“clean” vacuum), following best practice at major FEL facilities. This configuration ensures that operation with volatile or high-load samples does not degrade the overall beamline vacuum and allows for flexible adaptation to different experimental requirements.

10.2.1.2 Short focal length optics

To increase the photon density per area on the sample, besides exploiting the KB mirrors installed upstream, the AQUA endstation will allow installing short focal length optics. Since these elements require stable and well-characterized photon beams—with minimal angular jitter, low positional drift, stable intensity profiles, and well-defined wavefront and coherence properties [5–7]—their integration will be planned in a later development stage. It is therefore important to account for them already in the design phase, ensuring that sufficient space, flanges and flexibility are allocated for their future integration.

One option will consist of multilayer-coated off-axis parabolic (OAP) mirrors, optimized for high reflectivity, such as Sc/Cr or B_4C/Cr, capable of achieving sub-micron spot sizes [8] at the AQUA wavelength. An alternative is the use of Fresnel Zone Plates (FZPs) — compact diffractive optics capable of achieving sub-hundreds nm focusing [9, 10]. FZPs are widely used in FEL-based soft X-ray microscopy but require care under high-flux exposure. Both these devices are compatible with the AQUA chamber design.

It should be emphasized that both FZP and OAP focusing optics require exquisite alignment and mechanical stability. Achieving and maintaining sub-micron or sub-100 nm focal spots demands highly precise positioning, vibration isolation, and continuous monitoring of the beam position and intensity on target. Therefore, their implementation will only be pursued once the photon transport system demonstrates the required pointing and stability and will be made available to users after *P2* of the AQUA endstation.

10.2.1.3 External lasers

In order to fully exploit the ultra-short X-ray pulses and enable a broad range of time-resolved measurements, the chamber will be equipped with multiple laser access ports. These vacuum-compatible windows will allow the introduction of femtosecond optical laser pulses, synchronized with the FEL, into the interaction region. This capability is essential for conducting pump–probe experiments, where the sample is first excited or modified by an optical pump pulse and subsequently probed by the X-ray pulse, enabling the study of ultrafast structural and electronic dynamics on femto- to picosecond timescales.

The window geometry and positioning will be optimized to support a wide variety of experimental geometries, including collinear, orthogonal, and grazing incidence pump–probe configurations. A dedicated mirror system inside the chamber will allow flexible redirection and precise alignment of the laser beam relative to the X-ray beam, enabling parallel or angled propagation as required by the specific experiment (Figure 10.1).

Provisions will be made for future upgrades to accommodate different laser wavelengths and beam sizes, ensuring compatibility with anticipated user needs.

A dedicated chapter later in this document will provide a detailed description of the pump laser system and its integration with the AQUA endstation (see Section 12.4).

10.2.2 Sample delivery systems

Ultra-bright, pulsed photon sources such as the EuPRAXIA@SPARC_LAB FEL typically cause significant sample damage upon exposure. To fully exploit the potential of these sources, reliable sample delivery systems capable of replenishing fresh samples for every shot are essential. Key performance criteria for such systems include operational stability, low background levels, efficient sample consumption, and, being the FEL a pulsed source, capability of matching the FEL's repetition rate. In *P0*, positioners to mount solid test sample will be installed. In *P1*, gas-phase sources, such as supersonic nozzles [11], will be added. In *P2*, sample delivery systems focused on aerosols and liquid will be made available in the second, dedicated experimental chamber. Fig. 10.2 shows examples of sample injection systems for liquid and aerosol samples that will be available at

AQUA.

10.2.2.1 Fixed targets

Fixed-target delivery systems are commonly used for solid or semi-solid samples, providing a stable platform for experiments requiring high precision and repeatability. They can accommodate a variety of sample types, from thin films to crystals, enabling precise positioning and rapid exchange of targets in synchrony with the FEL repetition rate.

For experiments at the relatively low repetition rate, such as the 100 Hz of EuPRAXIA@SPARC_-LAB, a motorized fixed-target scanner will be installed to hold solid samples. This approach also permits the collection of multiple data points from a single sample—provided the FEL intensity does not cause irreversible damage upon exposure. One straightforward option is to deposit samples on thin membranes, such as graphene or Si_3N_4 [12], mounted or etched into robust supports like silicon chips. As an advanced alternative, a system to deliver continuously a sample on a moving tape, following the scheme of the CFEL TapeDrive, developed at the Center for Free-electron Laser Science [13], will be installed. Such a device indeed enables continuous sample replenishment on a moving tape, ensuring fresh material for every pulse while maintaining low sample consumption. In addition, it is fully compatible with mix-and-diffuse methods, making it particularly attractive for time-resolved studies of chemical reactions [14].
Although such systems will not constitute the primary operational mode for most AQUA experiments, they will play a crucial role during the commissioning phase and for ongoing diagnostics of beam performance and stability. Fixed targets provide an ideal and reliable platform for characterizing key FEL parameters—such as pulse duration, focal spot size, pointing stability, and fluence—in a controlled and repeatable manner.

In addition, for solid-state and thin-film samples used in reflectivity or grazing-incidence studies, the system will be designed with future rotational capabilities in mind—initially around the incidence angle, and potentially also around the azimuthal axis. This functionality is foreseen for the *P2* upgrade, but the mechanical design of the sample stages will ensure compatibility with such developments.

10.2.2.2 Gas-phase molecular injectors

The AQUA beamline will support the injection of isolated gas-phase molecules and clusters as part of its *P1* implementation, providing a complementary approach to liquid, aerosol, and fixed-target sample delivery methods. This capability enables high-resolution investigations of photoionization, dissociation, ultrafast molecular dynamics, and reaction pathways in a clean, collision-free environment [15, 16].

Gas-phase injection can be realized through several methods, depending on the thermophysical properties of the sample. For volatile compounds, a common approach involves expanding a mixture of the target molecules and a carrier gas (typically He or Ne) through a heated nozzle into vacuum, producing a collimated supersonic beam of cold, isolated molecules with narrow velocity and spatial distributions [17]. This is particularly well suited for FEL-based pump–probe experiments, ion imaging, and photoelectron spectroscopy. Less volatile species may require upstream thermal evaporation, in which an oven sublimates the material into a carrier gas before expansion through the nozzle, allowing stable and reproducible beam conditions with low background. In addition, filament-based cracking sources can be employed to dissociate precursor compounds, producing reactive species such as radicals or metastable intermediates, enabling studies in molecular physics and ultrafast chemistry.

To ensure compatibility with FEL operation in the XUV wavelength range — the injector system will incorporate multi-stage differential pumping to isolate high-pressure regions near the nozzle and maintain ultra-high vacuum in the interaction chamber. Careful confinement of the

gas expansion cone and optimized injection geometry will allow detector placement close to the interaction region while minimizing photon absorption and scattering losses.

Although gas-phase injection will not be the primarily delivery method for biological or soft-matter targets, it represents a crucial extension of AQUA's experimental capabilities. It will support atomic and molecular physics experiments, facilitate benchmarking of FEL performance (pulse duration, coherence, wavelength tuning), and provide a flexible testbed for future upgrades. A modular injector design will be adopted so that the interaction chamber and pumping infrastructure are pre-configured for phased integration and later developments.

10.2.2.3 Liquid jet injectors

Liquid jet injectors are tools designed to deliver samples in a continuous liquid stream at high velocities [18]. These injectors are critical for diffract-and-destroy experiments, allowing each FEL pulse to interact with a fresh sample. The design of these injectors focuses on minimizing sample consumption while ensuring a stable and uninterrupted flow, crucial for high-resolution imaging and spectroscopy studies. The technology enables exploring molecular and atomic structures and dynamics in real time, under natural or near-natural hydration conditions. As pointed out above, these systems will be installed in the second experimental chamber that will be made available in *P2*. Gas Dynamic Virtual Nozzles (GDVNs) are able to generate ultra-thin, highly focused liquid-jets, which are essential for delivering samples in a hydrated state, with low background and in a controlled manner. GDVNs use gas focusing to provide fast, thin liquid-jets. Since GDVNs require high-pressure gases (N_2 and He) up to 100 bar for operation, gas bottles will be installed in a dedicated cabinet located near the experimental endstation. The sample will be pushed into the injector by a syringe pump or by a high-performance liquid chromatography (HPLC) pump. Depending on the sample features and on the required jet velocity, the sample flow rates can be adjusted in the range between about 5 and 40 µL/min and diameters between 2 and 20 µm. For highly viscous samples, high viscosity extrusion injectors will be provided. This system is composed of a hydraulic cylinder, driven by a HPLC pump, a sample reservoir and a nozzle tip, and produces jet with thicker diameters, of the order of 50-100 µm. For time-resolved experiments, the injectors can be combined with mixing devices for fast and controlled diffusion-based mixing. The liquid-jet mechanical system will be installed on a side of the sample chamber. It will have an XYZ stage to position a shroud in which the sample is delivered, to allow the injector to be inserted and removed without venting the experimental chamber.

A major engineering challenge for liquid-jet injection is maintaining high vacuum in the interaction region, where pressures of 10^{-2} mbar down to 10^{-4} mbar are required. This is complicated by both the injected liquid load and, critically, the high flow of carrier gases (N_2, He) used in GVDNs. Efficient removal of these gases is essential, as photon absorption by the carrier gas can severely reduce XUV transmission and increase background levels at long wavelengths. To address these challenges, the endstation will employ a robust, multi-stage differential pumping system with optimized geometry: the region of elevated gas pressure around the nozzle will be tightly confined by small apertures and skimmers, and high-capacity turbo pumps will be positioned in successive pumping stages to extract excess gas before it can diffuse toward the detector region.

At the same time, scientific requirements often demand that detectors be placed as close as possible to the interaction point to maximize signal from weakly scattering samples. Balancing gas confinement, vacuum quality, and detector proximity therefore requires careful mechanical design, supported by vacuum simulations and prototyping. The injector chamber, skimmer design, and detector mount will be optimized to ensure minimal gas path length in the photon trajectory, thereby reducing absorption losses.

Disposal of the injected liquid is also critical for vacuum performance. Downstream of the interaction point, the design will incorporate either a catcher or a cold trap. The catcher collects the

spent jet, minimizing splashing and secondary evaporation, while a cold trap condenses residual vapor, both contributing to maintaining low background pressure. The final configuration will be selected based on detailed engineering evaluation during the development phase.

10.2.2.4 Aerosol injectors

Aerosol injection techniques complement liquid sample delivery systems by dispersing samples into monodisperse particles, thus allowing the FEL to probe samples, such as individual micro or nanoparticles, soot particles, cells, organelles and viruses, in the gas-phase [19–21]. Aerosol injectors can indeed keep the background signal lower than liquid or fixed-target delivery systems. At the same time, the particle density within an aerosol beam is lower than in a liquid-jet, thus resulting in a lower hit-rate with respect to liquid-jets. For this reason, the second experimental chamber will be able to host either the liquid-jet injector described in Sec. 10.2.2.3, or an aerosol source. The aerosol source will consist in a liquid-jet injector, such as the aforementioned GVDN, feeding an aerodynamic lens stack (ALS), designed to transmit and focus a beam of nanoparticles over a wide size range. The ALS will be mounted onto a motorized XYZ stage in order to move the particle beam across the X-ray focus and maximize the hit rate.

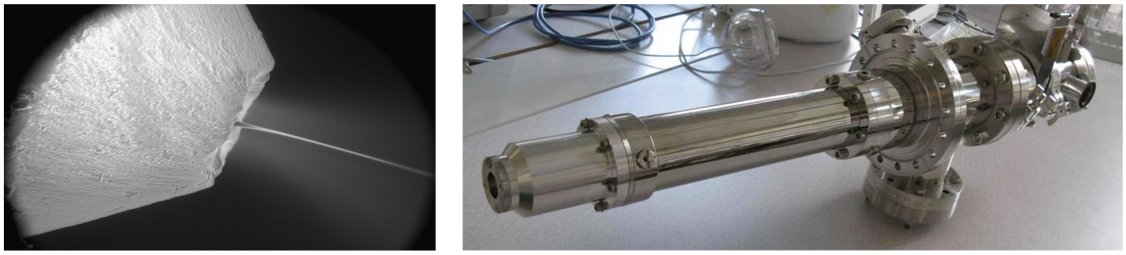

Figure 10.2: An overview of sample injection systems that will be installed at AQUA. An environmental scanning electron microscope picture of a GVDN producing a micrometer-sized water jet (left panel). A stack of aerodynamic lenses used for aerosol injection (right panel).

The second experimental chamber will also have the possibility of installing an electrospray injection system. Electrospray is a method where samples are ionized and sprayed into the vacuum chamber, offering a unique way to study charged particles or biomolecules in their native state [22, 23]. Setups aimed at further reducing the background levels, e.g. using low-scattering gases such as He for the electrospray operation, will also be considered [24]. The installed electrospray will consist of a silica capillary, with an inner diameter of 50 or 100 µm, and a grounded counterelectrode, positioned a few millimeters downstream of the capillary tip to provide the electric field to stabilize and direct the electrospray cone. The particle beam will then travel in a neutralization chamber equipped with a VUV lamp, and finally inside an ALS, where it will be focused into a narrow beam with a diameter on the order of tens of microns. A scheme, taken from the electrospray injector used at the EuXFEL, is given in Fig. 10.3. The electrospray injector assembly will be about 25 cm long and will be mounted on a DN63CF flange.
As a more elaborate optional extension, the integration of a mass spectrometry-coupled electrospray ionization source—similar to the prototype developed by the SPIDOC initiative [25, 26]—may also be considered at a later stage of *P2*. This would involve an ad hoc, external setup mounted on a dedicated port, designed to operate with minimal impact on the core configuration. Such a system would enable advanced control over sample composition by producing monodisperse, low-background, gas-phase streams with mass-to-charge selectivity.

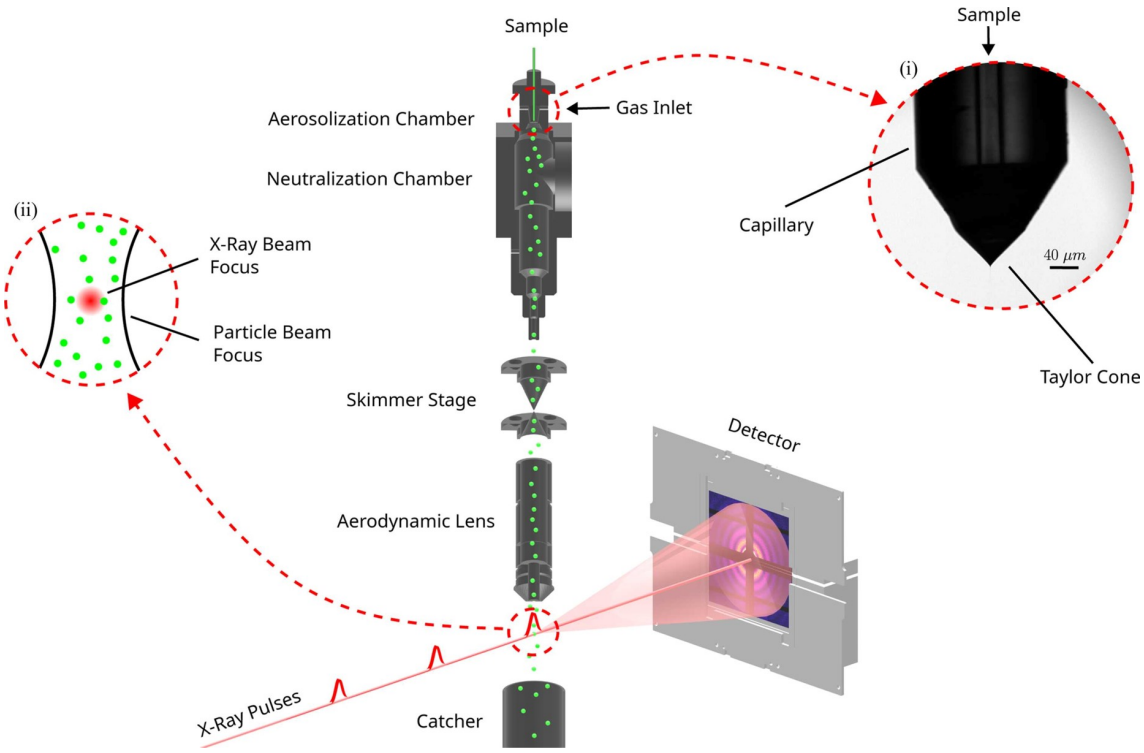

Figure 10.3: Schematic of the electrospray-based aerosol injector system used at the European XFEL for single-particle imaging. Image reproduced with permission from [23].

10.2.3 Detectors

Detectors play a critical role in FEL experiments, capturing data that reveal the interaction between intense X-ray pulses and various samples. To meet the demanding requirements of FEL-based experiments, the detectors must combine low intrinsic noise, high sensitivity, and response times matching the EuPRAXIA@SPARC_LAB repetition rate, and radiation hardness to ensure reliable performance under the operative conditions. Depending on the experiment, the detection system must balance spatial and temporal resolution, optimizing data collection for imaging, spectroscopy, and static or time-resolved experiments.
At AQUA, a suite of advanced detectors will support in the first operating phase coherent imaging and scattering and high-resolution photon spectroscopy, as well as, at a later stage, ion and electron spectroscopy, enabling precise measurements under a wide variety of experimental conditions.
The detection system combines photon detectors for capturing scattered or diffracted photons with dedicated ion and electron detectors for charged-particle spectroscopy. This integrated approach ensures full experimental versatility, enabling both photon-in/photon-out measurements — such as diffraction and scattering — and photon-in/particle-out studies for detailed spectroscopic investigations of photoionization and fragmentation dynamics.

All detectors at the AQUA endstation — including photon, ion, and electron detection systems — will be fully integrated into the facility-wide Data Acquisition (DAQ) system described in Section 10.3. This ensures that every detector signal is time-stamped and synchronized with accelerator diagnostics and pump–probe laser parameters, enabling reliable shot-to-shot correlation across different measurement channels. Such integration provides the backbone for both routine data collection and the advanced real-time analysis pipelines available to users.

10.2.3.1 Photon detectors

Different photon detectors will allow performing either CDI and scattering experiments or X-ray Absorption spectroscopy. For X-ray spectroscopy experiments, the beamline will incorporate a high-performance grating-based soft X-ray spectrometer operating in transmission geometry, inspired by the TIMEX (WEST) spectrometers at FERMI [27]. This system will feature a variable-line-spacing reflective grating designed to achieve spectral resolutions on the order of 10^4, enabling precise energy-resolved measurements while maintaining high photon throughput. It will be positioned 2 m downstream of the sample, between the interaction region and the 2D area detector, and mounted in an extension of the chamber.
A cryogenically cooled soft X-ray camera, either a CMOS or CCD, with high quantum efficiency, small pixel size (less than 20 µm), and low dark current, and a chip size on the order of 1–2 cm, will be positioned on the focal plane of the grating at a distance of a few tens of centimeters, depending on the FEL wavelength.
Additionally, a grating-based spectrometer — similar to the PRESTO system [28] at FERMI — will be installed upstream of the sample. This spectrometer, detailed in the Section 9.4.4, will record the incident FEL spectrum on a shot-to-shot basis, providing the necessary normalization for experimental signals and enhancing data accuracy.
For CDI and scattering experiments, the primary detector will be a high-performance pixel-array X-ray detector optimized for single-photon sensitivity and high spatial resolution. Similar detectors are widely employed at soft X-ray FEL endstations [29]. The AQUA detector will feature pixels of 50–75 µm and an active area of about 10×10 cm^2 ($\sim$1 Mpixel), a configuration well matched to the accessible wavelength range. Mounted on a motorized rail, it will allow sample-to-detector distances between 10 and 50 cm, providing a balance between wide angular coverage for high-angle CDI and enhanced resolution for scattering experiments.

To handle the large dynamic range of FEL diffraction signals, the system will include a motorized solid-state filter wheel positioned between sample and detector. Thin foils of Al, Si_3N_4, or Zr, with thicknesses ranging from tens of nanometers to several microns, will provide tunable attenuation while preserving spectral fidelity. These filters enable high photon flux on the sample while protecting the detector from saturation or damage, and allow rapid switching between attenuation factors depending on the experiment.

The detector itself adopts a split-sensor design, with two halves separated by an adjustable central gap to accommodate the direct FEL beam. Depending on experimental conditions, this gap can host either a beamstop or a central aperture for transmitting the unscattered beam. In non-blocking configurations, the transmitted FEL pulse can be directed to a Hartmann sensor for shot-to-shot pulse-front tilt characterization, supporting accurate reconstruction of the focal spot. More details on this apparatus are given in Section 9.4.6. Motorized translation stages will adjust the gap dynamically: narrower for improved low-angle coverage, wider for enhanced protection. Similar strategies are used at LCLS AMO/SXR [30, 31], FERMI EIS-TIMEX, and FLASH CAMP [1].

In summary, the AQUA photon detection suite combines high-resolution spectroscopic capability with a versatile pixel-array detector for CDI and scattering, integrated with dynamic attenuation, modular geometry, and advanced data processing. This ensures robust, high-quality performance aligned with established FEL standards while tailored to the specific photon-energy range and repetition rate of EuPRAXIA@SPARC_LAB.

10.2.3.2 Ions and electron detectors

For momentum- and energy-resolved photoelectron and ion spectroscopy experiments at the AQUA beamline, dedicated detection systems will be integrated into the endstation.
In the initial stage of operation in *P1*, the experimental focus will be on high-sensitivity electron

spectroscopy, which is widely recognized as one of the most broadly applicable and scientifically productive techniques at soft X-ray FELs [32–39]. To this end, a high-efficiency Magnetic Bottle Electron Spectrometer (MBES) [40] will be installed as the primary detection system, enabling comprehensive studies of photoelectron spectra and ultrafast electron dynamics across a wide range of atomic, molecular, and cluster targets.

The MBES will be positioned close to the interaction region (1–2 cm), offering near-4π solid-angle electron collection and good sensitivity across the AQUA photon energy range at its 100 Hz repetition rate. Utilizing a strong solenoid magnet and a long drift tube, the MBES efficiently guides electrons of varying kinetic energies (up to several hundred eV) to the detector. This configuration is ideal for total electron yield measurements and coincidence studies, and is particularly suited for experiments where angular resolution is less critical than detection efficiency and yield.

The adoption of the MBES in the early operational phase provides broad scientific applicability, enabling experiments in photoionization, electron correlation, and time-resolved dynamics for a wide user community. Building on this foundation, the AQUA endstation has been designed with future flexibility in mind: as the facility evolves, additional detection systems—including a Velocity Map Imaging (VMI) spectrometer, a Time-of-Flight (TOF) ion spectrometer, and a position-sensitive Multi-Channel Plate (MCP) detector—can be readily integrated. These upgrades, foreseen for *P2*, will expand the experimental capabilities to include momentum- and energy-resolved ion and photon detection, as well as ion coincidence and angularly resolved electron measurements.

The VMI spectrometer will be positioned approximately 200–400 mm from the interaction zone and mounted perpendicular to the FEL beam propagation axis. This geometry enables efficient collection of electrons emitted transverse to the beam direction and provides optimal conditions for angular-resolved measurements of electron emission, while minimizing distortions in the recorded distributions. The VMI spectrometer will be housed in a cylindrical vacuum chamber with an approximate length of 600 mm and a diameter of 400 mm, accommodating the electrostatic lens assembly and a large-area microchannel plate detector with a phosphor screen. The chamber design ensures compatibility with standard HV beamline setups and allows easy alignment with the FEL focus. To accommodate the broad photoelectron energy range — typically from a few eV up to nearly 300 eV — the VMI system will incorporate a set of electrostatic lenses with adjustable extraction voltages. This tunability enables precise focusing and velocity mapping optimized for specific kinetic energy windows and angular distributions, ensuring high-resolution momentum imaging.

Additionally, the system will support electron-ion coincidence measurements by integrating an ion detection arm opposite the electron detector. This configuration allows complete event characterization during ionization processes, providing simultaneous insights into both electron and ion dynamics induced by soft X-ray FEL pulses.

A TOF spectrometer, optimized for ion mass analysis and electron-ion coincidence measurements, will be positioned at approximately 300–500 mm perpendicular to the X-ray beam direction. Employing delayed extraction (the so-called Wiley–McLaren mode), the TOF spectrometer will achieve enhanced mass resolution by compensating for initial spatial and temporal spreads of the ions. Such a configuration provides precise identification of ion masses generated by photon energies corresponding to the soft X-ray wavelength range accessible at AQUA. The TOF's moderate-resolution electron measurement capability complements the detailed momentum analysis from the VMI, providing comprehensive characterization of the photoionization dynamics.

A MCP detector with a delay-line anode will be positioned about 500 mm downstream of the interaction region, along the ion detection axis, to enable precise time and position measurements of multiple charged fragments. This setup supports three-dimensional momentum reconstruction in Coulomb explosion imaging experiments by ensuring efficient multi-hit ion detection while maintaining a well-defined drift region for accurate time-of-flight analysis.

Similarly, the TOF spectrometer, intended for later integration, will be optimized for high-resolution ion mass analysis and electron-ion coincidence measurements, employing delayed extraction (Wiley–McLaren mode) to maximize mass resolution. The MCP with a delay-line anode will enable multi-hit, position-sensitive detection for advanced Coulomb explosion and momentum imaging experiments.
In summary, the initial deployment of the MBES for electron spectroscopy provides the AQUA beamline with immediate, high-impact experimental capability and serves the largest user base. The modular chamber and detection infrastructure ensure that additional systems for ion and photon spectroscopy can be efficiently integrated in future upgrade phases, progressively broadening the scientific reach of the facility.

10.3 Data Acquisition and Management

User experiments at AQUA will rely on an advanced computational infrastructure to manage the extensive data produced by state-of-the-art detectors and diagnostics. The Data Acquisition (DAQ) system will handle synchronized readout and event building for all detector classes described in Section 10.2.3, ensuring that photon, ion, and electron measurements are fully correlated with FEL and laser parameters on a shot-to-shot basis.

Integrated Data Acquisition System and synchronization

The EuPRAXIA@SPARC_LAB FEL will implement an advanced integrated DAQ system capable of comprehensively recording detailed information for every FEL pulse at the facility's nominal 100 Hz repetition rate (with provisions for future upgrades to 400 Hz).
The system will record thorough information for every FEL pulse, enabling detailed offline reconstruction and analysis of each experimental event. A central design principle is the unique timestamping of all data and metadata, ensuring reliable correlation of information from diverse sources (detectors, diagnostics, controls, environmental sensors) regardless of differing acquisition latencies.
The DAQ will acquire, for every pulse:

- Shot-to-shot pulse parameters: photon energy, pulse intensity, spectral distribution, beam position and profile diagnostics.
- Machine and experiment state: accelerator parameters, beamline configuration, optical laser parameters for pump–probe (pulse energy, wavelength, timing, delays), motor positions, and environmental sensor data (temperature, pressure, humidity, etc.).
- Synchronization information, including timing jitter and reference signals, enabling precise alignment of datasets from multiple sources.

A comprehensive online monitoring system will be deployed as part of the DAQ infrastructure. This system will allow users and operators to visualize key experimental data with minimal latency. Data visualization dashboards and quality metrics will be available through web-based interfaces and in control rooms, enabling immediate identification of issues and allowing for dynamic adjustment of experimental parameters.

Control System Integration and Operational Safety

The endstation control system will be closely integrated with the accelerator, laser, and beamline control systems through a unified, modular software framework EPICS, enabling seamless coordination across all facility subsystems. Integration will be achieved through standardized communication protocols and a centralized timing and event distribution network, ensuring all subsystems operate with consistent, synchronized control.

Data Integrity, Latency Management, and Event Building

Due to the different latency and throughput characteristics inherent to diverse detector technologies and DAQ devices, ensuring synchronized and accurate event reconstruction presents significant technical challenges. The DAQ infrastructure will explicitly include:

- Distributed hardware and software timestamping, implemented at the front-end electronics closest to each data source, thus minimizing synchronization uncertainties.
- Local buffering and intelligent queuing mechanisms tailored to handle device-specific readout times and network transmission delays, thereby preventing data loss and guaranteeing all recorded data are accurately matched to their corresponding FEL pulses.
- A centralized software event builder layer designed to assemble complete event datasets by correlating multiple incoming data streams based on their globally unique timestamps and pulse IDs. This layer ensures coherent event integrity, even during transient device or network delays.
- Continuous data integrity validation through real-time checksum algorithms and redundant data pathways, with additional hot-spare buffer storage capabilities to protect in-flight data from unexpected interruptions or hardware failures.

These strategies collectively ensure data reliability, minimize latency-related disruptions, and reinforce overall experimental robustness.

Data Reduction and Storage Infrastructure

Due to the intensive data generation expected from the EuPRAXIA@SPARC_LAB FEL, which, depending on the type of experiment might exceed terabytes per day, an optimized Data Reduction Pipeline (DRP) will be crucial. The DRP will deploy advanced algorithms for real-time, lossless or near-lossless compression, feature extraction, and event classification. Techniques such as sparsification (peak finding), region-of-interest extraction, and on-the-fly compression, widely used at facilities like the European XFEL and LCLS, will efficiently reduce data volume by one or two orders of magnitude.

Real-time, FPGA- or GPU-based data processing units situated near the experimental end-stations will rapidly execute these reduction tasks, minimizing latency. Detector-specific preprocessing techniques—such as adaptive pedestal subtraction, photon counting, and thresholding—will further streamline data volumes, particularly for pixel-array detectors commonly used in diffraction imaging and spectroscopy experiments.

The facility will offer a hierarchical, multi-tiered data storage solution to accommodate varying user requirements. High-speed NVMe SSD arrays or flash storage will provide temporary caching of raw and processed data during ongoing experiments. Long-term archival storage will be supported through petabyte-scale tape systems, augmented by redundant, high-capacity disk storage arrays for mid-term data preservation and accessibility. High-speed InfiniBand networking infrastructure will ensure seamless, real-time transfer of data streams from experimental hutches to the central data center, providing immediate access for users.

10.4 Sample preparation and characterization laboratories

Support laboratories will be made available to the users to prepare and characterize their samples on site and to test the experimental setups before the FEL experiments. These laboratories will be installed in the dedicated rooms located in the EuPRAXIA@SPARC_LAB building on the side of the experimental hall. The chemical laboratory, that will be maintained at a temperature between 20 and 24 °C by an air-conditioning system, will house standard equipment such as cabinets for chemicals, glassware, precision and analytical balances, ultrasonic bath, hot plates, a fume hood, a millipore water system, besides fridges and freezers for sample storage. Specialized equipment

including a vacuum oven, a microtome, a plasma system, a UV-VIS spectrophotometer, besides an optical and a fluorescence microscope will be also made available to the users. The biology laboratory will host a state-of-the-art wet lab area allowing cell culture, centrifugation, sonication and emulsification for cell lysis.
The sample delivery support laboratory will host the equipment to test liquid and aerosol sample injection. The instrumentation will closely resemble that installed at the beamline, thus allowing test in conditions very close to the experimental ones.
In a second phase, an advanced sample characterization laboratory, including an Atomic Force Microscope, a Dynamic Light Scattering system, a Nanoparticle Tracking Analysis, and a Raman Spectrometer, will be made available for the users.

10.4.1 Technology Readiness Level of the endstation components

Table 10.1 summarizes the Technology Readiness Level (TRL) of the main sub-systems of the experimental end-station. Overall, the set of sub-systems is mature and largely commercial (TRL 8–9). The experimental chamber, pump lasers, photon detectors, and sample-characterization instrumentation are at TRL 9, with off-the-shelf solutions available; the chamber's detailed engineering design is available; future steps will fine-tune and validate it. Sample-delivery systems (fixed-target supports, liquid-jets, aerosol injectors), the X-ray spectrometer (commercial crystals), ion/electron detectors, and the DAQ pipeline are at TRL 8: they are routinely used at FEL facilities but will require adaptation and optimization for the specific EuPRAXIA@SPARC_LAB beamline(s) (e.g., tailoring the spectrometer assembly, implementing optimized detector schemes, and integrating the DAQ). No sub-system is below TRL 8; therefore all listed instruments are planned for the first project phase, with the primary effort focused on integration and customization rather than fundamental R&D.

Table 10.1: TRL level of the endstation equipment.

Sub-systems	**TRL**	**Comments**
Experimental Chamber	9	A schematic design of the experimental chamber has been prepared.
Sample delivery systems	8	Sample delivery systems are at present installed at operational FEL facilities. However, some care must be taken to adapt them to the specific EuPRAXIA@SPARC_LAB beamline(s). Most of the sample delivery systems (fixed-target supports, liquid-jets, aerosol injectors) have already been used at FEL facilities and are commercially available.
Photon detectors	9	Photon detectors having the required features (vacuum compatibility, pixel size, intrinsic noise, readout rate) are commercially available.
X-ray spectrometer	8	Multilayers to build the X-ray spectrometer are also available on the market, but the details have to be tailored for the EuPRAXIA setup.
Ion & electron detectors	8	Ions and electron detectors are routinely used at similar facilities, but optimized schemes for EuPRAXIA have to be implemented.
DAQ systems	8	DAQ pipeline will be adapted - and then optimized - from those used by similar facilities.
Sample characterization laboratories	9	A list of general-purpose, commercially available instruments has been prepared.

Bibliography

[1] B. Erk et al. “CAMP@FLASH: an end-station for imaging, electron-and ion-spectroscopy, and pump–probe experiments at the FLASH free-electron laser”. In: *Synchrotron Radiation* 25.5 (2018), pp. 1529–1540.

[2] E. Pedersoli et al. “Multipurpose modular experimental station for the DiProI beamline of Fermi@ Elettra free electron laser”. In: *Review of scientific instruments* 82.4 (2011).

[3] C. Svetina et al. “The Low Density Matter (LDM) beamline at FERMI: optical layout and first commissioning”. In: *Synchrotron Radiation* 22.3 (2015), pp. 538–543.

[4] A. P. Mancuso et al. “The single particles, clusters and biomolecules and serial femtosecond crystallography instrument of the European XFEL: initial installation”. In: *Synchrotron Radiation* 26.3 (2019), pp. 660–676.

[5] A. J. Nelson et al. “Soft x-ray free electron laser microfocus for exploring matter under extreme conditions”. In: *Optics Express* 17.20 (2009), pp. 18271–18278.

[6] S. Ali and C. Jacobsen. “Effect of tilt on circular zone plate performance”. In: *Journal of the Optical Society of America A* 37.3 (2020), pp. 374–383.

[7] J. Ren et al. “Research on partially coherent light propagation through zone plates”. In: *Optics Express* 29.25 (2021), pp. 40947–40956.

[8] A. F. G. Leontowich et al. “Characterizing the focus of a multilayer coated off-axis parabola for FLASH beam at λ= 4.3 nm”. In: *Damage to VUV, EUV, and X-ray Optics IV; and EUV and X-ray Optics: Synergy between Laboratory and Space III*. Vol. 8777. SPIE. 2013, pp. 170–177.

[9] A. Ekman et al. “Extending imaging volume in soft X-Ray tomography”. In: *Advanced Photonics Research* 4.4 (2023), p. 2200142.

[10] J. Zhu et al. “Nanofabrication of 30 nm Au zone plates by e-beam lithography and pulse voltage electroplating for soft x-ray imaging”. In: *Microelectronic Engineering* 225 (2020), p. 111254.

[11] O. F. Hagena and W. Obert. “Cluster formation in expanding supersonic jets: Effect of pressure, temperature, nozzle size, and test gas”. In: *The journal of Chemical physics* 56.5 (1972), pp. 1793–1802.

[12] C. H. Yoon et al. “Conformation sequence recovery of a non-periodic object from a diffraction-before-destruction experiment”. In: *Optics express* 22.7 (2014), pp. 8085–8093.

[13] K. R. Beyerlein et al. “Mix-and-diffuse serial synchrotron crystallography”. In: *IUCrJ* 4.6 (2017), pp. 769–777.

[14] K. A. Zielinski et al. “Rapid and efficient room-temperature serial synchrotron crystallography using the CFEL TapeDrive”. In: *IUCrJ* 9.6 (2022), pp. 778–791.

[15] H. Zettergren et al. “Roadmap on dynamics of molecules and clusters in the gas phase”. In: *The European Physical Journal D* 75.5 (2021), p. 152.

[16] A. Odate et al. “Brighter, faster, stronger: ultrafast scattering of free molecules”. In: *Advances in Physics: X* 8.1 (2023), p. 2126796.

[17] R. Campargue. “Atomic and Molecular beams: The state of the art 2000”. In: (2012).

[18] M. Vakili et al. “3D printed devices and infrastructure for liquid sample delivery at the European XFEL”. In: *Synchrotron Radiation* 29.2 (2022), pp. 331–346.

[19] M. J. Bogan et al. “Aerosol imaging with a soft x-ray free electron laser”. In: *Aerosol Science and Technology* 44.3 (2010), pp. i–vi.

[20] M. J. Bogan et al. “Single-particle coherent diffractive imaging with a soft x-ray free electron laser: towards soot aerosol morphology”. In: *Journal of Physics B: Atomic, Molecular and Optical Physics* 43.19 (2010), p. 194013.

[21] R. A. Kirian et al. “Simple convergent-nozzle aerosol injector for single-particle diffractive imaging with X-ray free-electron lasers”. In: *Structural Dynamics* 2.4 (2015).

[22] J. Bielecki et al. “Electrospray sample injection for single-particle imaging with x-ray lasers”. In: *Science Advances* 5.5 (2019), eaav8801.

[23] S. Rafie-Zinedine et al. “Enhancing electrospray ionization efficiency for particle transmission through an aerodynamic lens stack”. In: *Synchrotron Radiation* 31.2 (2024), pp. 222–232.

[24] T. V. Yenupuri et al. “Helium-electrospray improves sample delivery in X-ray single-particle imaging experiments”. In: *Scientific Reports* 14.1 (2024), p. 4401.

[25] A. Kadek, K. Lorenzen, and C. Uetrecht. “In a flash of light: X-ray free electron lasers meet native mass spectrometry”. In: *Drug Discovery Today: Technologies* 39 (2021), pp. 89–99. ISSN: 1740-6749.

[26] T. Kierspel et al. “Coherent diffractive imaging of proteins and viral capsids: simulating MS SPIDOC”. In: *Analytical and bioanalytical chemistry* 415.18 (2023), pp. 4209–4220.

[27] E. Principi et al. “A versatile wide energy range spectrometer for soft X-ray FELs”. In: *Nuclear Instruments and Methods in Physics Research Section A: Accelerators, Spectrometers, Detectors and Associated Equipment* 1058 (2024), p. 168856.

[28] C. Svetina et al. “PRESTO, the on-line photon energy spectrometer at FERMI: design, features and commissioning results”. In: *Synchrotron Radiation* 23.1 (2016), pp. 35–42.

[29] L. Strüder et al. “Large-format, high-speed, X-ray pnCCDs combined with electron and ion imaging spectrometers in a multipurpose chamber for experiments at 4th generation light sources”. In: *Nuclear Instruments and Methods in Physics Research Section A: Accelerators, Spectrometers, Detectors and Associated Equipment* 614.3 (2010), pp. 483–496.

[30] J. D. Bozek. “AMO instrumentation for the LCLS X-ray FEL”. In: *The European Physical Journal Special Topics* 169.1 (2009), pp. 129–132.

[31] T. Osipov et al. “The LAMP instrument at the Linac Coherent Light Source free-electron laser”. In: *Review of Scientific Instruments* 89.3 (2018).

[32] A. Rudenko and D. Rolles. “Time-resolved studies with FELs”. In: *Journal of Electron Spectroscopy and Related Phenomena* 204 (2015), pp. 228–236.

[33] S. Owada et al. “Characterization of soft X-ray FEL pulse duration with two-color photoelectron spectroscopy”. In: *Synchrotron Radiation* 27.5 (2020), pp. 1362–1365.

[34] R. Boll et al. “X-ray multiphoton-induced Coulomb explosion images complex single molecules”. In: *Nature Physics* 18.4 (2022), pp. 423–428.

[35] M. Burt et al. “Coulomb-explosion imaging of concurrent CH 2 BrI photodissociation dynamics”. In: *Physical Review A* 96.4 (2017), p. 043415.

[36] T. Jahnke et al. “Direct observation of ultrafast symmetry reduction during internal conversion of 2-thiouracil using Coulomb explosion imaging”. In: *Nature Communications* 16.1 (2025), p. 2074.

[37] H. V. S. Lam et al. “Differentiating three-dimensional molecular structures using laser-induced coulomb explosion imaging”. In: *Physical Review Letters* 132.12 (2024), p. 123201.

[38] N. Berrah et al. “Femtosecond-resolved observation of the fragmentation of buckminsterfullerene following X-ray multiphoton ionization”. In: *Nature Physics* 15.12 (2019), pp. 1279–1283.

[39] B. F. Murphy et al. “Femtosecond X-ray-induced explosion of C60 at extreme intensity”. In: *Nature communications* 5.1 (2014), p. 4281.

[40] A. M. Rijs et al. “‘Magnetic bottle’spectrometer as a versatile tool for laser photoelectron spectroscopy”. In: *Journal of electron spectroscopy and related phenomena* 112.1-3 (2000), pp. 151–162.

11. Electron Diagnostics

11.1 Introduction

A high-brightness linear accelerator driving a free-electron laser (FEL) requires a comprehensive suite of diagnostic tools to accurately measure the full six-dimensional (6D) phase space of the electron beam at multiple locations along the accelerator. In the specific case considered here, the diagnostics must also be compact to preserve the high average accelerating gradient enabled by the plasma wakefield accelerator. This chapter describes the diagnostic systems for electron beams, ensuring measurement and control of beam parameters in compliance with EuPRAXIA@SPARC_-LAB design and user facility requirements.

For the purpose of describing the diagnostics, three main sections are identified:

- The S-band photoinjector and X-band linac, delivering a 200 pC drive bunch and a 30 pC witness bunch at an energy of 500 MeV.
- The 60-cm-long discharge plasma capillary, where the energy of the witness bunch is boosted to 1 GeV.
- The undulator section, where the witness bunch generates radiation via the FEL process.

The electron beams are characterized just after generation in the RF gun, before and after compression, and before injection into and after extraction from the plasma module, in front of the undulator section. The main parameters that must be monitored and controlled are listed in Table 11.1, together with the required resolution and the corresponding diagnostic tools. The diagnostics described here and foreseen for the facility meet the requirements of TRL 7, except for diagnostics at the plasma entrance, which are still under development. However, in the dedicated chapter, a risk mitigation strategy is considered.

Table 11.1: Relevant electron beam parameters, measurement range and resolution, and corresponding envisioned diagnostic tools.

Parameter	Range	Resolution	Tool
Charge	1–500 pC	$\mathcal{O}$(pC)	ICT, TurboICT, Combo-Turbo-Toroid, Faraday cup
Beam size (rms)	1 µm–1 mm	$\mathcal{O}$(5µm)	View screens (OTR and scintillating screens)
Beam size (rms)	1 µm–1 mm	$\mathcal{O}$(µm)	Wire scanner
Energy	5 MeV–1.2 GeV	$\mathcal{O}$(10 keV)	Magnetic spectrometer
Relative energy spread (rms)	>‰	0.01%	Magnetic spectrometer
Transverse position	1 µm-500 µm	$\mathcal{O}$(µm)	Cavity BPMs,
Transverse position	10 µm–2 mm	$\mathcal{O}$(10 µm)	Strip-line BPMs
Longitudinal distribution (rms)	3 fs–1 ps	$\mathcal{O}$(fs)	Transverse deflecting cavity (Polarix) and view screen, CDR
Transverse normalized emittance	>0.5 mm mrad	0.3 mm mrad	Quadrupole scan
Relative delay between bunches	0.2–2 ps	$\mathcal{O}$(fs)	Transverse deflecting structure (Polarix) and view screens, EOS

11.2 Electron beam diagnostics

11.2.1 Integrated current transformer

The bunch charge will be measured at several points along the accelerator to optimize transmission efficiency and ensure stable long-term operation. Non-destructive measurements will be performed using commercially available integrating current transformers (ICTs) [1]. These in-flange transformers are mounted directly on the beamline; they are ultra-high-vacuum (UHV) compatible, feature a short axial length (40 mm), and include a vacuum-brazed ceramic gap. They require no bellows, external electromagnetic shielding, or wall-current bypass systems. Their reliability is attested by their widespread use in many other accelerator facilities worldwide.

ICTs provide charge measurements with a few-picocoulomb (pC) accuracy over the full range of interest. The signal generated by a single electron bunch has a nominal duration of 70 ns, with a pulse amplitude calibrated to within 1% accuracy. The pulse area is directly proportional to the beam charge, and each signal will be digitized using a 16-bit ADC operating at 1 GS/s, enabling precise charge reconstruction.

Conventional ICTs detect both the bunch charge and any accompanying dark current. In modern accelerators, the RF photoinjector is typically the main source of dark current. However, only a small fraction of this current survives acceleration, as most electrons are not captured at the proper RF phase. Due to their poor transverse emittance, they usually appear as a diffuse halo. Dark current contributions can be isolated by disabling the photocathode laser.

The X-band structures can also contribute to dark current. While it is still too early to assess the extent to which this may affect charge measurements, a mitigation strategy is already in place. To enhance measurement precision at low charge levels and suppress dark current effects, a new generation of detectors (Turbo-ICTs, developed by Bergoz Instrumentation [2]) will be employed. These devices operate in the frequency domain rather than the time domain, making them effectively immune to dark current. They provide accurate measurements down to tens of femtocoulombs (fC). Turbo-ICTs will be installed immediately after the RF gun—where dark current is most significant—and before and after the plasma module, where high resolution is required for the low-charge witness bunch.

Turbo-ICTs incorporate a band-pass filter centered at 180 MHz to limit the output bandwidth. This produces a narrow resonance at 180 MHz, which is amplified by a low-noise amplifier and processed through detection electronics based on a logarithmic amplifier. The output is then handled by a track-and-hold circuit that captures the pulse envelope peak—logarithmically proportional to the bunch charge—triggered by a synchronous signal.

Although Turbo-ICTs are highly effective for low-charge, dark-current-free measurements,

they are not suitable for continuous dark current monitoring, which is essential for radiation safety compliance. Therefore, a separate device is required for this function. To address space constraints and improve integration, Bergoz has developed a Combo-Turbo-Toroid for SPARC_LAB at INFN-LNF. This compact hybrid device combines a conventional ICT and a Turbo-ICT within a single housing. It will be installed in the injector region, where dark current is always present and accurate monitoring is critical.

The combination of these devices enables online monitoring of both the beam charge and the dark current.

11.2.2 Faraday cup

The Faraday cup will be used in two regimes based on bunch charge: measuring the total charge (Q) pulse-by-pulse, or switching to the average current mode (C/s) for low-charge bunch (<1 pC) .

The design uses a simplified mechanical layout which, operating as a lumped element circuit with a limited useful bandwidth (50 MHz) and allowing an easy insertion and extraction from the vacuum chamber, is sufficient for obtaining an integral charge assessment at the expense of capturing the actual temporal bunch profile information.

It consists of a copper cup that can be inserted into the electron beam path approximately 1.2 m downstream of the cathode. The device is mounted on a linear actuator, electrically isolated from the grounded vacuum chamber by ceramic washers, and connected to the readout electronics via a 50 Ω coaxial cable through a vacuum feedthrough (Fig. 11.1).

As the electron bunch enters the cup, the collected charge generates a current directly proportional to the number of incident particles, enabling absolute pulse-by-pulse charge measurements.

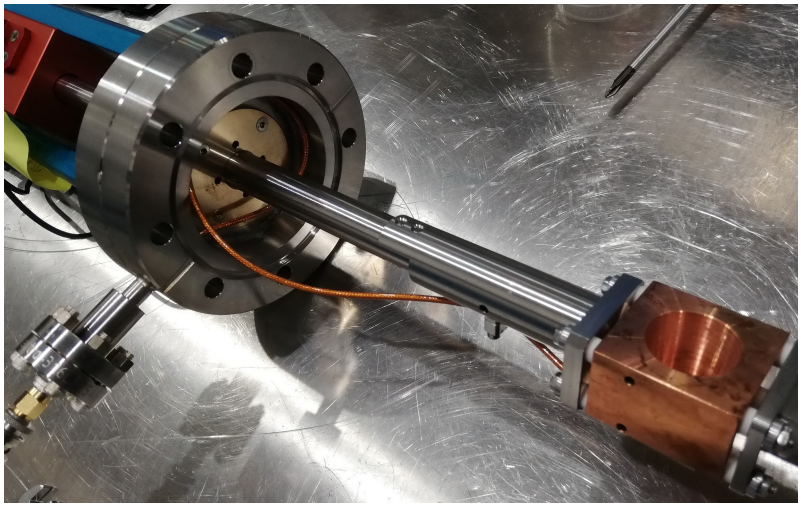

Figure 11.1: Picture of the Faraday Cup and linear actuator (SPARC).

For beams in the few-MeV energy range, charge loss mechanisms such as deep inelastic scattering or secondary electron emission are typically negligible. Nonetheless, to further minimize secondary electron effects and ensure measurement accuracy, the cup includes a suppressor electrode biased to a negative voltage.

Copper was chosen for the cup material due to its high electrical conductivity, good machinability, and relatively high atomic number. The cup is dimensioned to fully stop the incoming beam. For instance, a 5-cm-thick copper absorber (corresponding to several radiation lengths) is sufficient to absorb most of the energy from a 5 MeV electron beam, ensuring that energy deposition occurs predominantly within the cup body.

The electrical behavior of the Faraday cup can be modeled as a current source (representing

the beam) in parallel with an equivalent resistor (to ground) and a capacitor (representing the cup's capacitance to ground). The capacitance, determined by the cup geometry and surrounding environment, typically lies in the range of tens of picofarads. The resulting voltage signal across the 50 Ω termination is digitized with 16-bit resolution and integrated to determine the charge bunch by bunch.

For beams with < 1 pC charge per bunch, as an alternative to the standard bunch-by-bunch mode, the measurement system utilizes a Transimpedance Amplifier (TIA) to precisely determine the average current (C/s) by integrating over a sequence of N beam pulses. The dark charge background, which yields a significantly lower signal amplitude than that of the short accelerated beam pulse (due to its longer temporal duration relative to the system's time constant), will be subjected to background subtraction by disabling the photocathode laser. The TIA is preferred over a simple resistive readout because it offers superior sensitivity and lower noise by using high gain in the feedback loop while maintaining a low input impedance.

11.2.3 Strip-line Beam Position Monitors

Strip-line Beam Position Monitors (BPMs) will be used to measure the beam position relative to the machine axis. Each BPM pickup consists of four stainless steel electrodes mounted with $\pi/2$ rotational symmetry to form a transmission line with characteristic impedance Z_0 along the beam pipe. One end of the striplines, connected through coaxial vacuum feedthroughs, constitutes the output terminal; the other end is generally terminated to the wall via a load impedance R_l. The BPM frequency response is periodic and exhibits a sinusoidal shape.

A dedicated strip-line pickup has been designed to satisfy the following main requirements, which impose boundary conditions for the BPM design:

- Transfer impedance sufficient to maintain a root-mean-square (rms) resolution of 10 µm in the range 50–500 pC while also enabling single bunch measurements down to a charge as low as 10 pC with an expected rms resolution better than 100 µm.
- Installation inside quadrupole magnets in the S-band linac to save longitudinal space.
- Compatibility with existing commercial detection electronics centered at 500 MHz.

Figure 11.2 shows the technical drawing of the strip-line BPM, and the BPM parameters are summarized in Table 11.2.

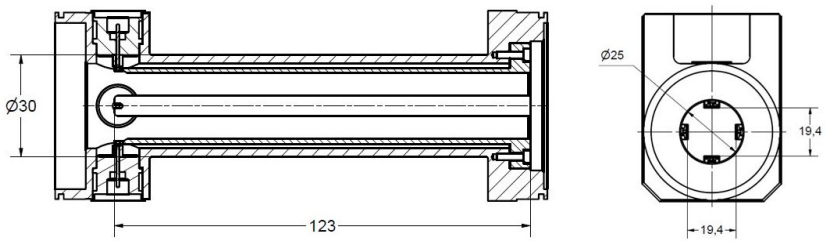

Figure 11.2: Technical design of the strip-line BPM pickup. All distances in mm.

The choice of shorted striplines ($R_1 = 0$), as opposed to the classical matched termination, was made to reduce the number of additional feedthroughs and resistive loads per BPM, thereby reducing the BPM's transverse footprint and simplifying its integration. Furthermore, the stripline length was specifically chosen as l=123 mm to ensure the entire assembly could be contained within the quadrupole magnets along the beamline.

This geometric constraint ensures that the BPM's transfer impedance exhibits a peak near the operating frequency of the detection electronics (500 MHz), while also providing sufficient sensitivity at the accelerating sections frequencies for the potential detection of parasitic bunches.

The distance d of the striplines from the vacuum chamber and the width w were selected to maintain the matched 50 ohm characteristic impedance and maximize electrode separation, thereby guaranteeing an adequate stay-clear (beam aperture).

The voltage signals induced in the striplines by the beam (pairs of pulses with opposite polarity, separated by twice the electrical length of the stripline) are transmitted via low-attenuation coaxial cables to the detection electronics, which compare the amplitudes of the individual signals to reconstruct the beam's transverse position.

A commercial BPM processor has been selected for use [3]. The short pulses from the pickup are first lengthened by band-pass filters on the RF front-end board (centered at 500 MHz with a 10 MHz bandwidth) and then digitized by a 16-bit ADC sampled at 125 MHz to extract the signal amplitude, which is used to calculate the beam transverse position. The sum signal, after proper calibration, can also be utilized to measure the total transmitted bunch charge.

An external trigger, synchronous with the beam signal, initiates the data processing. Linearity corrections for the reconstructed beam position will be based on bench calibration measurements and simulations.

Table 11.2: Strip-line BPM parameters

Vacuum pipe diameter D	mm	25
BPM total length	mm	155
Stripline distance r	mm	19
Strip coverage angle	degree	37
Strip length l	mm	123
Strip characteristic impedance Z_0	Ohm	50
Strip width	mm	1.5
Strip distance from chamber d	mm	1.5
1st lobe bandwidth	MHz	1219.5

11.2.4 Cavity Beam Position Monitors

Cavity Beam Position Monitors (cBPMs) are a type of BPM that use resonance cavities as electromagnetic pickups. They are non-destructive diagnostic devices capable of measuring the beam position (center of mass) in the transverse plane [4]. Cavity BPMs were chosen for their ability to provide the highest position precision, even for low-charge bunches. They will be installed in the X-band linac, on both sides of the plasma acceleration module, where a transverse beam position precision of 1 µm over a dynamic range of 1 mm is required, and between the undulators modules.

The beam position is calculated from the levels of the resonant modes excited in the pillbox cavities as a bunch passes through. Two cavities are used in series along the beam path: the *reference* cavity used to measure the monopole mode TM_{010} amplitude, the *position* cavity used to measure the dipole mode TM_{110} amplitude.

The TM_{010} amplitude is proportional to the bunch charge, whereas TM_{110} is proportional to both the charge and the transverse position of the bunch (i.e., the offset relative to the electromagnetic center of the pillbox). The dimensions of the pillbox cavities are designed such that the frequency of the dipole mode of the *position* cavity coincides with the frequency of the monopole mode of the *reference* cavity. The design is illustrated in Fig. 11.3. Four rectangular waveguides are matched to the position cavity via coupling ports. Antennas, connected to coaxial outputs, are placed inside the waveguides to couple to the extracted mode fields.

The readout electronics process the cBPM output signals to:

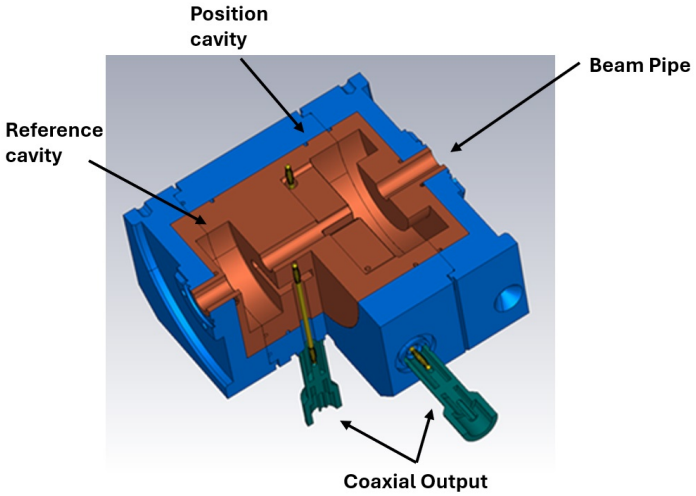

Figure 11.3: Cavity BPM PSI model "BPM8". ©2024 Fabio Marcellini (PSI)

1. Calculate the ratio between the two mode amplitudes, obtaining a quantity dependent only on the beam position, independent of the bunch charge.
2. Compare the phase of the two modes to determine the sign of the beam offset. The monopole mode has a fixed phase, while the dipole mode phase depends on the direction of the beam displacement.

By exploiting the horizontal and vertical polarization of the dipole mode fields and with appropriate cavity design, horizontal and vertical displacements can be measured independently. The chosen design for the cBPM is the PSI model “BPM8”, with an 8 mm beam aperture, developed at Paul Scherrer Institute. Table 11.3 summarizes the main parameters, and Fig. 11.4 shows a photograph of the device [5]. Between the undulator sections, PSI "BPM5" models are used instead of "BPM8". They have similar design and electromagnetic characteristics (e.g., resonance frequencies, Q_L) but with a 5 mm aperture (matching the beam pipe between undulators) and a total length of 80 mm instead of 100 mm.

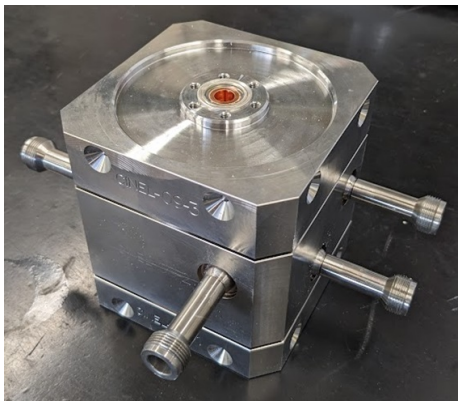

Figure 11.4: Cavity BPM PSI model "BPM8".

The readout electronics is the “LIBERA Cavity BPM” by Instrumentation Technologies (Fig. 11.5) [6]. Each module acquires signals from the position resonator (“X”, “Y”) and the reference resonator (“I”) of a single cBPM. At the front-end stage, signals are filtered to remove unwanted frequency components, and their amplitudes are adjusted via variable attenuators (0–32 dB)

Table 11.3: Main parameters of PSI cBPM models "BPM8" and "BPM5".

Parameter	**BPM8**	**BPM5**
General		
Material	Stainless Steel 316LN	Stainless Steel 316LN
Beam Acceptance [mm]	8	5
Total length [mm]	100	80
Position Cavity Resonator		
Length [mm]	12	12
Q_L	1000	1000
TM_{110} frequency [GHz]	4.92	4.92
Position Signal Sensitivity [V/(mm nC)]	4.3	4.7
Angle Signal Sensitivity [µm/mrad]	6.3	n.a.
Reference Cavity Resonator		
Length [mm]	14	14
Q_L	1000	1000
TM_{010} frequency [GHz]	4.92	4.92
Reference Signal Sensitivity [V/nC]	58	62

depending on beam conditions (charge, position). The signals are then down-converted to an intermediate frequency, filtered, and digitized. The local oscillator frequency and ADC sampling rate are generated by two PLLs locked to an external reference signal at 71.39 MHz. Main parameters of the LIBERA Cavity BPM are reported in Table 11.4.

Figure 11.5: "LIBERA Cavity BPM" by Instrumentation Technologies. Front and back panels view.

The absolute transverse position (x_b, y_b) of each bunch is obtained as:

$$x_b = K_x \frac{V_x}{V_i} \quad \text{and} \quad y_b = K_y \frac{V_y}{V_i} \tag{11.1}$$

where V_x, V_y, and V_i are the amplitudes of the signals ("X", "Y", "I"), computed via a sum-of-squares formula on the digital data, and K_x, K_y are calibration constants accounting for resonator sensitivity, applied attenuation, and cable losses.

To determine the sign of the transverse beam position, an I/Q demodulation of the signals is performed, comparing the phase of the position resonator signals ("X", "Y") with the reference resonator signal ("I") [7].

Table 11.4: Main parameters of the "LIBERA Cavity BPM".

Parameter	**Value**
General	
Number of RF inputs	3
Input connector type	SMA
Maximum input range [dBm]	16
Input signal frequency	4.926 GHz
FPGA	Zynq-7035
CPU	Dual Core ARM Cortex-A9
ADC	Analog Devices AD9680-500
Channels No.	4
Number of bits	14
Bandwidth	2 GHz
Sampling rate	500 MS/s
Maximum input range at ADC	2.06 V_{p-p}
Reference Signal	
Connector type	SMA
Signal level range	0–10 dBm
Signal frequency	71.39 MHz

11.2.5 View Screens

The primary tools for transverse beam diagnostics are the view screen systems. These devices measure the transverse beam profile, including the centroid and root-mean-square (rms) size, with a resolution of a few microns, typically not better than 4-5 μm at 1 GeV. When combined with a magnetic spectrometer, they enable beam energy measurements, and when used in conjunction with a transverse deflecting cavity, they allow characterization of the longitudinal bunch profile. All view screens are installed in an 80 mm-long vacuum chamber. Scintillator crystals, such as Ga:Ce, YAP, or GaGG, are commonly employed as the screen material due to their suitability for optical diagnostics. Figure 11.6 shows the mechanical drawing of the system.

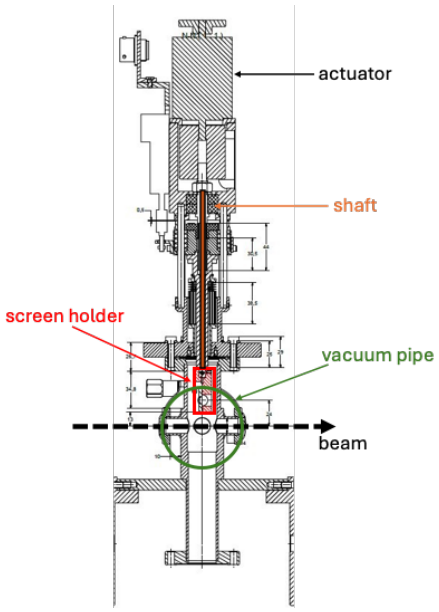

Figure 11.6: Mechanical drawing of the compact view screen, highlighting main components and beam propagation direction.

The screen is inserted into and retracted from the beam path (perpendicular to it) by a stepper motor driving a dual ball screw mechanism, ensuring high precision and reproducibility. A bellows assembly accommodates the actuator while preserving vacuum integrity. The screen holder is illustrated in Fig. 11.7. To minimize image blurring and improve spatial resolution, the screen is mounted perpendicular to the beam direction.

A 45° mirror, made of 300-µm-thick aluminized silicon, enables imaging of the scintillator's back side through a view window on one of the two CF16 flanges. The mounting is modular, allowing a second screen to be installed in a separate holder. By removing the scintillator, the mirror can also be used to generate optical transition radiation (OTR). Each screen is coupled to an optical system that collects emitted light and projects it onto a digital camera sensor. The field of view and spatial resolution are optimized according to the beam characteristics at each beamline location.

One of the main challenges in optical diagnostics of high-current electron beams is the generation of Coherent Optical Transition Radiation (COTR). COTR occurs when the electron bunch exhibits longitudinal density modulations with spectral components in the optical frequency range or higher. Figure 11.8 shows a typical COTR image recorded during LCLS commissioning [8]. This effect can distort the measured beam size, compromising the diagnostics. It is currently unclear whether bunches compressed via velocity-bunching will produce significant COTR; therefore, a mitigation strategy is considered.

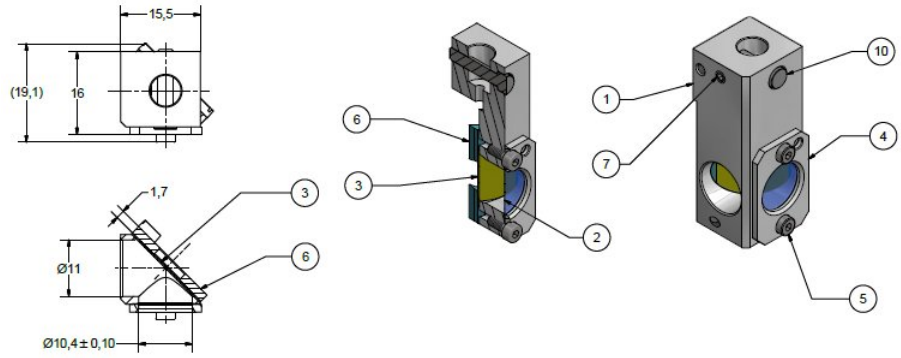

Figure 11.7: Mechanical drawing of the screen holder: 1) Base support; 2) Scintillator screen; 3) Mirror; 4) Scintillator casing; 6) Mirror casing; 7) Set screws with hex socket; 10) Plug.

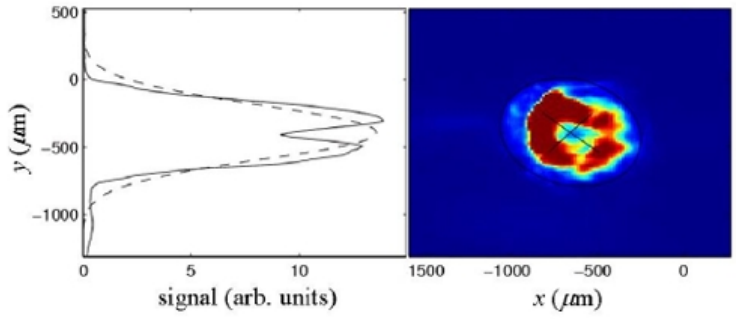

Figure 11.8: Example of a particle beam image in the presence of COTR [8].

At the PSI FEL facility, a method based on the directional properties of emitted radiation is employed [9]. Fluorescent screens emit light isotropically, whereas COTR is concentrated around the specular reflection direction within an angular spread of approximately $1/\gamma$. By careful optical design, it is possible to image only the isotropic fluorescence while excluding the directional COTR. Although effective, this approach requires a relatively large mirror system inside the vacuum chamber, which may be impractical in compact plasma accelerators.

To maintain flexibility and minimize system size, an alternative approach, tested at SACLA in Japan, is proposed [10]. Figure 11.9 illustrates the concept. Since COTR is highly directional, a small beam stop outside of the vacuum window blocks the coherent radiation while allowing isotropic light to reach the optical system. Residual stray light from reflections can be further suppressed by introducing a slight delay in the CCD camera triggering, improving measurement quality.

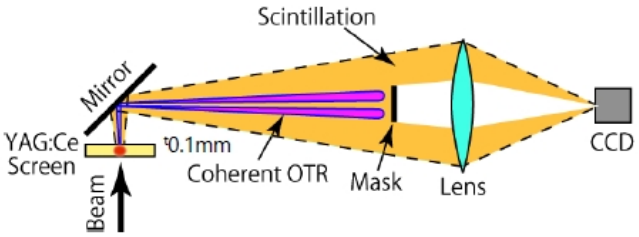

Figure 11.9: COTR filtering system using a spatial mask [10].

An RF shield will be installed at the end of the screen holder to continue the beam pipe when the screen is not in use. Fig. 11.10 shows design of the device installed at SwissFEL [11]. This element allows for mitigating the deleterious effect of the impedance discontinuities on the beams.

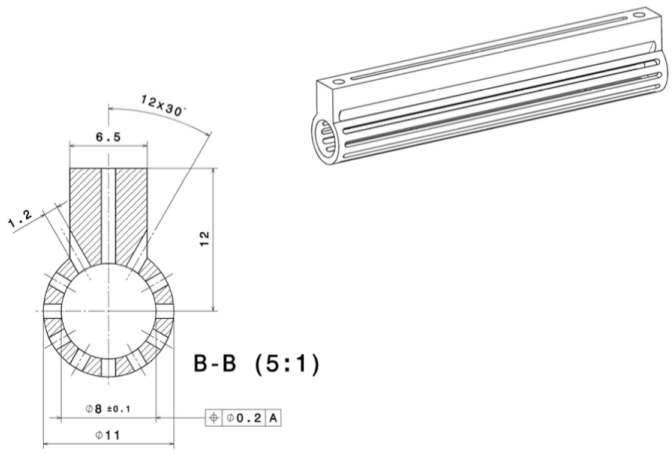

Figure 11.10: Technical design of the RF shield currently operational at SwissFEL [11].

11.2.6 Emittance Measurements

This section presents simulations of virtual quadrupole-scan measurements at three locations along the machine, aimed at evaluating measurement resolution and verifying the correct alignment of quadrupoles and view screens. Table 11.5 reports the nominal beam parameters at the diagnostic stations used for the measurement itself.

Emittance measurements will be conducted at the following locations:

- Downstream of the RF-photoinjector, after the laser heater, at a nominal energy of $E =$ 120 MeV.
- After the first X-band linac section and the bunch compressor, at nominal energy $E =$ 400 MeV.
- Downstream of the plasma module, just before the entrance to the undulator, at nominal energy $E = 1$ GeV.

Table 11.5: Nominal beam parameters for the Plasma acceleration and X-Band RF acceleration working points at the diagnostic stations.

Parameter	**Low-Energy**		**Mid-Energy**		**High-Energy**
Beam	**Witness**	**Driver**	**Witness**	**Driver**	**Witness**
Plasma acceleration					
Nominal Energy [MeV]	118	120	403	406	1004
Charge [pC]	30	200	30	200	30
Normalized Projected Emittance ε_N [mm-mrad]	0.7	1.5	0.7	1.5	1
rms Bunch Length [fs]	17	193	28	97	15
Energy Spread [%]	0.1	0.7	0.1	0.2	0.1
Full RF					
Nominal Energy [MeV]	170	–	592	–	1022
Charge [pC]	200	–	200	–	200
Normalized Projected Emittance ε_N [mm-mrad]	0.7 (x), 0.6 (y)	–	2.1 (x), 1.0 (y)	–	2.0 (x), 1.0 (y)
rms Bunch Length [fs]	392	–	49	–	49
Energy Spread [%]	0.7	–	0.5	–	0.2

Table 11.6: Parameters for emittance measurements at the diagnostic stations: Low-Energy (exit of photoinjector), Mid-Energy (after bunch compressor), and High-Energy (undulator entrance). The resolution is referred to both the driver and witness beams.

Parameter	**Low-Energy**	**Mid-Energy**	**High-Energy**
Nominal Energy [MeV]	120	400	1004
Distance Quadrupole–Screen [m]	4.065	4.039	4.840
Emittance Resolution [mm-mrad]	0.2	0.3	0.3

The emittance is determined using simulated quadrupole scan measurements [12]. At each station, three quadrupoles are optimized to minimize the beam size at the downstream screen in the measurement plane, maximizing the measurement resolution. The last quadrupole remains focusing in the measurement plane throughout the scan.

The measurement resolution is evaluated by simulating beams with varying emittance values. Each simulation accounts for camera magnification $M = 1$ and pixel size of 3.5 μm. Errors in quadrupole currents and distances are also included. The resolution is defined as the minimum emittance variation that can be reliably detected by the simulation.

Table 11.6 summarizes the parameters and results of the simulated measurements. The estimated resolution is sufficient to measure the emittance of the witness bunch at all stations along the accelerator.

To distinguish between the driver and witness, depending on the machine location, the use of the dipole or the transverse deflecting structure will enable us to separate the bunches and measure them independently [13].

11.2.7 Magnetic spectrometers

Magnetic spectrometers are commonly installed in linacs to measure the mean and rms energies of the beam [14–19]. Each spectrometer is made up of a dipole magnet, which disperses the beam by energy in the horizontal plane. A set of quadrupole magnets is usually installed before the dipole to focus the beam onto a viewing screen positioned after the dipole. The beam focusing is performed to minimize the contribution of the beta function to the rms bunch length at the screen position. The beam energy profile, and thus its mean and rms, is obtained by projecting onto the horizontal axis the transverse beam spot visible on the screen. To convert the horizontal axis to energy units, the following formulas can be used [20]:

$$E(x) \approx 0.29979 \frac{B_0 L_0}{\alpha_0 - \arctan \frac{x}{R}} \approx E_0 \left(1 + \frac{x}{\alpha_0 R}\right), \tag{11.2}$$

where E (in GeV) is the total energy associated with the horizontal displacement x on the screen, B_0 (in T) is the magnetic field in the dipole, L_0 (in m) and α_0 (in rad) are respectively the nominal length and bending angle of the dipole, R (same units as x) is the distance between the screen and the dipole center, E_0 is the nominal energy.

The horizontal resolution of the profile at the screen is the product of the camera-sensor pixel size and the inverse of the optical magnification [21]:

$$\frac{1}{|M|} = \frac{d_o}{d_i} = \frac{h_o}{h_i} = \frac{d_o - f}{f}, \tag{11.3}$$

where d_o and d_i are the distances from the lens to the object and to the camera sensor, respectively; h_o and h_i are the sizes of the object and of the image on the sensor, respectively, and f is the focal length of the optics system. The energy resolution of the profile at the screen is directly obtained after having converted the horizontal axis to energy units.

The dipole and quadrupole magnets, as well as the viewing screen, should be designed to meet the requirements in terms of energy resolution and accuracy at the screen position. Macroparticle simulations help significantly in the design of the energy measurements setup. The main idea is to track an initial bunch distribution from a starting point before the quadrupoles up to the screen position. Then, it is possible to compare the mean and rms of the energy profile at the screen with the corresponding quantities obtained from the initial energy profile, and this provides the accuracy of the simulated energy measurement.

Three spectrometers will be installed along the beamline to perform energy measurements at different stages of the acceleration process: downstream of the photoinjector and before the first X-band linac section (beam energy of 120 MeV), after the bunch compressor and before the high-energy X-band linac (400 MeV), after the plasma module and before the undulator (1 GeV). For each spectrometer, macroparticle simulations including synchrotron radiation effects were performed with the Elegant code to determine the optimal distance separating the dipole from the viewing screen (Fig. 11.11) [22]. The main parameters of the initial beam distributions, i.e. of the driver and witness at 120 MeV and 400 MeV, as well as of the witness at 1 GeV, are reported in Table 11.5.

The strengths of the quadrupoles installed before each dipole were determined with the MAD-X code, aiming at minimizing the horizontal beta function at the screen position. The quadrupole strengths were all below the limits derived by the maximum available quadrupole gradients. For a given beam spot at the screen, the magnification was chosen as high as possible to maximize the energy resolution, while allowing at most a negligible percentage of the macroparticles to be outside of the field of view (FOV). To obtain the horizontal projection of the simulated beam spot, it was assumed that the latter is acquired with a camera sensor having 1920 × 1200 pixels, and a pixel size of 3.45 µm. Other camera sensors could be used in different situations.

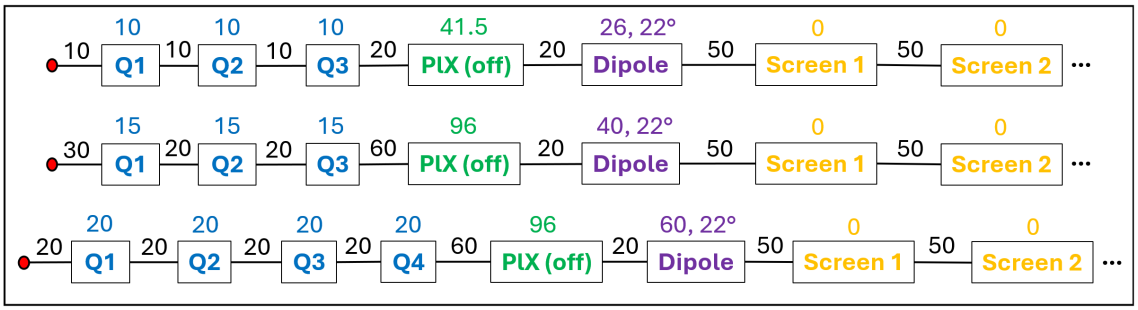

Figure 11.11: Lattice schemes assumed in the simulations, at the design energy of 120 MeV (top), 400 MeV (middle) and 1 GeV (bottom). The numbers without units indicate lengths in centimeters. The red dots indicate where the simulations start. The quadrupoles are represented in blue. The PolariX RF transverse deflecting structures (see Section 11.2.8) are in green. They are switched off during the beam energy measurements, so the tracked macroparticles see them as drifts. Design length and bending angle of each dipole are indicated in purple. The dipole operating at 120 MeV is rectangular, whereas the other two are sector magnets. In simulation, the beam spot is analyzed at six evenly-spaced positions ('screens' with zero length) after each dipole, starting from 50 cm from the dipole exit and ending at 3 m.

Figure 11.12 shows some important outcomes obtained from the simulations at 120 MeV. Even if not entirely separated from each other, the witness and driver bunches can be distinguished on the screen (Fig. 11.12, left). As a consequence, it is possible for each of these two bunches to compare the mean and rms energies obtained at the screen with the corresponding quantities of the initial bunch profile. Note that the shape of the input energy profile (red curve) is well retrieved at the screen (blue curve).

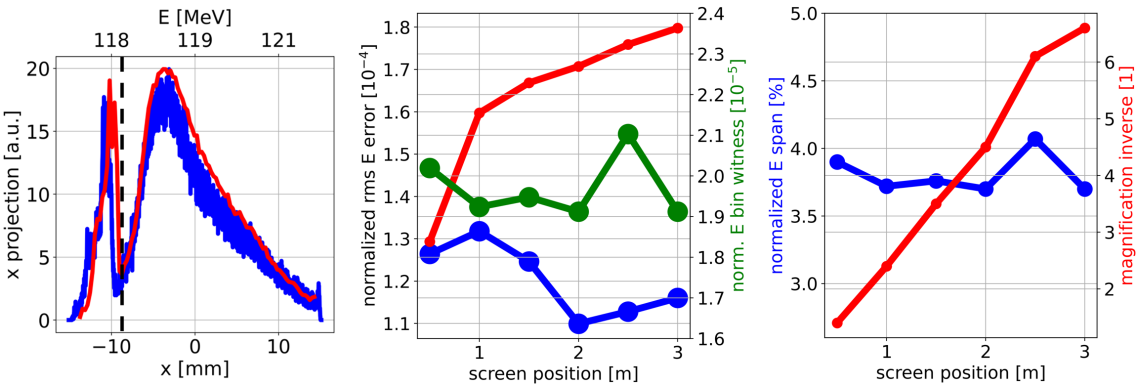

Figure 11.12: Simulation results for the driver and witness at 120 MeV. Left: projection (blue) of the camera FOV on the horizontal axis, for the screen placed at 2 m from the dipole exit. The energy axis is derived from the horizontal one by using the leftmost formula in Eq. 11.2. The energy profile of the initial beam distribution is in red. The witness and driver bunch profiles can be distinguished on the screen, respectively on the left and right of the dashed black line. Middle: normalized rms energy errors for the witness (blue) and driver (red), and the normalized energy resolution for the witness (green), as a function of the distance between the screen and the dipole exit. Normalizations are performed with respect to the mean of the corresponding initial energy profile. Right: energy span (blue), covered by the horizontal FOV and normalized by the mean of the initial beam energy profile. The inverse of the magnification is in red.

The rms energy error, normalized by the mean of the initial energy profile, is between $1.1 \cdot 10^{-4}$

and $1.8 \cdot 10^{-4}$ for both driver and witness, and for each screen position (Fig. 11.12, middle). The normalized energy resolution is around $2 \cdot 10^{-5}$ for the witness. The inverse of the magnification increases roughly linearly with the screen position, while the normalized energy span remains at around 4% (Fig. 11.12, right). For each screen position, the normalized mean energy error (not shown in Fig. 11.12) is between $8 \cdot 10^{-4}$ and $9 \cdot 10^{-4}$ for the witness, and equal to $1 \cdot 10^{-4}$ for the driver.

To indicate the most appropriate dipole-screen distance at 120 MeV, it should first be noted that the magnification values selected for the various screen positions (Fig. 11.12, right) lead to horizontal-FOV lengths (from 9 mm to 44 mm) which are all compatible with typical screen sizes. Then, one should observe that the mean and rms energy errors, as well as the energy resolution and span do not change significantly with the dipole-screen distance (Fig. 11.12, middle and right). Therefore, all the considered screen positions are acceptable. Nevertheless, choosing a lower dipole-screen distance would provide more margin for decreasing the magnification in case the measured beam spot will be larger than the simulated one. Increasing the FOV could be achieved by moving the camera away from the screen. As a consequence, the lower screen position of 0.5 m is preferable at 120 MeV.

For each considered scenario, Table 11.7 shows the recommended screen position and the values of the most important parameters that characterize the energy measurements. At 120 MeV and 400 MeV, the witness and driver can be distinguished on the screen, therefore they can be measured at the same time. The normalized mean and rms energy errors, within respectively $9 \cdot 10^{-4}$ and $2 \cdot 10^{-4}$, are sufficiently small for a precise tuning of the linac.

Table 11.7: From column 1 to 7: analyzed bunch with its initial mean energy, recommended screen position, error in mean energy, error in rms energy, bin size in energy units at the screen, energy span covered by the horizontal FOV, and inverse of the magnification. At 120 MeV and 400 MeV, the witness and driver bunches are measured at the same time on the screen. The energy mean error, rms error, resolution and span are normalized by the mean of the initial energy profile.

Bunch, mean energy	**Screen position**	**Energy mean error**	**Energy rms error**	**Energy resolution**	**Energy span**	M^{-1}
witness, 118 MeV	0.5 m	$8.6 \cdot 10^{-4}$	$1.3 \cdot 10^{-4}$	$2.0 \cdot 10^{-5}$	3.9%	1.4
driver, 120 MeV		$1.0 \cdot 10^{-4}$	$1.3 \cdot 10^{-4}$	$2.1 \cdot 10^{-5}$		
witness, 403 MeV	2.0 m	$1.1 \cdot 10^{-4}$	$4.0 \cdot 10^{-5}$	$1.0 \cdot 10^{-5}$	2.0%	2.5
driver, 406 MeV		$1.9 \cdot 10^{-4}$	$1.9 \cdot 10^{-4}$	$1.0 \cdot 10^{-5}$		
witness, 1004 MeV	2.5 m	$8.8 \cdot 10^{-5}$	$5.5 \cdot 10^{-7}$	$3.2 \cdot 10^{-6}$	0.6%	1

11.2.8 Transverse deflecting structure

The longitudinal properties of the bunch will be characterized through multi-shot measurements using an advanced X-band transverse deflecting structure (TDS), known as the Polarizable X-band (PolariX) TDS. This system is unique in its capability to modify the streaking direction by adjusting the polarization of the input electric field, as illustrated in Fig. 11.13. This feature enables beam tomography by acquiring images at different streaking angles, which can then be used to reconstruct the 3D charge distribution of the bunch [23].

When combined with quadrupole scans and energy measurements obtained from a dipole spectrometer downstream of the TDS, the system allows for complete 6D characterization of the beam. Furthermore, the ability to control the streaking direction enables slice emittance measurements in different transverse planes using the same transverse deflecting structure [24].

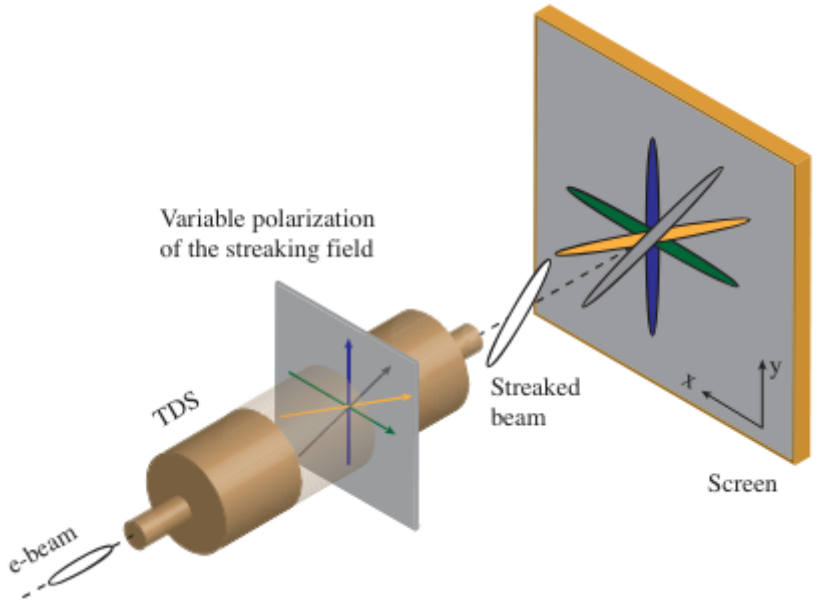

Figure 11.13: Working principle of the PolariX TDS, capable of streaking the beam along different directions by varying the field polarization [25].

The PolariX TDS supports the propagation of two TM_{110} (Transverse Magnetic) dipole-like modes. The final streaking direction is determined by the superposition of these two modes [26]. An E-Hybrid splits the incoming power into two equal branches; by introducing a phase shifter on one branch, the relative phase between the two can be controlled. An E-Rotator then recombines the two circularly polarized waves to produce a linearly polarized mode. The orientation of this linear polarization can be varied by adjusting the phase difference, with vertical and horizontal streaking corresponding to phase shifts of 0° and 180°, respectively.

The input RF power is split into two equal parts and fed through a dual-feed coupler, which injects the resulting signal into the cell section of the cavity. The coupler length is chosen to suppress evanescent modes generated by the E-Rotator before power is coupled into the TDS structure.

The cavity operates as a backward-traveling wave structure with constant impedance, featuring a $\frac{2\pi}{3}$ phase advance per cell. It is designed to operate at a nominal frequency of $\nu = 11.9952$ GHz at a temperature of $T = 33.9$ °C. Due to its constant-impedance design, the PolariX TDS can be easily adjusted in length by adding or removing cells, depending on the measurement requirements [27].

The screen coordinate along the streaking direction, Δu, is related to the longitudinal position along the bunch, Δt, by the following equation:

$$\Delta u = S \cdot c \cdot \Delta t \tag{11.4}$$

where S is the shear parameter which depends on the transport matrix element $M^u_{1,2}$ from the TDS centre to the downstream screen, the integrated voltage V_0, particle momentum p, and the RF frequency of the TDS structure ν:

$$S = M^u_{1,2} \frac{2\pi\nu\, eV_0}{c^2|p|}. \tag{11.5}$$

The shear parameter for each streaking direction can be determined by scanning over the cavity RF phase around the zero crossing, and measuring the beam centroid shift at the screen [28]. The integrated voltage V_0 is related to the power P_{in} fed into the system by the relation:

$$V_0 = D \cdot \sqrt{P_{in}} \tag{11.6}$$

where D is the voltage-to-power constant, which in this case is 6.1 $MV/MW^{\frac{1}{2}}$. Approximating the TDS by a drift plus an instantaneous kick induced in the middle of the device, the beam size measured at a screen σ is given by the beam size σ_{off} with deflector off and the streaked beam size $Sc\,\sigma_t$:

$$\sigma = \sqrt{\sigma^2_{off} + (Sc\,\sigma_t)^2}. \tag{11.7}$$

This equation leads to the definition of the longitudinal resolution R_t when the two terms on the right side are equal:

$$R_t := \sigma_t|_{limit} = \frac{\sigma_{off}}{c \cdot S}, \tag{11.8}$$

where $\sigma_t|_{limit}$ is the bunch length at which the terms in the right side of Eq. 11.7 are equal.

The diagnostic beamlines hosting the PolariX TDS consist of a series of upstream electromagnetic quadrupoles, which are used to match the beam optics to both the deflector and the downstream screen. The TDS is installed immediately after this matching section, followed by a drift space of several meters. The drift length is chosen to convert the temporal modulation imparted by the TDS into a measurable transverse displacement on the screen, ensuring the required resolution. At the end of the drift, a scintillating screen imaged by a camera records the streaked beam profile. A schematic representation of the beamline layout is shown in Fig. 11.14.

The diagnostic system has been developed and optimized to achieve a nominal temporal resolution of approximately 1 fs, consistent with the beamline layout and the limitations imposed by the RF system on the maximum gradient achievable in the cavity.

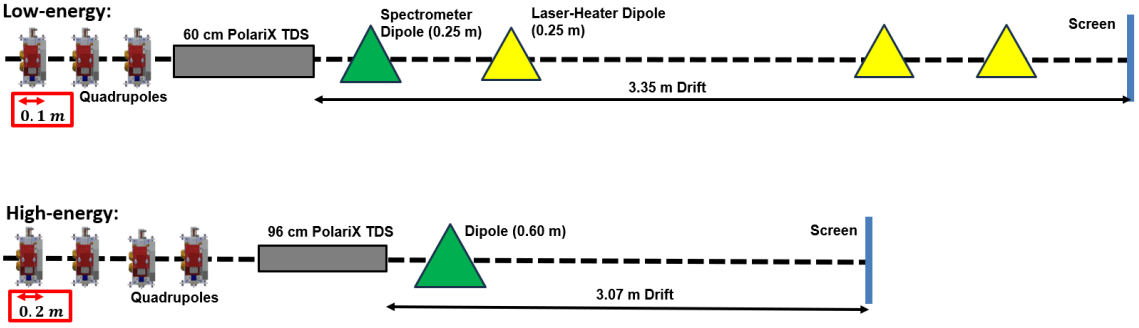

Figure 11.14: Simplified 2D layout of the diagnostic beamlines hosting the PolariX TDS. The setup includes matching quadrupoles, the TDS cavity (situated before the dipole spectrometer), a drift section, and a downstream screen.

Two configurations are foreseen: a 60 cm (flange to flange length consisting of 50 cells) TDS for the low-energy station (120 MeV) with a 3.0 m drift, and a 96 cm (flange to flange length consisting of 96 cells) TDS for the high-energy station (1 GeV) with a 3.07 m drift.

The parameters used for the longitudinal measurements in the simulations are reported in Table 11.8, while Fig. 11.15 shows the achievable resolutions as a function of the integrated voltage. The dashed line corresponds to a time resolution of 1.7 fs (0.5 µm on the spatial scale), which represents the target value required to resolve the slice length of interest. This line is therefore shown in the plot as a visual reference for the resolution needed for this measurement.

At low-energy, the estimated resolution is sufficient to clearly resolve the two bunches and to accurately determine the duration of each individual bunch. In the considered working point, the center-to-center separation of the driver–witness system is approximately 500 fs, while the net bunch separation is of the order of a few tens of femtoseconds.

Table 11.8: Parameters of TDS Measurements at the low-energy and high-energy diagnostics stations, considering the witness bunch as reference.

Parameter	Unit	Low-Energy	High-Energy
Nominal Energy	MeV	120	1004
Natural Beam Size	µm	60	14
Bunch Length	fs	17	15
Drift TDS-Screen	m	3.35	3.07
TDS Length	m	0.60	0.96
Max Voltage	MV	23	56
Max Resolution	fs	1.1	0.9

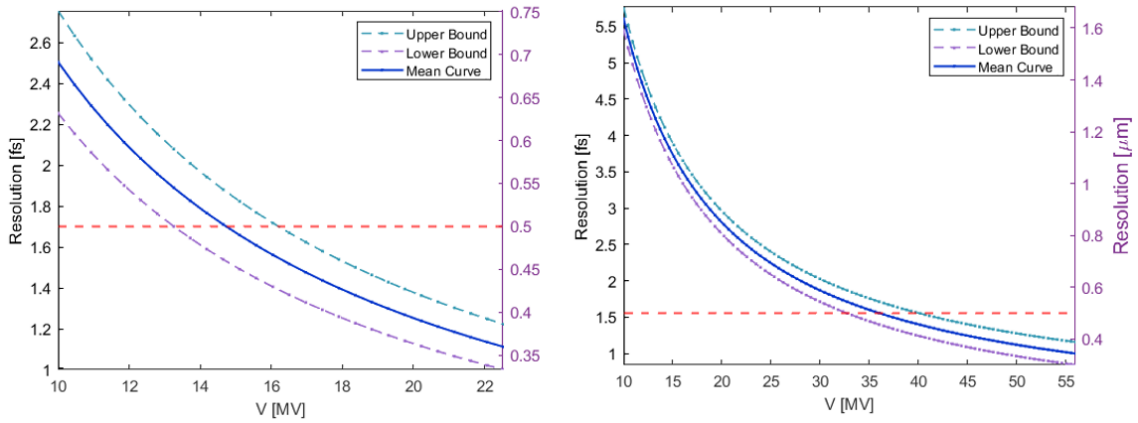

Figure 11.15: Left: Longitudinal resolution for the low-energy station, assuming a nominal natural beam transverse size of $\sigma_y \sim 60$ µm, and for a 0.6-m-long PolariX. Right: Longitudinal resolution for the high-energy station, assuming a nominal natural beam transverse size of $\sigma_y \sim 14$ µm, and for a 0.96-m-long PolariX. The red dashed lines correspond to time resolutions of 0.5 µm, which represents the target value achievable for this measurement. The upper and lower boundaries takes into accounts for shot-to-shot variations in the measured beam size.

In standard operation, the PolariX TDS is primarily used for two key diagnostics. The bunch length can be measured in both transverse planes by operating the structure with horizontal and vertical streaking. The two measurements provide independent reconstructions of the longitudinal profile, enabling a direct comparison of the results obtained with the two polarizations.

Moreover, the TDS allows slice-by-slice characterization of the beam. By dividing the streaked profile into temporal slices, it is possible to extract the slice emittance in both planes and the slice energy spread (via the downstream spectrometer).

Finally, the PolariX TDS also enables advanced techniques such as 3D and 5D phase space tomography, which have been experimentally demonstrated in previous works [29–31]. These methods provide full multidimensional reconstruction of the beam phase space and represent an additional capability of the diagnostic system.

11.2.9 Electro Optical Sampling

Electro-optical sampling (EOS) is a non-intercepting, single-shot diagnostic technique capable of measuring the longitudinal profile of an electron beam with temporal resolutions on the order of tens of femtoseconds [32].

The EOS system will be installed at the entrance of the plasma chamber, allowing detection of signals from both the driver and witness beams, as illustrated in Fig. 11.16. By correlating EOS data with the witness energy measured downstream of the plasma in the same shot, it is possible to quantify the effect of relative timing jitter between the two bunches on the acceleration process. Since different witness injection times correspond to varying accelerating fields within the plasma, this measurement provides a direct means to assess the stability of plasma-based acceleration.

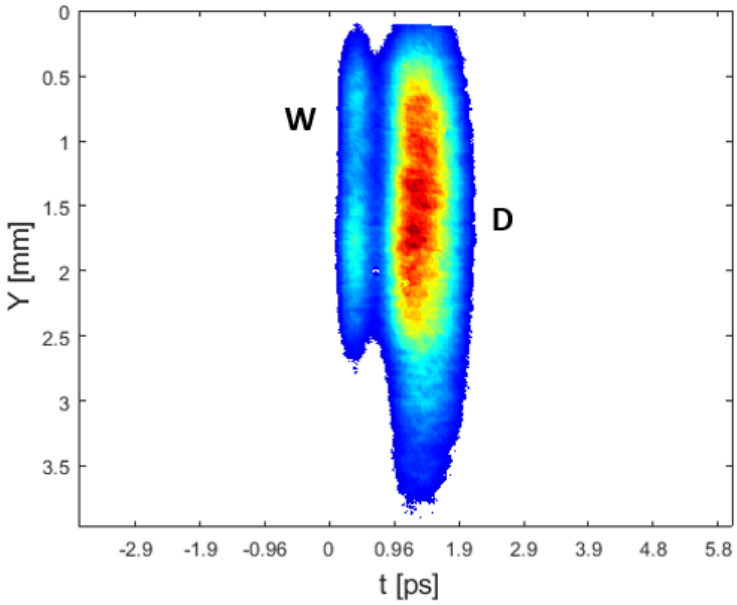

Figure 11.16: Measured signals of the driver (D) and witness (W) bunches, obtained at the SPARC_LAB facility [33]. The horizontal axis represents the longitudinal bunch distribution, while the vertical axis is the probe laser transverse profile. The measured relative distance is about ~ 1 ps.

The principle of EOS relies on an electro-optic crystal, typically zinc telluride (ZnTe) or gallium phosphide (GaP), whose optical properties change in response to an external electric field. In the context of particle accelerators, this field is provided by the Coulomb field of the electron bunch. As the field propagates through the crystal, it induces a transient change in the refractive index, which encodes the temporal structure of the beam's electric field in the THz frequency range.

This change is then probed by a polarized laser pulse traversing the crystal. The laser pulse is obtained as a bleed-through of the same beam generating the UV pulse, before higher harmonic generation. Thus, it is inherently synchronized with the electron bunches. The interaction between the laser and the electric field induces birefringence, resulting in a phase retardation between the laser's polarization components. The magnitude of the phase shift is directly proportional to the local electric field of the electron beam.

EOS typically employs a spatial decoding scheme, in which the probe laser crosses the crystal at an angle $\theta \approx 30°$. In this configuration, different longitudinal slices of the electron bunch correspond to distinct transverse positions along the laser profile. Consequently, the temporal profile of the bunch is directly mapped onto the spatial profile of the laser, as illustrated in Fig. 11.17.

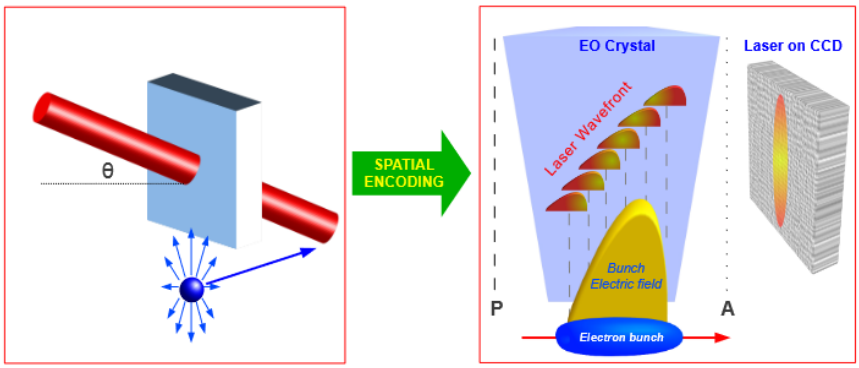

Figure 11.17: Spatial decoding configuration: the laser pulse crosses the crystal with angle $\theta \approx 30°$ and therefore different points on the pulse front wave are affected by a different external field and acquire a different polarization; then by the recorded laser pulse it is possible to reconstruct the beam longitudinal distribution [34].

At each instant, the external THz field interacts with only a spatial portion of the probe laser pulse. Consequently, different positions along the laser correspond to different time delays and experience distinct polarization rotations [35]. By measuring the transverse intensity distribution of the laser on a CCD camera, the temporal profile of the external field can be reconstructed.

The EOS measurement setup, illustrated in Fig. 11.18, comprises the probe laser generation system and the associated transport optics. The probe laser, with a wavelength of approximately 800 nm and a pulse energy on the order of mJ, is directly split from the same laser used for the photocathode, ensuring high synchronization with the electron bunch. Although in the velocity-bunching regime, the arrival time of the bunch can vary slightly due to RF phase fluctuations, this contribution is negligible compared to the EOS temporal resolution. Prior to entering the electro-optic crystal, the laser is horizontally polarized. As the electron bunch passes in proximity, it induces a transient electric field that, via the electro-optic effect, rotates the polarization of the laser pulse.

For the measurement, a GaP crystal has been chosen due to its superior temporal resolution compared to ZnTe and its broader frequency response (1–7 THz for GaP versus 1–3 THz for ZnTe). The crystal thickness is set to approximately 100 μm. The polarization modulation induced in the probe laser is then converted into an intensity modulation by passing the beam through a polarizer oriented orthogonally to the initial polarization. Finally, the transverse intensity profile, which encodes the temporal structure of the electron bunch, is imaged onto a CCD camera [36].

The temporal resolution of the EOS system is primarily determined by the duration of the probe laser pulse and by the temporal dispersion introduced by the electro-optic crystal, which depends on the crystal type and thickness. In the spatial decoding configuration, the achievable

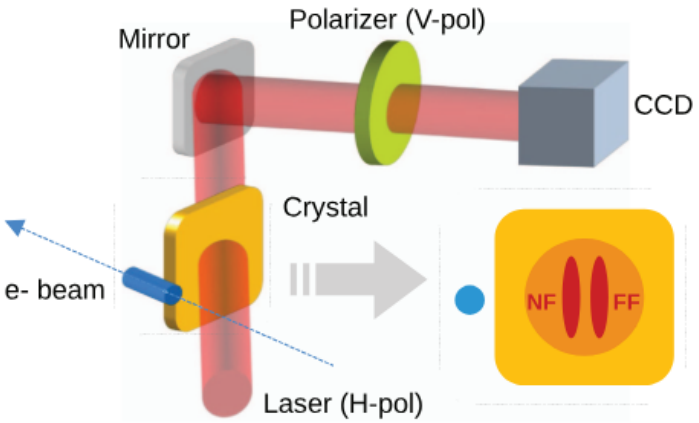

Figure 11.18: Experimental setup of the EOS system: the laser crosses the crystal and its polarization changes under the effect of the external field. The laser is then polarized vertically, and the signal is recorded by the CCD downstream of the crystal [36].

longitudinal resolution is on the order of tens of femtoseconds, while the beam arrival time can be measured with femtosecond-level precision. Although this resolution is insufficient for a complete reconstruction of the longitudinal charge distribution of the bunch, it is adequate for shot-to-shot measurements of both the beam arrival time and the driver–witness temporal separation. The main EOS parameters are summarized in Table 11.9.

Overall, the estimated resolution is sufficient to monitor the relative delay between the two bunches in real time. The EOS system will then be used to set up and constantly monitor the delay between driver and witness bunches.

Table 11.9: Typical EOS parameter employed at the SPARC_LAB facility.

Parameters	
Laser Wavelength	800 nm
Laser Energy	$\sim 1\,\mu$J
Laser RMS Pulse length	~ 80 fs
Incidence Angle	30°
Crystal type	GaP
Driver-Witness Distance	1 ps
Wavefront Resolution	$\sim$ fs
Longitudinal Resolution	$\mathcal{O}(10)$ fs

11.2.10 Coherent radiation monitor

Coherent Diffraction Radiation (CDR) will be employed for online, non-invasive monitoring of the longitudinal bunch distribution [37]. This type of radiation is generated when a charged particle moves near the edge of, or through, a boundary between two media, due to surface currents induced by the particle's electromagnetic field. As these surface currents evolve over time, the boundary emits radiation. When the particle crosses the boundary, the phenomenon is referred to as transition radiation; if it passes nearby without crossing, it is known as diffraction radiation.

In our setup, a diffraction radiation monitor is positioned at the entrance of the undulators, as it allows for real-time, non-destructive diagnostics of the longitudinal bunch profile by collecting the emitted coherent radiation.

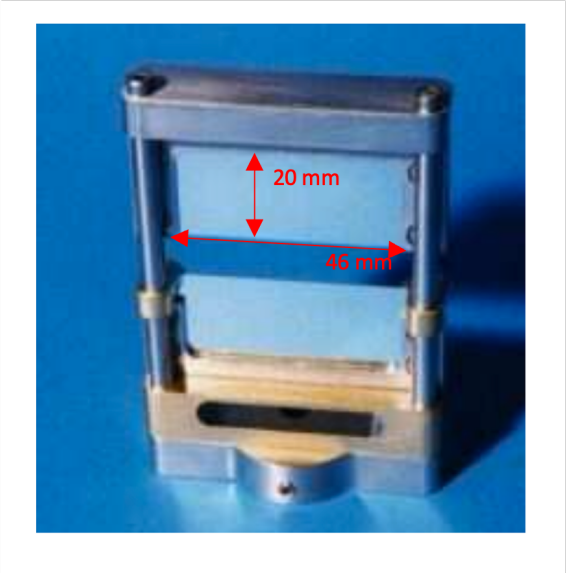

Figure 11.19: Picture of the CDR target. From [37].

For a distance ρ between the particle and the target edge, radiation is emitted with wavelength λ satisfying:

$$\rho \leq \frac{\gamma\lambda}{2\pi}, \tag{11.9}$$

where γ is the particle Lorentz factor.

The radiation is emitted both in the forward and backward directions, with an angular distribution similar to that of transition radiation. This is typically described by the Ginzburg-Frank formulation, assuming an infinitely wide, thin, and perfectly conducting target [38].

For a charged particle bunch with rms length σ_z, each particle emits radiation; however, when $\lambda \gg \sigma_z$, the emissions interfere coherently. The resulting radiation spectrum can be expressed as:

$$I_{tot}(\omega) = I_{sp}(\omega)\left[N + N(N-1)F(\omega)\right], \tag{11.10}$$

where ω is the radiation frequency, $I_{sp}(\omega)$ is the single-particle spectrum, N is the number of particles in the bunch, and $F(\omega)$ is the bunch form factor. At small observation angles θ, the form factor is determined by the longitudinal bunch distribution $S(z)$:

$$F(\omega) = \left| \int_{-\infty}^{\infty} S(z) e^{i\frac{\omega}{c}z} dz \right|^2. \tag{11.11}$$

Measuring the coherent emission spectrum thus provides direct access to the bunch form factor, revealing information on the longitudinal charge distribution. Since the coherent radiation intensity

scales with N^2, it dominates over the incoherent part, making the signal highly sensitive to short bunch lengths.

The primary goal of the CDR system is to monitor the length of the witness bunch as it enters the undulators, for feedback purposes. Consequently, the detector will be installed in the same vacuum chamber and mounted on the same holder as the view screen, positioned between the chicane—used to separate the driver and witness bunches—and the entrance of the first undulator.

The CDR monitor consists of the following components:

- A target positioned at 45° with respect to the beam direction, composed of two thin silicon foils coated with aluminum, separated by a variable gap.
- A quartz (or diamond) window, transparent to millimeter and submillimeter wavelengths, and compatible with ultra-high vacuum requirements.
- An off-axis parabolic mirror to collimate the radiation (in the THz range) emitted from the target.
- A pyrodetector coupled to a scope for measuring the intensity of the collected radiation.

Figure 11.19 shows a diffraction radiation target used at the TTF VUV-FEL facility at DESY. It consists of two silicon foils, each 300 nm thick and 46 mm wide, coated with aluminum. The gap between the two foils can be varied remotely within the range $0-10\,\text{mm}$.

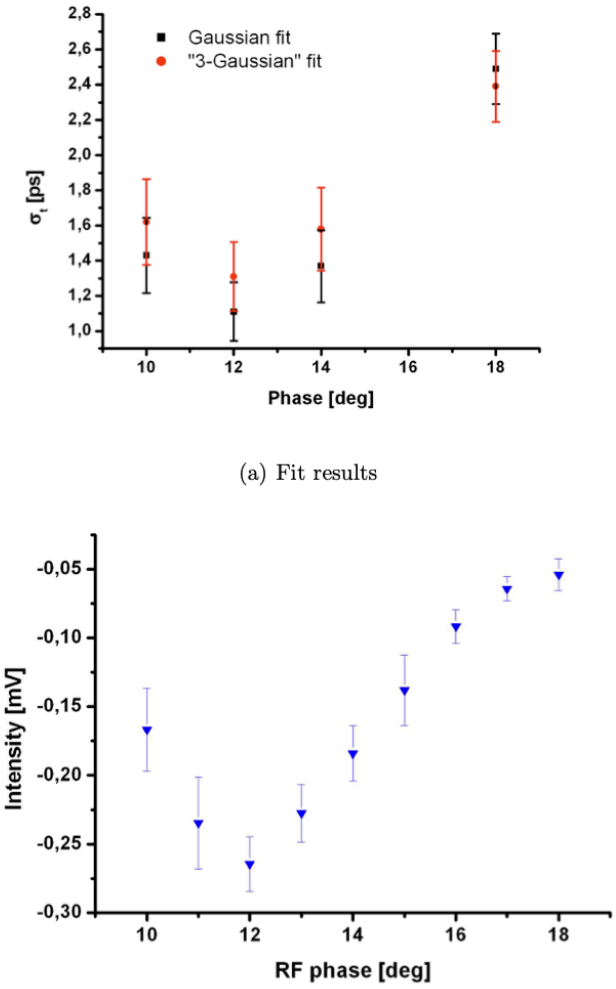

(a) Fit results

Figure 11.20: Top: bunch length, bottom: amplitude of the signal obtained from the CDR monitor as a function of phase compression at TTF VUV-FEL (DESY). From [37].

As the CDR-based bunch length monitor is non-invasive, it allows for real-time feedback, enabling automatic adjustment of compression parameters such as the RF phase or the R_{56} of the magnetic chicane. However, this diagnostic allows for a relative estimation of the bunch duration, while the absolute measurement is performed with the transverse deflecting structures, allowing for the calibration of the CDR monitor. Figure 11.20 shows the results obtained at TTV VUV-FEL (DESY) where the correlation between the amplitude of the CDR signal (bottom plot) and the bunch length (top plot) was shown (the absolute amplitude of the signal increases when decreasing the bunch length). The wavelength of the emitted radiation at EuPRAXIA@SPARC_LAB will be the same, since the energy of the beam will be similar, while the amplitude of the signal is expected to be even higher as the bunch duration will be shorter.

We note that, differently from the EOS system (Section 11.2.9), the CDR monitor does not require the use of a probe laser pulse, making its use and maintanance easier and more robust.

11.2.11 Plasma entrance diagnostics

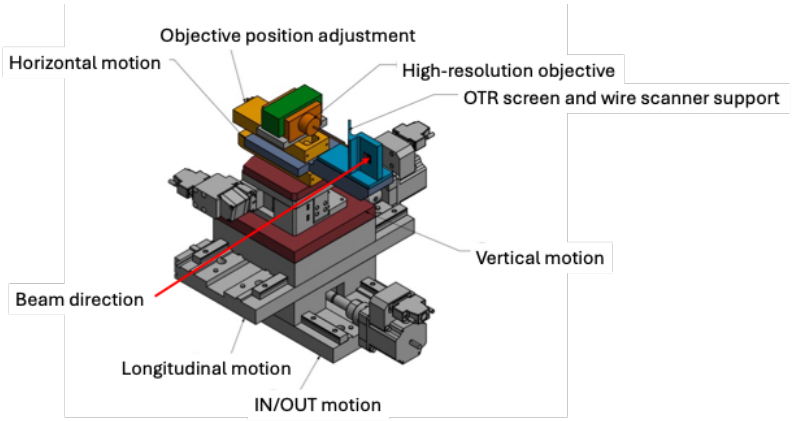

Figure 11.21: Axonometric projection of the diagnostic block at the entrance of the capillary. The beam direction is indicated by the red arrow.

The transverse distribution of the bunches at the plasma entrance is a critical parameter for optimizing plasma acceleration. To maximize the amplitude of the plasma wakefields, the drive bunch transverse size must be minimized to increase its charge density. At the same time, the witness bunch transverse size and divergence must be carefully matched to the plasma's focusing force—i.e., the ion column focusing force in the high-density plateau—to reduce emittance growth from transverse phase mixing.

Accounting for the focusing effect of the plasma entrance density ramp, the final focusing system is optimized to deliver the witness bunch with an rms transverse size of approximately 3 µm at the beam waist, located around 12 mm downstream of the plasma entrance.

For this reason, diagnostics of the witness bunch transverse distribution at the plasma entrance must provide µm-level resolution and allow mapping of the bunch envelope around the waist to also determine divergence (i.e., the longitudinal position of the waist). Two complementary devices will be implemented:

- A thin metallic screen (e.g., aluminized silicon wafer) generating optical transition radiation (OTR) upon beam passage, coupled to a high-resolution optical system that images the radiation onto a digital camera.
- A micrometric wire scanner, generating particle showers when intercepting the beam, with downstream scintillating fibers to detect beam losses.

Both systems provide time-integrated measurements; therefore, it is not possible to distinguish

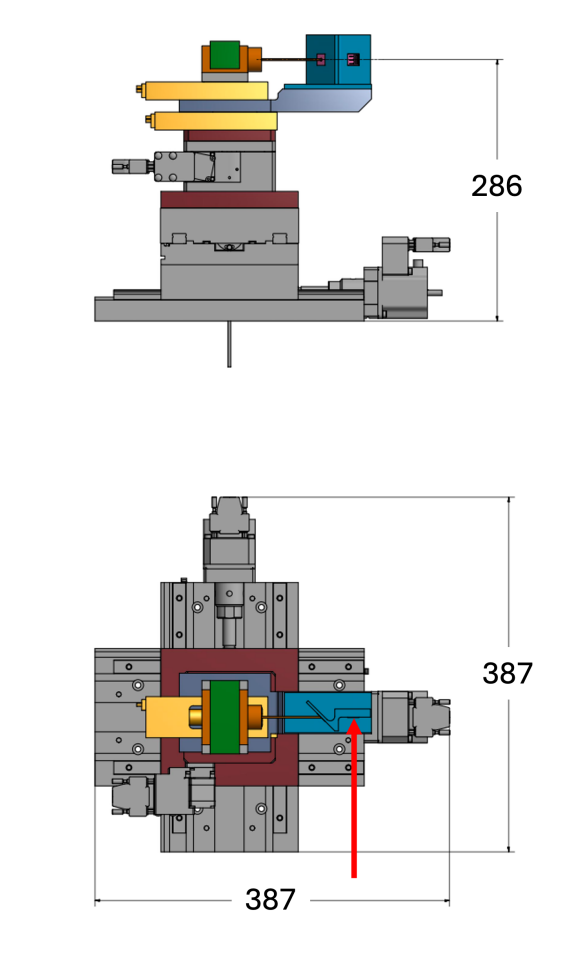

Figure 11.22: Design of the plasma entrance diagnostic device. Top: front view, with beam direction through the page. Bottom: top view, with beam direction indicated by the red arrow. Blue: holder containing the OTR screen (rotated at 45° with respect to the beam) and the microwires. Grey: remotely controlled translation stages for in-out and longitudinal motion, and for fine adjustment of the vertical and horizontal positions for microwire scans. Orange: microscopic objective. Yellow: translation stage for precise objective positioning. Dimensions in mm.

between the transverse distributions of the driver and the witness bunches. However, information on the witness bunch transverse distribution can be obtained by calculating the difference between the measured transverse distribution with both driver and witness bunches, and with the solely driver bunch. The measurement with only witness bunch is not significative because its parameters are significantly different when the driver bunch is not present, due to their mutual interaction during the velocity bunching process.

The OTR screen and the microwires are integrated into a single support (blue holder in Fig. 11.22). A horizontal translation stage allows either element to be inserted into the beamline when the capillary is retracted.

When the beam intercepts the OTR screen, the emitted radiation is collected by a high-magnification objective. The objective is mounted on a precision translation stage to enable accurate longitudinal alignment.

For the microwire scan, the system is first moved horizontally to insert the wire holder in the beam path. High-resolution vertical and horizontal translation stages are then used to scan the wire across the beam. Additionally, a longitudinal translation stage allows the measurement to be repeated at different longitudinal positions, using either the OTR screen or the microwires, thereby enabling a full mapping of the beam envelope.

The key dimensions of the system in mm are illustrated in Fig. 11.22.

11.2.11.1 OTR screen

Optical transition radiation (OTR) enables the direct imaging of the transverse bunch distribution using optical systems. The resolution of the system is limited by two main factors: the intrinsic point-spread function (PSF) of the radiation and the resolving power of the optical system. The PSF represents a fundamental limit of the detection method and cannot be overcome. For a 500 MeV electron bunch, the PSF becomes the dominant contribution for rms transverse spot sizes smaller than 4 µm [39].

The second limiting factor arises from the quality of the optical system. By carefully combining commercial microscopic objectives and lenses, spatial resolutions down to a few microns can be achieved. For instance, Ref. [40] reports a resolution of approximately 4 µm using a Cassegrain objective paired with a macro lens. Together, these factors define the ultimate resolution achievable when measuring the beam size at the waist.

A practical mitigation strategy consists of reconstructing the beam envelope by performing measurements on either side of the waist, away from its minimum. This method enables an indirect estimation of both the waist size and its longitudinal position, even when the spot size is smaller than the system's intrinsic resolution limit.

11.2.11.2 Microwire scanner

Wire scanners are widely used and well-established diagnostic tools in particle accelerators, functioning as nearly non-intercepting devices [41]. They have successfully enabled unperturbed lasing during measurements at facilities such as SwissFEL and FERMI [42].

The technique operates by transversely moving a micrometric wire through the bunch at discrete positions. The interaction between the beam and the wire produces a particle shower, which is detected by beam loss monitors—typically scintillating fibers—and correlated with the wire's position. Depending on the wire thickness and edge sharpness, even sub-micron resolution can be achieved [43].

Although wire scanning is delicate and relatively time-consuming, it remains the most suitable method for measuring the transverse distribution of the witness bunch for working points with transverse sizes $< 10\,\mu\text{m}$.

The interaction of the witness beam with a tungsten wire has been modeled using the GEANT4 framework [44]. The simulation incorporates all relevant aspects, including: (i) the wire geometry, (ii) material properties, (iii) primary particles (electrons), (iv) secondary particle production (electrons, positrons, photons, etc.), (v) particle tracking through materials, and (vi) physics processes such as bremsstrahlung, pair production, and multiple scattering.

For this study, the same driver and witness bunches obtained from start-to-end simulations is used as input. The entire interacting bunch contains 3×10^6 electrons, and the wire position is varied in 0.5 µm increments over the range from -20 to 20 µm with respect to the beam center. At each position, the interaction is independently simulated 10 times to ensure statistical reliability.

To reconstruct the bunch profile, secondary photons emitted within an angular range of [0,4] mrad are counted at each wire position. From the 10 simulations per step, both the mean photon count and its variance are computed.

Figure 11.23 presents the simulation results for the driver and witness couple with 200 and 30 pC and rms transverse size $\sigma_r = 4.9$ µm and 4.1 µm, respectively.

The blue curve represents the original transverse beam distribution, which is correctly reproduced by the wire scanner measurement (orange dots).

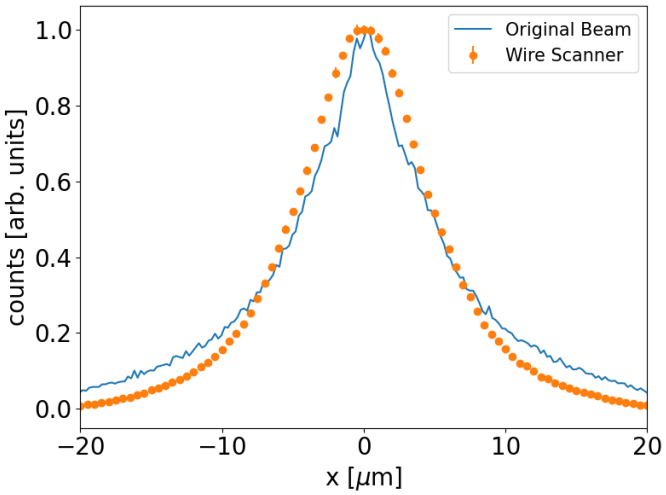

Figure 11.23: GEANT4 simulations of the wire scanner. Blue line: original transverse distribution of the driver and witness bunches from start-to-end simulations of the linac. Orange points: simulated secondary photons collected between 1 and 4 mrad with respect to the beam direction for different wire positions.

11.2.12 Beam Loss Monitors

Cherenkov radiation occurs when a charged particle travels in a dielectric medium with a velocity

$$v = c\beta > \frac{c}{n}, \tag{11.12}$$

where n is the refractive index of the material [45, 46]. Under this condition, the emitted electromagnetic waves interfere constructively, producing a coherent shockwave at an angle θ_c with respect to the particle trajectory, defined by:

$$\cos(\theta_c) = \frac{1}{\beta n}. \tag{11.13}$$

Measuring the Cherenkov angle θ_c allows the determination of the particle's velocity. The radiation is typically emitted in the ultraviolet (UV) range. A schematic of the detection principle is shown in Fig. 11.24.

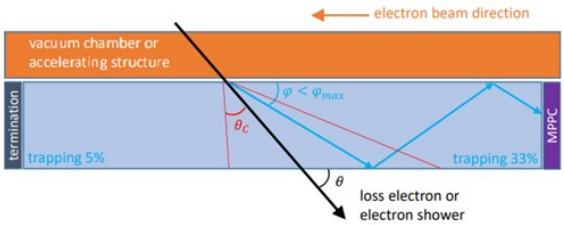

Figure 11.24: Cherenkov light produced by a lost electron is captured by an optical fiber. When the Cherenkov condition is satisfied, UV radiation propagates along the fiber under appropriate conditions.

The Cherenkov light is guided along an optical fiber composed of a core and a cladding with slightly different refractive indices ($n_{cl} < n_{co}$) [47]. Light entering the core at an angle smaller than the critical one is confined by total internal reflection and propagates toward the photodetector, as illustrated in Fig. 11.25. Otherwise, it is lost through the cladding.

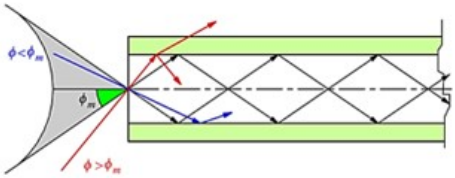

Figure 11.25: Cherenkov UV light propagates along the fiber if the incidence angle is smaller than the critical angle (blue line). Otherwise, the light is lost (red line).

The Cherenkov effect combined with an optical fiber can be exploited to construct a Beam Loss Monitor (BLM) [48]. In such a setup, an optical fiber is installed along the accelerator to detect Cherenkov photons generated by secondary electrons from beam losses. These photons are guided through the fiber and subsequently detected using a photomultiplier, which converts the optical signal into an electrical signal for acquisition and analysis.

By calculating the time of flight of Cherenkov photons, it is possible to determine the approximate position along the accelerator where a beam loss occurred [49]. A potential complication is the simultaneous detection of dark current, which must be distinguished from actual beam losses.

To locate the position of a beam loss within the accelerating structure—i.e., the point where Cherenkov light is produced—the arrival times of two signals are compared: the trigger signal from a scintillator and the Cherenkov light transmitted through the optical fiber to the photomultiplier. A schematic of this setup is shown in Fig. 11.26.

The time difference between the two signals can be expressed as:

$$\Delta t = \frac{\Delta x}{c} + \frac{n\Delta x}{c} + cst \tag{11.14}$$

where the first term corresponds to the electrons traveling in the accelerator, the second term to the photons propagating in the fiber plus constant. Solving for the distance Δx gives:

$$\Delta x = \frac{c\,\Delta t}{1+n}. \tag{11.15}$$

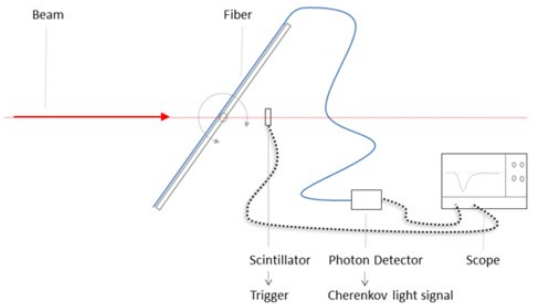

Figure 11.26: Schematic of the time-of-flight measurement setup, used to determine the location of a beam loss along the accelerator.

By measuring the Cherenkov photon time of flight relative to the trigger signal (which indicates when the electron bunch leaves the gun), the position of the beam loss can be estimated. However, since the ADC output is a sampled signal, the temporal resolution is limited by the sampling frequency. Consequently, the calculated Δx corresponds to the spatial resolution of the sampled signal, i.e., the length of the optical fiber associated with the time interval between two consecutive samples.

In our setup, the characteristics of the high-OH silica optical fiber used for Cherenkov detection are reported in Table 11.10 and illustrated in Fig. 11.27.

Table 11.10: Parameters of optical fiber.

Parameter	**Value**
nylon jacket	850 µm
polyimide buffer	370 µm
fluorine silica cladding	330 µm
high-OH silica core	300 µm
core refractive index	1.479

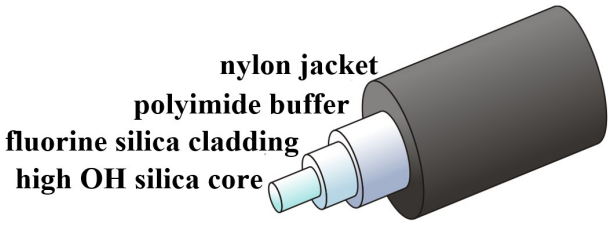

Figure 11.27: Internal structure of high-OH silica core fiber.

The electrons exiting the gun strike the optical fiber with energies of approximately 5–6 MeV. Under these conditions, the Cherenkov criterion is easily satisfied ($\beta > 0.67$).

The electronic devices described in this section are not intended as a definitive choice, but rather as examples illustrating the characteristics required for the project. The photomultiplier will consist of an array of 400 Avalanche Photodiodes (APDs) [50] connected in parallel. Each photodiode acts as an optical sensor, detecting photons at specific wavelengths and converting them

into an electrical current, often with internal amplification. Photodiodes are widely used at the end of optical fibers to generate electrical signals proportional to the incident light. In applications like the present one, they play a crucial role in converting optical signals into measurable electronic data. They are also commonly combined with scintillators, which emit light when traversed by ionizing radiation; the photodiode then converts this light into an electrical signal.

Since the incident light intensity is often low, the resulting electrical signal typically requires amplification. Thus, the photodetector may serve both as a transducer and an amplifier.

In the present application, the photomultiplier chosen is the Hamamatsu Multi-Pixel Photon Counter (MPPC). Figure 11.28 shows the sensor structure, and the relevant specifications of the photomultiplier are summarized below:

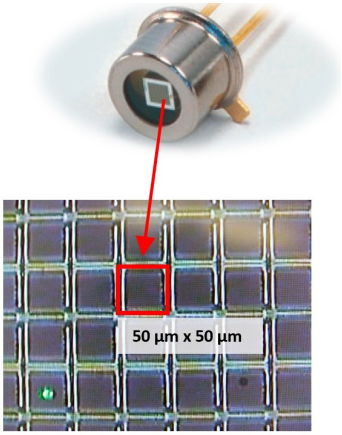

Figure 11.28: Hamamatsu MPPC sensor structure.

- Array of 400 avalanche photodiodes (APDs) in parallel
- Reverse bias (photon causes APD breakdown)
- Photomultiplier-like gain (10^5 – 10^6)
- Insensitivity to magnetic field
- Time resolution: rise time 100 ps
- Compact and Low cost

The signal amplified by the Hamamatsu MPPC then passes to a digitizer (ADC) that, in our case, is the 8-channel WaveCatcher [51] shown in the Fig. 11.29.

Figure 11.29: WaveCatcher 8-channels.

It makes use of an analog memory (SAMLONG) that allows sampling of the input signal between 400 MS/s and 3.2 GS/s at 12 bits with a bandwidth (BW) of 500 MHz. The specifications overview is reported in Tab. 11.11.

With such a sampling frequency (3.2 GS/s - 0.3125 ns/S), you would achieve a resolution of:

$$\Delta x = c\frac{\Delta t}{1+n} = 0.038\ m \sim 4\ cm \tag{11.16}$$

Table 11.11: Digitizer specifications.

Parameter	Value
sampling rate	3.2 GS/s
sample depth	12-bit
BW	0.5 GHz
memory	128 GB
cost/channel	€ 400

This information sets the minimum length of the fiber. If the fiber were indeed shorter than 4 cm, there wouldn't be enough resolution to obtain the desired information.

In the context of EuPRAXIA@SPARC_LAB, beam losses are expected to originate mainly from dark current, missteered bunches, or interactions with the vacuum chamber and diagnostics. The designed Cherenkov BLM system aims to detect localized losses corresponding to a small fraction of the nominal bunch charge, providing both timing and spatial information along the accelerating structure. Although no experimental calibration data are currently available, the estimated spatial resolution of approximately 4 cm suggests that the system will be capable of identifying the position of localized losses and discriminating them from background signals such as dark current or electronic noise.

The description of the detection flow is shown in Fig. 11.30.

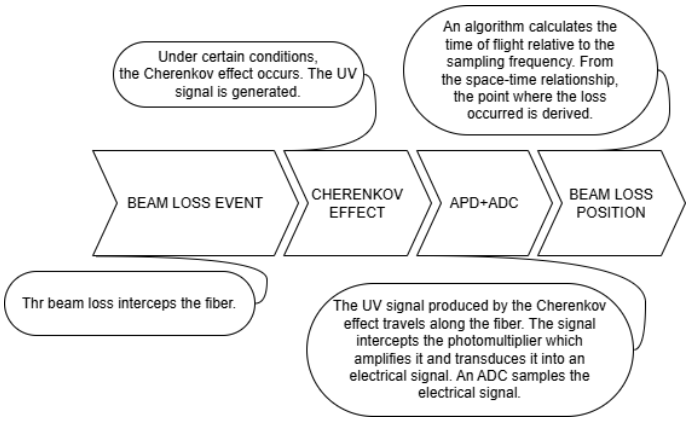

Figure 11.30: Description of the detection flow of Cherenkov BLM.

11.3 Layout integration

This chapter presents the positions of all diagnostic elements along the beamline. Figure 11.31 provides a schematic overview of the gun area. The first view screen is dedicated to laser alignment and cathode inspection. Downstream of this, a Turbo toroid is installed, followed by a second view screen and a Faraday cup, providing redundancy for charge measurements to better discriminate between bunch and dark current. The first BPM striplines are located immediately after these elements.

The location of all fundamental diagnostics are illustrated in Figures 11.32 through 11.38.

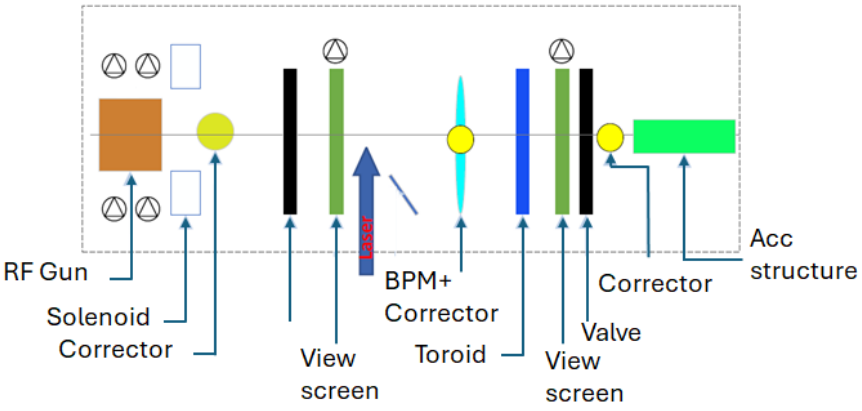

Figure 11.31: Diagnostics positions between RF gun and the first accelerating module.

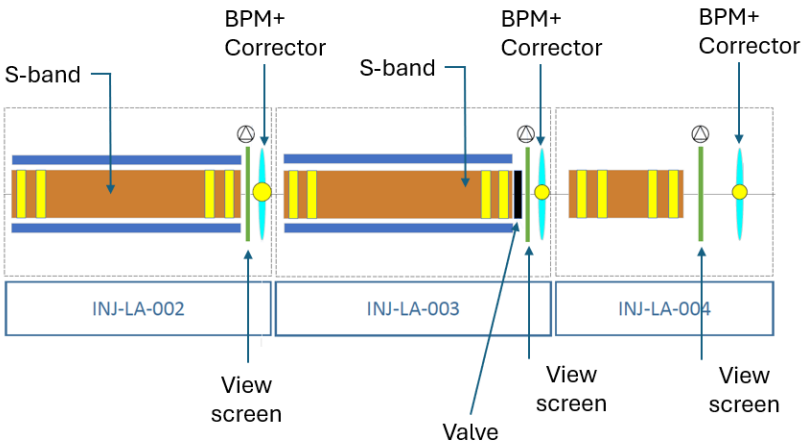

Figure 11.32: Diagnorstics positions in the injector area INJ-LA-002-003.

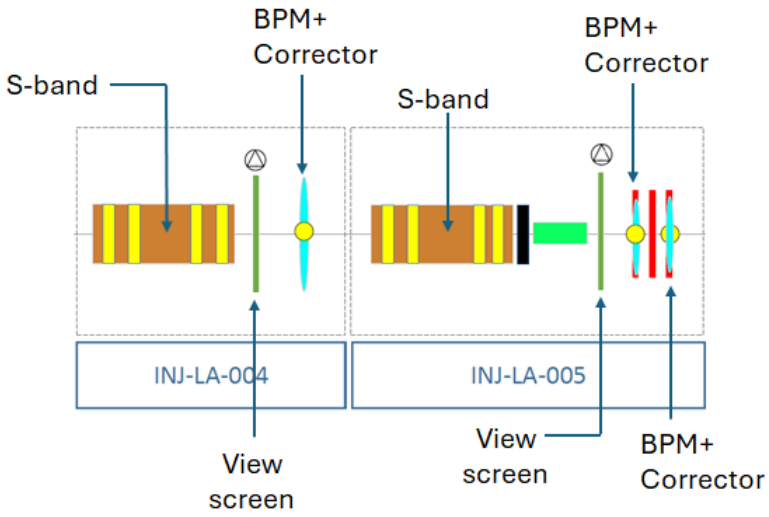

Figure 11.33: Diagnostics positions in the injector area section INJ-LA-004-005.

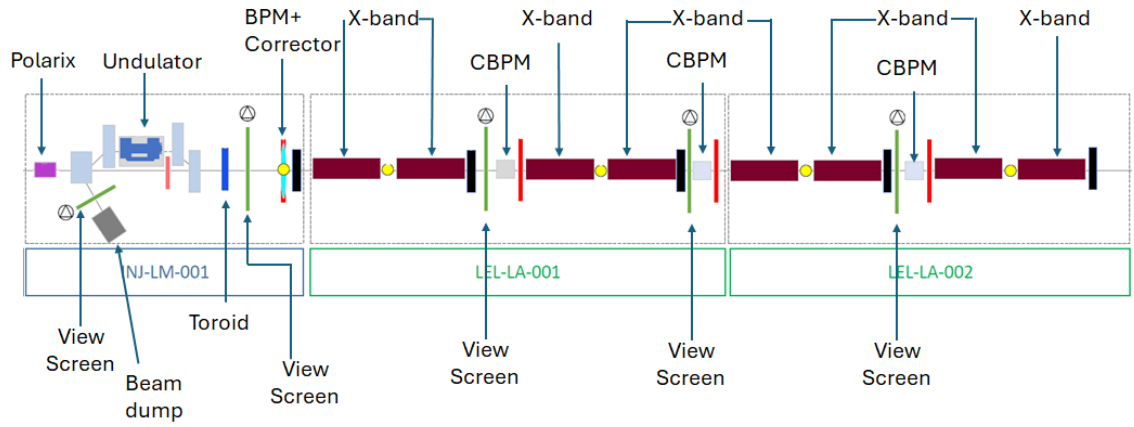

Figure 11.34: Diagnostics positions in low energy linac.

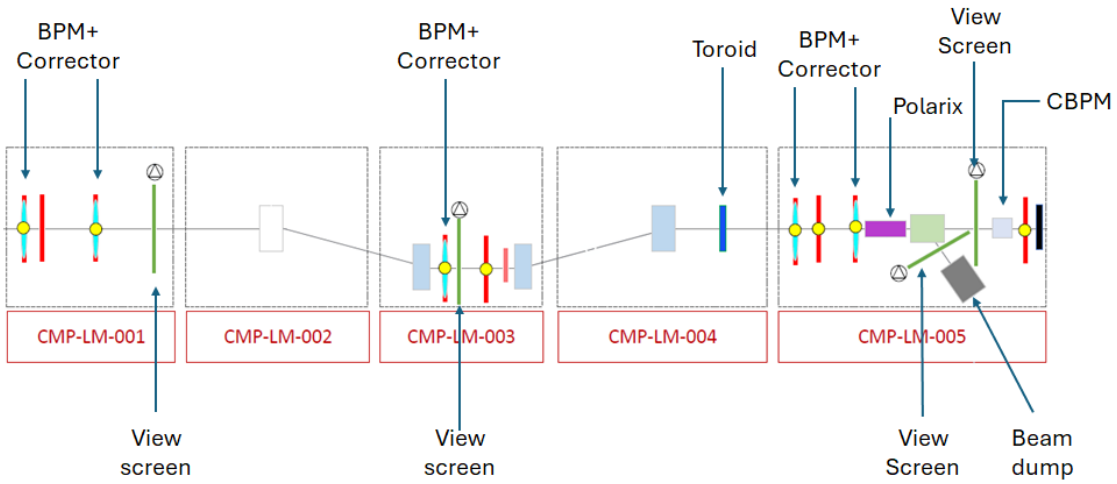

Figure 11.35: Diagnostics positions in bunch compressor

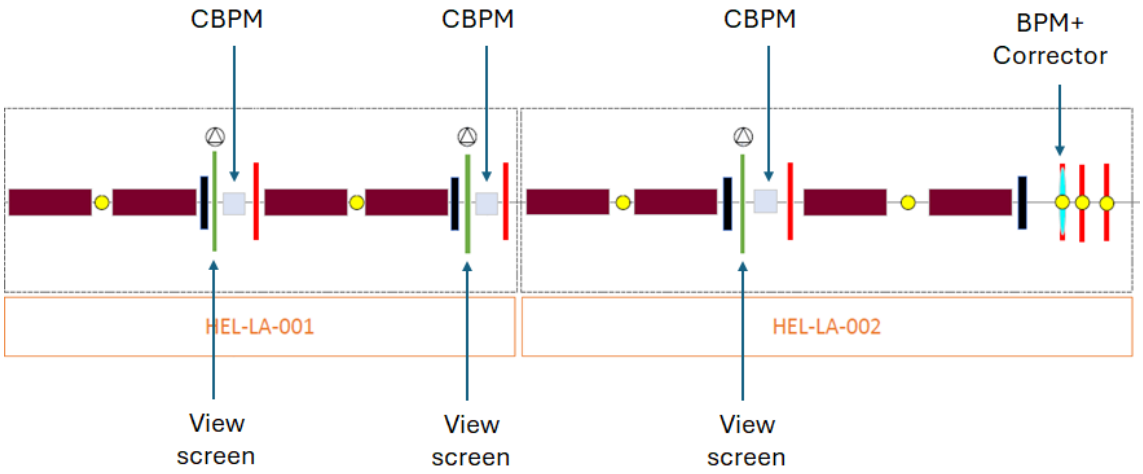

Figure 11.36: Diagnostics positions in the high energy linac.

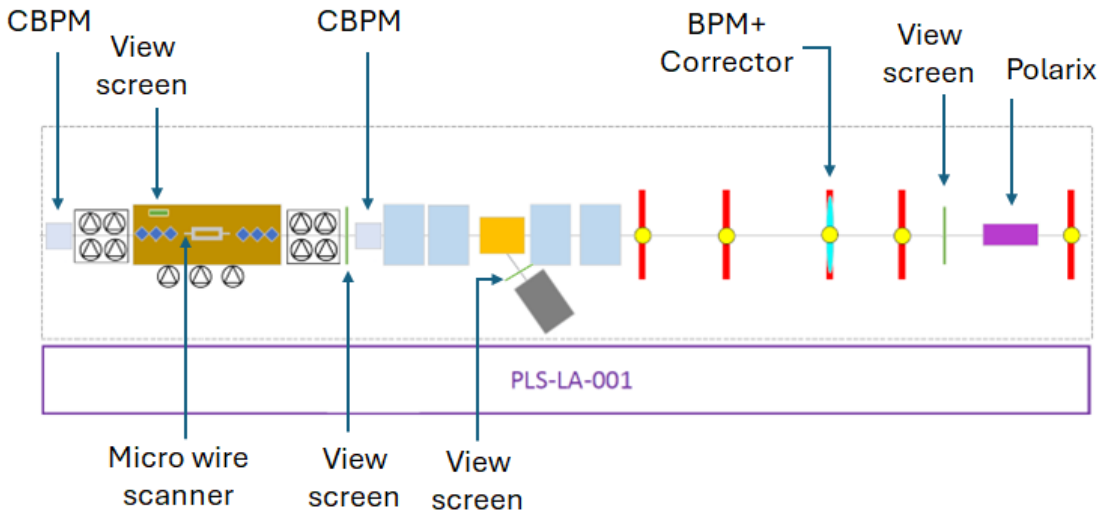

Figure 11.37: Diagnostics position in the plasma module. The view screen and the microwire scanner will be inserted in the beam line in alternation with permanent magnets and the plasma capillary, respectively.

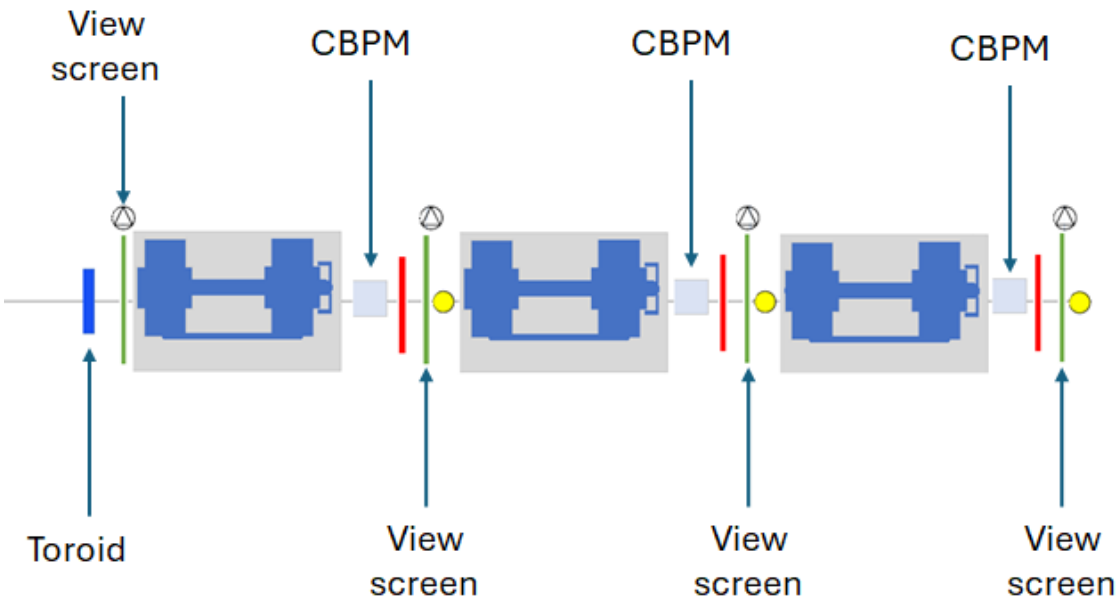

Figure 11.38: Diagnostics positions in the undulator. The lattice is equal in every undulator gap.

11.4 Technology Readiness Level and List of Elements

The Table below summarizes the Technology Readiness Level (TRL) of the components described in this Chapter.

Table 11.12: TRL level of the electron beam diagnostics

Sub - systems	TRL	Comments
Integrated Current Transformer	9	Commercially available (ICT Bergoz Instrumentation).
Faraday Cup	9	Commercially available.
Stripline BPM	7	Prototype under test at SPARC.
Cavity BPM	9	Already used at PSI.
View Screens	8	In-house design. Already used at SPARC.
Emittance Measurements	8	Quadrupole scan plus view screen.
Energy Measurement	8	Dipole plus view screen.
Transverse Deflecting Structure (PolariX)	7	One device positioned after the injector and one after the plasma.
EOS	7	Already used at SPARC.
Coherent Radiation Monitor	7	Already used in relevant beam test facilities.
Plasma Entrance Diagnostics	5	Design in the interaction chamber completed.
Beam Loss Monitors	9	Commercially available.

Table 11.13: List of electron beam diagnostics with section reference.

Diagnostics Element	Number of Items	Description
Current Monitor (ICT)	4	Sec. 11.2.1
Charge Monitor (Faraday Cup)	1	Sec. 11.2.2
Stripline BPM	14	Sec. 11.2.3
Cavity BPM	23	Sec. 11.2.4
View Screen	41	Sec. 11.2.5
Emittance Measurement Station	3	Sec. 11.2.6
Magnetic Spectrometers	3	Sec. 11.2.7
Transverse Deflecting Structures	2	Sec. 11.2.8
Electro-Optical Sampling	1	Sec. 11.2.9
Coherent Radiation Monitor	1	Sec. 11.2.10
Wire Scanner	1	Sec. 11.2.11.2
Beam Loss Monitor System	1	Sec. 11.2.12

11.5 Artificial Intelligence

Particle accelerators are complex systems composed of numerous sensitive components, requiring comprehensive diagnostic tools to determine beam parameters. Traditional measurements, such as beam size, emittance, and energy, are invasive and can interrupt operations.

To overcome these limitations, virtualized diagnostics based on simulations and machine learning (ML) are increasingly used. Simulation-based approaches rely on computational complexity, whereas ML models, such as Feedforward Neural Networks (FNNs) and Recurrent Neural Networks (RNNs), provide near-instantaneous predictions, with accuracy determined by the quality of the training data and the model architecture. Hybrid approaches combining simulation and ML can further enhance predictions. Recent applications at SLAC have demonstrated that neural networks can efficiently and non-invasively predict electron beam properties on accelerators such as LCLS, LCLS-II, and FACET-II [52–54].

Neural networks consist of interconnected artificial neurons with weights, biases, and activation functions. FNNs process information in a single direction, making them suitable for predicting parameters such as emittance, energy, or beam size. In contrast, RNNs retain memory of previous inputs, allowing for trajectory prediction from BPM data. Convolutional networks can predict beam images, and autoencoders reduce data dimensionality to optimize training.

It is essential to emphasize that virtualized diagnostics do not replace traditional diagnostic instruments and techniques, but rather serve as complementary support. They provide rapid measurements and predictions that integrate experimental data, enabling optimization of operations and reducing downtime without eliminating the need for conventional diagnostics.

These virtualized diagnostics, therefore, enable fast, non-invasive measurements, reducing downtime and allowing the exploration of new operational configurations in parallel with ongoing experimental activities, thereby supporting the goals of EuPRAXIA@SPARC_LAB.

11.6 Conclusions

The diagnostic systems implemented for EuPRAXIA@SPARC_LAB satisfy the performance requirements for commissioning and routine operation of the facility. They ensure comprehensive, high-resolution monitoring of all critical beam parameters and provide real-time feedback, which is essential for stable FEL user operation. Within current technological limits, these systems meet the design objectives and will be progressively optimized during commissioning to achieve the required performance.

Bibliography

[1] Bergoz Instrumentation. *Integrating Current Transformer (ICT)*. Tech. rep. 06.1. 2006.

[2] Bergoz Instrumentation. *Turbo-ICT& BCM-RF–E", User's Manual*. Tech. rep. Rev.3.1.

[3] Instrumentation Technologies. *Libera Single Pass E User Manual*. Tech. rep. Rev.1.04.

[4] T. Shintake. "Development of nanometer resolution RF-BPMs". In: *Proceedings of HEAC'99*. 1999, pp. 341–345.

[5] B. Keil et al. "Status of the SwissFEL BPM system". In: *Proceedings of IBIC2015*. 2015, pp. 497–501.

[6] Instrumentation Technologies. *Libera CavityBPM User Manual and Specifications*. Tech. rep. Rev.1.01.

[7] G. Franzini. *Studies and measurements on Cavity Beam Position Monitors for Novel Electron LINACS*. PhD Thesis on IRIS. 2020. URL: https://hdl.handle.net/11573/1357175.

[8] R. Akre et al. "Commissioning the linac coherent light source injector". In: *Physical Review Special Topics—Accelerators and Beams* 11.3 (2008), p. 030703.

[9] R. Ischebeck et al. "Transverse profile imager for ultrabright electron beams". In: *Physical Review Special Topics—Accelerators and Beams* 18.8 (2015), p. 082802.

[10] S. Matsubara et al. "Improvement of screen monitor with suppression of coherent-OTR effect for SACLA". In: *Proc. 1st Int. Beam Instrumentation Conf.(IBIC'12)*. 2012, pp. 34–37.

[11] R. Ischebeck et al. "Profile Monitors for the SwissFEL Injector Test Facility". In: *Linear Accelerator Conference LINAC2010* (Tsukuba, Japan). JACoW Publishing, Geneva, Switzerland, 2010.

[12] E. Chiadroni et al. "High Energy Emittance Measurement at SPARC". In: *Proceedings of the DIPAC 2009* (2009), pp. 402–404.

[13] A. Cianchi et al. "Six-dimensional measurements of trains of high brightness electron bunches". In: *Physical Review Special Topics—Accelerators and Beams* 18.8 (2015), p. 082804.

[14] L. Serafini et al. "Plasma Acceleration Experiment at SPARCLAB with External Injection". In: *Proc. IPAC'12* (New Orleans, LA, USA, May 2012). JACoW Publishing, Geneva, Switzerland, pp. 2169–2171. URL: https://jacow.org/IPAC2012/papers/WEEPPB002.pdf.

[15] F. Sannibale and M. Vescovi. *Linac to Accumulator Area Transfer Line (LAAT) & DAΦNE Linac Spectrometer DLS.* DAΦNE Technical Note LC-3. INFN-LNF, 1992.

[16] K. Techakaew, K. Kongmali, and S. Rimjaem. "Electron Energy Spectrometer for MIR-THz FEL Light Source at Chiang Mai University". In: *Particles* 6.3 (2023), pp. 703–712. DOI: https://doi.org/10.3390/particles6030043.

[17] S. Kasaei et al. "Spectrometer design for diagnostics in a wide range of energy at a linear accelerator". In: *Journal of Instrumentation* 13.06 (2018), P06021. DOI: https://doi.org/10.1088/1748-0221/13/06/P06021.

[18] J. O. Deasy et al. "A simple magnetic spectrometer for radiotherapy electron beams". In: *Medical Physics* 21.11 (1994), pp. 1703–1714. DOI: https://doi.org/10.1118/1.597271.

[19] F. Méot. *Understanding the Physics of Particle Accelerators*. Springer Nature, 2024, pp. 567–604. DOI: https://doi.org/10.1007/978-3-031-59979-8.

[20] J. Seeman. "Energy Measurement with Electron Beams". In: *Handbook of Accelerator Physics and Engineering*. Singapore: World Scientific, 1999. DOI: https://doi.org/10.1142/8543.

[21] R. Kingslake. *Optics in Photography*. SPIE Optical Engineering Press, 1992. DOI: https://doi.org/10.1117/3.43160.

[22] D. Quartullo et al. "Design of spectrometer energy measurement setups for the future EuPRAXIA@SPARC_LAB and SSRIP linacs". In: *Instruments* (2026). in press, paper accepted on 13/12/25.

[23] P. Craievich et al. "The Polarix-TDS Project: bead pull measurements and high power test on the prototype". In: *Proceedings of FEL*. 2019, pp. 396–399.

[24] B. Marchetti et al. "X-band TDS project". In: *Proc. IPAC'17* (2017), pp. 184–187.

[25] P. Craievich et al. "Novel X-band transverse deflection structure with variable polarization". In: *Physical review accelerators and beams* 23.11 (2020), p. 112001.

[26] B. Marchetti et al. "Experimental demonstration of novel beam characterization using a polarizable X-band transverse deflection structure". In: *Scientific reports* 11.1 (2021), p. 3560.

[27] A. Grudiev. *Design of compact high power rf components at x-band*. Tech. rep. 2016.

[28] S. Jaster-Merz et al. "5D phase-space reconstruction of an electron beam". In: *Proc. IPAC* 23 (), pp. 2566–2569.

[29] D. Marx et al. *Characterization of ultrashort electron bunches at the sinbad-ares linac*. Tech. rep. Deutsches Elektronen-Synchrotron Hamburg, Germany, 2019.

[30] S. Jaster-Merz et al. "5D tomographic phase-space reconstruction of particle bunches". In: *arXiv preprint arXiv:2305.03538* (2023).

[31] K. M. Hock and A. Wolski. "Tomographic reconstruction of the full 4D transverse phase space". In: *Nuclear Instruments and Methods in Physics Research Section A: Accelerators, Spectrometers, Detectors and Associated Equipment* 726 (2013), pp. 8–16.

[32] R. Pompili et al. "Femtosecond timing-jitter between photo-cathode laser and ultra-short electron bunches by means of hybrid compression". In: *New Journal of Physics* 18.8 (2016), p. 083033.

[33] F. Demurtas et al. "Experimental characterization of the timing-jitter effects on a beam-driven plasma wakefield accelerator". English. In: *Proc. IPAC'24* (Nashville, TN). IPAC'24 - 15th International Particle Accelerator Conference 15. JACoW Publishing, Geneva, Switzerland, May 2024, pp. 553–556. ISBN: 978-3-95450-247-9. DOI: 10.18429/JACoW-IPAC2024-MOPR43. URL: https://indico.jacow.org/event/63/contributions/3619.

[34] R. Pompili et al. "First single-shot and non-intercepting longitudinal bunch diagnostics for comb-like beam by means of electro-optic sampling". In: *Nuclear Instruments and Methods in Physics Research Section A: Accelerators, Spectrometers, Detectors and Associated Equipment* 740 (2014), pp. 216–221.

[35] R. Pompili et al. "Sub-picosecond snapshots of fast electrons from high intensity laser-matter interactions". In: *Optics Express* 24.26 (2016), pp. 29512–29520.

[36] M. Galletti et al. “Direct visualization of relativistic Coulomb field in the near and far field ranges”. In: *New Journal of Physics* 25.6 (2023), p. 063014.

[37] E. Chiadroni. “Bunch Length Characterization at the TTF VUV-FEL”. In: *PhD thesis, Università degli Studi di Roma Tor Vergata* (2005).

[38] J. D. Jackson. *Classical Electrodynamics*. John Wiley & Sons, 1962.

[39] M. Castellano and V. A. Verzilov. “Spatial resolution in optical transition radiation beam diagnostics”. In: *Phys. Rev. ST Accel. Beams* 1 (6 1998), p. 062801. DOI: 10.1103/PhysRevSTAB.1.062801. URL: https://link.aps.org/doi/10.1103/PhysRevSTAB.1.062801.

[40] B. Allen et al. “Experimental Study of Current Filamentation Instability”. In: *Phys. Rev. Lett.* 109 (18 2012), p. 185007. DOI: 10.1103/PhysRevLett.109.185007. URL: https://link.aps.org/doi/10.1103/PhysRevLett.109.185007.

[41] G. L. Orlandi et al. “Design and experimental tests of free electron laser wire scanners”. In: *Phys. Rev. Accel. Beams* 19 (9 2016), p. 092802. DOI: 10.1103/PhysRevAccelBeams.19.092802. URL: https://link.aps.org/doi/10.1103/PhysRevAccelBeams.19.092802.

[42] G. L. Orlandi et al. “Nanofabricated free-standing wire scanners for beam diagnostics with submicrometer resolution”. In: *Phys. Rev. Accel. Beams* 23 (4 2020), p. 042802. DOI: 10.1103/PhysRevAccelBeams.23.042802. URL: https://link.aps.org/doi/10.1103/PhysRevAccelBeams.23.042802.

[43] S. Borrelli et al. “Generation and measurement of sub-micrometer relativistic electron beams”. In: *Communications Physics* 1.1 (2018), p. 52. DOI: 10.1038/s42005-018-0048-x. URL: https://doi.org/10.1038/s42005-018-0048-x.

[44] S. Agostinelli et al. “Geant4-a simulation toolkit”. In: *Nuclear Instruments and Methods in Physics Research Section A: Accelerators, Spectrometers, Detectors and Associated Equipment* 506.3 (2003), pp. 250–303. ISSN: 0168-9002. DOI: https://doi.org/10.1016/S0168-9002(03)01368-8. URL: https://www.sciencedirect.com/science/article/pii/S0168900203013688.

[45] P. A. Cherenkov. “Visible luminescence of pure liquids under the influence of γ-radiation”. In: *Dokl. Akad. Nauk SSSR* 2.8 (1934), pp. 451–454. DOI: 10.3367/UFNr.0093.196710n.0385.

[46] I. M. Frank and I. E. Tamm. “Coherent visible radiation of fast electrons passing through matter”. In: *Compt. Rend. Acad. Sci. URSS* 14.3 (1937). Ed. by V. L. Ginzburg, B. M. Bolotovsky, and I. M. Dremin, pp. 109–114. DOI: 10.3367/UFNr.0093.196710o.0388.

[47] S. Pioli. *Advanced beam protection systems for high-brightness electron-beam and linac-based Compton sources*. Tech. rep. Frascati National Laboratories of INFN, Italy, 2019.

[48] M. Kastriotou et al. “A Versatile Beam Loss Monitoring System for CLIC”. In: *7th International Particle Accelerator Conference*. 2016, MOPMR024. DOI: 10.18429/JACoW-IPAC2016-MOPMR024.

[49] E. Nebot Del Busto et al. “Position Resolution of Optical Fibre-Based Beam Loss Monitors Using Long Electron Pulses”. In: *4th International Beam Instrumentation Conference*. 2016, WEBLA03. DOI: 10.18429/JACoW-IBIC2015-WEBLA03.

[50] R. Paschotta. *Avalanche Photodiodes*. RP Photonics Encyclopedia. DOI: 10.61835/pbn. URL: https://www.rp-photonics.com/avalanche_photodiodes.html (visited on 05/23/2024).

[51] D. Breton and J. Maalmi. *WaveCatcher Family User's Manual*. URL: https://www.hep.ucl.ac.uk/pbt/wikiData/manuals/WaveCatcher/WaveCatcherFamily_V1.2.pdf.

[52] A. Hanuka et al. "New machine learning tool diagnoses electron beams in an efficient, non-invasive way". In: *Scientific Reports (SLAC National Accelerator Laboratory press)* (2021). Demonstrated ML-based virtual diagnostics at LCLS, LCLS-II and FACET-II. URL: https://www6.slac.stanford.edu/news/2021-03-24-new-machine-learning-tool-diagnoses-electron-beams-efficient-non-invasive-way.

[53] C. Emma et al. "Machine learning–based longitudinal phase space prediction of particle accelerators". In: *Physical Review Accelerators and Beams* 21 (2018), p. 112802. DOI: 10.1103/PhysRevAccelBeams.21.112802.

[54] R. Roussel et al. "ML-assisted beamline optimization and hybrid modeling for accelerator control". In: *Proceedings of ICALEPCS 2025*. Examples of machine learning techniques applied to accelerator optimization at SLAC. 2025. DOI: 10.18429/JACoW-ICALEPCS2025-WESV001.

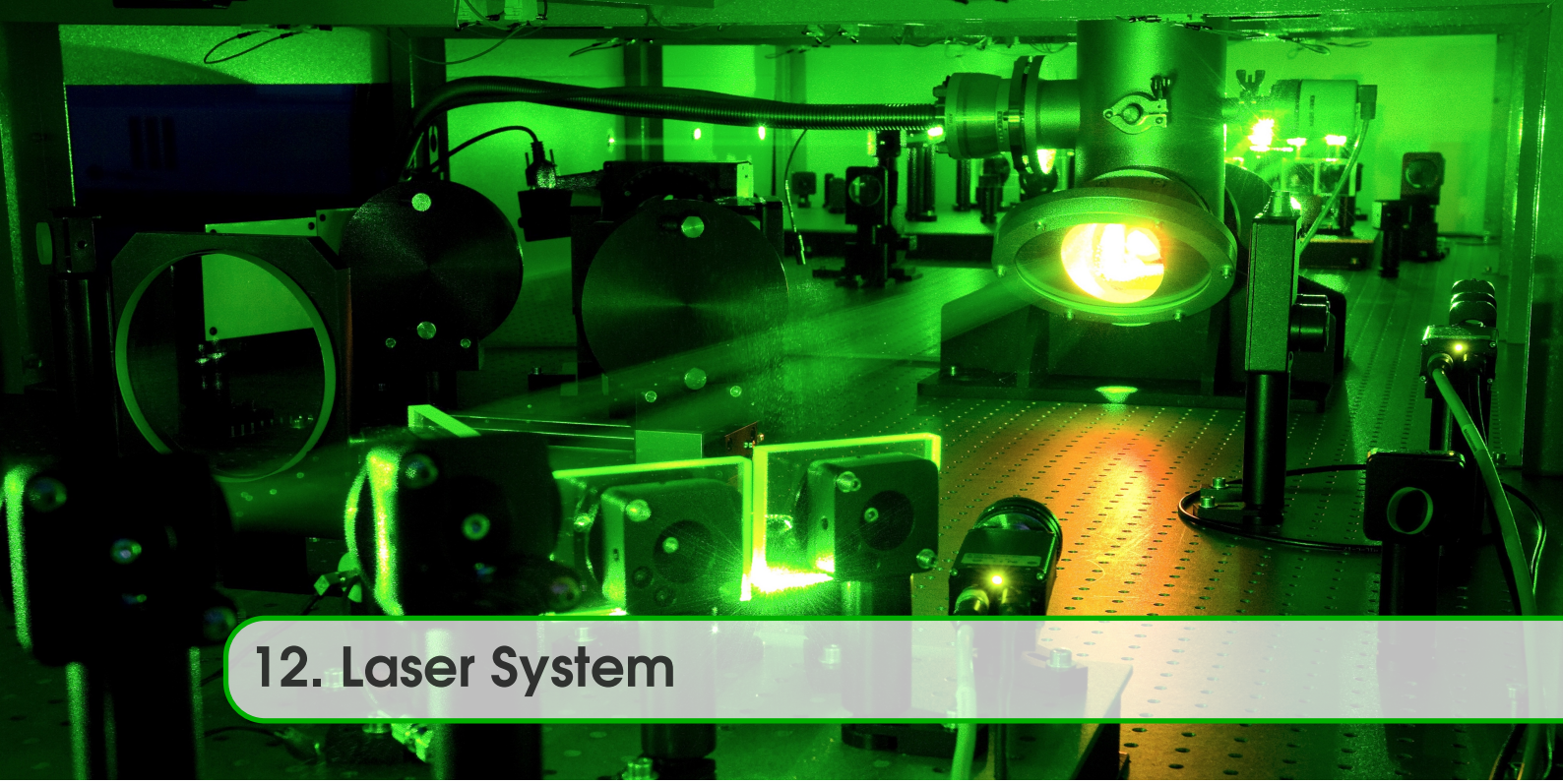

12. Laser System

12.1 Introduction

A central component of this project is the photocathode laser system, which plays a crucial role in generating high-brightness electron beams. Three additional laser systems are distributed along the linac and at the user experimental area.

This chapter provides a comprehensive overview of the photocathode laser system (Sec. 12.2), covering its design principles, implementation, and optimization strategies. We discuss the system specifications, the development process, and the improvements achieved through dedicated research and development efforts. Furthermore, we outline the rationale behind the selection of other laser systems (Sec. 12.3) employed for the laser heater and for user pump-probe experiments (Sec. 12.4). The focus is on tailoring the systems to meet the performance objectives of EuPRAXIA@SPARC_-LAB.

12.2 The Photocathode Laser

The performance of the photocathode laser system directly determines the quality and stability of the electron beam. For this reason, the system must satisfy strict requirements in terms of energy stability, beam uniformity, and pulse shaping. The following sections describe the system specifications and the design solutions adopted to meet these demands.

12.2.1 Location and Infrastructure

The photocathode laser system is strategically located to ensure optimal integration with the accelerator.

Laser Room: Situated at the same level as the LINAC (see Fig. 12.1a).

Rack Room: Located on the upper floor, close to the control room (see Fig. 12.1b).

The laser beam is transported from the cleanroom to the cathode via trenches, as shown in Fig. 12.2, where the laser transport line is highlighted in orange. The beam is guided beneath the floor to an optical table positioned close to the cathode.

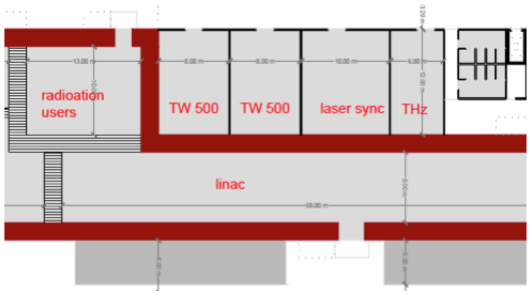

(a) Ground floor layout showing the room for the photocathode/synch laser.

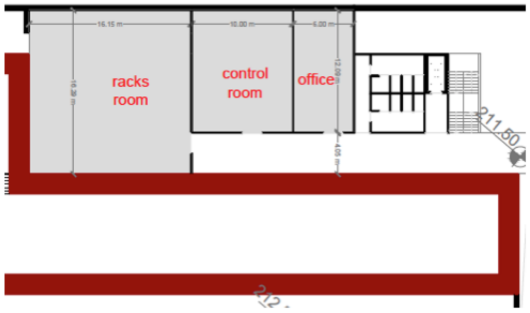

(b) Upper floor layout showing the racks for the photocathode/synch laser.

Figure 12.1: Overall layout of the laser rooms.

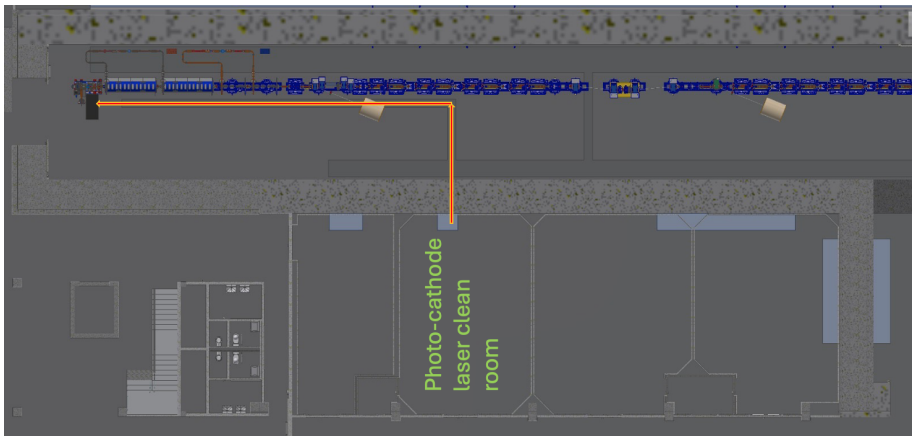

Figure 12.2: Transport beamline from cleanroom to cathode.

The optical transport from the laser room to the experimental chamber is carefully designed to minimize beam jitter in position and size, taking into account propagation distance and source pointing stability. All transport paths are fully enclosed to reduce disturbances caused by air currents, acoustic noise, and thermal gradients, while also ensuring compliance with safety regulations. Enclosures further mitigate temporal jitter induced by air fluctuations and enhance long-term stability.

Dedicated diagnostics (Sec. 12.2.9) are installed at key points along the transport line to continuously monitor spatial and temporal jitter. Real-time measurement of pulse arrival time and pulse profile enable active feedback and prompt correction when necessary. Comprehensive remote monitoring and automated control systems are employed to maintain optimal alignment and performance.

Near the gun area, a periscope raises the beam to the machine height on the optical table, where

it is further manipulated, characterized, and finally directed onto the cathode.

12.2.2 Laser Requirements

For the COMB scheme - where multiple electron bunches are injected into the plasma to establish a resonant acceleration mechanism - the laser system must satisfy the following requirements:

- **Multiple beam overlap:** the system must produce n laser pulses overlapping in space.
- **Variable spot sizes:** each pulse should have a tunable diameter.
- **Temporal flexibility:** each laser pulse must have an individually adjustable duration.
- **Transverse homogeneity:** each pulse profile must be highly uniform, with peak-to-peak variations below 10%.
- **High energy stability:** the system must maintain energy stability better than 1% to ensure reproducible electron beam generation.

12.2.3 Photocathode Laser Subsystems

The photocathode laser system is based on a Chirped Pulse Amplification (CPA) architecture and consists of the following elements:

- An ultrashort (15 fs), large-bandwidth oscillator operating at 71.39 MHz repetition rate (European S-band/42).
- A booster amplifier to increase the pulse energy and reduce the repetition rate from 71.39 MHz to 1 kHz.
- A stretcher to transform the short pulse into a temporally stretched, chirped pulse.
- A regenerative amplifier to increase the pulse energy from the nJ to the mJ level while reducing the repetition rate from 1 kHz to 100 Hz.
- One or two multipass amplifiers to further increase the pulse energy from the mJ up to 100 mJ.
- A compressor to compress the pulse duration back to the femtosecond regime (down to a minimum of 35 fs).
- A third harmonic generator to convert the wavelength from 800 nm to 266 nm.
- A UV stretcher to allow easy switching between short and long pulse durations depending on LINAC operational requirements.

The maximum UV energy delivered to the cathode is approximately 2 mJ, which can be attenuated down to a few µJ using an optical attenuator, allowing exploration of a wide range of laser/electron energies.

12.2.4 Example of a Commercial IR Laser System

A commercially available laser capable of meeting the required repetition rate and pulse energy is illustrated in Fig. 12.3.

The system parameters are as follows:

- Repetition rate: 100 Hz
- Energy per pulse (after compression): 100 mJ
- Pulse duration: $\geq$35 fs
- Central wavelength: 800 nm
- Energy stability: 0.5% (IR) and $<$1% (UV)

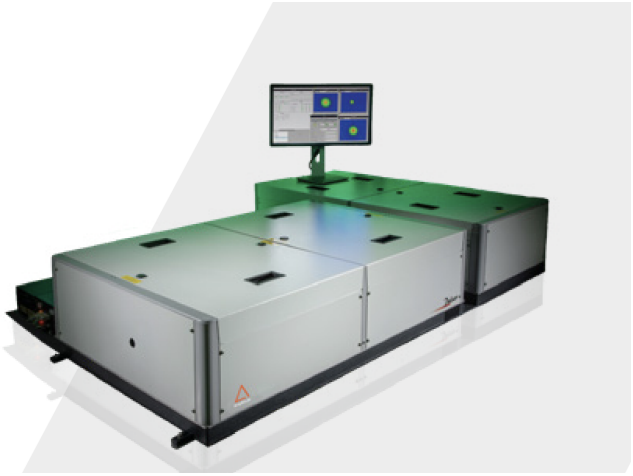

Figure 12.3: Commercial IR laser system suitable for photocathode applications.

12.2.5 Laser Layout after Pulse Compression

The schematic of the laser chain after compression is shown in Fig. 12.4.

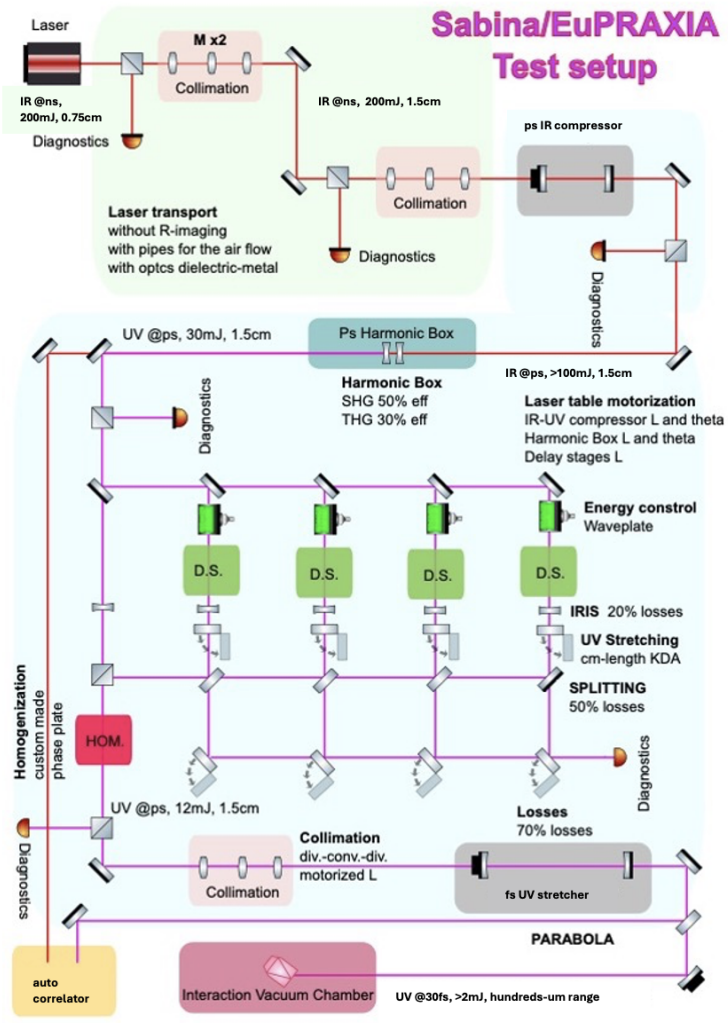

Figure 12.4: Schematic of the laser chain after compression.

This configuration has already been tested within the SABINA (Source of Advanced Beam Imaging for Novel Applications) project [1], in which the SPARC photocathode laser was upgraded and characterized. The schematic illustrates the beamline diagnostics, the third harmonic generator, and several delay lines, allowing the main pulse to be divided into up to four separate pulses. To satisfy LINAC operational requirements and maximize flexibility at the cathode, each pulse is individually manipulated. Specifically, each laser delay line is equipped with:

- A waveplate coupled to the polarizing beam splitter for controlling pulse energy.
- A delay stage to adjust the beam arrival time at the cathode.
- An iris to set the transverse beam size at the cathode.
- A dispersive material (e.g., KDA crystals) to control the pulse duration.

Finally, all pulses are recombined, homogenized, collimated, and directed to a UV compressor and an off-axis parabola for focusing onto the cathode.

12.2.6 Transverse Beam Profile on the Cathode

Within the SABINA project, a new photocathode laser for SPARC was procured and fully characterized. The specifications defined for the SABINA tender procurement are identical to those for EuPRAXIA@SPARC_LAB, making SABINA an effective test bench for the laser system. The only distinction concerns the repetition rate, which increases from 10 Hz to 100 Hz.

A key requirement is the transverse profile of the laser, which had to exhibit high uniformity (peak-to-peak variation $<10\%$) and energy stability (better than 1% in the IR).

12.2.6.1 Peak-to-peak uniformity

To ensure maximum peak-to-peak uniformity, the supplier has to measure the transverse beam profile over rectangular regions rotated in 30° increments, resulting in six independent measurements, as shown in Fig. 12.5. Within each region, a peak-to-peak variation below 10% is required. This criterion guarantees the absence of localized intensity depressions or hot spots within the beam, which could otherwise produce a non-uniform photoemission and degrade the electron bunch quality at the cathode.

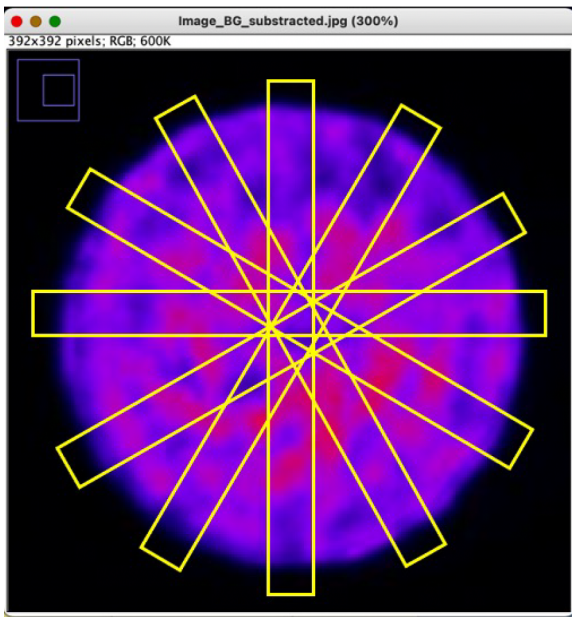

Figure 12.5: Transverse uniformity requirement of the laser beam.

Fig. 12.6 shows the measured transverse beam profile of the photocathode laser installed at

SPARC_LAB, obtained during the site acceptance test conducted within the SABINA project. The measured profile demonstrates excellent uniformity, fully meeting the requirements defined for both the SABINA and EuPRAXIA@SPARC_LAB projects.

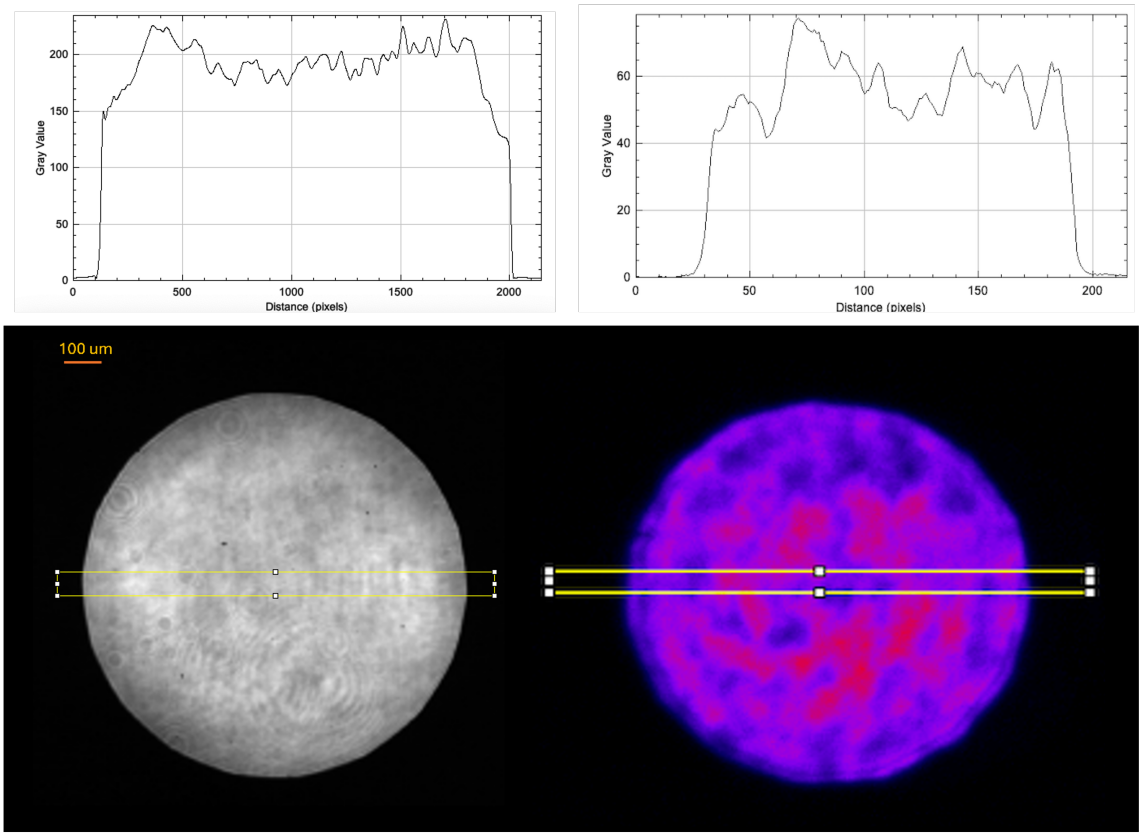

Figure 12.6: Measured transverse profile of the laser beam (IR left, UV right).

12.2.6.2 Energy Stability

To achieve energy stability better than 1%, the SABINA laser manufacturer (Amplitude) adopted a configuration featuring four pump lasers within the main IR amplifier. This design enhances the energy supply uniformity and improves pumping efficiency. Furthermore, a Diffractive Optical Element installed at the pump exit homogenizes the beam profile, ensuring uniform energy distribution across the crystal. This approach minimizes thermal gradients, mitigates optical distortions, and increases amplification stability. As a result, the final pulse energy stability after compression is maintained below 1%.

12.2.7 Estimation of Energy Losses

A schematic representation of the estimated energy losses is shown in Fig. 12.7.

Energy losses throughout the laser system arise from several processes, as listed below:

- Harmonic conversion.
- Splitting into multiple (n) pulses.
- Recombination of the n pulses overlapping in space.
- Collimation and propagation.

Two distinct scenarios are considered:

- Multiple pulses with identical pulse durations.
- Multiple pulses with individually optimized pulse durations.

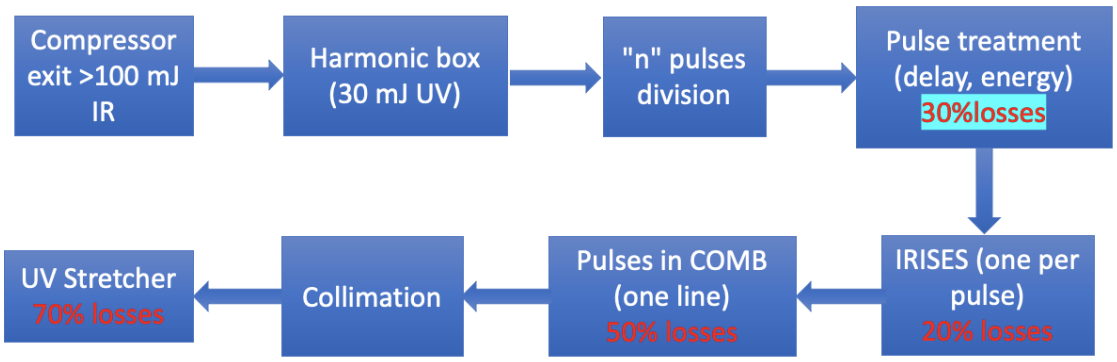

Figure 12.7: Estimated energy losses throughout the laser system.

In the first scenario, the total energy at the cathode (distributed among n pulses) is approximately 2.5 mJ, which is well above the maximum energy required for operation. In the second scenario, additional losses occur due to the dispersive material used to adjust the pulse duration, leading to an extra 30% energy reduction. Consequently, the total energy at the cathode is about 1.75 mJ, which remains sufficient for operational requirements and will be distributed among the n pulses.

12.2.8 Final Scheme of the Laser Systems

Figure 12.8 presents a simplified schematic of the overall laser chain.

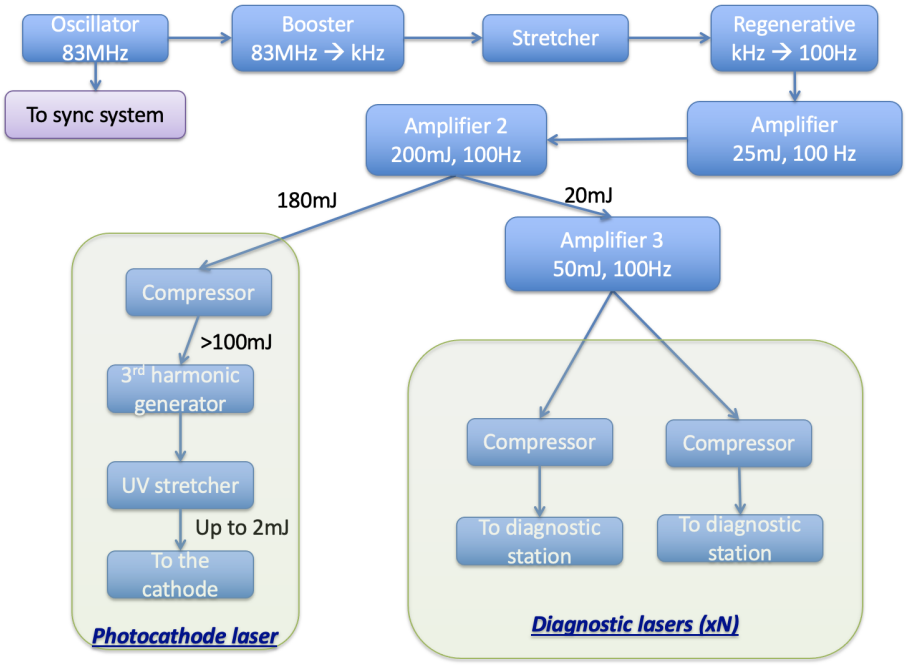

Figure 12.8: Simplified schematic of the complete laser systems.

As illustrated, a fraction of the oscillator output is split and directed to the synchronization system, which ensures precise temporal alignment between electron bunches and the various laser beamlines. Additional details on the timing and synchronization systems are provided in Chapter 14.

12.2.9 Laser Diagnostics

The complete laser characterization system is installed on the optical table positioned near the gun, as shown in Fig. 12.9.

Figures 12.10 and 12.11 illustrate the layout of the diagnostics system, which is fully described in this section.

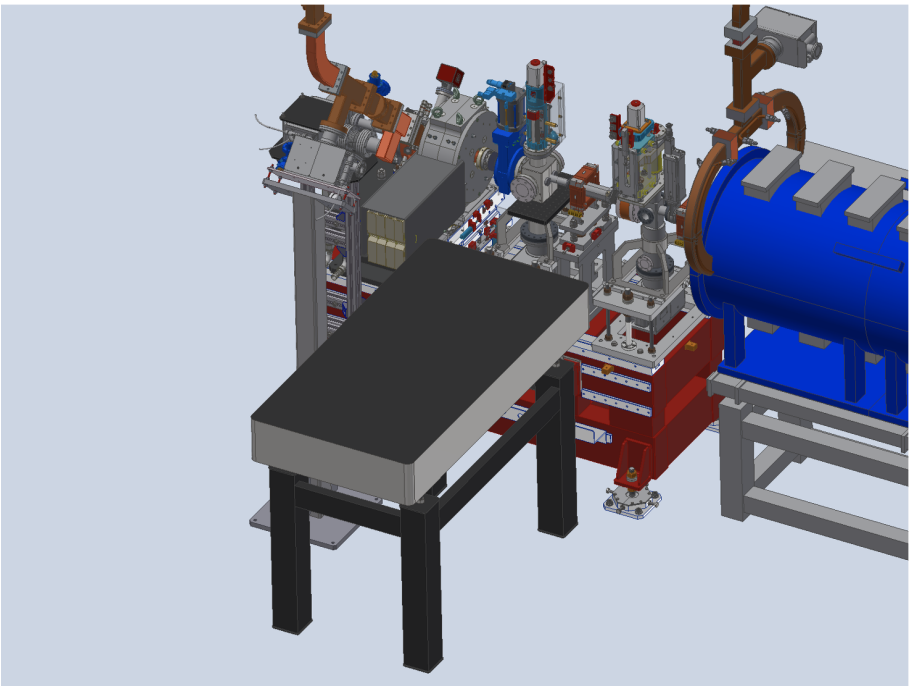

Figure 12.9: Side view of the gun with the optical table for laser diagnostics.

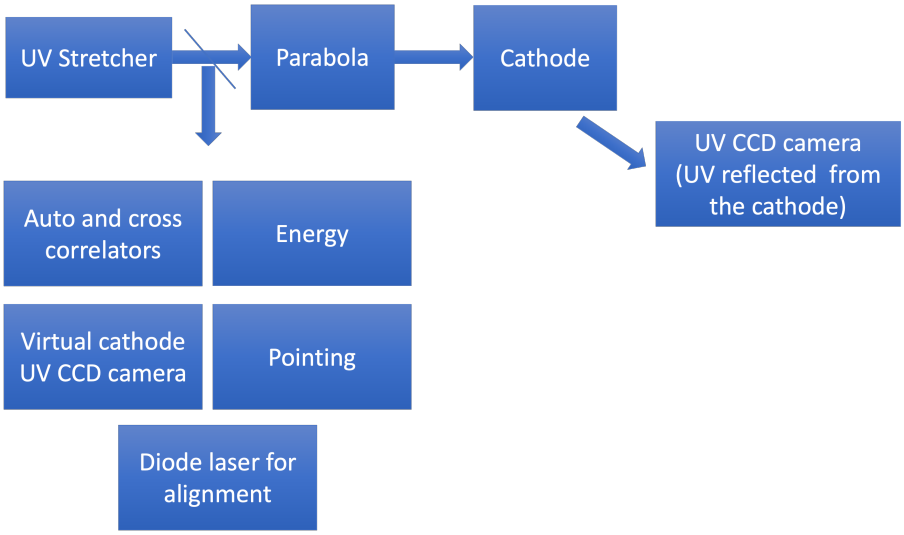

Figure 12.10: Schematic of the laser diagnostics installed on the optical table near the cathode.

The temporal characterization of the laser pulses is performed using autocorrelation and cross-correlation techniques. The 800 nm pulse is first analyzed with an autocorrelator, which measures the pulse duration by overlapping two replicas of the same pulse with a variable delay. The resulting autocorrelation trace provides the temporal profile and Full Width at Half Maximum (FWHM) of

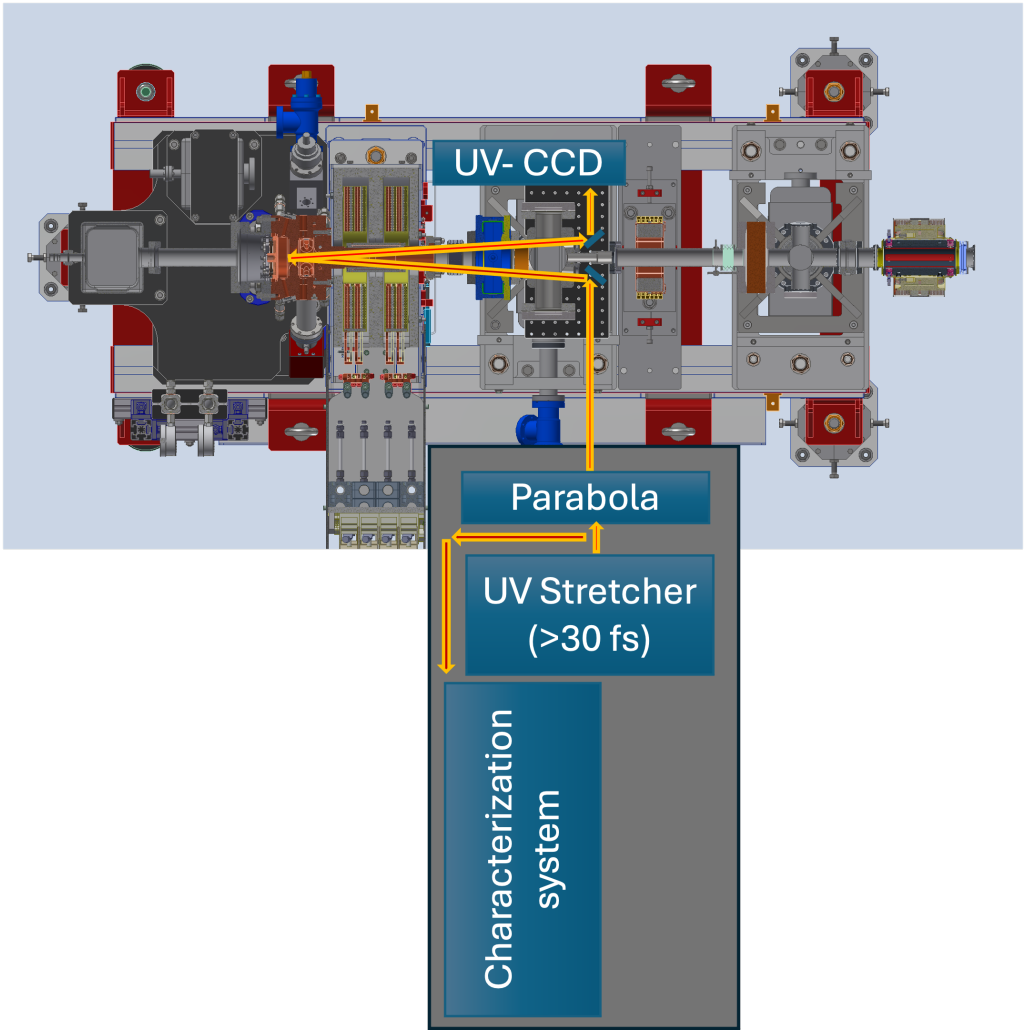

Figure 12.11: Top view of the gun and associated diagnostics.

the pulse.

The 266 nm pulse, generated as the third harmonic of the 800 nm pulse, is then characterized through cross-correlation with the fundamental pulse. The cross-correlator measures the relative delay between the two pulses, yielding a correlation trace from which the UV pulse duration is derived. Together, these measurements provide accurate information on the longitudinal pulse structure and timing.

The transverse beam profile is obtained using a UV-sensitive camera. The UV beam is directed onto the copper cathode, where the iris pattern is imaged. Part of the reflected beam, carrying the spatial imprint, is relayed on the camera to obtain an accurate reconstruction of the transverse intensity distribution. A uniform transverse profile indicates proper focusing and energy homogeneity, while irregularities may signal optical aberrations, damage, or misalignment.

The energy per pulse is monitored with a photodiode measuring the small fraction of the pulse transmitted by the mirrors. A pyroelectric energy meter (e.g. from Gentec-EO) can be remotely inserted in the pulse path to have absolute calibration of the photodiode readout. Photodiode measurement can also be used as a wide dynamic range laser arrival time monitor during initial commissioning or after significant modification of the laser configuration or transport.

Combined, these diagnostics provide a complete spatio-temporal characterization of the UV beam, ensuring optimal performance for high-precision photocathode applications.

12.2.10 Summary of the Laser Parameters

The main parameters of the IR and UV laser pulses are summarized in Tables 12.1 and 12.2.

Table 12.1: Infrared laser parameters.

Parameter	Specification Value
Central wavelength	780 ± 20 nm
FWHM Bandwidth	60 nm
Energy per pulse after compression	> 100 mJ
Energy stability (rms)	< 1 %
Pulse duration (FWHM)	≥ 35 fs
Repetition rate	100 Hz
Beam ellipticity (1-a/b)	< 10 %
Contrast ($100 - 10$ ps)	1×10^{-6}
Contrast ($300 - 100$ ps)	3×10^{-7}
Pointing stability	< 10 µrad
Polarization	Linear, Horizontal
Temporal shape	Gaussian

Table 12.2: Ultraviolet laser parameters.

Parameter	Specification Value
Central wavelength	263 ± 3 nm
FWHM Bandwidth	20 nm
Energy per pulse at the cathode	> 1.75 mJ
Energy stability (rms)	< 1 %
Pulse duration (FWHM)	≥ 30 fs
Repetition rate	100 Hz
Beam ellipticity (1-a/b)	< 10 %
Pointing stability	< 10 µrad
Polarization	Linear, Horizontal
Energy (to reach 500pC)	≤ 200 µJ
Temporal shape	Gaussian

12.3 The Probe Beamlines

Before the main compressor, a beam splitter extracts 10% of the main beam energy. This pulse is amplified independently to provide sufficient energy per pulse for diagnostics along the LINAC.

12.3.1 Laser Beams for Diagnostics

Transport to the diagnostic stations (e.g., EOS) is performed using the long IR pulse. Each diagnostic beamline is equipped with its own compressor to allow maximum flexibility in pulse

duration, with the minimum pulse duration matching that of the main beam (35 fs). Delay lines are incorporated to synchronize the pulses with the electron beam.

12.3.2 Laser System for the Laser Heater

The Laser Heater (LH) is designed to deliberately introduce a controlled uncorrelated energy spread onto the electron beam, using longitudinal Landau damping to mitigate microbunching instabilities. More details are provided in Sec. 5.3.

This section describes the laser system for the LH, its transport beamline, and the key beam characteristics.

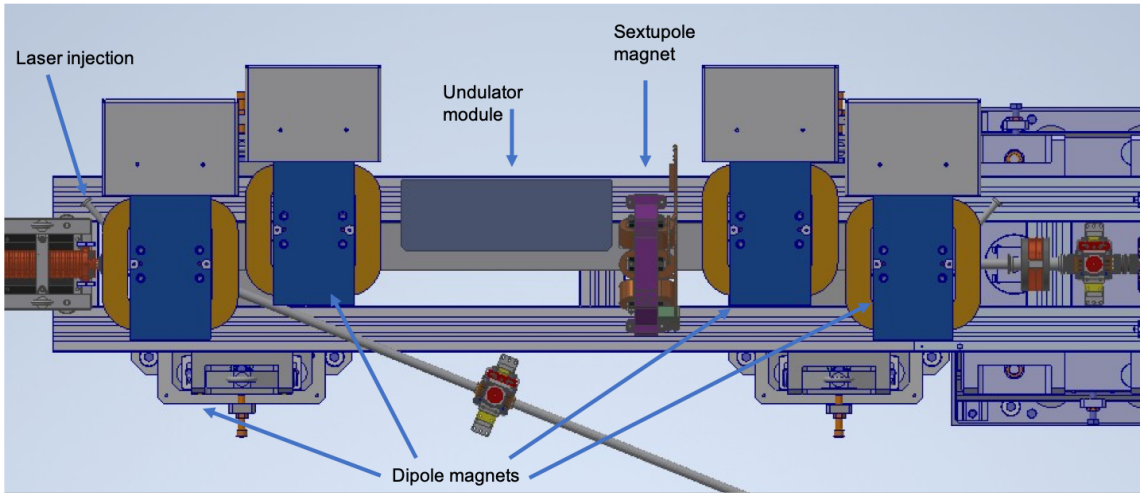

Figure 12.12: Schematic of the Laser Heater (LH) beamline.

Table 12.3 summarizes the laser parameters required for the LH.

Table 12.3: Laser Heater parameters.

Parameter	Unit	Value
Laser wavelength, λ_l	nm	400, 800
Laser pulse duration, FWHM	ps	≤ 10
Laser peak power	MW	≤ 5

The laser pulse for the LH is extracted from the second amplifier (similarly to all diagnostic beamlines) and transported to the chicane where it is required. This beamline is also equipped with its own pulse compressor to achieve the target pulse duration, employing chirping techniques to reach a duration on the ps scale.

12.4 Laser System for FEL Users

Time-resolved measurements, enabled by synchronizing ultrafast optical laser pulses with the FEL, are essential for the scientific mission of free-electron laser facilities. The EuPRAXIA@SPARC_-LAB facility will be equipped with laser systems specifically designed to meet stringent requirements for stability, precision, and flexibility needed by these experiments.

The user lasers will operate at a repetition rate matched to the 100 Hz FEL and will incorporate careful design of beam transport, monitoring, and control systems to ensure maximum stability. The system design will be continuously updated to meet evolving user requirements.

The primary laser employed in the AQUA endstation is a compact commercial Ti:sapphire femtosecond laser at 800 nm, capable of generating second (400 nm) and third (267 nm) harmonics. Pulse durations can be set as short as 35 fs FWHM, with fundamental pulse energies up to approximately 10 mJ. Harmonic conversion efficiencies are expected to be ∼50% for the second harmonic and ∼15% for the third harmonic.

This Ti:sapphire laser can also pump an Optical Parametric Amplifier (OPA), providing wide wavelength tunability from approximately 200 nm to 20 µm. To minimize spatial and temporal distortions, the OPA and harmonic generation modules will be installed close to the experimental endstation. A reference commercial system is the Light Conversion TOPAS PPRIME system [2].

Optical transport from the laser room to the experimental chamber—similar to the photocathode system—will be carefully designed to minimize pointing instability, spatial jitter, and temporal drifts. All optical paths will be enclosed to mitigate disturbances from air currents, acoustic noise, and thermal gradients. Dedicated diagnostics, as those described Sec. 12.2.9, will continuously monitor spatial and temporal stability, including near the user experimental chamber, with automated control systems maintaining alignment and performance.

Precise timing between the FEL and the external optical laser is critical for pump-probe experiments. The overall timing jitter at the experimental endstations must remain within a few tens of femtoseconds. The Ti:sapphire oscillator cavity is equipped with a piezo actuator to synchronize with the optical master oscillator, as detailed in Sec. 14.3.2.3, providing the required stabilization. Shot-to-shot pulse duration and arrival-time characterization is performed via optical cross-correlation with the master oscillator, on an optical breadboard near the user experimental chamber. A motorized delay line, installed on the transport line, corrects for long-term drifts.

12.5 Laser Safety System

The entire photocathode laser system is installed in a dedicated, environmentally controlled laser room adjacent to the accelerator tunnel. The optical table is enclosed for cleanliness and safety, while electronics and laser drivers are located in a separate control rack area. A comprehensive safety interlock system, compliant with current laser safety standards, protects personnel and equipment during operation and maintenance.

Given the inherent hazards associated with laser radiation—including burns, eye injuries, and fire risk—all personnel operating or working near the laser system undergo specialized training. Training covers laser classifications, beam paths, reflection hazards, emergency procedures, and system-specific configurations, and includes supervised hands-on operation.

Personal protective equipment is mandatory for all personnel in proximity to active lasers, including wavelength- and power-specific safety goggles. Warning signs are clearly posted, and access to laser areas is restricted to authorized personnel only. Interlocks, beam stops, and shutters prevent accidental exposure. Regular safety audits and maintenance of the laser and shielding structures ensure continued protection.

These measures collectively maintain a safe working environment, in full compliance with laser safety regulations.

12.6 Conclusions

The goal of this chapter was to describe the laser system needed by the facility and complete the information already given in the previous chapters on the subject. According to the reported contents, the laser systems will meet the requirements imposed by the machine and user needs. The technical readiness levels of the subsystems are reported in Tab. 12.4.

Table 12.4: Technological Readiness Level (TRL) of the laser subsystems.

Sub-systems	TRL	Comments
Photocathode laser (overall)	9	The photocathode laser is a well-established technology, successfully tested in operational facilities (including SPARC_LAB). These systems are now commercially available and can be considered almost off-the-shelf products.
Oscillator	9	Low-noise oscillators suitable for synchronization applications are fully available on the market as off-the-shelf products (two units have already been procured for SABINA and EuAPS).
100 Hz pumps	9	100 Hz laser pumps are commercially available as off-the-shelf components.
100 Hz compressor	9	100 Hz compressors are commercially available as standard products.
3rd Harmonic generator	9	Third harmonic generation units, typically based on nonlinear crystals, are fully available on the market.
UV stretcher	9	UV stretchers are commercially available and can be considered off-the-shelf products.
Laser for FEL user	9	Lasers of this type are well-proven technologies, tested in several operational facilities. They are now commercially available as standard products.

Bibliography

[1] L. Sabbatini et al. “Sabina: A research infrastructure at LNF”. In: *Proceedings of the 12th International Particle Accelerator Conference (IPAC’21), Campinas, Brazil*. 2021, pp. 24–28.

[2] *TOPAS-PRIME laser systems*. Ligth Conversion. URL: https://lightcon.com/products/topas-prime-opa/ (visited on 03/28/2025).

13. RF systems

Many details of the RF system characteristics are provided elsewhere in this TDR. In particular the injector RF layout, the RF photo-gun and the X-band 7-cells SW linearizer cavity are described in the Photoinjector Chapter 5, while the TW X-band accelerating structures and the complete linac modules accommodating them are described in details in the X-band linac Chapter 6. This chapter is devoted to complete the information on the RF systems with greater emphasis on S-band TW accelerating structures, RF power plants, waveguide network and LLRF systems.

13.1 Introduction and general description

As already described in detail in Chapters 3, 5 and 6, the electron beam is generated and shaped in the linac injector by S-band RF systems driving the photo-gun and 2 pairs of travelling wave (TW) accelerating sections. Then the beam is boosted to the energy required to the injection in the plasma channel by eight identical X-band RF modules consisting each of one klystron (25 MW peak power) followed by 1 BOC pulse compressor and feeding a pair of TW accelerating structures approximately 1 m long up to a gradient of 60 MV/m. Two additional X-band power sources will drive a linearizer structure placed in the injector, and two PolariX deflecting structures for advanced beam diagnostic and tomography, as reported in Diagnostics Chapter 11.

13.2 The S-band injector RF systems

The schematic layout of the S-band injector RF system is shown in Figures 4.6, 5.1, 5.15, 5.16. The European S-band standard frequency (f = 2998.55 MHz) has been chosen as the operating frequency for the RF Gun and the accelerating sections. The RF Gun will be powered by a dedicated klystron with a square RF pulse, while each pair of TW accelerating sections will be powered by a dedicated RF station through a pulse compressor producing a pseudo-triangular RF pulse. However, since the structures are of the constant impedance type, the accelerating field exhibits an almost constant gradient along the TW sections because of the attenuation and the absence of group velocity modulation along the structures (Figs. from 13.3 to 13.5). As already reported in Chapter 5, two X-band structures have also been included in the injector design: a Standing Wave, 7-cells

linearizer to optimize the beam longitudinal phase space (Sec. 5.2.2), and a PolariX transverse deflector, whose deflection angle can be adjusted over 360°, is capable of kicking the beam in both the horizontal and vertical planes for diagnostic purposes. The two structures will be powered by a single dedicated X-band RF station working at a power around 16 MW, where only a small fraction of the power will be diverted toward the SW linearizer (about 0.5 MW peak). Two variable attenuators will be used in series before the Polarix. The first acts as a power divider to properly split the power coming from the klystron between the linearizer line and the Polarix, while the second functions as an RF switch to ensure that the power delivered to the Polarix is truly zero when only the linearizer needs to be used. In this configuration, the RF power reflected by the standing-wave linearizer is sufficiently mitigated before reaching the klystron. The reflected signal experiences progressive attenuation ($\sim$2.5 dB) along the waveguide transmission line and undergoes additional suppression when traversing the variable attenuator in the reverse direction. As a result, the residual reflection incident on the klystron output window corresponds to an equivalent VSWR below 1.2, compliant with the operational limit specified for the tube. Finally, as reported in Fig. 5.16, an X-band phase shifter developed at PSI for the Polarix line, providing a full 360° tuning range, is installed upstream of the linearizer to allow adjusting its phase with respect to that of Polarix when both systems are operated simultaneously.

13.2.1 The RF Gun

The main description and function of the RF gun is provided in Sec. 5.2.1. The beam dynamics in the whole linac and beyond is very much sensitive and dependent on the quality and stability of the fields in the RF Gun that represents therefore a crucial device for the stability and the performances of the facility. A novel construction technique has been proposed, refined and now routinely adopted at LNF, based on clamping with special gaskets instead of brazing of the various device components. This technique clamps the copper parts of a structure together using special gaskets that ensure proper RF contact. This approach has been proved to substantially simplify the manufacturing process while preserving the original characteristics of the hard copper. By contrast, the high temperatures used in standard brazing procedures can compromise these properties by softening the material. LNF team has fabricated, tested and put in operation 5 of such devices of various frequencies in last few years [1–3]. Namely, three of them are US S-Band (2856 MHz) devices and are now operating at UCLA (US), SPARC_LAB (IT) and ELI-NP (SSRIP project, Ro). One is an EU S-Band (2998 MHz) device in operation at the CLEAR facility (CERN). The last realization of this kind is a C-band (5712 MHz) device, designed for an ultra-high peak electric field at the cathode (180 MV/m) and high rep-rate (400 Hz), preliminarily tested at PSI (CH) and presently installed at the TEX facility at INFN LNF for full tests at nominal specifications [4]. The development and testing of this gun may represent a future upgrade path for the EuPRAXIA@SPARC_LAB linac, enabling a fully C-band injector with improved brightness and increased compactness. Having chosen the EU S-band frequency for the injector, the RF Gun will be essentially a copy of the one already realized and successfully operated at CLEAR and shown in Fig. 13.1. More details on the RF Gun characteristics and specifications are presented in Sec. 5.2.1.

13.2.2 The Travelling Wave S-band accelerating sections

The design and optimization of the two types of S-band RF structures were carried out using a semi-analytical code developed and used to guide the design of the X-band linac TW accelerating structures. Starting from the simulated parameters of a single cell as a function of the iris aperture, and taking into account the pulse shape and the peak power gain provided by the RF pulse compressor, the code allows computing and maximizing the effective shunt impedance of a stack of a given number of cells while keeping the surface electric fields and the modified Poynting vector

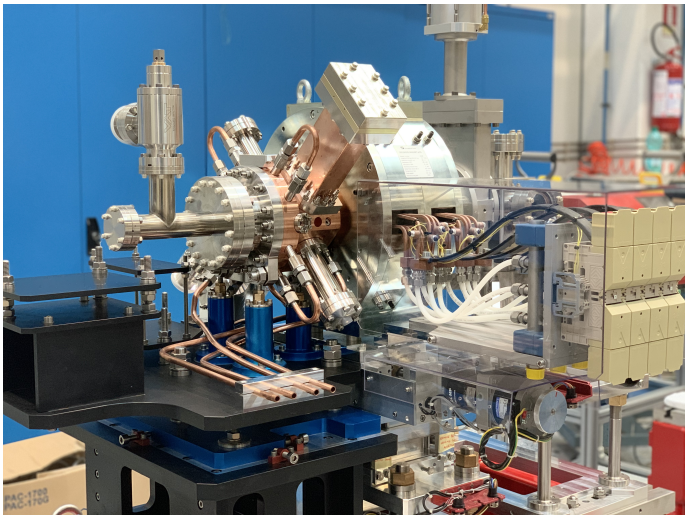

Figure 13.1: Picture of the S-band RF Gun realized for the CLEAR injector.

under control [5]. The effective shunt impedance is defined as:

$$R_s = V_a^2 / P_{in} L_s \ \ [\Omega/m]$$

where V_a is the integrated accelerating voltage, P_{in} is the structure input power and L_s is the structure length [6]. In order to maximize this parameter and obtain a quasi-constant accelerating gradient along the structure axis, the code allows scanning various parameters, such as the cell average iris radius and the coefficient of linear tapering of the cell iris radius along the structure, while some other parameters are assumed fixed by design (such as the structure length and the unloaded quality factor of the pulse compressors). Since the machine working point makes use of a single RF bucket, the pseudo-trapezoidal RF pulse profile produced by the RF pulse compressors does not need to be flattened with additional phase/amplitude manipulation provided by the Low-Level RF (LLRF) systems, and can be fed directly into the accelerating structures maximizing the global efficiency. The code showed that under these conditions a proper choice of the iris dimension of a travelling wave constant impedance (TW CI) structure can balance the power attenuation with the increasing profile of the RF pulse, resulting in an almost constant (to the first order) accelerating gradient experienced by the electron bunch along the structure. We considered this an optimal solution since it provides very good performance in terms of effective shunt impedance value and it simplifies the construction avoiding iris aperture variations along the structure.

Table 13.1 reports the main parameters for the 3 m sections used as RF longitudinal compressors and the 1.5 m sections for energy boosting; these values were obtained at the conclusion of the optimization process. Figures 13.2 and 13.4 show the RF pulse profiles at the input and output of the pulse compressor, as well as at the input of the accelerating structure, for both cases. Figures 13.3 and 13.5 show the accelerating gradient profile respectively for the 3 m and the 1.5 m long structures at the nominal maximum ratings.

Table 13.1: Parameters of the 3 m section used as RF longitudinal compressors and of the 1.5 m section for energy boosting.

Parameter	**Units**	**3 m long section**	**1.5 m long section**
Frequency	MHz	2998.55	2998.55
Length	m	3	1.5
Type		$2\pi/3$ CI	$2\pi/3$ CI
Maximum average acc. gradient	MV/m	25	35
Number of structures per source		2	2
Iris radius, a	mm	12	10.06
Number of cells		88	44
Shunt impedance R	MΩ/m	55	61
Effective shunt impedance R_{eff}	MΩ/m	117	128
Peak input power in the structure	MW	88.6	79
Input power averaged over the pulse	MW	58	52
Average dissipated power	kW	3.2	2.9
P_{out}/P_{in}	%	39.7	38.7
Filling time	ns	700	700
Peak modified Poynting vector	W/μm^2	0.5	0.8
Peak surface electric field	MV/m	73	100
Unloaded pulse compressor Q-factor Q_0		150000	150000
External pulse compressor Q-factor Q_e		22400	22400
Required klystron power per module	MW	31.4	28
RF pulse length at klystron	μs	4	4
Repetition rate	Hz	100	100

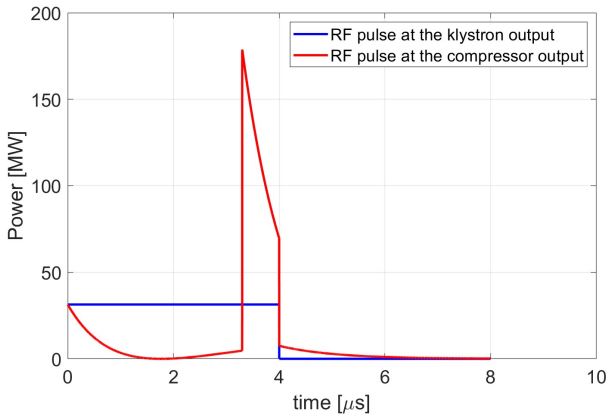

Figure 13.2: Computed RF pulses at the SLED input and output for the 3 m S-band structures.

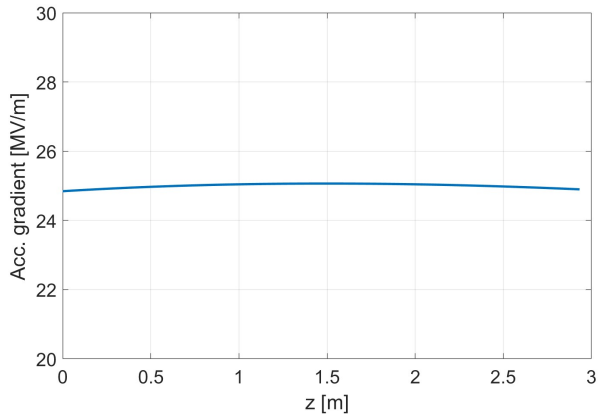

Figure 13.3: Quasi-constant accelerating gradient across the 3 m structure.

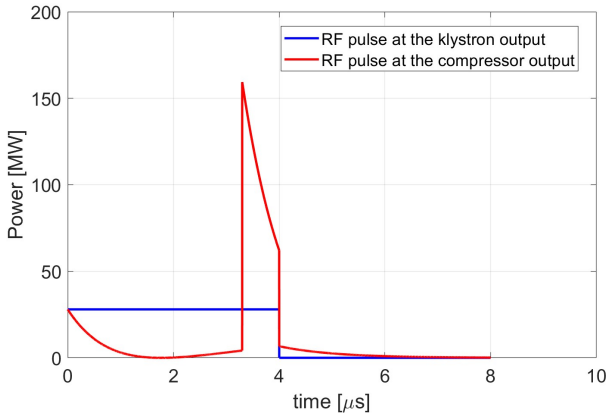

Figure 13.4: Computed RF pulses at the SLED input and output for the 1.5 m S-band structures.

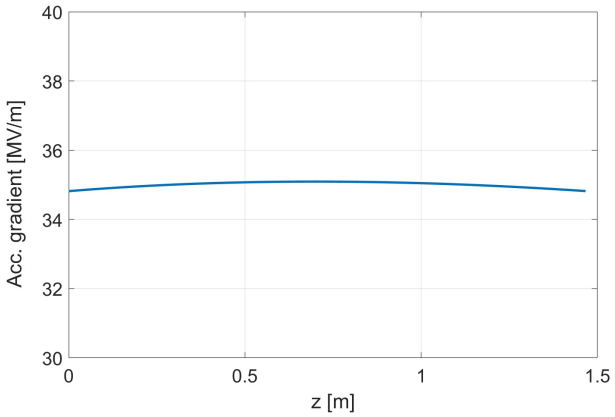

Figure 13.5: Quasi-constant accelerating gradient across the 1.5 m structure.

13.2.2.1 Brazing-free design and realization of sections

The baseline for the S-band accelerating sections manufacturing technology is the conventional brazing technique. However, the gasket-clamping method is being considered as a potential alternative for future developments, pending the outcome of dedicated R&D activities aimed at demonstrating its full applicability to high-gradient travelling wave structures.

Generally, accelerating structures are manufactured by machining single cells using high-precision lathes and/or milling machines. These copper components are then assembled through a brazing process, a metal joining technique in which two parts are bonded by melting a filler alloy that, at high temperature (typically above 800–900 °C), flows into the joint via capillary action. At each brazing step, a brazing alloy with a progressively lower melting point must be used to avoid compromising previous joints.

To prevent oxidation during brazing, the process is carried out in large, high-vacuum furnaces that are expensive and only available in a limited number of specialized facilities or companies. Moreover, the high temperatures involved induce annealing of the copper, increasing its ductility but reducing its mechanical hardness. Each brazing cycle also subjects the components to significant mechanical and thermal stress due to the elevated temperature variations involved.

In summary, the brazing process presents some drawbacks:

- the risk of failure is non-negligible (e.g., vacuum leaks, mechanical damage);
- it requires large, specialized vacuum furnaces available in only a few laboratories or companies;
- it can be performed by only a limited number of qualified manufacturers worldwide;
- it is generally expensive;
- the copper becomes annealed and loses its original mechanical strength.

Furthermore, studies on breakdown rate in X-band structures have shown that avoiding copper annealing, associated with the high temperatures of brazing, reduces the probability of breakdowns [7].

For these reasons, a novel fabrication technique known as the gasket-clamping method has been developed at INFN-LNF [8]. This method eliminates the need for brazing by employing specially designed RF and vacuum gaskets to join the machined components. The parts are mechanically clamped together using screws arranged radially around the cells. This technique has been successfully implemented in the construction of several RF guns developed at LNF in recent years, as reported in Section 13.2.1. Moreover, a preliminary study on the application of this technique to the fabrication of a complete travelling wave structure has already been carried out through the design of a small S-band prototype [9]. The good performance of these devices, in terms of achieved peak fields and low breakdown rates, opens the possibility of extending this approach to the realization of entire TW structures. To apply this technique, the mechanical design of the accelerating sections must be revised to make them compatible with the integration of gaskets and clamping screws. In particular, the electromagnetic and mechanical design of the couplers must be carefully optimized to allow the implementation of this technique while preserving the RF performance.

13.2.3 RF Power distribution network

The schematic layout of the power distribution system for the S-band structures of the photo-injector is shown in Fig. 5.15. The RF gun is powered independently by a dedicated S-band RF station. Since the gun is a standing wave cavity, a commercial 4-port differential ferrite circulator in S-band operating in an SF6 atmosphere, rated for 20 MW peak power, will be used to protect the RF source from potentially damaging reflected power.

The two S-band modules for the low and high gradient sections are powered in pairs using a pulse compressor. The compressor can be either a commercial SLED-type or a spherical-type design with an E-rotator, recently implemented on the FERMI linac in Trieste [10]. Since there is currently no confirmed evidence that a commercial S-band variable power divider can reliably withstand the high peak power at the output of the pulse compressor, the baseline solution includes a fixed power divider combined with two variable attenuators on each output port. This configuration maximizes flexibility and tunability of the power delivered to the accelerating structures. A possible

future upgrade could involve replacing the fixed power divider with a variable one, in order to have even more flexibility in the klystron power partition. Downstream of the second output port of each power divider, a waveguide phase shifter is cascaded to adjust the relative RF phase between sections of each pair. All waveguides used in these lines are of the WR284 type, equipped with LIL-standard flanges. To keep the lines under vacuum during the replacement of a klystron, an S-band ceramic RF window will be installed on each of the three S-band lines downstream of the klystron. No RF window is foreseen downstream of the X-band klystrons, since reliable RF windows at this frequency and at these peak power levels are not yet available. The schematic layout of the feeding arrangement for the X-band structures in the photo-injector is shown in Chapter 6 in Fig. 5.16. To split the power between two structures, a variable power divider is used. Along the PolariX line, an additional power divider terminated on an RF load is interposed as an additional RF switch, ensuring that no power is delivered to the PolariX when it is not in use. Both the power divider and the RF switch are based on the variable attenuator design developed at CERN, shown in Fig. 13.6, which has been successfully tested at high power [11]. Alternatively, they can be implemented by combining the X-band phase shifter developed and used at PSI with two custom-designed 3 dB hybrids.

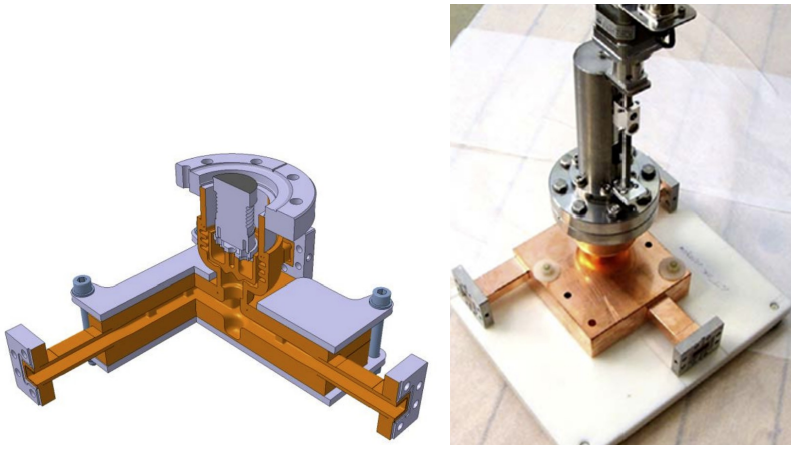

Figure 13.6: Mechanical design and realization of the variable RF power divider.

13.3 The S-band and X-band RF power sources

High-voltage pulsed power for the klystrons is provided by pulsed power converters also known as modulators. The most important parameters that specify a modulator are peak power, pulse duration, peak voltage and current. The modulators are connected to the klystrons via high-voltage pulse transformers designed with low leakage inductance and minimized parasitic capacitance, matched to the klystron impedance. The flat-top of the voltage pulse is tailored to match or slightly exceed the RF pulse duration specified for the klystron. The overall efficiency of the modulator is strongly influenced by the rise and fall times of the high-voltage pulses, which are targeted at approximately 1 µs and 2 µs (10 - 90%), respectively.

The klystrons used in the RF stations are high-gain, narrowband amplifiers such as the Canon E37119 reported in Fig. 13.7, featuring ultra-high vacuum RF windows ($\sim 10^{-9}$ mbar). Achieving high stability in RF phase and amplitude from shot-to-shot is critical, as any fluctuation can significantly affect FEL output characteristics such as arrival time, pulse energy, and wavelength. Once a stable RF distribution system is in place, modulator voltage stability becomes a primary factor in overall RF performance. To meet FEL requirements, the voltage pulse to pulse stability must be kept below 20 ppm for all RF sources. The RF signal generated and pre-shaped at low

power by the LLRF system must be pre-amplified to power levels of the order of tens to hundreds of watts before reaching the klystron input. This is achieved by means of solid-state driver amplifiers. As for the modulator and the klystron, their contribution to phase and amplitude stability must be carefully controlled, since any fluctuation introduced at this stage directly affects the final stability of the RF source.

Figure 13.7: Picture of the Canon E37119 klystron.

Linac RF modulators can generally be divided into two categories based on the primary energy storage element used to generate the high-voltage pulse:

- PFN-based (Pulse Forming Network) modulators, which use a transmission line-type network matched to the klystron impedance to store energy. The high-voltage pulse is generated through the discharge of this network via high-current switches such as thyratrons, producing fixed-duration pulses.
- Solid-state modulators, which utilize banks of capacitors as energy storage elements, each connected in parallel to an IGBT switch. Given the relatively low operating voltage of IGBTs (typically 2–4 kV), these systems require pulse transformers with high step-up ratios to achieve the required klystron voltage.

Both approaches have been evaluated in terms of performance, reliability, maintainability, and cost. PFN-based systems present two major drawbacks: limited lifetime of thyratron switches (typically $\sim 20,000$ hours), which affects reliability, and poorer pulse-to-pulse voltage stability. Additionally, the fixed pulse characteristics dictated by the PFN cell configuration reduce flexibility. The large component dimensions required to sustain high-voltage operation further constrain system compactness. At INFN-LNF, both PFN-based and solid-state modulators systems have been operated. At SPARC_LAB, two S-band RF stations operate with PFN-based modulators, while the C-band station, operational since 2012, uses a ScandiNova K400 solid-state modulator. In particular, substantial expertise in solid-state and X-band technology has been acquired through the

TEX facility, developed in collaboration with CERN's CLIC group for advanced X-band technology studies [12–16]. Operational since early 2023, TEX hosts a 50 MW X-band RF source powered by a ScandiNova K400 solid-state modulator and has recently been upgraded with the installation of two high-repetition-rate solid-state RF sources: a 25 MW X-band system and a 20 MW C-band system, both operating at 400 Hz. Fig. 13.8 shows the solid-state RF sources installed at TEX. The facility enables long-term testing and conditioning of RF stations under both high-peak and high-average power conditions, critical for validating component reliability, investigating breakdown phenomena, and assessing long-term operational stability. The knowledge and operational experience gained at TEX directly contribute to the design and development of the EuPRAXIA@SPARC_LAB linac.

Figure 13.8: Picture of the solid-state RF sources at the TEX facility. In order X-band 50 MW, 50 Hz source, X-band 25 MW, 400 Hz source and C-band 20 MW, 400 Hz source.

Operational experience has confirmed several advantages of solid-state modulators over traditional PFN systems:

- Simplified installation (electrical, cooling, and control only).
- High modularity (reduced spares, reconfigurable switch modules).
- Enhanced reliability and maintainability.
- Compact footprint.
- Adjustable pulse duration, allowing efficiency optimization.
- Good amplitude and phase stability from pulse to pulse.
- Improved safety (most high-voltage hardware enclosed in oil tanks).

Due to these advantages, especially the improved stability, all EuPRAXIA@SPARC_LAB RF stations will adopt solid-state modulator technology. As previously discussed in earlier sections, a total of three S-band RF stations are planned for the injector, each based on the Canon E37237A klystron. This particular model was selected not only for its technical specifications, which are well-suited to our requirements, but also for its widespread adoption and proven performances at other European facilities (i.e. Paul Scherrer Institute).

In addition, eight X-band RF stations, each one powering two accelerating structures, will be used to power the linac booster. Two additional X-band stations are also foreseen: one dedicated to the injector's X-band linearizer and deflector, and another to supply power to a second PolariX deflector located downstream of the plasma module. This power plant and its waveguide network will be very similar to the one feeding the injector PolariX, apart the line diverting a fraction of the RF power to the linearizer that is not present in this case. All X-band RF stations are based on the Canon E37119 klystron, which is designed to operate at repetition rates up to 400 Hz, an important feature that potentially opens the possibility of future upgrades of the facility.

The main parameters and specifications of the S-band and X-band sources are summarized in Table 13.2 while the nominal parameters for the S-band E37327A klystron and X-band E37119 klystron are reported in Table 13.3. Finally, the main specifications required for the S-band and X-band driver amplifiers are reported in Table 13.4.

Table 13.2: S-band and X-band RF sources parameters and main specifications.

	Units	**S-band**	**X-band**
Klystron		E37327A	E37119
Frequency	GHz	2.99855	11.9942
RF pulse length	μs	4.5	1.5
Max RF output power	MW	45	25
Max Average RF power	kW	20	4
Repetition Rate	Hz	1-100	1-100
Peak voltage	kV	330	320
Peak current	A	420	200
Modulator average power	kW	75	20
Flat-top flatness	%	± 1	± 1
Pulse-to-pulse voltage stability rms	ppm	≤ 20	≤ 20
Pulse to pulse time jitter	ns	$\leq \pm 4$	$\leq \pm 4$
Pulse width time jitter	ns	$\leq \pm 8$	$\leq \pm 8$
RF amplitude jitter	%	≤ 0.05	≤ 0.05
RF phase jitter	degree	≤ 0.02	≤ 0.1

Table 13.3: S-band and X-band klystrons nominal parameters.

	Units	E37327A	E37119
Frequency	GHz	2.99855	11.9942
Bandwidth	MHz	3	8
RF pulse length	µs	4.5	1.5
Max output power	MW	45	25
Max Average power	kW	20	15
Repetition Rate	Hz	1-100	1-400
Beam voltage	kV	330	320
Beam current	A	420	200
Gain	dB	51	47
Efficiency	%	40	40
Maximum RF drive power	W	1000	500
Nominal RF drive power	W	500	60
Filament Current	A	22	22
Filament Voltage	V	22	22
Solenoid model		VT-68931A	VT-68977
Solenoid current	A	21	32
Solenoid voltage	V	250	350
Solenoid coolant flow	L/min	> 10	> 16
Collector coolant flow	L/min	> 48	> 65
Body coolant flow	L/min	> 12	> 15
Window coolant flow	L/min	> 2	> 1.8

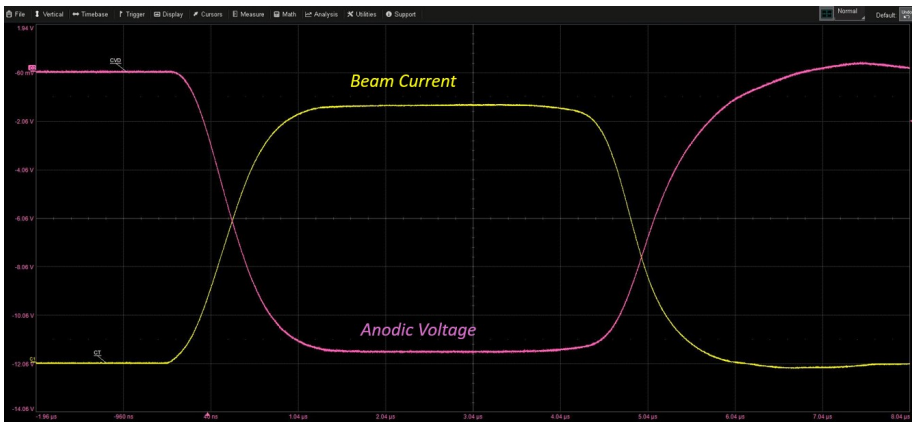

Figure 13.9: Example of measured klystron anode voltage and corresponding beam current waveforms.

13.3.1 RF source safety

The RF sources operate under stringent safety protocols aimed at protecting both personnel and equipment as reported in the European standard for machinery electrical safety EN 60204-1:2006.

Table 13.4: S-band and X-band RF solid state driver amplifier parameters and main specifications.

	Units	**S-band**	**X-band**
Frequency	GHz	2.99855	11.9942
Bandwidth	MHz	$\geq \pm 10$	$\geq \pm 20$
RF pulse length	μs	≥ 4.5	≥ 1.5
Peak output power	W	≥ 500	≥ 100
Repetition Rate	Hz	≥ 100	≥ 100
Input Power for rated output	dBm	$-5 \div 0$	$-5 \div 0$
RF amplitude jitter	%	≤ 0.02	≤ 0.02
RF phase jitter	degree	≤ 0.01	≤ 0.05

These safety measures are implemented throughout all phases of use, including installation, operation, and maintenance.

Access to the klystron gallery will be managed by a comprehensive interlock system, ensuring that all safety conditions are met before the systems are powered on. The interlock also verifies the absence of personnel in restricted areas during operation.

These safety protocols address multiple sources of risk associated with the operation of high-power RF systems, including:

- Electrical hazard: The modulator generates a high-voltage pulses inside a transformer tank in order to feed the klystron and amplify the RF signal. In a solid-state modulator the components outside the oil tank generate a maximum voltage lower than 10 kV. Each RF source is equipped with an emergency stop button that opens the main breaker, disconnecting the three-phase power supply to the modulator. The circuit breaker opens the circuit for whenever specific safety conditions are not satisfied, this ensures that the modulator cannot generate any high voltage on its terminals. Additionally, each modulator features an internal passive bleeder circuit that safely discharges all high-voltage potentials within the various modulator units within two minutes of shutdown. Therefore, there are no high voltage parts accessible on the outside of the RF source once it is turned off.
- Electromagnetic radiation hazard (RF fields): High-power radio-frequency electromagnetic fields are generated by the klystron and all waveguide components. To mitigate the risk of exposing workers to electromagnetic irradiation, the output of the klystron and all RF components are always properly sealed and terminated before powering on the RF source.
- Hot surface hazard: Some equipment surfaces may become hot during operation. To prevent injury, direct contact should be avoided, and a waiting period of at least 10 minutes is recommended before any intervention on the equipment after shutdown.
- Fire hazard: Smoke detectors will be installed inside the modulators and in the klystron gallery to detect the onset of any fire. The modulator uses mineral oil as a high-voltage insulating medium, enclosed in a sealed internal tank. This tank is installed within a retaining containment basin equipped with an interlock system that triggers an alarm if fluids, such as water or oil, are detected, indicating a potential leak.
- X-ray radiation hazard: The klystron is a vacuum tube that, during normal operation, emits X-rays. These are shielded by appropriate radiation lead protection provided by the manufacturer. The resulting dose rate is reduced to less than 1 μSv/h at a distance of 1 meter from the klystron. The area where these systems are installed is classified as a restricted area, and the presence of personnel is strictly prohibited during operation. In exceptional cases requiring intervention while the sources are active, authorized personnel may access the area only if

equipped with a personal dosimeter.

13.4 Low Level RF systems

The implementation of an advanced Low-Level RF (LLRF) system is crucial for the precise control and stability of the accelerating fields, particularly given the stringent amplitude and phase jitter requirements imposed by the plasma acceleration stage. One dedicated LLRF module is required for each RF power plant, three operating in the S-band and ten in the X-band.

13.4.1 LLRF System Architecture and Challenges

Each RF power plant is independently driven by its own LLRF system to provide maximum operational flexibility. The need for such an architecture arises from the diverse requirements of the accelerator, where independent phase and amplitude control of each RF source is mandatory for optimal beam performance. The integration of LLRF systems across multiple frequency bands presents significant engineering challenges, particularly in the X-band, where native LLRF solutions are currently unavailable.

A key function of the LLRF system is to ensure the control of the accelerating fields while minimizing drifts of RF amplitude and phase (by means of RF feedbacks) with possibly a negligible contribution to the pulse to pulse jitter. The plasma acceleration stage imposes exceptionally strict tolerances on the phase stability of the RF signals, since even minimal fluctuations can lead to significant degradation in beam quality. In the case of the X-band, the required operating frequency of 11.9942 GHz demands dedicated research and development (R&D) efforts from industry partners to develop new LLRF systems capable of meeting these specifications (summarized in Table 13.5). Moreover, commercial LLRF solutions available in lower frequency bands do not provide sufficient performance in terms of phase stability, necessitating novel design approaches.

13.4.2 R&D Efforts for X-Band and S-Band LLRF Systems

Given the absence of commercial X-band LLRF solutions, significant R&D investments are required to design and manufacture a system that meets the stringent phase noise and stability requirements. The main challenges include:

- Achieving stable operation at 11.9942 GHz adding minimal amplitude and phase jitter;
- Ensuring long-term stability and robustness under high-power RF operation;
- Improving the ADC sampling speed and front-end bandwidth with respect to off the shelf commercial S- and C-band systems to meet the X-band RF pulse requirements (maximum length 1.5 µs, 150 ns after pulse compression).

Similarly, while commercial S-band LLRF systems exist, they do not offer the necessary phase stability required for the project. Enhancements in phase noise performance and feedback control mechanisms are needed to meet the demanding specifications of this facility.

Moreover, as described in detail in Chapter 14.3.2.5, to ensure a wider safety margin within the overall jitter budget, the phase-jitter reduction techniques currently operational at SPARC_LAB will also be implemented, complementing the slow amplitude and phase control loops used to mitigate environmental drifts that affect the machine's operational stability. These techniques employ broadband feedback circuits capable of correcting the klystron phase within the same RF pulse, with reaction times on the order of a few hundred nanoseconds, a method commonly referred to as intra-pulse feedback. This approach has been successfully tested and has been in routine operation on PFN-modulator-driven RF stations at LNF since 2008, as reported in [17]. At SPARC_LAB a phase stability of 15 fs rms has been achieved for both S-band systems following the latest upgrade of the intra-pulse feedback system. To further optimize the implementation of such fast feedback, each LLRF system will be equipped with an additional RF output that is

phase-coherent with RF pulse modulation and maintains a constant amplitude. Further details about the achieved RF station stability are reported in Chapter 14.

13.4.3 Key Features of the LLRF System

The LLRF system is designed with advanced technical features to meet the demanding stability and precision requirements. The main characteristics include:

- Digital FPGA-based systems with the capability of arbitrary RF pulse modulation, allowing fine control over the acceleration process;
- Temperature-stabilized RF front-end to minimize long-term drifts, ensuring a phase stability of 100 fs over 24 hours (for a temperature drift of ± 2 °C);
- High-resolution ADCs (16-bit) with a minimum sampling frequency of 230 MHz, providing a sufficient number of samples to accurately represent the RF pulses typical of the project.

Table 13.5 summarizes the key technical specifications for the LLRF systems in both S-band and X-band. One of the most critical parameters for plasma acceleration is the phase stability of each RF station. For this reason the LLRF specifications on the maximum phase added jitter have been set to 0.005° rms and 0.015° rms for S and X band LLRF systems respectively. Detailed calculations on the RF power plants jitters have been carried out in Chapter 14.

Table 13.5: S-band and X-band LLRF main specifications.

	Units	**S-band**	**X-band**
Mode of operation		pulsed	pulsed
Carrier frequency	GHz	2.99855	11.9942
Nominal RF pulse length	µs	4.5	1.5
VM output rep. rate	Hz	$\geq$ 400	$\geq$ 400
Minimum MO input level	dBm	0	0
ADC Sampling rate	MHz	> 230	> 230
Time window	µs	> 7	> 3.5
Back-end rise time	ns	< 50	< 20
Back-end output level	dBm	> 10	> 10
N. RF output channels		2	2
Vector Modulator isolation	dBc	< -40	< -40
Vector Modulator pulse shaping		Arbitrary	Arbitrary
Front-end BW	MHz	> 20	> 20
N. of RF input channels		$\geq$ 15	$\geq$ 15
Avg. window (from RF pulse end)	µs	0.8	0.15
Min. detectable amplitude (400 pulses)	% rms	$\leq$ 0.015	$\leq$ 0.015
Min. detectable phase (400 pulses)	deg rms	$\leq$ 0.005	$\leq$ 0.015
Back-end added amplitude noise (400 pulses)	% rms	$\leq$ 0.015	$\leq$ 0.015
Back-end added phase noise (400 pulses)	deg rms	$\leq$ 0.005	$\leq$ 0.015
Long term drift performance (24 °C $\pm$ 2 °C)	fs rms	100	100
Amplitude and phase pulse to pulse feedback		Yes	Yes
Interlock on VSWR		Yes	Yes

13.5 Technology readiness level

Table 13.6 reports and comments on the Technology Readiness Level (TRL) of the RF systems across the different linac subsystems.

Table 13.6: TRL of RF subsystems

Sub - systems	TRL	Comments
Injector RF	9	S-band injectors are widely used in many facilities including SPARC_LAB. S-band technology is fully available in the market.
X-band Linac	6	X-band linacs are relatively new. Impressive progress has been made and the final testing of the accelerating section full prototype will upgrade the corresponding TRL level in the upcoming months.
X-band waveguide components	6	Technology demonstrated in other facilities and test benches but not widely and exactly at the same conditions.
RF power system	6	X-band RF power system has been already tested and operated in normal conditions in the test stand, but the Canon tube selected for our module is a novel device lacking operational experience. The final operational test will prove the validity and reproducibility of the technical choices in the real setting.
X-band LLRF	6	A commercial S-band system operating at X-band thanks to up/down converters made in-house has been successfully operated at TEX. A brand-new X-band native platform is being developed in collaboration with industry.

13.6 Conclusions

The goals of this chapter were to describe the various RF systems of the facility and complete the information already given in the previous chapters on the subject. According to the reported contents, the designed RF systems will meet the requirements imposed by the beam physics to reach the facility scientific goals. However, the margin to meet some of the system specifications is not very large, especially for what concerns the peak accelerating fields and the ultra-tight RF phase stability required to limit the shot-to-shot energy jitter downstream of the plasma channel. Continuing the R&D in this field at the LNF facilities SPARC_LAB and TEX is therefore crucial.

Table 13.7: Radiofrequency subsystems with section reference.

Subsystems	**Number**	**Description**
RF gun	1	Sec. 13.2.1
S-band structure 3 m	2	Sec. 13.2.2
S-band structure 1.5 m	2	Sec. 13.2.2
X-band structure	16	Chapter 6
X-band linearizer	1	Chapter 5
PolariX	2	Chapter 11
S-band power system	3	Sec. 13.3
X-band power system	10	Sec. 13.3
S-band LLRF	3	Sec. 13.4
X-band LLRF	10	Sec. 13.4

Bibliography

[1] D. Alesini et al. “New technology based on clamping for high gradient radio frequency photogun”. In: *Physical Review Special Topics—Accelerators and Beams* 18.9 (2015), p. 092001.

[2] D. Alesini et al. “Design, realization, and high power test of high gradient, high repetition rate brazing-free S-band photogun”. In: *Physical Review Accelerators and Beams* 21.11 (2018), p. 112001.

[3] V. Shpakov et al. “Design, optimization and experimental characterization of RF injectors for high brightness electron beams and plasma acceleration”. In: *Journal of Instrumentation* 17.12 (2022), P12022.

[4] D. Alesini et al. “Design, realization, and testing of a brazing-free C-band radio frequency photogun”. In: *Phys. Rev. Accel. Beams* (Oct. 2025). DOI: 10.1103/jrth-j9sf. URL: https://link.aps.org/doi/10.1103/jrth-j9sf.

[5] A. Grudiev, S. Calatroni, and W. Wuensch. “New local field quantity describing the high gradient limit of accelerating structures”. In: *Phys. Rev. ST Accel. Beams* 12 (10 2009), p. 102001. DOI: 10.1103/PhysRevSTAB.12.102001. URL: https://link.aps.org/doi/10.1103/PhysRevSTAB.12.102001.

[6] R. B. Neal. “Design of linear electron accelerators with beam loading”. In: *Journal of Applied Physics* 29.7 (1958), pp. 1019–1024.

[7] V. Dolgashev et al. “RF Breakdown in Normal Conducting Single-cell Structures”. In: (2005). URL: https://cds.cern.ch/record/928170.

[8] D. Alesini et al. *Process for manufacturing a vacuum and radio-frequency metal gasket and structure incorporating it*. International patent application PCT/IB2016/051464 assigned to INFN. 2016.

[9] F. Cardelli et al. “Design of Linac with the New Gaskets Clamping Fabrication Technique”. In: *Proc. of International Particle Accelerator Conference (IPAC’16), Busan, Korea, May 8-13, 2016* (Busan, Korea). International Particle Accelerator Conference 7. Geneva, Switzerland: JACoW, 2016, pp. 403–406. ISBN: 978-3-95450-147-2. DOI: doi:10.18429/JACoW-IPAC2016-MOPMW005. URL: http://jacow.org/ipac2016/papers/mopmw005.pdf.

[10] N. Shafqat et al. “Fabrication, conditioning and installation of the 1st high gradient S-band accelerating module for the energy upgrade of the FERMI free electron laser linac”. In: *Nuclear Instruments and Methods in Physics Research Section A: Accelerators, Spectrometers, Detectors and Associated Equipment* 1055 (2023), p. 168543. ISSN: 0168-9002. DOI: https://doi.org/10.1016/j.nima.2023.168543. URL: https://www.sciencedirect.com/science/article/pii/S0168900223005338.

[11] V. del Pozo Romano et al. “High Power Conditioning of X-Band Variable Power Splitter and Phase Shifter”. In: *Proc. 10th International Particle Accelerator Conference (IPAC’19), Melbourne, Australia, 19-24 May 2019* (Melbourne, Australia). International Particle Accelerator Conference 10. Geneva, Switzerland: JACoW Publishing, 2019, pp. 2964–2967. ISBN: 978-3-95450-208-0. DOI: doi:10.18429/JACoW-IPAC2019-WEPRB064. URL: http://jacow.org/ipac2019/papers/weprb064.pdf.

[12] F. Cardelli et al. “Status and Commissioning of the First X-Band RF Source of the TEX Facility”. In: *Proc. 13th International Particle Accelerator Conference (IPAC’22)*. International Particle Accelerator Conference 13, TUPOPT061 (July 2022), pp. 1148–1151. ISSN: 2673-5490. DOI: 10.18429/JACoW-IPAC2022-TUPOPT061. URL: https://jacow.org/ipac2022/papers/tupopt061.pdf.

[13] F. Cardelli et al. “X-band activities at INFN-LNF”. In: *JACoW* IPAC2023 (2023), MOOG1. DOI: 10.18429/JACoW-IPAC2023-MOOG.

[14] F. Cardelli et al. “Advancements in X-band technology at the TEX facility at INFN-LNF”. In: *Proc. IPAC'24*. IPAC'24 - 15th International Particle Accelerator Conference 15 (May 2024), pp. 1421–1424. ISSN: 2673-5490. DOI: 10.18429/JACoW-IPAC2024-TUPR02. URL: https://indico.jacow.org/event/63/contributions/3936.

[15] C. Di Giulio et al. “TEX (TEst stand for X-band) at LNF”. In: (2023). arXiv: 2308.03053 [physics.acc-ph]. URL: https://arxiv.org/abs/2308.03053.

[16] S. Pioli et al. “TEX - an X-Band Test Facility at INFN-LNF”. In: *Proc. IPAC'21* (Campinas, SP, Brazil). International Particle Accelerator Conference 12. JACoW Publishing, Geneva, Switzerland, Aug. 2021, WEPAB314, pp. 3406–3409. ISBN: 978-3-95450-214-1. DOI: 10.18429/JACoW-IPAC2021-WEPAB314. URL: https://jacow.org/ipac2021/papers/wepab314.pdf.

[17] L. Piersanti et al. “Design and Test of a Klystron Intra-Pulse Phase Feedback System for Electron Linear Accelerators”. In: *Photonics* 11.5 (2024). ISSN: 2304-6732. DOI: 10.3390/photonics11050413.

14. Timing and Synchronisation

14.1 Introduction

This chapter presents the design and implementation of the timing and synchronization system for EuPRAXIA@SPARC_LAB. It covers the distribution of precise trigger and reference signals, the generation of a stable master clock, phase-locking of optical and electrical clients, and intra-pulse stabilization of klystrons. The key performance specifications, system architecture, and strategies for mitigating environmental effects are comprehensively discussed, providing an overview of the optimized methodologies by which femtosecond-level synchronization is achieved throughout the entire facility.

14.2 System overview and specifications

14.2.1 Timing

The timing system is designed to distribute precisely timed trigger events to equipment, ensuring synchronized execution across the facility, including beam-related information for each pulse, timestamping, and pulsed or periodic signals.

For EuPRAXIA@SPARC_LAB, an event-based timing system has been preferred over absolute time synchronization, as it enables the definition and distribution of trigger and clock signals synchronized with the Reference Master Oscillator (RMO) based on pre-programmed sequences or specific events (e.g., "Injection Trigger," "Spectrometer Active", etc).

Its tree network topology efficiently distributes timing signals to hundreds of points across the accelerator, with ease of modification and scalability, and supports event propagation between network nodes through its event-driven architecture, delivering triggers with a jitter that is a fraction of the Radiofrequency (RF) period.

Essential system parameters for EuPRAXIA@SPARC_LAB include:

- Trigger Rate: bunch rate (up to 400 Hz)
- Synchronization Frequency: 2998.55 MHz
- Clock Frequency: $RF_{S\text{-}band}/42$ (photocathode laser oscillator frequency)
- Time Jitter: < 35 ps RMS with respect to the synchronization signal

- Timestamping Resolution aligned with bunch rate
- Total Users: > 100 trigger points

14.2.2 Synchronization

The synchronization system has two main responsibilities:

1. Reference signal generation and distribution
   - Provides the low jitter *master clock signal*, at the S-band RF frequency, to accelerator subsystems (lasers, LLRF, diagnostics);
   - Delivers the 42nd sub-harmonic of the master clock (hereinafter referred as *reference synchronization signal*) for use as reference for the timing system and for coarse laser repetition-rate locking.
2. Phase coherence
   - Ensures that the oscillators of critical subsystems remain phase-locked to the master clock signal.

Reference generation is achieved by means of an ultra-stable microwave oscillator (RMO, see Section 14.3.2.1). The resulting signal is subsequently transmitted to each subsystem utilizing dedicated fiber-stabilized links (see Section 14.3.2.2). Coaxial cable distribution is employed exclusively for the low frequency reference synchronization signal, which serves the laser systems by providing coarse pulse alignment. The master clock distribution guarantees the femtosecond-level synchronization. To maintain coherence between the master clock signal and the local oscillators of each subsystem, dedicated locking electronics are utilized. Specifically, each laser oscillator is equipped with a feedback system designed to stabilize its repetition rate relative to the master clock frequency (see Section 14.3.2.3). The complete schematic layout of the synchronization system is presented in Figure 14.2.

Performance specifications for the synchronization system are derived from jitter tolerance studies discussed in the beam physics chapter (see Table 3.9). We report the values in Table 14.1, translated in fs to facilitate understanding of the jitter studies discussed later in this chapter:

Component	**Maximum Jitter** (RMS)	**Equivalent** (fs RMS)
Photo-injector laser	20 fs	20
S-band power stations	0.02°	18.5
X-band power stations	0.10°	23.1

Table 14.1: Timing jitter specifications

For each subsystem, the maximum tolerable jitter, denoted as $\sigma_{\text{subsystem}}$, is the root mean square combination of three uncorrelated contributions:

$$\sigma_{\text{subsystem}} = \sqrt{\sigma_{\text{distr}}^2 + \sigma_{\text{lock}}^2 + \sigma_{\text{client}}^2} \tag{14.1}$$

- σ_{distr} is the jitter added by the distribution system delivering the master clock signal to each client;
- σ_{lock} is the residual jitter of the locked client oscillator due to the non-ideal locking device (limited bandwidth, gain, or added noise);
- σ_{client} is the jitter introduced by the subsystem itself, i.e. downstream the locked oscillator.

14.3 System implementation

The physical implementation and spatial distribution of the synchronization system components are detailed in Figure 14.1. This comprehensive diagram of the accelerator highlights the specific

locations where the primary generators and the distributed timing and synchronization receivers are placed. The layout indicates the strategic positioning of these devices across key areas of the facility—including the laser clean room, the linac tunnel, and the klystron gallery—emphasizing the integration points where the low-jitter reference signals and the timing information are delivered to both electrical (LLRF) and optical (laser) clients.

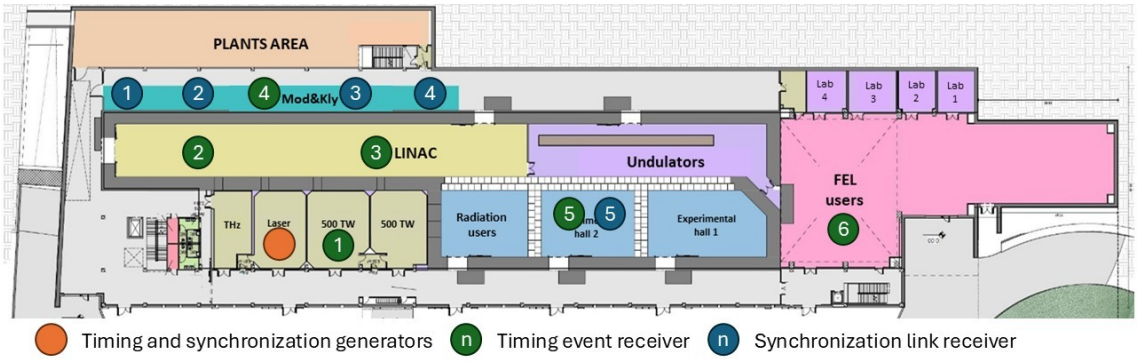

Figure 14.1: Map of the Timing and synchronization hardware on the level L0 building plan.

14.3.1 Timing system

A commercial system, built by Micro-Research Finland Oy, already extensively tested at LNF accelerators and in numerous facilities worldwide, is proposed for use. It allows a modular architecture within a tree network topology, incorporates recent hardware updates by the manufacturer, and is adapted to the mTCA.4 standard, aligning with current market technologies [1].

This is an event-based timing system, working by generating event codes that are synchronized to a master clock reference locked to the main accelerator frequency, with a typical jitter of less than 25 ps RMS. It uses a base clock at $f_{ck} = 71.39$ MHz driven by the 42^{nd} sub-harmonic of the RMO. A distribution network provides timing signals using three hardware components: an Event Generator (EVG) acting as timing master, Event Receivers (EVRs) acting as slaves, and fan-out modules.

Events are sent at the rate of the beam pulse repetition rate (and/or any submultiple of the base clock) from the EVG to EVRs through a bidirectional fiber optic cabling network. The EVRs are able to generate actions in response to received events, such as pulses with configurable delay (resolution $1/f_{ck} = 14$ ns, fine tunable to 10 ps steps on selected outputs), polarity and width and/or software notifications about event reception. These pulses are connected to the hardware equipment such as beam diagnostics, modulators, and Low-Level Radiofrequency (LLRF) systems among others. The system is easily configurable and scalable to support all required users.

EVRs can also send event codes to the event generator upon detecting input activity. The generator can then redistribute this event again in downwards direction to all the receivers.

Logging of events with globally distributed timestamps is available in the receivers and allows association of timestamp to collected data or performed actions, with a resolution equal to the period of the base clock. Additionally, the system capabilities are extended to include an absolute clock reference. This is provided by a White Rabbit node integrated with the MRF EVG and distributed to the EVRs to achieve enhanced sub-nanosecond absolute time synchronization across the facility, which can be highly beneficial for data correlation performed by the user-side equipment [2].

The event generator is also capable of distributing up to eight arbitrary digital signals using another feature called the Distributed Bus. An active delay compensation mechanism measures the propagation delay between every two nodes directly connected at any level of the network, so that the total delay from the EVG to each node can calculated, in order to counteract the effects of

thermal changes and other environmental factors on the signal's travel time between nodes.

14.3.2 Synchronization system

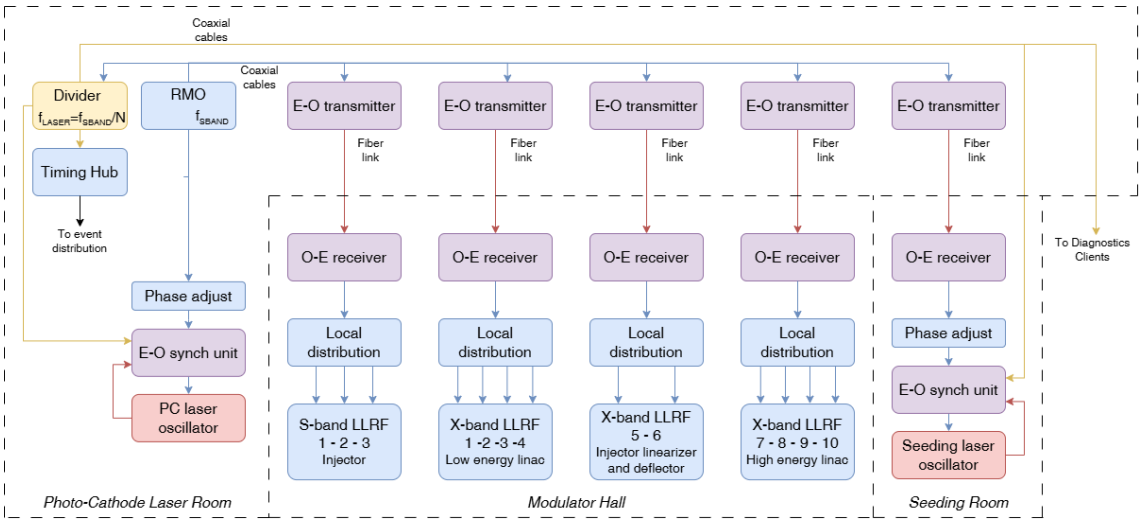

Figure 14.2: Layout of the synchronization system.

14.3.2.1 Reference generation

The RMO constitutes the central component of the synchronization system. This oven-controlled crystal oscillator (OCXO) generates the *master clock signal* for the facility at 2998.55 MHz. As stated in the introduction, also a *synchronization reference signal*, essential for the timing system and laser locking, is also required at 71.39 MHz (derived from the master clock as 2998.55/42). Since the stability requirements for this sub-harmonic are less stringent (maximum jitter <1 ps RMS), it can be generated externally using electronic frequency dividers.

The short-term performance specification for the RMO requires an integrated absolute timing jitter of less than 30 fs RMS (integrated across the offset frequency range of 10 Hz to 10 MHz from the carrier). Moreover, the long-term frequency stability must not exceed 1×10^{-7} per year. Commercial off-the-shelf devices are currently capable of achieving these stringent specifications. For example, the single-sideband phase spectral density (SSB PSD) of a Rohde & Schwarz SMA100B microwave generator, shown in Figure 14.3, meets the machine requirements and identifies this unit as a viable candidate for the RMO implementation.

14.3.2.2 Reference distribution

Commercial off-the-shelf components were selected for the timing distribution system, as they provide an added jitter contribution below 10 fs with respect to the RMO, thereby fulfilling the phase-noise and timing-stability requirements listed in Table 14.1 and further discussed later in this chapter.

Given the compact scale of the accelerator facility, a Continuous Wave (CW) laser distribution architecture, where the optical carrier is amplitude-modulated by the master clock and transmitted through stabilized fiber links, was adopted instead of a pulsed-laser timing system. This configuration was chosen due to its enhanced cost-effectiveness, reduced architectural complexity, and improved long-term operational robustness, all of which are advantageous for maintaining synchronization across accelerator subsystems. Each link utilizes a dual-fiber configuration: the primary fiber transmits the reference signal, while a secondary probe fiber measures the optical path

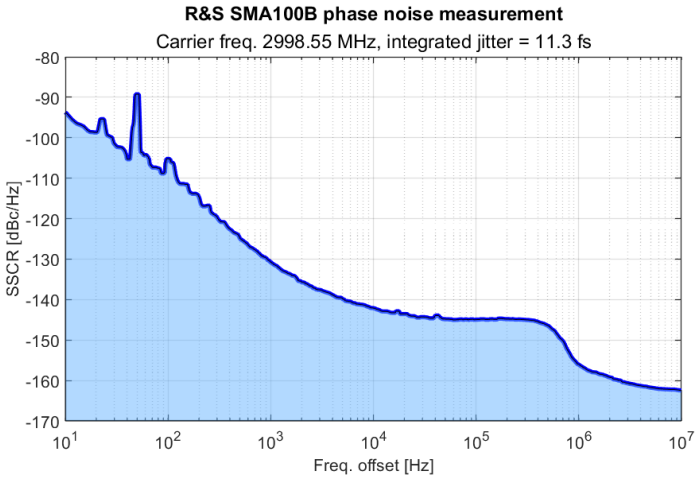

Figure 14.3: SSB PSD of Rohde & Schwarz© SMA100B microwave signal generator [3] (with ultra low noise option) and its timing jitter from integrated between 10 Hz and 10 MHz from the carrier

length. The probe fiber enables optical path stabilizers to actively compensate for environmental fluctuations, thereby maintaining a constant effective length. Downstream of each link, a receiver converts the optical signal back into the electrical domain for local distribution. Similar systems have been successfully implemented in facilities such as PSI SwissFEL and are commercially available [4]. This established technology is capable of distributing the master clock signal with an added jitter $\sigma_{\text{distr}} < 8$ fs and a peak-to-peak drift between 10 fs and 30 fs over a 24-hour period, under environmental variations of $\pm$ 1 °C and $\pm$ 5 % RH (Relative Humidity).

Given that the various areas of the EuPRAXIA@SPARC_LAB facility exhibit environmental parameter specifications that may be either more stringent (e.g., the bunker) or more permissive (e.g., the klystron gallery) than those required by the reference distribution system (see Table 18.15), the optical fibers and RF cables will be routed within thermally insulated, vibration-damping conduits. These ducts will be equipped with internal water pipes to help temperature stabilization. It is worth to noting that the cooling pipes must provide a water laminar flow to avoid unwanted vibrations.

This mitigation technique has been successfully validated at the PAL-XFEL facility [5] and will be replicated at the LNF, with initial prototype tests conducted at SPARC_LAB. The primary objective of these studies is to evaluate the request for the water cooling system (in terms of water temperature average value and stability), the contribution of mechanical vibrations to the overall timing jitter and to assess the system's performance under realistic operational conditions. The conceptual cross-section design for this ductwork is reported in Figure 14.4. The complete layout of the duct network along the facility is illustrated in Section 14.3.2.4.

The link receivers, in conjunction with the associated RF amplification and splitting electronics, will be located within the same racks as the client subsystems. This strategic placement is implemented to minimize coaxial cable lengths, restricting them to approximately 1 m for RF clients and less than 3 m for laser clients. To further mitigate drifts in this local distribution, temperature-stabilized coaxial cables [6] will be employed. For the LLRF modules located in the klystron gallery, the estimated drift is approximately 5 fs peak-to-peak per meter ($\text{fs}_{\text{pp}}/\text{m}$) under (23 ± 2) °C conditions (see Table 18.15). Conversely, in the laser clean room, where the temperature is four times more stable (23.0 ± 0.5) °C, the expected drift is substantially lower, estimated at 1.25 fs peak-to-peak per meter ($\text{fs}_{\text{pp}}/\text{m}$).

The low frequency synchronization reference signal will be distributed using only coaxial

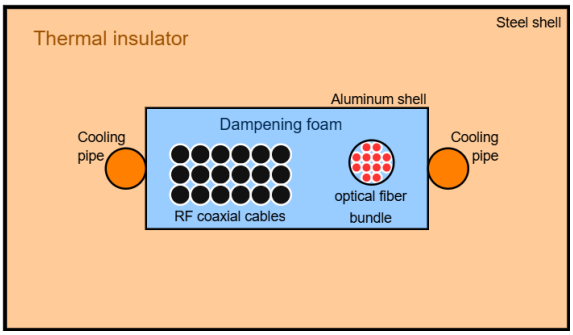

Figure 14.4: Conceptual cross-section design of the thermal-insulating vibration-dampening cable duct

cables, given that attenuation is negligible at this frequency and the precision requirements are less stringent. These cables will also be housed within the previously described stabilized ducts. While optical fiber length exhibits considerable sensitivity to humidity, coaxial cables are substantially less affected by this environmental variable (as indicated by the absence of explicit warnings or specifications from the manufacturer). Nevertheless, placing both distribution media within the insulated ducts is expected to strongly reduce the overall impact of humidity, though dedicated laboratory tests will be conducted prior to final installation to confirm this performance.

14.3.2.3 Client locking systems

The primary clients of the synchronization system can be systematically categorized into two main groups:

- Electrical (LLRF modules and cavity BPMs);
- Optical (laser oscillators - photocathode and pump-probe laser system).

The electrical clients use the master clock or the synchronization reference signals directly. This approach eliminates the need for supplementary locking electronics, thereby inherently preventing the introduction of additional accumulated jitter into these subsystems. It is worth noting that also the X-band LLRF modules accept the master clock frequency as input since they generate internally the X-band clock and all the necessary ancillary reference signals (LO, ADC and DAC clocks, ...).

Optical clients, unlike purely electrical components, require additional locking electronics to synchronize the repetition rate of their laser oscillators to an external reference (i.e., the master clock). The first step in this procedure is to establish temporal overlap between the pulse trains generated by the different oscillators. Since the laser oscillator repetition rate corresponds to the 42^{nd} sub-harmonic of the S-band frequency, an initial feedback loop (referred to as the fundamental loop) operates at this lower frequency. Once the fundamental loop is active, the system automatically transitions to the higher frequency feedback (harmonic loop), which works at the main S-band frequency. Operation of the harmonic loop provides significantly enhanced phase detection resolution and enables the optical client to be phase-locked to the reference with a residual relative timing jitter well below 20 fs RMS.

To implement this high-precision locking system, a balanced optical–microwave phase detector (BOMPD) was selected. This device enables precise phase comparison (with a demonstrated sensitivity of hundreds of mV/ps) between a continuous optical pulse train and a CW microwave reference, typically achieved using a fiber-coupled Sagnac interferometer [7]. The resulting error signal is subsequently processed by dedicated locking electronics, which drives a piezo-mounted mirror. This mechanism forces the laser cavity's natural frequency to match that of the reference within an active bandwidth of several tens of kHz. Such BOMPDs are available as commercial off-the-shelf products [8] and can guarantee a residual jitter with respect to the reference signal

of approximately 15 fs RMS. A validation test utilizing a commercial device has already been scheduled on the laser oscillators currently operating at LNF, which share similar characteristics with those planned for the EuPRAXIA@SPARC_LAB facility.

14.3.2.4 Residual drift compensation

Residual temporal drifts occurring over long timescales (minutes to hours) are corrected using shot-by-shot RF feedbacks. As phase values are sampled at the machine repetition rate, compensation is inherently limited to variations with spectral components below the corresponding Nyquist frequency (half the repetition rate).

The phase of each facility subsystem, whether RF or laser, can be controlled independently to maximize operational flexibility. For RF clients, the phase signal is sampled directly from the accelerating structure and processed by the LLRF system, which employs its built-in Proportional-Integral-Derivative (PID) digital controller to achieve phase stability (see Section 13.4).

For optical clients, phase readback obtained using a fast photo-diode illuminated by the laser oscillator. This signal, properly filtered, is sent to a LLRF module that measures the phase. This technique has been extensively used for measuring the SPARC_LAB photo-cathode laser oscillator and a jitter resolution below 20 fs RMS has been achieved. Further studies to minimize the photo-detection AM/PM conversion are foreseen. Slow feedback stabilization exploits the average phase information extracted by the photo-diode and is achieved by introducing a correction via a phase shifter located on the RF reference line that feeds the laser synchronization unit (see Figure 14.2).

To prevent environmental conditions from corrupting these crucial phase readback signals, the coaxial cables transporting the RF signals from the linac to the klystron gallery will be routed through the previously described insulated duct system [5]. This dedicated duct network spans the entire facility, featuring two main actively temperature-stabilized backbones: one traversing the linac tunnel and one traversing the klystron gallery. These two backbones are positioned using dedicated mechanical supports and they are locally connected by means of short, thermally insulated, corrugated pipes, as illustrated conceptually in Figure 14.5.

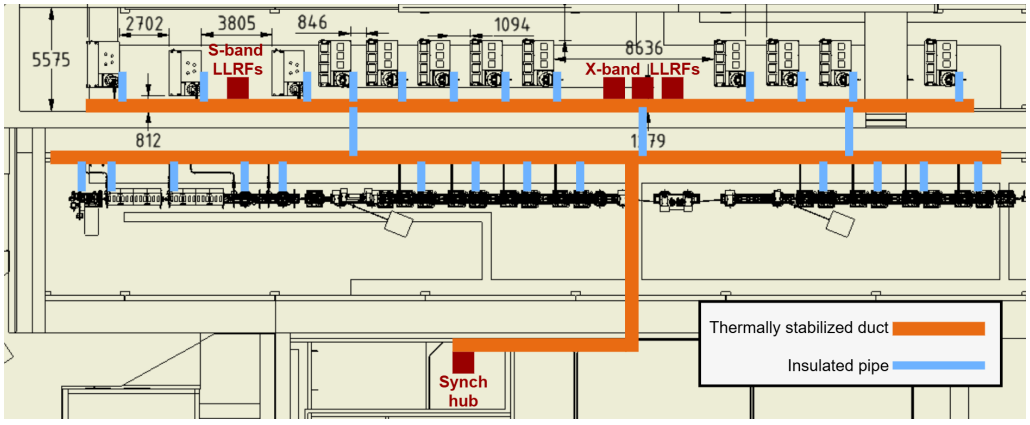

Figure 14.5: Conceptual network layout of the insulated ducts across the facility. This system is specifically designed to accommodate the coaxial cables and optical fibers utilized for both the reference signal distribution and the RF signal readbacks

14.3.2.5 RF plant stability enhancement

To assess the stability of the RF plant, dedicated measurements were performed on an X-band station at the LNF TEX facility. Because the LLRF system used during these tests was not optimized for the X-band operation (low ADC sampling frequency, limited bandwidth), the resulting values

were subsequently treated as upper limits for calculations.

Specifically, an added phase jitter of 0.05° RMS (corresponding to 11.6 fs RMS) was measured from the driver amplifier, and 0.07° RMS (corresponding to 16.2 fs RMS) was measured from the klystron.

Moreover, the LLRF specifications, as detailed in Table 13.5, require that the maximum phase jitter introduced by the LLRF must not exceed 0.005° RMS (corresponding to 4.6 fs RMS) for S-band systems and 0.015° RMS (corresponding to 3.5 fs RMS) for X-band systems.

Based on these specifications, the total RMS jitter of the RF plant, calculated using Equation 14.2, is expected to be 0.09° RMS for the X-band and 0.021° RMS for the S-band. These calculated results are already approaching the limits of the overall tolerances defined in Section 14.2.2, even prior to the inclusion of the added jitter from the reference distribution system.

$$\sigma_{\text{RF plant}} = \sqrt{\sigma_{\text{LLRF}}^2 + \sigma_{\text{DRI}}^2 + \sigma_{\text{KLY}}^2} \tag{14.2}$$

To satisfy the stringent beam physics requirements and provide an operational margin against potential power plant performance deviations, intra-pulse phase stabilization of klystrons will be implemented. This advanced technique, initially developed at LNF and in continuous operation at SPARC_LAB since 2007, has been recently upgraded and successfully validated on both solid-state and Pulse-Forming Network (PFN) modulators.

Stabilization is achieved by comparing the klystron output signal against the LLRF drive using a broadband mixer. The resulting error signal is processed by an analogue active loop filter and subsequently applied to a fast phase shifter, enabling phase corrections to be executed within the duration of a single RF pulse. Detailed implementation specifics of this system are documented in [9].

This stabilization method has demonstrated significant performance enhancement, reducing the RF power plant jitter to less than 10 fs for a C-band solid-state based power plant, and less than 15 fs for an S-band PFN based power plant.

Theoretically, given that the control loop operates on baseband signals, comparable performance could be achieved across S-, C- and X-band systems, although the characteristics of certain key components (e.g., fast phase shifters, RF mixers) may exhibit variation. Consequently, the jitter measured on the C-band plant with solid-state modulators is designated as the reference client jitter (σ_{client}) for budgetary purposes across both RF plant types.

14.4 Conclusions

Table 14.2 summarizes the expected timing jitter contributions from the main facility subsystems. For the reference distribution system and the laser phase lock implementation, the values used in this budget were derived from the datasheets of commercial products currently under consideration. Specifically, residual jitters of < 8 fs and < 15 fs were assumed for the reference distribution and the laser phase lock, respectively. Regarding the optical clients, a client jitter of less than 5 fs was assumed for the laser amplification chain following the oscillator, which is well within the maximum tolerated limit of 10 fs.

These results confirm that the proposed synchronization system, inclusive of klystron intra-pulse phase feedback, satisfies the stringent tolerances required by the beam dynamics criteria.

Continuous R&D efforts at the LNF are essential to validate the most critical design choices for the synchronization system. These critical areas include the phase-locking of optical oscillators, the implementation of a thermally stabilized duct network for distributing coaxial cables and optical fibers carrying the machine RF references, and the intra-pulse phase stabilization of the klystrons.

Table 14.3 reports the Technology Readiness Level (TRL) for the timing and synchronization systems, providing a detailed description of the sub-systems and critical devices and components.

Table 14.2: Synchronization system expected performance for the RF and laser clients.

Subsystem	$\sigma_{\textbf{distr}}$ (fs)	$\sigma_{\textbf{lock}}$ (fs)	$\sigma_{\textbf{client}}$ (fs)	$\sigma_{\textbf{subsystem}}$ (fs)	**Required** σ (fs)
Lasers	< 8	< 15	< 5	< 17.7	20
S-band stations	< 8	n/a	< 10	< 12.8	18.5 (0.02°)
X-band stations	< 8	n/a	< 10	< 12.8	23.1 (0.10°)

Table 14.3: TRL level of the timing and synchronization systems

Sub - systems	**TRL**	**Comments**
Event generator & receiver modules	9	System already proven in operational environment. Technology is fully commercialized and operational.
Reference generation	9	Reference Master Oscillators are commercially available, extensively tested in accelerator environment delivering excellent performance.
Reference distribution	9	Stabilized fiber links for master clock signal distribution (including both the transmitter and receivers) are commercially available, extensively tested in accelerator environment delivering excellent performance (e.g. SwissFEL).
RF locking system	9	LLRF modules directly fed by the master clock signal received from stabilized links. Locking electronics is not needed and no added jitter is foreseen.
Laser locking system	8	Commercial laser locking systems, including phase detectors and control electronics, satisfy EuPRAXIA@SPARC_LAB requirements. A joint test with an industry leader is scheduled at LNF to verify performance.
Klystron intra-pulse phase feedback	7	The system has been in operation at SPARC_LAB since 2006 on S-band RF power stations and has been tested on the C-band station using solid state modulator. Tests are planned at TEX to confirm the compliance on the X-band RF stations using the same architecture of EuPRAXIA@SPARC_LAB.
Stabilized cable duct	7	Similar system already used in other facilities (e.g. PAL-XFEL), but it needs to be realized and tested at LNF.

Bibliography

[1] J. Pietarinen (Micro-Research Finland Oy). “Complete MRF Timing System on MicroTCA.4”. In: *Proceedings of Workshop for Research and Industry*. IHEP, Beijing, 2019.

[2] White Rabbit Collaboration. *White Rabbit: Sub-Nanosecond Synchronization and Deterministic Ethernet*. 2025. URL: https://white-rabbit.web.cern.ch/.

[3] Rohde & Schwarz© GmbH. *SMA100B - RF and microwave signal generator*. URL: https://www.rohde-schwarz.com/it/prodotti/misura-e-collaudo/generatori-di-segnali-analogici/rs-sma100b-rf-and-microwave-signal-generator_63493-427776.html. (accessed: 25.03.2025).

[4] P. Orel et al. “Test results of the Libera Sync 3 CW reference clock transfer system”. In: *Proc. IPAC'14* (2014), pp. 1751–1753.

[5] C.-K. Min et al. “RF Timing Distribution and Laser Synchronization Commissioning of PAL-XFEL”. In: *Proc. IPAC2016, Busan, Korea* (2016).

[6] Andrew©. *FSJ1-50A, HELIAX® Superflexible Low Density Foam Coaxial Cable, corrugated copper, 1/4 in, black PE jacket*. URL: https://www.andrew.com/products/fiber-power-rf-connectivity-accessories/rf-connectivity/coaxial-cables/itemfsj1-50a/. (accessed: 15.03.2025).

[7] K. Şafak et al. “Balanced optical-microwave phase detector for 800-nm pulsed lasers with sub-femtosecond resolution”. In: *Proc. of FEL2019, WEP003* (2019), pp. 322–324.

[8] Cycle© GmbH. *Balanced Optical Microwave Phase Detector*. URL: www.cyclelasers.com/synchronization-modules/bompd/#details. (accessed: 15.03.2025).

[9] L. Piersanti et al. “Design and test of a klystron intra-pulse phase feedback system for electron linear accelerators”. In: *Photonics*. Vol. 11. 5. MDPI. 2024, p. 413.

15. Control System

15.1 Introduction

This chapter presents the design and implementation of the EuPRAXIA@SPARC_LAB control system. It provides an overview of the general requirements that guide its development, the adopted technologies—chiefly the EPICS 7 framework—and the structure of the system in its different tiers, from hardware interfaces to high-level services (Sec. 15.2). Furthermore, it illustrates the services design and architecture (Sec. 15.3), the interfaces (Sec. 15.4), and the integration of advanced tools such as Artificial Intelligence (Sec. 15.5). Sec. 15.6 describes the data management and networking of the facility.

15.2 Overview

Control systems of large experimental physics facilities [1], as EuPRAXIA@SPARC_LAB, need to address several general top-level requirements listed in Table 15.1. The intention of the general requirements list is to emphasize the requirements that are not obvious, or which are likely to be forgotten in a bottom-up development process, resulting in difficulties during integration, commissioning or operation.
Control system design expects that the variation of similar device types is minimal in the control system in order to meet the following requirements: REQ-1000/3000/4000/5000.
It is very important to provide unified access to the all devices that are used in the project to reduce system maintenance costs and possible human errors during usage (REQ-5000).
The EuPRAXIA@SPARC_LAB control system will provide facility-wide monitoring and control, integrating all the accelerator subsystems into a unified infrastructure. It will extend from the interfaces of the equipment to be controlled within the technical subsystems during the machine operation, up to the data management and services such as alarm propagation and high-level applications for data analysis and advanced functionalities.

Table 15.1: Generally applicable requirements for control systems of large experimental physics facilities

REQ-1000	Scalability. The facility will be large in terms of the number of signals (order-of-magnitude estimation between 10^5 and 10^6). The control system must be designed to efficiently handle such a scale without significantly impairing performance.
REQ-2000	Performance.The control system must provide the means to handle slow and mid-rate signals, with sampling rates ranging from a few Hz up to several kHz (e.g. temperature sensors, vacuum gauges, auxiliary systems - ref. Vacuum Chapter 16), as well as fast-rate signals up to the MHz range, as required by the RF system and selected beam diagnostics (ref. Diagnostics Chapter 11 and RF System Chapter 13).
REQ-3000	Maintainability. It must be possible to efficiently adapt the control system to the requirement and technology changes during the long lifetime of the facility. As one part of the control system is changed, the unintended impact on other subsystems must be minimal.
REQ-4000	Reliability. The mean time between failures (MTBF) of the control system (either due to faults in software or hardware failures) must meet the overall availability objectives of the facility (ref. Executive Summary Chapter 1). With a control system availability target in line with that of other hyperconverged infrastructures (>99%), and a mean time to repair of 1 week considering the presence of spare objects provisions, we aim at a year-reliability of >98%.
REQ-5000	Usability. The control system must provide human-machine and programmatic interfaces to its users (operators, physicists and engineers) that allow for efficient, ergonomic and intuitive operation in order to reduce the possibility of human error. For example, the look-and-feel of the graphical interfaces should be consistent (use of colors, fonts, layouts), it should be possible to easily transfer information between the tools (drag & drop / copy & paste), guidance should be handily available, etc. The system should be in compliance with the accessibility requirements Directive (EU) 2019/882 in terms of user experience and interoperability across graphical and programmatic interfaces.
REQ-6000	Longevity. The facility is expected to be in operation for several decades. The design of the control system must allow for continued operation throughout the lifetime of the facility, in spite of the need to reconfigure it, as well as failures and obsolescence issues of control equipment.

15.2.1 Architecture

The EuPRAXIA@SPARC_LAB control system, as usually for large experimental physics facilities, will be structured in three tiers [2], as shown in Fig. 15.1:

- User interface (upper right in Fig. 15.1). These are graphical and non-graphical user interfaces. Most or all of these will be in the control room. However, there could be some user interfaces used elsewhere during commissioning and maintenance.
- Central services (upper left in Fig. 15.1). Computer services that need to run continuously irrespective of user activities, e.g., for archiving process variables' values, high level applications (HLA), monitoring alarm states, etc.
- Equipment interfaces (bottom in Fig. 15.1). This tier is responsible for interaction with equipment and devices. It provides an abstract representation of equipment to higher layers through which the equipment can be monitored and controlled. The elementary entity on this level is called an Input Output Controller (IOC).

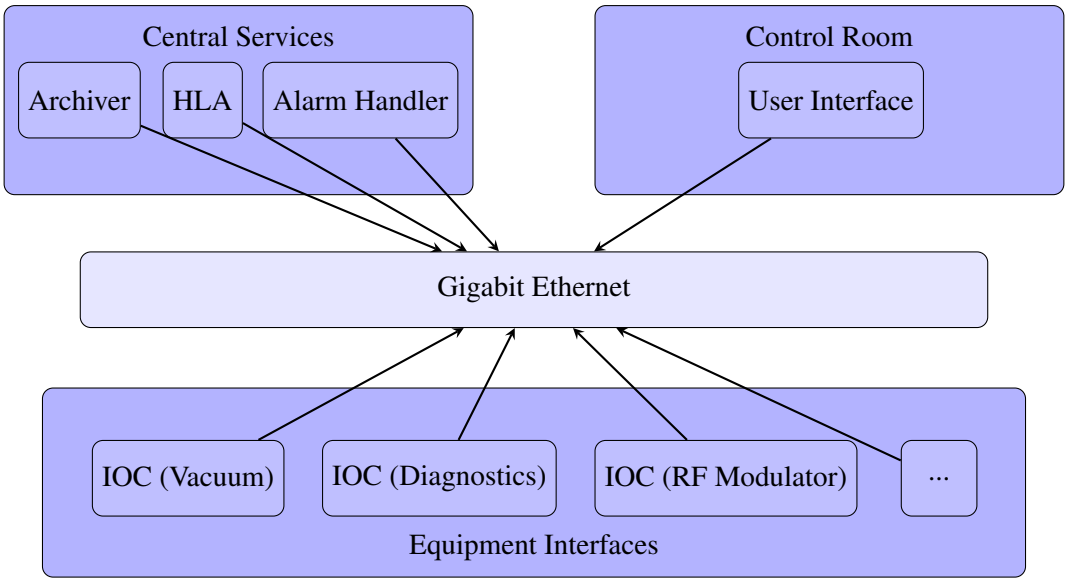

Figure 15.1: Three tier architecture scheme.

Such a structure of a control system conforms to REQ-1000, REQ-3000, REQ-5000.
The control system of the EuPRAXIA@SPARC_LAB project will be based on EPICS (Experimental Physics and Industrial Control System) [3]. EPICS is a distributed control system framework based on client-server architecture. It uses an Ethernet network for communication via the Channel Access (CA) and PVAccess (PVA) protocols. The EPICS server part, runs on IOCs. EPICS Input/Output controllers communicate with hardware devices and expose their parameters through CA. Central services (archiver, high level applications, machine protection tools and alarm handler) and the graphical OPerator Interfaces (OPIs) are EPICS clients that use CA to access device parameters. The EPICS framework is a common standard for many other scientific facilities over the world, which ensures that REQ-3000 and REQ-6000 are met.

15.2.2 Hardware and Software Integration Schemes

A vertical column is an abstraction which describes how the concrete device type is integrated into the control system. It starts from the device sensors and progresses up to the GUI (Fig. 15.2) [4].

A vertical column defines such common parts as: interfaces between an IOC and the operator's workstation and the IOC and operator workstation platform on the hardware (HW) level. From the software (SW) perspective, the vertical column describes the server and client frameworks,

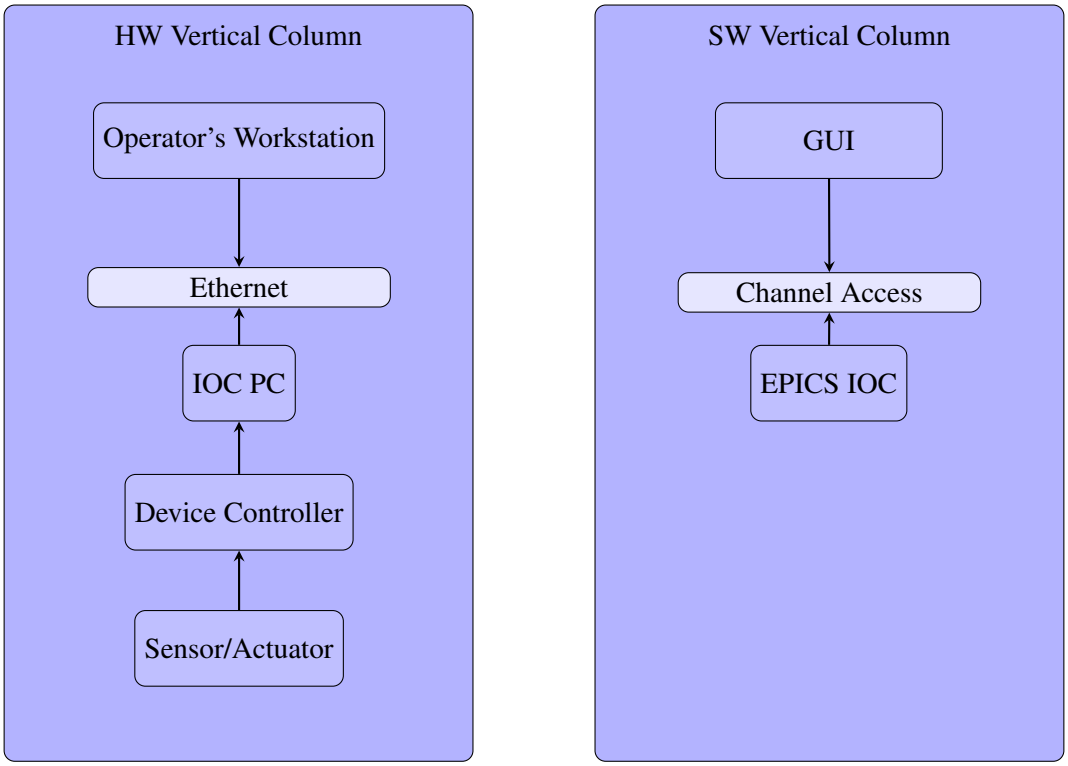

Figure 15.2: Hardware and software vertical columns.

required SW packages and communication interfaces between these components. Common parts of all vertical columns are described in this chapter. In addition, for a specific device type, the vertical column defines at the HW level:

- hardware of host computer.
- required device controller based on the sensor's interface (like ADC, relay, motion controller etc.)
- physical interfaces between all components

while at the SW level:

- Operating System (OS),
- hardware drivers,
- EPICS modules,
- device specific OPIs.

Device specific information is provided in related chapters.

15.2.2.1 Hardware

The communication interface between client/server applications is the EPICS Channel Access (CA) protocol. CA uses the TCP protocol on a transport layer. The physical interface between the IOC and the operator workstation is an Ethernet based network.

Devices can have physical interfaces of varying complexity and type. An Input/Output controller is an abstraction which hides all types of device interfaces from the control system client and exposes data through CA.

Devices that require high-speed or real-time acquisition, such as RF modulators or selected beam diagnostics (ref. Diagnostics Chapter 11 and Vacuum Chapter 16), will be handled by dedicated embedded controllers (e.g., micro-TCA or industrial PCs) located close to the apparatus. These controllers can achieve sampling rates beyond the 1 ms latency limit of the Ethernet network,

ensuring deterministic real-time performance. Other non-critical devices with moderate sampling rates (from a few Hz up to kHz), such as motors, temperature sensors components, etc. will operate via the standard Ethernet network within typical latency limits. The IOCs for these devices will be deployed as virtualized processes managed by a container orchestrator, while embedded controllers handle devices requiring real-time acquisition. This ensures REQ-2000 is met.

15.2.2.2 Software

As already mentioned, the EuPRAXIA@SPARC_LAB control system will be based on EPICS, an open-source software framework including libraries, applications and support modules developed by the collaborative effort of several scientific facilities worldwide (REQ-3000 and REQ-6000). This framework is based on a client-server structure, where the IOC represents the server component. The IOC is a virtual unit that standardizes data from different hardware devices, ensuring that the data are extracted and subsequently presented to the user in a coherent format and unit (REQ-5000).

The power of the EPICS framework stems from its modularity and capability to provide communication among a large number of devices installed throughout the entire facility, all interconnected via the same network using the CA and PVAccess protocols. This simplifies the integration of additional devices in the control system (REQ-1000) and ensures that the user's workstation can access the control and monitoring of all the facility elements (REQ-2000).

Device parameters such as measured physical quantities or status/alarm flags are represented in an EPICS IOC as Process Variables (PVs). A PV is a data container storing the parameter value and associated meta-data (e.g. units, lower and upper limits, processing configurations). The name of a PV must be unique according to the established EuPRAXIA naming convention, as it is exposed to the CA and serves as the key to identify and access the associated parameter by the control system and OPIs. The PVs are defined within the IOC as instances into a database record file.

Device support modules are available in EPICS to manage different communication methods and to handle specific functionalities of diverse hardware devices (e.g. motors, cameras).

15.2.3 Control Equipment Catalogue

The hardware devices to be integrated into the control system of EuPRAXIA@SPARC_LAB can be distinguished in families: motors, cameras, vacuum system components, magnets, RF system components, timing and synchronization systems, diagnostics. These will include almost 10^3 devices across all subsystems, with an expected number of integrated EPICS process variables between 10^5 and 10^6. The EPICS application support modules and OPIs of different types of device belonging to the same family require minimal modifications, so that all the developments are performed in a standardized and coherent manner. The operator's workstations will be connected to the same network as the IOCs, ensuring the access to the control system.

Motors

Stepper motors, piezo motors and servo motors will be employed for the motion of several components such as laser mirrors and diagnostic devices (ref. Photoinjector Chapter 5, Undulators Chapter 8, Photon Beamline Chapter 9, Endstation Chapter 10, Diagnostics Chapter 11, Laser Chapter 12). All the developments are based on the EPICS support module for motors control (*motor*). The control of these devices will be provided by motion controllers connected to the motors themselves. The controllers can be connected to a serial-to-ethernet converter and then to the network, or to the network directly, depending on the motor type.

Cameras

CCD-cameras are usually employed as optical diagnostic devices for the photoinjector laser beam, the electrons and photon beams, and for plasma (ref. Photoinjector Chapter 5, Plasma Chapter 7,

Photon Beamline Chapter 9, Endstation Chapter 10, Diagnostics Chapter 11, Laser Chapter 12). The control system will provide a functional EPICS application and OPI using the required EPICS device support module (*areaDetector*) and device drivers for the provided CCD-camera (*Aravis*). The application and the OPI will allow for images acquisition, arrays for displaying acquired images, as well as images saving. The cameras will be connected via gigabit Ethernet to the IOC.

Vacuum System

Both accelerators and FEL require a vacuum system for their operation (ref. Vacuum Chapter 16). This consists of scroll pumps, turbo pumps, ionic pumps, NEG pumps, pump controllers, chillers, pressure gauges, gauge controllers and gate valves. These components will be integrated into the control system as well as into the interlock handling of the Machine Protection System (ref. Section 19.5). These IOCs load the EPICS device support modules *StreamDevice* and *asynDriver* and will provide the monitoring and control of the physical parameters of interest, devices status, operating modes, configuration settings, and interlocks.

- **Vacuum pumps** Scroll, turbo, ionic and NEG pumps will be responsible for reaching and maintaining the required vacuum level and will be placed throughout the facility. Depending on the pump type, it can be connected to a controller, which in turn links to a serial-to-ethernet converter before reaching the network, to the network through a serial-to-ethernet converter, or directly to the network.
- **Vacuum gauges** The vacuum gauges will be responsible for monitoring the pressure inside the vacuum chambers and sections. The sensors will be connected to multi-channel controllers linked to the network.
- **Chillers** Turbo pumps may require a chiller water cooling circuit. The chillers will be connected to a serial-to-ethernet converter and then to the network.
- **Vacuum valves** Gate valves dividing the vacuum sections will be integrated into the machine protection system, which will control their operation in response to machine interlocks.

Magnet System

Different type of magnets, such as solenoids, dipoles, quadrupoles, sextupoles, and correctors, will be installed across the accelerator structure (ref. Magnets Chapter 17). These will be equipped with power supply controllers that will be integrated in the EPICS control system. This will provide access to remote control and monitoring of crucial parameters as current, status, power supply configuration settings, operating modes, and magnet temperature.

RF System

The following components of the RF System (ref. Chapter 13) will be integrated into the EPICS the control system:

- **RF modulators** RF Modulators will be connected to the network via Ethernet to an EPICS IOC, with an RF modulator device support module.
- **Low Level Radio-Frequency (LLRF)** Each LLRF instance will have an integrated EPICS IOC.
- **RF waveguides** This system includes motors and vacuum components. The integration of such devices will be the same as previously described.

Timing and Synchronization Systems

The Timing and Synchronization Systems (ref. Chapter 14) will respectively distribute the timed trigger events across the machine devices, and provide the signal reference and phase coherence required by critical subsystems. These two crucial systems will be equipped with dedicated IOCs and will be integrated into the EPICS control system.

Other diagnostic components

Other devices that will be integrated into the control system such as the various types of Beam Position Monitors (BPMs), the Current Transformer (CT), Gas Monitor Detectors (GMDs), etc. are described in the Diagnostics Chapter 11 and Photon Beamline Chapter 9.

15.3 Services

The Services tier [5] is an intermediate layer that includes functionalities such as alarm handling, data archiving, logging, and high level applications. These are responsible for more advanced functionalities as pre-processing or historization of the data collected from EPICS IOCs. Processed data information is then sent to the OPI.

15.3.1 Design and Architecture

The Services applications and functionalities act as Channel Access clients, as they collect data from the IOCs. In turn, Services are based on a client-server architecture, where each service constitutes the server component and the OPIs machines in the user's workstations act as clients. A simplified scheme of such architecture is shown in Fig. 15.3.

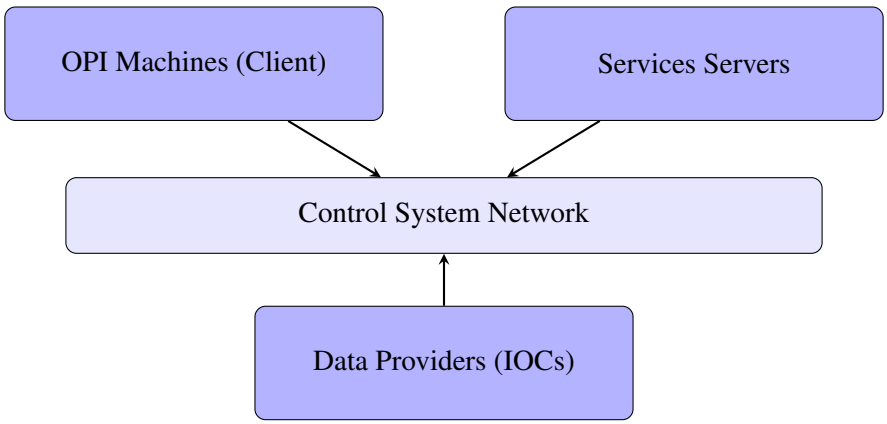

Figure 15.3: Control System Services architecture scheme.

15.3.2 Functionality

- **Archiving** - Data historization is crucial to monitor the systems conditions over time or for waveforms visualization. The Archiver Appliance will be used as the data archiving framework, as it is implemented for EPICS-based control systems [6]. This allows to access and store millions of PVs. All PV values are acquired at a fixed scan rate or upon change, leading to the collection of a vast amount of data in a short time. The Archiver Appliance provides efficient data management, as data storage is organized on a three-level basis: short, medium and long-term storage. As data are acquired, they are initially stored in the high-performance short-term storage, and after a certain time they are automatically moved to the subsequent storage level. This ensures an efficient management of resources in terms of disk space usage and performance (REQ-2000). The interface between the control system and the timing system (ref. Chapter 14) will provide access to time information through EPICS time stamping of each PV update, ensuring data consistency on a shot-to-shot basis and allowing correlation of the accelerator data.

- **Alarm handling** - It is possible to associate alarms to each EPICS PV. Upper and lower thresholds can be set to the PV value through the record meta-data, and when these are exceeded, the alarm for that PV is triggered. Since PVs can be linked to each other, an alarm can be propagated to the linked ones in a hierarchical manner, so that lower level alarms propagate up. All the EPICS clients that have access to these PVs are notified through the CA, so that the operators have immediate knowledge of the machine alarm status.
- **Logging** - EPICS IOCs are equipped with logging tools. The error logging system includes routines passing error messages and the *iocLogClient* and *iocLogServer* modules. Error messages can be generated with different severity levels and are passed to *errlog Task*, which elaborates and forwards them to logfiles or network servers. *iocLogClient* forwards log messages to the log server, *iocLogServer*, which receives them in the local area network and writes them to a file. A logging tool for CA put operations is also available. The EPICS *CaPutLog* module is designed to send logs of these actions in a text format to a remote logging server. This system follows the same principle of the *iocLogClient* and *iocLogServer* modules.
- **Machine Protection System** - The Services layer also includes a Machine Protection System. Details can be found in the dedicated Section 19.5.

15.3.3 High Level Applications

Applications for more complicated data analysis or advanced functionalities as AI lean on and are integrated into the control system as well.

- **pyEpics** - The *pyEpics* package provided by EPICS includes several modules and classes allowing to interact with the CA through Python programs via the *caget()*, *caput()*, *camonitor() cainfo()* functions. Python routines can be developed to read and write the IOC PVs and perform various data analysis tasks, such as pre-processing and implementing state machines. Results of any processing can be put into other PVs and then displayed on OPIs.
- **AI** Automation tools will be integrated in the EuPRAXIA@SPARC_LAB control system as well. This aspect is detailed in Section 15.5.

15.4 Graphic and Not-Graphic Interfaces

The graphical OPI framework chosen for the EuPRAXIA@SPARC_LAB project is CSS Phoebus. This is a Java-based graphical environment that is widely used for developing OPIs for large scale facilities with EPICS-based control systems, and acts as an EPICS client. Phoebus is the current implementation of CSS and features a scalable and modular architecture (REQ-1000). It allows for the realization of OPIs for device control and monitoring by accessing the EPICS PVs from the IOCs database in read and/or write mode through CA and PVAccess protocols. A databrowser tool allows to display data trend over time, both for real-time data and for archived ones. Each hardware device instance will be equipped with a dedicated OPI. Additionally, synoptical panels aggregating the relevant PVs of similar device types as well as geographical screens will be made available to the users and to the scientific operators, in order to facilitate the device control and monitoring during the machine operation as well as throughout the test and commissioning phases. Access to the more advanced tools of dedicated OPIs for each device will be only allowed to authorized expert users for debugging purposes, in order to minimize human error (REQ-5000).

EPICS also provides a non-graphical interface to access PVs. As previously mentioned, communication among IOCs occurs through CA and PVAccess protocols. The CA protocol is UDP-based when sending queries to PVs, and TCP-based for information exchange. An easy-to-use interface similar to the basic command-line tools is provided with few simple commands:

- *caget* retrieves the current PV value;

- *caput* writes a value into a PV;
- *camonitor* monitors the PV value printing an update message at every change;
- *cainfo* monitors the PV value and prints an update message whenever the value changes.

An interactive console is also provided by the IOC to list and inspect the available PVs, to check the status of the IOC and to diagnose communication issues. These tools are widely used during the development and debugging phases.

15.5 AI for EuPRAXIA@SPARC_LAB control system

Within the EuPRAXIA@SPARC_LAB infrastructure, extensive research, meticulous design, and the progressive development of advanced Artificial Intelligence (AI) systems are actively being pursued with the goal of automating, optimizing, and enhancing a broad spectrum of control processes. The overarching objective of this ambitious initiative is to significantly improve the overall operational efficiency of the accelerator by enabling a more precise, highly adaptive, and intelligent management of a wide array of critical system parameters in real time. This, in turn, ensures not only greater stability and reliability of the entire facility but also enhances its long-term performance, making the system more resilient to variations in operating conditions and unforeseen perturbations.

Unlike the AI solutions developed specifically for the beam diagnostics group—whose primary objective is to leverage advanced machine learning techniques to optimize, refine, and virtualize the diagnostic processes associated with the characterization and analysis of the particle beam—AI systems designed for the overall control of the infrastructure operate on a significantly broader scale as shown in the Figure 15.4.

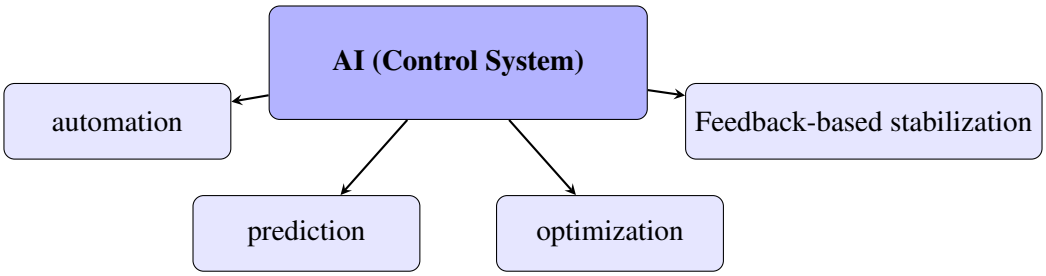

Figure 15.4: AI functionality for control system

These systems are responsible for overseeing the comprehensive management of the entire accelerator, which includes not only the continuous real-time monitoring of a wide array of critical operational parameters but also the dynamic adaptation and fine-tuning of these parameters to ensure optimal performance, stability, and efficiency of the facility.

One of the most significant and impactful aspects of this implementation concerns the capability for advanced data analysis, encompassing both real-time processing and the examination of historical datasets. Through the integration of sophisticated machine learning models, the vast amount of data continuously collected from the numerous sensors strategically distributed along the entire facility can be efficiently processed and analyzed. This will make it possible to detect and identify potential anomalies in the system's operation with greater accuracy and speed. As a result, issues such as beam instabilities, malfunctions in magnetic elements, irregularities within the RF systems, likely issues with the RF power sources, LLRF, and any deviations from the optimal operating conditions can be recognized and addressed in a more timely and proactive manner, ultimately contributing to enhanced system reliability, stability, and overall performance.

An additional significant advantage provided by the integration of Artificial Intelligence lies in the implementation of predictive maintenance, a proactive approach that enables the prevention

of failures before they have the opportunity to cause system interruptions, unexpected downtime, or critical malfunctions. By continuously monitoring and analyzing the operational behavior of essential components over extended periods such as RF sources, magnetic elements and other key devices, it becomes possible to accurately predict when a specific element is approaching a state of degradation or reduced efficiency. This predictive capability enables maintenance activities to be strategically planned in advance, ensuring that necessary interventions are performed before a failure occurs and allowing for the timely provision of spare parts. As a result, unplanned machine downtime can be significantly minimized, overall system reliability can be greatly improved, and the long-term operational stability of the accelerator can be effectively maintained, ultimately enhancing both performance and efficiency.
One particularly valuable application of Artificial Intelligence within this context will be the implementation of a sophisticated forecasting algorithm specifically designed for time series analysis [7]. By leveraging this approach, it will be possible to continuously analyze the evolution of signals originating from critical systems, such as the integrating current transformers or vacuum pumps, on a pulse-by-pulse basis.
A possible real-time implementation involves the analysis of recurrence plots between pre-processed time series and the training of a convolutional machine learning algorithm capable of classifying the input.
This analysis will be especially crucial in the moments leading up to an interlock event, where identifying subtle deviations from normal operating conditions can provide key insights into potential failures or instabilities.
By detecting anomalies in advance and understanding the specific conditions under which these irregularities arise, the system will be able to proactively predict scenarios where it becomes necessary to either shut down the RF systems or, more broadly, activate safety protocols to protect the accelerator infrastructure. This predictive capability will not only enhance the overall reliability and operational continuity of the facility but also contribute to minimizing downtime and reducing the risk of damage to critical components, ultimately ensuring a more stable and efficient long-term performance of the accelerator.
In addition to its role in diagnostics and fault prevention, Artificial Intelligence will be actively employed in the real-time control of the particle beam trajectory. Specifically, the adoption of reinforcement learning algorithms will enable the development of an advanced system capable of dynamically adjusting the accelerator parameters in response to environmental variations or unforeseen instabilities. This intelligent control system will not only contribute to maintaining a more stable and consistent beam over time but will also serve as a valuable support tool for the beam physicists/machine development team and diagnostics group. By leveraging the data generated through AI-driven optimization, they will be able to monitor, analyze, and further refine beam parameters more effectively and in an increasingly automated manner.
The implementation strategy includes the use of advanced machine learning techniques, such as recurrent neural networks [8] and Q-learning [9], which will allow for the simultaneous adjustment of beam position monitor parameters or RF phase and power. This approach aims to identify and achieve the optimal configuration necessary to meet specific performance targets, such as desired beam energy levels, minimized emittance, and other key beam properties. An example of Q-learning algorithm training procedure is shown on Figure 15.5.

By integrating these AI-driven methodologies, the system will enhance operational efficiency, improve overall beam quality, and contribute to the long-term stability of the accelerator.
All of these systems will communicate with the central control system as well as with the control room, enabling seamless interaction with the operator and facilitating communication with various interface devices. This integration will allow for real-time monitoring and management

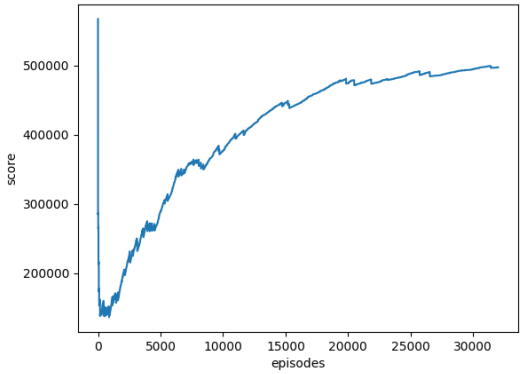

Figure 15.5: Q-learning system to adjust the beam energy changing the RF power and phase. The target energy is 511 MeV. The final energy after 30000 episodes ($\sim$ 42 s) is 514 $\pm$ 3 MeV.

of the accelerator, ensuring that operators can easily access and control critical parameters. As shown in Figure 15.6, this interconnected framework will enhance the overall efficiency of system management, providing a comprehensive and user-friendly interface for operators to effectively monitor and intervene as needed.

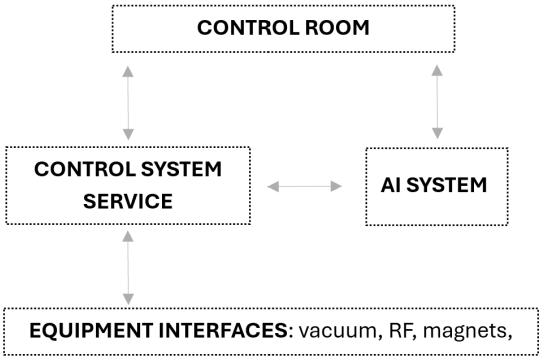

Figure 15.6: Communication between AI framework and control system

The integration of these AI techniques represents a significant step forward towards achieving a more autonomous and intelligent control of the accelerator, reducing the need for manual interventions while simultaneously enhancing the overall performance of the infrastructure. As these systems continue to evolve and mature, new opportunities emerge for optimizing the operations of EuPRAXIA@SPARC_LAB, positioning it as a leading-edge laboratory in the application of artificial intelligence to accelerator physics. This ongoing development not only promises to improve operational efficiency, but also paves the way for groundbreaking advancements in accelerator technology and research.

15.6 E-infrastructure

15.6.1 Data Management & Access Policy

EuPRAXIA is fully committed to Open Science and to implementing a Data Management Plan ensuring FAIR data principles, i.e. that all research data and accelerator data produced during the operational phase, including failure events for fault analyses and training algorithms, are Findable,

Accessible, Interoperable, and Reusable. During its operation, EuPRAXIA@SPARC_LAB will produce large volumes of such data, estimated at ∼100 PB/year in total. About 2 PB/year of these data are expected to be preserved for long-term re-use and open access [10]. The data storage will be handled by EPICS Archiver Appliance, as discussed in Sec. 15.3.2.

A common, open, and self-describing data format will be adopted across all EuPRAXIA sites to guarantee interoperability and ease of access. The preferred choice is the NeXus/HDF5 format, that is widely used by research infrastructures worldwide. The data will include standardized metadata allowing the user to properly read and interpret the dataset. These will provide contextual information such as the time stamp, experimental parameters, instruments references, calibration data, and any other relevant data referring to the experimental conditions. Metadata will follow community conventions and will be licensed under CC0, while data will be published under Creative Commons license CC BY 4.0 for open use and citation promotion. A persistent identifier will be assigned to each dataset, in accordance with European Open Science Cloud principles. Published data will remain available for at least 10 years after their production at the EuPRAXIA@SPARC_-LAB facility. The EuPRAXIA Computing Center, that is currently under construction at LNF, will serve as the main hub for data storage and access, providing the interface both between the data management infrastructure and the facility network. This center will host the repositories and services for data conservation, processing and retrieval; INFN CNAF of Bologna may be used in support of data archiving and interoperability when required. A dedicated online data access portal will be made available to allow users to search and retrieve published data from these repositories.

Access policies will distinguish between public and private users: data produced through open or competitive programs will be publicly available, while for users purchasing beam time the possibility of applying an optional embargo of up to three years may be provided. In all cases, access to open data will be provided through standardized, free access protocols defined in collaboration with the chosen repositories. To ensure high data quality, EuPRAXIA will implement periodic assessments addressing both fitness for use (reliability and usability) and fitness for purpose (adequacy for reuse). Technical, scientific, and stewardship checks will be performed regularly. A dedicated Data Management Team, supported by a Data Management Committee, will oversee implementation, policy decisions, and quality assurance.

15.6.2 Network

The facility network will be implemented as a single physical data infrastructure, within which separated VLANs will be created. Each VLAN will be dedicated to a different purpose, such as machine control, user activities, beamline scientists experiments and tests, and other services. This approach will ensure both security and operational efficiency. It will follow a hierarchical star topology (Fig. 15.7), with a central core connected through redundant >100 Gbit optical fiber links to the new EuPRAXIA Computing Center. Besides serving as the main data hub, this computing center will also host core services, storage systems, high level applications, simulation and data analysis environments. The central core will be also connected through >40 Gbit optical links to multiple local switches located in user areas, technical zones, and rack rooms. The connection between these field switches to accelerator devices for data acquisition and to dedicated PCs for real-time data acquisition will consist of >1 Gbit copper links. Each device connected to the control system will be assigned at least one dedicated network port. Based on a number of almost 10^3 objects under the control system, we expect around 20 distribution switches. A 20% spare capacity will be included to ensure scalability and operational margin. The final network layout and number of rack rooms will be optimized during the detailed design phase, according to the final distribution of the technical systems across the facility.

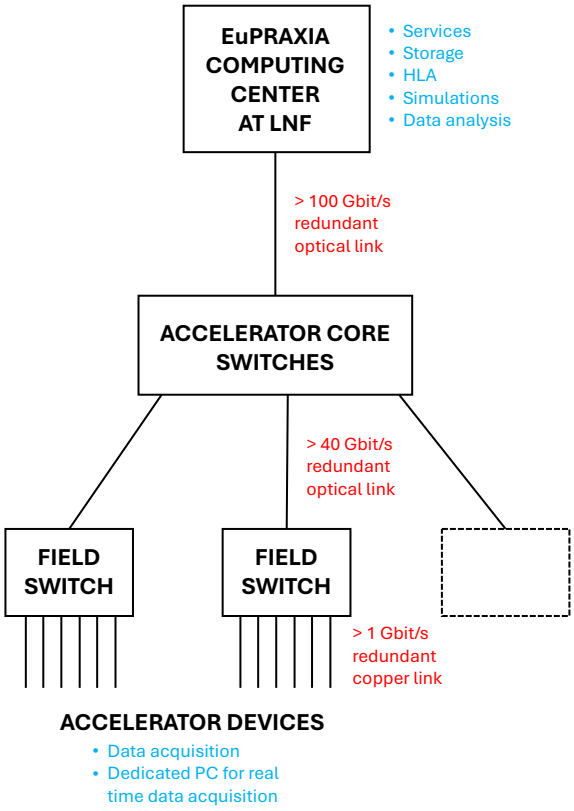

Figure 15.7: EuPRAXIA network design scheme.

15.7 Conclusions

The current technology readiness level of the diverse EuPRAXIA@SPARC_LAB Control System sub-components is reported in Fig. 15.2. The robustness of EPICS-based control systems has been extensively proven worldwide; as regards the other subsystems, we can state that their technology has been demonstrated or is actually in operational environments of other facilities. At the present stage, building on the experience gained with TEX, EuAPS, SPARC, and SSRIP, most of the EPICS IOC and hardware integration development for the devices we expect to include in EuPRAXIA@SPARC_LAB is mature. While additional developments will be likely required as the project progresses, this work provides a solid background towards a complete implementation of the control system. The goals of the chapter are satisfied by the presented discussion.

Table 15.2: Technology Readiness Level of Control System sub-components.

Subsystem	TRL	Comments
EPICS IOCs development	8	EPICS-based control systems are widely used in experimental facilities. IOCs already developed for most of elements (motors, cameras, vacuum system components, RF system components), software is open source and accessible, few still in development.
Archiving tool development	9	Technology proven in other facilities (TEX, SPARC_LAB, EuAPS).
Alarm handler	9	Technology proven in other facilities (TEX, SPARC_LAB, EuAPS).
AI system	7	Technology demonstrated in other facilities (TEX, Daphne LINAC, SPARC_LAB).
Graphical User Interfaces	7	Technology based on widely used platforms.

Bibliography

[1] G. Di Pirro et al. “SPARC Control System”. In: *Proc. ICALEPCS’07* (2007), pp. 214–216.

[2] P. D. Sheriff. “Fundamentals of N-tier architecture”. In: *Barnes & Noble* (May 2006).

[3] *EPICS Home Page*. URL: https://epics.anl.gov.

[4] S. Pioli, Giampiero Di Pirro, et al. “The Turn-key Control System For The ELI-NP Gamma Beam System”. In: *Proc. IPAC’16* (2016), pp. 4091–4092. DOI: 10.18429/JACoW-IPAC2016-THPOY003.

[5] S. Pioli et al. “Control and Functional Safety Systems Design for Real-Time Conditioning of RF Structures at TEX”. In: *Proc. IPAC’22* (2022), pp. 751–753. DOI: 10.18429/JACoW-IPAC2022-MOPOMS047.

[6] M. Shankar et al. “The EPICS Archiver Appliance”. In: *Proc. ICALEPCS’15* (2015), pp. 761–764. DOI: 10.18429/JACoW-ICALEPCS2015-WEPGF030.

[7] G. Bontempi, S. Ben Taieb, and Y.-A. Le Borgne. “Machine Learning Strategies for Time Series Forecasting”. In: vol. 138. Jan. 2013. ISBN: 978-3-642-36317-7. DOI: 10.1007/978-3-642-36318-4_3.

[8] M. Ghasemi and D. Ebrahimi. *Introduction to Reinforcement Learning*. 2024. arXiv: 2408.07712 [cs.AI]. URL: https://arxiv.org/abs/2408.07712.

[9] C. Watkins and P. Dayan. “Technical Note: Q-Learning”. In: *Machine Learning* 8 (May 1992), pp. 279–292. DOI: 10.1007/BF00992698.

[10] R. Fonseca. *Deliverables Report - EuPRAXIA-PP Data Management Plan*. 2023.

16. Vacuum System

16.1 Introduction

This chapter is dedicated to description of EuPRAXIA@SPARC_LAB vacuum system. After a general introduction to the vacuum system (Sec. 16.2), a schematic layout of the vacuum configuration for the different areas of the machine will be presented, along with preliminary simulations of pressure behavior carried out using the Monte Carlo code MolFlow+ [1]. These simulations support the overall machine design and the prototyping of the more complex components (Sec. 16.3). Specific description of some chambers and devices is also addressed in dedicated paragraphs within the corresponding chapters where the devices are actually included. The last section before the conclusions (Sec. 16.4) introduces some best practices for manufacturing, storage, and installation which, given the characteristics of the vacuum system, must be followed to ensure proper vacuum setup and operation of the machine.

16.2 Vacuum System: Requirements and General Evaluations

The vacuum system of EuPRAXIA@SPARC_LAB is a non-cryogenic setup composed of beampipes and devices with average diameters ranging from 8 to 15 mm. Due to these dimensions, the system has to be considered conductance-limited. The requirements for the machine operation are generally between $\approx 5.0 \cdot 10^{-8}$ mbar and $\approx 5.0 \cdot 10^{-9}$ mbar with a gas composition predominantly consisting of H_2, smaller amounts of H_2O, CO, O, CO_2, and negligible traces of species with molecular masses above 50. The more demanding areas of the machine are the X-band accelerating structures while the less demanding are the S-band waveguides network. To address these requirements, the pumping configuration follows a lumped pumping distribution, where the pumping devices are usually installed below the electron diagnostic chambers along the linac or installed to the T-Pumping units along the waveguide networks. As it will be explained in Sec. 7 the plasma chamber area is an exception to this general layout, both for the operating vacuum levels and for the pumping system employed. In this area, the vacuum will range from about $\approx 10^{-3}$ mbar in the gas injection zone to $\approx 10^{-9}$ mbar in the connections with the rest of the machine. The pumping system is instead based on the use of turbomolecular pumps.

The machine's vacuum system primarily relies on Ion Sputtering Pumps and Non-Evaporable Getter (NEG) Pumps. Ion pumps will be installed within the S-band waveguide systems and along the machine near the electron diagnostic chambers. NEG pumps have been selected for their high pumping speed—particularly for hydrogen—and for their ease of installation due to their compact size and low weight. The NEG will be then installed along the X-band waveguide network and on X-band accelerating structures.

The vacuum system is divided in areas (Fig. 16.1) that can be isolated from the adjacent ones by pneumatic gate valves. Consequently, every section is equipped with its own dedicated pumping system and at least one manual valve, allowing for independent intervention procedures such as venting and pumping down without affecting adjacent sections. The valves installed throughout the machine are Ultra-High Vacuum (UHV) all-metal gate valves. Similarly, the valves used for venting and pumping-down operations are UHV all-metal angle valves. Pressure monitoring is performed using Cold Cathode Gauges for UHV readings during operation, and Pirani Gauges for measurements during pumping down and venting procedures. Additionally a pilot vacuum gauge, typically a Triode Cold Cathode type, is connected to fast gate valves located at the following critical points:

- Between the RF-gun area and the first accelerating structure of the S-band injector;
- At both ends of the low-energy X-band linac section;
- At both ends of the high-energy X-band linac section;
- At both ends of the undulator section.

The distribution of these valves secures these more sensitive areas from sudden pressure rush coming from the adjacent areas (for example chicane, beamlines etc…). All devices selected for the vacuum system comply with UHV specifications and are listed and classified in Tab. 16.1. All joints within the machine use metal seals, chosen to meet UHV specifications described above and ensure long-term durability. Along the machine, joints are of the Quick-Conflat type, secured using chain clamps. This choice was made for its practicality and reduced axial space requirements during assembly. The waveguide network, on the other hand, uses LIL-type flanges for the S-band and International-type flanges for the X-band. All these specifications of the vacuum system, together with the procedures described in the Sec. 16.4, allow to fulfill the requirements for the machine operations.

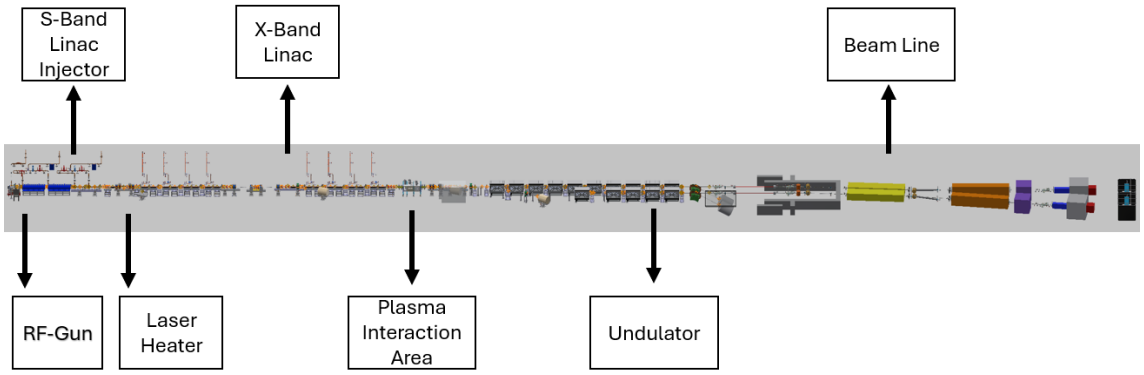

Figure 16.1: Vacuum Schematic Layout Legend

16.3 Vacuum Layout

Below is reported a short description of each key area of the machine, including specific characteristics of the section, a schematic of the vacuum system, and a preliminary Monte Carlo simulation for pressure profile estimation. Since the primary materials used in the vacuum system are stainless

Table 16.1: Vacuum System Main Elements

Element	Quantity
Ion Pumps	234
Turbo Pumps	11
Primary Pumps	5
Valves	40
Vacuum Gauges	9

steel and copper, for calculation and simulation purposes, the assumed thermal out-gassing rates are generally set to $1 \cdot 10^{-12}$ mbar·L/s·cm^2 for stainless steel and $1 \cdot 10^{-11}$ mbar·L/s·cm^2 for copper, unless otherwise specified.

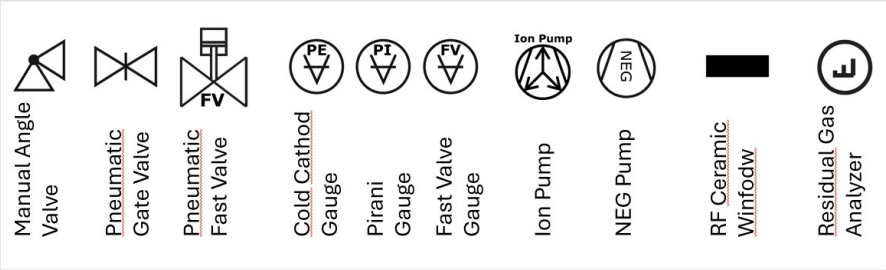

Figure 16.2: Vacuum Schematic Layout Legend

16.3.1 RF-Gun Section

This 1.3-meter-long section is the first part of the machine. It includes the RF-gun, a laser entrance chamber, and the first diagnostic chamber for the electron beam. The main material used in this area is stainless steel. The section is isolated from the waveguide vacuum layout by an RF ceramic window, and from the rest of the machine by gate valves. Due to the high sensitivity of this area to vacuum quality and pressure levels, a fast gate valve is installed upstream to protect the section in case of sudden incidents. Additionally, a mass spectrometer is mounted on the diagnostic chamber to characterize the vacuum composition and quality.

This section is equipped with both Ion Pumps and NEG Pumps, as illustrated in Fig. 16.3. The NEG Z100 pumps are installed directly on the RF-gun, while the Ion pumps (two 20 L/s) are located around it, on the laser entrance chamber (75 L/s), on the diagnostic chambers (75 L/s) and on the waveguide near the RF window (55 L/s) (Fig. 16.4). The simulation shown in Fig. 16.5 indicates a relatively uniform pressure profile, with values below $1 \cdot 10^{-10}$ mbar.

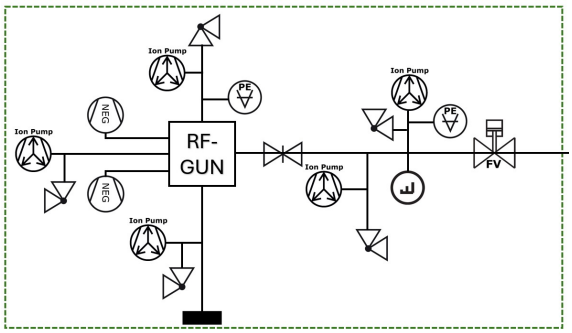

Figure 16.3: RF-gun Vacuum System: Schematic Layout

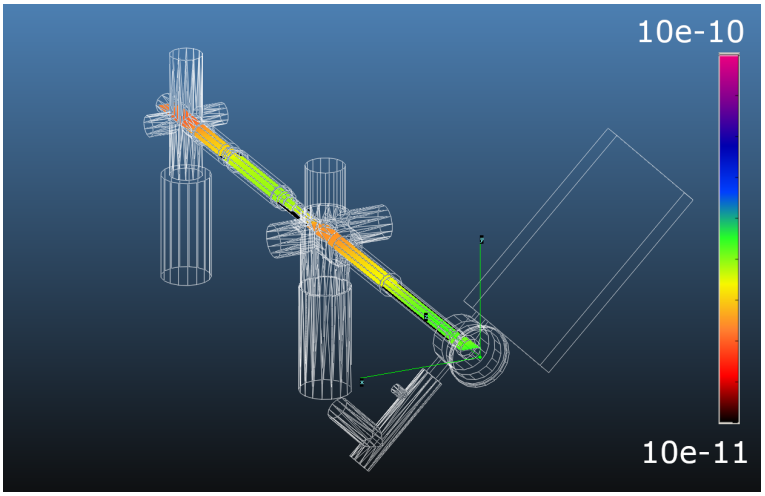

Figure 16.4: RF-gun Vacuum System: CAD Layout

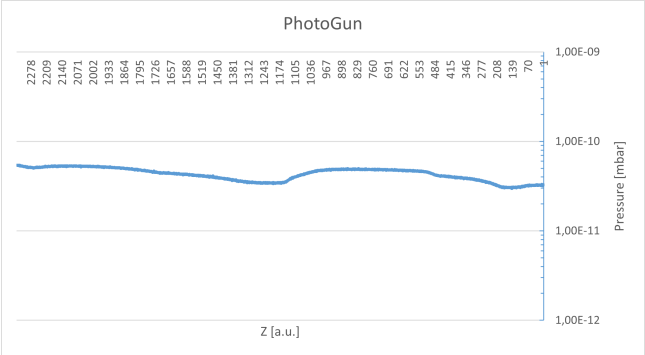

Figure 16.5: RF-gun Vacuum System: Pressure Simulation

16.3.2 S-Band Linac Injector

This section primarily consists of one X-band linearizer cavity, two 3 meters long S-band accelerating structures and other two 1.5 meters long S-band accelerating structures. Diagnostic chambers for the electron beam are placed in the remaining spaces between the structures, where ion pumps and vacuum gauges are installed. The total length of this section is approximately 10.4 m. The vacuum system is segmented downstream by a gate valve, while RF ceramic windows separate the vacuum system of the S-band structures from their waveguide layout. The X-band linear cavity, however, does not include RF windows and therefore maintains a continuous vacuum system with

its associated waveguide network.

As illustrated in Fig. 16.6, the pumping system includes:

- Three 55 L/s ion pumps installed at the diagnostic chambers,
- Four 55 L/s ion pumps installed on the waveguides
- Four 75 L/s ion pumps installed on the RF loads of the S-band structures,
- One NEG Z100 pump installed on the X-band waveguides of the linear cavity.

A preliminary vacuum simulation indicates a pressure profile with peaks located at the center of the accelerating structures, reaching a maximum of $1.5 \cdot 10^{-8}$ mbar (Figs. 16.7 and 16.8).

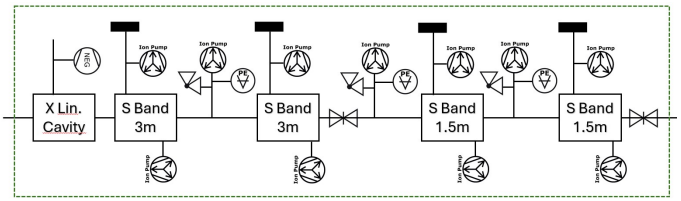

Figure 16.6: S-Band Linac: Schematic Vacuum Layout

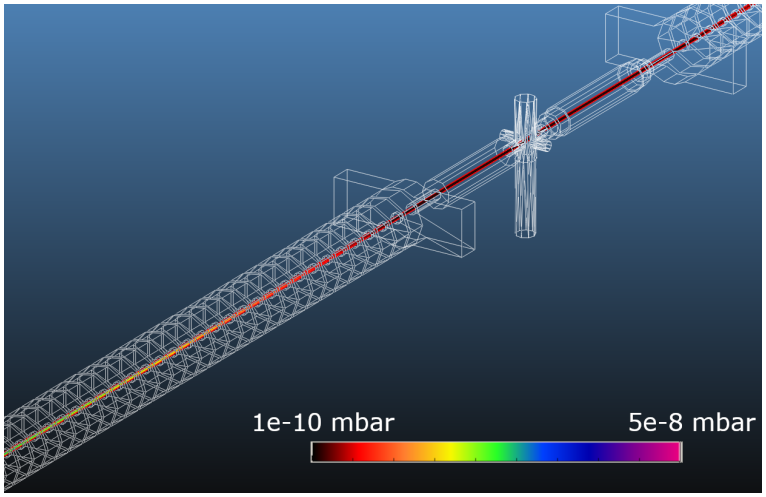

Figure 16.7: S-Band Linac: detail of pressure simulation in the area of the diagnostic chamber between 2nd and 3rd S-band accelerating structures

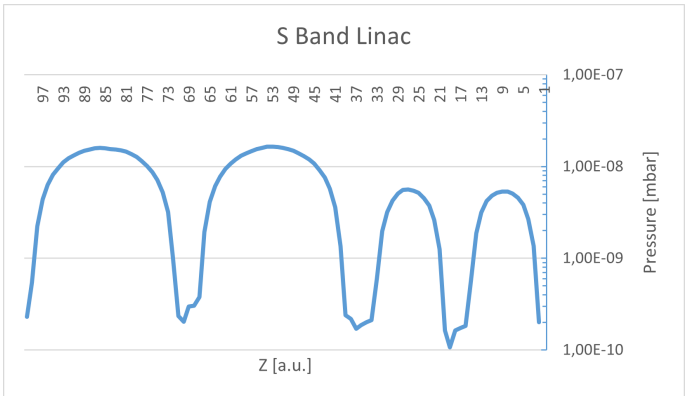

Figure 16.8: S-Band Linac: Simulated Pressure Distribution

16.3.3 Laser Heater

This section features a vacuum chamber designed to allow the electron beam to pass through a magnetic chicane with a central undulator, while simultaneously allowing laser injection. The mechanical constraints of this configuration are defined by the laser entrance and exit windows, and the gaps allowed by the magnetic elements: 30 mm in the dipole regions and 15 mm in the undulator region. The total length of this chicane is approximately 2.5 m.

Given this geometry, the pumping system is envisioned to be installed in an antechamber located on the long side of the chamber but outside the magnetic region, designed to provide distributed pumping. For this preliminary layout, assuming a modest integrated pumping speed of 10 L/s, the pressure at the center of the chamber does not exceed $5.1 \cdot 10^{-8}$ mbar (Fig. 16.10).

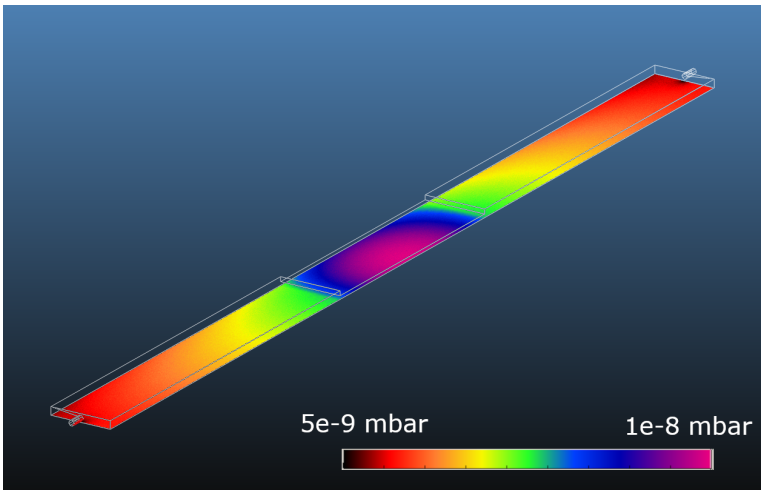

Figure 16.9: Laser Heater Chamber: Pressure simulation for a 100 l/s pumping system

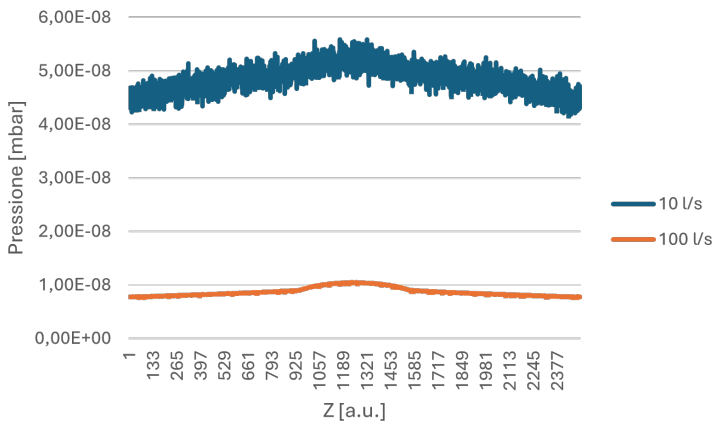

Figure 16.10: Laser Heater Chamber: Pressure Distribution for 10 L/s and 100 L/s

Distributed pumping may be implemented using alternatively:

- NEG strips directly installed inside the vacuum chamber;
- Distributed ion pump elements;
- lumped pumping stations based on ion pumps;

During the future design phase of the chamber, the characteristics of these three alternative pumping approaches will be evaluated in terms of pumping efficiency, beam interaction, and ease of integration. At this preliminary stage, the most promising solution appears to be the application of

NEG pumps. Additionally, the area includes three diagnostic chambers and two gate valves located upstream and downstream. Vacuum Gauges and 55 L/s ion pumps are installed at the diagnostic chambers.

16.3.4 X-Band Linac

The X-band linear accelerator is a vacuum system composed of modular sections separated by gate valves. Each module includes two accelerating structures, an electron diagnostics chamber, and a cavity beam position monitor (cBPM). Due to the absence of RF windows, the vacuum system of the accelerating sections is directly connected to the X-band waveguide network.

The pumping system consists of Z100 NEG pumps installed on the RF loads, one at the end of the structure and one on the waveguides near the power feed of the accelerating structures (Fig. 16.11). Additionally, each diagnostics chamber will be equipped with a 55 L/s ion pump and a pressure sensor. Preliminary simulations performed on a single accelerating structure indicate a peak pressure at the section center, with values varying according to the outgassing rate. The simulations investigated the behaviour for three different orders of magnitude of outgassing rates, showing that $1.0 \cdot 10^{-12}$ mbar l/s cm^2 the peak value not exceeds $4 \cdot 10^{-9}$ mbar (Figs. 16.12 and 16.13).

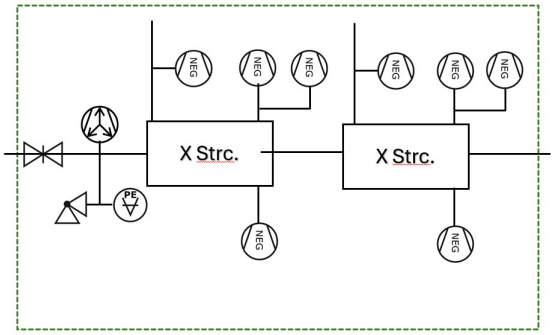

Figure 16.11: X-Band Linac Module: Vacuum Schematic Layout

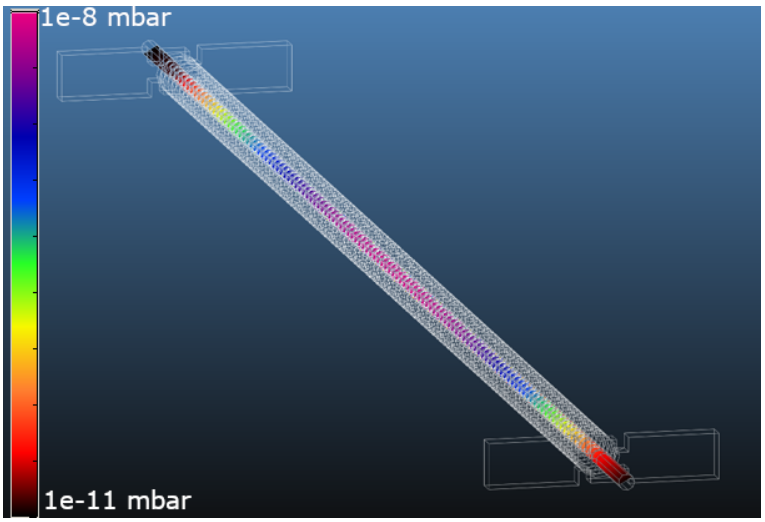

Figure 16.12: X-Band Accelerating Structure: pressure distribution simulated for q = $1 \cdot 10^{-12}$ mbar l/s cm^2

In the mechanical layout of the machine, the X-band linac can be divided into two stages: a Low Energy and a High Energy stage, each composed of four accelerating modules, for a total of

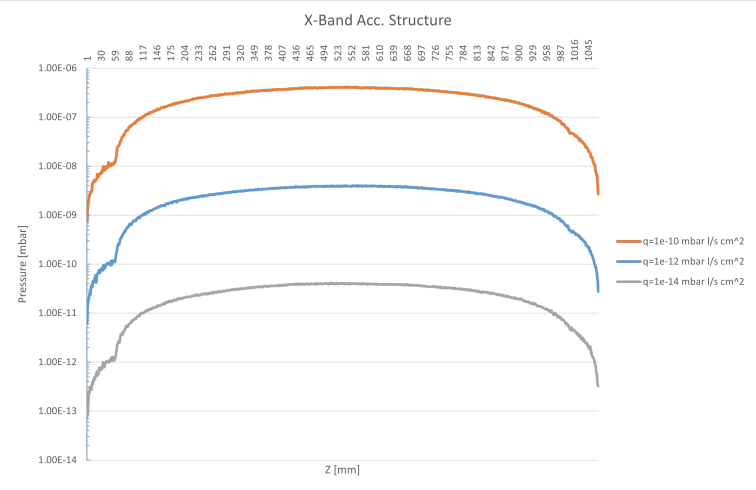

Figure 16.13: X-Band Accelerating Structure: Pressure Distribution

eight accelerating structures and approximately 10.5 m long. Both lines are further segmented at their ends by fast-closing valves to protect against sudden pressure surges. Simulations of a four modules linac show pressure profiles with peak values at the center of the accelerating structures not exceeding $4.5 \cdot 10^{-9}$ mbar along whole X-band linac (Fig.16.14).

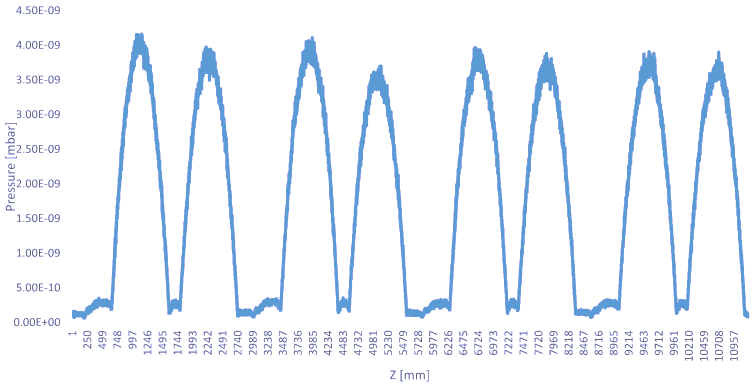

Figure 16.14: X-Band Linac: Simulation of Pressure Distribution

16.3.5 Plasma Interaction Area

The plasma interaction area is the only one within the machine where controlled gas injection occurs. The vacuum system, including chambers and pumping units, has been designed to maintain pressure below $1 \cdot 10^{-8}$ mbar at the interface with both upstream X-band and below $1 \cdot 10^{-7}$ mbar downstream, while a gas flow of approximately 12 mbar l/s is injected into the capillary within the main chamber. This area, with a total length of approximately 3.5 m, is segmented at both ends by gate valves and features a quasi symmetric design. As described in Plasma Chapter 7, the central part houses the vacuum chamber where the capillary is installed, the location of the discharge and gas injection. At both ends of the capillary chamber, additional chambers have been designed to serve both diagnostic purposes and as functional pumping stages. These stages gradually reduce the pressure to levels acceptable for the rest of the machine. Specifically, upstream a main chamber segmented into four stadiums by known conductances (pipes with d = 12 mm, L = 120 mm), each

equipped with a turbo-molecular pump, is designed. On the opposite side, downstream, the chamber following the same conceptual design includes only 2 stadiums.

The entire pumping system is composed of turbo-molecular pumps: the capillary chamber will be equipped with two 2300 l/s turbo-molecular pumps, while each diagnostic chamber stadium is equipped by one 500 l/s turbo-molecular pump (Fig. 16.15). Preliminary calculations, also reported in Chapter 7, indicate a pressure of $5 \cdot 10^{-3}$ mbar within the capillary chamber and a pressure of approximately $1 \cdot 10^{-11}$ mbar at the end of the last stage of the diagnostic chambers (Fig. 16.16). For the downstream region, since the pumping chamber consists of only two stadium, the pressure calculated up to the second stage, as reported in Tab. 16.2, must be considered. However, the refinement of the calculations performed by Monte Carlo simulation, makes evident a difference with the preliminary 1D model in the final stadium, where the last stage shows an average pressure of about $5 \cdot 10^{-9}$ mbar. The discrepancy between the two predictions becomes increasingly evident as the distance from the capillary chamber increases toward the ends of the region. In 1D diffusion-based calculations, geometric factors are considered only in the conductance calculations, while directional propagation diffusion effects are entirely neglected. These directional effects, however, are included in the Monte Carlo simulations performed using Molflow software, which explains the differences between the two models. As the distance from the capillary region increases, these effects become more significant, resulting in higher pressure values but remaining in the limit of acceptable requirements.

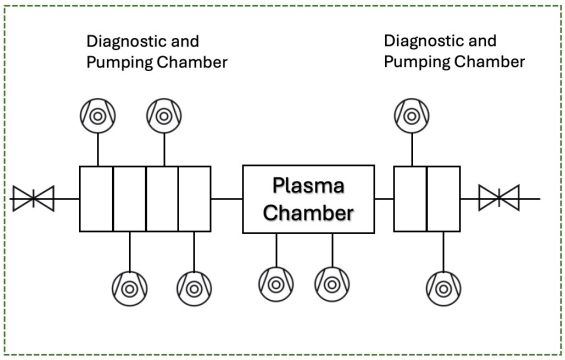

Figure 16.15: Plasma Area: Vacuum Schematic Layout

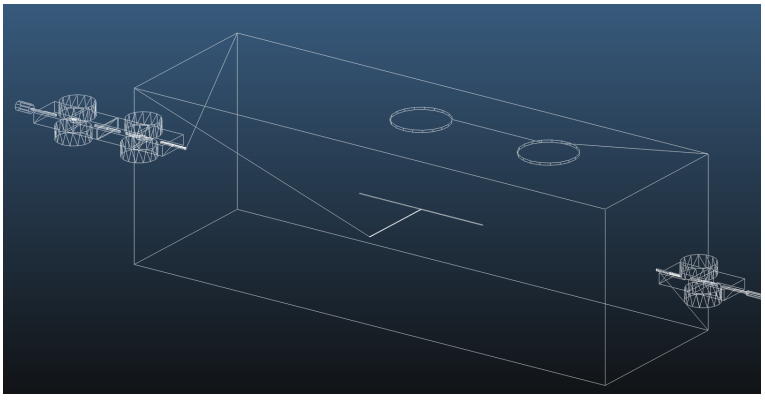

Figure 16.16: Plasma Area: CAD representation for simulation. At center the rectangular box simulates the Capillary Chamber. On the left the four cylinders simulate the four upstream Diagnostic/Pumping Chamber stadium. On the right the two cylinders simulates the two downstream Diagnostic/Pumping Chamber stadium.

Table 16.2: Plasma Chamber: Calculated and Simulated Pressure Distribution

	1D Model Calculation	Montecarlo Simulation
Capillary Chamber	$5 \cdot 10^{-3}$ mbar	$7 \cdot 10^{-3}$ mbar
Diagnostic Stadium 1	$1 \cdot 10^{-5}$ mbar	$1 \cdot 10^{-5}$ mbar
Diagnostic Stadium 2	$4 \cdot 10^{-8}$ mbar	$1.6 \cdot 10^{-7}$ mbar
Diagnostic Stadium 3	$3 \cdot 10^{-10}$ mbar	$2 \cdot 10^{-8}$ mbar
Diagnostic Stadium 4	$1 \cdot 10^{-11}$ mbar	$5 \cdot 10^{-9}$ mbar

16.3.6 Undulator Section

The undulator section is a modular vacuum system characterized by the presence of a chamber located within the magnetic structure of the undulator, with an outer diameter of 5.5 mm and a length of approximately 2 m. Each module consists of the thin chamber inside the undulator, an electron diagnostics chamber and a cavity BPM. The entire section comprises 10 modules, each featuring this type of vacuum system, segmented upstream and downstream by gate valves. Additionally, the system is safeguarded at both ends by two fast-closing safety valves (Fig. 16.17).

Due to the small diameter and relatively long length of the internal chamber, the vacuum system is particularly critical at the center of this chamber. Simulations (Fig. 16.19) indicate that, for a thermal out-gassing rate estimated at $1 \cdot 10^{-10}$ mbar L/s cm^2, the pressure peak reaches approximately $6.5 \cdot 10^{-7}$ mbar. By using the same simulations is possible to obtain the threshold value of $5.0 \cdot 10^{-10}$ mbar L/s cm^{-2} for the thermal out-gassing rate to ensure that the pressure peak remains below the required limit of $3.0 \cdot 10^{-6}$ mbar (Sec. 8.5.2). Hence for this area the prototyping phase of the chamber becomes especially important to accurately characterize its specific out-gassing rate. This prototyping phase will thoroughly address the selection of materials to meet vacuum requirements, mechanical strength, and thermal/electrical conductivity specifications of the chamber. The pumping system consists of a 55 L/s Ion Pump located below the diagnostic chamber between the undulator. As in the other areas, on the diagnostic chamber are also located vacuum gauges and manual angle valve for venting and pumping down operations.

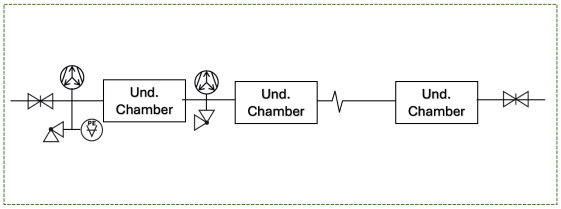

Figure 16.17: Undulators: Vacuum Schematic Layout

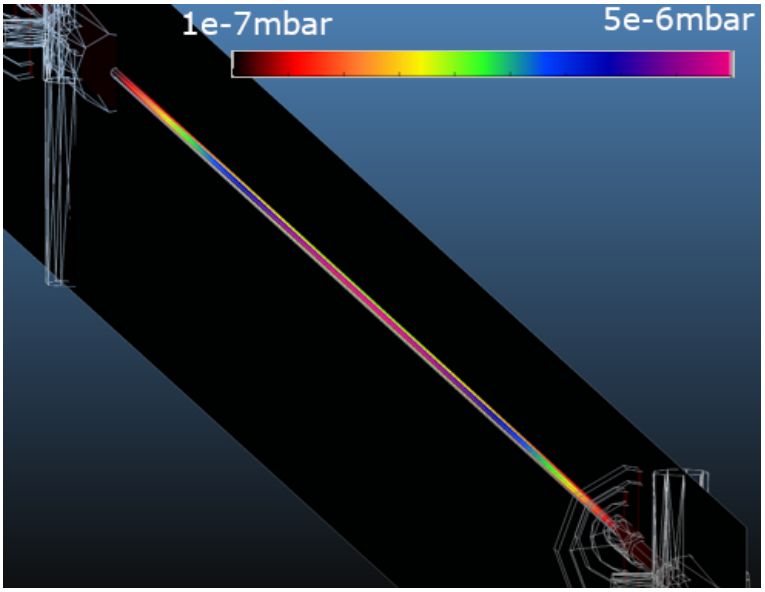

Figure 16.18: Undulators: Detail of pressure distribution inside one of the Undulator vacuum chamber

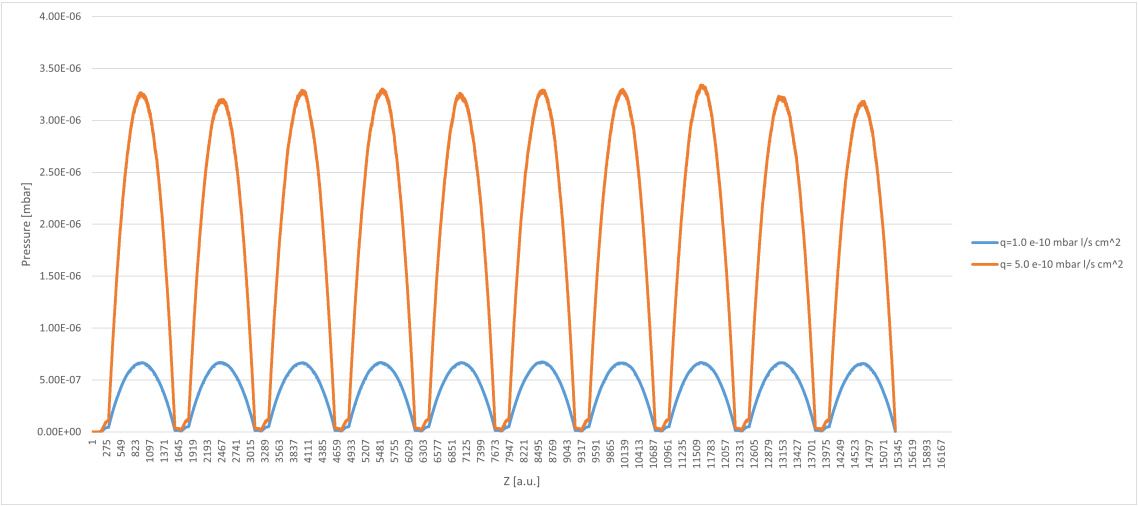

Figure 16.19: Undulators: Simulated pressure distribution along undulator series

16.3.7 Photon beamline

The photon transport area for the AQUA beamline consists of a vacuum beamline with a total length of approximately 50 m. As described in Chapter 9, several devices will also be considered to be included in this area. Devices such as gas attenuators operate by filling specific zones with selected gases at controlled low vacuum pressures. The detailed design of these devices will be outsourced, with the requirement that they must not interfere with in-line components, ensured through differential pumping zones. In the same technical specification will be also included a special attention to all optical elements: these optical chambers require a total pressure of $\approx 10^{-9}$ mbar with attention at the partial pressures of C, CO, CO_2, CH_4 or generally Carbon compounds. This includes both the components adjacent to the optical chambers and those located within the chambers themselves.

The vacuum system for the photon transport sections will be based on pumping stations

equipped with 150 L/s ion pumps, and vacuum reading chambers fitted with cold cathode and pirani pressure sensors capable of monitoring pressures ranging from Low to Ultra High Vacuum. These vacuum reading chambers will also be equipped with manual angle valves for pumping down and venting operations.

16.3.8 Waveguide Systems

The waveguide systems include the vacuum infrastructure extending from the klystrons to the accelerating structures. Two main vacuum system layouts are distinguished: X-band and S-band.

In the X-band layout, the system features rectangular-section waveguides with relatively low conductance, interspersed with low RF attenuation circular-section segments that offer higher conductance. Along the waveguide network, T-Pumping Units are installed, each equipped with a pump, a pressure sensor, and a manual valve for venting and pump-down operations. The pumping system utilizes NEG Z100 pumps, selected for their high pumping speed, compact design, and low weight. This configuration allows for a more efficient distribution of pumping capacity, ensuring a more uniform pressure profile along the line. The X-band waveguide lines terminate directly at the corresponding accelerating structures without any ceramic RF window, resulting in a continuous vacuum system from the accelerating module to the klystron separation RF window, as described in Chapter 6.

The S-band layout features a vacuum system with sufficiently high conductance to ensure pressure uniformity along the waveguide. The pumping system consists of 55 L/s ion pumps. Pressure readings are obtained by interpreting the current absorption of the ion pumps, which can be directly converted into pressure values. Some ion pumps will be equipped with CF40 flanges, on which UHV manual angle valves will be mounted to enable pump-down and venting operations. For this configuration, the waveguide network is separated from the corresponding accelerating structure by a ceramic RF window, resulting in fully isolated vacuum systems. This separation facilitates maintenance, modifications, and operational interventions.

16.4 Manufacturing and Cleaning Procedures

Given that the vacuum system is conductance-limited, particular attention must be paid to maintaining low specific out-gassing rates of all components, as well as to adhering strictly to standard UHV procedures. First and foremost, all standard cleaning and surface treatment procedures for UHV components are required. These will be supplemented by ex-situ thermal treatments aimed at reducing the out-gassing rate. Component preparation will utilize existing thermal treatment facilities at the LNF Vacuum Laboratory, which include:

- A vacuum furnace capable of reaching up to 1200 °C, suitable for firing stainless steel components.
- A Thermic Vacuum Chamber for thermal treatments up to 450 °C, used to reduce contaminant emissions and water content.

The most commonly used materials for vacuum components are stainless steel and copper. Stainless steel is primarily used for beam pipes and diagnostic chambers, while copper is employed in accelerating structures and the waveguide network. Due to the conductance-limited nature of the system, the specific out-gassing rates of materials are critical. For stainless steel, a value of $\approx 1{\cdot}10^{-12}$ mbar L/s cm^2 is considered, while for copper, an initial value of $\approx 1{\cdot}10^{-11}$ mbar L/s cm^2 is assumed, with potential reduction to $\approx 1{\cdot}10^{-12}$ mbar L/s cm^2 after RF conditioning. For specialized components, other UHV-compatible materials such as aluminum, ceramics, and titanium may be used, selected based on dedicated out-gassing studies and their impact on the vacuum system.

The final design will rely on an out-gassing characterization facility already in operation at the

LNF Vacuum Laboratory. This facility will be used to characterize both low out-gassing materials (e.g., metals) and high out-gassing components (e.g., cables, actuators), correlating their rates with the gas species spectrum via an in-line Residual Gas Analyzer. Prior to installation, components will undergo ex-situ thermal treatment and be stored in dry nitrogen. Additionally, an in-situ bake-out system will be prepared, should it be necessary to reduce the partial pressure of water in the final vacuum level. For the installation of components sensitive to dust and contamination, mobile clean rooms will be deployed to ensure proper assembly conditions. Venting procedures will be carried out using dry nitrogen, while pump-down operations will be performed using portable turbo-molecular pumping systems backed by scroll pumps. The same systems will be used for the activation of NEG pumps installed in various areas of the machine, including the gun region, X-band linac, and X-band waveguide network. The coexistence of ion-sputtering pumps and NEG pumps within the same vacuum system requires strict control over NEG activation procedures to extend the lifetime of the pumping system, reduce maintenance costs, and optimize overall vacuum performance.

16.5 Conclusions

The goal of this chapter was to describe the vacuum systems needed by the facility and complete the information already given in the previous chapters on the subject. According to the reported contents, the vacuum systems will meet the requirements imposed by the machine needs. To comprehensively address the entire vacuum system, from the injector to the endstations, the vacuum requirements and the solutions to be implemented in the experimental area are described in Chapter 10. Although the general layout and main features of the vacuum system are well defined, certain specific areas and chambers still require prototyping or advancement to the final design stage. The technology readiness levels of the subsystems are reported in Tab. 16.3.

Table 16.3: TRL level of the Vacuum

Sub - systems	TRL	Comments
Pumps – Gauges - Valve	9	ll these devices are fully commercialized and such solutions are based on previous experiences or tested in our actual facilities (TEX – SPARC etc..)
Cleaning procedure and storaging	9	All the systems required for these procedures are currently in use at LNF - Vacuum Laboratory.
Installation and Intervention Procedures	9	These Procedures are well known and all the components or devices needed are fully commercialized
Outgassing characterization and Heat Treatments	8	These procedures are well known and operated at LNF - Vacuum Laboratory.
Undulator Chamber Prototype	6	The final prototype needs more laboratory test and characterization in order to fulfill specification.

Bibliography

[1] Roberto Kersevan, Marton Ady, et al. “Recent developments of Monte-Carlo codes molflow+ and synrad+”. In: *10th International Particle Accelerator Conference*. Vol. 6. 2019.

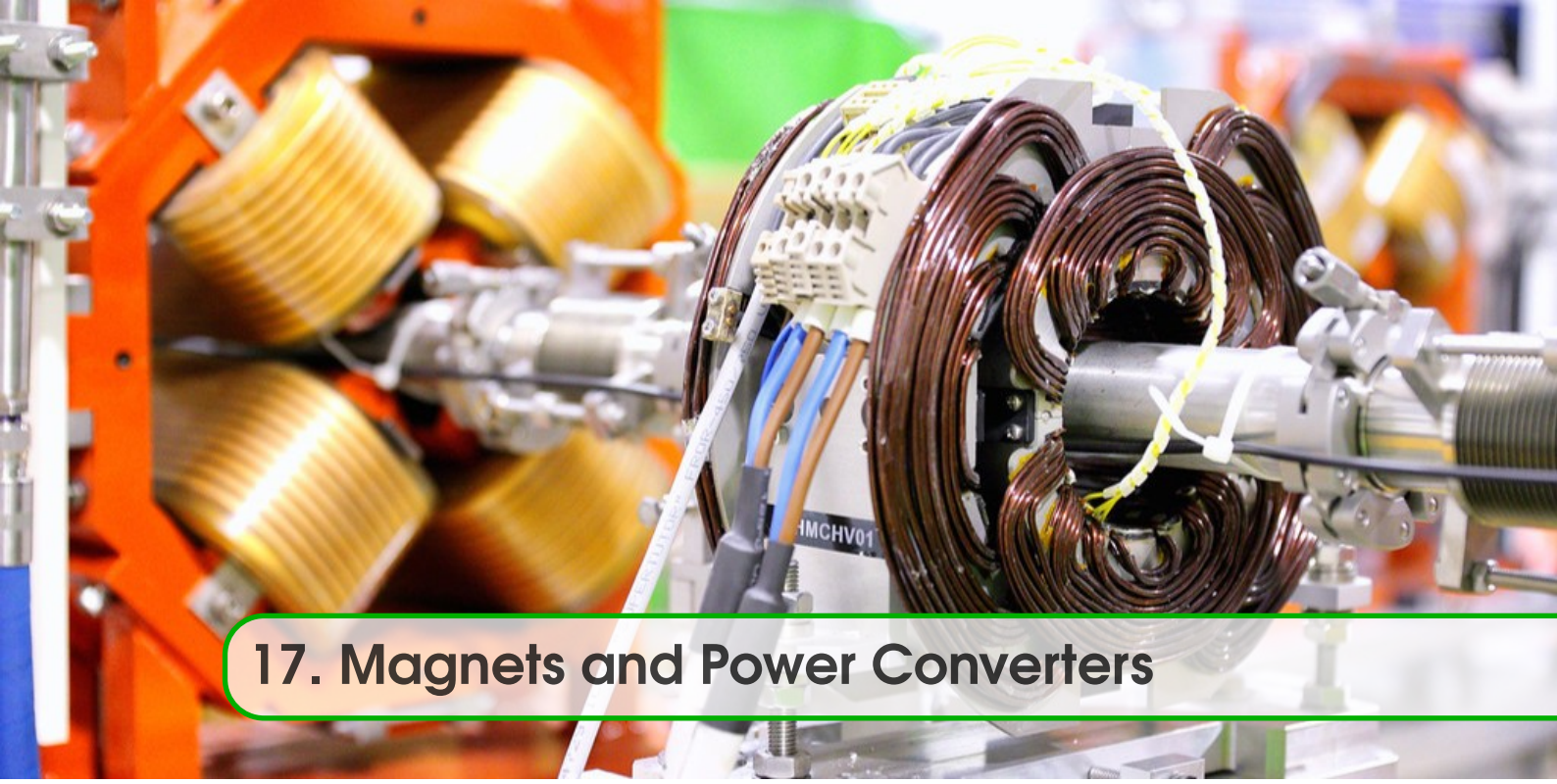

17. Magnets and Power Converters

17.1 Introduction

This chapter presents all the magnetic elements implemented in the machine. For each magnet, or family of magnets, a magnetic design has been performed using the Opera 3D software by Dassault Systèmes. The design process was carried out in close collaboration with the Beam Physics and Undulators working areas, in order to understand and interpret the specific requirements of each component. In parallel, continuous interaction with the Integration working area ensured proper evaluation of boundary constraints, such as space limitations, mechanical interferences, and integration challenges. The magnetic design includes the sizing of the yoke and windings, as well as the selection of electrical parameters. For water-cooled magnets, hydraulic parameters were also considered, including the pancake configuration of windings, cooling water flow rate and velocity, and the corresponding temperature variation. For some of the more conventional magnetic elements, preliminary sizing was based on the working group's previous experience, using as reference similar magnets developed for other facilities (such as ELI, STAR, BTF, and SPARC_LAB among others). Conversely, for the more specialized magnetic components, the design process was significantly more detailed and rigorous. A major constraint throughout the entire machine is the longitudinal space available. As a result, a considerable part of magnetic design focused on developing compact solutions. Examples include integrating quadrupoles and correctors into a common yoke, or mounting correctors on top of bellows, as in the drift space between two X-band sections. The engineering of all components will be completed during the preparation of the technical specification documents required for procurement. The following sections provide a magnetic overview of the various parts of the machine, from the gun to the dump, presenting the main parameters for each magnet or family of magnets in tabular form.

The design parameters for all magnetic elements have been defined in accordance with the specifications provided in the Beam Physics Chapter 3, Injector Chapter 5 and Undulators Chapter 8, ensuring full consistency with the machine's overall performance objectives.

Table 17.1 lists the magnetic elements contained in the accelerator, together with their number, and indicates the paragraph in this chapter where they are described.

Table 17.1: Table of magnets classified by type and position along the accelerator, including the number of elements and the corresponding section reference.

Magnet type	**Position**	**Number**	**Section**
SOLENOIDS	Gun	1	Sec. 17.2.1
	Accelerating sections	2	Sec. 17.2.4
DIPOLES	Laser heater chicane	4	Sec. 17.2.7
	Bunch compressor chicane	4	Sec. 17.4.1
	Driver-witness separator chicane	4	Sec. 17.6
	Septum	1	Sec. 17.6
	Spectrometers	2	Sec. 17.7
	Dump dipole	1	Sec. 17.9
STEERERS	Gun	2	Sec. 17.2.3
	Between S-bands	3	Sec. 17.2.5
	Linac 1	4	Sec. 17.3.1
	Linac 2	4	Sec. 17.3.1
	Intra-undulators	10	Sec. 17.8.2
QUADRUPOLES	Gun	1	Sec. 17.2.2
	Injector	4	Sec. 17.2.6
	Linac 1	3	Sec. 17.3.2
	Bunch compressor chicane	9	Sec. 17.4.2
	Linac 2	3	Sec. 17.3.2
	Plasma section (PMQ)	16	Sec. 17.5
	Intra-undulators	10	Sec. 17.8.1
SEXTUPOLES	Laser heater chicane	1	Sec. 17.2.8
	Bunch compressor chicane	1	Sec. 17.4.3

17.2 Magnets for the injector

17.2.1 Gun solenoid

The Radio-Frequency photo-injector is designed to provide high-brightness, high-current electron beam. One of its key elements is the solenoid for the gun, whose main task is to limit the beam emittance growth in the first acceleration stages by imposing a spiraling motion to the beam [1]. The magnetic design is based on the following requirements:

- an integrated field of the longitudinal component of 62.6 T mm with an integrated field quality better than $5 \cdot 10^{-4}$ in a good field region of 30 mm radius;
- a focusing strength, corresponding to the field integral of B_z^2 along z direction, at least equal to 0.015 T^2 m;
- a minimization of the field on cathode aiming to avoid undesired emittance growth.

The solenoid [2] is composed of two coils surrounded by an iron shield that ensures a limitation of stray field over the magnet ends and reduces the power current for a given peak field. Although the ++ configuration is typically expected to be used, the choice of two coils allows to have a better compensation of the possible misalignment between them by powering each coil with an opposite current polarity (+- configuration). The inner diameter has been sized to guarantee easy access to the mirror for the laser beam transport on the cathode putting it out of vacuum. The magnet is equipped with a remote-controlled motorized support aiming to have a fine adjustment of its transverse position by means of beam-based alignment. Figure 17.1 shows the gun solenoid and its 3D model, while Figure 17.2 shows the magnet undergoing Hall probe measurements at LNF. Table 17.2 presents the final specifications of the gun solenoid.

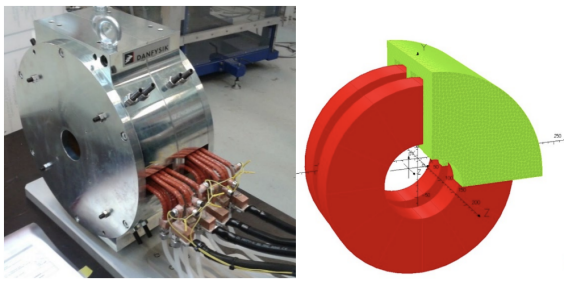

Figure 17.1: SPARC_LAB gun solenoid and its 3D model

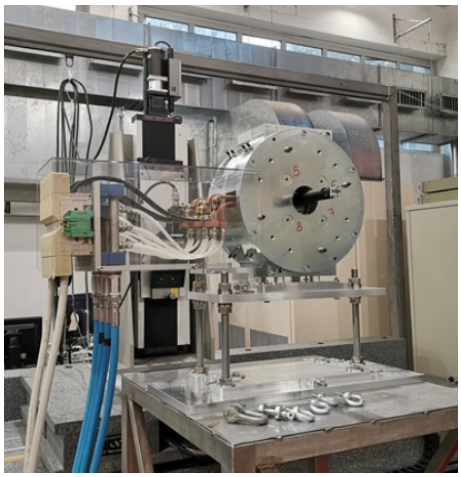

Figure 17.2: SPARC_LAB gun solenoid during the Hall probe measurements at LNF

Table 17.2: Final specifications of solenoid for the gun

Parameter	Units	Value
B_{max} in ++ config	T	0.39
B_{max} in +- config	T	0.36
Yoke material	-	St.37
Integrated field on axis, B_z	T mm	62.6
Integrated field quality	-	$4 \cdot 10^{-5}$
Good field region radius	mm	30
Minimum free aperture diameter	mm	308
Focusing strength on axis in +- config.	T^2 m	0.015
B_{max} on cathode	G	8.5
Number of turns per coil	-	136
Cooling	-	water cooled
Conductor size (hole diameter)	mm×mm (mm)	5×5 (∅ 3)
Water pressure drop	bar	3
Water flow rate	l/min	4.2
Water ΔT	°C	25
Nominal current in ++/+- config.	A	182/192
Nominal voltage	V	35
Inductance	mH	35
Resistance	mΩ	191

17.2.2 Gun quadrupole

The gun also includes a normal and a skew quadrupole with variable polarity, embedded in the solenoid, for tuning the x-y emittances and compensating for residual transverse beam spot asymmetries. The skew quadrupole, air cooled, is based on the design made at PSI [3], with a maximum gradient of 32 mT/m (both for normal and skew) and a magnetic length of 100 mm. The quadrupole is mounted on the vacuum chamber at the center of the solenoid. A similar solenoid with integrated skew quadrupole has been recently designed, built, characterized and installed at SPARC_LAB, and is currently in successful operation (Figure 17.3 and 17.4).

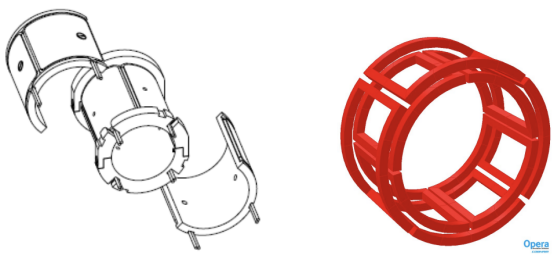

Figure 17.3: Design of the skew quadrupole mounted in the gun solenoid

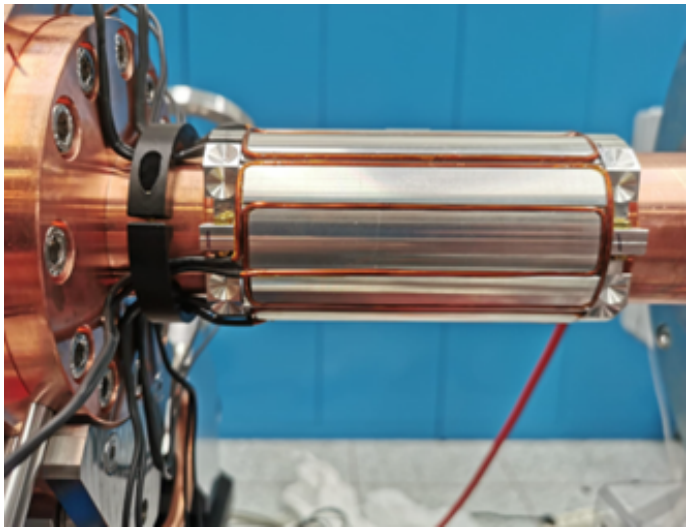

Figure 17.4: Skew quadrupole mounted on the SPARC_LAB gun vacuum chamber

17.2.3 Gun steerers

The layout also includes a vertical and horizontal steerer downstream the solenoid for trajectory optimization and beam energy measurements. A similar air cooled steerer has been designed, built and installed at SPARC_LAB (see Figure 17.5): it has a maximum field of about 25 G, with a magnetic length of 152 mm, allowing a deflection of an electron beam with an energy of about 6 MeV of approximately 19 mrad. The current version has been slightly upgraded, reaching an integrated field of about 0.4 T mm, in order to achieve a beam deflection of 20 mrad, with the parameters reported in Table 17.3. Its integrated field quality is within $2 \cdot 10^{-3}$ in a good field region of $\pm$ 15 mm with respect to the magnet axis. A copy of this steerer is also foreseen just after the gun for trajectory correction.

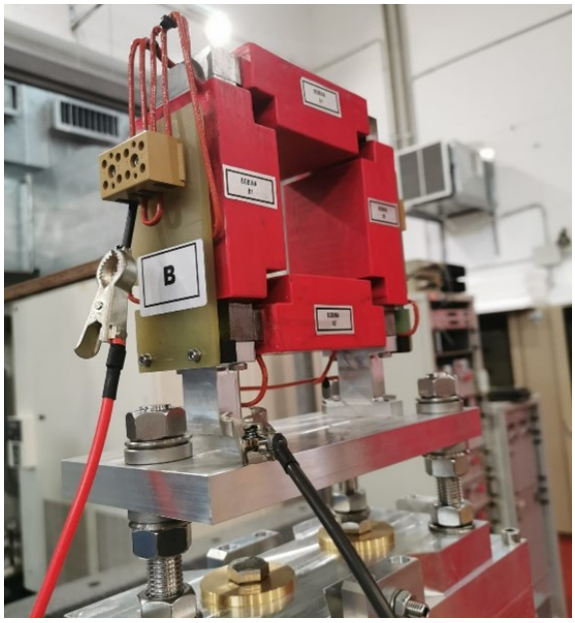

Figure 17.5: SPARC_LAB gun steerer during tests at LNF

Table 17.3: Main parameters of the gun steerers.

Parameter	Units	Value
Energy	MeV	6
Deflection angle	mrad	20
Integrated field	T mm	0.4
Peak field	G	25
Magnetic length	mm	160
Good field region	mm	± 15
Field quality	-	$2 \cdot 10^{-3}$

17.2.4 Focusing solenoids for accelerating sections

The injector configuration includes the presence of two S-band accelerating structures contained within two solenoids, to allow the focusing needed to prevent the growth of the transverse emittance during the velocity bunching RF compression. The two solenoids are therefore two identical electromagnets, 3 m long each, composed of 12 oxygen free copper coils, surrounded by an iron shield. The minimum free aperture diameter is imposed by the accelerating structure mechanical measures. From the magnetic point of view, the request of having a maximum field of 0.18 T and the $5 \cdot 10^{-4}$ integrated field homogeneity on a good field region of 30 mm radius can be accomplished with the configuration proposed in Table 17.4. The solenoid is requested to have a maximum value of the field of 20 Gauss at 300 mm from the end of the iron yoke to prevent interaction with the photocathode. From an electrical point of view, the coils are connected in series in groups of 3 (therefore each solenoid is made up of four triplets), each group is powered by a dedicated power supply, to allow choosing the running configuration.

From a mechanical point of view, the iron shield is divided lengthwise into two halves: the lower one is in one piece and fixed, while the upper one is composed of four parts (one for each triplet), which can be opened to intervene either on the coils, on the section, or on the correctors located inside the solenoid (and described in the next paragraph). The iron shield is provided with an adjustable support with fiducials; each of the removable upper parts is also provided with fiducials. In this way, the positioning of the whole magnet and the repeatability of the positioning of the upper parts are allowed after each intervention. The alignment between magnetic axis and mechanical axis is of primary importance: the magnetic axis misalignment allowable tolerance must be within 140 μm, i.e. the axis shall be contained in a cylindrical surface of radius 70 μm with respect to the alignment reference frame. For this reason, each coil is provided with a dedicated alignment support and with four alignment fiducial sockets. The coil alignment system as well as the fiducial points are mechanically decoupled from the iron shield and accessible for the operations. With the shield closed, under normal operating conditions, the alignment adjustment can be operated from outside. The fiducial sockets are designed to accommodate a laser tracker target holder. The whole solenoid (coils and iron shield) is mounted on a main support dedicated to the position adjustment, having a rough positioning system to accommodate for the unevenness of the floor and a precise one for the alignment. The support for the RF accelerating structure located inside the solenoid is independent from the solenoid, having the legs passing through the iron shield without mechanical contact. The accelerating structure will have its own references. This configuration allows for independent alignment with laser tracker even with the iron shield in closed position. Figures 17.7 and 17.8 show one of the SPARC_LAB solenoids during the installation phases: the first before the closure of the iron shield, and the second with the shields closed and in place, during the coils alignment procedure.

From a hydraulic point of view, each solenoid is equipped with an inlet and an outlet water manifolds, appropriately sized for cooling the solenoid. Each pancake is provided with thermal switches on the warm ends, activating at a temperature of 70 °C. The magnetic, electrical and hydraulic characteristics of each of the two solenoids are shown in the Table 17.4.

Table 17.4: Magnetic, electrical and hydraulic parameters of the injector accelerating-structure solenoids.

Parameter	**Units**	**Value**
Quantity	-	2
Number of coils	-	12
Maxium integrated field in ++ config, B_{max}	T	0.18
Integrated field on axis, B_z	T mm	527.3
Integrated field homogeneity in ++ config	-	$5 \cdot 10^{-4}$
Good field radius	mm	30
Minimum free aperture diameter	mm	308
Mechanical length	mm	3000
Maximum field on axis at 300 mm from the iron yoke end plates, B_z^{out}	G	20
ELECTRICAL INTERFACE		
Maximum nominal current allowed	A	190
Maximum nominal voltage allowed for the 3 coils series	V	100
Inductance for 3 coils in series ++	mH	13
Conductor size (hole diameter)	mm×mm (mm)	8×6 (∅ 4)
Number of turns	-	192
COOLING INTERFACE		
Maximum pressure drop at the manifolds	kPa	200
Maximum total water flow rate	m^3/h	3.6
Inlet water temperature	°C	32

Similar solenoids have been recently built, tested and installed at SPARC_LAB [4], and are currently operated successfully. The experience acquired with this activity has highlighted few key points:

- Magnetic measurements: the alignment of magnetic and mechanical axis requires a well-defined measurements run with proper instrumentation. The state of the art provides as best option a laser tracker and a Hall probe bench with a probe holder of adequate length to reach at least the center of the solenoid from the two sides, with an overlapping central zone. An example of such measurement done for the SPARC_LAB's solenoids is shown Figure 17.6.
- Transport and positioning: the solenoids are long (3 m) and heavy (3.5 ton) items; it is of vital importance to have adequate tools for the unloading, the movement in the experimental area and the final positioning (crane, transpallet, ...).
- Mechanical alignment: SABINA solenoids share the idea of decoupling the coil alignment from the solenoid iron shield, but not for the acceleration structure. This experience also indicates that the effort made to decouple the mechanical support from the shielding will guarantee more precise and feasible alignment operations. Such structure and alignment operations are shown in Figures 17.7 and 17.8.

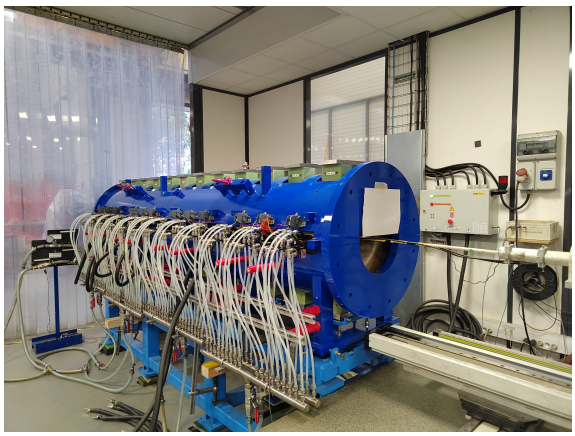

Figure 17.6: SPARC_LAB solenoid during magnetic measurements and mechanical alignment of coils

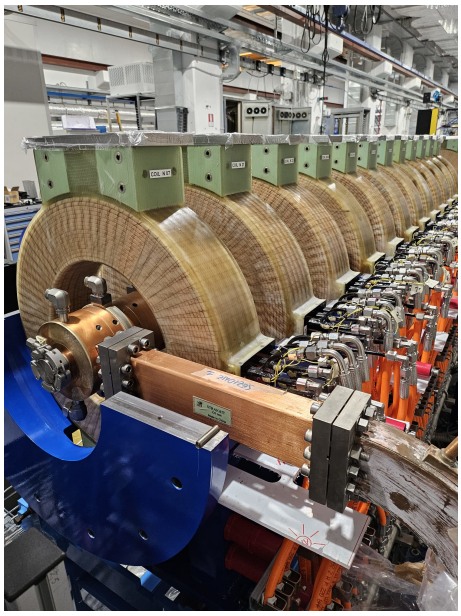

Figure 17.7: SPARC_LAB solenoid during installation at SPARC_LAB, without the iron shield upper half

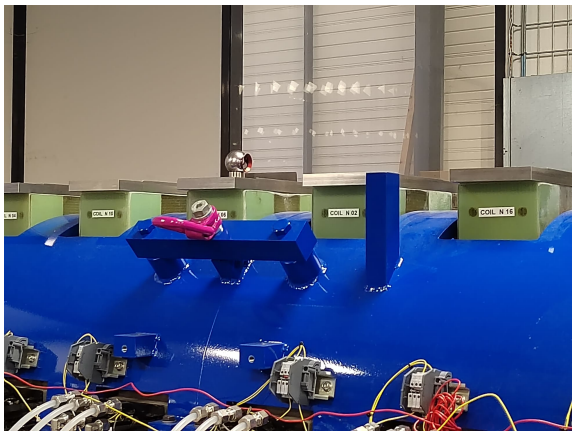

Figure 17.8: The solenoid with the iron shield during the coils alignment

17.2.5 Steerers between accelerating sections

Between the accelerating sections, three steerers are positioned to adjust the beam trajectory prior to the next acceleration section. To simplify the design, procurement, and operation phases, these steerers are identically designed and dimensioned for the highest beam energy, ensuring that their use at lower energies still provides adequate resolution. They are designed to incorporate a beam position monitor (BPM), requiring a sufficiently large aperture to accommodate the BPM and allow space for alignment. The correctors provide horizontal and vertical steering and are based on a square iron yoke geometry. A view of the magnetic design is reported in Figure 17.9.

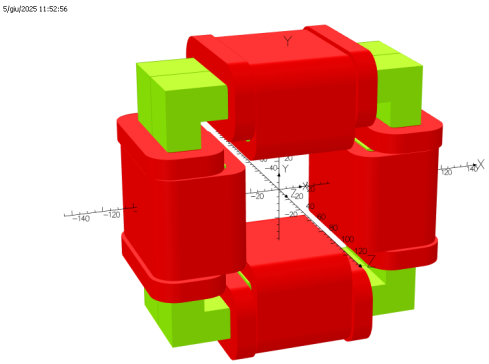

Figure 17.9: The 3D design of H-V steerer between accelerating sections.

Table 17.5: Main parameters of the steerers between accelerating sections.

Parameter	**Units**	**Value**
Energy	MeV	300
Deflection angle	mrad	4
Integrated field	T mm	4.0
Peak field	G	220
Magnetic length	mm	180
Yoke length	mm	70
Free aperture	mm $\times$ mm	70 $\times$ 70
Good field region	mm	$\pm$ 10
Field quality	-	$6 \cdot 10^{-4}$
Conductor size	mm $\times$ mm	1.0 $\times$ 2.2
Number of turns per coil	-	528
Current	A	3.2

17.2.6 Quadrupoles before laser heater chicane

A quadrupole triplet is placed upstream of the laser heater chicane to match the beam parameters required for injection into the chicane; another quadrupole is located after the chicane. With respect to the triplet, two of the three quadrupoles - the first and the last - are located at positions where beam position monitors are installed. Consequently, their bore diameter must be large enough to accommodate the BPMs and allow for proper alignment. The quadrupoles feature octagonal yokes, specifically designed to also house windings for integrated horizontal and vertical steerer. The

single quadrupole after the chicane is designed in the same way. Although integrating two magnetic elements into a single yoke requires more precise mechanical design, this configuration was chosen to minimize the longitudinal footprint of the system. The central quadrupole of the triplet, although it does not require either a BPM or a steerer, is designed identically to the others for standardization. Preliminary design data for these quadrupoles are summarized in Table 17.6.

Table 17.6: Main parameters of the quadrupoles before the LH chicane.

Parameter	Units	Value
Energy	MeV	300
Field gradient	T/m	18
Bore diameter	mm	56
Magnetic length	mm	160
Yoke length	mm	90
Integrated gradient	T	2.88

17.2.7 Laser heater chicane dipoles

The laser heater chicane is designed to deflect the electron beam by a total angle of 14.5° (253 mrad) at a maximum beam energy of 300 MeV. It consists of four identical C-shaped rectangular dipole magnets, positioned with their faces orthogonal to the beam original trajectory. The distance between the centers of the first and second dipoles (and symmetrically between the centers of the third and fourth) results in a lateral offset of about 100 mm between the incoming and outgoing beam trajectories. The central gap, between the second and third dipoles, provides space for a sextupole and for the laser heater undulator, which can be up to 600 mm long. To assess magnetic interference and evaluate the extent of cross-talk due to the close proximity of magnetic elements, the detailed design of the individual dipole (see Figure 17.11) was followed by a full 3D analysis of the entire chicane (reported in Figure 17.10). The magnetic design was carried out assuming a 30 mm gap. Given the beam energy and, consequently, its magnetic rigidity (1 T m), the required deflection corresponds to an integrated field of 0.253 T m. Beam dynamics simulations request for a magnetic length of 250 mm, which would correspond to a central field of approximately 1.0 T. However, since the first dipole in the chicane must also act as a spectrometer—deflecting the beam in the opposite direction by 22°—and all four dipoles must remain identical, they are all designed to operate with a peak magnetic field of 1.54 T. The main constraint for the chicane layout is the longitudinal footprint of the magnets: their close proximity requires a detailed study to minimize magnetic crosstalk. For that reason, the coils are more distributed in vertical direction instead of horizontal one. The geometry of the yoke has been defined in order to avoid saturation of the iron. The pole width has been defined to provide adequate coverage of the beam when the magnet is used as spectrometer. Engineering of the dipoles will include proper tapering of the pole.

17.2.8 Laser heater chicane sextupole

As discussed in the Full RF configuration Section 3.3, the inclusion of a sextupole magnet between the second and third dipoles of the laser heater chicane may become necessary if the chosen working point differs from the baseline configuration adopted in this document. A preliminary study was therefore carried out to assess the space requirements of such a sextupole and to verify its compatibility with the overall layout of the laser heater area. The configuration of the laser heater chicane including the sextupole is reported in Laser Heater Section 5.3.

Table 17.7: Preliminary parameters for the laser heater chicane dipoles.

Parameter	**Units**	**Value**
Energy, E	MeV	300
Pole gap, h	mm	30
Magnetic length, L_{mag}	mm	250
Iron length, L_y	mm	210
Total length, L_{TOT}	mm	360
Number of turns per pole, N	-	112 (= 8×14)
Conductor size (hole diameter)	mm×mm (mm)	6 × 6 (∅ 3)
USED AS SPECTROMETER		
Bending angle, θ	deg	22
Integrated Field, BL	T mm	384
Field, B	T	1.536
Current, I	A	190
Current density, J	A/mm^2	6.83
Inductance, L	mH	130
USED AS CHICANE DIPOLE		
Bending angle, θ	deg	14.5
Integrated Field, BL	T mm	253
Field, B	T	1.0
Current, I	A	110
Current density, J	A/mm^2	3.87

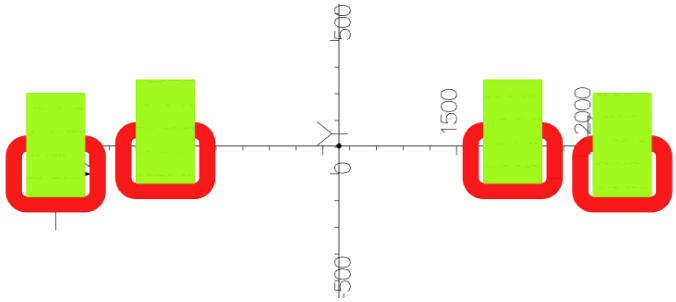

Figure 17.10: Top view of the 3D design of the magnets for the Laser Heater chicane.

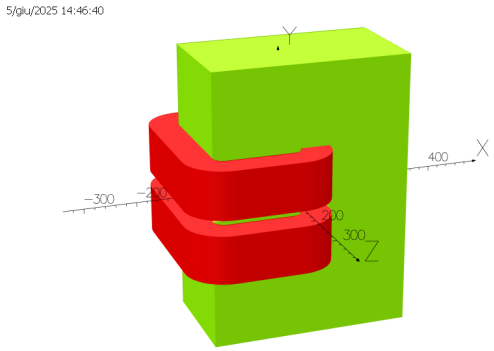

Figure 17.11: The 3D design of C-shaped dipoles for the Laser Heater chicane.

The transverse size of the sextupole, in its preliminary air cooled layout, appears to be sufficiently compact to allow installation without interfering with the vacuum chamber of the straight section of the chicane. It is important to note that, should the final design result in a transverse footprint exceeding the space available between the two branches of the vacuum chamber, a design solution is foreseen that allows the straight-section vacuum chamber to be accommodated by creating a lateral space within the yoke. Similar designs, which exploit three-fold symmetry to preserve beam quality, have been successfully implemented and are in operation at other facilities. The normalized sextupole strength k_2 is 250 m^{-3}, with a magnetic length of 100 mm. The main parameters of the preliminary design are summarized in Table 17.8 and a front view of the magnet is represented in Figure 17.12.

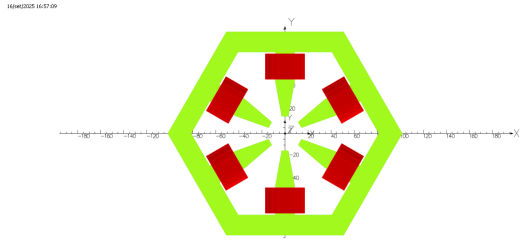

Figure 17.12: Front view of the 3D design of the sextupole for the Laser Heater chicane.

Table 17.8: Preliminary parameters for the laser heater chicane sextupole.

Parameter	Units	Value
Energy, E	MeV	300
Normalized sextupole strength	m^{-3}	250
Sextupole gradient	T mm^2	250
Bore diameter	mm	30
Pole shape	-	cubic + straight line
Magnetic length, L_{mag}	mm	100
Iron length, L_y	mm	90
Total length, L_{TOT}	mm	110
Amp-turns per pole, NI	A turns	225
Insulated conductor diameter	mm	2.2
Number of turns per pole	mm	40
Current	A	5.1

17.3 Magnets for the linac

Both the low-energy linac (L1) and the high-energy linac (L2) require magnetic elements—steerers and quadrupoles—to adjust the beam position and focusing during acceleration. To optimize the longitudinal footprint, the proposed layout places a combined horizontal-vertical steerer between two RF sections powered by the same modulator, and a quadrupole magnet between two sections served by different modulators. This configuration is applied to both L1 and L2. Although the beam energy differs at each location, the goal is to streamline the procurement, production, and operation of these magnets by grouping them into two families, based on the maximum beam energy reached in each linac section. Specifically, magnets for L1 are designed for a maximum beam energy of 0.67 GeV while magnets for L2 are dimensioned for up to 1 GeV, as determined by beam dynamics simulations. This strategy reduces the number of steerer families to two (each consisting of four units) and the number of quadrupole families to two (each consisting of three units).

17.3.1 Steerers between X band accelerating sections

For both L1 and L2, intra-X band sections steerers are placed across the bellows to avoid increasing the longitudinal footprint that would result from placing the steerer and the bellow in series. This placement requires a larger magnet aperture but allows for increased magnetic length and, consequently, a higher integrated field. The required correction capability is 0.2 mrad in both horizontal and vertical planes for each part of the linac. To maximize the integrated magnetic field, air-cooled squared iron-yoke magnets are adopted. A view of the design is reported in Figure 17.13.

17.3.2 Quadrupoles between X band accelerating sections

The quadrupoles placed between the X-band accelerating sections are designed with a 30 mm bore. The chosen configuration, taking into account the maximum longitudinal footprint, consists of water-cooled octagonal quadrupoles with a gradient of 30 T/m and a magnetic length of 100 mm for L1 and 150 mm for L2. Cavity beam position monitors are installed in series with the quadrupoles. The relevant data are summarized in Table 17.10.

Table 17.9: Main parameters of the steerers between X band accelerating sections.

Parameter	Units	Value for L1	Value for L2
Energy	MeV	670	1000
Deflection angle	mrad	0.2	0.2
Integrated field	T mm	0.45	0.67
Peak field	G	56	84
Magnetic length	mm	80	80
Yoke length	mm	44	44
Total length	mm	60	60
Free aperture	mm × mm	28 × 28	28 × 28
Insulated conductor diameter	mm	1	1
Number of turns	-	214	214
Current density	A/mm^2	1.35	2
Current	A	0.9	1.3

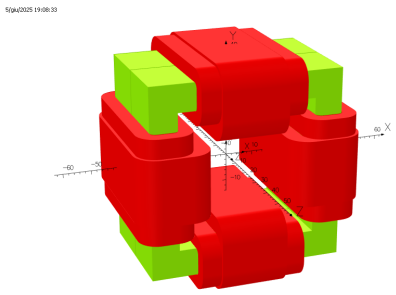

Figure 17.13: The 3D design of H-V steerer between X band accelerating sections.

Table 17.10: Main parameters of the quadrupoles between X band accelerating sections.

Parameter	Units	Value for L1	Value for L2
Energy	MeV	670	1000
Field gradient	T/m	30	30
Bore diameter	mm	30	30
Magnetic length	mm	100	150
Yoke length	mm	86	136
Total length	mm	156	206
Integrated gradient	T	3.0	4.5
Good field region	mm	$\pm$ 10	$\pm$ 10
Field quality	-	$5{\cdot}10^{-4}$	$5{\cdot}10^{-4}$
Conductor size (hole diameter)	mm$\times$mm (mm)	5 $\times$ 5 ($\varnothing$ 3)	5 $\times$ 5 ($\varnothing$ 3)
Number of turn per pole	-	32	32
Current density	A/mm^2	5.3	5.3
Current	A	90	90
Voltage	V	5	7
Inductance	mH	6	8
Power	kW	0.5	0.6

17.4 Bunch compressor magnets

17.4.1 Bunch compressor chicane dipoles

The bunch compressor chicane is designed to deflect the beam by 4.1° (as reported in Table 3.19), based on simulations indicating a maximum beam energy of 670 MeV. This deflection is achieved with an integrated magnetic field of approximately 160 T mm. Each dipole has a magnetic length of about 300 mm and a central field of 0.53 T. All four dipoles are identical, with the parameters resumed in Table 17.11; their design in shown in Figure 17.14. The selected configuration uses C-shaped, rectangular dipole magnets arranged in a 0 - θ - θ - 0 geometry, orthogonal to the main beamline.

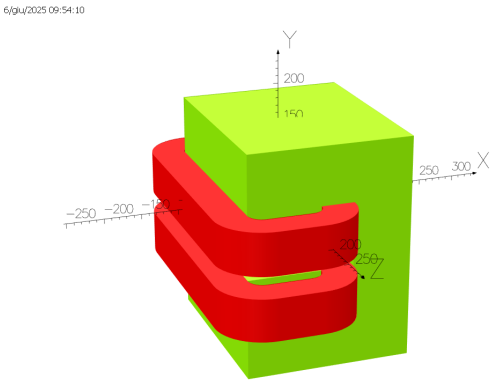

Figure 17.14: The 3D design of C-shaped dipoles for the Bunch Compressor chicane.

Table 17.11: Main parameters of the dipoles for the bunch compressor chicane.

Parameter	Units	Value
Energy, E	MeV	670
Pole gap, h	mm	30
Bending angle	deg	4.1
Integrated field, BL	T mm	160
Magnetic length, L_{mag}	mm	300
Yoke length, L_y	mm	260
Total length, L_{TOT}	mm	390
Field, B	T	0.53
Number of coils per pole	-	48 (= 6×8)
Conductor size (hole diameter)	mm×mm (mm)	6 × 6 (∅ 3)
Current density	A/mm^2	4.75
Current	A	135

The center-to-center spacing between the first and second dipoles — and symmetrically between the third and fourth - is approximately 2.2 m, resulting in a lateral offset of about 158 mm between the incoming and outgoing beam trajectories. The distance between the second and third dipoles is 900 mm, which provides the necessary space to install two quadrupoles and one sextupole described hereafter.

17.4.2 Bunch compressor section quadrupoles

The section of the beamline related to the bunch compressor also includes two quadrupole triplets (one upstream and one downstream of the chicane) and a doublet within the chicane itself. These magnets are designed with additional windings to allow for beam corrections, also acting as horizontal and vertical steerers. The bore diameter is sized to accommodate a beam position monitor, integrated within the first and third quadrupoles in the triplets, and in the first quadrupole of the doublet, to ensure precise beam diagnostics and correction.

17.4.3 Bunch compressor chicane sextupole

A sextupole is foreseen between the second and third dipole of the chicane. It is characterized by a normalized strength K_2 of 300 m^{-3}, with a magnetic length of 200 mm. The parameters of this sextupole are listed in Table 17.12, and its front view is shown in Figure 17.15.

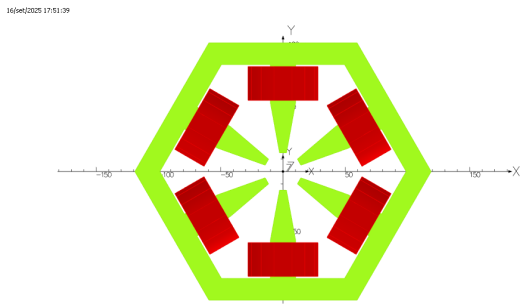

Figure 17.15: Front view of the 3D design of the sextupole for the Bunch Compressor chicane.

Table 17.12: Preliminary parameters for the bunch compressor chicane sextupole.

Parameter	Units	Value
Energy, E	MeV	670
Normalized sextupole strength	m^{-3}	300
Sextupole gradient	T mm^2	670
Bore diameter	mm	30
Pole shape	-	cubic + straight line
Magnetic length, L_{mag}	mm	200
Iron length, L_y	mm	192
Total length, L_{TOT}	mm	220
Amp-turns per pole, NI	A turns	600
Insulated conductor diameter	mm	3
Number of turns per pole	mm	54
Current	A	10

17.5 Magnets for the plasma section

Due to the strong focusing requirements in the plasma section, particularly downstream of the capillary, a compact and tunable focusing system compatible with ultra-high vacuum is needed. Tunable Permanent Magnet Quadrupoles (TPMQs) offer a promising solution. Several TPMQ designs exist [5–10], and for EuPRAXIA@SPARC_LAB, a design based on the QUAPEVA experience [11, 12] has been proposed and optimized for compactness [13]. This section outlines the main beam focusing requirements and summarizes the key parameters of the proposed TPMQ designs.

17.5.1 Beam focusing requirements

In the EuPRAXIA@SPARC_LAB linac, the X-band booster accelerates the beam up to 500 MeV upstream of the plasma, with the energy reaching ∼1 GeV downstream. Beam focusing is achieved through a symmetric TPMQ triplet upstream and a set of 13 quadrupoles downstream of the plasma capillary. Two types of quadrupoles—"long" and "short," based on magnetic length—are used on both sides. The tunability specifications are based on the estimated energy spread at the entrance and exit of the plasma capillary. The main requirements for these magnets are summarized in Table 17.13.

Table 17.13: TPMQ requirements upstream and downstream plasma capillary

	UPSTREAM		DOWNSTREAM	
Parameter	**Value**	**Value**	**Value**	**Value**
Energy	500 MeV	500 MeV	1 GeV	1 GeV
Aperture diameter	7 mm	7 mm	7 mm	7 mm
Average gradient	300 T/m	300 T/m	510 T/m	510 T/m
Tunability	±10%	±10%	±17%	±17%
Magnetic length	55 mm	100 mm	17.5 mm	35 mm
Integrated gradient range	16.5±1.7 T	30±3 T	8.9±1.6 T	17.8±3.2 T

17.5.2 Tunable permanent magnet preliminary design

A preliminary design of the Tunable Permanent Magnet Quadrupoles (TPMQs) has been carried out using Opera 3D with the TOSCA solver (see Figure 17.16). The design is based on the QUAPEVA concept developed for the COXINEL facility at SOLEIL [11, 12]. Each TPMQ consists of a fixed 8-sector hybrid Halbach array made of NdFeB and AISI1010 blocks, surrounded by four radially magnetized NdFeB tuning cylinders. By rotating the cylinders around the longitudinal axis, the magnetic gradient—and thus the focusing strength—can be adjusted. Opposite rotation directions reduce skew components at half of the maximum gradient. An upgrade using FeCo instead of AISI 1010 blocks is under evaluation to increase gradient, although it may raise cost and activation risks.

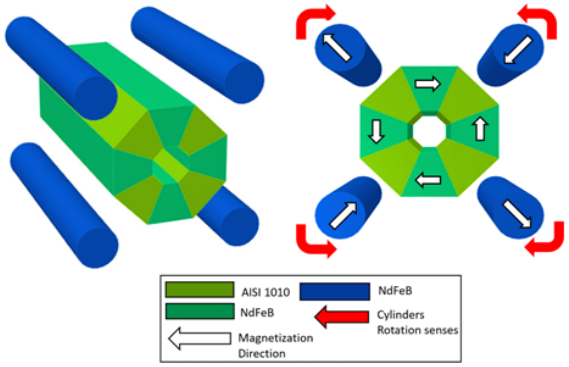

Figure 17.16: 3D view (left) and front view (right) of TPMQ. Legend of the blocks material, magnetization direction and cylinders rotation sense are shown (down).

The comparison between the requirements from beam dynamics and the main TPMQ parameters defined by the simulations is shown in Table 17.14 and 17.15 for the magnets upstream and downstream the plasma capillary respectively.

Simulations confirm that all models meet the required integrated gradient range, used as the key figure of merit. Downstream TPMQs require higher gradients and tunability, which leads to larger transverse dimensions. To mitigate spatial constraints in the vacuum chamber, a compact version of the short TPMQ has been developed. This design brings tuning cylinders closer to the air gap and modifies the AISI1010 poles to house them efficiently (see Figure 17.17). Feasibility will be tested with a prototype: magnetic design and measurements will be done in-house, while manufacturing will be handled by an external company.

Table 17.14: Requirements and simulations parameters for "Short" and “Long” TPMQ upstream the plasma capillary.

	SHORT TPMQ		LONG TPMQ	
Parameter	**Requirements**	**Simulations**	**Requirements**	**Simulations**
Energy	500 MeV	500 MeV	500 MeV	500 MeV
Aperture diameter	7 mm	7 mm	7 mm	7 mm
Average gradient	300 T/m	307 T/m	300 T/m	294 T/m
Tunability	±10%	±12%	±10%	±14%
Magnetic length	55 mm	54 mm	100 mm	102 mm
Integrated gradient range	16.5±1.7 T	16.4±1.7 T	30±3 T	30±4 T
Overall dimensions (W×H×L)	-	32×32×50 mm^3	-	36×36×100 mm^3
Weight	-	200 g	-	400 g

Table 17.15: Requirements and simulations parameters for "Short" and “Long” TPMQ downstream the plasma capillary.

	SHORT TPMQ		**LONG TPMQ**	
Parameter	**Requirements**	**Simulations**	**Requirements**	**Simulations**
Energy	1 GeV	1 GeV	1 GeV	1 GeV
Aperture diameter	7 mm	7 mm	7 mm	7 mm
Average gradient	510 T/m	433 T/m	510 T/m	492 T/m
Tunability	$\pm$17%	$\pm$22%	$\pm$17%	$\pm$19%
Magnetic length	17.5 mm	21 mm	35 mm	35 mm
Integrated gradient range	8.9$\pm$1.6 T	8.82$\pm$1.7 T	17.8$\pm$3.2 T	17.4$\pm$3.0 T
Overall dimensions (W$\times$H$\times$L)	-	125$\times$125$\times$17 mm^3	-	125$\times$125$\times$33 mm^3
Weight	-	1.2 kg	-	2.3 kg

Table 17.16: Comparison between compact and normal design for short TPMQ downstream the plasma capillary.

	Short compact design	**Short normal design**
Parameter	**Value**	**Value**
Energy	1 GeV	1 GeV
Aperture diameter	7 mm	7 mm
Average gradient	495 T/m	433 T/m
Tunability	$\pm$15%	$\pm$22
Magnetic length	23 mm	21 mm
Integrated gradient range	11.4$\pm$1.7 T	8.8$\pm$1.7 T
Overall dimensions (W$\times$H$\times$L)	45$\times$45$\times$20 mm^3	**1**25$\times$125$\times$17 mm^3
Weight	1.3 kg	1.2 kg

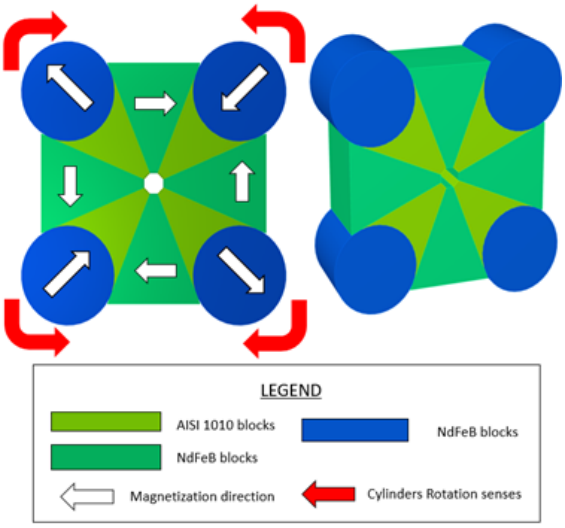

Figure 17.17: 3D front (left) and general (right) views of the TPMQ compact design for the short quadrupole downstream the plasma capillary. Blocks material, magnetization direction and cylinders rotation senses are depicted with colors and symbols of the legend.

Table 17.16 shows the comparison for the short quadrupole downstream the plasma between the compact and the "normal" design already presented in Table 17.15.

17.5.3 Current status and next steps

Further validation with the Beam Physics team and a cross-talk analysis are ongoing before finalizing the design. Interaction forces between components are being studied to properly size the tuning cylinder servomotors. A translation table, as used in the QUAPEVA system at SOLEIL, will be included to compensate residual magnetic axis shifts during gradient adjustment. Prototyping will follow, involving precision machining companies for assembly and testing. Magnetic measurements will be performed at LNF's dedicated facility. Upon successful validation, to be carried out at INFN through magnetic measurements, series production will begin, handled by an external company.

17.6 Driver-witness separator

The separation of the driver and witness beams is achieved by exploiting their different energies, using a magnetic chicane and a septum dipole. In the first dipole, the deflection angle differs for the two beams due to their energy difference, resulting in a transverse separation that is preserved through the second dipole. As a result, between the second and third dipoles, the two beams propagate parallel to each other with a transverse offset: at this point, a septum C dipole is inserted. The geometry of the chicane dipoles is shown in Figure 17.18.

As shown by the simulations, the witness beam reaches an energy on the order of 1 GeV, while the driver contains particles with energies ranging from 180 to 560 MeV. This implies that the dipoles in the chicane must be designed for a reference energy of 1 GeV. It is evident that, due to their energy spread, the driver particles will be deflected over a range of angles, spanning from the minimum to the maximum corresponding to their energy distribution.

The chicane design foresees a total length of approximately 2 meters. It is essential to find an optimal compromise for the deflection angle of the first dipole: a large angle would provide sufficient spatial separation between the driver and the witness, facilitating the insertion of the septum dipole; on the other hand, a small angle is required to keep the quality of the accelerated

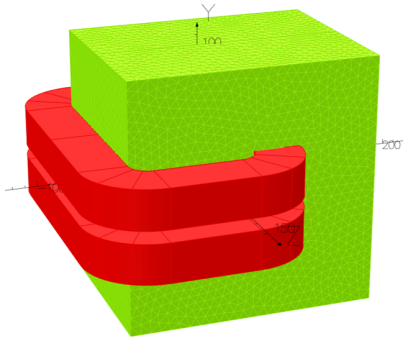

Figure 17.18: The 3D design of C-shaped dipoles for the driver-witness separator chicane.

beam. Moreover, a sufficient distance between the second and third dipole magnets must be ensured to allow the installation of the septum dipole and to provide enough space for the deflected driver trajectory to reach the dump without passing through the magnetic field of the third dipole. A reasonable compromise was found with a deflection angle for the witness of 2.5°, which allows for beams separation of about 17 mm. This choice also enables the first two dipoles (and symmetrically the last two) to be placed closer together, increasing the available space in the central region where the septum dipole is to be positioned (see Figure 17.19). The deflection of 2.5° at 1 GeV is obtained by an integrated field of 145 T mm, that is achieved with a 0.8 T and a magnetic length of 182 mm. This choice allows the magnet to operate well below saturation and helps to limit the overall length of the magnetic yoke. Table 17.17 reports the main parameters of the chicane dipoles.

Table 17.17: Main parameters of the four dipoles for the driver-witness separation chicane.

Parameter	**Units**	**Value**
Quantity	-	4
Type	-	C-shape
Energy, E	GeV	1
Pole gap, h	mm	10
Bending angle	°	2.5
Integrated field, BL	T mm	145
Field, B	T	0.8
Magnetic length, L_{mag}	mm	180
Yoke length, L_{mag}	mm	162
Pole width, W_{pole}	mm	120
Number of coils per pole	-	42 (= 6×7)
Conductor size (hole diameter)	mm×mm (mm)	6 × 6 (∅ 3)
Coil size	mm × mm	40 × 48
Current density	A/mm^2	4.1
Current	A	120

With these parameters of the dipoles, the chicane may have the overall geometry reported in Table 17.18 and shown in Figure 17.19.

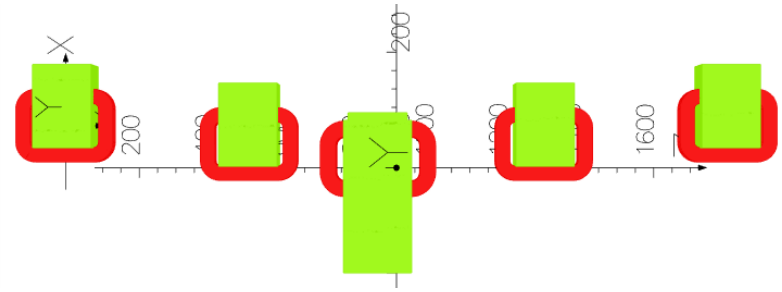

Figure 17.19: The 3D view of the driver-witness separator chicane, showing from left to right: dipoles D1 and D2, the septum, and dipoles D3 and D4.

Table 17.18: Geometrical parameters of the driver-witness separation chicane.

Parameter	Units	Value
D1-D2 and D3-D4 distance	mm	400
D2-D3 distance	mm	1000
Displacement in transverse	mm	50
D2-septum dipole distance	mm	350

The magnet responsible for the beam separation is a C-type dipole, shown in Figure 17.20, positioned between the second and third dipoles of the chicane, . It features a septum designed such that the driver beam passes under the magnet pole, while the accelerated beam (witness) travels outside the iron septum and thus experiences no magnetic field. The septum dipole is not placed at the center of the space between the second and third dipoles, but closer to the second dipole, in order to provide sufficient space for the deflected driver trajectory before it is directed toward the dump.

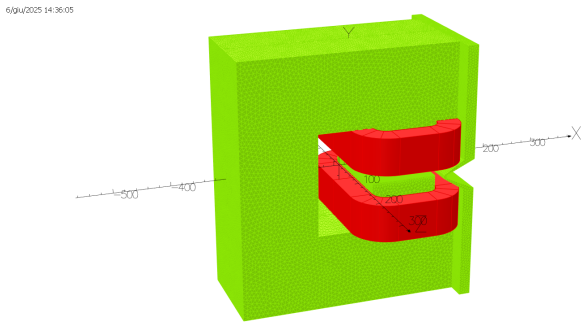

Figure 17.20: The 3D design of the septum dipole.

The magnet is configured to deflect the central portion of the driver beam, corresponding to an average driver energy of approximately 370 MeV, by 10°. This deflection is achieved with an integrated field of approximately 216 T mm. The chosen configuration includes a central field of 1.04 T and a magnetic length of 208 mm. The total yoke length is 180 mm. The pole width has to be large enough to cover the entire area swept by the driver. To mitigate further broadening of the driver beam, which already reaches the septum dipole with a transverse size due to the dispersion introduced by the first dipole, the pole face is transversally tapered, effectively creating a combined-function magnet. The gap reported in Table 17.19 corresponds to the value at the magnet center.

As previously noted, the separation between the two beams at the septum dipole location is estimated to be 17 mm. The transverse geometry, shown in Figures 17.21 and 17.22, includes a septum with a thickness of 5 mm in the central plane. Longitudinally, the septum extends beyond the magnet yoke to suppress fringe field effects, which would otherwise result in a non-negligible integrated field acting on the witness beam, which is meant to remain unaffected.

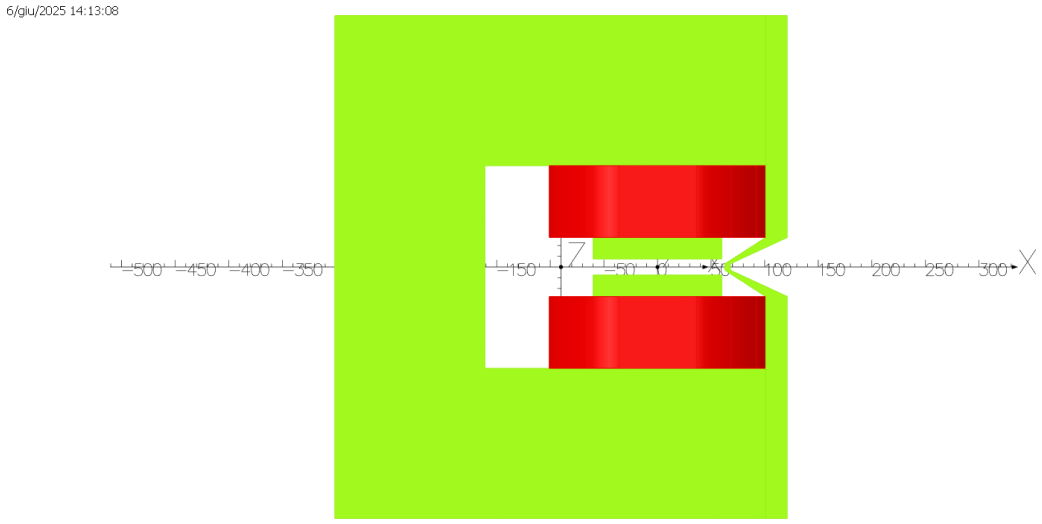

Figure 17.21: The section of the septum dipole.

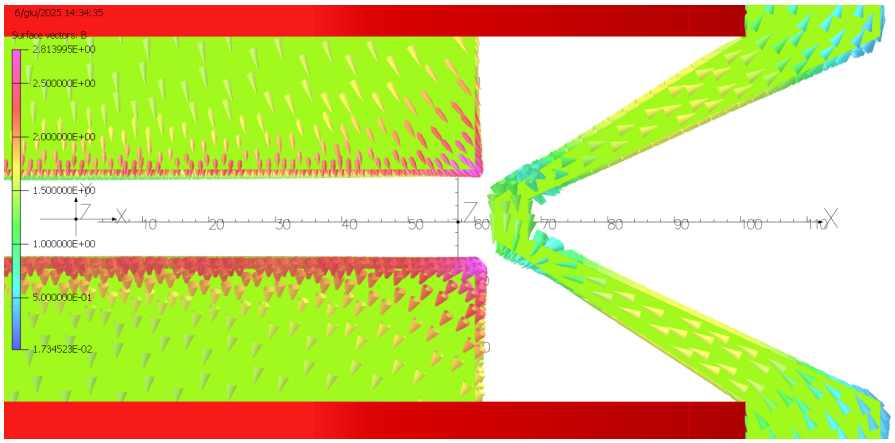

Figure 17.22: Details of the field in the septum.

Table 17.19: Main parameters of the septum dipole for the driver-witness separation.

Parameter	Units	Value
Type	-	Septum, C-shape
Energy, E	MeV	370
Pole gap, h	mm	10
Bending angle	°	10
Integrated field, BL	T mm	216
Field, B	T	1.04
Magnetic length, L_{mag}	mm	208
Yoke length, L_{mag}	mm	180
Pole width, W_{pole}	mm	120
Number of coils per pole	-	60 (= 6×10)
Conductor size (hole diameter)	mm×mm (mm)	6 × 6 (∅ 3)
Coil size	mm × mm	41 × 67
Current density	A/mm^2	3.8
Current	A	106

17.7 Spectrometer Dipoles

The layout includes two dipole magnets acting as spectrometers for beam energy measurement: one is located downstream of the bunch compressor chicane, and the other is positioned at the end of the plasma acceleration stage, just before the undulator line. Both dipoles are designed as sector-type C-shaped magnets, corresponding to maximum beam energies of 670 MeV and 1 GeV, respectively. The first dipole provides a bending angle of 22°, while the second bends the beam by 14°. In both cases, the magnetic gap is 30 mm. The magnetic field is chosen as a compromise between minimizing the magnet length and ensuring operation well below saturation. The preliminary parameters of these magnets are summarized in Table 17.20.

Table 17.20: Main parameters of the dipoles used as spectrometers.

Parameter	Units	Value	Value
Type	-	Sector C-shape	Sector C-shape
Energy, E_{max}	MeV	670	1000
Pole gap, h	mm	30	30
Bending angle	°	22	14
Integrated field, BL	T mm	856	813
Field, B	T	1.4	1.4
Magnetic length, L_{mag}	mm	611	581
Amp-turns per pole, NI	A turns	33,400	33,400

17.8 Magnets for the undulator line

In the drift section between each pair of consecutive undulators, a quadrupole and a horizontal-vertical steerer are installed to control the beam focusing and to correct its entrance angle into the subsequent undulator. While these magnetic elements are primarily designed for a 1 GeV beam, they have been dimensioned with a design margin to ensure reliable operation under varying conditions, anticipating possible future upgrades of the machine. A critical aspect in this context is their longitudinal length, which must be as compact as possible due to the high density of components (mechanical structures, vacuum equipment, and diagnostics) within the limited available space of about 60 cm.

17.8.1 Intra-undulators quadrupoles

Regarding the quadrupoles, the required focusing strength, as defined in the Undulators Chapter 8, corresponds to an integrated gradient of 1.7 T. The quadrupole will be installed adjacent to the cavity beam position monitor, sharing a dedicated motorized support structure to enable precision alignment. The quadrupole has a squared geometry (see Figure 17.23), even though an octagonal configuration could be easily implemented in the engineering phase to simplify positioning and alignment. It is an air-cooled magnet, with an iron yoke and coils made of enameled copper wire of 1.6 mm in diameter. Its main parameters are reported in Table 17.21.

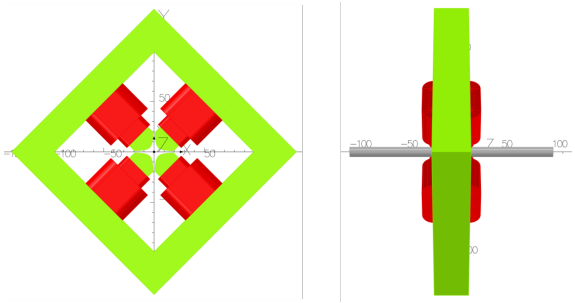

Figure 17.23: The Opera 3D model of the intra-undulators quadrupoles (front and side view).

17.8.2 Intra-undulators steerers

For the horizontal-vertical steerers, an air-core magnet configuration — without an iron yoke — has been selected. Although this solution is less efficient magnetically compared to a yoke-based design, it was preferred due to the close proximity of the magnet to the undulator, in order to avoid unwanted magnetic field closure effects. Moreover, the air-core configuration is better suited for potential future upgrades of the machine, which may involve increasing the repetition rate up to 400 Hz. Air-core magnets can be operated more rapidly, enabling faster trajectory corrections at such frequencies. The steerer is designed to provide an angular deflection of approximately 0.3 mrad for a 1 GeV beam in both transverse planes (x and y). Its design builds upon the experience gained from the SABINA steerers [14], where geometry has been studied to optimize longitudinal footprint. To facilitate assembly and improve integration, the coils support structure is 3D printed. The coil aperture has been dimensioned taking into account the mechanical support constraints. The magnet is designed assuming the same current density for both horizontal and vertical correction elements, with the number of windings adjusted accordingly. The total length of the steerer is less than 120 mm. Thanks to a design margin, in the event that future upgrades of the machine lead to a higher energy, the steerer would still be able to operate, ensuring the same deflection of 0.3 mrad by increasing the current density. The magnetic design of the coils is in Figure 17.24, while main parameters are reported in Table 17.22.

Table 17.21: Preliminary parameters for the intra-undulators quadrupoles.

Parameter	Units	Value
Bore diameter	mm	12
Gradient	T/m	40.7
Integrated gradient	T/mm	1.7
Magnetic length, L_{mag}	mm	41.7
Yoke length, L_y	mm	34
Yoke external side	mm	200
Yoke thickness	mm	30
Pole width	mm	26
Pole profile	-	Hyperbolic
Number of windings, N	-	192 (= 2×30 + 6×22)
Insulated conductor diameter	mm	1.6
Current density, J	A/mm^2	1.8
Current, I	A	3.18
Total length, L_{TOT}	mm	56

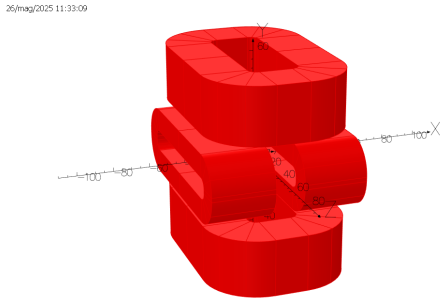

Figure 17.24: The Opera 3D model of the coils for the intra-undulators steerers.

Table 17.22: Preliminary parameters for the intra-undulators steerers.

Parameter	**Units**	**Value**
Energy, E	GeV	1
Deflection angle, θ	mrad	0.3
Integrated Field, BL	T mm	1
Insulated conductor diameter	mm	1.6
Current density, J	A/mm^2	2.0
Current, I	A	3.5
Total length, L$_{TOT}$	mm	120
INTERNAL STEERER		
Coil aperture	mm	16
Coil straight section	mm	80
Number of windings		176 (= 8×22)
EXTERNAL STEERER		
Coil aperture	mm	52
Coil straight section	mm	60
Number of windings		320 (= 16×20)

17.9 Dump dipole

The dipole magnet located at the end of the undulator line is designed to deflect a 1 GeV beam downward by 30°. It is a C-type curved, sector dipole with a 32 mm magnetic gap. The dipole geometry has been designed by balancing the magnetic flux within the yoke and considering the three main cross-sectional regions: the pole width (W$_p$), the coil window (W$_c$) and the return leg width (W$_R$). Three curvature radii are defined: the beam curvature radius (rho), the maximum curvature radius (Rmax) and the minimum curvature radius (Rmin), the latter two corresponding to the outer and inner edges of the yoke, respectively. The longitudinal coil overhang causes an effective increase in the beam curvature radius of the curvature radius. This effect was initially estimated analytically and then refined through 3D electromagnetic modelling. The main parameters are reported in Table 17.23.

The design has been carried out with an appropriate design margin to ensure reliable operation and accommodate potential future upgrades of the machine. Should higher performance be required, the magnetic field could be increased by applying a higher current density, within the capabilities of the design.

Table 17.23: Main parameters for the dump dipole.

Parameter	Units	Value
Energy, E	GeV	1
Pole gap, h	mm	32
Bending angle, θ	deg	30
Integrated Field, BL	T m	1.75
Nominal Field, B	T	1.13
Magnetic length, L_{mag}	m	1.54
Pole width, W_p	mm	170
Ampere-turn, NI	A-turn	14,400
Number of windings, N	-	144 (= 12×12)

17.10 Power Converter Sizing and Specifications

The 3D electromagnetic design of the magnets leads to the definition of the appropriate sizing of the power converters required for their excitation. In this phase, the operating current ranges, dynamic requirements, and regulation performance are evaluated in order to identify the most suitable power converter for each magnet type under all expected conditions. The resulting power converter size identified for each magnet type is reported in Table 17.24. In addition, Table 17.25 provides a comprehensive summary of the technical specifications of all selected power converters, including stability, accuracy, reproducibility, resolution, and output ripple, which constitute the key parameters governing their performance within the system.

17.11 Safety for magnets and power supplies

The operation of magnets and power supplies complies with established safety protocols to ensure the protection of personnel, equipment, and facility infrastructure. Safety measures are implemented to mitigate electrical, thermal, mechanical, and environmental risks associated with these subsystems, as summarized below.

17.11.1 Magnets

Electrical safety

Electromagnets are powered by power converter. Their live parts will be under 1 kV voltage. The following measures will be implemented for the safety risk mitigation:

- Appropriate protection against direct and indirect contact (e.g., grounding, insulation, physical barriers). All the live components will be properly insulated including the electrical coils terminals that will be protected with a IP30 protection rating.
- Interlocks to automatically disconnect power in the event of a fault.
- Overcurrent and short-circuit protection devices (e.g., fuses, circuit breakers).

Thermal risk

Magnets dissipate heat during operation; hence, it will be implemented:

- Cooling systems (either water- or air-cooled) with monitoring of flow, temperature, and pressure.
- Thermal alarms and interlocks (e.g., thermostats or thermoswitches) to detect overheating.

Table 17.24: Table of power converter size for each magnet type, classified by type and position along the accelerator, including the number of elements. The converter size is expressed in terms of required current and voltage.

Magnet type	**Position**	**Number**	**Current (A)**	**Voltage (V)**
SOLENOIDS	Gun	1	200	50
	Accelerating sections	8	200	100
DIPOLES	Laser heater chicane	4	200	50
	Bunch compressor chicane	4	150	20
	Driver-witness separator chicane	4	150	20
	Septum	1	120	30
	Spectrometers	2	120	30
	Dump dipole	1	200	100
STEERERS	Gun	4	5	10
	Between S-bands	6	5	10
	Linac 1	8	5	10
	Linac 2	8	5	10
	Intra-undulators	20	5	10
QUADRUPOLES	Gun	2	10	10
	Injector	4	200	50
	Linac 1	3	120	30
	Bunch compressor chicane	9	200	50
	Linac 2	3	120	30
	Intra-undulators	10	5	10
SEXTUPOLES	Laser heater chicane	1	20	30
	Bunch compressor chicane	1	20	30

Table 17.25: Table of the technical specifications of the power converters.

Parameter	**Specification**	**Unit**
Stability, 8 hours	$\pm$ 150	ppm
Accuracy	$\pm$ 500	ppm
Reproducibility	$\pm$ 200	ppm
Analogue programming resolution	$\leq$ 120	ppm
Power factor	$\geq$ 0.92	–
V/I ripple (resistive load)	$\leq$ 150	ppm pk-pk

Mechanical and structural safety

Magnetic fields generate significant internal forces. The following measures will be taken to ensure:

- Robust mechanical design to withstand electromagnetic stresses.
- Proper anchoring and support structures to prevent displacement or vibrations.
- Protection against crushing or impact hazards during installation and maintenance activities.

Residual magnetic fields

Although non-ionizing, the following precautions will be taken to minimize hazards due to residual magnetic fields:

- Clearly marked and restricted areas to prevent access by individuals with sensitive medical devices (e.g., pacemakers).
- Static magnetic field risk assessments in accordance with applicable standards (e.g., ICNIRP or EN 50500).
- Magnetic field levels limited to < 0.5 mT in areas accessible to the general public or untrained personnel.
- All the magnets have been designed with the purpose to maximize the magnetic field intensity in the air region between the poles where there will be the interaction with the particles beam. Therefore, the fringe field outside the magnet will be limited and properly mapped during the design phase and in the magnetic measurements test.

Environmental and material considerations

- Use of flame-retardant and non-toxic materials for insulation and coverings.
- Adequate ventilation to prevent heat accumulation or release of volatile substances

Operational procedures and signage

- Clear and visible signage (e.g., high voltage, magnetic field, hot surfaces).
- Controlled access procedures in areas where magnets are in operation.
- Staff training on electrical, magnetic, and mechanical hazards.

Applicable standards and regulations

- IEC 61010, IEC 60204-1 (electrical safety)
- EN 50500 (static magnetic field exposure)
- European Directives: Low Voltage Directive (LVD); Machinery Directive; EMC Directive.

17.11.2 Cables

The power cables will connect the current terminals of the power converter with the magnets coils terminal. The cables will be sized following the EU directive standards avoiding overheating during normal machine operations and choosing proper insulation materials. The insulation materials are non-propagation of flame; non-spread of fire; very low emission of fumes, toxic and corrosive gases. The typical cable type will be the FG7OR family.

Applicable Standards and Regulations

- (UE) n. 305/2011
- EN 50575
- CEI 64-08
- CEI 20-67

17.11.3 Power converters

Power converters will deliver power from AC network to the magnets. All the live parts will be under 1kV voltage and protected with insulation rating IP30. The power converter will be air-cooled and in case of overheating, internal thermoswitches will open the circuit breaker switching off the devices. In case of overload or insulation loss a circuit brake with differential switch will protect the device and the personnel from indirect contacts. All the exposed conductive parts will be grounded to a node inside the racks who will be connected to earth equipotential node of the racks hall. The personnel devoted to power converter operations will be trained with safety courses according to EU regulations. All the power converters will be marked with CE marking.

Applicable Standards and Regulations

- IEC 61204
- IEC 61204-3
- IEC 61204-4
- IEC 61010-1
- LVD 2014/35/UE
- EMC 2014/30/UE
- EN 61326-1

17.12 Conclusions

The magnetic design carried out for this TDR has demonstrated the feasibility of the beamline, particularly with respect to the longitudinal footprint of the machine, which is considered a critical aspect for defining the layout and the construction choices of the components. The analysis identifies which magnets require special attention, particularly those associated with the driver-witness separator chicane, due to the complexity of the septum magnet, as well as the permanent magnets required for the plasma section.

Overall, the Technology Readiness Level (TRL) associated with magnet technology is considered to be very high, with a detailed breakdown of the various components as reported in Table 17.26. The technology of electromagnets, the use of high-accuracy 3D simulation software, the possibility of selecting appropriate materials (for the yoke, windings, electrical insulation, etc.), the expertise of the suppliers in manufacturing, and the ability to perform magnetic measurements even directly on site, all contribute to ensuring the feasibility of the project.

Table 17.26: TRL level of the magnets

Sub - systems	TRL	Comments
Magnets for the gun	9	Solenoid, quadrupole and steerers: already designed and successfully operating on the SPARC_LAB gun.
Accelerating sections solenoids	9	Experience gained with SABINA focusing solenoids. Only minor adjustment are required to decouple the mechanical support of the accelerating sections.
Steerers	9	Different types of steerers are foreseen in the machine (air-dominated or with iron yoke). The technology is well established.
Quadrupoles	8	Different types of quadrupoles are also included in the layout, including combined function quadrupoles with integrated steerers. The technology is well established.
Dipoles for chicanes	8	Standard dipoles with non-critical magnetic fields and parameters. May include magnetic shielding to reduce crosstalk. The technology is well established.
Magnets for the plasma section	6	PMQ design based on similar implementations at other accelerators. A prototype, based on our specifications, is to be built and tested.
Separator chicane	7	Four chicane dipoles and one septum magnet. The septum design is delicate, although the technology is well known.
Dump dipoles	9	Optimization efforts are focused on minimizing the overall size.

Bibliography

[1] D. Alesini et al. “The New SPARC_LAB RF Photo-Injector”. In: *Proc. IPAC’22*. 2022. DOI: 10.18429/JACoW-IPAC2022-MOPOMS019.

[2] A. Vannozzi et al. “Design and Realization of New Solenoids for High Brightness Electron Beam Injectors”. In: *Proc. IPAC’21* (Campinas, Brazil, May 2021). JACoW Publishing, Geneva, Switzerland, 2021, pp. 2374–2377. DOI: 10.18429/JACoW-IPAC2021-TUPAB366. URL: https://jacow.org/ipac2021/papers/TUPAB366.pdf.

[3] T. Schietinger et al. “Commissioning experience and beam physics measurements at the SwissFEL Injector Test Facility”. In: *Phys. Rev. Accel. Beams* 19 (10 2016), p. 100702. DOI: 10.1103/PhysRevAccelBeams.19.100702.

[4] L. Sabbatini et al. “SABINA: A Research Infrastructure at LNF”. In: *12th International Particle Accelerator Conference*. Aug. 2021. DOI: 10.18429/JACoW-IPAC2021-THPAB372.

[5] T. Mihara et al. “Variable Permanent Magnet Quadrupole”. In: *IEEE Transactions on Applied Superconductivity* 16.2 (2006), pp. 224–227. DOI: 10.1109/TASC.2006.873248.

[6] G. Tosin et al. “Super hybrid quadrupoles”. In: *Nuclear Instruments and Methods in Physics Research Section A: Accelerators, Spectrometers, Detectors and Associated Equipment* 674 (2012), pp. 67–73. ISSN: 0168-9002. DOI: https://doi.org/10.1016/j.nima.2012.01.036. URL: https://www.sciencedirect.com/science/article/pii/S0168900212000769.

[7] S. C. Gottschalk and D. J. Taylor. “Magnetic and Engineering Analysis of an Adjustable Strength Permanent Magnet Quadrupole”. In: *Proc. PAC’05* (Knoxville, TN, USA, May 2005). Particle Accelerator Conference 21. JACoW Publishing, Geneva, Switzerland, 2005, pp. 2122–2124. URL: https://jacow.org/p05/papers/MPPT030.pdf.

[8] M. Modena et al. “Design, Assembly and First Measurements of a short Model for CLIC Final Focus Hybrid Quadrupole QD0”. In: *Conf. Proc.* C1205201 (2012), THPPD010. URL: https://cds.cern.ch/record/1470334.

[9] N. A. Collomb, J. A. Clarke, and B. J. A. Shepherd. “Construction and Measurement of Novel Adjustable Permanent Magnet Quadrupoles for CLIC”. In: *Conf. Proc. C* 1205201 (2012). Ed. by Vic Suller, pp. 3530–3532.

[10] J. A. Clarke et al. “Novel Tunable Permanent Magnet Quadrupoles for the CLIC Drive Beam”. In: *IEEE Transactions on Applied Superconductivity* 24.3 (2014), pp. 1–5. DOI: 10.1109/TASC.2013.2289357.

[11] F. Marteau et al. “Variable high gradient permanent magnet quadrupole (QUAPEVA)”. In: *Applied Physics Letters* 111.25 (Dec. 2017), p. 253503. ISSN: 0003-6951. DOI: 10.1063/1.4986856. eprint: https://pubs.aip.org/aip/apl/article-pdf/doi/10.1063/1.4986856/13296044/253503_1_online.pdf. URL: https://doi.org/10.1063/1.4986856.

[12] A. Ghaith et al. “Tunable high gradient quadrupoles for a laser plasma acceleration based FEL”. In: *Nuclear Instruments and Methods in Physics Research Section A: Accelerators, Spectrometers, Detectors and Associated Equipment* 909 (2018). 3rd European Advanced Accelerator Concepts workshop (EAAC2017), pp. 290–293. ISSN: 0168-9002. DOI: https://doi.org/10.1016/j.nima.2018.02.098. URL: https://www.sciencedirect.com/science/article/pii/S0168900218302869.

[13] A. Vannozzi et al. “New Tunable High Gradient Permanent Magnet Quadrupole for Plasma Wake Field Acceleration at SPARC_LAB”. In: *Journal of Physics: Conference Series* 1596.1 (2020), p. 012009. DOI: 10.1088/1742-6596/1596/1/012009. URL: https://doi.org/10.1088/1742-6596/1596/1/012009.

[14] A. Selce et al. “Intra-undulator magnets for the SABINA THz FEL line: magnets design, manufacturing and measurements”. English. In: *Proc. IPAC’24* (Nashville, TN). IPAC’24 - 15th International Particle Accelerator Conference 15. JACoW Publishing, Geneva, Switzerland, May 2024, pp. 1534–1536. ISBN: 978-3-95450-247-9. DOI: 10.18429/JACoW-IPAC2024-TUPR50. URL: https://indico.jacow.org/event/63/contributions/3938.

18. Civil Infrastructures

18.1 Civil engineering

This chapter describes the design and implementation of the civil infrastructures for the EuPRAXIA@SPARC_LAB facility, including the main building layout, utilities, power distribution, HVAC (Heating Ventilation & Air Conditioning) systems, and supporting infrastructure. It aims to ensure that the facility meets the requirements of accelerator operations, radiation protection, and sustainability, in alignment with with the minimum environmental criteria (CAM) required by Italian law, Decreto Ministeriale 23.06.2022, see also Chapter 21. The design of the infrastructure has been developed to fulfill the the requirements of the equipment described in the Executive Summary Chapter 1 and Machine Layout Chapter 4.

The new infrastructure will be built inside the INFN LNF area (Figure 18.1). LNF is situated about two kilometers North of Frascati and about thirty kilometers from Rome. It is near ENEA and ESA.

As per September 2025 the design activities have been completed, also the administrative aspects foreseen by the Italian law, and the process to issue the tender for the construction has been started.

18.1.1 Geology and environment

Several site investigations were carried out. First of all, a geological investigation of the site with an exploratory drillings survey campaign was performed in December 2017 and updated in August 2021. The survey was done to a depth of about 37 m. The morphology is typical of plan-altimetric sub-flat trends of the Colli Albani area. From a geological point of view, the site is related to the Latium Volcano activity.

The soil consists of volcanic products with different physical-mechanical characteristics and a good degree of stability. Starting from the ground surface, the soil includes the following main stratigraphic levels (see Figure 18.2):

- layer of vegetable soil and fill material (about 1 to 3 m);
- epivolcanic layer (1 to 2.5 m);
- ash deposit layer of phreatomagmatic origin (1 to 3 m layer);

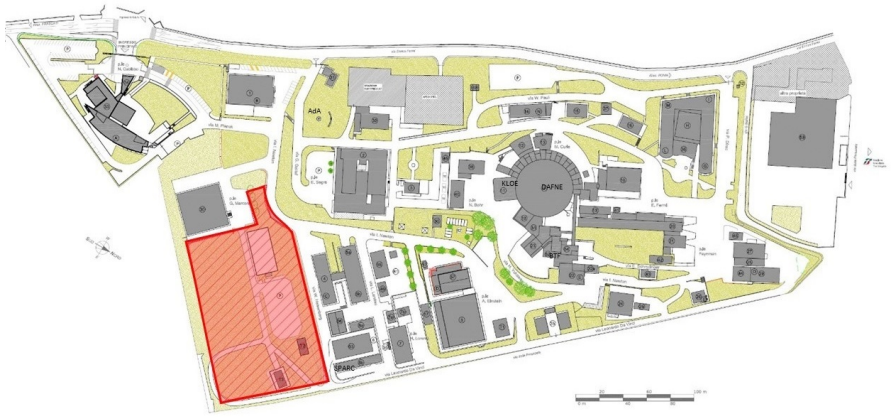

Figure 18.1: INFN-LNF and EuPRAXIA@SPARC_LAB area.

- lava rocks (1 to 2 m, max 4 m);
- other layers of gray pyroclastic material, including pockets of scoria, lava tuff elements.

From this surveys outcome the presence of underground water was not detected. From a seismic point of view, the site is classified 2B seismic area, in accordance with Lazio Region classification. The site is able to damp vibrations coming from natural sources and cultural noise, as confirmed by vibration measurements carried out for SuperB project [1].

About the environmental impact assessment, this type of project is not included in the categories referred to in art. 6, paragraphs 6 (verification of subjection to EIA) and 7 (EIA), of part II of Legislative Decree no. 152/06 and subsequent amendments. About war remains risk, no specific investigations have been carried out because within the LNF area and near the EuPRAXIA@SPARC_LAB site similar buildings have been built and not any problem related to these type of risk has been detected. For the characterization of the soils coming from excavations, specific investigations were carried out in October 2024. The characteristics of the soil allow it to be used in other construction sites for backfilling. Otherwise, after a thorough chemical laboratory analysis, it can be disposed of in landfills for non-hazardous waste or in landfills for inert waste with appropriate exceptions.

From a city planning point of view, the area is classified by Frascati general land-use plan as a zone with a special destination. A detailed urban plan specifies the available volumetric dimensions and the maximum height of new buildings inside the LNF area. Frascati area is bounded by archaeological and environmental restriction, as defined by the Piano Territoriale Paesistico Regionale of Lazio Region. An archaeological investigation was performed in July 2022: the results have been evaluated by the Archaeological and Landscape Superintendence (Area Funzionale Archeologia della Soprintendenza) and there are not archaeological obstacles (prot. N. 19194 – 2022.09.15).

18.1.2 Buildings

The EuPRAXIA@SPARC_LAB facilities will be set in the South-East part of LNF site, on the slope of a little hill. They will be built near the current facilities and offices of the Labs. The new building complex that will host the new LNF facility includes the construction of a new building that will house the accelerator machine and the systems needed for its operation, a building to house a fire-prevention tank and a large car park with 55 spaces for users.

The main building, hosting the new accelerator machine, occupies an area of approximately 5,600 m^2 and a volume, including open spaces and technical rooms, of almost 50,000 m^3 (Fig. 18.3).

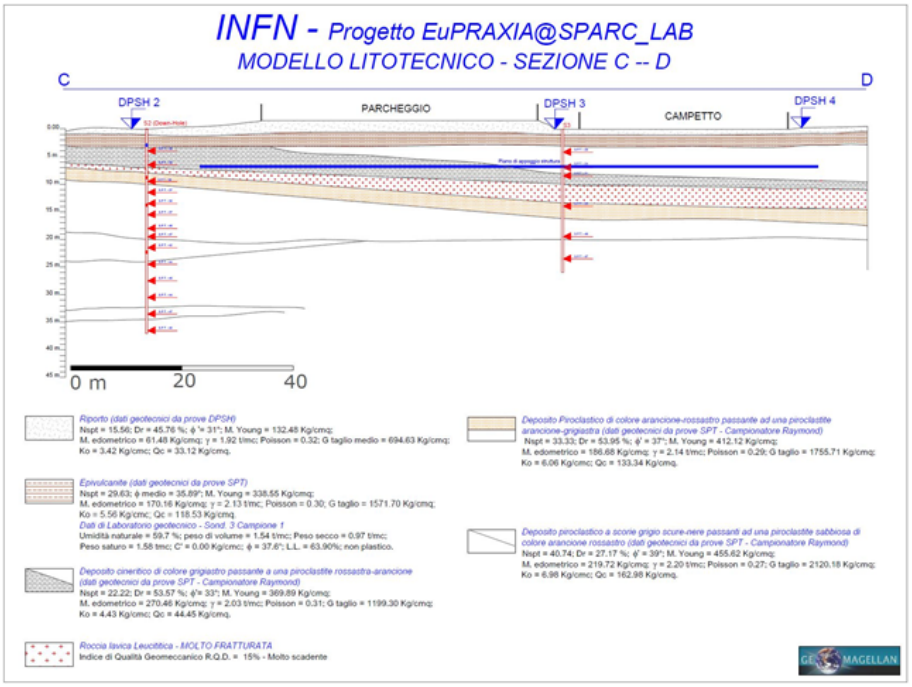

Figure 18.2: Excerpt from the geological report: stratigraphic section of the soil in longitudinal direction.

Figure 18.3: EuPRAXIA@SPARC_LAB facilities top view.

Figure 18.4: 3D view (North-West side) of the EuPRAXIA@SPARC_LAB facilities.

It exploits the height difference of the site, developing in the south-west/north-east direction against the ground. The building has a regular layout and is strongly characterized by functional reasons that determine its articulation around the central core of the LINAC. It consists of two floors above ground with main vehicular and pedestrian accesses from via W. Heisemberg (north-west facade), while, in the upstream part (south-east facade) only one floor above ground provides secondary accesses reserved purely for maintenance. At its maximum extension above ground, the building is approximately 140 m long and 45 m wide, with a narrowing to 36 m towards the north-west; it ends on the ground floor with a rectangular appendix measuring 21 m by 13 m completely underground.

The secondary building intended for the water-fire tank is a parallelepiped buried on three sides, with a rectangular base of approximately 19 m by 16 m. The building is made of reinforced concrete cast in place and divided internally into 4 different areas: two are reserved for the tanks that will contain the water reserve and the water-fire tank, and the other two areas are the respective control cabins.

The final design for the new complex was delivered on December the 2nd, 2022; after an internal verification, it was validated on December the 15th, 2022. The project has obtained the formal authorization on May the 30th, 2023, with archaeological and landscape superintendence, planning and building permission included.

18.1.2.1 Main Buildings

The architectural layout of the main building has been developed in order to fulfill the experimental equipment requirements.

At ground floor (Figure 18.5) there are:

- the LINAC tunnel housing the injector, the main linear accelerator, plasma and matching. Its dimensions are approximately 62 by 8 m^2 with a height of 6 m;
- four clear rooms (THz, Laser Sync, 2$\times$500 TW rooms), with different dimensions, distributed along the LINAC tunnel. A large corridor from via W. Heisemberg allows access into them;
- a radiation users room adjacent to the LINAC and near the last TW lab;
- the Undulator/FEL hall, located downstream the LINAC tunnel, whose dimensions are approximately 36 by 8 m^2 with a height of 6 m;
- two experimental rooms dedicated to High Energy Physics (HEP) experiments, adjacent to the undulator hall. 2 m thick wall separates the two halls;

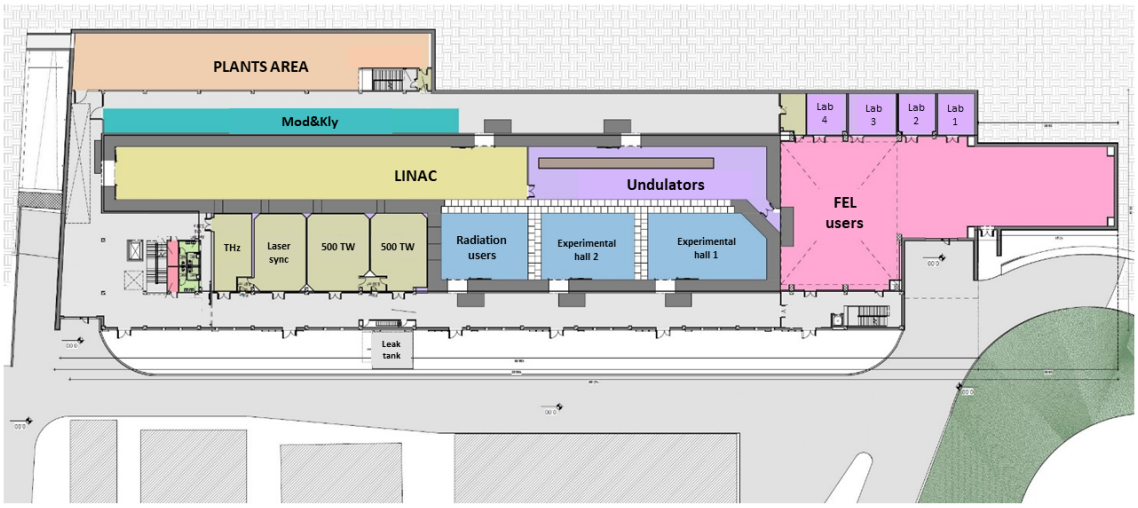

Figure 18.5: EuPRAXIA@SPARC_LAB building functional layout - Level 0.

- a Modulators and Klystrons gallery adjacent and parallel to the LINAC tunnel, 6 m wide and 6 m high, allows the access of the waveguides feeding the LINAC sections, through proper penetrations;
- the FEL Users Hall is a large open space of approximately 50 by 23 m^2, with a free height of 7.5 m (under beam) which reaches 8.9 m at the ceiling and drops to 4.35 m in the narrowest part (west side of the hall);
- 4 users laboratories near the FEL user hall, to allow samples preparation;
- an additional area designated for plants (pumps room), near the Modulators and Klystrons gallery.

Regarding the access to level zero, from via W. Heisemberg the building has two large vehicle entrances, one at the beginning of the LINAC and one at the FEL Users Hall, and seven large pedestrian entrances (Figure 18.6).

LINAC, Undulator hall, radiation users hall and two experimental halls have walls and a roof made of reinforced concrete with a thickness of 2 m and above the roof there is an additional shielding of natural soil (1.8 m). These halls are 6 m full height. The external walls of the experimental area are made of cast concrete, while the internal dividing walls are made of removable blocks in precast concrete up to 3 m high (Figure 18.7).

At the end of the Undulators hall, before the dividing wall with the FEL users room, there is an area for housing two dumps inside the floor slab. Its dimensions are 4 m $\times$ 4.4 m $\times$ 2.2 m.

Each experimental room has access through external shielding doors (closed when the machine is in operation) and through internal fire doors during the maintenance phase. Every access is 3 m wide and 3 m high but LINAC hall has two entrances located on opposite sides, one 4 m wide behind the RF Gun and the other 3 m wide close to the Undulators hall (Figure 18.6). A 5 tons overhead crane will be installed in the LINAC hall and in the Undulator hall. The two halls are separated by a dividing wall with a connecting door. The Modulator and Klystron gallery is instead accessed through a driveway door with a fire-break function. It expands to the overall length of the building to allow access to Users hall and to house the main electrical and cooling distribution. In this area a 5 tons crane will be installed to facilitate klystrons handling.

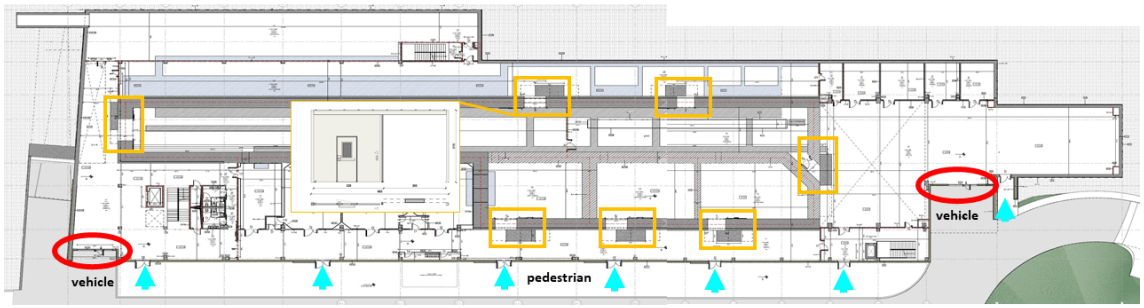

Figure 18.6: EuPRAXIA@SPARC_LAB building Level 0 - Entrances.

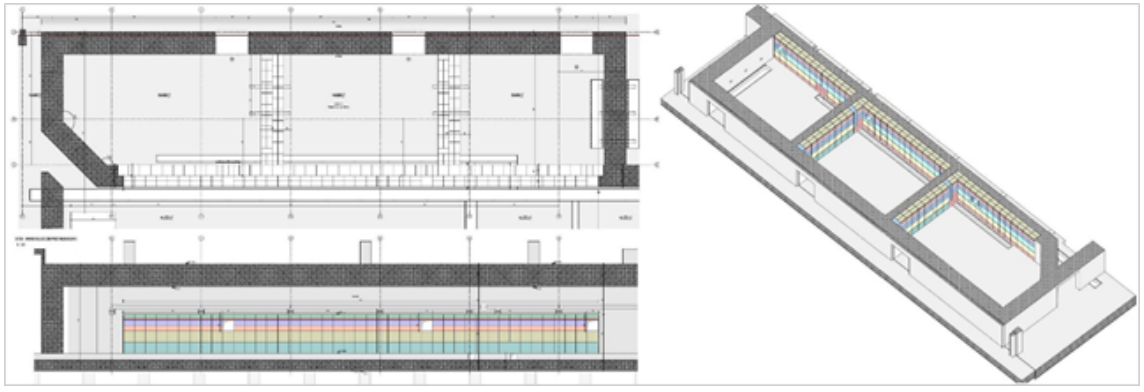

Figure 18.7: Layout, section and axonometric view of the dividing walls in removable blocks between Undulators and Experimental halls.

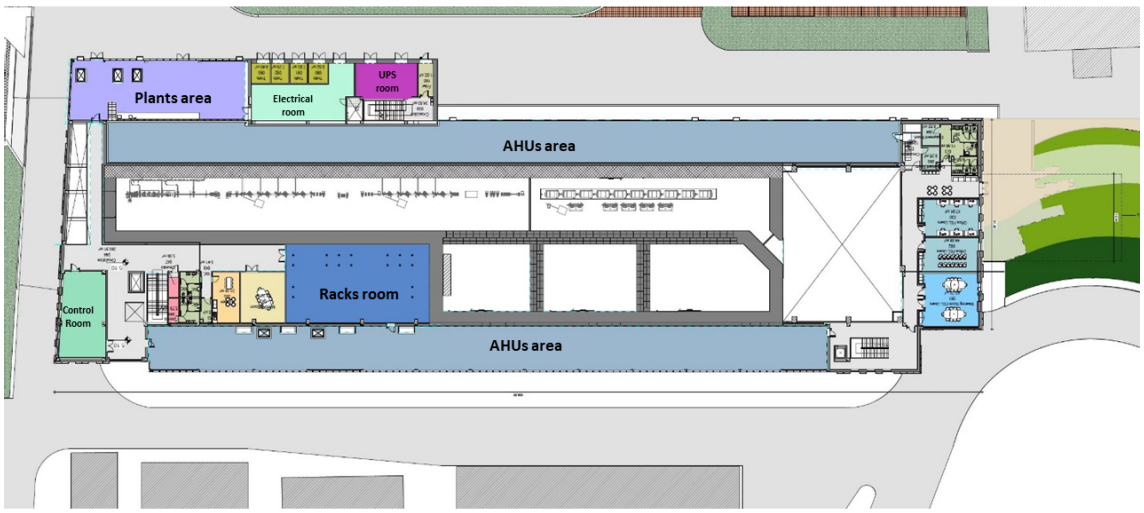

Figure 18.8: EuPRAXIA@SPARC_LAB building functional layout - Level 1.

On the first floor (Figure 18.8) there are a Control Room, the Racks Room, a meeting room, offices and services. Access to the first floor is through two lifts and two staircases. The control room is located approximately in the East part, far enough from the experimental area for radiation exposure reasons; the rack room is above the ancillary laboratories.

At this level the layout envisages some areas intended for Air Handling Units (AHUs) hosting but conveniently hidden and with appropriate paths for maintenance; above the pumps room there are also a UPS and electrical cabin and a large plants area, accessible from the outside.

The electrical and mechanical systems are distributed in all the rooms through appropriately designed services ducts and penetrations (Figure 18.9). In the experimental areas the ducts are inside the floor slab and are equipped with a walkable wire covering. Furthermore, a system for collecting any water leaks from utility systems is also provided in the ducts. This water is conveyed into a special tank outside the building and separated from the rainwater collection system for radio-protection reasons.

The slab stability is very important for accelerator reliable operation: the slab of accelerator rooms must be able to accommodate the machine mounting and handling and allow its repositioning without unsatisfactory deflection or settlement over time. The vibration limits are intended to fulfill user-supplied research instruments requirements. A campaign of detailed ground motion measurements at LNF is available (performed for the SuperB project [1]).

Table 18.1 summarizes the acceptable tolerance defined for Soleil Synchrotron (France), here used as reference.

In order to limit ancillary systems vibrations transmission to the accelerator machine the building is made by a jointed structure that separates the experimental halls from the remain areas (external part). Therefore, the EuPRAXIA@SPARC_LAB building is composed of two structures separated by 5 cm joint (Figure 18.10). In some areas the joint is in correspondence with the cast wall of the experimental area: here the wall of experimental area is composed of 0.30 m concrete, 0.05 m gap, 1.70 m concrete, to respect the 2 m thickness required for radio-protection. This gap must be filled with polyethylene for radio-protection reason (Figure 18.11).

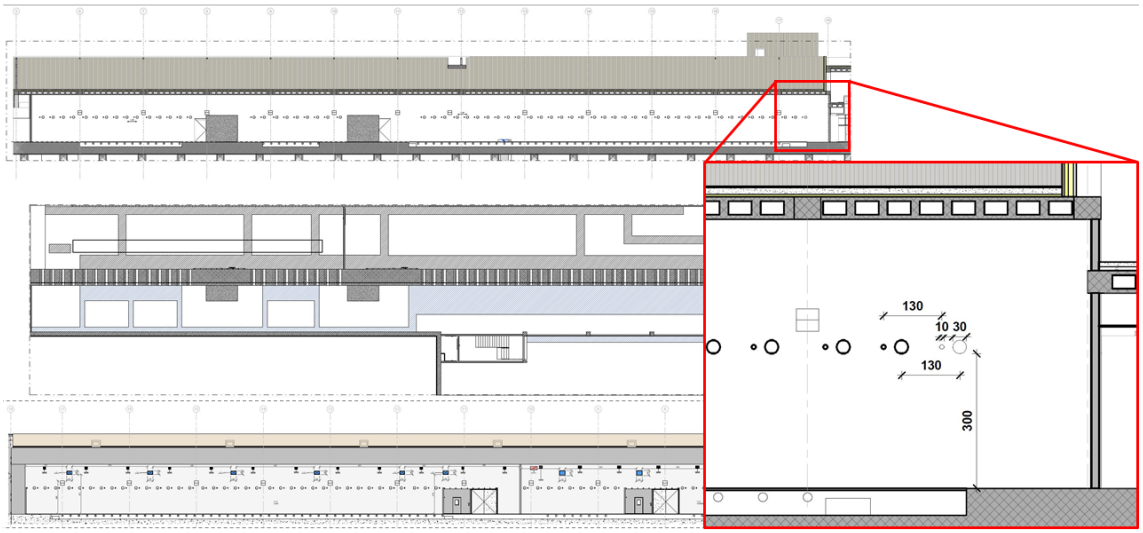

Figure 18.9: Layout and section views of the Experimental halls with systems ducts and penetrations.

Table 18.1: Soleil Synchrotron long time settlement (Extract from SuperB Committee report)

LONG TERM SETTLEMENT (vertical)	100 µm over 10 m per year 10 µm over 10 m on a diurnal cycle 1 µm over 10 m in short-term (about 1 hour)
PUNCTUAL STATIC LOAD OF 500 kg	$\Delta z < 6$ µm under the load $\Delta z < 1$ µm at 2 m
DYNAMIC LOAD OF 100 kg	$\Delta z < 1$ µm peak to peak at 2 m
VIBRATIONS (0,1-70 Hz) due to all effects induced by the facility, added to the external effects	$\Delta z < 1$ µm peak to peak $\Delta z < 4$ µm peak to peak

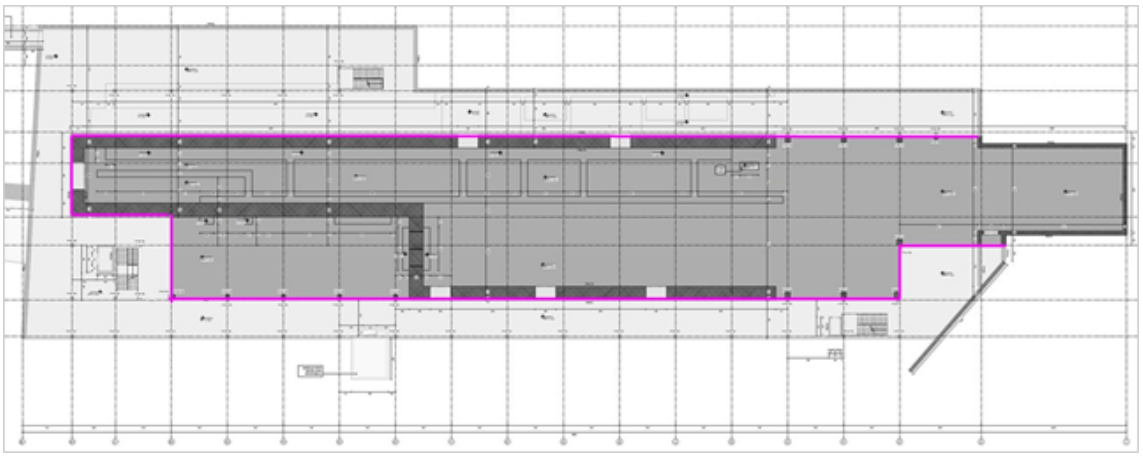

Figure 18.10: Structural joint of the EuPRAXIA@SPARC_LAB building.

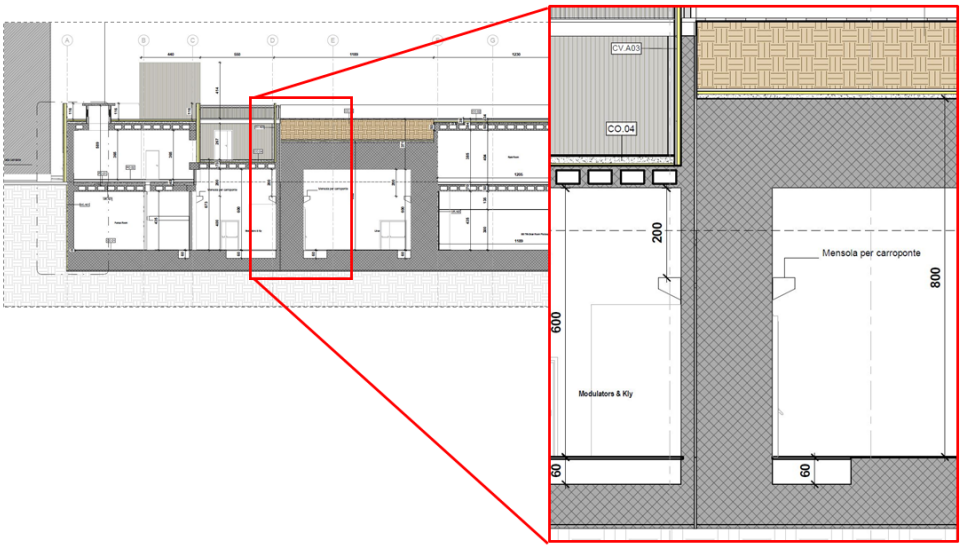

Figure 18.11: EuPRAXIA@SPARC_LAB Building cross section.

The ceiling of the experimental area is made of 2 m thick solid reinforced concrete; this thickness is required for radio-protection reasons (Section 19.4).

The two structures of the building are based on a foundation slab in reinforced concrete with a thickness of 1 m in the external area and 1.50 m in the central part. The slab is supported by reinforced concrete piles with a diameter of 1 m and a length that varies from 17 to 20 m and is joined as in the elevated part. The load-bearing capacity of the ground floor slab is 10 tons per square meter, while on the first floor it is 5 tons per square meter. The following Tables (18.2, 18.3, 18.4, 18.5) summarize the characteristics of the main rooms of the building.

To ensure maintenance of the utility systems (electrical, mechanical and overhead crane), an accessibility plan for the equipment to be used during maintenance phases has been studied (Figure 18.12).

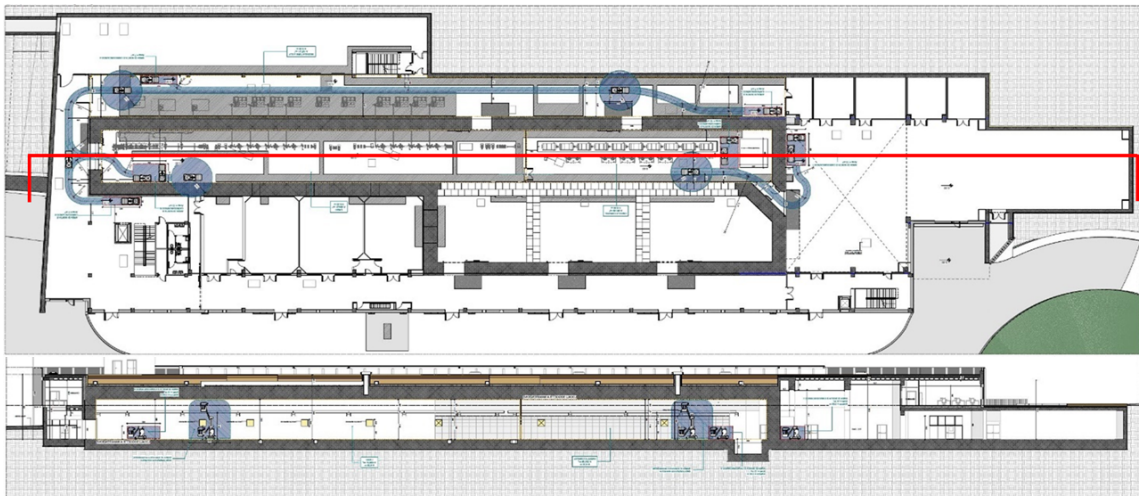

Figure 18.12: Layout and section view for equipment accessibility during maintenance stops.

Table 18.2: EuPRAXIA@SPARC_LAB Building Level 0 main halls dimensions

HALL	LENGHT [m]	WIDTH [m]	HEIGHT [m]	AREA [m^2]	VOLUME [m^3]	SLAB LOAD [Tons/ m^2]	CRANE [Tons]
Linac	61.94	8	6	494.21	2965.26	10	5
Undulator hall	35.84	8	6	261.54	1569.24	10	5
FEL Users hall	50-18.25	23-12	8.9-4.35	810.71		10	
Users labs 1	5.53	6.25	3	34.37	103.11	10	
Users labs 2	5.60	6.25	3	34.27	102.81	10	
Users labs 3	7.23	6.25	3	45.09	135.27	10	
Users labs 4	5.92	6.25	3	36.59	109.77	10	
Rad. users	13.05	9.99	6	130.38	782.28	10	
Exper. Hall 1	17.12	9.99	6	171.41	1028.46	10	
Exper. Hall 2	14	9.99	6	139.89	839.34	10	
THz CR	5.64	11.76	3	61.91	185.73	10	
Laser sync CR	7.78	11.76	3	90.08	270.24	10	
TW 500 CR 1	9.31	11.76	3	104.45	313.35	10	
TW 500 CR 2	8.50	11.76	3	92.00	276.00	10	
Mod&Kly gall.	53.50	6	6	321.00	1926.00	10	5
Pumps room	53.63	8.58	4.40	422.45	1858.78	10	
Circulation						10	

Table 18.3: EuPRAXIA@SPARC_LAB Building Level 1 main halls dimensions

HALL	LENGHT [m]	WIDTH [m]	HEIGHT [m]	AREA [m^2]	VOLUME [m^3]	SLAB LOAD [Tons/ m^2]
Rack room	21.48	11.82	3.85	256.22	986.45	5
Control room	6.75	12.84	3.85	85.13	327.75	5
UPS room	9.26	5.01	3.60	46.42	167.11	5
Electrical room	14.16	8.60	3.60	123.72	445.39	5
Plants area						5

Table 18.4: EuPRAXIA@SPARC_LAB Building Level 0 main halls interior finishes

HALL	FLOOR	WALLS	CEILING
Linac	R.01	F.01	F.01
Undulator hall	R.01	F.01	F.01
FEL Users hall	R.01	F.01	F.01
Users labs 1	R.01	F.01	CT.01
Users labs 2	R.01	F.01	CT.01
Users labs 3	R.01	F.01	CT.01
Users labs 4	R.01	F.01	CT.01
Rad. users	R.01	F.01	F.01
Exper. Hall 1	R.01	F.01	F.01
Exper. Hall 2	R.01	F.01	F.01
THz CR	R.01	HP.01	CT.01
Laser sync CR	R.01	HP.01	CT.01
TW 500 CR 1	R.01	HP.01	CT.01
TW 500 CR 2	R.01	HP.01	CT.01
Mod&Kly gall.	R.01	F.01	F.01
Pumps room	R.01	F.01	F.01
Circulation	R.01	F.01	CT.01

Table 18.5: EuPRAXIA@SPARC_LAB Building Level 1 main halls interior finishes

HALL	FLOOR	WALLS	CEILING
Rack room	PG.01	F.01	F.01
Control room	PG.01	F.01	CT.01
UPS + Electrical rooms	PG.01	MR.01a	MR.01a
Plants area	CO.04	SC.01b	No ceiling

Table 18.6: Legend of Tables 18.4 and 18.5

R.01	industrial resin
PG.01	raised floor
CO.04	concrete tile floor
F.01	breathable, dust-proof paint
HP.01	HPL wall 45 mm thickness
MR.01a	plastered wall
SC.01b	micro-perforated aluminium sheet panel
CT.01	false ceiling

18.2 Electrical installations

The construction of the new infrastructure includes the power plants. This starts from LNF main substation point of delivery down to the general purpose distribution and the powering of high technology devices up to the busbars. Final hookup of the users will be performed by specialized firms; busbars tap-off units placed near the user, in order to have the shortest cable length possible, will feed the devices through cable trays and ducts studied to avoid cables interferences with other passages in order to have a tidy area. This installation configuration allows for maximum flexibility for future upgrades and new integrations of the equipment.

18.2.1 LNF Power supply

The INFN-LNF are powered by the high voltage public grid at 150 kV by the adjacent node of the grid served by two lines. 10 MW are available on the point of delivery. The 150/20 kV substation is under responsibility of LNF as the MV network. This kind of power supply ensures high levels of reliability. The experience in the past 25 years of operation reports only 3 events of unanticipated outages, one was the national black-out in 2003, and two short interruptions due to local faults. Scheduled outages for maintenance or fault fixing on the public grid have a frequency less than once per year and are usually shared also for the internal maintenance. Main disturbance coming from the grid is represented by voltage dips. The resilience of the system in these events is increased adopting devices with higher compatibility level. Supercapacitors UPS are adopted for modulators with the multiple purpose to reduce unbalance and harmonics, and fix voltage dips. The main substation is equipped with 2 transformers 10 MVA in redundant configuration. The maximum LNF power demand is limited at 4.5 MW during run of the Dafne accelerator complex, which contributes to this demand with 3 MW, so there's large space for new users. 8 MV substations are in service, and a new one is under construction for the new data centre.

18.2.2 EuPRAXIA@SPARC_LAB Load estimation

EuPRAXIA@SPARC_LAB facility is an experimental area for accelerator devices and, for its purpose, future expansions and unpredictable installations must be considered. As an example the 400 Hz repetition rate, that at the moment is under evaluation for future expansion, is out of the scope of work because is far from technological readiness and heavily impacting on the sizing of the auxiliary plants. Sizing of the electrical infrastructure comply with the baseline project (Chapter 1), and only the availability of space and penetration for eventual power increase has been considered. As an example, a fourth transformer bay is reserved in case of necessity, allowing for 1.6 MVA expansion. The electrical installations design in based on the load analysis summarized in Table 18.7.

The expected power demand, used for the electrical installation sizing, is about **2.8 MVA** for all the facility. This figure (2.5 times the estimated consumption for the AQUA baseline) consider different configurations of the machine and a sensible amount of additional power required by limited expansion of beamlines (ARIA beamline) and experimental devices and users (PW Laser, etc.). The MV Substation has been sized to be capable to supply up to 3.2 MVA (two 1.6 MVA transformers fully loaded).

A realistic estimation of the power consumption for the baseline AQUA beamline operation at 100 Hz, 1 GeV has been performed considering a set of RF and magnets PS and the auxiliaries related to the linac at 1 GeV, excluding loads of other experimental areas, as detailed in Table 18.8.

Table 18.7: EuPRAXIA@SPARC_LAB Main loads estimation

Electrical loads	**kVA**
RF Modulators	720
Magnet PSU	580
Laser	150
Experimental users	300
Vacuum, electronics and controls	100
Cooling magnet + RF	200
Backup chiller for cooling	80
HVAC	550
Lighting	20
General purpose power	50
Tot power demand	**2750**

Table 18.8: Expected power consumption for the AQUA beamline operation at 100 Hz, 1 GeV

Electrical loads	**kW**
RF Modulators	575
Magnet PSU	300
Laser	15
Experimental users	10
Vacuum, electronics and controls	30
Cooling magnet + RF(avg)	45
HVAC	120
Expected power consumption	**1095**

18.2.3 Electrical network and Redundancy criteria

The EuPRAXIA@SPARC_LAB substation will be supplied by the 20 kV LNF grid, through two feeders, the main one from the 150/20 kV substation, the backup one from the closest cabin. A MV/LV substation equipped with three 1.6 MVA transformers, located in a technical building central with respect to the electrical load. Power is distributed at level 400/230 V as TN-S distribution system. LSOH Cables (fire retardant, Low Smoke – Zero Halogen) will be adopted for internal wiring. Power cables will be drawn in metal ducting systems distinct and far from control and signal ducting system in order to minimize the electromagnetic coupling with electronic cables and devices. Protection against indirect contact has to be achieved by over-current protective devices. Residual current devices will be adopted only on the load. As a general consideration, important loads, over 125 A, will be feed by dedicated switch units of the low voltage main switchboard. Lower size devices will be supplied using 400 A busbars trunking systems that will serve all the power supply rooms. Busbar Tap-off units will be equipped with circuit breaker. Conventional reactive power compensating system will not be implemented, considering that most of the users are inverter driven or power electronic devices with high power factor. UPS supercaps adopted to mitigate the impact of the modulators power converters will also contribute to the power factor correction. Fault resilience criteria have been considered for main components as the transformer bay and

MV feeders. The unavailability of one component of a transformer bay, like MV or LV breaker, protection devices, auxiliary services, busbars, as well as the transformer doesn't compromise the operation. Transformers will be sized in order to be fully loaded in case of unavailability of one per substation. Otherwise, they will be loaded at 50% capacity. This configuration allows for most of maintenance activities avoiding power cut. Due to the high availability of the power source a backup power source can be considered useless. Only critical users, like vacuum and control devices, underground emergency lighting, some ventilation, auxiliary services and some UPS loads must be ensured during planned outages. The existing main back-up 560 kW power generator, hosted in the main substation, is available to supply up to 100 kW and is used as emergency power source.

18.2.4 Critical issues and proposed solutions

The state of art of RF source is based on Scandinova modulators series K300 and K400. Limitations due to the not complete compliance with EMC standards EN 61000-3-12 is well known. In particular, at 100 Hz a high harmonic content and phase load unbalance require special care. Due to the grid reference phase synchronization lock of all the 12 modulators required by the RF system, the compensation of the phase unbalance with a phase shift is completely ineffective. Figures 18.13 and 18.14 show typical current waveform and FFT.

Figure 18.13: Current Waveform for 100 Hz operated Modulator.

In some installation an active filter has been adopted successfully to solve the problem. At the moment another solution based on a complete decoupling from the network adopting a supercapacitor-based UPS is under test at TEX facility at LNF. This solution could represent a cost-effective alternative with the plus represented by the improvement of resilience to network disturbances. With these devices, equipped with a limited capacitor bank, few seconds of interruption can be withstand and the more usual voltage dips would be neglected.

18.2.5 Electrical installation in the accelerator tunnel

Special care will be given to minimize radiation damage for electrical devices. Radiation tolerant materials and low maintenance systems will be selected for every component that has to be installed in the beam area. Electronic devices not absolutely necessary will be banned by the accelerator area, like electronic ballasts and control devices. With respect to lighting devices, polycarbonate and electronics suffer by radiations. Metal and glass luminaries with fluorescent bulbs with non electronic ballast will be adopted, and a central emergency lighting system will be preferred with

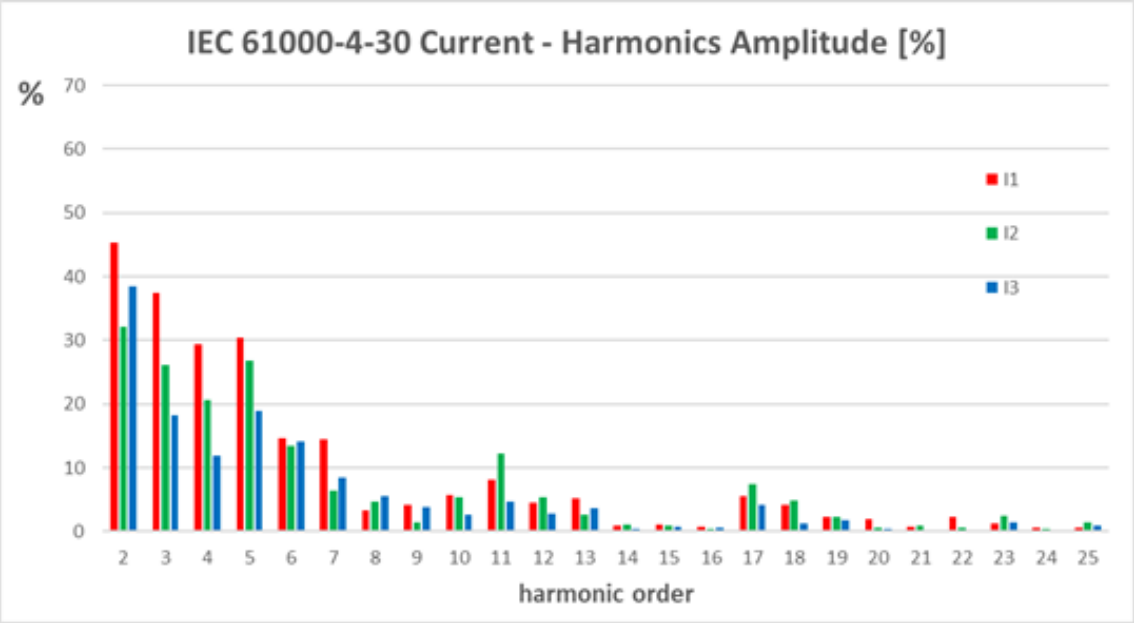

Figure 18.14: Current Waveform FFT.

respect to self-powered devices. Fire resistant cable FGT10OM1 will be adopted for the safety lighting power distribution. Reduced maintenance devices and solutions will be adopted in the radiation safety restricted access area. Electrical switchboards will be placed out of the beam area of influence.

18.2.6 Grounding, bonding and low voltage distribution system

Following best practices [2, 3] a dedicated buried earth electrode, integrated with the metal reinforcement of concrete and structural metalwork of all the building site will be integrated in the LNF grounding system. A meshed Common Bonding Network (CBN) will be distributed with 250 mm^2 copper bar in all the beam and power supplies area and will be used to bond all the devices in the beam line and the auxiliaries besides the proper protection earth. The low voltage distribution system will be delivered as TN-S, whit separate neutral and protective earth (PE) wires. The PE will be distributed and bonded on the CBN wherever is possible, in order to minimize conducted and radiated interference. CBN will be the only reference potential inside the site.

18.2.7 Electromagnetic compliance

With respect to technical rules CEI-EN 50160, 61000-2-2, and 61000-2-12, electrical installations have to comply with CEI-EN 61000-2-4 level 2. Nevertheless, higher harmonic current distortion level has to be expected for power converter that will be powered by a “dirty” transformer bay.

18.2.8 Technological plants automation and control

All plants will be controlled through industrial based devices, PLC and SCADA. The HW platform adopted for the more recent applications for DAFNE and SPARC accelerators will be used both for building and accelerator facilities in order to take advantage of internal personnel knowledge for reliable operation and maintenance. At the moment a new generation of SCADA is under evaluation with a test application on the EuAPS@SPARC_LAB project.

The aim of the control system is to deliver a unique interface, both for technical specialists and machine operators, for all the auxiliary plants. The system will allow a reliable operation, ensuring

a tool for tuning of devices and commissioning of the accelerator. The first step of the SCADA implementation will be set with the building construction contract, for the electrical and HVAC control. Afterwards the high technology system and accelerator auxiliaries automation, as magnet safety system, will be added in the same framework.

The database will be shared with the accelerator control system in order to allow easy correlations with the machine. Special care will be given at the power management.

18.3 Fluid plants

The main characteristics of the Cooling and Ventilation systems of the accelerator machine, its auxiliary equipment and its experimental areas are here described.

The design guidelines were:

- high system performance;
- reliability (2n components to avoid single points of failure);
- energy efficiency;
- rooms free from cooling and ventilation equipment in the accelerator installation areas;
- operation easiness;
- spare parts availability policy to reduce MTTR (Mean Time To Repair).

18.3.1 Process Cooling System

The cooling system for EuPRAXIA@SPARC_LAB is essential to ensure stable operational conditions for the magnets, RF systems and power supplies. The cooling system will be composed by a primary circuit and secondary circuits (demineralized water). The layout below (Figure 18.15) presents the conceptual design of the system.

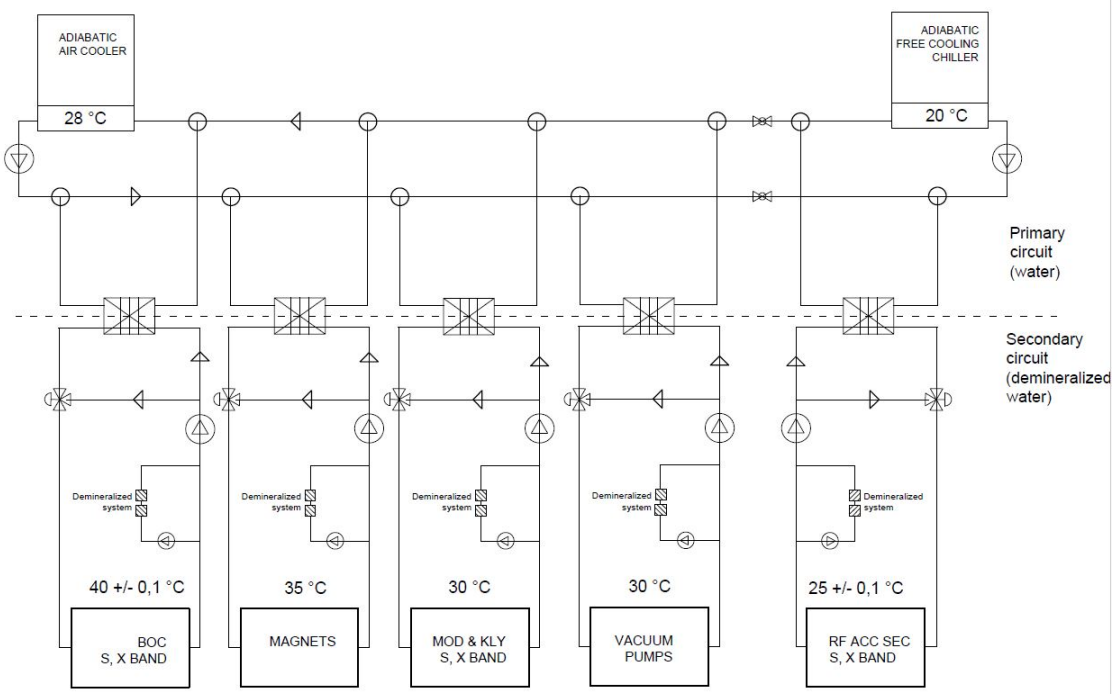

Figure 18.15: Cooling System Schematic.

18.3.1.1 Primary Water Cooling System

The primary water cooling system is divided into two distinct circuits in order to optimize different operational temperatures requested by the secondary circuits. The maximum total thermal power to be dissipated for the baseline accelerator configuration is 700 kW. Users requiring a temperature set above 28 °C are served by adiabatic dry coolers, while loads requiring lower temperature set, for example the RF accelerating structures, which require thermal stability at 25 °C, are served by an adiabatic free cooling chiller that can operate in free cooling mode as long as the outdoor temperature allows it, and the compressor is optimized for water production at temperatures above 20 °C (Table 18.9).

Table 18.9: Power demand for the primary cooling circuits.

Cooling machine	Cooling Power Demand[kW]
Adiabatic Dry Cooler	680
Free Cooling Chiller	20

18.3.1.2 Secondary Water Cooling System

The secondary cooling system manages the different cooling lines dedicated to specific subsystems as shown in Table 18.10.

Table 18.10: Secondary Cooling System Users

LINE	USER	Thermal Load [kW]	Operating Temperature [°C]
1	Magnets	240	35 ± 2
2	RF Modulators	414	30 ± 1
3	RF Accelerating S Band, X Band	20	25 ± 0.1
4	RF Boc X Band	10	43.5 ± 0.1
5	Vacuum Pumps	17	30 ± 1

Each subsystem is equipped with temperature control system based on a combination of heat exchanger and three-way valves in order to ensure stable operation conditions. Furthermore, for all the components requiring high accuracy temperature control, such as the accelerating sections and the BOC, an electric heater system is integrated in order to maintain extremely stable temperature.

Electrical Power Demand of Cooling Systems

The electrical power demand of the process cooling system can be estimated starting from the thermal power to be dissipated in the accelerator base line configuration. The electrical power demand is driven primarily by the thermal load, which determines the type and size of the cooling units required. Equipment selection, sizing, and operation are strongly affected by the installation site's climate conditions. Ambient dry-bulb and wet-bulb temperatures determine the number of available free-cooling hours and significantly affect the performance and efficiency of chillers and coolers.

In addition to the electrical power demand of the cooling units, the electrical power required for pumping must be included. The primary and secondary hydraulic circuits are detailed in Table 18.11.

Table 18.11: Primary and secondary circuits pumps design data

CIRCUIT	Thermal Load [kW]	ΔT [°C]	Flow Rate [l/min]	Pressure Head [bar]	Pump Electrical Power [kW]
Primary circuit Dry Cooler Pump	680	5	1943	4	16.61
Primary circuit Chiller Pump	20	5	57	2	0.24
Secondary circuit RF BOC Pump	10	1	143	2	0.61
Secondary circuit Magnet Pump	240	15	229	4	1.96
Secondary circuit RF Modulator Pump	414	5	1183	7	17.7
Secondary circuit Vacuum Pump	17	5	49	3	0.31
Secondary circuit RF Structures Pump	20	1	286	2	1.22

In total, the estimated electrical power demand for the adiabatic dry cooler, chiller, pumps, and other auxiliaries of the process cooling system is approximately 90 kW (Table 18.12).

Table 18.12: Total Electrical Power demand.

Equipment	Electrical Power [kW]
Adiabatic Dry Cooler	40
Free Cooling Chiller	8
Pumps	38

The annual electrical consumption of the cooling plants for the accelerator baseline configuration has been simulated considering the variation of power demand as a function of outdoor air temperature and humidity. The simulation was carried out using the Test Reference Year, with hourly weather data, developed by the LNF Technical Division specifically for energy analysis applications.

The annual energy consumption of the cooling system, including adiabatic dry coolers (≈ 34 MWh), adiabatic free cooling chiller (≈ 15 MWh), and all primary and secondary pumps (≈ 333 MWh), sums to 382 MWh/year, corresponding to an average electrical power demand of 45 kW since the accelerator is expected to run continuously.

The detailed energy consumption of the primary circuit cooling machines with water at 28 °C is reported below (Table 18.13, Figure 18.16).

The detailed energy consumption of the primary circuit adiabatic free cooling chillers with water at 20 °C is reported below (Table 18.14, Figure 18.17).

18.3.1.3 Demineralized Water Production System

The demineralization system is designed to ensure optimal water quality with specific configurations for each circuit. The demineralization process will combine reverse osmosis and cation-anion exchange resins to ensure continuous water treatment. Each system will be individually managed to maintain the required water quality, with automated monitoring of conductivity and operational parameters.

For circuits serving Magnets, coils and solenoids, the system will maintain water conductivity in a low range (0.5 to 1.5 µS/cm) to meet strict cooling requirements. Other circuits, as Power

Table 18.13: Total Electrical Power demand, Water @28 °C

Month	Dry Cooling Mode [h]	Adiabatic Cooling Mode [h]	Total Energy Consumption [MWh]
JANUARY	744	0	0.24
FEBRUARY	672	0	0.33
MARCH	744	0	0.51
APRIL	720	0	1.23
MAY	730	14	3.46
JUNE	470	250	5.20
JULY	350	386	7.15
AUGUST	386	354	7.55
SEPTEMBER	571	149	4.69
OCTOBER	744	0	2.24
NOVEMBER	720	0	0.56
DECEMBER	744	0	0.29
SUB-TOT	7595	1153	33.44
TOT			**≈34 MWh**

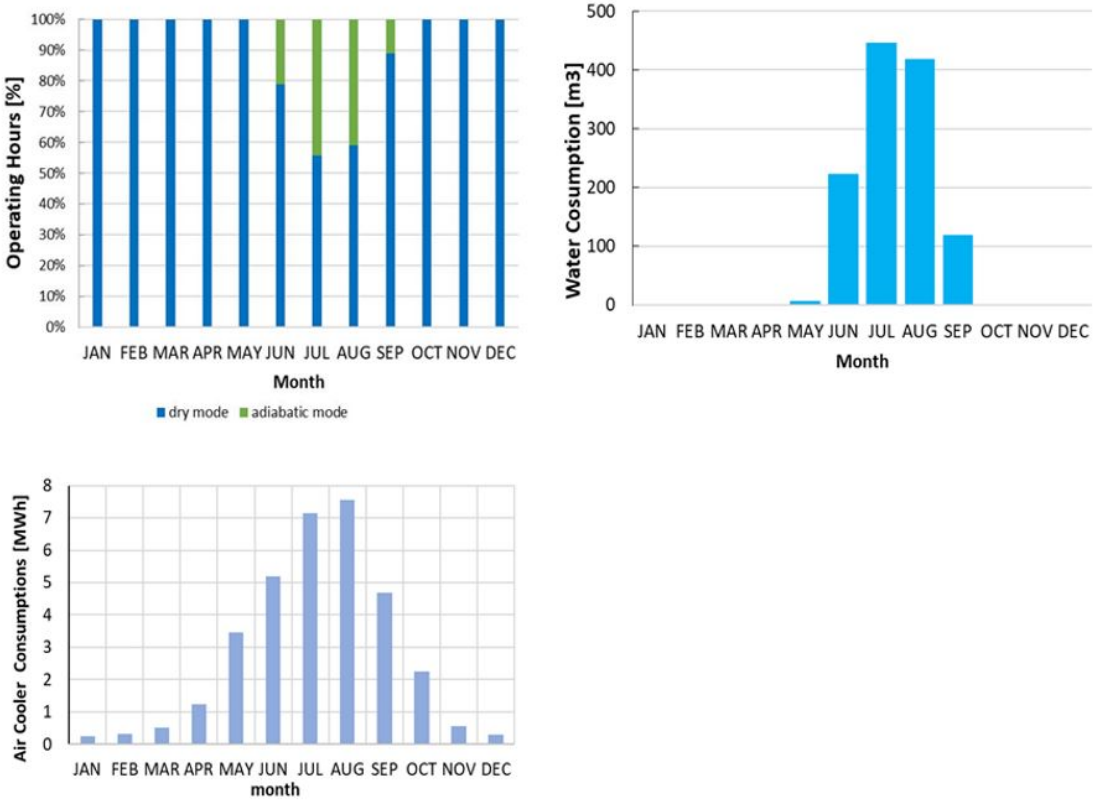

Figure 18.16: Top-left: Monthly operating hours – dry mode and adiabatic mode; Top-right: Monthly water consumption of the dry cooler in adiabatic mode; Bottom-left: Monthly electrical consumption of the air cooling system.

Table 18.14: Total Electrical Power demand, Water @20 °C

Month	Dry Cooling Mode [h]	Adiabatic Cooling Mode [h]	Covered by Chiller [h]	Total Energy Consumption [MWh]
JANUARY	744	0	0	0.01
FEBRUARY	672	0	0	0.01
MARCH	701	43	0	0.02
APRIL	465	251	4	0.04
MAY	356	237	151	0.81
JUNE	128	78	514	2.83
JULY	27	85	632	3.68
AUGUST	7	66	671	3.84
SEPTEMBER	175	40	505	2.65
OCTOBER	456	118	170	0.87
NOVEMBER	666	41	13	0.08
DECEMBER	744	0	0	0.01
SUB-TOT	5141	959	2660	14.81
TOT	8760			**≈15 MWh**

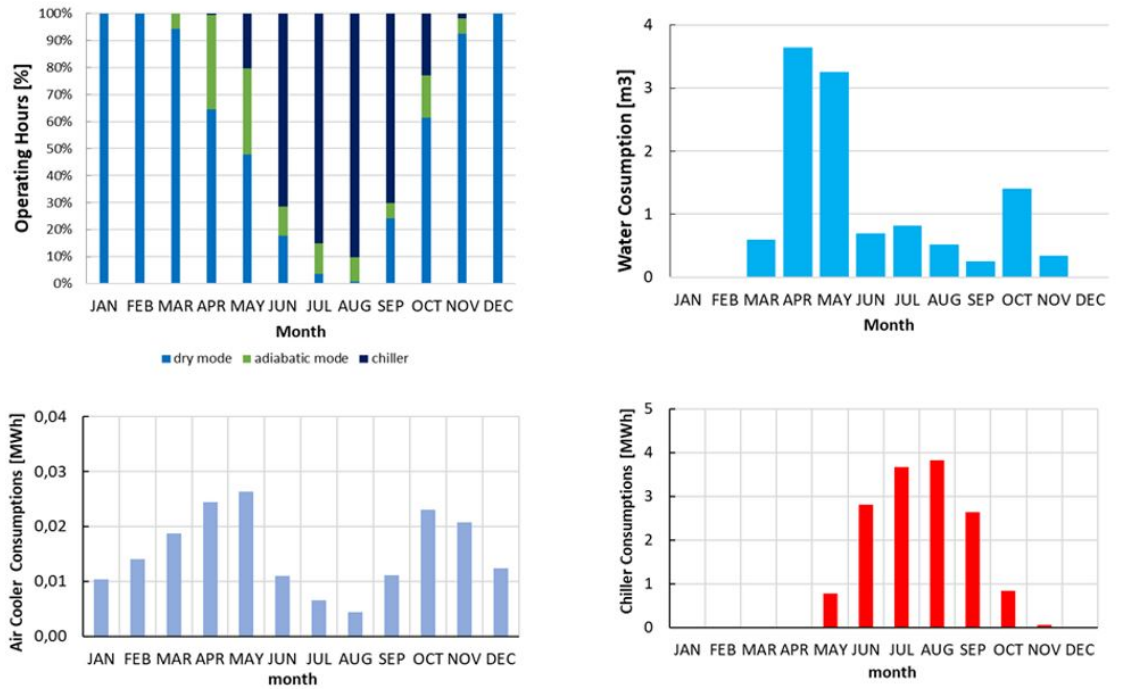

Figure 18.17: Top-left: Monthly operating hours of the chiller in free cooling dry mode, adiabatic mode, and chiller-only mode; Top-right: Monthly water consumption of the chiller in adiabatic mode; Bottom-left: Monthly electrical consumption of the chiller in free cooling mode; Bottom-right: Monthly electrical consumption in only chiller mode.

Supplies, RF system and other, while still using demineralized water, will require a less intense treatment.

18.3.1.4 Leak Control and Water Collection System

To prevent and manage potential water leaks, a dedicated leak control system will be implemented. This system will include sensors in key areas and a collection network to gather any water leakage and convey them into a tank (Figure 18.5).

18.3.2 Ventilation and HVAC Systems

This section concerns the ventilation system that provide the required room conditions for processes and occupants comfort.

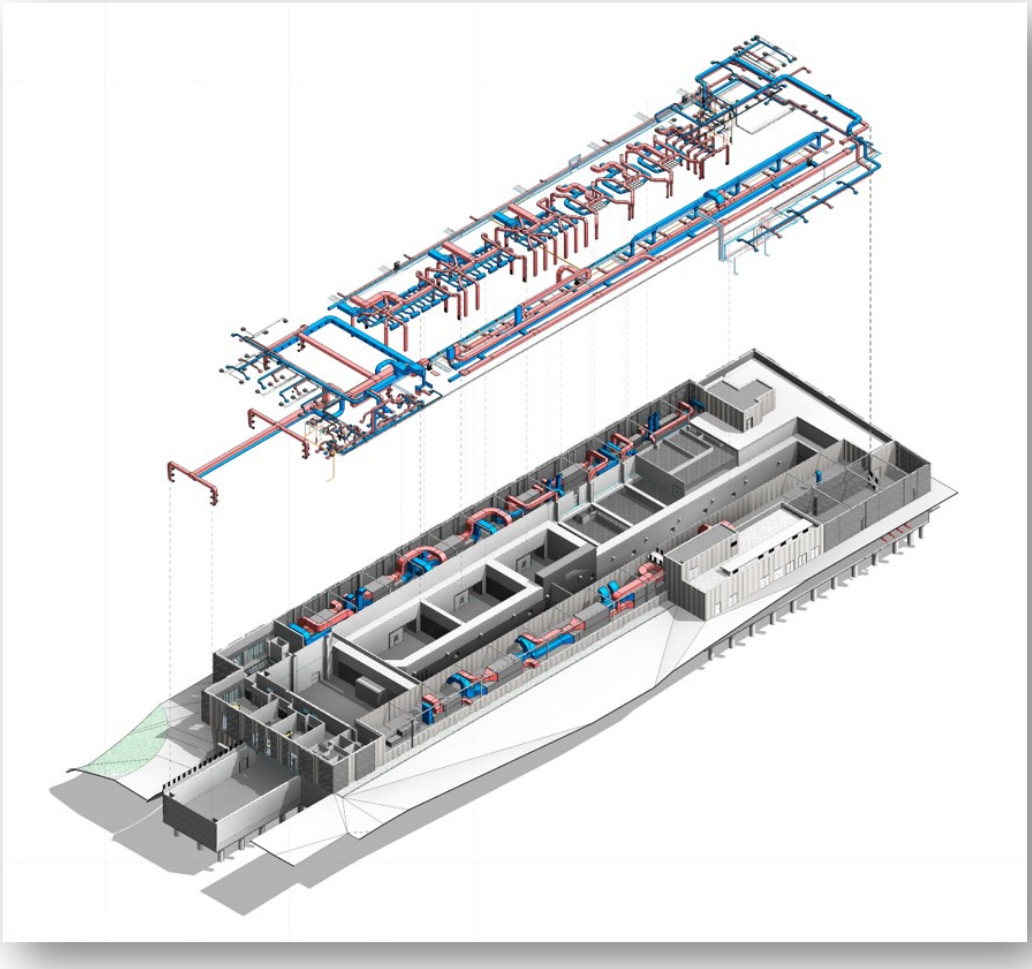

Figure 18.18: HVAC ducts and distribution.

Selection of the air conditioning systems depends on three main factors including the building configuration, the climate conditions (temperature, humidity, pressure) and the equipment constraints. Design criteria are building thermal capacity, spatial requirements, operating and maintenance costs, life cycle assessment, reliability and flexibility.

The following extreme outdoor atmospheric conditions are considered:

- winter: -2 °C (dry bulb temperature), 80% RH

- summer: 35 °C (dry bulb temperature), 55% RH

The air conditioning system is supplied by two multipurpose units, operating with a temperature range of 40-35 °C and 7-12 °C, and two heat recovery chillers, operating with a temperature range of 40-35 °C and 15-20 °C. The heat transfer fluids produced supply the heat exchange coils of the AHUs (Air Handling Units), the fancoils and the radiators located in the toilets.

The experimental rooms have dedicated air conditioning systems (all-air systems), whereas the remaining rooms are equipped with air-water systems with fancoils as terminal units, except for the toilets served by radiators. Each AHU is provided with adiabatic humidifier with atomized water and cross-flow plate heat exchanger, except for the AHUs serving the cleanrooms, that are equipped with steam humidifiers and run-around heat exchangers to avoid cross contamination.

Design values for the ventilation system are shown in Table 18.15.

Table 18.15: Design values for the ventilation system

ROOM	TEMPERATURE [°C]	RH [%]	THERMAL LOAD [kW]
LINAC	23 ± 0.5	40-60	52
500 TW-1	23 ± 0.5	45-55	10
500 TW-2	23 ± 0.5	45-55	10
LASER SYNC	23 ± 0.5	45-55	10
LASER THz	23 ± 0.5	45-55	10
UNDULATORS	23 ± 0.5	40-60	31
EXPERIMENTAL HALL1	23 ± 1	40-60	26
EXPERIMENTAL HALL2	23 ± 1	40-60	26
FEL USERS	23 ± 2	40-60	62
RADIATION USERS	23 ± 1	40-60	26
MODULATORS	23 ± 2	40-60	100

The following list describes the main features of the AHUs for the experimental rooms:

- **AHU LINAC** provides the air handling for the linear particle accelerator (LINAC) room. The AHU is able to work in all air recirculation, in all external air or in partially recirculation, thus being able to meet the needs of the three operating modes: run, pre-shutdown, shut-down. In the run phase the AHU works in all air recirculation with slight expulsion of air in order to ensure the necessary underpressure in the room, while in the pre-shutdown the AHU works with all outside air ensuring a complete washing of the entire volume of the room in less than 10 minutes. The use of air motorized dampers allows the management of the shutdown phase, guaranteeing a share of external air (for sanitary purposes) and recirculated air (to avoid an unjustified excessive energy consumption). The main tunnel is virtually divided into six sectors which are cooled by six coils connected to the chilled water network. This design allows the system to react to the thermal loads not uniform along the axis of the accelerator. The ventilation system for LINAC is shown in Figure 18.19.
- **AHU FEL-OND** provides supply air to the undulators room. The temperature is controlled by post coils and the relative humidity is controlled on the basis of the average value measured on the main branch of the air handling unit or by special ambient hygrometers (Figure 18.20).
- **AHU RAD-USERS** is dedicated to the radiation users room. The AHU can work both fully and partially in recirculation mode, with external air flow for hygienic and sanitary purposes.

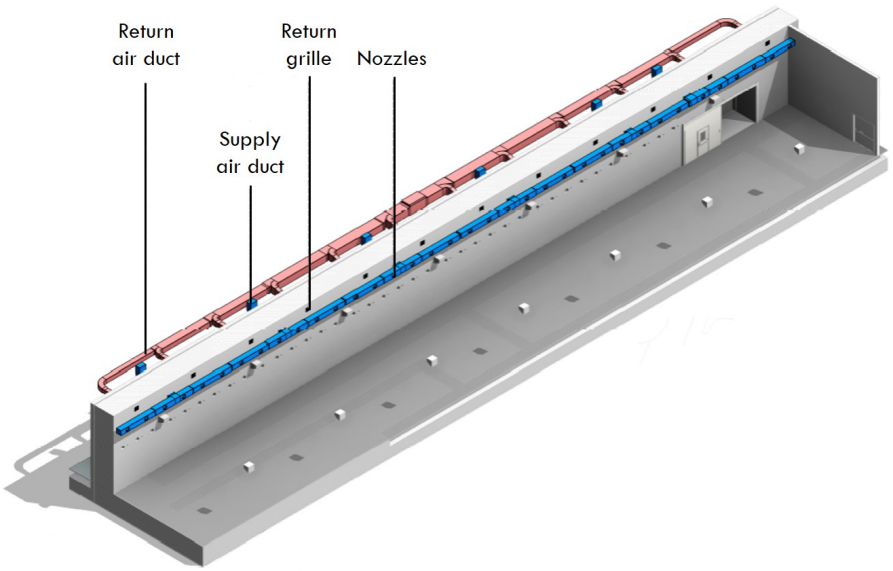

Figure 18.19: LINAC ventilation system.

It operates at constant air flow with post treatment coil to achieve independent temperature control. Given the reduced volume of the room, the ventilation supply works on the cold lake principle: high air flow at low speed. The supply grilles are distributed on the ceiling, whereas the exhaust grilles on the lower part of the wall.

- **AHU EXP-HALL 1** is dedicated to the experimental hall 1. The AHU can work both fully and partially in recirculation mode with external air flow for hygienic and sanitary purposes. It operates at constant air flow with post treatment coil to achieve independent temperature control. Given the reduced volume of the room, the ventilation supply works on the cold lake principle: high air flow at low speed. The supply grilles are distributed on the ceiling, whereas the exhaust grilles on the lower part of the wall.
- **AHU EXP-HALL 2** is dedicated to the experimental hall 2. The AHU can work both fully and partially in recirculation mode with external air flow for hygienic and sanitary purposes. It operates at constant air flow with post treatment coil to achieve independent temperature control. Given the reduced volume of the room, the ventilation supply works on the cold lake principle: high air flow at low speed. The supply grilles are distributed on the ceiling, whereas the exhaust grilles on the lower part of the wall. The ventilation system for EXPERIMENTAL HALL is shown in Figure 18.21.
- **AHU FEL-USER** is dedicated to the FEL users room. It operates at constant air flow with post treatment coil to achieve independent temperature control. The supply air is introduced into the room through long range nozzle jet diffusers for the double height area and through micro perforated ducts for the remaining area, the return air grilles are installed at medium height of the wall to avoid interference with the nozzle range (aeraulic shortcut).
- **AHU 500 TW-1** is dedicated the 500 TW-1 room, which is an ISO7 cleanroom. Filtration is done with HEPA filters. The cleanroom design uses a negative pressure plenum with HEPA fan filter units in the ceiling and incorporated low wall air returns to achieve laminar air flow. The HEPA filtered air sweeps dirt down to the floor and horizontally to the low wall air returns. The AHU is equipped with a run-around heat exchanger system, which consists of at least one heat exchanger in the supply and extract air flow which are connected to one another by an hydraulic circuit. This system is a regenerative heat recovery system in which the airflows are completely separated from one another. As a result, no leakages occur

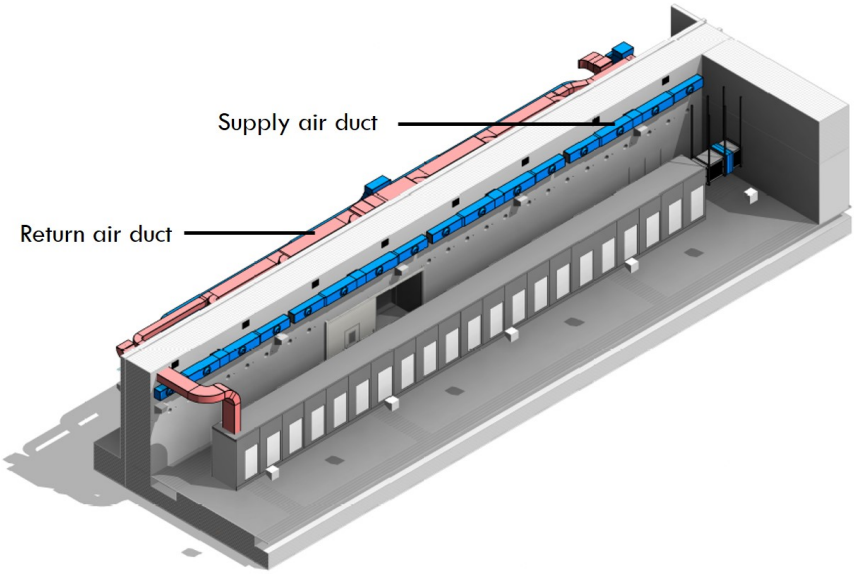

Figure 18.20: Undulators Hall ventilation system.

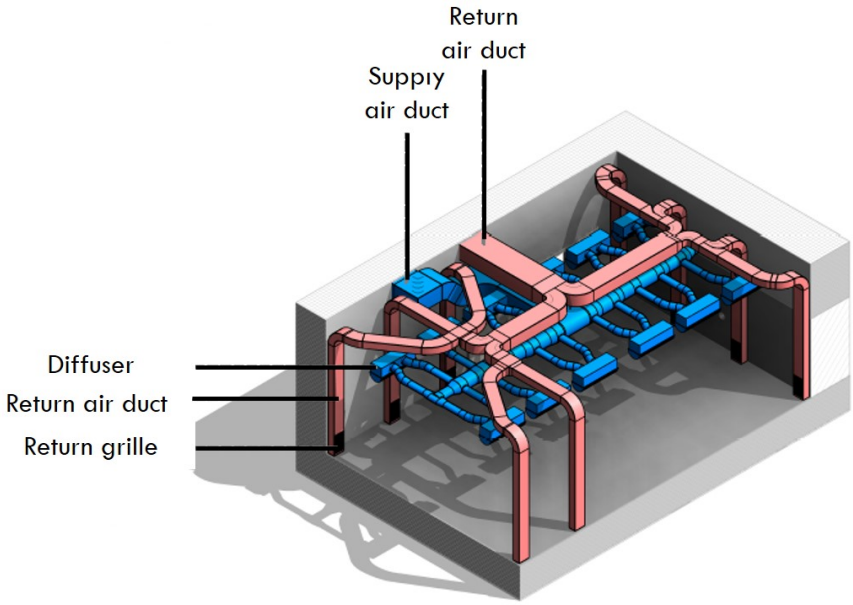

Figure 18.21: Experimental Hall ventilation system.

between the supply and extract air. The AHU is installed on the technical deck located on the North side of the building so that it is close to the room served.

- **AHU 500 TW-2** is dedicated the 500 TW-2 room, which is an ISO7 cleanroom. Filtration is done with HEPA filters. The cleanroom design uses a negative pressure plenum with HEPA fan filter units in the ceiling and incorporated low wall air returns to achieve laminar air flow. The HEPA filtered air sweeps dirt down to the floor and horizontally to the low wall air returns. The AHU is equipped with a run-around heat exchanger system, which consists of at least one heat exchanger in the supply and extract air flow which are connected to one another by an hydraulic circuit. This system is a regenerative heat recovery system in which the airflows are completely separated from one another. As a result, no leakages occur between the supply and extract air. The AHU is installed on the technical deck located on the North side of the building so that it is close to the room served.
- **AHU LASER SYNC** is dedicated the laser synchronization room, which is an ISO7 cleanroom. Filtration is done with HEPA filters. The cleanroom design uses a negative pressure plenum with HEPA fan filter units in the ceiling and incorporated low wall air returns to achieve laminar air flow. The HEPA filtered air sweeps dirt down to the floor and horizontally to the low wall air returns. The AHU is equipped with a run-around heat exchanger system, which consists of at least one heat exchanger in the supply and extract air flow which are connected to one another by an hydraulic circuit. This system is a regenerative heat recovery system in which the airflows are completely separated from one another. As a result, no leakages occur between the supply and extract air. The AHU is installed on the technical deck located on the North side of the building so that it is close to the room served. A P&ID and a 3D view of the ventilation system for ISO7 cleanroom is shown in Figures 18.22 and 18.23.

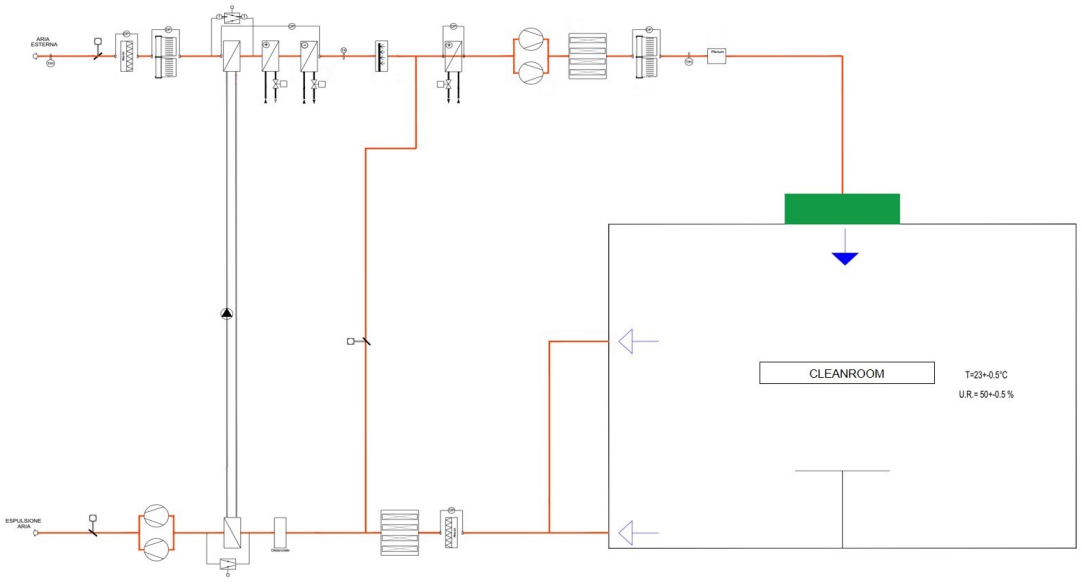

Figure 18.22: CleanRoom HVAC schematic.

- **AHU THz** is dedicated to the THz room. The AHU can work both fully and partially in recirculation mode, with external air flow for hygienic and sanitary purposes. It operates at constant air flow with post treatment coil to achieve independent temperature control.
- **AHU Modulators** dedicated to the modulators room. The AHU operates at constant air flow with post treatment coil to achieve independent temperature control. The supply air is introduced into the room through long range nozzle jet diffusers reaching the portion of the room characterized by high endogenous thermal loads and avoiding interference between

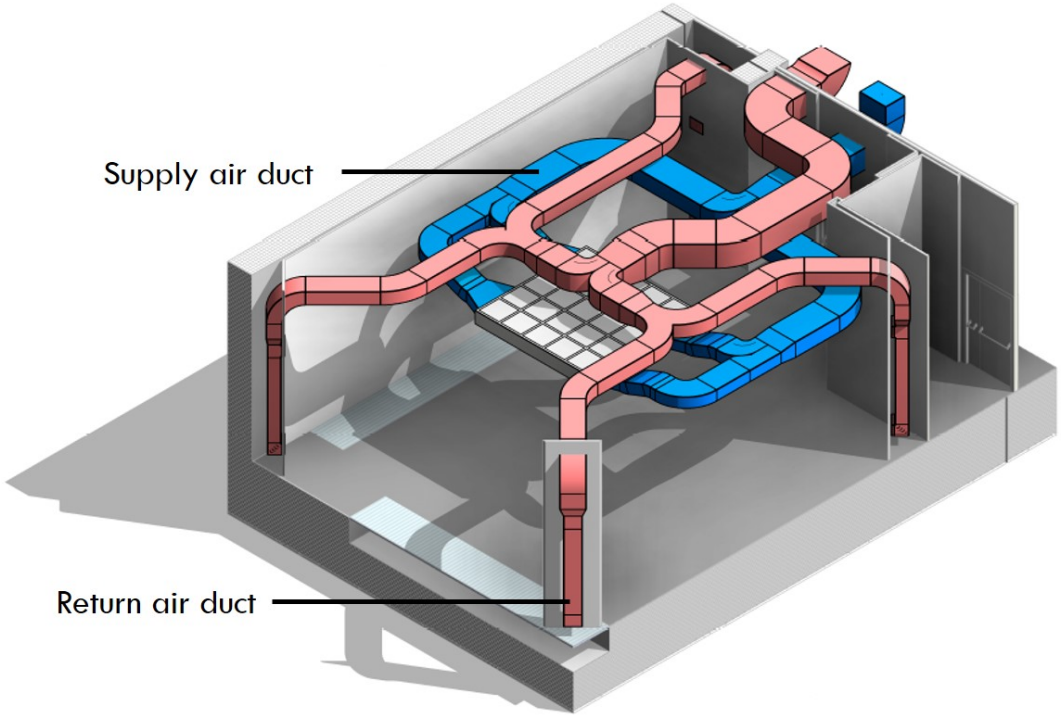

Figure 18.23: CleanRoom ventilation system.

supply and return air although the grilles are installed both on the ceiling.
The main AHUs values are presented in Table 18.16.

The portions of the building dedicated to AHUs are the North and South facing balconies, that constitute the technical area (blue highlighted areas in Figure 18.24). Access from the outside facilitates operations and maintenance, so that not only the equipment life is extended but also operating, downtime and troubleshooting costs can be reduced. It helps mitigate the majority of these expenses because the issues are caught ahead of time.

A thermal analysis of the LINAC room has been performed to explore the thermal management of the system, including a CFD simulation to estimate the effectiveness of typical thermal approximations made during the design process and to verify the real functionality and reliability of the ventilation system. The model presents some simplifications including:

- LINAC is considered to have a parallelepiped shape with height, width and maximum length relative to the accelerator machine to be installed;
- the heat dissipation is considered uniformly distributed equal to 50 kW.

The simulation results (Figures 18.25 and 18.26) show how the design choices respect the constraints imposed in the area around the machine:

- temperature equal to 23 °C $\pm$ 0.5 °C;
- air velocity less than 0.1 m/s.

The whole undulator system is hermetically encased in an enclosure. It has walls which can be easily opened and removed if needed. The enclosure completely separates its internal air flow from the rest of the tunnel. An air conditioning system located on the downstream end of the enclosure provides an air flow of 3500 m^3/h. It stabilizes the undulator system locally better than $\pm$ 0.1 °C. Along the undulator system, a slight but very stable temperature gradient of about 2 °C is permitted going from the downstream to upstream end. The air flow inside the enclosure moves in direction

Table 18.16: AHUs main values

AHU	AIR SUPPLY [m^3/h]	AIR EXTRACTION [m^3/h]	PRE-HEATING COIL [kW]	COOLING COIL [kW]	POST-HEATING COIL [kW]	POST-COOLING COIL [kW]
LINAC (RUN)	16 575	17 425	-	-	-	52.8
LINAC (PRE-SHUTDOWN)	16 575	17 425	125	226	65	-
FEL-UNDULATORS	14 825	15 500	10.7	22.5	17	51
RADIATION USERS	12 425	13 500	10.7	22	15	26
EXPERIMENTAL HALL1	12 425	13 675	10.7	22	15	26
EXPERIMENTAL HALL2	12 425	13 500	10.7	22	15	26
FEL USERS	29 875	28 000	25.9	61	35	62.5
500 TW-1	10 500	9 450	11	75	25	-
500 TW-2	10 500	9 450	11	80	26	-
LASER SYNC	10 500	9 450	11	75	24.5	-
THz	5 025	4 525	5.2	9.5	6	10.5
MODULATORS 1	14 500	16 550	10	10	15	49.5
MODULATORS 2	13 750	12 400	15	25	15	43

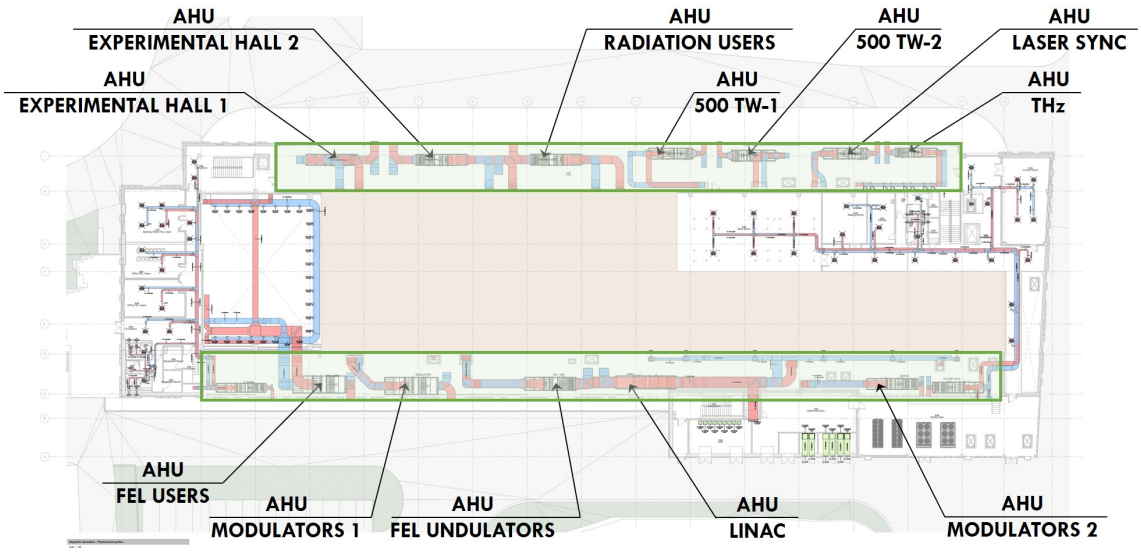

Figure 18.24: Technical balconies for AHUs.

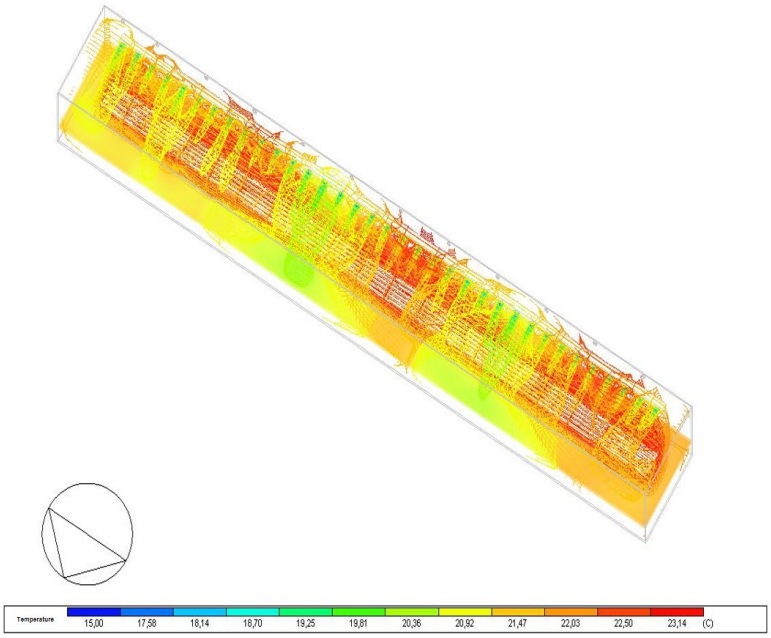

Figure 18.25: LINAC room Temperature simulation map.

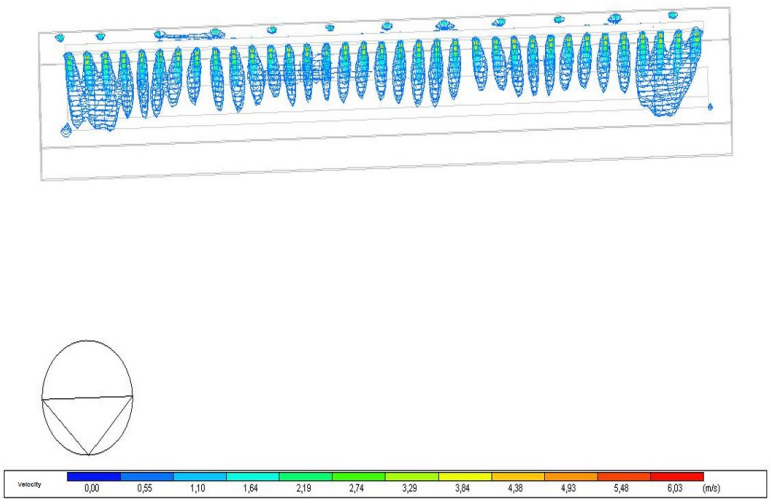

Figure 18.26: LINAC room Velocity vectors simulation map.

opposite to the beam inside the "beam pipe", creating a sort of counter-current exchanger. Indoor conditions in the undulators enclosure are 24 °C ± 0.1 °C and 40% - 60% RH. The ventilation system for undulators enclosure is shown in Figure 18.27.

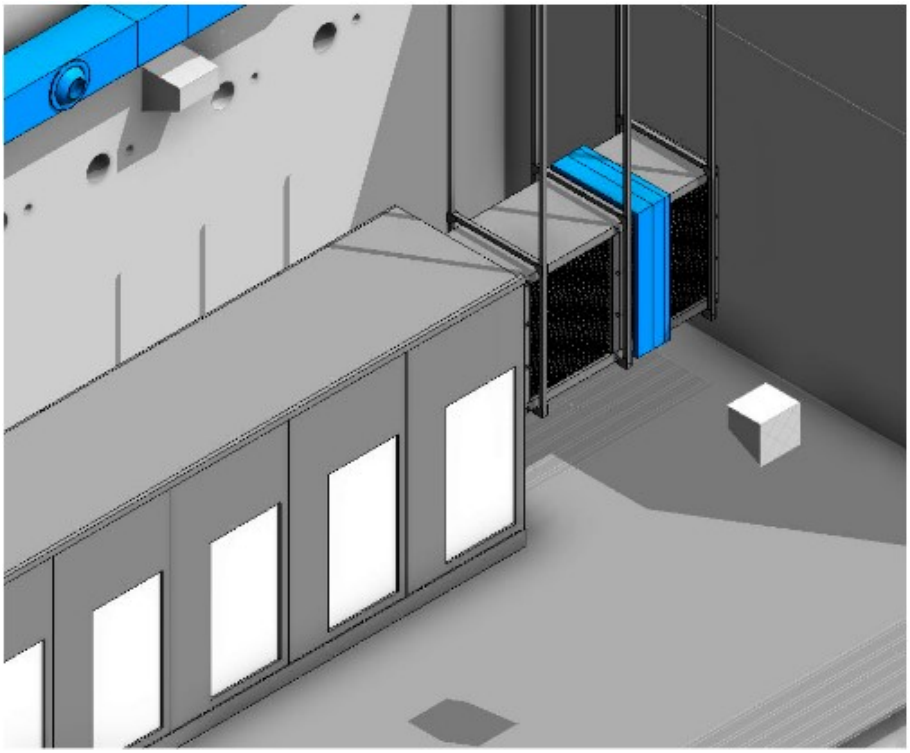

Figure 18.27: Undulators enclosure ventilation system.

18.3.3 Compressed Air System

The compressed air system is designed to supply the necessary air for actuating valves and other pneumatic devices across the entire particle accelerator complex. The centralized system will supply compressed air through a branching network, reaching all experimental halls and ensuring reliable and efficient operation. The infrastructure will be configured to maintain stable pressure levels, ensuring high performance for the pneumatic components in each part of the facility. Automated monitoring will be implemented to control air quality and pressure, optimizing system reliability and reducing downtime across the experimental zones.

18.4 Conclusions

The design of the civil infrastructures for EuPRAXIA@SPARC_LAB fully meets the functional and technical goals, defined in the Technical Annex to the tender for the awarding of the engineering design, set for the facility . The new 5,600 m² building layout ensures adequate space allocation, radiation protection, vibration control, and operational flexibility for all accelerator systems and user areas. The electrical, cooling, and HVAC systems have been dimensioned to support nominal and upgrade operation up to 3.2 MVA total power, with provisions for redundancy, efficiency, and future expansion. All construction solutions comply with INFN standards for safety, sustainability, and long-term resilience, as required by Italian law according to the minimum environmental criteria (CAM), Decreto Ministeriale 23.06.2022.

Bibliography

[1] B. Bolzon et al. “Preliminary ground motion measurements at LNF site for the super B project”. In: *1st International Particle Accelerator Conference (IPAC 2010)*. 2010, pp. 1482–1484.

[2] T. Williams and K. Armstrong. *EMC for Systems and Installations*. Newnes, 1999.

[3] F. Szoncsó. “Supplying high-energy physics detector systems”. In: *Nuclear Instruments and Methods in Physics Research Section A: Accelerators, Spectrometers, Detectors and Associated Equipment* 300.1 (1991), pp. 115–126.

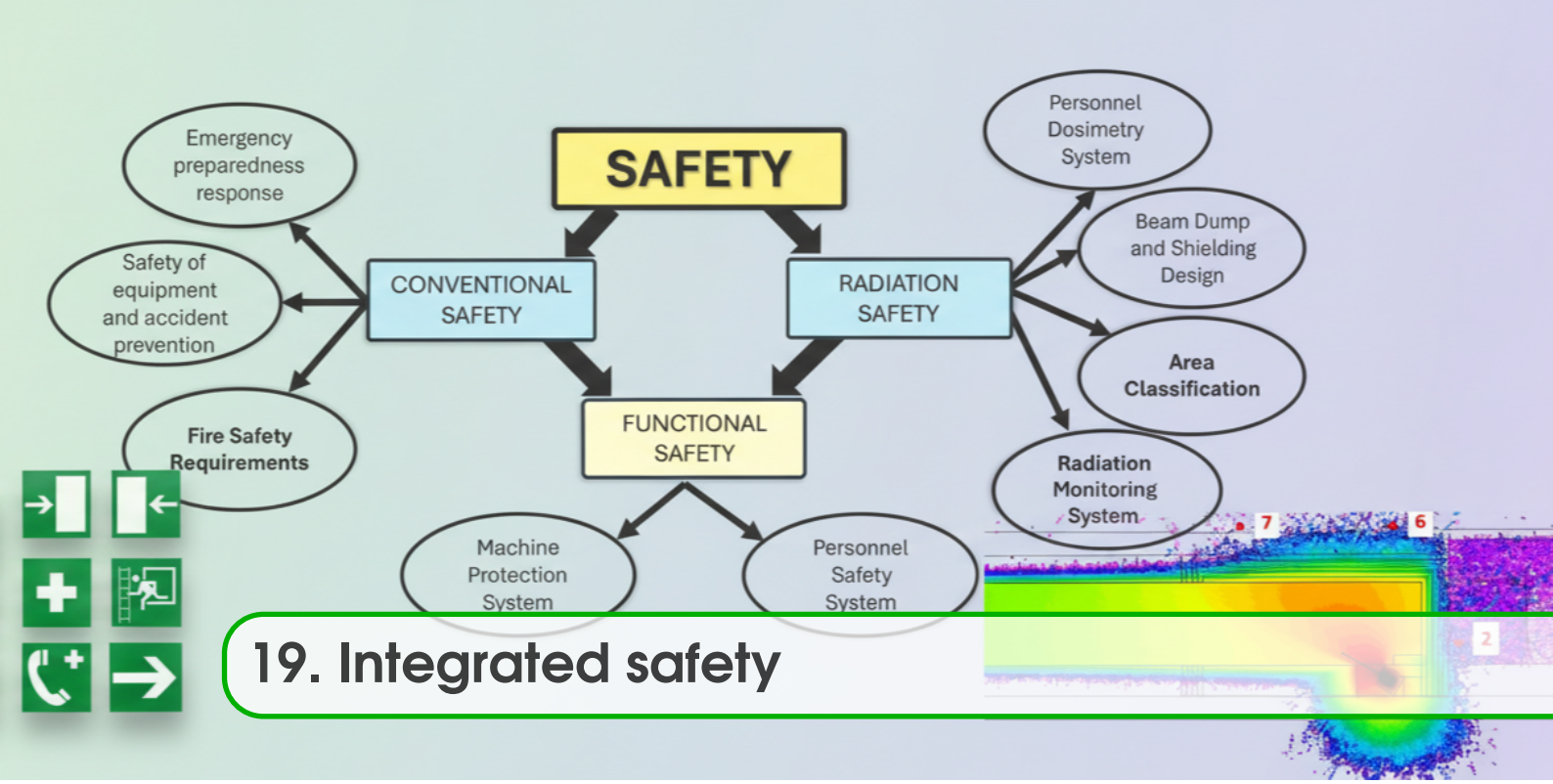

19. Integrated safety

19.1 Introduction

The goal of this chapter is to describe the adopted approach, specifications, and design choices of the facility's Integrated Safety System. This system encompasses both conventional and radiological safety aspects and implements operational Functional Safety through two distinct and dedicated subsystems: the Machine Protection System and the Personnel Safety System. The concept of safety in the implementation of a complex system such as the EuPRAXIA@SPARC_LAB linear accelerator is articulated into two distinct areas: conventional safety and radiological safety.
Conventional safety comprises all regulations, engineering controls, and organizational measures aimed at preventing risks related to infrastructure, equipment, working environments, occupational health and safety and emergency situations. In particular, the conventional safety domain encompasses fire safety, which is fully defined in the executive design and compliant with the applicable national and European standards. It also includes all provisions related to the safety of equipment and accident prevention, covering both the technical requirements for the safe operation of systems and installations and the organizational requirements for occupational health and safety during both the construction and operational phases, in full compliance with Legislative Decree 9 April 2008, No. 81. Access control systems and procedures are also implemented as part of accident prevention strategies, serving to restrict entry to hazardous areas and prevent unauthorized operations in safety-critical zones. In addition, conventional safety incorporates emergency preparedness and response, structured around formal emergency planning and dedicated training initiatives for staff and emergency response teams. These aspects are addressed through a combination of validated design solutions, approved by the competent Italian authorities, and proactive risk management procedures. The implementation of conventional safety at EuPRAXIA@SPARC_LAB ensures that all physical hazards are controlled through appropriate design, engineering systems, and operational protocols, thereby supporting the overall integrity of the integrated safety strategy adopted for the facility.
Radiation safety, on the other hand, refers to all subsystems and protection measures adopted to manage the ionizing radiation generated by the accelerator, with the aim of safeguarding personnel and users and ensuring that the infrastructure operates within the limits established by current regu-

lations. In the context of EuPRAXIA@SPARC_LAB, the Health Physics team is responsible for the design and implementation of radiation protection measures across all operational phases of the facility, including both beam-on and beam-off conditions. These activities involve the assessment of the dosimetric contributions associated with the various radiation components generated in the different operating scenarios—such as the primary electron beam, bremsstrahlung photons, and photoneutrons—and the design of the required radiation shielding and beam dumps. Based on these evaluations, the team defines the radiological zoning of the areas according to potential exposure levels and establishes the corresponding controlled-access procedures.
The team is also responsible for the selection, management, and analysis of data from monitoring and detection systems including dosimetric stations, installed in the most sensitive locations, and personal dosimeters. These systems are essential for the continuous verification of dose levels throughout the facility. Another key responsibility concerns the definition of the safety interlocks required for the correct operation of the Personnel Safety System (PSS), which is designed to prevent access to irradiated areas during accelerator operation.
All implemented measures ensure compliance with the dose limits established by current regulations, in particular Legislative Decree 31 July 2020, No. 101. The team is also in charge of training personnel on the principles of radiological safety, the risks associated with ionizing radiation, and the proper operating procedures to be followed. The technical and regulatory assessments related to both conventional and radiological safety define the design requirements for the Machine Protection System (MPS) and the PSS. The MPS is a functional safety system designed to protect the accelerator and safeguard its most critical components, preventing damage in case of hazardous conditions or interlocks triggered during operation. The PSS, by contrast, is the functional safety system dedicated to protecting people, intervening to ensure their safety in the event of accidental or abnormal situations that could threaten the health of operators or users. As safety systems, both must be designed and implemented in compliance with the international standard IEC 61508, which ensures their reliability and conformity with functional safety requirements. The interconnection between the safety domains and the associated safety systems is illustrated in Figure 19.1.

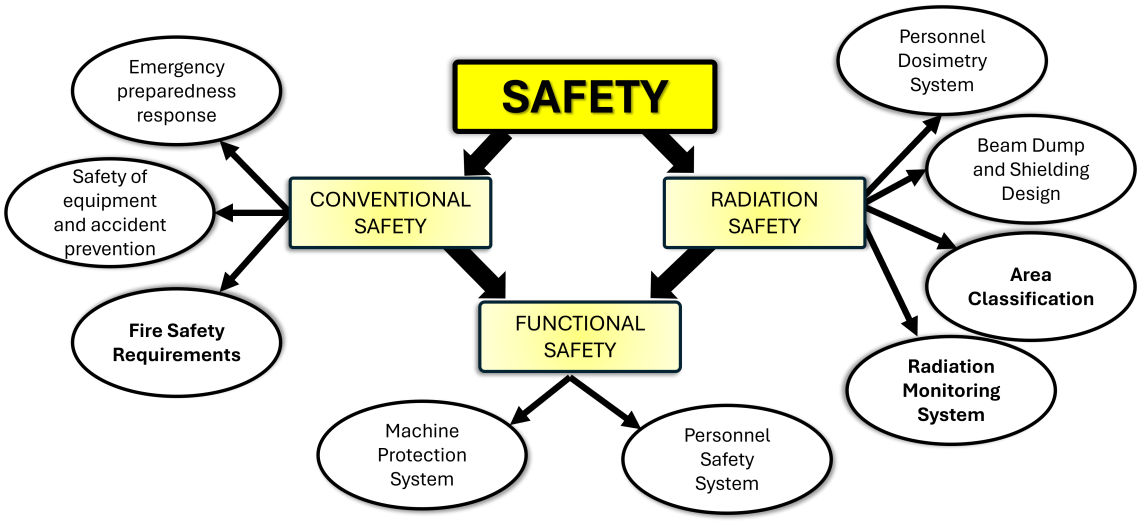

Figure 19.1: Interconnections between Conventional Safety, Radiation Safety and Functional Safety. The requirements and subsystems highlighted in black in the figure form the basis for the design and definition of some of the functions of the MPS and the PSS.

19.2 Reference Regulations

19.2.1 Building Works and structures

- Presidential Decree No. 246 of 21/04/1993 “Regulation implementing Directive 89/106/EEC on construction products” (Official Gazette No. 170 of 22/07/93)
- Presidential Decree No. 380 of 06/06/2001 “Consolidated text of legislative and regulatory provisions on construction” (Official Gazette No. 245 of 20/10/2001 - Ordinary Supplement No. 239)
- (Correction Official Gazette No. 47 of 25/02/2002) and subsequent amendments (Legislative Decree 301/2002, Law 166/2002, Ministerial Decree 37/2008)
- Ministerial Decree of 16 February 2007: Classification of fire resistance of construction products and elements.
- Ministerial Decree of 17 January 2018 “Update of the Technical Standards for Constructions (Official Gazette General Series No. 42 of 20-02-2018 - Ordinary Supplement No. 8)”
- CNR Instructions 10011/97 “Steel constructions: instructions for calculation, execution, testing, and maintenance”
- CNR UNI 11018 “Instructions for the calculation and use of support devices to be provided in constructions”
- UNI EN 1991-1-1:2004 “Eurocode 1: Actions on structures - Part 1-1: General actions - Densities, self-weight, imposed loads for buildings”
- UNI EN 1998-5:2005 “Eurocode 8: Design of structures for earthquake resistance - Part 5: Foundations, retaining structures and geotechnical aspects”
- UNI EN 1990:2006 “Eurocode: Basis of structural design”
- UNI 10722-1:2007 “Qualification and control of the project of new constructions – general criteria and terminology”
- UNI 10722-2:2007 “Qualification and control of the project of new constructions – definition of the intervention program”
- UNI 10722-3:2009 “Qualification and control of the project of new constructions – project planning and execution of project controls in a building intervention”
- UNI EN 1997-1:2013 “Eurocode 7: Geotechnical design - Part 1: General rules”
- UNI EN 1993-1-10:2014 “Eurocode 3: Design of steel structures - Part 1-10: Material toughness and through-thickness properties”
- UNI EN 1992-1-1:2015 “Eurocode 2: Design of concrete structures - Part 1-1: General rules and rules for buildings”
- UNI EN 206-1:2016 “Concrete – Part 1: specification, performance, production, and conformity”

19.2.2 Occupational Health & Safety

- Legislative Decree 9 April 2008, No. 81 “Consolidated text on health and safety in the workplace”
- Legislative Decree 3 August 2009, No. 106 “Integrative and corrective provisions of Legislative Decree 9 April 2008, No. 81, on health and safety in the workplace”
- EN ISO 12100:2010 “Safety of machinery – General principles for design – Risk assessment and risk reduction”
- UNI EN ISO 45001:2023 “Occupational health and safety management systems – Requirements with guidance for use”

19.2.3 Radiation Protection

- Legislative Decree 31 July 2020, No. 101 "Implementation of Directive 2013/59/Euratom, which lays down basic safety standards for protection against the dangers arising from exposure to ionizing radiation, and repeals Directives 89/618/Euratom, 90/641/Euratom, 96/29/Euratom, 97/43/Euratom, and 2003/122/Euratom, and reorganizes the legislation in the sector in implementation of Article 20, paragraph 1, letter a), of Law No. 117 of October 4, 2019"

19.2.4 Installations

- Law No. 615 of 13 July 1966 "Measures against air pollution"
- Law No. 186 of 1 March 1968 "Provisions concerning the production of materials, equipment, machinery, installation of electrical and electronic systems"
- Presidential Decree No. 1391 of 22 December 1970 "Regulation for the implementation of Law No. 615 of 13 July 1966 regarding measures against air pollution"
- Law No. 791 of 18 October 1977 "Implementation of EEC Directive No. 73/23 concerning the safety requirements of electrical equipment intended to be used within certain voltage limits"
- Presidential Decree of 14 November 1997 "Determination of the limit values for noise sources"
- Ministerial Decree No. 37 of 22 January 2008 "Regulation concerning the implementation of Article 11-quaterdecies, paragraph 13, letter a), of Law No. 248 of 2 December 2005, on the reorganization of provisions regarding the installation of building systems"
- Legislative Decree No. 28 of 03 March 2011 "Implementation of Directive 2009/28/EC on the promotion of the use of energy from renewable sources"

19.2.5 Fire Prevention

- Ministerial Decree of 16 February 2007 "Classification of fire resistance of construction products and elements"
- Ministry of the Interior Decree of 9 March 2007 "Fire resistance performance of constructions in activities subject to the control of the National Fire Brigade"
- Presidential Decree No. 151 of 1 August 2011 "Regulation on the simplification of fire prevention procedures, pursuant to Article 49, paragraph 4-quater, of Decree-Law No. 78 of 31 May 2010, converted with amendments by Law No. 122 of 30 July 2010"
- Ministerial Decree of 7 August 2012 "Provisions regarding the submission of applications for fire prevention procedures and related documentation, pursuant to Article 2, paragraph 7, of Presidential Decree No. 151 of 1 August 2011"
- DCPREV (Direzione Centrale per la Prevenzione e la Sicurezza Tecnica – Dipartimento dei Vigili del Fuoco, del Soccorso Pubblico e della Difesa Civile) Note No. 1324 of 7 February 2012 "Guidelines for the installation of photovoltaic systems – Edition 2012"
- Circular 1324/2012 "Guidelines for the installation of photovoltaic systems – Edition 2012"
- Ministry of the Interior Decree of 3 August 2015 "Approval of fire prevention technical standards, pursuant to Article 15 of Legislative Decree No. 139 of 8 March 2006" and subsequent amendments
- Ministry of the Interior Decree of 12 April 2019 "Amendments to the decree of 3 August 2015, concerning approval of fire prevention technical standards, pursuant to Article 15 of Legislative Decree No. 139 of 8 March 2006"
- Ministry of the Interior Decree of 18 October 2019 "Amendments to Annex 1 of the decree of 3 August 2015, concerning approval of fire prevention technical standards, pursuant to Article 15 of Legislative Decree No. 139 of 8 March 2006"

- Legislative Decree No. 101 of 31 July 2020 “Provisions on the protection against ionizing radiation and the safety of radioactive materials, repealing Legislative Decree No. 230 of 17 March 1995”
- Ministry of the Interior Decree of 2 September 2021 “Criteria for the management of workplaces in operation and in emergencies and characteristics of the specific fire prevention and protection service, pursuant to Article 46, paragraph 3, letter a), point 4 and letter b) of Legislative Decree No. 81 of 9 April 2008”
- Ministry of the Interior Decree of 3 September 2021 “General fire safety criteria and emergency management in workplaces”
- UNI EN 1992-1-2:2005 “Eurocode 2: Design of concrete structures – Part 1-2: General rules, Structural fire design”
- UNI EN 1125:2008 “Building hardware - Panic exit devices operated by a horizontal bar, for use on escape routes - Requirements and test methods”
- UNI EN 1838:2013 “Lighting applications – Emergency lighting”
- UNI EN 7010:2017 “Graphical symbols – Safety colors and safety signs – Registered safety signs”
- UNI 9494-1:2017 “Smoke and heat control systems – Part 1: Design and installation of Natural Smoke and Heat Exhaust Ventilation Systems (NSHEVS)”
- UNI 9494-2:2017 “Smoke and heat control systems – Part 2: Design and installation of Smoke and Heat Exhaust Ventilation Systems (SHEVS)”
- UNI EN 15004-10:2018 “Requirements specific to systems using IG-541”
- UNI 10779:2021 “Fire extinguishing systems – Hydrant networks – Design, installation, and operation”
- UNI 9795:2021 “Fixed fire detection and fire alarm systems – Design, installation, and operation”
- UNI EN 1991-1-2:2024 “Eurocode 1: Actions on structures – Part 1-2: Actions on structures exposed to fire”
- UNI EN 15004-1:2025 “General requirements for gas extinguishing systems”

19.3 Conventional safety

As part of the broader integrated safety framework of the EuPRAXIA@SPARC_LAB facility, this section addresses the strategies and measures adopted to ensure conventional safety and emergency preparedness and response throughout all project phases, from construction to full operation. The conventional safety concept is grounded in the executive design developed by a qualified external engineering firm with recognized experience in high-complexity scientific infrastructures, particularly accelerator facilities. This design has already undergone a rigorous validation and authorization process by the competent Italian authorities, and it fully complies with national and European regulatory requirements and safety standards. The conventional safety framework reflects a structured, risk-based approach aimed at protecting personnel, equipment, and infrastructure under both routine and emergency conditions. Key elements include fire prevention, structural compartmentalization, smoke and heat control systems, and the safe design of evacuation routes. These technical measures are complemented by organizational actions such as emergency preparedness procedures, personnel training, and coordinated health and safety management. The EuPRAXIA@SPARC_LAB facility is fully integrated into the overarching Internal Emergency Plan and emergency procedures of INFN LNF, which govern all aspects of emergency organization, alarm management, evacuation, and coordination with external responders. This ensures consistency, regulatory compliance, and alignment with established institutional emergency management practices. Overall, the conventional safety strategy of EuPRAXIA@SPARC_LAB is aligned with international best practices and embodies a proactive, integrated approach to risk management, ensuring the highest standards of safety and compliance in support of the facility's scientific mission. The conventional safety requirements defined in this section, particularly with regard to fire prevention and control, fire detection and alarm systems, safe operating procedures for equipment, and occupational health and safety measures, will serve as the basis for the design of the MPS and the PSS, which are described in detail in Sections 19.5.2 and 19.5.3.

19.3.1 Fire safety

The general safety requirements are established in alignment with the fire prevention strategy detailed in the technical report on fire safety for the EuPRAXIA@SPARC_LAB complex. Fire protection measures are enforced throughout all operational phases — including construction, shutdown, testing, maintenance, and routine operation — to ensure consistent risk mitigation. Access to tunnels and buildings is strictly regulated and granted only to personnel who have received adequate training and instructions, in order to guarantee safe working conditions.

Taking into account the nature of indoor activities, the possibility of ignition, the minimal presence of combustible materials, the proper storage of flammable liquids in approved containers, the limited access granted to a small number of authorized expert personnel, and in accordance with the outcomes of fire safety modeling and analysis [1], the potential ignition sources and the overall fire hazard for the office activity are classified as: **MEDIUM FIRE RISK**.

The building (Figs. 18.5 and 18.8) is organized into compartments based on functional activities:

- FEL User Area
- Experimental Halls
- Clean Room/Laser Sync/THz
- Undulators Tunnel
- LINAC
- Modulator & Klystron Gallery
- Plants area
- Offices FEL user
- Racks room
- Control room

- Circulation
- Electrical substation

Fire prevention operations are categorized into the following ten activities as mandated by the Consolidated text of Annex I to the Ministry of the Interior Decree of 3 August 2015:

1. Reaction to fire
2. Fire resistance
3. Compartmentation
4. Evacuation
5. Fire safety management
6. Fire control
7. Fire detection and alarm
8. Smoke and heat control
9. Firefighting operations
10. Safety of technological systems

According to the Ministry of the Interior Decree of 3 August 2015, each activity is assigned a specific performance level. Depending on the type of activity, these levels range from I up to V. For all activities, corresponding compliant design solutions have been implemented in accordance with the assigned level.

19.3.1.1 Reaction to fire

All compartments are classified as performance level **II** for reaction to fire, in accordance with the applicable fire safety requirements. As a result, materials of class **GM3**, acceptable for standard-risk areas and compliant with regulatory provisions, have been selected. For vertical escape routes and connecting sections of horizontal escape routes (such as corridors, lobbies, refuge areas, and smoke lobbies), materials must meet at least **GM2** classification, offering improved fire performance with low combustibility and limited flame spread.

19.3.1.2 Fire resistance

All compartments are classified as performance level **III** for resistance to fire, ensuring that the fire resistance requirements are maintained for a duration consistent with the expected development of a fire. Tunnels and building compartments are constructed using fire-resistant materials rated for a **minimum fire resistance of 120 minutes**. These specifications comply with the fire resistance criteria established for critical areas, as defined in the regulatory framework described in Section 19.2.

19.3.1.3 Compartmentation and evacuation

Compartments are designed to prevent fire spread between operational zones and to confine fires to localized areas. All compartments are classified as performance level **II**, ensuring that the fire is effectively contained for a period of time comparable to its expected duration, thereby limiting its extension both inside and outside the compartment. The evacuation strategy adopted is **simultaneous evacuation**, ensuring that all occupants begin evacuating at the same time. This is consistent with performance level **I** which requires that everyone must reach a place of safety before conditions become incapacitating. Evacuation routes are planned to ensure a safe evacuation within a **maximum of 120 minutes**, including for personnel using protected escape routes, based on the fire resistance characteristics of the materials used. Key evacuation design criteria, aligned with current fire safety regulations, include:

- Maximum evacuation path length: 60 meters;

- Maximum dead-end corridor length: 30 meters;
- Three evacuation routes are provided: one smoke-proof (ventilated or pressurized to prevent smoke entry) and two protected (enclosed and fire-resistant, but not necessarily smoke-free);
- Doors installed along escape routes: In compliance with Ministry of the Interior Decree of 3 August 2015, they must be easily identifiable and operable by all occupants. Their opening must not obstruct the flow of people along the evacuation paths. The fire resistance characteristics of the doors must comply with the provisions of the previous paragraph, i.e. they must provide a **minimum fire resistance of 120 minutes**. The doors located along the escape routes will be equipped with electromagnetic holders for normally open doors;
- Emergency exits: Manual-operated doors that open outward, equipped with UNI EN 1125-compliant panic exit devices for emergency egress. These exits will be provided with a sign stating "Emergency exit – Keep clear" both in Italian and English (Figure 19.2).

Figure 19.2: Example of emergency exit sign

Emergency signage and safety lighting will be installed to facilitate recognition and navigation of escape routes [2], in accordance with applicable standards such as UNI EN ISO 7010 (Figure 19.3).

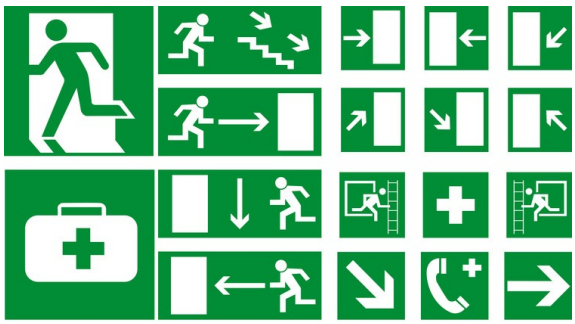

Figure 19.3: Example of emergency signage compliant with UNI EN ISO 7010

The emergency lighting system consists of dedicated luminaires powered by a central power supply system (CPS) and autonomous safety luminaires with backup batteries, centralized through a dedicated control unit.

The CPS will consist of a control panel with a variable number of inputs and outputs, each output powering a lamp circuit. The power supply cables to the lamps will be of fire-resistant type up to the entrance of the relevant compartment. The distribution network will use fire-resistant cable type FTG10(O)M1 0.6/1kV (in accordance with CEI 20-36 and CEI 20-45 standards).

The central battery system is intended to power and monitor 230 V emergency luminaires. The central unit will be designed to charge sealed, maintenance-free batteries with a charging voltage of 2.3 V per cell, housed either within the power supply unit or in a dedicated cabinet. The system will

allow monitoring of each individual luminaire with individual status indication and identification through communication that does not require additional components inside the lighting fixture.

The luminaires for emergency lighting will be of the centralized type, powered by the central power supply unit. Exit signage fixtures, complete with green-and-white pictograms indicating emergency exits and escape routes, compliant with European standardization, will consist of dedicated autonomous, self-powered and centralized lamps.

The system, equipped with supervision software, will allow visualization of the status of luminaires and batteries (where provided) and will also be able to perform the periodic tests required by Legislative Decree 9 April 2008, No. 81, and by EN 62034.

In all service penetrations crossing compartmentalized structures, appropriate sealing and restoration measures have been provided to ensure the same fire resistance rating as the affected compartment. In particular:

- All ducts crossing fire compartments will be equipped with fire dampers of the appropriate resistance class.
- All combustible plastic pipes (PEAD and PVC) will be protected with firestop collars.
- All non-insulated steel pipes will be protected with suitable fire-resistant sheathing.
- All insulated and multilayer steel pipes will be protected with two-component polyurethane firestop foam.

19.3.1.4 Fire safety management

The performance level assigned to fire safety management is **II**, which requires the implementation of management procedures during both normal operations and emergency situations, ensuring continuous compliance with fire safety protocols. This level also entails maintaining operational conditions and emergency response capabilities through a dedicated support structure. The person responsible for the activity must appoint a fire safety coordinator and establish a fire safety team. The facility has established a set of organizational, managerial, and emergency procedures, which include the following categories:

- Organizational and management measures.
- Measures for fire hazard mitigation.
- Measures concerning escape routes.
- Measures for fire detection and alarm systems.
- Measures for fire suppression.
- Measures for evacuation and safety signage.
- Measures for fire safety information and communication.

Additionally, compliance with Articles 31 and 32 of Legislative Decree 9 April 2008, No. 81, is required. These articles outline the provisions regarding the prevention and protection service, as well as the skills and professional qualifications required for internal and external fire safety personnel and supervisors.

Regarding fire safety management during normal operations, the training and information procedures follow the requirements defined in the Ministry of the Interior Decree of 18 October 2019 and the Ministry of the Interior Decree of 2 September 2021.

These decrees also define the procedures for emergency preparedness, which, as part of fire safety management, include:

- Planning of emergency procedures, to be executed in response to various hypothetical incident scenarios;
- Periodic training and drills to ensure personnel are prepared to implement the emergency and evacuation plan.

Emergency planning must be reviewed regularly and updated whenever there are changes to

structures, systems, or fire protection equipment that affect fire safety conditions.

During an emergency, once an incident is detected, the immediate activation of the emergency procedures outlined in the plan is expected. The continuous presence of designated emergency personnel must be ensured throughout the event.

Fire safety management during an emergency must also include:

- Activation of public emergency services.
- Evacuation of occupants.
- Securing of equipment and systems.

Fire safety management is included as a component of the broader Emergency Preparedness and Response framework, which is discussed in detail in Section 19.3.3.

19.3.1.5 Fire control

In compartments classified as performance level **II** for fire control (all compartments except racks room and electrical substation), where manual fire control and suppression is required, basic fire protection is ensured through the installation of portable fire extinguishers with the following specifications:

- **Class A coverage (for solids):** Extinguishers with a minimum rating of 21A, placed so that the distance between any two consecutive extinguishers does not exceed 40 meters and, in any case, allowing an extinguisher to be reached from any point in the facility along a path no longer than 20 meters.
- **Class B coverage (for liquids):** One type 144B fire extinguisher for each room located within a TK compartment (i.e., a fire compartment designated for the storage or handling of flammable liquids) of the facility, as well as for any areas where flammable liquids are present, either temporarily or permanently. Furthermore, at least one extinguisher with a minimum rating of 233B must be installed near each energized electrical device.
- **Electrical apparatus operating at specific voltage level (former Class E coverage):** Fire extinguishers suitable for use on electrical equipment operating at voltages up to 1000 V and compliant with EN 3-7 standards, as specified by the manufacturer, will be installed in rooms housing electrical equipment rated up to 1000 V.

In addition, a manually operated external fire hydrant network designed, installed, and operated in accordance with UNI 10779:2021 is available to support firefighting operations. A new integrated fire water storage system is also installed. This system will include a partially underground water reserve and pump room, with a usable fire water storage capacity of 150 m^3.

In performance level **IV** compartments (racks room and electrical substation), fire suppression is managed through automatic systems designed to inhibit, control, or extinguish fires within designated areas. In the racks room, the system utilizes inert gas agents, specifically IG-541 (Inergen), a blend of nitrogen, argon, and carbon dioxide, which is safe for use in occupied areas and effective in reducing oxygen concentration to suppress combustion. The system is designed and operated in compliance with UNI EN 15004-1 (General requirements for gas extinguishing systems) and UNI EN 15004-10 (Requirements specific to systems using IG-541). An example of the system is shown in Figure 19.4. In the electric substation, containing electrical panels or sensitive equipment, carbon dioxide (CO_2) is used instead, due to its high extinguishing efficiency and non-conductive properties.

The activation of the automatic fire suppression system, or the manual triggering of the fire alarm in the laser room and in the modulator & klystron gallery, initiates an interlock procedure that safely disables the accelerator systems. This safety response is implemented through the functional safety infrastructure, as described in detail in Section 19.5.

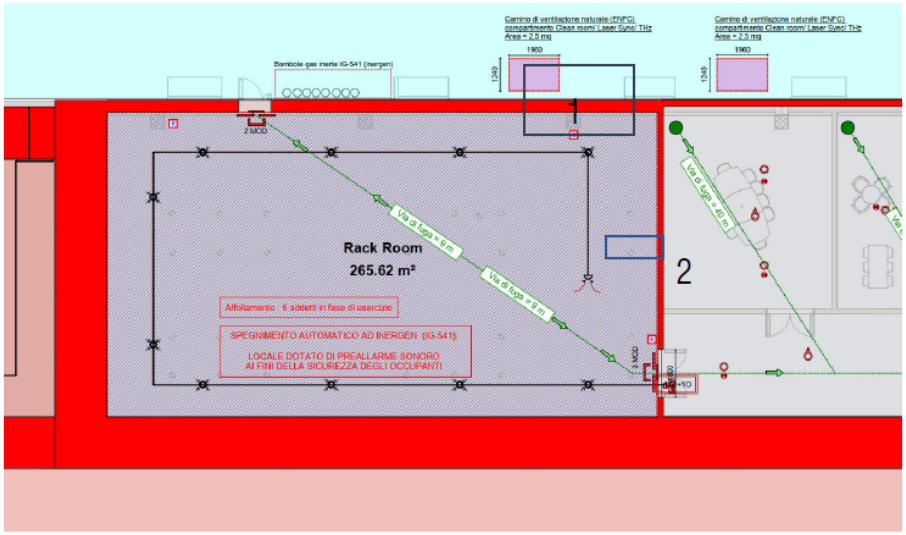

Figure 19.4: Example of first floor plan with identification of the area served by the automatic extinguishing system

19.3.1.6 Fire detection and alarm

All compartments are equipped with fire detection and alarm systems. In accordance with the Ministry of the Interior Decree of 3 August 2015, compartments featuring automatic fire suppression systems (rack room and electrical substation), those equipped with Mechanical Smoke and Heat Exhaust Ventilation Systems – SHEVS (the undulators tunnel and LINAC), as well as areas where activated particles are expected (experimental halls), and the modulator and klystron gallery, are classified as performance **III**. In these compartments, fire detection and alarm systems operate through automated continuous monitoring and the automatic distribution of alarm signals. All remaining areas are classified as performance level **II**. In these compartments, fire detection and alarm are performed manually by the occupants. The automatic fire detection and alarm system, based on addressable digital technology, will comply with UNI 9795:2021. Each field device (point smoke detectors, optical-acoustic indicators, alarm push buttons, and interfaces to technological systems) will be uniquely addressable and displayed at both the control panels and the Control Room via supervision software. The software will feature graphical maps to identify individual components and visualize any alarms. Each detector will also include analog functions for sensitivity adjustment and recalibration. The system is designed to detect the onset of a fire as quickly as possible within the building. It will consist of an electronic control panel, operating 24/7 and located on the ground floor, connected to sensors capable of detecting smoke, flames, or heat. Protection will primarily be provided by analog optical smoke detectors with individual addressing and triple detection technology. These will be connected through fire-resistant loop cabling rated at 30 minutes, 750 °C (CEI 20-45 compliant). Coverage will extend to all areas with high fire load or high occupancy, such as offices, control rooms, and corridors, as well as to locations where flammable materials are stored, including the warehouse and the technological plant room. Alarm push buttons will be installed at suitable points on every floor to allow manual alarm activation. Each floor will also be equipped with at least one optical-acoustic alarm device with a flashing light and high-intensity siren, activated either automatically by detectors or manually by a call point. These devices will be powered by fire-resistant cabling rated at 3 hours, 750 °C (CEI 20-45 compliant).

The microprocessor-based control panel, compliant with EN 54-2 and EN 54-4, will be an analog addressable type capable of managing up to four loops. Each loop can support up to

127 analog sensors and 127 input/output devices. The maximum length of each loop will not exceed 1000 m, using 2×1.5 mm^2 cabling. Because it is addressable, each sensor will be uniquely identifiable by its specific address. The control panel will support the connection of:

- Smoke detectors.
- Alarm push buttons.
- Internal and external sirens.
- Relay modules for I/O devices.

In the event of a fire, upon receiving an alarm signal, the control panel in the first-floor Control Room will issue both optical and acoustic alarms, clearly identifying the activated detector or call point. It will also control and command the fire damper actuators installed in the extraction system and at other points where compartmentation must be maintained.

The system will also be equipped with:

- Low-profile optical smoke detectors with LED status indicators.
- Low-profile optical smoke detectors with LED status indicators and alarm repeaters for suspended ceilings.
- Linear smoke detectors.
- Smoke detectors for AHU return ducts with analysis chambers.
- Visual indicators (LED repeaters) for detector status.
- Self-powered optical-acoustic indicators with Ni-Cd backup batteries, LED illumination, and programmable functions.
- Addressable manual call points with integrated isolators.

This configuration guarantees rapid and reliable fire detection, continuous system supervision, and full compliance with both national and European standards.

The building will be provided with a sound diffusion system. The system will include:

- A central sound diffusion and evacuation unit compliant with CEI EN 50849, consisting of a main signal management unit and console input module.
- A secondary audio input module, secondary signal management unit, audio output module with self-diagnosis, and a voice message module. The system will be capable of managing up to four independent channels, each with a dual loudspeaker connection line.
- An operator workstation for the evacuation sound diffusion system, also compliant with CEI EN 50849. This will feature a digital microphone console with programmable functions, zone control, message management, and alarm management. A dedicated microphone will be provided for direct communication with the fire brigade station.
- Ceiling-mounted loudspeakers equipped with fire-resistant covers and ceramic terminals, specifically designed for evacuation sound diffusion.

19.3.1.7 Smoke and heat control

In accordance with the Ministry of the Interior Decree of 3 August 2015, the entire building is classified as performance level **II**, meaning that all compartments must allow for the removal of smoke and heat in the event of a fire, in order to support the operations of firefighting and rescue teams, even in the event of a main power supply failure. Effective smoke and heat removal is essential to facilitate rescue operations and ensure safe access for emergency response teams. Where smoke and heat cannot be evacuated through natural openings due to the nature of the activities, both natural (NSHEVS) and mechanical (SHEVS) smoke and heat evacuation systems are installed on the roof.

These systems must comply with the following standards:

- UNI 9494-1:2017, Appendix G for NSHEVS
- UNI 9494-2:2017, Appendix H for SHEVS

For the FEL user area, the experimental halls and the circulation compartments, an NSHEVS has been provided. For the undulators tunnel and LINAC compartments, a SHEVS has been provided. These systems are designed without the need to create smoke stratification or a smoke-free layer, serving solely to assist firefighting operations and to reduce the impact of fire on the structural components of the building. The exhaust openings are located on the roof of the building, allowing combustion products to be discharged directly outside. Fresh air intake from outside the compartment will be ensured through mechanical ventilation at the lower part of the space, with a flow rate equal to 20 air changes per hour of the compartment's volume. The roof openings are designed to prevent smoke discharge from interfering with evacuation routes or contributing to fire spread to adjacent rooms, floors, or compartments. These openings will allow for effective smoke removal from all zones within the compartment. They will be protected against accidental obstruction during normal activity and can be easily managed as part of the facility's emergency response plan. The uniform distribution of the openings will be ensured by applying an influence radius of 20 meters for each opening. With the exception of the FEL User Area and the Circulation compartments, the operation of the machine may cause radiogenic activation of the air within certain compartments during normal operation. In an emergency, this air cannot be discharged directly to the outside environment. Therefore, activated carbon filters will be installed downstream of the exhaust system, designed to limit the release of any radiation-activated combustion byproducts into the environment. Furthermore, each forced extraction opening of the SHEVS will be designed with a "double-L" structure to ensure a radiological shielding function for the surrounding environment, even in emergency conditions (Figure 19.5).

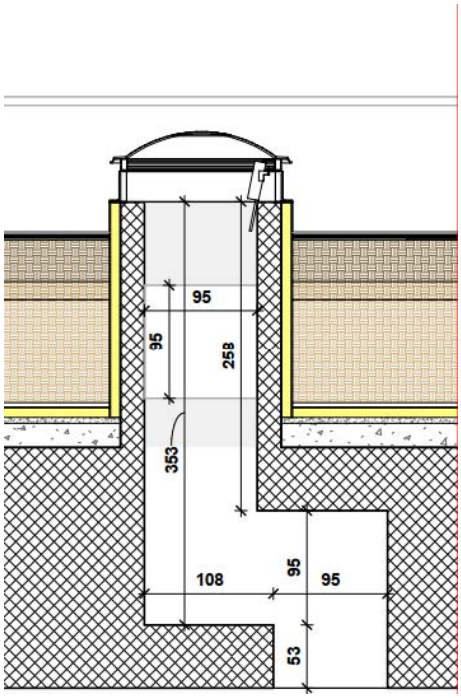

Figure 19.5: Section of a SHEVS exhaust opening showing the "double-L" structure

19.3.1.8 Firefighting operations

The entire facility ensures accessibility for firefighting and emergency response vehicles in accordance with performance level **II**. Figure 19.6 shows the access routes for firefighting vehicles together with the locations of the single fire pump connections (Standard UNI 70) and pillar-type or underground hydrants (Standard DN70), in the vicinity of the building.

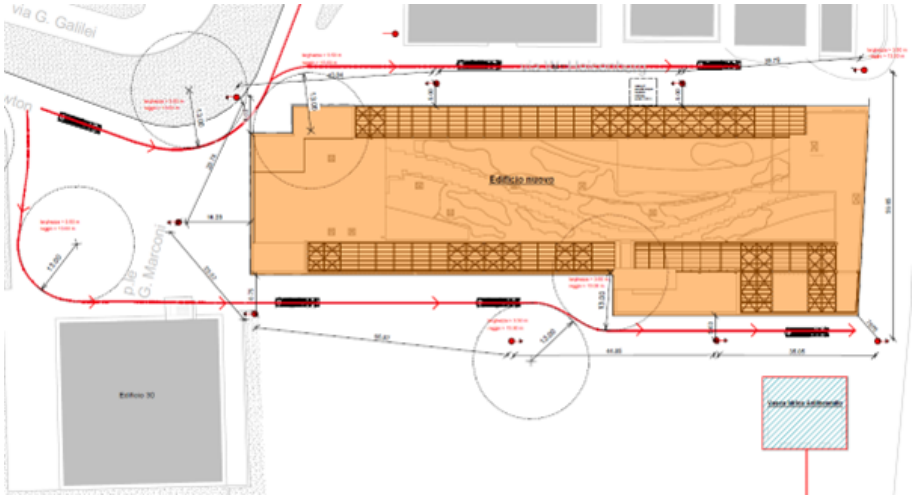

Figure 19.6: Access routes for firefighting vehicles showing single fire pump connection (UNI 70), and pillar-type or underground hydrants (DN70)

19.3.1.9 Safety of technological systems

For all activities, the systems are designed, installed, operated, and maintained according to recognized best practices, in compliance with applicable regulations, and in accordance with specific fire safety requirements as mandated by the performance level **I**.

19.3.2 Safety of equipment and accident prevention

19.3.2.1 Requirements for the safe operation of equipment

The conventional safety framework includes specific measures to ensure the safe operation of technical equipment and systems throughout the facility. This is achieved through the definition and implementation of clear operational procedures, standard operating protocols, and access control strategies. These procedures are developed in accordance with international best practices, current regulation, and the most up-to-date safety management approaches, and they are tailored to the specific operational contexts of the EuPRAXIA@SPARC_LAB facility. Prior to commissioning, all equipment will undergo rigorous safety inspections, following the guidelines of the Ministry of the Interior Decree of 2 September 2021, which defines the criteria for fire safety management during operation and maintenance. Periodic inspections will also be carried out throughout the facility's lifecycle to ensure continued compliance with applicable safety standards and to promptly identify and address potential hazards. A key element of this safety approach is the regulated access to equipment areas. Access is granted only to authorized and trained personnel, following role-based criteria and procedural authorization. This access control is not limited to radiation protection purposes but also functions as a primary layer of accident prevention, particularly in areas containing high-voltage systems, pressurized components, cryogenic equipment, or other operational hazards. The physical architecture and logic regulating access control is discussed in Section 19.5.3. The overarching objective of this approach is to minimize the likelihood of incidents and equipment failures, while ensuring a safe working environment for operators and maintenance teams. These measures are aligned with technical standards such as EN ISO 12100, which defines the basic methodology for identifying hazards and reducing associated risks through both engineering and procedural means.

19.3.2.2 Occupational Health & Safety requirements for the construction phase

The implementation of conventional safety principles extends beyond the operational phase to include all activities associated with construction, installation, commissioning, and maintenance. Occupational health and safety requirements are applied systematically in compliance with Legislative Decree 9 April 2008, No. 81, which constitutes the legal framework for workplace safety in Italy and incorporates the core principles of prevention, risk assessment, and worker protection as defined by EU Directive 89/391/EEC. During the construction phase, a dedicated Health & Safety Coordination Plan will be implemented for all worksites, under the responsibility of a designated Safety Coordinator. This includes the identification and mitigation of risks related to construction machinery, site layout, fire hazards, falls from height, confined spaces, hazardous material management, emergency evacuation procedures and other relevant factors. The safety coordination effort ensures alignment between all contractors and INFN-LNF internal procedures. In the operational phase, risk assessment documents and specific emergency response protocols are maintained and regularly updated, ensuring continuity of protection as the facility transitions from installation to routine use. This dual-phase approach aims to reduce the likelihood of workplace accidents, enhance personnel safety, and ensure compliance with national legal obligations. It also supports the long-term reliability of technical infrastructure by promoting safe working conditions and preventing damage due to improper handling or procedural deficiencies.

19.3.3 Emergency preparedness and response

The EuPRAXIA@SPARC_LAB facility is fully integrated into the emergency preparedness and response system established by INFN-LNF. This means that the facility is subject to the Emergency Plan and the associated organizational procedures adopted at the Frascati National Laboratories. These measures are designed to ensure a coordinated and effective response to potential emergency situations, encompassing the protection of workers, visitors, critical infrastructure, and the surrounding environment. The inclusion of EuPRAXIA@SPARC_LAB within the existing emergency framework guarantees alignment with the legal requirements of Legislative Decree 9 April 2008, No. 81 and Legislative Decree 31 July 2020, No. 101, as well as with internationally recognized best practices in emergency planning, occupational safety, radiation protection, and environmental management.

The emergency response strategy relies on the high level of professionalism of on-site personnel, the structured organization of the Health, Safety and Environment (HSE) service, the specialized contributions of Health Physics and Occupational Medicine, and the operational readiness of trained Emergency Response Teams.

To ensure the full effectiveness of the Internal Emergency Plan, the following preconditions must be met:

- Awareness and training of personnel involved in laboratory activities.
- Clear and timely information for guests regarding emergency behavior protocols.
- Clear and visible signage for evacuation routes leading to assembly points and safe areas.
- Proper installation and marking of fire extinguishing equipment and emergency devices throughout the facility.
- Formal and precise assignment of roles and responsibilities for emergency management, with clearly defined operational procedures for each designated person.

19.3.3.1 Staff Training

To ensure effective intervention in emergency situations, all internal personnel must be adequately trained, with the primary objective of reducing the risk of confusion or panic. Designated personnel shall attend specific theoretical and practical training courses, tailored to their respective operational roles.

19.3.3.2 Specialized Training for the Emergency Response Teams

This course is mandatory for Emergency Response team members and focuses on the operational aspects of the Emergency Plan, as well as general and specific principles of fire prevention and workplace safety. The training should cover the following topics:

- Basic principles of fire prevention and accident mitigation, and identification of major fire causes.
- Active and passive fire protection measures implemented in the facility.
- Emergency operating procedures, including evacuation protocols.
- Proper use of fire extinguishers and other emergency response equipment available on-site.
- Basic life support techniques with the use of an automated external defibrillator.

19.3.3.3 General Training for All Personnel

A second course, intended for all personnel, including research fellows, students, associates, and any other users of EuPRAXIA@SPARC_LAB facilities, provides a general understanding of workplace safety and emergency procedures, with particular focus on the following topics:

- Basic fire and accident prevention and protection principles.
- General knowledge of firefighting and first response equipment available at the facility.
- Operational organization and management structure of the Emergency Plan.
- Essential behavioral and response procedures in the event of an emergency.

19.3.3.4 General Emergency Drills

In compliance with Legislative Decree 9 April 2008, No. 81 and the provisions of the Ministry of the Interior Decree of 2 September 2021 on fire emergency management in workplaces, the employer must ensure the regular performance of emergency drills aimed at:

- Verifying the effectiveness of the Internal Emergency Plan.
- Training personnel in evacuation procedures in the event of imminent danger.
- Testing the functionality of the command chain and alarm systems, and continuously improving emergency management systems.
- Training emergency response teams (firefighting, first aid, evacuation).
- Raising awareness among all personnel, including authorized external personnel (contractors, interns, visitors), and providing general instructions on possible risks, alarm procedures, and protective actions that may be required in an emergency.

Drills must:

- Be conducted at least once a year and whenever significant changes occur in work organization, space layout, or emergency measures.
- Be planned and documented through a formal report including the simulated scenario, involved personnel, evacuation times, identified issues, and improvement suggestions.
- Be coordinated by the HSE.

Drills should simulate conditions as realistically as possible, including:

- Activation of the alarm system.
- Partial or full evacuation.
- Verification of escape route accessibility and emergency equipment functionality.
- Involvement (if applicable) of external emergency services (Fire Brigade, Medical Emergency Services, Law Enforcement).
- Possible use of fire extinguishers on controlled fires for firefighting personnel.

All workers must be adequately informed and trained on proper emergency behavior. The

outcomes of each drill must be analyzed to update the Emergency Plan if necessary. Participation in drills is mandatory for all personnel—internal or external—present at LNF during the exercise.

19.3.3.5 Radiological Emergency Drills

Periodic drills involving potential radiological emergency scenarios must be organized. These drills must simulate:

- Fires in areas containing activated materials.
- Damage to or loss of radioactive sources.
- Accidental contamination events.

The drills must be conducted at least annually and include:

- Actual or simulated use of radiological personal protective equipment and portable radiation detectors.
- Activation of the Response Chain of Command defined in the emergency plan.
- Evaluation and documentation of all actions carried out during the exercise.

19.4 Radiation Safety and protection

Radiation safety represents a fundamental component of any facility operating an electron accelerator. Its primary role is to ensure that all activities involving ionizing radiation are conducted under conditions that protect personnel, equipment, and the environment. Effective radiation safety prevents life-threatening exposures, limits accidental or unintended doses, and provides a structured framework for identifying, controlling, and mitigating radiological hazards throughout the installation.

This section presents the main aspects that define the radiation-safety approach adopted for the installation. It first introduces the preliminary radiation safety program, focusing on the elements addressed within this report: area classification, the radiation-monitoring system, and the personal-dosimetry system. Other components of the radiation-safety program, although essential, are described in separate sections (Sec. 19.5). The final part of the section reports on the study carried out on both lateral shielding, diagnostic and fixed beam dump design, highlighting the optimization in terms of radiological protection as well as their consistency with the planned area classification. It is crucial to outline the main components of high-energy electron accelerators and the key design parameters that influence radiation production, in order to provide the necessary protection strategies.

Prompt radiation and radioactivity resulting from particle - nuclear interactions within beamline components and shielding materials constitute the primary radiation hazards in high energy accelerators fields. The accelerator's design parameters play a critical role in determining both the characteristics and intensity of these radiation sources. The most important parameters to take into account are:

- particle energy;
- beam power;
- target material;
- work load;
- beam losses;
- the geometrical layout.

19.4.1 Preliminary Radiation Safety Program

For every electron accelerator facility, a Radiation Safety program is required, which ensures that the use of the installation, or specific parts of it, is conducted under safe conditions. The primary objective of the program is to prevent life-threatening exposures and to minimize any accidental, yet potentially significant, exposure to personnel. The program includes the fundamental elements of radiation protection, such as the PSS, the access control system, and the interlock system. The PSS will be discussed in Sections 19.5.3, while the requirements for the access control system and the interlock system are described in Sections 19.4.1.4 and 19.4.1.5, respectively. In addition, the area classification, the monitoring system and the personnel dosimetry one are addressed in the following sections.

19.4.1.1 Radiation monitoring System

The EuPRAXIA@SPARC_LAB Radiation monitoring System will consist of:

- 12 active detectors for photon radiation (e.g. ionization chambers);
- 12 active detectors for neutron radiation (e.g. rem counters);
- 1 detector for the measurement of radioactive gas activity concentration in air;
- 1 central data acquisition system;
- 1 computer for control, data storage, and data processing.

All detectors are connected via LAN to the radiation-monitoring service of the Health Physics team (FISMEL). The Laboratories are already equipped with a dedicated network infrastructure

that enables the integration of radiation monitors from the various facilities and ensures a reliable, seamless interface with the central monitoring and alarm system. Each monitoring station is also equipped with hardwired safety contacts that provide a direct and independent interface with the facility's PSS.

The monitors are interlocked with accelerator operation through a configurable dose-rate alarm threshold. When this threshold is exceeded, irradiation is immediately interrupted, and machine operation cannot resume until the measured dose falls below the preset limit. Photon and neutron detectors will be installed in the bunker surrounding areas, with particular emphasis on supervised zones.

The planned spatial distribution of the detectors is shown in Fig. 19.7, while the detailed location and designation of each unit are reported in Tab. 19.1.

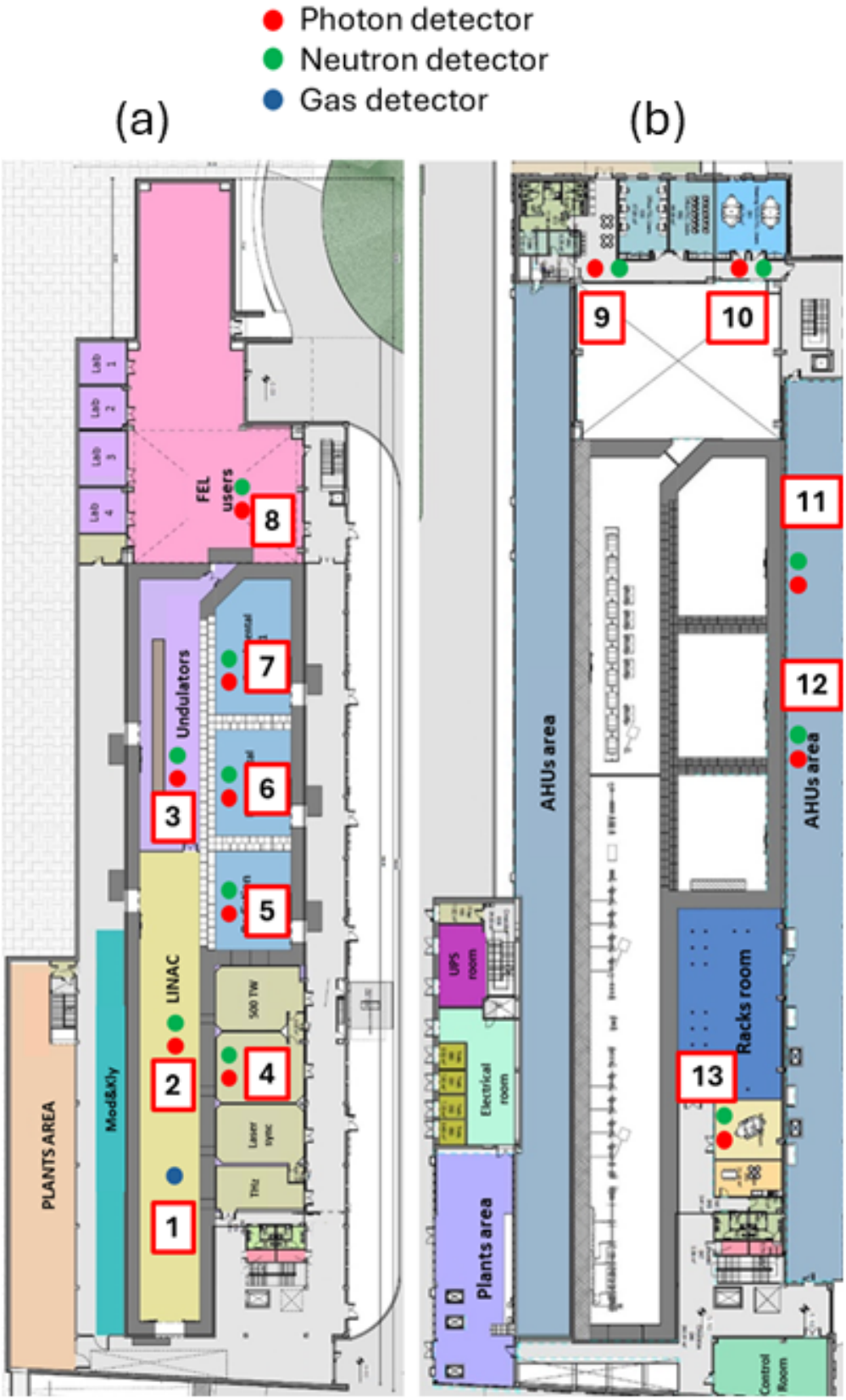

Figure 19.7: Planned detector position on the first (b) and ground (a) floor.

Table 19.1: Detector location.

Point	Place
1*	Roof - LINAC tunnel
2*	Roof - LINAC tunnel
3*	Roof - Undulator tunnel
4	Clean room
5	Experimental hall 1
6	Experimental hall 2
7	Experimental hall 3
8	FEL user area
9	Corridor 1
10	Corridor 2
11	AHUS area 1
12	AHUS area 2
13	Rack room

With reference to Table 19.1, the points marked with an asterisk (*) correspond to the detectors installed on the roof, where point 1 specifically refers to the gas detector. Points 4 through 8 refer to those located on the ground floor, while points 9 through 13 correspond to the detectors installed on the first floor.

For special installations, the system allows the detector head to be separated from its associated electronics by a distance of at least 5 m. This option is intended for high-radiation environments to reduce the risk of electronic degradation or failure.

Photon Detectors Requirements

Detectors for photon radiation have to be preferably high pressure ionization chambers. Each detector has to be compliant with the following characteristics:

1. Response in term of Ambient Dose Equivalent rate, $\dot{H}^*(10)$, in a wide energy range, from few tens of keV up to 10 MeV.
2. Measurement range from 0.1 µSv/h up to 0.1 Sv/h.
3. Neutron insensitivity.
4. Generation of a pre-alarm signal when the radiation level exceeded a pre-settable alert level in the measurement range at pt. 2.
5. Generation of an alarm signal when the radiation level exceeded a pre-settable alarm level in the measurement range at pt. 2.
6. Alarm and alert signals must activate a buzzer and warning lights (red = alarm, yellow = alert, green = proper operation).
7. Possibility to introduce a delay, pre-settable in the range 10 s - 1 min, in the generation of the alarm signal in order to avoid any false signal or spike.
8. Automatic reset of pre-alarm and alarm signal when the radiation level come back under the relative threshold.
9. Indication of proper operation, available after the switch-on and every time it is required.
10. Generation of an interlock fail safe signal if the radiation level measured is greater than the pre-settable alarm level for the pre-settable length (of time), opening four independent contacts normally open of internal relays. The signal should be extracted through a connector

to be agreed.
11. Relays referred at pt. 10 must be compliant with SIL – 3 safety integrity level of IEC (61508)* or better.
12. Each unit must be equipped with a backup battery.
13. Calibration certificate for each detector in term of $\dot{H}^*(10)$.

Neutron Detectors Requirements

Detectors for neutron radiation have to be constituted by rem-meters. Each detector has to be compliant with the following characteristics:

1. Response in term of $\dot{H}^*(10)$, in the energy range from thermal energy up to up to hundreds MeV.
2. Measurement range from 0.1 µSv/h up to 0.1 mSv/h.
3. Photon insensitivity to photon radiation up to 1 Sv/h.
4. Generation of a pre-alarm signal when the radiation level exceeded a pre-settable alert level in the measurement range referred to in point 2.
5. Generation of an alarm signal when the radiation level exceeded a pre-settable alarm level in the measurement range referred to in point 2.
6. Alarm and alert signals must activate a buzzer and warning lights (red = alarm, yellow = alert, green = proper operation).
7. Possibility to introduce a delay, pre-settable in the range 10 s - 1 min, in the generation of the alarm signal in order to avoid any false signal or spike.
8. Automatic reset of pre-alarm and alarm signal when the radiation level come back under the relative threshold.
9. Indication of proper operation, available after the switch-on and every time it is required.
10. Generation of an interlock fail safe signal if the radiation level measured is greater than the pre-settable alarm level for the pre-settable length (of time), opening four independent contacts normally open of internal relays. The signal should be extracted through a connector to be agreed.
11. Relays referred to in point 10 must be compliant with SIL – 3 safety level of IEC (61508)* or better.
12. Each unit must be equipped with a backup battery.
13. Calibration certificate for each detector in term of $\dot{H}^*(10)$.

Radioactive Gas Detector Requirements

Detectors for monitoring radioactive gases can be chosen among gas detectors, such as proportional detectors, that enables the greatest possible sensitivity with low sensitivity to external gamma radiation and thus outstanding detection limits. This because the gas to detect are mainly beta emitters. Moreover, the use of scintillator detectors in addition is preferred, such as NaI detector for gamma spectrometry.

The detector has to be compliant with the following characteristics:

1. Measurement range from 0.1 Bq/g up to 10 Bq/g for a radioactive gas mixture mainly consisting of ^{11}C, ^{13}N, ^{15}O, ^{41}Ar with spectrometric detection type.
2. Generation of a pre-alarm signal when the radiation level exceeded a pre-settable level in the measurement range referred to in point 1.
3. Generation of an alarm signal when the radiation level exceeded a pre-settable alarm level in the measurement range referred to in point 1.
4. Alarm and alert signals must activate a buzzer and warning lights (red = alarm, yellow = alert, green = proper operation).
5. Automatic reset of warning and alarm signal when the radiation level come back under the

relative threshold.
6. Indication of proper operation, available after the switch-on and every time it is required.
7. Generation of an interlock fail safe signal if the radiation level measured is greater than the pre-settable alarm level for the pre-settable length (of time), opening 4 independent contacts, normally open of internal relays. The signal should be extracted through a connector to be agreed.
8. Relays referred to in point 7 must be compliant with SIL – 3 safety level of IEC (61508)* or better.
9. Calibration certificate for gases referred at pt. 1.
10. Predisposition of a possible installation of a calibration radioactive source.
11. Each unit must be equipped with a backup battery.
12. Calibration certificate for each detector in $\dot{H}^*(10)$.

19.4.1.2 Data acquisition and management

The data acquisition and management software has to be installed on a work station, at least equipped with processor i7, 1 Tb of memory with a RAM not less 8 Gb. The data acquisition system should be able to connect up to 50 detectors and must allow the following operation:

- Remote control of detectors.
- Storage of data, coming from each detector, every minute on files of 24 hours. File name GGMMAAAA (start acquisition at 00:00 stop acquisition at 24:00).
- Storage with time/date of maximum instant value of quantities measured, in case of exceeding the pre-settable alert or alarm level for the pre-settable length of time.
- Real time display of all detectors with automatic switch to a pre-alarming and alarming detector, using yellow color in case of a pre-alarm and red color in the case of an alarm.
- Storage of all signals of alert and alarm on files of 24 hour. File names are in the format "DetectorNameDDMMYYYY".
- Display for a single detector of the Ambient Dose Equivalent integrated on 24 hour or on any programmable time interval.
- Query archive independently from the data acquisition.
- Possibility to print stored data.
- Graphic display and print of stored data.
- Possibility to perform mathematical operations on selected portion of data.
- Quick scroll of entire archive.
- Possibility to display the graphical representation of all detectors or a selected number of detectors.
- Password access to various part of program.
- The system is equipped with a DC-UPS.

19.4.1.3 Personnel Dosimetry Systems

It is necessary to define a Personnel Dosimetry Systems for External Radiation Exposures, considering the classification of workers and workplaces and the type of risk from ionizing radiation expected for the EuPRAXIA@SPARC_LAB facility.

These dosimeters are needed for monitoring exposures to external radiation and guarantee that the exposures are kept at the lowest level reasonably achievable, on the basis of Optimization principle.

Dosimeters are devices used to measure the amount of energy deposited by ionizing radiation. This measurement is used to estimate the effective dose received by the human body through exposure to external ionizing radiation. Doses received following internal exposure from incorporation of radioactivity are not assessed by these dosimeters, but if necessary determined through

other methods. Dosimeters only measure external radiation exposure and do not offer radiation protection.

The different types of dosimeter and systems proposed for the EuPRAXIA@SPARC_LAB are:

- personal dosimeter (TLD and/or DIS-1 + CR39);
- operational dosimeter (DMC2000 or DMC3000);
- extremities dosimeter, usually for hands, feet or eyes.

The personal dosimeter is mandatory for all workers occupationally exposed to ionizing radiation. The operational dosimeter is complementary and required only for certain areas or activities, if required by the FISMEL Group. Extremity dosimeters have to be worn if required by FISMEL group, usually when high local doses to the extremities or eyes can be expected.

Dosimeters are released once the suitability assessment has been obtained and by following the required radiation protection training programs.

Evaluations of the doses received by exposed workers have to be performed by the Radiation Protection Expert within an appropriate time period, as well as the dose evaluation of the environment.

19.4.1.4 Access control system requirements

The requirements for the interlock system are as follows:

- allow the passage of only one person at a time, both at entry and exit;
- record each individual access in order to count and identify the persons present inside the area;
- ensure personal identification of workers accessing the area, for example by means of a magnetic badge;
- be interlocked with the machine operation: if there is no correspondence in number and identity between persons entering and leaving the area, the machine shall not be enabled for operation.

19.4.1.5 Interlock requirements

The main principles and requirements governing the design and operation of the safety interlock system are outlined, namely:

- The aim of a safety interlock is to prevent injury or damage from radiation;
- The interlock must operate with a high degree of reliability (at least SIL-2);
- All components should be of high grade for dependability, long life, and radiation resistance;
- All circuits and components must be fail-safe (relay technology preferably);
- All cables must run in separate conduits, and all logic equipment must be mounted in locked racks to reduce the likelihood of accidental damage or deliberate tampering;
- Two independent chains of interlocks are required, where each interlock consists of two micro-switches in series, and each micro-switch consists of two contacts;
- Emergency-off buttons must be clearly visible in the dark and readily accessible, with reset performed locally;
- Emergency exit mechanisms must be provided at all doors;
- Warning lights must be flashing and an audible warning must be given inside radiation areas before the accelerator is turned on, as well as inside the control room;
- A radiation area search must be initiated before starting the accelerator, with "search start", "search confirmation" and "search complete" buttons provided along the path;
- Accelerator restarting must be prevented if the search is not performed in the correct order or if the time expires;
- The interlock system must ensure that the beam cannot be turned on until the audible and visual warning cycle has ended;

- Any violation of the radiation areas must trigger the interlock system. Restarting must be impossible before a new search;
- Access control procedures to accelerator vaults or tunnels must be implemented and monitored;
- Routine entry into accelerators is allowed through a turnstile and a gate controlled by a magnetic card reader connected to a PC;
- Accelerator restart is not possible unless there is parity between entries and exits.

19.4.1.6 Area classification

The classification of areas according to radiation protection criteria is mandatory, as it enables the regulation of access and the implementation of appropriate safety measures based on the potential exposure risk.

The definitions of classified areas, namely controlled and supervised areas, follow the standard radiation protection guidelines [3]:

- a radiation workplace defined as "controlled area" means an area subject to special rules for the purpose of protection against ionizing radiation or preventing the spread of radioactive contamination and to which access is controlled. Generally, it is a workplace where the exposure of workers is liable to exceed an effective dose of 6 mSv per year;
- a workplace is considered "supervised area" where the exposure of workers is liable to exceed an effective dose of 1 mSv per year, but does not exceed 6 mSv per year. Supervised area means an area subject to supervision for the purpose of protection against ionizing radiation;
- a workplace is considered "free access area" when the exposure worker cannot exceed the effective dose of 1 mSv/y, therefore supervision or other radiation protection controls are not required.

For the execution phase of the EuPRAXIA@SPARC_LAB project, the planned area classification is reported in Tab. 19.2.

Table 19.2: Area classification planned for the EuPRAXIA@SPARC_LAB facility.

Area	Classification
Linac tunnel Undulator tunnel	**prohibited area** during machine operation **controlled area** during no operation
FEL user area Modulator & Klystron gallery Experimental Halls	**supervised area** during machine operation **free access area** during no operation
THz Clean room Laser Sync.	**free access area** during machine operation **free access area** during no operation

The proposed classification will go through a comprehensive review upon licence approval process.

19.4.2 Radiation protection evaluations

This section presents all radiation-protection assessments carried out for the LINAC and undulator tunnel shielding design, as well as for the beam dumps foreseen for the facility. The “operating parameters” adopted for the various evaluations are first introduced, together with the shielding-design criteria applied. Subsequently, the source terms considered in the radiological analyses are described, while the detailed results of the evaluations are provided at the end of this section.

19.4.2.1 Operating parameter

The EuPRAXIA@SPARC_LAB project consists of an XUV Free Electron Laser facility in which an electron beam, transported by a linear accelerator with an average current of 50 nA (50 W), is accelerated up to an energy of 1 GeV , as extensively described in the Beam Physics Chapter 3.
All radiological protection assessments have been carried out following a conservative approach based on these operating conditions. The main objective was to maintain the doses below 1 µSv/h, within the areas beyond the shield which will be frequently accessed by the staff, and within 0.25 µSv/h within the areas outside the shield which will be accessible to members of public or not exposed worker, thus ensuring that the bunker surrounding areas will be classified as free-access or, at most, supervised zones.
In greater detail, the operational parameters used for the shielding and beam dump design are summarized in Table 19.3.

Table 19.3: Operational parameter considered for radiation protection evaluations.

	Energy E	**Charge** Q	**Frequency** f	**Average current** $\bar{I}$
Shielding	1.2 GeV	500 pC	100 Hz	50 nA
Diagnostic Beam Dump n.1	300 MeV	500 pC	15 Hz	7.5 nA
Diagnostic Beam Dump n.2	800 MeV	500 pC	2 Hz	1 nA
Diagnostic Beam Dump n.3	1.2 GeV	500 pC	1 Hz	1 nA
FEL Beam Dump	1.2 GeV	300 pC	100 Hz	30 nA
Driver Beam Dump	600 MeV	400 pC	100 Hz	40 nA

With reference to Table 19.3:

- the lateral shielding design was dimensioned assuming a 5% electron beam loss on an optimized target (see Section 19.4.2.2);
- for the diagnostic beam dumps (see Section 19.4.3.3), different beam energies were considered, depending on their position along the beamline. For these dumps, the frequency reported in the table refers to the maximum operational repetition rate that allows the surrounding areas to remain classified as free-access, or at most, supervised zones;
- the Full RF operation mode was considered for the FEL beam dump, as it represents the most radiologically critical condition (Section 19.4.3.6);
- for the driver beam dump (Sec. 19.4.3.7), the expected beam characteristics described in the Chapter 3, and reported in Table 19.3 were used. In particular, the beam energy reported in the table corresponds to the maximum energy within the driver's electron spectrum.

It is important to note from Table 19.3 that some parameters differ from the nominal operating conditions of the machine—specifically, an energy of 1.2 GeV (instead of 1 GeV) and a driver charge of 300 pC (instead of 200 pC). These values were selected to ensure that the following evaluation remains conservative, thereby covering potential future upgrades or operational enhancements of the machine.

19.4.2.2 Shielding Approach and Design Criteria

The facility general layout has been presented in Chapter 4, and the shielding evaluation has been carried out using the parameters described above. Owing to the several precautionary assumptions introduced, the resulting estimates represent conservative upper bounds on the expected dose rates under operational conditions. These assumptions will be verified during the commissioning phase, and additional protective measures will be implemented if required.

The shielding design criteria has been based on the Italian legislation requirements (Sec. 19.2.3), that include the European Directives as well as the recent ICRP recommendations [3]. According to these documents, the individual dose limit is 20 mSv/y for radiation exposed worker, and 1 mSv/y for the public and not exposed worker.

Taking into account the dose levels normally found around accelerators, the shielding thickness was dimensioned to maintain the doses below 1 μSv/h, within the areas beyond the shield which will be frequently accessed by the staff, and within 0.25 μSv/h within the areas outside the shield which will be frequently accessed by public or not exposed worker. A shifting from these values could at most change the radiation classification of some areas. In normal working condition the dose rate outside shielding should not exceed a fraction of μSv/h.

19.4.2.3 Radiation Source Terms

For shielding evaluation purposes several components of the radiation field have to be considered [4–6], which are produced when an electron beam with an energy of hundred of MeV impacts a vacuum chamber wall or a thick target. The fields present when the facility is working are called prompt radiation: these are bremsstrahlung photons, neutrons, muons and gas bremsstrahlung. Other radiation field, produced when the facility is not working, is composed by the photons emitted by activated materials.

Bremsstrahlung

Prompt photon fields, produced by Bremsstrahlung, constitute the most important radiation hazard from high energy electron accelerators with thin shielding. Bremsstrahlung yield is very forward peaked, and increasingly so with increasing energy. The half emission angle, expressed in degree, in the forward direction is described through the following equation:

$$\theta_{1/2} = 100/E_0 \tag{19.1}$$

where E_0 is the initial electron energy expressed in MeV. An optimized “thick target” - a target of sufficient thickness to maximize bremsstrahlung production - was considered in order to evaluate the shield thickness. Photon yield from a thick target as a function of the angle is composed by two components: sharply varying forward component, described in Equation 19.1, and a mildly varying wide-angle component. Forward peaked bremsstrahlung contains the most energetic and penetrating photons, while bremsstrahlung at wide angles is much softer. The source term (per unit beam power) for bremsstrahlung at 90° is independent of energy differently from the peak component, that depends linearly from it.

Neutrons

Photons have larger nuclear cross-sections than electrons, so neutrons and other particles resulting from inelastic nuclear reactions are produced by the bremsstrahlung radiation. Neutrons from photonuclear reactions are outnumbered by orders of magnitude by electrons, positrons and photons emerging from the electromagnetic shower. However, some of these neutrons constitute the most penetrating component for radiation fields behind thick shielding. Depending on the photon energy, three different photon neutron productions can occur: giant resonance, pseudo-deuteron and photo-pion production.

- **The giant resonance production**
  This process can be subdivided in two steps:
  1. the nucleus excitation by photon absorption;
  2. the subsequent de-excitation by neutron emission, where memory of the original photon direction has been lost.

  The cross-section has a maximum around 20-23 MeV for light nuclei (mass number A $\leq$ 40) and 13-18 MeV for heavier nuclei. The angular yield of giant resonance neutrons is nearly isotropic. The giant resonance constitutes the primary mechanism responsible for photoneutron production in electron accelerators across all electron-energy regimes.
- **Pseudo-deuteron production**
  At photon energies beyond the giant resonance, the photon is more likely to interact with a neutron-proton pair rather than with all nucleons collectively. This mechanism is important in the energy interval of 30 to $\sim$ 300 MeV, contributing to the high-energy end of the giant resonance spectrum. Because the cross-section is an order of magnitude lower than giant resonance, with the added weighting of bremsstrahlung spectra, this process never dominates.
- **Photo-pion production**
  Above the threshold of $\sim$140 MeV, pions production (and other particles) becomes energetically possible. These pions then generate secondary neutrons as byproduct of their interactions with nuclei. While substantially less numerous than giant resonance neutrons, the photopion neutrons are very penetrating representing the component of the initial radiation field from a target (with the exception of muons at very high energies) that determines the radiation fields outside very thick shields.

Muons

Muon production is analogous to e^+/e^- pair production by photons in the field of target nuclei when photon energy exceeds the threshold $2m_\mu c^2 \approx 211$ MeV. Above a few GeV the muon yield per unit electron beam power become approximately proportional to electron energy E_0. Muon angular distribution is extremely forward-peaked, and this distribution narrows further with increasing energy. At energies of a few GeV adequate photon and neutron shielding will be also sufficient for muons.

Gas Bremsstrahlung

The gas bremsstrahlung is produced by the interaction of the electron beam with residual low-pressure gas molecules in the vacuum pipe. Bremsstrahlung on residual gas is one of the main cause of beam loss in a storage ring and may represent a radiation hazard at synchrotron radiation facilities. In literature, this type of radiation has been thoroughly investigated at circular storage rings, where the average beam current is much more intense. It is mainly in the straight section that a radiation problem could arise, since pointing toward the corresponding photon beam line. At EuPRAXIA@SPARC_LAB the straight length where gas bremsstrahlung is produced correspond to the FEL line, at least 38 m long, as shown in Machine Layout Chapter 4, cause the chicane presence along the LINAC structure. According to calculation methods available in the literature [7, 8], and under worst-case emission conditions, the gas bremsstrahlung contribution to the ambient dose is estimated to be approximately 60 nSv/h. Although this value is negligible, a dedicated absorber will nonetheless be implemented in order to fully suppress this component.

Induced Activity

When the accelerator facility is turned off, the radiation level is strongly reduced and only the induced material activation remains. Personnel exposure from radioactive components is of concern mainly around beam lines, collimators, slots, beam stopper or beam dump, where the entire beam -

or a large fraction of it - is dissipated continuously, while unplanned beam losses result from beam mis-steering due to inaccurate orbit adjustment or devices failure.
Beam losses induce activation in machine component as well as in:

- the metallic structures, such as stainless steel vacuum chamber, copper RF structure (^{60}Co, ^{54}Mn, ^{51}Cr, ^{46}Sc, ^{22}Na, ^{11}C, ^{7}Be);
- the cooling water (^{3}H, ^{7}Be, ^{15}O, ^{13}N, ^{11}C);
- the air (^{15}O, ^{13}N, ^{38}Cl, ^{41}Ar);
- the concrete walls (^{152}Eu, ^{154}Eu, ^{134}Cs, ^{60}Co, ^{54}Mn, ^{22}Na).

The activation of soil as well as the groundwater by neutrons and other secondary particles can have an environmental impact, but at electron accelerators the radioactivity levels are generally low and absolutely negligible, considering the given beam parameters.
A more precise evaluation is in progress, following the final definition of the beam parameters and the beam losses and the characteristic of cooling water system, the air circulation system and the beam dump layout. Furthermore, depending on the water cooling system to be implemented, a dedicated drainage network will be installed. In the event of system failure, this network will channel any potentially activated water into dedicated collection tanks, ensuring safe containment and handling.

Beam line local shielding design

The local shielding will be designed along the beam line, or in any sensitive part, once the facility commissioning starts.

19.4.3 Lateral shielding and beam dumps design

19.4.3.1 Lateral shielding design

For the LINAC and undulator tunnel lateral shielding designs, a conservative approach was adopted. This approach assumes the incidence of an electron beam, with characteristics reported in Table 19.3, on an optimized target (Section 19.4.2.3).

The dose estimation for the various radiation field components was performed using the Swanson rules of thumb [4–6], which allow the absorbed dose to be quantified as a function of the beam power deposited on the target.

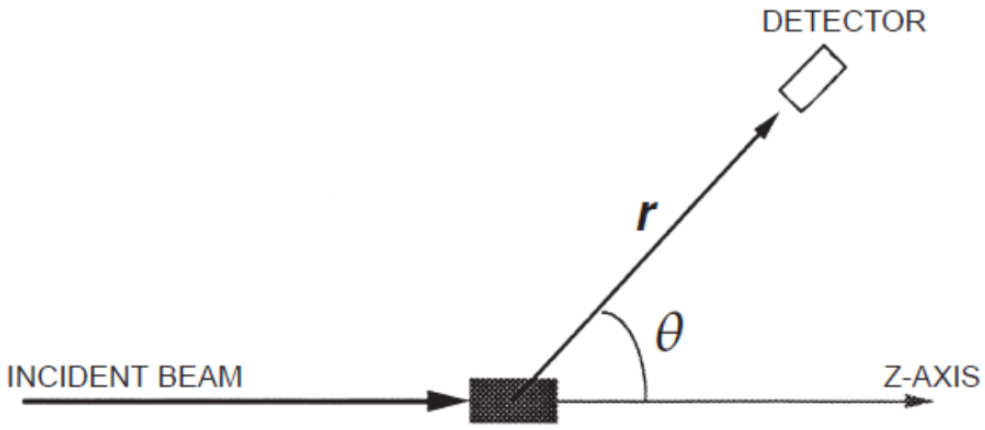

Figure 19.8: Irradiation geometry considered for the lateral shielding evaluation.

Assuming a loss of 5% of the total beam power on the optimized target (Fig. 19.8), it was

possible to quantify the expected dose under unshielded conditions at 90°. Based on this, using appropriate attenuation coefficients [9], the dose attenuation as a function of the ordinary concrete thickness was evaluated (Fig. 19.9 and 19.10).

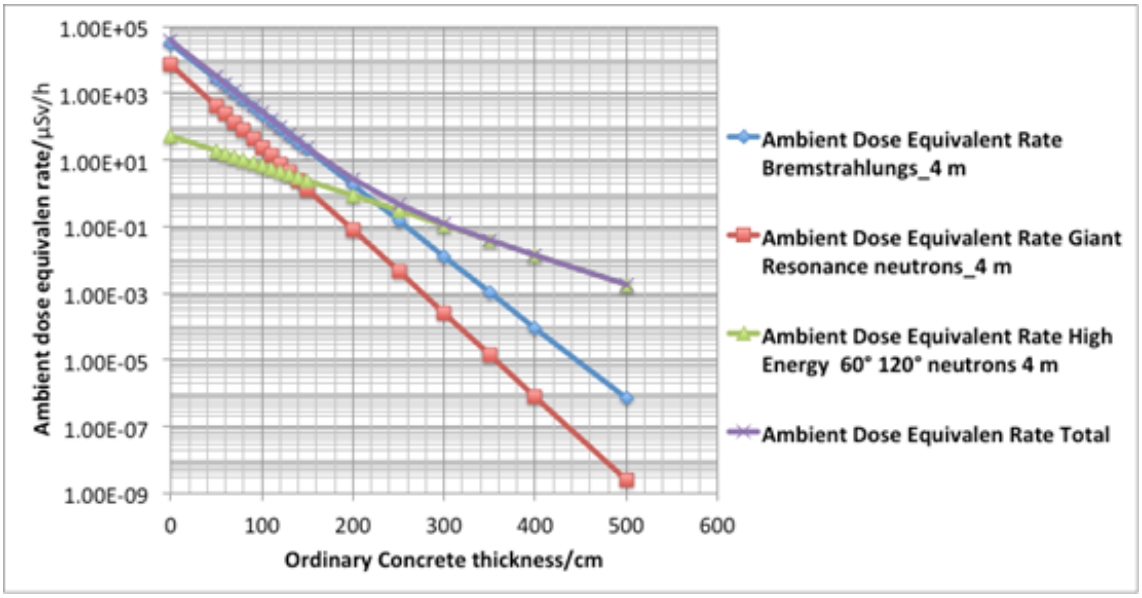

Figure 19.9: Ambient dose equivalent rate (4 m - 90°).

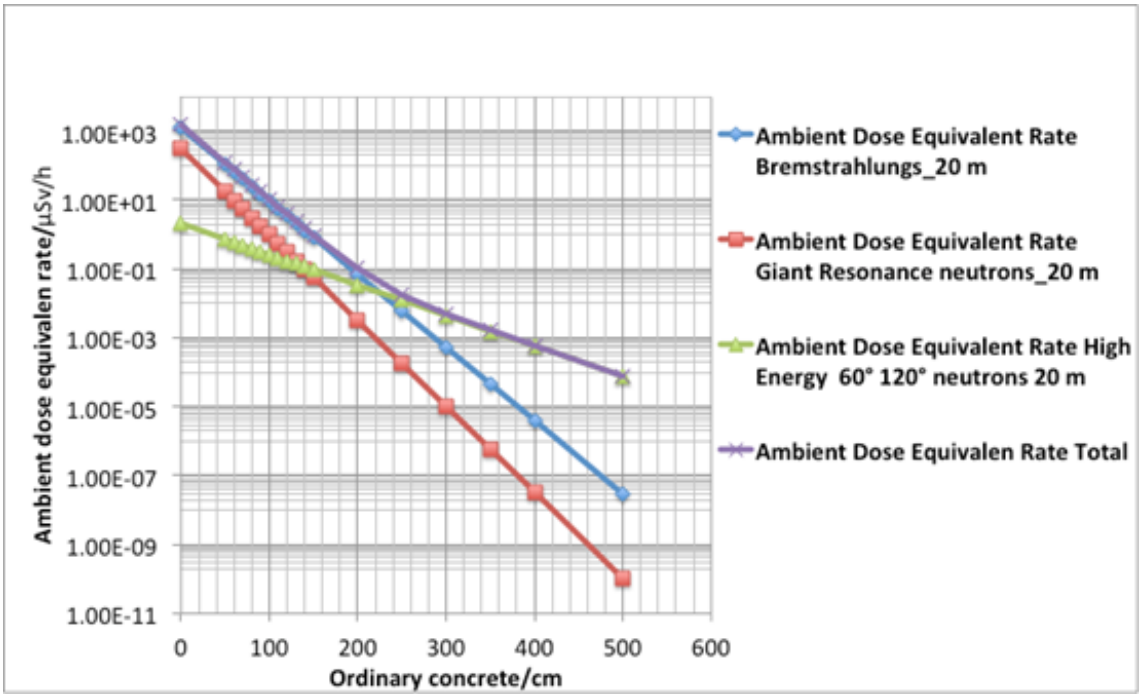

Figure 19.10: Ambient dose equivalent rate (20 m - 90°).

This attenuation was evaluated to estimate the dose in areas adjacent to the bunker (4 m – Fig. 19.9) and in areas outside the shielding (20 m – Fig. 19.10). The results show that a concrete thickness of 2 meters ensures compliance with radiation protection requirements discussed in Sec. 19.4.2.2.

19.4.3.2 Electron Beam Dump design

The beam dump is a dedicated device designed to fully absorb a beam particle during various operation phases. Its structure must be highly optimized to control the dose contributions arising from the beam–dump interaction. The design is strongly dependent on the incident particles type, their energy, and the average beam current. It is essential to distinguish between two main dump categories: diagnostic and main ones.

- The diagnostic beam dump is intended to absorb the primary beam during measurement and diagnostic operations, such as charge, energy, or emittance checks. The beam current directed onto this structure can be adjusted as needed, primarily for radiation protection purposes or to meet diagnostic requirements;
- The fixed beam dump, on the other hand, is designed to absorb the beam during standard operation, excluding diagnostic phases. In this case, the beam current cannot be modified at will, so the dump must be dimensioned to comply with all radiation protection requirements at full beam power.

The design and dosimetric assessments for the beam dumps planned for our facility have been performed using Monte Carlo simulations with the FLUKA - INFN code [10–12].

19.4.3.3 Diagnostic Beam Dumps

The EuPRAXIA@SPARC_LAB facility includes three diagnostic beam dumps, positioned along the beamline at the end of different acceleration stages of the S-band and X-band LINAC structures, described in Facility Layout Chapter 4.

The first two dumps are designed to interact with 300 and 800 MeV electron beam, respectively, and these are tilted horizontally at 22° with respect to the beam line axis. The third one, which will interact with a 1.2 GeV beam, is located before the undulator tunnel and it is characterize by an inclination of 25°. All three dumps have the same structural design (Fig. 19.11), featuring cylindrical symmetry, with overall dimensions of 104 cm in diameter and 125 cm in length.

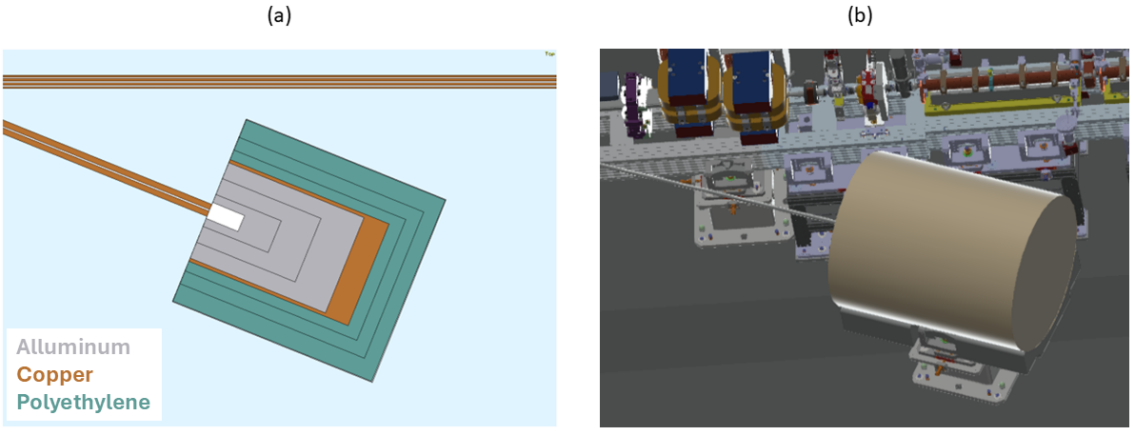

Figure 19.11: Diagnostic beam dump layout in 2D (a) and 3D (b).

From a construction standpoint, each diagnostic beam dump is composed of:

- an aluminum core, used to obtain the complete electromagnetic cascade development, minimizing the number of photons produced and consequently of the photoneutrons;
- a copper layer, placed immediately downstream of the core and surrounding it, serving the dual purpose of attenuating the forward-directed electromagnetic component and enhancing heat dissipation resulting from beam absorption;
- a polyethylene cover, needed to attenuate, moderate and absorb the different neutron component emitted by the photo-production reactions;

- a few millimeters of aluminum, covering the polyethylene are used to prevent potential fire hazards associated with the plastic material.

The structure has been optimized to ensure an ambient dose equivalent rate beyond the shielding below 0.25 µSv/h, in order to maintain the surrounding areas classification as free access zones or, at most, as supervised ones.

19.4.3.4 Diagnostic Beam Dump FLUKA simulation

The simulated environment, used in the FLUKA simulations, include the complete building geometry, that means bunker, adjacent areas and air ducts ones, obtained from the technical design (Fig. 19.12).

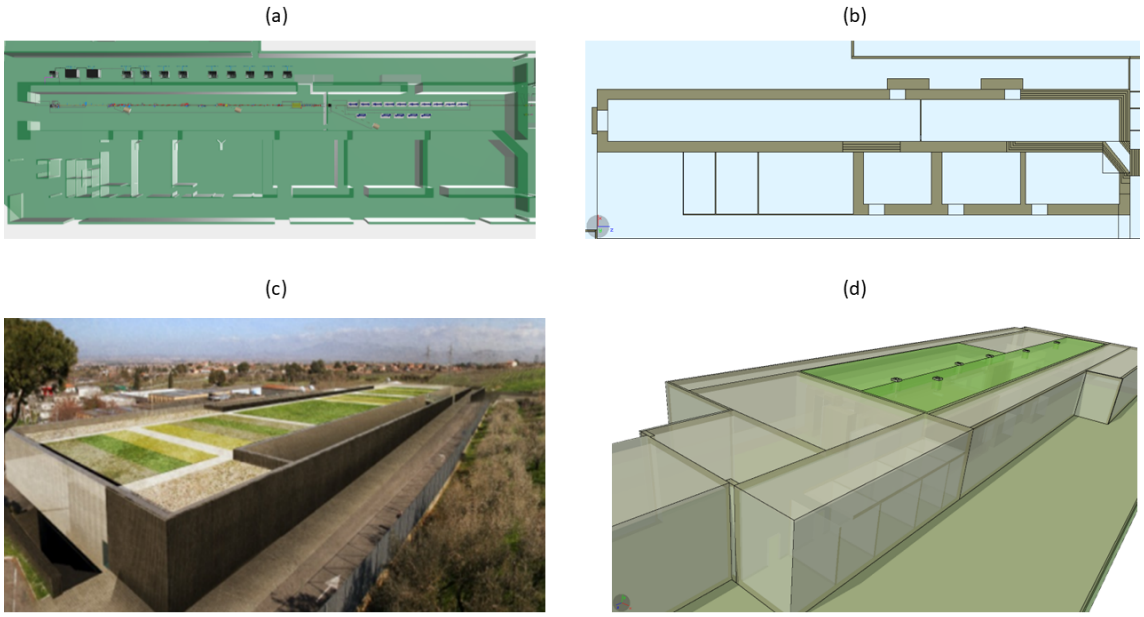

Figure 19.12: Technical and simulated layout in 2D (a-b) and 3D (c-d).

A dedicated FLUKA simulation was performed for each beam dump. The incident beam used was modeled as a pencil beam with a radius of 10 µm and a spot size of 3.14×10^{-6} cm^2, impinging orthogonally on the beam dump, to reflect the typical beam extraction geometry during diagnostic procedures. The measurement points considered in the simulations are shown in Fig. 19.13, and their references are listed in Table 19.4.

Preliminary studies, carried out under the irradiation conditions reported in Table 19.1, indicate that the maximum repetition rates ensuring that the surrounding areas remain classified as free-access or, at most, supervised zones are 15 Hz for a 300 MeV beam, 2 Hz for 800 MeV, and 1 Hz for 1.2 GeV.

Therefore, a repetition rate of 1 Hz will be proposed as the recommended operational setting for diagnostic cases, and it is the basis for all subsequent dose evaluations.

The Figures from 19.14 to 19.19 show the total ambient dose equivalent rate spatial distribution H*(10), obtained for the three diagnostic beam dump scenarios (see Tab. 19.3), while the resulting ambient dose equivalent rates at relevant locations are summarized in Table 19.5.

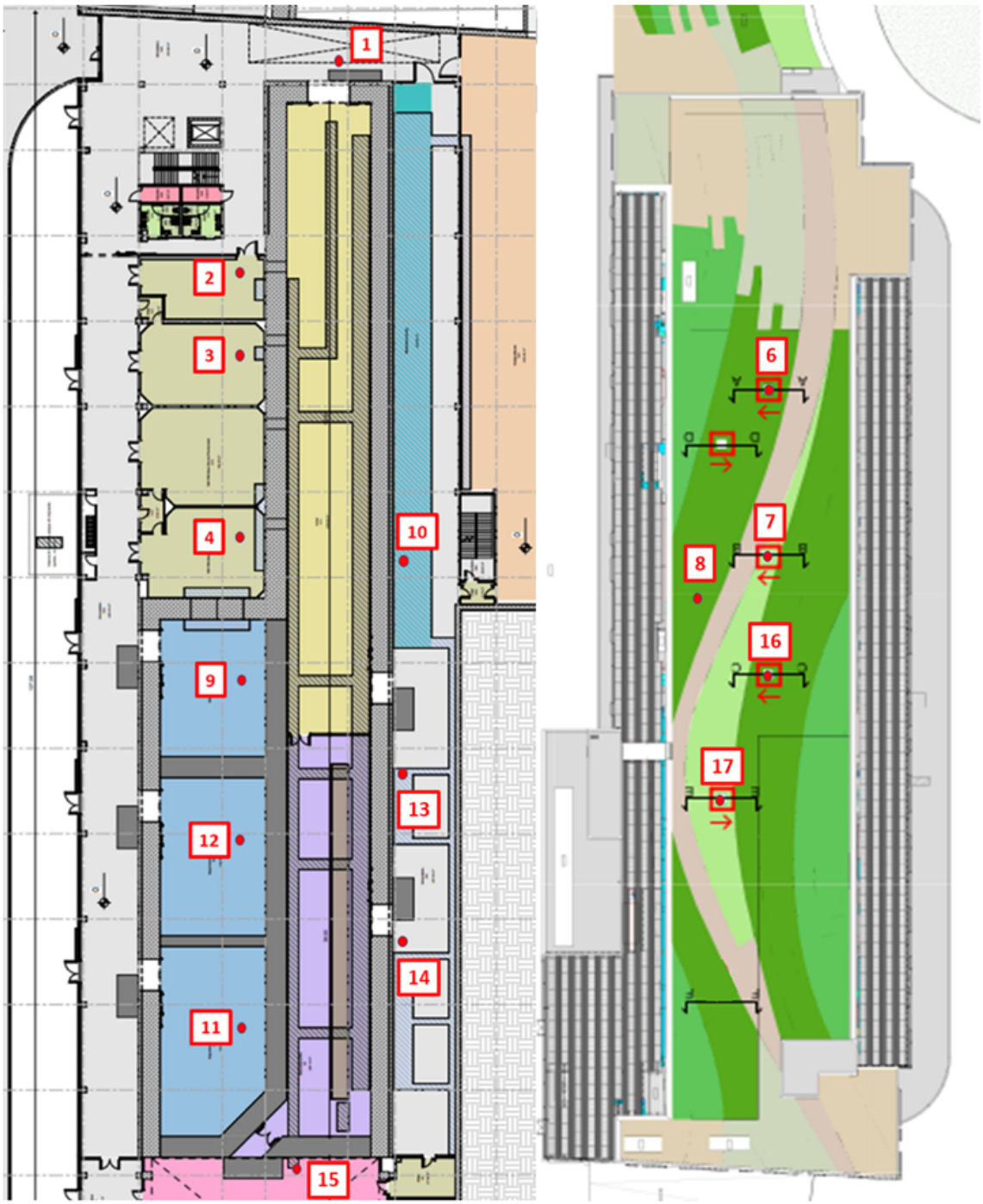

Figure 19.13: Measurement points - diagnostic beam dump simulations.

Table 19.4: Measurement point - Diagnostic Beam Dump Simulation.

Point	Place
1	Circulation 1
2	THz
3	Laser Sync.
4	Clean room
5	Offices
6	Air duct 1
7	Air duct 2
8	Roof
9	Experimental Hall 1
10	Modulator & Klystron Gallery
11	Experimental Hall 2
12	Experimental Hall 3
13	Circulation 2
14	Circulation 3
15	Front end
16	Air duct 3
17	Air duct 5

300 MeV Beam Dump

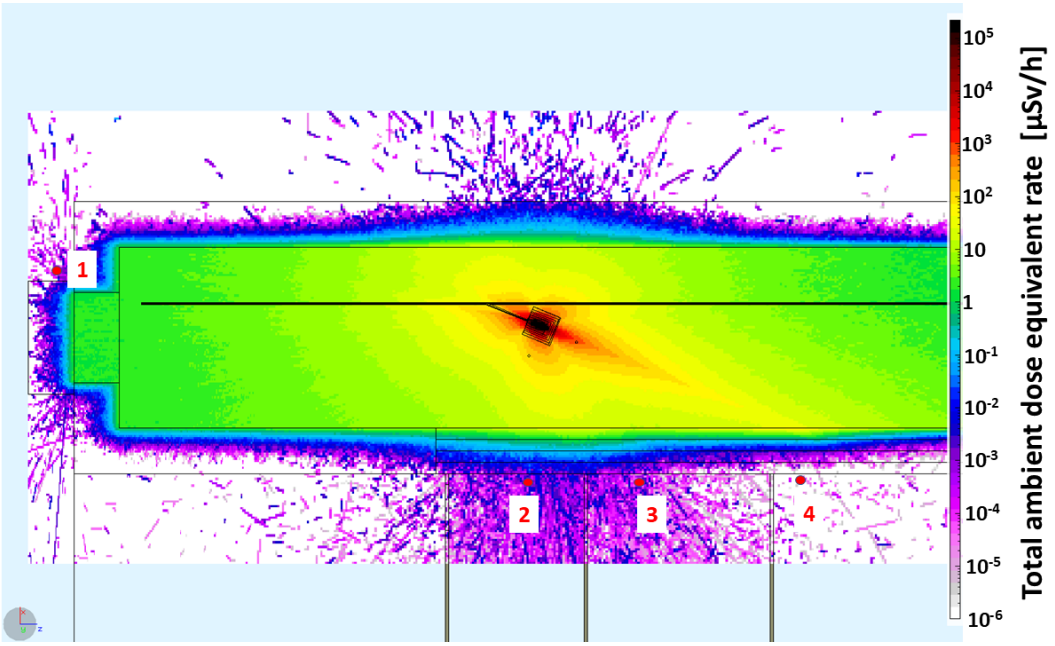

Figure 19.14: H*(10) - 300 MeV diagnostic beam dump - xz plane.

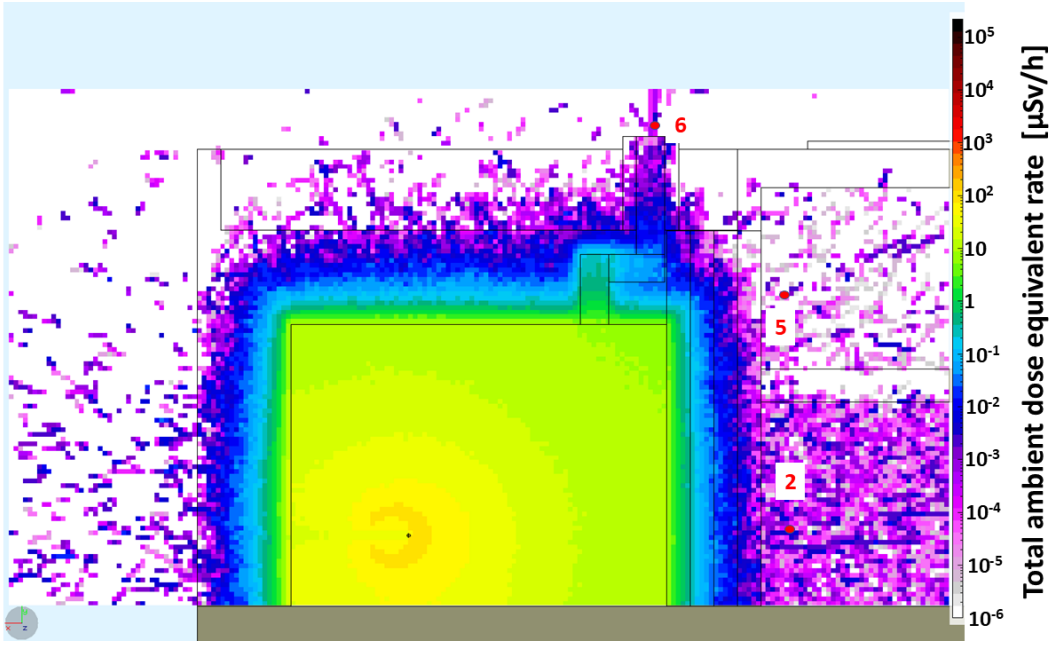

Figure 19.15: H*(10) - 300 MeV diagnostic beam dump - xy plane.

800 MeV Beam Dump

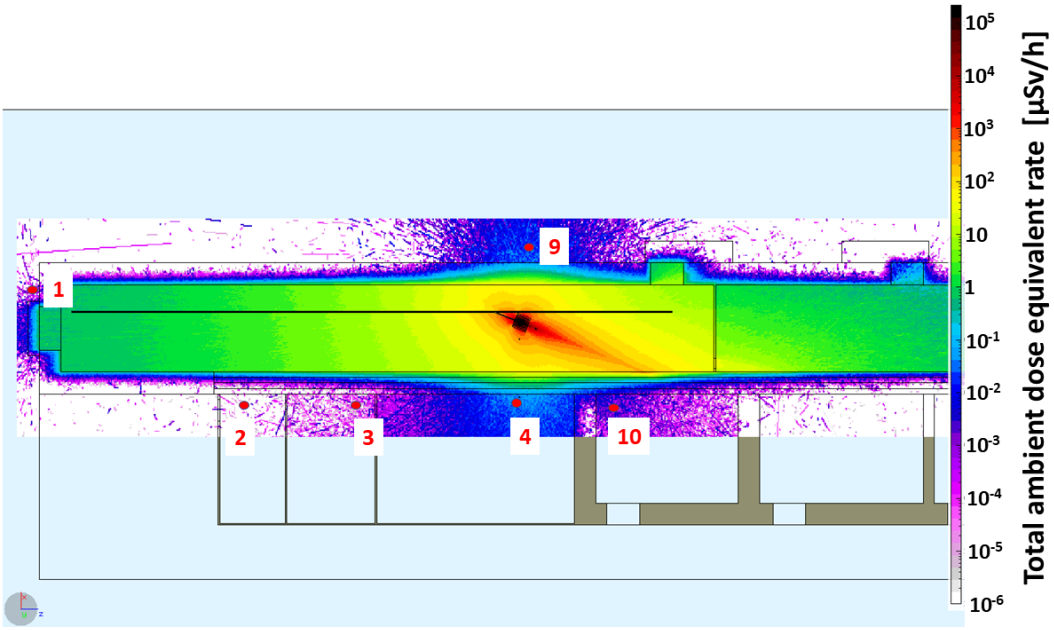

Figure 19.16: H*(10) - 800 MeV diagnostic beam dump - xz plane.

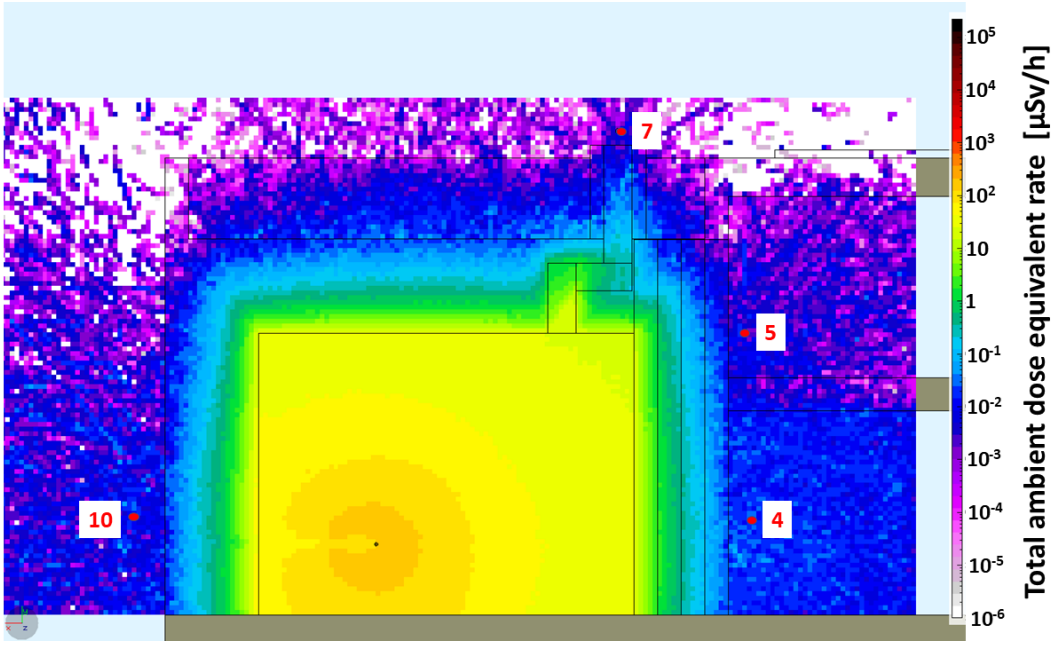

Figure 19.17: H*(10) - 800 MeV diagnostic beam dump - xy plane.

1.2 GeV Beam Dump

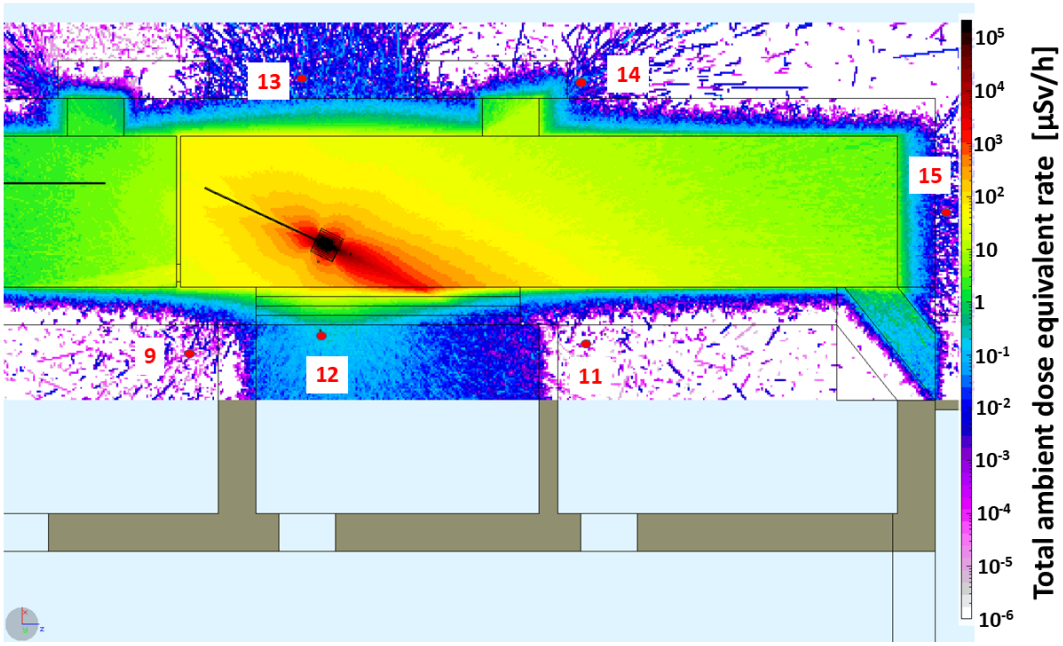

Figure 19.18: H*(10) - 1.2 GeV diagnostic beam dump - xz plane.

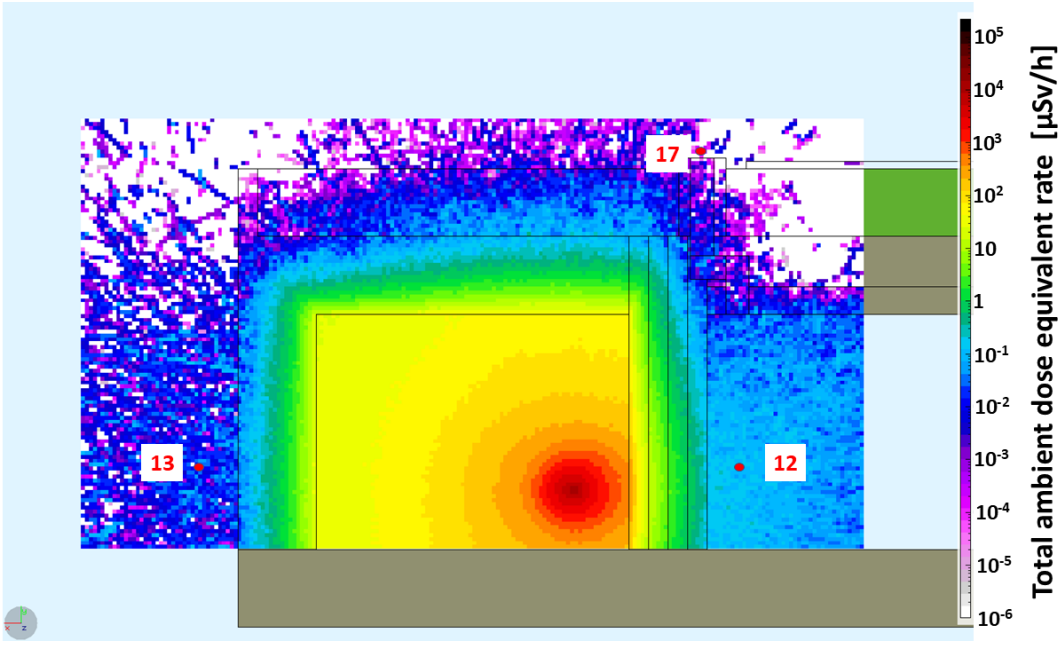

Figure 19.19: H*(10) - 1.2 GeV diagnostic beam dump - xy plane.

Table 19.5: H*(10) values for diagnostic scenarios.

Point	H*(10) [µSv/h] 300 MeV	H*(10) [µSv/h] 800 MeV	H*(10) [µSv/h] 1.2 GeV
1	3.37×10^{-3}	7.87×10^{-3}	
2	1.12×10^{-2}	2.25×10^{-3}	
3	3.37×10^{-3}	3.37×10^{-3}	
4	1.12×10^{-3}	8.99×10^{-3}	
5	2.25×10^{-3}	2.25×10^{-2}	
6	1.12×10^{-3}	4.49×10^{-4}	
7	2.25×10^{-4}	1.12×10^{-2}	
8	3.37×10^{-3}	8.99×10^{-3}	3.37×10^{-2}
9		8.99×10^{-3}	8.99×10^{-3}
10		5.62×10^{-2}	
11			6.74×10^{-3}
12			1.57×10^{-1}
13			1.01×10^{-1}
14			6.74×10^{-2}
15			3.37×10^{-2}
16			1.12×10^{-3}
17			4.49×10^{-3}

From the previous Fig. from 19.14 to 19.19 and the Tab. 19.5, it is evident the total ambient dose equivalent rate values remain under 0.15 µSv/h in the surrounding zones beyond the shield, for all the diagnostic beam dump cases analyzed.

19.4.3.5 Fixed Beam Dump

This section presents the simulations concerning the two planed fixed beam dumps: one positioned at the end of the FEL AQUA beamline and another designed to completely absorb the driver during the plasma acceleration stage.
The placement of these structures affects several areas beyond the shielding, during irradiation conditions. Therefore, although they may be irradiated simultaneously during the plasma acceleration stage, it is possible to perform two independent and separate evaluations, as will be highlighted in the following sections.

19.4.3.6 FEL Beam Dump (AQUA beamline)

The FEL beam dump has been designed as fully buried, installed at an inclination of 30° with respect to the floor, and located downstream of the AQUA beamline undulators.
Its structural design shows small differences from the diagnostic one, features a cylindrical symmetry with a diameter of 150 cm and a length of 160 cm, as schematically illustrated in Fig. 19.20. The difference from the diagnostic beam dumps consists in a lead layer, placed between the copper and polyethylene one, used to further attenuate the forward and high energy photons component emitted by the electromagnetic cascade.

The structure described above has been optimized to absorb the electron beam under RF-only operating conditions, as these represent the most demanding case from a radiological protection

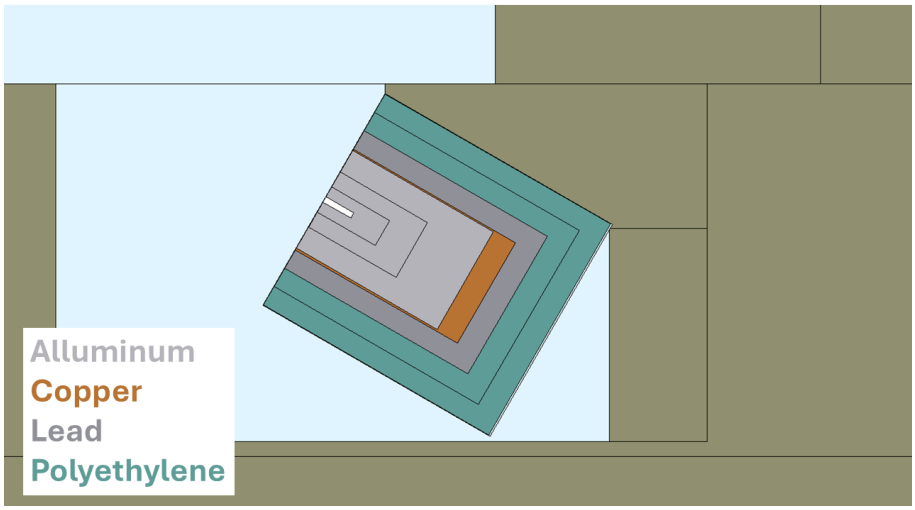

Figure 19.20: FEL Beam Dump (AQUA beamline) layout on yz plane.

standpoint. In fact, in the plasma acceleration mode, the charge impinging on the beam dump decreases by almost one order of magnitude, as described in Beam Physics Chapter 3. The irradiation parameters used in FLUKA simulations are summarized in the Table 19.4.
This simulation aim to evaluate the expected ambient dose equivalent rate spatial distribution extended to the area of interest and for seven measurement points, placed around the undulator tunnel as shown in Fig. 19.21 and detailed in Tab. 19.6.

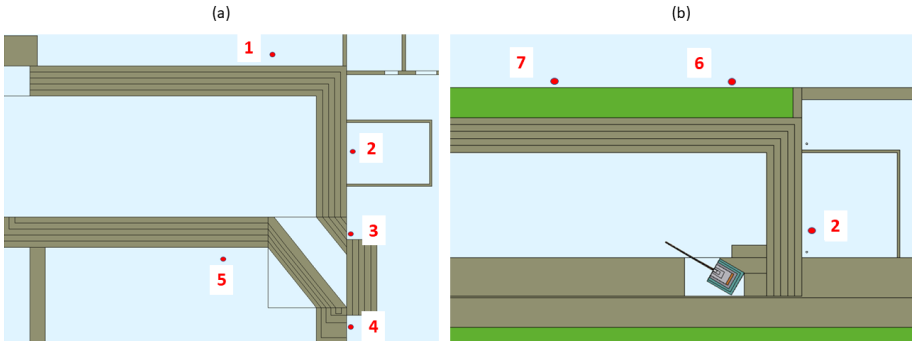

Figure 19.21: Measurement points - FEL beam dump FLUKA simulation on xz (a) and yz (b) plane.

Table 19.6: Measurement point - FEL Beam Dump Simulation.

Point	Place
1	Circulation 3
2	Front end
3	Experimental Hall 3
4	FEL user area 1
5	FEL user area 2
6	Roof
7	Air duct 3

The corresponding spatial distribution for the Full RF acceleration case is shown in Fig. 19.22 and Fig. 19.23, while the resulting ambient dose equivalent rates at the defined measurement points are summarized in Tab. 19.7.

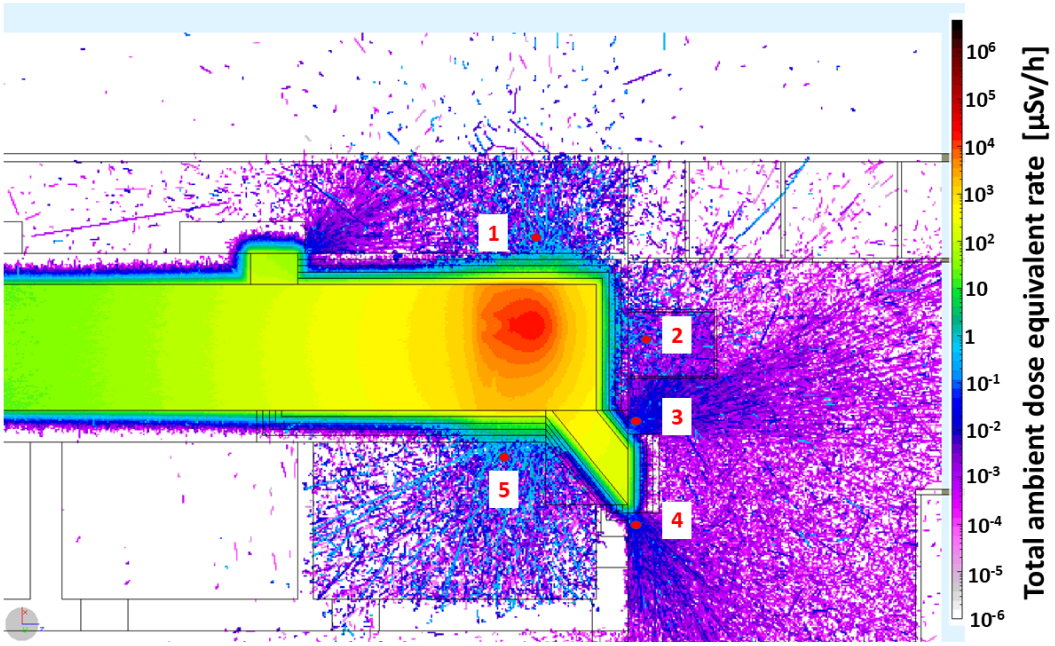

Figure 19.22: H*(10) - FEL beam dump - without plasma acceleration - xz plane.

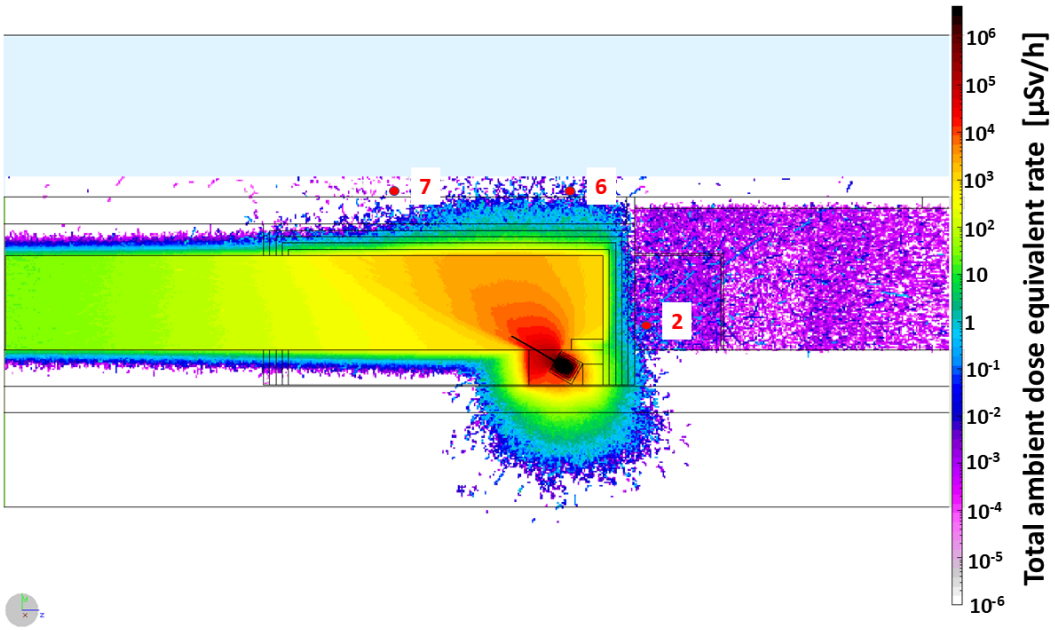

Figure 19.23: H*(10) - FEL beam dump - without plasma acceleration - yz plane.

Table 19.7: H*(10) - FEL beam dump - only RF scenario.

Point	H*(10) [µSv/h]
1	3.71×10^{-1}
2	5.93×10^{-2}
3	1.48×10^{-1}
4	5.93×10^{-2}
5	1.11×10^{0}
6	1.20×10^{-1}
7	4.80×10^{-2}

From the Fig. 19.22 to 19.23 and Tab. 19.7 it is possible to note as the ad hoc beam dump structure proposed for these configuration modes, ensure ambient dose equivalent rate values less then 1.1 µSv/h, avoiding any area classification change.

19.4.3.7 Driver Beam Dump

Another type of fixed beam dump, dedicated to absorbing the driver electron bunches, is located near the capillary section for plasma acceleration. In the FLUKA simulation the separating septum (described in Magnets Chapter 17) was implemented ensuring the driver–witness separation along the chicane, in order to take into account all relevant variables. More specifically the corresponding magnetic field map was also included, in addition to the geometric features. The expected driver spectrum, described in Beam Physics Chapter 3 and shown in Fig. 3.11, was used as the source term in the simulations, in order to take into account both its deflection and its energy spread. Furthermore, conservative irradiation conditions were assumed (Tab. 19.4).
The driver beam dump is composed of:

- an aluminum core, ensuring the full development of the electromagnetic cascade while minimizing photoneutron production;

- a copper layer surrounding the core, designed both to absorb the forward spike of the electromagnetic shower and to enhance heat dissipation outward;
- a local concrete shielding surrounding part of the inner layers.

The local concrete shielding is essential not only to attenuate the prompt radiation components produced in the driver–dump interaction, but also to mitigate the photon contributions arising from the activation of the inner layers structure. The proposed design includes approximately 50 cm of concrete in all directions, including the ceiling, with the only exception being the beamline axis, which remains open due to geometrical constraints. Nevertheless preliminary conservative estimates of dose contributions from dump activation indicate no critical values, and any residual contributions can be adequately managed through controlled access during potential maintenance operations. The beam dump schematic layout is shown in Fig. 19.24.

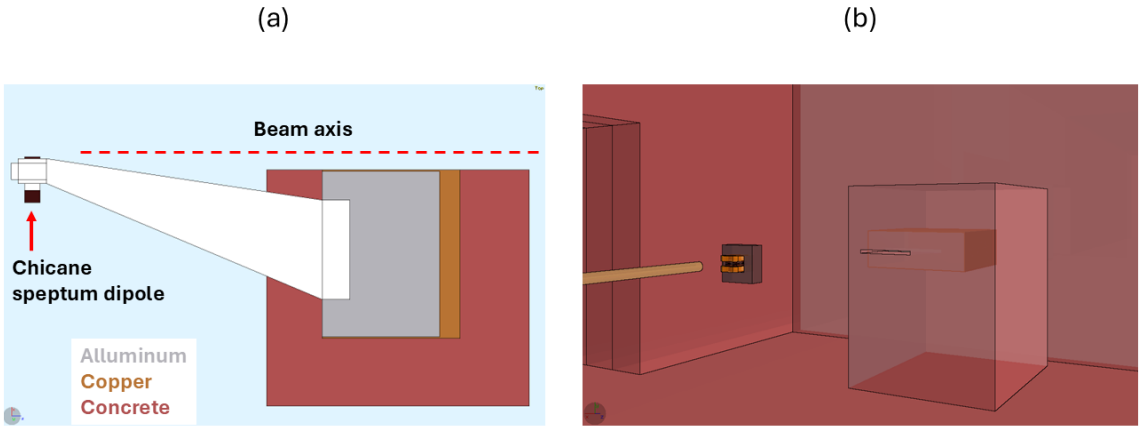

Figure 19.24: Driver beam dump layout 2D (a) and 3D (b).

These simulations are focused on the ambient dose equivalent rate spatial distribution extended to the area of interest and for three measurement points, placed as shown in Fig. 19.25 and detailed in Tab. 19.8.

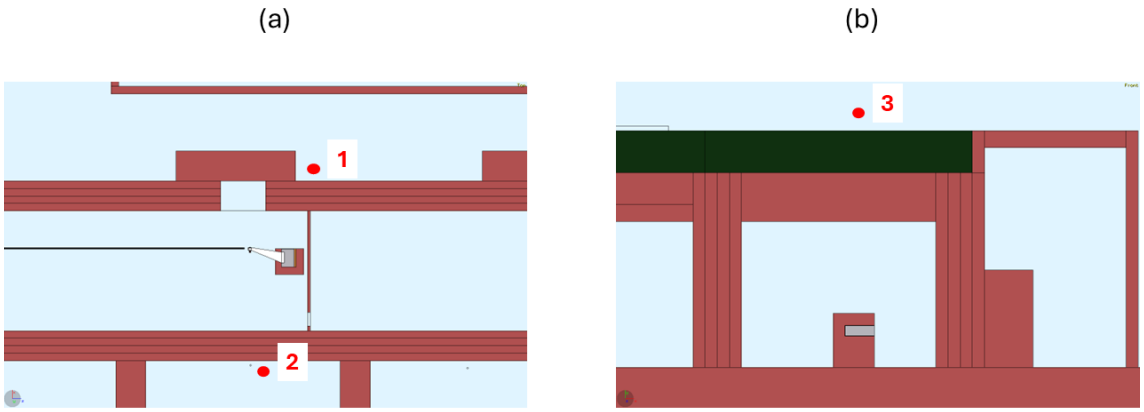

Figure 19.25: Measurement points - driver beam dump simulations on xz (a) and xy (b) plane.

Table 19.8: Measurement point - Driver Beam Dump Simulation.

Point	**Place**
1	Modulator & Klystron gallery
2	Experimental Hall 2
3	Roof

The spatial distributions of the ambient dose equivalent rate are reported in Fig. 19.26 and 19.27, while the dose in the measurement points in Tab. 19.9.

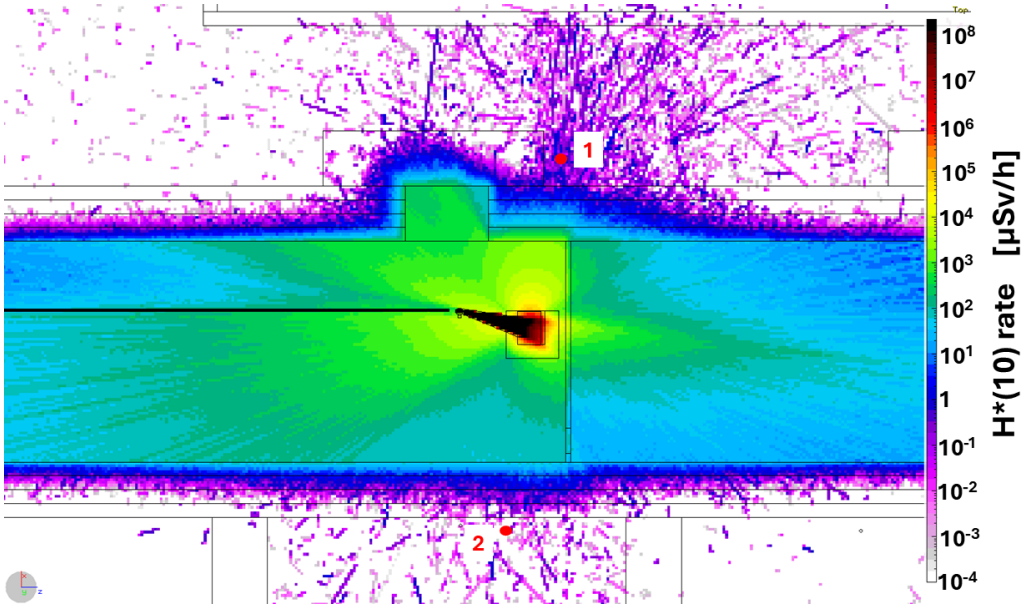

Figure 19.26: H*(10) - driver beam dump - xz plane.

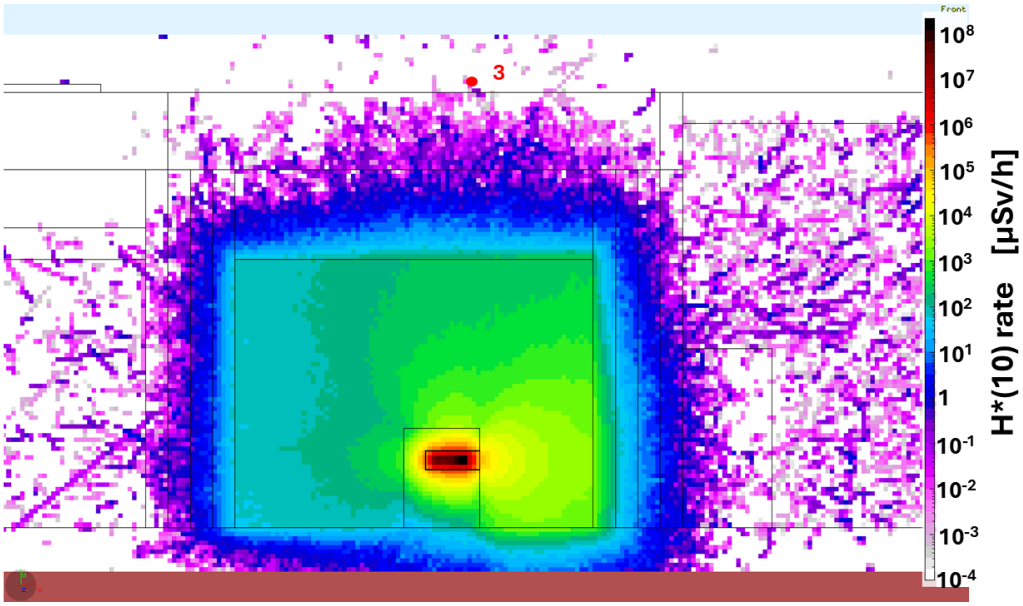

Figure 19.27: H*(10) - driver beam dump - xy plane

Table 19.9: H*(10) values - Driver Beam Dump

Point	H*(10) [µSv/h]
1	8.0×10^{-1}
2	1.1×10^{-1}
3	3.2×10^{-3}

The results presented in Tab. 19.9 and in the Fig. 19.26 and 19.27 demonstrate that the proposed driver beam dump design ensures ambient dose rates below 1 µSv/h in the bunker surrounding

areas, fully compliant with the project requirements.

19.4.4 Other Radiation Sources

RF power is provided by a number of RF station (Modulator and Klystron) operating at different frequencies and peak power level, as reported in Tab. 13.2.
The klystrons will arrive already self shielded from factory. Additional shield will be installed in order to eliminate and/or to reduce radiation escape. An interlocked fence around klystrons area is foreseen in order to reduce as low as possible the radiation level behind the fence and avoid the presence of personnel around these source.

19.5 Functional Safety

Given the complexity of the devices integrated into the EuPRAXIA@SPARC_LAB accelerator and the cutting-edge nature of the technologies involved, the implementation of Instrumented Safety Systems (SIS), namely the Personnel Safety System and the Machine Protection System, is essential to ensuring the safety of personnel and the protection of critical equipment. A SIS is a combination of hardware and software used to implement Safety Instrumented Functions (SIF) in accordance with the international standard IEC-61508 [13]. Each SIF is classified with a Safety Integrity Level (SIL), which is required to define and quantify the functional safety of the EuPRAXIA@SPARC_-LAB safety systems under design. The PSS is tasked with minimizing the risk of accidental exposure of personnel to ionizing radiation within the accelerator facility. The MPS continuously monitors interlocks, reacts promptly to any anomalies and it also supports optimization procedures through dedicated software routines. The development workflow of both systems is carried out in compliance with the Conventional Safety and Radiation Safety Requirements described in the previous sections (see Figure 19.1).

19.5.1 Compliance and Risk Assessment Procedure

Both the PSS and MPS are classified as SIS in accordance with IEC 61508 standard, which defines the lifecycle and design principles required to ensure their functional safety. The PSS is also designed to be in compliance with ANSI N43.1 standards "Radiological Safety in the Design and Operation of Particle Accelerators" [14] and NCRP Report 88 on Radiation Alarms and Access Control Systems" [15]. The design of both systems requires performing a risk assessment aimed at identifying operational hazards, analyzing and estimating the associated risks while evaluating their acceptability (Risk Analysis), and finally defining the necessary mitigation measures according to the block diagram shown in the Fig. 19.28.

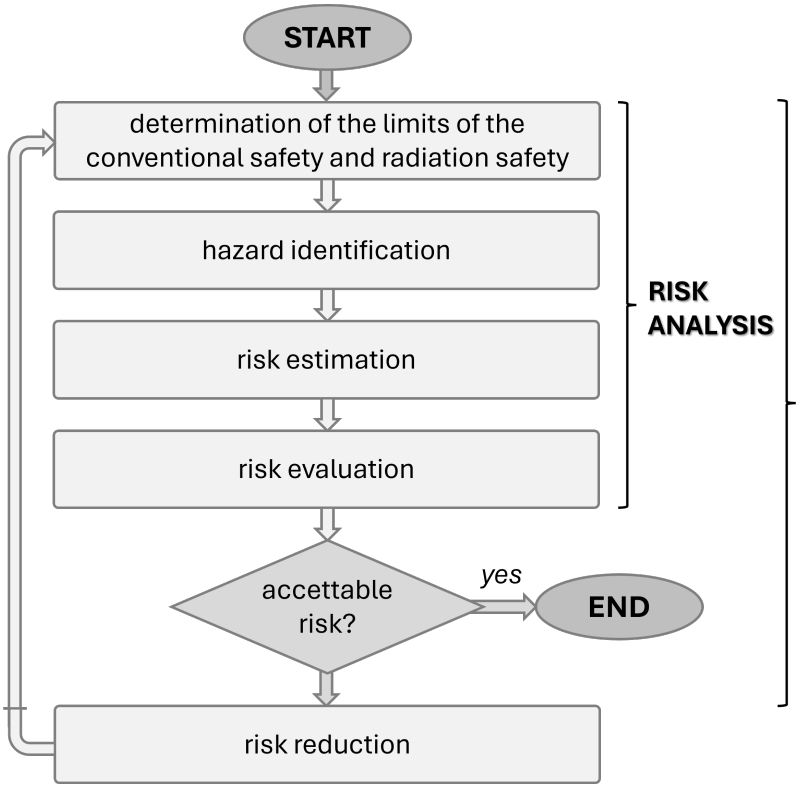

Figure 19.28: Risk assessment procedure to evaluate risk reduction measures.

19.5.2 Machine Protection System

The Machine Protection System is a functional safety system intended to protect the accelerator by safeguarding its most critical components and preventing damage when hazardous conditions arise or interlocks are activated during operation. In the EuPRAXIA@SPARC_LAB it disables RF signal (driver amp), closed photon and laser shutter in front of hazardous conditions arise or activated interlocks from the following devices or subsystems shown in the following Fig. 19.29.

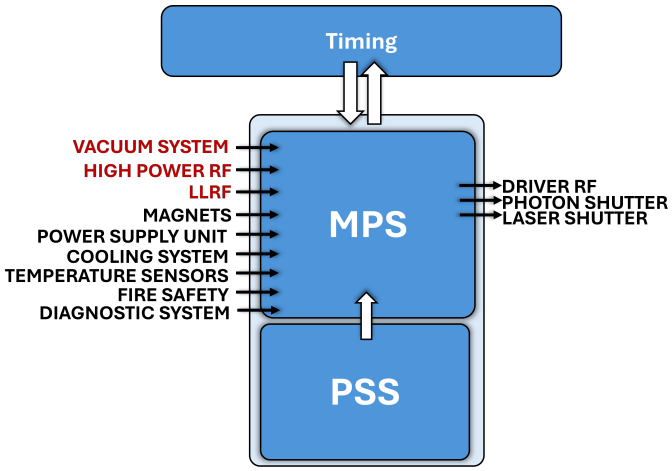

Figure 19.29: Overview of the devices and subsystems connected to the MPS, both for input, to read the interlocks, and for output, to enable or disable the systems. Critical subsystems that require a fast response to interlocks are highlighted in red.

The red subsystems are critical and request fast interlock responses respect to timing machine (100 Hz). The MPS reads an enable signal from the PSS and is also connected to the machine Timing system, which provides synchronization signals for its interlocks and control logic. The MPS enters a Fail-Safe state when the PSS inhibits machine operation in accordance with the defined safety functions and requirements.

19.5.2.1 MPS Requirements and Specifications

Table 19.10 summarizes the MPS requirements in according to Conventional Safety requirements described in the previous sections (see Figure 19.1 and Sections 19.3.1 and 19.3). Each requirement is labeled for traceability.

Table 19.10: MPS System Requirements

ID	Requirement Description
SR01	Monitor systems and subsystems reported in Fig. 19.29
SR02	Provide automated procedure to manage accelerator operation in response to issues
SR03	Ensure device management is synchronized with the timing system
SR04	Record all significant device signals
SR05	Operate reliably during electrical anomalies or outages
SR06	Respect Conventional Safety requirements (see Sec. 19.3.1 and 19.3)
SR07	Ensure coordination and correct functionality with the PSS

All requirements must be linked to at least one specifications. For verification purposes, the traceability matrix is provided on Table 19.12.

Table 19.11: MPS Technical Specifications

Each requirement is translated into a technical specifications in the following Table 19.11:

ID	Specification Description
SS01	A multi-head system is required for signal monitoring.
SS02	PT100 temperature sensors are required, for BOC and modulator, with spare channels.
SS03	A wired network must connect to all systems and subsystems to monitor and control.
SS04	Fast interlock detection is needed for High Power RF, LLRF, and vacuum systems.
SS05	Data from monitoring systems must be processed with an update rate of $\sim$ 100 ms, aligned with EPICS.
SS06	The system must include a CPU, FPGA and I/O interface (system core) with appropriate digital/analog I/O modules.
SS07	The core PSU must be backed by a UPS to guarantee 10 minutes (600 s) of operation during outages.
SS08	A watchdog must monitor the UPS–core connection and trigger corrective action if interrupted.
SS09	The fire safety signal must be monitored. Upon alarm, the modulator and driver RF must be turned off, photon and laser shutters must be closed.
SS10	The core checks for interlocks before enabling the trigger, ensuring a safe state before the next RF pulse.
SS11	The core checks for interlocks and turns off the modulator and driver RF, closes photon and laser shutters.
SS12	An advanced system using Machine Learning must detect breakdowns using RF waveform, Cherenkov BLM, and Faraday cup with detection masks.
SS13	An enable signal from the PSS must be integrated to avoid operational conflicts.

Table 19.12: Traceability Matrix: Requirements vs Specifications

ID	SS01	SS02	SS03	SS04	SS05	SS06	SS07	SS08	SS09	SS10	SS11	SS12	SS13
SR01	X		X							X		X	
SR02		X				X					X	X	
SR03				X	X	X				X		X	
SR04		X	X										
SR05							X	X					
SR06			X						X				
SR07													X

19.5.2.2 MPS Architecture and device support

The MPS system architecture shown on Fig. 19.30 consists of following macroblocks:

- **HW DEVICES**: All systems under MPS have hardwire link including 24 VDC digital contacts.
- **MPS CHASSIS**: National Instrument compact RIO [16] units configured as MODBUS TCP slaves for direct control and monitor all devices.
- **EPICS SERVER**: EPICS IOC based on Database and Records to communicate and manage Process Variables (PVs), with data logging capabilities. All status changed by MPS are

monitored by control system on TCP/IP communication using EPICS framework.

- **EPICS CLIENT**: Multi-monitor workstations installed in the control room, featuring a LabVIEW-based and CSS-Phoebus graphical interface for real-time supervision and operational data analysis. It's linked to EPICS SERVER with Channel Access Protocol.

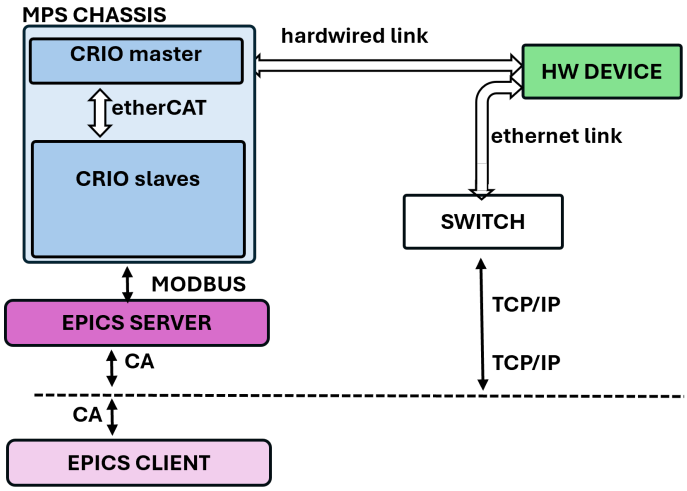

Figure 19.30: MPS Architecture

19.5.2.3 MPS Risk Assessment

In accordance with Figure 19.28, the first phase of Risk Analysis of the MPS is referred to Section 19.3 and to the requirements section. To comply with IEC-61508, SIFs are defined to ensure safety requirements and to mitigate risk. For the MPS, the functions are:

- **SIF-1**: Real-time control and intervention for critical subsystems (LLRF, High Power RF, vacuum), known as the Fast Interlock System. High reliability is essential to prevent hardware damage.
- **SIF-2**: Online control and monitoring via a Supervisor that also handles interlocks through predefined routines. Failures can also impact hardware integrity.

In the context of IEC-61508, a SIF is subject to the assignment of a SIL only if it directly contributes to risk reduction to an acceptable level or if it is implemented through hardware and/or safety-related software means that act deterministically on hazard mitigation. A purely software/management function (e.g., supervision, data logging, monitoring or signaling) does not result in a direct risk reduction and therefore does not require SIL classification. For these reasons, SIL assignment will be carried out only for SIF-1. The devices controlled by the MPS are listed in Table 19.13.

The system consists of four cRIO units in a master–slave configuration: three slaves allocated in the facility and one master allocated in rack room. The cRIO are equipped with 36-channel digital I/O interface modules, sufficient to handle approximately 600 Digital Input (DI) signals and 160 Digital Output (DO) signals. In total, 25 DI modules and 5 DO modules are distributed across the system. According to the system dependencies (i.e., which modules and cRIOs operate in parallel and which operate in series with MTBF reported in Table 19.14), the resulting system reliability, calculated using the formula shown in Eq. 19.2, is 0.391. This value is evaluated for a time period of 10 years of continuous operation and is obtained according to Eq. 19.3 and Eq. 19.4.

Table 19.13: Overview of the quantity of devices connected to the MPS, highlighting the number of components monitored and controlled to ensure safe accelerator operation and the protection of critical equipment.

Device	Quantity
Magnets	80
Valves	21
Ion Pump + NEG controller	66
Gauges Controller	23
Modulator	13
LLRF	13
Laser and Photon Shutter	2

Table 19.14: MTBF values hardware devices

Device	MTBF [h]
NI cRIO-9038 (Master)	1.00×10^5
NI cRIO-9144 (Slave)	4.50×10^5
NI-9476 (Digital Output Module)	1.09×10^6
NI-9425 (Digital Input Module)	1.25×10^6

$$r = e^{-t/MTBF} \tag{19.2}$$

$$r_{parallel} = 1 - \prod_{i=1}^{N}(1 - r_i) \tag{19.3}$$

$$r_{series} = \prod_{i=1}^{N} r_i \tag{19.4}$$

$$PFH = (1 - r)/t \tag{19.5}$$

From the relationship between reliability and Probability of Failure for Hour (PFH) reported in Eq. 19.5, it is found that the MTBF is 10.65 years, corresponding to a PFH of the order of 10^{-5}.

Based on the Risk Matrix shown on Table 19.15, the system with PFH between 10^{-6} and 10^{-5} the system has a SIL of 1. This value is compliance with Functional Safety standard IEC-61508 for MPS [17].

Table 19.15: SIF versus PFH according to mode of operation.

SIL	PFH for On Demand mode	PFH for Continuous mode
SIL – 1	$\geq 10^{-2}$ to $< 10^{-1}$	$\geq 10^{-6}$ to $< 10^{-5}$
SIL – 2	$\geq 10^{-3}$ to $< 10^{-2}$	$\geq 10^{-7}$ to $< 10^{-6}$
SIL – 3	$\geq 10^{-4}$ to $< 10^{-3}$	$\geq 10^{-8}$ to $< 10^{-7}$
SIL – 4	$\geq 10^{-5}$ to $< 10^{-4}$	$\geq 10^{-9}$ to $< 10^{-8}$

19.5.2.4 MPS Software and Hardware Design

The FPGA implements a state machine with a "read–search–set" cycle, as shown in Fig. 19.31. This ensures fail-safe operation and quick response.

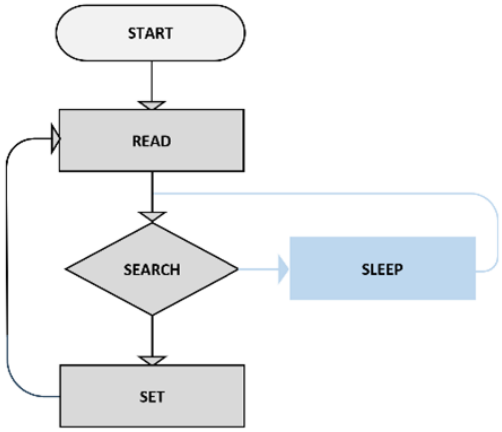

Figure 19.31: FPGA state machine implementing the read–search–set cycle used by the MPS, ensuring fail-safe operation and fast response to interlocks.

- **Read**: Signals are acquired from devices and passed to the FPGA I/O modules.
- **Search**: Interlocks are checked against the logic matrix.
- **Set**: Appropriate outputs are set. If the CPU–FPGA connection fails, the system enters a fail-safe loop.

The entire MPS system is developed in LabVIEW, using the graphical G-language. This enables programming of both the FPGA and the user interface. The FPGA executes routines within 1 ms, ensuring rapid and reliable operation.

19.5.2.5 Validation and Verification

Validation and verification activities are planned to ensure compliance with safety requirements. The Verification phase confirms each development phase meets its input requirements through reviews, inspections, and unit testing. The Validation phase compares the final system with initial requirements via functional tests, interlock response checks, and fault injection. This dual process ensures the final MPS aligns with design goals and regulatory compliance.

19.5.3 Personnel Safety System

The PSS is a functional safety system designed to ensure that personnel are protected from exposure to ionizing radiation by preventing access to hazardous areas during accelerator operation. In the EuPRAXIA@SPARC_LAB facility, the PSS controls and monitors all safety-related systems, including fire safety (described in Section 19.3.1), radiation monitoring, alarm systems, doors (gates), and search and emergency buttons, as shown in Figure 19.32 and according with Area Classification from Tab. 19.2. Figure 19.32 represents the connection between MPS and PSS.

Based on the status of these devices and in accordance with the defined safety functions, the PSS generates an enable signal that allows or inhibits accelerator operation. In unsafe conditions or when safety interlocks are activated, the PSS removes the trigger to the RF modulators, inhibiting beam generation and forcing the system into a safe state. In addition, the PSS directly commands the photon and laser shutters, operating them in parallel with the MPS to ensure redundancy and a coherent safety response.

The requirements governing the design and implementation of the PSS are defined by international safety standards, including IEC-61508, ANSI N43.1, and NCRP Report 88, and are further specified by the Radiation Protection Service of the INFN LNF. The requirements, which represent mandatory constraints for personnel and radiation safety, are detailed in the corresponding reference Section 19.4. It is important to emphasize that the PSS enters a Fail-Safe state when inhibits machine operation in accordance with the defined safety functions and requirements.

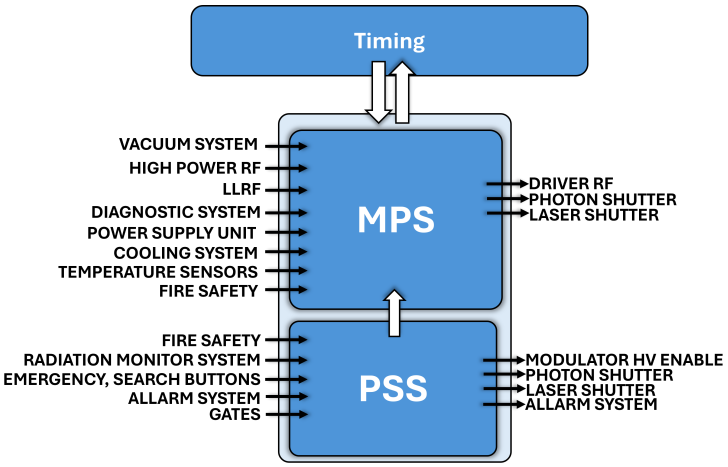

Figure 19.32: Diagram of the PSS at EuPRAXIA@SPARC_LAB, showing its control and monitoring of all safety-related systems, including fire protection, radiation monitoring, alarm systems, access gates, and search and emergency buttons, and its role in sending an enable signal to the MPS to ensure the system operates safely according to PSS requirements.

19.5.3.1 PSS Requirements and Specifications

The Table 19.16 summarizes the PSS requirements in according to Conventional Safety requirements and Radiation Safety Requirements described in the previous sections (see Figure 19.1 and Sections 19.3 and 19.4). Each requirement is labeled for traceability.

Table 19.16: PSS Requirements for EuPRAXIA@SPARC_LAB

ID	Requirement Description
SR01	Ensure personnel safety during accelerator operation.
SR02	Prevent access to hazardous areas while the beam is active.
SR03	Continuously monitor the status of doors, barriers, photon and laser shutters, and sensors in controlled zones (Sec. 19.4.1.6).
SR04	Provide accessible, redundant patrol and emergency stop buttons, LEDs, and status indicators.
SR05	Log and maintain records of safety events and access attempts.
SR06	Ensure system integrity in case of faults or power failure.
SR07	Be certifiable according to safety standards (e.g., IEC-61508).
SR08	The control system shall have real-time visibility of all status changes.
SR09	Allow for both automatic and manual periodic testing.
SR10	Restrict access to authorized and traceable personnel only.
SR11	Guarantee electrical isolation, continuity and automatic safe-state transition in case of hardware, software, or power failure, avoiding undetected hazardous conditions.
SR12	Safety must also be guaranteed on the FEL/experimental line.

Each requirement is translated into a technical specifications in the following Table 19.17:

All requirements must be linked to at least one specifications. For verification purposes, the traceability matrix is provided on Table 19.18.

Table 19.17: PSS System Specifications for EuPRAXIA@SPARC_LAB

ID	Specification Description
SS01	The PSS shall automatically close laser shutter, photon shutter and disable trigger to modulator if unauthorized access is detected or f a fire alarm/interlock condition is asserted by the Fire Control
SS02	The system shall operate in a fail-safe mode (defaulting to "safe" in case of faults).
SS03	Electromechanical and redundant micro-switches shall be installed on all controlled-area gates (see Sec. 19.4)
SS04	Beam activation shall only be allowed when all gates are closed and locked and the patrol procedure is completed.
SS05	The system shall poll all sensors at $\geq$100 Hz.
SS06	A Human-Machine Interface (HMI) shall display real-time status of each controlled zone.
SS07	Emergency and patrol buttons shall be placed every few meters along the accelerator, especially in low-visibility areas. LEDs and labels must clearly communicate the PSS and accelerator status (Alarm System).
SS08	All critical safety events shall be logged with timestamps and user IDs.
SS09	An Uninterruptible Power Supply (UPS) shall provide at least 30 minutes of backup power. Automatic diagnostics of CPUs and safety I/O shall be performed every 10 seconds.
SS10	All components must be certified in accordance with IEC-61508 guidelines.
SS11	An enable signal from the PSS shall be provided to prevent conflicts with the Machine Protection System.
SS12	Periodic testing (both manual and automatic) shall be conducted to verify system integrity.
SS13	Access shall be controlled via magnetic card, and all access attempts must be logged with date, time, and user ID.
SS14	The system must implement a dual-channel (1oo2) redundant architecture with cross-checking functions to detect failures, logic inconsistencies, or power loss. All cables must run in separate conduits, and all logic equipment must be mounted in locked racks to reduce the likelihood of accidental damage or deliberate tampering. An independent hardware watchdog must trigger beam shutdown if the control logic cycle fails.

Table 19.18: Traceability Matrix showing the relationship between Safety Requirements (SR) and System Safety Specifications (SS) for the PSS at EuPRAXIA@SPARC_LAB, highlighting how each specification addresses the relevant safety requirements

ID	SR01	SR02	SR03	SR04	SR05	SR06	SR07	SR08	SR09	SR10	SR11	SR12
SS01	X											X
SS02	X											
SS03		X										
SS04		X										
SS05			X									
SS06			X									
SS07				X								
SS08					X							
SS09						X						
SS10							X					
SS11								X				
SS12									X			
SS13										X		
SS14											X	

19.5.3.2 PSS Architecture and device support

The PSS system architecture shown on Fig. 19.33 consists of following macroblocks:

- **HW DEVICES**: All systems under PSS have hardwired link including 24 VDC redundant digital contacts.
- **PSS CHASSIS**: National Instrument compact RIO [16] units configured as MODBUS TCP slaves for direct control and monitor all devices.
- **EPICS SERVER**: EPICS IOC based on Database and Records to communicate and manage PVs, with data logging capabilities. All status changed by MPS are monitored by control system on TCP/IP communication using EPICS framework.
- **EPICS CLIENT**: Multi-monitor workstations installed in the control room, featuring a LabVIEW-based and CSS-Phoebus graphical interface for real-time supervision and operational data analysis. It's linked to EPICS SERVER with Channel Access Protocol.

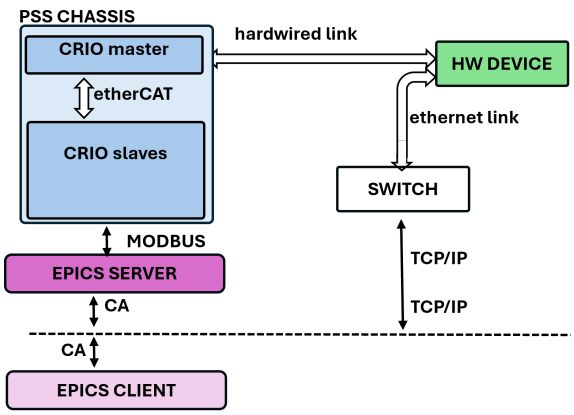

Figure 19.33: PSS Architecture

19.5.3.3 PSS Risk Assessment

In accordance with Figure 19.28, the first phase of Risk Analysis of the PSS is referred to Sections 19.3 and 19.4 and to the requirements section. To comply with IEC-61508, SIFs are defined to ensure safety requirements and to mitigate risk. For the PSS, the functions are:

- **SIF-1**: Real-time access control and intervention by monitoring all safety-related contacts and stopping the timing and RF systems to ensure personnel safety.
- **SIF-2**: Alarm systems using audible and visual signals.

In the context of IEC-61508, the SIF scope is limited to functions that directly contribute to reducing risk to an acceptable level or are implemented through deterministic hardware and/or safety-related software acting on hazard mitigation. Functions related solely to the control of lights and audio (e.g., warning lights, acoustic alarms) do not directly reduce the hazard risk; they serve only as alerting or signaling mechanisms. Therefore, these functions fall outside the scope of the SIF and do not require SIL assignment. For these reasons, SIL assignment will be carried out only for SIF-1.

The quantity of devices controlled by the PSS are reported in the specific Sections 19.4 and 19.3. Table 19.19 lists the quantity of remaining devices and subsystems that are not specified in the corresponding paragraphs.

Table 19.19: Quantity of devices monitored and controlled by the PSS

Device	Quantity
Photon and Laser Shutter	2
Gates	Sec. 19.4.1.6
Modulator	13
Fire Safety	1
Radiation Monitor System	Sec. 19.4.1.1
Emergency/Search Buttons	Sec. 19.4.1.6

The devices controlled by the PSS are total of 50 DI signals and 17 DO signals. The designed PSS consists of a redundant NI-cRIO master and slave unit and configurable I/O interfaces, which represent the core of the safety system.

Each cRIO is equipped with 36-channel digital I/O modules, sufficient to handle all available signals. In total, 2 DI modules and 1 DO module are used.

According to the system dependencies (i.e., which modules and cRIOs operate in parallel and which operate in series with MTBF reported in Table 19.14) the overall reliability is calculated (Eqs. 19.2-19.5) to be 0.825 over 10 years of continuous operation. From the relationship between reliability, MTBF, and PFH, the MTBF is found to be approximately 50 years, corresponding to a PFH on the order of 10^{-6}. According to Table 19.15 and the IEC-61508 standard, the system is therefore classified as SIL-2.

19.5.3.4 PSS Software and Hardware Design

The PSS software architecture is based on tight integration between FPGA logic and real-time software on the NI cRIO-9038. The safety logic is implemented as a deterministic state machine with three core phases: read, search, and set (see Fig. 19.31):

- **Read**: Acquire signals from devices distributed along the beamline.
- **Search**: Evaluate these signals against the interlock matrix.
- **Set**: Trigger outputs to shut down systems or activate alarms.

The entire PSS system is developed in LabVIEW, using the graphical G-language. This enables programming of both the FPGA and the user interface. The FPGA executes routines within 1 ms, ensuring rapid and reliable operation.

19.6 Conclusions

Based on the objectives outlined at the beginning of this chapter, the approach, specifications, and design of the facility's Integrated Safety System have been systematically described. The resulting architecture demonstrates how operational Functional Safety is achieved by integrating conventional and radiological safety requirements through two dedicated and clearly separated subsystems: the Machine Protection System and the Personnel Safety System.

The integrated safety framework developed for the EuPRAXIA@SPARC_LAB facility is based on a comprehensive and harmonized approach that encompasses conventional safety, radiation protection, and functional safety. These three components interact to ensure the protection of personnel, infrastructure, equipment and environment throughout all operational phases of the facility. The safety strategy combines validated technical solutions, regulatory compliance, and organizational measures to achieve a high level of operational reliability and risk control.

The conventional safety strategy is the result of a structured and validated process, grounded in the executive design developed by a qualified external engineering firm with recognized expertise in large-scale scientific infrastructure. This design has been fully reviewed, approved, and authorized by the competent Italian verification authorities, ensuring strict compliance with national and European safety regulations and standards. The adopted approach reflects a mature and proactive risk management system, integrating technical and organizational measures to safeguard personnel, infrastructure, and equipment under both normal and emergency conditions. The conventional safety concept includes structural compartmentalization, fire prevention systems, smoke and heat control solutions, evacuation route design, and the integration of emergency preparedness and response measures within the broader INFN LNF Emergency Plan framework. These elements, fully described in Section 19.3, represent consolidated and operationally effective solutions. For this reason, all conventional safety aspects discussed are considered to have reached the highest level of technological readiness.

The radiation safety and protection section has addressed the key aspects of radiation protection for the facility. In particular, the source terms associated with the generated radiation fields have been described, as they are essential for evaluating dosimetric contributions, along with the shielding designs conceived to ensure their adequate attenuation. A preliminary radiation protection program has also been presented, including area classification, the monitoring system, the personnel dosimetry system, as well as the requirements for the interlock and access control systems. Furthermore, the studies conducted on the different beam dumps—both diagnostic and fixed—planned for the facility have been illustrated. The results obtained confirm that the proposed beam dump designs can be safely operated and are fully consistent with the area classification defined at this stage of the project. At the current stage, the Technology Readiness Level (TRL) of the various sub-components can be summarized as shown in Tab. 19.21. It should be noted that the TRLs currently assigned to each subsystem are provisional and may be updated as the project progresses.

In conclusion, the aim of Sec. 19.5 was to describe the MPS and the PSS of the facility, complementing and extending the information already presented in Sec. 19.3 and 19.4. The systems were designed in accordance with the requirements defined in the previous sections devoted to Conventional Safety and Radiation Safety, ensuring the integration and consistency of safety

functions within the overall facility architecture. Based on the contents and analyses reported, the proposed systems are compliant with the applicable safety regulations and standards. Although the technologies available on the market during the implementation years may partially differ from those currently considered, it is reasonable to expect that future technological developments will further improve the performance and reliability of the systems. The corresponding TRL of the systems are reported in Table 19.22.

Table 19.20: TRL of the Conventional Safety.

Safety aspects	TRL	Comments
Fire safety systems	9	Fire detection, alarm, and suppression systems are fully defined in the executive project and compliant with national and EU standards. The fire prevention strategy has been approved by the competent Italian verification authorities.
Evacuation measures	9	Evacuation routes, emergency lighting, signage, and smoke management systems have been fully developed in accordance with regulatory standards and are ready for implementation.
Emergency preparedness	9	The facility's emergency management is fully integrated into the INFN-LNF Emergency Plan, with defined roles, procedures, and coordination with institutional stakeholders.

Table 19.21: TRL level of the radiation protection system.

Sub - systems	TRL	Comments
Diagnostic Beam Dumps	9	The design and dimensions have been validated through FLUKA simulations.
FEL Beam Dump	9	Similar to diagnostic dumps: validated by FLUKA studies.
Driver Beam Dump	9	Optimization in progress through dedicated FLUKA - INFN simulations.
Radiation Shielding	9	The barrier design has been evaluated analytically.
Safety Interlock System	9	The concept has been outlined, but detailed design and implementation planning are still pending.
Radiation Detector/Monitor	9	The technical specifications are defined.

Referring to the Table 19.21:

- The beam dump structures, both diagnostic and fixed, are highlighted in green, since their design has been developed exclusively through Monte Carlo simulations using the FLUKA-INFN code, in accordance with guidelines available in the literature;
- The interlock and safety systems have been designed based on the expected machine operation modes and the surrounding structural layout. During the construction phase of the facility, further refinements are foreseen to enhance their operational effectiveness;
- The bulk shielding barrier has been dimensioned according to conservative approaches to ensure adequate radiation protection. While not yet realized, several examples—both at LNF facilities and at other laboratories worldwide—demonstrate the effectiveness of such shielding solutions across different operating conditions and beam energies;
- The monitors foreseen for the EuPRAXIA@SPARC_LAB project fully comply with the requirements detailed in Section 19.4.1.1. Their specifications are already consistent with commercially available solutions, requiring no additional customization.

Table 19.22: TRL of the functional safety subsystems.

Sub - systems	TRL	Comments
PSS	9	The PSS architecture has already been defined based on a proven configuration, currently in use at the TEX, SSRIP and soon at EuAPS facilities, where it has been validated with the same operational logic and hardware setup.
MPS	9	The MPS architecture has been defined and validated based on a configuration already implemented at the TEX, SSRIP and soon EuAPS facilities and further tested in other accelerator environments, confirming its reliability and scalability.

Bibliography

[1] E. Ronchi et al. “A fire safety assessment approach for evacuation analysis in underground physics research facilities”. In: *Fire Safety Journal* 108 (2019), p. 102839. ISSN: 0379-7112. DOI: https://doi.org/10.1016/j.firesaf.2019.102839.

[2] E. Kinkel, C. N. van der Wal, and S. P. Hoogendoorn. “The effects of three environmental factors on building evacuation time”. In: *Heliyon* 10.5 (2024), e27128. ISSN: 2405-8440. DOI: https://doi.org/10.1016/j.heliyon.2024.e27128.

[3] ICRP. *The 2007 Recommendations of the International Commission on Radiological Protection*. ICRP Publication 103, Ann. ICRP 37(2–4). 2007.

[4] NCRP. *Radiation Protection for Particle Accelerator Facilities*. NCRP Report No. 144. 2003.

[5] IAEA. *Radiation Protection and Safety in Accelerators*. IAEA Safety Report Series No. 188. 2018.

[6] Fermilab. *Radiation Physics for Personnel and Environmental Protection*. Tech. rep. TM-1834. Fermilab, 1993.

[7] A. Ferrari et al. “Estimation of fluence rate and absorbed dose rate due to gas bremsstrahlung from electron storage rings”. In: *CERN Report* (1993).

[8] A. Esposito et al. “Gas Bremsstrahlung: A Comparison of Measurements and Simulations”. In: *Nucl. Instr. and Meth. in Phys. Res. B* (1993).

[9] S. Dierker and BROOKHAVEN NATIONAL LABORATORY (United States). *NSLS-II Preliminary Design Report*. Tech. rep. BROOKHAVEN NATIONAL LABORATORY (United States), 2007. DOI: 10.2172/1010602.

[10] F. Ballarini et al. “The FLUKA code: Overview and new developments”. In: *EPJ Nuclear Sci. Technol.* 10 (2024), p. 16.

[11] A. Ferrari et al. *FLUKA: A Multi-particle Transport Code (Program Version 2005)*. Tech. rep. CERN-2005-10. CERN, 2005.

[12] T. T. Böhlen et al. “The FLUKA code: Developments and challenges for high energy and medical applications”. In: *Nuclear Data Sheets* 120 (2014), pp. 211–214.

[13] *Functional Safety*. URL: https://www.iec.ch/functionalsafety/.

[14] Scott Walker et al. *ANSI N43.1 “Radiological Safety in the Design and Operation of Particle Accelerators*. 2004.

[15] *Report No. 088 – Radiation Alarms and Access Control Systems*. 1986.

[16] *National Instruments*. URL: https://www.ni.com/it-it.

[17] G. Latini et al. “Machine protection system for TEX facility”. In: *Proc. IPAC’24*.

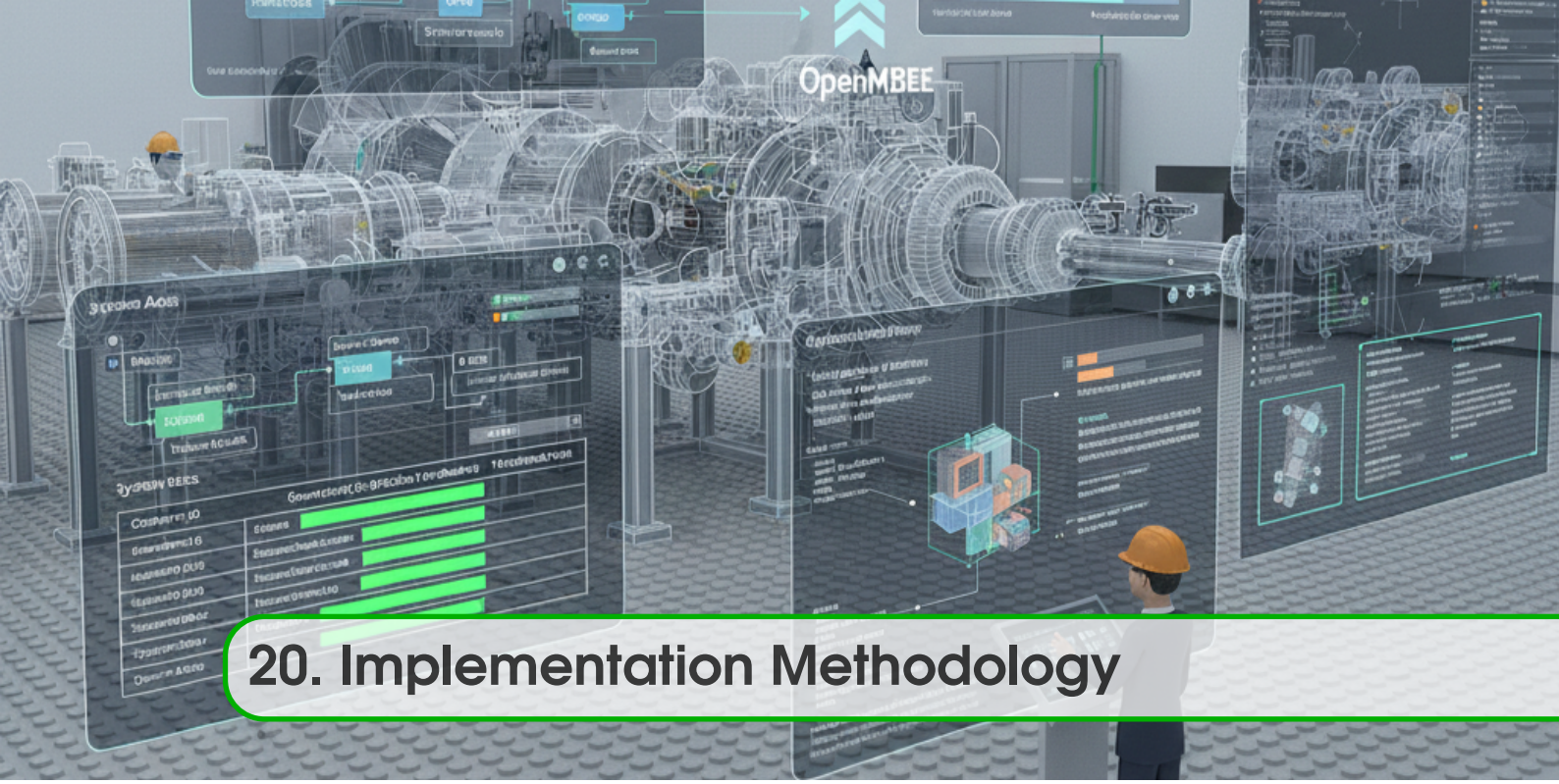

20. Implementation Methodology

20.1 Introduction

The realization of EuPRAXIA@SPARC_LAB requires an integrated approach that combines project management with the technological implementation of systems. Systems Engineering [1], as part of Project Management, provides methodologies and tools to develop, design, and integrate complex subsystems, ensuring coordination among engineers, physicists, and technicians. This process, structured into phases such as requirements analysis, system design, integration, verification, and optimization, enables monitoring of the accelerator's entire lifecycle—from initial configuration to maintenance and decommissioning.

At the same time, technological implementation is not a sequential activity but a collaborative and concurrent effort involving the harmonious integration of mechanical, electrical, and control systems with civil infrastructure. Such integration is essential to guarantee high performance, stability, and future adaptability, transforming the project from concept to operational reality. Project integration management ensures that processes, resources, and interfaces are coordinated while maintaining a balance among scope, schedule, cost, and quality constraints.

Finally, the experience gained through previous projects such as SPARC_LAB, EuAPS, Tex, and SABINA has enabled the validation of key technologies—from X-band accelerating structures to plasma systems—and the development of innovative solutions for RF cabling, gas handling, and vacuum system cooling. This synergy between system-level management and technological implementation forms the cornerstone for the harmonious and safe development of the infrastructure, ensuring scientific excellence and long-term success [2–4].

20.2 Integration of the Accelerator Machine with Civil Infrastructure

The interface between the accelerator machine and civil infrastructure involves a co-designed, co-optimized system, where the mechanical, electrical, and environmental needs of the machine are intrinsically embedded into the structural, spatial, and utility systems of the building. This chapter provides an analytical overview of this integration, identifying challenges, best practices,

and strategic approaches for successful project realization. The integration of a plasma-based particle accelerator with its civil infrastructure is essential to the successful implementation of the machine. Unlike conventional particle accelerators, plasma-based systems—such as Laser Wakefield Accelerators (LWFA) and Plasma Wakefield Accelerators (PWFA)—introduce new architectural, environmental, and structural requirements due to their compactness, high precision, and sensitivity to external disturbances. For example, the use of centrally cooled vacuum systems is being evaluated, replacing the current configuration based on dedicated chillers. Furthermore, the distribution of plasma gas from dedicated external storage areas is planned, improving maintenance, safety, and operational flexibility—particularly in scenarios requiring different gases for specific experiments.

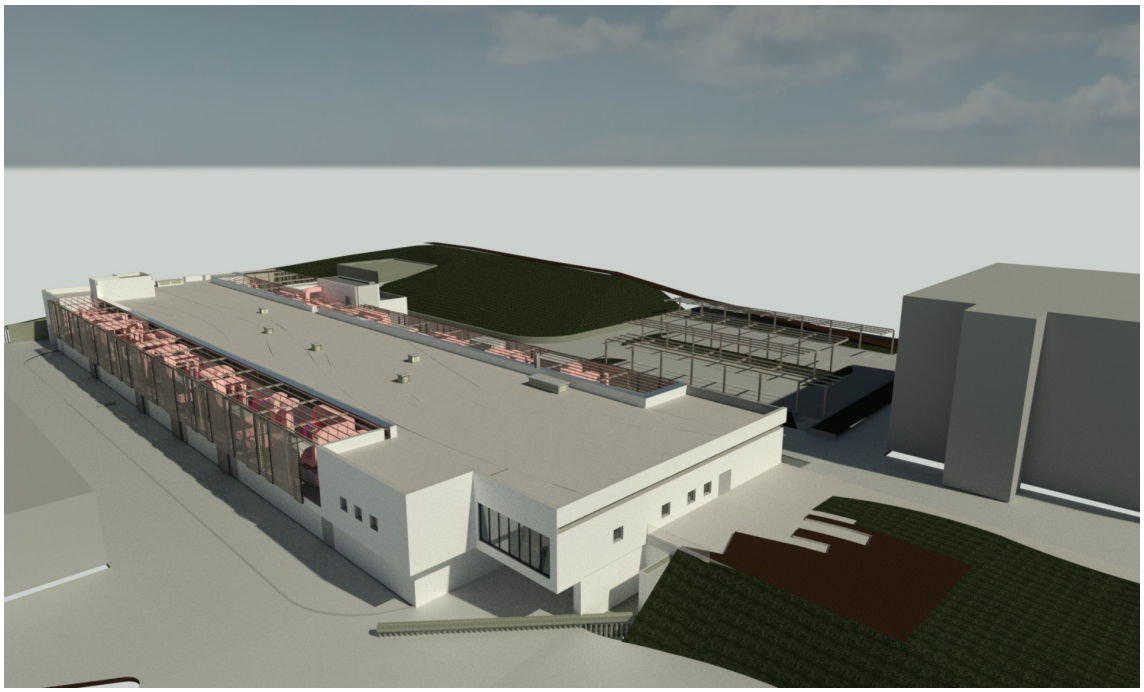

Figure 20.1: EuPRAXIA 3D View Project

20.2.1 Building Acceptance Test

The purpose of this chapter is to list the technical characteristics and the geometric and dimensional parameters (required dimensions and geometries, along with an acceptable range of values) that must be identified, checked, and verified against the nominal values reported in the 2D project drawings before starting the machine installation. The goal of this procedure is to minimize the risk of delays and non-conformities during the installation and integration of the machine. Monitoring of slab settlement during construction and upon completion of the works. Measurements will be carried out by the Contracting Authority using its own instruments, in the presence of and jointly with the executing contractor. The measurements shall be performed in accordance with the following schedule:

The first settlement measurement shall be taken upon completion of the floor, including the final finish.

The second measurement shall be taken after installation of the mechanical/electrical systems and the overhead cranes.

The third measurement shall be taken upon completion of the shielding cover with soil.

The fourth measurement shall be taken upon completion of the entire building and issuance of

the Works Completion Certificate by the Site Supervisor.

20.2.1.1 Geometric and Dimensional Characteristics of the Building

This section lists the main geometric and dimensional characteristics to be checked, along with their allowable tolerances, compared to the nominal project measurements. A cross-check will also be performed using a 3D Laser Scan model. This system provides an accuracy of less than 1 mm and allows for a fast and reliable comparison between the nominal 2D project values and the 3D model produced by the measuring instrument.

1. Parallelism of the machine installation plane with the ideal plane orthogonal to the Earth's vertical (datum): 10 mm
2. Floor flatness, both local and total, of the machine installation area: 5 mm every 3 m^2 of surface
3. Parallelism between partition walls: 10 mm
4. Parallelism between longitudinal walls: 10 mm
5. Parallelism between floor and ceiling: 10 mm
6. Perpendicularity between the floor and all walls: 10 mm
7. Perpendicularity between longitudinal walls and partition walls: 10 mm
8. Dimensions of the LINAC and undulator rooms: $\pm$20 mm
9. Dimensions of experimental rooms (LINAC, undulator room, radiation users room, laser room, experimental hall, modulator room): $\pm$5 mm
10. Dimensions of cable ducts: $\pm$20 mm
11. Positioning accuracy of cable ducts relative to building walls: $\pm$20 mm
12. Verification of the number of all openings
13. Positioning of their entry and exit centers relative to the walls: $\pm$5 mm
14. Hole diameter: $\pm$2 mm
15. Hole cylindricity: 4 mm

20.2.1.2 Short- and Long-Term Building Settlements

The facility is intended for experiments requiring precision measurements, so short- and long-term settlements caused by both static and dynamic loads must be limited according to the specifications below, which are to be considered valid as structural design requirements. All medium- and long-term measurements will be carried out by the Alignment Department of the Laboratories' Engineering Service. The procedures and instrumentation required for this purpose are already available and are routinely employed for analogous operations, both in internal bunker facilities housing accelerator machines and in collaborative activities with national and international partners.

- Long-term vertical settlements:
  100 µm over 10 m per year.
- Short-term vertical settlements:
  100 µm over 10 m within a daily cycle.
  1 µm within one hour.
- Static point load of 5000 N:
  $\Delta z < 6$ µm under the load.
  $\Delta z < 1$ µm at 2 m distance.
- Dynamic load of 100 kg:
  $\Delta z < 1$ µm peak-to-peak at 2 m distance.
- Vibrations (0.1–70 Hz) due to all effects induced by the facility combined with external effects:
  $\Delta z < 1$ µm peak-to-peak.
  $\Delta x < 1$ µm peak-to-peak.

20.2.2 Key Integration Areas Between Machine and Civil Infrastructure

- Structural and Spatial Integration:
  - The building must physically accommodate the machine layout, which includes beamlines, laser transport paths, shielding walls, target areas, and diagnostic stations.
  - Structures must allow for overhead cranes, floor hatches, or removable panels to support installation and maintenance.
  - The architectural layout must support modularity and future upgrades or reconfiguration of experimental zones.
  - Integration must consider access corridors for large optics or vacuum components and equipment clearance envelopes.
  - Seven through-openings have been provided in the shielding separation walls between the Linac and Undulators tunnels and the four laser and experimental halls. These openings are square, with dimensions of 1 m $\times$ 1 m, and their centers are located at a height of 2.3 m above floor level. The purpose of these seven openings is to enable synchronization between the local networks of the individual halls and the main machine network defined along the two tunnels, Linac and Undulators, in order to allow component alignment. The number of network nodes and their spatial distribution will be defined through a simulation carried out using dedicated software, following a procedure known as USMN (Unified Spatial Metrology Network). This procedure is used to predict the achievable accuracy and associated uncertainty with which the points measured by the laser tracker can be defined, under real operating conditions, within the various areas with respect to the alignment network, reaching the accuracy levels required by the project for the different elements along the machine or within the halls (Figure 20.2).

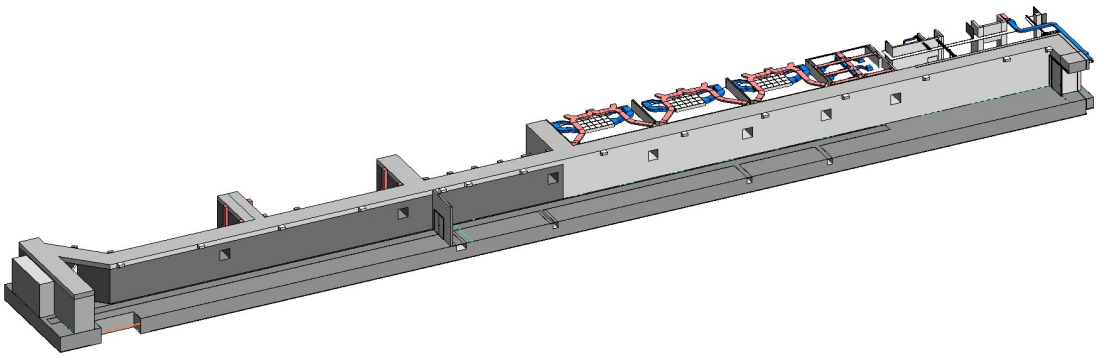

Figure 20.2: Alignment apertures

- Vibrational and Mechanical Stability:
  - Plasma-based systems are highly sensitive to floor vibration. Even minor tremors can cause optical misalignment or diagnostic drift (see Sec. 18.1.2.1).
  - Civil infrastructure must include:
    - Reinforced concrete slabs with vibration damping properties.
    - Isolation pads or floating floor systems.
    - Analysis of natural frequencies of structures to avoid resonance with mechanical systems.
  - Facilities near railways, elevators, or mechanical plants require site-specific vibration attenuation strategies.
- Thermal and Environmental Coupling (see also Table 18.15):
  - Temperature fluctuations in the building envelope affect laser pointing, beamline align-

ment, and plasma density.
  - Civil HVAC systems must be integrated with the machine's thermal stability needs:
    * Zoning for critical environments like laser halls.
    * Laminar flow systems in optics zones.
  - Thermal insulation of walls, ceilings, and floors must be modeled to prevent gradients.
- Shielding and Radiation Protection:
  - Although plasma accelerators are compact, they can still produce high-energy secondary particles, requiring radiation shielding.
  - Civil design must include:
    * Concrete shielding walls, ceilings, and labyrinths (Figure 20.3).

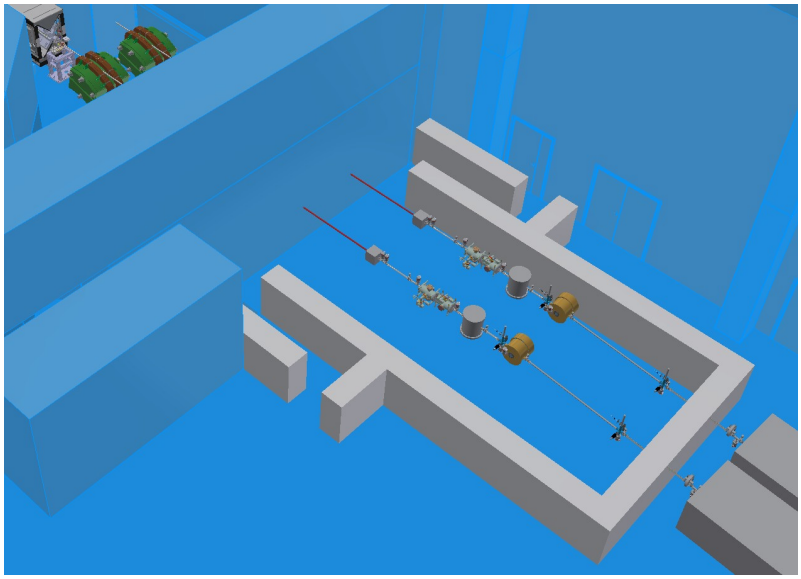

Figure 20.3: Labyrinths in Experimental Area

    * Integration of shielded access doors, chicanes, and emergency interlock zones (Figure 20.4).

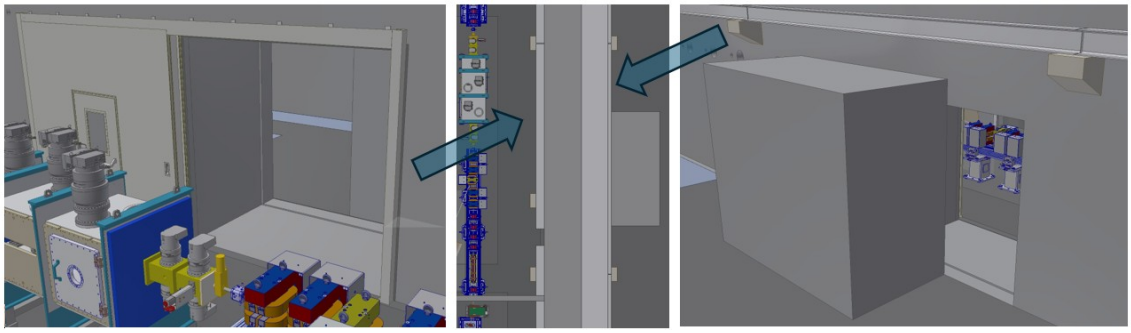

Figure 20.4: Left: View from Plasma Area; Center: Top View; Right: View from Service Tunnel.

    * Compliance with international radiation protection standards (e.g., ICRP, IEC, NCRP).
- Utilities and Routing Infrastructure:
  - Plasma accelerators require complex utility networks:
    * Cooling water systems for lasers, power supplies, diagnostics.
    * Electrical power with clean, isolated grounding.

        * Gas lines for plasma generation (e.g., hydrogen, helium, argon).
        * Vacuum lines, signal cables, and optical fibers.
    - Civil infrastructure must support:
        * Cable trays, underfloor ducts, ceiling-mounted tracks, see Sec. 18.1.2.1.
        * Utility chases designed with accessibility and electromagnetic shielding in mind.
        * Isolation zones for high-voltage or pulsed-power components.

20.2.3 Design and Implementation Strategy

- Co-Design from Concept Stage:
    - Early involvement of civil engineers, physicists, and mechanical designers in a cross-disciplinary design team is essential.
    - Use of Building Information Modeling (BIM) and integrated CAD platforms enables real-time coordination and spatial conflict resolution.
    - Regular interface definition workshops help align machine layout with architectural elements.
- Layout Optimization and Functional Zoning (see also Sec. 18.1.2.1):
    - Strategic allocation of building zones:
        * Laser rooms require high stability, low vibration, and clean conditions.
        * Experimental halls must allow for shielding and modularity.
        * Technical galleries accommodate racks, water pumps, and power supplies.
        * Control rooms must provide visual and electronic interfaces without compromising safety.
    - Ensure fire separation, RF shielding, and EMC compliance across different facility zones.
- Construction Phase Coordination:
    - Civil construction must follow a phased implementation schedule aligned with machine delivery and installation (see Figure 20.5).
    - Ensure floor flatness and leveling are verified before beamline alignment.
    - Infrastructure must include provisions for:
        * Temporary clean zones.
        * Access for large component insertion.
        * Laser-safe interlock installations.
- Commissioning and Integration Testing:
    - Once civil construction is complete, comprehensive environmental testing (vibration, temperature, humidity, noise) must be conducted.
    - Conduct dry runs of utility systems before equipment installation.
    - Install reference fiducials and alignment monuments within the building structure to assist long-term calibration.

20.2.4 Designing for Mechanical and Thermal Stability

A major consideration in the integration process is the need for exceptional mechanical stability. Since plasma accelerators rely heavily on ultra-precise laser and beamline alignment, the floor structure must be engineered to suppress vibrations from both external sources (such as nearby roads or mechanical systems) and internal operations (such as pumps or power units). For this reason, buildings are often designed with isolated foundation slabs, floating floors, or reinforced structural zones around critical components. Equally important is the control of thermal conditions, see Sec. 18.3.2. Even small temperature gradients across a laser room or experimental hall can lead to expansion or contraction of optical benches, misalignment of diagnostic systems, or changes in the refractive index of the air. As such, the air conditioning and environmental control systems must

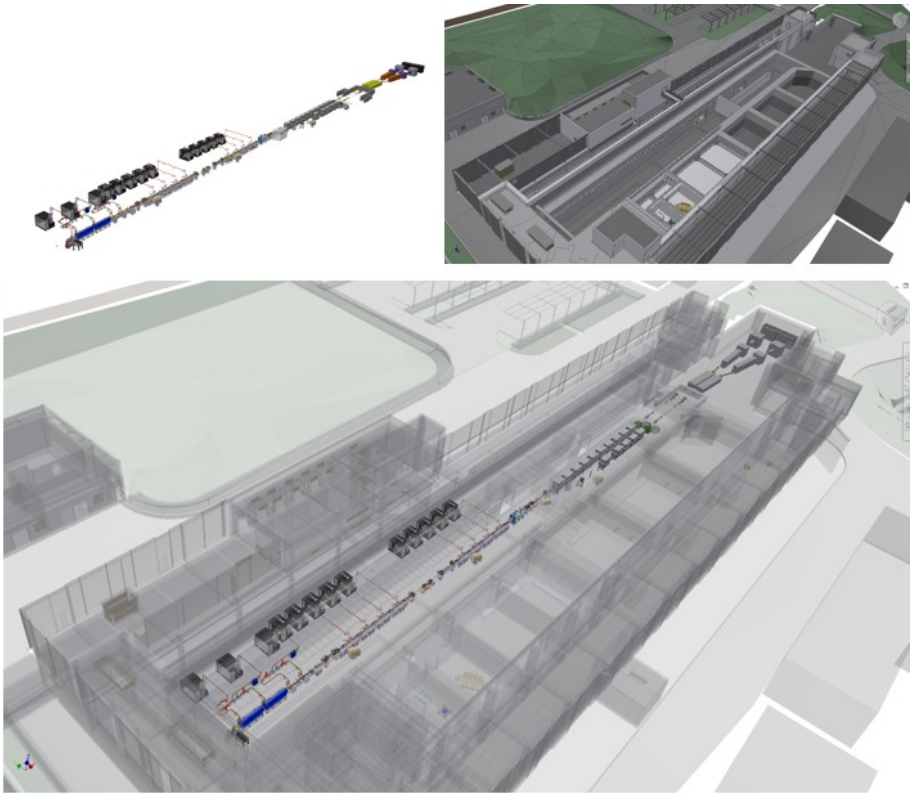

Figure 20.5: Top Left: Machine; Top Right: Civil Infrastructure; Bottom: Matching between Machine with Civil Infrastructure.

be tightly integrated with the architectural and mechanical design, ensuring stable conditions often within fractions of a degree Celsius. These considerations have been implemented in Chapter 18.

20.2.5 Spatial Planning and Functional Layout

Another key aspect of integration is space management and zoning. The building must be laid out in such a way that it reflects the functional needs of the accelerator. Areas like the laser hall, which require pristine conditions, must be physically and environmentally separated from technical zones such as power supply rooms or maintenance corridors. The design should anticipate the flow of personnel, equipment, and services, ensuring ease of access for installation and maintenance, while maintaining safety and environmental control. Moreover, flexibility is crucial. Plasma accelerator projects are often experimental in nature, evolving over time as new technologies and research needs emerge. The infrastructure must be modular and adaptable, capable of accommodating reconfigurations or expansions without major structural changes. This is particularly relevant for test facilities or pilot lines intended to evolve into operational systems. These considerations have been implemented in Chapters 4 and 18.

20.2.6 Utilities and Infrastructure Services

No accelerator can function without a carefully designed network of supporting utilities. In plasma-based systems, this includes power delivery with minimal electromagnetic interference, stable water-cooling circuits for lasers and electronics, controlled gas supply for plasma sources, and a network of signal and data lines for control and diagnostics. Routing these utilities within the building requires forethought and precision. Civil design must consider how these services will be distributed—whether through underfloor channels, ceiling-mounted tracks, or wall-integrated

conduits—without introducing unwanted vibrations or thermal imbalances. Furthermore, utility access must remain serviceable, ensuring that maintenance or upgrades do not interfere with operational uptime. These considerations have been implemented in Chapter 18.

20.2.7 Radiation Safety and Shielding

While plasma accelerators are generally more compact than their conventional counterparts, they can still produce significant levels of ionizing radiation during operation. This requires the building to incorporate appropriate shielding elements, such as thick concrete walls, labyrinth-style access points, and embedded radiation protection systems. These features must be seamlessly integrated into the architectural and mechanical design, conforming to international safety standards and allowing for safe operation and personnel access. These considerations have been implemented in Chapters 18 and 19.

20.2.8 From Design to Commissioning

The integration process begins early in the design phase, ideally with a collaborative approach that brings together accelerator physicists, civil engineers, architects, and systems engineers. Using shared digital environments—such as BIM systems and integrated CAD platforms—teams can develop coordinated layouts that identify and resolve spatial conflicts, optimize environmental control, and plan for installation sequencing. During construction, precision becomes paramount. Floor flatness, alignment reference points, and tolerance to vibration must all be verified. Before equipment is installed, environmental qualification tests—including vibration surveys, thermal mapping, and airflow modeling—are performed to ensure that the infrastructure meets the design criteria. Once the machine is installed, commissioning involves not just bringing the accelerator components online but also validating the performance of the building systems in real-world conditions. Any discrepancies between the expected and actual performance must be addressed through fine-tuning or, in some cases, structural modifications.

20.3 Naming Convention

This paragraph outlines the guidelines and recommendations that designers have followed to define a consistent and unambiguous naming convention for the EuPRAXIA@SPARC_LAB project. The naming structure has been developed in accordance with the principles of the ISO standard UNI EN ISO 41001:2018 [5], and has been adapted to meet the specific needs of the project. The objective is to provide a detailed description of the criteria required to assign a code that fully identifies each project element. These guidelines apply to all components that make up both the accelerator machine and the auxiliary systems necessary for its operation within the EuPRAXIA@SPARC_LAB infrastructure. In particular, the components included in this naming convention are:

- Beam elements.
- Beam-related elements (power supplies, controllers, modulators, etc.).
- Mechanical elements (supports, bases, etc.).
- Secondary system elements (coolers, valves, etc.).
- Functional safety elements (conventional safety devices, access controls, radiation protection, and machine safety systems).
- Circuits and wiring.

To correctly define a valid naming convention, the following requirements have been established:

- Usability.
- Uniqueness.
- Self-explanatory nature.

- Machine-independence.
- Adaptability.
- Traceability to the reference Work Packages.
- Integration with the machine's configuration database.

To uniquely identify a component, the system name is defined as a combination of two codes (Fig. 20.6):

- **Component Code:** Identifies the system itself. Identical components may share the same code.
- **Functional Code:** Provides additional details to ensure the uniqueness of the component.

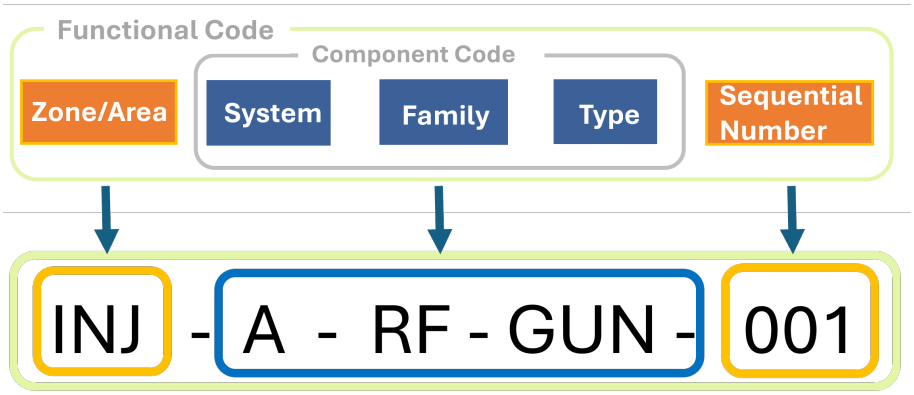

Figure 20.6: Identification code of the GUN on the beamline of EuPRAXIA@SPARC_LAB.

Specifically, the Functional Code identifies the specific zone or area of the machine where the component is installed and reflects the function it serves within the system. These areas include:

- Injector.
- Low-Energy Linac.
- High-Energy Linac.
- Plasma Section.
- Undulator Section.
- Experimental Halls.
- Modulator Rooms.
- Rack Room.

Meanwhile, the Component Code is composed of three fields: **SYSTEM** – **FAMILY** – **TYPE**. The **SYSTEM** field identifies the group of devices that perform homogeneous functions and is defined according to the classification Table 20.1.

Table 20.1: System Descriptions.

Letter	System	Description
A	Acceleration	Elements that vary the beam energy
B	Beam Instrumentation	Measurement of beam characteristics (diagnostics)
C	Controls / Communications	Control systems and network
D	DC Electrical Distribution	DC power distribution
E	Electricity (AC Distribution)	AC power distribution
F	Fluids	Fluid systems and cooling
G	Survey & Geodesy	Alignment network elements
H	Mechanics, Support	Mechanical supports
I	Circuits	Electromagnetic connections (waveguides and related components)
J	Infrastructures	Infrastructural elements (e.g. overhead crane)
K	Racks	Racks and similar structures
L	Layout & Assembly	Mechanical components housing multiple distinct systems
M	Magnets	Magnets
N	Particle Source	Particle sources
O	Operation	-
P	Power Supply	Power supply units
Q	Cryogenic	Cryogenic elements
R	RF Power Source	RF sources
S	Functional Safety	Radiation protection, access system, conventional safety & MPS
T	Targets	Collimators, targets, dumps
U	Undulators	Undulators
V	Vacuum	Vacuum systems
W	Laser & Optical System	Lasers, optical transport systems (including beamlines)
X	Experiments / User	-
Y	-	-
Z	Electrostatic System	Electrostatic beam elements

The **FAMILY** defines a functional subset of the system, identifying the nature of the object. For example, within the vacuum system, families may include pumps, valves, and other related components. Finally, the **TYPE** further specifies the model, variant, or unique technical characteristics of the object within its family, allowing for unambiguous identification. For instance, vacuum pumps may be classified as ion, turbo, or scroll, while valves may be categorized as manual or fast-acting. In summary, this naming convention enables precise identification and differentiation of components within the system [6]. In addition to the machine-level naming convention, there is a separate code not represented in the naming structure but stored within the configuration database. This code is an unstructured alphanumeric identifier that uniquely identifies the physical object and is assigned permanently. It is referred to as a UUID (Universally Unique Identifier).

20.4 Schematic Layout

For this Technical Design Report, the schematic layout of the EuPRAXIA@SPARC_LAB accelerator includes the complete beamline configuration, component naming, working zones, and a legend explaining the geometric elements represented.

Figures (Fig. 20.8, 20.9, 20.10, 20.11) are intended to provide an overview of the main areas of the accelerator while also conveying the number and variety of elements distributed along and around the machine. As an illustrative example, to clarify how the indications of individual components are displayed, a dedicated zoom of the injector is shown in Fig. 20.7.

The principal areas represented are:

- **Linac Area**, comprising the accelerating sections and the Plasma section.
- **Undulator Area**.
- **User Beamlines Area**.
- **Klystron Gallery**, with a schematic representation of the RF distribution connected to the various Linac sections.

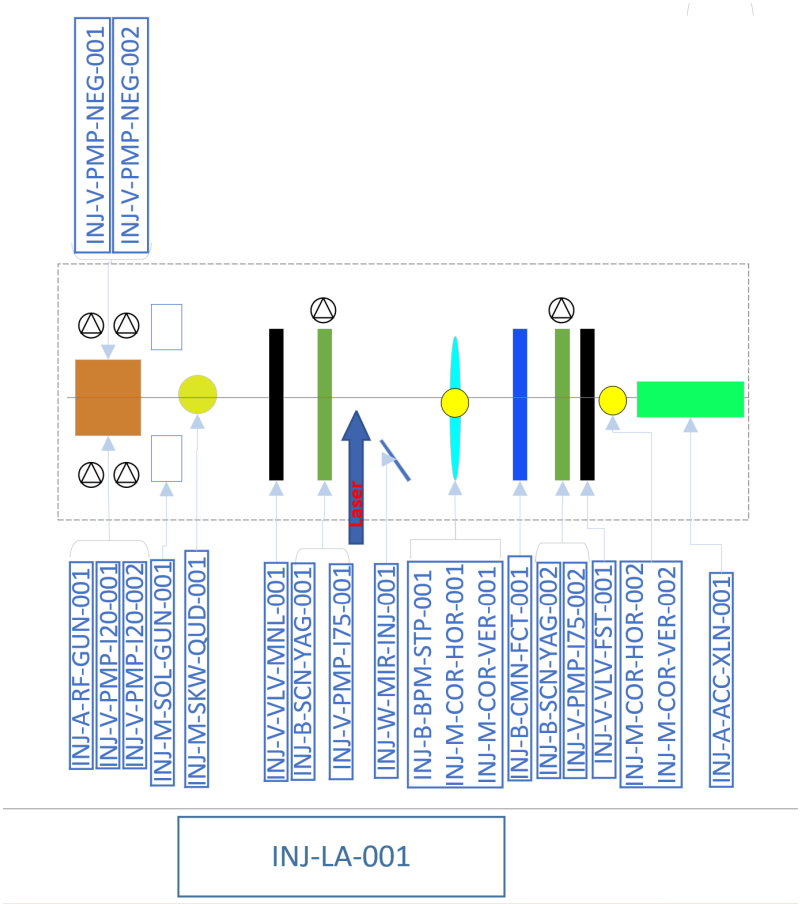

Figure 20.7: ZOOM INJ-LA-001 ZONE

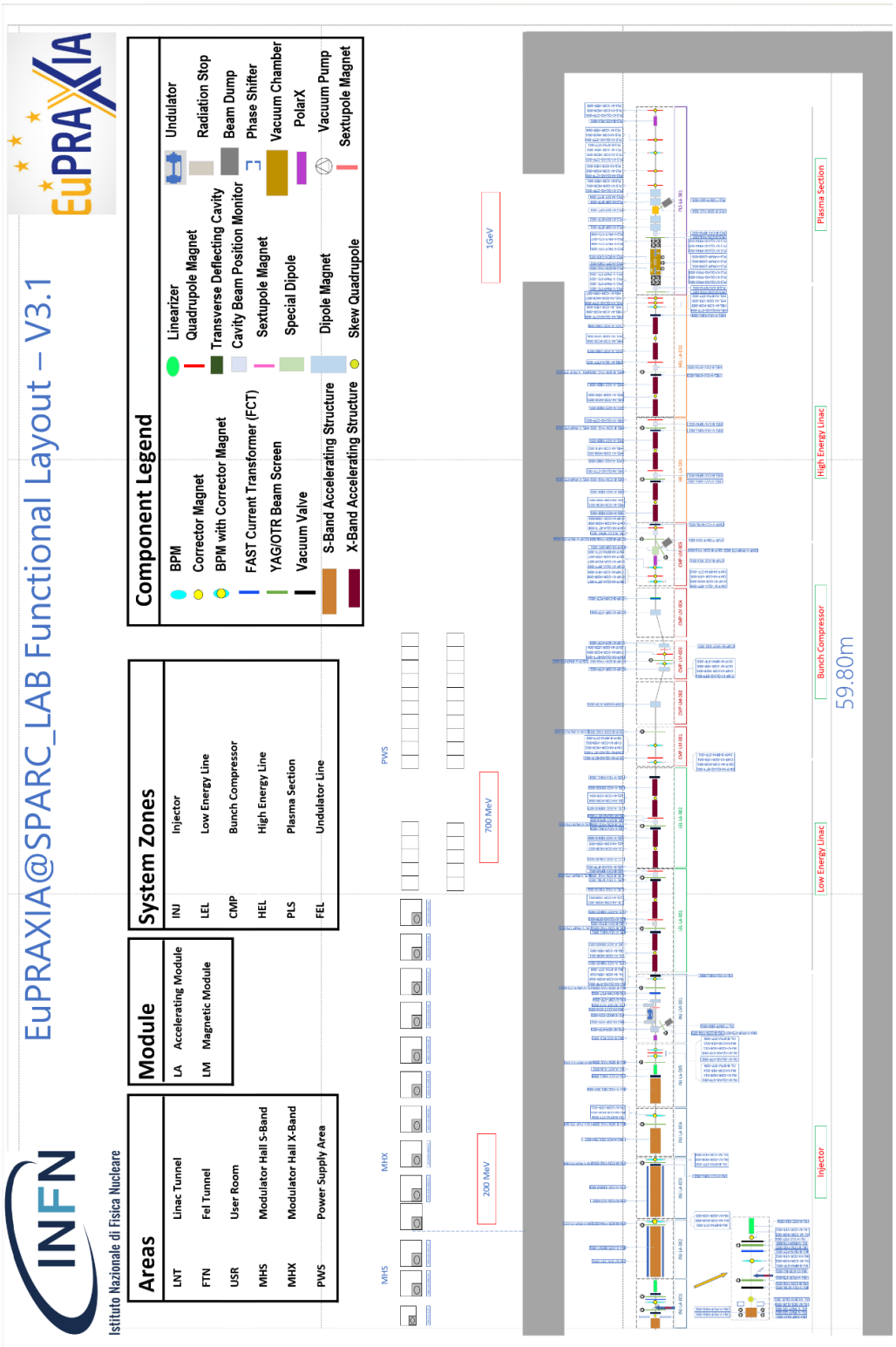

Figure 20.8: LINAC AREA

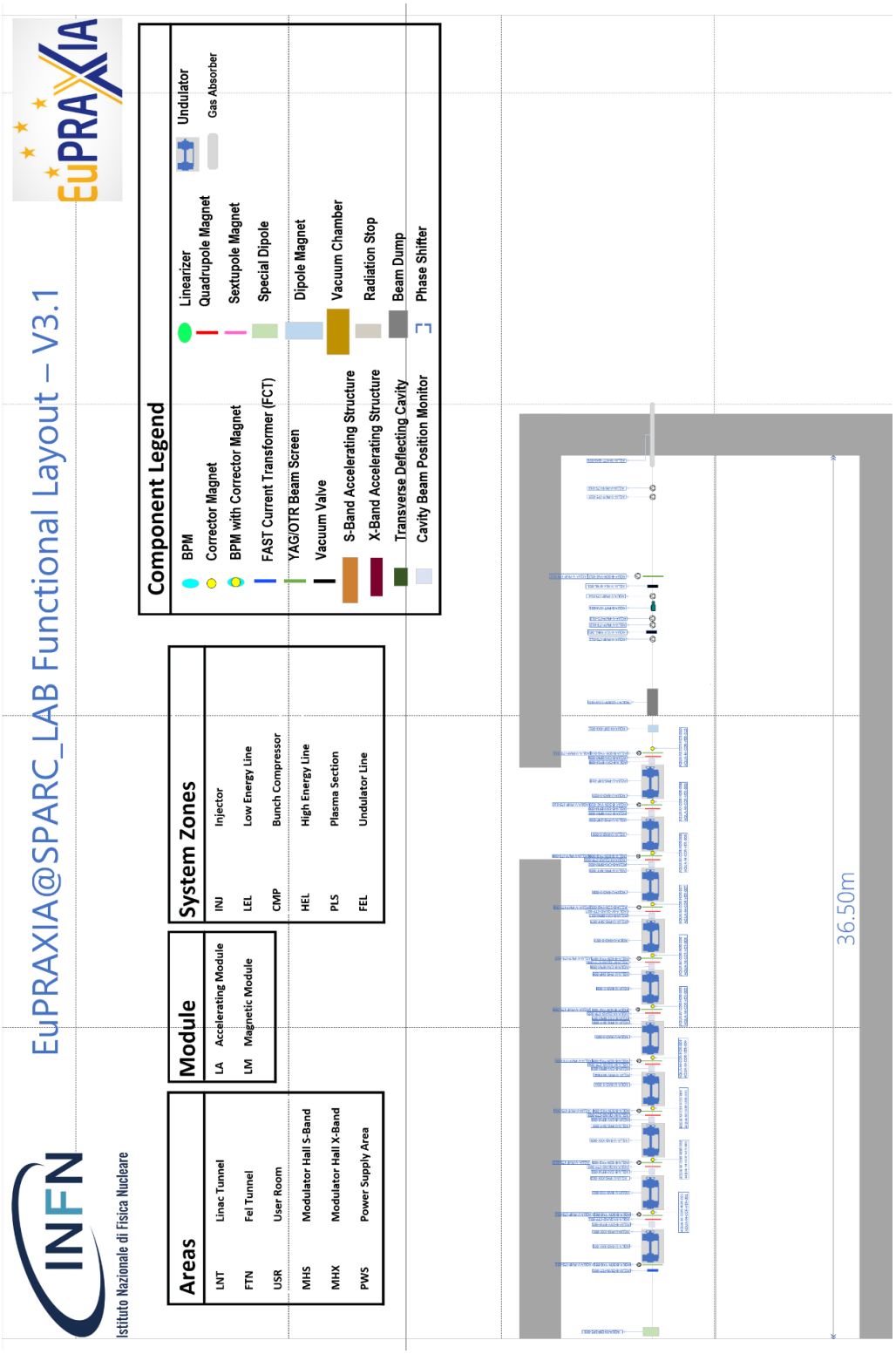

Figure 20.9: UNDULATOR AREA

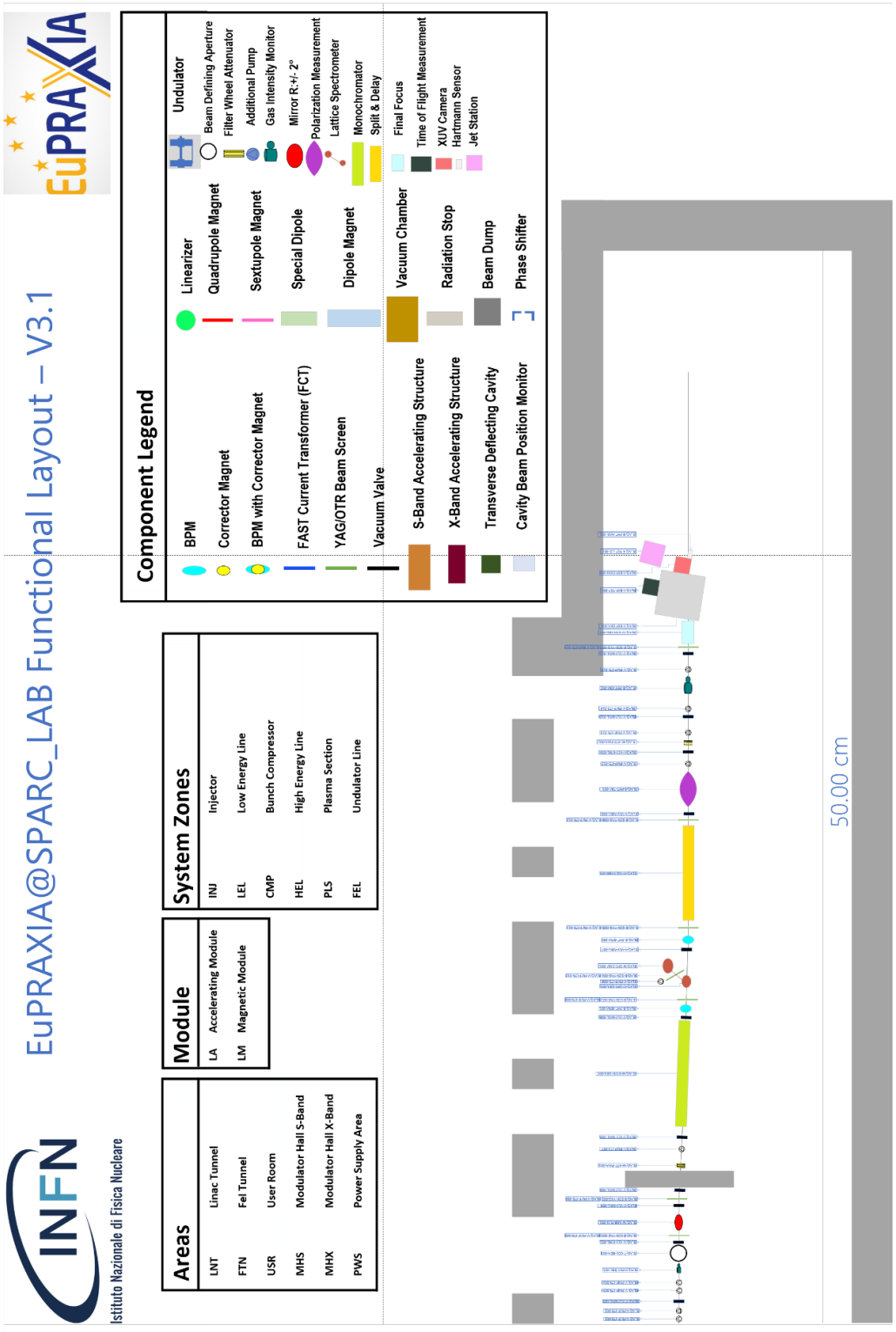

Figure 20.10: AQUA BEAMLINE AREA

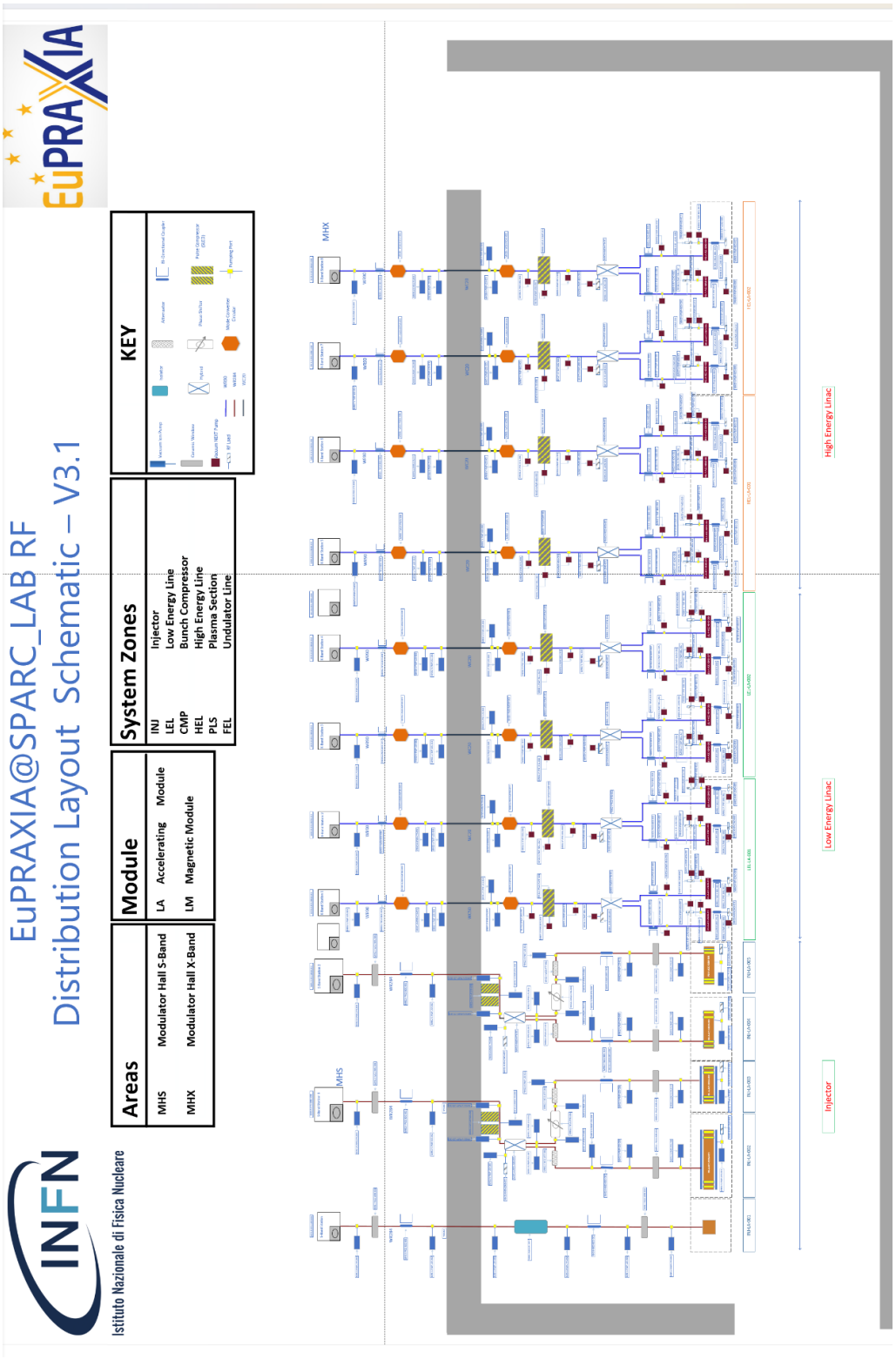

Figure 20.11: KLYSTRON GALLERY

20.5 Asset Management

Asset Management (AM) has been adopted as a strategic approach for the efficient and sustainable management of the project's technical and infrastructural resources. By integrating advanced technologies for real-time monitoring, failure prediction through artificial intelligence based on historical data [7], optimized maintenance planning, cost control, and risk analysis, AM ensures high operational performance, reduced downtime, and sustainable, cost-effective management. Within this framework, the PMO Service has implemented an advanced system based on a dedicated database, enabling detailed cataloging of resources, monitoring of operational conditions, maintenance tracking, fault analysis, and performance evaluation. For the initial phase, the software Hexagon EAM – Essential Bundle [8], compliant with ISO 55000 standards [9], was selected to improve operational efficiency and extend asset lifecycle. The system provides functionalities such as asset tracking, automated work order planning, inventory optimization, mobile access, and BIM integration. A pilot phase has been launched with the development of a structured database organized as a tree, representing hierarchical relationships and inter dependencies among subsystems. This model, aligned with the Project Breakdown Structure (PBS), facilitates life-cycle monitoring, operational integration, and maintenance activities, thereby supporting efficient and sustainable management of the accelerator. Fig. 20.12 illustrates how the database is structured using the described tool, providing a comprehensive overview of the project elements according to their respective reference areas. In this context, the application of the Verification & Validation

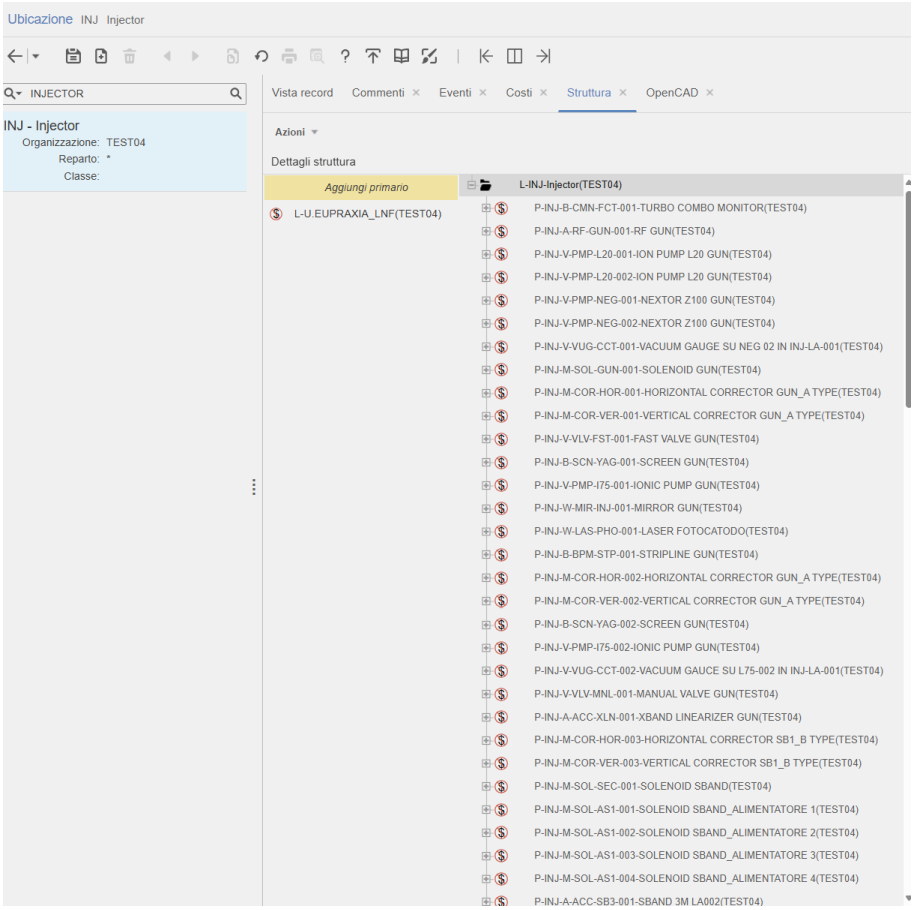

Figure 20.12: List of machine components entered into the Hexagon database filtered by work areas/zones such as the Injector.

(V&V) model proves particularly valuable as a method for assessing the project's progress, from the

implementation phase through to operational deployment. Through documented verifications and validations, the model enables an objective measurement of compliance with requirements, correct technical implementation, and the system's functional adequacy, providing a solid foundation for progress control and the timely identification of potential issues [10]. Moreover, by aligning these activities with the Capability Maturity Model Integration (CMMI) [11] framework, the project can benchmark the maturity of its processes and progressively evolve toward higher levels of operational excellence. The integration of V&V with CMMI maturity levels ensures that verification and validation outcomes are not only technical checks, but also indicators of organizational growth, process optimization, and continuous improvement across subsystems and project management practices.

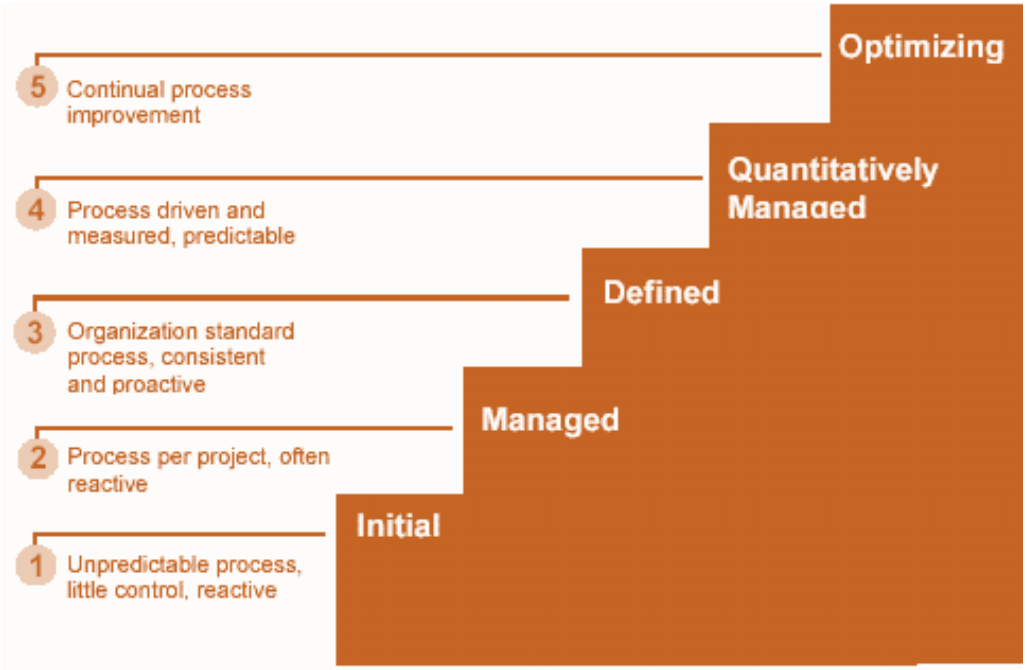

Figure 20.13: Scale of Maturity Levels in Project Configuration Management.

20.5.1 The PBS and Utility Matrix in the Context of EuPRAXIA@SPARC_LAB

The PBS [12] is a fundamental tool for analyzing, documenting, and making all planned physical deliverables visible to the entire project team. It is a hierarchical tree structure that decomposes the project into clear, controllable sub-products (deliverables), aligned with the technical competencies involved. The PBS begins with the final product and breaks it down into subsystems based on criteria of uniformity, expertise, and manageable complexity, thereby facilitating control using the available resources. Each element is uniquely identified according to the specific nomenclature detailed in the preceding paragraphs of this chapter. In addition to providing a graphical representation of the relationships between components, the PBS serves as a key instrument for:

- valuating and controlling material costs;
- assigning responsibilities;
- monitoring project maturity;
- ensuring effective communication among team members.

The methodology adopted for defining and managing the PBS is inspired by the standards of the Project Management Body of Knowledge (PMBOK®), the openSE methodology used within INFN, and engineering best practices from scientific and technological organizations. A practical

example of how the PBS structure was developed within System Engineering for managing machine components in our facility is illustrated through the second low-energy X-band accelerating module. This structure is applicable to the remaining modules, considering their repeatability at both low and high energy levels, with appropriate adjustments based on the energy used. The image below (Fig. 20.14) shows the schematic layout section of the low-energy accelerating module, which includes the following components:

- **4 X-Band Accelerating Sections.**
- **2 Horizontal/Vertical Correctors.**
- **2 Manual Valves.**
- **1 YAG Screen with associated Ion Pump.**
- **1 Cavity BPM.**
- **1 Quadrupole.**

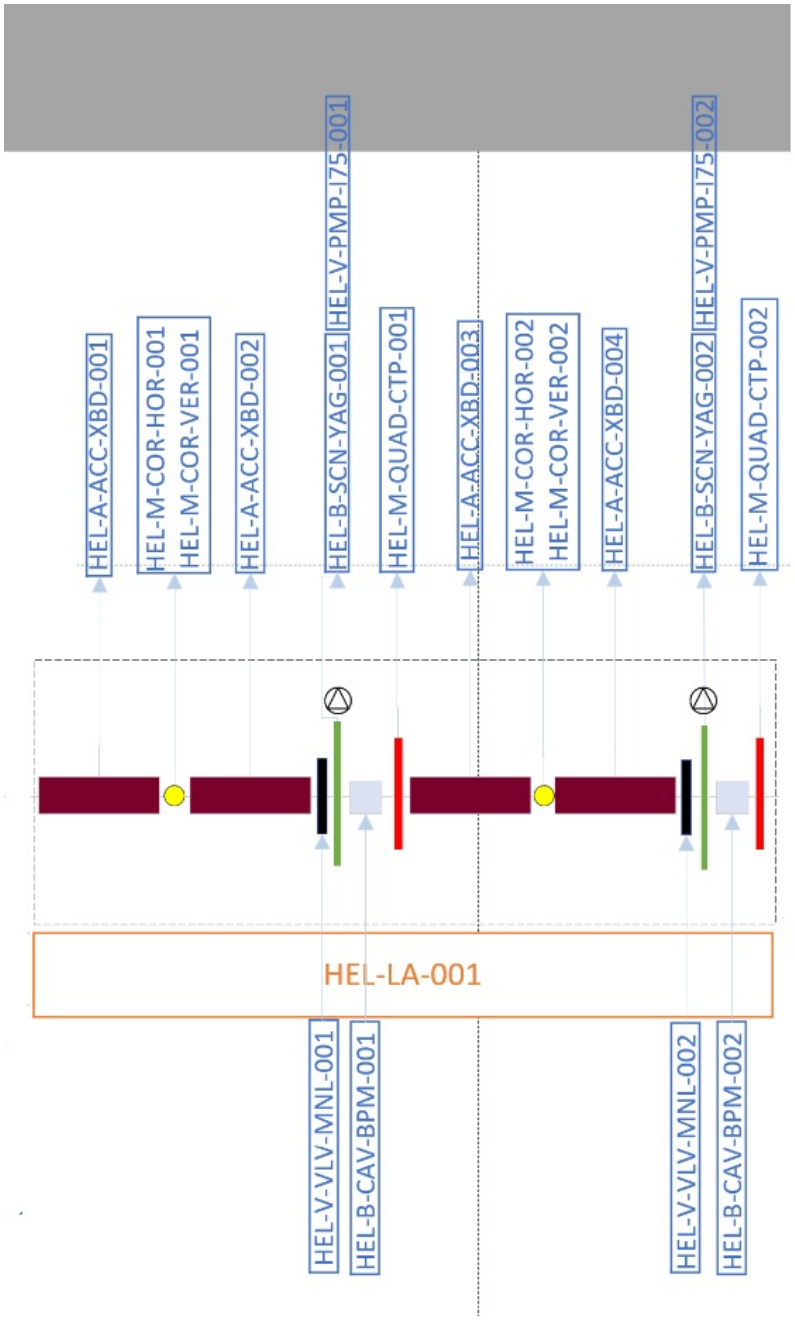

Figure 20.14: Schematic Layout of the Second Module of the X-Band Accelerating Section.

For each machine component, the PBS structure includes a set of common identification requirements, which are as follows:

- **ID**: a unique identifier automatically generated by the system.
- **WA Code**: identifies the relevant Working Area (WA).
- **WBS Code**: refers to the associated Work Package (WP).
- **Area/Zone**: indicates the physical location of the component.
- **System**: specifies the type of system to which the component belongs (A, V, M, etc., as described in Sec. 20.3).
- **Family**: denotes the family or category of the component.
- **Type**: defines the specific type within the same family.
- **Sequential Number**: used to identify the sequence of identical components along the line.

- **PBS Code**: encapsulates most of the above information related to the component.
- **Description**: a field for providing additional details about the component when necessary.
- **Module**: indicates the type of module (Accelerating or Magnetic) in which the component is located.
- **Unit Cost**.
- **Notes**.

Once these general attributes are defined, more specific and component-dependent parameters are added. For example, in the case of the X-band accelerating section of the second low-energy module, identified by PBS Code: LEL-A-ACC-XBD-005, additional structural and functional details are provided, as listed in Table 20.2.

Table 20.2: Technical specifications for component LEL-A-ACC-XBD-005.

Component	Technical Requirements
LEL-A-ACC-XBD-005	STRUCT. EFFECTIVE LENGTH [m]
	NUMBER OF CELLS
	AVERAGE ACC. GRADIENT [MV/m]
	FREQUENCY [GHz]
	IRIS RADIUS A [mm]
	TAPERING ANGLE [deg]
	MATERIAL
	SHUNT IMPEDANCE R [MΩ/m]
	EFFECTIVE SHUNT IMP. Rsh_eff [MΩ/m]
	PEAK INPUT POWER IN THE STRUCTURE [MW]
	INPUT POWER AVERAGED OVER THE PULSE [MW]
	AVERAGE DISSIPATED POWER [kW]
	KLYSTRON MAXIMUM AVAILABLE POWER [MW]
	QUALITY FACTOR
	Pout/PIN [%]
	RF-PULSE LENGTH [μs]

These additional entries enable the development of the Utility Matrix, a strategic tool that links each facility component to its corresponding datasheet, which contains both functional and performance requirements. This matrix serves as a foundation for designing the systems that will support the building housing the machine, as discussed in Civil Infrastructure Chapter 18. The Utility Matrix also facilitates the verification of consistency between the specifications dictated by beam dynamics and the technical and operational requirements, ensuring alignment with the design objectives of EuPRAXIA@SPARC_LAB. Fig. 20.15 displays the interface containing all relevant information for section LEL-A-ACC-XBD-005, as presented in the Hexagon database. Within this environment, the PBS is integrated, encompassing all elements included in the Schematic Layout.

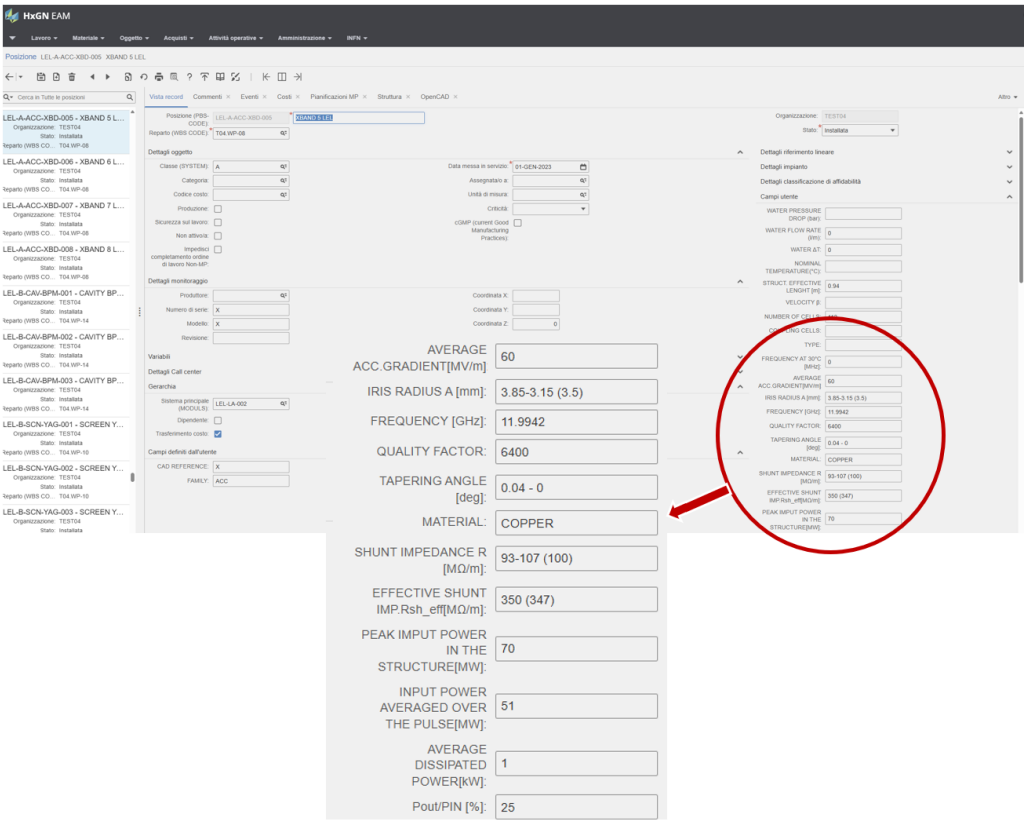

Figure 20.15: Example of Machine Component Classification.

Finally, the PBS proves to be a fundamental tool not only for the hierarchical representation of machine elements, but also for the development of an effective *procurement planning* strategy implemented by the Project Office. The summary Table 20.3 of the main systems, which synthesizes the content discussed in previous chapters, enables clear identification of the items to be procured, thereby facilitating purchase planning in alignment with the project's timeline and resource allocation. Furthermore, the PBS is tightly integrated into the Work Breakdown Structure (WBS), ensuring a perfect correspondence between the deliverables to be produced and the activities required for their realization. This integration provides a comprehensive and coordinated view between technical deliverables and operational processes, enhancing the overall management of the project.

Table 20.3: Summary of Main Machine Elements by System.

System	Element	Quantity
A - Acceleration	RF Gun	1
	S-Band 3 meters sect.	2
	S-Band 1.5 meters sect.	2
	Low Energy Linac sect. – X-band	8
	High Energy Linac sect. – X-band	8
	Linearizer	1
B - Diagnostic	Stripline BPM	14
	Cavity BPM	23
	Current Monitor	4
	View Screen	41
	PolariX TDS	2
M - Magnets	Solenoid	3
	Corrector H or V (Steerer)	46
	Dipole	16
	Quadrupole	30
	Permanent Quadrupole	16
	Sextupole	2
V - Vacuum	Ion Pump	234
	Turbo Pump	11
	Primary Pump	5
	Valve	40
	Vacuum Gauge	9

20.6 Conclusions

Not all components of the Project have reached the level of detailed (executive) design. The 3D layout of the Infrastructure, which includes the machine and experimental beamlines, has enabled a macroscopic verification of compatibility with the Beam Dynamics specifications and, consequently, with the Magnetic Layout. This assessment considered the approximate position and dimensions of all elements. It can be stated that the proposed infrastructure is suitable to host the EuPRAXIA Project. Structural solutions and provisions have been incorporated to ensure adequate installation and positioning tolerances for the components. These include aerial and floor connection openings between the klystron tunnel and the linac and undulator hall for RF distribution and signal/power cabling, as well as the dimensions of the floor trenches for laser line and cooling system distribution. From this point forward, until the complete definition of EuPRAXIA@SPARC_LAB's hardware design, it is essential to monitor the development and finalization of all remaining design elements to ensure compatibility, dimensional compliance, and expected performance. The desired implementation would require the availability of components according to a conventional chronological sequence. It is crucial to adhere to this sequence as closely as possible to optimize logistics, installation, testing, and commissioning.

In conclusion, the EuPRAXIA@SPARC_LAB project stands out as an advanced scientific

infrastructure, managed through a digital and systemic approach. The integration of the Hexagon EAM platform, or equivalents tools, enabled the development of an asset information model, ensuring traceability, consistency, and optimization. Furthermore, the adoption of international standards and Configuration Management tools (PBS, Utility Matrix, KPIs, and the V&V model) has facilitated change control, documentation efficiency, compliance with requirements, and overall system quality. This approach can therefore be considered a benchmark for the sustainable and integrated management of complex infrastructures [13].

Bibliography

[1] P. Bonnal et al. “openSE: A Systems engineering framework particularly suited to particle accelerator studies and development projects”. In: *arXiv preprint arXiv:1801.03836* (2018).

[2] M. Ferrario et al. “EuPRAXIA@SPARC_LAB Design study towards a compact FEL facility at LNF”. In: *Nuclear Instruments & Methods in Physics Research Section A 909, 134-138* (2018). URL: https://doi.org/10.1016/j.nima.2018.01.094.

[3] P. A. Walker et al. “Horizon 2020 EuPRAXIA design study”. In: *Journal of Physics: Conference Series*. Vol. 874. 1. IOP Publishing. 2017, p. 012029.

[4] R. B. Assmann, P. Walker, et al. “EuPRAXIA Conceptual Design Report”. In: *The European Physical Journal Special Topics* 229.24 (2020), pp. 3675–4284. DOI: 10.1140/epjst/e2020-000127-8. URL: https://doi.org/10.1140/epjst/e2020-000127-8.

[5] European Standard. *Facility Management - Sistemi di Gestione - Requisiti con guida di Utilizzo*. 2018.

[6] A. Falone. *EuPRAXIA@SPARC_LAB Naming Convention*. Internal Note INFN-LNF, 2020.

[7] A. Apollonio and L. Serio. *Data-driven operation and maintenance for particle accelerators*. TE-MPE, EN-ARP. 2020. URL: https://indico.cern.ch/event/985701/contributions/4150743/attachments/2164877/3653487/20201123_SMARTLinac-proposal_MZ.pdf.

[8] Hexagon. *HxGN EAM: Il software gestionale leader di mercato per la gestione degli asset*. Brochure ufficiale. 2025. URL: https://hexagon.com/products/hxgn-eam.

[9] European Standard. *Gestione dei beni(Asset Managementi)- Line guide per l’applicazione della ISO 55001*. 2020.

[10] A. Oppermann. *V mmodel*. 2023. URL: https://builtin.com/software-engineering-perspectives/v-model.

[11] J. Yamfashije. *Capability Maturity Model Integration*. 2017. DOI: 10.13140/RG.2.2.35219.94247.

[12] A. Falone. *Criteri per la redazione della Project Breakdown Structure - PBS- EuPRAXIA@SPARC_LAB*. Internal Note INFN-LNF, 2018.

[13] A. Florentina. *Gestione dei progetti attraverso la tecnica SCRUM*. 2016.

21. Sustainability

21.1 Introduction

The goal of this appendix is to define and document the sustainability strategies adopted in the design, construction, and operation of the EuPRAXIA@SPARC_LAB facility. It aims to demonstrate compliance with European and national environmental regulations—particularly the Do No Significant Harm (DNSH) principle and the Italian Criteri Ambientali Minimi (CAM)—and to quantify the measures implemented to reduce the project's carbon footprint and resource consumption.

The chapter covers energy production and efficiency, HVAC and process-cooling optimization, sustainable materials, waste and water management, greenhouse gas reduction, and Life Cycle Assessment (LCA) activities. It provides a unified framework for sustainability across all facility subsystems and cross-references related chapters (Civil Engineering, RF Systems, and System Engineering) to ensure technical and operational consistency within the TDR.

21.2 LNF campus greening strategies

LNF has been committed, for several years, to reduce its carbon footprint both due to general services and particle accelerator devices.

The long term annual log of energy demand (Fig. 21.1), divided in base load and accelerators, shows the continuous reduction in terms of energy demand both for DAΦNE accelerator and for the base load.

In the last ten years the base load has been reduced of about 20% with several activities that involved the renewing of inefficient devices but also a growing sensitivity of users to the energy and the environmental aspects.

About particle accelerators it is worth remembering the DAΦNE upgrade, between 2007-2012, that has reduced its power demand from 5.9 to 3.3 MW in some steps (i.e. in Fig. 21.2 the difference can be appreciated on the annual consumption comparing years 2000 and 2017 that have similar run days of the accelerator.).

Decarbonization, in terms of usage of natural gas for winter heating has been realized with some rationalizations, some heat pump installations, but mainly by the realization of the Data

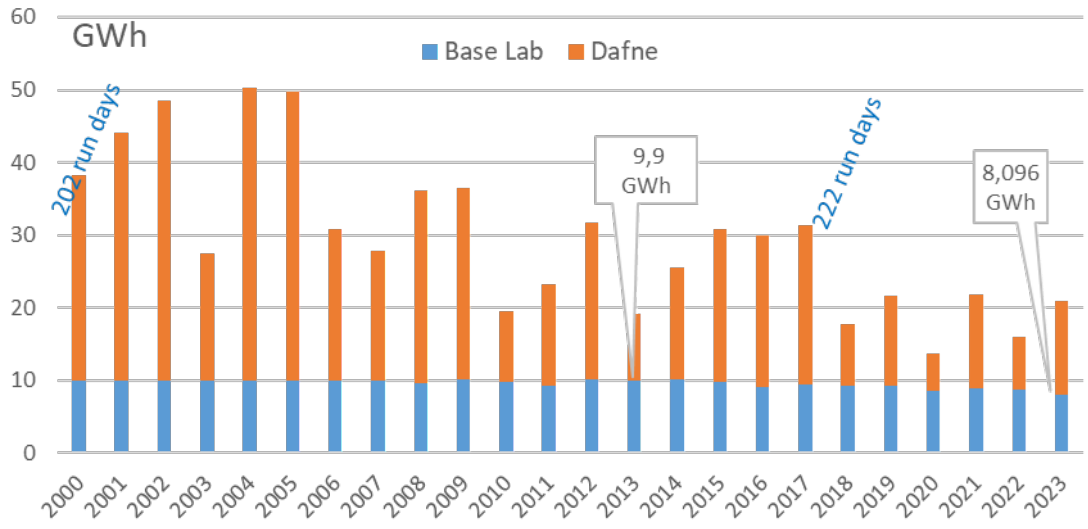

Figure 21.1: Annual electrical power demand

Center heat recovery system that has been delivering about 1 GWh/year of recovered heat from 2015. Fig. 21.2 shows the trend of the Natural gas usage.

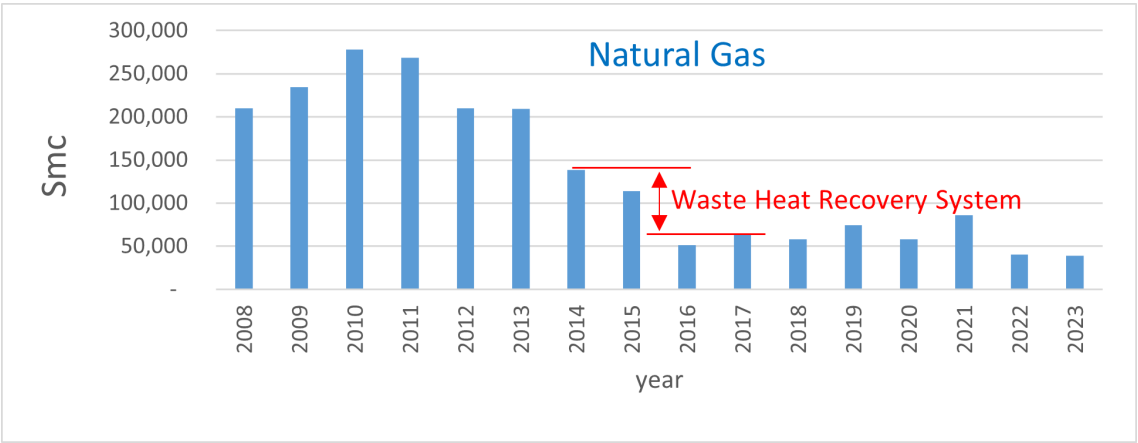

Figure 21.2: Trend of Natural gas annual demand (in standard cubic meter of gas)

Based on this experience, the heat recovery concept along with the usage of low-grade heat have been adopted as a standard for future projects and also for EuPRAXIA@SPARC_LAB.

1.1 MW of photovoltaic generation on LNF buildings will be completed in 2025. This will produce about 1.5 GWh/year of green energy. The new building EuPRAXIA@SPARC_LAB will add 217 kW of photovoltaic as external technical areas shading. About 400 kW of additional photovoltaic sources are now under evaluation over the roof of building 59, recently acquired.

In 2024 the first INFN Environmental Report has been published, that offers a survey of sustainability key aspects. LNF Carbon footprint assessment results of the report is available on [1].

21.3 Sustainability Regulation and duties in Italy

EuPRAXIA, as every procurement procedure, must comply current regulations also in therms of sustainability. In particular, the DNSH principle and the Green Public procurement regulation have to be satisfied.

The DNSH principle (Do No Significant Harm) [2], key element of the EU Taxonomy's environmental regulation, focuses on avoiding significant negative impacts on the environment and society and is mandatory in all public procurements. This approach covers several aspects of the conventional activities, from the design to the decommissioning.

The European *Green Public Procurement regulation* has been implemented in Italy with a list of action and environmental requirements named "CAM" that specifies minimal requirements for public procurement, mainly related to building, HVAC and electronic equipment. CAM are mandatory and inserted in the building tender.

21.4 EuPRAXIA@SPARC_LAB Building

The building project includes design solutions that comply with the minimum environmental criteria (CAM) required by Italian law, Decreto Ministeriale 23.06.2022 [3].

The application of environmental design criteria concerns:

- integration of the new building into the naturalistic and landscape context;
- design techniques to ensure good energy performance;
- choice of building products and materials;
- specific design choices for the construction phase.

21.4.1 Integration of the new building into the naturalistic and landscape context

The building project aims to improve the area's environmental quality by enhancing a system of diversified and integrated spaces, reflecting its peri-urban vocation and serving science while respecting the context. Integration, functionality and safety, clear pathways, and biodiversity are the primary objectives.

Permeability of the territorial surface and reduction of the "summer heat island" effect

The project guarantees a permeable surface equal to 64% (minimal acceptable 60%) of the total surface area with:

- green areas with grassy surface with a permeability index of 100%;
- parking areas with interlocking paving, 80% permeable.

The green roof of the building guarantees an SRI, Solar Reflectance Index, index of at least 76 (roofs with a slope less than or equal to 15%). The paved surfaces of the roof will feature light-coloured materials compliant with the SRI ≥ 76 requirement (point and slope less than 15%).

The outdoor areas intended for parking or vehicle storage are shaded by trees for at least 10% of the area. The perimeter of the area is bordered by a green belt no less than 1 m high. There are 5 motorcycle parking spaces and 12 bicycle spaces.

Collection, purification and reuse of rainwater

The project includes the construction of a rainwater harvesting, which conducts the first rainfall into an underground first flush basin located. This basin will have a capacity similar to that of the nearby retention basin, with which it will work for the sustainable management of stormwater runoff.

Water from drainage surfaces not subject to pollution will be collected to be reused for irrigation purposes and to fill the toilet cisterns.

Energy supply

A photovoltaic system with an installed peak power of approximately 217 kWp is planned. The collection fields will consist of monocrystalline silicon photovoltaic panels with a unit power of 500 Wp, installed above the AHUs and heat pumps on special metal support structures with a 25° inclination from the horizontal. The inverters for photovoltaic conversion will be installed outdoors on the terraces where the AHUs are located.

21.4.2 Design techniques to ensure good energy performance

The project includes various solutions that allow for the control of the building's energy performance:

1. the surface mass and periodic thermal transmittance requirements of the external envelope have been verified in accordance with current legislation;
2. the lighting system includes an automatic on/off and dimming management system that operates on a time-based basis, considering brightness and the presence of people;
3. the building's air conditioning system complies with Class 2 of the UNI EN 16798-1 standard in accordance with the very low polluting building requirement;
4. the use of screening panels made of perforated press-formed sheet metal placed on the outside (the expected perforation percentage equal to 50% of the surface) will guarantee at the same time the contribution of natural light and shielding from harmful radiation.

21.4.3 Choice of building products and materials

The project requires the construction of a concrete shield for a total of approximately 20,000 tons for the tunnel linac and undulator hall and other experimental halls. Building a new infrastructure will involve large carbon emissions.

Anyway, the building design includes also requirements for the choice of building materials: e.g., for non-structural masonry structures, the project includes products in autoclaved aerated concrete and in vibro-compressed concrete with a content of recovered or recycled material, or of by-products, of at least 5% of the weight of the product. This is valid also for steel, PVC and polypropylene pipes.

21.4.4 Specific design choices for the construction phase

Building construction phase is among the most impactful on the environment.

During the design phase, a preliminary soil analysis was carried out to characterize the site. This analysis revealed that excavation materials can be reused as by-product. So, the excavation work will produce approximately 97,000 cubic meters of soil and rock. Of this, approximately 14,000 cubic meters will be reused for backfilling, while nearly 19,000 cubic meters will be landfilled. The remain will be reused in backfilling quarries and mines or in other site construction, where technically appropriate, if there is a market for them.

In accordance with the Italian law for the CAM, the building design includes an end-of-life and disassembly study (Life Cycle Analysis) with an analysis of the recycling percentages of the individual types of materials used in the project. In addition, in the tender for the works, we ask the companies for a technical offer that includes proposals for improving the environmental impact of the work, for example, proposals for low-carbon solutions during the construction phase with the use of certifiable eco-friendly materials, means and/or techniques.

21.5 Sustainability Aspects of RF systems

In the framework of the EuPRAXIA@SPARC_LAB project, sustainability has been identified as a key guiding principle in the future operation of the linear accelerator. Particle accelerators are inherently power-intensive infrastructures, and international roadmaps increasingly emphasize the need to minimize their environmental footprint through life-cycle-conscious engineering and energy-efficient subsystem choices.

Within this context, the energy consumption of the radiofrequency (RF) systems represents a substantial portion of the total power budget. For the EuPRAXIA@SPARC_LAB linac, this contribution is estimated to be in the range of 40–50%, highlighting the need to improve RF system efficiency. The RF power system of the EuPRAXIA@SPARC_LAB linac consists of thirteen RF

Table 21.1: Main specification of the VKX83113 CPI klystron high efficiency prototype

Parameter	Value	Unit
RF Frequency	11.9942	GHz
Peak RF power	50	MW
RF pulse width (at -3dB)	1.5	ms
Pulse repetition rate	100	Hz
Average RF Power	7.5	kW
Klystron peak voltage	430	kW
Klystron peak current	212	A
Perveance	0.75	$mA/V^{1.5}$
Gain at peak power	50	dB
Bandwidth (at -3 dB)	50	MHz
Efficiency at saturation	55	%

stations, each comprising a high-voltage (HV) pulsed modulator driving a klystron as the final amplification stage. Efforts are underway to improve the overall efficiency of these RF stations, in particular the X-band sources, which account for 10 out of the 13 stations.

Klystrons currently available for scientific applications typically achieve efficiencies between 43% and 45%, which results in significant energy losses even under pulsed operation. The efficiency of a klystron is defined as the ratio of RF output power to the beam power delivered to the electron beam from the modulator, the latter being calculated as the product of beam current and voltage. The RF drive power at the input is negligible and typically amounts to a few tens of watts. To increase klystron efficiency, we are actively supporting R&D programs in close collaboration with CERN. In recent years, this effort has led to the successful design, and in some cases, prototyping and testing, of novel high-efficiency klystrons, achieving efficiency improvements of up to 10% [4]. As part of this broader initiative, a high-efficiency X-band 50 MW klystron prototype, jointly developed by CERN and CPI and named VKX83113, is currently being procured by INFN. This device is expected to reach efficiency levels higher than 55%, compared to the 46% efficiency of standard commercial models. Table 21.1 summarizes its main design parameters.

Testing of this klystron is scheduled to take place at INFN-LNF in January 2026. In parallel, under the EU-funded PACRI (Plasma Accelerator Systems for Compact Research Infrastructure) project [5], in the WP06 “High efficiency RF generator” development is ongoing on a second high-efficiency (> 50%) X-band klystron prototype, rated at 25 MW, specifically designed to operate at repetition rates exceeding 400 Hz. These efforts, involving both the 50 MW and 25 MW X-band klystrons, reflect a coordinated European strategy to improve the sustainability of RF sources for next-generation accelerators. The development of these high-efficiency X-band devices is expected to directly benefit the EuPRAXIA@SPARC_LAB project by increasing overall RF system efficiency, thus enhancing the energy performance and in particular long-term sustainability of the linac infrastructure.

The pulsed modulator, which supplies the high-voltage pulse to the klystron, also plays a key role. To ensure a flat-top RF output, the HV pulse must be longer than the RF pulse itself, accommodating both the rise and fall times. For EuPRAXIA@SPARC_LAB, the choice of solid-state modulators is central to improving energy efficiency and reducing environmental impact. These systems enable faster voltage transitions, which reduce pulsed power losses and improve energy transfer to the klystron. Additionally, they allow electronic shaping of the pulse duration to

match the RF signal envelope, minimizing excess power delivery. Unlike conventional modulators based on thyratrons, solid-state systems do not rely on consumable or hazardous components such as gas-filled tubes or mercury-based elements. This greatly reduces maintenance requirements and eliminates issues related to the disposal and handling of such materials. Moreover, their modular architecture enables simplified maintenance, extended operational lifetime, and seamless integration into sustainable facility operation models.

Finally, significant efforts have been made to minimize power losses in the X-band waveguide distribution system. As reported in Chapter 13, conventional WR90 rectangular waveguides operating in X-band exhibit a relatively high attenuation coefficient of approximately 0.1 dB/m. For this reason, a dedicated R&D activity, carried out in collaboration with CERN, has focused on the development of double-height waveguides and the adoption of circular waveguides. Both solutions enable more efficient long-distance power transmission with significantly reduced losses.

21.6 HVAC

In the EuPRAXIA@SPARC_LAB project, the HVAC (Heating, Ventilation and Air Conditioning) system is designed to ensure optimal indoor conditions, supporting both technical operations and occupant comfort and is developed with a strong focus on sustainability, integrating advanced technologies and design strategies aimed at minimizing environmental impact and reducing energy consumption. Importantly, its role extends beyond basic cooling: it is specifically tasked with keeping the accelerator hall temperature highly stable. This level of control is essential, as temperature deviations greater than 0.5 °C can adversely affect the instrument spatial and temporal resolution, ultimately impacting the accelerator performance.

High-efficiency chillers and heat pumps equipped with inverter technology are adopted to optimize energy use across varying load conditions. The system includes variable-speed drives on fans and pumps, allowing continuous adaptation to real-time thermal demands and significantly improving operational efficiency. Free cooling and heat recovery solutions are also in place, enabling the use of ambient air or recovered waste heat to reduce the load on refrigeration equipment. Environmentally friendly design choices are made throughout, including the use of low-GWP refrigerants and materials selected for durability, recyclability, and compliance with LCA principles. The entire system has been conceived to support long-term operational sustainability, reduce greenhouse gas emissions and contribute to the achievement of environmental performance targets and green building certifications.

The air conditioning system is sustained by thirteen Air Handling Units (AHUs), two multi-purpose units operating with a temperature range of 40-35 °C and 7-12 °C and two heat recovery chillers with integrated free cooling function operating with a temperature range of 40-35 °C and 15-20 °C. The heat transfer fluids produced supply the heat exchange coils of the AHUs, the fan coils and the radiators located in the toilets.

The system design considers the following extreme outdoor climatic conditions: during the winter season, a dry bulb temperature of -2 °C with 80% relative humidity; during the summer season, a dry bulb temperature of 35 °C with 55% relative humidity. These boundary conditions are used for the sizing and performance assessment of HVAC components and thermal exchange systems.

An analysis is carried out to evaluate the efficiency of the refrigeration units (Figs. 21.3 to 21.8).

In relation to the potential recovery of thermal energy from the EuPRAXIA@SPARC_LAB building (through the use of polyvalent and heat recovery units), an analysis is carried out on the energy consumption of nearby buildings, as well as on their current heating and cooling generation systems. Specifically, several buildings are currently served by heat pump chillers, while others rely on dedicated boiler systems. As a reference, the winter season 2022-2023 is considered, characterized by 170 days of operation (from early November to approximately April 7th). Based

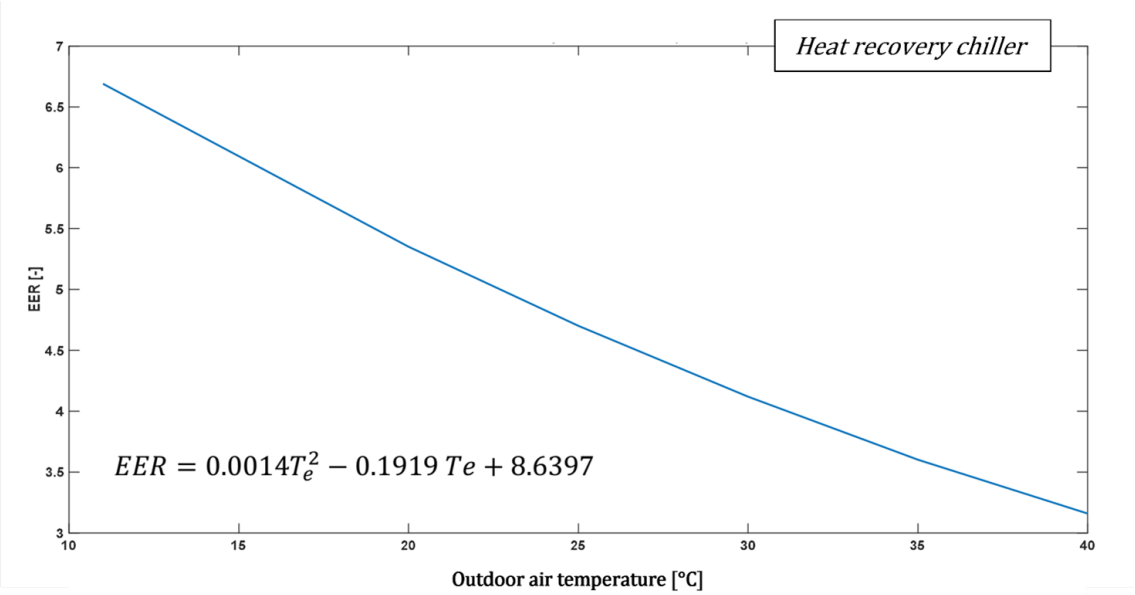

Figure 21.3: EER depending on outdoor air temperature (under peak load conditions), operating mode without free cooling

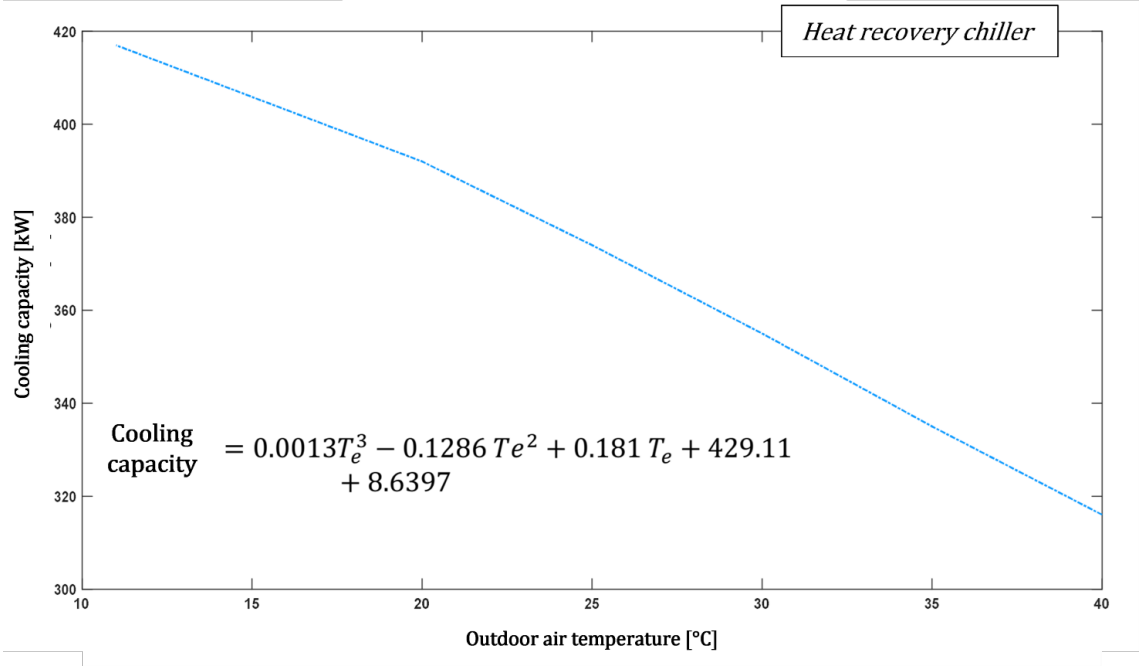

Figure 21.4: Cooling capacity depending on outdoor air temperature (under peak load conditions), operating mode without free cooling

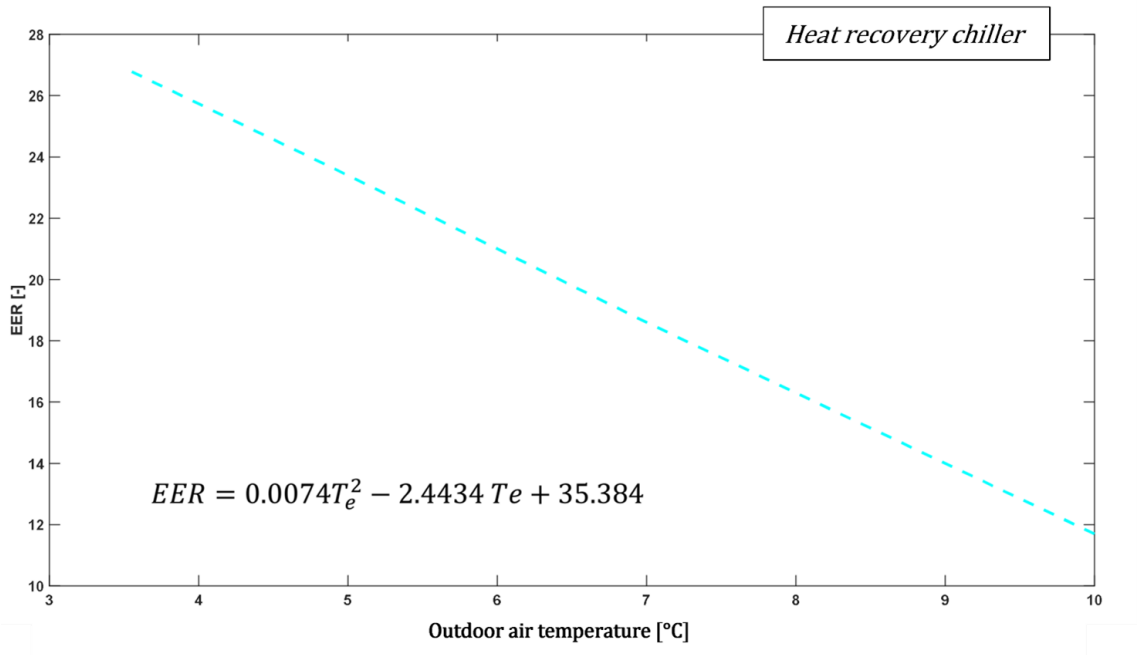

Figure 21.5: EER depending on outdoor air temperature, free cooling operating mode

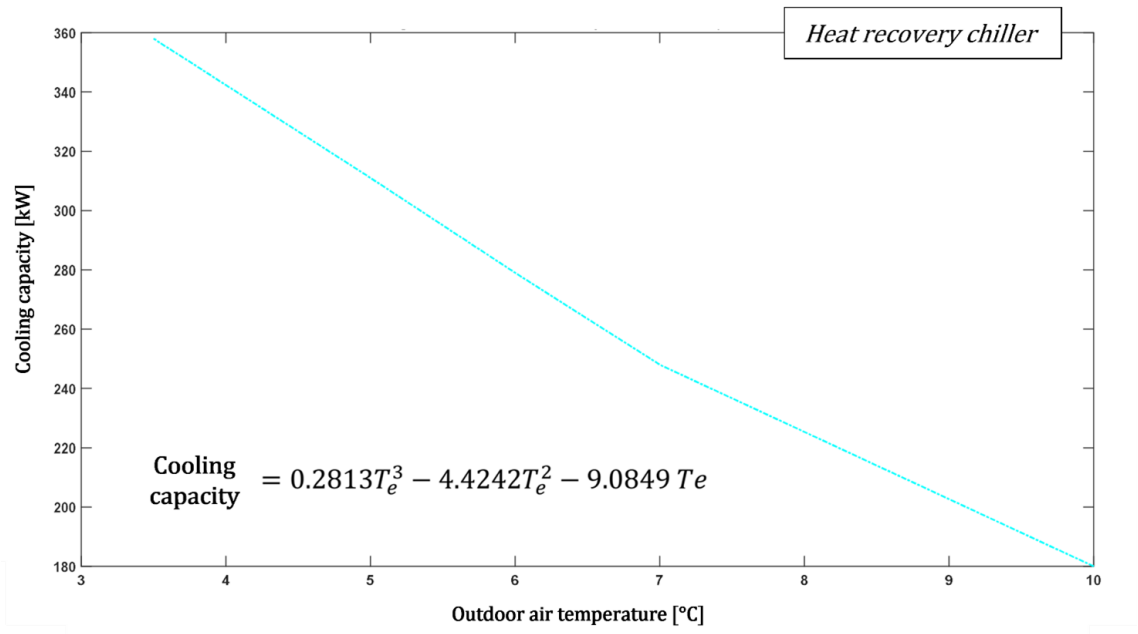

Figure 21.6: Cooling capacity depending on outdoor air temperature, free cooling operating mode

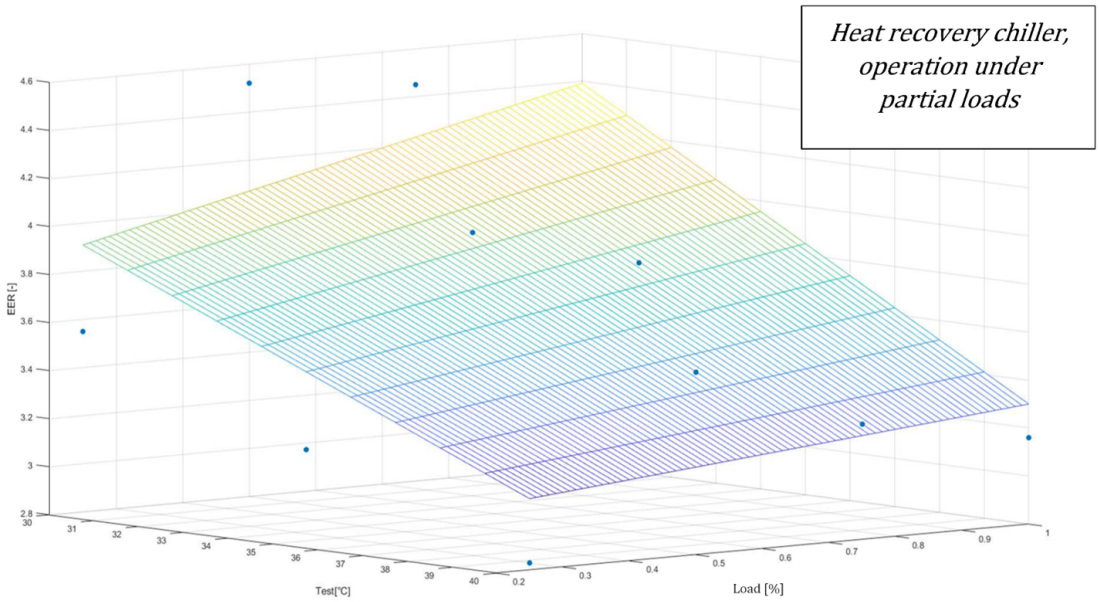

$$EER = 5.91 - 0.072\,T_{est} + 1.758\,Perc - 0.0372\,T_{est}Perc$$

Figure 21.7: Interpolating surface for partial load operation

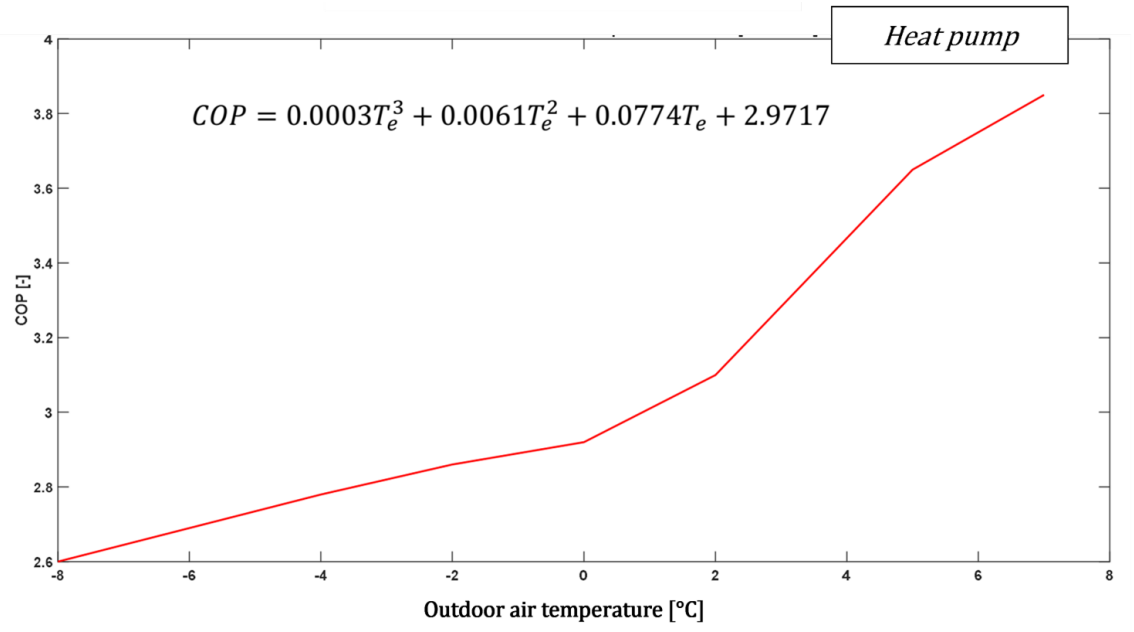

Figure 21.8: COP depending on outdoor air temperature

on the operating period and the specific outdoor temperatures, a back-fitting analysis is performed using tailored climatic curves, in order to replicate the measured energy consumption values during the specified operating hours (typically from 7:00 a.m. to 5:00 p.m.). This approach enables the reconstruction of hourly energy consumption profiles for the different buildings, allowing for an accurate sizing of the thermal energy recovery system to be implemented.

The estimated energy consumption over a year for HVAC systems is around 1000 MWh, including the thermal energy supply for nearby buildings covered in part by the heat recovery from the EuPRAXIA@SPARC_LAB system and, to a lesser extent, by the equipment currently serving the buildings.

An advanced control architecture, based on Programmable Logic Controllers (PLCs) and integrated into a centralized Building Management System (BMS), regulates temperature, humidity, and airflow dynamically, ensuring precise environmental control while minimizing energy waste.

With these strategies fully implemented, the HVAC infrastructure not only ensures high thermal comfort and reliability but also represents a significant step toward a low-carbon, energy-efficient facility.

21.7 Process cooling

Particle accelerators are among the most energy-intensive scientific instruments, absorbing large amounts of electrical power to generate high-energy particle beams. A significant fraction of this energy consumption is not directly used to accelerate particles, but rather to support essential auxiliary systems - chief among them, the cooling infrastructure. Thermal management plays a crucial role to ensure safe and reliable functioning, without adequate cooling, thermal expansion and overheating can degrade beam quality, shorten equipment lifespan and compromise the integrity of experiments.

Given these tasks, improving the energy sustainability of cooling systems is a key area of focus for the design, upgrade and operation of EuPRAXIA@SPARC_LAB facility. The integration of high-efficiency cooling technologies, advanced control systems and energy recovery methods is not only a matter of operational cost, but a crucial step toward reducing the carbon footprint.

To address the substantial energy demands associated with cooling, a range of strategies have been developed and implemented. These approaches aim to enhance thermal efficiency, reduce operational costs and minimize environmental impact, all without compromising performance or reliability.

EuPRAXIA@SPARC_LAB high efficiency cooling system relies on closed water loop and employs variable speed pumps that adapt to the thermal load in real time, reducing unnecessary energy use during partial load operation, high performance heat exchangers with optimized surface area for effective heat transfer and advanced water treatment and purification system that extends component life and improve thermal conductivity. As part of the design, refrigeration units operating with low GWP (Global Warming Potential) refrigerants are selected. This design choice is driven by the need to reduce the environmental impact associated with direct refrigerant emissions, in line with the current European F-Gas Regulation and international climate policies.

Based on a standard chiller, the overhead for refrigeration and pumping of the cooling water is estimated to be around 35% of the base power requirement for each water-cooled component. The use of units equipped with adiabatic cooling allows the energy overhead to be limited to within 10% of the base power requirement. The climatic conditions at the installation site allow for the use of adiabatic cooling, thanks to the implementation of adiabatic dry coolers (the minimum operating temperature is 28 °C, based on outdoor air conditions of 35 °C and 50% relative humidity), that involve minimal use of water for adiabatic operation over a year, useful for facilitating heat transfer. Approximately 0.2% of the mass to be cooled evaporates, thus returning to the environment (typically in medium-hot periods a specific section is sprayed with water to reduce

the air temperature). Almost 97% of the total cooling power demand is provided by the adiabatic dry cooler with an electrical power consumption of about 40 kW. The use of the dry cooler as the primary cooling device enables efficient thermal management of the equipment, reducing reliance on more energy-intensive refrigeration methods and contributing to overall system sustainability.

Subsystems requiring operating temperatures below the limits of the adiabatic dry coolers are cooled using chillers. In the case of air-cooled machines use of electrical energy is only for refrigerant gas compression and the use of one or more fans for the refrigerant condensing phase with the possibility of free cooling solutions which allows for energy savings of up to 50%, implemented during cooler seasons.

The estimated electrical power demand for the adiabatic dry cooler unit, chiller, pumps and other auxiliaries of the process cooling system is around 90 kW. The annual electrical energy consumption for the cooling plants of the accelerator baseline configuration has been simulated considering the Test Reference Year, with hourly weather data, developed by the LNF Technical Division. As a result, the energy consumption is 382 MWh/year, corresponding to an average electrical power demand of 45 kW.

The contribution to the carbon footprint from the manufacturing machines can be reduced focusing on a careful choice of materials to be used in the construction of them, this is through research into components that encourage recycling at the end of their life (green cooling solutions). Moreover, the use of remanufactured cooling systems offers a sustainable solution for the environment due to the lower use of energy and raw materials. The analysis of the most optimized solution should be accompanied by LCA analysis, electricity use and water use to evaluate the carbon footprint impact. The implementation of PLC management for all machines enables energy saving in the order of 80% over lifecycle.

Instead of rejecting waste heat, EuPRAXIA@SPARC_LAB facility is designed to repurpose thermal energy for supplying LNF heating network and pre-heating facility air or water systems. These strategies improve the facility's energy balance and reduce dependence on external heating sources.

The implementation of a smart thermal management that consists of advanced sensors, real-time diagnostics and AI-driven control systems allows for predictive maintenance and adaptive load balancing. These techniques ensure optimal energy usage under varying operational conditions.

In conclusion, improving the energy sustainability of EuPRAXIA@SPARC_LAB requires a holistic approach in which cooling system plays a central role. By adopting high-efficiency cooling infrastructure, reusing waste heat, leveraging smart controls and designing for compactness, EuPRAXIA@SPARC_LAB exemplifies how advanced technologies and strategic facility design can work together to minimize environmental impact.

21.8 Greenhouse gas

Very small amount of SF6 (GWP 22.800) are used only for RF circulators, and a recovery system is foreseen. Medium voltage devices are completely SF6 free, and vacuum switch and dry-air insulated switchboard are in the design. Refrigerators use gases with GWP < 675.

21.9 Energetic mix and CO2

Most of electric power is supplied by the grid. Average composition of the sources and their carbon intensity depend on the suppliers, but referring to the national data (Tab. 21.9), 59% of energy is not renewable.

Carbon Intensity of the Italian mix based on 2024 data is 297 gCO2eq/kWh.

At LNF 2.3 GWh per year of renewable energy will be generated by 1.7 MW of photovoltaic fields on the LNF building, that have to be compared to 8 GWh of the LNF baseload and 7.5 GWh

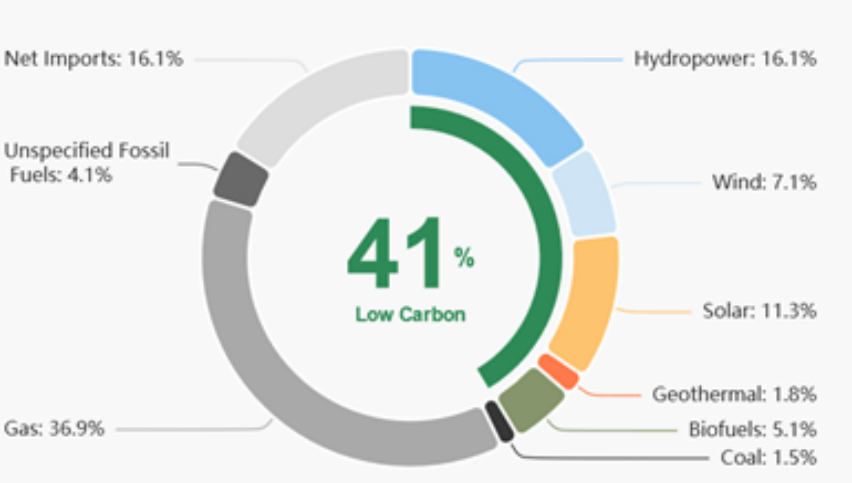

Figure 21.9: Italian energy mix

of EuPRAXIA@SPARC_LAB baseline annual energy demand.

21.10 Sustainability Benefits of Plasma-Based Acceleration

Although the current RF LINAC layout has been intentionally designed to be longer than strictly necessary for risk mitigation, an optimized EuPRAXIA@SPARC_LAB configuration would accelerate the beam to approximately 550 MeV using only the S-band injector (about 120 MeV in velocity-bunching configuration) and four X-band modules operating at 60 MV/m (providing an additional ~ 480 MeV), with the remaining energy supplied by the plasma booster.

Operating in this minimized-RF mode would reduce the RF power demand from 575 kW to 400 kW, corresponding to a reduction greater than 30% with respect to the Full RF linac configuration. The plasma booster also replaces a significant fraction of conventional RF infrastructure: a plasma module approximately 6 m long (including matching sections, vacuum chamber (3.7 m) and the driver–witness separator (2.3 m)) substitutes for about 10 m of X-band linac, reducing the associated capital investment from roughly 9.8 M€ to about 2.2 M€.

Plasma acceleration therefore enables GeV-scale beam energies with a substantially **smaller RF footprint, reduced capital costs, and significantly lower electrical power consumption, cooling requirements, and associated CO_2 emissions over the facility lifetime**.

More generally, the sustainability benefit of the plasma accelerator module improves with increasing target beam energy and can be expressed in closed form using asymptotic scaling relations. For a single-stage plasma wakefield accelerator operating with transformer ratio T, the relative reduction of installed RF power asymptotically approaches:

$$\frac{\Delta P}{P_{\mathrm{RF}}^{\mathrm{RF}}} \to 1 - \frac{1}{T},$$

independently of injector length and low-energy details. In the energy-doubling configuration ($T = 2$) considered here, this corresponds to an intrinsic RF power reduction approaching 50% in the multi-GeV regime, with even larger savings achievable for higher transformer ratios.

The corresponding reduction in total accelerator length reflects the competition between the high accelerating gradient achievable in plasma and the additional length associated with beam transport and driver–witness separation. In the high-energy limit, the relative length reduction can be written as:

$$\frac{\Delta L}{L_{\mathrm{tot}}^{\mathrm{RF}}} \to \left(1 - \frac{1}{T}\right)\left(1 - \frac{G_X}{G_p}\right) - L_{0,\mathrm{sep}}\, G_X,$$

where G_X and G_p are the effective RF and plasma gradients, respectively, and $L_{0,\mathrm{sep}}$ (2.3 m/GeV in our case) parameterizes the linear energy scaling of the separator length. (The separator length is assumed to scale linearly with beam energy corresponding to a field-limited chicane providing comparable transverse separation at higher energies. Alternative scalings are possible with redesigned optics and/or higher-field magnets). A net footprint reduction is therefore preserved as long as the separator contribution remains smaller than the effective gradient advantage of the plasma stage. Under realistic assumptions for X-band and plasma gradients, this condition is satisfied over the energy range relevant for EuPRAXIA@SPARC_LAB and its future upgrades, leading to total length reductions of order 20% at $\sim$ 1 GeV and increasing to $\sim$ 30% in the multi-GeV regime.

From an energy-efficiency perspective, modern X-band RF technology already achieves RF-to-beam efficiencies in the range of 45–60% when operated with optimized beam loading. Consequently, the sustainability advantage of plasma acceleration does not arise from a fundamentally higher RF-to-beam conversion efficiency, but rather from the substantial reduction in the amount of RF acceleration required to reach a given beam energy. The overall wall-plug-to-beam efficiency of a plasma-based system therefore depends critically on the efficiency of energy transfer from the driver to the witness beam in the plasma stage [6].

Overall, the plasma accelerator module provides a robust and scalable contribution to facility sustainability by reducing installed RF infrastructure, electrical power consumption, cooling demand, and associated embodied and operational CO_2 emissions, while preserving a clear upgrade path toward higher beam energies. These benefits are structural, rooted in the fundamental scaling of gradients and transformer ratio, and become increasingly significant in the multi-GeV regime.

21.11 Conclusions

The EuPRAXIA@SPARC_LAB project has integrated sustainability into every stage of its design and implementation, making environmental performance a central driver of technical decisions. The facility's energy demand is mitigated through a combination of high-efficiency systems, renewable power generation, and extensive energy-recovery solutions. The adoption of the EU DNSH and Italian CAM frameworks ensures full regulatory compliance for all construction and procurement activities. Reuse of excavation materials, employment of recycled and low-carbon construction products, the use of low-GWP refrigerants, and the elimination of SF6 in power systems further reduce the environmental footprint. Advanced HVAC and process-cooling technologies, together with smart control architectures, enable substantial energy savings and operational flexibility. The forthcoming LCA will quantify the overall carbon and material footprint, providing a benchmark for continuous improvement and transparent reporting. LCA of all the facility is at early study phase and will be performed in the next year. Recommendation collected in the "Sustainability Assessment of Future Accelerators" [7] will be adopted as baseline for the LCA approach.

In conclusion the sustainability objectives of EuPRAXIA@SPARC_LAB have been met by integrating energy-efficient technologies, renewable power generation, and circular-economy design principles consistent with INFN and EU environmental directives."

Bibliography

[1] INFN. *Environmental Report 2023*. URL: https://www.infn.it/wp-content/uploads/2025/01/Environmental_Report_23.pdf (visited on 10/02/2025).

[2] The European Parliament and the Council of the European Union. "Regulation (EU) 2020/852 of the European Parliament and of the Council of 18 June 2020 on the establishment of a framework to facilitate sustainable investment, and amending Regulation (EU) 2019/2088". In: *Official Journal of the European Union* L 198.63 (2020), p. 13. URL: https://eur-lex.europa.eu/legal-content/EN/TXT/PDF/?uri=CELEX:32020R0852.

[3] Il Ministro della transizione ecologica. "Criteri ambientali minimi per l'affidamento del servizio di progettazione di interventi edilizi, per l'affidamento dei lavori per interventi edilizi e per l'affidamento congiunto di progettazione e lavori per interventi edilizi". In: *Gazzetta Ufficiale della Repubblica Italiana* 183 (2022). URL: https://www.gazzettaufficiale.it/eli/id/2022/08/06/22A04307/sg.

[4] N. Catalan-Lasheras et al. "JACOW: High-efficiency klystrons from a dream to a reality". In: *JACoW IPAC* 2024 (2024), FRYD1.

[5] *PACRI project*. URL: https://www.pacri.eu/ (visited on 10/02/2025).

[6] C. A. Lindstrøm et al. "Beam-driven plasma-wakefield acceleration". In: *arXiv preprint arXiv:2504.05558* (2025).

[7] C. Bloise et al. "Sustainability Assessment of Future Accelerators". In: *arXiv preprint arXiv:2504.01235* (2025).

22. Project Cost, Timeline and Management Structure

22.1 Introduction

The goal of this chapter is to establish the cost baseline, implementation timeline, and management framework that will guide the realization of the EuPRAXIA@SPARC_LAB facility. These elements define the financial and organizational structure required to achieve operational readiness by 2031, in line with the ESFRI Landmark objectives and the national funding commitments supporting the project. In this chapter the main Project Management Framework that will guide the implementation phase will be presented. The overall Project Management structure including the monitoring & control tools via Earned Value Management technique will be part of a separate document namely the Project Management Plan. A short overview of the main strategic goals of the Project Management activities, tools and processes will be also described. In particular will be presented: Work Breakdown Structure, Project Breakdown Structure, Cost Baseline and High level strategic planning, risk assessment and management. The aim is to provide a comprehensive baseline that covers all the relevant aspect of the project.

22.2 Project Management Methodology

The methodology used for the implementation of EuPRAXIA project is based on a clear definition of the baseline in terms of:

- Scope;
- Cost;
- Schedule.

These will be complemented with a well defined management structure and procedures which will include:

- Change management;
- System engineering;
- EVM - Earned Value Management for project monitoring & control;
- WBS - Work Breakdown structure;
- OBS - Organization Breakdown Structure.

The methodology adopted for this project is based on a traditional waterfall approach, which has been deemed appropriate given the anticipated predictability of the implementation phase. It is important to emphasize, however, that the cost and schedule baselines presented at this stage should be regarded as high-level estimates. These initial figures serve as a strategic reference framework and the corresponding high level milestones are check-points used for monitoring and control. As the project progresses and more information becomes available, a detailed schedule will be developed and refined in alignment with the project's natural evolution. This detailed schedule will be subject to regular updates to accurately reflect the current status and any adjustments arising from ongoing developments and insights gained during execution.

22.3 Cost Baseline and cost assessment methodology

The methodology to consolidate the cost assessment starts with the beam physics layout provided by beam dynamics simulations. Additional systems and subsystems are then developed as example RF power sources, Diagnostics, Vacuum, Controls. A functional and a mechanical layout is then composed as described in Chapter 20. The functional layout which refers to the system engineering is then the baseline for the Project Breakdown Structure database. Each item is recorded with a proper naming convention plus a set of other relevant technical information. In addition estimated cost and maturity level complete the attributes for each item. The subsystem cost are then aggregated together with their error assessment in different ways. Cost assessment is based on bottom up approach using the Project Breakdown structure as described in the System Engineering Chapter 20 and it is therefore PBS and WBS based following the workflow described in Fig. 22.1.

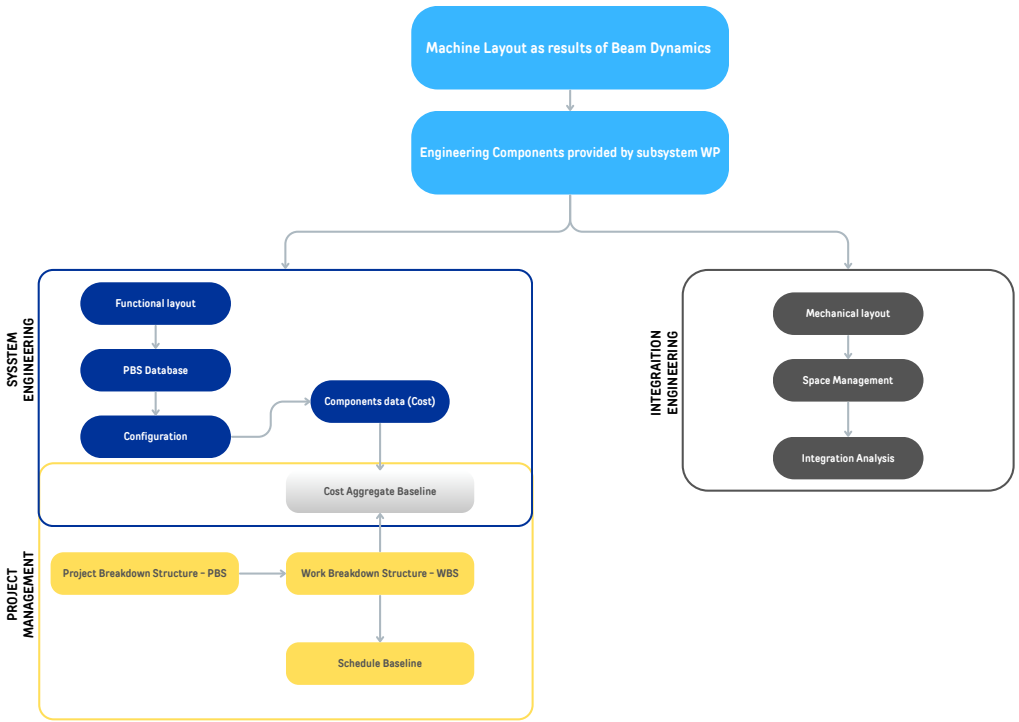

Figure 22.1: Cost and schedule baseline methodology

The cost coming from the PBS are then aggregated in two different way:

- Aggregation per functional area.
- Aggregation per work package (System).

They are then summarized in the Tabs. 22.2 and 22.3 note that the amount presented is the expected case. Some contingencies are considered (in cost or, in case of repetitive items, in the total number) with an average of 5%. As already mentioned the ARIA Beamline is included in the cost baseline as result of an additional funding line (10 M€) from local government (Regione Lazio). It is important to highlight that the additional funding source (co-funding 10 M€ Reg. Lazio and 10 M€ INFN) is meant to add a significant value to the whole infrastructure therefore it must be used for the additional FEL beamline.

The error in the estimation follows AACE (*Association for the Advancement of Cost Engineering, guidelines - International Recommended Practice No. 18R-97*) recommendation, based on the maturity of the design for each item an estimated error has been assessed.

Table 22.1: Methodology for cost accuracy assessment

Class	**Accuracy (%)**	**Note**
1	-5%/+5%	Quotation from vendor from identical items recently purchased
2	-5%/+10%	Comparison with similar items recently purchased
3	-10% / +20%	Cost incurred in similar activities in the past
4	-10% / +25%	Expert judgment

Considering the current maturity level the LINAC is essentially in class 1, while the FEL and Beamline are in class 2. Additional elements are considered in class 3 but they have a marginal impact on the overall cost (e.g. beam dumps etc..).

The total **BAC - Budget At Completion** is estimated in 116 M€. This has to be considered as the expected baseline and the ARIA beamline has to be summed up. In Tab. 22.2 the cost distribution per functional area is summarized, data are visualized in Fig. 22.2.

Table 22.2: Aggregated cost per functional area (values in k€)

Functional Area	**Estimated Cost (k€)**
Injector	11,000
Low Energy Line	9,600
Bunch Compressor	1,200
High Energy Line	9,800
Plasma Module	2,300
AQUA FEL	12,000
AQUA Beamlines	7,100
General Elements	4,000
Building Construction	47,935
Building Ancillary costs	4,765
Hi-Tech Utilities	6,000
TOTAL	**115,700**

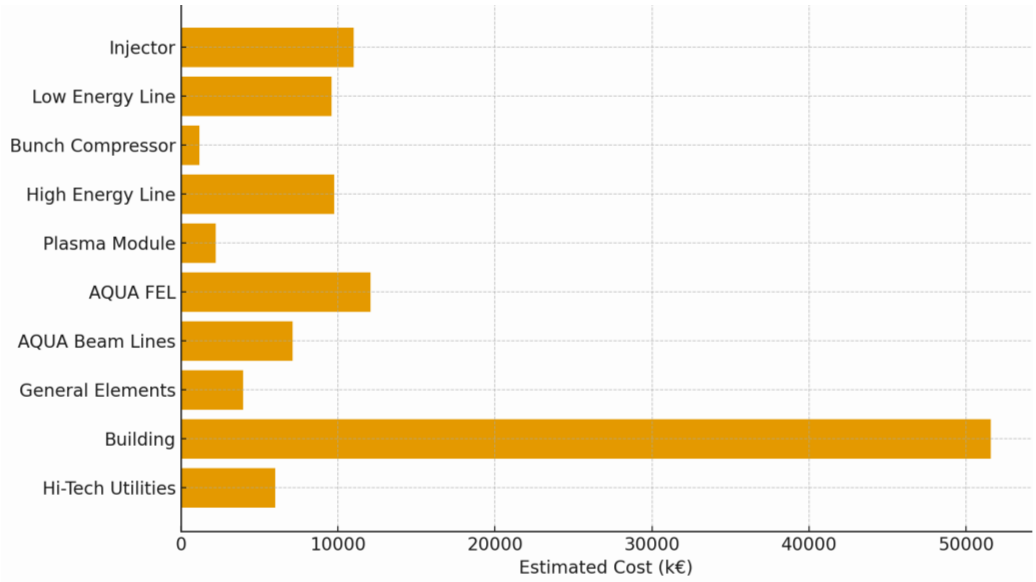

Figure 22.2: Cost distribution per functional area.

The ARIA beam line has not been considered in this assessment, but it is part of a separate study, due to the fact that this FEL Line has been recently funded and it is not part of the current technical design report.

The expected cost distribution per functional is presented in Tab. 22.3 together with the expected accuracy, providing thus an interval of the cost estimated (best and worse case). Data are visualized in Fig. 22.3.

It has to be pointed out that the cost of the building is coming from the executive design in which a detailed computation of the expected costs have been developed. It is expected a reduction in the tender phase, but the final cost of the building at this stage is not predictable, in any case it will not exceed the amount considered in this document. It also to be pointed out that in the building cost estimation a substantial amount are allocated as contingencies and reserves that might not be fully deployed during the building execution. The expected BAC (*Budget at Completion*) has been computed through a Monte Carlo analysis considering a triangular distribution of the expected items cost. The mean value is around 116 M€. The project cost distribution is sketched in Fig.22.4 and the corresponding cumulative probability distribution in Fig.22.5.

Table 22.3: Estimated costs by system with expected values, margins of error, and projected best/worst-case scenarios.

SYSTEM	Exp. (k€)	Error	Best Case (k€)	Worst Case (k€)
A - Acceleration	5,000	-5% – +5%	4,750	5,250
B - Beam Instrumentation	3,440	-5% – +5%	3,268	3,612
I - Circuits	2,500	-5% – +10%	2,375	2,750
M - Magnets	5,700	-5% – +10%	5,415	6,270
R - RF Power Source	15,500	-10% – +10%	14,725	17,050
T - Target	260	-10% – +10%	234	286
U - Undulators	10,500	-10% – +10%	9,450	11,550
V - Vacuum	4,000	-5% – +5%	3,800	4,200
W - Laser & Optical System	3,200	-5% – +5%	3,040	3,360
X - Experimental Users	2,900	-10% – +25%	2,610	3,625
General Elements	4,000	-5% – +5%	3,600	4,800
Building	47,935	-10% – +0%	43,141	47,935
Building Ancillary costs	4,765	0% – +0%	4,765	4,765
Hi-Tech Utilities	6,000	-10% – +20%	5,400	7,200
TOTAL COST	115,700	-	106,600	122,700

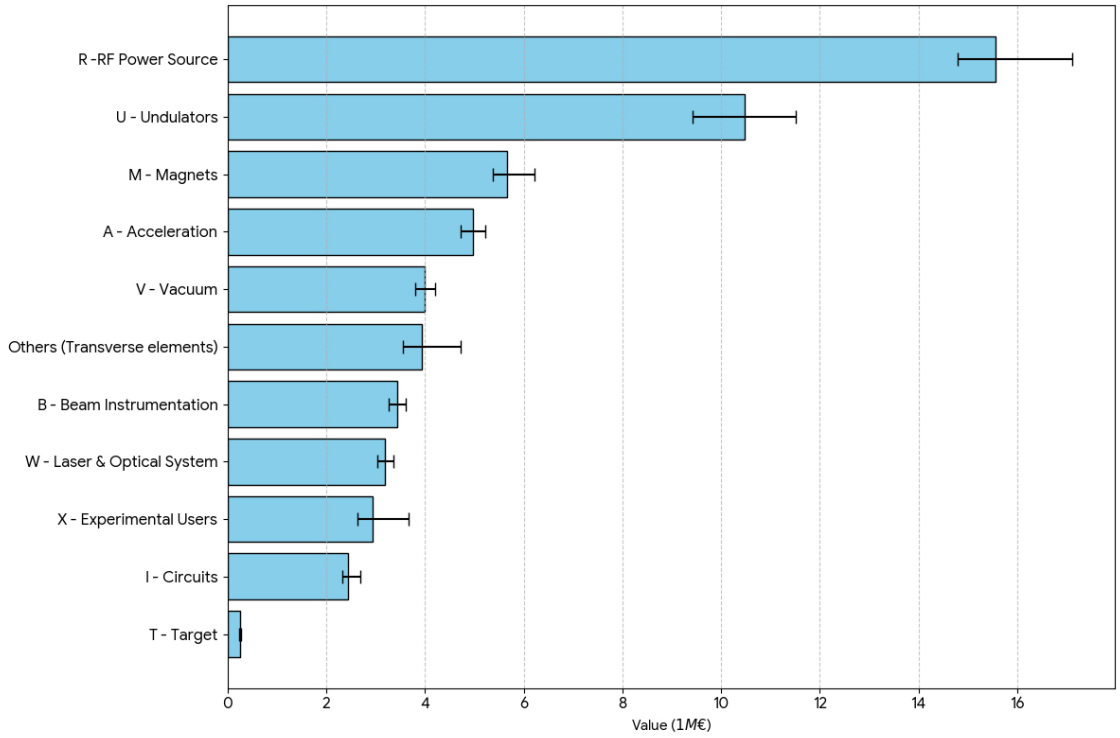

Figure 22.3: Cost distribution per subsystem.

The Monte Carlo cost analysis provides a quantitative assessment of the uncertainty associated with the project cost estimate. By propagating the individual cost ranges of all major cost through a large number of simulations (400,000), the analysis generates a probabilistic distribution of the

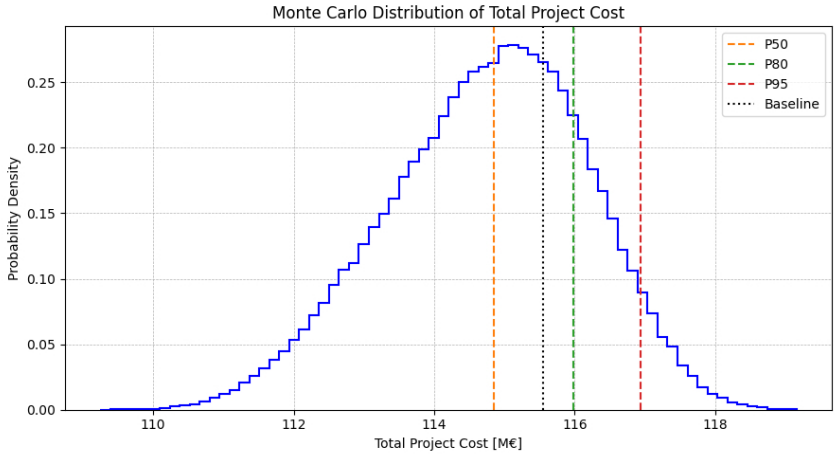

Figure 22.4: Cost distribution

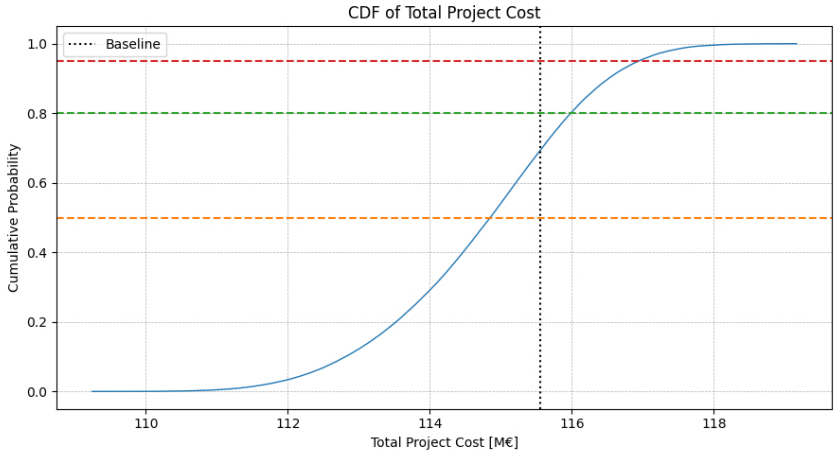

Figure 22.5: Cumulative Distribution Function of the project cost.

total project cost rather than a single deterministic value. This approach allows the identification of confidence levels (e.g. P50, P80, P90) and therefore supports an informed evaluation of cost risk and the definition of appropriate contingency margins. In particular, it highlights the likelihood of cost overruns, the expected variability of the total cost, and the main contributors to overall uncertainty, thus offering a robust basis for risk-aware budgeting and decision-making. In particular the probability of over cost with respect to the baseline is 30% which has to be fully considered in the procurement plan. The current budget allocation is of 108 M€ which part of them has been already used in the R&D phase (9 M€). It is evident that there is a budget gap of about 16M€ that must be addressed. The following strategy will be adopted:

- Priority to the more mature items;
- Priority to the minimum configuration scenario needed;
- Make or buy scenario;
- Additional funding line to support the activities;
- Phasing approach.

The first (and largest) procurement will be the building construction for which the full budget will be allocated. The final offer will be expected to be lower, the difference will be used as additional resources for the machine implementation. Additional funding lines might be in synergy

with the machine implementation providing a more structured and elaborated financial framework. For the machine implementation priority will be given to the RF power stations, Injector, ARIA Beamline (which is funded by a different funding line) and the X-band accelerating sections. The above mentioned initiative will be fully analyzed and structured in the project management plan.

22.3.1 Time Line

The overall project timeline is primarily shaped by the strategic commitments set forth by the European Strategy Forum on Research Infrastructures (ESFRI). In particular, these commitments mandate that EuPRAXIA must achieve the status of a "Landmark" on the ESFRI Roadmap by the year 2031, thereby formally establishing its role as a distributed European research infrastructure of reference. To meet this objective, it is essential that by 2031 a minimum level of operational readiness is demonstrably achieved. This implies that, at the very least, a pilot user facility should be operational, or that the infrastructure should have reached an advanced stage of commissioning, clearly validating its readiness to serve the scientific community. A second key milestone, equally critical to the timely execution of the implementation phase, concerns the availability of the dedicated building infrastructure. According to the current project schedule, the building must be fully completed and ready for use by mid-2029. This deadline is vital, as it directly influences the subsequent installation, integration, and commissioning of the various technical components required to bring EuPRAXIA to operational status in alignment with the 2031 ESFRI target. The different schedules at high level schedule for the machine implementation phase, general infrastructure implementation and building construction are presented in Fig. 22.6.

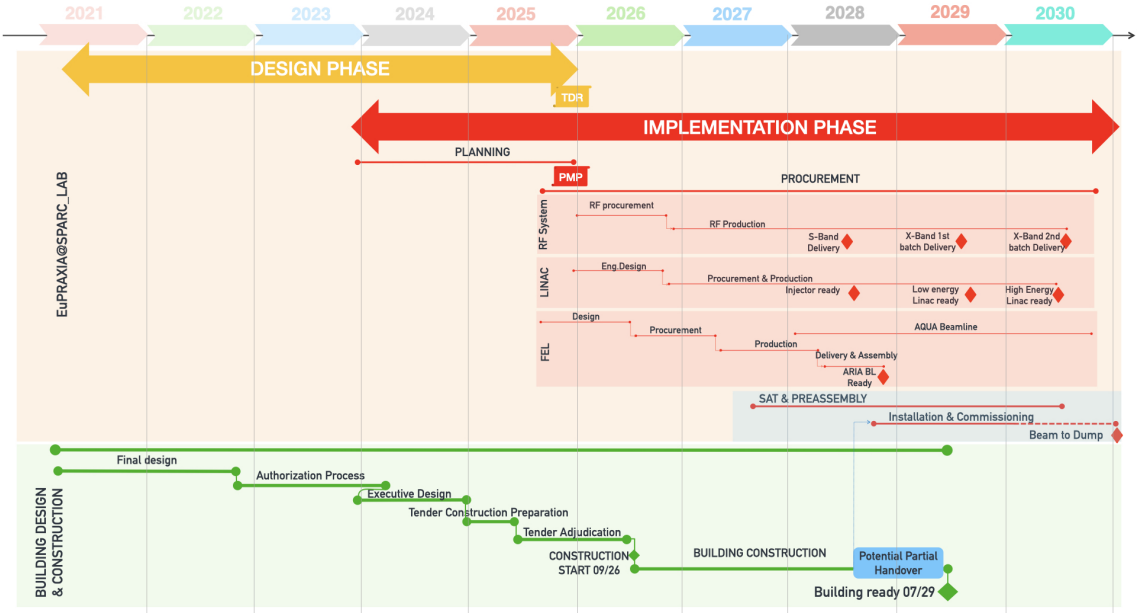

Figure 22.6: High Level time line - Machine & Building

A comprehensive and detailed breakdown schedule is presently under development and will be formally included as a key component of the *Project Management Plan*. Within this plan, all relevant action items and tasks to be performed will be clearly identified and structured in order to provide full transparency and traceability throughout the implementation process. The scheduling effort will be anchored to a series of well-defined and significant milestones, which will serve as reference points to closely monitor and evaluate progress. These milestones will ensure the proper tracking of all critical phases, including the engineering design activities, the procurement

process, and the subsequent integration of each subsystem, thereby providing a robust framework for effective project oversight and timely delivery.

22.3.2 Work Breakdown Structure, resource associated and correlation with Lab structure

The Work Breakdown Structure (hereafter WBS) is the main tool for organizing the work required to perform the implementation phase. The work-packages resemble the structure of the TDR with some minor deviation for easiness purposes. Two main families of workpackages are identified. The Functional Areas workpackages also referred to integration work-packages and the system workpackages which will deal with the design, realization and test of each system and sub-system. The overall structure is presented in Tab. 22.4. In the management plan a detailed resource loaded WBS will be elaborated and in addition the missing resources will be highlighted.

Table 22.4: Main structure of the Work Breakdown Structure

WP Id	WP Name
WP.0	Project Management & System Engineering
WP.1	Beam Physics
WP.2	Injector Modules
WP.3	Linac Modules
WP.4	Plasma Modules
WP.5	FEL Modules
WP.6	Photon Beam lines & users
WP.7	RF systems (LLRF, Timing & Synch)
WP.8	Accelerating Sections
WP.9	Diagnostics
WP.10	Laser
WP.11	Control System
WP.12	Vacuum System
WP.13	Magnets and Power supplies
WP.14	Civil infrastructures
WP.15	Radioprotection
WP.16	Mech. Engineering and Integration

Each work package is composed of personnel drawn primarily from the laboratory's internal functional units, known as *Servizi*, with the majority of contributors belonging to the Accelerator Division and the Technical Division. These divisions represent the core technical competencies required for the successful execution of the work plan. While the present overview focuses on these primary contributors, it is important to note that other divisions within the laboratory—such as Administration, Safety, and General Services—will also provide support and resources as necessary throughout the course of the project, even though their contributions are not explicitly detailed in this breakdown. The resource allocation estimates have been developed using a conservative approach, aiming to ensure both feasibility and sustainability over the duration of the project. In particular, a balanced distribution of effort between the two key personnel categories *Technologists* and *Technicians* has been pursued, reflecting a realistic projection of the technical manpower available and required. A central assumption underpinning this resource plan is that a significant portion of the required human resources is already available in-house, within the existing workforce

of the laboratory. In cases where specialized expertise or additional personnel are found to be necessary, these needs will be addressed through consultation and coordination with INFN central management, which will support recruitment or reallocation strategies as appropriate. It is also essential to underscore that the current estimation does not account for the substantial contributions expected from external institutions, including other INFN laboratories (e.g., INFN-MI), universities, and collaborating research organizations. These partners are anticipated to provide critical expertise and manpower across multiple areas of the project, and their involvement will be integrated into future planning documents as the implementation phase progresses. At this stage around **70 FTE - 80 FTE** are expected to be needed for the implementation of the project adn to comply with the aggressive and successfull-oriented project plan. This will be assessed during the course of the implementation phase. It is also worth highlighting that the *Project Management Office* of INFN-LNF will take care of the actual allocation and will monitor deviation with respect the given baseline also considering other activities in which the Lab is involved. This will provide a strategic view of the overall allocation and support the management for informed decision-making process.

22.3.3 Correlation with the European context

This section explores the inter dependencies and implications of the cost assessment processes adopted within the EuPRAXIA project, focusing on both methodological aspects and substantive content in the broader context of European research infrastructure development. Particular emphasis is placed on the role that European-level initiatives—especially the ESFRI Roadmap—have played in shaping EuPRAXIA's strategic trajectory.

The inclusion of EuPRAXIA in the 2021 ESFRI Roadmap significantly enhanced the project's visibility at both national and international levels. This recognition not only underscored the scientific and technological relevance of the initiative but also substantially increased its attractiveness to potential funding bodies. As a result, the inclusion acted as a catalyst, facilitating the mobilisation of resources and political support necessary for its advancement.

Within this framework, the EuPRAXIA Preparatory Phase Project, supported by a Horizon Europe grant, has been instrumental in guiding the initiative from its conceptual stage toward a level of maturity appropriate for launching the implementation phase. According to ESFRI guidelines, the life cycle of a research infrastructure typically progresses through distinct and consecutive phases: concept development, design, preparatory, implementation, and operational. This idealized progression is illustrated in Figure 22.7. However, it is important to note that in real-world projects, these phases frequently overlap. The EuPRAXIA initiative exemplifies this dynamic. While the Preparatory Phase is still ongoing, the Implementation Phase has already commenced—a situation largely driven by the availability of funding and by the nature of the funding model adopted, which heavily depends on national contributions during the implementation stage.

At the core of EuPRAXIA's vision within the ESFRI framework is the ambition to establish a distributed European research infrastructure capable of hosting cutting-edge user facilities based on advanced plasma acceleration technology. This ambition is being addressed through a coordinated sequence of projects: the current Preparatory Phase Project and the upcoming Early Implementation Phase Project. Both initiatives are designed to systematically resolve technical, organizational, and financial challenges associated with the realization of a new European Research Infrastructure. A key priority of these projects is the comprehensive evaluation of investment and operational costs, the development of a viable and sustainable funding model, and the formulation of service-cost structures. These are all critical to ensuring the long-term feasibility and success of EuPRAXIA. The infrastructure is structured around two major implementation pillars: the Beam-Driven Pillar, located at the INFN-LNF site, and the Laser-Driven Pillar, based at ELI-ERIC. In this context, EuPRAXIA@SPARC_LAB represents Phase 1 of the Beam-Driven Pillar's implementation. The cost estimation process for this phase—including the methodology employed and the resulting

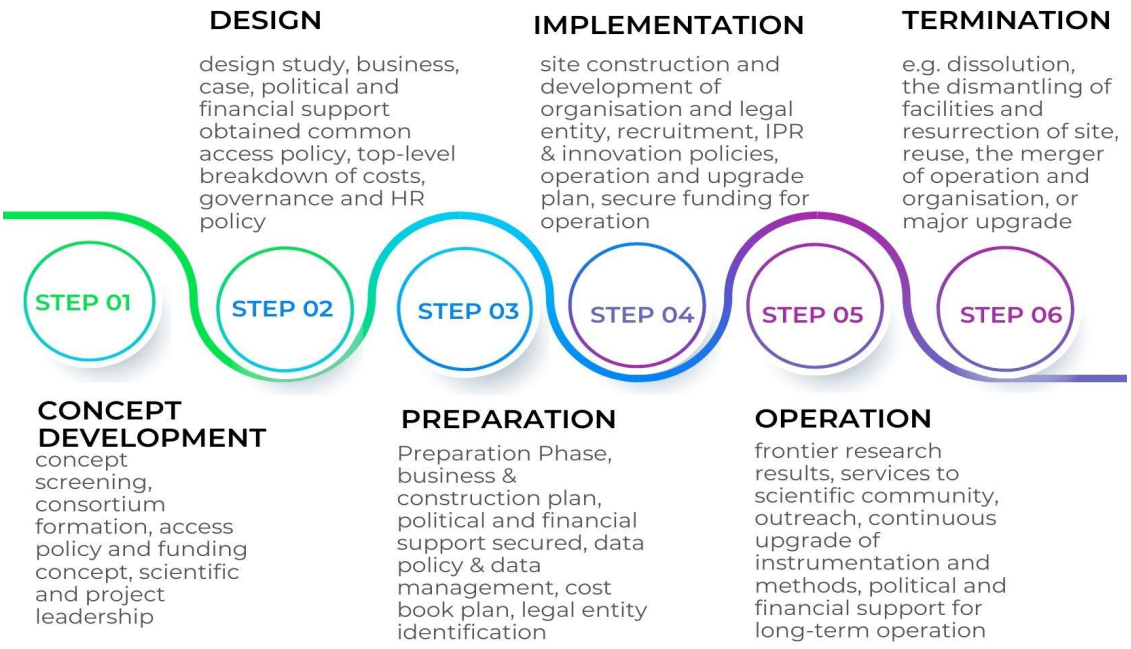

Figure 22.7: RI Lifecycle approach in the ESFRI Context

assessment—holds strategic importance not only for the preparatory work but also as a foundation for subsequent stages of development. It provides critical input for refining budget forecasts, risk assessments, and investment planning. Furthermore, the successful execution of EuPRAXIA requires the adoption of a robust and harmonized project management framework, aligned with best practices in large-scale European research collaborations. Such an approach must account for the complex, distributed nature of the EuPRAXIA consortium and ensure coherence across institutional, national, and international levels.

In summary, the cost assessment exercise plays a dual role: it is a technical requirement for financial planning and resource allocation, but it is also a strategic tool for ensuring the project's alignment with European research policy objectives, financial sustainability, and long-term operational success.

22.4 Conclusions

The analyses presented in this chapter confirm that the project cost baseline and implementation schedule are coherent with the strategic objectives of EuPRAXIA@SPARC_LAB. Despite the limited uncertainties related to procurement and inflation, the overall financial and temporal framework remains robust and sufficient to ensure the successful completion of the facility by 2031. The proposed management methodology, based on Earned Value Management and WBS control, provides the necessary tools to track deviations and maintain consistency with the project's technical scope.

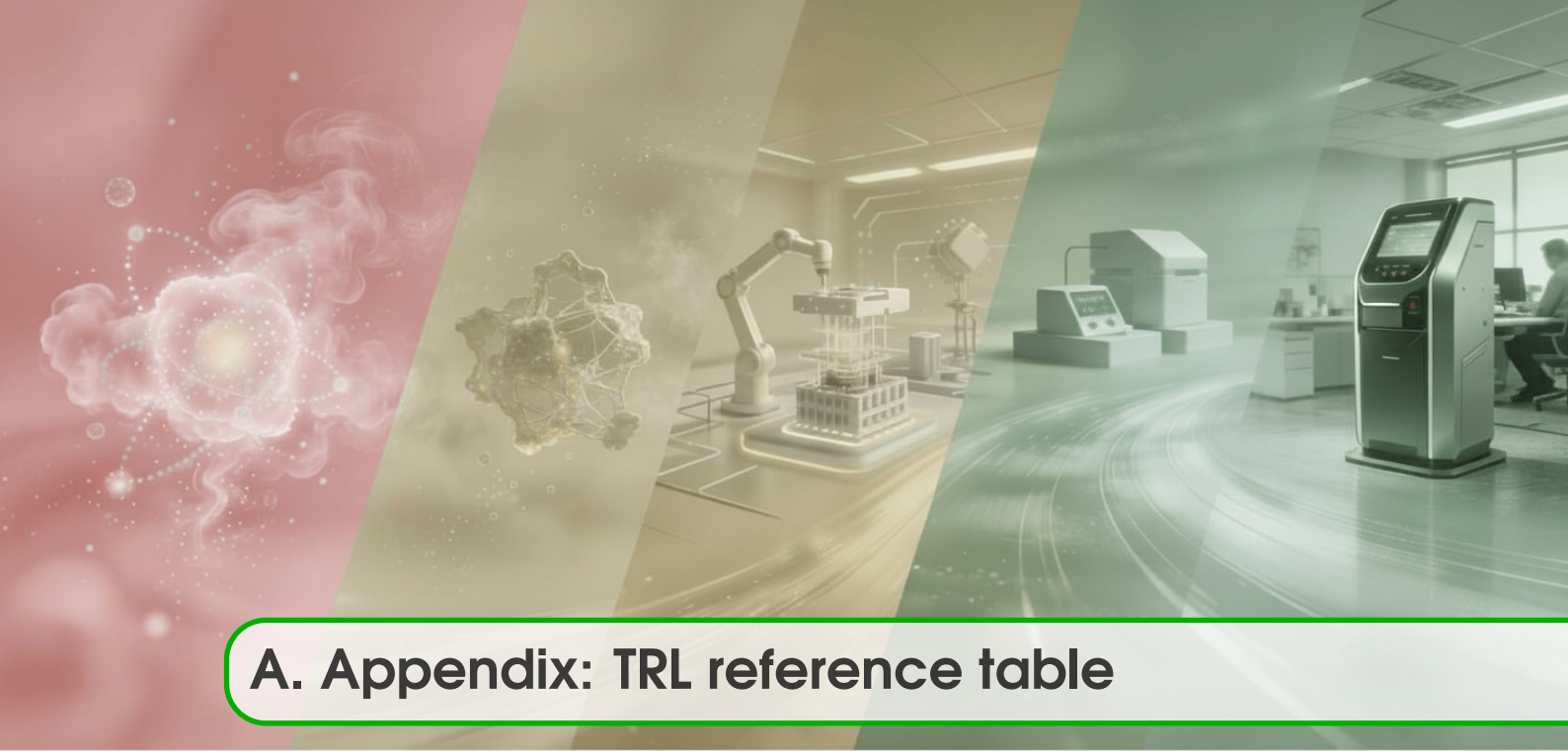

A. Appendix: TRL reference table

The Technology Readiness Level tables reported in this TDR follow those references for the TRL values:

Sub - systems	TRL	Comments
TRL 9	9	Actual system proven in operational environment - The technology is fully commercialized and operational in its intended setting.
TRL 8	8	System complete and qualified - The technology is proven to work in its final form and under expected conditions.
TRL 7	7	System prototype demonstration in operational environment - A working prototype is demonstrated in a real operational setting.
TRL 6	6	Technology demonstrated in relevant environment - A prototype system is tested in an environment similar to the operational one.
TRL 5	5	Technology validated in relevant environment - The technology is tested in a simulated or relevant environment.
TRL 4	4	Technology validated in lab - Basic technological components are integrated to establish that they work together.
TRL 3	3	Experimental proof of concept - Active R&D is initiated, including analytical and laboratory studies to validate predictions.
TRL 2	2	Technology concept formulated - The basic principles are explored and practical applications are identified.
TRL 1	1	Basic principles observed - Scientific research begins to be translated into applied research and development (R&D).

Table A.1: Reference TRL description